R-08-78

Hydrogeological conceptualisation and parameterisation

Site descriptive modelling SDM-Site Laxemar

Ingvar Rhén, Torbjörn Forsmark
Sweco Environment AB

Lee Hartley, Peter Jackson, David Roberts, Dave Swan
Serco Assurance

Björn Gylling, Kemakta Konsult

December 2008

Svensk Kärnbränslehantering AB
Swedish Nuclear Fuel
and Waste Management Co

Box 250, SE-101 24 Stockholm
Phone +46 8 459 84 00

ISSN 1402-3091
SKB Rapport R-08-78

Hydrogeological conceptualisation and parameterisation

Site descriptive modelling SDM-Site Laxemar

Ingvar Rhén, Torbjörn Forsmark
Sweco Environment AB

Lee Hartley, Peter Jackson, David Roberts, Dave Swan
Serco Assurance

Björn Gylling, Kemakta Konsult

December 2008

Keywords: Laxemar, Hydrogeology, Deformation zone, Fracture domain, Hydraulic domain, Hydraulic properties, Hydrogeological DFN.

Summary

The Swedish Nuclear Fuel and Waste Management Company (SKB) has conducted site investigations at two different locations, the Forsmark and Laxemar-Simpevarp areas, with the objective of siting a final repository for spent nuclear fuel according to the KBS-3 concept. Site characterisation should provide all data required for an integrated evaluation of the suitability of the investigated site and an important component in the characterisation work is the development of a hydrogeological model. The hydrogeological model is used by repository engineering to design the underground facility and to develop a repository layout adapted to the site. It also provides input to the safety assessment. Another important use of the hydrogeological model is in the environmental impact assessment.

The current report (R-08-78) is a level III report that describes the analysis of the primary data and the parameterisation of the hydrogeological DFN model and associated hydraulic rock domains (HRD) and deterministic deformation zones (HCD). In a second level III report the hydrogeological conceptual model, the regional scale numerical groundwater flow modelling is presented (R-08-91). In a concluding level II report (R-08-92) the analysis and results of the two level III reports are summarised.

Single-hole tests for main hydraulic characterisation

The hydraulic parameterisation of the deformation zones and fracture domains forming the base for the Hydraulic Conductor Domains (HCD) and Hydraulic Rock Domains (HRD) models (the rock between the HCDs) is based on single-hole tests in boreholes. Difference flow logging pumping tests (PFL) and double-packer injection tests (PSS) were used in the deep, cored boreholes, whereas pumping tests in open holes (HTHB) were performed in the shallow percussion-drilled boreholes. The PFL and PSS test methods have different advantages and disadvantages. For this reason, the two methods were both run in several cored boreholes (PFL-tests in 44 core holes, PSS; 100/20/5 m test scales in 23/22/13 core holes respectively) , in order to enable quantification of the consequences for the site characterisation and subsequent hydrogeological discrete fracture network modelling and groundwater flow modelling.

In total the HRDs are informed by 3,412 observations of flowing features (with transmissivity $<$c. $1 \cdot 10^{-9}$ m^2/s), 3,692 PFL-s evaluated tests with a test scale of 5 m, and 898/ 775/ 304 evaluated PSS tests of test scales 5 m/ 20 m/ 100 m section length, respectively, collected in 46 cored boreholes (although not all test types and test scales were employed in all boreholes). Some 304 tests with a test scale of 100 m also include data from tests in percussion boreholes made with HTHB equipment.

The total transmissivity of HCDs tested in cored boreholes tends to decrease with depth, tends to increase with zone size and is also dependent on the orientation of the zones. For the zone orientation (strike) groupings; E-W, NW-SE, N-S, NE-SW, as defined by Geology, the E-W group is slightly more conductive (less than an order of magnitude) than the others, based on data from the regional model volume. Data shows that there are significant heterogeneity within HCDs as well as in identified Minor Deformations Zones (MDZ), the latter modelled as part of the hydrogeological DFN of the HRDs.

The depth dependency of the hydraulic conductivity in the HRDs and the hydraulic conductivity of the HCDs is found to be similar. Using test results obtained at test scale 100 m, it is noted that the hydraulic conductivity within a HCD is c. 10 times higher compared to the rock in HRDs.

The fracture intensities for all fractures characterised in the core mapping, and for the mapped by Geology as being open fractures show little depth dependence. However, the intensity of flowing fractures detected by PFL-f, shows a significant decrease in fracture intensity with depth for all types of rock subdivision.

Hydrogeological DFN

The hydrogeological DFN model is based on four defined fracture sets, named (after mean pole direction): WNW, ENE and N-S striking sub-vertical sets and a sub-horizontal set SH. The model parameters are also defined for four depth intervals:

- down to –150 masl,
- –150 masl to –400 masl,
- –400 masl to –650 masl,
- below –650 masl.

and four hydraulic rock domains (HRDs):

- HRD_EW007 (corresponding to Fracture Domain FSM_EW007),
- HRD_N (corresponding to FSM_N),
- HRD_W (corresponding to FSM_W),
- HRD_C (corresponding to an amalgam of FSM_C, FSM_NE005 and FSM_S).

Three alternative relationships between fracture transmissivity and fracture size were considered; a completely correlated model, a semi-correlated model, and an uncorrelated model. Results indicate that the uncorrelated model is a less likely model compared to the two others and the semi-correlated is considered more hydrogeologically plausible compared to the correlated model.

The hydrogeological DFN has also been used to calculate block model directional and effective hydraulic conductivities at support scales of 5, 20 and 100 m for most combinations of HRD and depth zone. The results show a prominent maximum hydraulic conductivity oriented about 80–140 degrees for HRD_C, i.e. WNW. This orientation coincides with the current orientation of maximum horizontal stress. This orientation is distinct on all scales, but especially for the 100 m scale. It was demonstrated that the distribution of open fracture sizes derived in the hydrogeologcial DFN is consistently a sub-set of all the distribution of all fractures, as modelled by the geological DFN (which was derived independently) on all scales and at all depths.

Contents

1 Introduction

The Swedish Nuclear Fuel and Waste Management Company (SKB) is undertaking site characterisation at two different locations, the Forsmark and Laxemar-Simpevarp areas, with the objective of siting a geological repository for spent nuclear fuel. The investigations are conducted in campaigns punctuated by data freezes. After each data freeze, the site data are analysed and site descriptive modelling work is carried out. A site descriptive model (SDM) is an integrated model for geology, rock mechanics, thermal properties, hydrogeology, hydrogeochemistry and transport properties, and a description of the surface system.

So far, three full versions of a site descriptive model have been completed, Simpevarp 1.1 and 1.2 and Laxemar 1.2. Version 0 /SKB 2002/ established the state of knowledge prior to the site investigation. Simpevarp version 1.1 /SKB 2004/, which essentially was a training exercise, was completed during 2004 and Simpevarp version 1.2 during 2005 /SKB 2005a/. The latter formed the basis for a preliminary safety evaluation (PSE) of the Simpevarp subarea /SKB 2005b/ and completed the initial site investigation stage (ISI) in the Simpevarp subarea. A preliminary repository layout (D1) for the Simpevarp subarea was presented in 2006 /SKB 2006a/. Laxemar version 1.2 was presented 2006 /SKB 2006b/ and this preliminary site descriptive model completed the initial site investigation stage (ISI). It formed the basis for a PSE of the Laxemar subarea /SKB 2006c/, a preliminary repository layout /SKB 2006d/, and the first evaluation of the long-term safety of this layout for KBS-3 repository layout in the context of the SR-Can project /SKB 2006e/.

After the completion of the initial site investigations of the Simpevarp and Laxemar subareas /SKB 2005a, 2006b/, an evaluation of the site data from the two subareas, results from site modelling, repository layouts and preliminary safety evaluations were carried out. Based on this evaluation, a decision was made to continue with the complete site investigation (CSI) in the central, southern and western parts of the Laxemar subarea /SKB 2007a/. Three modelling stages were initially planned for the complete site investigation work. An important component of each of these planned stages was to address and continuously try to resolve uncertainties of importance for repository engineering and safety assessment. The primary objective of the geological modelling during stage Laxemar 2.1 /SKB 2006f/, was to analyse available new data at data freeze Laxemar 2.1 (June 30, 2005) to provide feedback to ensure that adequate geological information was obtained during the complete site investigation stage at Laxemar /SKB 2006g/. However, in order to maximise the feedback to the site investigation, a successive evaluation of data that became available in the time period between June 30, 2005 and the end of March 2006 were also included in the Laxemar 2.1 modelling work. Based on an integrated analysis of all available site data, a decision was made at the turn of the year 2006–2007 to expand the focused area of the site investigation to the south to include also an additional area south of the Laxemar subarea. This decision also raised an urgent need for a complementary cored borehole to minimise the uncertainty in the final geological models in the focussed area/volume. The outcome of this drilling of the complementary borehole has been considered in the geological modelling of rock domains and deformation zones presented here. Hence, due to projected lack of critical data from southern Laxemar at the time for data freeze Laxemar 2.2 (December 31, 2006), a decision was made to allow inclusion of data from the final data freeze Laxemar 2.3 (August 31, 2007) in the concluding site-descriptive modelling work. This modelling work based on the data available at data freeze Laxemar 2.3 is referred to as modelling stage SDM-Site Laxemar.

As part of the preliminary Site Descriptive Modelling (SDM) for the Initial Site Investigation (ISI) phases at Forsmark, Simpevarp and Laxemar, a methodology was developed for constructing hydrogeological models of the crystalline bedrock at the studied sites. The methodology combined a deterministic representation of major deformation zones (DZ) with a stochastic representation of the less fractured bedrock between these zones using a Discrete Fracture Network (DFN) concept, the latter subsequently upscaled in regional scale flow models.

The geological DZ and fracture network are parameterised hydraulically using data from single-hole Posiva Flow Log (PFL) pumping tests and single-hole Pipe String System (PSS) injection tests, see e.g. /Pöllänen et al. 2007/ and /Enachescu et al. 2006b/. The hydrogeological descriptions of the major deformation zones and the less fractured bedrock outside/between these zones are referred to as Hydraulic Conductor Domains (HCD) and Hydraulic Rock Domains (HRD), respectively, according to SKB's systems approach to bedrock hydrogeology /Rhén et al. 2003/.

The hydraulic properties of the HCD and DFN models form the basis of constructing regional-scale Equivalent Continuum Porous Medium (ECPM) flow models, which are e.g. used to simulate the palaeohydrogeological evolution over the last 10,000 years (Holocene). This modelling is conducted as a coupled process between variable density groundwater flow and the hydrodynamic transport of several reference waters, taking into account the process of rock-matrix diffusion. Results obtained from these simulations include prediction of hydrochemical constituents (e.g. major ions and environmental isotopes) for the present-day situation along boreholes, which is subsequently compared with results of groundwater samples acquired from the corresponding boreholes/borehole sections. By comparing the model predictions with measurements, the models developed can be partially calibrated to improve model parameterisation, thus improving our understanding of the principal controls of the hydrogeological system, thereby building confidence in the conceptual models developed for the studied site. As the calibration results are dependent on the conceptual models, these models should be hydrogeologically relevant and sound.

The methodology has achieved reasonable success given the restricted amounts, and types of data available at the time of models preceding the SDM-Site models. Notwithstanding, several issues of concern have surfaced following the reviews of the preliminary site descriptions of the Simpevarp and Laxemar subareas conducted internally by SKB's modelling teams /SKB 2005a, 2006b/, by SKB's external review group (SIERG) and by the SKI's international review group (INSITE) /SKI 2005/. Moreover, the safety implications of the preliminary site descriptions have been assessed in the Preliminary Safety Evaluations (PSE) /SKB 2005b, 2006c/ and in SR-Can /SKB 2006e/.

Of particular importance for the work reported here are the concerns raised regarding the uncertainties in the derivation of hydraulic properties of the deterministically modelled deformation zones and the less fractured bedrock outside/between the deterministically modelled deformation zones. These uncertainties involve, among other things:

- the understanding of deformation zone genetics and its implication for hydraulic material properties and hydrogeology,
- the spatial variation of hydraulic properties over the plane of a deformation zone,
- the support in data for dividing the less fractured bedrock between the deterministically modelled deformation zones into subvolumes of different hydrogeological DFN properties, e.g. with due consideration of possible depth dependence and anisotropy,
- the upscaling approach used for constructing regional scale ECPM flow models based on discrete feature representation, and
- the intrinsic complexity of the DFN concept, the properties of which are described in terms of probability distributions for the orientation, size, intensity, spatial distribution and transmissivity of fractures making up discrete fracture networks.

It is recognised that a main reason for uncertainties in the model version 1.2 site descriptive model (SDM) of Laxemar /SKB 2006b/ are associated with relatively few hydraulic observations compared to the large volume investigated and the high variability found in the existing data, as well as the uncertainty demonstrated by the geological (geometrical) DFN modelling derived.

For the complete site investigation (CSI) phase, the integrated use of geological, hydrogeological, hydrogeochemical and transport models has identified the need for more robust, discipline-consistent and at least 'partially validated' models to be produced by the final stage of the site descriptive modelling. As part of the solution for obtaining more robust models, an integrated view and strategy has been formulated, see Figure 1-1. This "updated strategy" is not an entirely new direction in methodology, but rather a refocusing on and clarification of the key aspects of the hydrogeological SDM, i.e.:

- assessing the current understanding of the hydrogeology at the analysed site, and
- providing the hydrogeological input descriptions needed for the end users, design, safety assessment and environmental impact assessment. These input descriptions should especially focus on properties in the potential repository volumes of the explored sites and assess the distribution of flow paths at potential repository depth.

/Follin et al. 2007a/ suggested a procedure for integrating four kinds of data in the groundwater flow (GWF) modelling of the final SDM, see Figure 1-2, as a means of approaching the issue of confirmatory testing (Step 4 in Figure 1-1).

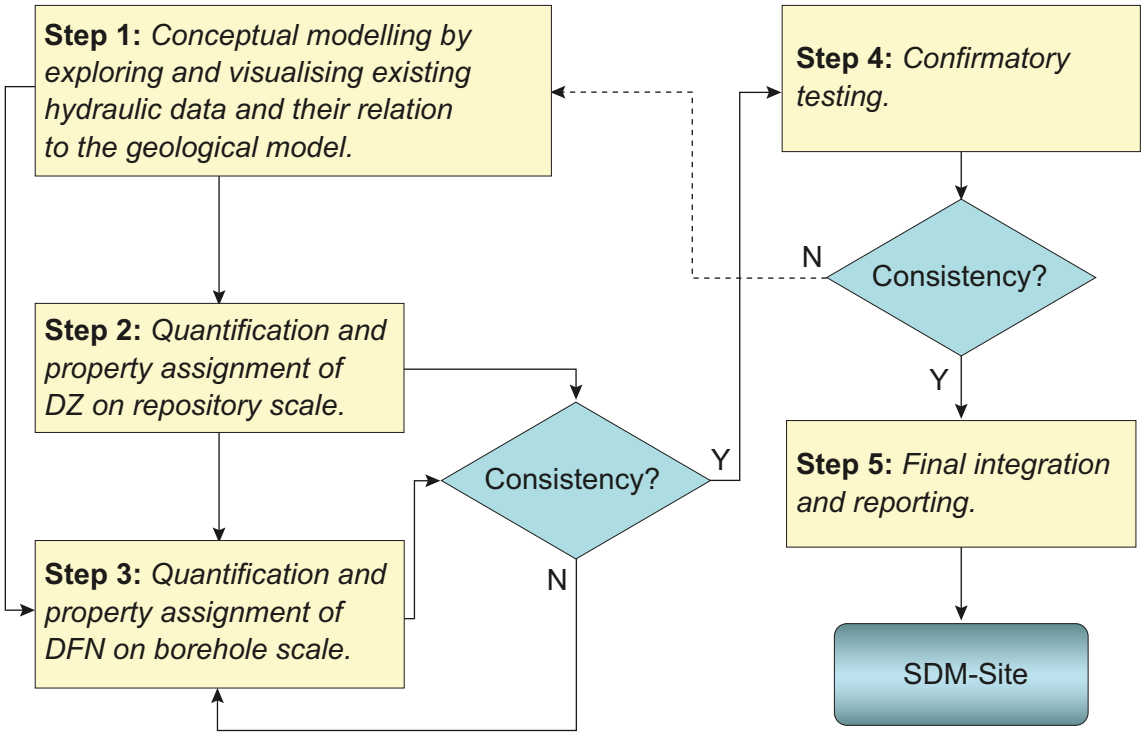

Figure 1-1. *Flow chart of the five steps suggested for the hydrogeological modelling of the complete site investigation (CSI) phase.*

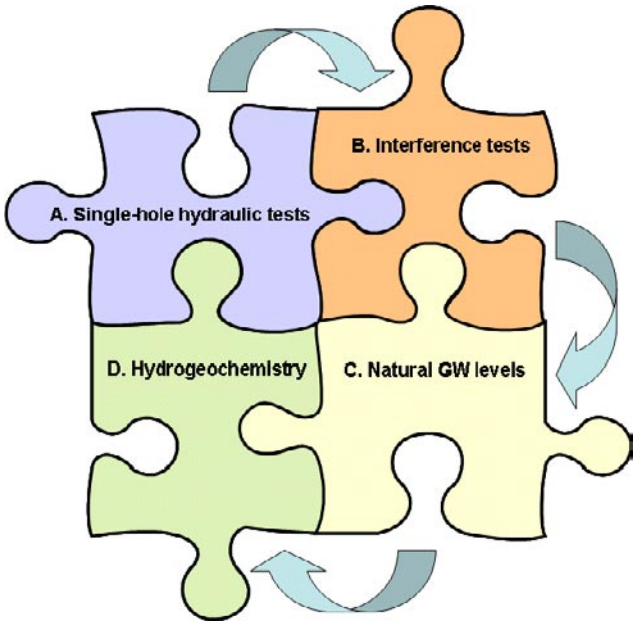

Figure 1-2. *Four kinds of data are used in the numerical groundwater flow modelling of the final SDM as a means of approaching the issue of confirmatory testing, cf. Step 4 in Figure 1-1: A) Hydraulic properties of deformation zones and discrete fracture networks as deduced from single-hole hydraulic tests (this report); B) Interference tests; C) Natural groundwater levels; D) Hydrogeochemistry. Figure from /Follin et al. 2007b/).*

At Laxemar the hydrogeological HCD and DFN models derived as part of model version 1.2 and the hydrogeological and hydrochemical information from data freeze Laxemar 2.1 were used to explore some issues raised in the reviews of Laxemar version 1.2. The aim was not a full SDM update, but rather to constitute preparatory modelling studies of regional boundary conditions /Holmén 2008/, modelling studies intended to provide insight into new aspects of the suggested procedure and the use of field data (e.g. interference tests) and the possible effects in Laxemar of the nearby underground laboratory Äspö Hard Rock Laboratory (Äspö HRL) /Hartley et al. 2007/, thereby providing premises and support for the work reported here.

It is noted that an underlying idea behind Figure 1-2 is that the same groundwater flow model is used for each type of simulation to make it transparent that a single implementation of the conceptual model can be calibrated against all four types of field observation (a is rather used for conditioning borehole near-field and B-D for confirmatory testing), although it might have been possible to improve the model performance further in relation to a particular data type by refining, e.g. the geometry or material property distribution around a particular observation borehole.

1.1 Scope and objectives

The primary objectives of the work reported here are to:

- provide the hydrogeological input descriptions of the Laxemar bedrock needed for the end users Repository Engineering, Safety Assessment and Environmental Impact Assessment, and
- provide a basis for subsequent construction of a 3D regional groundwater flow model of Laxemar and surrounding area to allow quantitative assessment and illustration of the conceptual understanding of the site. Furthermore, to build confidence in the flow model by testing it against a variety of field data, such as interference tests, palaeo-hydrogeology and near-surface hydrogeology.

The input descriptions should especially focus on the hydraulic properties of deformation zones (HCDs) as well as the rock between the deformation zones in the potential repository volume (HRDs), the latter which is defined in a late stage of the site investigations. This requires consideration of how to build on and parameterise the geological DZ and hydrogeological DFN models representative of the rock between geologically defined DZs based on hydraulic measurements along boreholes, applicable to the entire regional scale 3D groundwater flow domain, a volume of ca 600 km^3 (the corresponding local model volume is ca 20 km^3), cf. Section 1.3. Part of this is achieved by deriving specific:

- hydrogeological deformation zone models (HCD models) for deterministic deformation zones interpreted in the regional model domain /Wahlgren et al. 2005, 2008/,
- hydrogeological DFN models for the set of hydraulic (rock) domains based on representative fracture domains which cover the local model volume and the defined rock domains accounting for the remaining part of the regional model. The geological fracture domain model is presented by /LaPointe et al. 2008/ and the rock domains in /Wahlgren et al. 2005, 2008/ and briefly in Chapter 3.

This said, there is still the issue of how the deformation zones defined by geology should be modelled hydrogeologically and judged (e.g representative hydrogeological thickness, associated hydrogeological barrier effect etc). Another issue is how to model the hydrogeology of the upper part of bedrock (100 m or so) which is generally characterised to a much lesser degree by the cored boreholes, but is known to generally be more permeable than below 100 m depth. Recommendations on how to address these three issues in the upcoming groundwater flow modelling for SDM-Site Laxemar are reported here.

The modelling and conceptualisation is an iterative process with interactions with other disciplines, mostly geology and geochemistry. The presentation of some data is based on conclusions made late in this process such as elevation intervals for statistics of data presented in Chapters 7–9. The motivation for these elevation intervals are provided in Chapter 9. However, data processed and analysed in preceding chapters were also processed according to this division in elevation interval as this was found useful for description of depth dependency and for maintaining an overall consistency of the report as such. Also Hydraulic Rock Domains (HRD) are briefly introduced to the reader in Chapter 3 together with the geological models, but the motives for the construction of HRDs are provided in Chapter 9.

1.1.1 Disposition

This remainder of the report is organised as follows:

- Chapter 2 presents SKB's systems approach to groundwater flow and solute transport in fractured crystalline rock as employed in the SDM work. This chapter constitutes an important premise for Chapters 4, 9 and 10.
- Chapter 3 presents an overview of the deformation zone model and the fracture domain model for SDM-Site Laxemar as derived by the geological modelling group. This chapter is important for Chapters 7, 9, and 10.
- Chapter 4 presents an overview of the hydraulic testing carried out up to data freeze Laxemar 2.3 for SDM-Site Laxemar, and a review of the data selected for hydrogeological analysis and modelling in the work reported here.
- Chapter 5 presents the structural-hydraulic data as obtained in core-drilled boreholes.
- Chapter 6 presents the structural-hydraulic data as obtained in percussion-drilled boreholes.
- Chapter 7 introduces the concept of 'deterministically modelled deformation zones' and presents a working hypothesis for their hydraulic parameterisation for SDM-Site Laxemar.
- Chapter 8 provides the hydraulic material property assignment to interpreted minor deformation zones.
- Chapter 9 provides the hydraulic properties of the rock between the deterministically modelled deformation zones. The chapter also presents the statistical analyses of hydraulic data in relation to various subdivisions (e.g. defined fracture domains, rock domains and depth intervals).
- Chapter 10 presents the assumptions and conceptual model development for hydrogeological DFN modelling as well as the model set-up and the results from the hydrogeological DFN modelling undertaken for SDM-Site Laxemar.
- Chapter 11 contains a summary of the observations made and the conclusions drawn.

1.2 Regional and local model areas

The regional and local model areas employed for model version SDM-Site Laxemar are shown in Figure 1-3. The *Laxemar-Simpevarp regional (scale) model area/volume* (later in the report referenced as the *Regional model area/volume*) for SDM-Site Laxemar, is the same as the one used in model version Laxemar 1.2.

The coordinates outlining the surface area of the Regional model volume, cf., Figure 1-3 are (in metres):

RT90 (RAK) system: (Easting, Northing):
(1539000, 6373000), (1560000, 6373000), (1539000, 6360000), (1560000, 6360000).

RHB 70; elevation: +100 masl, –2,100 masl.

Volume: $21 \times 13 \times 2.2$ km^3 = 600.6 km^3.

The coordinates defining the *Laxemar local (scale) model area/volume* (later in the report referenced as *Laxemar model area/volume or Local model area/volume*) for model version SDM-Site Laxemar are (in metres):

RT90 (RAK system: (Easting, Northing): (1546150, 6368200), (1550390, 6368200), (1550390, 6364250), (1546150, 6364250).

RHB 70: elevation: +100 masl, –1,100 masl.

Volume: $4.24 \times 3.95 \times 1.2$ km^3 = 20.1 km^3.

Focused area/volume is the central, southern and western parts of the local model area.

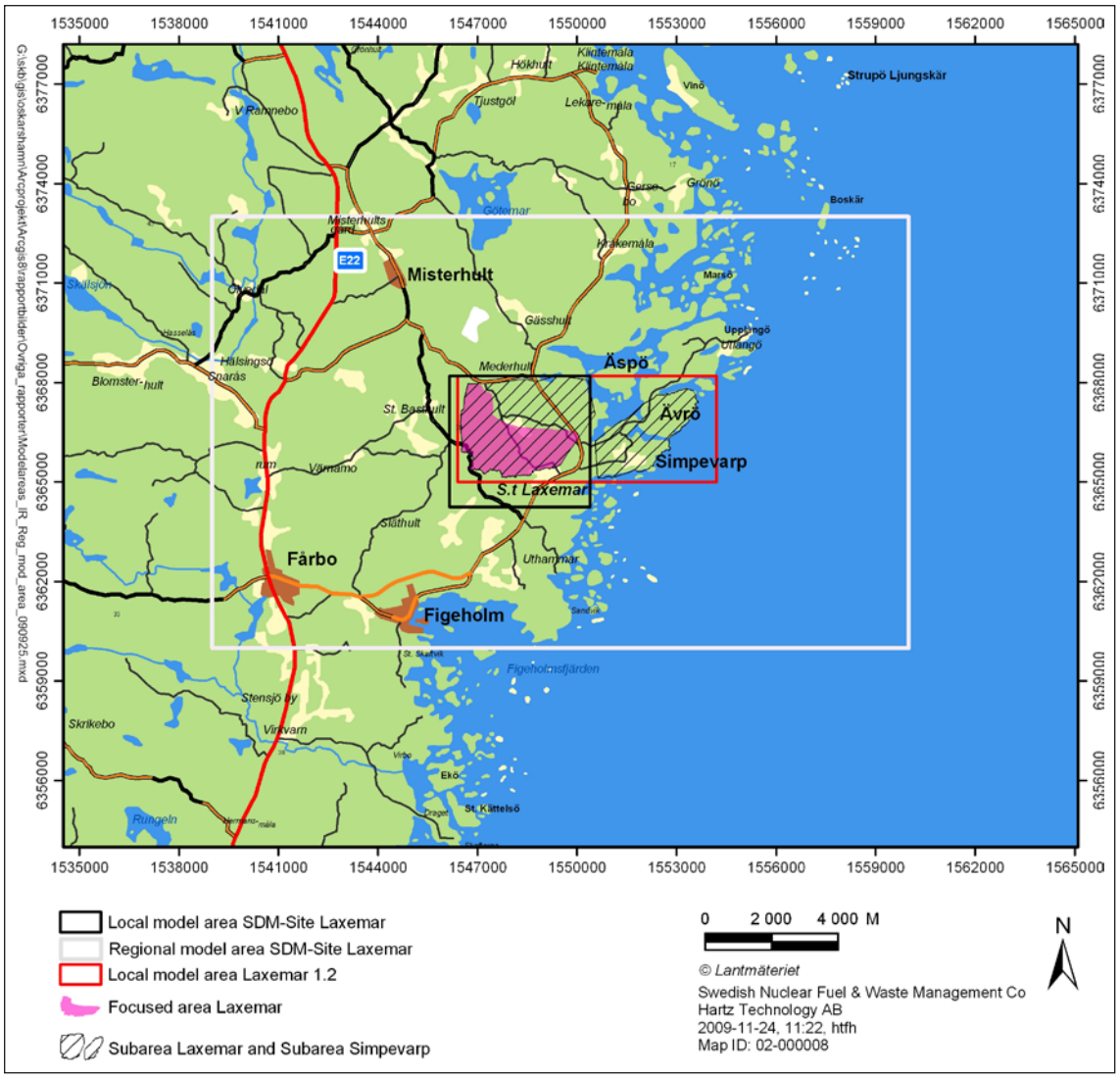

Figure 1-3. *Regional and local model areas used for model version SDM-Site Laxemar. The area coverage of the regional model is the same as that employed in previous model versions, whereas the local model area is significantly reduced compared to that employed in model version Laxemar 1.2. Laxemar subarea and Simpevarp subarea defined the investigations areas during the initial stage of the site investigations.*

2 SKB's systems approach to hydrogeological modelling in the SDM

2.1 General

The hydrogeological SDM modelling is conducted on two different scales, regional scale as well as local scale. In model version SDM-Site Laxemar, particular attention is paid to the local model volume, see Section 1.3. In order to meet the two objectives listed in Section 1.1 the groundwater system is divided into different hydraulic domains. Figure 2-1 illustrates schematically SKB's systems approach as employed in the hydrogeological SDM for Laxemar. The groundwater system consists of three basic hydraulic domain types, namely HSD, HCD and HRD, where:

- HSD represents the Quaternary deposits /reported in Rhén et al. 2009/,
- HCD represents the deterministic deformation zones (or "hydraulic conductors"), and
- HRD represents the fractured bedrock between the deterministic deformations zones.

The systems approach constitutes the basis for the conceptual modelling, the site investigations and the numerical simulations carried out in support of the hydrogeological SDM.

The hydrogeological investigations and modelling of the groundwater system are subdivided between the surface systems and the bedrock hydrogeology (bedrock hydrogeology modelling group called HydroNet within Site Investigations), where the former treat the near-surface system (surface hydrology and the hydrogeology of surface bedrock and HSD), and the latter the deeper (bedrock hydrogeology and hydraulic properties of the HCD and HRD). However, the hydrogeology modelling group also uses hydraulic properties of HSDs and interacts with the surface systems modelling group in the assessment of the hydraulic properties. This division is purely pragmatic and the interface between the different descriptions is seamless from a conceptual modelling point of view. For instance, the hydraulic properties of the bedrock and the head distribution at the bottom boundary of the near-surface hydrogeological system are provided by the numerical flow modelling undertaken for the entire system A description of the approach taken by SKB for the near-surface hydrogeological for Laxemar model version 1.2 is found in /Bosson 2006/. The SDM-Site regional groundwater flow modelling is presented in /Rhén et al. 2009/.

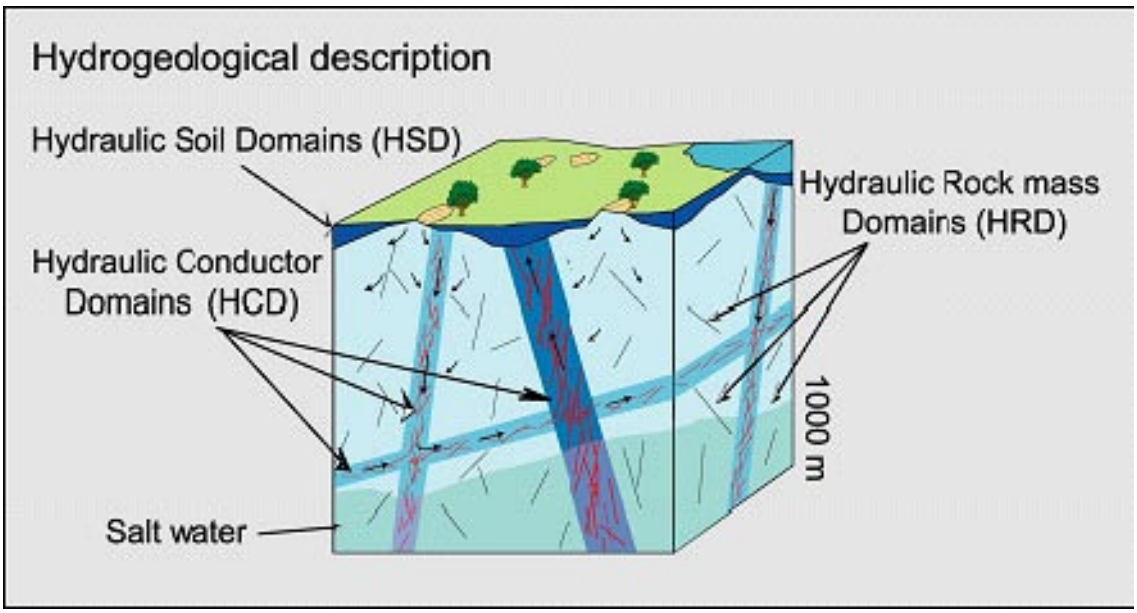

Figure 2-1. *Schematic illustration showing the division of the crystalline bedrock and the overburden (Quaternary deposits) into hydraulic domains. Within each domain, the hydraulic properties are represented by equivalent values, or by spatially distributed statistical distributions /Rhén et al. 2003/.*

2.2 Bedrock hydrogeology

A cornerstone of the bedrock hydrogeological description concerns the hydraulic characterisation of the more intensely fractured deterministic deformation zones and the fractured bedrock between these zones. The approach taken by SKB combines a deterministic representation of the major deformation zones (DZ) with a stochastic representation of the fractured bedrock between these zones using a Discrete Fracture Network (DFN) concept. The hydraulic description of the deformation zones is particularly important for Repository Engineering and the hydraulic description of the less fractured bedrock between the deformation zones is especially important for Safety Assessment. The hydraulic characterisation of the fractured bedrock between the deterministic deformation zones at repository depth is a vital task, yet complex given the relatively minute number of data collected at these depths. The hydrogeological SDM is based on data from investigations in cored boreholes drilled from the surface typically extending to depths between 400 to 1,000 m, and the current understanding of the groundwater system at depth is constrained by this fact, where subvertical boreholes tend to favour sampling of subhorizontal structures.

Geology interpret zones with associated surface lineaments longer than 1,000 m as being deterministic (major local or regional) deformation zones, whereas those with length less than 1,000 m are referred to as minor local deformation zones and are consequently modelled stochastically using DFN models, cf. Section 3.4. Deformation zones with inferred true thickness of 10 m or more in boreholes that are not possible to trace to a structure (lineament) on ground surface, are modelled deterministically as discs with a size equivalent to a 1,000×1,000 m square. The geological DZ and DFN models are parameterised hydraulically using data from single-hole Posiva Flow Log (PFL) pumping tests and single-hole Pipe String System (PSS) injection tests, cf. Section 4.3.

In relation to the two methods used for hydraulic borehole investigations in Laxemar, PFL and PSS, the hydraulic characterisation of fractured bedrock between deterministic deformation zones may be envisaged as illustrated in Figure 2-2. The constituent parameters measured, where the fractures intersects the borehole, are the flow rate Q and the pressure p. Since the two entities are coupled the material property parameter studied is really the specific discharge $Q/\Delta p$. The specific discharge is dependent on several important aspects, among which are particularly noted:

- Q_{limit}; the lower measurement limit of the flow rate for the test method.
- T_{bh}; the transmissivity of the tested fracture intersecting the borehole. Evaluation of transmissivities (T_{bh}) can be affected by the hydraulic resistance close to the borehole (positive or negative skin factor), with either reduced or enhanced hydraulic communication between the borehole and the rock, respectively.
- C; the connectivity of the tested fracture to other fractures away from the borehole. Some fractures are isolated, or are a part of an isolated cluster of fractures. Others are well connected and a part of the overall connected hydrological system.
- T/S; the hydraulic diffusivity of the fracture system within the radius of influence.
- T/S; the hydraulic diffusivity of the fracture system.
- t; the duration of the hydraulic testing, i.e. the test time.
- ΔL; the length of the test interval (test section) in the borehole.

The pros and cons of the two test methods used in Laxemar, PFL and PSS, are described in detail in Section 4.3. From a site descriptive modelling point of view it is noted that the modelling approach taken by SKB focuses on the conductive fracture frequency (CFF) measured by the so called PFL-f method. This emphasis on the PFL-f method means, among other things, that fracture network situations such as A and B in Figure 2-2 are not honoured in the SDM-Site modelling, neither in the hydrogeological DFN modelling nor in the subsequent ECPM groundwater flow modelling[1].

[1] The reason why the PFL method cannot address situations like A and B in G Figure 2-2, in contrast to the PSS method, is explained in Section 4.3. It is also explained in Section 4.3 why the PSS method has problems in distinguishing situations A and B from situations C–E.

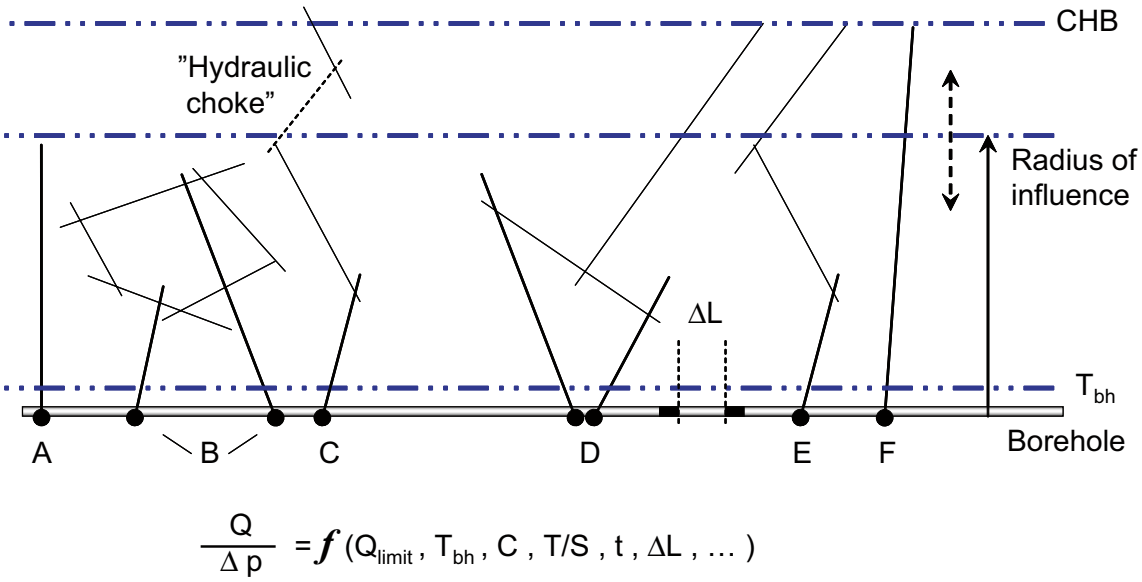

Figure 2-2. *Cartoon showing a borehole with six different symbolic fracture network situations, cases A–F. The specific capacity, Q/Δp, measured along the borehole is dependent on several factors, e.g. the measurement limit, Q_{limit}, of the test method, the transmissivity of the fracture intersecting the borehole, T_{bh}, the fracture connectivity, C, the hydraulic diffusivity, T/S, of the fracture network, the test time, t, the length of the test section, ΔL, etc. The hydraulic characterisation of the fracture system varies depending on the method used as well as on the in situ conditions, e.g. the occurrence of "hydraulic chokes". Cases A–C represent isolated fracture networks and cases D–F represent fracture networks connected to the overall hydrogeological system. The overall hydrogeological system for the latter is here indicated by a constant head boundary (CHB) suggesting a pseudo steady-state flow regime at long test times. The cartoon is rotated 90° to improve the readability. Reproduced from /Follin et al. 2007c/.*

Neglecting situations like A and B does not mean that they are unimportant. On the contrary, the role of compartmentalised fracture systems is well recognised by the hydrogeological modelling group and a procedure has been suggested for its handling in the repository modelling carried out in the forthcoming safety assessment project SR-Site. However, situations such as C–E, cf. Figure 2-2, with larger systems of connected fractures that connect to (a) positive boundaries(y), are regarded as more important for the groundwater flow modelling addressed in the hydrogeological SDM modelling (PSS tests may indicate compartmentalised fracture systems where PFL-f indicates low-permeable rock, or rather no fractures with transmissivities above the measurement limit of the PFL-method).

A pertinent question to be answered in due time, is the role of the presumably connected fractures of transmissivity less than the practical lower measurement limit of the PFL-f method, which is c. $1 \cdot 10^{-9}$ m^2/s. This matter is discussed further in Section 4.3. Another circumstance to consider is that not all boreholes in the potential deposition volumes in Laxemar will be hydraulically tested with both test methods, cf. Chapter 4 (It differs slightly between Formark and Laxemar in that PSS with 5 m test sections were in Laxemar only performed in the elevation interval –300 to –700 m whereas in Forsmark generally these tests were made in the entire borehole below casing).

The hydraulic characterisation of the deformation zones is fairly straightforward. All hydraulic data between the upper and lower bounds of an interpreted deformation zone interval in a borehole (the latter given by the single-hole geological interpretation) are considered, regardless of the test method used. The collected hydraulic data are pooled, i.e. lumped together, to form basis for an integrated single transmissivity value for the particular borehole interval.

Figure 2-3 illustrates the structural-hydraulic approach taken by SKB in the hydrogeological modelling within SDM-Site Laxemar.

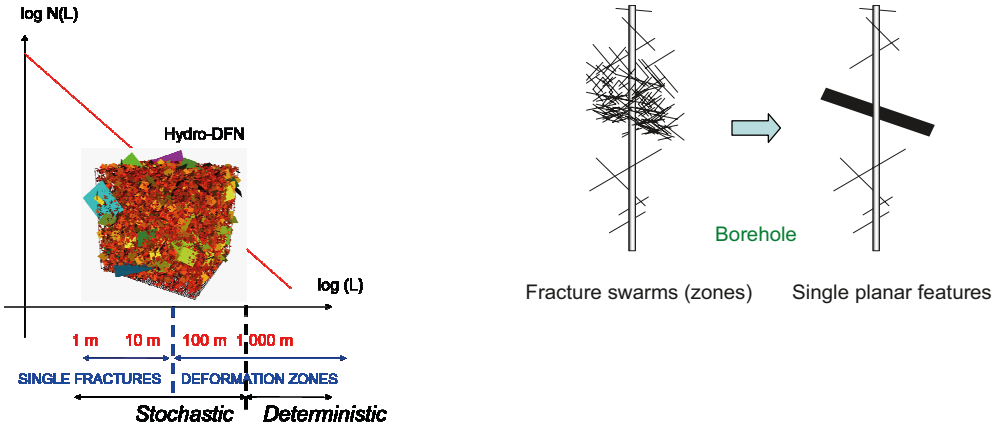

Figure 2-3. *Left: The tectonic continuum hypothesis invokes that the frequency of fractures of different sizes can be approximated through the use of a single power-law density function. Structures up to L = 1,000 m (r = 564.2 m) are regarded as uncertain and are treated stochastically using the discrete fracture network (DFN) concept. The same distinction was used in the geological DFN modelling. Right: The fracture data collected between the upper and lower bounds of a deformation zone interval are lumped together to form a single planar feature. In the same fashion, all hydraulic data in the interval are also lumped together to form a single transmissivity value. Reproduced from /Follin et al. 2007c/.*

2.3 The ECPM approach

Any groundwater model is a simplified parameterisation of a real physical groundwater system. The Equivalent Continuous Porous Medium (ECPM) approach is used in the hydrogeological SDM for the transformation of geometrical and hydraulic properties of a modelled system consisting of 2D discrete features (HCD and hydrogeological DFN features) into a 3D continuous porous medium, see Figure 2-4. Since each ECPM model studied is based on a particular underlying stochastic DFN realisation, the ECPM models are inherently also stochastic. It should be mentioned that within the Safty Assessment the hydrogeological DFN is used to model the flow pattern in the within the repository volume and not the ECPM.

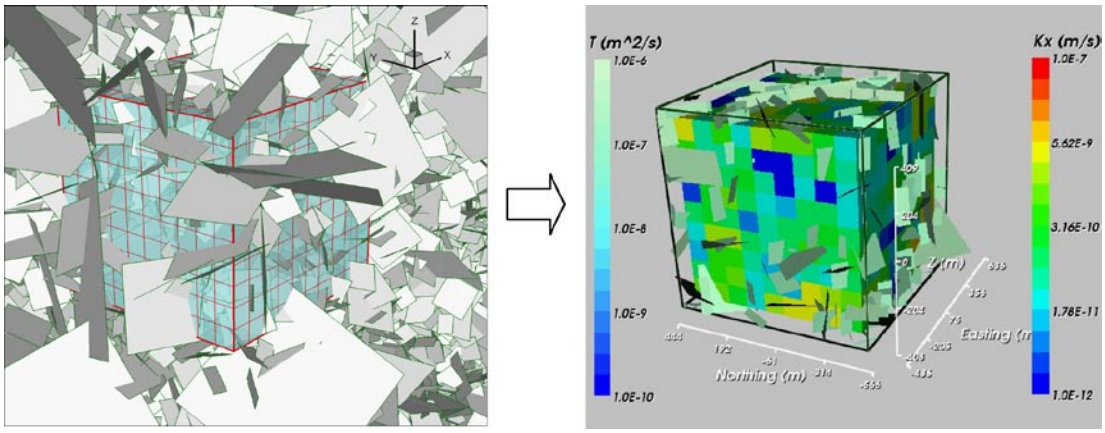

Figure 2-4. *Illustrations showing of the ECPM concept. Geometrical and hydraulic properties of modelled 2D discrete features (DZ and DFN) are transformed into a 3D equivalent continuous porous medium. Reproduced from /Follin et al. 20007c/.*

3 Geological setting

3.1 Laxemar

Laxemar is situated in north-eastern Småland within the municipality of Oskarshamn, about 300 km south of Stockholm. Figure 3-1 and Figure 3-2 illustrate the local model area, c. 4×4 km^2 , and the eastern part of the regional model area (essentially covering the Simpevarp subarea), indicating the boreholes available for interpretation of the bedrock conditions in the area. Figure 3-3 and Figure 3-4 illustrate the drilled soil pipes that in part have helped to define the bedrock surface, but mainly characterise the Quaternary deposits.

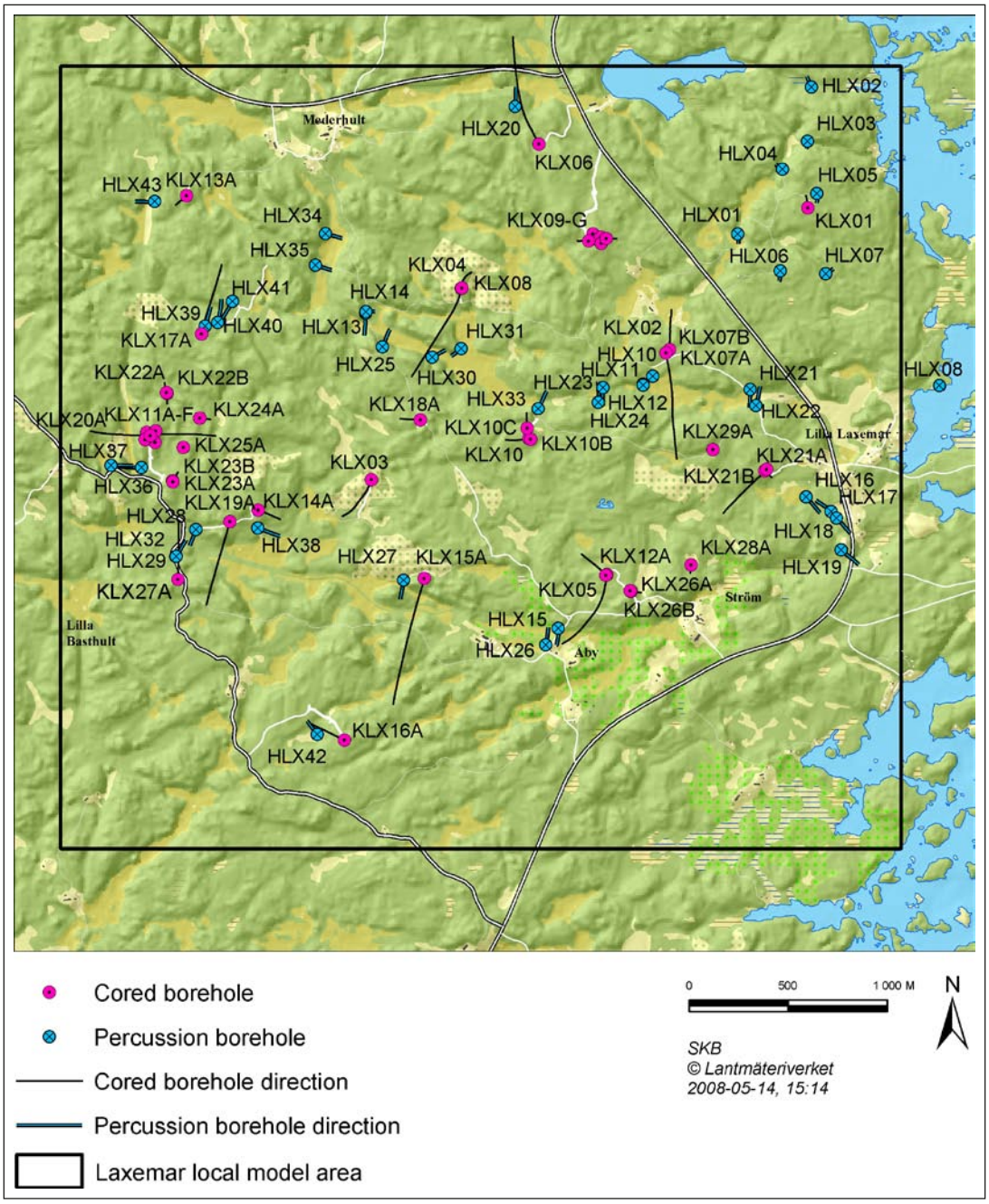

Figure 3-1. *Cored and percussion drilled boreholes within and close to the Laxemar local model area. Data from borehole KLX27A have not been used for primary data analysis and for hydrogeological DFN model as the data were made available late in the project.*

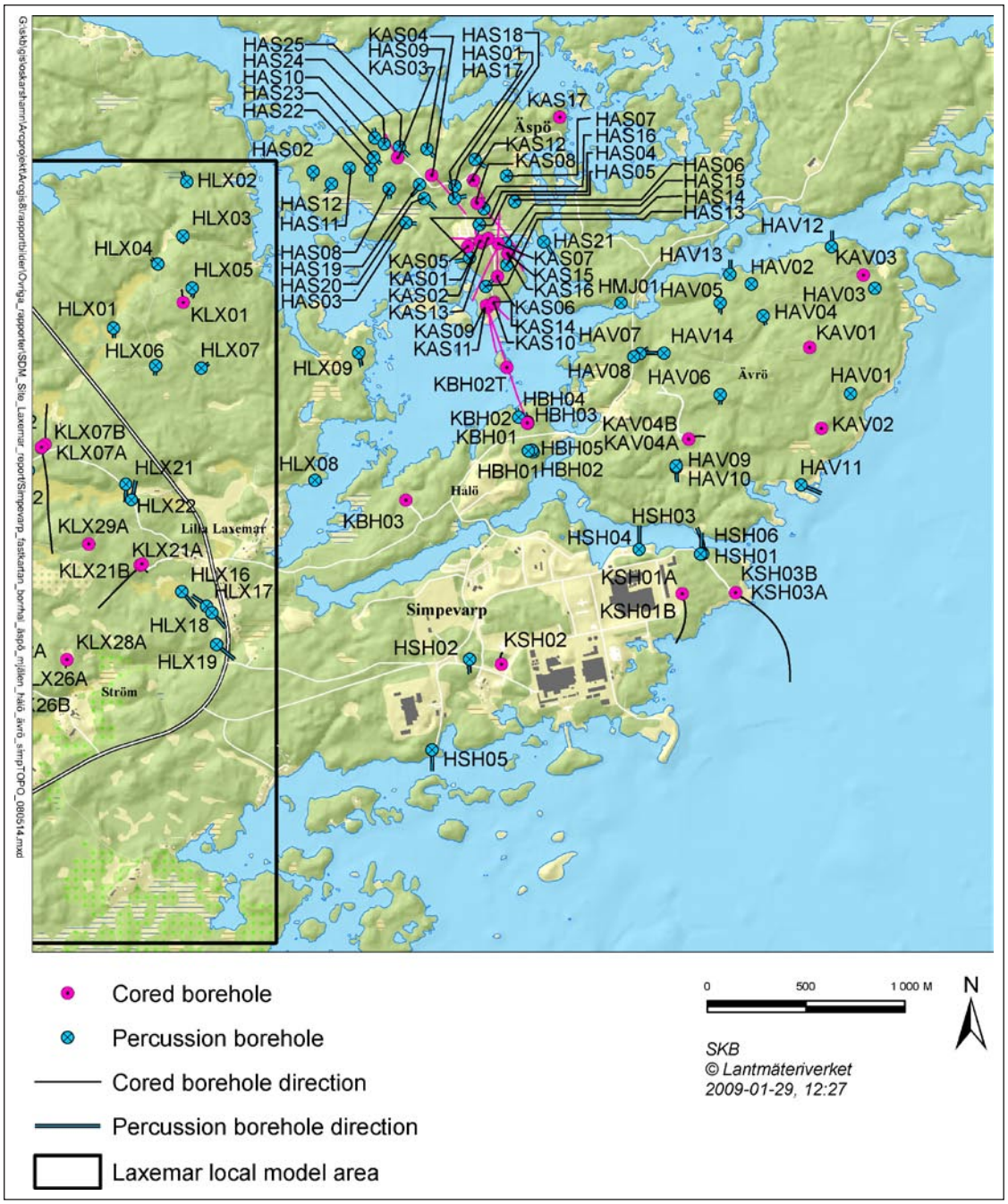

Figure 3-2. *Cored and percussion drilled boreholes within the regional model area covering Äspö, Hålö, Ävrö, Mjälen and Simpevatp peninsula (i.e. parts of the Simpevarp subarea).*

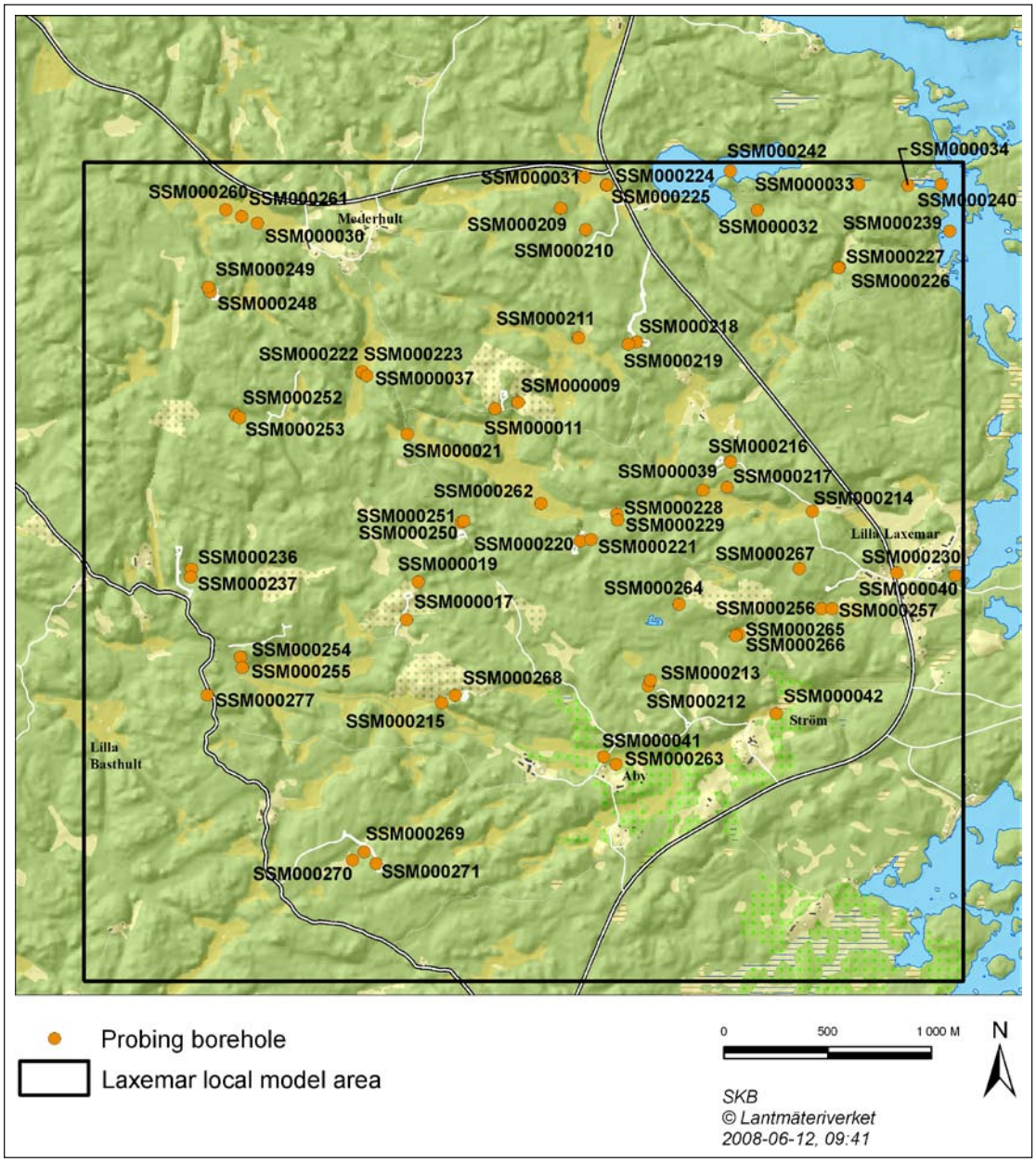

Figure 3-3. *Soil pipes within and close to the Laxemar local model area.*

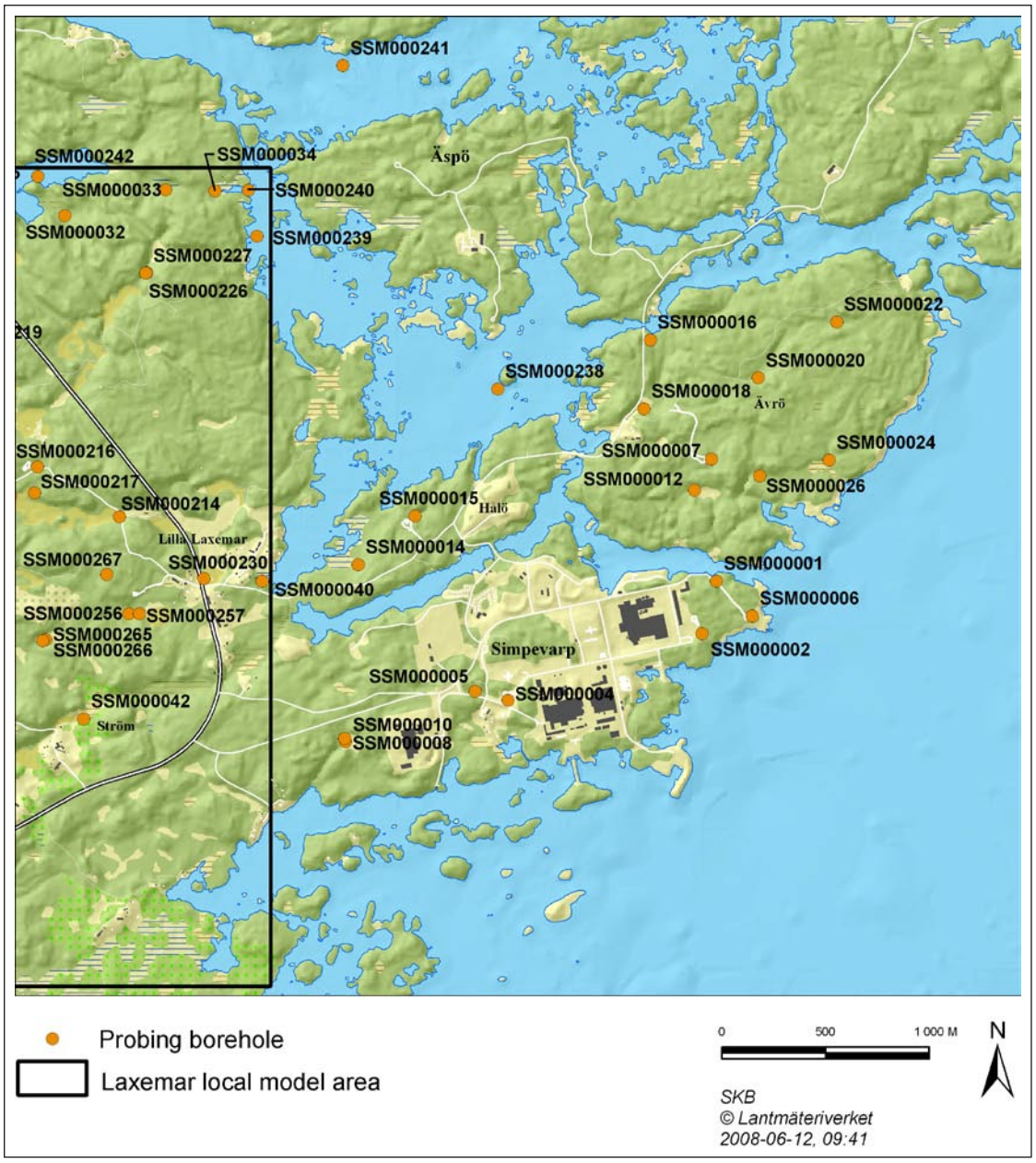

Figure 3-4. *Soil pipes within the regional model area covering Äspö, Hålö, Ävrö, Mjälen and Simpevatp peninsula (i.e. parts of the Simpevarp subarea).*

During the site investigations of Laxemar boreholes have mainly been drilled within the Laxemar subarea (HLX10–43, KLX03–29A), cf. Figure 3-1. Boreholes have also been drilled on the Simpevarp peninsula (HSH01–06, KSH01–KSH03B) and Ävrö (HLX09–14, KAV04A,B) as part of investigations of the Simpevarp subarea, cf. Figure 3-2. The additional boreholes, e.g. KLX01 and KLX02, cf. Figure 3-1, were drilled during projects preceding the site investigations in the Laxemar-Simpvarp area. These boreholes generally have less geological and hydrogeological data and are sometimes based on methodologies other than those employed in the current site investigations. Data from cored borehole KLX27A, cf. Figure 3-1, drilled late in complete site investigations, have not been used for the hydrogeological DFN model, as data became available late in the project.

3.2 Overview of the deformation zone model

The term deformation zone is used in all phases of the geological work, bedrock surface mapping, surface based interpretations, single-hole geological and hydrogeological interpretations and 3D modelling. Hence, a deformation zone is a general term referring to an essentially 2D structure along which there is a concentration of brittle, ductile or combined brittle and ductile deformation. Table 3-1 presents the terminology for brittle structures based on trace length and thickness as presented in /Andersson et al. 2000a/. The geometric borderlines between the different structures are highly approximate.

Deformation zones are considered to have a variable thickness and a spatial variability of the properties that is important for the evaluation of data /Wahlgren et al. 2008/, cf. Figure 3-5.

Table 3-1. Terminology and general description (length and width are approximate) of brittle structures (modified after /Andersson et al. 2000a/).

Terminology	Length	Width	Geometrical description
Regional deformation zone	>10 km	>100 m	Deterministic
Local major deformation zone	1 km–10 km	5 m–100 m	Deterministic (with scale-dependent description of uncertainty
Local minor deformation zone	10 m–1 km	0.1–5 m	Statistical (if possible, deterministic)
Fracture	<10 m	<0.1 m	Statistical

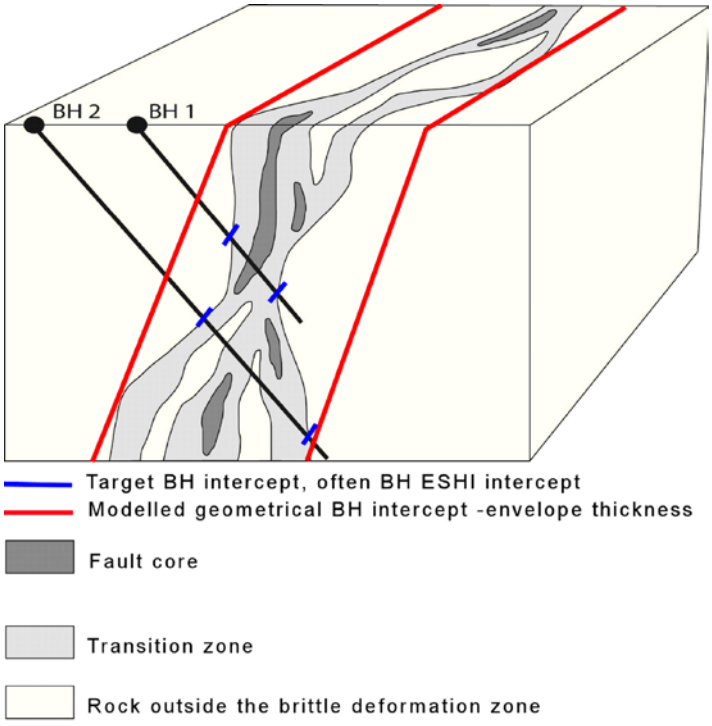

Figure 3-5. *Three-dimensional schematic conceptual geometric model for a brittle deformation zone in Laxemar along which shear displacement has occurred (redrawn after /Caine et al. 1996/). Note the variable character of the deformation zone along the two borehole intersections. From /Wahlgren et al. 2008/,*

The 3D deformation zone model for SDM-Site Laxemar /Wahlgren et al. 2008/ contains 202 (187 if DZ-segments with the same name but different extension A, B etc counted as one single (e.g. ZSMNS001A, ZSMNS001B etc)) deterministically modelled deformation zones within the regional model volume, of which 70 (64 if DZ-segments with the same name extension A, B are counted as one single DZ) are included in the local model volume, see Figure 3-6 through Figure 3-9. Most of these deterministic deformation zones are referred to as ZSMxxx. A subset (N=24) of the deterministic zones are interpreted on the basis of the single-hole interpretation but are devoid of an associated surface lineament. In doing so, only those zones with a interpreted true thickness of 10 m or more in a borehole are interpreted to have a size (length) in excess of 1,000 m. These DZs are named Borehole-ID_DZ-unit, where the DZ-unit is defined by the geological single-hole interpretation. The latter 24 DZs are modelled deterministically as discs with radius 564 m (based on an equal area of 1×1 km^2).

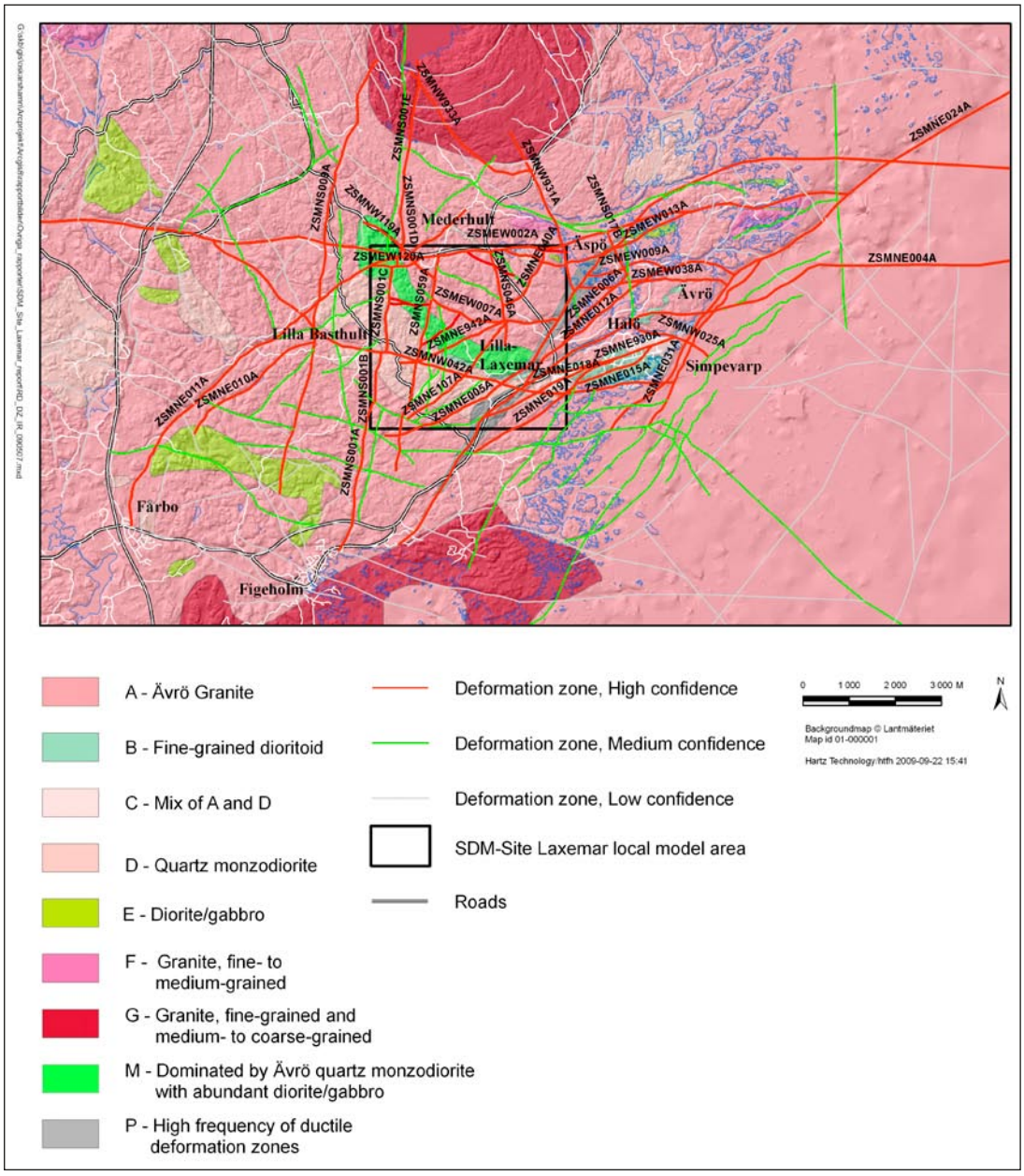

Figure 3-6. *Deformation zones and rock domains bounded by the regional model area. From /Wahlgren et al. 2008/.*

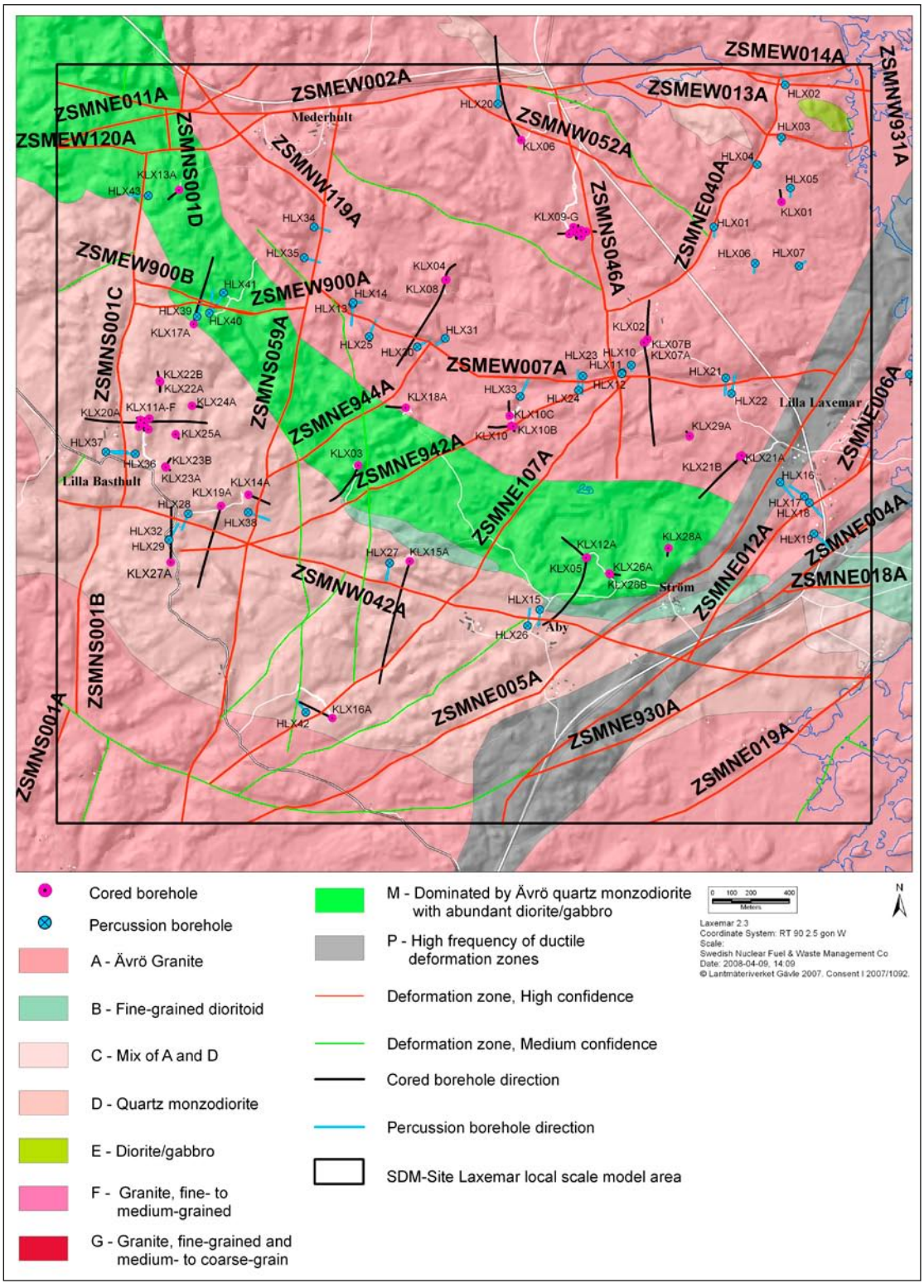

Figure 3-7. *Interpreted deterministic deformations zones and rock domains within the local model area. From /Wahlgren et al. 2008/.*

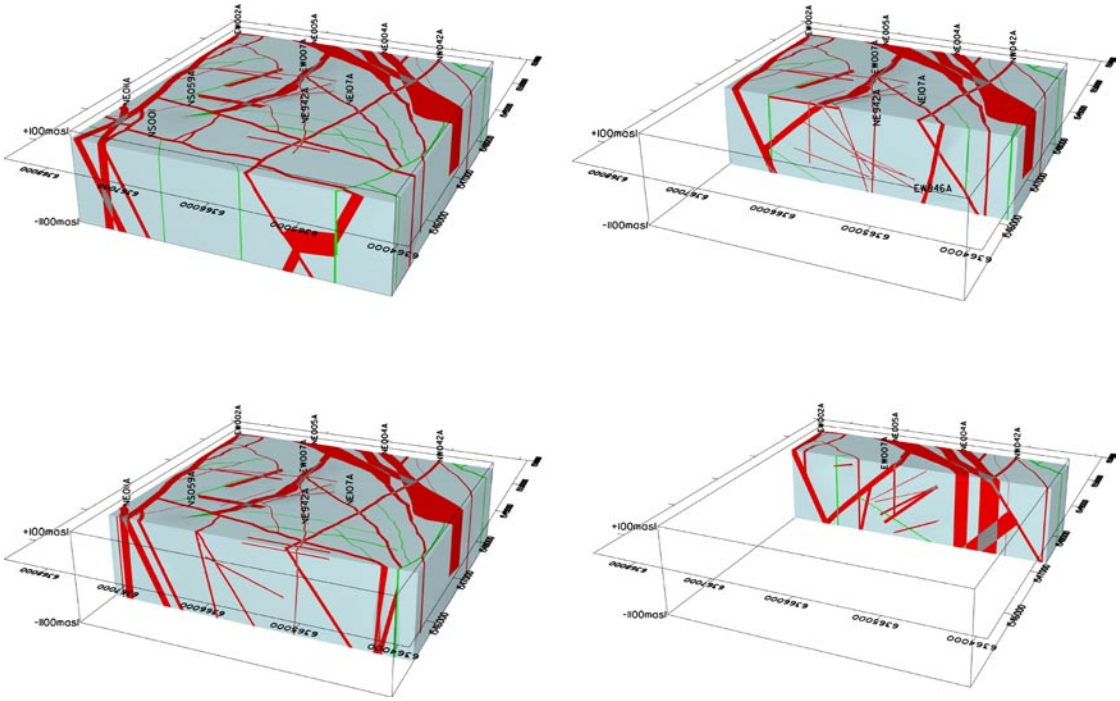

Figure 3-8. *3D visualisation of the deformation zones modelled deterministically in the local model volume for SDM-Site Laxemar. View from west-south-west, with vertical cut in N-S. From /Wahlgren et al. 2008/.*

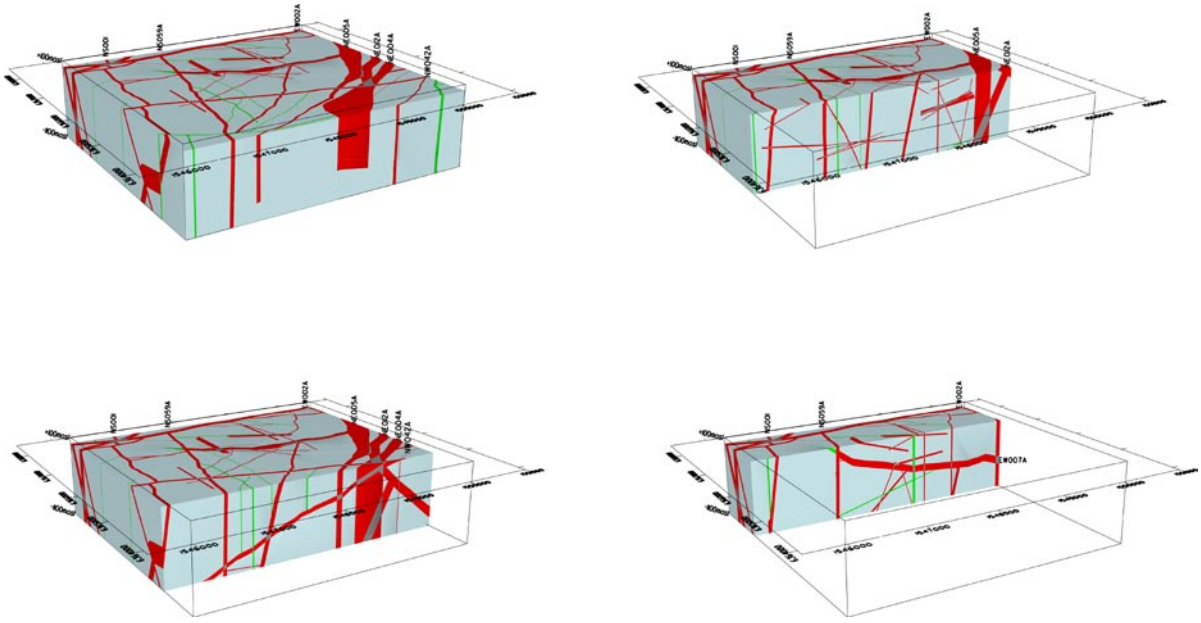

Figure 3-9. *3D visualisation of the deformation zones modelled deterministically in the local model volume for SDM-Site Laxemar. View from south-west, with vertical cut in E-W. From /Wahlgren et al. 2008/.*

Within the local model, see Figure 3-7 , the deterministically modelled deformation zones are of modelled size (trace length at surface) of 1 km or longer whereas within the regional model, see Figure 3-6, but outside the local model volume, deterministic are modelled with a size of 1.6 km or longer /Wahlgren et al. 2005, 2008/.

Deformation zones may be of hydraulic importance both as planar extensive conductive elements with higher permeability than the surrounding bedrock, but some deformation zones may also act as hydraulic barriers by influence of geology, e.g. through association to dolerite dykes or fault gouge, cf. Chapter 7.

A number of minor deformation zones are not modelled deterministically by geology but are described in /Hermanson et al. 2008/. These were analysed hydraulically in Chapter 8 and treated according to Section 2.2 and Chapter 9–10.

Dolerite has not been observed in outcrops within the Laxemar local model area but on Äspö Island. However, observations have been made of dolerite in a number of cored and percussion boreholes in western Laxemar, namely KLX14A and HLX38 along deformation zone ZSMNS059A, KLX20A, HLX36, HLX37 and HLX43 along deformation zone ZSMNS001C, plus additional observations in KLX19A and HLX13. The dolerite dykes in HLX38 are very thin. /Triumf 2007/. The probable and possible dolerite dykes, according to /Triumf 2007/, are shown in Figure 3-10. Three of these dolerite dykes have been modelled deterministically /Wahlgren et al. 2008/:

- ZSMNS001,
- ZSMNS059A,
- klx19_dz5-8_dolerite (devoid of associated surface expression, assumed to me 1,000 m in size, with strip/dip: 185/81).

Thicker dolerite dykes are of hydraulic importance as they have the potential to act as hydraulic barriers, due to the low-permeable characteristics of the dolerite. However, the rock bordering the dolerite dykes may be quite permeable. These hydraulic implications of the dolerite dykes are further discussed in Chapter 7. Hydraulic conductor domains (HCD) are based on the deformation zones presented in this section and analysis of their hydraulic properties are presented in Chapter 7.

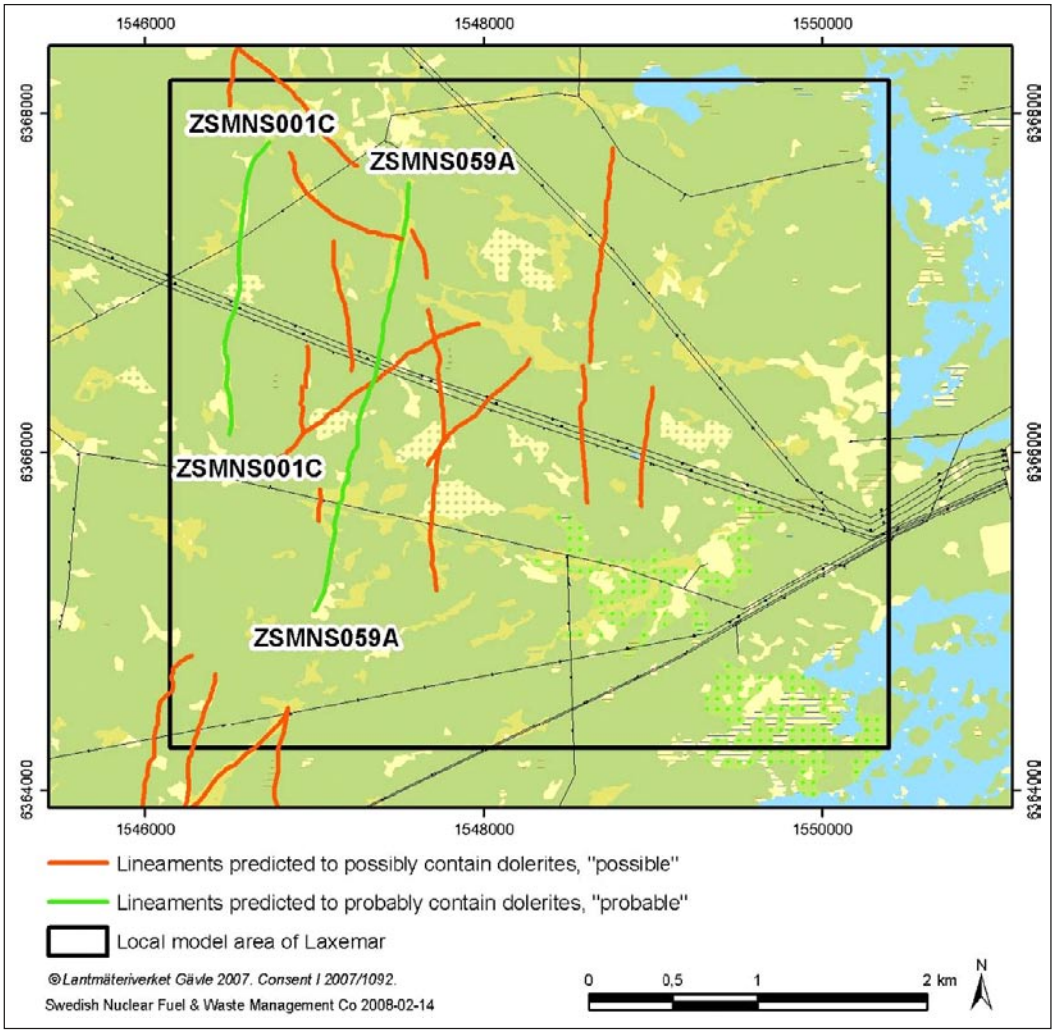

Figure 3-10. *Two lineaments (green line) are predicted as "probable" regarding their potential content of dolerite in the Laxemar area – they coincide with the deformation zones ZSMNS001C and ZSMNS059A. The lineaments (red line) are predicted as "possible" regarding their potential content of dolerite as part of their sources. From /Triumf 2007/.*

3.3 Overview of the rock domain model

The rock domains are defined on the basis of a combination of composition, grain size, texture, homogeneity and ductile structural overprinting. The rock domain model is discussed in /Wahlgren et al. 2008/ and shown here in Figure 3-6 , Figure 3-7 and Figure 3-11. The Ävrö granite (Domain A) is dominant in the regional model area, whereas Domain M (dominated by Ävrö quartz monzodiorite with abundant diorite/gabbro) and Domain D (Quartz monzodiorite) make up large parts of the local model volume.

The rock domains have been given different codes where domains denominated with the same capital letter are dominated by the same characteristics as displayed below:

RSM**A**-domain: dominated by Ävrö granite;

RSM**B**-domain: dominated by fine-grained dioritoid;

RSM**BA**-domain: characterized by a mixture of Ävrö granite and fine-grained dioritoid;

RSM**C**-domain: characterized by a mixture of Ävrö granite and quartz monzodiorite;

RSM**D**-domain: dominated by quartz monzodiorite;

RSM**E**-domain: dominated by diorite/gabbro;

RSM**G**-domain: dominated by the Götemar type granite;

RSM**M**-domain: characterized by a high frequency of minor bodies to small enclaves of diorite/gabbro in particularly Ävrö quartz monzodiorite;

RSM**P**-domain: characterized by a high frequency of low-grade ductile shear zones in the above mentioned rock types.

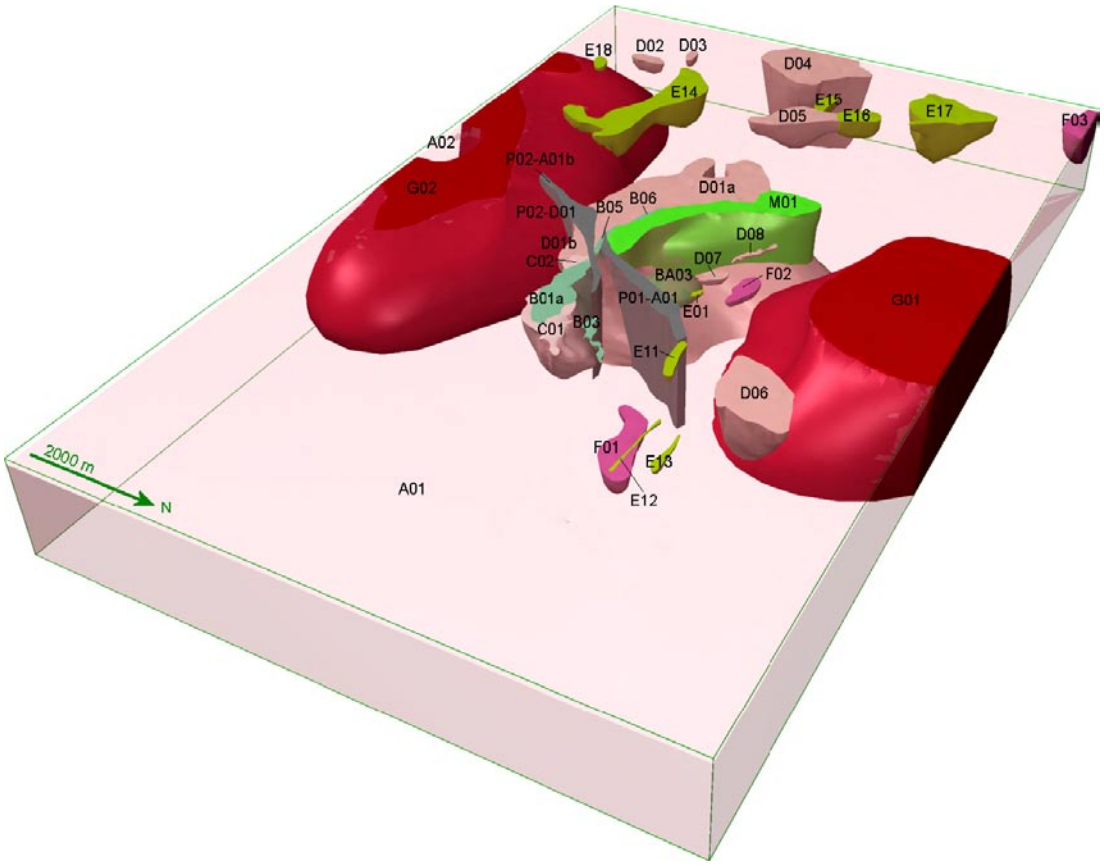

Figure 3-11. *Rock domains visualized in 3D, bounded by the regional model area. Ävrö granite shown transparent. From /Wahlgren et al. 2008/.*

One rock domain, RSMBA03, characterised by a mixture of Ävrö granite and fine-grained dioritoid, is intersected by only borehole KLX02 at borehole length 540 –960 m, and is geologically modelled as a large ellipsoidal body. It is in the northern part of the model and occupies a rather small volume.

Rock domains may have variable hydraulic properties due to differences in composition, grain size, texture, homogeneity and ductile structures between rock domains.

3.4 Overview of the fracture domain model

Fracture domains are rock volumes outside the bounds of modelled deterministic deformation zones in which the rocks show similar fracture characteristics. The key objective of the fracture domain assignment is the reduction of the total model uncertainty through the delineation of volumes of rock that possess similar geological characteristics. Detailed analysis of the spatial distribution of the fractures and other geological characteristics motivated the definition of fracture domains /La Pointe et al. 2008/, see Figure 3-12 and Figure 3-13. The fracture domains and rock domains have been the base geometrical models to study the spatial variation of hydraulic properties for definition of hydraulic rock domains (HRD), see Chapters 5 and 9.

Fracture domains are potentially significant hydraulically as the intensity and orientations of open fractures, a subset of all fractures, govern the permeability of the rock.

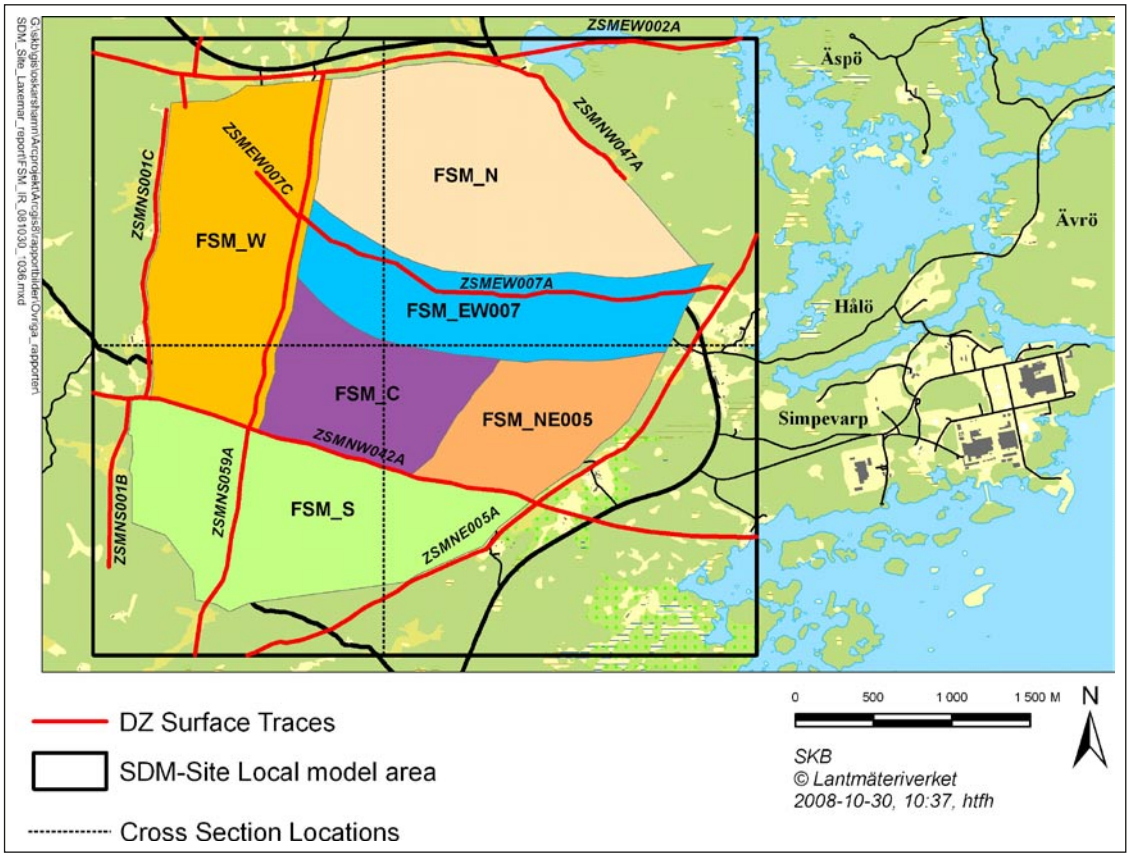

Figure 3-12. *Illustration of the SDM-Site Laxemar Fracture Domain Model. Based on /La Pointe et al. 2008/.*

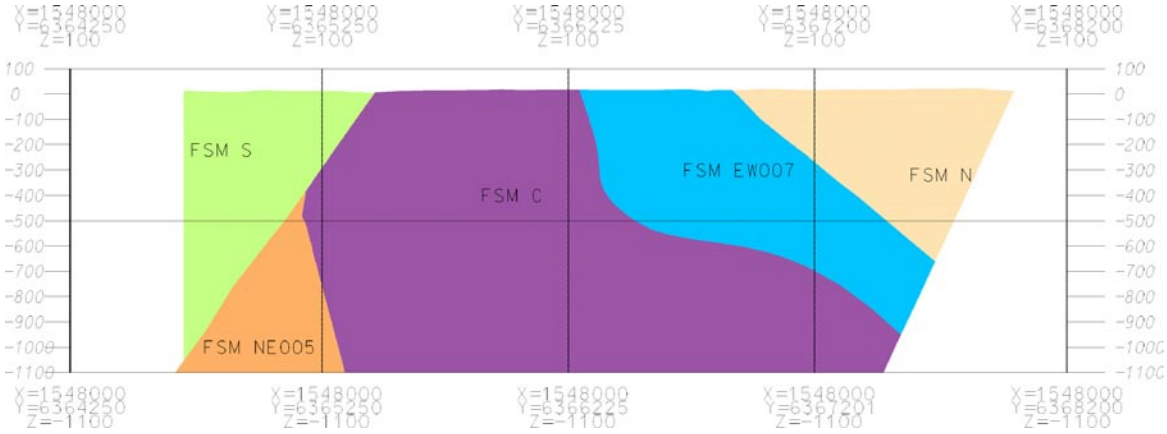

Figure 3-13. *RVS cross-section, oriented north-south through the middle of the Laxemar local model volume, through identified fracture domains. Vertical section from south (left) to north at Easting's X=154,800 m. From /La Pointe et al. 2008/.*

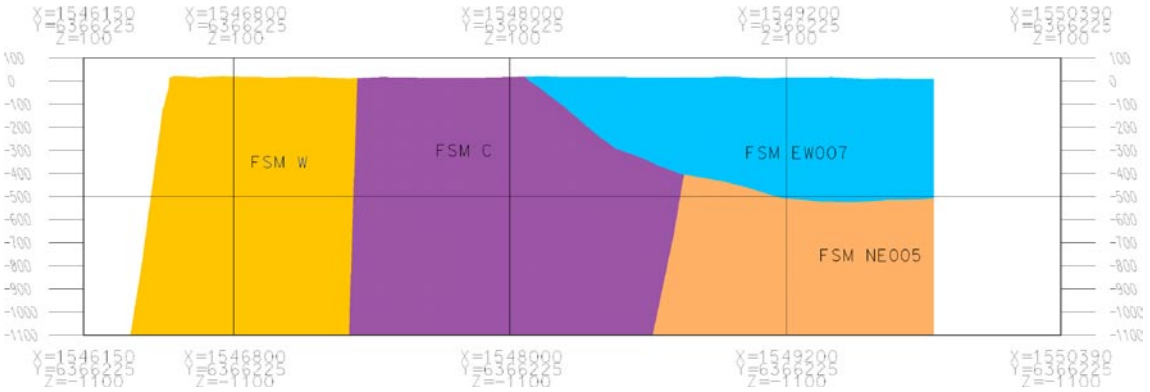

Figure 3-14. *RVS cross-section, oriented east-west through the middle of the Laxemar local model volume, through identified fracture domains. Vertical section from west (left) to east at Northing's Y=6,366,225 m. From /La Pointe et al. 2008/.*

3.5 Hydraulic rock domains

Hydraulic rock domains are parameterised based on the spatial distribution of hydraulic properties, and analysis have shown that some fracture domains can be used as hydraulic domains directly, whereas some fracture domains in combination can be considered as a single hydraulic rock domain, see Chapter 9. Figure 3-15 through Figure 3-17 show the HRDs (HRD_N, HRD_EW_007, HRD_C, HRD_W) corresponding to fracture domains, but the motivation for the formation of the individual HRDs is provided in Chapter 9. Given that the fracture domains are not defined outside the bounds of the envelope seen in Figure 3-15, hydraulic rock domains outside this envelope are motivated and based on the hydraulic properties of rock domains as outlined in /Rhén et al. 2006/, see also Chapter 10.

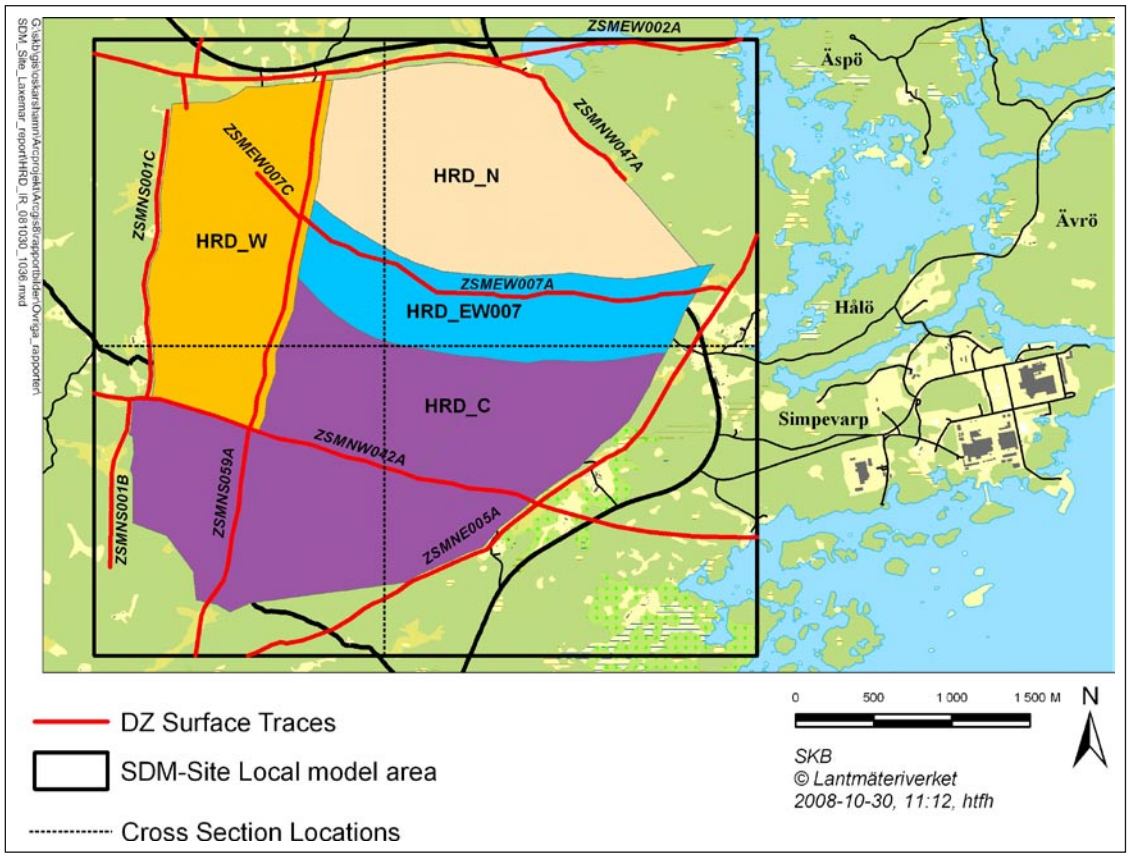

Figure 3-15. *Illustration of the SDM Site Laxemar Hydraulic Rock Domain Model.*

Figure 3-16. *Illustration of the SDM Site Laxemar Hydraulic Rock Domain Model, vertical section from south (left) to north at Easting's X=154,800 m.*

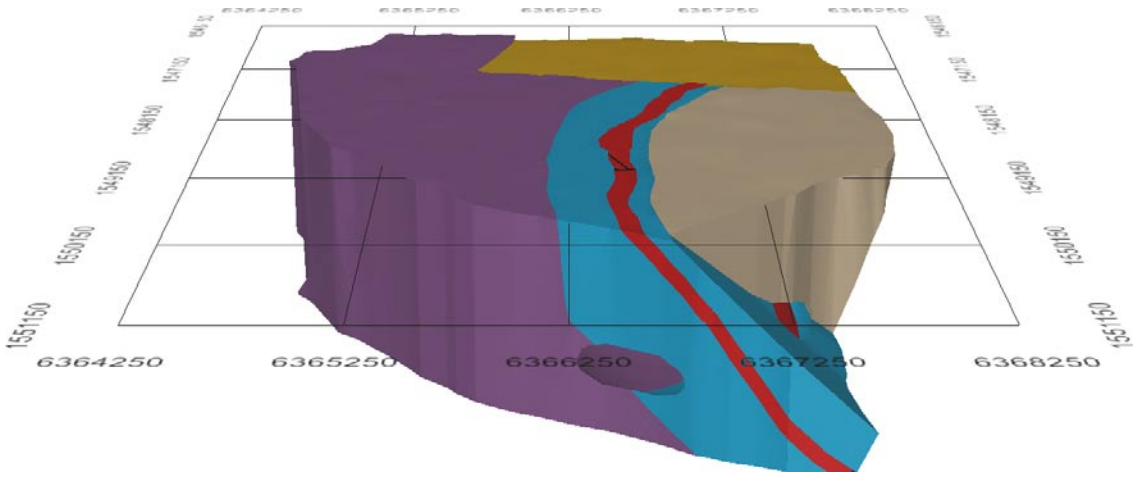

Figure 3-17. *Illustration of the SDM Site Laxemar Hydralic Rock Domain Model, 3D view looking westward.*

4 Hydraulic single-hole investigations

In this chapter a brief summary is presented of test methods and primary test results. Hydraulic results in relation to geology and the definition of hydraulic domains are shown in subsequent chapters.

The description in this chapter of test methods is important for understanding the hydraulic test results limitations, but also advantage of one method compared to another, concerning different hydrogeological modelling issues discussed in Chapter10.

The chapter also provides a brief overview of the quantity of available hydraulic data and is depth distribution.

Finally, the chapter summarizes some field and laboratory data of matrix properties that is of importance for the large-scale groundwater flow modelling, which will be presented in /Rhén et al. 2009/.

4.1 Available primary data

Table 4-1 lists the boreholes available within the regional model area. The logging and test methods as well as the core mapping procedures applied to the drill cores employed by SKB have developed significantly over the years and consequently the borehole data from the current site investigation period (2002–2007) are more comprehensive and also based on new methodologies. These data therefore constitute the corner stone of the results reported in this report. Some of the older data have been used for assessing properties of deformation zones (in some instances denoted DZ) and for assessing probable ranges of hydraulic properties for some rock domains (Götemar granite), properties of deformation zones, and in some cases properties of rock between deformation zones (using the 100 m test scale).

Table 4-2 lists the cored boreholes investigated with the Posiva Flow Log (PLF) method and the Pipe String System (PSS) method, respectively. PFL is used to measure 5 m sections (PFL-s) and fracture/feature specific transmissivities (PFL-f), see Section 4.3 for details. In the older boreholes, equipment similar to the PSS was used, but in some cases only steady-state tests were performed. The spatial distribution of PSS and PFL tests within different fracture domains (cf. Chapter 3) and elevation is shown in Figure 4-1 through Figure 4-4.

A number of laboratory tests on cores and borehole logging have also been made and selected results are presented in Section 4.2.

All new percussion-drilled boreholes in the Laxerma-Simpevarp area have been investigated with the HTHB method (combined pumping and impeller flow logging) in conjunction with drilling, except those showing a very poor total yield. Only a few percussion boreholes have been investigated with impeller flow logging or injection/pumping tests within limited test sections in boreholes using a dual-packer system. Therefore, observations during drilling (bit penetration rate, core losses and loss of drilling fluid circulation) are generally the only indications as to where there are possible conductive fractures and zones along percussion drilled boreholes.

Table 4-1. List of cored and percussion-drilled boreholes drilled from ground surface relative to different geographical locations within the Laxemar-Simpevarp area. Boreholes drilled during the site investigations are indicated "new" and those completed before the site investigations (before year 2002) are indicated "old". No. of core drilled boreholes: All boreholes (long boreholes/short boreholes). Long core holes: >300 m, Short core holes : < 300 m. NB. KLX27A included in the table.

Area	No. of core drilled boreholes	Kzzxxx	No. of percussion drilled boreholes	Hzzxx
Laxemar-new	44 (19/25)	KLX03–KLX29A	34	HLX10–43
Laxemar-old	2 (2/0)	KLX01–02	9	HLX01–09
Simpevarp-new (1)	5 (3/2)	KSH01A–KSH03	6	HSH01–06
Ävrö, new	2 (1/1)	KAV04A,B	6	HAV09–14
Ävrö-old	3 (1/2)	KAV01–03	8	HAV01–08
Äspö-old	17 (13/4)	KAS01–17	25	HAS01–25
Hålö, Mjälen -old	2 (1/1)	KBH01–02	6	HBH01–05, HMJ01
Götemar granite-old	3 (3/0)	KKR01–03	0	

(1): There are a few boreholes also near the CLAB facility on the Simpevarp peninsula, but they are all fairly short.

Table 4-2. List of PFL and PSS tests in the Laxemar-Simpevarp area made in boreholes from ground-surface. PSS: Test scale 100 m, 20 m and 5 m. (KLX27A included in the table.) The model version Laxemar 1.2 was mainly based on the KAV, KSH and KLX01–04 boreholes. KLX05–KLX29A were drilled and investigated after data freeze for model version Laxemar 1.2.

Area	No. of PFL tested borholes. PFL: All (PFL-s/ PFL-f).	PFL-s. Test scale (m)	PFL tested boreholes Kzzxxx (9)	No. of PSS (and similar tests) tested boreholes (1)	PSS (and similar tests). Test scales (m) (2) (9)	PSS (and similar tests) tested boreholes Kzzxxx (3) (9)
Laxemar-new	44 (42/44)	5 m	KLX03–KLX29A	43	**5** (KLX02, 04, 10, 11A, 12A, 15A, 17A, 18A, 19A, 21B, 27A), **20** (KLX02–07A, 08, 10, 11A–13A, 15A–21B, 27A), **100** (KLX02–10B, 11A–13A, 15A–24A, 26A, 27A, 28A)	KLX02–KLX29A
Laxemar-old	1 (1/0)	3	KLX02 (8)	2	**3** (KLX01), **30** KLX01), ca **200–500** (KLX02)	KLX01–02 (4)
Simpevarp-new	2 (2/2)	5	KSH01A–KSH02	3	**5** (KSH01A, 02), **20** (KSH01A, 02), **100**	KSH01A–KSH03
Ävrö, new	3 (2/3)	5	KAV01, KAV04A,B	1	**20**, **100**	KAV04A
Ävrö-old	0			3	**2** (KAV02), **10** (KAV01,03)	KAV01–03 (6)
Äspö-old	0			15	**3** (7 bh), **30**(2 bh), **100** (13 bh)	KAS01–17 (4)
Hålö, Mjälen -old	0			2	Ca **100**	KBH01–02 (7)
Götemar granite-old	0			3	**2**, **3**, **20**(KKR01)	KKR01–03 (6)

(1): Tests in boreholes, with any test scale.

(2): If no comments with brackets, all bh were tested with the test scale shown.

(3): If no note is made, then PSS was used.

(4): Airlift test, short pumping test or injection tests similar equipment as PSS.

(5): 20 and 100 m test scale made systematically in borehole. 5 m tests limited to depth interval –300 to –700 m.

(6): Injection test with similar equipment as PSS.

(7): Airlift test or short pumping test.

(8): Flowing features between 200 to 1,000 m bh-length has been assessed based on Boremap data, BIPS and PFL-s data.

(9): If several boreholes have been drilled from the same drill site they are named with A, B etc (e.g. KLX11A, KLX11B. KLX11C etc). In some cases one short borehole B have been drilled near a longer borehole but near KLX10, KLX09A and KLX11A 2/6/5 short boreholes, respectively, were drilled.

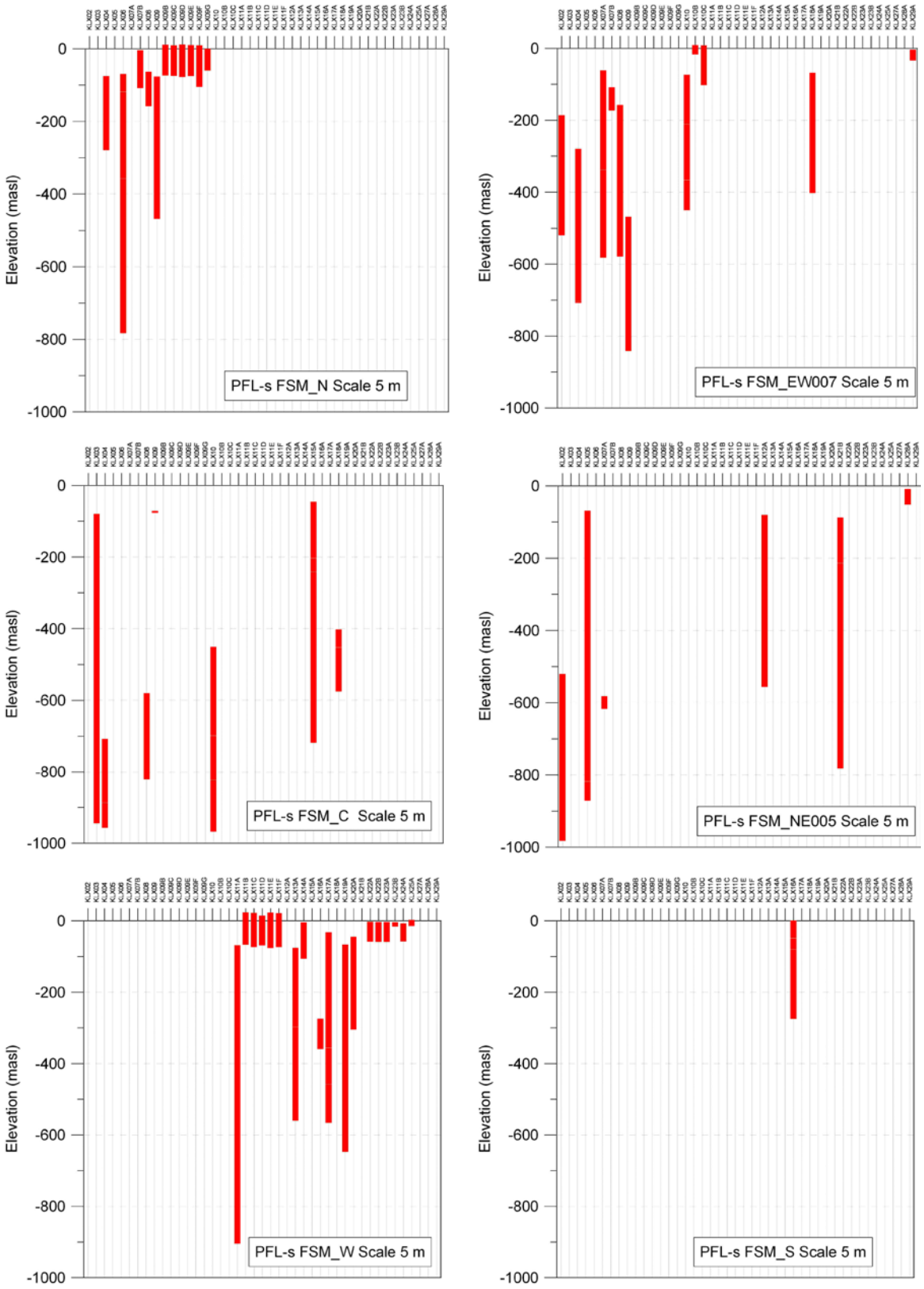

Figure 4-1. *PFL-s tests in different boreholes and fracture domains versus elevation.*

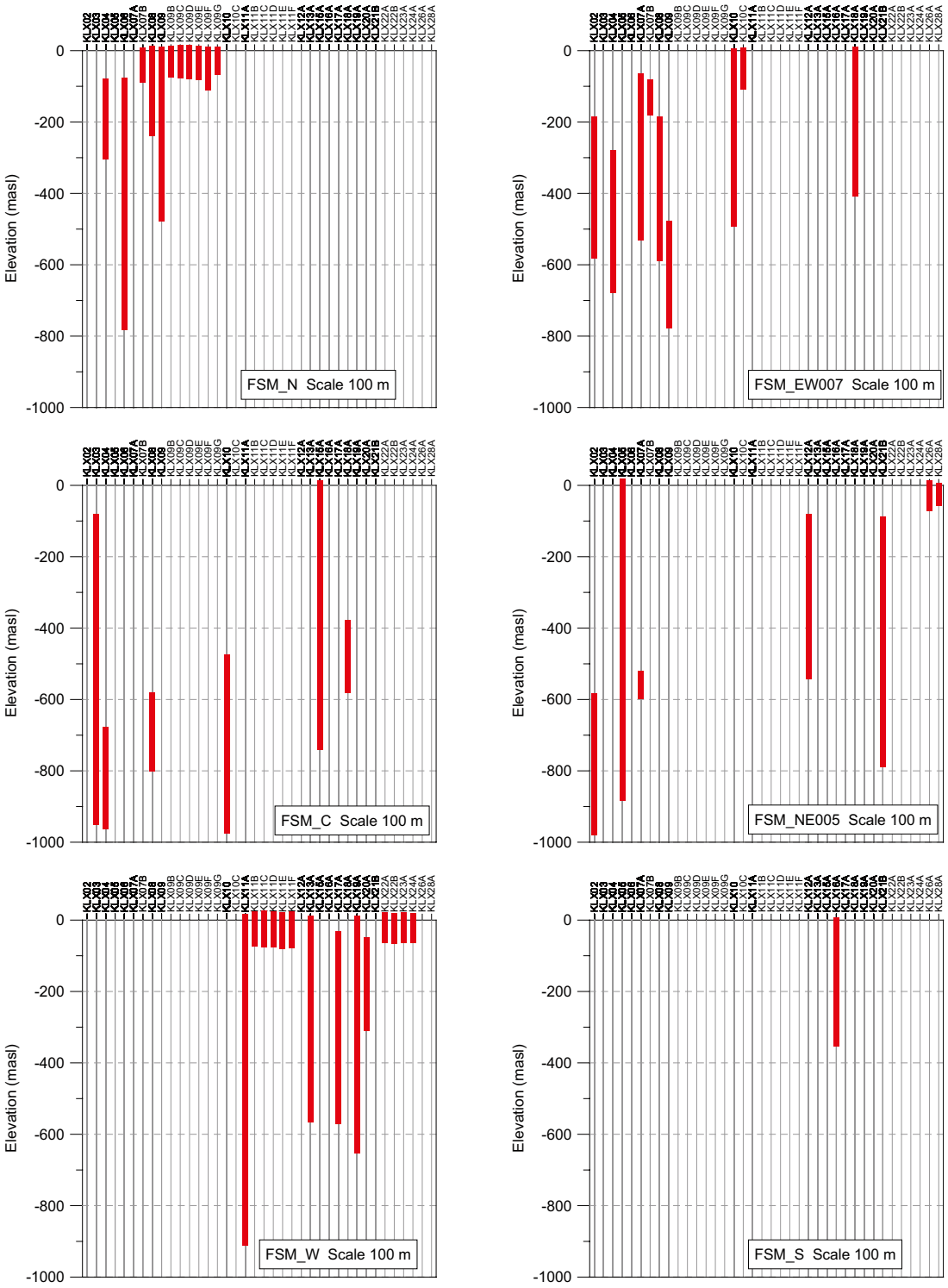

Figure 4-2. *PSS tests, test scale 100 m, in different boreholes and fracture domains versus elevation.*

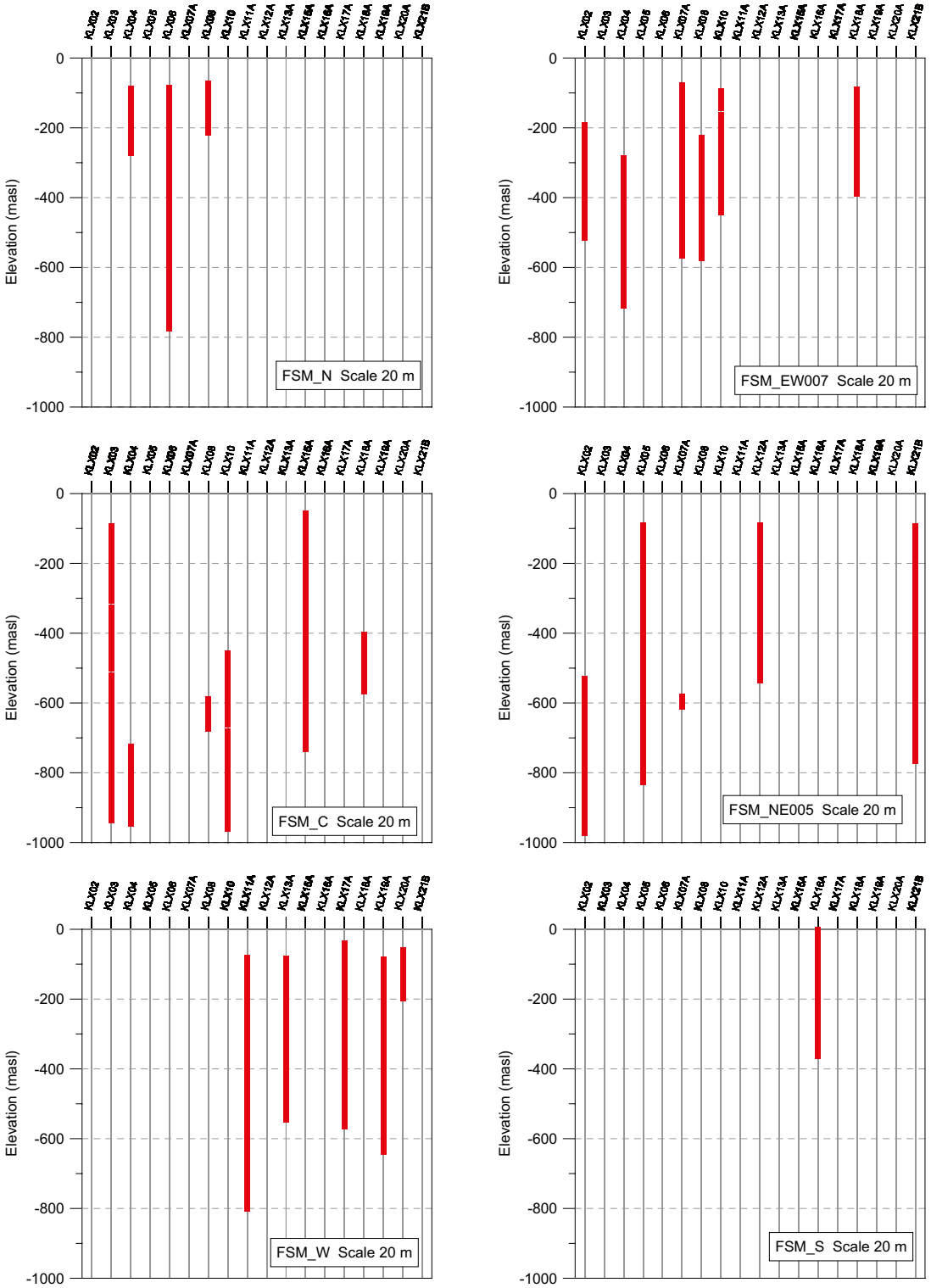

Figure 4-3. *PSS tests, test scale 20 m, in different boreholes and fracture domains versus elevation.*

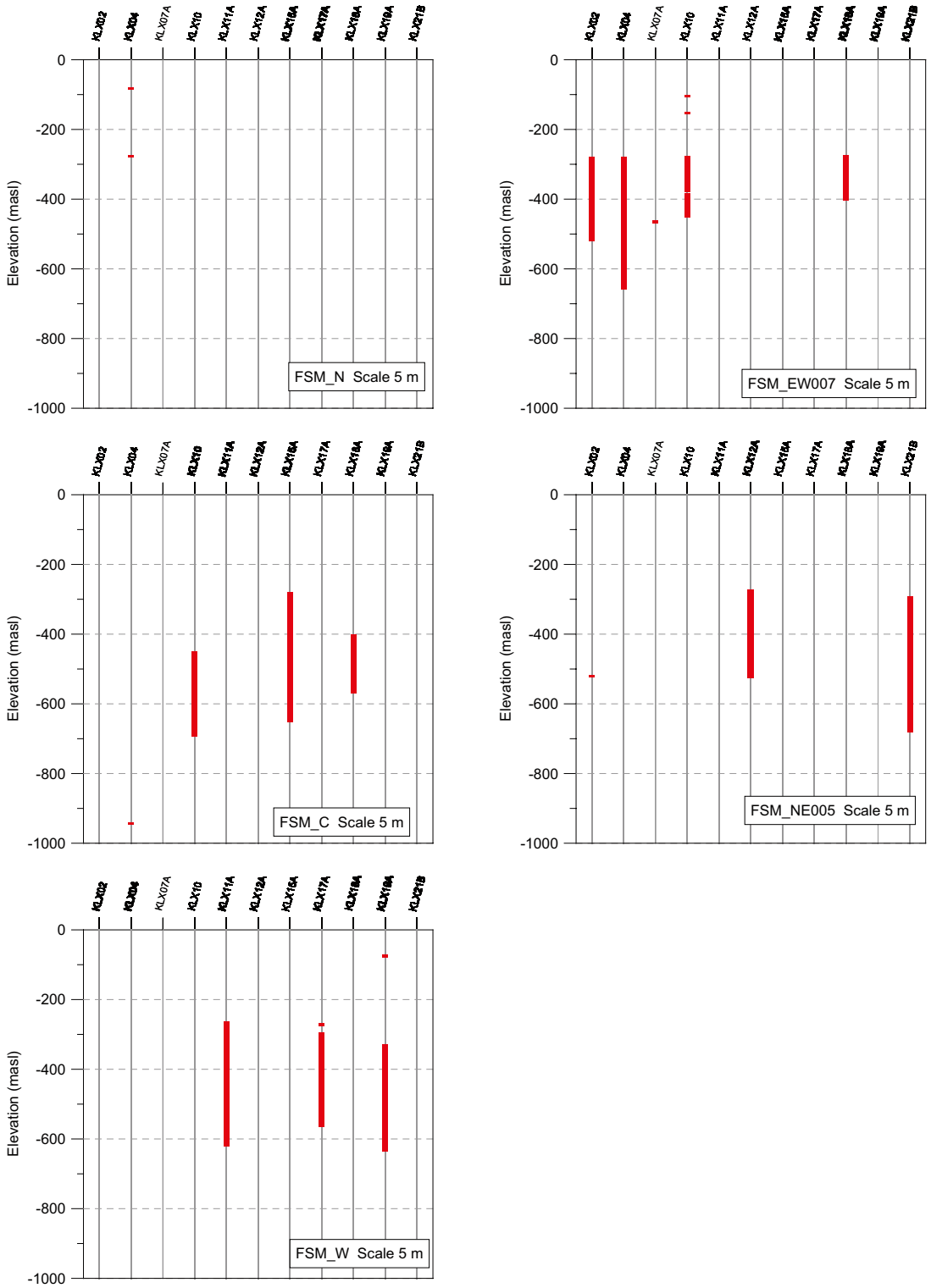

Figure 4-4. *PSS tests, test scale 5 m, in different boreholes and fracture domains versus elevation.*

Table 4-3. List of HTHB tests in the Laxemar-Simpevarp area performed in boreholes from ground-surface. Pumping or airlift tests: No. of boreholes (No. of bh with no test results).

Area	Pumping or airlift tests	Flow logging	Injection tests	Tested boreholes Hzzxxx	Comment
Laxemar-new	31 (0)	12		HLX13–43	
Laxemar-old	12 (2)	0		HLX01–12	HLX11 and HLX12 has not been tested
Simpevarp-new	6 (1)	4	3 tests in HSI03 and HSI04	HSH01–06	HSH06 was not tested
Ävrö, new	5 (0)	4		HAV09–14	
Ävrö-old	7 (1)	0		HAV01–08	HAV08 have not been tested
Äspö-old	21	0		HAS01–21	
Hålö, Mjälen -old	6 (1)	0		HBH01–05, HMJ01	HBH05 was not tested
Götemar granite-old	0	0	0	–	

4.2 Hydraulic tests of matrix properties

The hydraulic properties of the rock matrix plays a role when long time simulations are performed and the hydrogeochemical water composition is simulated, assuming conservative transport or involving chemical reactions, since exchange of chemical constituents between the flowing fracture system and the rock matrix can be significant. On a longer time scale, the water compositions in the flowing fractures and the rock matrix are affected by diffusion between matrix and fractures driven by concentration gradients. The matrix properties are therefore important for the paleohydrogeological modelling and there are results available from laboratory measurements of the water composition of the matrix water to compare with simulation results. Hydraulic diffusivity for the rock matrix, in terms of formation factor, is also presented in this section based on *in situ* resistivity logging.

Laboratory measurements have been made to estimate matrix properties. In /Vilks 2007b/ methods for measuring the matrix permeability and results at different confining pressures are reported.

In /Gustavsson 2006/ results from laboratory measurements on rock samples and drillcores are presented for:

- matrix porosity (defined as open porosity in SS-EN 1936),
- matrix diffusivity (equivalent to effective diffusivity),
- BET, specific surface area,
- CEC, cation exchange capacity,
- sorption coefficients for a number of combinations of rock materials, radionuclides and groundwater compositions.

/Gustavsson 2006/ presents measurement methods and data from the cored boreholes KSH01A, KSH01B, KSH02, KSH03A, KLX02, KLX03, KLX04, KLX05, KLX06, KLX07A, KLX08, KLX10, KLX11A, KLX12A and KLX13A. Matrix porosity applicable to Laxemar conditions is compiled below. A more complete presentation of data than that in /Gustavsson 2006/ is provided in /Selnert et al. 2007, 2009/.

/Waber et al. 2009/ reports results of laboratory tests on pore water composition.

The formation factor estimated from borehole logging can be found in /Crawford and Sidborn 2009/.

4.2.1 Matrix permeability

The matrix permeability of intact rock core samples has been estimated at various confining pressures /Vilks 2007b/ using the HPRM apparatus, described by /Drew and Vandergraaf 1989/. The HPRM consists of a core holder assembly, which is placed in a pressure vessel that can be operated with a maximum pressure of about 17 MPa. The core samples, with lengths of 0.5 to 2.0 cm, were placed between two stainless steel cylinders, see Figure 4-5

Six core samples were taken from borehole KLX03 at borehole lengths ranging from about 355 m to 978 m. The matrix permeability measurements were conducted at AECL's Whiteshell Laboratories, Canada, using a range of confining pressures to simulate *in situ* burial conditions. Measured permeability values in fracture free samples ranged from $7 \cdot 10^{-24}$ to $1 \cdot 10^{-19}$ m^2, corresponding to hydraulic conductivity values of $6 \cdot 10^{-17}$ to $1 \cdot 10^{-12}$ m/s, respectively. The presence of a fracture in one sample increased the permeability to $1 \cdot 10^{-16}$ m^2.

The effect of confining pressure on permeability measurements is illustrated in Figure 4-6. Note that sample LAX-1 is not included in this figure because the confining pressure for this sample did not go beyond 7 MPa. When the confining pressure was increased from 2 MPa to 15 MPa most samples displayed reductions in permeability that ranged from a factor 4 to 154. This suggests that the permeability of the rock samples may have been altered by stress relief and/or damage due to drilling.

The estimated permeabilities increase with sample depth, possibly because with increasing depth and confining pressure there is more sample alteration during drilling. The permeabilities values measured parallel to the core axis were higher than permeabilities measured normal to the core axis by factors of 4 to 19. This difference can possibly be interpreted as an effect of sample disturbance (stress unloading, widening of micro-cracks, and possibly formation of new micro-cracks – parallel to the core axis) and damage due to drilling increases longitudinal permeability compared to transverse.

Table 4-4 and Table 4-5 show sample data and average permeability and conductivity values for confining pressures greater than 14 MPa, which are assumed to be more representative of *in situ* conditions.

Corresponding measurements on samples from Forsmark, reported in /Vilks 2007a/ show permeability values ranging from $6 \cdot 10^{-22}$ to $6 \cdot 10^{-19}$ m^2, corresponding to hydraulic conductivity values of $5 \cdot 10^{-15}$ to $5 \cdot 10^{-12}$ m/s, respectively. Permeability measured normal to the core axis was a factor 3 to 5 lower than measured parallel to the core axis.

The LTDE-SD (Long term diffusion experiment) at Äspö HRL (elevation around –400 m) measured the permeability of a core sample at the same laboratory as above and the results were similar to the figures for samples from KLX03; $4.7 \cdot 10^{-21}$ m^2 (K= $4.1 \cdot 10^{-14}$ m/s) /Vilks 2005/.

Figure 4-5. *Rock core sample enclosed by end pieces of stainless steel cylinders to be used in a permeability measurement. Reproduced from /Vilks 2007b/.*

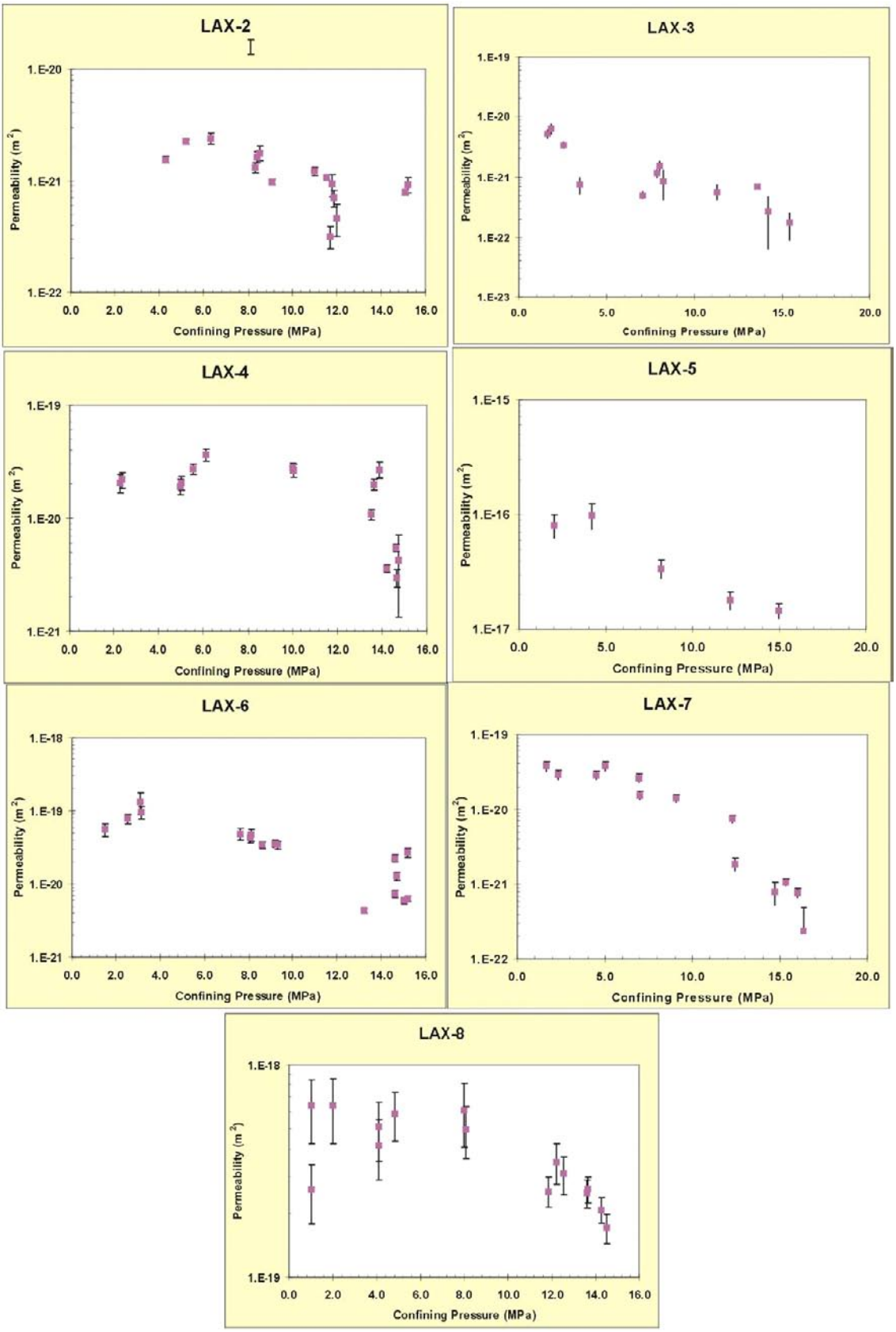

Figure 4-6. *Effect of confining pressure on matrix permeability. From /Vilks 2007b/.*

Table 4-4. Sample positions along the borehole /Vilks 2007b/.

Sample	Core sample	Borehole length (m)	Rock type	
LAX -1*	KLX03–5	355.66	Ävrö granite	Cut **parallel** to core axis
LAX-2	KLX03–8	524.63	Ävrö granite	Cut **parallel** to core axis
LAX-3	KLX03–9	590.12	Ävrö granite	Cut **normal** to core axis
LAX-4	KLX03–9	590.12	Ävrö granite	Cut **parallel** to core axis
LAX-5	KLX03–12	803.21	Quartz monzodiorite	Cut **parallel** to core axis
LAX-6	KLX03–14	894.53	Quartz monzodiorite	Cut **parallel** to core axis
LAX-7	KLX03–14	894.53	Quartz monzodiorite	Cut **normal** to core axis
LAX-8	KLX03–16	979.78	Quartz monzodiorite	Cut **parallel** to core axis

Table 4-5. Average matrix permeability and corresponding hydraulic conductivity for confining pressures greater than 14 MPa /Vilks 2007b/.

Sample	Sample size	Permeability (m^2)	Conductivity (m/s)
LAX -1*	5	$(4\pm4)\times10^{-23}$	$(3\pm4)\times10^{-16}$
LAX-2	2	$(8.6\pm0.9)\times10^{-22}$	$(7.5\pm0.8)\times10^{-15}$
LAX-3	2	$(2.2\pm0.7)\times10^{-22}$	$(1.9\pm0.6)\times10^{-15}$
LAX-4	4	$(4.1\pm1.1)\times10^{-21}$	$(3.6\pm0.9)\times10^{-14}$
LAX-5	1	1.45×10^{-17}	1.27×10^{-10}
LAX-6	6	$(1.4\pm0.9)\times10^{-20}$	$(1.2\pm0.8)\times10^{-13}$
LAX-7	4	$(7.2\pm3.5)\times10^{-22}$	$(6.3\pm3.1)\times10^{-15}$
LAX-8	2	$(1.9\pm0.3)\times10^{-19}$	$(1.7\pm0.2)\times10^{-12}$

* Average for confining pressures from 1.7 to 7.0 MPa.

4.2.2 Matrix porosity

Results of matrix porosity measurements are reported in /Gustavsson 2006/. The statistics of the matrix porosity, based on division of the bedrock in Hydraulic Rock Domains (HRD) and depth zones used for the hydrogeological DFN model (see Chapter 9), are shown in Figure 4-7 to Figure 4-9 and Table 4-6. In Appendix 1 the corresponding statistics based on rock domains (RSM) are shown. Some core samples have been collected in borehole sections mapped as deformation zones; either deterministically modelled deformation zones or minor deformation zones (MDZ). The few core samples within minor deformation zones are included in the statistics for rock matrix between the deterministic deformation zones.

As can be seen in Figure 4-8 the porosity is clearly lognormally distributed and there does not seem to be any depth dependence. Reported matrix porosity ranges from c. 0.01% to 6%, with geometric means of 0.13–0.37% for HRDs (between deterministic deformation zones) and 0.40% within deformation zones, cf. Table 4-6. The probability distributions indicate that 95% of the population is expected to be within a range of 0.01–1.4% for HRDs and within a range of 0.06–2.5% within deterministic deformation zones. The hydraulic rock domains HRD_B-C, HRD_C and HRD_EW007 have a rather similar geometric mean but the standard deviation decreases in order: HRD_B-C → HRD_C → HRD_EW007. HRD_N has a higher geometric mean and lower standard deviation compared to HRD_B-C, HRD_C and HRD_EW007 but the sample size is small, cf. Table 4-6. HRD_W has a lower geometric mean matrix porosity and a higher standard deviation compared to HRD_B-C, HRD_C and HRD_EW007 but it is noted that the sample size is rather small.

In /Waber et al. 2009/ the water-loss porosity values of samples on rock matrix are in the range ca. 0.2–1%, which is in a similar range as those presented in Table 4-6.

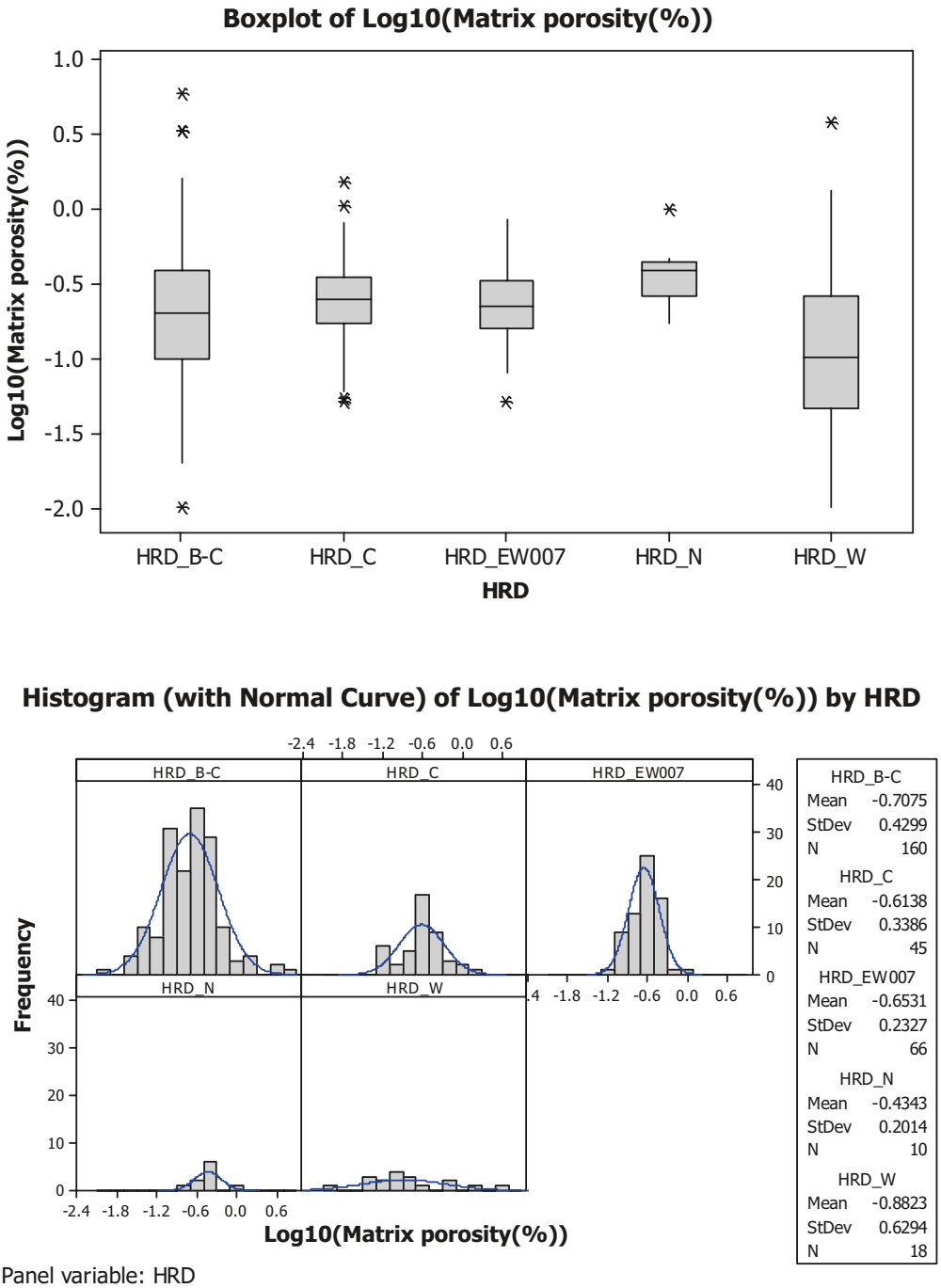

Figure 4-7. *Matrix porosity outside the deterministic deformation zones. A few core samples are within borehole sections mapped as "Minor deformation zones". Based on data presented in /Gustavsson 2006/.*

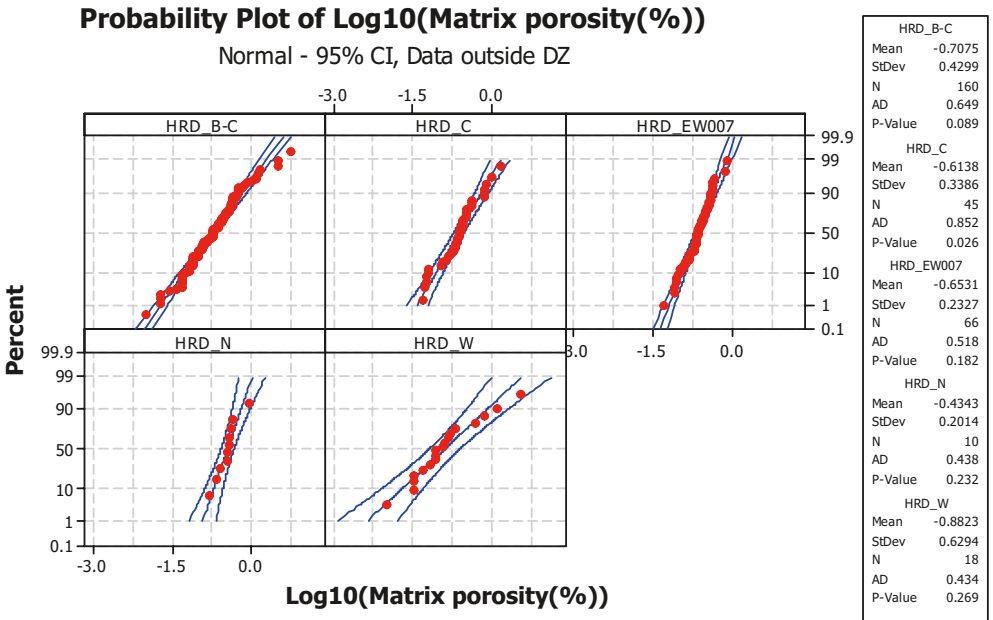

Panel variable: HRD

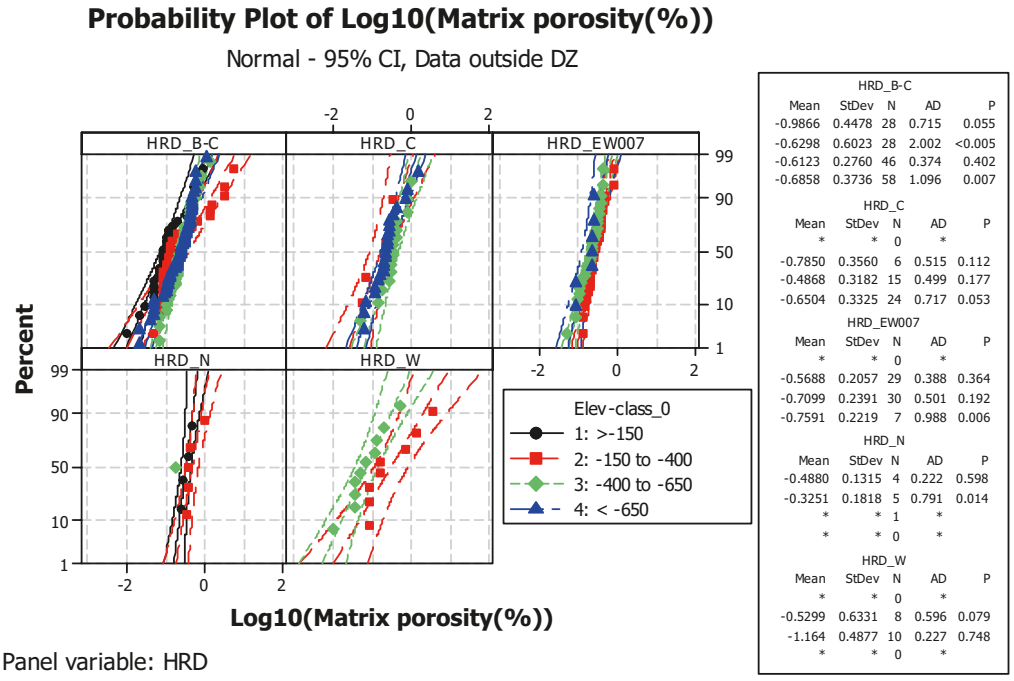

Panel variable: HRD

Figure 4-8. *Matrix porosity outside the deterministic deformation zones. A few core samples are within borehole sections mapped as "Minor deformation zones". Based on data presented in /Gustavsson 2006/.*

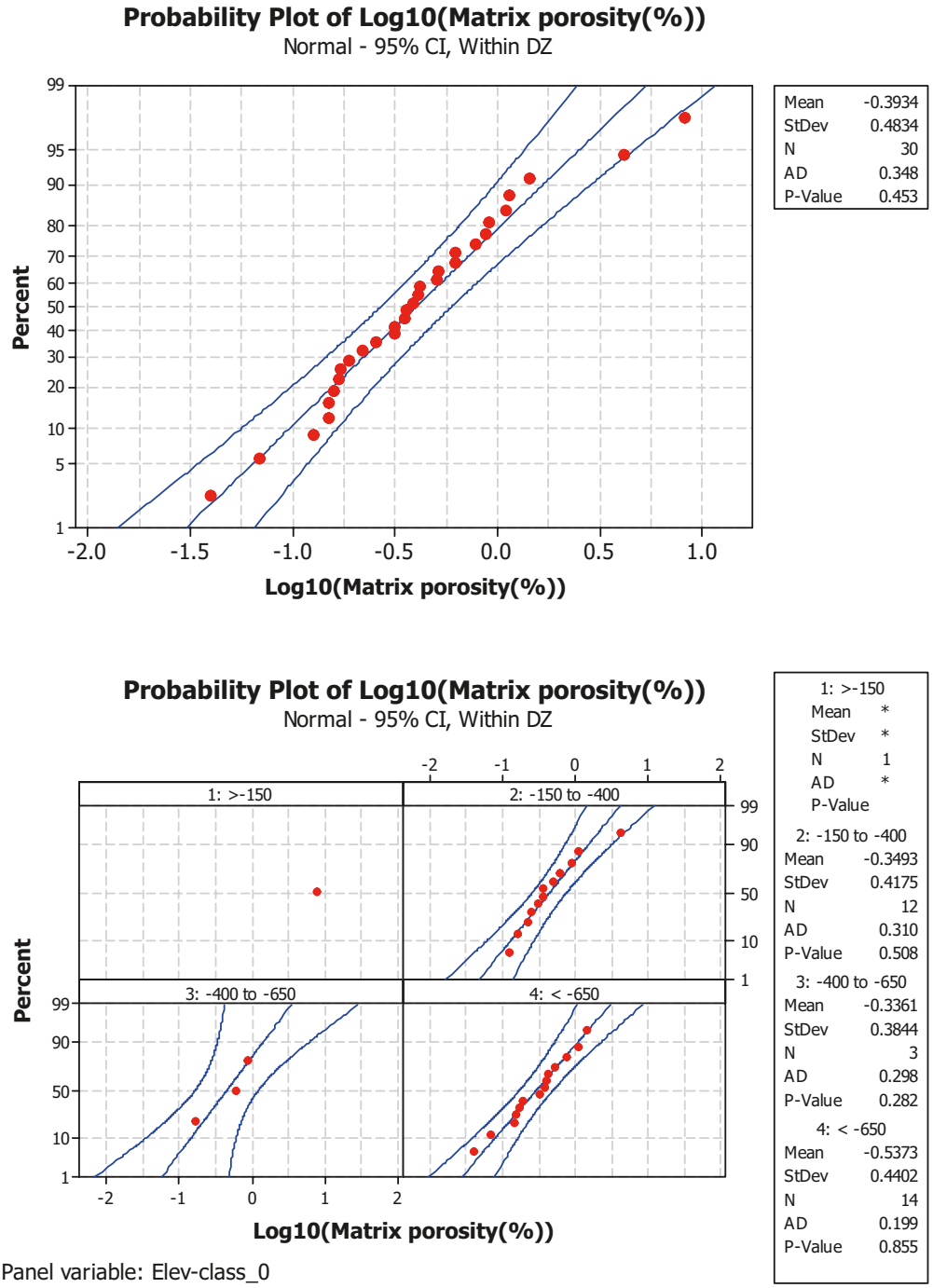

Figure 4-9. *Matrix porosity inside the deterministic deformation zones. Based on data presented in /Gustavsson 2006/.*

Table 4-6. Matrix porosity of rock between the deterministic deformation zones (A few core samples are within borehole sections mapped as "Minor deformation zones") and inside the deterministically defined deformation zones. Confidence interval for Mean Log10(n). Based on data presented in /Gustavsson 2006/.

Object	Data type	Depth interval (masl)	Sample size	Geom. Mean n (%)	Mean $Log_{10}(n)$ (n: %)	STD $Log_{10}(n)$ (n: %)	95% Conf. Int. $Log_{10}(n)$ Low (n: %)	95% Conf. Int. $Log_{10}(n)$ High (n: %)	Arithmetic mean (estimate from log-normal distr.) E(x) (%)
HRD_B-C	Between DZ	> –1,000	160	0.20	–0.71	0.43	–0.77	–0.64	0.32
HRD_C	Between DZ	> –1,000	45	0.24	–0.61	0.34	–0.72	–0.51	0.33
HRD_EW007	Between DZ	> –1,000	66	0.22	–0.65	0.23	–0.71	–0.60	0.26
HRD_N	Between DZ	> –1,000	10	0.37	–0.43	0.20	–0.58	–0.29	0.41
HRD_W	Between DZ	> –1,000	18	0.13	–0.88	0.63	–1.19	–0.57	0.38
All HRD	DZ	> –1,000	30	0.40	–0.39	0.48	–0.57	–0.21	0.75

4.2.3 Matrix diffusivity

The matrix diffusivity measured in laboratory is presented in /Gustavsson 2006/. Data indicate that the effective diffusivity (D_e) is generally within the range $10^{-14} – 10^{-12}$ m^2/s.

In /Waber et al. 2009/ the D_e estimates are in the range $10^{-13} – 10^{-12}$ m^2/s for chloride, based on out-diffusion experiment.

4.2.4 In situ formation factor

Resistivity logging in the cored boreholes has been used to estimate the formation factor. The effective diffusivity, D_e (m^2/s), can be estimated as the Formation factor, F (–), multiplied by the free diffusivity in water, D_w (m^2/s). The statistics of the measured formation factors evaluated from site specific borehole logging data from Laxemar are presented in /Crawford and Sidborn 2009/. Formation factors derived from *in situ* measurements are empirically corrected for measurement bias and represent "rock matrix" (i.e. ≥ 0.5 m distant from the nearest mapped, open fracture). The data include rock from the HRD and HCD (deterministic deformation zones) considered together.

The mean value of formation factors are approximately within the in the range $8 \cdot 10^{-6}$ to $2 \cdot 10^{-5}$ (–) for different rock types. With the free diffusivity in water D_w set to $1.1 \cdot 10^{-9}$ m^2/s (at 12°C according to /Crawford 2008/) the effective diffusivity (in terms of geometric mean) is in the range $1 \cdot 10^{-14}$ to $2 \cdot 10^{-14}$ (–).

4.3 Hydraulic tests conducted in cored boreholes

4.3.1 Hydraulic test methods

Most of the cored boreholes have been characterised hydraulically with both the PFL-s and PFL-f methods as well as the PSS method in order to allow for consistency checks of the hydraulic data acquired from repository depth. During drilling, the wireline probe was used to make transient tests with test scale ca 100 m to get preliminary data /Rhén et al. 2006/.

The two test methods PFL and PSS have different pros and cons. In particular, it is important to recognise the significant differences between the PFL and PSS methods in terms of field operation, spatial resolution and lower measurement threshold (detection limit). It is also important to recognise the fairly intricate evaluation procedure used for the interpretation and reporting of transmissivity

data for the PSS method. In summary, all these differences combined have a profound impact on the resulting transmissivity values and their subsequent usage in hydrogeological modelling. In short, the PFL-method measures hydraulically connected fractures that connect to some distant boundary. The PSS-method characterise hydraulically connected fractures near the tested borehole, with the implication that in some of the tests the conductive fractures may just be a local cluster of fractures not connected to the surroundings, see Chapter 2.

PFL

Schematic drawings of the PFL (Abbreviation for *Posiva Flow Log*) equipment used in Laxemar are shown in Figure 4-10 and Figure 4-11. Two different measurement strategies have been used, named here PFL-s and PFL-f. The PFL-s provides an estimate of the transmissivivity within a certain test section length, in the Laxemar case 5 m, that is moved stepwise 0.5 m. PFL-s (s stands for section) also provides the undisturbed flow rate distribution with indicated flow direction (in or out of the borehole) along the borehole. The PFL-f (f stands for fracture or feature) method is a geophysical logging device developed to detect *continuously flowing fractures* in sparsely fractured crystalline bedrock by means of difference flow logging, see Figure 4-10, using a 1 m test section that is moved stepwise 0.1 m. Flow rate is measured either with the thermal dilution method or using the thermal pulse method /Pöllänen et al. 2007/. The single point resistance electrode is important for the length correction of the measured section, as it is possible to detect the length markers made during drilling at every 50 m along the borehole, but also enables an indication of the precise location of conductive fractures within a few decimetres or better. However, most important for the length correction is the calliper tool and single point resistance measurements applied on the PFL-probe as a first part of a logging sequence, to obtain a calibration function (length correction) using the single point resistance measurements applicable to subsequent measurements in the borehole, including flow rate measurements. The physical limitations of the measurement device and the principles for operation are explained in detail in e.g. /Pöllänen et al. 2007/.

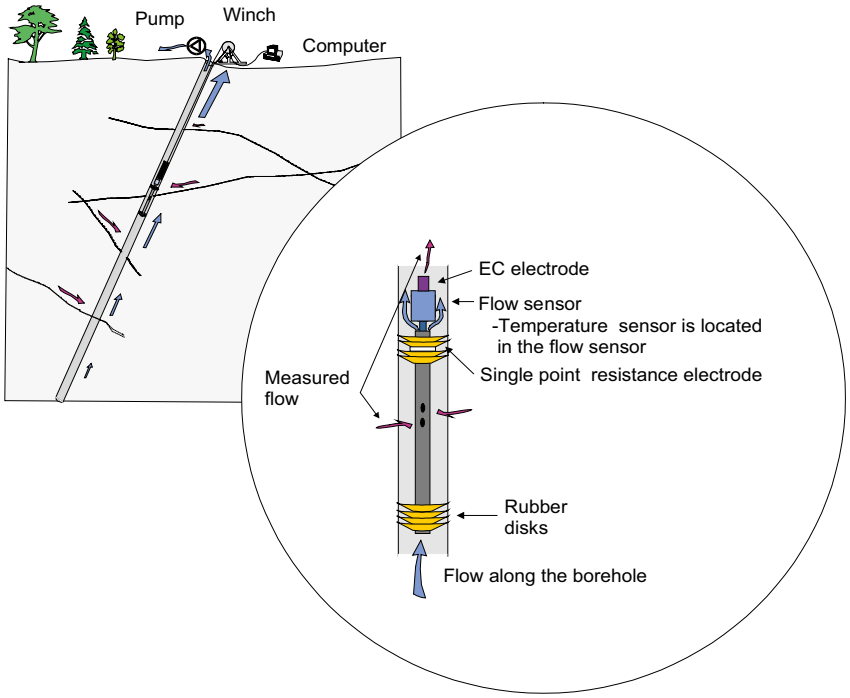

Figure 4-10. *PFL-logging tool. Schematic drawing of the down-hole equipment used for difference flow logging in the Laxemar-Simpevarp area. Reproduced from /Pöllänen et al. 2007/.*

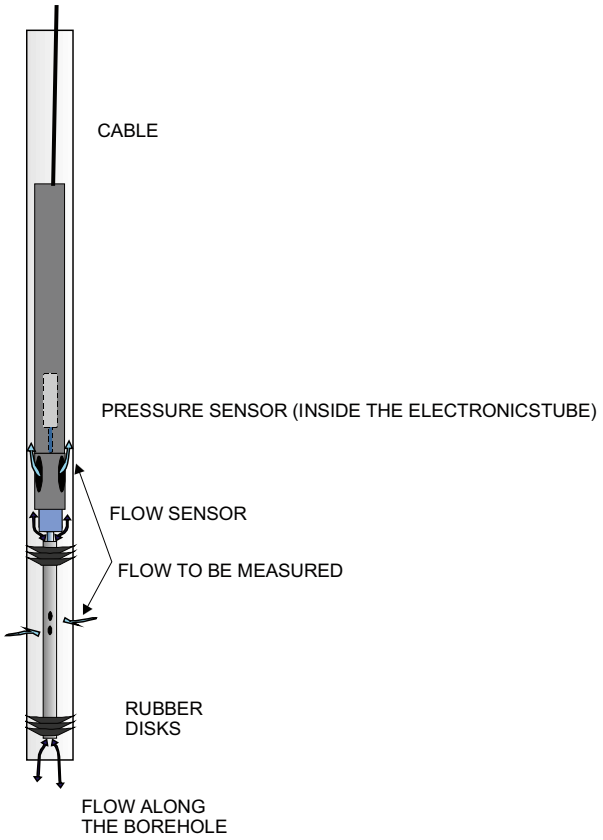

Figure 4-11. *PFL-logging tool. The absolute pressure sensor is located inside the electronics tube and is connected through a tube to the water in the borehole section. Reproduced from /Pöllänen et al. 2007/.*

The flowing fractures detected with the so called PFL-f method have previously been called "flow anomalies", or simply "PFL-anomalies", but "flowing feature/-s detected by PFL"or "PFL-f features" are preferred and used here.

The PFL-s and PFL-f measurements are based on c. one week of pumping (~ 10,000 minutes), where the entire borehole acts as a line sink. The test configuration means that a radial, steady-state flow regime is prevailing.

The accuracy of the flow rate measurements is estimated to ±10% of actual reading, the accuracy of the absolute pressure in the test section to ±0.01% of full scale (range 0–20 MPa) and the accuracy of the groundwater level sensor in the borehole to ±1% of full scale (range 0–0.1 MPa) /Pöllänen et al. 2007/.

The detection limit varies depending on the *in situ* conditions. As a rule of thumb, the lower detection limit of the flow meter device used is c.30 mL/h ($0.833 \cdot 10^{-8}$ m^3/s) for thermal dilution method which is fast and generally used. For the thermal pulse method the lower detection limit of the flow meter device used is c.6 mL/h ($0.167 \cdot 10^{-8}$ m^3/s) but the latter method was only used every 5^{th} m (every 10^{th} measurement when the test section is moved 0.5 m) for PFL-s when natural (undisturbed) flow was measured. Flow direction (in or out of the borehole) is also documented when the natural (undisturbed) flow rate is measured. Drilling debris and gas bubbles may disturb the measurements, and in such cases a practical measurement limit is estimated from the noise level found in the measurements. However, in some cases with good measurement conditions, flowing features can be observed below 30 mL/h with the thermal dilution method, but of course the estimated flow rate is uncertain. During pumped conditions the drawdown in the boreholes is generally c. 10 m, but if the upper measurement limit is reached (300,000 mL/h=$0.833 \cdot 10^{-4}$ m^3/s) for a test section, the test section is later repeatedly measured with a smaller drawdown.

In a few cases water has been injected instead of pumped, to enable measurements in the upper part of the borehole close to the ground surface. Furthermore, PFL-f is only measured during pumped conditions as it is judged that data from the non-pumped phase of the PFL-s can be used to extract the parameters needed for calculation of the PFL-f transmissivities.

The PFL-f method has the following characteristics:

- A radial, steady-state flow regime prevails around each test interval. The test interval is probably small enough to mostly characterise the flow from individual fractures. By combining the PFL-f method with the results from the borehole imaging system (BIPS) and the geological mapping of the core, the orientation of the flowing fracture can be assessed. The maximum uncertainty in position along the borehole of the PFL-f method is c. ± 0.3 m but generally the position is judged to be within ±0.2 m /e.g. Wikström et al. 2007a/.
- There are no problems with flowing fractures short-circuiting with the borehole above and below the rubber discs since the borehole acts as a line sink. Problems with the rubber discs may arise however, e.g. when there are significant cavities in the borehole wall or large axial flows in the borehole below the test interval.
- The flow rate of isolated fractures or isolated clusters of fractures connected to the pumped borehole are not investigated; that is, only connected open fractures with a sufficient flow rate are detected and analysed.
- Fracture transmissivity values are only defined and reported to the SICADA data base for those 0.1 m long test intervals where measurable flow rates are observed. Non-flowing test intervals with open fractures are not assigned a threshold value for PFL-f. This means that the numbers of flowing features is most likely truncated at the measurement limit for PFL-f, and hence underestimated.

The PFL-f transmissivity $T_{PFL\text{-}s}$ and $T_{PFL\text{-}f}$ is calculated using Thiem's equation /Thiem 1906/, which assumes a radial, steady-state flow regime with a known radius of influence (for evaluation of the transmissivity from PFL tests it is assumed that the radius of influence divided by borehole radius is; R_0/r_w=500. With r_w=0.038 m, R is estimated at 19 m). The undisturbed head (h_0) in the borehole test section (using a pressure sensor at test section) and natural flow into/out from the tests section (Q_0) are measured initially with the PFL-s method, followed by pumping of the entire borehole during which the head (h_1) in the borehole test section and the flow into the tests section (Q_1) are measured. The transmissivity ($T_{PFL\text{-}s}$) within test section and the undisturbed formation head near the test section (h_i) are estimated with the equations below.

$$T_{PFL-s} = \frac{Q_{s0} - Q_{s1}}{h_1 - h_0} \cdot \frac{\ln(R_0/r_w)}{2 \cdot \pi} \qquad (4\text{-}1)$$

$$h_i = \frac{h_0 - h_1 \cdot (Q_{s0}/Q_{s1})}{1 - Q_{s0}/Q_{s1}} \qquad (4\text{-}2)$$

(With R_0/r_w=500; $\ln(R_0/r_w)/(2\cdot\pi)$=0.99).

As pointed out previously, the PFL-f metod is only performed during pumping and therefore Q_0 and h_0 from the PFL-s test is used for the transmissivity estimation according to the equation below:

$$T_{PFL-f} = \frac{Q_{s0(PFL-s)} - Q_{s1}}{h_1 - h_{0(PFL-s)}} \cdot \frac{\ln(R_0/r_w)}{2 \cdot \pi} \qquad (4\text{-}3)$$

Since the actual flow geometry, borehole skin effects, and actual radius of influence are unknown, transmissivity values should be taken as indicative of orders of magnitude. In summary, the practical transmissivity measurement limit varies depending on the actual field conditions, but the typical measurement limit for the conditions in Laxemar is c. $1\cdot10^{-9}$ m^2/s assuming 10 m drawdown. The upper measurement limit is approximately c. $1\cdot10^{-5}$ m^2/s assuming a drawdown of 10 m.

/Pöllänen et al. 2007/ note that the calculated hydraulic heads do not depend on geometrical properties (fracturing) but only on the ratio of the flow rates measured at different heads in the borehole. Hence, they should be less sensitive to unknown fracture geometry. A discussion of potential uncertainties in the estimation of transmissivity and undisturbed hydraulic head from PFL tests is provided in /Ludvigson and Hansson 2002/.

PSS

The PSS (*Pipe String System*) measurements apply the classic test approach known as constant-head injection within a test section limited within a double-packer system. A schematic drawing of the test equipment used in Laxemar is shown in Figure 4-12 and Figure 4-13. The PSS measurements are run with different test section lengths. The test section lengths and injection periods used in the Laxemar site investigations were 5, 20 and 100 m with corresponding injection times 20, 20 and 30 minutes, respectively. The evaluation of the flow-time envelope was made after 20–30 minutes of injection, which means that the duration of the PSS measurements is much shorter than for the PFL-f measurements.

The accuracy of the flow rate measurements is estimated to < ±1.5% of the actual reading for the flow rate range $60 \cdot 10^5$ –$60 \cdot 10^3$ mL/h ($1.67 \cdot 10^{-3}$ –$1.67 \cdot 10^{-5}$ m^3/s) and ±0.5–30% of actual reading for the flow rate range $60 \cdot 10^3$ –60 mL/h ($1.67 \cdot 10^{-5}$ –$1.67 \cdot 10^{-8}$ m^3/s), i.e. accuracy depends on the actual flow rate. The accuracy of the differential pressure in the test section is estimated to < ±5 kPa of used differential pressure 200 kPa /Harrström et al. 2006a/). As a rule of thumb, the lower detection limit of the PSS flow meter device used is c. 60 mL/h ($1.67 \cdot 10^{-8}$ m^3/s) defining the measurement limit for flow.

First the tests employing 100 m test sections were performed. For 100 m test-sections showing flow rates above the measurement limit for the flow, tests with 20 m test sections were performed. Subsequently the tests with a test section length of 5 m were performed in 20 m tests sections showing flow rates above the measurement limit for the flow. For the site investigations within Laxemar-Simpevarp area, PSS tests with a test scale of 5 m were only performed in the depth interval –300 m to –700 m, covering the foreseen repository depth.

The PSS method has the following characteristics:

- The test section is generally so long that several conductive fractures are investigated simultaneously. Their individual contribution or geometry cannot be inferred and distinguished without an additional set of assumptions of statistical nature.
- The flow regime (linear, radial, and spherical) and the state of flow (steady-state or transient) cannot be assumed with confidence, because the tested section acts more or less like one or several point sources. Hence, the flow regime and the state of flow must be analysed and evaluated using the entire flow-time envelope, preferably using time-derivates of the pressure.
- In places there may be problems with locally connected fractures short-circuiting the borehole above and below the inflatable packers (cf. Figure 4-13), in particular at locations where the fracture intensity is high.
- The transmissivity of some isolated fractures, or isolated clusters of fractures, connected to the test section may also be measured; that is, it is not only the interconnected open fractures (in the sense connected to a far-field conductive fracture network.) that are detected and analysed. The hydraulic diffusivity of the more compartmentalised parts of the fracture network is also investigated. In order to resolve the connectivity issue of distinguishing possible compartmentalised parts, the boundary effects must be evaluated and/or another methodology must be used.
- A test section transmissivity value is always defined and reported to the SICADA database regardless of whether a measurable flow rate or not was detected during the injection period. If the test section is estimated to have no flow, a transmissivity corresponding to the estimated measurement limit estimate is entered in SICADA and a value type flag indicates that it is a measurement limit value. The standard lower detection limit of the flow meter device used is c. 60 mL/h ($1.67 \cdot 10^{-8}$ m^3/s), which corresponds to a measurement limit transmissivity of c. $6.7 \cdot 10^{-10}$/$8.5 \cdot 10^{-10}$/$1.1 \cdot 10^{-9}$ m^2/s for test scales 5/20/100 m, respectively, and injection pressure of 200 kPa, when using Moye's formula for steady-state flow /Moye 1967/. However, sometimes the noise level is sufficiently low to allow definition of a test-specific lower measurement limit in the order of c. 20 mL/h (ca $0.5 \cdot 10^{-8}$ m^3/s), cf. e.g. /Harrström et al. 2006a/).

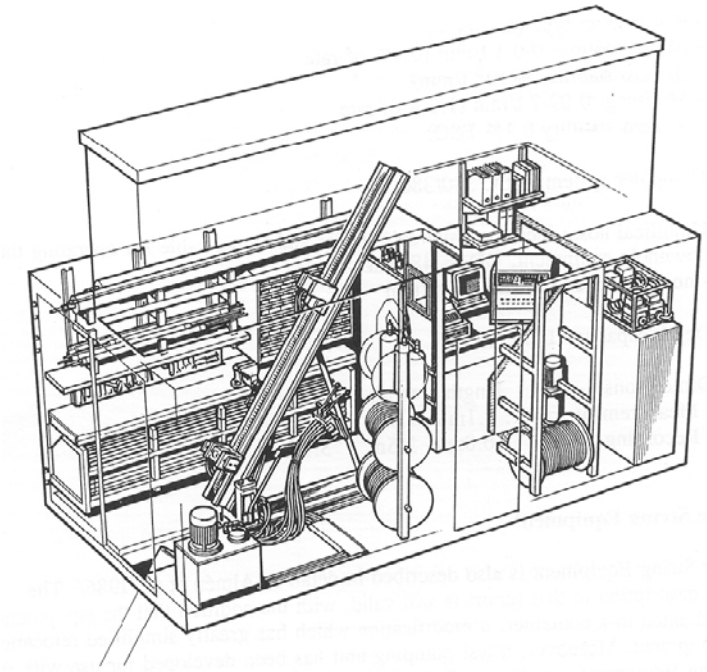

Figure 4-12. *A view of the layout and equipment of PSS2. From /Harrström et al. 2006a/.*

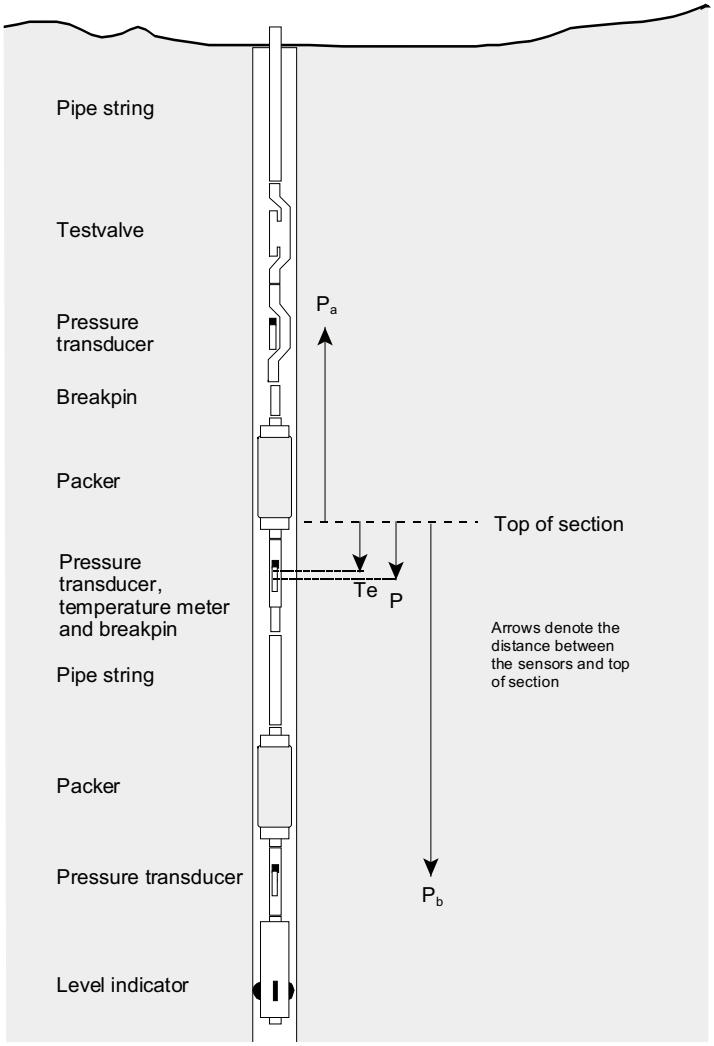

Figure 4-13. *Schematic drawing of the down-hole equipment in the PSS system. Reproduced from /Harrström et al. 2006a/.*

Two transmissivity values should be reported to SICADA for each PSS test conducted according to the methodology instructions for single-hole hydraulic testing; a steady-state transmissivity value T_M and a transient value T_T, regardless of the *in situ* borehole flow conditions. The steady-state transmissivity evaluation is based on the flow rate at shut-in time (c. 20/20/30 min for test scales 5/20/100 m, respectively) using Moye's formula /Moye 1967/. The base for /Moye 1967/ is the injection/pumping flow rate at the end of the injection/pumping period (Q) and head increase/decrease above natural head (Δh), test section length (L_w) and borehole radius (r_w) are the base for the transmissivity estimation based on /Moye 1967/.

$$T_M = \frac{Q}{\Delta h} \cdot \frac{1 + \ln\left(L_w / \left(2 \cdot r_w\right)\right)}{2 \cdot \pi} \qquad (4\text{-}4)$$

(With L_w=5/20/100 m and r_w=0.038 m; $(1+ \ln(L_w/(2 \cdot r_w)))/(2 \cdot \pi)$=1.67/1.89/2.14).

The transient transmissivity evaluation may employ several options. Ideally, the evaluation is made for the first acting radial part of the flow-time envelope using type curve interpretation methods derived by the petroleum industry and transferred to hydrogeology, e.g. AQTESOLVE /HydroSOLVE Inc. 2007/. If there exits no acting radial acting part, the test section transmissivity value is calculated using classic linear or spherical flow models. In case of very low-conductive sections, pulse tests have occasionally been performed. These tests are evaluated as pulse tests and are also reported in SICADA as pulse tests, T_P. If apparent boundary effects can be observed at shut-in time this is also reported to SICADA. The information stored in SICADA is accompanied by a recommendation regarding the best transmissivity value to be used for each test section, i.e. the steady-state transmissivity value or the transient transmissivity value. The recommended transmissivity values are denoted by T_{BC} (BC for "Best Choice") and are based on the transient evaluated transmissivity (T_T), if available; otherwise the steady-state transmissivity value (T_M) value is used. In case of very low transmissivity, only the transmissivity based on pulse-test analysis (T_P) is provided or an estimated measurement limit value is used as T_{BC}.

4.3.2 Transient and steady state evaluation of PSS tests

As described in previous sections, tests with PSS have been performed using 3 different test scales and in several boreholes. The individual single-hole tests are reported in /Enachescu and Rohs 2007a, b, Enachescu et al. 2006b, c, 2007a, b, c, d, e, f, Harrström et al. 2006a, b, Ludvigson et al. 2004, Rahm and Enachescu 2004a, b, c, d, e, f, 2005a, b, c, d/. The evaluation methods used are discussed in more detail in /Enachescu and Rahm 2007, Ludvigson et al. 2007/. Test results from KLX27A and transient evaluation of the PFL-pumping tests /Enachescu et al. 2008c, d/ were not available for evaluation.

In this section the parameters based on transient and steady state evaluation of the PSS tests are presented and discussed. In the next Section 4.3.3 the PSS and PFL tests are compared.

Skin factor

Wellbore skin is a concept developed by the petroleum industry to describe the hydraulic contact between a production well and the geological formation surrounding the well /Earlougher 1977/. A positive skin factor means, conceptually, that there is a resistance to flow (head loss) close to the well. Thus, a positive skin reduces the specific capacity of the well. A negative skin means the opposite; the hydraulic contact with the geological formation is enhanced near the well and the specific capacity is improved. The concept of skin is not readily transferred to fractured crystalline rock, in particular not a positive skin. However, the majority of the skin factors inferred from transient analyses of the 444/627/165 PSS tests performed in Laxemar, at test scales 5/20/100 m respectively, with PSS measurements in Laxemar-Simpevarp area have a negative skin, see Figure 4-14. The calculated skin factor has been corrected using the relation between the storage coefficient (S) and the evaluated transmissivity (T) as shown in Section 7.5. Originally the skin factor was reported using a preliminary assessed storage coefficient S, generally assumed to be 10^{-6} (–).

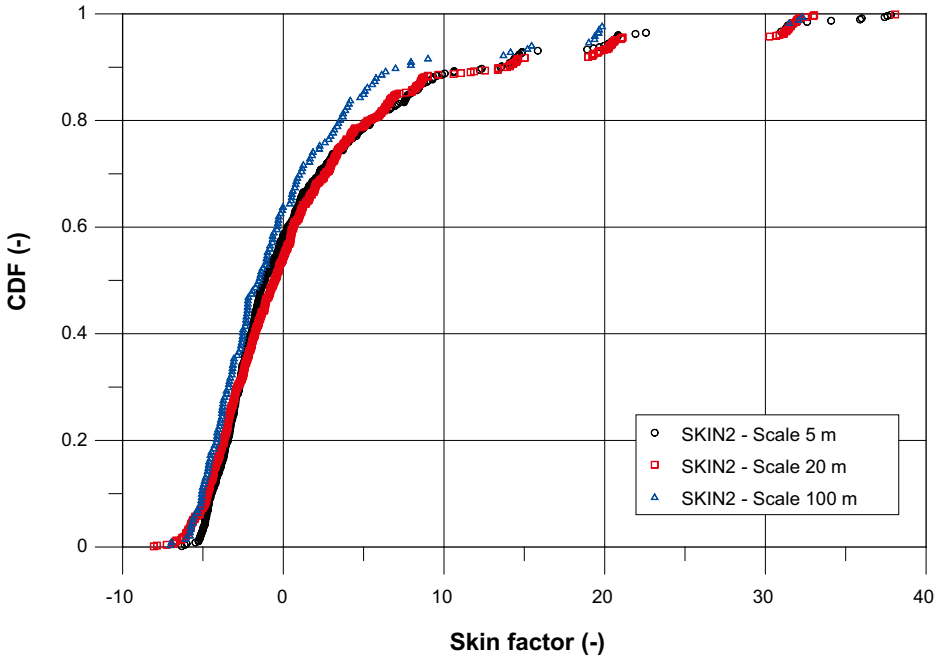

Figure 4-14. *Cumulative distribution plot of the skin factors inferred from transient analyses of 444/627/165 PSS measurements with 5/20/100 m test section length, during the investigations in Laxemar-Simpevarp area.*

From a site characterisation point of view, a negative skin factor is preferable since the radius of influence is enhanced; that is, the hydraulic testing senses the hydraulic properties of the bedrock farther away from the immediate borehole surroundings. In contrast, a positive skin factor can be detrimental for the testing since it not only restricts the radius of influence, but also endangers the transmissivity interpretation resulting in lower values than otherwise, being non-representative of the formation. The steady-state interpretations are particularly sensitive to positive skin. Figure 4-14 does not suggest that there is significant problem with large positive skin factors in Laxemar although positive skin factor is evident for a large number of the tests.

Boundary effects

It was previously mentioned that the flow condition at the shut-in time of the injection period is reported to SICADA. An index of three possible values (–1, 0, +1) is used to indicate whether *recharge boundary* (–1, tested feature connected to a feature with a higher transmissivity or an apparent constant head boundary), *infinitely acting* (0) or *barrier boundary* (+1, tested feature connected to a feature with a lower transmissivity or an apparent impermeable boundary), respectively, could be observed (indicated) after the time period for the transient transmissivity evaluation. Figure 4-15 shows a histogram of reported "apparent boundary effects" coupled to the 5, 20 and 100 m test-scales of the PSS tests conducted in Laxemar. The plot indicates that the tested feature acts as an infinite feature during the test duration for c. 45–55% of the tests. For c. 20–25% of the tests, a barrier boundary (or rather a more low conductive volume) is indicated after the first radial period, and for the remaining 25–30%, a recharge boundary (or rather a more high conductive volume) can be observed after the first radial period. Heterogeneity can thus be readily observed in the transient data.

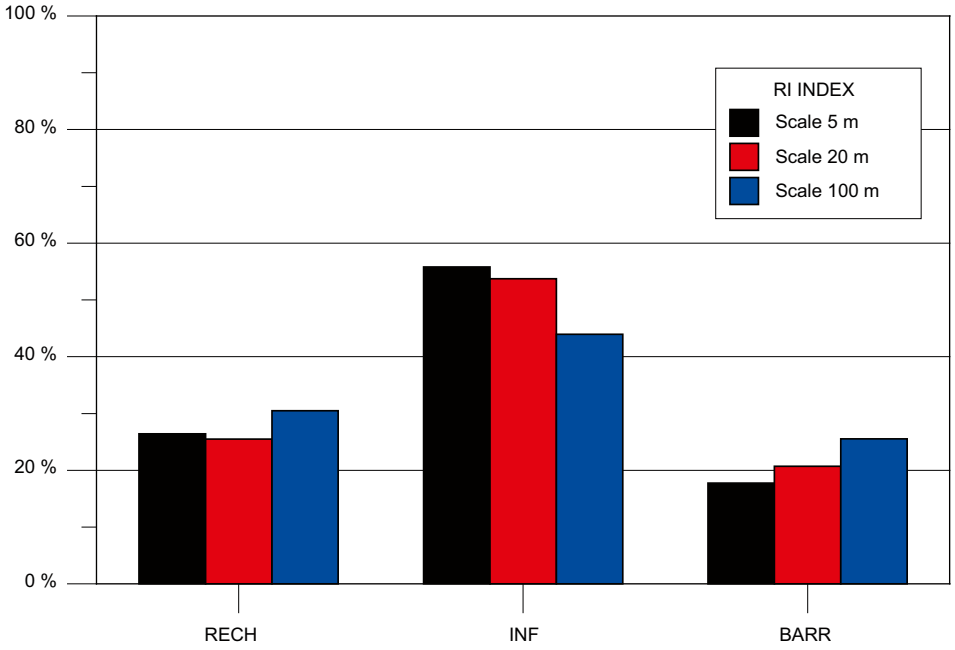

Figure 4-15. *Histogram of the "boundary effects" sensed (RECH: recharge boundary, INF: infinitely acting or BARR: barrier boundary) at the shut-in time for the 5, 20 and 100 m test scales PSS tests conducted. Data from the Laxemar local model volume.*

Cross-correlation of PSS transient versus steady state

In Figure 4-16 the transmissivities (T) based on transient evaluation (T-T) and steady state (T-M) are shown. As can be seen in the figure there is a tendency that for a low T-T the T-M is a bit larger than T-T, and for large values of T-T the T-M is smaller than T-T. The difference is most pronounced for test scales 5 and 20 m (also 8 tests in percussion holes with test scale 100 m are included in the data for "100 m-PSS").

This means that the positive skin observed mainly relates to the transmissivities T-T in the higher end. This can be observed also in Figure 4-24, looking at the PSS-xm (x in PSS-xm indicates scale 5, 20 or 100 m) curves for data based on T-BC that mostly are based on transient evaluation and PSS-Moye-xm that is based on steady state evaluated T, except for T evaluated as pulse tests (the later provides estimates of T in the lower region).

The generalised radial flow (GRF) approach proposed by /Barker 1988/ was used in an attempt to assess the role of fractional flow dimension and boundary effects for one borehole; KLX11A /Enachescu et al. 2006b/. GRF analysis was possible to perform on 35 tests (12/15/8 tests for test scales 5/20/100 m, respectively), see Figure 4-17. As can be seen, nearly all tests have a flow dimension between. 1.5 to 2.3, indicating that these tests are rather close to radial flow (flow dimension = 2), which both evaluation methods for PSS and PFL assumes. There is some tendency that the 5 m tests are less "canalised" (fewer data with lower flow dimension than 2) compared to the 20 m tests and perhaps 100 m tests, but one should remember that the sample sizes are small. The transmissivities evaluated with the GRF method (T-GRF) are fairly similar to T-T, which it should be when the flow dimension is around 2, see Figure 4-18. Low T-T values are coupled to a bit higher T-GRF values, which indicate that flow dimension below 2 is generally coupled to low transmissive features. High T-T values, on the other hand, do couple to slightly lower T-GRF, indicating flow dimension above 2 for these values. It should be remembered that values of T-GRF are always strongly linked to the interpreted flow dimension and are not comparable with the common definition of transmissivity.

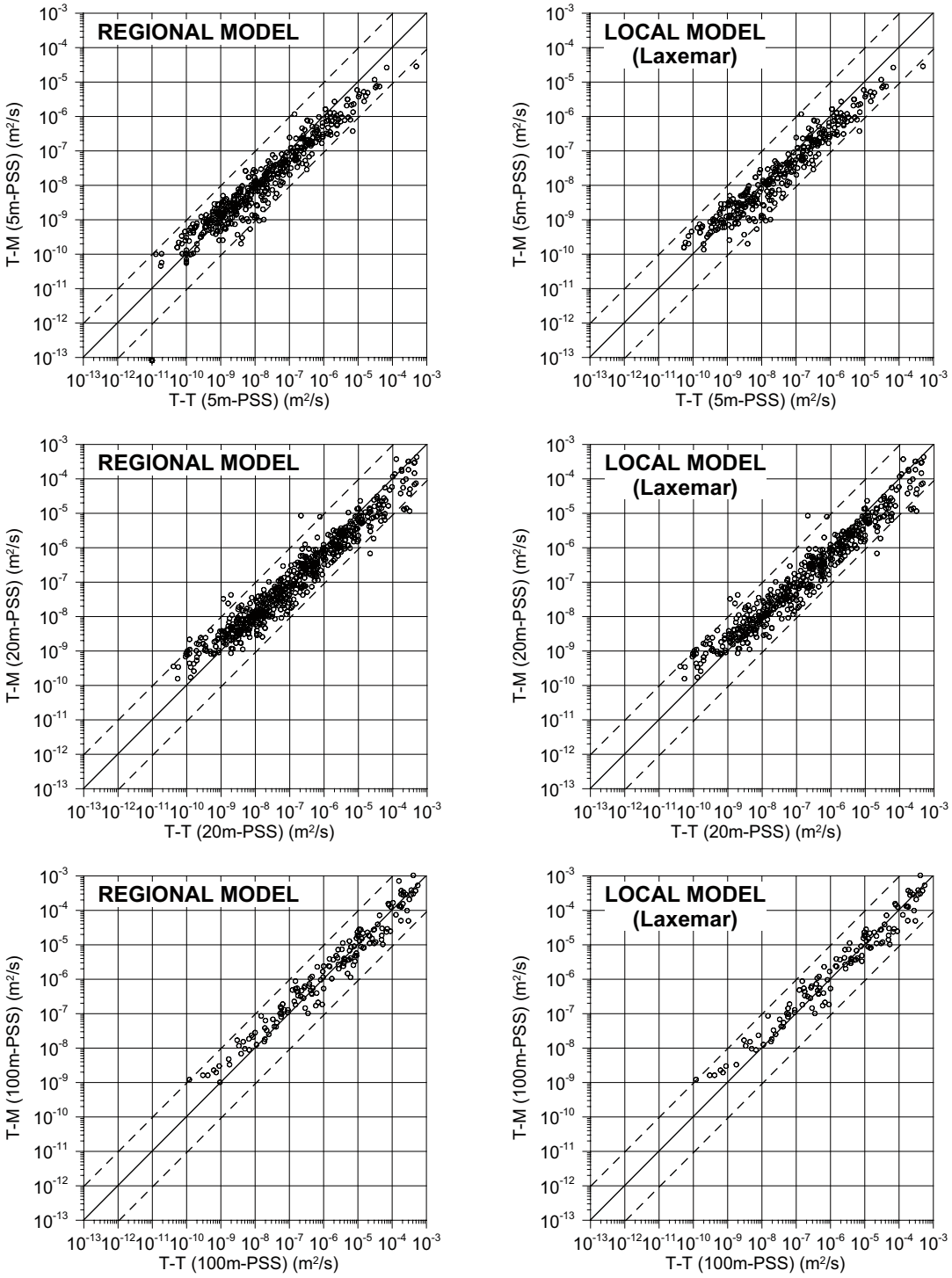

Figure 4-16. *Summary cross-plot of PSS 5, 20, 100 m steady-state transmissivity data vs. PSS 5, 20, 100 m transient transmissivity data gathered in cored boreholes. The solid line indicates a 1:1 slope and the dotted lines a spread of ± 1 order of magnitude.*

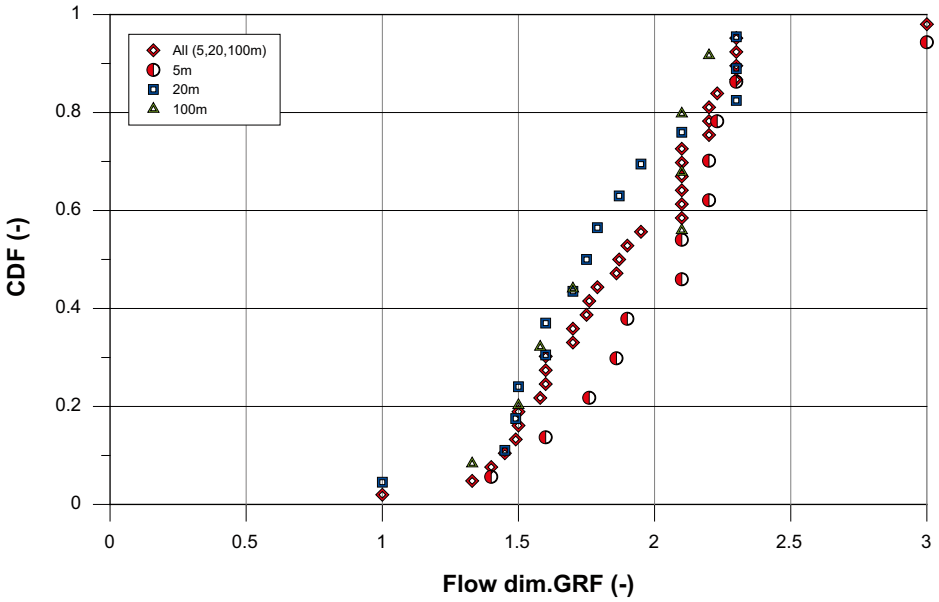

Figure 4-17. *Cumulative distribution plot for the fractional flow dimensions inferred from GRF analyses of 35 tests (12/15/8 tests for test scales 5/20/100 m, respectively) in KLX11A.*

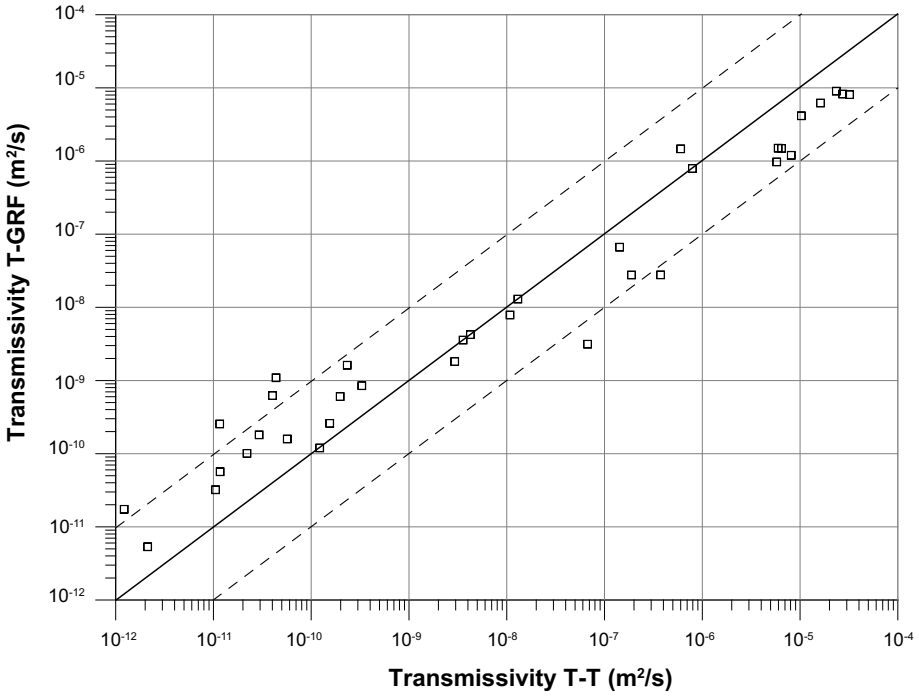

Figure 4-18. *Cross-plot of transmissivities derived with the GRF approach T_{GRF} vs. the transmissivities "Best Choice" transmissivities T_{BC} reported to SICADA for KLX11A. The cross-plot indicates a fairly good agreement between the T_{GRF} and the T_{BC} values.*

Figure 4-19 shows a cross-plot of the fractional flow dimensions interpreted from the injection period versus the observed pressure recovery at the end of the recovery period for borehole KLX11A. The pressure recoveries for the sections show rather complete recovery for most sections but in some sections there is a slow recovery, which suggests poorly connected fracture network geometries for the associated test sections, i.e. compartmentalised fracture networks. This suggests that some test sections with transmissivities evaluated from PSS-tests may represent local transmissivities but are possibly less relevant for assessment of transmissivities of hydraulic features and their intensities for a larger volume of connected fractures.

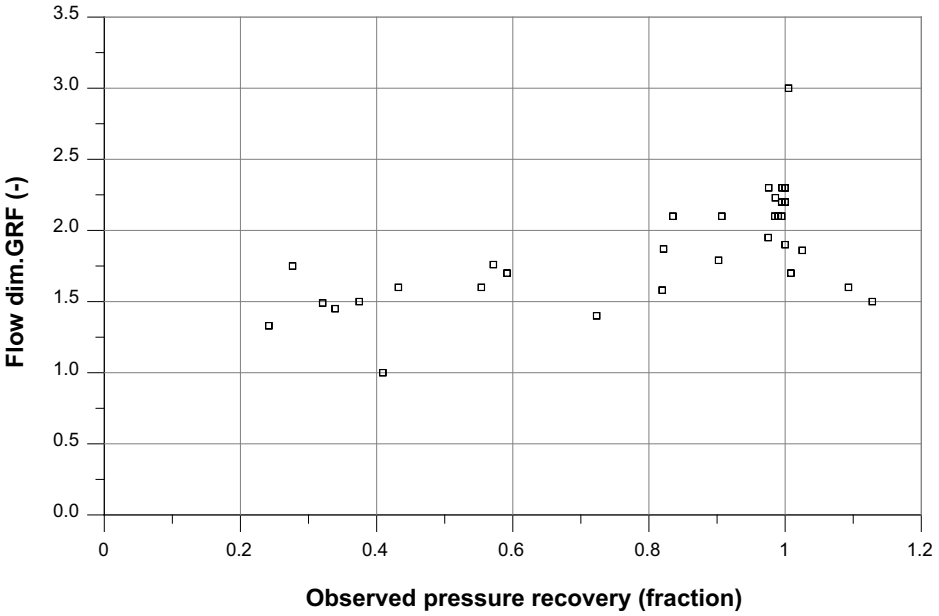

Figure 4-19. *Cross-plot of computed fractional flow dimension vs. measured pressure recovery for PSS tests in KLX11A.*

4.3.3 Correlation between PSS and PFL

A large number of boreholes have been tested with the PFL method, as indicated in the first section of this chapter. The PFL-measurements are reported in /Ludvigson and Hansson 2002, Kristiansson 2006, Kristiansson et al. 2006, Kyllönen and Leppänen 2007, Pöllänen 2007a, b, c, Pöllänen and Sokolnicki 2004, Pöllänen et al. 2007, 2008, Rouhiainen 2000, Rouhiainen and Sokolnicki 2005, Rouhiainen and Pöllänen 2003a, b, Rouhiainen and Pöllänen 2004, Rouhiainen et al. 2005, Sokolnicki 2006, Sokolnicki and Rouhianien 2005a, b, c, Sokolnicki and Pöllänen 2005, Sokolnicki and Pöllänen 2007, Sokolnicki and Väisäsvaara 2006, Sokolnicki and Kristiansson 2006, 2007, Väisäsvaara 2006, 2007, Väisäsvaara and Pekkanen 2006, Väisäsvaara et al. 2006a, b, c, Väisäsvaara et al. 2007/.

The transmissivities of the hydraulic features identified with PFL-f were summed up to correspond to 5 and 20 m sections (Tsum (xm-ΣPFL-f), x indicating sum over 5 or 20 m sections) measured with the PSS (T-BC(xm-PSS), x indicating PSS-test scales 5 or 20 m), to explore the difference between the methods. The number of section compared were 689/601 for test scales 5/20 m, respectively, including all test sections with values at and above the measurement limit (although excluding the data from KLX02 as there are measurements in this borehole that differ from those made during the site investigations.). These numbers of tests includes also those 100-m or 20-m long PSS-packer intervals with no quantifiable flow above the lower detection limit, hence all non-flowing 5-m intervals envisaged were not measured directly[1] but were assigned measurement limit values. Figure 4-20 shows an overview of all data and Figure 4-21 to Figure 4-23 show the individual boreholes with PSS and PFL data. In Section 9.4.1 the similar plots as Figure 4-20 are made but observations are also divided into HRDs and HCD. KLX02 data were excluded in Figure 4-20 as the identification of PFL-f features (made on pre-Site Investigation tests) was considered uncertain compared to other boreholes tested during the site investigation, which also can be seen readily in Figure 4-21.

[1] A telescopic approach is used for the PSS testing conducted in Laxemar. Each borehole is measured with consecutive 100-m long, 20-m long and 5-m long packer intervals beginning with the longest packer interval. However, non-flowing 100-m long packer intervals are not studied with 20-m long packer intervals, etc. The telescopic measurement approach saves time but it assumes that low transmissive sections are correctly characterised.

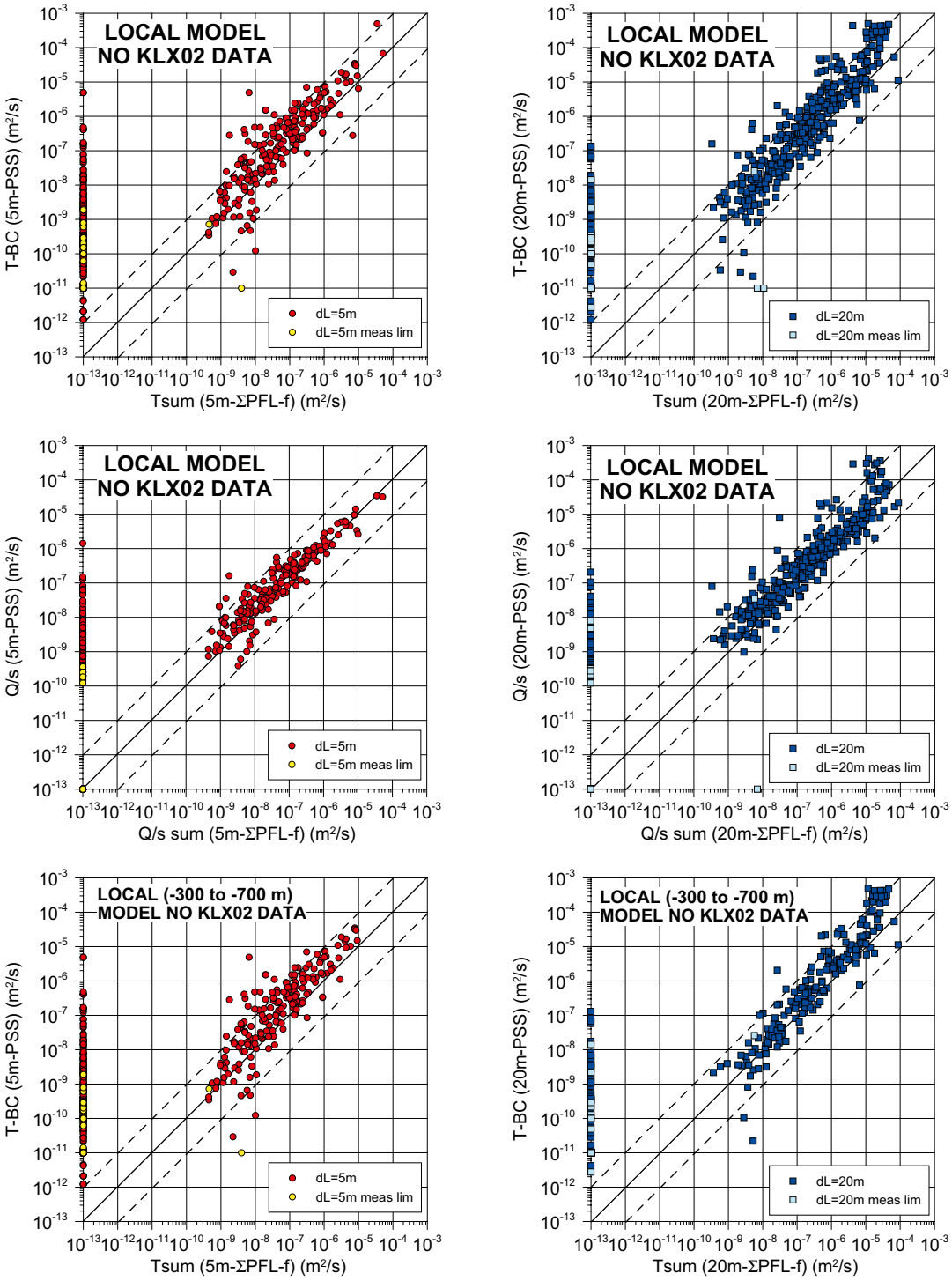

Figure 4-20. *Cross-plot of PSS BC- transmissivity(T) data (or Q/s) vs. Σ PFL-f T (or Q/s) data. The solid line indicates a 1:1 slope and the dotted lines a spread of ± 1 order of magnitude. Data are shown for two test section lengths dL between the PSS packers, i.e. 5 m and 20 m. Transmissivity data from PSS test sections without PFL-f anomalies are plotted to the left at an arbitrary low value on the abscissa. Top and middle: all Laxemar data. Bottom; data for the elevation. interval. –300 to –700 m.*

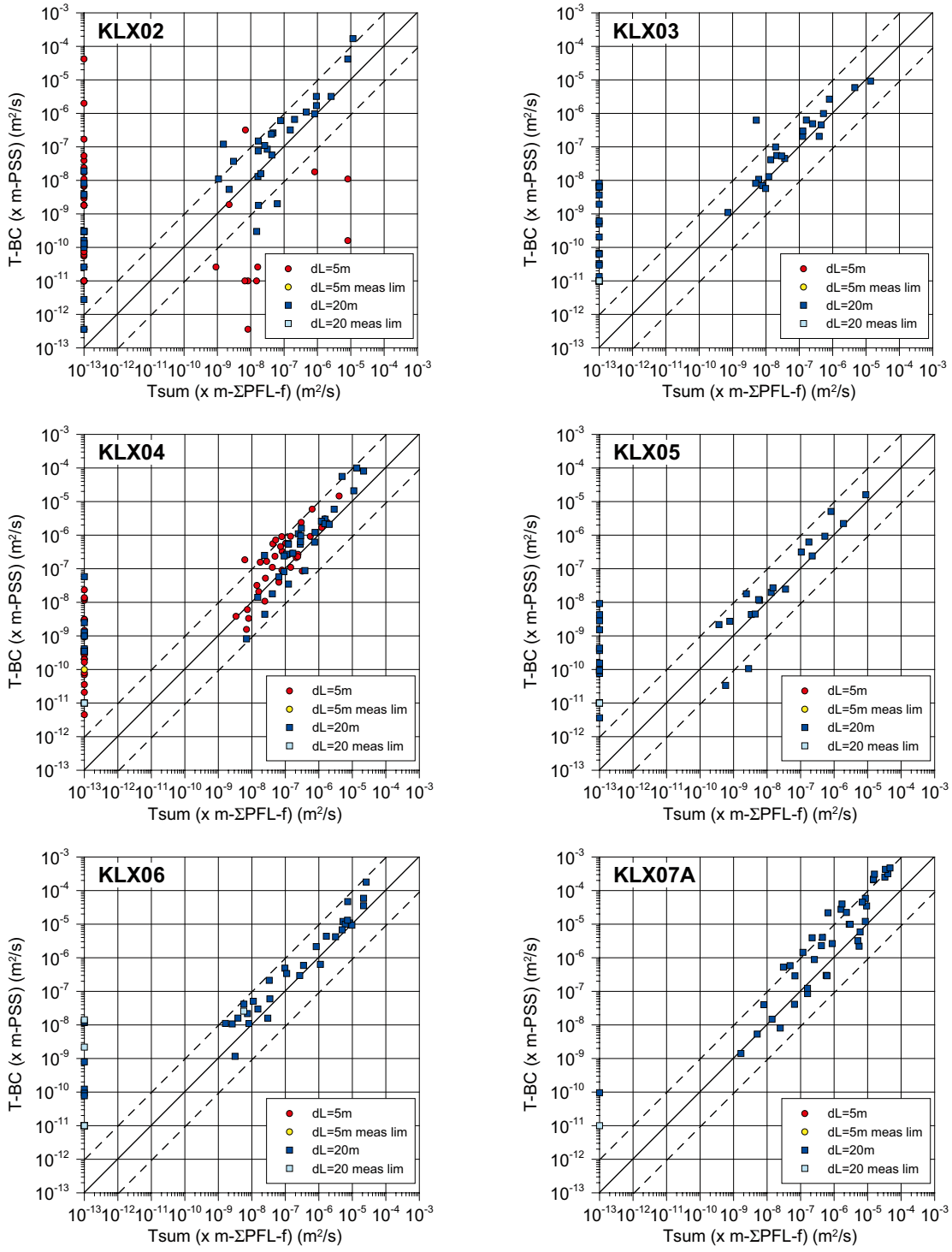

Figure 4-21. *Cross-plot of PSS BC- transmissivity data vs. Σ PFL-f transmissivity data. The solid line indicates a 1:1 slope and the dotted lines a spread of ± 1 order of magnitude. Data are shown for two test section lengths dL between the PSS packers, i.e. 5 m and 20 m. Transmissivity data from PSS test sections without PFL-f anomalies are plotted to the left at an arbitrary low value on the abscissa.*

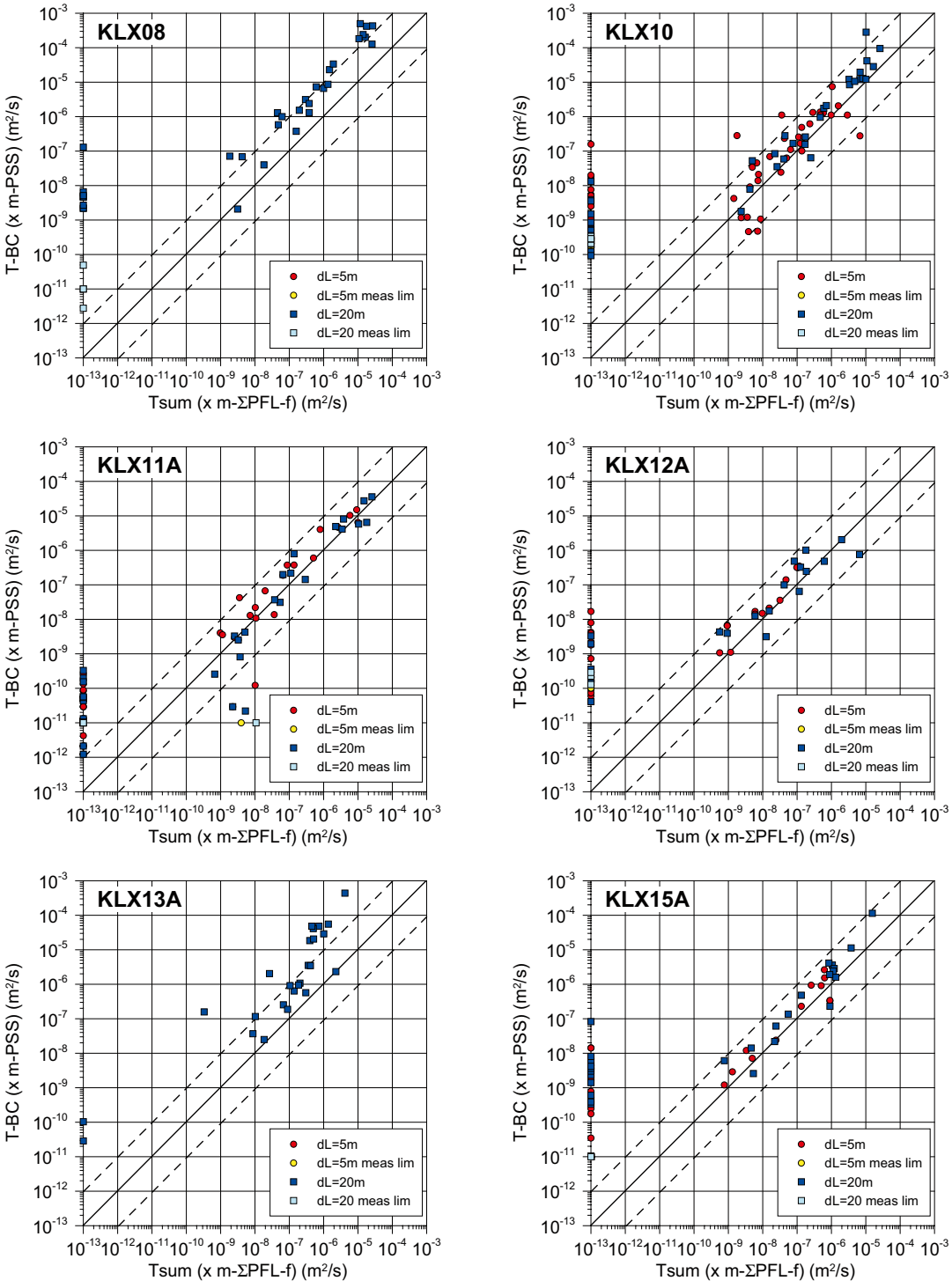

Figure 4-22. *Cross-plot of PSS BC- transmissivity data vs. Σ PFL-f transmissivity data. The solid line indicates a 1:1 slope and the dotted lines a spread of ± 1 order of magnitude. Data are shown for two test section lengths dL between the PSS packers, i.e. 5 m and 20 m. Transmissivity data from PSS test sections without PFL-f anomalies are plotted to the left at an arbitrary low value on the abscissa.*

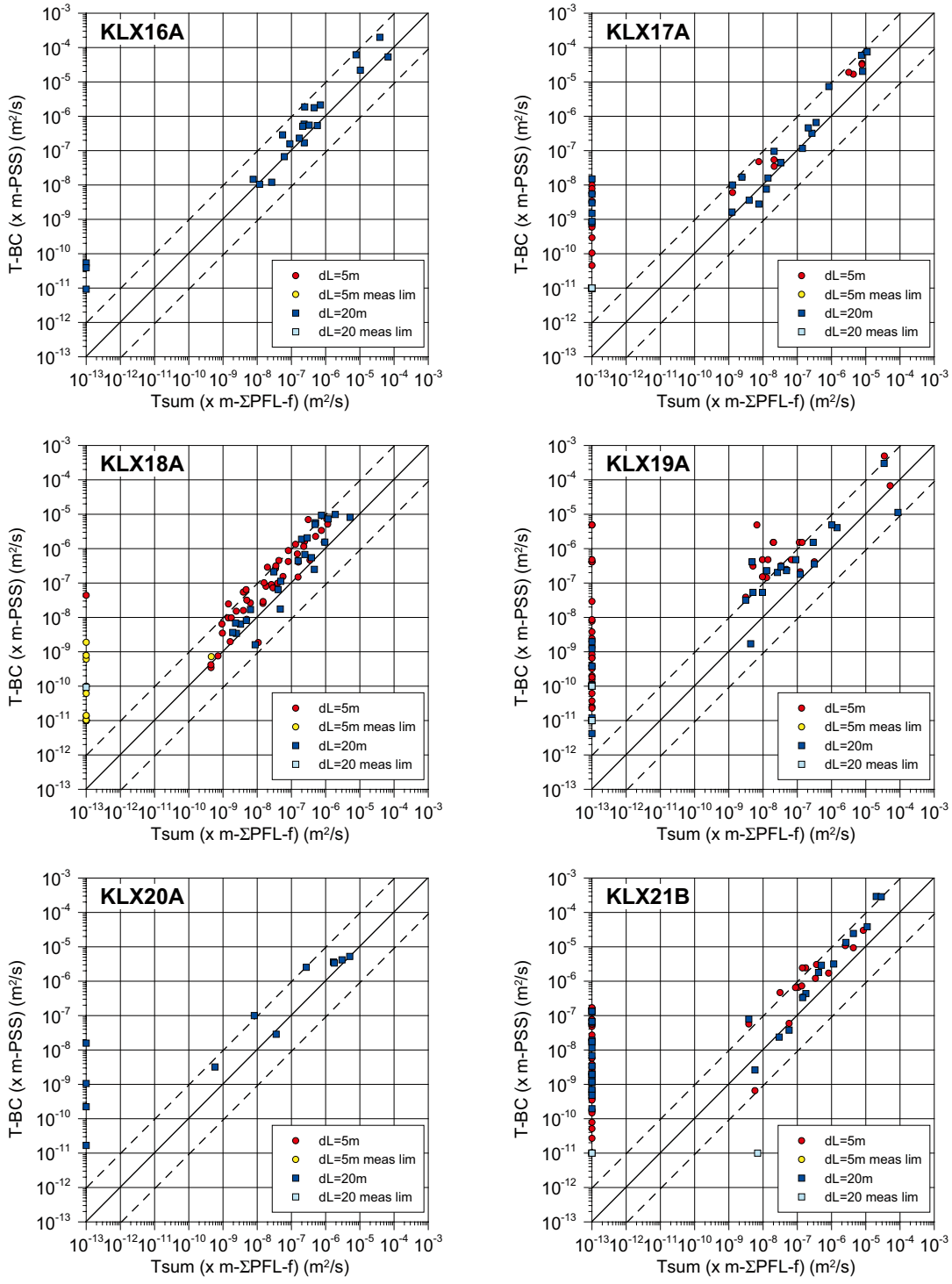

Figure 4-23. *Cross-plot of PSS BC- transmissivity data vs. Σ PFL-f transmissivity data. The solid line indicates a 1:1 slope and the dotted lines a spread of ± 1 order of magnitude. Data are shown for two test section lengths dL between the PSS packers, i.e. 5 m and 20 m. Transmissivity data from PSS test sections without PFL-f anomalies are plotted to the left at an arbitrary low value on the abscissa.*

Transmissivity data from PSS test sections without PFL-f anomalies are plotted to the left at an arbitrary low value on the abscissa. One reason for the presence of these values is that these test sections probably partly represents compartmentalised parts of the fracture network that carry no continuous flow during tests with PFL. However, some of these test sections may also be related to the uncertainties of the positioning of PFL-f and PSS test sections in the borehole; occasionally a PFL-f feature may be wrongly connected to a certain PSS section. A third reason is that the lower measurement limit is slightly lower for PSS compared with PFL, which indicates that possibly some of the sections with no PFL-f features may in fact still have connected fractures with very low transmissivities. These sections with possibly compartmentalised parts of the fracture network generally have transmissivities lower than 10^{-8} m^2/s but occasionally up to c. 10^{-7} m^2/s as can be seen in Figure 4-21 to Figure 4-23.

As can be seen in Figure 4-20 there is a tendency that (T-BC(xm-PSS)) is slightly higher than (Tsum (xm-ΣPFL-f)) but overall the values for corresponding sections are within a factor of 10 in difference. There seems to exist a bit lager deviation for 20 m sections with high T-values; (T-BC(xm-PSS)) is higher than (Tsum (xm-ΣPFL-f)). It may be because that PFL has an upper measurement limit that possibly has been reached and that no repeated measurements were made with a lower drawdown for these test sections, although some tests were re-made with a lower head in 22 of the tested core holes.

There are a few sections with significantly higher (Tsum (xm-ΣPFL-f)) compared to (T-BC(xm-PSS)). For tests employing test section length 5 m they originate from KLX11A and for test section lengths 20 m they originate from KLX05, KLX11A and KLX21B, respectively.

Looking at the individual boreholes, it is difficult to see that there are any greater systematic differences that can be connected to a few specific boreholes besides perhaps KLX07A, KLX08, KLX13A and KLX19A that show a bit larger differences between (T-BC(xm-PSS)) and (Tsum (xm-ΣPFL-f)). A possible reason is that parts of these boreholes are a bit more intensively fractured than most other boreholes, and if many of these fractures are interconnected it may be manifested as generally lower steady state transmissivities from the PFL with a forcedly large scale radial flow compared to transmissivities based on 20–30 minutes of transient injection.

The complementary cumulative density distribution of transmissivities greater than the lower detection limit, $1\cdot10^{-9}$– $1\cdot10^{-10}$ m^2/s with respect to the total number of measurement intervals, are shown in Figure 4-24.

In Figure 4-24 the PSS-xm curves are based on *PSS-T-BC-xm* that mostly are based on transient evaluation and *PSS-Moye-xm* that are based on a steady state evaluated T, except for T evaluated as pulse tests (the latter provides estimates of T in the lower region). The figure shows that the two evaluation methods provide rather similar distributions. For test scale of 5 m it seems that *PSS-Moye-5 m* estimates more conductive sections below T c. $1\cdot10^{-6}$ m^2/s compared with *PSS-T-BC-5 m*. Down to T=$1\cdot10^{-9}$ m^2/s c. 30% of 5 m sections with PFL-f (*Sum-PFL-5 m*) are conductive whereas c. 40% of PSS-sections are conductive (i.e. more transmissive than $1\cdot10^{-9}$ m^2/s). This difference between methods can be interpreted as a quantification of test sections with hydraulically connected fractures. However there are a few uncertainties, as also pointed out earlier in the text. To some extent, low transmissive PFL-f features may have been missed in the interpretation as the interpretation near the lower measurement limit of c. 10^{-9} m^2/s is uncertain. PSS tests, on the other hand, may in some cases (believed to be few) have fractures that connect back to the borehole above or below the test section, indicating a transmissive section that in reality is non-conductive. This means that possibly 5–10% of PSS-tested 5 m sections only represent local systems that are not, or just slightly, connected to a large conductive system that can provide flow for long test times as indicated by the PFL-tests.

The test sections for 20 m are a bit different. This set of data covers the depth interval c. –100 m to –1,000 m, whereas 5 m test sections cover the depth interval –300 to –700 m. As can be seen the curves are parallel and the differences seem to be coupled to high T-values. As indicated above, this may be related to the fact that PFL has an upper measurement limit that possibly has been reached and no repeated measurements were made with a lower drawdown in some cases. Assuming that this

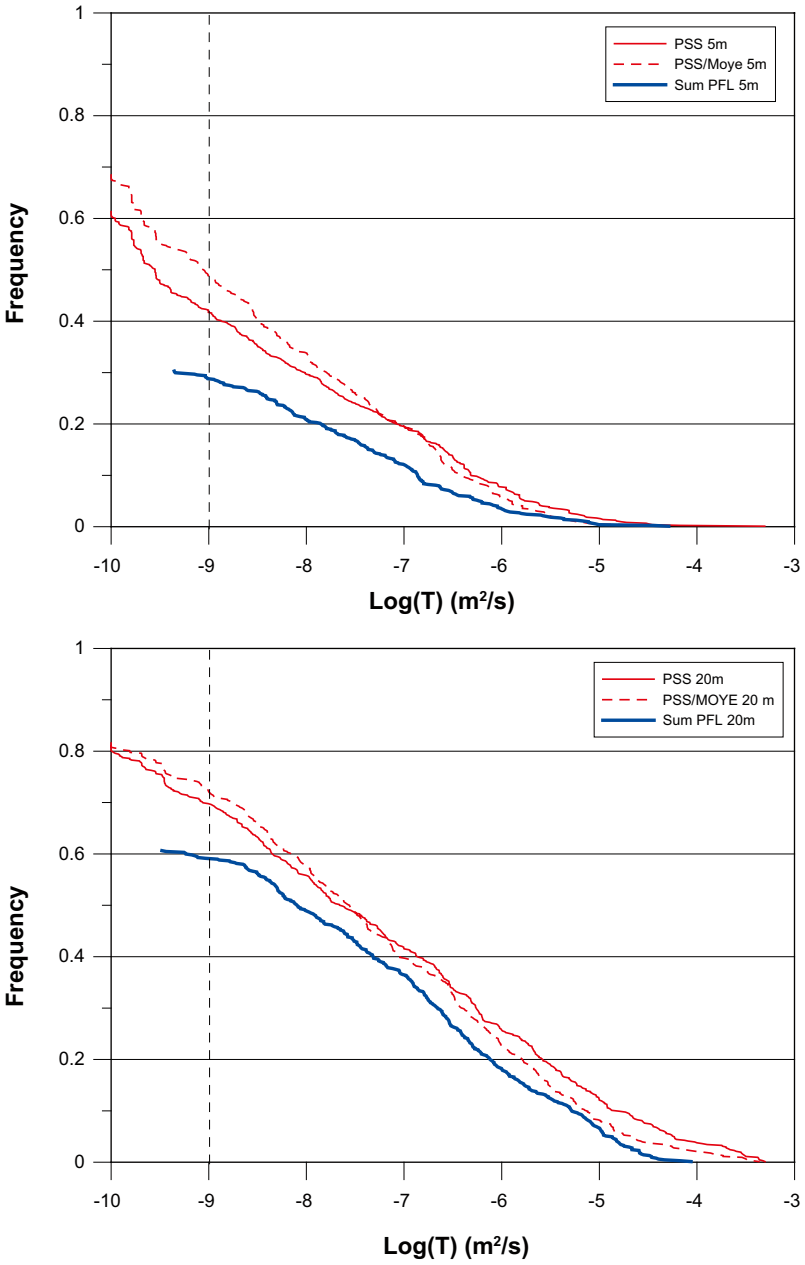

Figure 4-24. *Complementary cumulative distribution plot for the frequency of Log(T) in 5 and 20 m intervals for the PSS measurements and the PFL-f measurements grouped according to the same 5 or 20 m intervals. The frequency is normalised according to the total number of 5 or 20 m intervals measured by the PSS technique (i.e. total borehole length of PSS measurements / 5 or 20 m), then also counting sections which have been assigned measurement limit values due to that a longer test scale have shown to be at or below measurement limit (measurements in 5 and 20 m sections are continuous along each borehole). The typical detection limit of the PFL-f technique is shown by the dotted line. PSS_T-BC represents all Best Choice values of T. PSS_T-Moye represents tests possible to evaluate with Moye and the rest are evaluated with pulse test or are measurement limit values, which both of the last represents very low T-values.*

is correct; c. 65% of 20 m sections with PFL-f (*Sum-PFL-20 m*) are conductive whereas c. 70% of PSS-sections are conductive (i.e. more transmissive than $1 \cdot 10^{-9}$ m^2/s) for a test scale of 20 m. This observation seems consistent with the findings for the 5 m sections as one would expect that the proportion of flowing test sections increases as test scale increases.

According to the preceding text one can also point out that the steady state evaluation, with the same specific capacity (Q/s) results in 1.5–2 times lager T using Moye compared to the Thiem formulation and the assumed influence radius used for PFL, which shows that the steady state evaluation methods give similar results.

In Figure 4-15 the flow condition at the shut-in time of the injection period is shown as a RI-index; *recharge boundary* (tested feature connected to a feature with a higher transmissivity or an apparent constant head boundary), *infinitely acting* or *barrier boundary* (tested feature connected to a feature with a lower transmissivity or an apparent impermeable boundary), respectively. As can be expected, one finds that PSS sections without PFL-f features are mostly present in the shorter test sections compared to the longer ones, cf. Figure 4-25. One also finds that PSS sections without PFL-f features can be found for all three types of RI-index probably indicating that the test duration for the PSS tests was not long enough to capture the closed or very low-conductive boundary indicated by the PFL measurements for the same test sections. As previously commented, these test sections without PFL-f features generally have PSS- based transmissivities that are lower than 10^{-8} m^2/s but occasionally reaching c. 10^{-7} m^2/s. One can also observe that the sections without PFL-f features are to some extent clustered, see Figure 4-26, which possibly indicates the size of compartmentalised parts of the fracture network that carries no (measurable) continuous flow during the tests with PFL.

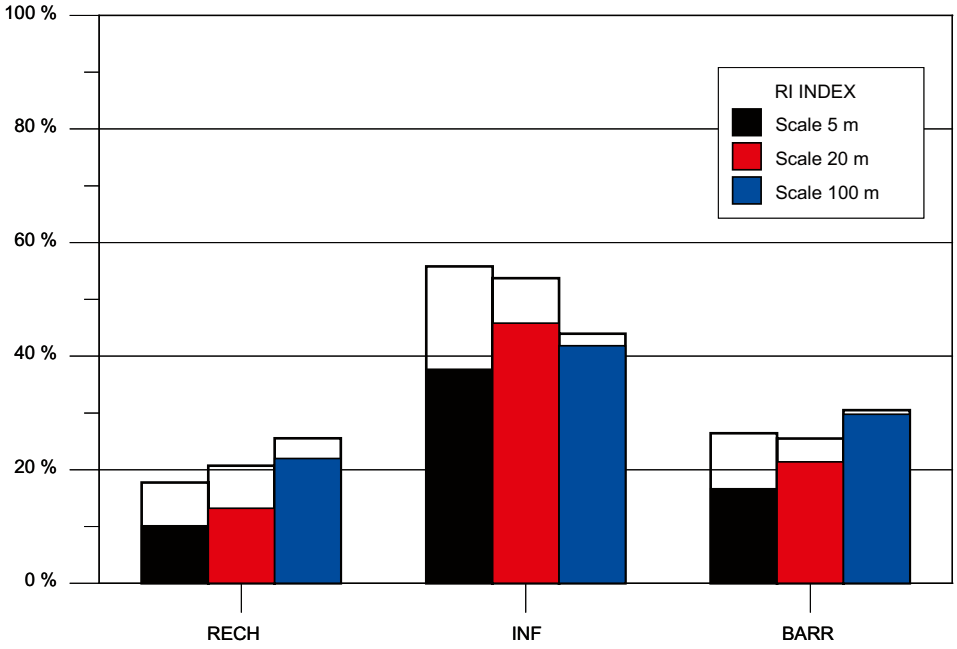

Figure 4-25. *Histogram of the "boundary effects" sensed (RECH: recharge boundary, INF: infinitely acting or BARR: barrier boundary) at the shut-in time for the 5, 20 and 100 m test scales PSS tests conducted. Proportions of PSS section without PFL-f features are indicated non-coloured upper part of histogram. Data from Local model volume.*

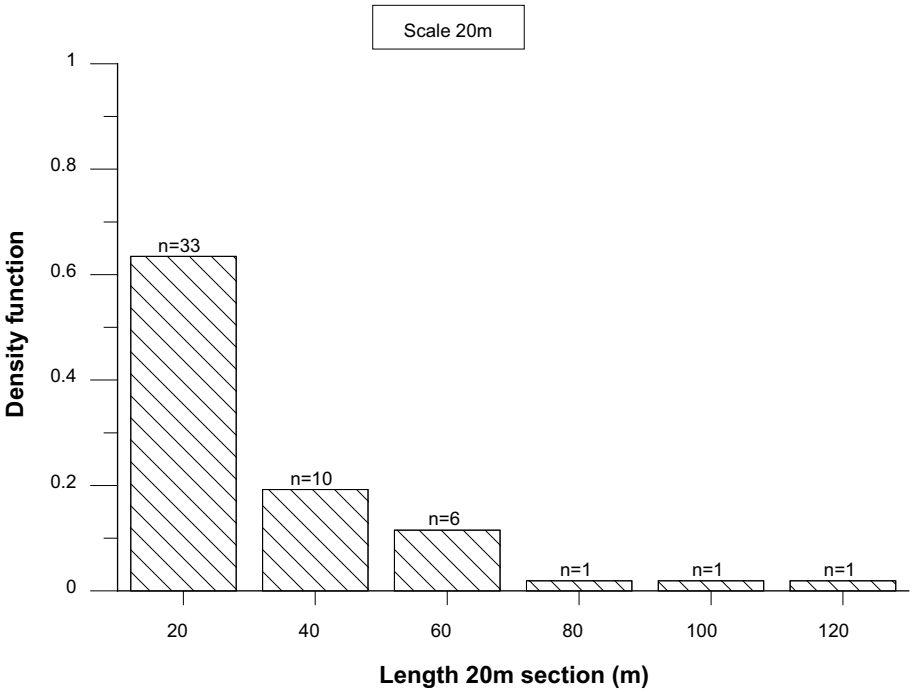

Figure 4-26. *Length of consecutive 20 m sections without PFL-f features (sections with T<c. 10^{-9} m^2/s) but with transient evaluated transmissivity above measurement limit based on PSS tests. n: the sample size within each length category.*

4.4 Hydraulic tests in percussion-drilled boreholes

4.4.1 Hydraulic test methods

Percussion-drilled boreholes have been characterised with the HTHB method predominantly. The equipment called HTHB (Swedish abbreviation for *Hydraulic Test System for Percussion Boreholes* (*Hydro Testutrustning i Hammar-Borrhål*)) is a modular tool for testing boreholes up to ca. 200 m depth (see schematic drawing in Figure 4-1). The HTHB is designed for percussion boreholes and used to perform pumping and injection tests in open boreholes, or in packed-off sections of the borehole. It is possible to combine a pump test in an open borehole with a flow logging survey along the same borehole, cf. Figure 4-27. Tests can be performed with a constant hydraulic head, or alternatively with a constant flow rate. Hydraulic tests can also be performed in packed-off borehole sections down to a total depth of 200 m cf, Figure 4-28.

The general schedule for the performed pump tests consisted of a pump phase of approximately 8–10 hours, sometimes combined with flow logging (impeller) and monitoring of observation wells nearby. The flow phase was followed by a recovery phase of approximately 8–15 hours.

The measurement range for flow rate during pumping is 5–80 L/min ($8.33 \cdot 10^{-5}$ – $1.33 \cdot 10^{-3}$ m^3/s) and during injection the minimum flow rate can be as low as 1 L/min ($6 \cdot 10^{-5}$ m^3/s). The accuracy of the flow rate is ±0.5% of actual reading. Assuming a drawdown during a pumping test of 50 m in a borehole with a radius/test-section length ratio of: 0.07 m/200 m, the measurement limit for transmissivity is: c. $2 \cdot 10^{-6}$ m^2/s. Assuming injection at an excess pressure of 20 kPa and the same radius/test section length ratio as for the pumping test, the measurement limit for transmissivity becomes c. $1 \cdot 10^{-6}$ m^2/s. During flow logging with impeller the drawdown is usually 10 m and a flow change can be identified if it is greater than c. 1 L/min ($1.67 \cdot 10^{-5}$ m^3/s), which then corresponds to a measurement limit for transmissivity of: c. $2 \cdot 10^{-6}$ m^2/s. The accuracy of the flow rate is ±20% of actual reading. The accuracy of the pressure is ±10 kPa. /Rahm and Enachescu 2004a/.

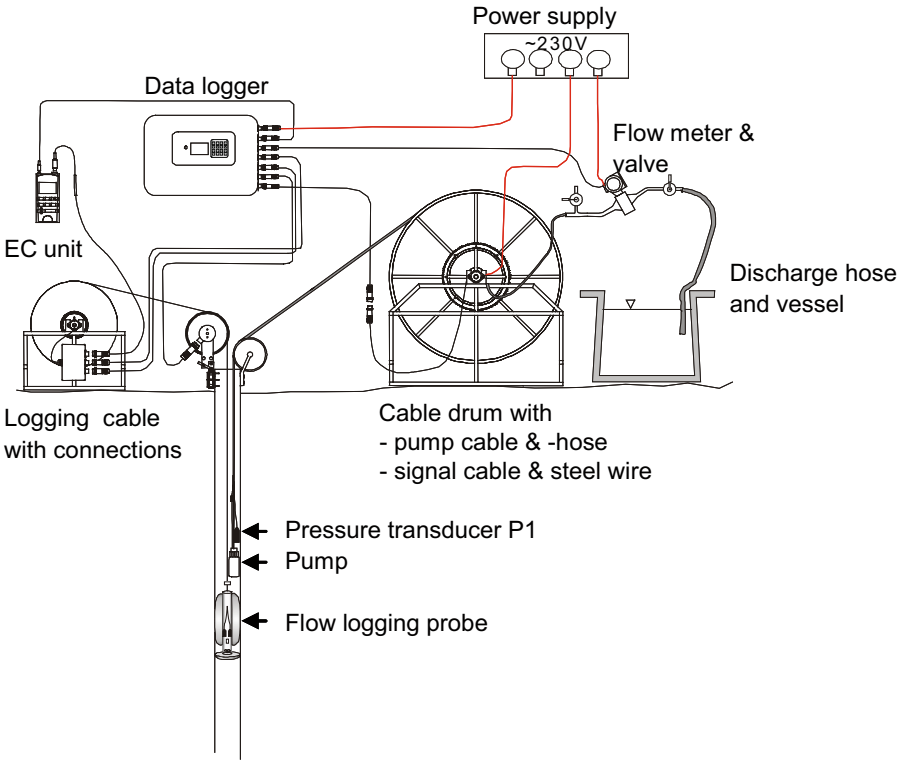

Figure 4-27. *Schematic test set-up for a pumping test in an open borehole in combination with flow logging with HTHB. Reproduced from /Rahm and Enachescu 2004a/.*

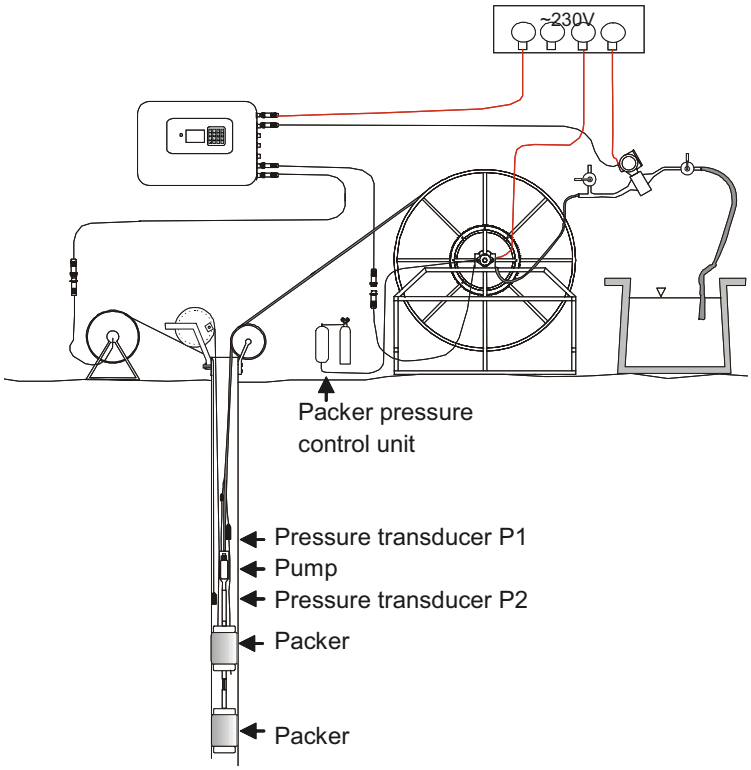

Figure 4-28. *Schematic test set-up for a pumping test in an isolated borehole section with HTHB. Reproduced from /Rahm and Enachescu 2004a/.*

4.4.2 Test results

Pumping tests, and on a few occasions flow logging, have been performed in the percussion boreholes and are reported in /Ludvigson et al. 2003, Rahm and Enachescu 2004a, 2005e, Rohs 2006, Rohs et al. 2006, Svensson 2004/. In some cases the borehole was judged to be so low-conductive, after examining data from drilling, that a pumping test was found not feasible. Instead, data from airlift pumping during drilling could sometimes be used, either to estimate a transmissivity or set a measurement limit value to the borehole (if flow rate was estimated to 0). The drilling and hydraulic tests in conjunction with the drilling are reported in the drilling reports. All drilling reports for percussion and core holes as well as monitoring wells in overburden: /Ask 2003, 2004, 2005, 2006a, b, c, Ask and Samuelsson 2003, 2004a, b, c, Ask and Zetterlund 2005, Ask et al. 2003, 2004a, b, c, 2005a, b, c, d, e, f, 2006a, b, c, d, e, 2007a, b, c, d, Johansson and Adestam 2004, Sigurdsson and Ekström 2005, Sigurdsson et al. 2005/ .

An overview of primary data is provided in Chapter 6.

4.5 Overview of the hydraulic characterisation of the bedrock at repository depth

At repository depth (–300 to – 700 masl) all test scales are represented for PSS, given that 5 m test sections were employed in this depth interval and furthermore PFL-f as well as PFL-s data are available in all tested cored boreholes. The data set available south of deformation zone ZSMEW007A comprises PSS tests in the following cored boreholes between –300 to –700 m (Hydraulic rock domains (HRD) are defined in Chapter 9 but also shown in a figure in Chapter 3):

- 5 m tests in;
  - **HRD_C:** KLX10, -12A, -15A, -18A and -21B,
  - **HRD_W:** KLX11A, -17A, -19A,
- 20 m tests in:
  - **HRD_C:** KLX03, -05, -10, -12A, -15A, -18A and -21B,
  - **HRD_W:** KLX11A, -17A, -19A (Note: Data from KLX13A are not considered representative for HRD_W while the borehole parallels and is affected by an interpreted deformation zone (ZSMEW120A) and are therefore excluded from the analysis for hydrogeological DFN),

and PFL tests between elevations –300 to –700 m:

- **HRD_C:** KLX03, -05, 7A, -10, -12A, -15A, -18A and -21B,
- **HRD_W:** KLX11A, -17A, -19A (Note: not for KLX13A above for PSS tests).

4.6 Overview of the hydraulic characterisation of the near-surface bedrock

Near surface PSS measurements generally start below elevation –100 m and comprise only test scales 20 and 100 m down to elevation –300 m. The bedrock transient tests in top 100 m are only performed with test scale 100 m using with HTHB or airlift tests during drilling. In a number of short cored boreholes, in general both PFL-s and PFL-f tests have been performed, and in a few cases PFL-f tests alone. It has generally not been possible to test the uppermost 10 m of the bedrock due to emplacement of steel casing and in some cases also due to the fact that pumping was used during the flow logging and no extra tests were made in the top-most section using injection of water. At two sites, around KLX09 and KLX11A, several short core holes were drilled and comprehensive information on geological features as well as on hydrogeological feature characteristics are available, see Appendix 2 and Chapter 9. Injections of water in the uppermost sections were also made in KLX11B–F, providing data a bit closer to bedrock surface compared to KLX09 site.

A number of short cored boreholes were also drilled with the purpose of investigating minor deformation zones, which resulted in geological and hydraulic data representative of the near surface rock /Olsson et al. 2006/. Results of PFL-f tests above elevations –100 m can be found in Chapter 9. Data within brackets indicate that data are few and/or are to be found immediately above elevation –100 m:

- HRD_N: (KLX04, -06), 07B, (-08, -09), -09B to 09G,
- HRD_EW007: (KLX07A, -10), -10B, -10C, (-18A), -29A,
- HRD_C: (KLX03, -05, -12A, -15A, -21B), -26A, 26B, -28A,
- HRD_W: (KLX11A), -11B to -11F, 14A, (-17A, -19A, -20A), -22A, -22B, -23A, -23B, -24A, -25A (Note : Data from KLX13A are not considered representative for HRD_W while the borehole parallels and is affected by an interpreted deformation zone (ZSMEW120A) and data from this borehole are therefore excluded from the analysis).

Borehole KLX01 provides only some injection test data below c. elevation –100 m of test scales 3 and 30 m and has not been used for the assessment of the near-surface properties.

5 Structural-hydraulic data in cored boreholes

This chapter and Appendix 2 presents primary PFL-f data plotted versus geological interpretations of deterministically modelled deformation zones, minor local deformation zones (MDZ), interpreted fracture domains (FSM) and rock domains (RSM, only shown in Appendix 2) to provide an overview of how these data correlate. In Chapter 3 the deterministically modelled deformation zones, minor deformation zones, the interpreted fracture domains and rock domains were introduced and defined.

The hydraulic properties of deterministically modelled deformation zones and interpreted minor deformation zones are evaluated in Chapters 7 and 8, respectively.

The evaluation of hydraulic rock domains (HRD) has been an iterative process testing the significance in property differences using interpreted fracture domains and rock domains and mainly PFL-s, PFL-s and PSS 100 m test scale data. As fracture domains showed to be the most relevant basis for HRDs, statistics and illustrations of data subdivided on the basis of fracture domains (or combinations thereof) are presented in the main text and supporting presentations in appendices. The detailed basis and argumentation for defining HRDs and the quantification of their hydrogeological DFN properties are provided in Chapter 9.

5.1 Deformation zones, minor deformation zones and fracture domains

PFL-f results in the long cored boreholes are plotted together with the fracture domain interpretations /La Pointe et al. 2008/ and the interpreted borehole intercepts of the deterministic deformation zones and interpreted minor deformation zones /Wahlgren et al. 2008, Hermanson et al. 2008/.

In Appendix 2, Section A.2.1,, the cored boreholes and pole plots for depth intervals of 200 m are shown. In Appendix 2, Section A2.2, data from cored boreholes are plotted together with the rock domain interpretations and the interpreted borehole intercepts of the deterministic deformation zones and minor deformation zones /Wahlgren et al. 2008/. Details of core mapping, hydraulic tests in cored boreholes and some hydrochemical sampling in the cored boreholes are provided in /Hermanson et al. 2008/.

The main references to PFL- measurements are provided in Section 4.3.3.

The correlation between the coremapping and the PFL-f data is reported in /Forssman et al. 2005a, b, Teurneau et al. 2007, Wikström et al. 2007a, b, c, Forsmark et al. 2007/.

5.2 Hydro-structural cross-correlation

Examples of detailed presentations of PFL-f versus fracture domains (FSM), deformation zones and MDZs are provided in Figure 5-1 and Figure 5-2 for the cored boreholes in the Local model volume. In Appendix 2, Section A.2.1, similar figures are shown for all cored boreholes. The figures show the main data that have been the base for the hydrogeological DFN model development described in Chapters 9 and 10. The PFL-f data versus rock domains (RSM), deformation zones and MDZ presented in Appendix 2, Section A.2.2, have constituted an additional base for the analysis of data before defining the Hydraulic Rock Domains (HRD) as described in Chapter 9.

The Figure 5-1 and Figure 5-2 in this section show the following:

Upper left: The PFL-f – features transmissivities are plotted versus elevation (left side of the figure) and the borehole length (right side of the figure). The fracture domain (FSMxxxx) is shown by name and colour. The deterministic deformation zones are indicated by name: NNxxxx (leaving out the preceding prefix ZSM) and MDZ by the name (DZx) used in the geological extended single-hole interpretation (ESHI).

Upper right: The pole plots show the pole vector, with its trend/dip, of each PFL-f feature found between the deformation zones for the entire borehole. Each pole vector symbol indicates the fracture domain and the transmissivity range for each PFL-feature.

Lower left and right: The PFL-f – feature orientations (strike/dip) are plotted versus elevation (left side of the figure) and the borehole length (right side of the figure). The fracture domain (FSMxxxx) is shown by name and colour. The deterministic deformation zones (s) are indicated by name: NNxxxx (leaving out the preceding prefix ZSM) and MDZ by the name (DZx) used in the geological extended single-hole interpretation (ESHI).

Some general characteristics can be seen in the figures:

- The intensities of PFL-f features decreases with depth.
- Generally, the PFL-f feature intensities seem to be higher within defined deformation zones compared to rock in between deformation zones, but there is a great variability and some deformation zones have none, or just a few PFL-fs.
- Boreholes intersecting, or that are near, deformation zone ZSMEW007A generally seem to have higher intensities of PFL-f features and the orientation of steep E-W features are more dominating (e.g. in KLX07).

Three boreholes show characteristics that through the integration process of geological data and hydrogeological data have lead to the following conjectures:

The KLX02 intersection with RSMBA03 has not been modelled as an FSM as it is just a small local domain at depth with no outcrop /La Pointe et al. 2008/, but shows similarities with FSM_NE005 and FSM_C at corresponding depths.

KLX13A seems to have a higher intensity of PFL-f features, possibly affected by a couple nearby larger deformation zones. This has led to the conclusion that the borehole is not representative for the later defined HRD_W, as further discussed in Chapter 9.

The geological modelling of rock domains (RSM) indicates a domain M in the bottom of KLX13A and KLX18A. However, the rock units more correspond to RSM_A but were not possible to model geometrically by geology. However, in the hydrogeological evaluation of the properties of RSMs this (small) deviation from the geological RSM model was accounted for.

KLX18A and KLX10, south of EW007 show a bit higher intensities of PFL-f features. The higher intensities in KLX10 can possibly be coupled to the large structure ZSMEW007A. The situation in the vicinity of KLX18A seems to be more complicated to explain, besides that the intensities of MDZs is rather high in the borehole.

5.2.1 Data from KLX27A

Data from KLX27A are not used in the hydrogeological DFN modelling as the borehole was drilled late in the project. However, the hydraulic data in KLX27A are commented upon in relation to the performed modelling in Appendix 10.

Borehole KLX03.

Poles for PFL-f feature planes between deterministic deformation zones.

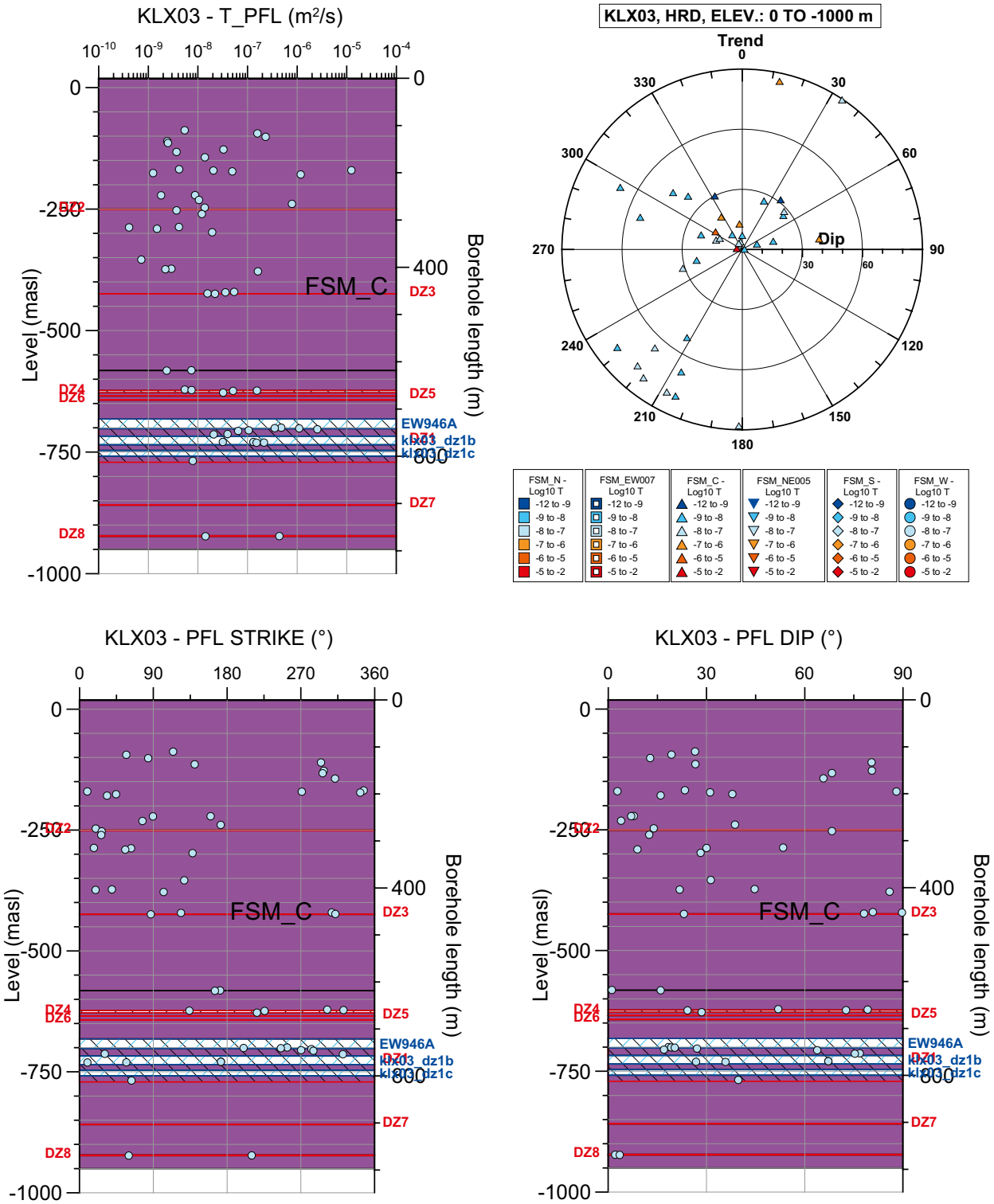

Figure 5-1. *Summary plots of geological and hydraulic data in the cored borehole based on the cross-correlation analyses carried out by /Forssman et.al. 2005b/.*

Borehole KLX04.

Poles for PFL-f feature planes between deterministic deformation zones.

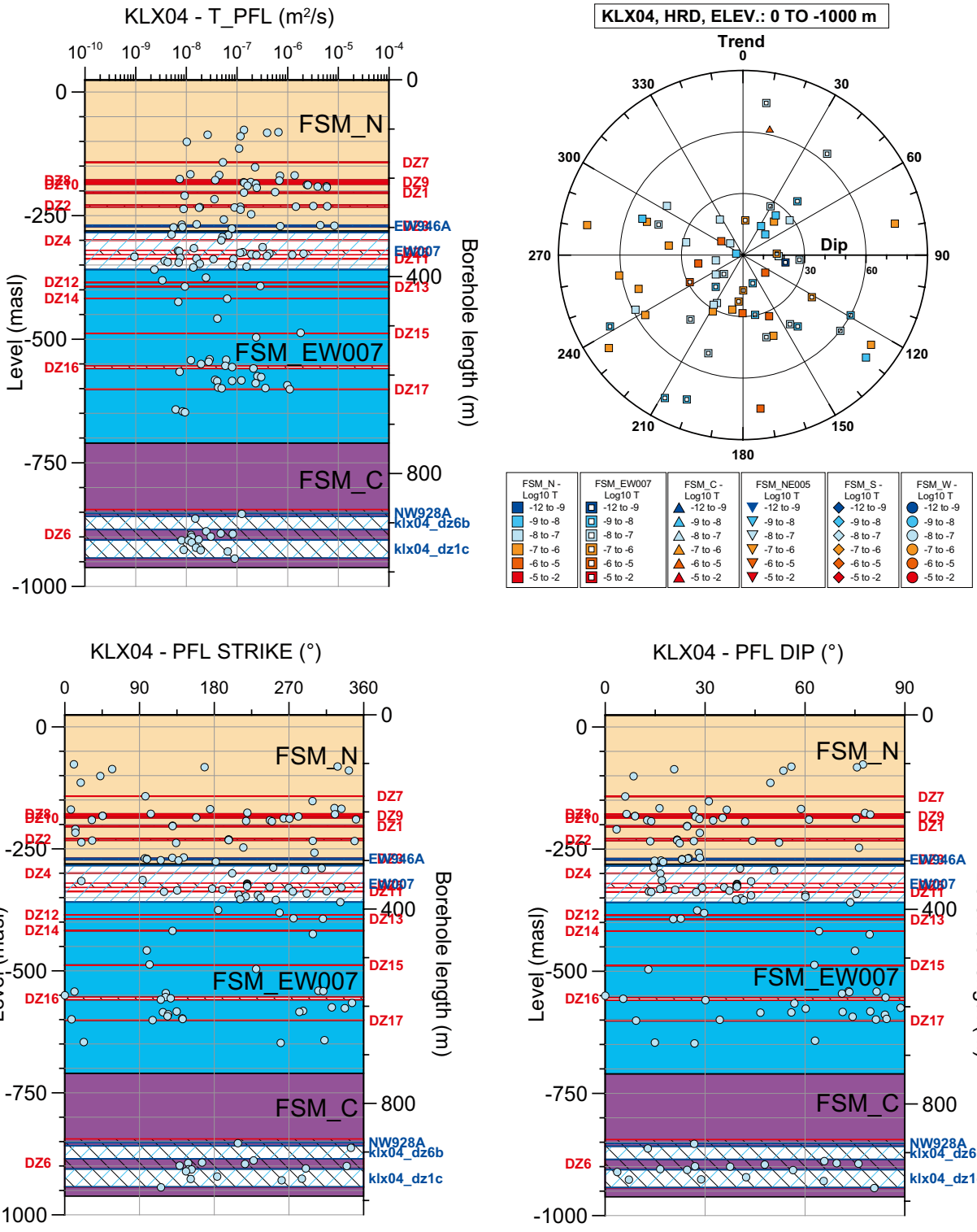

Figure 5-2. *Summary plots of geological and hydraulic data in the cored borehole based on the cross-correlation analyses carried out by /Forssman et.al. 2005b/.*

5.2.2 Comments on open fractures and crushed rock

/Hermanson et al. 2008/ provide detailed information on data used for the geological DFN modelling and data available in cored boreholes and percussion boreholes. An overview is also provided of some characteristics related to PFL-f features, open fractures and crush, which is briefly commented here. It should be emphasised that the figures mentioned below represent the entire measured borehole lengths as described in the database for the borehole mapping and hence include data from all interpreted deformation zones. Possibly a few of the data representing "crush zones" can be attributed to damage during drilling as interpreted by the geological extended single-hole interpretation.

The mean frequency of open fractures within PFL-s measured intervals in the boreholes are for Certain/Probable/Possible/Certain+Probable+Possible: 0.40/0.87/1.36/2.63 (frequency: m^{-1}), respectively. There are very few fractures mapped as partly open in the boreholes (mean per borehole: c. 6 partly open fractures and 727 open fractures (Certain+Probable+Possible)). Inclusion of open fractures, partly open fractures and crush zones (assuming 40 fractures/m in the crush zone) increases the mean frequency of total open fractures within PFL-s measured interval to 2.91 m^{-1}.

Boreholes KLX02 and KLX10B seem to constitute extremes among the boreholes when looking at some of the presented plots. However, KLX02 was drilled before the site investigations and was subsequently re-mapped down to c. 1,000 m borehole length and essentially only fractures mapped as certain or possible are in the database. Looking at the total fracture frequency (All open, partly open and crush zone fractures (40 fractures/m assumed for crush zones)), results from KLX02 do not differ significantly from the other cored boreholes. KLX10B differs from other boreholes concerning open fractures but it is a very short borehole and the data are from borehole length 10.7–43.5 m, i.e. relatively close to the ground surface.

The mean of the relative proportions in boreholes of Certain/Probable/Possible/ for open fractures within PFL-s measured interval are: 0.11/0.34/0.55 (given as relative proportion of certain open fractures in a borehole : No of Certain open fracture/ Total No. of open fractures, etc).

The frequency of PFL-f features within PFL-s measured intervals is 0.30 m^{-1}. That is, c. every tenth open fracture has a transmissivity $T > c\ 10^{-9}$ m^2/s (i.e. the approximate measurement limit for the PFL).

Along the boreholes the mean frequency of crush zones is 0.029 m^{-1}, and.45% of all crush zones have one or several PFL-f features associated with the crush zone Approximately 9% of the PFL-f are within crush zones.

Approximately 31% of all PFL-f are within deformation zones defined in the geological single-hole interpretation.

5.2.3 Errors and uncertainty in fracture orientation

/Stigsson 2008/ investigated the orientation uncertainty of flowing fractures identified to be flowing by the Posiva Flow Log in 43 cored boreholes in the Laxemar subarea. It was found that generally the uncertainties were rather small for most fractures. Of the 1957 studied fractures 566 have a maximum uncertainty, Ω, larger than 10° and 156 of them a maximum uncertainty larger than 30°. The greatest uncertainties can be coupled to a few boreholes, e.g. KLX09B which is a short vertical borehole showing the largest uncertainties. KLX11B (a short vertical borehole), KLX12A, KLX18A and KLX20A all have greater uncertainties than most of boreholes, but still most fractures with PFL-features have maximum uncertainty, Ω, around 10°.

It can be concluded that this indicates that the uncertainty in orientations of fractures is not a major problem for the confidence in the data used in the SDM-Site Laxemar hydrogeological DFN modelling. For more details, see /Stigsson 2008/.

6 Structural-hydraulic data in percussion-drilled boreholes

6.1 Overview

This chapter presents data from all percussion boreholes in the Laxemar subarea, Äspö and the Simpevarp subarea (including Ävrö, Hålö and Mjälen) with the purpose of providing an overview the entire hydraulic dataset informing the regional model area. As pointed out in Chapter 4, generally the entire percussion borehole has been pumped and impeller flow logging was performed only in some select boreholes to detail the flowing features along the borehole. However, observations during drilling have been useful for better understanding the hydraulic character of the bedrock sampled by the borehole, although associated with uncertainties, particularly regarding location of the flowing fractures and zones along the borehole. Geological documentation and hydraulic test results/observations in the boreholes are presented in /Hermanson et al. 2008/ The type of hydraulic observations made during drilling which are given in the figures in /Hermanson et al. 2008/ are transmissivity estimates from HTHB tests, flow logging with HTHB equipment and inflow rates, and the positions of these inflows in boreholes. Section 6.2 provides an overview of estimated borehole transmissivities and associated intercepts with deterministic deformation zones.

6.2 HTHB transmissivity data

Figure 6-1 displays the HTHB transmissivity estimated from tests in the percussion-drilled boreholes in within the regional model area. The associated deterministic deformation zones intersecting the percussion boreholes, if any, are also given in the figure.

Notable is that most percussion boreholes in the HLX-series of boreholes are associated with deterministic deformation zones – this simply due to the fact that most of these boreholes have been used to verify the existence and geometry of zones interpreted on the basis of surface information alone.

This stands in contrast to the boreholes in the HAS- and HAV- series of percussion boreholes. This need not necessarily imply that these boreholes are not directed on lineaments/zones, but it simply means that the lineaments/zones intersected by the boreholes are not part of the deterministic deformation zone model as presented by /Wahlgren et al. 2008/.

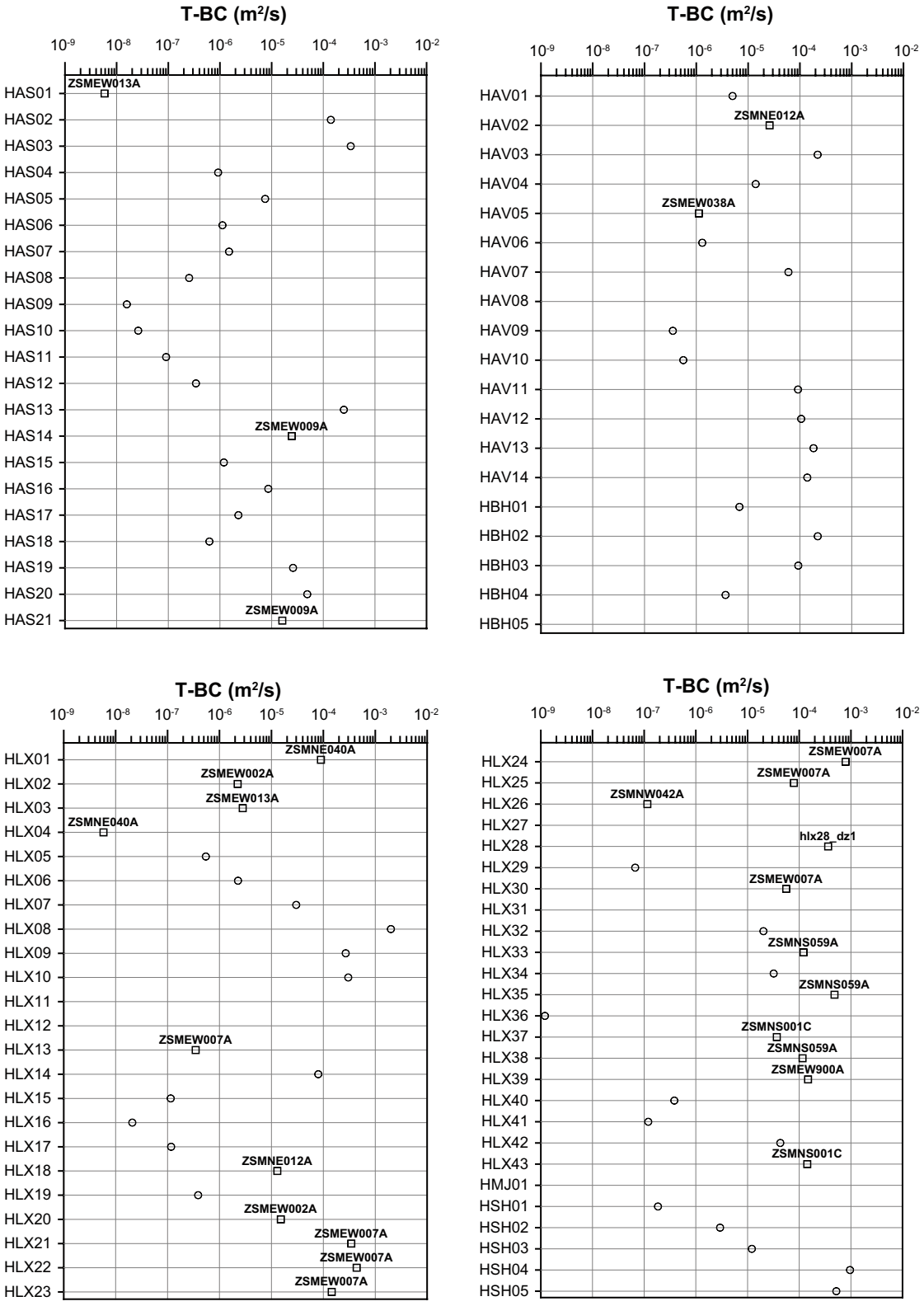

Figure 6-1. *Transmissivity measured in percussion holes located in Laxemar (HLX), Simpevarp(HSH), Ävrö (HAV), Äspö (HAS). The name of the deterministic deformation zones are shown in the plot if it is judged that the respective deformation zone intersects the borehole.*

7 Hydrogeological data synthesis for deterministic deformation zones

The chapter provides proposals as to how transmissivity and flowing feature intensities should be assigned to deterministic deformation zones, including those subjected to hydraulic tests and those that have not been tested hydraulically. The data analysed cover both the Laxemar-Simpevarp regional and the Laxemar local model volumes. The structure of the chapter is as follows:

- Brief overview of available data.
- Description of evaluation methodology.
- Brief description of a few interference tests that have been important for the hydraulic description of some deformation zones.
- Description of dolerite dykes of hydraulic importance.
- Discussion of correlations related to deformation zones that possibly affect the hydrogeological descriptive models of deformation zones.
- Suggested transmissivity model for deformation zones.
- Suggested storage coefficient model for deformation zones.
- Suggested kinematic porosity model for deformation zones.
- Description of heterogeneity within deformation zones.

7.1 Summary of data and evaluation methodology

7.1.1 Data

The deformation zones that are longer than c. 1 km are modelled deterministically in the SDM-Site Laxemar deformation zone model, cf. Chapter 3. Details on the geological data and the modelling of these deformation zones are presented in /Wahlgren et al. 2008/. All deterministic deformation zones are modelled as Hydraulic Conductor Domains (HCD) using the geometries defined by Geology. There are however a few exceptions. Thickness was increased for one deformation zone to capture the character of its hydraulic barrier function and a few local minor deformation zones were lumped together and were modelled as a HCD as they were also considered to form a possible local hydraulic barrier, see Sections 7.2 and 7.3. Late in the process of data evaluation and hydraulic modelling a need was identified to model an additional 4 minor deformation zones as HCDs. These 4 new HCDs (klx09_dz9, klx09_dz14, klx16_dz6 and klx19_dz2) are discussed in Appendix 3 but the statistics of HCDs in this chapter does not take this last step into consideration as it is was judged that it had only minor influence on the statistics.

Hydraulic information is available for a large number of the deformation zones within the regional model area, but far from all. The distribution of hydraulic data in relation to the deterministic deformation zones interpreted by Geology is summarised in Table 7-1. The geologically defined borehole intercepts in boreholes for deformation zones (local major and local minor deformation zones) in the single hole interpretation /Wahlgren et al. 2008/ are used when the hydraulic properties for each HCD are evaluated. As indicated above, there are two exceptions that are discussed in Sections 7.2 and 7.3, respectively.

The deepest mid-point of a test section in the data has an elevation of –991 m. The data therefore covers approximately the upper 1,000 m of the rock volume. A total of 18 of the core holes KLX01 to KLX29A (KLX27A excluded) covers depth interval –400 to –650 m, or parts of the depth interval, within the local model volume. Of these 18 cored boreholes 14 intercepts the local volume south of deformation zone ZSMEW007A.

The transmissivity characteristics for each deformation zone (or Hydraulic Conductor Domain, HCD) are provided in Appendix 3.

Table 7-1. Distribution of hydraulic data for deterministic deformation zones (DZ) in the Laxemar-Simpevarp regional model volume modelled as HCDs. X(Y/Z): X= objects in the regional model volume (Y=objects belonging to deformation zones in the local model volume, thus including a few borehole intercepts outside the local model volume but with part of HCD within the local model volume/ Z=objects based on local model volume).

Object	Depth interval (masl)	No of DZ	Sample size of hydraulic observations	Comment
DZ	> –1,000	189[1]		
DZ with hydraulic data	> –1,000	57 (50/48)	158 (131/100)	
DZ with >1 observation of hydraulic data		24 (18/16)	125 (99/68)	2 to 19 observation in a single DZ, with mean observations=4
DZ with hydraulic data	> –150		73 (67/55)	
DZ with hydraulic data	–150 to –400		43 (28/16)	
DZ with hydraulic data	–400 to –650		19 (17/13)	
DZ with hydraulic data	< –650		23 (19/16)	

[1] Some of these 189 deformation zones are modelled as individual segments of a given numbered zone (e.g. ZSMxxxxxxA, ZSMxxxxxxB, etc, including the 4 HCD defined by hydrogeology).

Deformation zone transmissivities are grouped according to depth zones defined for the hydrogeological DFN model, cf. Chapter 9 (> –150, –150 to –400, –400 to –650, < –650 m) and if several observations exist within a depth zone for a certain HCD, the mean (log10 (T)), std log10 (T)) and mean elevation are calculated. In Appendix 3 the borehole names for each observation are also presented, thus enabling local conditioning of deformation zone transmissivity to available borehole data.

7.1.2 Evaluation methodology

In several cases different types of hydraulic tests have been performed over borehole sections interpreted to represent a given deformation zone. Data selected as “Best Choice” for the transmissivity (T-BC) of the entire deformation zone are generally based on the sum of PFL-s tests (5 m test sections) (cf. Chapter 4). These tests have been performed systematically in a large number of boreholes. For deformation zones with PFL-s data there are generally also PFL-f data (1 m tests in 0.1 m increments) (cf. Chapter 4) that indicate the frequency of flowing features and the transmissivity distribution of these features. If PFL-s data are missing, PSS data (cf. Chapter 4) were used for cored boreholes in terms of the sum of 20 m test section data over interpreted deformation zone thickness. For deformation zone intercepts in percussion boreholes and for intercepts in the upper 100 m of the cored boreholes, data from HTBH (cf. Chapter 4), generally with test scale 100 m, have been used, assuming that the transmissivity value is dominated by the properties of the deformation zone (as flow logging generally was not performed to facilitate a more precise estimate of the properties of deformation zones). PSS data of 5 m test scale only covered a limited number of deformation zones and have not been used for HCD property estimations.

As indicated above, most HCD transmissivities are based on PFL-s data which means that for the most part similar data are used and they cover well the defined thickness of the respective deformation zone. Tests have been made to judge what the difference would be to use the PSS-20 m data. It can be concluded that mostly they are fairly similar (PSS 20 m tests on average indicate a slightly higher transmissivity, generally up to c. 5 times larger for individual observations but a few values show larger differences. PSS tests available cover in some cases lager parts of the borehole compared to PFL-s and than defined borehole intercept for the deformation zones, which in a few cases resulted in that PSS tests included some high flowing features not part of defined deformation zones intercepts.). The choice of using PFL-s for transmissivity estimates is judged to be sufficient as there are also uncertainties related to using PSS 20 m tests (PSS 20 m tests generally covering a larger part of the borehole than defined by the geologically defined thickness of a given deformation zone)

As discussed in Chapter 4, transiently evaluated transmissivities are based on the first radial flow period, which has been judged to be the best estimate for further processing of the data for different purposes. One might suggest that a late time radial flow period would be more representative as average property for a HCD. This can be the case, but generally one do not have a very precise structural control of the flowing system and other hydraulically important structures may intersect

the tested deformation zone some hundreds of meters from the pumping hole, that may result in non-representative interpretation of a late time mean effective transmissivity for the studied deformation zone in question. The transmissivities from the first radial period also provides better data for discussion of spatial variability within deformation zones.

It is also important to point out that the transmissivities of HCDs presented in Chapter 7 and in Appendix 3 will be used as input in the regional-scale numerical groundwater flow model, and the typical values of deformation zones may change due to the calibration using interference tests, natural (undisturbed) heads and hydrogeochemical data as part of paleohydrogeological simulations.

7.2 Interference tests and indications of connectivity

Interference tests have been performed in a number of boreholes and are reported in /Enachescu et al. 2006a, 2007g, h, 2008a, Gokall-Norman and Ludvigson 2007, Gustafsson and Ludvigson 2005, Harrström et al. 2007, Morosini and Jönsson 2007, Morosini et al. 2009, Morosini and Wass 2006, Rahm and Enachescu 2004a, Svensson et al. 2007, Thur et al. 2007, Walger et al. 2007/. Interference test data involving observations in KLX27A /Enachescu et al. 2008b/ were not available for the evaluation.

Some of these tests have been of fairly short duration and involving only a few observation sections, but some tests have both a long duration and several observation sections, which make their results more interesting for comparison with the structural model.

Response variables that are considered when judging the magnitudes in responses in the observation sections are: Spherical distance squared divided by response time (dt_L = f(drawdown 0.1 m); r_s^2/dt_L) or specific drawdown; s_p/Q_p or distance weight specific drawdown; $(s_p/Q_p)\cdot\ln(r_s/r_0)$.

Below a few interference tests are described that are important for the HCD model development.

7.2.1 Deformation zone ZSMEW007A

A few tests have been performed along the surface extent of deformation zone ZSMEW007A, cf. Figure 3-6, that support the geological interpretation that the structure dips towards the north. Figure 7-1 illustrates the hydraulic pressure responses in a few boreholes when HLX10 was pumped. Very clear responses were noted in a KLX02 borehole section at borehole length c. 200–300 m but no responses deeper down. This fits well with the geologically interpreted geometry of the zone ZSMEW007A /Wahlgren et al. 2008/, as the zone ZSMEW007A is interpreted to be a feature more conductive than the surrounding rock.

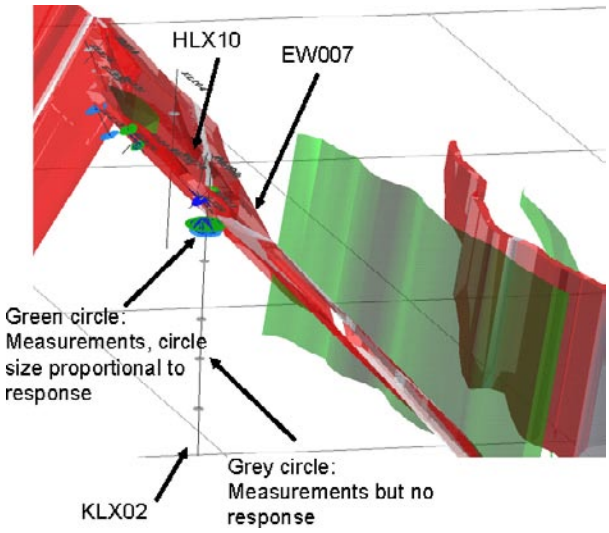

Figure 7-1. *Responses when HLX10 was pumped. View from the east-southeast.*

Later tests provided an insight in that hydraulic features along ZSMEW007A seemed to be steep with strike around E-W. The reason for this conclusion was the distribution of responses along borehole KLX07, which is drilled from the north through ZSMEW007A towards the south during the period when borehole HLX33 was pumped. As there were no responses in the deeper part of KLX07, there seemed to be no splays of ZSMEW007A (or other conductive zones dipping south and in hydraulic contact with ZSMEW007A) that were dipping south. Later, pumping tests along KLX07 confirmed this picture as pumping deeper sections in KLX07 did not seem to generate reponses towards the north.

7.2.2 Deformation zone ZSMNS001

Deformation zone ZSMNS001 is of particular interest as it is associated with a dolerite dyke, and as such, a potential hydraulic barrier as thicker dolerite dykes are expected to be low-conductive.

Two pumping tests were conducted in KLX20A and, due to some practical considerations, KLX19A was also pumped during the same period. Observations were made in two packed-off percussion boreholes; HLX37 and HLX43, cf. Figure 7-2. The responses from these three hydraulic disturbances as measured in HLX37 are shown in Figure 7-3 . It is concluded from the responses that ZSMNS001 must have a tight core but permeable wall rock, at least in the southern part of ZSMNS001 near KLX20A, see Figure 7-3 for the interpreted hydraulic communication paths:

- Pumping in KLX20A on the west side of the dolerite dyke in ZSMNS001 generates responses in borehole HLX37 west of the dolerite dyke in ZSMNS001 and no responses east of the dolerite dyke (Test 1).
- When pumping in KLX20A on the east side of the dolerite dyke in ZSMNS001 generates responses in borehole HLX37 east of the dolerite dyke in ZSMNS001 and no responses west of the dolerite dyke (Test 2).
- Pumping in KLX19A gives clear responses East of dyke but not west of the dolerite dyke.

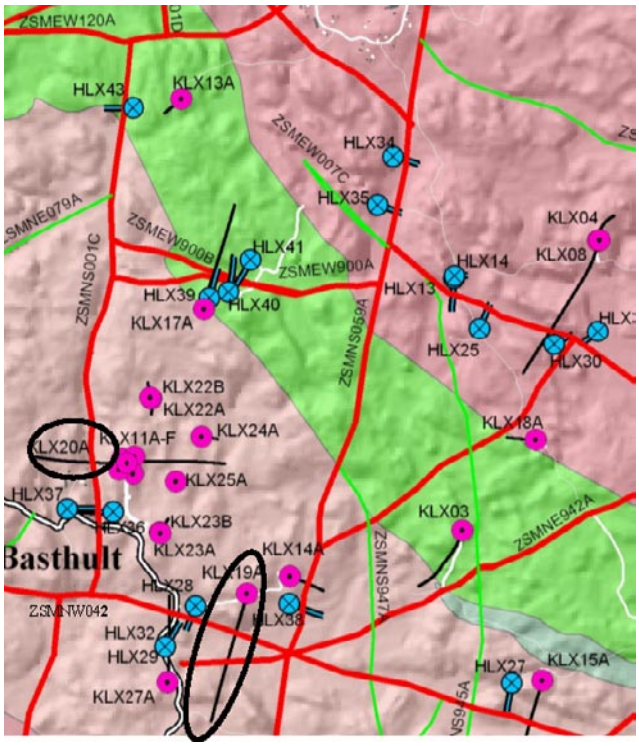

Figure 7-2. Pumping in KLX20A and KLX19A with observations in nearby percussion holes HLX37 and HLX43.

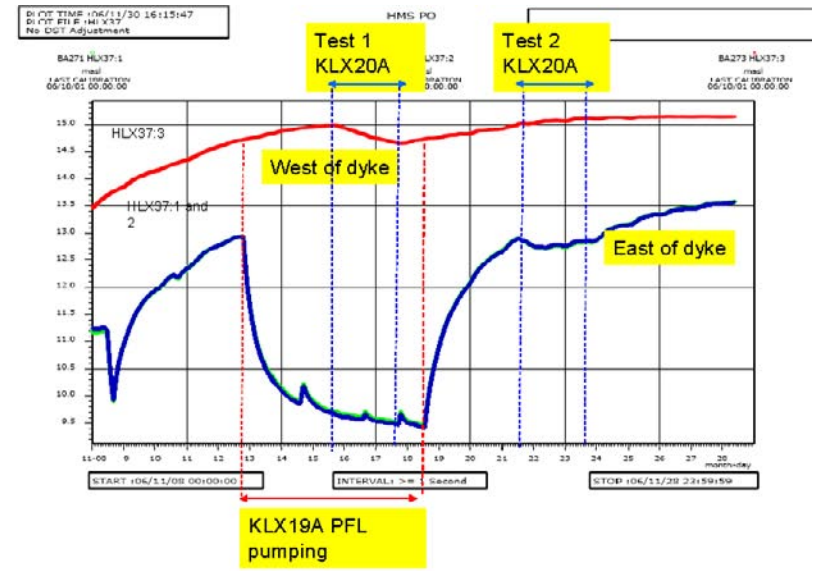

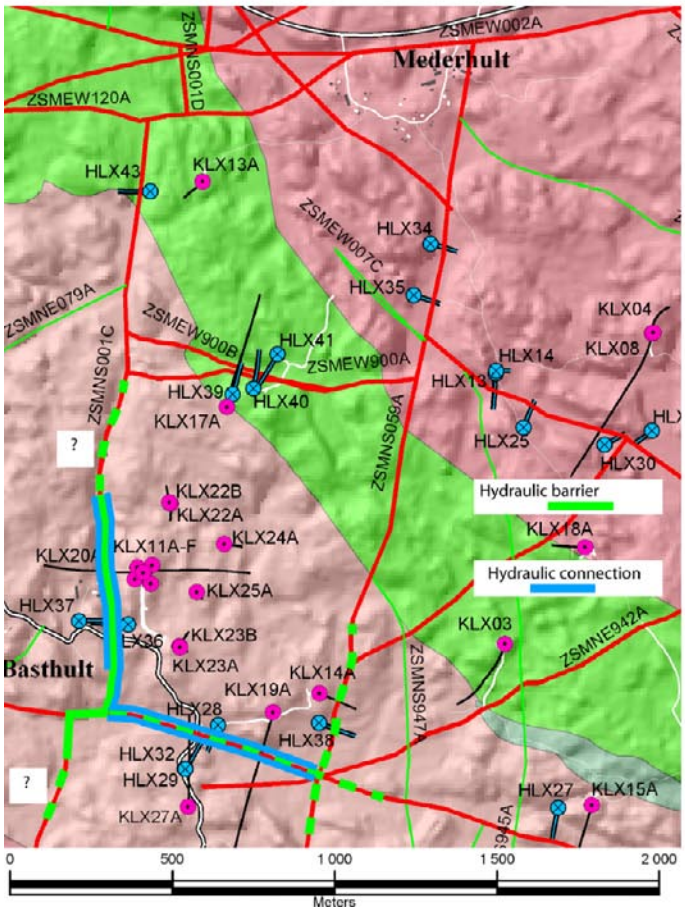

Figure 7-3. *Pumping in KLX20A and KLX19A. Top: observations in nearby percussion holes HLX37. Bottom: interpreted hydraulic connections and interpreted hydraulic barrier function.*

7.3 Dolerite dykes

Parts of three of the deformation zones are associated with or made up of dolerite dykes:

- ZSMNS001 (see also Section 7.2.2),
- ZSMNS059A,
- klx19_dz5-8_dolerite (dolerite devoid of associated surface expression, assumed to be 1,000 m in size).

The interpretation of HCD klx19_dz5-8_dolerite was inferred by hydrogeology due to hydraulic test results indicating a local barrier function. Dolerite dykes at Laxemar are expected to have a low hydraulic conductivity, see Table 7-2, but are still heavily fractured and the wall rock outside the dolerite dykes is fairly transmissive along the sides of the dyke, cf. Figure 7-4 and Figure 7-5.

Only 3 tests from the PSS measurements are entirely within the interpreted dolerites, see Figure 7-6. Dolerite is found in cored boreholes KLX01 (one, only ca 1 cm thick), KLX14 (several, centimetre to decimetre wide sections), KLX19A (three long sections) and KLX20A (two long and several centimetre to decimetre wide sections). Additional observations in percussion boreholes indicate dolerite sections from centimetres to several metres in length. In Figure 7-4 the dolerite and the wall rock in KLX20A is shown together with some mapped and measured entities. Based on Table 7-3 the following estimates can be made.

Dolerite dyke thicknesses have been estimated based on the deformation zone orientation, mapped dolerite lengths along the borehole and borehole orientation /Wahlgren et al. 2008/ as follows:

- ZSMNS001 is interpreted to be c. 30 ±10 m thick,
- ZSMNS059A is interpreted to to be c. 5 ±5 m thick,
- klx19_dz5-8_dolerite is interpreted to be c. 5 ±5 m thick.

The hydraulic conductivity (K) is c. $1{\cdot}10^{-7}$ to $1{\cdot}10^{-6}$ m/s for HCDs ZMSNS001, ZMSNS059 and klx19_dz5 using the mean transmissivity accross the HCD estimated, that represents flow along the HCD plane, divided by the HCD thickness. This indicates that anisotropy ratio of c. 1:1000 may be reasonable as the hydraulic conductivity of the dolerite in the centre of the HCD is in the range $1{\cdot}10^{-10}$ to $1{\cdot}10^{-9}$ m/s or possibly lower.

7.4 Correlations of deformation zone properties

Various deformation zone characteristics have been explored in relation to evaluated transmissivity of deformation zones. The former characteristics include; size, orientation and principle genetic appearance in terms of Ductile/Ductile-Brittle/ Brittle and depth of observation. This analysis is needed in order find a possible logic in how data relate to the various entities which could help structure the data in a meaningful way, and also to help inform deformation zones which lack borehole intercepts, and consequently are devoid of hydraulic data.

As stated in Section 7.1, in several cases different hydraulic tests have been performed covering borehole sections interpreted to represent a deformation zone. In most cases the geologically defined target borehole intercept of the zones in the boreholes, cf. /Wahlgren et al. 2008/ and Figure 3-5, have been used to select the relevant hydraulic test data applicable to the given deformation zone. The exception is zone ZSMNS001, which is a dolerite dyke surrounded by fractured conductive rock, see also Section 7.2.2, the latter which is outside the target borehole intercept of the zone in the applicable boreholes, where in fact this conductive fractured rock should be attributed to the hydraulically active HCD ZSMNS001, this albeit the dolerite itself being highly fractured shows a low hydraulic conductivity. However, one should also remember that the available hydrogeological observations in ZSMNS001 are limited to a few boreholes in the south-western part of the local model area and the hydraulic character is uncertain in other parts of the zone. As pointed out above, the HCDs klx19_dz5-8_dolerite klx09_dz9, klx09_dz14, klx16_dz6 and klx19_dz2 were also defined by Hydrogeology and are not part of the geologically defined deformation zones defined by Geology.

Table 7-2. Hydraulic conductivity of interpreted dolerite occurrences in boreholes.

Object	Borehole	Test type	Test sec. from (m)	Test sec. to (m)	Test scale (m)	Sample size	Mean Log_{10}(K-BC) (K: m/s)	Std Log_{10}(K-BC) (K: m/s)	Comment
ZSMNS001C	KLX20A	PFL-s	182.97	233.1	5	10	<–9.3	–	All data below measurement limit
klx19_dz5-8_ dolerite	KLX19A	PFL-s	484.06	544.07	5	12	<–9.7	–	All data below measurement limit
ZSMNS001C, klx19_dz5-8_ dolerite	KLX19A, KLX20A	PSS			20	3	–10.8	0.5	Tests sections are within dolerite dyke

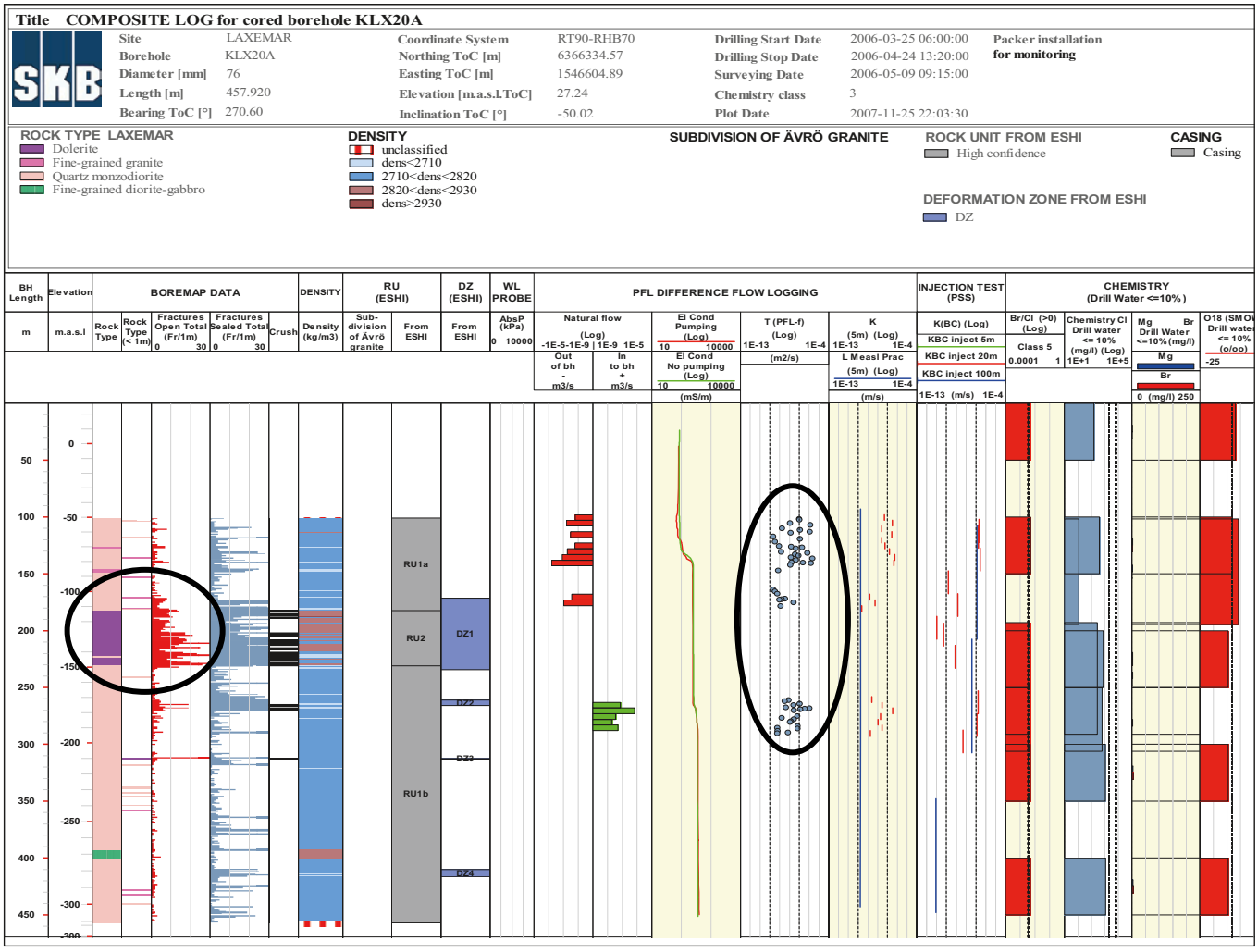

Figure 7-4. *KLX20A showing the properties of the dolerite (violet) and the wall rock /Hermanson et al. 2008/.*

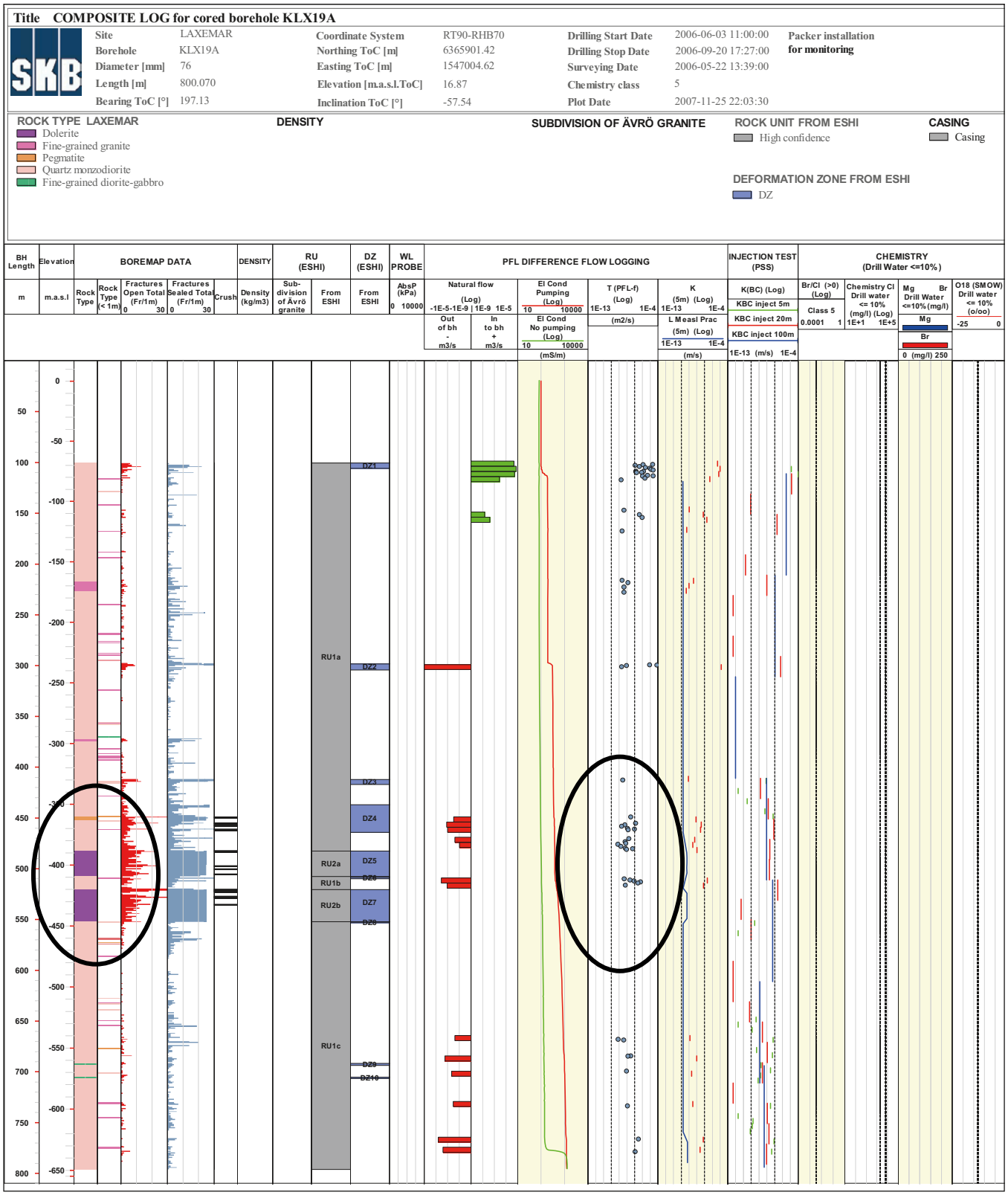

Figure 7-5. *KLX19A showing properties of the dolerite (violet) and the wall rock /Hermanson et al. 2008/.*

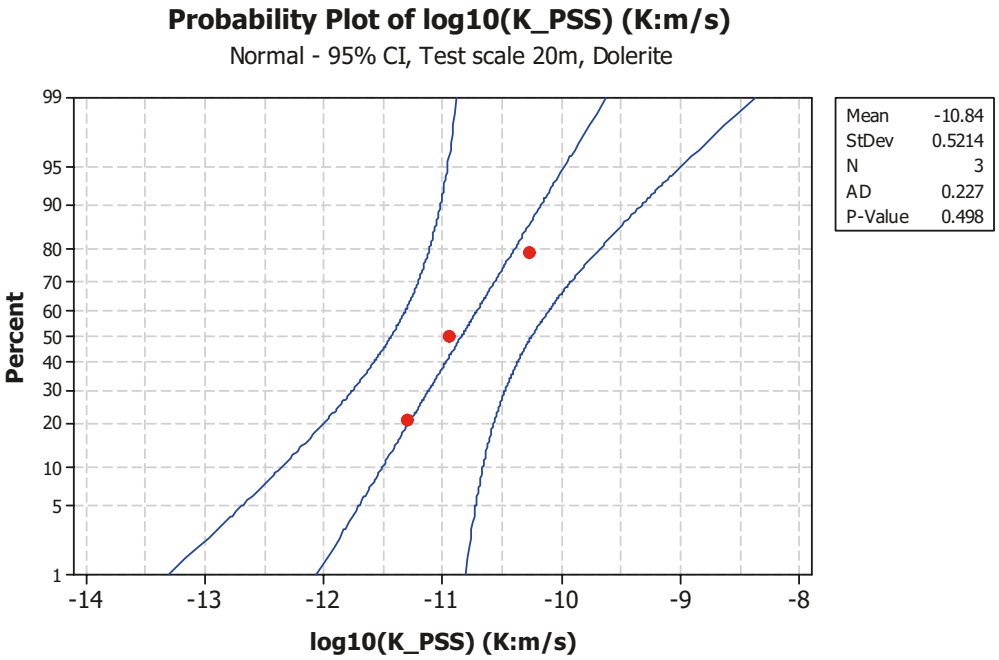

Figure 7-6. *Probability plot of PSS measurements in the dolerite. Test scale 20 m.*

Table 7-3. Geometrical considerations related to deformation zones modelled as dolerite dykes with conductive wall rock alongside.

DZ	Borehole	Bh-length, SecUp (m)	Bh-length, SecLow (m)	Rock type	Length along bh (m)	True thickness (m)	Comment
ZMSNS059	KLX14A	75.366	76.554	Dolerite	1.188	0.84	(1)
klx19_dz5	KLX19A	482.603	507.675	Dolerite	25.072	0.13	(3)
klx19_dz5	KLX19A	520.439	522.403	Dolerite	1.964	0.01	(3)
klx19_dz5	KLX19A	522.403	552.213	Dolerite	29.81	0.16	(3)
ZMSNS001	KLX20A	182.371	222.704	Dolerite	40.333	21.36	(2)
ZMSNS001	KLX20A	223.983	230.898	Dolerite	6.915	3.66	(2)
	HLX13	75.080	107.783	Dolerite	32.703	4.27	(4)
ZMSNS001	HLX36	112.006	191.367	Dolerite	79.361	39.67	(2)
ZMSNS001	HLX37	122.279	146.708	Dolerite	24.429	17.24	(2)
ZMSNS001	HLX43	32.441	73.723	Dolerite	41.282	19.92	(2)

(1): (Assumed strike/dip of dolerite dyke: ZSMNS059A: 188/85.

(2): (Assumed strike/dip of dolerite dyke: ZSMNS001: 185/81.

(3): Assuming strike 170 or 210 degree the true thickness becomes ca 5 m. It is unlikely that the true thickness is just a few cm when the length along the borehole is 25–30 m.

(4): Assuming strike 170 or 210 degree the true thickness become ca 1 or 10 m.

7.4.1 Deformation zone size versus deformation zone thickness

Deformation zone thickness is shown to vary along the extent of a given deformation zone. /Wahlgren et al. 2008/ presents interpreted mean thickness, zone mean strike and dip and borehole length of the borehole intercept. The deterministic deformation zones are generally larger than 1 km in size, as seen in lineament data on surface. A few of the deformation zones modelled deterministically are shorter than 1 km. In some cases a deformation zone is interpreted on the basis of a borehole intercept but lacks an associated surface outcrop. On the basis of correlation established between interpreted length and true thickness the size (or length) of a zone with a true thickness > 10 m is assumed to be associated with a size (length) > 1,000 m and with a thickness around 0.01 of the deformation zone length /Wahlgren et al. 2008/. A more detailed discussion on the interpretation of deformation zone size and thickness is found in /Wahlgren et al. 2008/.

7.4.2 Transmissivity versus elevation

In Figure 7-8 the deformation zone mean transmissivity (mean log10(T)) is given as function of elevation. As can be seen there is an obvious depth trend considering geometric mean transmissivities for the four defined depth zones but also considering the maximum observed transmissivities.

7.4.3 Transmissivity versus ductility and brittleness

/Wahlgren et al. 2008/ provide the deformation zone characteristics Ductile, Ductile-Brittle or Brittle. For the deterministic deformation zones, which generally are larger than 1 km, only zones of character Ductile-Brittle (DB, meaning that there is clear evidence of ductile character but also clear evidence of subsequent brittle deformation) and Brittle (B, meaning that there is clear evidence of brittle deformation but no clear evidence of ductile deformation) are defined. Ductile character (D, meaning that there is clear evidence of ductile character but no clear evidence of subsequent brittle deformation) is not attributed to these larger deformation zones but indeed to minor deformation zones (as presented in the subsequent Chapter 8).

In Figure 7-9 the deformation zone mean transmissivity (mean log10(T)) for depth zones is plotted for groups DB and B, as defined above. As can be seen there is no correlation between T and ductility/brittleness as defined by the B/DB groupings. The sample size of B is about half of DB, the latter sustained by 111 observations.

7.4.4 Transmissivity versus deformation zone size

In Figure 7-10 and Figure 7-11 the deformation zone mean transmissivity is plotted versus size. Initially several size-groups were tested but the sample size become small in several of the groups and the significance of the results become low. A better choice seems to be to only use two size groups; 1–2 km and >2 km, see Figure 7-10, which indicates that there is a significant difference considering all regional scale data. A similar picture can be seen in the data for the local model volume, cf. Figure 7-11. It is interpreted that the regional data set probably is more relevant to judge the possible presence of a size-transmissivity correlation as this data set is larger.

7.4.5 Transmissivity versus deformation zone dip

If the dips of deformation zones is divided into two classes; dip<30°, dip≥30°, see Figure 7-12, it seems that the more subhorizontal zones are less transmissive. However, looking at the size distribution versus dip of the deformation zones, cf. Figure 7-13, it is evident that it is nearly only small deformation zones that are subhorizontal and the lower transmissivity can instead be explained by size differences.

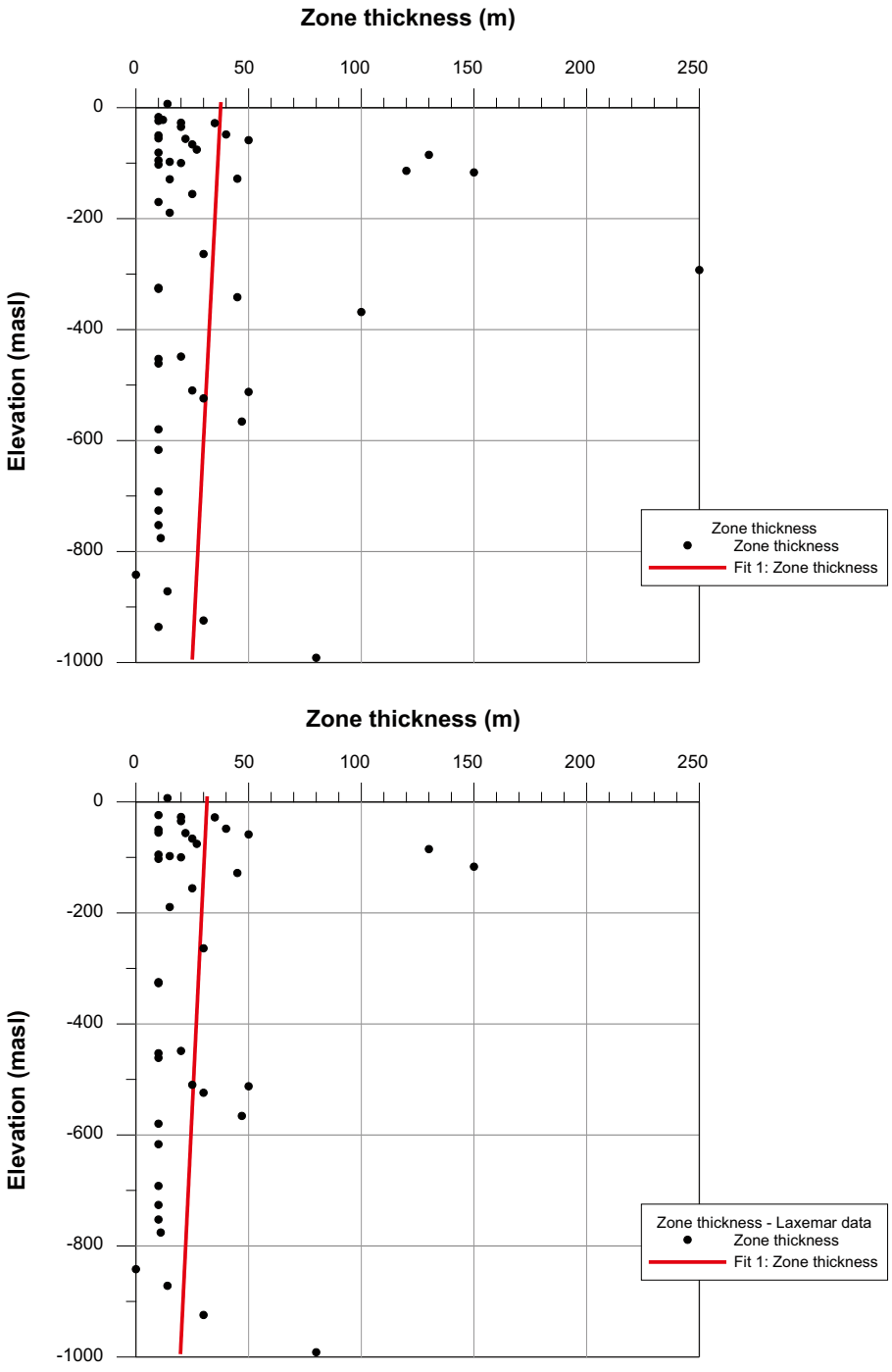

Figure 7-7. *Deformation zone thickness versus elevation. (Data Top: regional model. Bottom: local model).*

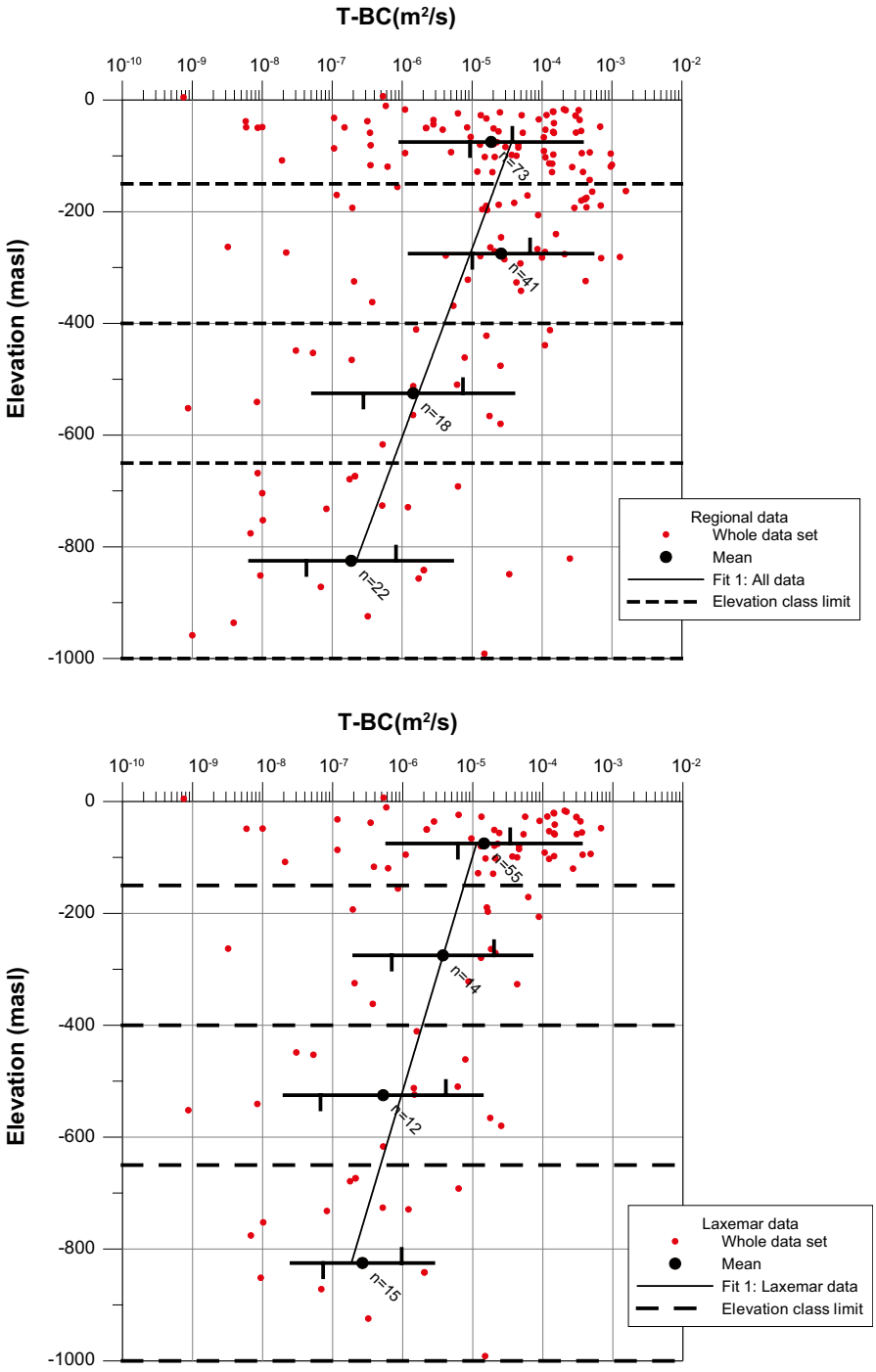

Figure 7-8. *Deformation zone transmissivity (T) versus elevation: For depth zones the number of observations (n) for depth zones, geometric mean T (Mean), 95% confidence limits for mean log10(T)(vertical bars on horizontal line) and ±1 standard deviation log10(T)(entire horizontal line) are plotted. The line is fitted to the 4 Geometric mean values. Top: regional model volume, Bottom: Local model volume.*

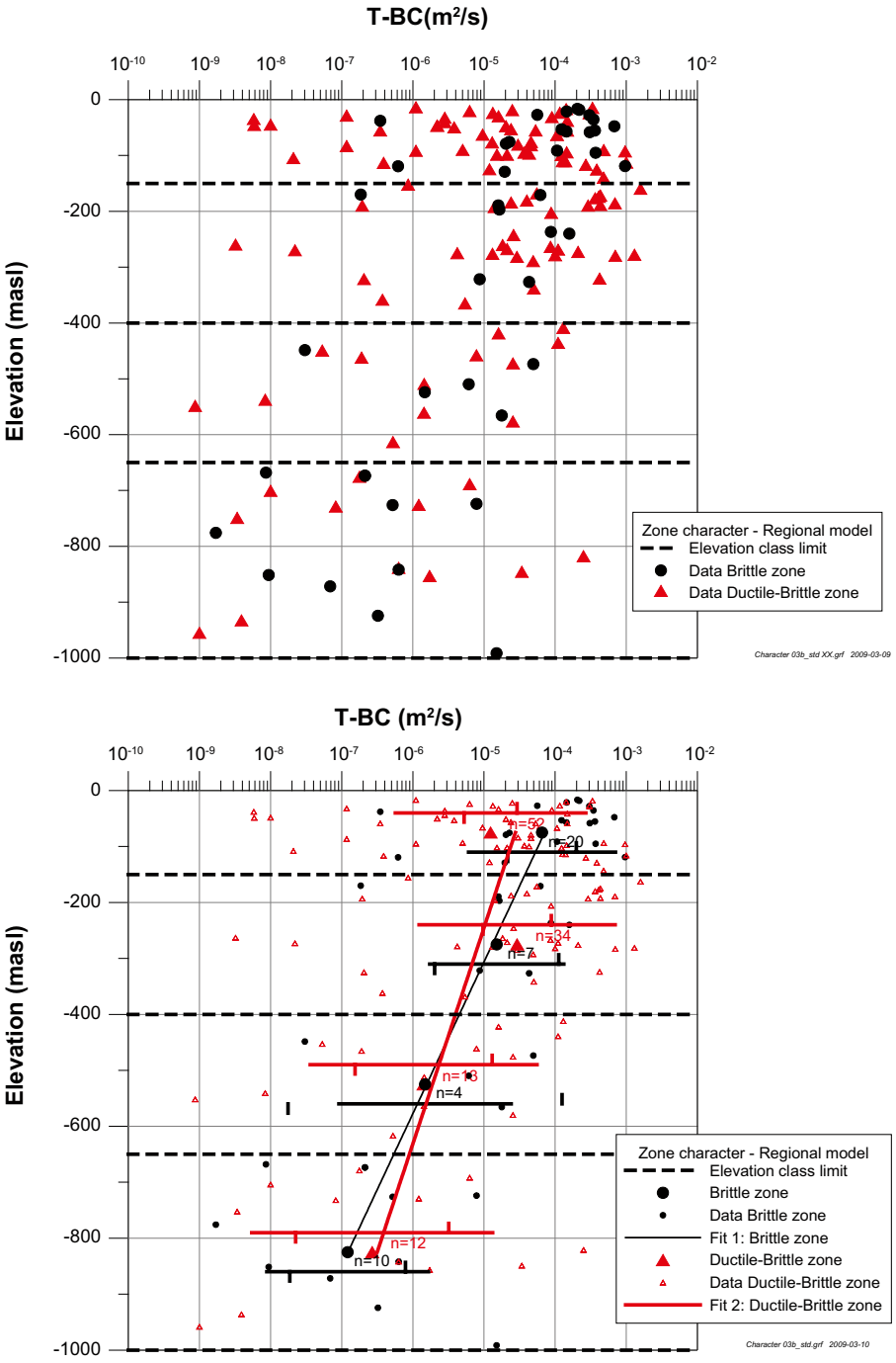

Figure 7-9. *Deformation zone transmissivity (T) related to deformation zone characteristics expressed as; Ductile-Brittle(DB) and Brittle(B), versus elevation. Top: data points, Bottom: data points and statistics. For depth zones the number of observations (n) for depth zones, geometric mean T (Mean), 95% confidence limits for mean log10(T)(vertical bars on horizontal line) and ±1 standard deviation log10(T)(entire horizontal line) are plotted. The line is fitted to the 4 Geometric mean values. Data from regional scale model volume.*

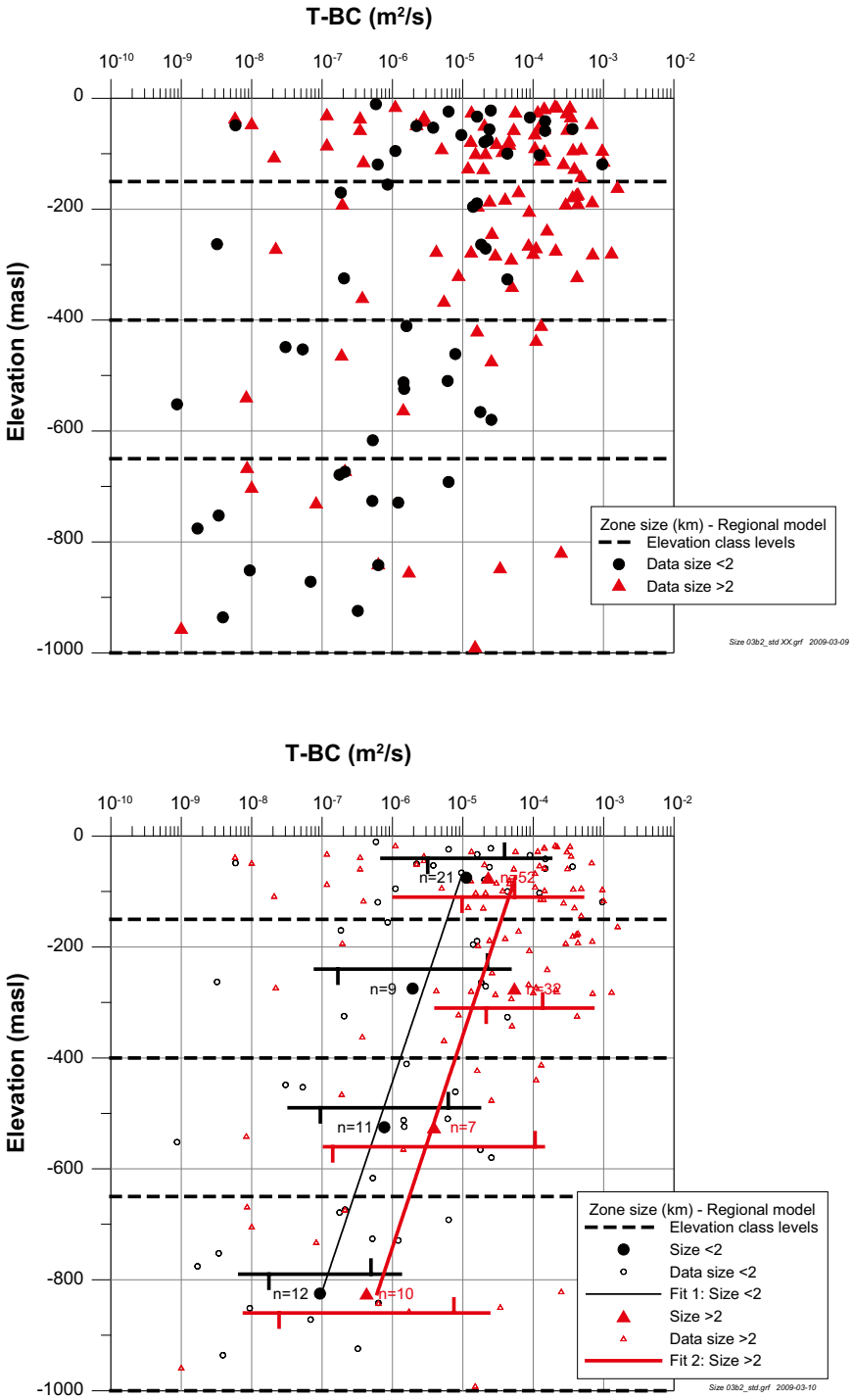

Figure 7-10. *Deformation zone transmissivity (T) related to deformation zone size, versus elevation. Top: data points, Bottom: data points and statistics. For depth zones the number of observations (n) for depth zones, geometric mean T (Mean), 95% confidence limits for mean log10(T)(vertical bars on horizontal line) and ±1 standard deviation log10(T)(entire horizontal line) are plotted. The line is fitted to the 4 Geometric mean values. Data from regional scale model volume.*

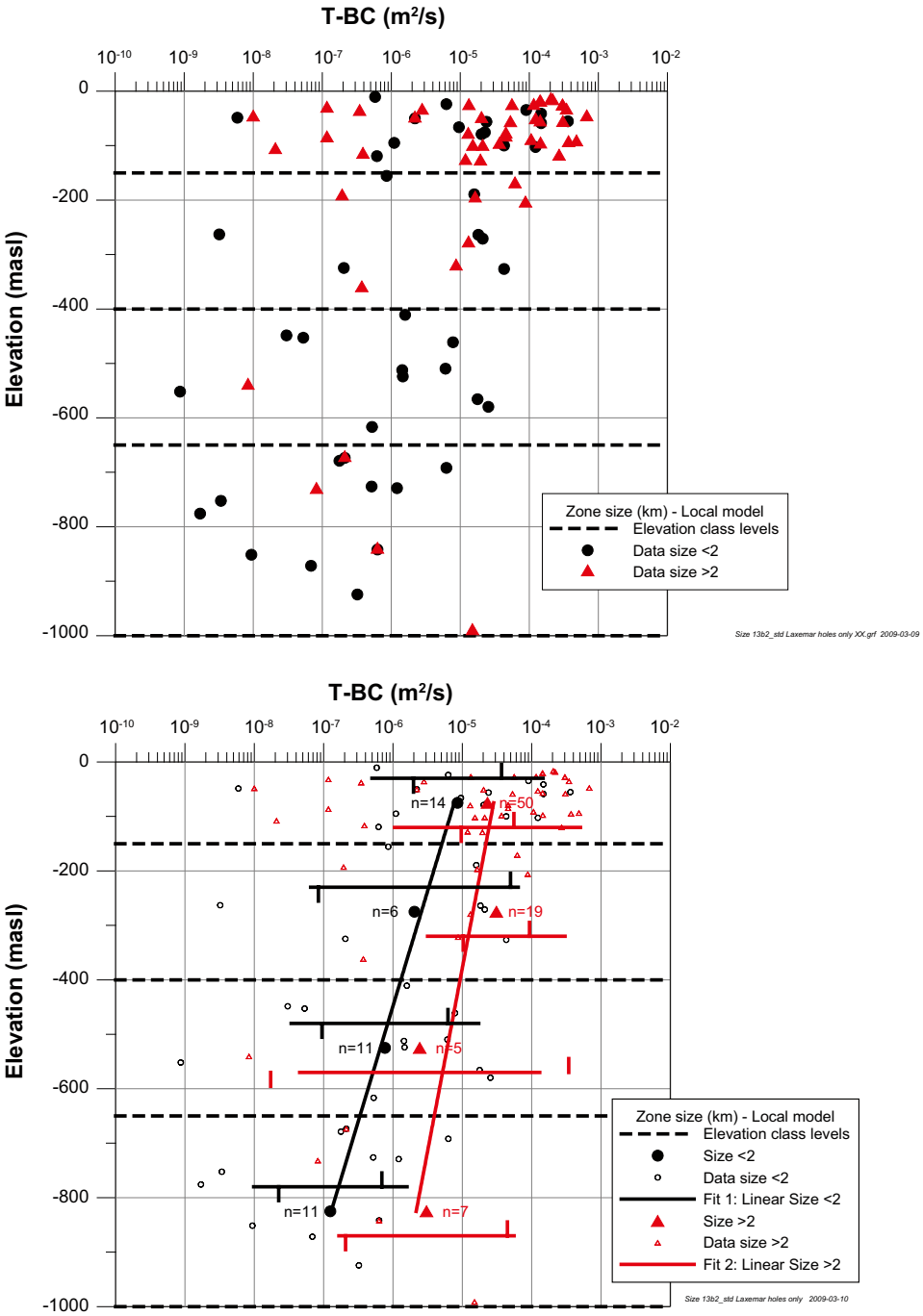

Figure 7-11. *Deformation zone transmissivity (T) related to deformation zone size, versus elevation. Top: data points, Bottom: data points and statistics. For depth zones the number of observations (n) for depth zones, geometric mean T (Mean), 95% confidence limits for mean log10(T)(vertical bars on horizontal line) and ±1 standard deviation log10(T)(entire horizontal line) are plotted. The line is fitted to the 4 Geometric mean values. Data from local scale model volume.*

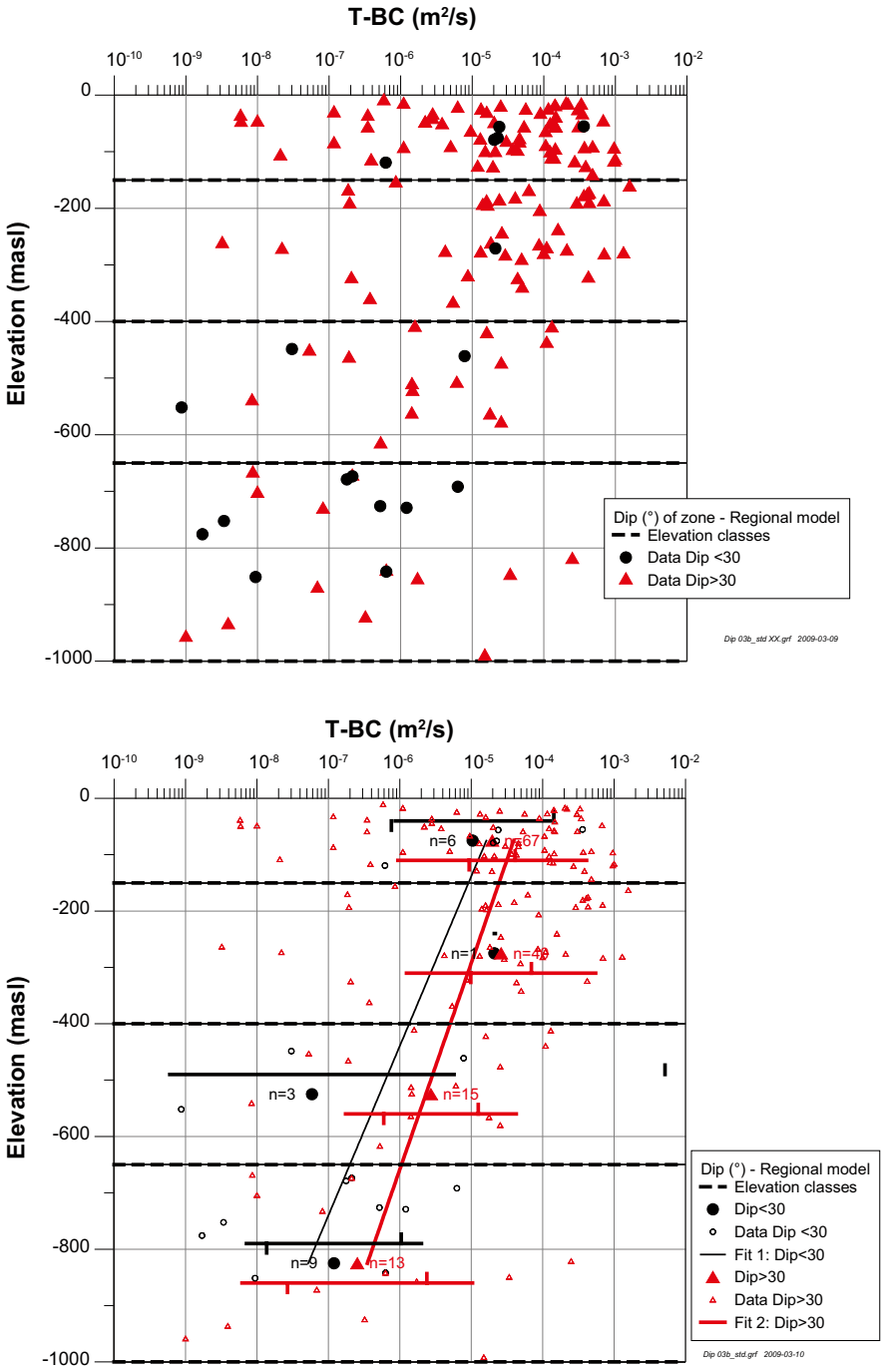

Figure 7-12. *Deformation zone transmissivity (T) related to deformation zone dip, versus elevation. Mean of log10(T), max and min T are plotted as well as the number of observations (n) for elevation intervals. (Data: regional model.)*

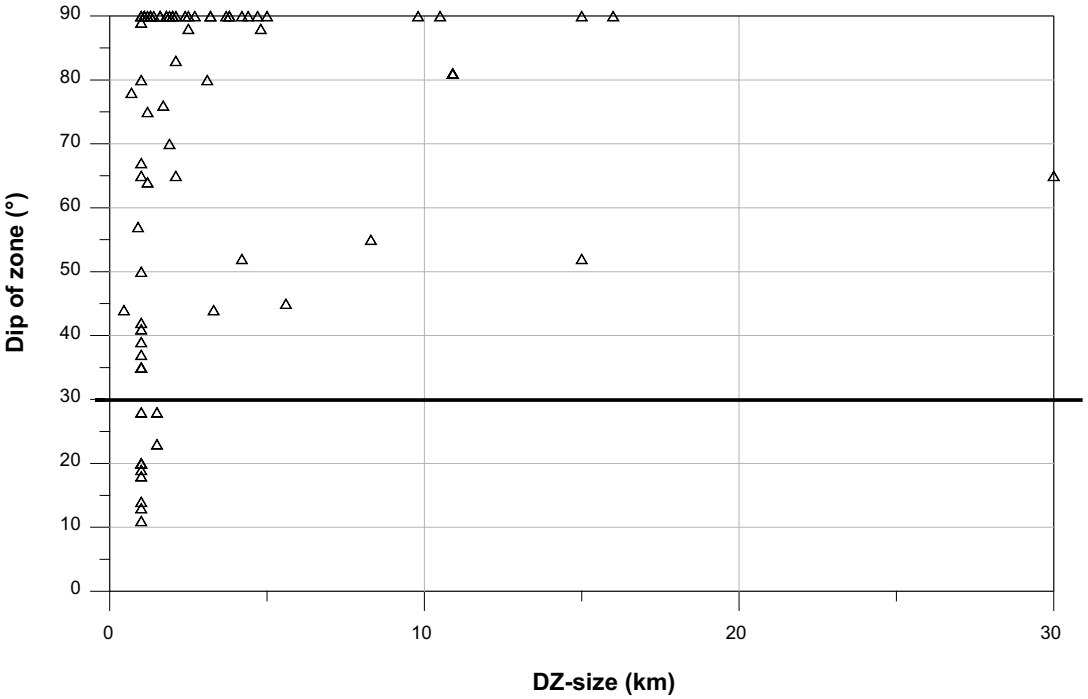

Figure 7-13. *Deformation zone size versus deformation zone dip. Data from regional scale model volume.*

7.4.6 Transmissivity versus deformation zone orientation

In Figure 7-14 the deformation zone mean transmissivity (mean log10(T)) for depth zones is plotted for the orientation (strike) groups; E-W, NW-SE, N-S, NE-SW, respectively. There seems to be a notable difference between NW-SE deformation zones relative to the other orientation groups. The sample size of N-S deformation zones is limited but one can probably state that E-W, N-S and NE-SW deformation zones have similar transmissivity distributions. However, incorporation also of the size distribution provides a somewhat different view, see Section 7.4.7.

7.4.7 Transmissivity versus deformation zone orientation and size

Figure 7-15 and Figure 7-16 show the deformation zone mean transmissivity (mean log10(T)) for depth zones plotted for the orientations (strike) groups; E-W, NW-SE, N-S, NE-SW and size. According to the figure there seems to be a difference between the orientation groupings when also separated in two size-groups, at least when considering the regional data.

The local model data seem to indicate that it is only the E-W grouping of size >2 km that differs from the others. The sample sizes of each grouping is small and the group E-W with size >2 km is dominated by data from the large deformation zones ZSMEW005A and ZSMEW002A, which provide a plausible explanation for the noted difference.

For preliminary assignments of properties in groundwater flow models, it is suggested that for the regional and local model volumes to use the regional models for size and orientation groups. However, as an alternative for the local model volume it seems reasonable to use a trend model for all Laxemar data, cf Figure 7-8, and not use size and orientation groups.

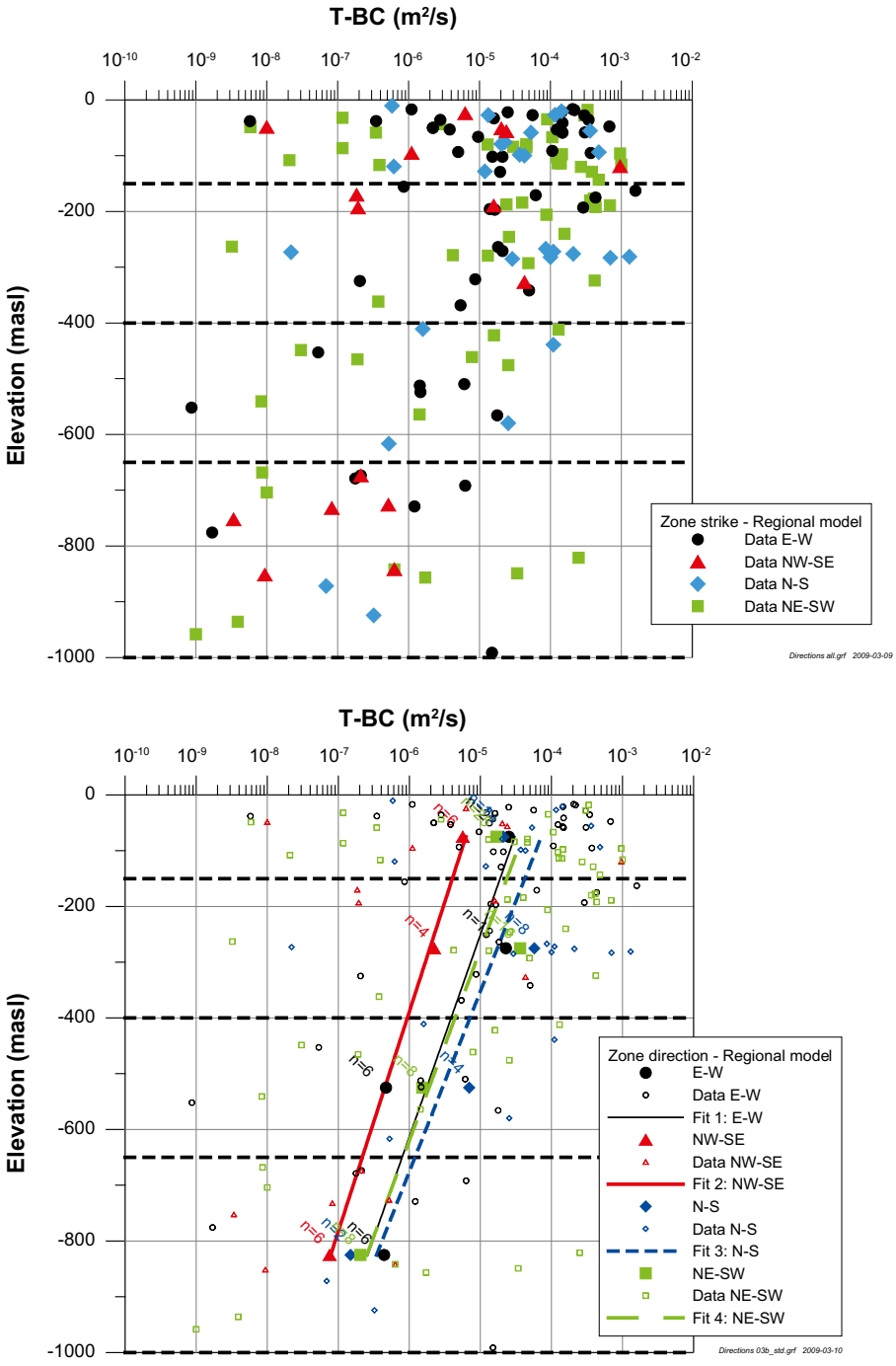

Figure 7-14. *Deformation zone transmissivity (T) related to deformation zone orientations in the horizontal plane, versus elevation. Top: data points, Bottom: data points and statistics. For depth zones the number of observations (n) for depth zones, geometric mean T (Mean), 95% confidence limits for mean log10(T) (vertical bars on horizontal line) and ±1 standard deviation log10(T)(entire horizontal line) are plotted. The line is fitted to the 4 Geometric mean values. Data from regional scale model volume.*

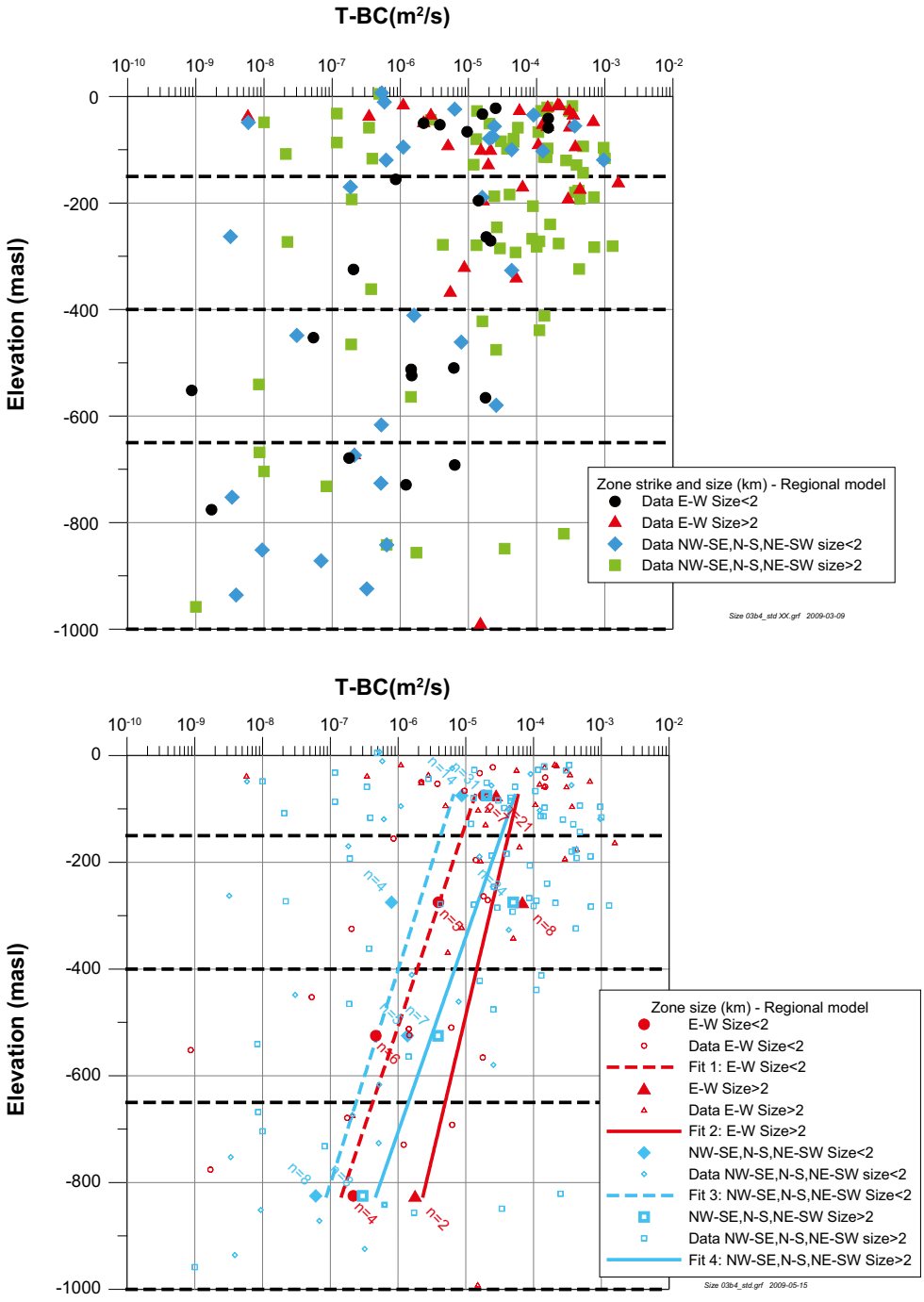

Figure 7-15. *Deformation zone transmissivity (T) related to deformation zone orientations in the horizontal plane and size, versus elevation. Top: data points, Bottom: data points and statistics. For depth zones the number of observations (n) for depth zones, geometric mean T (Mean), 95% confidence limits for mean log10(T)(vertical bars on horizontal line) and ±1 standard deviation log10(T)(entire horizontal line) are plotted. The line is fitted to the 4 Geometric mean values. Data from regional model volume.*

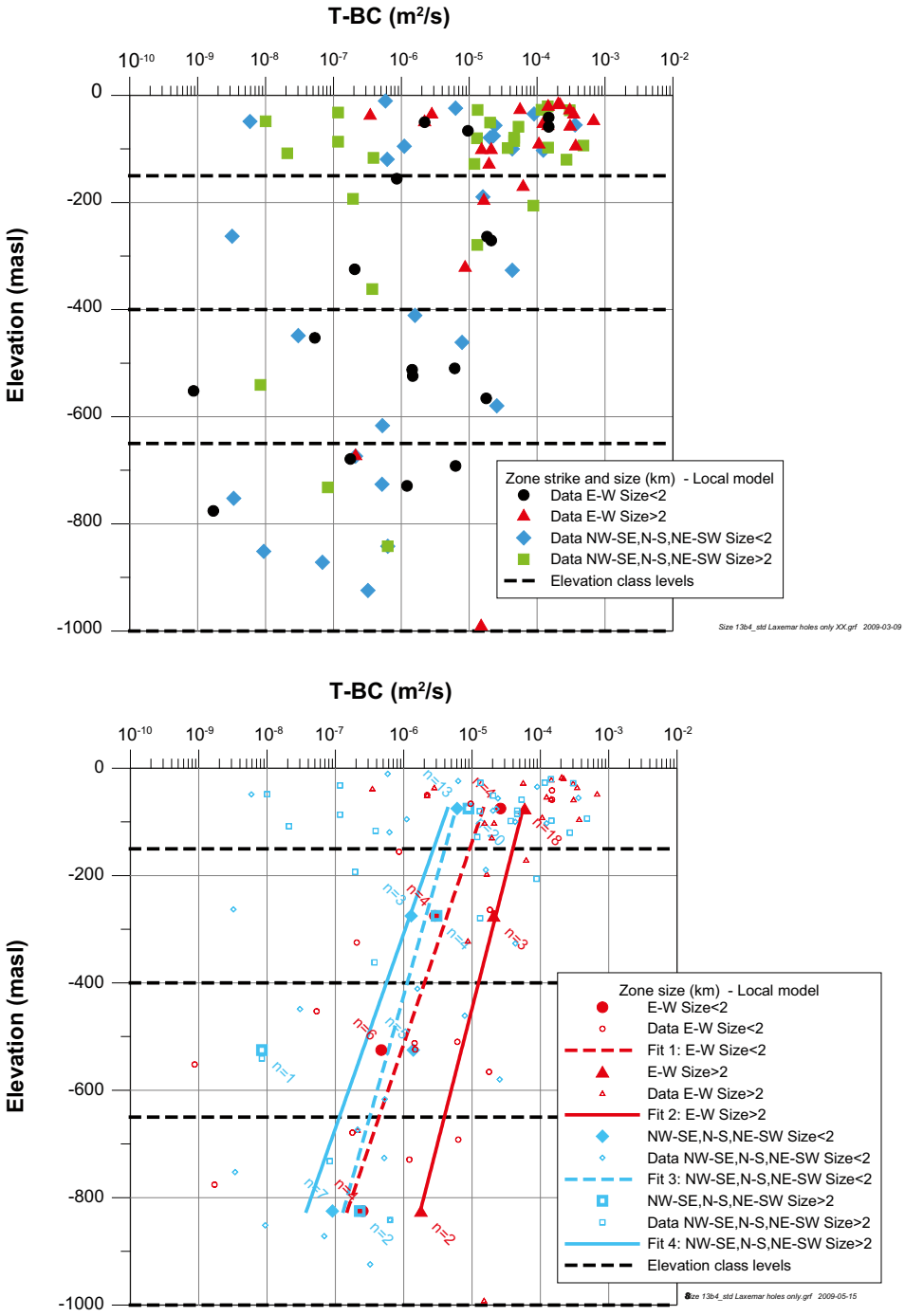

Figure 7-16. *Deformation zone transmissivity (T) related to deformation zone orientations in the horizontal plane and size, versus elevation. Top: data points, Bottom: data points and statistics. For depth zones the number of observations (n) for depth zones, geometric mean T (Mean), 95% confidence limits for mean log10(T)(vertical bars on horizontal line) and ±1 standard deviation log10(T)(entire horizontal line) are plotted. The line is fitted to the 4 Geometric mean values. Data from local model volume.*

7.5 Preliminary hydrogeological models for deterministically modelled deformation zones

The transmissivity models of HCDs presented in this section and in Appendix 3 will be used as input to the subsequent regional-scale numerical groundwater flow model. Due to the calibration using interference tests, natural (undisturbed) heads and hydrogeochemical data as part of paleohydrogeological simulations, the final assessment of individual HCD parameterisation will be reported in /Rhén et al. 2009/.

7.5.1 Conceptual model

The transmissivity of a deformation zone decreases with depth but the standard deviation is fairly constant by depth (cf. Figure 7-19).

The transmissivity of a deformation zone increases with size, but the variability is high. The reason seems to be that the number of flowing fractures increases due to possibly more extensive brittle deformation in the larger zones, resulting in more fractures and a thicker fractured deformation zone, cf. Section 7.8.

NW-SE, N-S and NE-SW deformation zones are less transmissive than E-W deformation zones within the regional model volume. Possibly there are no differences within the local model volume, cf. Figure 7-15 and Figure 7-16.

Those deformation zones that are associated with dolerite dykes (ZSMNS001C, ZSMNS059A and klx19_dz5-8_dolerite) are assumed to have a fractured, but yet impermeable core, representing the dolerite, but have permeable contacts with/in the wall rock along either side of the dolerite. The continuity of these impermeable cores and conductive flanks is uncertain. The transmissivities provided in this report represents the total expected transmissivity of these deformation zones that should be related to the permeable rock outside the dolerite.

Some deformation zones may have fault gauge that affects the hydraulic characteristics of the zone. Clay has not been reported but fault gouge has been documented in the cores of the faults in both ZSMEW002A (KLX06), ZSMEW007A (trench) and ZSMNW042A (KLX27A). However, it is difficult to state whether the fault gouge is continuously distributed along the deformation zones. Probably the gauge is not continuously distributed as most deformation zones are heterogeneous along strike what relates to both true thickness, the relation between fault core and transition zone and the types of fault rocks etc.

7.5.2 Parameterisation of non-tested deformation zones

There are a large number deformation zones in the regional model volume that lack site-specific hydraulic data. The general characteristics inferred for deformation zones with hydraulic data are used in the assessments of possible hydraulic characteristics of non-tested deformation zones in the following way.

Deterministic deformation zones without site specific hydraulic data are divided into four categories:

- Orientation group E-W, Size <2 km.
- Orientation group E-W, Size >2 km.
- Orientation group NW-SE, N-S and NE-SW, Size <2 km.
- Orientation group NW-SE, N-S and NE-SW, Size >2 km.

The suggested trend functions for these categories are shown in Table 7-6 and Table 7-7.

The following basic trend models for variables (denoted X in trend function); total HCD transmissivity within HCD etc, are used:

- Power-law trend model (Power): $X = a \cdot (-Z)^B$ (7-1)
- Linear trend model (Linear): $X = a + B \cdot (Z)$ (7-2)
- Exponential trend model (Exp): $X = (10^Y =) 10^{(a+B \cdot Z)}$ (7-3)

Z: Elevation in m (masl) (Z defined positive up). The coefficients in the Exponential trend model are based on a linear regression of Log10(X_i) and this trend model is generally just used for transmissivity and hydraulic conductivity.

Trend functions can be used directly to assign properties to individual elements of the 3D mesh of the regional groundwater flow model, or to estimate values for the four depth zones; >–150 m, –150– to –400 m, –400 to –650 m, <–650 m.

If a thickness estimate is explicitly given for a certain deformation zone, the thickness of the deformation zone is assumed to be given by 0.01·DZ-size, cf. Section 7.4.1 . (NB. Where "DZ-size" is the interpreted length of the surface expression of any given zone.)

Figure 7-17 shows the two trend functions used for the entire HCD data set (regional model volume) and Figure 7-18 shows HCD data from the local model volume. Viewing the confidence limits for transmissivity (T) it is observed that T above elevation –150 m is greater than below elevation –400 m, indicating that there is in fact an actual depth trend.

Using the suggested trend functions for T will generate unrealistically low transmissivities at great depths compared with what is expected in HRDs and even matrix hydraulic conductivity. As the mean deformation zone thickness at elevation –1,000 m is around 30 m and matrix hydraulic conductivity is expected to be in the range 10^{-14} to 10^{-12} m/s, a lower limit for HCD transmissivity can probably be set to about 10^{-10} m^2/s.

As can be seen in Figure 7-17 through Figure 7-22, Table 7-4 and Table 7-5, the standard deviation (log10(T)) is fairly constant with depth. For stochastic simulations without spatial correlation probably a constant std Log10(T) = 1 to 2 can be used. The trend functions of the standard deviation in the figures are questionable. In principle the standard deviation indicated in Figure 7-22 and Table 7-5 should be more representative for an estimate of standard deviation within an individual HCD as it is based on several samples in individual zones, but the difference is small compared with the standard deviations for the total samples within the respective depth zones.

Trend functions vs. depth for the regional model HCD transmissivities, taking HCD orientation and size into account, are shown in Table 7-6, Figure 7-10, Figure 7-14 and Figure 7-15, respectively. Trend functions for the local model HCD transmissivities related to HCD orientation and size are shown in Table *7-7*, Figure 7-11 and Figure 7-16.

As a first alternative it is suggested to use the four categories mentioned above, both for the regional model and the local model (Models DZ-R-19 to DZ-R-22, in Table 7-6). As a second alternative, just one model for deformation zones within the local model volume should be used (Model DZ-L-4 in Table 7-7, cf. Figure 7-18).

The deformation zone transmissivity has been divided by the estimated true thickness of the zone, to estimate the hydraulic conductivity of each deformation zone subject to hydraulic tests. The results are presented in Figure 7-23, Figure 7-24 and Table 7-8, respectively.

Comments to the fitted models

One can observe that the two Exponential trend models for the local model hydraulic parameterisation of deformation zones (DZ-L-L3 and DZ-L-L4) are essentially coincide and are more or less identical to the parameterisation of the regional model (DZ-R-R2) fitted to the means of the depth zone. When applied to the regional model deformation zone data, the trend for both the linear and power law becomes steeper compared to the fit to the four means associated with the defined depth zones. This is not surprising as more weight is put on the very large number of observations near the surface in order to fit to all data. The fits to the means are considered more relevant as it features equal weights for the depths intervals.

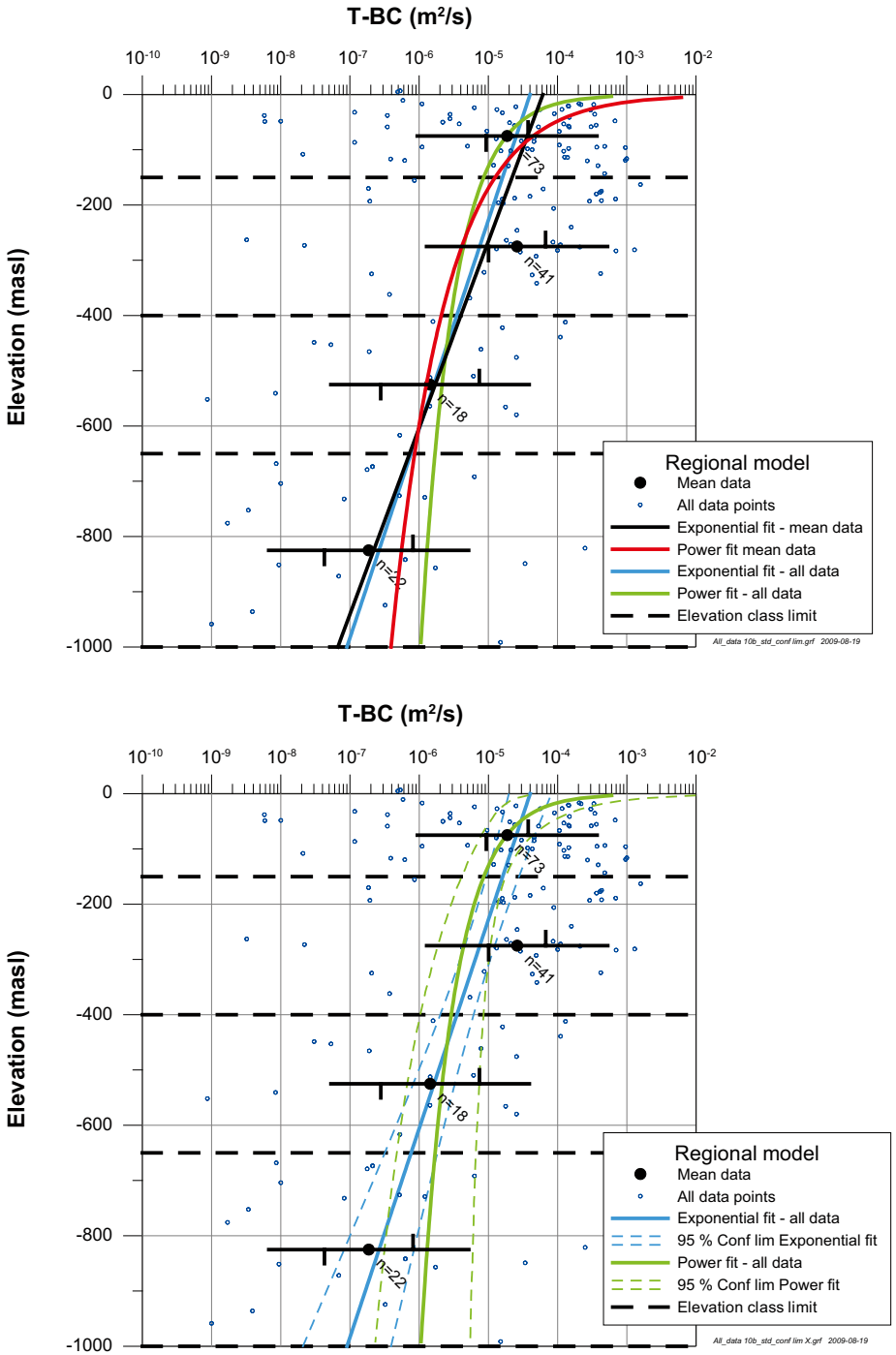

Figure 7-17. *HCD transmissivity (T) versus elevation: For depth zones Geometric mean T, 95% confidence limits for mean log10(T)(vertical bars on horizontal line) and ±1 standard deviation log10(T)(entire horizontal line) are plotted. Curves are fitted to the 4 geometric mean values or all data. Confidence intervals for fitted lines are shown for lines fitted to all data. Data from regional model volume.*

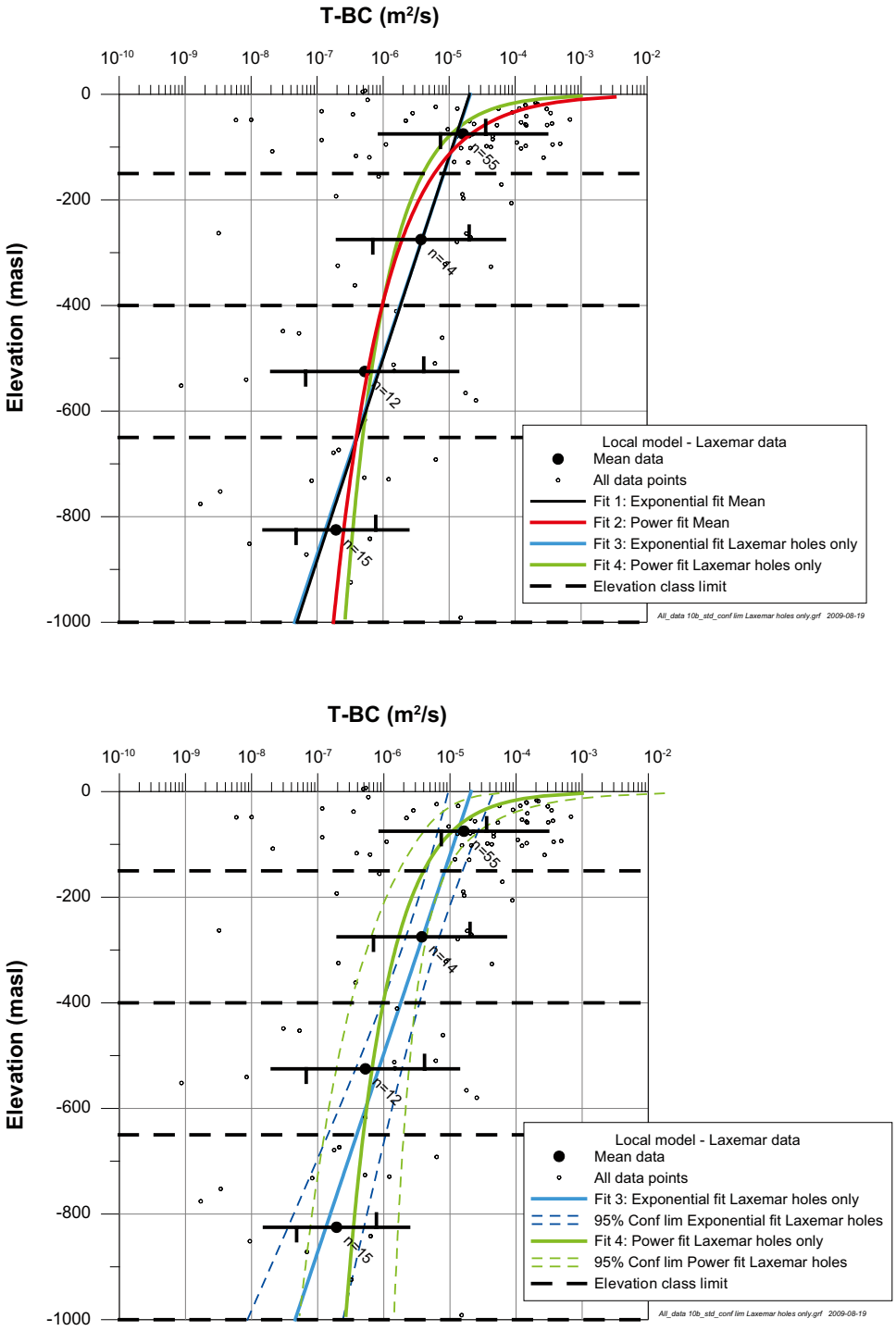

Figure 7-18. *HCD transmissivity (T) versus elevation: For depth zones Geometric mean T, 95% confidence limits for mean log10(T)(vertical bars on horizontal line) and ±1 standard deviation log10(T)(entire horizontal line) are plotted. Curves are fitted to the 4 geometric mean values or all data. Confidence intervals for fitted lines are shown for lines fitted to all data. Data from local model volume.*

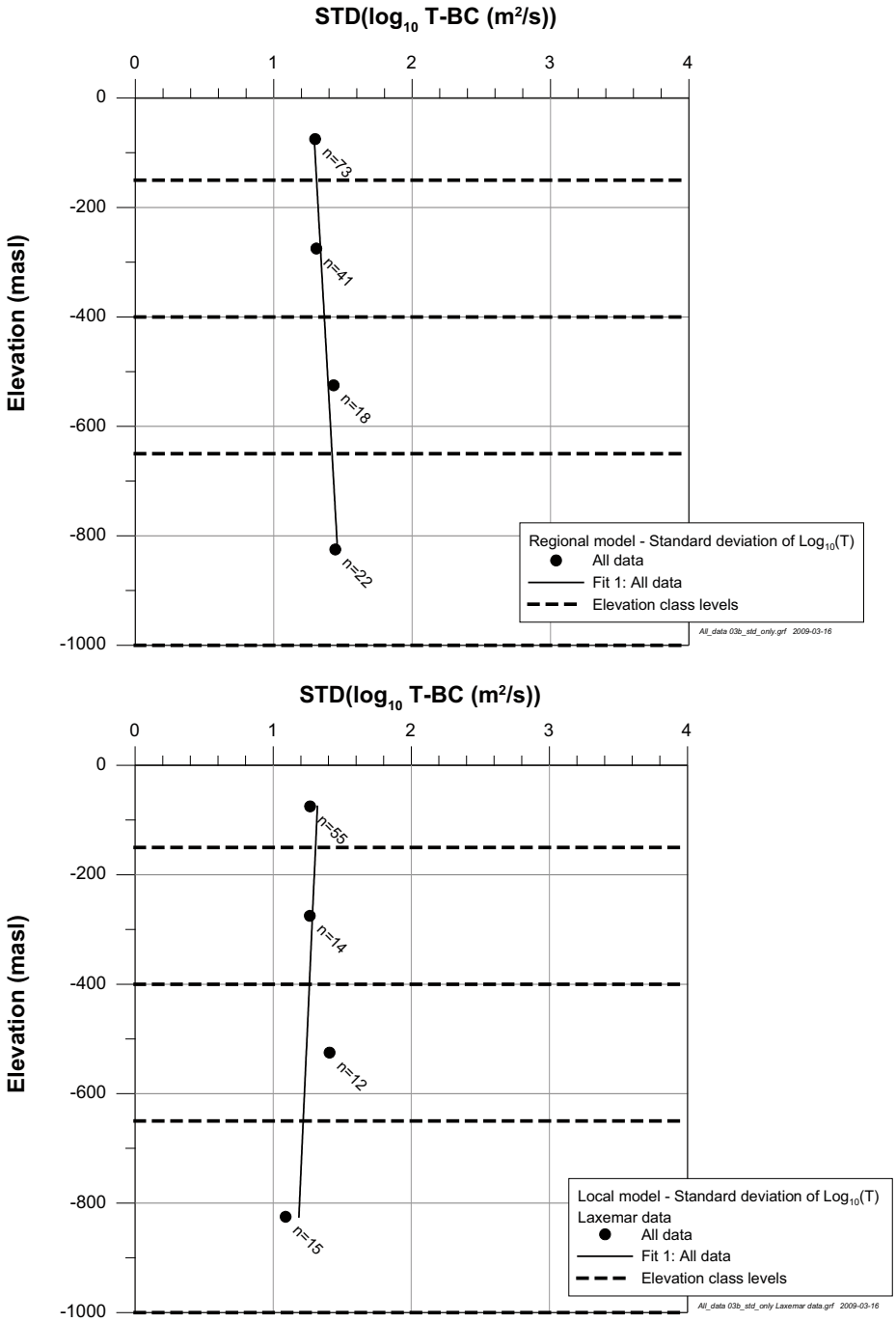

Figure 7-19. *Standard deviation of HCD transmissivity (T) versus elevation based on all data. For depth zones, 1 standard deviation of log10(T) are plotted. Data from regional model volume (top) and local model volume (bottom), respectively.*

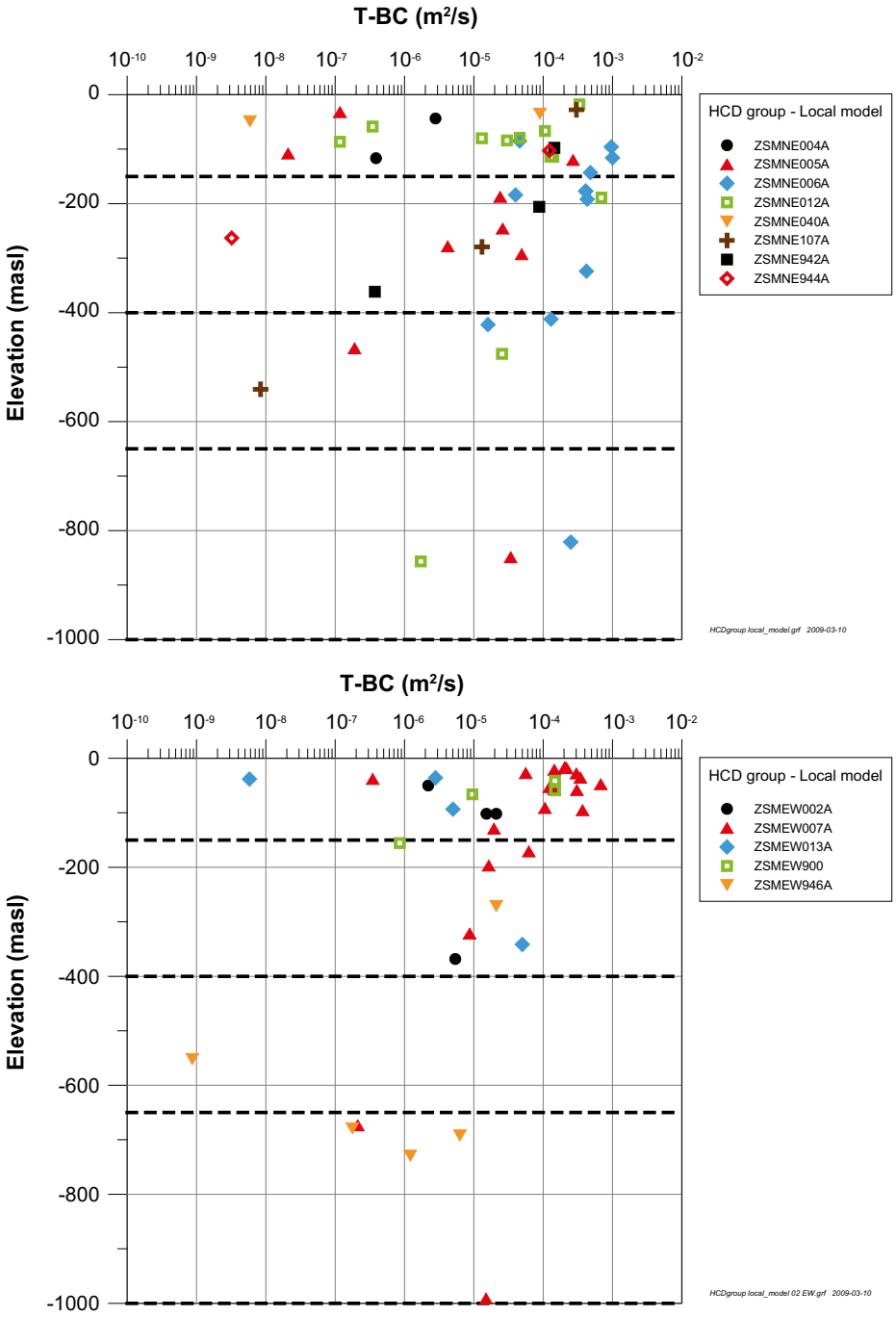

Figure 7-20. *HCD transmissivity (T) versus elevation: Transmissivity for HCDs with more than 1 borehole intercept plotted. Data from local model volume.*

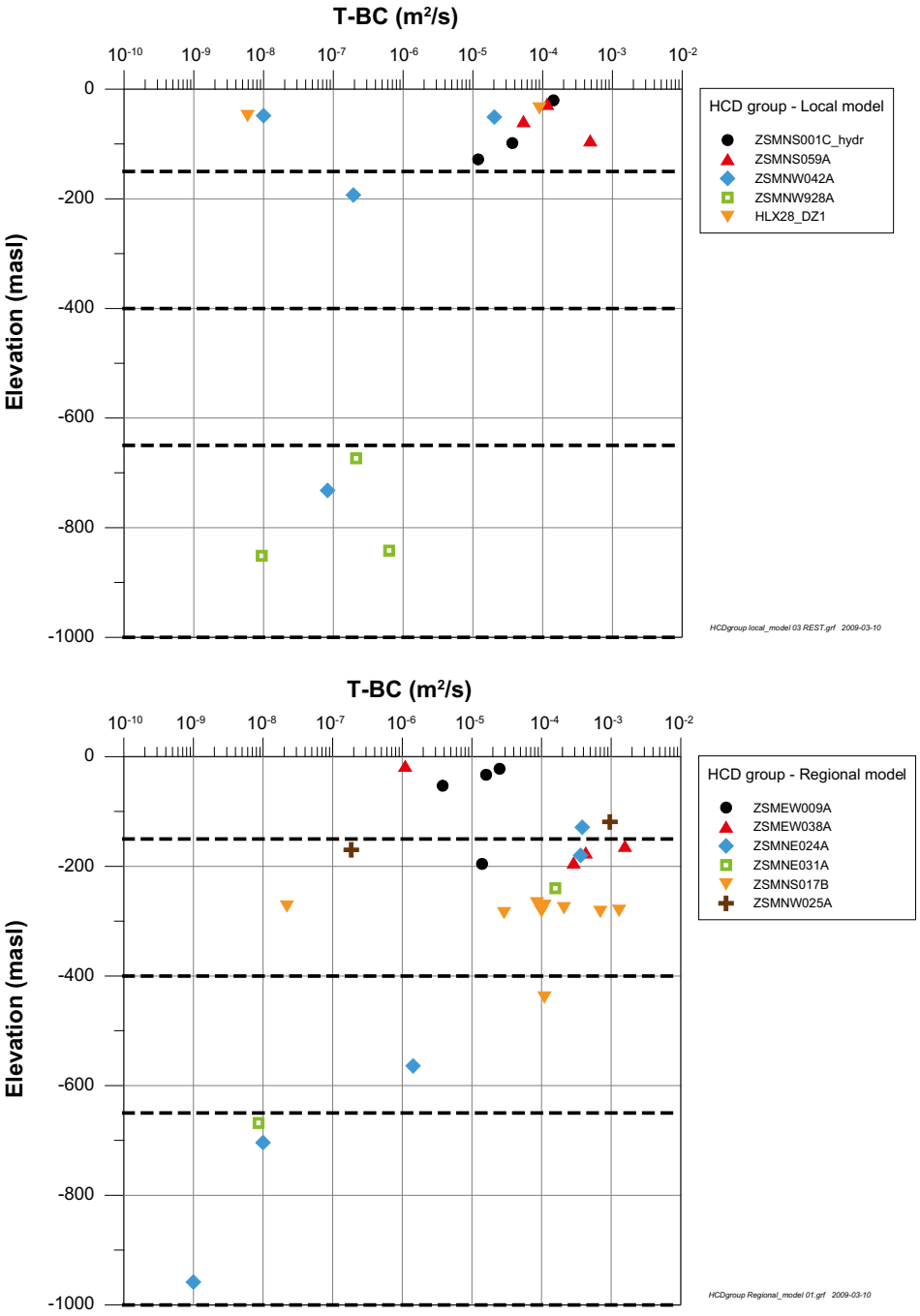

Figure 7-21. *HCD transmissivity (T) versus elevation: Transmissivity for HCDs with more than 1 borehole intercept plotted. Data from local model volume.*

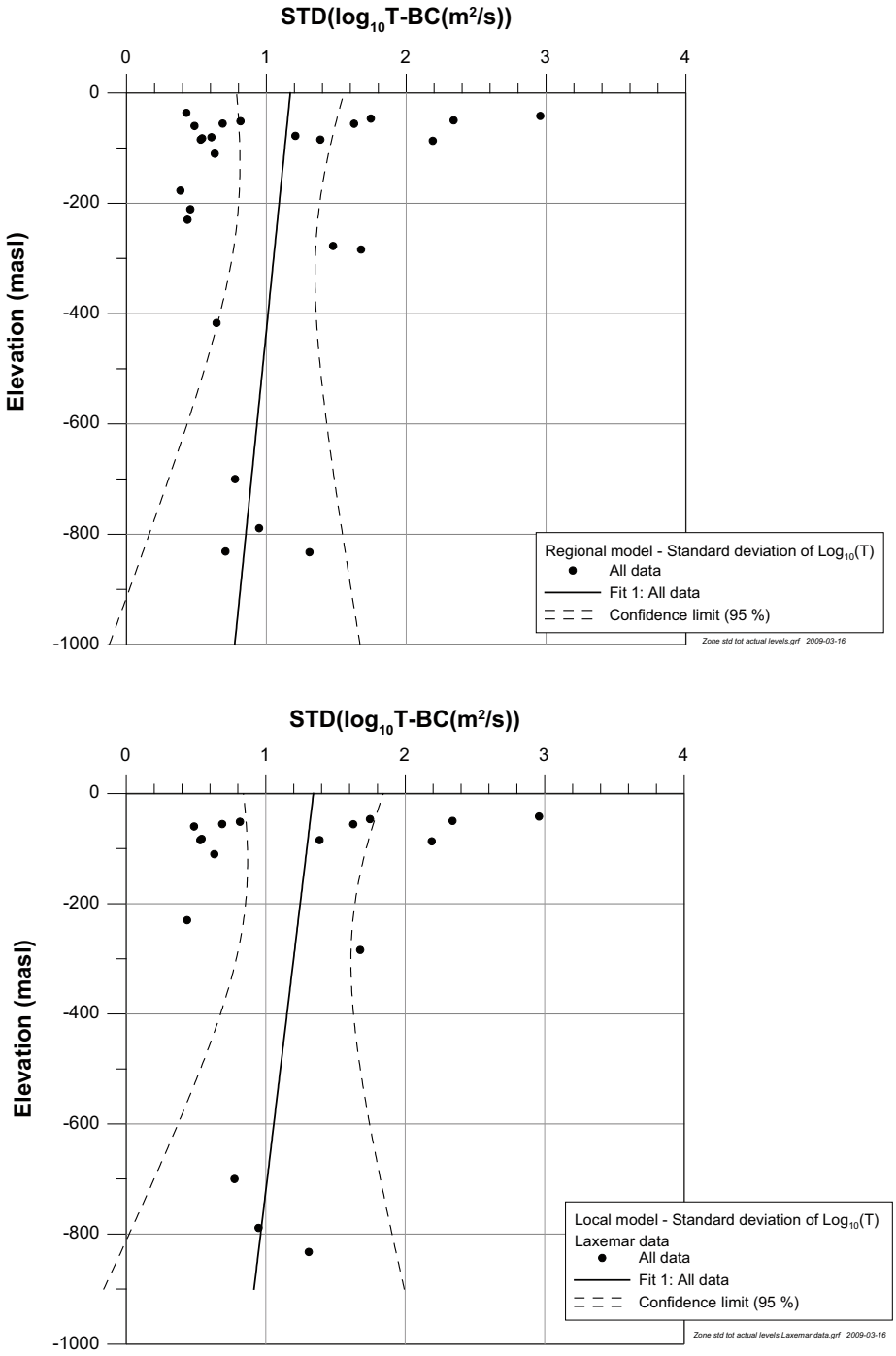

Figure 7-22. *Standarad deviation of HCD transmissivity (T) versus elevation based on zones with several observations of transmissivity within a single HCD. Confidence intervals for fitted lines are shown. Data from regional model volume (top) and local model volume (bottom), respectively.*

Table 7-4. Table of results for all data samples in HCDs. Statistics for depth zones, also shown in Figure 7-17 and Figure 7-18. Data from regional and local scale model volumes.

Object	Data type	Depth zone (masl)	Mean elevation (masl)	Sample size	Mean Log_{10}(T-BC) (T: m^2/s)	STD Log_{10}(T-BC) (T: m^2/s)	95% Conf. Int. Log_{10}(T-BC) Low (T: m^2/s)	95% Conf. Int. Log_{10}(T-BC) High (T: m^2/s)
HCD	All data	> –150	–75	73	–4.73	1.30	–5.03	—4.42
HCD	All data	–150 to –400	–275	41	–4.58	1.31	–5.00	–4.17
HCD	All data	–400 to –650	–525	18	–5.84	1.43	–6.55	–5.13
HCD	All data	< –650	–825	22	–6.63	1.41	–7.26	–6.01
HCD	Local model	> –150	–75	55	–4.84	1.38	–5.21	–4.47
HCD	Local model	–150 to –400	–275	14	–5.43	1.27	–6.16	–4.70
HCD	Local model	–400 to –650	–525	12	–6.28	1.41	–7.17	–5.38
HCD	Local model	< –650	–825	15	–6.58	1.01	–7.14	–6.01

Table 7-5. Standard deviation relation for Log_{10} (T-BC) for all data samples in HCDs. Models shown in Figure 7-19 and Figure 7-22. Data from regional scale model volume.

Model ID	Depth trend model	Object	Data type	Coeff. a	Coeff. B	Corr, coeff. r^2
DZ-R-S1	Linear	HCD	Standard deviation of total transmissivity within a HCD. X=Std(log10(sum T-BC)). Regional data, DZ with several tests with an depth zone: >–150 m, –150– to –400 m, –400 to –650 m, <–650 m.	1.303	0.000603	–
DZ-R-S2	Linear	HCD	Standard deviation of total transmissivity within a HCD. X=Std(log10(sum T-BC)). Regional data, All data, standard deviation for interval.	1.355	–0.00007412	0.226

Table 7-6. Trend models for transmissivity in HCDs. Data from regional scale model volume. Shaded model IDs: recommended models.

Model ID	Figure	Depth trend model	Object	Data type	Coeff. a	Coeff. B	Corr, coeff. r^2
DZ-R-1	Figure 7-17	Power	HCD	Total transmissivity within a HCD. X=(T_BC). Regression on geometric means of (T_BC) for interval (4 data points). Regional data.	0.1177	–1.82558	0.67
DZ-R-2	Figure 7-17	Exp	HCD	Total transmissivity within a HCD. X=(T_BC). Regression on means of log10(T_BC) for interval (4 data points). Regional data.	–4.211	0.00296	0.90
DZ-R-19[1]	Figure 7-15	Exp	HCD	T (1). Regional data, Zone E-W size < 2 km.	–4.665	0.00263	0.95
DZ-R-20[1]	Figure 7-15	Exp	HCD	T (1). Regional data, Zone E-W size > 2 km.	–4.091	0.00187	0.773
DZ-R-21[1]	Figure 7-15	Exp	HCD	T (1). Regional data, Zone NW-SE,N-S,NE-SW size < 2 km.	–4.997	0.00250	0.83
DZ-R-22[1]	Figure 7-15	Exp	HCD	T (1). Regional data, Zone NW-SE,N-S,NE-SW size > 2 km.	–4.070	0.00274	0.83

T(1): Total transmissivity within a HCD. X=(T_BC). Regression based on mean values of log10(T_BC) for depth zones (4 data points).

[1]: The regional groundwater flow modelling in /Rhén et al. 2009/ is based on regression curves very similar to the ones shown in Table 7-6, but not exactly, cf. Appendix 3. The updates of a few data points included in the regression analysis as shown in Table 7-6 were done late in the modelling process. However, as the changes to the regression curves as presented here are small, the regional groundwater simulation cases, based on the original regression analysis, were not re-run.

Table 7-7. Trend models for transmissivity(m^2/s) in HCDs. Data from local scale model volume. Shaded model IDs: recommended models.

Model ID		Depth trend model	Object	Data type	Coeff. a	Coeff. B	Corr, coeff. r^2
DZ-L-1	Figure 7-18	Power	HCD	Total transmissivity within a HCD. X=(T_BC). Regression on individual points. Local model data.	0.005292	–1.4343	0.26
DZ-L-2	Figure 7-18	Power	HCD	Total transmissivity within a HCD. X=(T_BC). Regression on means for interval (4 data points). Local model data.	0.06493	–1.85488	0.95
DZ-L-3	Figure 7-18	Exp	HCD	Total transmissivity within a HCD. X=(T_BC). Regression on individual points. Local model data. Local model data.	–4.6799	0.002661	0.26
DZ-L-4	Figure 7-18	Exp	HCD	Total transmissivity within a HCD. X=(T_BC). Regression on means of log10(T_BC) for interval (4 data points). Local model data.	–4. 6900	0.002617	0.97
DZ-L-5	Figure 7-16	Exp	HCD	Total transmissivity within a HCD. X=(T_BC). Regression on means of log10(T_BC) for interval (4 data points). Local model data, Zone E-W size < 2 km.	–4.635	0.002657	0.90
DZ-L-6	Figure 7-16	Exp	HCD	Total transmissivity within a HCD. X=(T_BC). Regression on means of log10(T_BC) for interval (4 data points). Local model data, Zone E-W size > 2 km.	–4.101	0.002006	0.99
DZ-L-7	Figure 7-16	Exp	HCD	Total transmissivity within a HCD. X=(T_BC). Regression on means of log10(T_BC) for interval (4 data points). Local model data Zone NW-SE, N-S,NE-SW size < 2 km.	–5.067	0.002202	0.88
DZ-L-8	Figure 7-16	Exp	HCD	Total transmissivity within a HCD. X=(T_BC). Regression on means of log10(T_BC) for interval (4 data points). Local model data Zone NW-SE, N-S,NE-SW size > 2 km.	–5.151	0.002755	0.44

Table 7-8. Trend models for hydraulic conductivity (m/s) in HCDs. Data from regional and local scale model volumes.

Model ID	Figure	Depth trend model	Object	Data type	Coeff. a	Coeff. B	Corr, coeff. r^2
DZ-R-K1	Figure 7-23	Power	HCD	Hydraulic conductivity within a HCD. X=(K_BC). Regression on individual points. Regional model data.	0.0000275	–0.96562	0.1
DZ-R-K2	Figure 7-23	Power	HCD	Hydraulic conductivity within a HCD. X=(K_BC). Regression on means for interval (4 data points). Regional model data.	0.000876	–1.58804	0.61
DZ-R-K3	Figure 7-23	Exp	HCD	Hydraulic conductivity within a HCD. X=(K_BC). Regression on individual points. Regional model data.	–6.0628	0.00235	0.18
DZ-R-K4	Figure 7-23	Exp	HCD	Hydraulic conductivity within a HCD. X=(K_BC). Regression on means of log10(K_BC) for interval (4 data points). Regional model data.	–5.8874	0.00264	0.87
DZ-L-K5	Figure 7-24	Power	HCD	Hydraulic conductivity within a HCD. X=(K_BC). Regression on individual points. Local model data.	0.0000357	–1.12429	0.18
DZ-L-K6	Figure 7-24	Power	HCD	Hydraulic conductivity within a HCD. X=(K_BC). Regression on means for interval (4 data points). Local model data.	0.0002498	–1.43967	0.90
DZ-L-K7	Figure 7-24	Exp	HCD	Hydraulic conductivity within a HCD. X=(K_BC). Regression on individual points. Local model data.	–6.32566	0.002095	0.18
DZ-L-K8	Figure 7-24	Exp	HCD	Hydraulic conductivity within a HCD. X=(K_BC). Regression on means of log10(K_BC) for interval (4 data points). Local model data.	–6.29184	0.002099	0.98

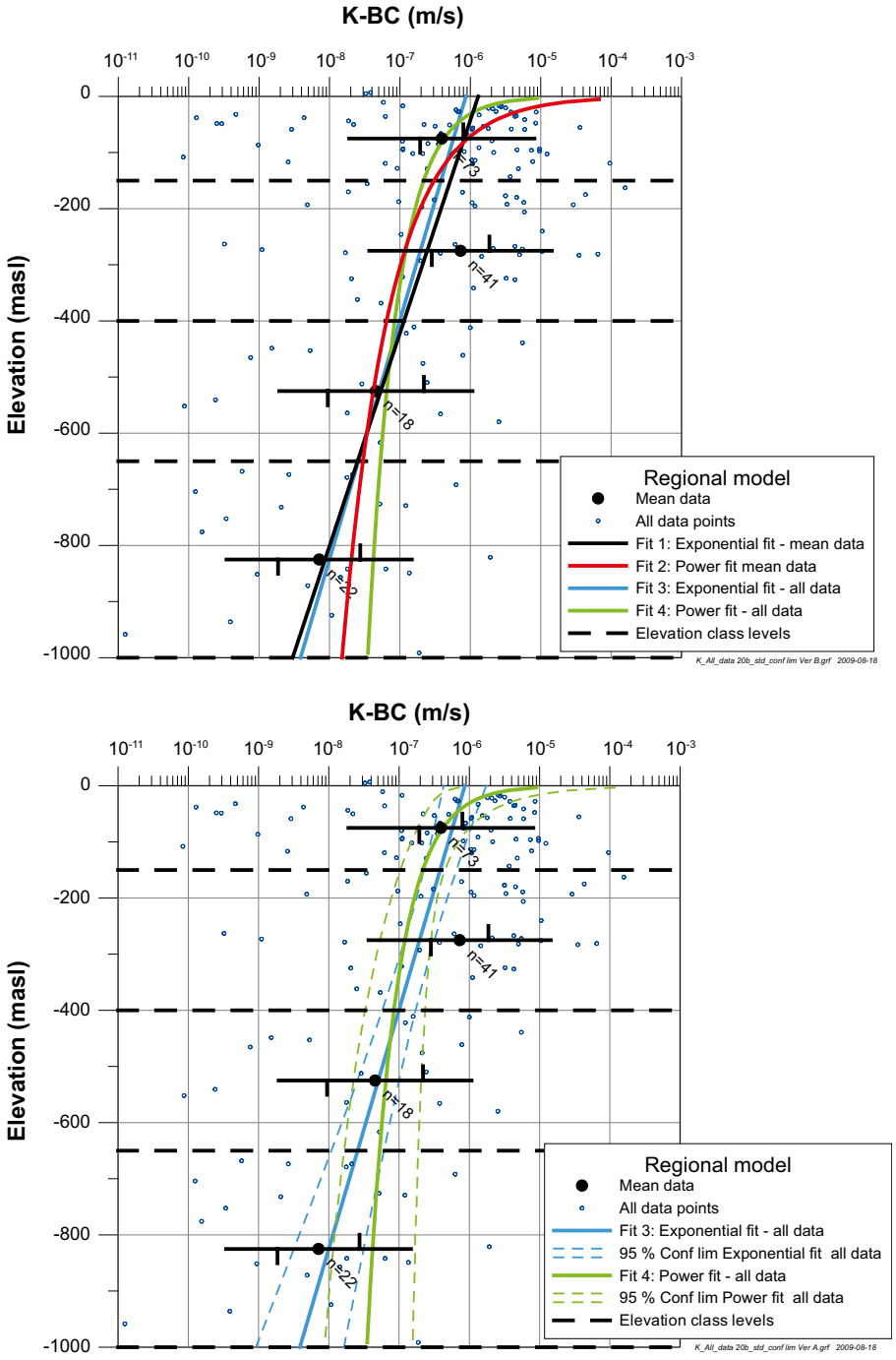

Figure 7-23. *HCD Hydraulic conductivity (K) versus elevation: For depth zones Geometric mean K, confidence limits for mean log10(K)(vertical bars on horizontal line) and ±1 standard deviation log10(K) (entire horizontal line) are plotted. Curves are fitted to the 4 geometric mean values or all data. Confidence intervals for fitted lines are shown for lines fitted to all data. Data from regional model volume.*

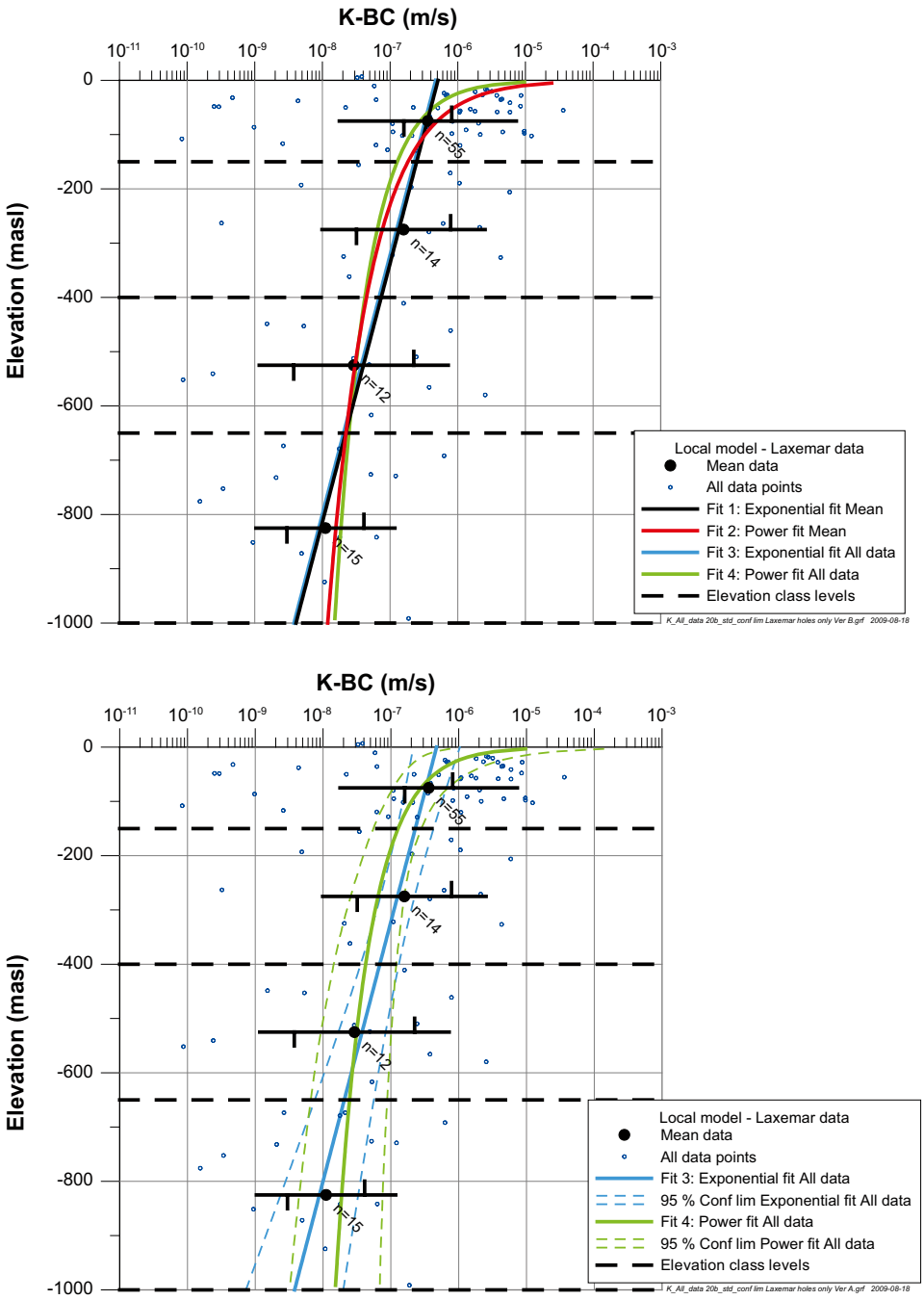

Figure 7-24. *HCD Hydraulic conductivity (K) versus elevation: For depth zones Geometric mean K, confidence limits for mean log10(K)(vertical bars on horizontal line) and ±1 standard deviation log10(K) (entire horizontal line) are plotted. Curves are fitted to the 4 geometric mean values or all data. Confidence intervals for fitted lines are shown for lines fitted to all data. Data from local model volume.*

7.5.3 Parameterisation of HCDs subjected to hydraulic tests

The deterministic deformation zones subjected to hydraulic tests are presented in Appendix 3. There are from 1 single up to 19 transmissivity estimates in each of these 24 deterministic deformation zones (HCDs), and in cases with more data points within a defined deformation zone and within the depth zones employed (>–150,–150 to –400, –400 to –650, <–650 m), mean and standard deviation have been calculated as well as the mean elevation of the observations.

If there are data from several depth zones (as given above) a linear trend function between elevation and log10(T) has been calculated. If there are only data from one depth zone, the slope of the general trend function for all Laxemar data (DZ-L-3), cf. Table *7-7*, is used to adapt a trend function to the size specific value for the depth zone. Appendix 3 provides all trend functions for all applicable HCDs in a table and associated figures and two examples of such adapted trend functions are shown in Figure 7-25.

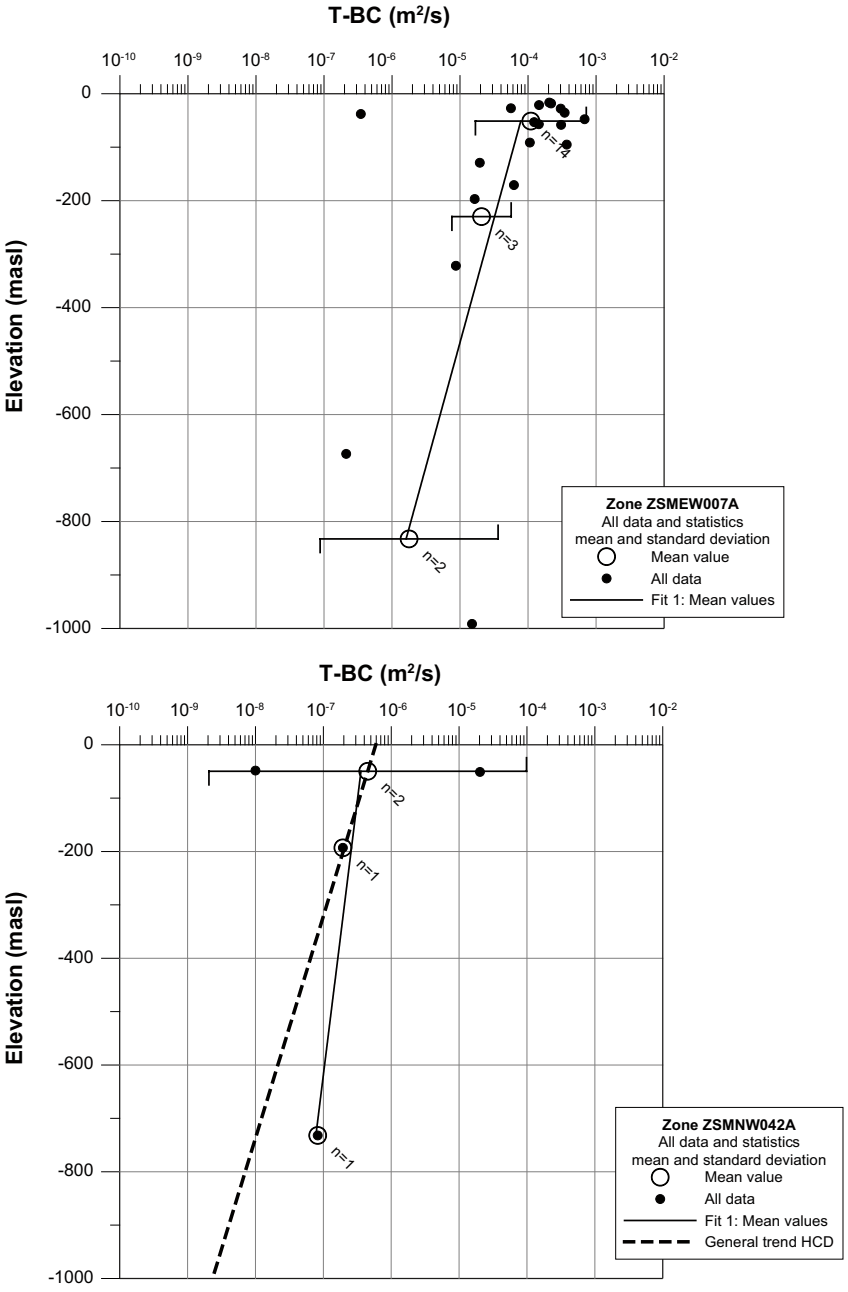

Figure 7-25. *Examples of suggested relations of transmissivity versus elevation for two specific deformation zones. Top: The trend function is considered reliable. Bottom: The trend function is considered uncertain and hence the general trend function should be used.*

The table for trend functions in Appendix 3 should be used to assign the properties to the respective deterministic deformation zone (HCD) which has available hydraulic test data. As preliminary estimates in the numerical groundwater model, only trend functions of seven deformation zones (as suggested in Appendix 3) with several tests within at least two depth zones should be used. For the 17 HCDs in Appendix 3 marked as uncertain, the trend functions for the deformation zones without hydraulic tests should be used, cf. Section 7.5.2.

The values proposed in this section and in Appendix 3 may later be subject to change if the regional model calibration suggests that the transmissivity should be modified. The data in Appendix 3 can then be used for conditioning the transmissivity near boreholes producing estimates of the local transmissivities. The thickness of each zone with hydraulic data is also found in Appendix 3.

A few deformation zones must be modelled with an impervious core and permeable sides attributed to dolerite dykes, see Section 7.3.

One deformation zone that deserves further comment is ZSMNE005A, the so-called Äspö Shear zone. This zone corresponds more or less to rock domains RSMP01 and RSMP02. Its character at Äspö HRL shows that there are transmissive features along the structure, but across the relatively wide structure there are also low-conductive parts that seem to limit/dampen the hydraulic responses across the zone. In Laxemar there are no observations from cored boreholes that penetrate the zone that can add to its local hydraulic characteristics, although a few percussion boreholes provide additional information. However, the zone's geological character at Laxemar is assumed to be similar to that observed at Äspö and Äspö HRL and it is therefore suggested that ZSMNE005A should be modelled with a low conductive core and permeable sides. As a first estimate in sensitivity studies $K_{transverse}$ can be assumed to be $0.1 \cdot K_{longitudinal}$, where $K_{longitudinal}$ is estimated from the transmissivity model and the thickness of ZSMNE005A, as given in Appendix 3.

7.6 Storage coefficient of deformation zones

During interference tests the storage coefficient (S) can be estimated if:

- the observation section is fairly close to the pumped section in a deformation zone. At longer distances from the pumped section the responses will be more affected by intersections with hydraulic features that will make the estimate of S unreliable,
- it can be assumed that the observation section response is well-connected to the deformation zone studied,
- there are no other major hydraulic features than the deformation zone studied interacting/interfering during the evaluation period, such that the radial flow assumption for a single feature can be assumed approximately valid.

Tests with observation sections within a distance of 300 m from the pumping section have been examined, and among them, tests with what seem to be a complex geometry or deformation zones between, or very near, the pumped section and observation sections (as inferred from the deformation zone model) have been excluded. Furthermore, for tests where the deformation zone model indicates a well defined (and singular) deformation zone, results from observation sections with low and/or slow responses have been excluded. For the remaining observation sections the geometric mean of S has been estimated and plotted vs. the transmissivity of the corresponding pumped borehole section, cf. Figure 7-26, the latter which is judged to be the best estimate of the transmissivity of the deformation zone compared to T evaluated from observation sections. However, using the geometric mean of T of the observation sections hardly change the relation shown in Figure 7-26. all that much. Results from a few other projects have also been included. Tests from the investigations at the Äspö HRL are based on estimates of T and S as above but for one case the geometric mean of T from several observation wells close to the pumped section was used instead of the transmissivity from the pumped section /Rhen et al. 1997/. Several interference tests made as part of the TRUE Block Scale project at Äspö HRL have also been used /Andersson et al. 2000b, 2001a, b/. Tests from features that were considered relevant at the end of the project were selected and geometric mean of T and S from

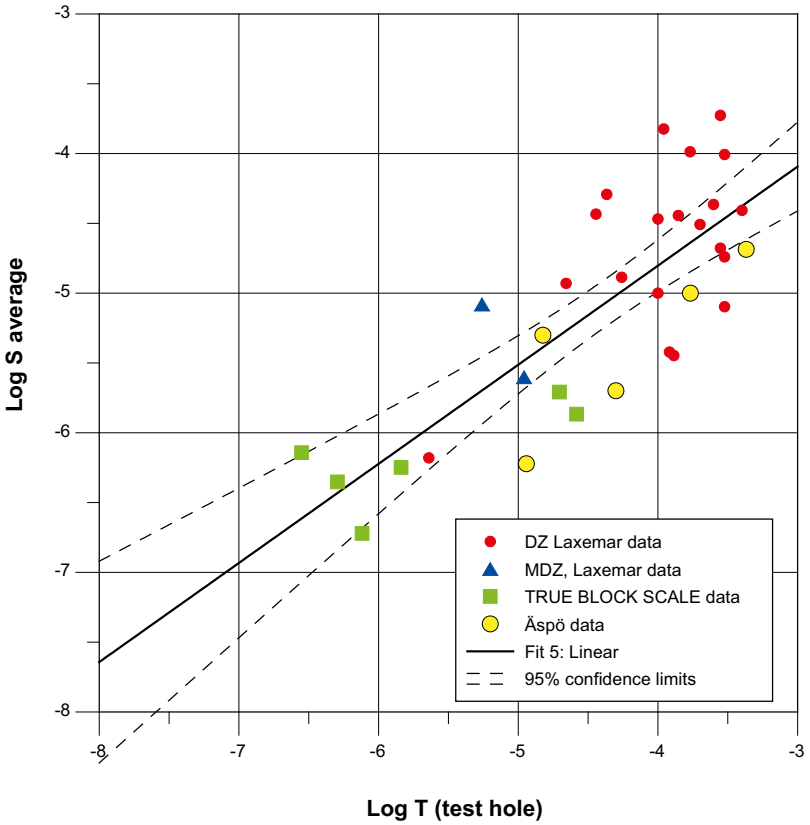

Figure 7-26. *Correlation between T and S for deformation zones.*

observation wells were used, excluding observations that were considered uncertain. In Figure 7-26 and Table 7-9 the correlation between T and S is shown. The data cover roughly tests performed down to c. 500 m depth. As indicated, also a few minor deformation zones (MDZ) are included, see /Olsson et al. 2006/. Additional treatise of minor deformation zones is presented in Chapter 8 and 10.9.

The hydraulic diffusivity is a useful parameter for evaluating the radius of influence in hydraulic transient tests. The hydraulic diffusivity (T/S) can be estimated from relation in Table 7-9. $T=1\cdot10^{-7}$ m^2/s and $.1\cdot10^{-3}$ m^2/s corresponds to T/S of c. 0.9 and 12 respectively. As indicated in Figure 7-26 there is spread of the observations along the regression line, which indicates that there is an uncertainty in the estimate of the hydraulic diffusivity that probably depends both on actual difference between hydraulic features with similar transmissivities but possibly also the uncertainty in the evaluations of the different tests.

Table 7-9. Correlation between T and S for deformation zones. $S=a\cdot T^B$.

Model ID	Object	Data type	Coeff. a	Coeff. B	Corr, coeff. r^2
DZ-TS1	DZ, MDZ	Storage coefficient as function of Transmissivity in deformation zones	0.0109	0.71	0.62

7.7 Preliminary assessment of kinematic porosity of deformation zones

The kinematic porosity (n_e) is here defined as the mean transport aperture (e_T) divided by the hydraulic thickness of the HCD (b_T), the latter being the true thickness of a HCD, to which the evaluated transmissivity for the corresponds), cf. Equation 7-1 /Dershowitz et al. 2003/. The knowledge of kinematic porosity (n_e) is very limited. A few estimates found in the literature of the coefficients of the relationship in Equation 7-1 are shown in Table 7-10.

$$n_e = \frac{e_T}{b_T} \qquad (7\text{-}1)$$

The coefficients provided by /Dershowitz et al. 2003/ are rather similar to the ones reported in /Rhén et al. 1997/, with a=1.428 and b=0.523, the latter based on a compilation of tracer tests in crystalline rock, ranging from tests of a single to up larger test scales with densely fractured rock and fracture zones. A more comprehensive compilation of tracer test results is provided by /Hjerne et al. 2009/ and a preliminary relation for e_T, Equation 3 in Table 7-10, was available for the calculations made in Chapter 10 in this report and Equation 4 was their final suggestion. However, the equations should be regarded as uncertain but as kinematic porosity is considered a calibration parameter, the relation 4 may be used as first estimates of the kinematic porosity.

7.8 Heterogeneity

The HCDs are generally the most conductive elements in the rock mass and are important components in groundwater flow models but are also important for repository layout and design. The estimated total transmissivity or deformation zones, as presented in the preceding sections, provide data for the flow capacity of the HCDs. However, if one would like to incorporate heterogeneity within a HCD on a smaller scale, or to assess e.g. the grouting needs and potential within a HCD, the hydraulic character and spatial distribution of individual flowing features within a HCD is of interest. In this section some basic PFL-f statistics pertinent to HCDs are summarised.

7.8.1 Summary of data and evaluation methodology

Data represent the local model (KLX27A not included) and cover some 49 intercepts of HCDs (in a few cases several HCDs within a single borehole and some intercepts in several borehole represents the same HCD).

The compiled statistics of the individual deformation zones, or rather HCDs in the hydrogeological context, are always based on PFL-f features covered by the local apparent thickness of the HCD, i.e. borehole length where the HCD intersects the borehole, cf. Figure 7-27 and Figure 3-5. Figure 7-27 illustrates how the heterogeneity within a deformation zone (DZ) (and also MDZ in Chapter 8) have been analysed. The intensities of PFL-f features along the borehole (P_{10}) are based on the DZ (or MDZ) apparent thickness.

Depth dependence of the individual PFL-f features within the large deformation zones has been analysed for the depth zones; >–150 m, –150– to –400 m, –400 to –650 m, <–650 m, respectively, using the data from the local model volume.

Table 7-10. Estimation of mean transport aperture for HCD from transmissivity (T). $e_T = aT^b$. T (m^2/s), e_T(m).

Equation	Approximate test scale (m)	Coefficient a	Coefficient b	Reference
1	5–100	0.46	0.5	/Dershowitz et al. 2003/
2	5–100	1.428	0.523	/Rhén et al. 1997/
3	5–100	0.705	0.404	/Hjerne et al. 2009/, (preliminary model available for this report, cf. Chapter 10)
4	5–100	0.28	0.30	/Hjerne et al. 2009/ (Model suggested)

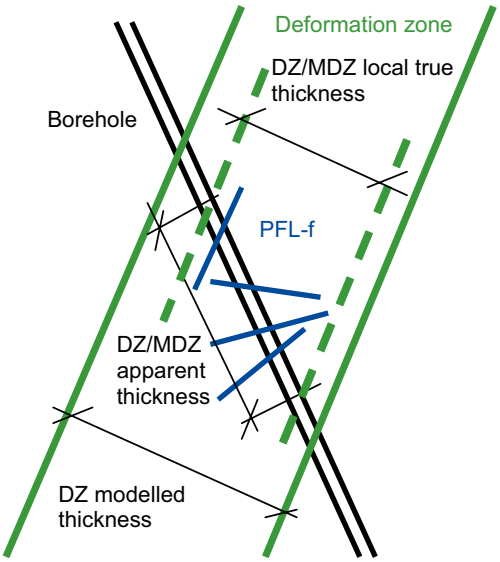

Figure 7-27. *Illustration forming the base for how PFL-f features within a deformation zone (or MDZ) have been interpreted. The single hole interpretation provides the interpreted borehole length where the deformation intersects each borehole. The 3D modelling of the deformation zones, taking several borehole and surface observations into account, results in e.g. a modelled thickness of the deformation zone. Statistics of PFL-f in terms of intensity (P_{10}) is based on the local thickness of the deformation zone.*

7.8.2 Transmissivity models and heterogeneity

The results of the compilation of HCDs internal properties with at least one PFL-f feature are presented in Table 7-11 and Figure 7-28 through Figure 7-33. In Appendix 3 the detailed results for each deformation zone are provided. These figures can be used to assess the intensity of flowing features within HCDs.

Table 7-11 covers local model HCDs showing the statistics of PFL-f within HCDs and depth zones for the HCDs and includes the following columns:

- *Bh-length(HCD)*: Lengths of individual HCDs (with PFL-f features) along the borehole.
- *HCD-thickness at bh*: Estimated true thickness of individual HCDs (with PFL-f features).
- *N-PFL-f*: Number of PFL-f features within individual HCDs.
- *N-corr-PFL-f*: Number of PFL-f features, Terzaghi corrected due to PFL-f feature orientations, within individual HCDs.
- *P10 (PFL-f)* and *P10-corr(PFL-f)*: Intensity of PFL-f features within a HCD. N-PFL-f and N-corr-PFL-f divided by HCD length along the borehole, for each individual HCD.
- *T(sum T-PFL-f)*: Sum of T-PFL-f, where T-PFL-f is the transmissivity of individual PFL-f features within a HCD (sum T-PFL-f= total transmissivity of a HCD).
- *log10 (sum T-PFL-f)*: Log10(sum T-PFL-f), where T-PFL-f is the transmissivity of individual PFL-f features within a HCD (sum T-PFL-f= total transmissivity of a HCD).
- *Mean T-PFL-f*: Arithmetic mean of T-PFL-f within each HCD, where T-PFL-f is the transmissivity of individual PFL-f features within a HCD.
- *10^(Mean log10(T-PFL-f))*: Anti-log of the calculated values for Mean log10(T-PFL-f) shown below.
- *Mean log10(T-PFL-f)*: Arithmetic mean of log10(T-PFL-f) within each HCD, where T-PFL-f is the transmissivity of individual PFL-f features within a HCD.
- *Std log10(T-PFL-f)*: Standard deviation of log10(T-PFL-f) within each HCD, where T-PFL-f is the transmissivity of individual PFL-f features within a HCD.

For each of these column variables; Min, Max, Mean (arithmetic) and std(standard deviation) is shown for the values within a depth zone (Object). The std cannot always be calculated due to small sample size, marked as NA: Not available.

Table 7-11 is based on the figures shown in Appendix 3, Section A.3.4.

Table 7-11. PFL-f statistics related to HCDs. Data from local model volume, data from KLX27A excluded.

Object		Bh-length (HCD) (m)	HCD thickness at bh (m)	N PFL-f (–)	N-corr PFL-f (–)	P10 (PFL-f) (m^{-1})	P10-corr (PFL-f) (m^{-1})	T (sum T-PFL-f) (m^2/s)	log10 (sum T-PFL-f) (m^2/s)	Mean T PFL-f (m^2/s)	10^(Mean log10 (T-PFL-f)) (m^2/s)	Mean log10 (T-PFL-f) T: (m^2/s)	Std log10 (T-PFL-f) T: (m^2/s)
> –1,000 All data	Sample size	49	49	49	49	49	49	49	49	49	49	49	45
	Min	1.0	0.7	1	1	0.04	0.04	1.5E–08	–7.82	3.5E–09	3.3E–09	–8.48	0.08
	Max	246.0	130.0	137	383	1.03	2.23	4.2E–04	–3.38	4.9E–05	4.9E–05	–4.31	2.22
	Mean	50.5	28.7	17.14	33.64	0.39	0.68	2.3E–05	–5.56	2.7E–06	7.8E–08	–7.11	0.81
	std	57.0	28.5	23.58	58.65	0.26	0.53		1.06			0.82	0.38
> –150	Sample size	13	13	13	13	13	13	13	13	13	13	13	13
	Min	14.0	10.0	2	3	0.21	0.34	5.5E–07	–6.26	7.2E–08	1.6E–08	–7.79	0.18
	Max	188.0	130.0	55	92	0.96	2.23	9.9E–05	–4.00	4.0E–06	2.9E–07	–6.53	1.67
	Mean	42.1	38.2	18.00	34.44	0.46	0.93	2.2E–05	–5.10	1.1E–06	8.7E–08	–7.06	0.93
	std	46.4	36.9	16.54	30.00	0.24	0.64		0.73			0.46	0.33
–150 to –400	Sample size	17	17	17	17	17	17	17	17	17	17	17	16
	Min	1.0	0.7	1	1.34	0.06	0.09	1.5E–07	–6.84	2.1E–08	8.9E–09	–8.05	0.54
	Max	246.0	100.0	137	382.57	1.03	1.82	4.2E–04	–3.38	2.2E–05	2.1E–05	–4.67	2.22
	Mean	63.4	28.5	25.12	52.85	0.49	0.85	4.3E–05	–5.19	3.7E–06	1.1E–07	–6.98	0.89
	std	71.4	29.7	34.72	91.88	0.29	0.51		1.01			0.85	0.40
–400 to –650	Sample size	10	10	10	10.00	10	10	10	10	10	10	10	9
	Min	16.7	6.2	1	1.00	0.06	0.06	2.1E–08	–7.68	3.5E–09	3.3E–09	–8.48	0.17
	Max	148.0	50.0	39	67.33	0.53	0.95	4.9E–05	–4.31	4.9E–05	4.9E–05	–4.31	1.07
	Mean	49.6	21.8	13.30	21.47	0.28	0.41	8.6E–06	–5.84	5.1E–06	5.0E–08	–7.30	0.75
	std	43.4	16.0	11.44	21.73	0.15	0.24		1.07			1.20	0.29
< –650	Sample size	9	9	9	9.00	9	9	9	9	9	9	9	7
	Min	2.0	9.0	1	1.06	0.04	0.04	1.5E–08	–7.82	1.5E–08	8.3E–09	–8.08	0.08
	Max	190.0	80.0	23	51.43	0.50	0.69	7.8E–06	–5.11	3.9E–06	9.1E–07	–6.04	1.32
	Mean	39.4	23.1	5.11	9.73	0.20	0.30	1.3E–06	–6.58	5.5E–07	6.0E–08	–7.22	0.51
	std	57.8	23.4	6.95	16.13	0.15	0.22		0.83			0.75	0.41

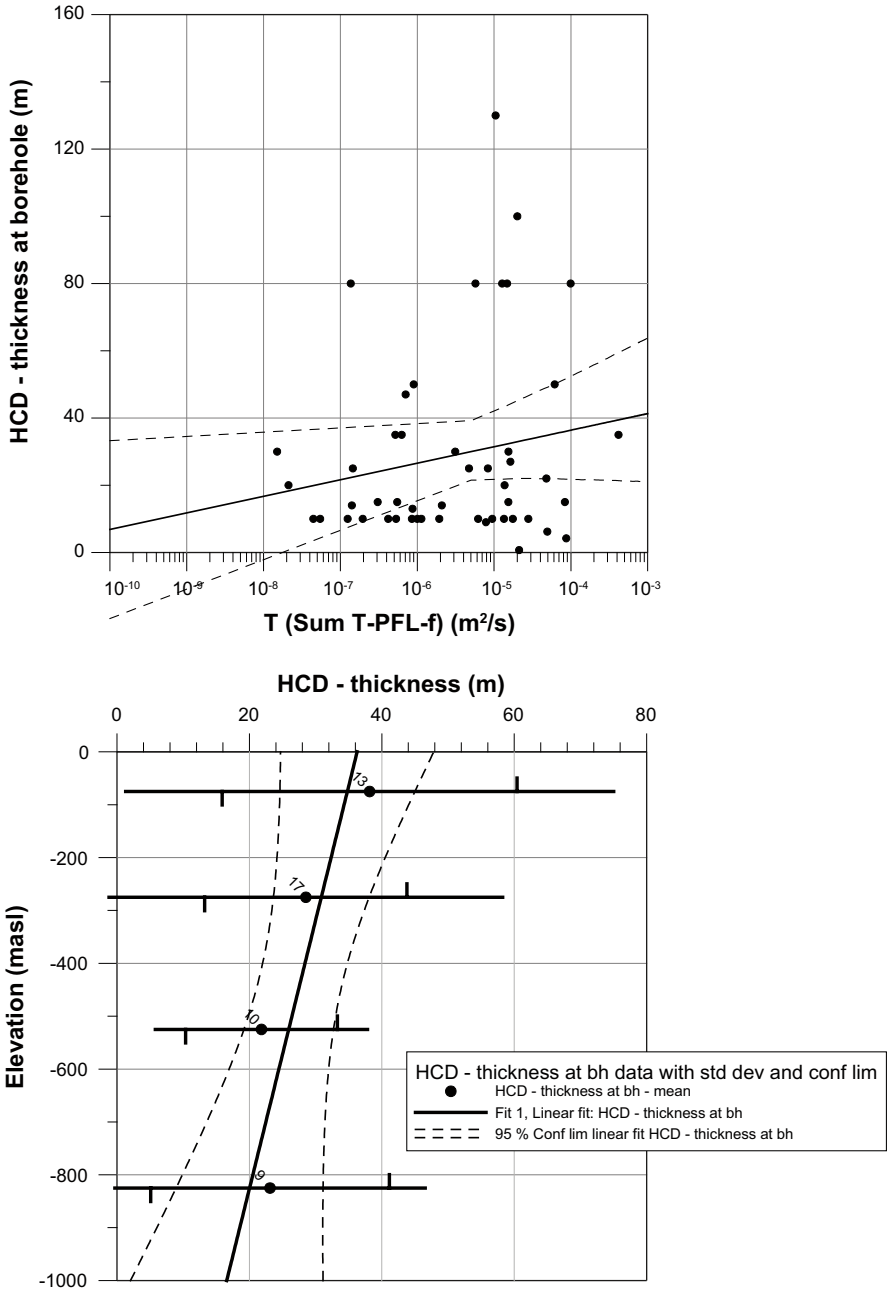

Figure 7-28. *Top: Transmissivity of a HCD versus HCD true thickness. Transmissivity based on sum of T-PFL-f. Estimated thickness of a HCD at borehole intercept providing the actual T-estimates. Bottom: HCD true thickness versus elevation. For depth zones the following parts are plotted; mean thickness, confidence limits for mean thickness (vertical bars on horizontal line) and ±1 standard deviation thickness (entire horizontal line) are plotted. Curves are fitted to the 4 arithmetic mean values of all data. The mean and standard deviation are based on the number of samples shown near the mean value. Confidence intervals for fitted lines are shown for lines fitted to the 4 interval means. Data from local scale model volume.*

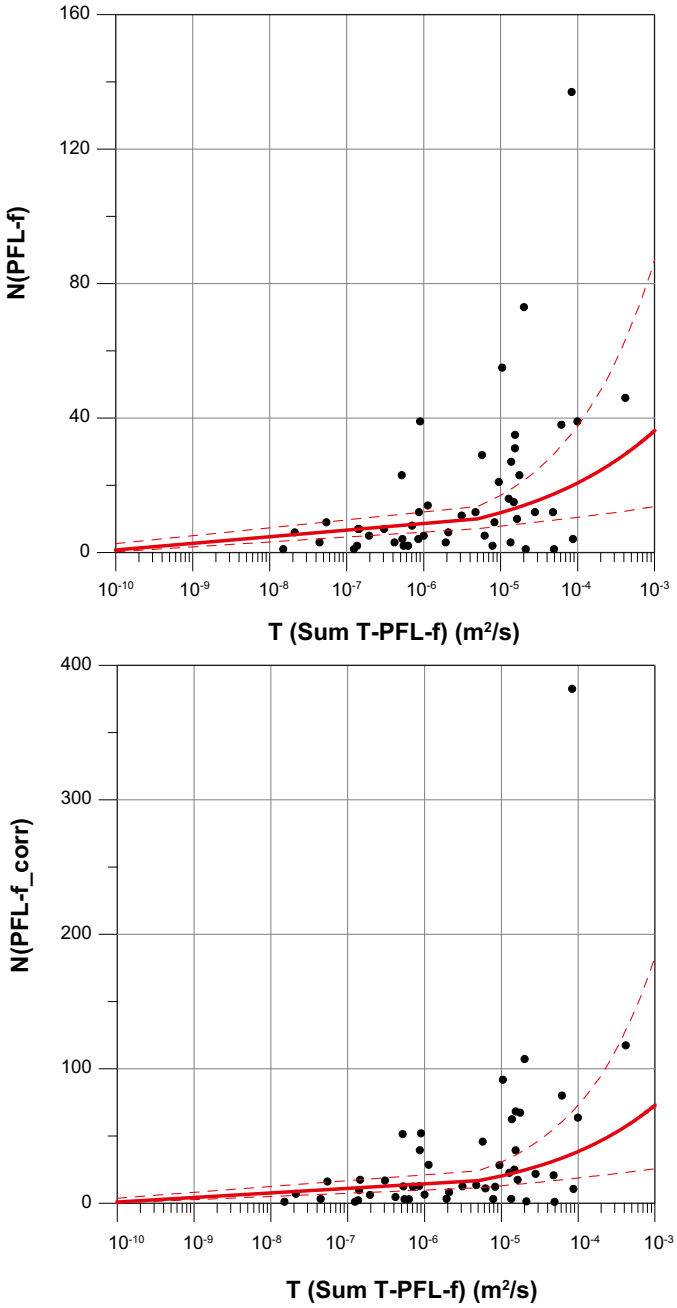

Figure 7-29. *No. of PFL-f within a HCD. Top: No. of PFL-f within a HCD as observed along the borehole. Bottom: Terzaghi corrected No. of PFL-f within a HCD, with max correction factor of 7. Data from local scale model volume.*

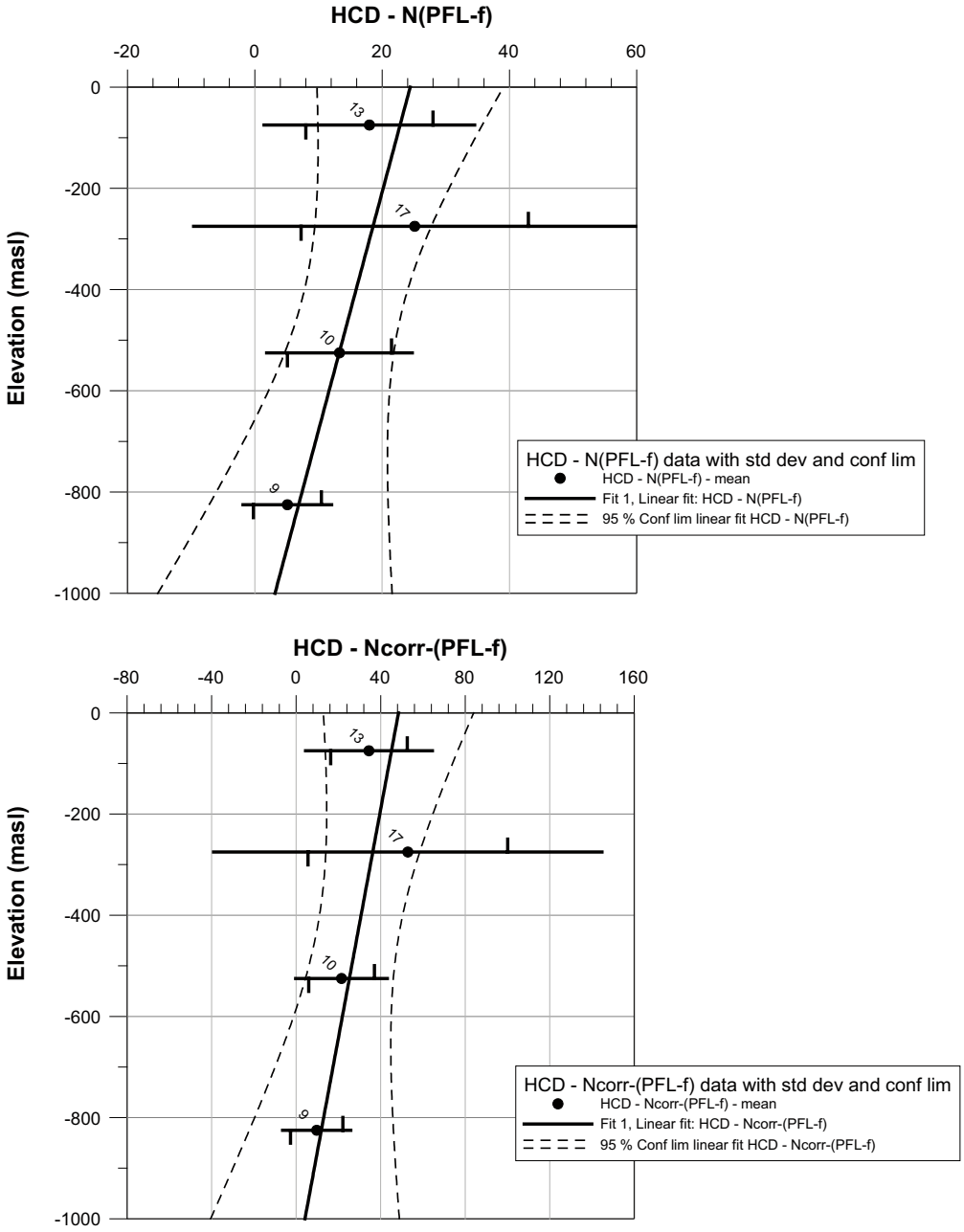

Figure 7-30. *No. of PFL-f:s within a HCD (N: number of PFL-f features along borehole, N-corr: N Terzaghi corrected) versus elevation. Top: N. Bottom: N-corr. For depth zones the following parts are plotted: mean N (or N-corr), confidence limits for mean N (or N-corr), (vertical bars on horizontal line) and ±1 standard deviation of N (or N-corr), (entire horizontal line). Curves are fitted to the 4 mean values and the confidence intervals for fitted lines are shown. The mean and standard deviation are based on the number of samples shown near the mean value. Confidence intervals for fitted lines are shown for lines fitted to the 4 interval means. Data from local scale model volume.*

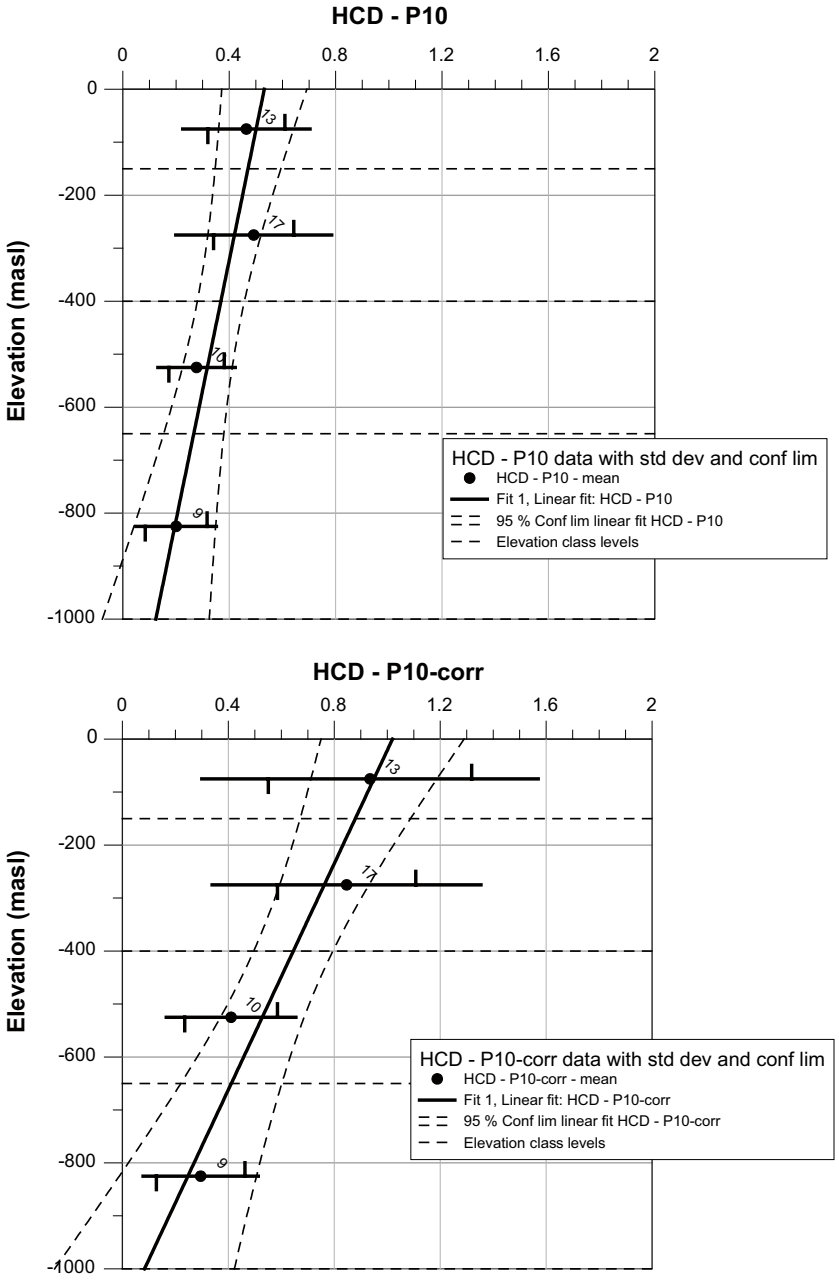

Figure 7-31. *Frequency of PFL-f:s within a HCD (P10: frequency of PFL-f features along borehole, P10-corr: P10 Terzaghi corrected) versus elevation. Top: P10. Bottom: P10-corr. For depth zones the following parts are plotted: mean P10 (or P10-corr), confidence limits for mean P10 (or P10-corr (vertical bars on horizontal line) and ±1 standard deviation of P10 (or P10-corr), (entire horizontal line). Curves are fitted to the 4 mean values and the confidence intervals for fitted lines are shown. The mean and standard deviation are based on the number of samples shown near the mean value. Confidence intervals for fitted lines are shown for lines fitted to the 4 interval means. Data from local scale model volume.*

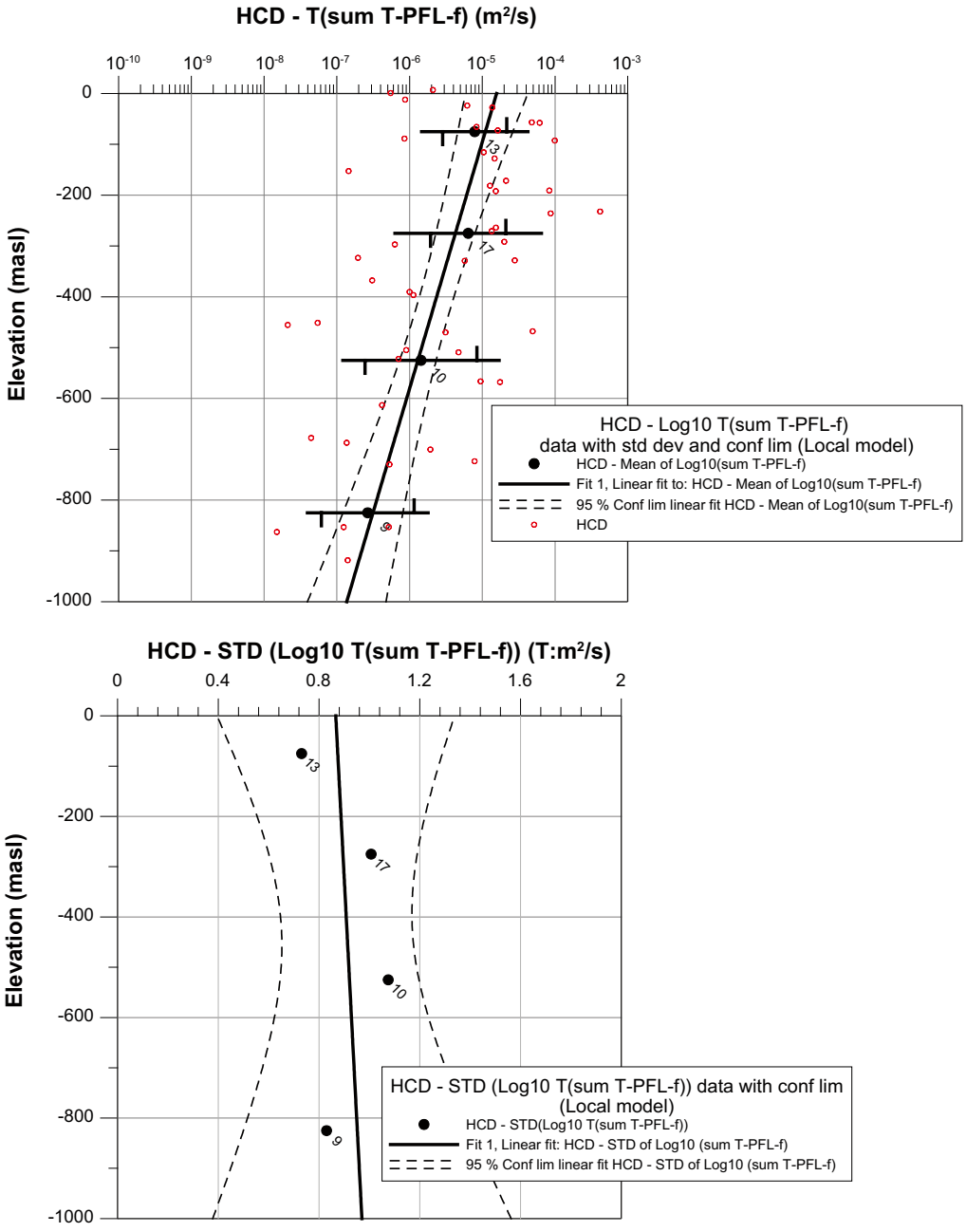

Figure 7-32. *Total transmissivity (sum of T-PFL-f) of a HCD versus elevation. Top: T(sum T-PFL-f). Bottom: Standard deviation of log10(T(sum T-PFL-f)). For depth zones the following parts are plotted: mean log10(T(sum T-PFL-f)) (or std log10(T(sum T-PFL-f))), confidence limits for mean log10(T(sum T-PFL-f)) (vertical bars on horizontal line) and ±1 standard deviation of mean log10(T(sum T-PFL-f)), (entire horizontal line). Curves are fitted to the 4 mean (or 4 standrad deviation values) and the confidence intervals for fitted lines are shown. The mean and standard deviation are based on the number of samples shown near the mean value. Confidence intervals for fitted lines are shown for lines fitted to the 4 interval means (or std). Data from local scale model volume.*

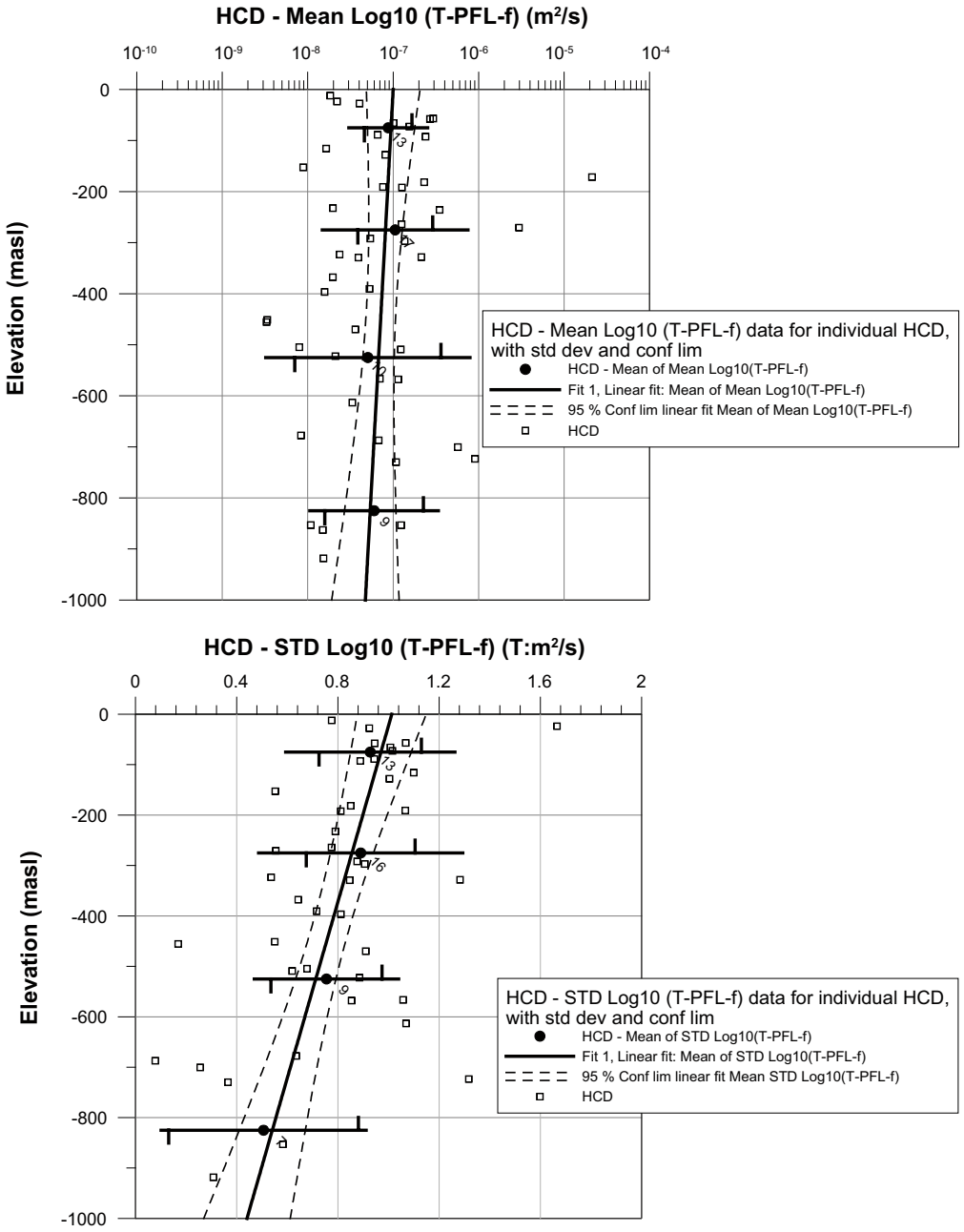

Figure 7-33. *Tranmissivity of individual of PFL-f:s (T-PFL-f) within a HCD versus elevation. Top: mean log10(T-PFL-f) within a HCD. Bottom: Standard deviation of log10(T-PFL-f)) within a HCD. For depth zones the following parts are plotted: mean of mean- log10(T(sum T-PFL-f)) (or mean of std log10(T(sum T-PFL-f))), confidence limits for mean of mean- log10(T(sum T-PFL-f)) (or mean of std log10(T(sum T-PFL-f))), (vertical bars on horizontal line) and ±1 standard deviation of mean of mean- log10(T(sum T-PFL-f)) (or mean of std log10(T(sum T-PFL-f))), (entire horizontal line). Curves are fitted to the 4 mean values and the confidence intervals for fitted lines are shown. The mean and standard deviation are based on the number of samples shown near the mean value. Confidence intervals for fitted lines are shown for lines fitted to the 4 interval means. Data from local scale model volume.*

As seen in Figure 7-28 the total transmissivity (total T for a HCD) increases as the thickness of the HCD increases (but with very large variation). The HCD thickness seems to decrease with depth, but the confidence limits do not support this depth dependence, see Figure 7-28. The range for the thickness of a HCD is c. 10–100 m, with a mean around c.20–40 m and a standard deviation of c. 20–40 m.

Not surprisingly, the number of flowing features also increases when the total transmissivity of the HCD increases, see Figure 7-29 and Table 7-12.

The number PFL-f per HCD and the frequency of PFL-f features within HCD seems to weakly decrease with depth, but the confidence limits do not support this depth dependence except for P10-corr, see Figure 7-30 and Figure 7-31. The range for the N and N-corr within a HCD is c. 1–140 and c. 1–400 respectively, with mean around c. 5–25 and 10–50, respectively, and a standard deviation of c. 5–30 and 10–100, respectively. The range for the P10 and P10-corr within a HCD is c. 0.05–1 and 0.05–2 respectively, with a mean around 0.2–0.5 and 0.3–1 respectivly and a standard deviation of c. 0.15–0.25 and 0.2–0.6 respectivly.

The total transmissivity (sum over the apparent thickness) of a HCD decreases with depth, see Figure 7-32 whereas the standard deviation of the log10(sum T-PFL-f) does not. The range for the mean of log10(sum T-PFL-f) within a HCD is c. –8 to –3 with mean around –5 to –6.6 and a standard deviation of c. 0.7–1.1 (T unit : m^2/s).

The statistical distribution of transmissivity of the individual PFL-f features within a HCD does not decrease with depth, cf. Figure 7-33. The range of the mean of log10(T-PFL-f) within a HCD is c. –8.5 to –4.3 with a mean around –7.3 to –7 (T: m^2/s).

The statistical distribution of standard deviation of the transmissivity of the individual PFL-f features within a HCD seems to decrease with depth, but the confidence limits do not support this depth dependence, see Figure 7-33. The range for the standard deviation of log10(T-PFL-f) within a HCD is c. 0.1–2.2 with mean around 0.5–0.9 (T unit: m^2/s).

The following basic trend models for variables (denoted X in trend function); total HCD transmissivity, PFL-f transmissivity within HCD etc, are proposed, cf. Table 7-12:

- Power-law trend model (Power): $X = a \cdot (-Z)^B$
- Linear trend model (Linear): $X = a + B \cdot (Z)$
- Exponential trend model (Exp): $X = (10^Y =) 10^{(a+B \cdot Z)}$

Z: Elevation in m (masl) (Z defined positive up). The coefficients in the Exponential trend model are based on a linear regression of $Log10(X_i)$ and Exponential trend model is generally just used for transmissivity and hydraulic conductivity.

Table 7-12. Regression models for HCDs fitted to depth zone mean values: Models shown in Figure 7-28 through Figure 7-33. Data from local model volume.

Model ID	Depth trend model	Object	Data type	Coeff. a	Coeff. B	Corr, coeff. r^2
HCD-L-T1	Exp	HCD	Total transmissivity within a HCD. X=(sum T- PFL-f). Local model data.	–4.80347	0.002061	0.96
HCD-L-S1	Linear	HCD	Standard deviation of total transmissivity within a HCD. X=Std(log10(sum T-PFL-f)). Local model data.	0.86635	–0.000104	–
HCD-L-TF1	Exp	HCD	Mean transmissivity of a PFL-f features within a HCD. X=Geometric mean (T-PFL-f). Local model data	–7.00063	0.0003250	0.51
HCD-L-SF1	Linear	HCD	Standard deviation of log10(T-PFL-f) of PFL-f features within a HCD. X=Std (log10(T-PFL-f)). Local model data.	1.01288	0.0005724	0.95
HCD-L-N1	Linear	HCD	N for PFL-f features within a HCD. X=Mean N. Local model data.	24.4127	0.021248	0.67
HCD-L-N2	Linear	HCD	N-corr for PFL-f features within a HCD. X=Mean N-corr. Local model data.	48.4368	0.044267	0.60
HCD-L-P1	Linear	HCD	P10-corr for PFL-f features within a HCD. X=Mean P10-corr. Local model data.	1.01984	0.000936	0.92

8 Hydrogeological data synthesis for local minor deformation zones

Deformation zones with trace length shorter than 1,000 m are called Minor Deformation Zones (MDZ) and are geologically assessed by /Hermanson et al. 2008/ and /Wahlgren et al. 2008/. The MDZs are included as single features in the hydrogeological DFN model presented in Chapter 10. However, the PFL-f features within a MDZ are not treated individually in the hydrogeological DFN model as pointed out in Chapter 2 and 9. If one would like to model heterogeneity within a minor deformation zone (MDZ) or assess the grouting possibilities within a MDZ, the hydraulic character and spatial distribution of individual flow features within a MDZ are of interest. In this chapter some basic PFL-f statistics related to MDZs are summarised.

8.1 Summary of data

The data (excluding data from borehole KLX27A) are from the local model volume. MDZs interpreted in the geological single-hole interpretation interpreted as being hydrogeologically defined HCDs, as discussed in Chapter 7, are excluded from the statistics presented.

Figure 7-27 illustrates how the heterogeneity within a MDZ (and also HCD) has been analysed. The compiled statistics of the individual MDZs are always based on PFL-f features within the local apparent thickness defined by the borehole intercept with the MDZs.

Within the local model volume itself a total of 281 MDZs have been identified (KLX27A not included) and of these 213 MDZs represent rock between the HCDs. PFL-f measurements cover all boreholes with the 213 MDZs with the exception of borehole KLX01 where DZ1 represents a deterministic deformation zone. Among the 213 MDZs representing the rock between the HCDs, 123 (58%) have at least one PFL-f feature associated with the individual MDZ, cf. Table 8-1. That is, grossly about 60% of the MDZs can be expected to have a conductive feature with a transmissivity T >1E–9 m^2/s (the measurement limit for the PFL-tool).

The depth zones; >–150 m, –150– to –400 m, –400 to –650 m, <–650 m have been used when analysing depth dependence of the PFL-f data within the minor deformation zones (MDZ).

Statistics of MDZs are presented in this chapter but also in Section 10.9. One should observe that the statistics in Section 10.9 are based on all MDZs, including those without any PFL-f features, but in Section 8.2 the statistics are based on MDZ with at least one PFL-f feature within a MDZ.

Table 8-1. Statistics of MDZs within the local model volume (data from KLX27A excluded).

Depth zone (m)	PFL-f in MDZ[1]	No. MDZ	Total bh-length (/MDZ)[2] (m)	Total MDZ thickness at bh[2] (m)	Mean N PFL-f[3] (–)	Mean N-corr PFL-f[3] (–)	Mean P10, PFL-f[4] (m^{-1})	Mean P10-corr, PFL-f[4] (m^{-1})	Mean P10-corr, All MDZ[4] (m^{-1})
> –150	PFL-f>0	63	203.40	147.2	2.52	4.24	1.34	2.18	
> –150	PFL-f=0	18	25.20	20.1					
> –150	All	81	228.6	167.3					1.94
–150 to –400	PFL-f>0	36	118.7	81.9	2.17	3.48	1.64	2.34	
–150 to –400	PFL-f=0	31	53.20	42.54					
–150 to –400	All	67	171.90	124.44					1.62
–400 to –650	PFL-f>0	21	78.1	60.7	2.29	5.01	1.12	2.38	
–400 to –650	PFL-f=0	31	64.40	45.5					
–400 to –650	All	52	142.50	106.2					1.30
< –650	PFL-f>0	3	8.9	6.6	1.33	1.55	0.85	0.95	
< –650	PFL-f=0	10	13.70	7.3					
< –650	All	13	22.60	13.9					0.38
> –1,000	PFL-f>0	123	409	296					
> –1,000	PFL-f=0	90	157	115					
> –1,000	All	213	566	412					

[1] PFL-f in MDZ: MDZs with PFL-f features(PFL-f>0) or without PFL-f features(PFL-f=0).

[2] Total bh-length(MDZ): total length of MDZ along the borehole. Total MDZ thickness at bh: sum of thickness of MDZ along the borehole.

[3] Mean N PFL-f: Mean number of PFL-f features within a MDZ. Mean N-corr PFL-f: Mean number of PFL-f features within a MDZ with Terzaghi correction of N.

[4] Mean P10 PFL-f: Mean N PFL-f/(Bh length(MDZ) for PFL-f>0). Mean P10-corr, PFL.f: Mean N-corr PFL-f/(Bh length(MDZ) for PFL-f>0). Mean P10-corr All MDZ: Mean N-corr PFL-f/((Bh length(MDZ) for All)

8.2 Transmissivity models and heterogeneity

The results of the compilation of internal properties of MDZs with at least one PFL-f feature, are presented in Table 8-2 through Table 8-3 and Figure 8-1 to Figure 8-4. In Appendix 4 the detailed results for each minor local deformation zone are shown.

Table 8-2 covers local model MDZs showing the statistics of PFL-f within MDZs and depth zones for the MDZs and includes the following columns:

- *Bh-length(MDZ)*: Lengths of individual MDZs (with PFL-f features) along the borehole.
- *MDZ-thickness at bh*: Estimated true thickness of individual MDZs (with PFL-f features).
- *N-PFL-f*: Number of PFL-f features within individual MDZs.
- *N-corr-PFL-f*: Number of PFL-f features, Terzaghi corrected due to PFL-f features orientations, within individual MDZs.
- *P10 (PFL-f)* and *P10-corr(PFL-f)*: Intensity of PFL-f features within a MDZ. N-PFL-f and N-corr-PFL-f divided by MDZ length along the borehole, for each individual MDZ.
- *T(sum T-PFL-f)*: Sum of T-PFL-f, where T-PFL-f is the transmissivity of individual PFL-f features within a MDZ (sum T-PFL-f= total transmissivity of a MDZ).
- *log10 (sum T-PFL-f)*: Log10(sum T-PFL-f), where T-PFL-f is the transmissivity of individual PFL-f features within a MDZ (sum T-PFL-f= total transmissivity of a MDZ).
- *Mean T-PFL-f*: Arithmetic mean of T-PFL-f within each MDZ, where T-PFL-f is the transmissivity of individual PFL-f features within a MDZ.
- *10^(Mean log10(T-PFL-f))*: Anti-log of the calculated values for Mean log10(T-PFL-f) shown below.
- *Mean log10(T-PFL-f)*: Arithmetic mean of log10(T-PFL-f) within each MDZ, where T-PFL-f is the transmissivity of individual PFL-f features within a MDZ.
- *Std log10(T-PFL-f)*: Standard deviation of log10(T-PFL-f) within each MDZ, where T-PFL-f is the transmissivity of individual PFL-f features within a MDZ.

For each of these column variables; Min, Max, Mean (arithmetic) and std(standard deviation) are shown for the data points within a depth zone (Object). The std cannot always be calculated due to small sample size, labelled as NA: Not available.

Table 8-2 is based on the figures shown in Appendix 4.

Table 8-2. PFL-f statistics related to minor deformation zones. Data from local model volume, data from KLX27A excluded.

Object		Bh-length (MDZ)	MDZ thickness at bh	N PFL-f	N-corr PFL-f	P10 (PFL-f)	P10-corr (PFL-f)	T (sum T-PFL-f)	log10 (sum T-PFL-f)	Mean T-PFL-f	10^(Mean log10 (T-PFL-f))	Mean log10 (T-PFL-f)	Std log10 (T-PFL-f)
Object/Depth zone		(m)	(m)	(–)	(–)	(m^{-1})	(m^{-1})	(m^2/s)	(m^2/s)	(m^2/s)	(m^2/s)	T: (m^2/s)	T: (m^2/s)
> –1,000 All data	**Sample size**	123	123	123	123	123	123	121	121	121	121	121	64
	Min	0.0	0.0	1	1	0.10	0.11	6.8E–10	–9.17	6.8E–10	6.8E–10	–9.17	0.00
	Max	24.3	10.2	10	27	10.00	24.48	6.4E–05	–4.19	3.7E–05	3.7E–05	–4.43	2.02
	Mean	3.3	2.4	2.35	4.08	1.38	2.23	4.3E–06	–6.70	2.0E–06	6.9E–08	–7.16	0.66
	std	3.8	2.4	1.89	4.04	1.32	2.72		1.28			1.06	0.46
> –150	**Sample size**	63	63	63	63	63	63	61	61	61	61	61	34
	Min	0.1	0.0	1	1	0.15	0.15	6.8E–10	–9.17	6.8E–10	6.8E–10	–9.17	0.00
	Max	22.4	9.6	10	27	10.00	24.48	6.4E–05	–4.19	3.2E–05	1.9E–05	–4.72	2.02
	Mean	3.2	2.3	2.52	4.24	1.34	2.18	6.5E–06	–6.44	2.9E–06	1.2E–07	–6.91	0.62
	std	3.6	2.3	2.16	4.48	1.36	3.10		1.33			1.13	0.48
–150 to –400	**Sample size**	36	36	36	36	36	36	36	36	36	36	36	18
	Min	0.3	0.0	1	1.00	0.10	0.11	8.3E–10	–9.08	8.3E–10	8.3E–10	–9.08	0.10
	Max	24.3	10.2	7	12.83	6.06	11.67	3.7E–05	–4.43	3.7E–05	3.7E–05	–4.43	1.69
	Mean	3.3	2.3	2.17	3.48	1.64	2.34	3.1E–06	–6.79	1.7E–06	5.5E–08	–7.26	0.77
	std	4.5	2.4	1.59	3.06	1.39	2.21		1.26			0.97	0.47
–400 to –650	**Sample size**	21	21	21	21.00	21	21	21	21	21	21	21	11
	Min	0.0	0.0	1	1.00	0.11	0.13	1.3E–09	–8.89	1.3E–09	1.3E–09	–8.89	0.01
	Max	9.0	8.2	6	18.86	5.00	9.71	5.8E–06	–5.24	1.2E–06	1.1E–06	–5.96	1.32
	Mean	3.7	2.9	2.29	5.01	1.12	2.38	5.1E–07	–7.20	1.7E–07	2.2E–08	–7.65	0.64
	std	3.3	2.7	1.59	4.26	1.11	2.55		1.01			0.80	0.43
< –650	**Sample size**	3	3	3	3.00	3	3	3	3	3	3	3	1
	Min	0.7	0.6	1	1.03	0.29	0.35	3.7E–09	–8.43	1.8E–09	1.5E–09	–8.83	0.43
	Max	7.0	4.8	2	2.47	1.43	1.64	4.4E–07	–6.36	4.4E–07	4.4E–07	–6.36	0.43
	Mean	3.0	2.2	1.33	1.55	0.85	0.95	1.6E–07	–7.43	1.6E–07	2.7E–08	–7.57	0.43
	std	3.5	2.3	0.58	0.80	0.57	0.65		1.04			1.24	NA

(1) Two transmissivities was not possible to estimate for two PFL-f s.

(2) Thickness at borehole intercept has not been estimated for a few boreholes, mostly outside the local model volume. In such cases the Bh-length/MDZ was used as approximation for thickness in the P10 estimates.

Table 8-3. Regression models for MDZs fitted to depth zone means. Models shown in Figure 8-1 through Figure 8-6. Data from local model volume.

Model ID	Depth trend model	Object	Data type	Coeff. a	Coeff. B	Corr, coeff. r^2
MDZ-L-T1	Exp	MDZ	Total transmissivity within a MDZ. X=(sum T- PFL-f). Local data.	–6.39954	0.001333	0.97
MDZ-L-S1	Linear	MDZ	Standard deviation of total transmissivity within a MDZ. X=Std(log10(sum T- PFL-f)). Local data.	1.34648	0.0004376	0.79
MDZ-L-TF1	Exp	MDZ	Mean transmissivity of a PFL-f features within a MDZ. X=Geometric mean (T- PFL-f). Local data.	–6.96331	0.009006	0.76
MDZ-L-SF1	Linear	MDZ	Standard deviation of log10(T-PFL-f) of PFL-f features within a MDZ. X=Std (log10(T- PFL-f)). Local data.	0.745850	0.0003115	0.49
MDZ-L-N1	Linear	MDZ	N for PFL-f features within a MDZ. X=Mean N. Local data.	2.67970	0.001417	0.79
MDZ-L-N2	Linear	MDZ	N-corr for PFL-f features within a MDZ. X=Mean N-corr. Local data.	4.76336	0.002810	0.38
MDZ-L-P1	Linear	MDZ	P10-corr for PFL-f features within a MDZ. X=Mean P10-corr. Local data.	2.62696	0.001566	0.56

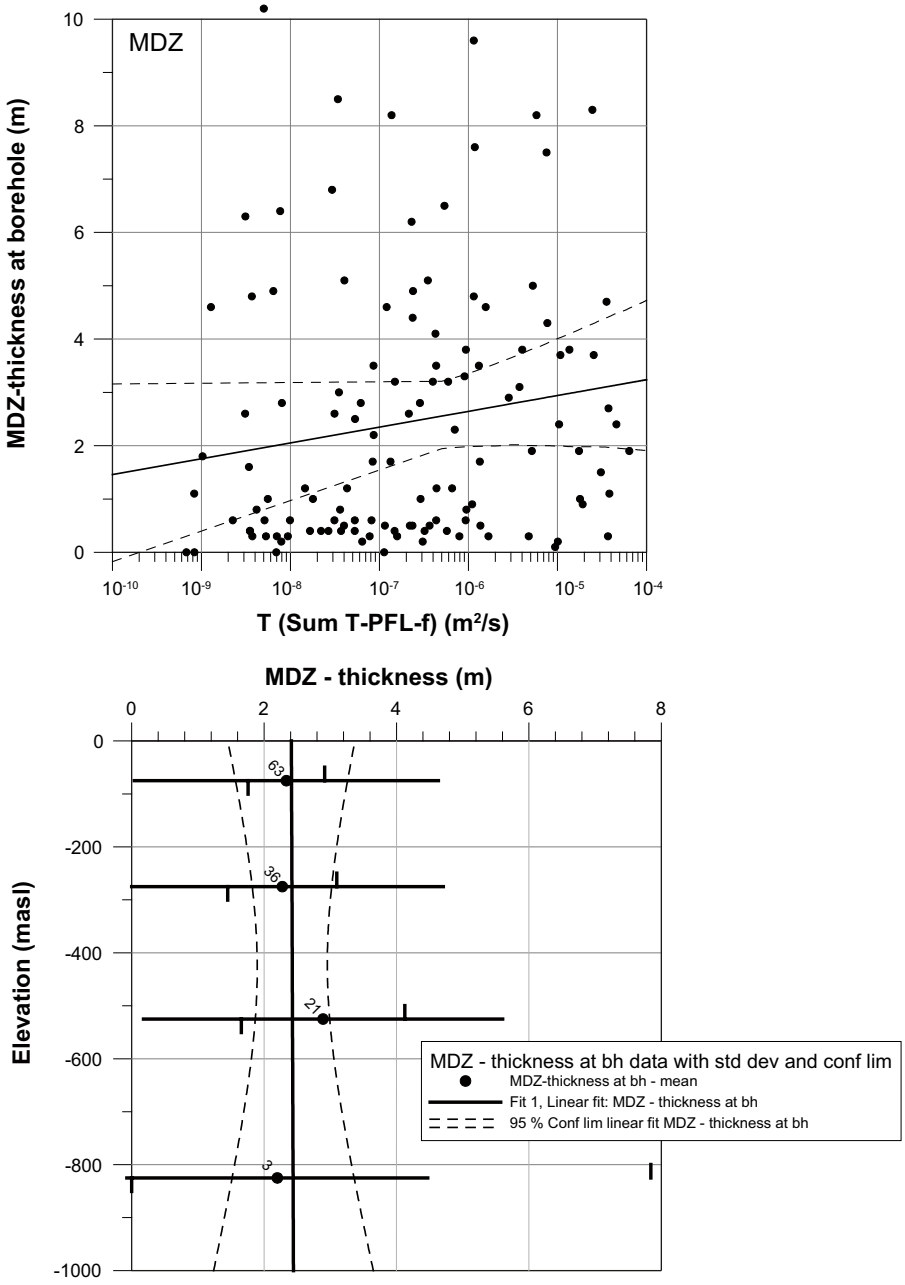

Figure 8-1. *Top: Transmissivity of a MDZ versus MDZ true thickness. Transmissivity based on sum of T-PFL-f. Estimated thickness of a MDZ at borehole intercept providing the actual T- estimates. Bottom: MDZ true thickness versus elevation. For depth zones the following parts are given; mean thickness, confidence limits for mean thickness (vertical bars on horizontal line) and ±1 standard deviation thickness (entire horizontal line) are plotted. Curves are fitted to the 4 Arithmetic mean values of all data. The mean and standard deviation are based on the number of samples shown near the mean value. Confidence intervals for fitted lines are shown for lines fitted to the 4 depth zone means. Data from local scale model volume.*

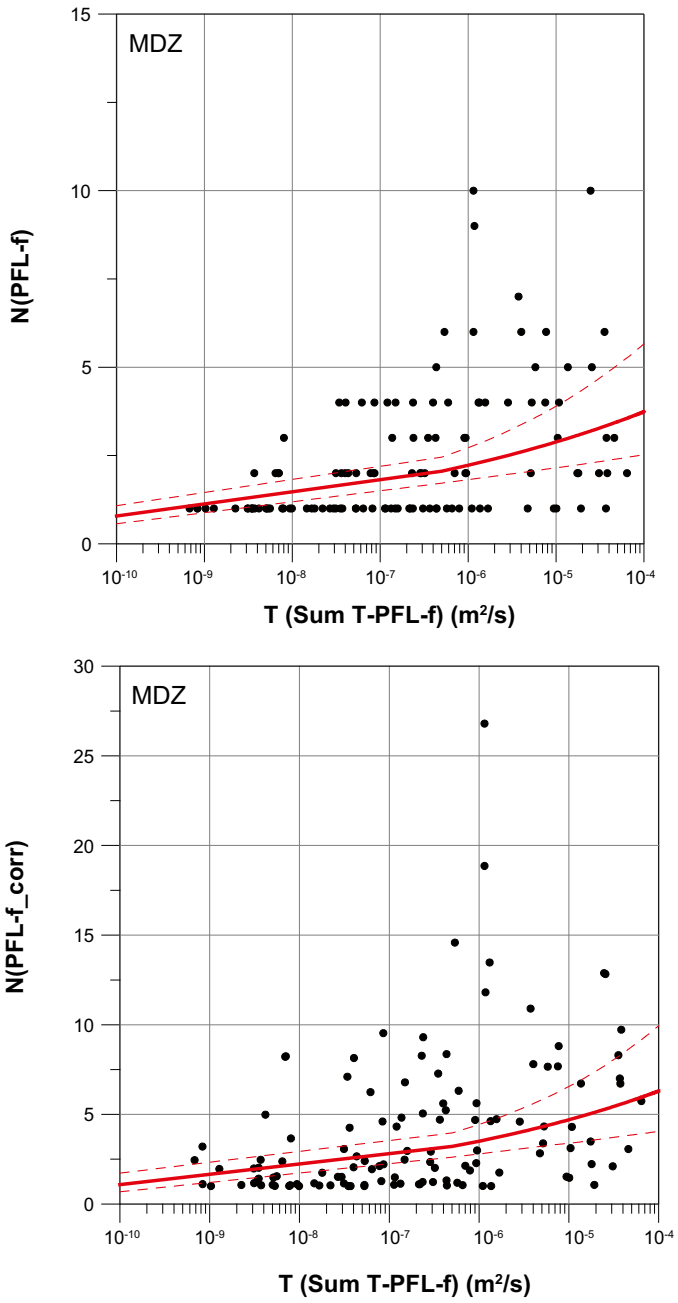

Figure 8-2. *No. of PFL-f within a MDZ. Top: No. of PFL-f within a MDZ as observed along the borehole. Bottom: Terzaghi corrected No. of PFL-f within a MDZ, with max correction factor of 7. Data from local scale model volume.*

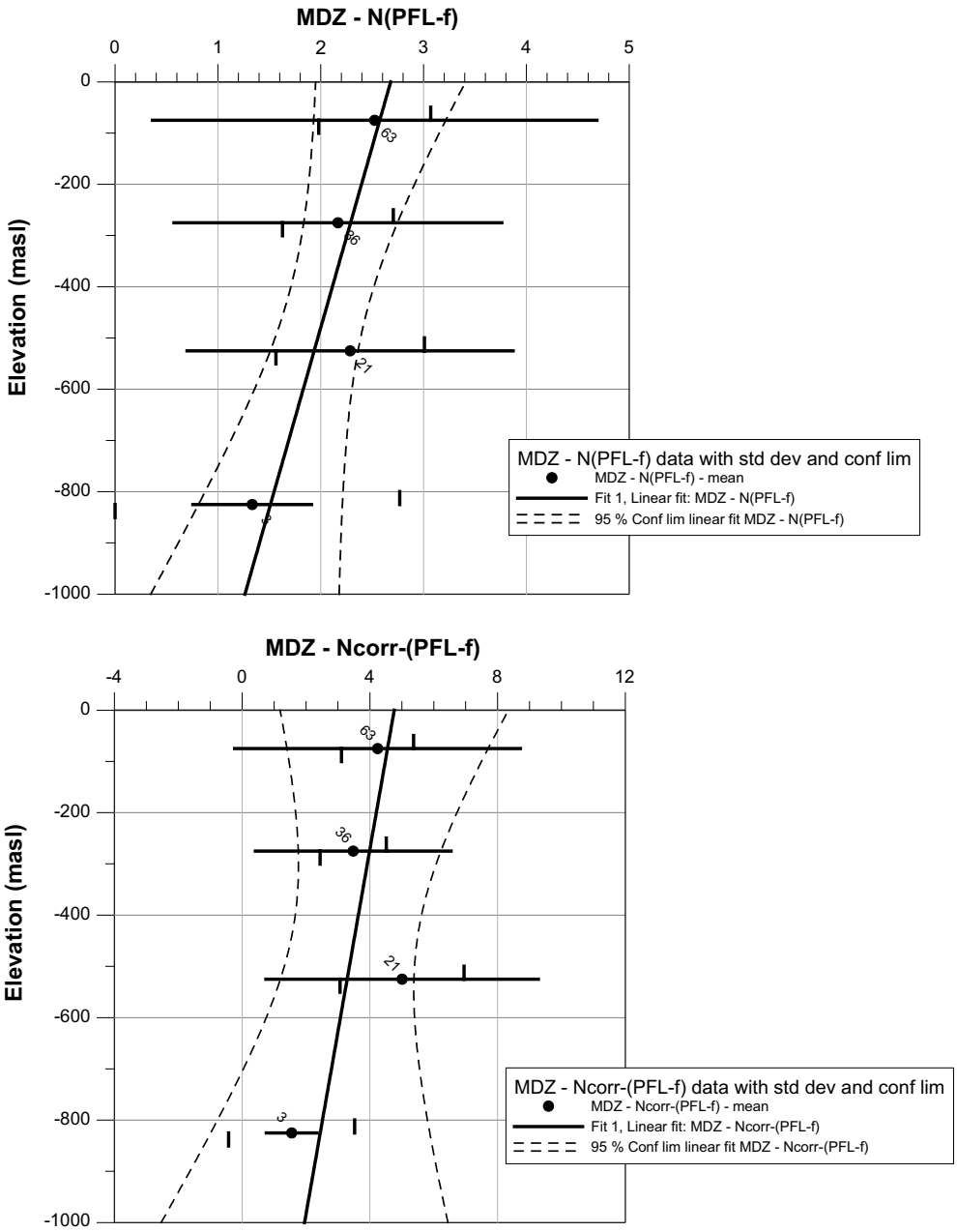

Figure 8-3. *No. of PFL-f:s within a MDZ (N: number of PFL-f features along borehole, N-corr: N Terzaghi corrected) versus elevation. Top: N. Bottom: N-corr. For depth zones the following parts are plotted: mean N (or N-corr), confidence limits for mean N (or N-corr), (vertical bars on horizontal line) and ±1 standard deviation of N (or N-corr), (entire horizontal line). Curves are fitted to the 4 mean values and the confidence intervals for fitted lines are shown. The mean and standard deviation are based on the number of samples shown near the mean value. Confidence intervals for fitted lines are shown for lines fitted to the 4 depth zone means. Data from local scale model volume.*

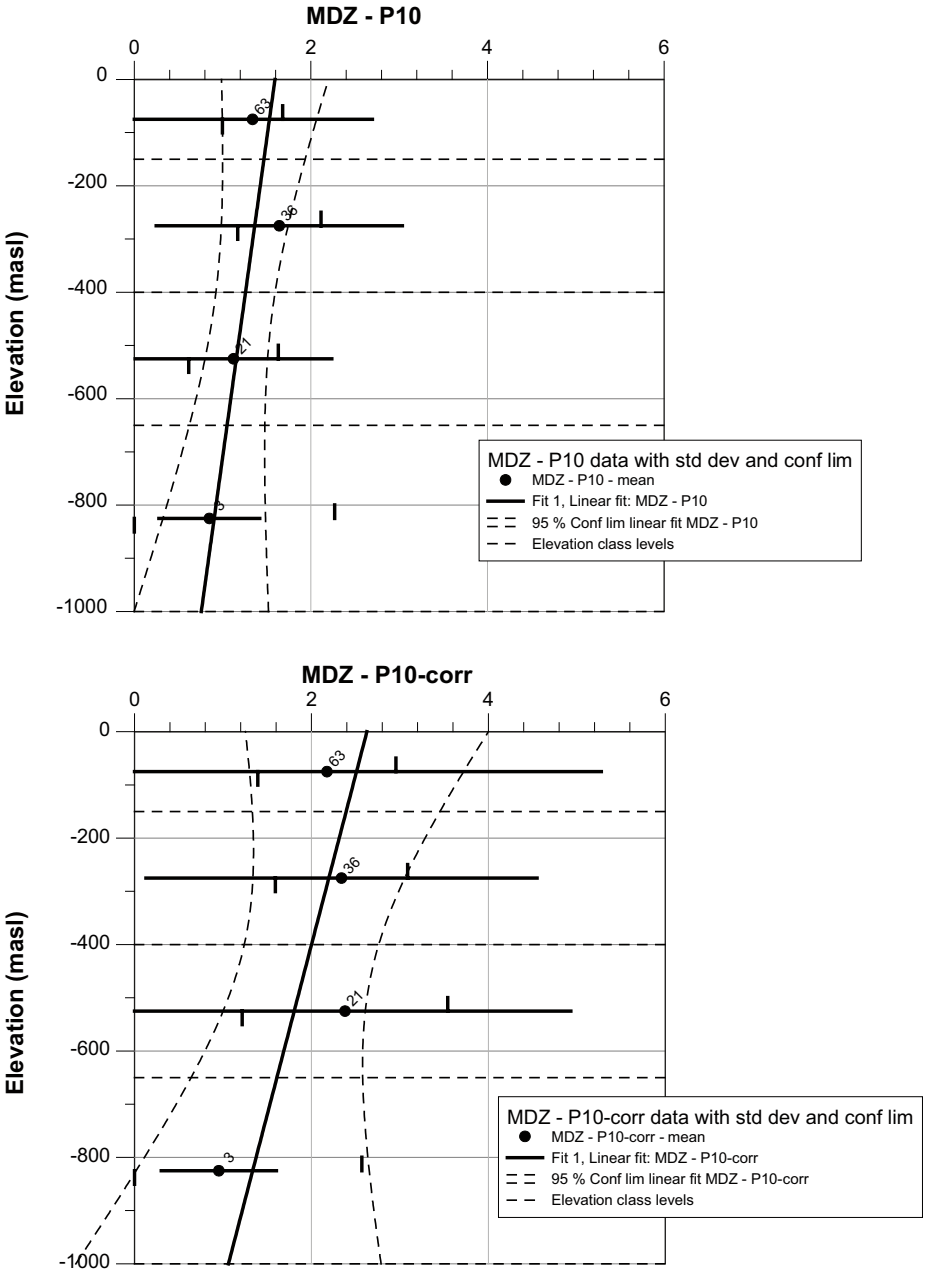

Figure 8-4. *Frequency of PFL-f:s within a MDZ (P10: frequency of PFL-f features along borehole, P10-corr: P10 Terzaghi corrected) versus elevation. Top: P10. Bottom: P10-corr. For depth zones the following parts are plotted: mean P10 (or P10-corr), confidence limits for mean P10 (or P10-corr (vertical bars on horizontal line) and ±1 standard deviation of P10 (or P10-corr), (entire horizontal line). Curves are fitted to the 4 mean values and the confidence intervals for fitted lines are shown. The mean and standard deviation are based on the number of samples shown near the mean value. Confidence intervals for fitted lines are shown for lines fitted to the 4 depth zone means. Data from local scale model volume.*

As seen in Figure 8-1 the total transmissivity (total T for a MDZ) increases as the thickness of the MDZ increases (but with very large variation). A large proportion of the MDZs are very thin, as can be seen in the figure. The figure also shows that there is no indication that the MDZ thickness changes with depth for the sample studied, see Figure 8-1. The range for the true thickness of a MDZ with a least one PFL-f is c. 1–10 m, with a mean around 2 m and a standard deviation of c. 2 m.

The number of flowing features also increases when the total transmissivity of the MDZ increases, see Figure 8-2 and Table 8-2.

The number of PFL-f features per MDZ and frequency within MDZ seem to weakly decrease with depth, but the confidence limits do not support this depth dependence, see Figure 8-3 and Figure 8-4. However, on average, one can expect that the P10corr for PFL-f of a MDZ decreases with depth as the frequency of MDZ without PFL-f features increases with depth, cf. Table 8-1. The range for the N/N-corr within a MDZ is c. 1–10/ c. 1–40, with mean around 2/4 and a standard deviation of c. 2/4. The range for the P10/P10-corr within a MDZ is c. 0.1–10/ 0.2–25, with mean around 1–1.5/2–2.5 and a standard deviation of c. 1–1.5/2–3. One can observe that P10/P10-corr is higher for MDZs compared to HCDs in Section 7.8. This is probably due to that most MDZ are rather narrow features with some relevant characteristics for MDZs, while a HCD (and the underlying deformation zone) generally are more complex, with several MDZs and less fractured parts of rock between the MDZs within defined thickness of the HCD.

The total transmissivity (sum over the apparent thickness) of a MDZ decreases weakly with depth, but the confidence limits do nearly not support this depth dependence, see Figure 8-5. However, on average, one can expect that the total transmissivity of a MDZ decreases by depth as the frequency of MDZ without PFL-f features increase by depth, cf. Table 8-1. The standard deviation of log10(T-PFL.f) decreases weakly with depth, but the confidence limits do not support this depth dependence, see Figure 8-5. The range for the mean of log10(sum T-PFL-f) within a MDZ is c. –9 to –4 with mean around –7.4 to –6.4 and a standard deviation of c. 1–1.4 (T: m^2/s).

The statistical distribution of transmissivity of the individual PFL-f features within a MDZ seems to weakly decrease with depth, but the confidence limits do nearly not support this depth dependence, see Figure 8-6. The range for the mean of log10(T-PFL-f) within a MDZ is c. –9 to –5 with mean around –7.7 to –7 (T unit: m^2/s).

The statistical distribution of standard deviation of the transmissivity of the individual PFL-f features within a MDZ seems to weakly decrease with depth, but the confidence limits do not support this depth dependence, see Figure 8-6. The range for the standard deviation of log10(T-PFL-f) within a MDZ is c. 0.2–1.5 with mean around 0.6–0.8 (T unit: m^2/s).

MDZs that are judged to be brittle or ductile/brittle, cf. /Hermanson et al. 2008/, can generally be expected to have a conductive feature with a transmissivity $T > 10^{-9}$ m^2/s but a MDZs judged to be mostly ductile can generally be expected to show no conductive feature with a transmissivity $T > 10^{-9}$ m^2/s, see Figure 8-7 and Table 8-4.

The storage coefficient as function of transmissivity in deformation zones is presented in Section 7.6 and probably this relation is applicable also for MDZs as well. In fact, some of the low-transmissive features included in the regression should be considered as MDZs.

The following basic trend models for variables (denoted X in trend function); total MDZ transmissivity, PFL-f transmissivity within MDZ etc, are proposed, cf. Table 8-3:

- Power-law trend model (Power): $X = a \cdot (-Z)^B$
- Linear trend model (Linear): $X = a + B \cdot (Z)$
- Exponential trend model (Exp) $X = (10^Y =) 10^{(a+B \cdot Z)}$

Z: Elevation in m (masl) (Z defined positive up). The coefficients in the Exponential trend model are based on a linear regression of $Log10(X_i)$ and Exponential trend model is generally just used for transmissivity and hydraulic conductivity.

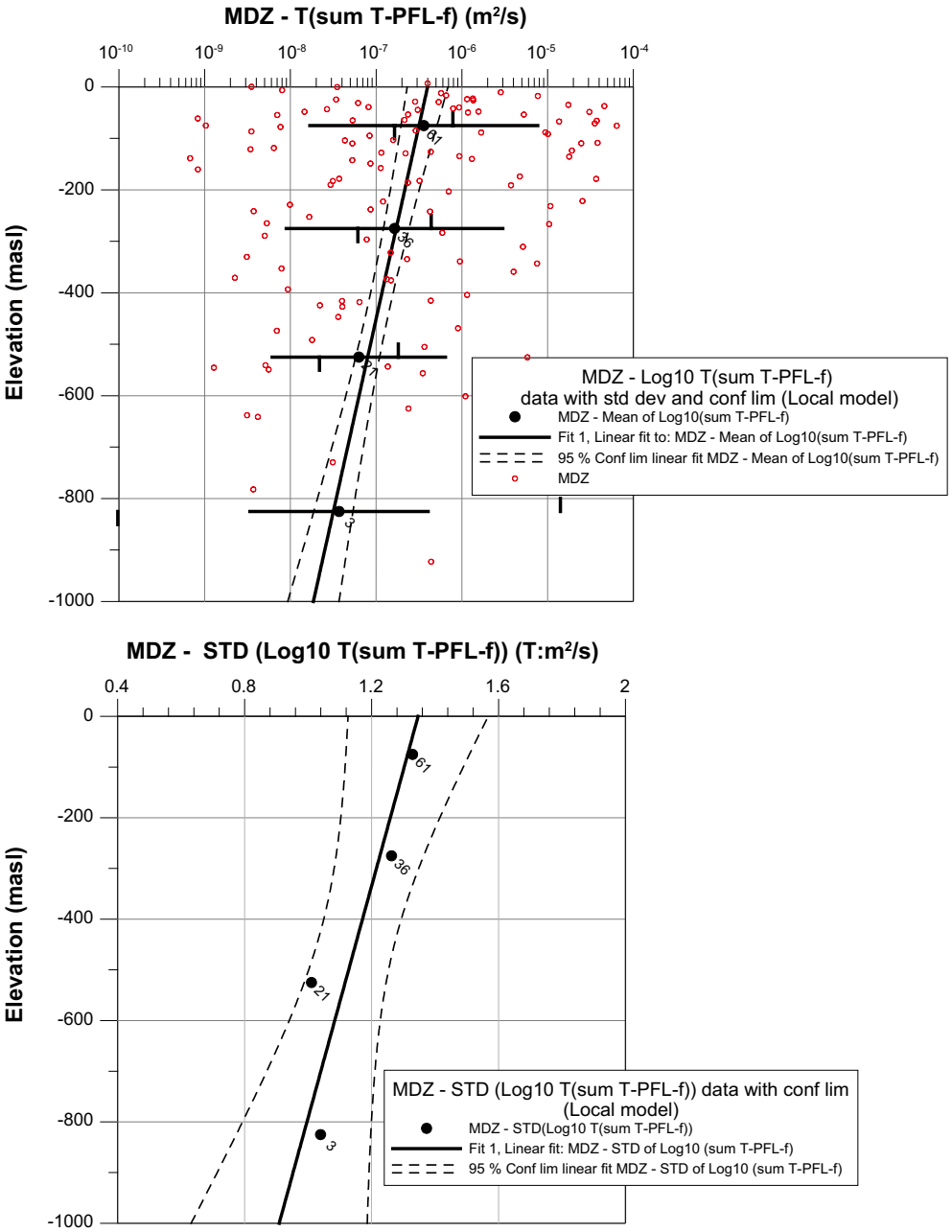

Figure 8-5. *Total transmissivity (sum of T-PFL-f) of a MDZ versus elevation. Top: T(sum T-PFL-f). Bottom: Standard deviation of log10(T(sum T-PFL-f)). For depth intervals the following parts are plotted: mean log10(T(sum T-PFL-f)) (or std log10(T(sum T-PFL-f))), confidence limits for mean log10(T(sum T-PFL-f)) (vertical bars on horizontal line) and ±1 standard deviation of mean log10(T(sum T-PFL-f)), (entire horizontal line). Curves are fitted to the 4 mean (or 4 standard deviation values) and the confidence intervals for fitted lines are shown. The mean and standard deviation are based on the number of samples shown near the mean value. Confidence intervals for fitted lines are shown for lines fitted to the 4 depth zone means (or std). Data from local scale model volume.*

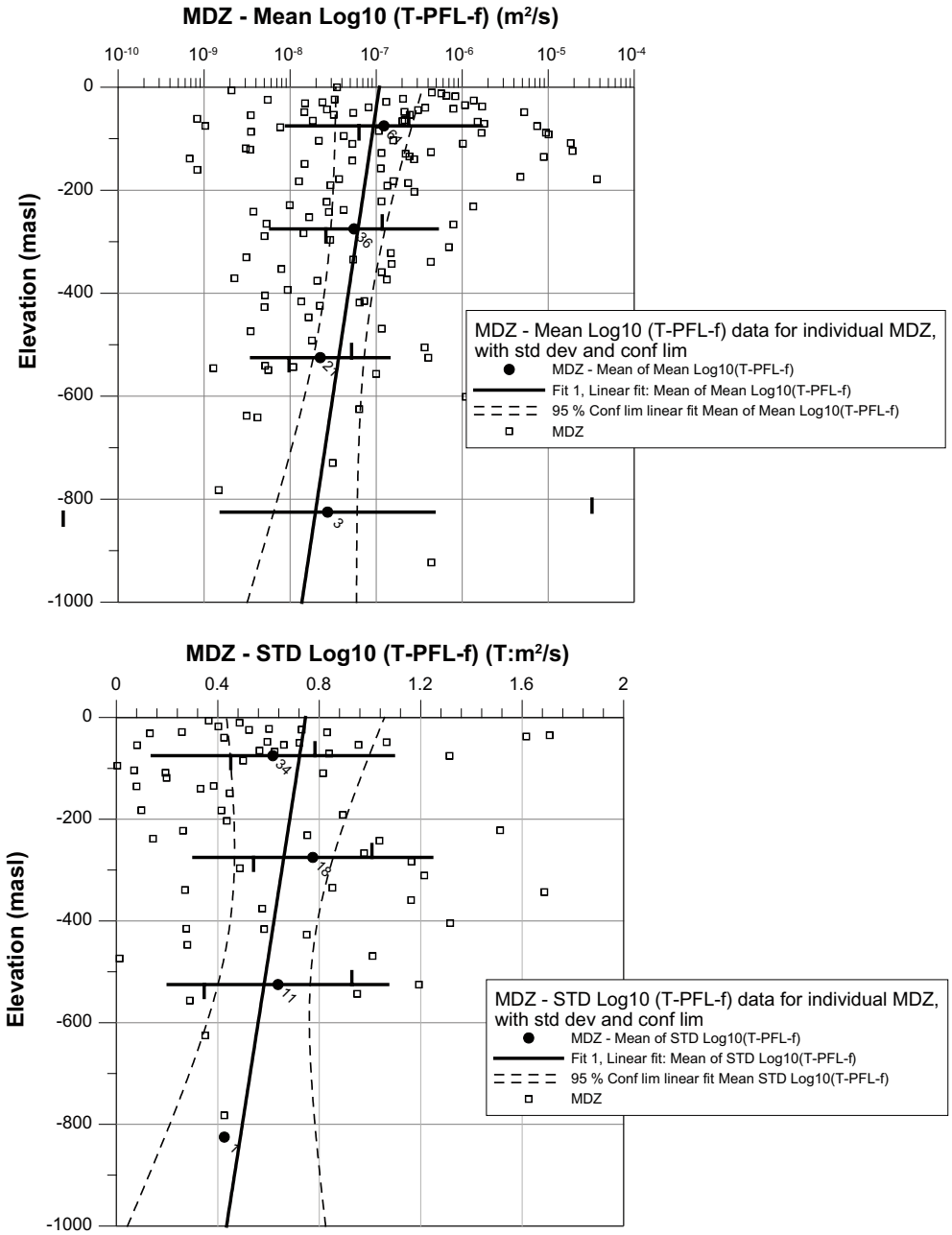

Figure 8-6. *Tranmissivity of individual PFL-f:s (T-PFL-f) within a MDZ versus elevation. Top: mean log10(T-PFL-f) within a MDZ. Bottom: Standard deviation of log10(T-PFL-f)) within a MDZ. For depth zones the following parts are plotted: mean of mean- log10(T(sum T-PFL-f)) (or mean of std log10(T(sum T-PFL-f))), confidence limits for mean of mean- log10(T(sum T-PFL-f)) (or mean of std log10(T(sum T-PFL-f))), (vertical bars on horizontal line) and ±1 standard deviation of mean of mean- log10(T(sum T-PFL-f)) (or mean of std log10(T(sum T-PFL-f))), (entire horizontal line). Curves are fitted to the 4 mean values and the confidence intervals for fitted lines are shown. The mean and standard deviation are based on the number of samples shown near the mean value. Confidence intervals for fitted lines are shown for lines fitted to the 4 depth zone means. Data from local scale model volume.*

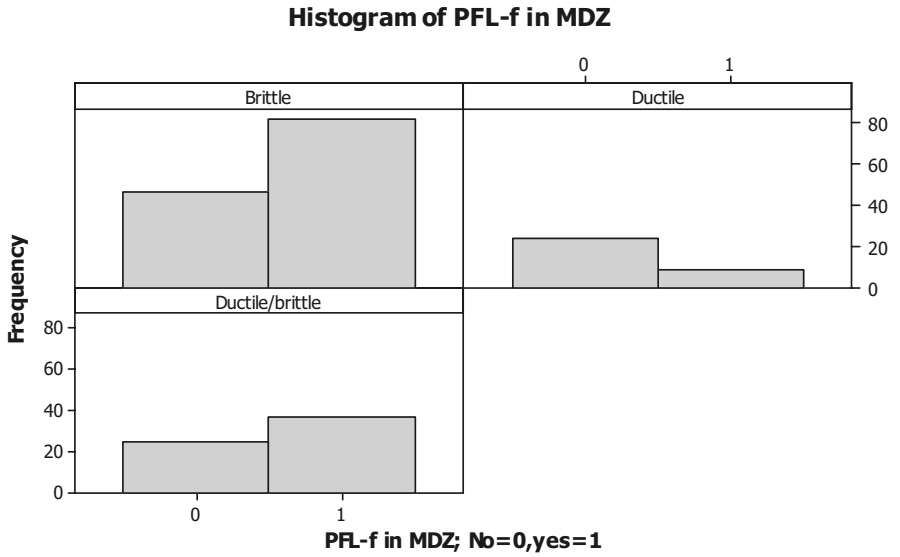

Panel variable: Z type

Figure 8-7. *Number of MDZ with and without PFL-f features versus character: Brittle, Ductile/Brittle, Ductile. Data from local model volume, data from KLX27A excluded.*

Table 8-4. Number of MDZ with and without PFL-f features versus character: Brittle, Ductile/ Brittle, Ductile. Data from local model volume, data from KLX27A excluded.

Object	Data type	No. with PFL-f	No. without PFL-f	Total No.
MDZ	Brittle MDZ	77	44	121
MDZ	Ductile/Brittle MDZ	36	22	58
MDZ	Ductile MDZ	9	24	33

9 Hydrogeological data synthesis for bedrock between the deterministic deformation zones

This chapter explores and discusses different aspects of the hydraulic characteristics and properties of the rock in between the interpreted deterministic deformation zones (including the minor deformation zones (MDZ) that are not part of the deterministic deformation zones in the analysed data). Data in this chapter explores details that are essential for the hydrogeological DFN model construction, but also scale dependencies and depth trends in HRDs as shown by injection tests data based on different test.scales that are useful for testing hydrogeological DFN models and for generating properties for simplified ECPM models.

The first sections; Section 9.1 through 9.5, form the basis for the hydrogeological DFN models presented in Chapter 10. The remaining sections; Sections 9.6 through 9.9, describe PSS and PFL-s tests, cf. Chapter 4, at different test scales, estimates of hydraulic conductivity of rock types and specific storage. More specifically, the hydraulic characteristics and properties of the rock in between the interpreted deterministic deformation zones are discussed in relation to:

- Orientation and intensity of mapped fractures in the core and flowing features (PFL-f features), which are the base for the definition of Hydraulic Rock Domains (HRD) and the depth zones used for processing data in Chapters 7 through 9 and the ensuing hydrogeological DFN modelling described in Chapter 10. Depth zones are defined in Section 9.3.5 and HRDs are defined in Section 9.3.6.
- Gross differences in hydraulic conductivity between deformation zones and rock between DZ. In this context 100 m test scale is used as it is a large data set with good spatial coverage, cf. Section 9.6.
- Scale issues related to test scales and statistics of test results (100, 20 or 5 m PSS tests are used as the same methodology for testing and evaluation are employed). These data can be used to compare with the block modelling results based on the hydrogeological DFN model described in Chapter 10, but also as an indication of how up- and down scaling can be performed, cf. Section 9.6.
- Properties of rock types, which may be of interest at the tunnel and deposition hole scale, cf. Section 9.7.
- Hydraulic conductivity in relation to the frequency of open fractures and presence of crush zones. Entries here serve as a brief overview of how the existence of open fractures and crush zones relate to measured hydraulic conductivity. In Sections 9.1 through 9.5 a more differentiated view of the coupling between open fractures and PFL-f features is provided (cf. Section 9.8).
- Specific storage in relation to hydraulic conductivity, in support of the performance of transient groundwater flow modelling, cf. Section 9.9).

Section 9.6 provides an evaluation of the hydraulic properties of the deformations zones, contrasted and compared with a case where the entire data set (including data associated with deformation zones) is evaluated for comparison. However, concerning the actual proposed properties for deterministically defined deformation zones, Chapter 7 constitutes the main reference.

This chapter dicusses both PFL and PSS test data since both methods have different capabilities important for the discussion, cf. Chapter 4.

9.1 Fracture data analysis – Methodology

In previous work for Forsmark /Follin et al. 2007b/ and Laxemar /Hartley et al. 2006, Hartley et al. 2007/, a methodology was developed and refined for the analysis of the geological and hydrogeological fracture information and the subsequent development of a hydrogeological DFN model. This methodology comprises:

1. Collate the fractures from the borehole core- and image-logs (boremap data) and classify them according to whether they are inside one of the interpreted regional deformation zones, one of the local major deformation zones, one of the local minor deformation zones or the fractured rock between interpreted deformation zones.
2. For each local minor deformation zone, determine an effective planar feature that represents the overall geometry of the zone (see Figure 9-1). Each local minor deformation zone is regarded as being a single feature in the overall distribution of features, and are considered as being among the larger features of the fracture distribution. The orientation of the planar feature representing a minor deformation zone has been determined from several sources /see Hermanson et al. 2008, cf. Appendix 3 therein/ and their transmissivity local to a borehole is taken to be equal to the sum of the transmissivities of the fractures within the interpreted intersection interval along the borehole.
3. Collate the PFL-f features and classify them according to whether they are inside one of the interpreted regional deformation zones, one of the local major deformation zones, one of the local minor deformation zones, or the fractured rock between interpreted deformation zones.
4. For the PFL-f features, determine the fracture that is considered most likely to correspond to the PFL-f feature. Use the orientation of this fracture to provide an orientation to the fracture corresponding to the given PFL-f feature.
5. Identify major fracture sets from the stereographic density plots for the fractures (Terzaghi corrected to account for the bias in sampling fractures at different orientations to a given borehole).
6. Classify the fractures and planar features representing minor local deformation zones in various categories such as by borehole, by fracture set, by depth, by whether the fractures are open, or partly open or closed and by the associated confidence (certain, probable or possible).
7. Calculate linear fracture intensities, P_{10}, for the various categories of fractures and for the PFL-f features.
8. Calculate Terzaghi corrected linear fracture intensities, $P_{10,corr}$, for the various categories.
9. Investigate possible correlations between fracture intensity and the various categories (e.g. defined rock domain, fracture domain, depth, etc).
10. Generate equal-area lower-hemisphere stereonets for various categories of fractures to investigate possible variations in fracture orientations between different categories, such as variations between boreholes and variations with depth.
11. Generate stereographic pole plots for the fractures associated with PFL-f features, with the poles coloured according to the interpreted transmissivity to identify the orientation of fractures with the greatest hydrogeological significance.
12. Generate realisations of fractures potentially carrying flow for suitable sub-division of the bedrock and predict the occurrence of fractures belonging to each defined set in a vertical borehole.
13. Check the consistency of the generated realisations (in terms of fracture intensity along boreholes) with the statistics taken from the boremap data.
14. Calibrate the model parameters, mainly fracture size and transmissivity distrubtions, i.e. determine the model that best matches observations (in terms of the distribution of flow within PFL-f features in the boreholes).

Steps 1-11 are essential steps in the data analysis and are covered in this chapter. The aim of these analyses is to support the development of a conceptual model for the hydraulically signicant fractures, including correlations of orientation or intensity with, for example, depth. Steps 12 to14 relate to DFN modelling and are covered in Chapter 10.

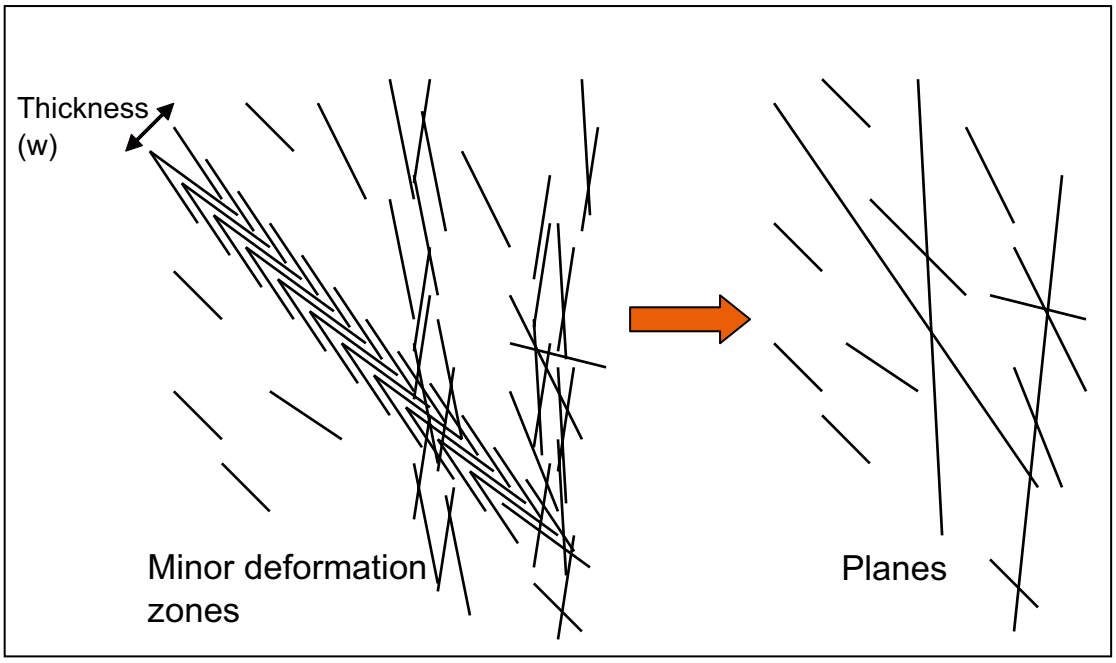

Figure 9-1. *Representation of minor deformation zones as effective stochastic planar features.*

Here, the term "PFL-f feature" is used to denote a flowing feature detected using the PFL-f technique to identify discrete changes in flow-rate over short sections of borehole, typically 0.1 m.

9.2 Fracture data analysis – Assumptions

The following assumptions have been made in the data compilation:

- Fracture sets can be categorised based on orientation using defined hard sectors.
- Fracture with dips ≥ 45° belong to subvertical sets. Fractures with dips < 45° are assigned to the subhorizontal set.
- The Terzaghi correction can be used to estimate fracture intensities unbiased by the direction of a borehole relative to individual fracture geometries. Having calculated unbiased or corrected linear fracture intensities, $P_{10,corr}$ [1/m], for individual boreholes, these can be combined pooling data from boreholes of varying geometries to estimate average areal fracture intensities, P_{32} [m^2/m^3].
- The maximum correction factor used in the Terzaghi correction process is 7, equivalent to a minimum angle of 8.2° between the borehole and the individual fracture plane.
- Stereonets are plotted as equal area lower hemisphere plots with stereographic density plots, all Terzaghi corrected.
- The PFL-f features identified in each borehole are comparable, i.e. have similar practicable measurement limits.
- The errors in interpreted fracture orientations and positions based on borehole image-logs (BIPS) in the Laxemar 2.3 data are small.
- The measurement process for recording length down the borehole for the occurrence of PFL-f features is sufficiently consistent with the measurement process for the image-logs (BIPS) such that the correlations of PFL flow difference logging with individual fractures are valid.
- Potentially water-bearing fractures are a subset of all fractures, and the PFL-f features are a subset of the potentially water-bearing fractures.

Terzaghi correction

As indicated above, measurements along a borehole (or scanline) are biased in that the closer the fractures are to being orthogonal to the borehole, the more readily the fractures are detected. Estimating the fracture intensity from the ratio of the number of fractures to the length of borehole therefore gives a biased estimate. The bias can be corrected by giving each fracture a weight, which depends on its orientation relative to the borehole (see Figure 9-2). The correction process is called Terzaghi weighting. Using measures of fracture intensity corrected in this way means that the intensities in boreholes with different orientation can be sensibly compared.

As indicated in Figure 9-2, the weight is given by cosec(α) where α is the angle between the fracture and the borehole. This correction is, in principle, unlimited. In order to avoid giving extremely large weight to fractures that are closely aligned with the borehole (bearing in mind that the measurement of the orientation of the fracture will be subject to experimental error) it is standard practice to limit the maximum value of the Terzaghi correction factor. For the analyses presented in this report the upper limit for the Terzaghi correction was set to be 7 (corresponding to an angle of about 8 degrees).

Identification of fractures associated with PFL-features

To help interpret the flow data measured by the PFL-f method, flowing features have been linked to particular fractures seen in the drill core and borehole image logs. The methodology followed is described in e.g. /Wikström et al. 2007a/. The methodology followed by Wikström and co-authors when assigning a fracture orientation to each PFL-f feature is summarised below.

For each PFL-f feature, the fracture or the crush zone most ‘consistent’ with the flowing feature is selected. The assumptions made by Wikström and co-authors when correlating the Boremap data to the PFL-f features were:

- As a first assumption, the open and partly-open fractures as well as crush zones are assumed to be **possible flowing features**. This is an important assumption on which all subsequent analysis relies. Alternative possibilities, which were not considered in this work, include the suggestion that fractures mapped as sealed could contain flow. For instance, fractures that are considered sealed when viewed from the Boremap data within the diameter of the borehole may have a conductive (flowing) section further away from the borehole.
- It is assumed that the **precision of the position** (L) in the borehole of the PFL-f feature is not on the 1 dm level. If an open, partly-open fracture or crush zone is within ±0.5 m of a PFL-f feature it is assumed that it could potentially correspond to the PFL-f feature (in a few cases larger differences have been accepted). However, the estimated maximum error of the positioning in the borehole is c. ±0.3 m and even less than that near length markers in the borehole, cf. Section 4.3.1). The nearest distance in decimetres from the fracture trace (a sinus-shape line) on the borehole wall to depth L is judged and documented in the database (called “PFL-anom. Confidence” in the data base). This distance is estimated in decimetres as the deviation of each potential open, partly-open fractures or crush zones from L, defined positive if the fracture is located below L.
- In a few cases no open fracture could be found within 0.6 m of the PFL-f feature (or the nearest open fracture is positioned closer than 0.6 m but matches another anomaly very well) but could be matched to a broken fracture interpreted by the core mapping team to be sealed. There is a possibility that the broken sealed fracture should have been mapped as a possible open fracture, and it can thus be interpreted as a flowing feature if no nearby options for open fractures are available. When interpreting these broken/sealed fractures, only those located ±0.1 m from the flowing feature have been mapped. These are fractures considered to be very uncertain and consequently “PFL-confidence” is set to zero (0) in the database for these cases.
- Occasionally, several **open fractures** are within ±0.2 m of L for the PFL-anomaly and it is judged that one or all of them may be flowing features. In a few cases, the mapped open fractures are so close (< 1 cm) that possibly one could consider them as being one fracture. In some cases where open fractures have been identified within ±0.2 m of L, there may be more open fractures at a distance ±0.2–0.5 m that are not included in the database as possible flowing features.

- In a few cases several PFL-f features may be connected to a single geological feature, generally a crush zone but sometimes also an steep open fracture, see next bullet.
- Some open, possibly flowing, fractures have very high amplitudes in the BIPS log, stretching over up to several meters of the borehole wall. These fractures can, because of their geometry, have an influence on the flow conditions over quite a long distance from the level indicated by the fractures' "secup"-value. When evaluating the data, these fractures are given a lower "PFL-confidence" than suggested only by the distance between the fractures secup and the level of the PFL-f feature. If the fracture cuts the level of the PFL-f feature, the PFL-confidence is set to unity (1, which is the highest confidence), irrespective of the distance between the secup value and the level of the flowing feature. In consequence, some fractures with high amplitudes that almost (±0.2 m) cut the PFL-f feature level are also included in the analysis. The PFL-confidence has been set to 2 in these cases.

Generally, there are only one or sometimes two possible fractures linked to a PFL-f feature (based on the critera used to couple mapped fractures to a PFL-f feature), but in a few cases there are 3–5 equally possible fractures within ±0.5 m of a PFL-f feature. Based on how visble the open fracture is in BIPS (Borehole Image Processing System), the open fracture characteristics as certain/probable/possible etc, one fracture is chosen as "Best Choice", cf, e.g. /Wikström et al. 2007c/ for details.

The orientation a PFL-f feature coupled to a fracture is based on the orientation of the fracture that is judged to be the most likely ("Best Choice") to be linked to the PFL-f feature. The orientation of a PFL-f feature coupled to a crush is based on the mean orientation (mean pole vector) of the upper and lower limits of the crush. If the PFL-f features belong to a MDZ , the modelled flowing feature representing the MDZ in the hydrogeological DFN has the MDZ interpreted orientation, cf. Sections 2.2 and 9.3.2.

9.3 Analysis of fracture data

In this section, statistical analyses of the attributes of the fractures in Laxemar are described. The Laxemar 2.3 data freeze includes data from 46 cored boreholes (including KLX01, KLX13A and KLX27A) including a variety of measurements in each borehole. In some boreholes, the fractures and their orientations were mapped over the entire length, or parts of the borehole. The fractures were classified (as either open, partly open, or sealed) and the level of confidence in this description was classified (as certain, probable or possible). Likewise, the Posiva Flow Log (PFL) measurements were carried out over the entrire length, or parts of the length of the borehole.

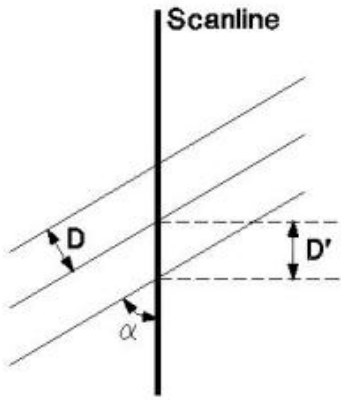

Figure 9-2. *α = minimum angle between plane and the borehole scanline, D' = apparent spacing along traverse, D = D' sin(α) = D' (1/W) = true spacing of discontinuity set, W = cosec(α) = weighting applied to individual pole before density calculation.*

Three boreholes were not included in the analysis. KLX01 had incomplete information and was excludced. After careful consideration, it was decided to also exclude data from borehole KLX13A from the analysis. The reason being that for the majority of its length it follows a trajectory in or very near deformation zone ZSMEW120A which dips to the south, parallel to ZSMEW002A, and hence does not usefully contribute to our understanding of the bedrock between deformation zones. KLX27A data, late incoming, were reserved for use in a validation study (see Section 10.5.5).

The statistics of the fracture attributes were analysed in various ways to try to discover possible patterns in the occurrence and nature of open, interconnected, flowing fractures. The analyses were undertaken for two different basic subdivisions of the rock: a subdivision on the basis of the Rock Domains /Wahlgren et al. 2008/ and a subdivision based on the geologically defined Fracture Domains /La Pointe et al. 2008, Wahlgren et al. 2008/. This was done in order to examine which approach to subdividing the rock would provide the best basis for describing the hydrogeology. The rock domains considered were RSMA01 (Ävrö Granite), RSMD01 (Quartz monzodiorite) and RSMM01 (mix of Ävrö quartzmonzodiorite and diorite gabbro) as shown in Figure 9-3, and the fracture domains considered were FSM_EW007, FSM_NE005, FSM_C, FSM_N, FSM_W and FSM_S shown in Figure 9-4, respectively.

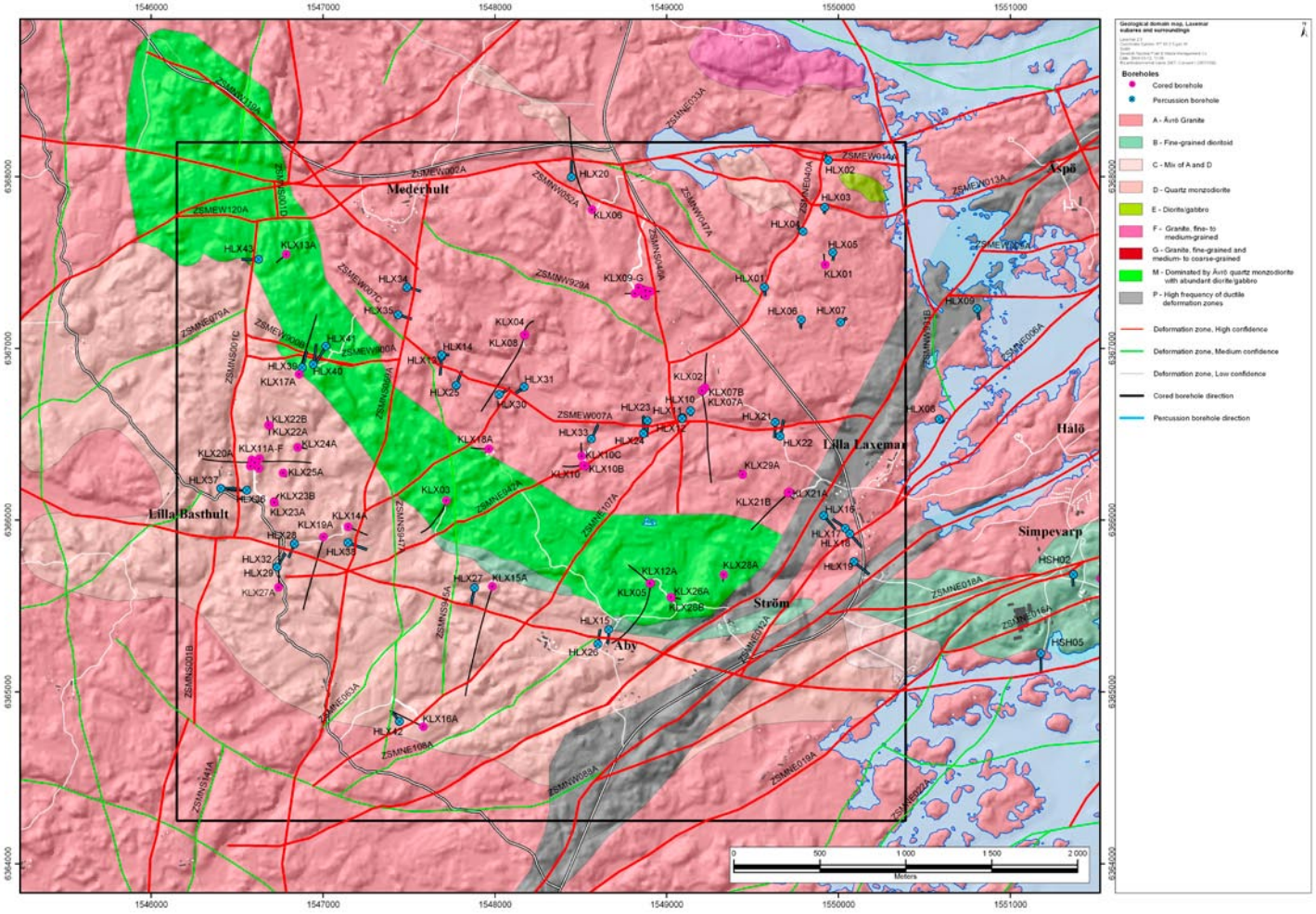

Figure 9-3. *The distribution of defined rock domains at the surface of the bedrock with cored and percussion drilled boreholes within the Laxemar subarea. Based on /Wahlgren et al. 2008/.*

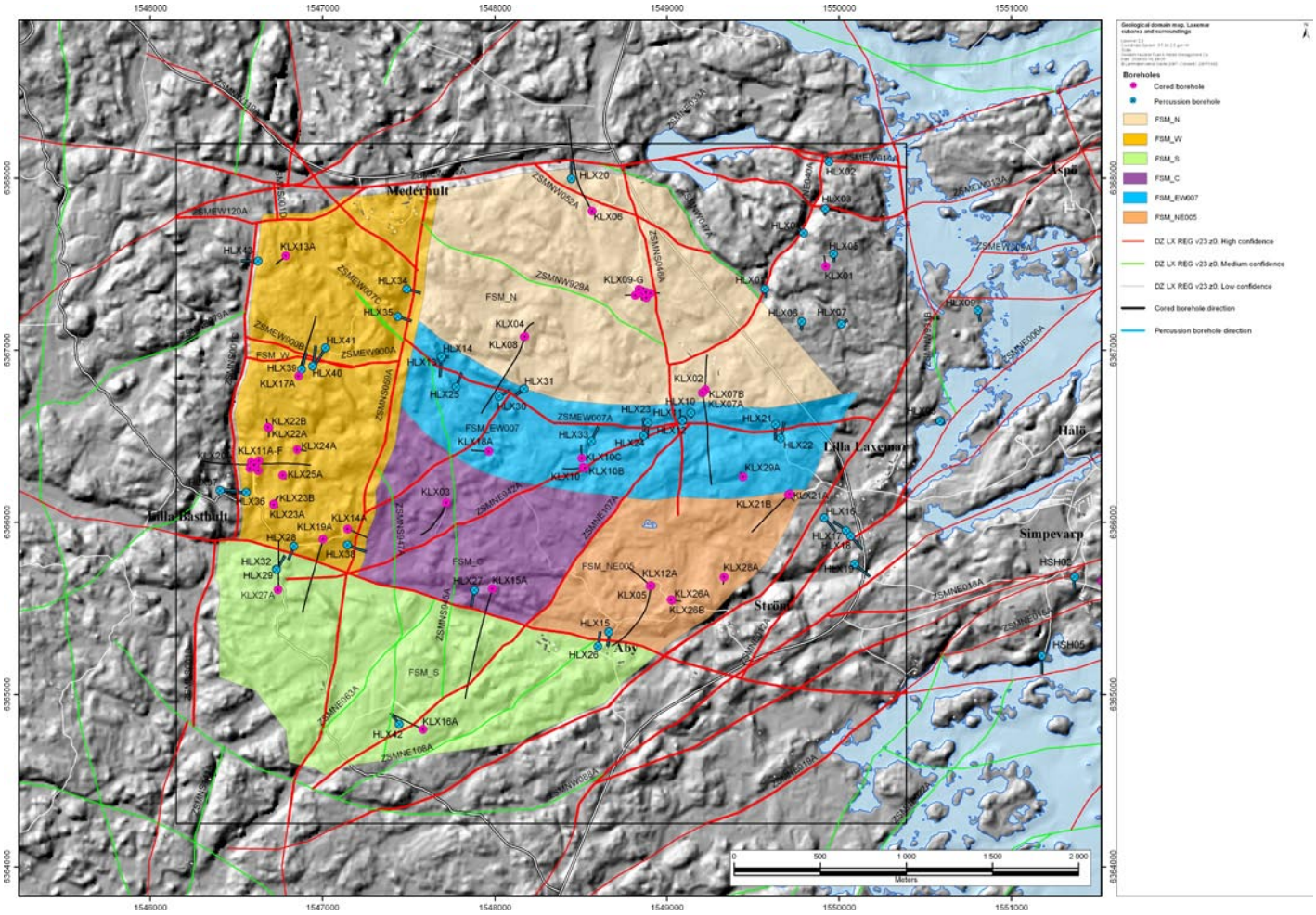

Figure 9-4. *The distribution of defined fracture domains at the surface of the bedrock with cored and percussion drilled boreholes within the Laxemar subarea. Based on /La Point et al. 2008/.*

In the analysis of borehole data, the intensities of various categories of fractures and of the PFL-f features were calculated, and compared. In general, there are slight differences between the mutual coverage of sections of each borehole mapped for fractures (boremap data) and over which PFL measurements were made. In most boreholes these sections are only up to about 20 m in length, but in KLX02 there is about 700 m at the bottom of the borehole where fracture mapping has not been carried out with the methodology applied in the site investigations. In order to ensure that the fracture and PFL intensities, respectively, were determined on a consistent basis, and therefore in order to be justifiably compared when looking for possible patterns, all intensities were calculated for those sections of boreholes that were both mapped for fractures and over which PFL-f/PFL-s measurements had been made. Such sections will hereafter be referred to as 'fully characterised' sections. For each borehole and each sub-division of the rock analysed, Table 9-1 gives the lengths of fully characterised boreholes sections excluding sections within interpreted regional deformation zones or local major deformation zones. In total this amounts to around 13 km of fracture logging of bedrock between deterministic deformation zones. NB. some parts of the boreholes are outside the fracture domains and hence there is a slightly lower total length for the fracture domains than rock domains.

Table 9-1. Account of fully characterised lengths (mapped for fractures and PFL-f features) for each borehole and each rock domain and fracture domains (excluding identified major zones).

	Fully characterised lengths (m)								
	FSM_ EW007	**FSM_ NE005**	**FSM_N**	**FSM_C**	**FSM_W**	**FSM_S**	**RSMA01**	**RSMD01**	**RSMM01**
KLX02	333	46					380		
KLX03				799				281	518
KLX04	281		346	149			776		
KLX05		879						514	365
KLX06			698				698		
KLX07A	439	32					471		
KLX07B	21		104				125		
KLX08	372		80	270			338	48	336
KLX09	292		402				694		
KLX09B			85				85		
KLX09C			102				102		
KLX09D			105				105		
KLX09E			71				71		
KLX09F			125				125		
KLX09G			43				43		
KLX10	124			509			497	12	124
KLX10B	23						23		
KLX10C	87						87		
KLX11A					832			832	
KLX11B					90			90	
KLX11C					110			110	
KLX11D					100			100	
KLX11E					111			111	
KLX11F					109			109	
KLX12A		495						69	426
KLX14A					100			100	
KLX15A				885				885	
KLX16A						231		231	
KLX17A					577				577
KLX18A	317			161			246		187
KLX19A					576			576	
KLX20A					159			159	
KLX21B		625					543	83	
KLX22A					81			81	
KLX22B					80			80	
KLX23A					75			75	
KLX23B					30			30	
KLX24A					75			75	
KLX25A					30			30	
KLX26A		79							79
KLX26B		28							28
KLX28A		42							42
KLX29A	47						47		
Total	**2,337**	**2,226**	**2,160**	**2,773**	**3,135**	**231**	**5,454**	**4,682**	**2,682**

The following analyses were carried out:

- an analysis to support the division of the fracture orientations into a number of fracture sets (fracture orientation analysis were also in parallel performed by geology and the comparison with the sets defined by geology is commented later in this section),
- an analysis of the fracture intensities for various categories of fractures,
- an analysis of the fracture intensities for the identified fracture sets for various categories of fractures,
- an analysis of the variation of fracture intensity with depth for various categories of fractures,
- an analysis of the variation of fracture intensity with fracture set and depth for various categories of fractures,
- an analysis of the fracture intensities for the local minor deformation zones and crush zones,
- a comparison of the result of two types of transmissivity measurement in boreholes,
- an analysis of the overall statistics of measured *in situ* transmissivity.

These analyses are described in the following. For clarity, the results of the analyses are mainly presented pictorially in the body of this report. Supplementary results are given in Appendix 5. In the plots of fracture intensity presented in Sections 9.3.2 through 9.3.5, indicative error bars are shown to give an idea of the statistical errors. The error bars correspond to 2 standard deviations on either side of the central value, and were determined on the basis that the data correspond to samples from a simple Poisson distribution (i.e. a distribution without clustering) and that the fracture orientations are uniformly distributed. In fact, as will be seen, the fracture orientations are indeed clustered. However, error bars calculated on the basis of the actual distributions of orientation differ by less than 5% from those shown. Details are given in Appendix 5, Section A.5.2.

9.3.1 Fracture orientation

Stereonet plots showing the orientation of the fractures for each fracture domain (see Figure 9-5 to Figure 9-10) were made to guide the definition of appropriate fracture sets and understand any clustering of fractures around particular orientations (Similar analysis of the rock domains is shown in Appendix 5). By definition, the fracture domains exclude sections of borehole inside interpreted deterministic deformation zones. The plots are Terzaghi-corrected density plots using equal-area lower-hemisphere projection. Concentration plots are used rather than simple pole plots to identify clustering around particular orientations. The concentration plotted at a point is a relative concentration equal to the percentage of the number of poles in 1% of the area of the hemisphere around the point. For each fracture domain density plots are shown for:

- all fractures (sealed + open + partly open fractures),
- fractures that are open or partly-open with either certain or probable confidence (which will hereafter be referred to as OPO-CP fractures),
- fractures associated with PFL-f features.

An additional pole plot is added showing the orientations of PFL associated fractures with the pole coloured according to interpreted transmissivity. Stereonets for FSM_EW007, FSM_NE005, FSM_N, FSM_C, FSM_W and FSM_S are shown in Figure 9-5 to Figure 9-10. Stereonets for rock domains RSMA01, RSMD01, and RSMM01 are shown in Appendix 5, Section A.5.1. A plot of the combined hydraulic rock domain HRD_C, cf. Section 9.3.6, is shown in Figure 9-11.

As can be seen, the fracture orientations are not uniformly distributed, but clustered around particular orientations. After inspection of all the plots, it was deemed that the fractures for every subdivision could be classified in terms of four principal fracture sets:

- a set striking roughly North-South,
- a set striking roughly ENE,
- a set striking roughly WNW,
- a sub-horizontal (SH) set.

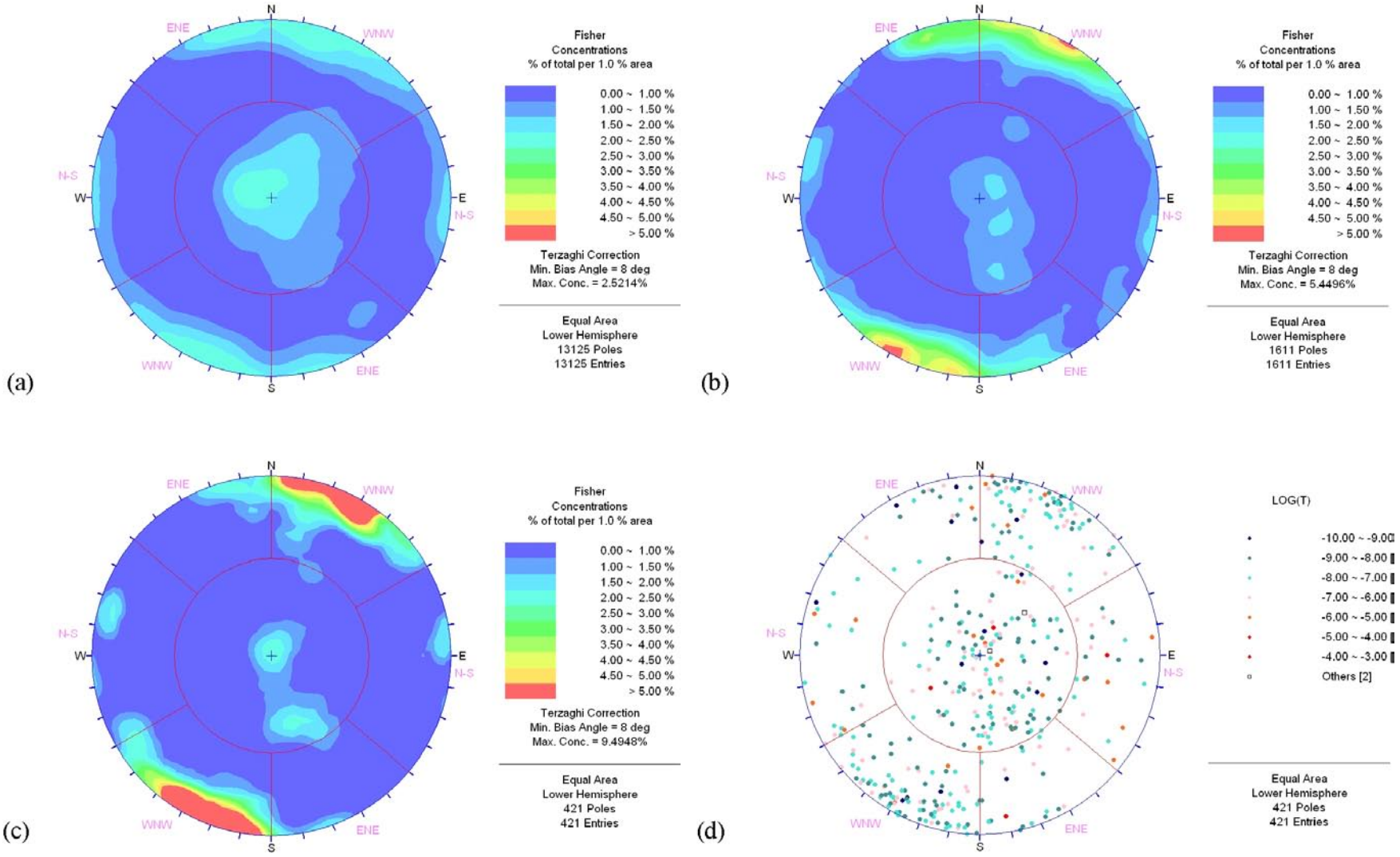

Figure 9-5. *Stereonets for FSM_EW007: (a), (b),(c) Terzaghi-corrected intensity for all fractures, OPO-CP fractures and PFL-f features. (d) poles for PFL-f features (coloured by transmissivity).*

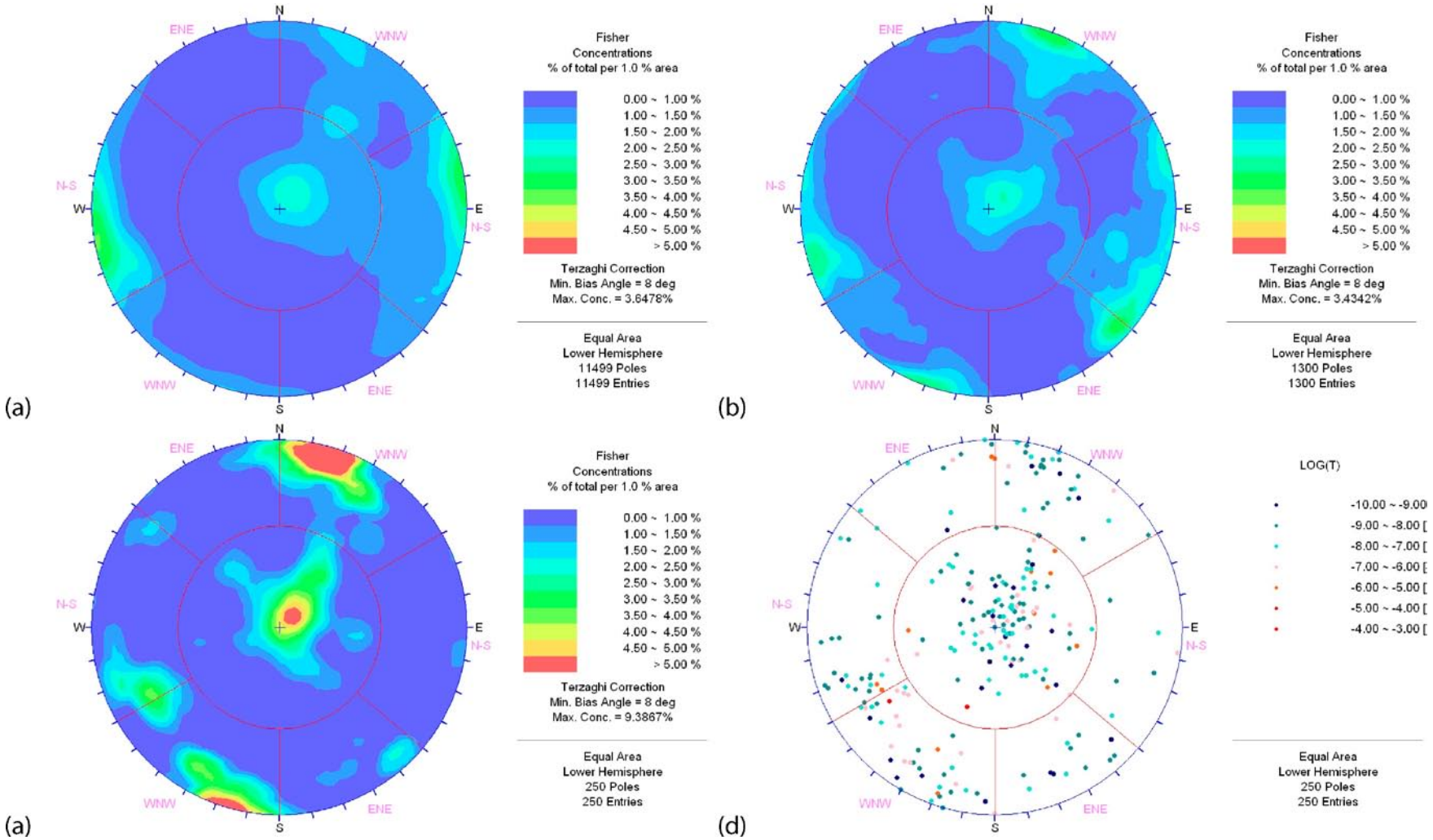

Figure 9-6. *Stereonets for FSM_NE005: (a), (b),(c) Terzaghi-corrected intensity for all fractures, OPO-CP fractures and PFL-f features. (d) poles for PFL-f features (coloured by transmissivity).*

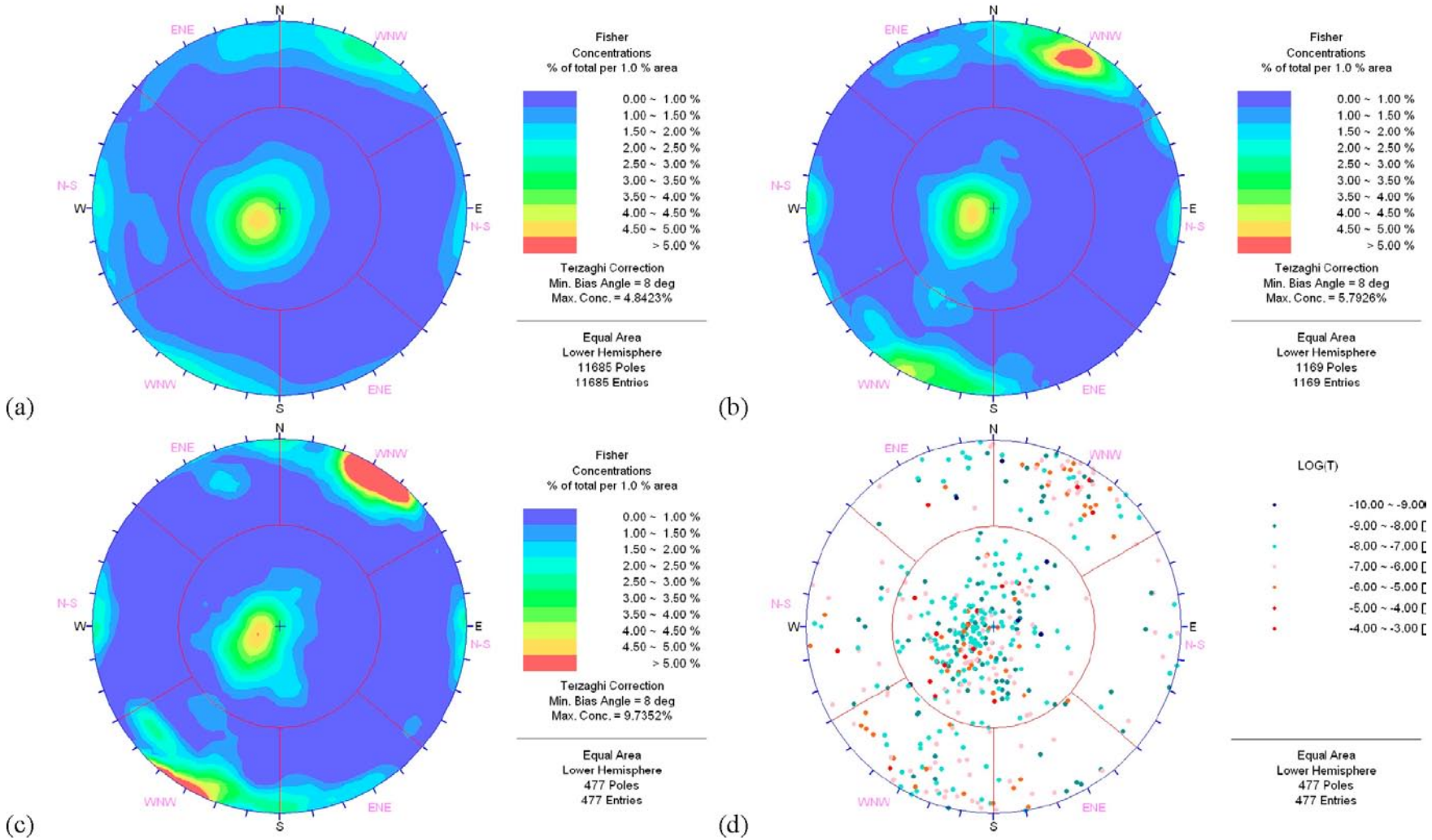

Figure 9-7. *Stereonets for FSM_N: (a), (b),(c) Terzaghi-corrected intensity for all fractures, OPO-CP fractures and PFL-f features. (d) poles for PFL-f features (coloured by transmissivity).*

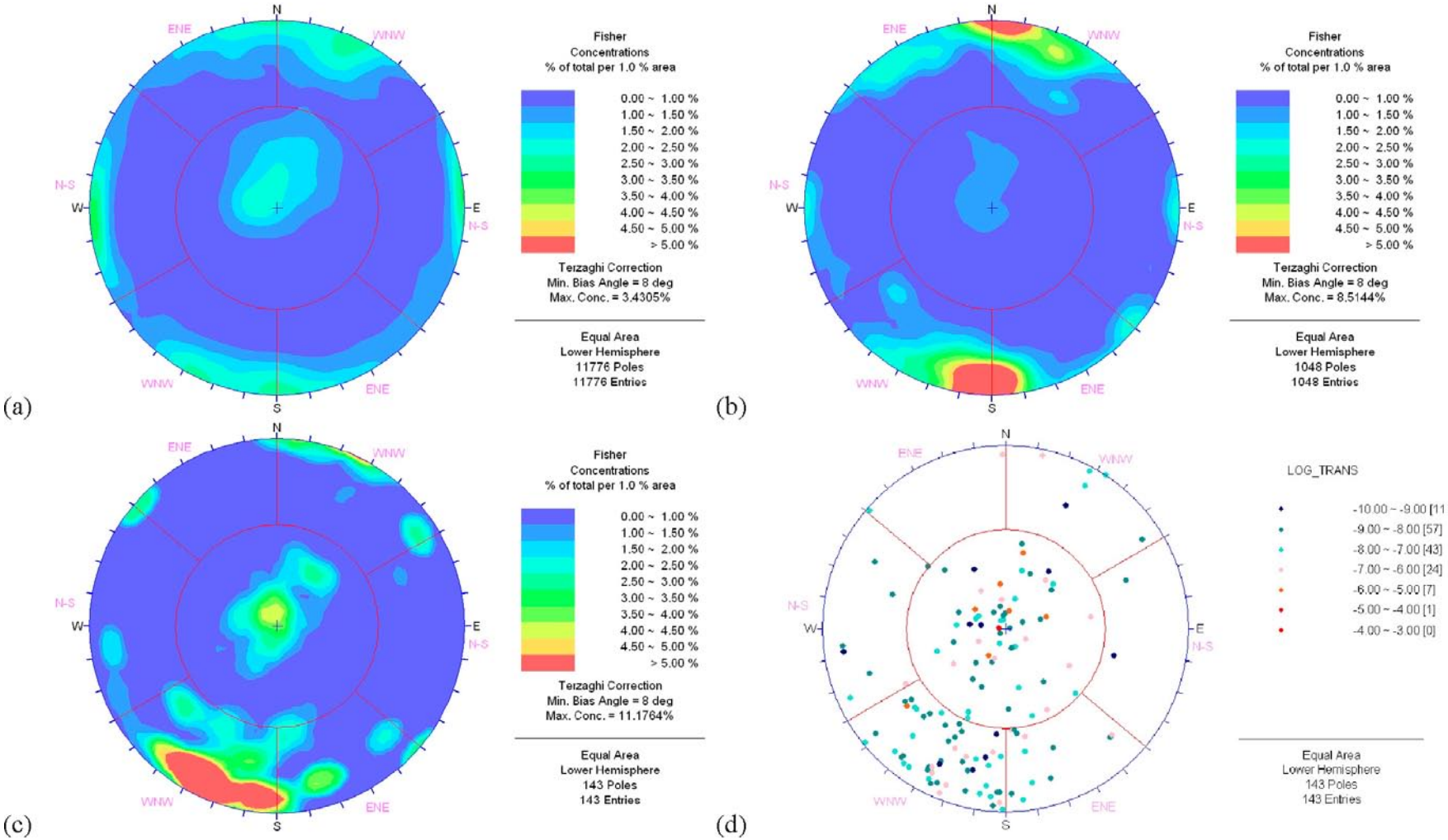

Figure 9-8. *Stereonets for FSM_C: (a), (b),(c) Terzaghi-corrected intensity for all fractures, OPO-CP fractures and PFL-f features. (d) poles for PFL-f features (coloured by transmissivity).*

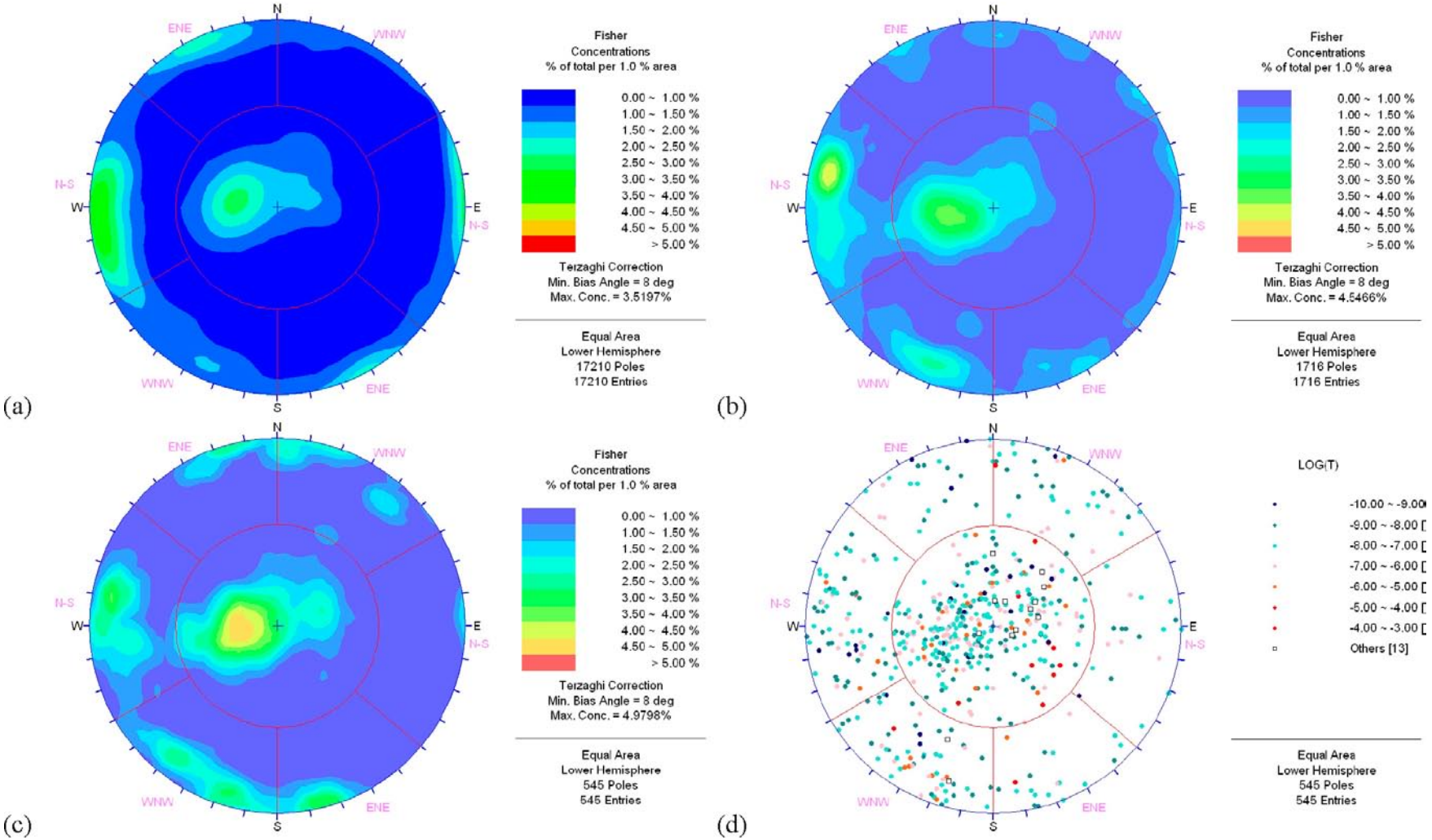

Figure 9-9. *Stereonets for FSM_W: (a), (b),(c) Terzaghi-corrected intensity for all fractures, OPO-CP fractures and PFL-f features. (d) poles for PFL-f features (coloured by transmissivity).*

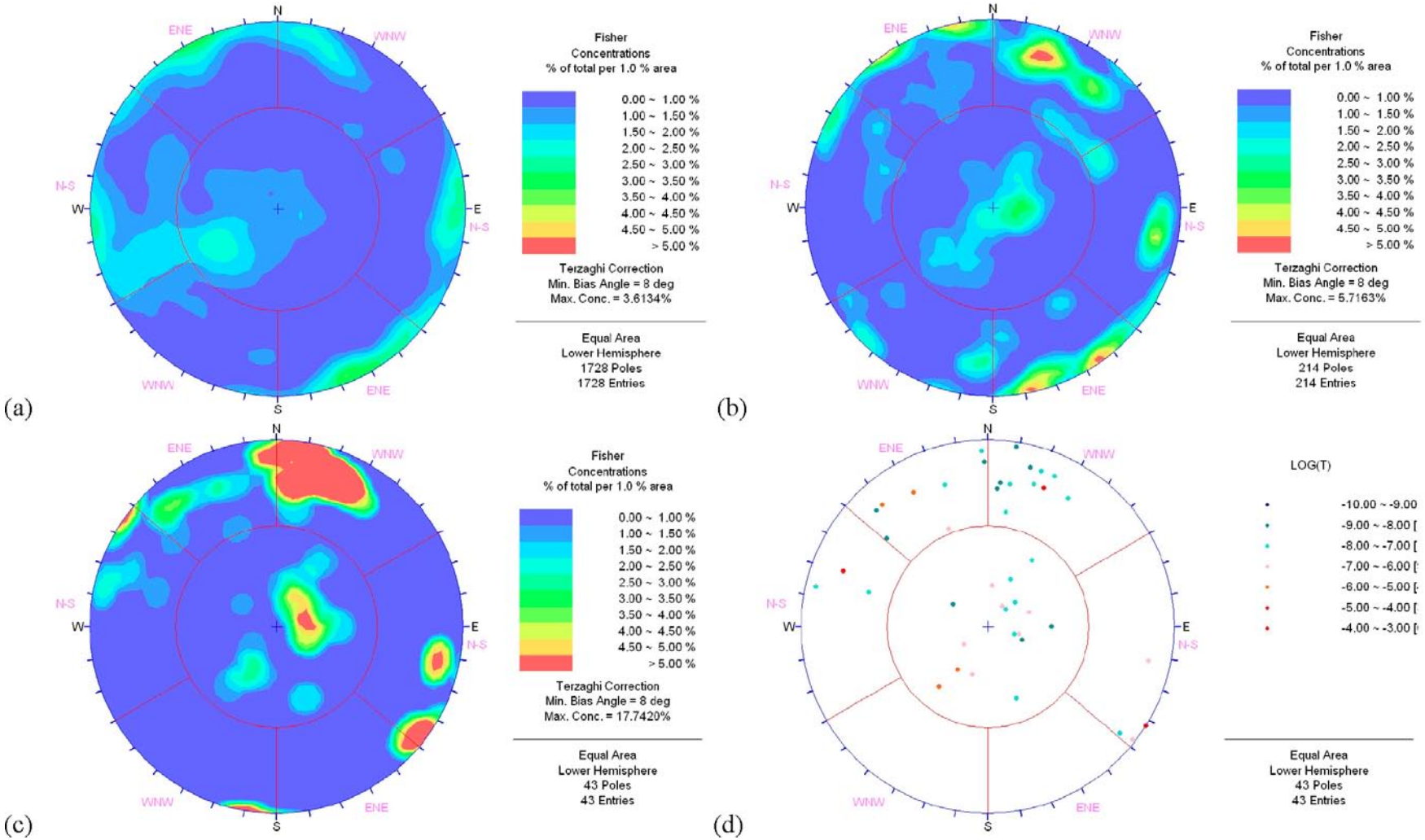

Figure 9-10. *Stereonets for FSM_S: (a), (b),(c) Terzaghi-corrected intensity for all fractures, OPO-CP fractures and PFL-f features. (d) poles for PFL-f features (coloured by transmissivity).*

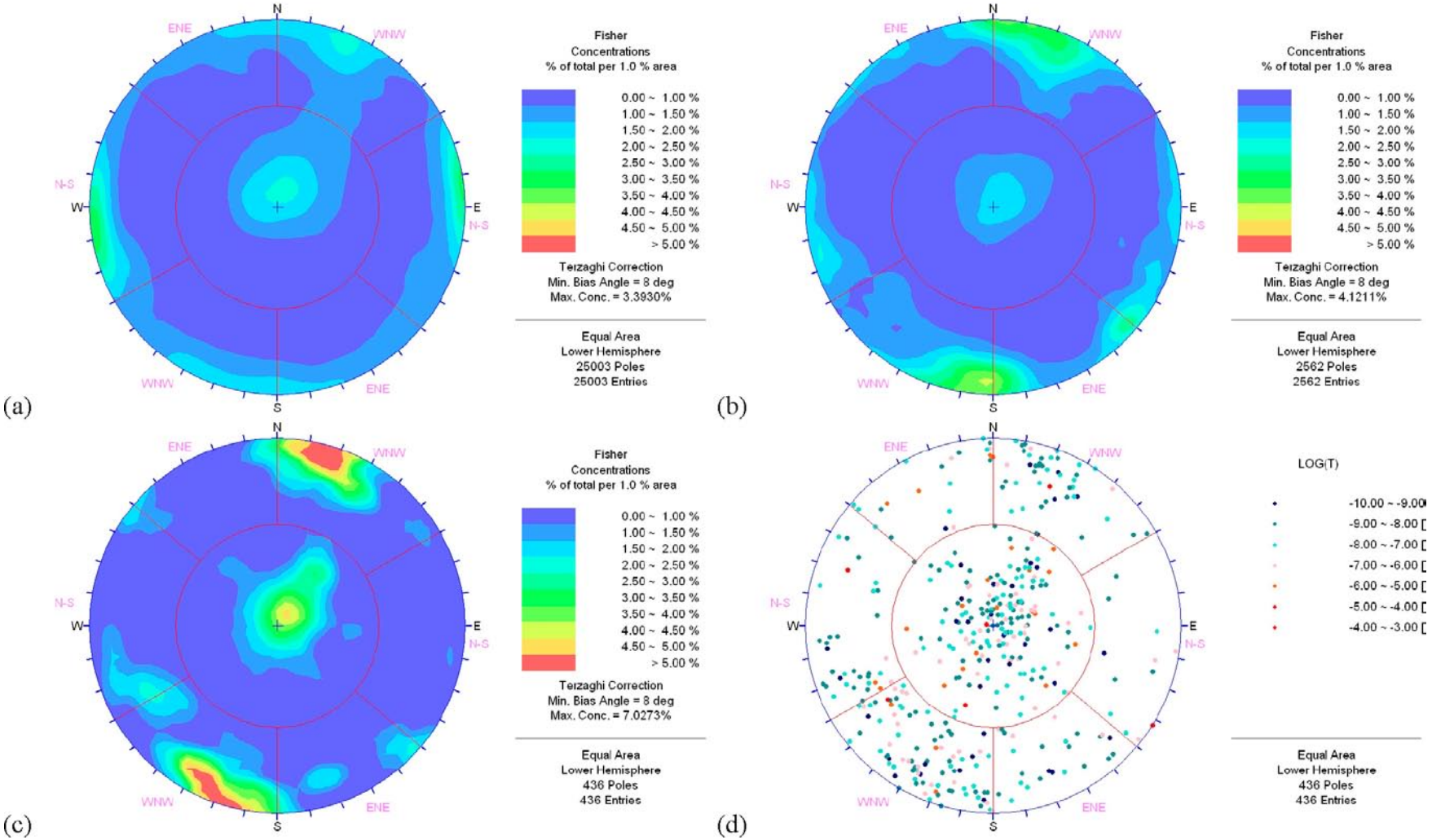

Figure 9-11. *Stereonets for HRD_C: (a), (b),(c) Terzaghi-corrected intensity for all fractures, OPO-CP fractures and PFL-f features. (d) poles for PFL-f features (coloured by transmissivity).*

The boundaries between the different sets are not precise and vary slightly between different subdivisions of the rock. However, in order to evaluate and analyse the fracture intensities for the orientations, simplified prescriptions of the intervals of strike and dip corresponding to each fracture set were made (the same for each subdivision). These so-called hard-sector set definitions are given in Table 9-2. The boundaries between the hard sectors sets are marked on the plots.

As an initial guide for this choice of hard sectors, the Laxemar 1.2 geological DFN model /Hermanson et al. 2005/ was used, being based on an analysis of Laxemar 1.2 outcrop data. Appropriate modifications were then made primarily considering the OPO-CP and PFL-f feature fractures, although some consideration was also given to stereonets based on Laxemar 2.3 outcrop data.

Although this fracture set definition was essentially done independently from Geology's assessment of the Laxemar 2.3 data, the corresponding definitions made in the geological DFN modelling /La Pointe et al. 2008/ are very similar to the fracture sets given here.

There is a strong consistent theme for most of the bedrock subdivisions that the dominant set for OPO-CP fractures and PFL-f features is the WNW set, and with SH usually as the secondary set. However, for FSM_W, the dominant set for OPO-CP fractures is the N-S set and the dominant set for PFL-f features is the SH set; and for FSM_N, the SH set also gives a major contribution for PFL-f features. For the rock domains, SH is dominant for RSMD01, and N-S is important in RSMM01.

It should be noted that some of the differences in orientations between the bedrock subdivisions may not necessarily be due to lateral trends, but rather may be a consequence of a dependence upon some other aspect of the system, such as depth, which is being sampled differently for the different rock subdivisions by the available boreholes. It should also be noted that there are very few measurements from fracture domain FSM_S, so the statistical errors for this rock subdivision are likely to be large.

9.3.2 Fracture intensity

Fracture intensity was quantified in terms of the Terzaghi corrected linear intensity along boreholes, $P_{10,corr}$, treating them as a scanline (the number of open fractures partly penetrating the borehole diameter being small). In order to derive an appropriate spatial model of fracture occurrence, particularly those potentially contributing to flow, fracture intensity was analysed in various ways. Possible correlations were considered between:

- fracture intensity and position (indicated by borehole location),
- fracture intensity and depth,
- fracture intensity and fracture set.

The analyses were carried out for various subdivisions of the bedrock (into Fracture Domains (FSM), Rock Domains (RSM) and ultimately Hydraulic Rock Domains (HRD)).

Table 9-2. Hard sector definitions of fracture sets.

Identification	Trend	Plunge	Dip	Strike
N-S	240–310	0–45	45–90	0–40
	60–130			150–220
				330–360
ENE	310–360	0–45	45–90	40–90
	130–180			220–270
WNW	0–60	0–45	45–90	90–150
	180–240			270–330
SH	0–360	45–90	0–45	0–360

Underlying the analyses is the view that flow can only take place through the fractures which contain some void space (i.e. not entirely sealed) and which connect with other such fractures to form continuous open channels that make up a network of connected open fractures. It is assumed that the intensity of potential water-conducting fractures can be estimated from the fractures that are identified as open or partly-open in the borehole core- and image-logs. Fractures are recorded as being open with a varying degree of confidence (certain, probable or possible), and so there is an uncertainty in defining the sub-group of potential water-conducting fractures. For the Forsmark hydrogeological DFN /Follin et al. 2007b/, fractures associated with PFL-f features predominantly belonged to the sub-group of open fractures that had either certain or probable confidence (OPO-CP fractures), and hence the fractures considered by the Forsmark hydrogeological DFN modelling was restricted to OPO-CP fractures as the assumed sub-group of potential water-conducting fractures. An appropriate restriction of open fractures for the Laxemar hydrogeological DFN is assessed in Section 9.3.3. The implications for restricting the fractures considered as part of the hydrogeological DFN are quantified in Table 9-3 through Table 9-8 by summarising the number of fractures in different fracture categories for the boreholes associated with each fracture domain. The categories used are:

- all fractures,
- open or partly open fractures (OPO),
- open or partly-open fractures with certain or probable confidence (OPO-CP),
- open or partly open fractures with certain confidence (OPO-C),
- PFL-f features,
- the number of interpreted local minor deformation zones (MDZ).

Note: in the case of the minor deformation zones (MDZ), any fractures that fall within the interpreted extent of the zone in the borehole are grouped together and counted as one single fracture with an appropriate orientation interpreted from several sources, see /Hermanson et al. 2008, cf. Appendix 3 therein/, and the transmissivities are summed over the individual PFL-f features within the zone, if any, and attributed to the single fracture in question (cf. Chapter 2). These tables combine the information for all the rock subdivisions irrespective of whether the fractures are associated with fully characterised sections of borehole or not, but excluding the identified deterministic deformation zones. Corresponding tables for the rock domains are presented in Appendix 5, Section A.5.1.

Table 9-3. Numbers of fractures in each category for each borehole for the fully characterised sections of fracture domain FSM_EW007, excluding interpreted deterministic deformation zones.

	Number					
	All	OPO	OPO-CP	OPO-C	PFL	MDZ
KLX02	560	327	205	205	54	3
KLX04	1,425	382	77	28	25	3
KLX07A	3,342	724	509	49	108	8
KLX07B	180	22	10		5	
KLX08	1,880	587	199	74	36	3
KLX09	1,756	436	171	14		8
KLX10	922	349	100	46	40	1
KLX10B	197	74	49	12	17	1
KLX10C	676	161	53	16	16	4
KLX18A	1,873	626	200	32	97	5
KLX29A	311	118	79	25	22	2
Total	**13,122**	**3,806**	**1,652**	**501**	**420**	**38**

Table 9-4. Numbers of fractures in each category for each borehole for the fully characterised sections of fracture domain FSM_NE005, excluding interpreted deterministic deformation zones.

	Number					
	All	OPO	OPO-CP	OPO-C	PFL	MDZ
KLX02	230	170	140	140	2	1
KLX05	3,372	296	212	41	71	12
KLX07A	275	110	21	1	3	
KLX12A	2,838	1,088	413	64	75	12
KLX21B	3,746	829	354	86	37	10
KLX26A	543	249	122	18	22	3
KLX26B	220	167	26	10	17	
KLX28A	269	106	55	2	23	1
Total	**11,493**	**3,015**	**1,343**	**362**	**250**	**39**

Table 9-5. Numbers of fractures in each category for each borehole for the fully characterised sections of fracture domain FSM_N, excluding interpreted deterministic deformation zones.

	Number					
	All	OPO	OPO-CP	OPO-C	PFL	MDZ
KLX04	2,258	670	90	44	70	12
KLX06	3,458	535	350	70	81	2
KLX07B	484	206	86	31	54	2
KLX08	560	264	137	95	48	1
KLX09	1,498	477	215	43	49	9
KLX09B	475	144	39	3	41	2
KLX09C	613	188	73	16	32	2
KLX09D	624	207	65	32	32	2
KLX09E	582	150	37	11	21	1
KLX09F	735	197	80	30	32	4
KLX09G	395	79	34	2	14	
Total	**11,682**	**3,117**	**1,206**	**377**	**474**	**37**

Table 9-6. Numbers of fractures in each category for each borehole for the fully characterised sections of fracture domain FSM_C, excluding interpreted deterministic deformation zones.

	Number					
	All	OPO	OPO-CP	OPO-C	PFL	MDZ
KLX03	3,418	419	95	22	40	7
KLX04	408	87	9	2		
KLX08	841	282	80	27	2	1
KLX10	2,159	535	146	11	7	
KLX15A	4,343	1,327	690	136	62	18
KLX18A	603	176	56	10	32	2
Total	**11,772**	**2,826**	**1,076**	**208**	**143**	**28**

Table 9-7. Numbers of fractures in each category for each borehole for the fully characterised sections of fracture domain FSM_W, excluding interpreted deterministic deformation zones.

	Number					
	All	OPO	OPO-CP	OPO-C	PFL	MDZ
KLX11A	4,259	627	229	36	44	16
KLX11B	351	124	33	5	36	2
KLX11C	433	125	38	8	41	
KLX11D	481	135	64	20	43	3
KLX11E	449	133	29	11	25	4
KLX11F	347	95	25	9	22	1
KLX14A	712	276	150	25	33	4
KLX17A	3,499	666	280	43	27	8
KLX19A	1,427	318	109	22	30	5
KLX20A	603	138	41	2		2
KLX22A	586	216	69	17	43	1
KLX22B	520	177	39	5	28	1
KLX23A	139	41	25	7	17	
KLX23B	34	15	4	1	4	
KLX24A	619	254	86	22	37	4
KLX25A	199	57	15	6	6	1
Total	**14,658**	**3,397**	**1,236**	**239**	**436**	**52**

Table 9-8. Numbers of fractures in each category for each borehole for the fully characterised sections of fracture domain FSM_S, excluding interpreted deterministic deformation zones.

	Number					
	All	OPO	OPO-CP	OPO-C	PFL	MDZ
KLX16A	1,725	473	223	65	41	9
Total	**1,725**	**473**	**223**	**65**	**41**	**9**

Overall fracture intensities

Taken overall, the Terzaghi-corrected fracture intensities are generally of order 2 to 3 times the uncorrected fracture intensities.

For an overview of the relative intensities of the different categories of fractures and the variability between boreholes within the same fracture domain, Figure 9-12 and Figure 9-17 present comparisons of the Terzaghi-corrected fracture intensities for each fracture domain. Equivalent plots for the rock domains are included in Appendix 5, Section A.5.1. Error bars are included to give an indication of the statistical uncertainty associated with the sample size (see Appendix 5, Section A.5.2).

It can be seen that the Terzaghi-corrected fracture intensities for all fractures are generally of order times the intensities for OPO fractures, which are generally of order 2 times the intensity of OPO-CP fractures, which are generally of order 2 times the intensity of OPO-C fractures, which have similar or slightly larger intensity to the PFL-features. The ratios vary somewhat from borehole to borehole. Overall, the Terzaghi-corrected fracture intensity for all fractures is about 10 m^{-1}, the Terzaghi-corrected fracture intensity for OPO fractures is about 2.5 m^{-1} and the Terzaghi-corrected fracture intensity for PFL-f features is about 0.5 m^{-1}. Notably, these averages are fairly consistent across all the fracture domains, and so there does not appear to be strong general spatial trends between the different fracture domains. Equally, there are no major variations between the rock domains.

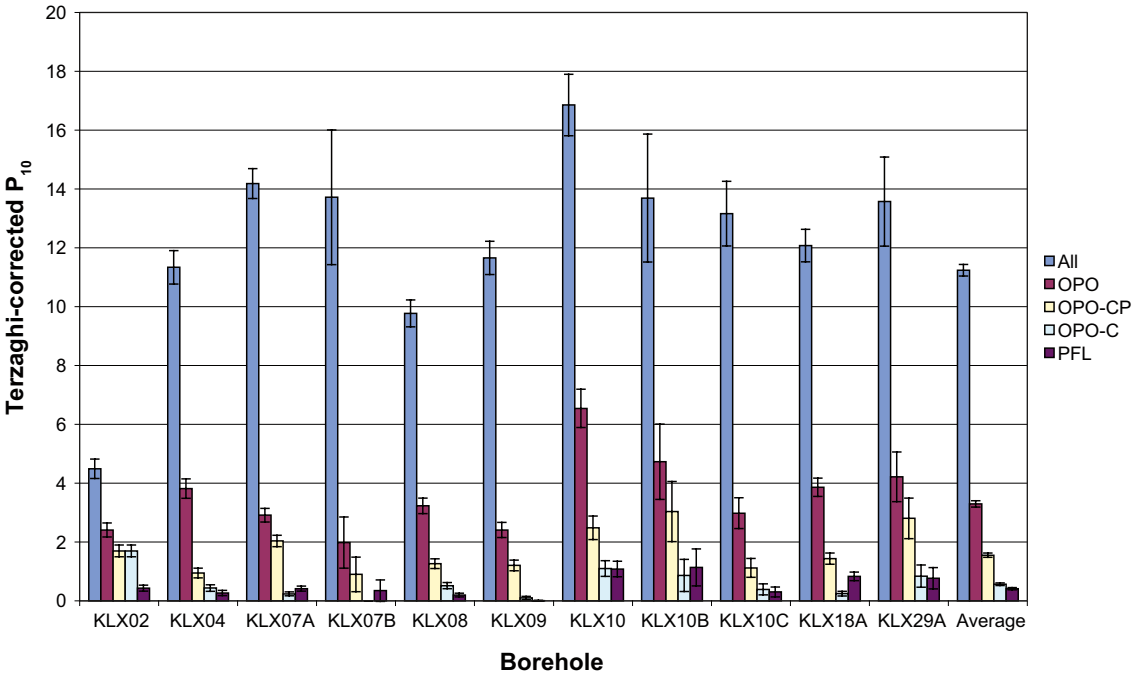

Figure 9-12. *Comparison of the Terzaghi-corrected fracture intensities for the different categories for fully characterised sections of boreholes penetrating fracture domain FSM_EW007.*

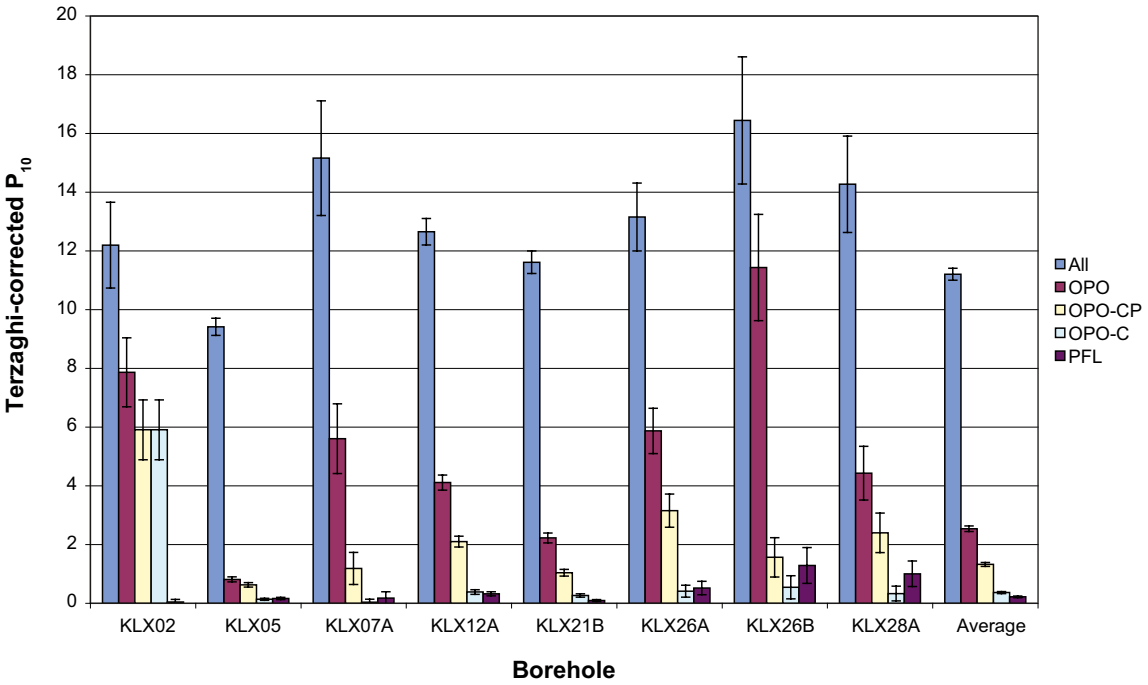

Figure 9-13. *Comparison of the Terzaghi-corrected fracture intensities for the different categories for fully characterised sections of boreholes penetrating fracture domain FSM_NE005.*

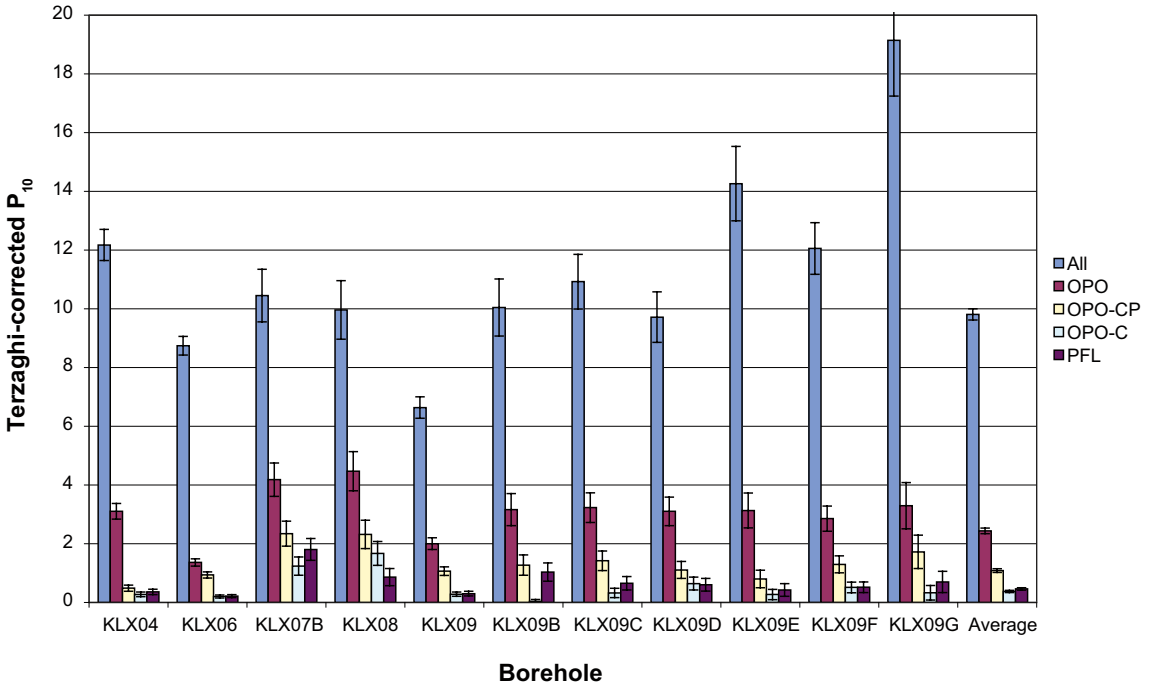

Figure 9-14. *Comparison of the Terzaghi-corrected fracture intensities for the different categories for fully characterised sections of boreholes penetrating fracture domain FSM_N.*

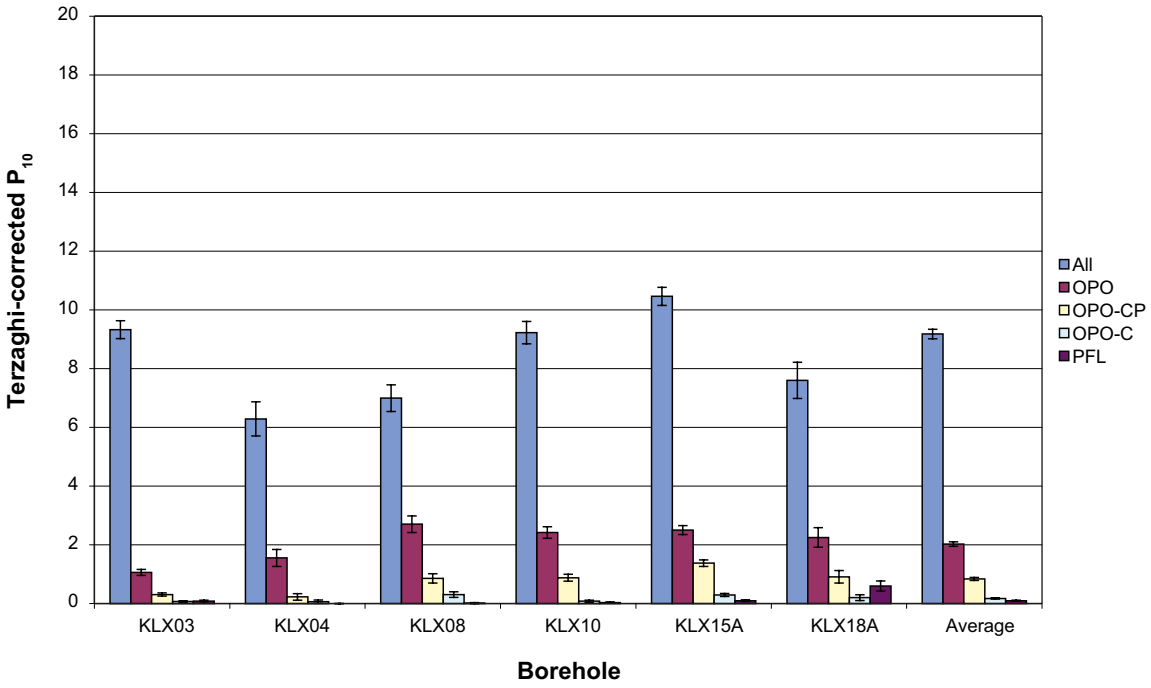

Figure 9-15. *Comparison of the Terzaghi-corrected fracture intensities for the different categories for fully characterised sections of boreholes penetrating fracture domain FSM_C.*

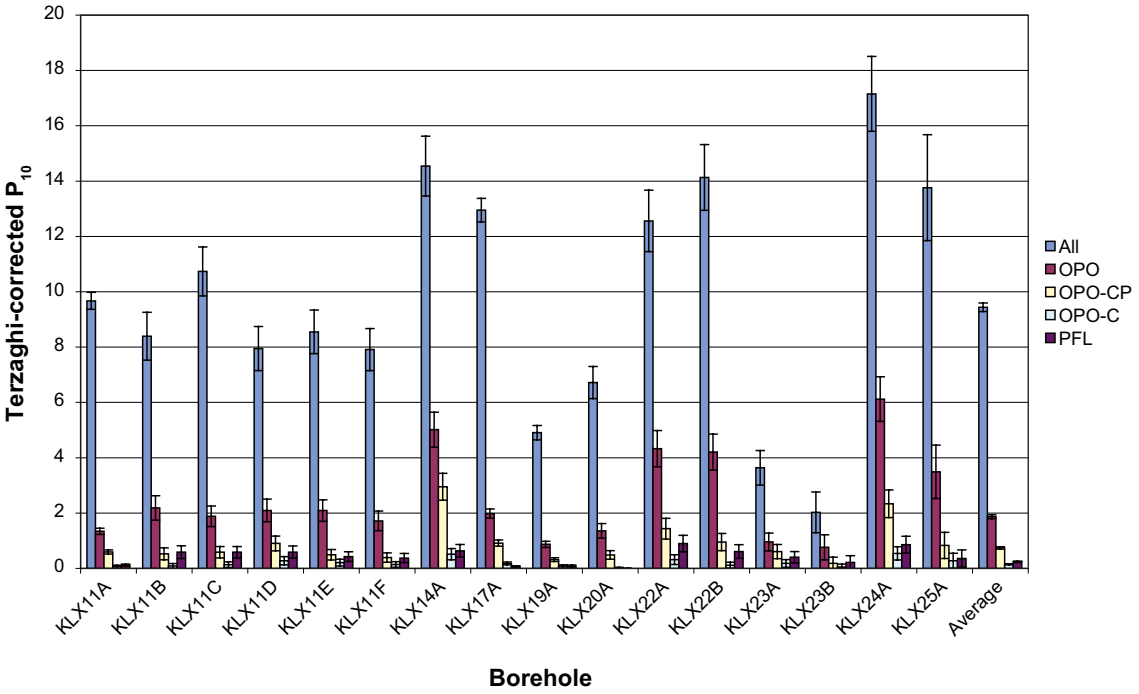

Figure 9-16. *Comparison of the Terzaghi-corrected fracture intensities for the different categories for fully characterised sections of boreholes penetrating fracture domain FSM_W.*

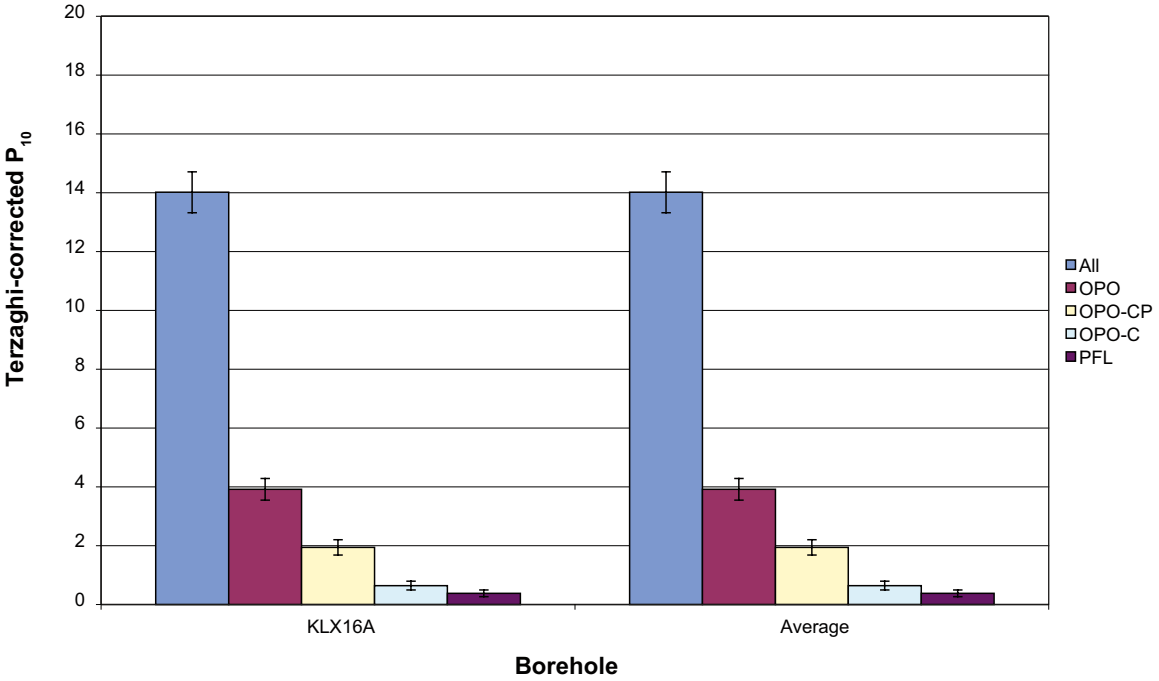

Figure 9-17. *Comparison of the Terzaghi-corrected fracture intensities for the different categories for fully characterised sections of boreholes penetrating fracture domain FSM_S.*

9.3.3 Correlation of geological fractures and hydrogeological flowing features

As discussed at the beginning of Section 9.3.2, it is important to decide on an appropriate restriction of the characterised fractures which are potentially water-conducting fractures that can be used as the basis for the hydrogeological DFN model development. The reasons for being interested in making this distinction between the subset of fractures that only have a potential to carry flow, and the smaller subset that actually have flows that can be detected by the PFL method, are to address safety assessment issues such as characterising potential flows below the resolution of the PFL method and in assessing the enhancement of hydraulic connectivity by construction of the repository, i.e. connecting fractures that were hitherto isolated from network of water-conducting fractures. It is assumed that the intensity of all open fractures (OPO) provides an upper limit for the intensity of potential water conducting fractures. The question is whether the geological classification of open fractures based on confidence can be used to further restrict the subset of hydrogeologically significant fractures.

In order to assess the restriction of fractures considered in the hydrogeological DFN, Table 9-9 gives the percentages of flowing fractures identified by the PFL method that fall within the different confidence indicators of open or partly-open fractures. The results show that almost all the flowing features detected by PFL correspond to open or partly-open fractures. The results also show that the flowing features detected by PFL do not just correspond to the fractures that have been classified as open or partly-open with certain confidence, but those fractures that have been classified as open or partly-open with probable confidence also need to be taken into account. Indeed, there is an indication that perhaps some fractures that have been classified as open or partly-open with possible confidence in some boreholes might also need to be taken into account. This may reflect differences in the ways in which the levels of confidence have been ascribed for different boreholes, which have been investigated at different stages in the site characterisation programme, and by different personnel. Table 9-9 suggests that a restriction to OPO-CP fractures cannot be justified for the majority of boreholes and hence the hydrogeological DFN model should be based on all OPO fractures, with OPO-CP fractures being considered as a variant.

In conclusion, for the purposes of the modelling, a realistic estimate of potentially water-conducting fractures can be made on the basis of the subset of OPO fractures, although the correspondence between geological characterisation of the core and hydraulic testing is sufficiently erratic to justify an alternative scenario where only OPO-CP fractures are potentially water-conducting, serving as an uncertainty analysis.

9.3.4 Fracture intensities by depth

In order to investigate a possible depth dependency, Terzaghi corrected fracture intensities were calculated for consecutive 50 m vertical sections according to elevation relative to sea-level. 50 m was used to give a reasonable level of resolution without being reduced to such small samples that trends could not be identified due to a lack of statistical significance. Figure 9-18 through Figure 9-26 show the variation of fracture intensity for OPO fractures and PFL-f features for each fracture domain. In general, there is a slight decrease with depth in the intensity of OPO fractures. Only in fracture domains FSM_W and FSM_N is there a clear and significant decrease in OPO fractures with depth. In Figure 9-20 the anomalous looking values at elevations between –900 to –1,000 masl in fracture domain FSM_NE005 come from a relatively short interval in one borehole (KLX02) and may be associated with the margins of an interpreted thick regional deformation zone (ZSMNW928A) that extends from –747 to –936 masl, while 2 PFL-f features occur at –955 and –958 masl. Similarly, there is little variation in the intensity of all fractures with depth.

For PFL-f features there is a marked decrease in the intensity with depth for all rock subdivisions. Intensity is greatest at elevations above –150 to –200 masl and significantly lower below about –650 masl. Between –150 and –650 masl there is a less pronouced decrease with depth. For all the fracture categories, there is significant variability in the fracture intensity. The anomalous looking value in fracture domain FSM_W at depths of –350 to –400 masl comes from one borehole (namely KLX11A – where a cluster of 7 PFL-f features are found at –392 to –393 masl), and may be associated with a conductive zone. Similar plots are given in Appendix 5, Section A.5.1 for the rock domains.

Table 9-9. Fractions of the flowing features detected by PFL that are classified as OPO, OPO-C and OPO-CP. (Crush zones are not included and that is the main reason for why OPO fractures do not include all PFL-f features.)

Borehole	OPO	OPO-CP	OPO-C
KLX02	0.92	0.78	0.78
KLX03	0.94	0.42	0.21
KLX04	0.97	0.44	0.25
KLX05	0.67	0.48	0.14
KLX06	0.97	0.86	0.32
KLX07A	0.98	0.91	0.30
KLX07B	1.00	0.70	0.30
KLX08	0.99	0.85	0.73
KLX09	0.98	0.86	0.47
KLX09B	0.98	0.52	0.07
KLX09C	1.00	0.83	0.39
KLX09D	1.00	0.56	0.34
KLX09E	1.00	0.65	0.26
KLX09F	1.00	0.81	0.42
KLX09G	1.00	0.76	0.21
KLX10	0.97	0.68	0.53
KLX10B	1.00	0.83	0.46
KLX10C	1.00	0.38	0.13
KLX11A	1.00	0.79	0.44
KLX11B	1.00	0.49	0.08
KLX11C	0.98	0.49	0.15
KLX11D	0.98	0.71	0.27
KLX11E	1.00	0.59	0.30
KLX11F	1.00	0.33	0.24
KLX12A	1.00	0.79	0.37
KLX14A	1.00	0.92	0.58
KLX15A	0.97	0.92	0.60
KLX16A	1.00	0.82	0.45
KLX17A	1.00	0.80	0.38
KLX18A	0.98	0.65	0.17
KLX19A	1.00	0.91	0.29
KLX20A	1.00	0.76	0.25
KLX21B	0.97	0.95	0.75
KLX22A	0.98	0.65	0.30
KLX22B	1.00	0.33	0.11
KLX23A	0.88	0.65	0.18
KLX23B	1.00	0.25	0.00
KLX24A	1.00	0.71	0.22
KLX25A	1.00	0.75	0.50
KLX26A	1.00	0.91	0.22
KLX26B	1.00	0.41	0.29
KLX28A	1.00	0.74	0.03
KLX29A	1.00	0.78	0.44
Average	0.97	0.73	0.36

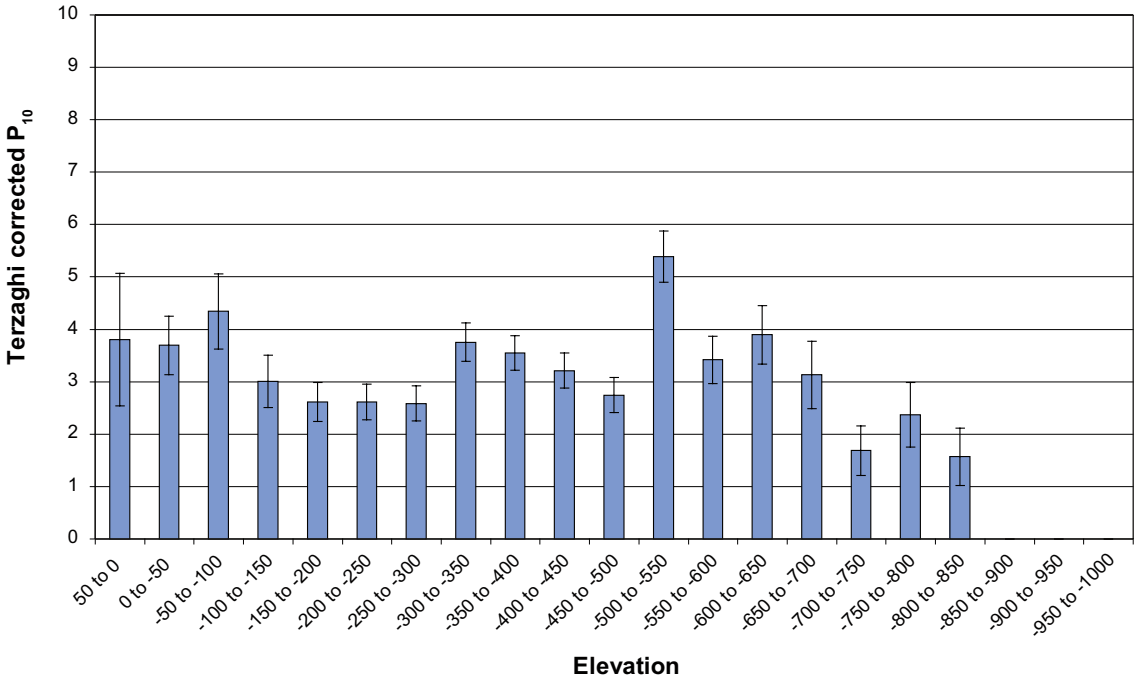

Figure 9-18. *Variation of the Terzaghi-corrected fracture intensity for OPO fractures with elevation (masl) for the fully characterised sections of boreholes penetrating fracture domain FSM_EW007.*

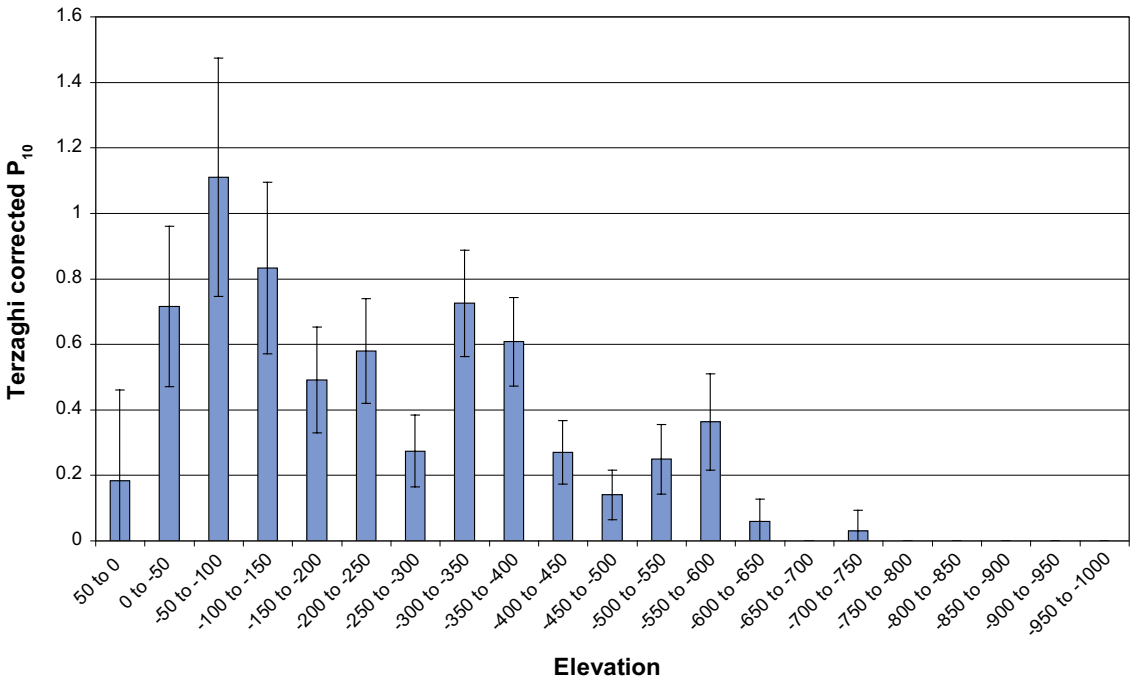

Figure 9-19. *Variation of the Terzaghi-corrected fracture intensity for PFL-f features with elevation (masl) for the fully characterised sections of boreholes penetrating fracture domain FSM_EW007.*

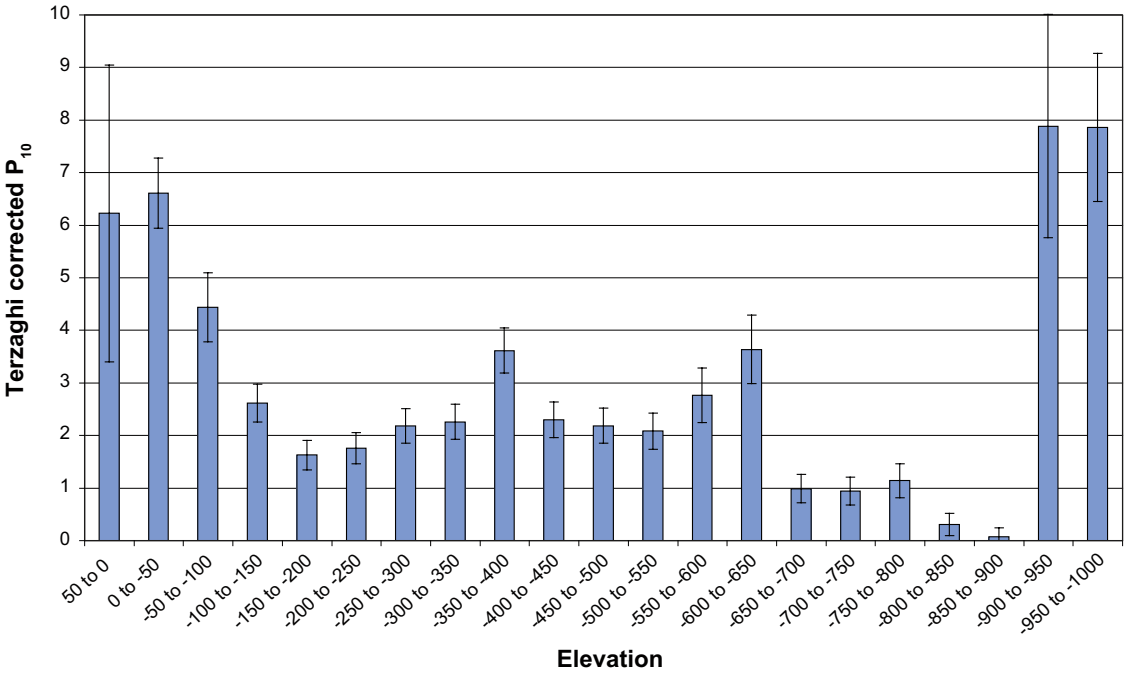

Figure 9-20. *Variation of the Terzaghi-corrected fracture intensity for OPO fractures with elevation (masl) for the fully characterised sections of boreholes penetrating fracture domain FSM_NE005.*

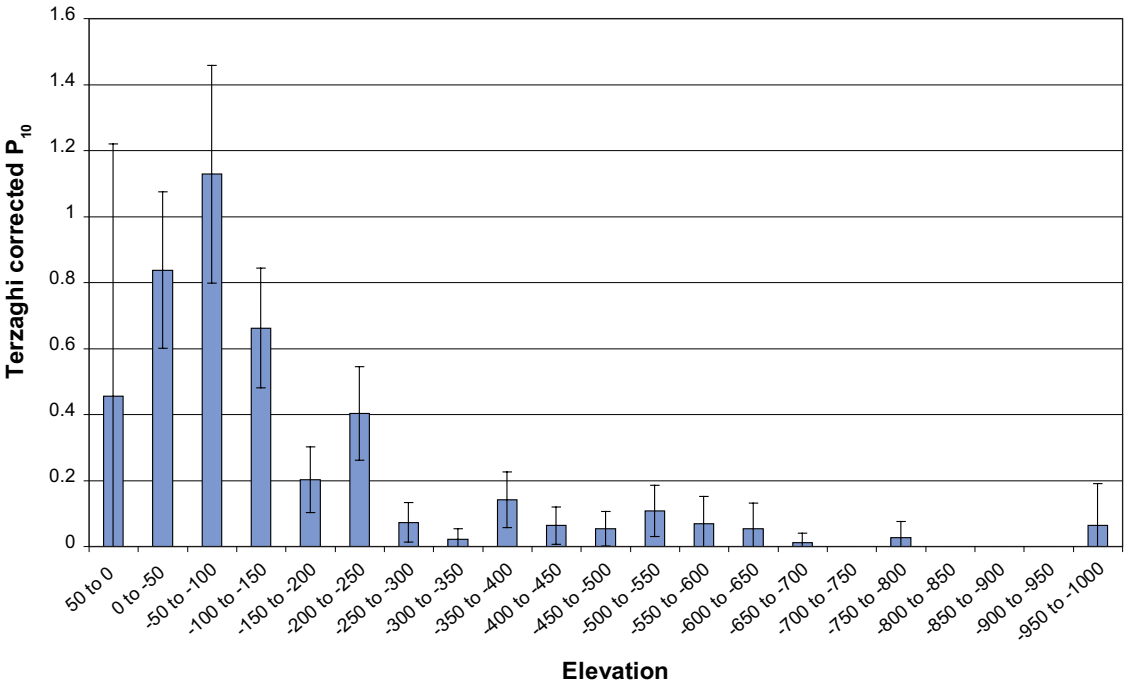

Figure 9-21. *Variation of the Terzaghi-corrected fracture intensity for PFL-f features with elevation (masl) for the fully characterised sections of boreholes penetrating fracture domain FSM_NE005.*

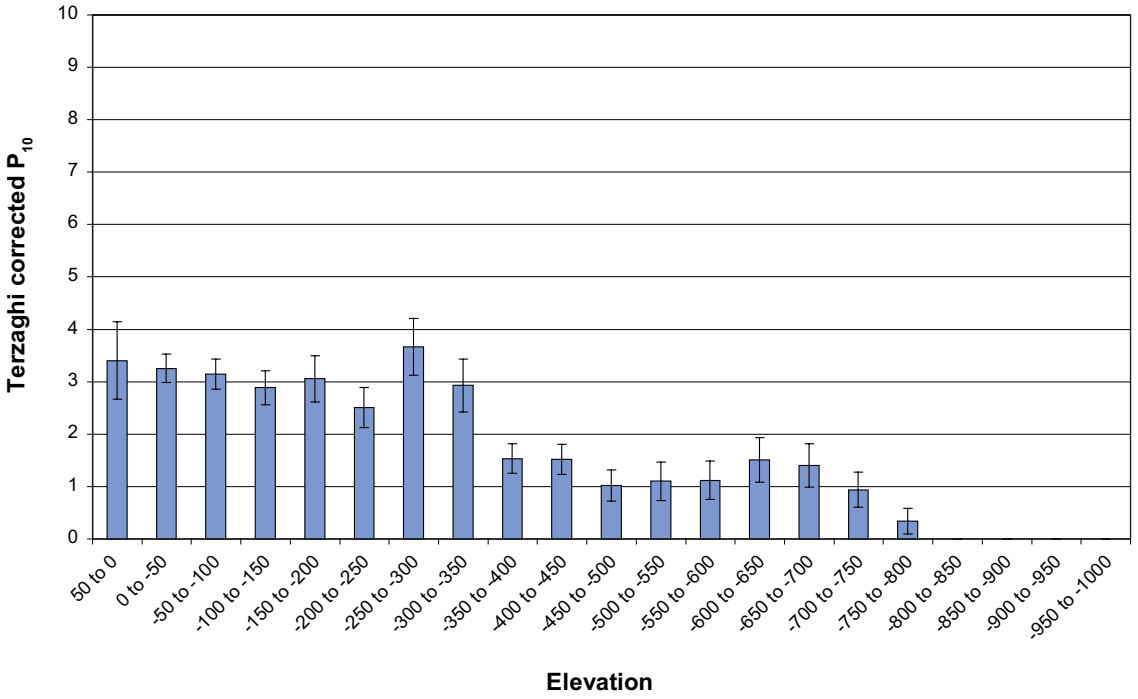

Figure 9-22. *Variation of the Terzaghi-corrected fracture intensity for OPO fractures with elevation (masl) for the fully characterised sections of boreholes penetrating fracture domain FSM_N.*

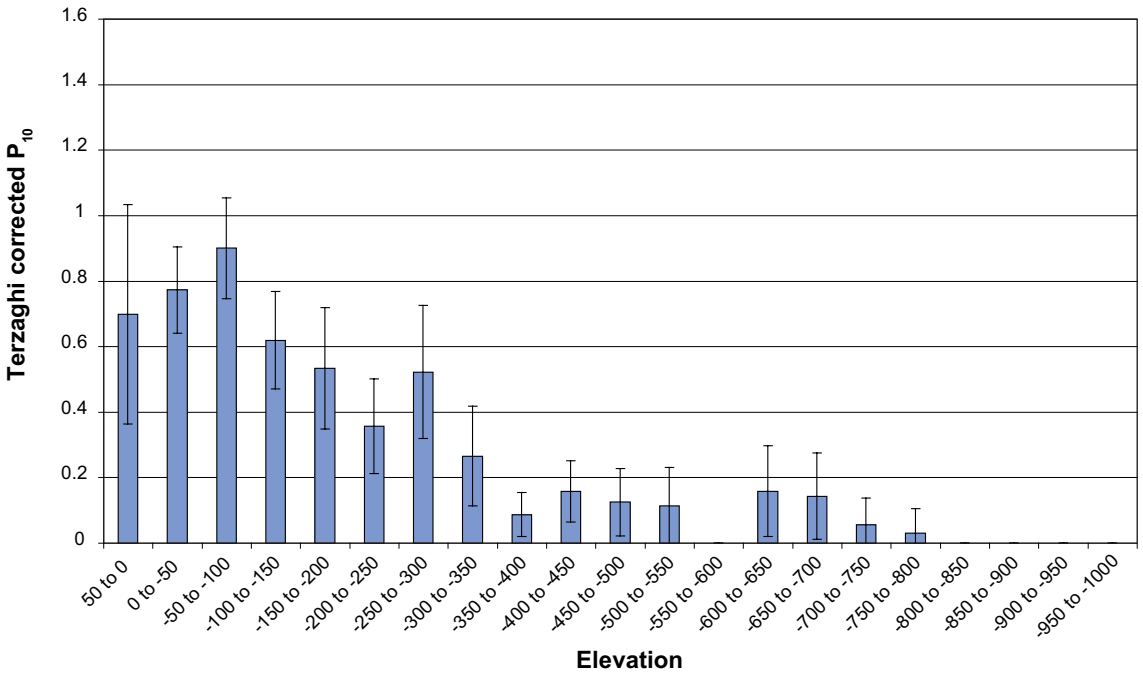

Figure 9-23. *Variation of the Terzaghi-corrected fracture intensity for PFL-f features with elevation (masl) for the fully characterised sections of boreholes penetrating fracture domain FSM_N.*

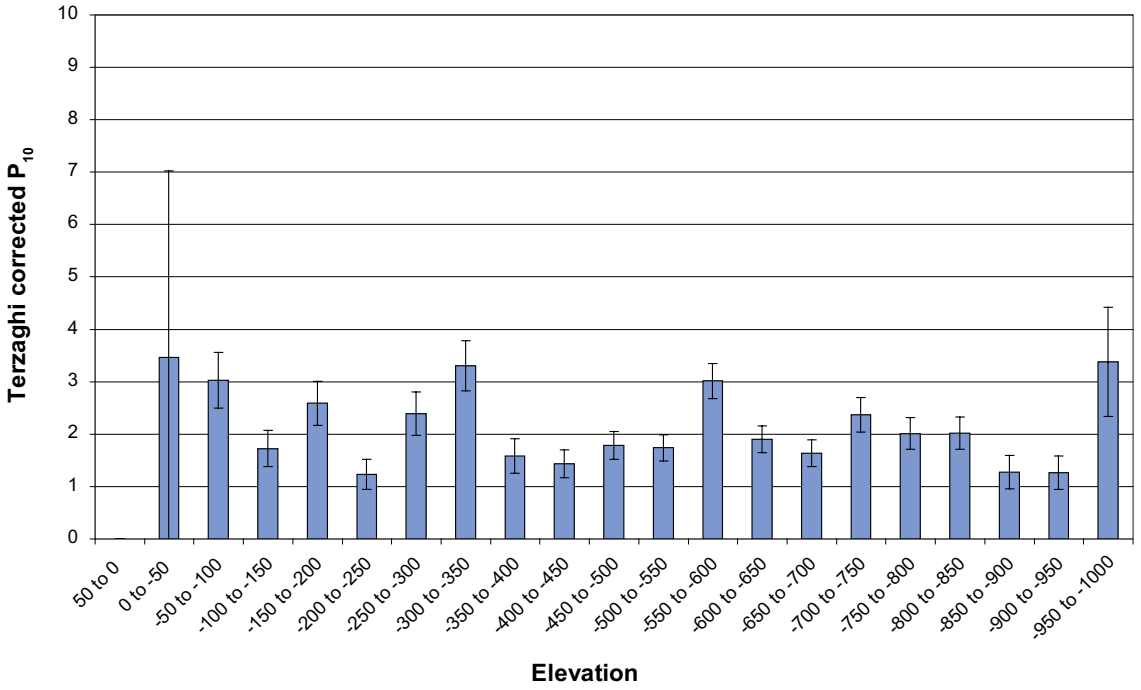

Figure 9-24. *Variation of the Terzaghi-corrected fracture intensity for OPO fractures with elevation (masl) for the fully characterised sections of boreholes penetrating fracture domain FSM_C.*

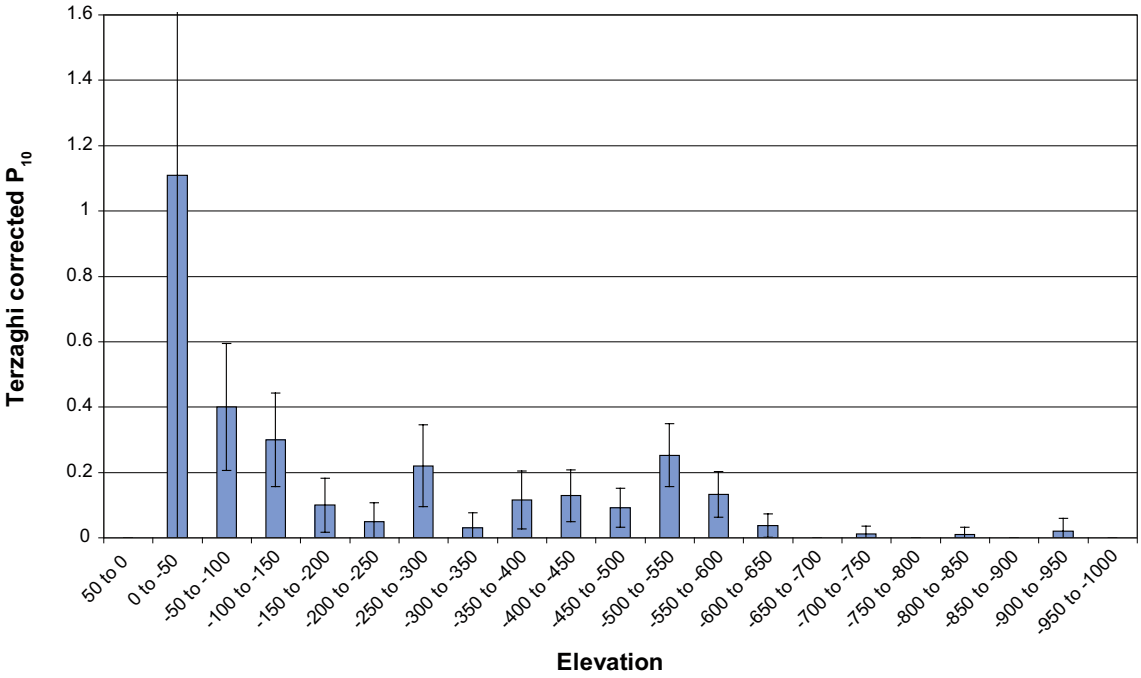

Figure 9-25. *Variation of the Terzaghi-corrected fracture intensity for PFL-f features with elevation (masl) for the fully characterised sections of boreholes penetrating fracture domain FSM_C.*

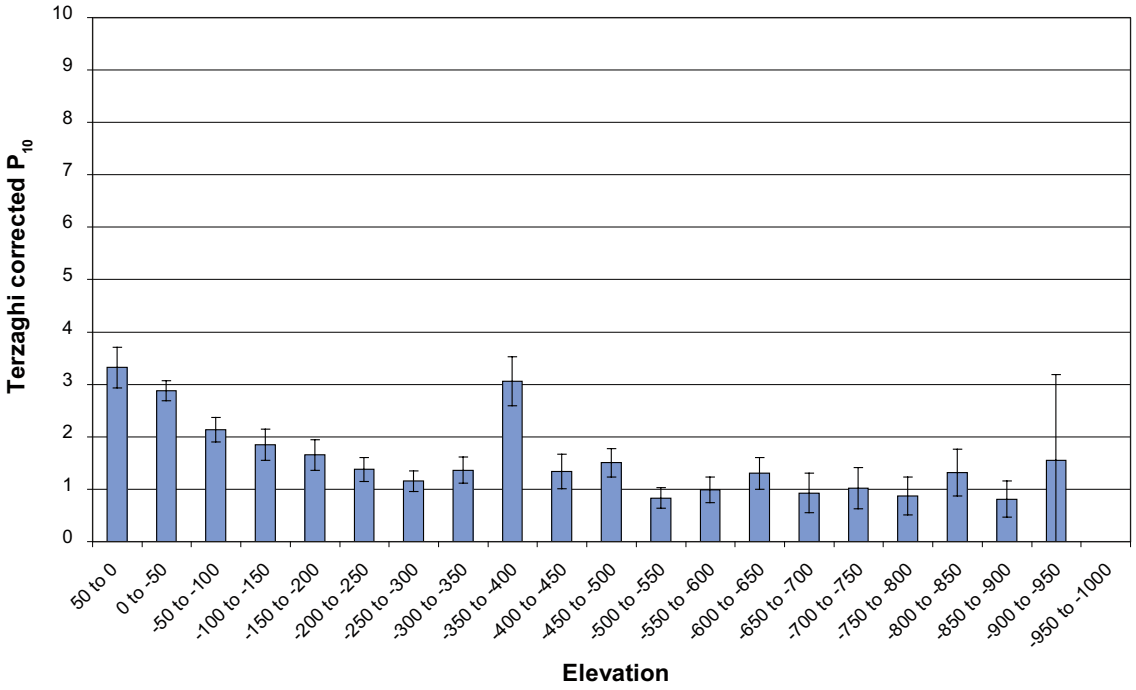

Figure 9-26. *Variation of the Terzaghi-corrected fracture intensity for OPO fractures with elevation (masl) for the fully characterised sections of boreholes penetrating fracture domain FSM_W.*

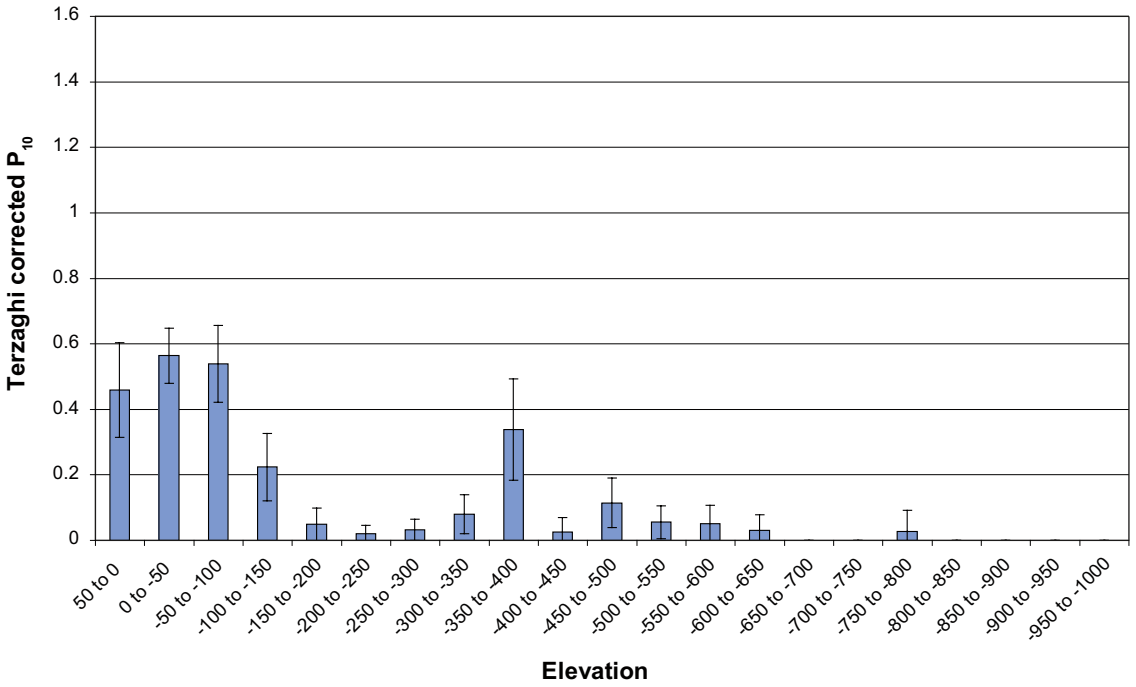

Figure 9-27. *Variation of the Terzaghi-corrected fracture intensity for PFL-f features with elevation (masl) for the fully characterised sections of boreholes penetrating fracture domain FSM_W.*

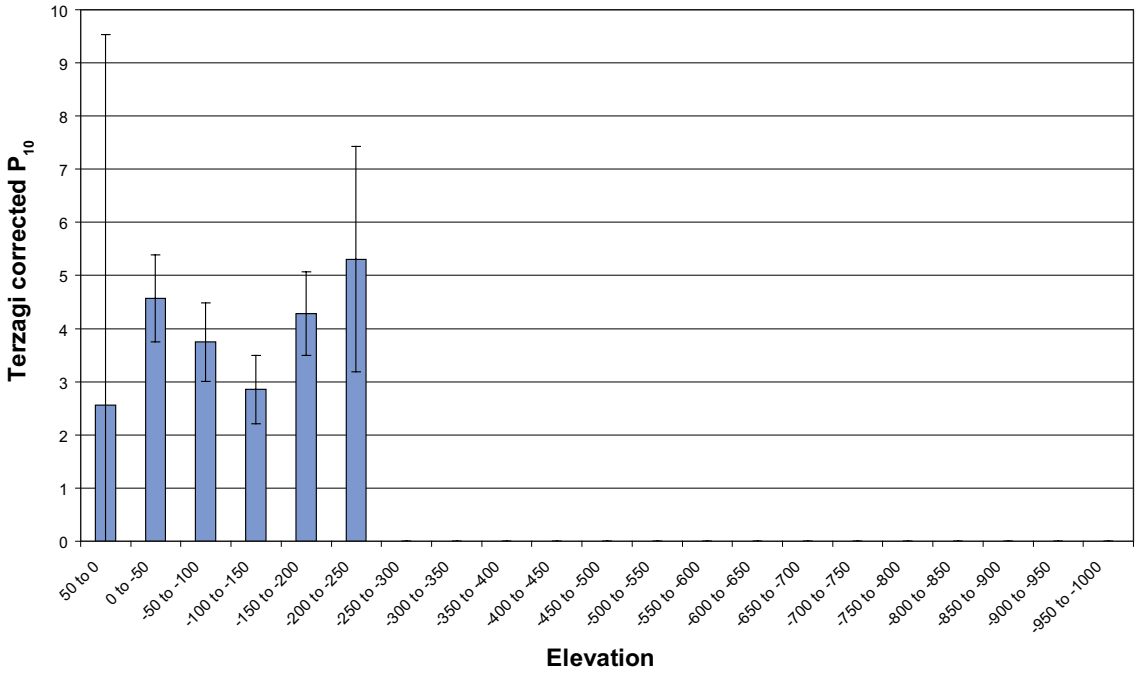

Figure 9-28. *Variation of the Terzaghi-corrected fracture intensity for OPO fractures with elevation (masl) for the fully characterised sections of boreholes penetrating fracture domain FSM_S.*

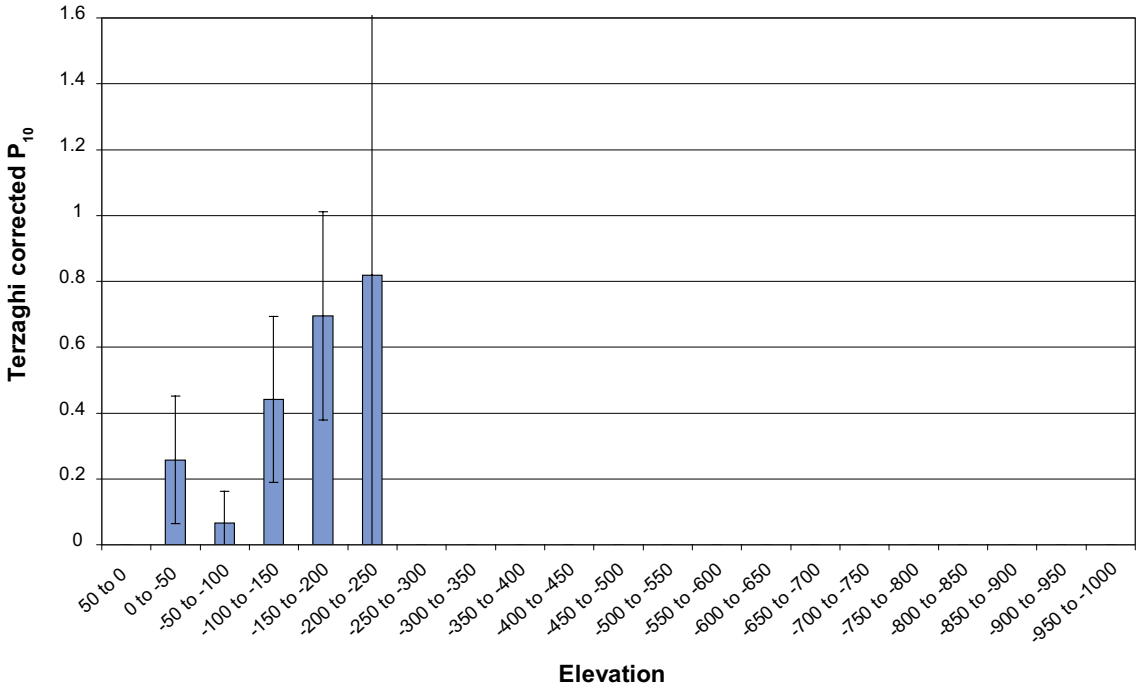

Figure 9-29. *Variation of the Terzaghi-corrected fracture intensity for PFL-f features s with elevation (masl) for the fully characterised sections of boreholes penetrating fracture domain FSM_S.*

The possible existence of a trend with depth for PFL-f features but not for OPO fractures is interesting in light of our conceptual model of how flow through a network of features. In this concept fractures that are identified as open or partly-open have the potential to carry flow, but will only do so if they are both connected and transmissive; these fractures correspond to the PFL-f features. This suggests that there may be depth trends in the distributions of either fracture size – making connections more likely – or fracture transmissivity (or both), rather than trends in fracture intensity with depth. This interpretation is reflected in the parameters produced by the hydrogeological DFN calibration, cf. Section 10.4.4 and Sections 10.5.2 to 10.5.4), where both fracture size distributions and fracture transmissivity distributions vary with depth.

Fracture intensities by depth and fracture set

The analyses described above indicated that there is a significant trend in the variation of the intensity of PFL-f features with depth. Since this seemed to be the key dependence of the water-conducting fractures, this aspect deserved further scrutiny to assess whether the orientations of PFL-f features were dependent on depth. Figure 9-30 through Figure 9-35 show the variation of the intensity of PFL-f features within individual sets according to depth for each fracture domain. In general, the WNW set is the dominant set at elevations greater than about –100 to –200 masl. At shallower depths, the SH set is generally the dominant set.

The equivalent plots for the rock domains are included in Appendix 5, Section A.5.1. For the rock domains, being of broader extent, the possibility of any general horizontal spatial trends was considered (see Appendix 5, Section A.5.1), but this did not reveal any clear trends.

9.3.5 Choice of appropriate depth zones for modelling

In order to honour the depth variation of the intensity of PFL-f features within the hydrogeological DFN model it is necessary to characterise the hydraulic properties of the fracture system for an appropriate number of depth zones. In doing so, the zones should be of sufficient extent that they have good statistical significance, still capture the sharp transitions at the higher elevations, and be sufficiently few for practical modelling considerations. After careful inspection of the results for the analyses of the overall and indivicual fracture set intensities according to the 50 m depth zones, it was decided that a reasonable choice for the depth zones for all the rock subdivision would be:

(i) from ground surface down to –150 masl,

(ii) from –150 to –400 masl,

(iii) from –400 to –650 masl,

(iv) below –650 masl.

There is not a unique best choice for the depth zones. The above choice enables a good representation of the main features of the distribution of fracture intensity. The top interval allows the higher fracture intensity and the higher intensity for the SH fracture set in the near-surface rocks to be represented. The lowest interval allows the much lower intensity of PFL-f features below about –650 masl to be represented. The division of the intervening rock into two depth zones allows the slight trend with elevation over this range to be represented. Furthermore, depth zone(iii) effectively straddles the typical repository elevation at –500 masl. It might be possible to obtain a modest improvement in the representation by, for example, adopting different depth zones for different rock types, or even different fracture sets, or by adopting more depth zones. However, an unnecessarily complicated prescription should be avoided, and it is considered that the prescription given above provides a sensible balance in terms of the level of detail given the available data.

In Figure 9-36 through Figure 9-47 the variation of the fracture intensity for OPO fractures and PFL-f features with depth zone and fracture set is shown for each fracture domain. The equivalent for the rock domain is given in Appendix 5, Section A.5.1. The Terzaghi corrected fracture intensities for the OPO fractures for the different fracture sets and the depth zones are key input for the hydrogeological DFN simulations, and the equivalent for the PFL-f features are the key calibration target for the flow modelling. These statistics are also tabulated in Table 9-10.

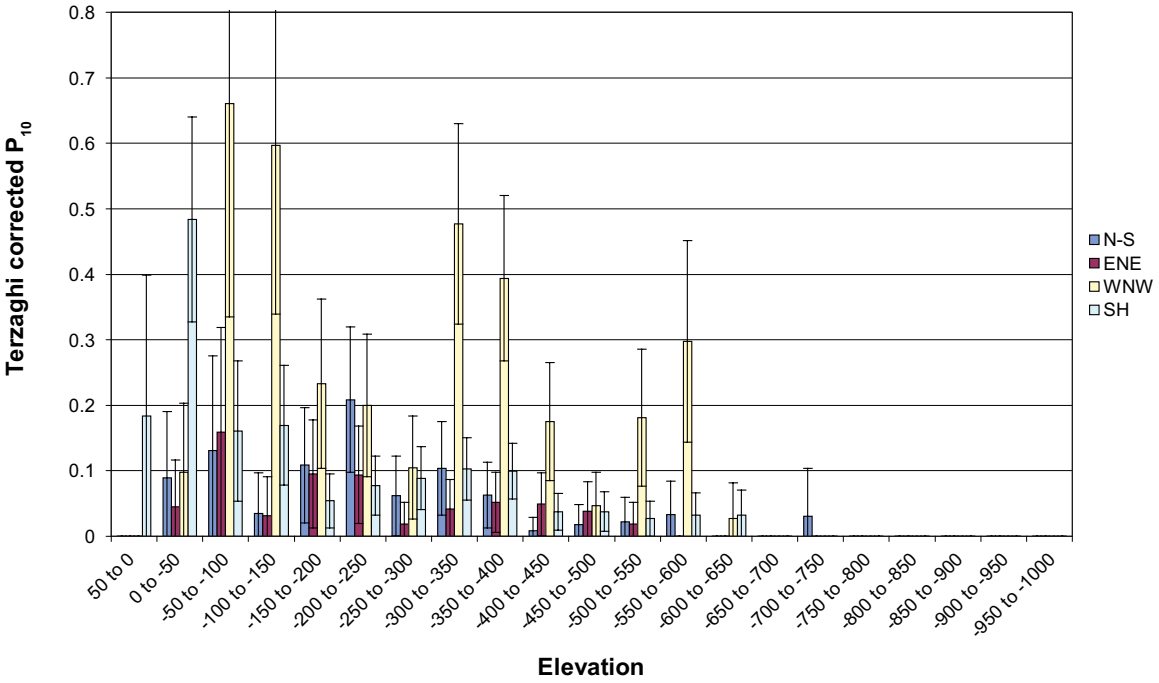

Figure 9-30. *Variation of the Terzaghi-corrected fracture intensity for PFL-f features with elevation (masl) and fracture set for the fully characterised sections of boreholes penetrating fracture domain FSM_EW007.*

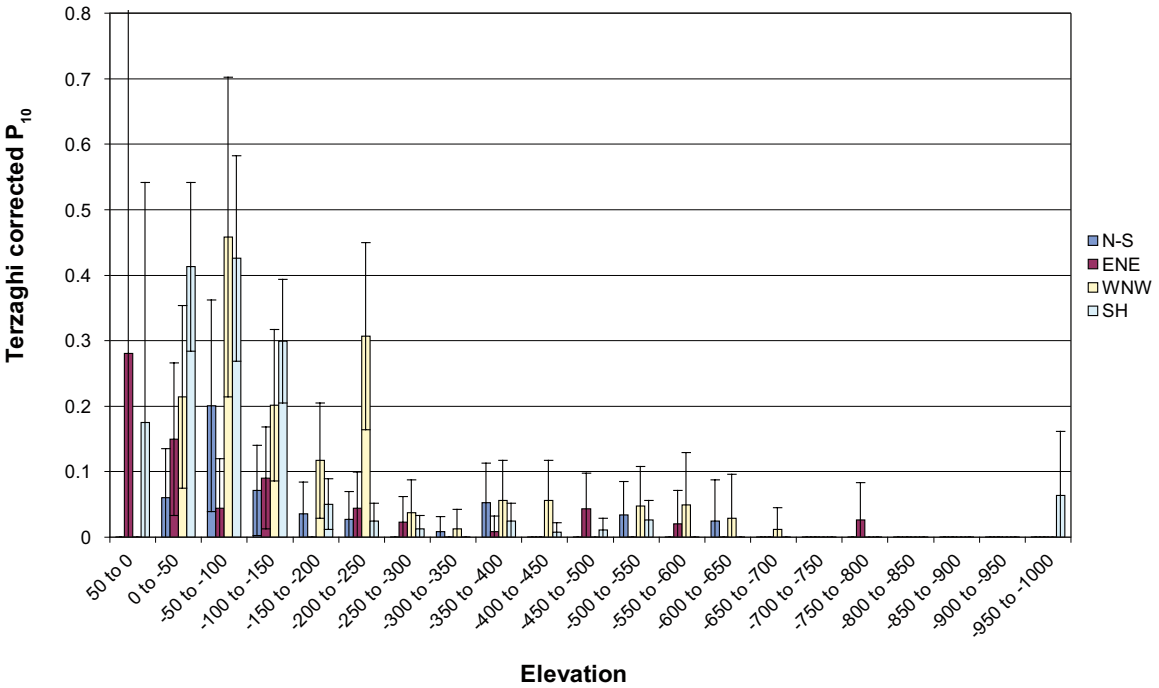

Figure 9-31. *Variation of the Terzaghi-corrected fracture intensity for PFL-f features with elevation (masl) and fracture set for the fully characterised sections of boreholes penetrating fracture domain FSM_NE005.*

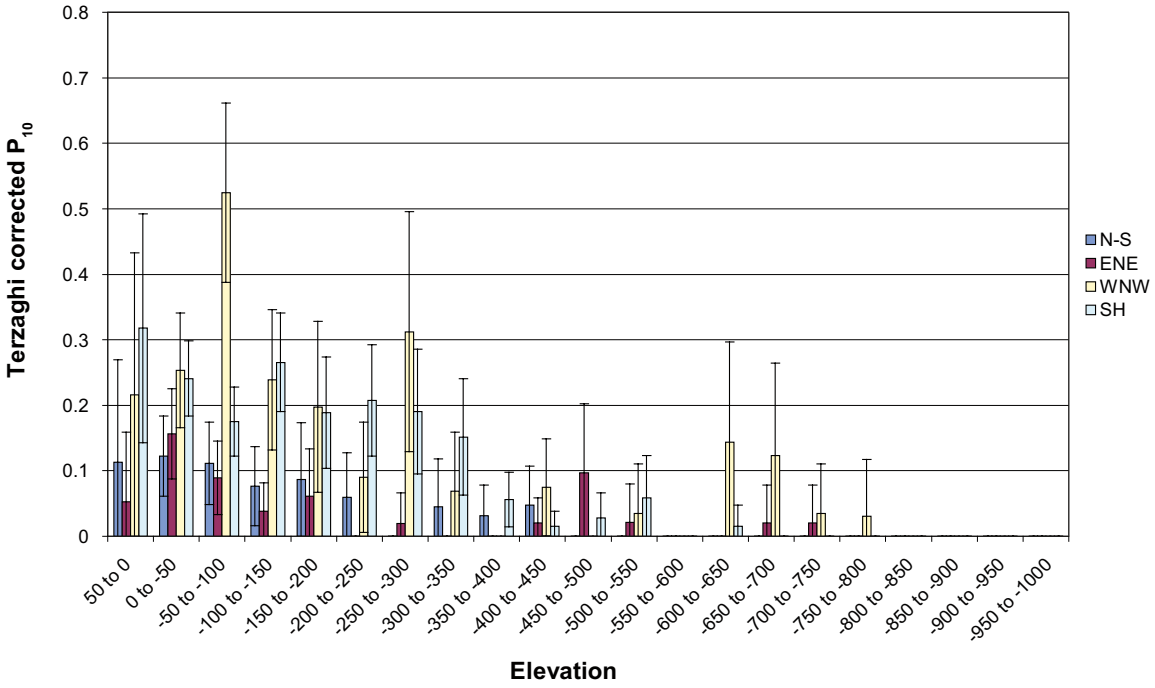

Figure 9-32. *Variation of the Terzaghi-corrected fracture intensity for PFL-f features with elevation (masl) and fracture set for the fully characterised sections of boreholes penetrating fracture domain FSM_N.*

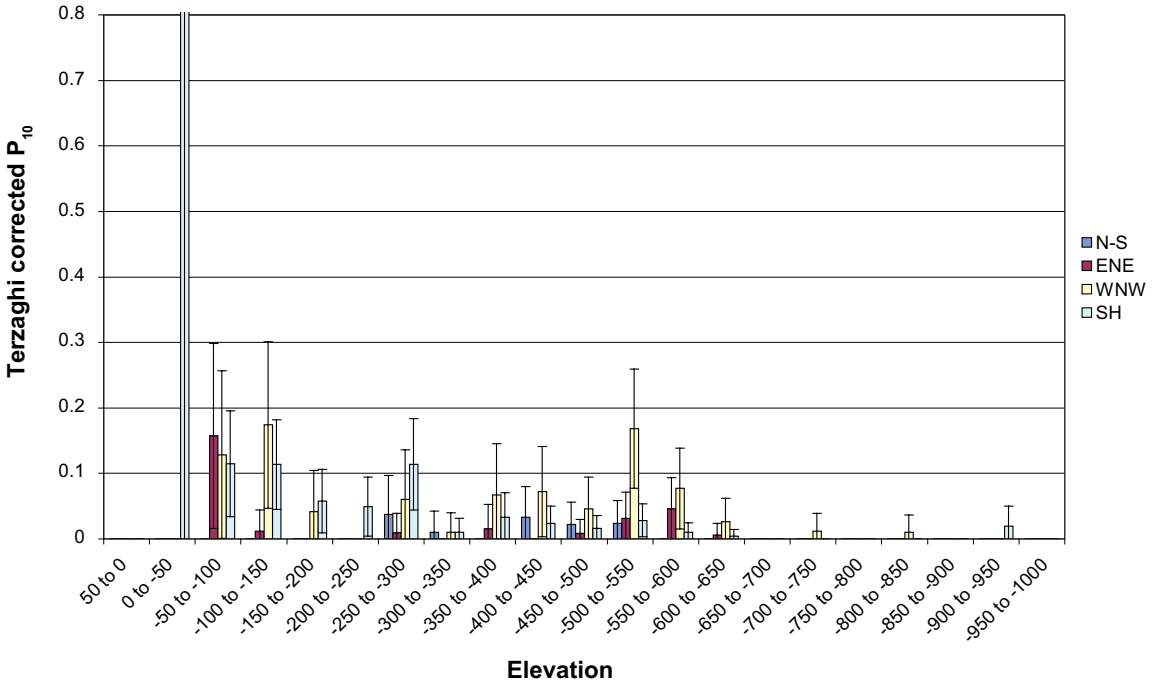

Figure 9-33. *Variation of the Terzaghi-corrected fracture intensity for PFL-f features with elevation (masl) for the fully characterised sections of boreholes penetrating fracture domain FSM_C.*

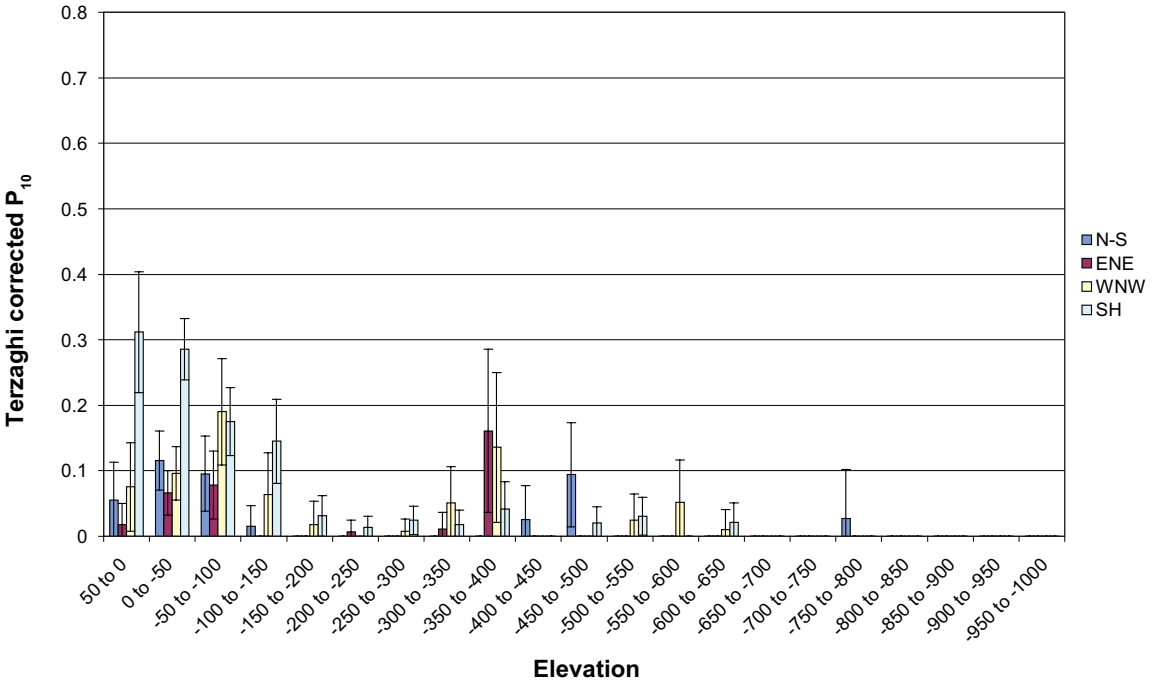

Figure 9-34. *Variation of the Terzaghi-corrected fracture intensity for PFL-f features with elevation (masl) and fracture set for the fully characterised sections of boreholes penetrating fracture domain FSM_W.*

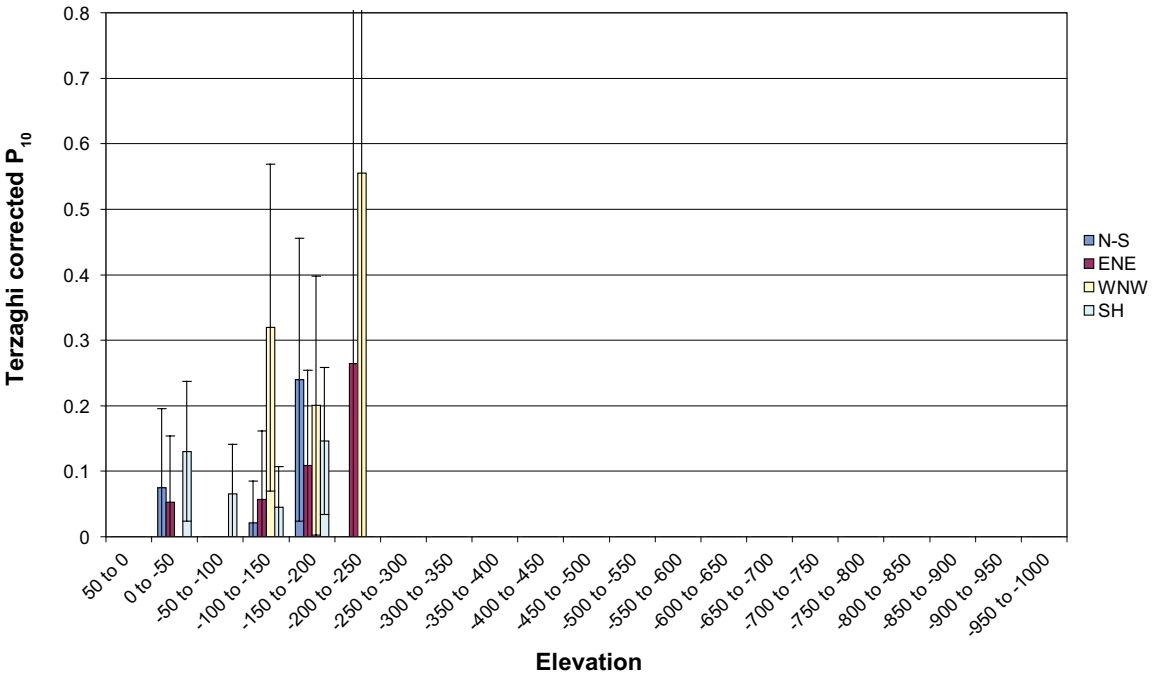

Figure 9-35. *Variation of the Terzaghi-corrected fracture intensity for PFL-f features with elevation (masl) and fracture set for the fully characterised sections of boreholes penetrating fracture domain FSM_S.*

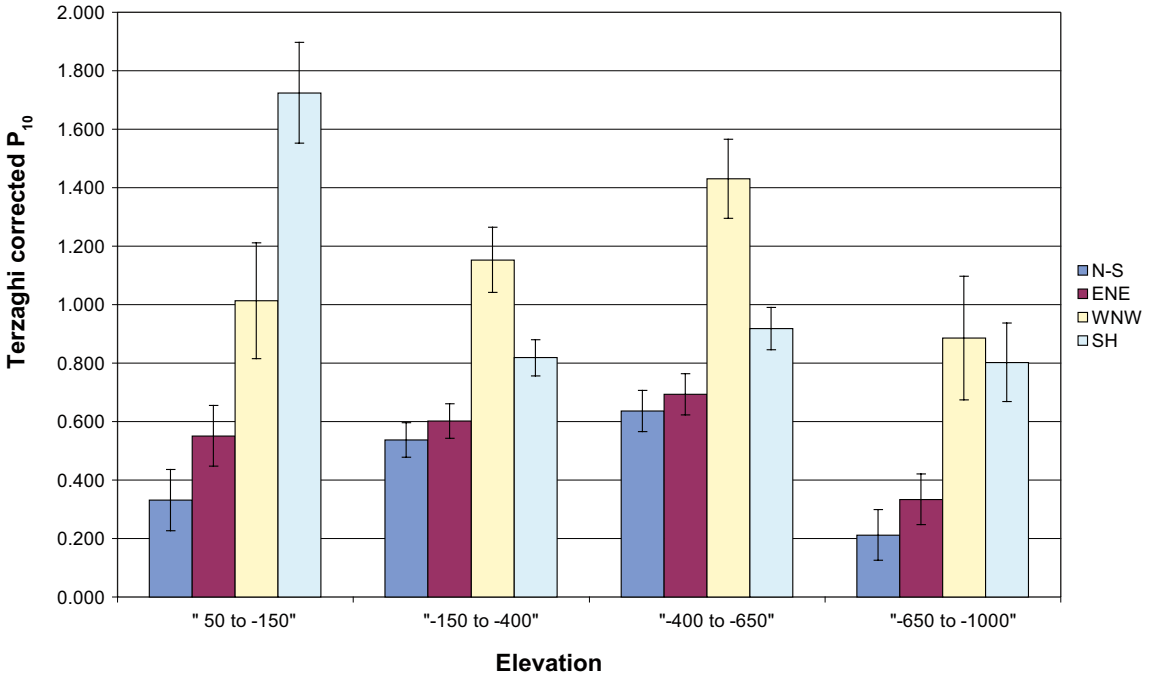

Figure 9-36. *Variation of the Terzaghi-corrected fracture intensity for OPO fractures with depth zone and fracture set for the fully characterised sections of boreholes penetrating fracture domain FSM_EW007.*

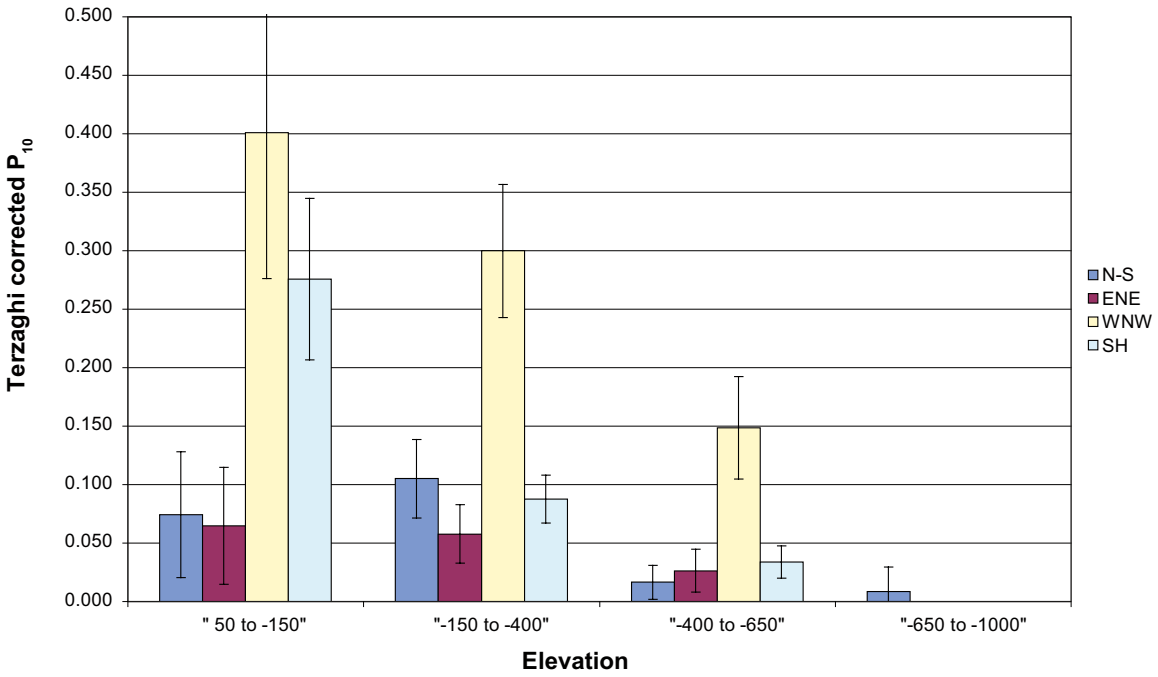

Figure 9-37. *Variation of the Terzaghi-corrected fracture intensity for PFL-f features fractures with depth zone and fracture set for the fully characterised sections of boreholes penetrating fracture domain FSM_EW007.*

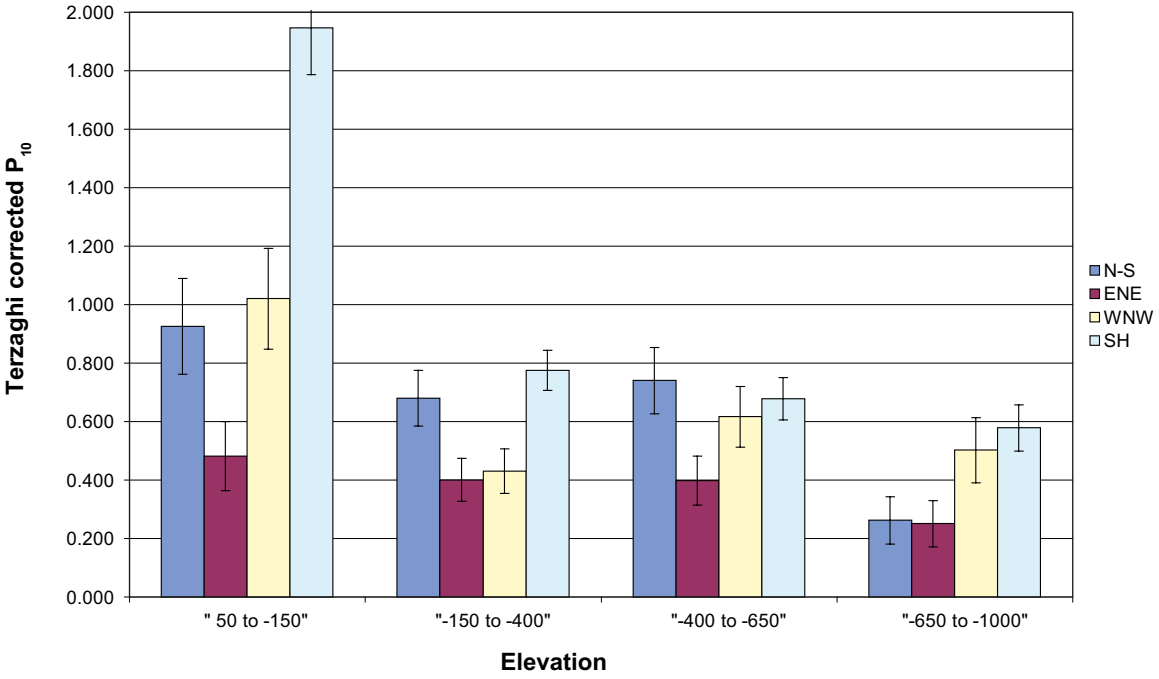

Figure 9-38. *Variation of the Terzaghi-corrected fracture intensity for OPO fractures with depth zone and fracture set for the fully characterised sections of boreholes penetrating fracture domain FSM_NE005.*

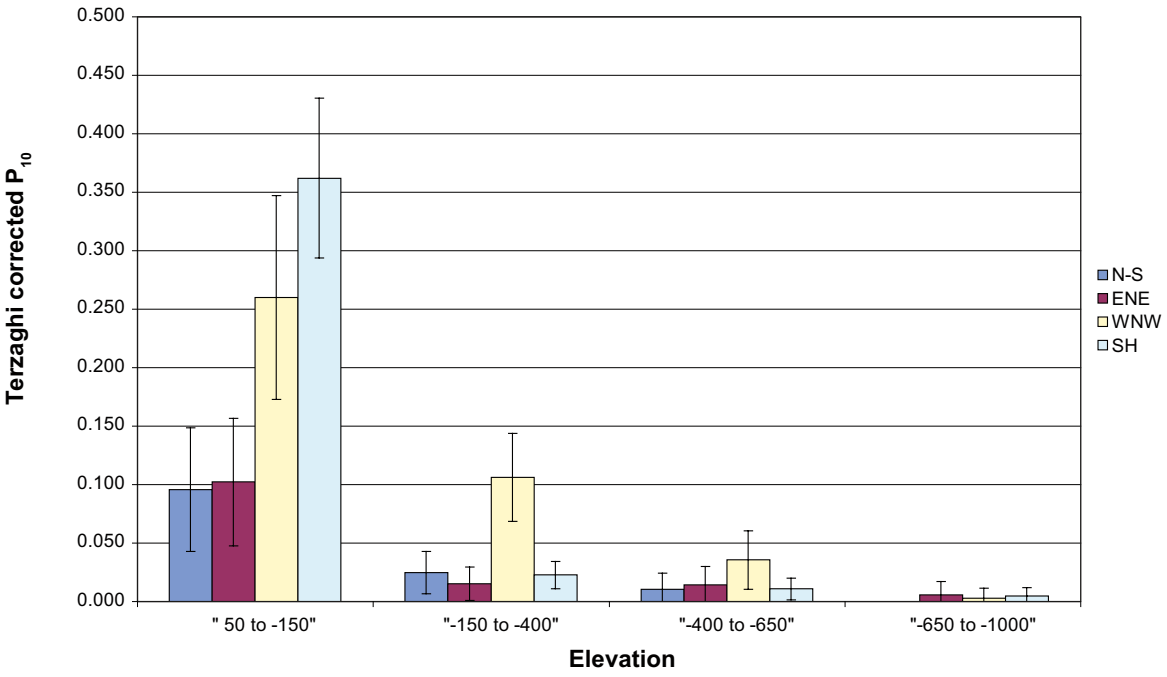

Figure 9-39. *Variation of the Terzaghi-corrected fracture intensity for PFL-f features with depth zone and fracture set for the fully characterised sections of boreholes penetrating fracture domain FSM_NE005.*

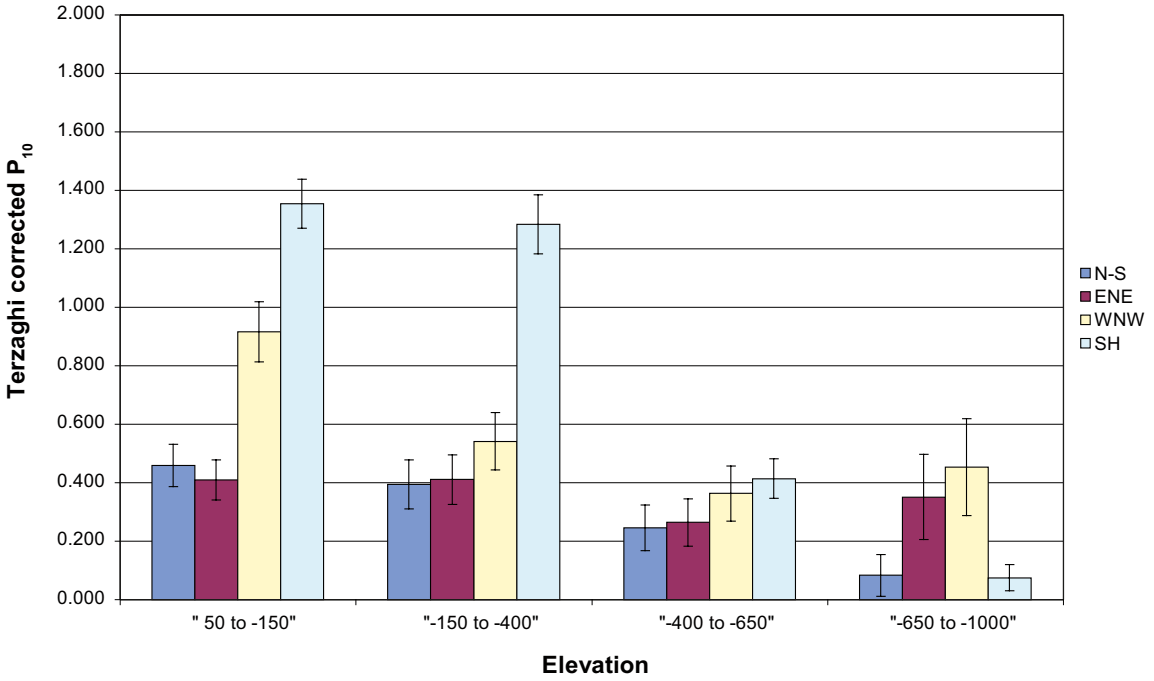

Figure 9-40. *Variation of the Terzaghi-corrected fracture intensity for OPO fractures with depth zone and fracture set for the fully characterised sections of boreholes penetrating fracture domain FSM_N.*

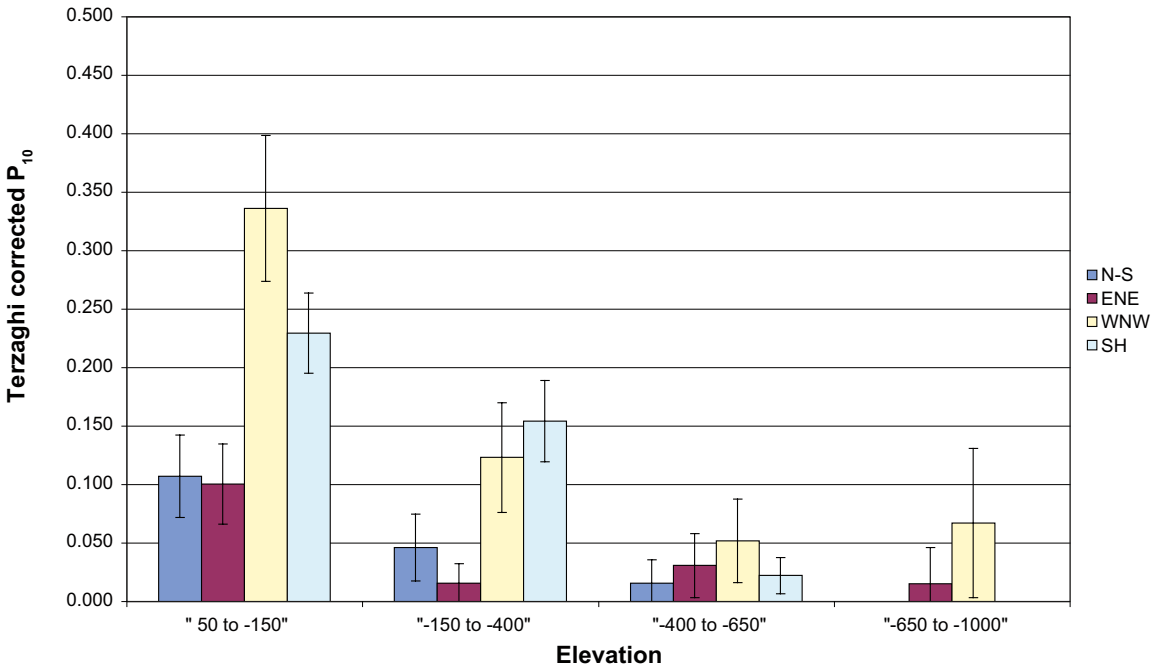

Figure 9-41. *Variation of the Terzaghi-corrected fracture intensity for PFL-f features with depth zone and fracture set for the fully characterised sections of boreholes penetrating fracture domain FSM_N.*

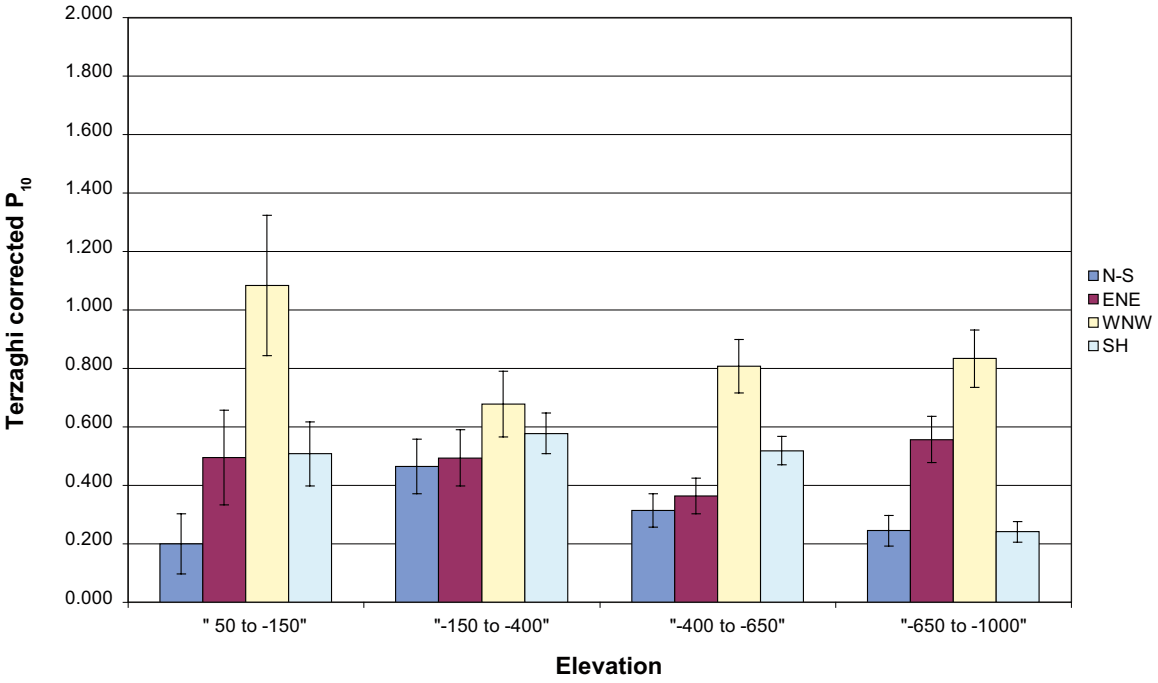

Figure 9-42. *Variation of the Terzaghi-corrected fracture intensity for OPO fractures with depth zone and fracture set for the fully characterised sections of boreholes penetrating fracture domain FSM_C.*

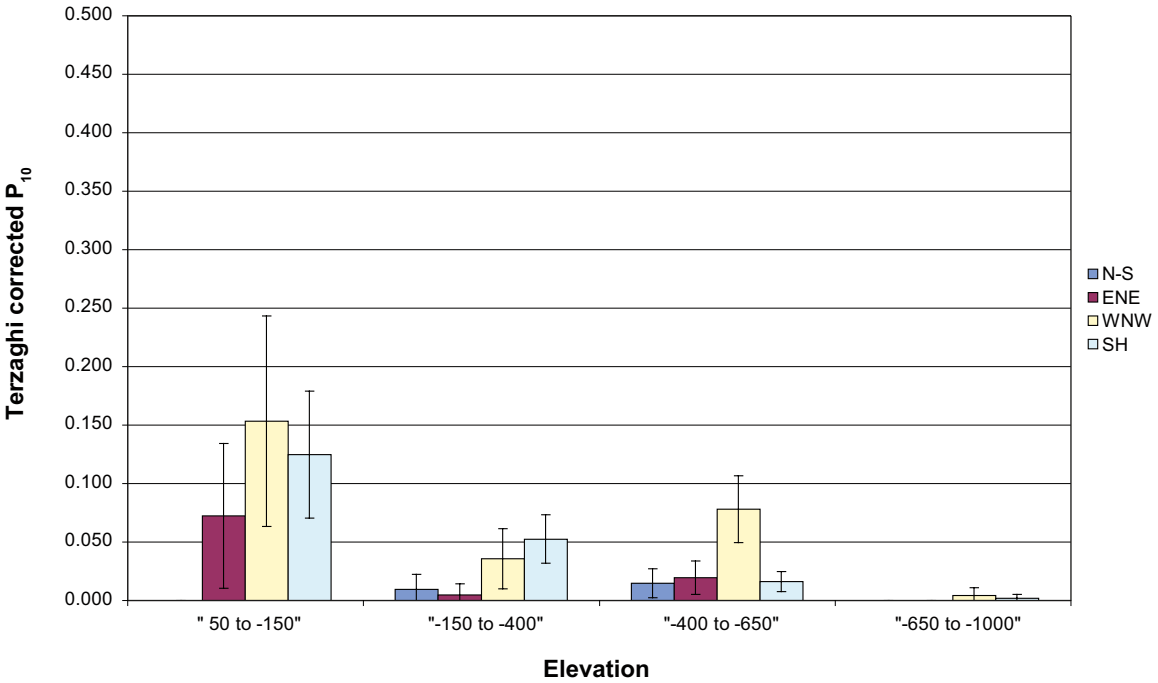

Figure 9-43. *Variation of the Terzaghi-corrected fracture intensity for PFL-f features with depth zone and fracture set for the fully characterised sections of boreholes penetrating fracture domain FSM_C.*

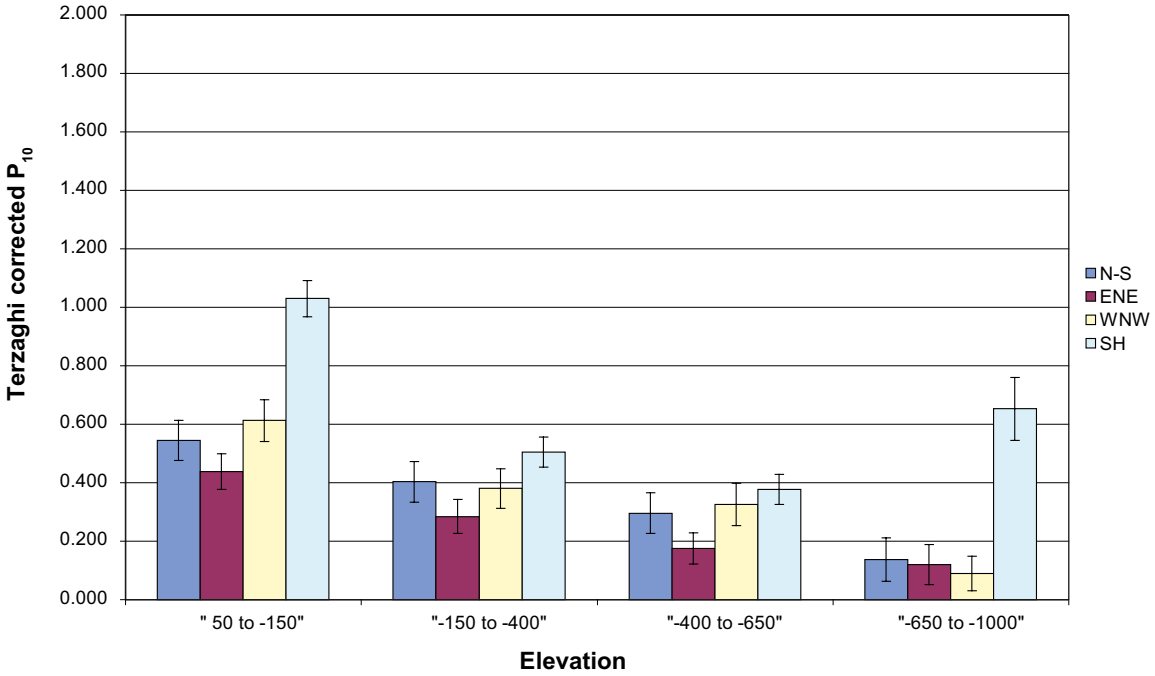

Figure 9-44. *Variation of the Terzaghi-corrected fracture intensity for OPO fractures with depth zone and fracture set for the fully characterised sections of boreholes penetrating fracture domain FSM_W.*

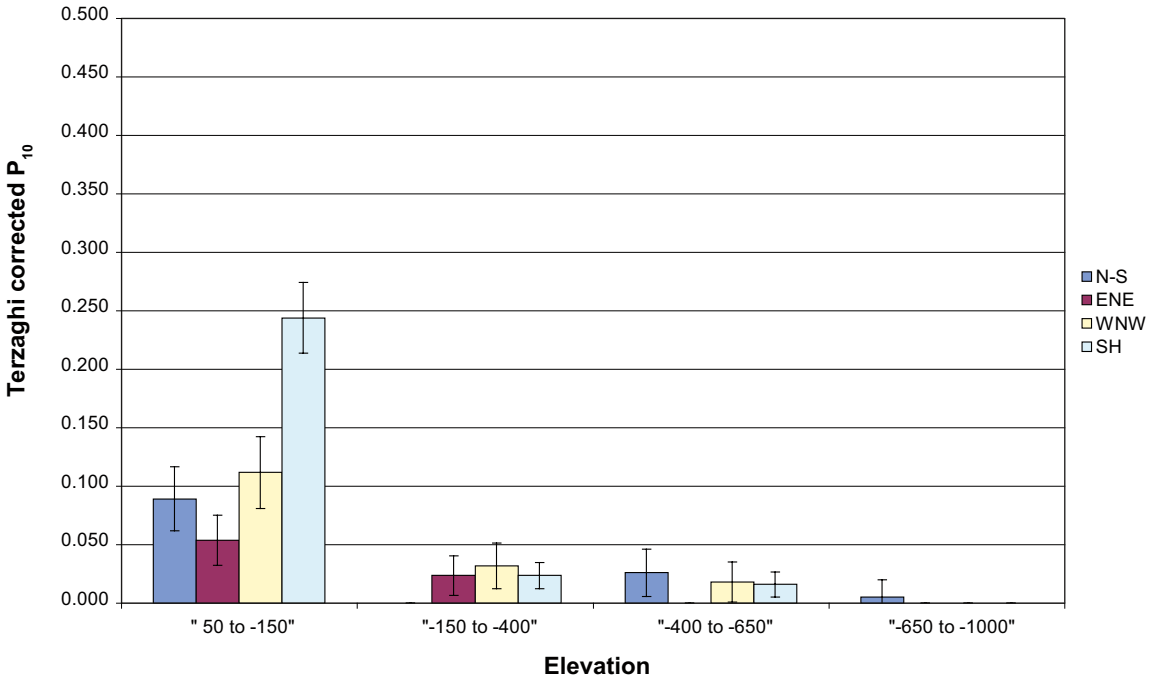

Figure 9-45. *Variation of the Terzaghi-corrected fracture intensity for PFL-f features with depth zone and fracture set for the fully characterised sections of boreholes penetrating fracture domain FSM_W.*

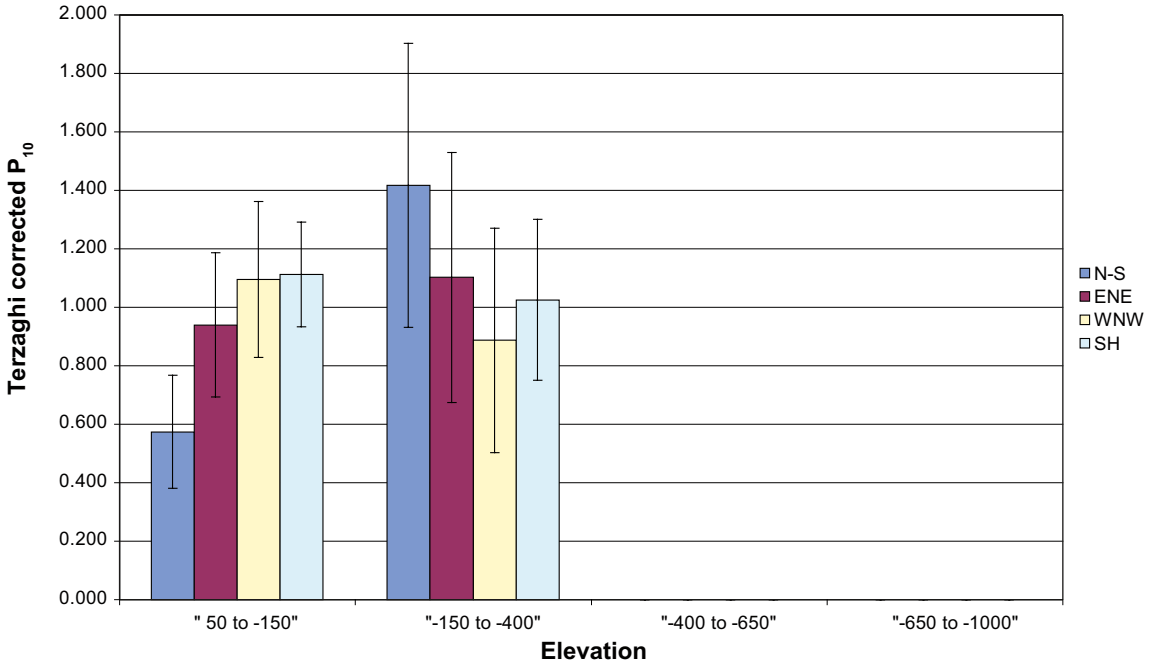

Figure 9-46. *Variation of the Terzaghi-corrected fracture intensity for OPO fractures with depth zone and fracture set for the fully characterised sections of boreholes penetrating fracture domain FSM_S.*

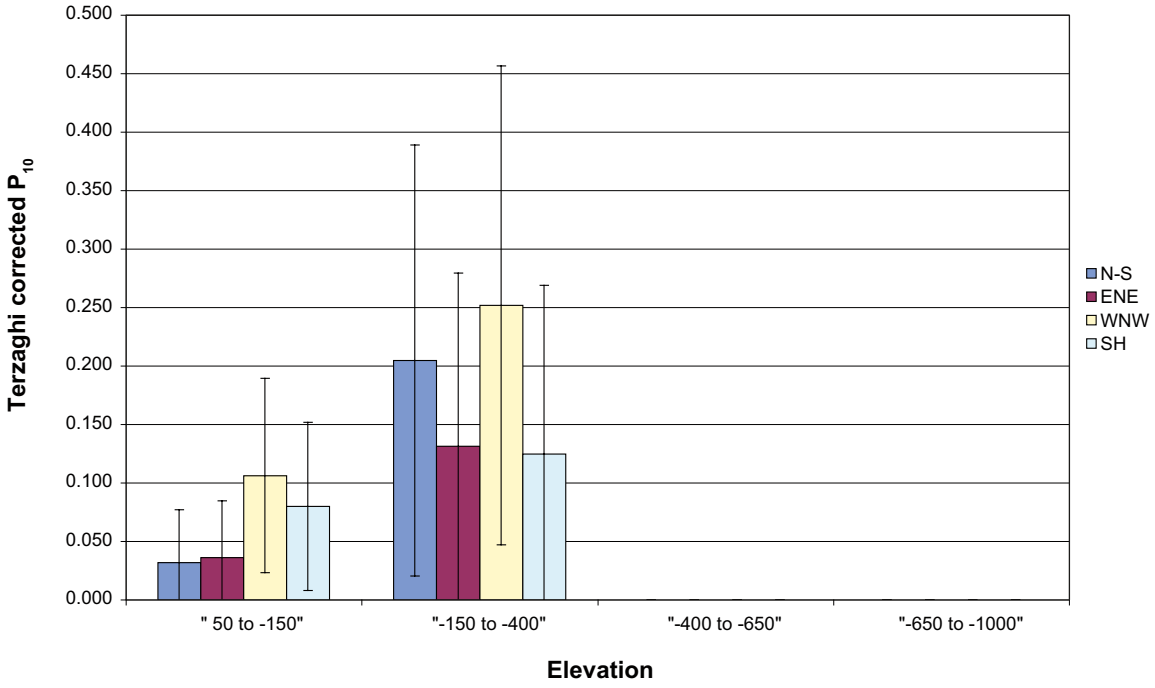

Figure 9-47. *Variation of the Terzaghi-corrected fracture intensity for PFL-f features with depth zone and fracture set for the fully characterised sections of boreholes penetrating fracture domain FSM_S.*

Table 9-10. Terzaghi-corrected fracture intensities for OPO fractures and PFL-f features for the depth zones and fracture sets for each rock subdivision. Depths intervals are defined in terms of elevation (masl).

		OPO Depth zone				PFL Depth zone			
		+50 to –150	–150 to –400	–400 to –650	–650 to –1,000	+50 to –150	–150 to –400	–400 to –650	–650 to –1,000
FSM_EW007	N-S	0.332	0.536	0.637	0.212	0.074	0.105	0.017	0.009
	ENE	0.551	0.601	0.694	0.334	0.065	0.058	0.026	0
	WNW	1.013	1.153	1.431	0.885	0.401	0.300	0.149	0
	SH	1.724	0.818	0.917	0.803	0.276	0.087	0.034	0
FSM_NE005	N-S	0.926	0.680	0.740	0.262	0.096	0.025	0.011	0
	ENE	0.482	0.401	0.398	0.251	0.102	0.015	0.014	0.006
	WNW	1.020	0.431	0.617	0.502	0.260	0.106	0.036	0.003
	SH	1.946	0.775	0.678	0.578	0.362	0.023	0.011	0.005
FSM_N	N-S	0.459	0.395	0.246	0.083	0.107	0.0386	0.016	0
	ENE	0.409	0.411	0.264	0.351	0.101	0.016	0.031	0.015
	WNW	0.915	0.541	0.363	0.453	0.336	0.123	0.052	0.067
	SH	1.354	1.284	0.414	0.075	0.230	0.154	0.022	0
FSM_C	N-S	0.199	0.465	0.314	0.245	0	0.009	0.015	0
	ENE	0.495	0.494	0.363	0.557	0.072	0.005	0.019	0
	WNW	1.084	0.677	0.808	0.833	0.153	0.036	0.078	0.004
	SH	0.508	0.578	0.519	0.242	0.125	0.053	0.016	0.002
FSM_W	N-S	0.545	0.403	0.296	0.138	0.089	0	0.026	0.005
	ENE	0.438	0.284	0.175	0.120	0.054	0.024	0	0
	WNW	0.613	0.380	0.326	0.089	0.112	0.032	0.018	0
	SH	1.030	0.505	0.377	0.653	0.244	0.024	0.016	0
FSM_S	N-S	0.574	1.418			0.032	0.205		
	ENE	0.939	1.102			0.036	0.132		
	WNW	1.095	0.887			0.106	0.252		
	SH	1.112	1.025			0.080	0.125		
RSMA01	N-S	0.425	0.510	0.487	0.347	0.096	0.076	0.021	0.002
	ENE	0.424	0.529	0.497	0.661	0.092	0.039	0.026	0.003
	WNW	0.899	0.864	0.927	0.669	0.326	0.212	0.119	0.017
	SH	1.465	0.953	0.750	0.572	0.241	0.104	0.028	0.002
RSMD01	N-S	0.543	0.427	0.441	0.110	0.080	0.014	0.020	0.002
	ENE	0.529	0.457	0.270	0.165	0.061	0.032	0.001	0.002
	WNW	0.758	0.527	0.580	0.392	0.124	0.044	0.023	0.001
	SH	1.010	0.405	0.443	0.350	0.229	0.029	0.013	0.002
RSMM01	N-S	0.704	0.625	0.375	0.205	0.076	0.023	0	0
	ENE	0.437	0.354	0.382	0.399	0.068	0.011	0.026	0
	WNW	0.906	0.516	0.748	1.436	0.245	0.102	0.048	0.008
	SH	1.473	0.877	0.509	0.142	0.268	0.044	0.014	0
HRD_C	N-S	0.647	0.627	0.472	0.250	0.055	0.027	0.013	0
	ENE	0.589	0.469	0.376	0.461	0.079	0.016	0.017	0.002
	WNW	1.055	0.550	0.737	0.730	0.196	0.085	0.062	0.004
	SH	1.363	0.708	0.578	0.347	0.233	0.039	0.014	0.003

9.3.6 Definition of hydraulic rock domains (HRD)

Reviewing the variations of the fracture intensity by fracture set and depth zone for the fracture domains shown in Figure 9-36 to Figure 9-47 and in the rock domains shown in Appendix 5, Section A.5.1, the variation are summarised in Table 9-11.

Table 9-11. Characteristics of Terzaghi corrected intensity for the different subdivisions of the rock.

Rock subdivision	OPO fractures	PFL-f features
FSM_EW007/ HRD_EW007	The dominant set in the near-surface is the SH set	The WNW and SH set are the dominant sets in the near surface
	At depth the WNW set is the dominant set and its intensity falls off gradually with depth	The WNW set is the dominant set at depth
FSM_NE005	The dominant set in the near surface is the SH set	The dominant set in the near surface is the SH set
	At depth the N-S and WNW sets have comparable intensity	The WNW set is the dominant set at depth
FSM_N/ HRD_N	The dominant sets in the near surface are the WNW and SH sets	The dominant sets in the near surface are the WNW and SH sets
	The intensities of the WNW and SH sets decrease with depth	The intensities of the WNW and SH sets decrease with depth
FSM_C	The dominant set is the WNW set, and the SH set is less important	The dominant set in the near surface is the WNW set
	The intensity of the WNW is high in the near surface but does not fall of with depth below the near surface	
FSM_W/ HRD_W	The dominant set in the near surface is the SH set	The dominant set in the near surface is the SH set
	At depth the N-S and WNW sets have comparable intensity	The N-S set is less important at depth
FSM_S	There are few data	There are few data
RSMA01	The WNW and SH sets are the dominant sets in the near surface	The WNW set is the dominant set at all depths, with the SH set also have high intensity in the near surface
	The WNW set is the dominant set at depth	
RSMD01	The SH set has slightly higher intensity in the near surface, but all the sets have similar intensities	The dominant set in the near surface is the SH set
RSMM01	The SH set has slightly higher intensity in the near surface	The WNW and SH sets are the dominant sets in the near surface
	The WNW set is the dominant set at depth	The WNW set is the dominant set at depth
HRD_C	The WNW and SH sets are the dominant sets in the near surface	The SH set is the dominant set in the near surface
	The intensity does not fall off significantly with depth below the near surface	The intensity of the WNW set falls off with depth

After inspection of the results in Section 9.3.5 it was decided to use a simplified subdivision of the rock for the purposes of the hydrogeological DFN modelling by defining the following 4 Hydraulic Rock Domains (HRD):

- HRD_EW007 corresponding to FSM_EW007,
- HRD_N corresponding to FSM_N,
- HRD_W corresponding to FSM_W,
- HRD_C corresponding to a combination of FSM_C, FSM_NE005 and FSM_S.

The distribution of HRDs at the bedrock surface is shown in Figure 9-48.

It was decided that the characteristics of FSM_C and FSM_NE005 are sufficiently similar that they can justifiably be combined. Further, it was decided that it is sensible to combine FSM_S with the former two because there are so few data for FSM_S. The Terzaghi corrected fracture intensities for the amalgamated HRD_C by depth zone are given in Figure 9-49 to Figure 9-50 for OPO fractures and PFL-f features.

A consequence of this choice is that hydrogeological description focuses on the potential differences in hydraulic properties within the repository deposition area, likely to be within HRD_C, HRD_W and in part in HRD_EW007. The price paid in achieving this detail is that hydrogeological description becomes confined to the immediate vicinity of the Laxemar subarea, shown in Figure 9-48, while the hydrogeological description of the larger Laxemar-Simpevarp area becomes harder to extrapolate than if a hydrogeological description linked to the defined rock domains had been devised.

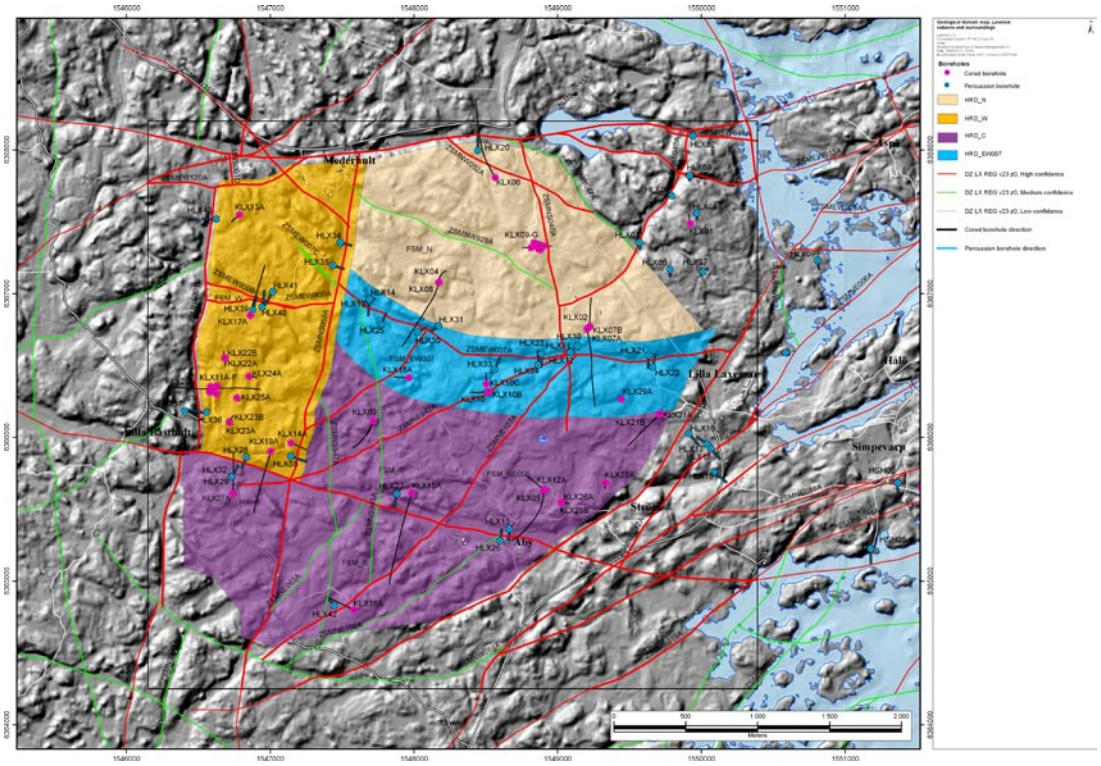

Figure 9-48. *The distribution of defined hydraulic rock domains (HRD) at the surface of the bedrock with cored and percussion drilled boreholes within the Laxemar sub-area.*

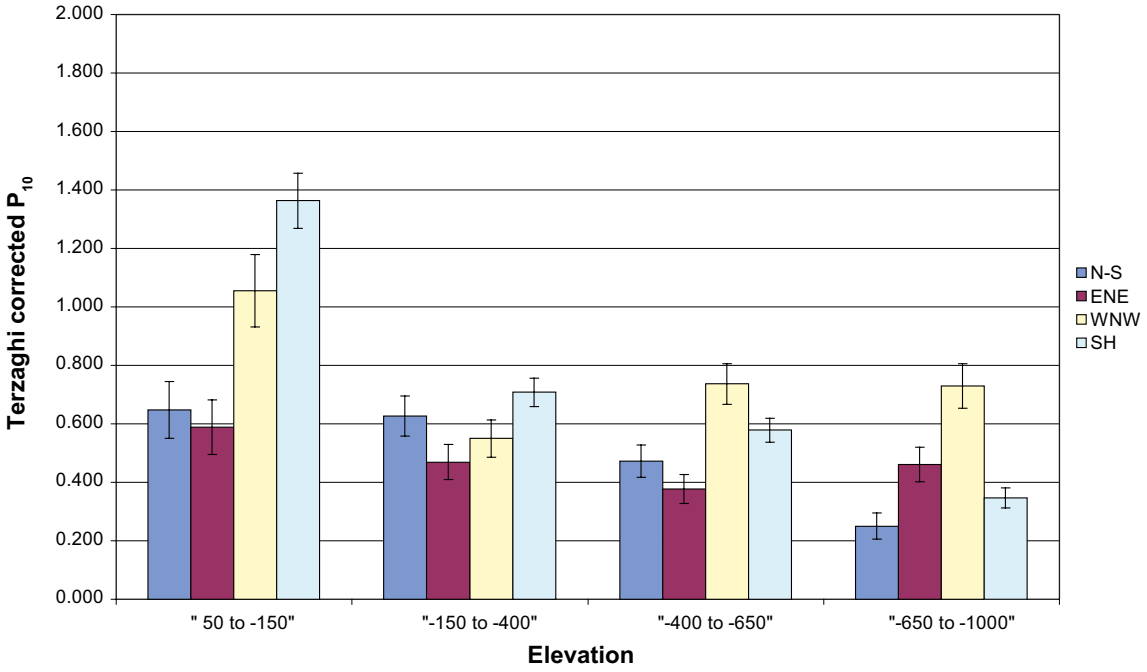

Figure 9-49. *Variation of the Terzaghi-corrected fracture intensity for OPO fractures with depth for the fully characterised sections of boreholes penetrating hydraulic rock domain HRD_C.*

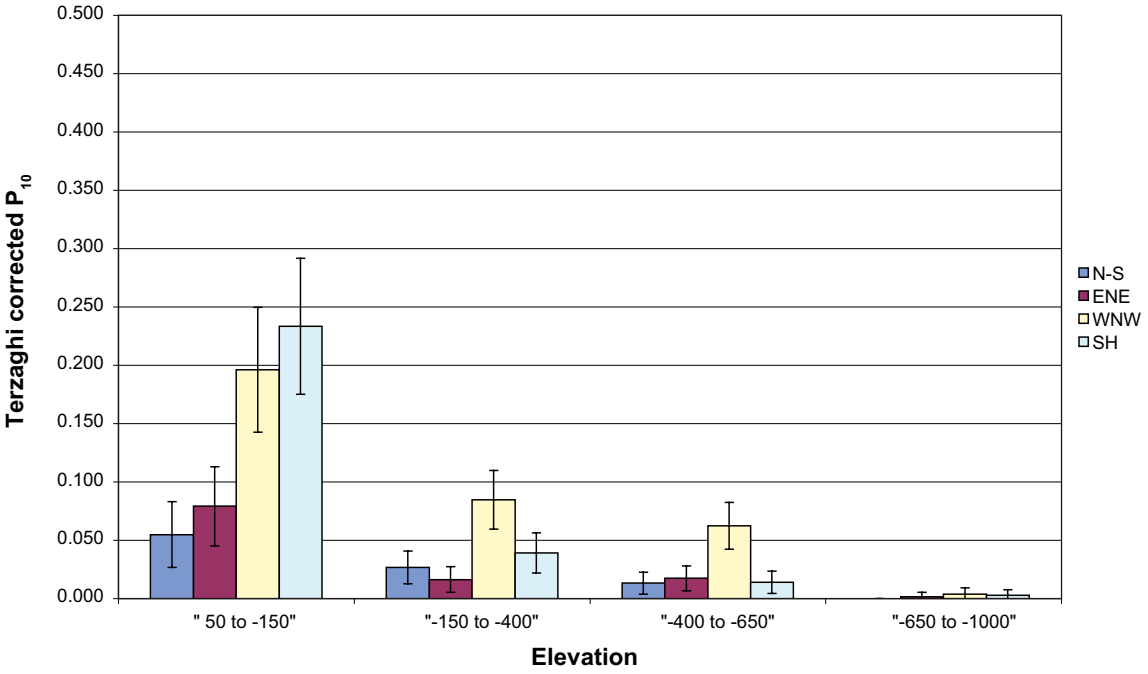

Figure 9-50. *Variation of the Terzaghi-corrected fracture intensity for PFL-f features with depth for the fully characterised sections of boreholes penetrating hydraulic rock domain HRD_C.*

9.4 Analysis of flowing features

This section analyses the flow measurements made by hydraulic testing and considers some confidence issues in using this data to construct a hydrogeological DFN.

9.4.1 Comparison of PFL and PSS transmissivity measurements

Transmissivities associated with borehole intervals have been measured in two ways: using the Posiva Flow Log (PFL) and using the Pipe String System (PSS) method. These two approaches measure different, but related quantities and are decribed in more detail in Chapter 4. In this section part of the analysis in Section 4.3.3 is expanded by dividing the data on HRDs and HCD.

In order to quantify any potential bias in using transmissivity values derived from the PFL method over the PSS method, Figure 9-51 to Figure 9-53 present comparisons of the transmissivities associated with borehole intervals obtained from PSS tests with the sum of the transmissivities of the flowing features detected by PFL crossing the interval. Borehole sections with deterministic deformation zones (HCD) are plotted separatly in Figure 9-51 to Figure 9-53, cf. Section 4.3 where all data are cross plotted. To aid interpretation, a red dashed line corresponding to equality of PFL and PSS transmissivity, and dashed lines corresponding to an order of magnitude difference are also plotted. The points along the vertical axis correspond to intervals for which a significant PSS transmissivity was obtained although the interval was not intersected by any flowing features detected by PFL. These points were plotted against an arbitrary PFL transmissivity of $1 \cdot 10^{-13}$ m^2/s. As discussed above, these points may be associated with isolated parts of the fracture network. The plots are generally in accord with the discussion above, lending support to the view that the transmissivities of the flowing features detected by PFL provide a better guide than the PSS transmissivities to the transmissivities of the fractures that form part of the interconnected network of flowing fractures, or at least, because of the measurement limit for flowing features detected by PFL, the most transmissive fractures in this network

The cross correlation was also separated on HRDs, see Figure 9-51 to Figure 9-53, but no systematic greater difference could be seen between the HRDs, except for HRD_N that indicated a minor difference.

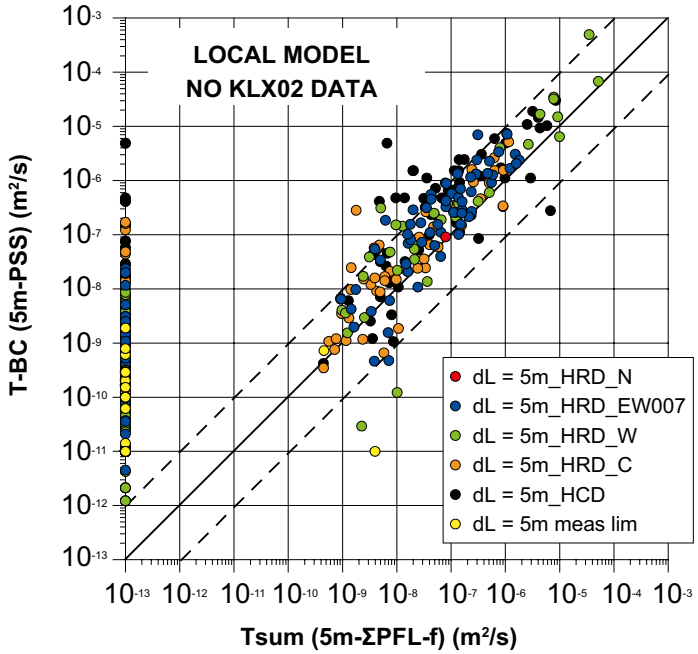

Figure 9-51. *Comparison of PSS transmissivities for 5 m intervals with the sum of the transmissivities of flowing features detected by PFL crossing the interval, for all boreholes.*

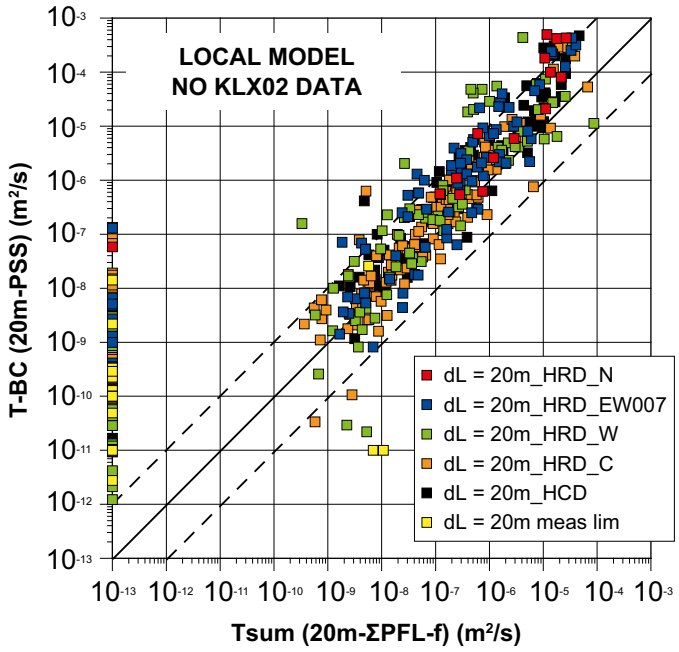

Figure 9-52. *Comparison of PSS transmissivities for 20 m intervals with the sum of the transmissivities of flowing features detected by PFL crossing the interval, for all boreholes.*

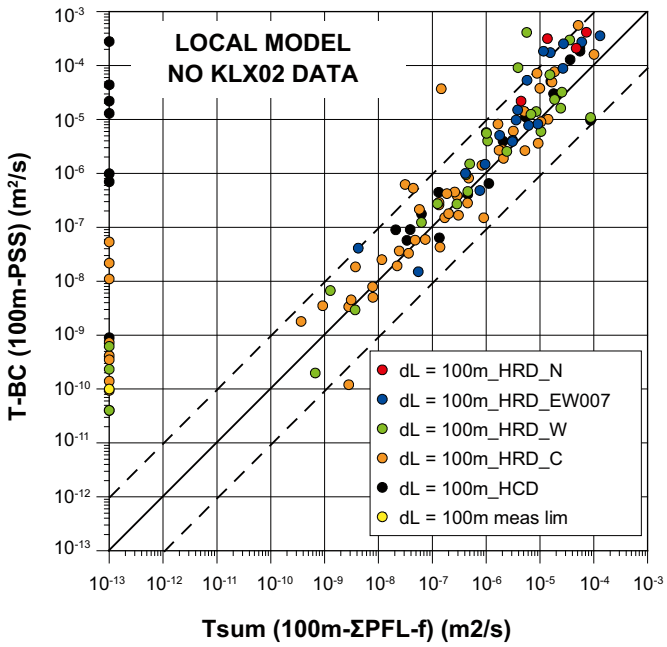

Figure 9-53. *Comparison of PSS transmissivities for 100 m intervals with the sum of the transmissivities of flowing features detected by PFL crossing the interval, for all boreholes.*

9.4.2 Orientation and statistics of flowing features

Figure 9-54 through Figure 9-57 show stereonet plots of the poles for flowing features detected by PFL coloured by interpreted transmissivity for each of the hydraulic rock domains. Although there is no absolute correlation of transmissivity with fracture set (both high and low values occurring in most fracture sets), there appear to be a higher density of high transmissivities in the WNW and SH sets. HRD_W stands out as being a bit different with a significant presence of flowing features in the N-S set in addition. These results would suggest significant hydraulic anisotropy.

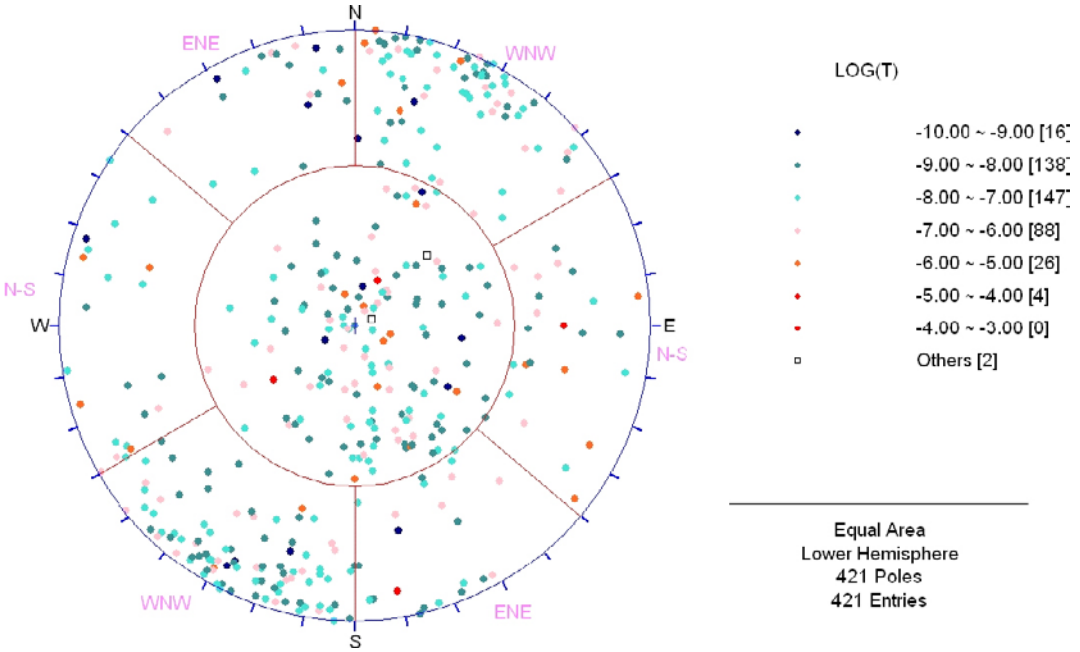

Figure 9-54. *Stereonet plot of the poles for flowing features detected by PFL coloured by transmissivity for sections of boreholes penetrating hydraulic rock domain HRD_EW007.*

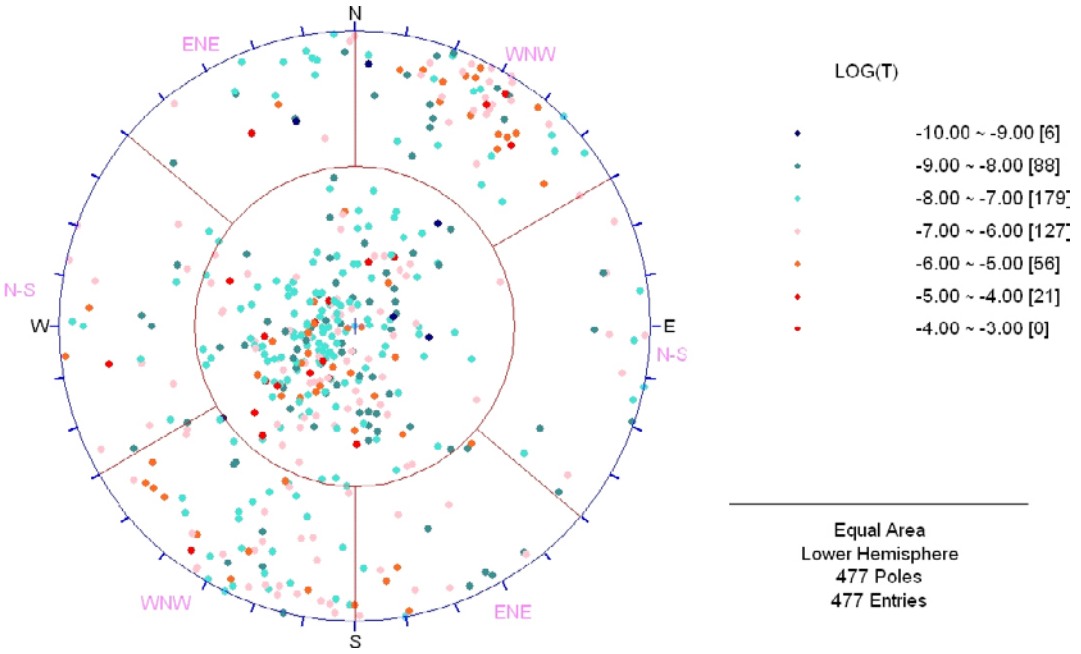

Figure 9-55. *Stereonet plot of the poles for flowing features detected by PFL coloured by transmissivity for sections of boreholes penetrating hydraulic rock domain HRD_N.*

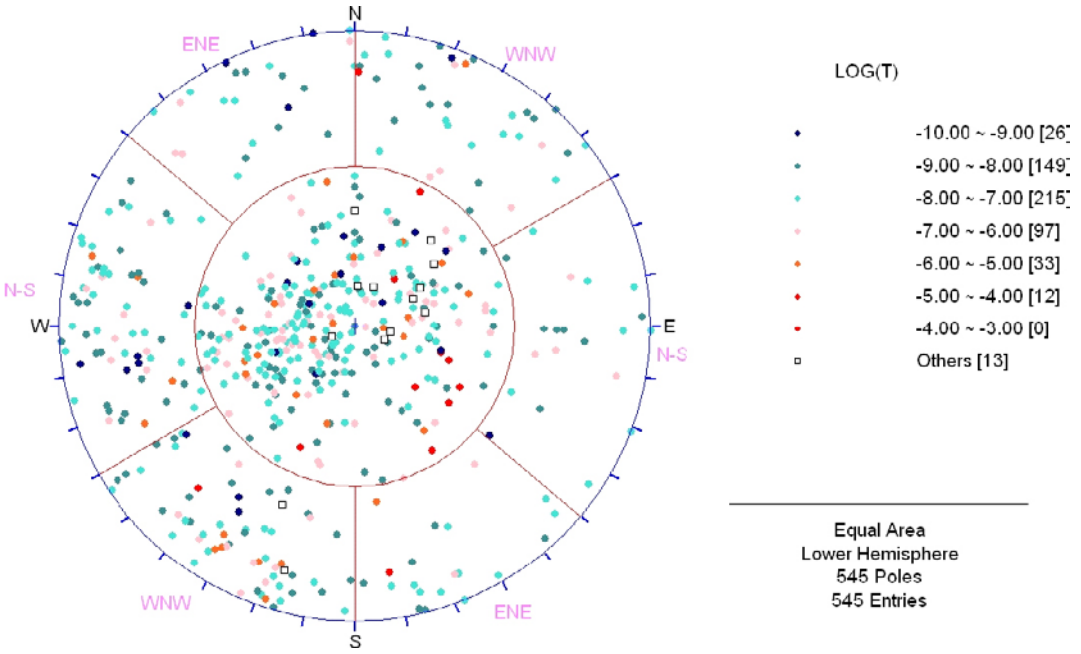

Figure 9-56. *Stereonet plot of the poles for flowing features detected by PFL coloured by transmissivity for sections of boreholes penetrating hydraulic rock domain HRD_W.*

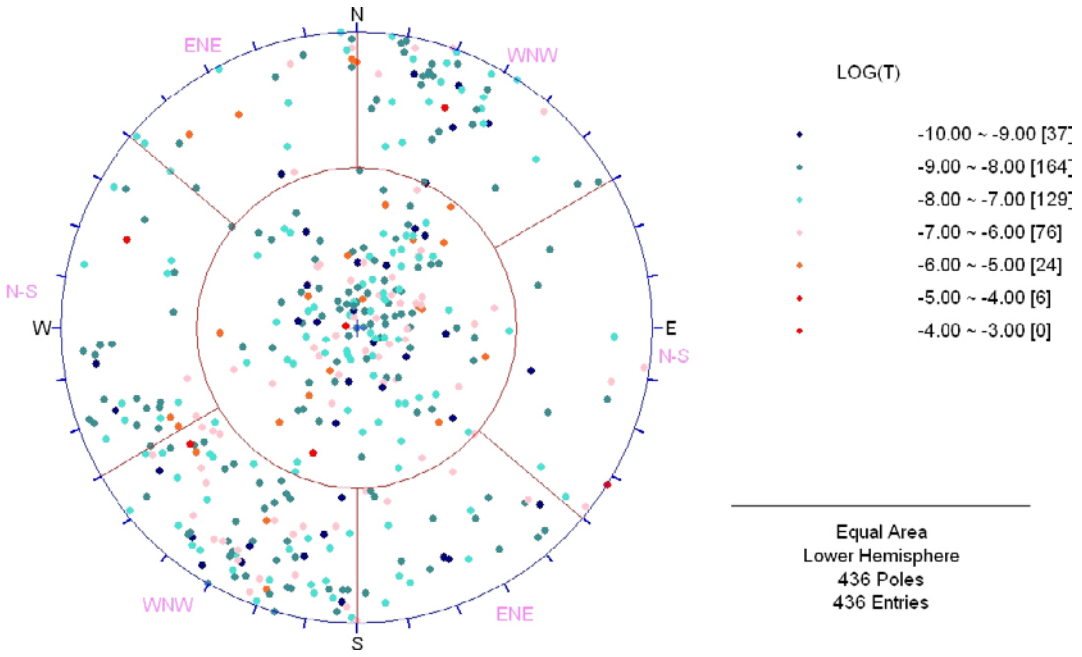

Figure 9-57. *Stereonet plot of the poles for flowing features detected by PFL coloured by transmissivity for sections of boreholes penetrating hydraulic rock domain HRD_C.*

The statistics of the transmissivity of the features carrying flow in each fracture domain and rock domain were also analysed, see Table 9-12. As discussed in Section 9.3.2, each local minor deformation zone (or crush zone) is regarded as being effectively a single feature in the overall distribution of features. The transmissivity of the feature local to a borehole is taken to be the sum of the transmissivities of the fractures within it that intersect the borehole. The first step in the analysis was therefore to calculate, for each local minor deformation zone, its effective transmissivity, that is, the sum of the transmissivities of the fractures within the zone. As indicated above, the PFL-f measurements are considered to provide the best information about the transmissivities of individual fractures. It should be noted that in some of the boreholes where the casing ends close to ground surface, then the drawdown during the abstraction in the borehole can de-water fractures within the very top of the boreholes leading to underestimation of the number of transmissive features near surface. Hence, the hydraulic conductivity of the very near-surface could be considerably higher than those given for the top depth zones given in Table 9-12.

Having combined the individual fractures within each local minor deformation zone and given an effective transmissivity, various intensity statistics of the features carrying flow were calculated and are presented in Table 9-13. It can be seen that, for all the rock subdivisions, the Terzaghi corrected fracture intensity (and the uncorrected fracture intensity) decrease with depth. The intensity is highest above –150 masl and markedly lower below –650 masl.

The sum of the transmissivities divided by the total borehole length involved (which is presented in Table 9-12) is a very crude measure of the hydraulic conductivity (K) of the rock. From the results presented in Table 9-12 it appears that all the rock subdivisions have similar hydraulic conductivity in the upper depth zone (i.e. above –150 masl), apart from RSMM01, which is about an order of magnitude less permeable. FSM_NE005 appears to be the least permeable rock subdivision at depths between –150 masl and –650 masl and FSM_N appears to be the most permeable rock subdivision at such depths. Generally, rock domain RSMM01 appears to be the least permeable of the defined rock domains. However, for RSMM01 below –650 masl elevation, the calculated value of the sum of transmissivities divided by the total borehole length involved is a very unreliable overall estimate of the sum of transmissivities divided by the total borehole length involved for the rock domain overall. This is because the estimate is obtained from the transmissivities of only two features. The very low value obtained might simply have arisen by chance, the two features in question having particularly low transmissivity; and a significantly higher value might be obtained were a greater length of borehole in RSMM01 to be considered. In terms of the HRDs, HRD_C is the least permeable, followed by HRD_W, then HRD_EW007, and NRD_N is the most permeable generally.

Table 9-12. Summary of transmissivity statistics of flowing features detected by PFL for the borehole intervals outside of interpreted deterministic deformation zones. MDZs are included in these statistics, but the transmissivity of individual PFL fractures are summed within an MDZ such that each is treated as a single feature. (Length = Mapped length – length deterministic DZ. Mapped borehole length is approximated with a straight line for each domain in the calculations.)

Domain	Depth zone (m)	Sum *T*/ Length (m/s)	Min T m^2/s)	Max *T* (m^2/s)	Mean log*T*	SD log*T*	Geometric mean (m^2/s)	Length (m)
FSM_	50 to –150	3.1E–07	4.4E–10	3.2E–05	–7.4	1.2	3.58E–08	279
EW007/	–150 to –400	1.2E–07	3.1E–10	3.7E–05	–7.5	0.9	3.0E–08	1,001
HRD_	–400 to –650	1.2E–08	7.9E–10	1.8E–06	–7.6	0.7	2.6E–08	843
EW007	–650 to –1,000	0.0E+00	0.0E+00	0.0E+00	N/A	N/A	N/A	213
FSM_	50 to –150	2.4E–07	3.9E–10	1.4E–05	–7.6	1.1	2.61E–08	371
NE005	–150 to –400	4.0E–09	3.7E–10	1.2E–06	–8.2	0.7	6.9E–09	806
	–400 to –650	2.2E–09	3.3E–10	8.1E–07	–8.1	0.9	8.5E–09	615
	–650 to –1,000	1.6E–10	1.5E–09	6.1E–08	–8.3	0.5	5.5E–09	434
FSM_N/	50 to –150	6.7E–07	7.7E–10	6.5E–05	–6.9	1.0	1.14E–07	933
HRD_N	–150 to –400	2.1E–07	8.3E–10	3.6E–05	–7.1	1.0	7.4E–08	608
	–400 to –650	1.5E–08	1.1E–09	5.2E–06	–7.8	0.9	1.6E–08	441
	–650 to –1,000	4.1E–10	1.3E–09	2.6E–08	–8.3	0.2	4.6E–09	177
FSM_C	50 to –150	1.0E–07	2.4E–09	9.4E–06	–7.4	0.8	3.74E–08	204
	–150 to –400	3.4E–08	4.1E–10	1.2E–05	–7.8	1.2	1.4E–08	579
	–400 to –650	4.2E–09	3.9E–10	1.1E–06	–8.1	0.9	8.4E–09	1,040
	–650 to –1,000	7.3E–10	1.4E–08	4.4E–07	–7.0	0.4	9.4E–08	950
FSM_W/	50 to –150	2.8E–07	3.7E–10	4.6E–05	–7.5	1.0	4.39E–08	1,282
HRD_W	–150 to –400	2.9E–08	1.1E–09	1.0E–05	–7.9	1.2	1.4E–08	904
	–400 to –650	2.8E–08	6.7E–10	9.2E–06	–7.5	1.4	2.9E–08	677
	–650 to –1,000	1.4E–11	3.7E–09	3.7E–09	–8.4	N/A	3.7E–09	272
FSM_S	50 to –150	2.9E–07	1.3E–10	3.8E–05	–6.8	0.6	1.77E–07	166
	–150 to –400	1.9E–07	3.8E–09	6.7E–06	–7.6	1.0	2.4E–08	65
	–400 to –650	N/A	N/A	N/A	N/A	N/A	N/A	N/A
	–650 to –1,000	N/A	N/A	N/A	N/A	N/A	N/A	N/A
RSMA01	50 to –150	6.3E–07	4.4E–10	6.5E–05	–7.0	1.1	1.07E–07	1,228
	–150 to –400	1.4E–07	5.6E–10	3.7E–05	–7.4	0.9	4.4E–08	1,699
	–400 to –650	1.2E–08	3.9E–10	5.2E–06	–7.8	0.9	1.6E–08	1,710
	–650 to –1,000	3.7E–10	1.3E–09	1.7E–07	–8.2	0.5	7.0E–09	817
RSMD01	50 to –150	2.9E–07	3.7E–10	4.6E–05	–7.5	1.0	4.79E–08	1,470
	–150 to –400	2.7E–08	7.6E–10	1.0E–05	–7.8	1.0	1.4E–08	1,023
	–400 to –650	1.7E–08	3.3E–10	9.2E–06	–7.7	1.3	2.0E–08	1,222
	–650 to –1,000	4.8E–10	2.8E–09	4.4E–07	–7.9	0.9	1.2E–08	967
RSMM01	50 to –150	5.0E–08	3.9E–10	5.8E–06	–7.8	0.8	1.46E–08	537
	–150 to –400	2.8E–08	3.1E–10	1.2E–05	–8.1	1.0	8.2E–09	1,196
	–400 to –650	1.6E–09	7.9E–10	3.7E–07	–7.9	0.5	1.3E–08	685
	–650 to –1,000	2.8E–10	7.4E–08	7.4E–08	–7.1	N/A	7.4E–08	263
HRD_C	50 to –150	2.1E–07	3.9E–10	3.8E–05	–7.5	1.1	3.33E–08	741
	–150 to –400	2.4E–08	3.7E–10	1.2E–05	–8.0	0.9	1.1E–08	1,451
	–400 to –650	3.4E–09	3.3E–10	1.1E–06	–8.1	0.9	8.5E–09	1,655
	–650 to –1,000	5.5E–10	1.5E–09	4.4E–07	–7.6	0.8	2.3E–08	1,384

Table 9-13. Summary of intensity statistics of flowing features detected by PFL for the borehole intervals outside of interpreted deterministic deformation zones. MDZ are included in these statistics, but the numbers of individual PFL-f features are summed up within an MDZ such that each is treated as one single feature. (Length = Mapped length – length deterministic DZ. Mapped borehole length is approximated with a straight line for each domain in the calculations.)

Domain	Depth zone (m)	Length	Count	PFL $P_{10,corr}$ (m^{-1})	PFL P_{10} (m^{-1})
FSM_	50 to –150	279	107	0.816	0.384
EW007/	–150 to –400	1,001	241	0.550	0.241
HRD_	–400 to –650	843	72	0.225	0.085
EW007	–650 to –1,000	213	0	0.000	0.000
SM_	50 to –150	371	167	0.820	0.451
NE005	–150 to –400	806	62	0.169	0.077
	–400 to –650	615	17	0.071	0.028
	–650 to –1,000	434	4	0.013	0.009
FSM_N/	50 to –150	933	331	0.773	0.355
HRD_N	–150 to –400	608	115	0.339	0.189
	–400 to –650	441	20	0.115	0.0385
	–650 to –1,000	177	9	0.082	0.051
FSM_C	50 to –150	204	48	0.350	0.235
	–150 to –400	579	40	0.103	0.069
	–400 to –650	1,040	51	0.129	0.0389
	–650 to –1,000	950	4	0.006	0.004
FSM_W/	50 to –150	1,282	379	0.499	0.296
HRD_W	–150 to –400	904	33	0.078	0.037
	–400 to –650	677	23	0.060	0.034
	–650 to –1,000	272	1	0.005	0.004
FSM_S	50 to –150	166	21	0.254	0.126
	–150 to –400	65	20	0.655	0.308
	–400 to –650	N/A	N/A	N/A	N/A
	–650 to –1,000	N/A	N/A	N/A	N/A
RSMA01	50 to –150	1,228	442	0.756	0.360
	–150 to –400	1,699	347	0.431	0.204
	–400 to –650	1,710	119	0.194	0.070
	–650 to –1,000	817	12	0.023	0.015
RSMD01	50 to –150	1,470	429	0.494	0.292
	–150 to –400	1,023	58	0.114	0.057
	–400 to –650	1,222	37	0.057	0.030
	–650 to –1,000	967	5	0.007	0.005
RSMM01	50 to –150	537	182	0.656	0.339
	–150 to –400	1,196	106	0.180	0.089
	–400 to –650	685	27	0.088	0.039
	–650 to –1,000	263	1	0.008	0.004
HRD_C	50 to –150	741	236	0.564	0.319
	–150 to –400	1,451	122	0.164	0.084
	–400 to –650	1,655	68	0.107	0.0381
	–650 to –1,000	1,384	8	0.008	0.006

The hydraulic conductivities below –650 masl elevation are the most variable, perhaps to lower statistical significance, although only in HRD_EW007 is it greater than 10^{-9} m/s.

For the needs of different end users, Table 9-14 collates Table 9-12 and Table 9-13 in a different format.

Table 9-14. Selected statistics of flowing features detected by PFL for the borehole intervals outside of interpreted deterministic deformation zones. (Note that each MDZ is considered to be a single feature, even if it corresponds to several PFL within a borehole.) (Length = Mapped length – length deterministic DZ. Mapped borehole length is approximated with a straight line for each domain in the calculations.)

Domain	Depth zone (m)	Length	PFL $P_{10,corr}$ (m^{-1})	Sum *T* / L	Min T (m^2/s)	Max *T* (m^2/s)
FSM_	50 to –150	279	0.816	3.1E–07	4.4E–10	3.2E–05
EW007/	–150 to –400	1,001	0.550	1.2E–07	3.1E–10	3.7E–05
HRD_	–400 to –650	843	0.225	1.2E–08	7.9E–10	1.8E–06
EW007	–650 to –1,000	213	0.000	0.0E+00	0.0E+00	0.0E+00
FSM_	50 to –150	371	0.820	2.4E–07	3.9E–10	1.4E–05
NE005	–150 to –400	806	0.169	4.0E–09	3.7E–10	1.2E–06
	–400 to –650	615	0.071	2.2E–09	3.3E–10	8.1E–07
	–650 to –1,000	434	0.013	1.6E–10	1.5E–09	6.1E–08
FSM_N/	50 to –150	933	0.773	6.7E–07	7.7E–10	6.5E–05
HRD_N	–150 to –400	608	0.339	2.1E–07	8.3E–10	3.6E–05
	–400 to –650	441	0.115	1.5E–08	1.1E–09	5.2E–06
	–650 to –1,000	177	0.082	4.1E–10	1.3E–09	2.6E–08
FSM_C	50 to –150	204	0.350	1.0E–07	2.4E–09	9.4E–06
	–150 to –400	579	0.103	3.4E–08	4.1E–10	1.2E–05
	–400 to –650	1,040	0.129	4.2E–09	3.9E–10	1.1E–06
	–650 to –1,000	950	0.006	7.3E–10	1.4E–08	4.4E–07
FSM_W/	50 to –150	1,282	0.499	2.8E–07	3.7E–10	4.6E–05
HRD_W	–150 to –400	904	0.078	2.9E–08	1.1E–09	1.0E–05
	–400 to –650	677	0.060	2.8E–08	6.7E–10	9.2E–06
	–650 to –1,000	272	0.005	1.4E–11	3.7E–09	3.7E–09
FSM_S	50 to –150	166	0.254	2.9E–07	1.3E–10	3.8E–05
	–150 to –400	65	0.655	1.9E–07	3.3E–11	6.7E–06
	–400 to –650	N/A	N/A	N/A	N/A	N/A
	–650 to –1,000	N/A	N/A	N/A	N/A	N/A
RSMA01	50 to –150	1,228	0.756	6.3E–07	4.4E–10	6.5E–05
	–150 to –400	1,699	0.432	1.4E–07	5.6E–10	3.7E–05
	–400 to –650	1,710	0.193	1.2E–08	3.9E–10	5.2E–06
	–650 to –1,000	817	0.023	3.7E–10	1.3E–09	1.7E–07
RSMD01	50 to –150	1,470	0.494	2.9E–07	3.7E–10	4.6E–05
	–150 to –400	1,023	0.114	2.7E–08	7.6E–10	1.0E–05
	–400 to –650	1,222	0.057	1.7E–08	3.3E–10	9.2E–06
	–650 to –1,000	967	0.007	4.8E–10	2.8E–09	4.4E–07
RSMM01	50 to –150	537	0.656	5.5E–08	3.9E–10	5.8E–06
	–150 to –400	1,196	0.180	2.8E–08	3.1E–10	1.2E–05
	–400 to –650	685	0.088	1.6E–09	7.9E–10	3.7E–07
	–650 to –1,000	263	0.008	2.8E–10	7.4E–08	7.4E–08
HRD_C	50 to –150	741	0.564	2.1E–07	3.9E–10	3.8E–05
	–150 to –400	1,451	0.164	2.4E–08	3.7E–10	1.2E–05
	–400 to –650	1,655	0.107	3.4E–09	3.3E–10	1.1E–06
	–650 to –1,000	1,384	0.008	5.5E–10	1.5E–09	4.4E–07

One interesting observation is that the geometric mean transmissivity does not show a clear depth trend (generally log$T$ (m^2/s) ~ –8 to –7.5), although the maximum value of T does tend to decrease with depth. The main reason for the reduction in hydraulic conductivity with depth then is due to a decrease in the intensity of flowing features above the measurement limit for the PFL (PFL $P_{10,corr}$) rather than in the transmissivity of individual flowing features.

9.5 Summary of fracture and PFL-f data analysis

The key findings of this analysis to derive basic statistical measures of flowing fracture intensity and transmissivity detected by the PFL method are:

- Revised hard sector fracture set definitions have been developed on the basis of the borehole fracture mapping. The revised sets, which are broadly consistent with the subdivisions adopted in the geological DFN /La Pointe et al. 2008/, consist of WNW, ENE and N-S striking sets and a subhorizontal set.
- There are significant variations in fracture intensity between different boreholes, indicating variation in fracture intensity with location. There does not appear to be any obvious structure to this variation.
- There are significant variations in fracture intensity between the different fracture sets. The WNW striking set generally has the largest fracture intensity.
- The fracture intensity for all fractures, OPO fractures and OPO-CP fractures does not show a significant trend with depth for most of the rock subdivisions, although for the OPO fractures in the FSM_W Fracture Domain, there appears to be a slight decrease in fracture intensity with depth.
- For all rock subdivisions, there is a significant decrease with depth in fracture intensity for PFL-f features. The intensity is highest above about –150 masl, is somewhat lower at elevations down to about –650 masl, and is considerably lower at depths below about –650 masl. An extra division between –150 masl and –650 masl at –400 masl is made to better resolve the gradual decrease in both intensity of PFL-f features and transmissivity with depth toward repository depth at around –500 masl.
- On the basis of the above (and depth trends in the geometric mean transmissivity), it was decided that for the hydrogeological DFN model, it would be sensible to work in terms of four depth zones (defined in terms of elevation):
  - down to –150 masl,
  - –150 masl to –400 masl,
  - –400 masl to –650 masl,
  - below –650 masl.
- The subdivision of rock according to fracture subdomains was used as the basis for defining an appropriate subdivision for the hydrogeological DFN model into the following 4 hydraulic rock domains (HRD):
  - HRD_EW007 corresponding to FSM_EW007,
  - HRD_N corresponding to FSM_N,
  - HRD_W corresponding to FSM_W,
  - HRD_C corresponding to a combination of FSM_C, FSM_NE005 and FSM_S.
- It is recommended that the subset of OPO fractures be used as an estimate of potentially water-conducting fractures, although the correspondence between geological characterisation of the core and hydraulic testing is sufficiently erratic between boreholes to consider a more pessimistic scenario where only OPO-CP fractures are potentially water-conducting as a variant.
- There is some correlation between the occurence of high transmissivity values with the WNW and SH sets for all rock subdivisions, and with some high transmissivities in the N-S set for HRD_W.
- Rock domain RSMM01 appears to be the least permeable of the rock domains.

- Fracture Domain FSM_NE005 appears to be the least permeable of the fracture domains, and FSM_N appears to be the most permeable.
- The transmissivities of the flowing features detected by the PFL method provide a more realistic indication of the connected open fracture network than the PSS method, or at least, because of the measurement limit for PFL method, for flows through the most transmissive fractures in this network.

A summary of the files used in this analysis are included in Appendix 5, Section A.5.3 for traceability and quality assurance purposes.

9.6 Hydraulic conductivity in test scales 100, 20 and 5 m

A large number of *in situ* tests have been performed in packed-off borehole sections at test scale 100, 20 or 5 m, using PSS, HTHB, or tests with similar methods employing older equipment in coreholes and percussion holes. These tests have been divided in three groups; "HCD": Test sections that includes one or several HCDs, "HRD": Test sections that includes HRD but no HCDs, "All": including all tests (both HRD and HCD). The data are based on the so called best Choice (BC) transmissivites, mainly based on transient evaluation. The methodologies for the tests providing the data are described in Chapter 4.

The depth zones used in the hydrogeological DFN model, cf. Section 9.5, have been used for analysing possible depth dependence in the test data; > –150 m, –150– to –400 m, –400 to –650 m, < –650 m.

The estimation of distribution characteristics is based on the assumption of a lognormal distribution and censored data are taken into account to provide distributions that fit the values above the measurement limit in an appropriate way (see e.g. /Helsel 2004/ and /Jensen et al. 2000/).

Statistics are provided based on regional model data and in some cases on local model data. The use of regional model data yields a better statistical support as the sample becomes larger. The difference between the regional and local model model data is discussed below. Results are presented in a number of tables in Appendix 9.

In the Figure 9-72 and similar figures with fitted line and a confidence band the "95% CI" means that the confidence interval is 95% for the fitted line.

9.6.1 Test scale 100 m

In total 304 tests of test scale 100 m are available. The statistics and trend models are shown in Figure 9-58 to Figure 9-61 and are summarised in tables in Appendix 9. The figures clearly indicate that there exists depth trends, and looking at Figure 9-60 it is evident that the average hydraulic conductivity is c. 10 times higher in HCDs than in the rock mass. This difference could possibly constitute an underestimation of the difference given that the data set "HCD" for 100 m test sections also includes sections of rock in between the defined deterministic deformation zones, but a comparison with results shown in Chapter 7 (Figure 7-23 and Figure 7-24) indicates a quite similar picture concerning the HCD properties.

The basic trend models for hydraulic conductivity (K) shown in the figures, are tabulated in Appendix 9.

9.6.2 Test scale 20 m

A total of 775 test results of test scale 20 m are available. The associated statistics are shown in Appendix 9.

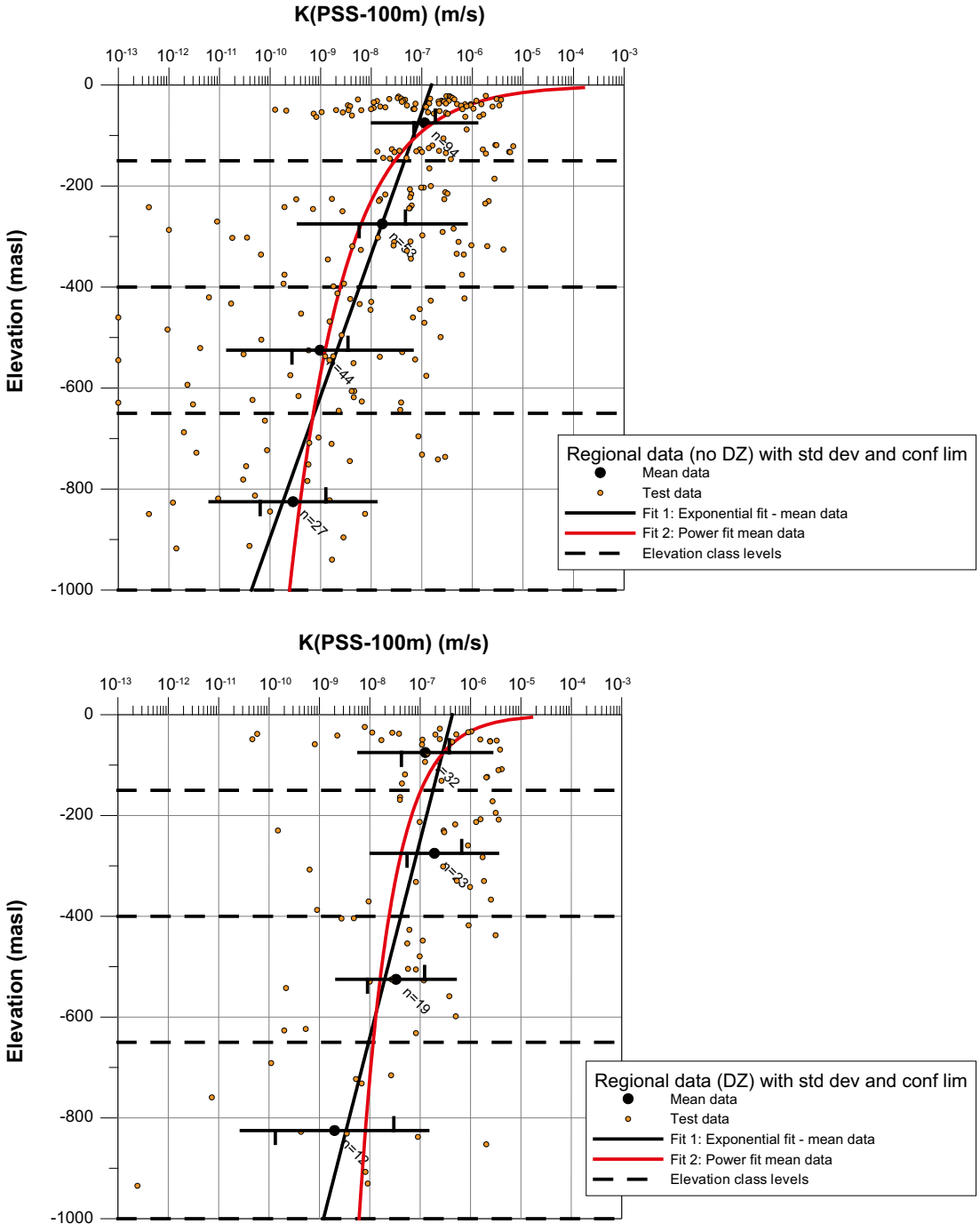

Figure 9-58. *Hydraulic conductivity (K) for test scale 100 m versus elevation. Top: Data from test sections between deterministic deformation zones (DZ). Bottom: Data from test sections including one or more HCD. For the defined depth intervals; geometric mean K, confidence limits for mean log10(K)(vertical bars on horizontal line) and ±1 standard deviation log10(K) (entire horizontal line) are plotted. Curves are fitted to the calculated four geometric mean values and all data, respectively.*

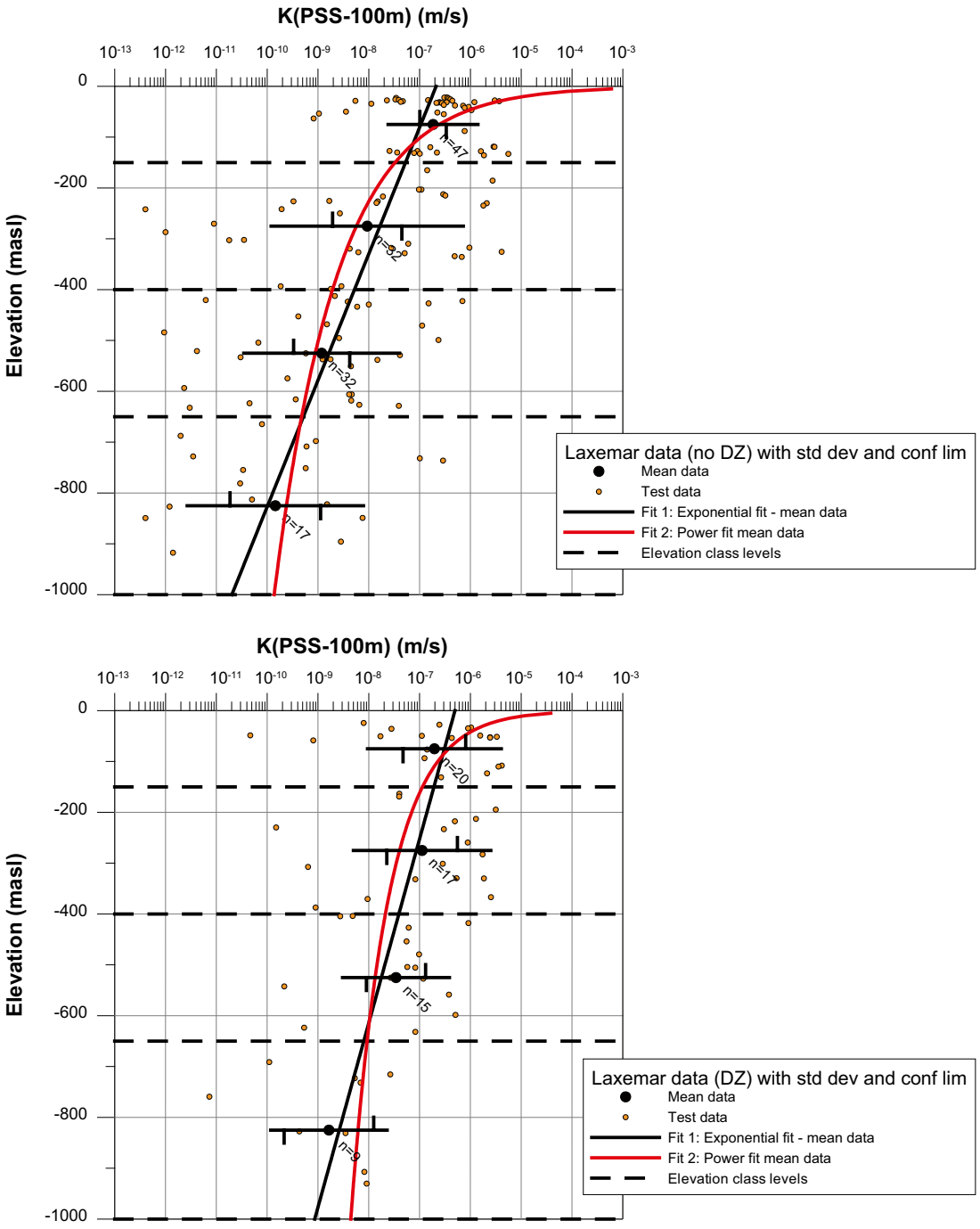

Figure 9-59. *Hydraulic conductivity (K) for test scale 100 m versus elevation. Top: Data from test sections between deterministic deformation zones (DZ). Bottom: Data from test sections including one or more HCD. For the defined depth zones; geometric mean K, confidence limits for mean log10(K)(vertical bars on horizontal line) and ±1 standard deviation log10(K) (entire horizontal line) are plotted. Curves are fitted to the calculated four geometric mean values and all data, respectively.*

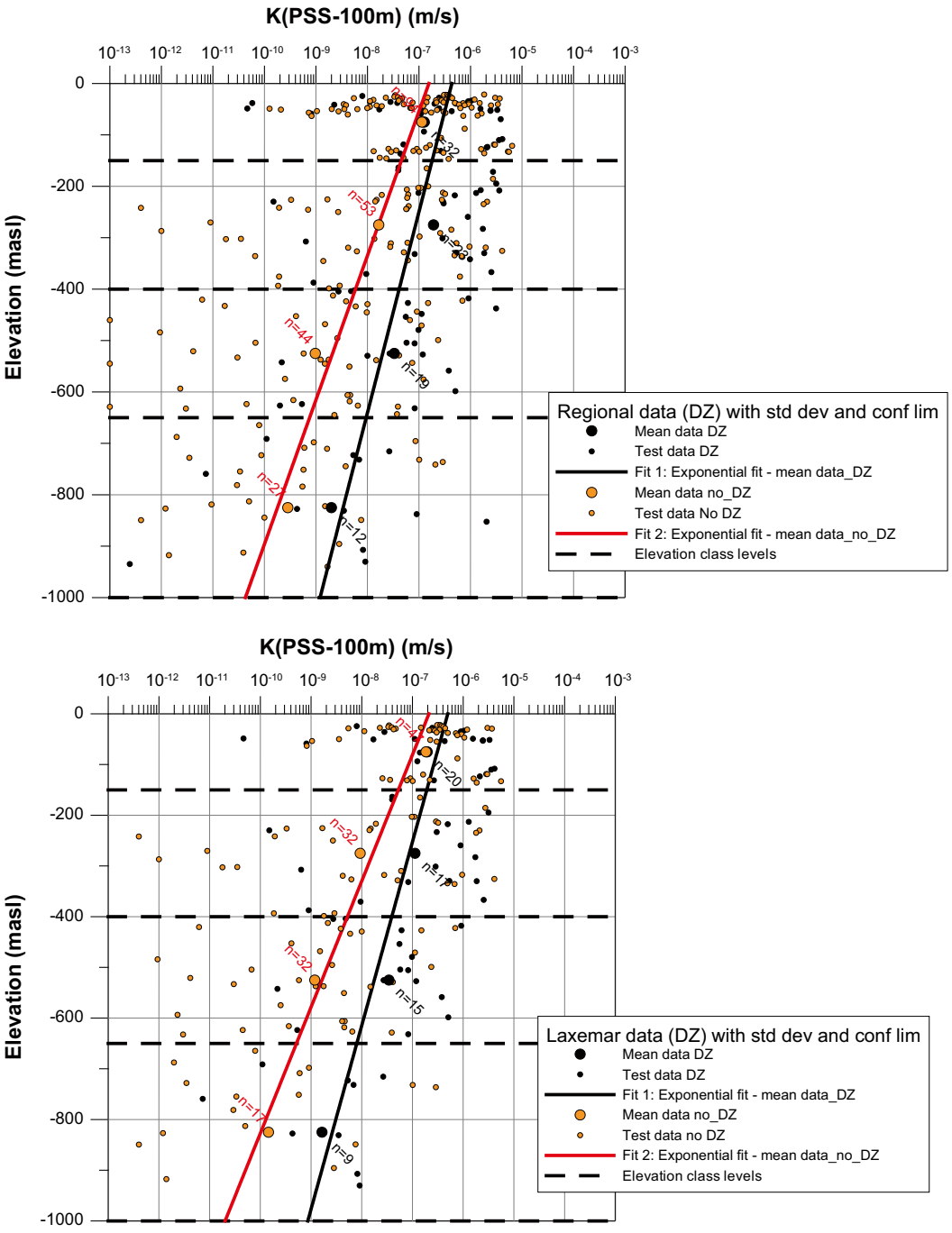

Figure 9-60. *Hydraulic conductivity (K) for test scale 100 m versus elevation. K shown from test sections between deterministic deformation zones (DZ) and test sections intersected by a HCD. Top: regional model. Bottom: local model. For depth intervals; geometric mean K, confidence limits for mean log10(K)(vertical bars on horizontal line) and ±1 standard deviation log10(K) (entire horizontal line) are plotted. Curves are fitted to the 4 geometric mean values or all data.*

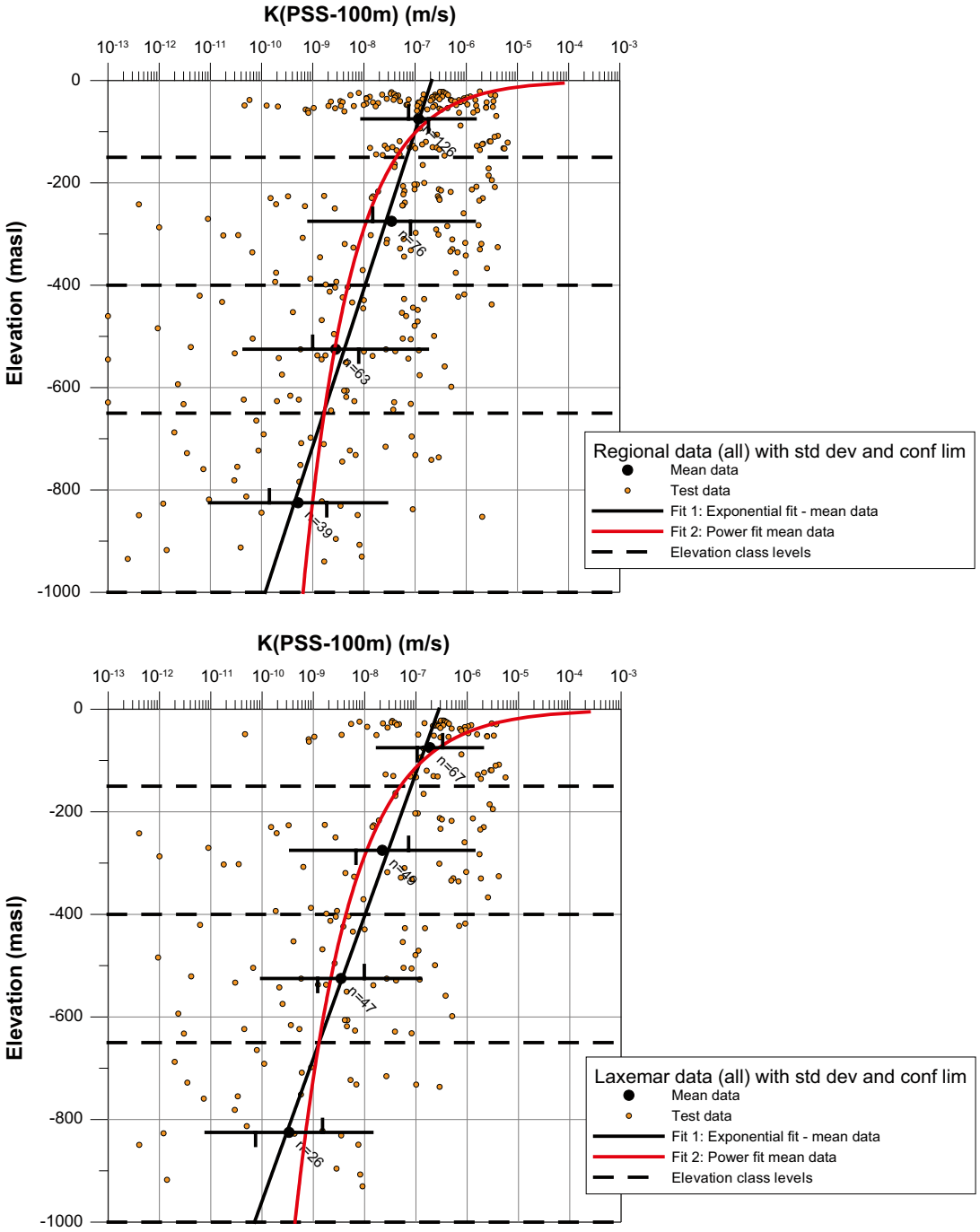

Figure 9-61. *Hydraulic conductivity (K) for test scale 100 m versus elevation. Top: Data from test sections between deterministic deformation zones (DZ). Bottom: Data from test sections including one or more HCD. For the defined depth intervals; geometric mean K, confidence limits for mean log10(K)(vertical bars on horizontal line) and ±1 standard deviation log10(K) (entire horizontal line) are plotted. Curves are fitted to the calculated four geometric mean values and all data, respectively.*

9.6.3 Test scale 5 m

A total of 898 test results of test scale 5 m are available. The associated statistics are shown in Appendix 9. As almost all tests in 5 m test scale have been performed between elevation –300 m and –700 m, the statistics based on the few samples above elevation –150 m and below –650 m are considered very uncertain.

9.6.4 Summary of observations related to test scales

As can be seen from Figure 9-62 through Figure 9-67, in general the geometric mean hydraulic conductivity increases and the standard deviation for $Log_{10}(K)$ decreases with increasing test scale. As there are very few measurements above elevation –150 m and below –650 m, these data have been excluded in the plots. In the depth zone –150 to –400 m, the test scale 5 m generally covers only part of the depth zone, but still the samples are quite large.

It seems that the difference between calculated means and standard deviations of hydraulic conductivity within each depth zone are similar between test scales but especially the geometric mean hydraulic conductivity decreases with depth. The geometric mean hydraulic conductivity (mean Log10(K-PSS) and the standard deviation of Log10(K-PSS) were therefore normalised by dividing the means and standard deviations with corresponding values for test scale 100 m. The results are shown in Figure 9-68 through Figure 9-70. From these figures one can see that the geometric mean increases c. two orders of magnitude going from test scale 5 m to 100 m. Similar behaviour is seen in the data representing deformation zones but the geometric mean increases c. one order of magnitude going from test scale 5 m to 100 m. This type of general behaviour was also noticed by /Rhén et al. 1997/ but the noted increase was less than that reported here.

In those cases where regional and local statistics can be compared it is shown that quite similar statistics for the two data sets are obtained. It is thus proposed that regional scale statistics are assumed valid also for the local model volume for those cases discussed below where only statistics for the regional model are available.

The scale effect seen in geometric mean depends mainly on the fact that it is more likely that one feature with high transmissivity will occur within a long test section compared to a short one. With the positive correlation between transmissivity and storage cofficient indicated in Section 7.6 and that the fact that most tests exhibit radial flow conditions at end of full test time, cf. Section 4.3.2, the radius of influence for the evaluated transmissivities is assumed to increase with increasing transmissivity. Thus, a large transmissity value can generally be assumed to be coupled to a large hydraulic feature.

As was discussed in Chapter 4, some of the lower transmissivities (below c. 10^{-8} m^2/s) obtained with the PSS method probably represent local clusters (compartments) of fractures that are not hydraulically connected, or at least not well-connected, to the surroundings. PFL-f features that are observed are by necessity part of a larger connected fracture system, and fractures belonging to the former isolated compartments cannot be observed using PFL. It was also concluded in Chapter 4 that PSS tests indicate on average slight higher transmissivities than corresponding sum of PFL-f features but overall the cross correlation of values above the two methods' measurement limitss show a fair correspondence. This probabaly means that the geometric mean values are slight overestimated if one considers the larger connected fracture systems for test scale 5 and 20 m. in this section possiby slightly The geometric means for 100 m scale are proabaly correct for lager connected fracture systems, as there frequently are fractures with higher transmissivities (with fairly large radius of influence) within the test sections and hardly any test sections show values below the measurement limit. Most likely the 100 m tests are testing some fractures belonging to hydraulically connected fractures within a large volume.

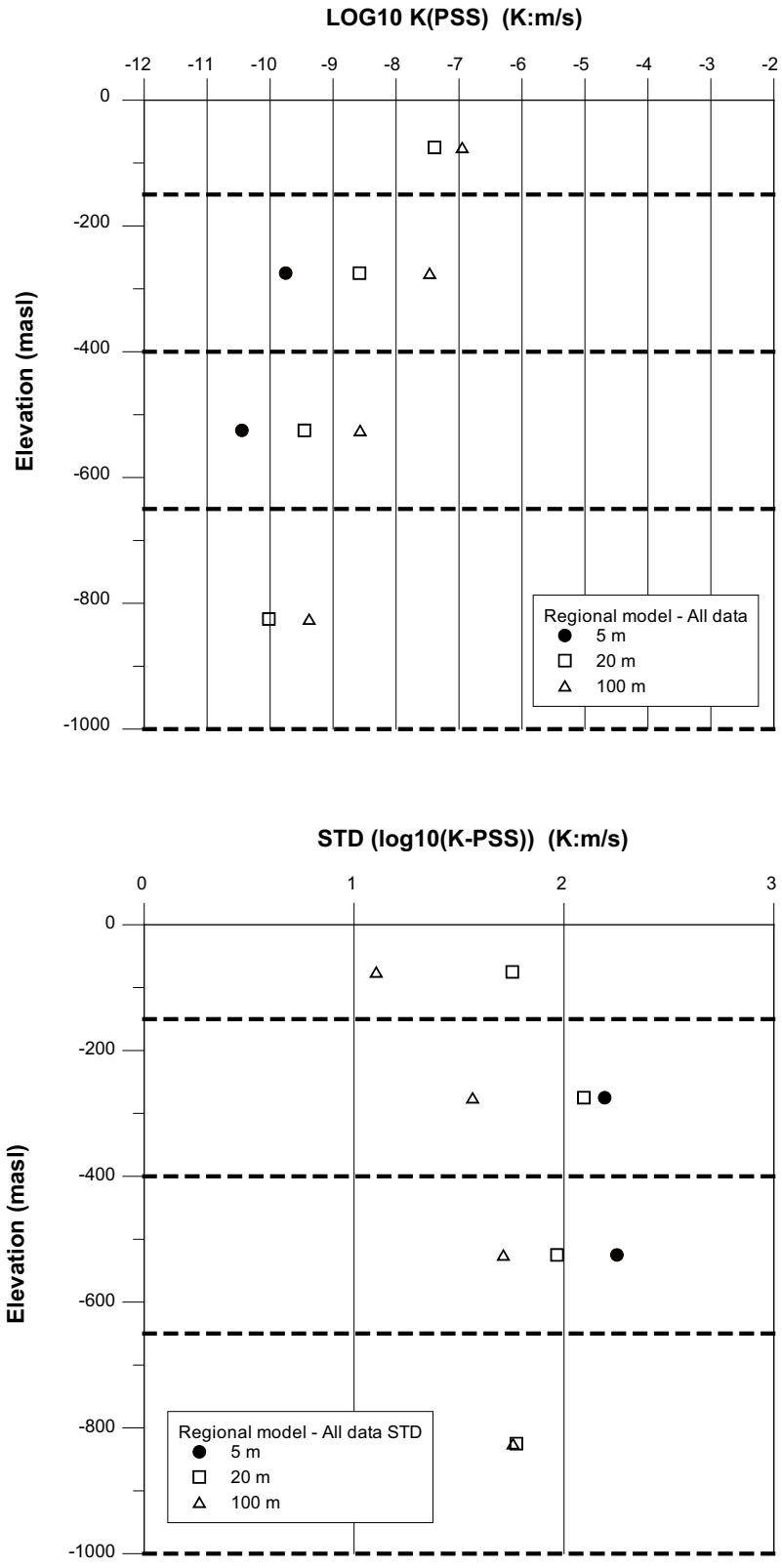

Figure 9-62. *Results for all data samples in test scales 100, 20 and 5 m. Statistics for depth intervals. Top: mean of log10(K), bottom standrad deviation of log10(K). Based on All data and regional model volume cf. Appendix 9.*

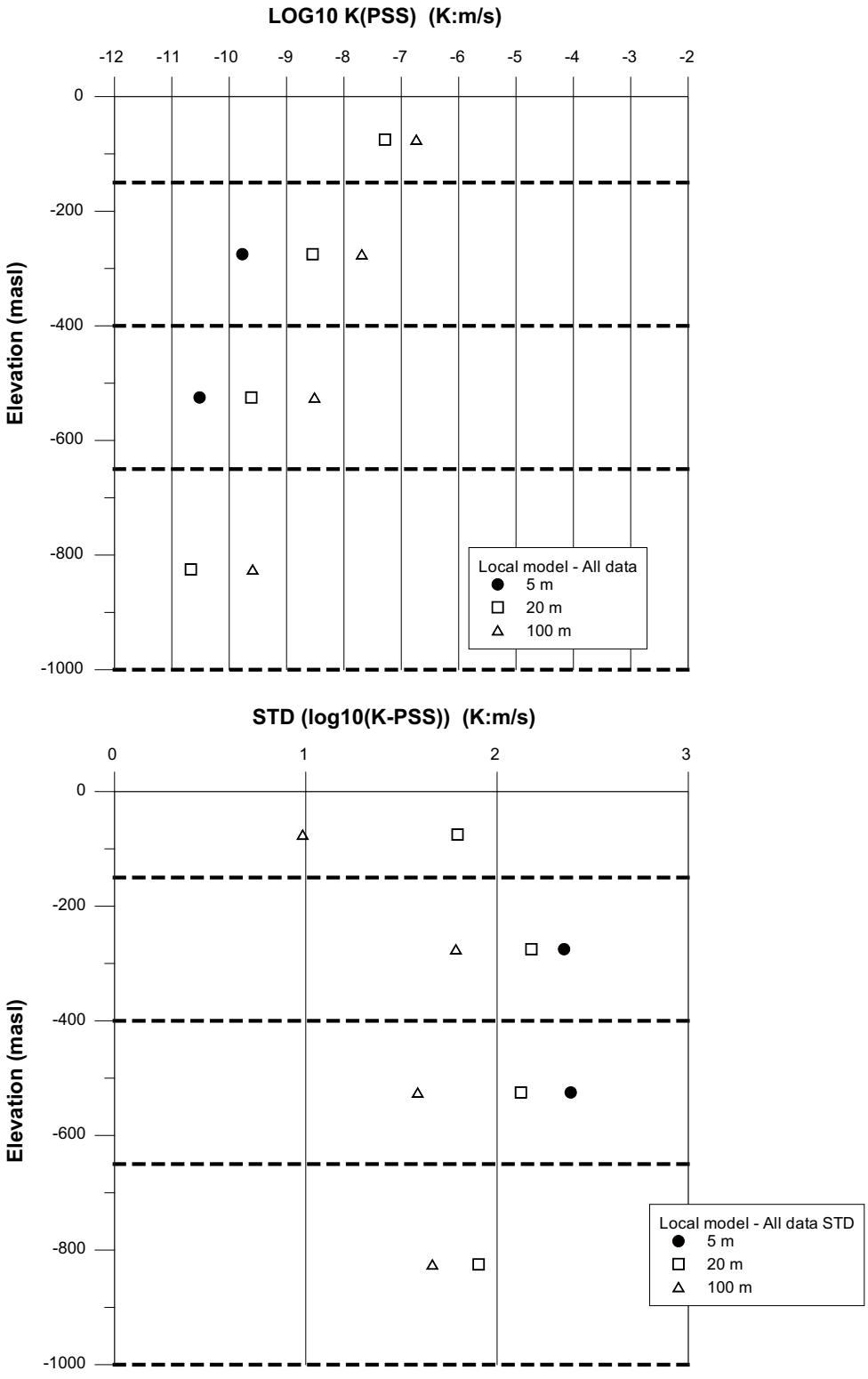

Figure 9-63. *Results for all data samples in test scales 100, 20 and 5 m. Statistics for depth intervals. Top: mean of log10(K), bottom standard deviation of log10(K). Based on All data and local model volume cf. Appendix 9.*

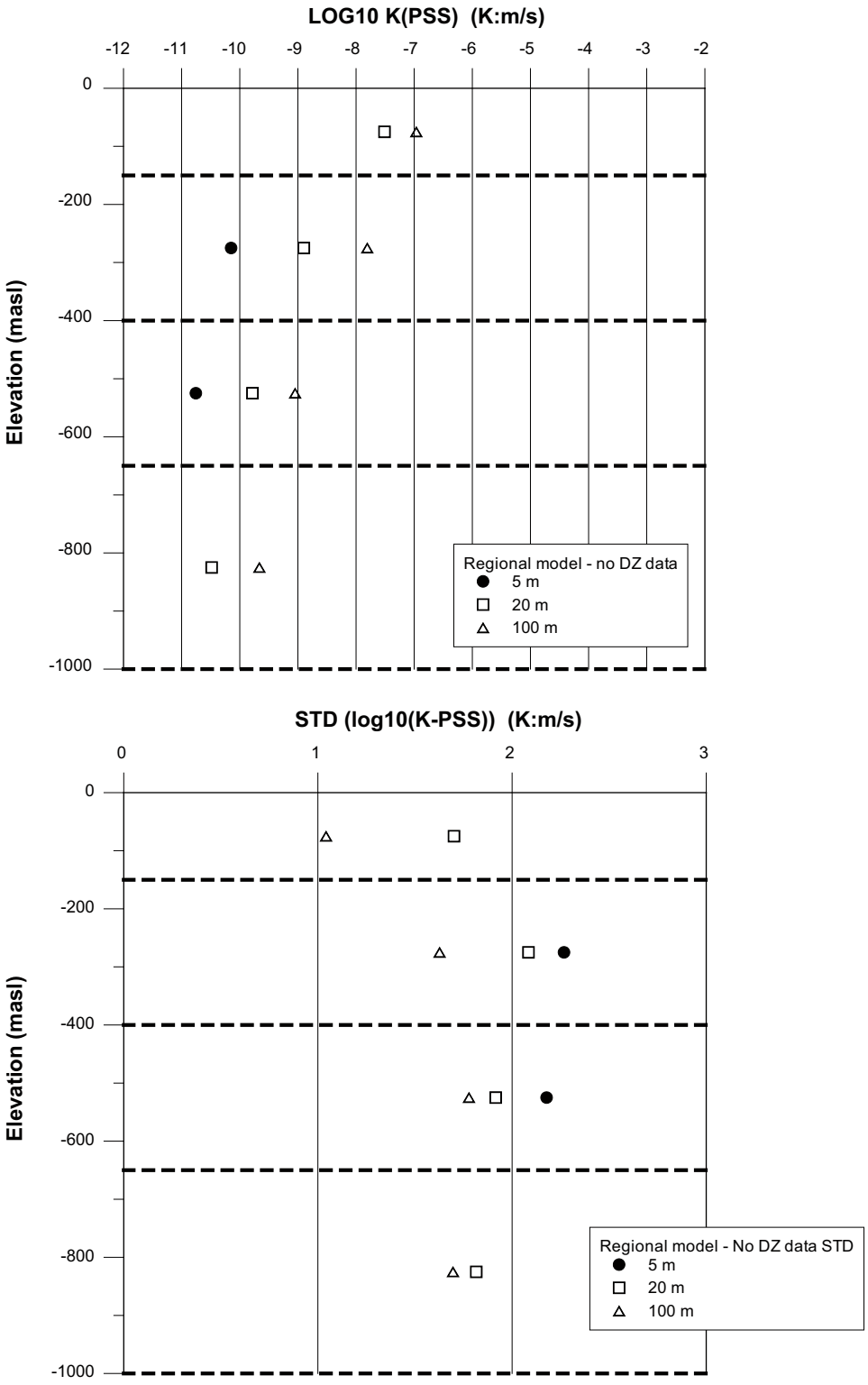

Figure 9-64. *Results for all data samples in test scales 100, 20 and 5 m. Statistics for depth intervals. Top: mean of log10(K), bottom standard deviation of log10(K). Based on HRD between deterministic deformation zones and regional model volume cf. Appendix 9.*

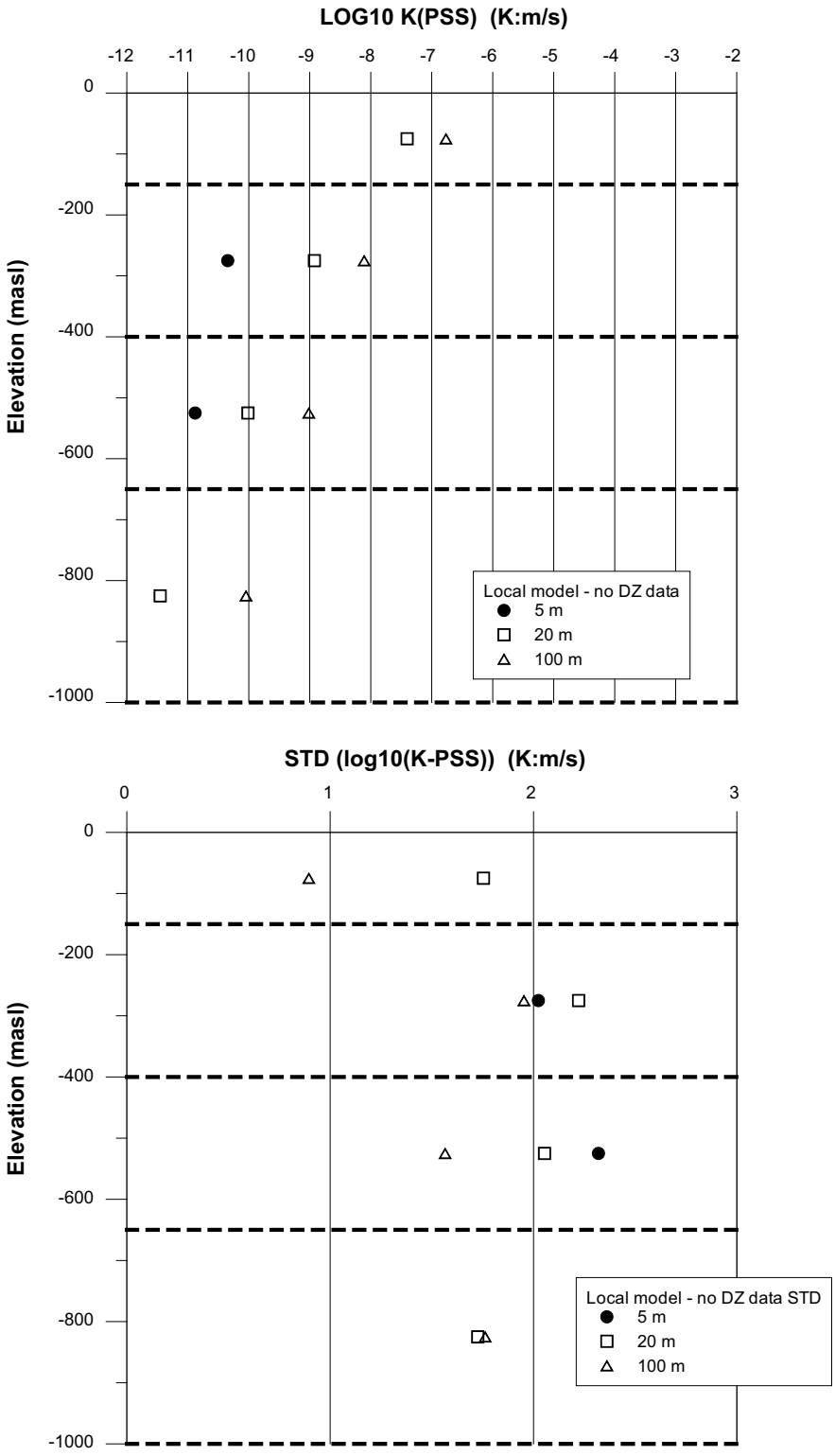

Figure 9-65. *Results for all data samples in test scales 100, 20 and 5 m. Statistics for depth intervals. Top: mean of log10(K), bottom standard deviation of log10(K). Based on HRD between deterministic deformation zones and local model volume cf. Appendix 9.*

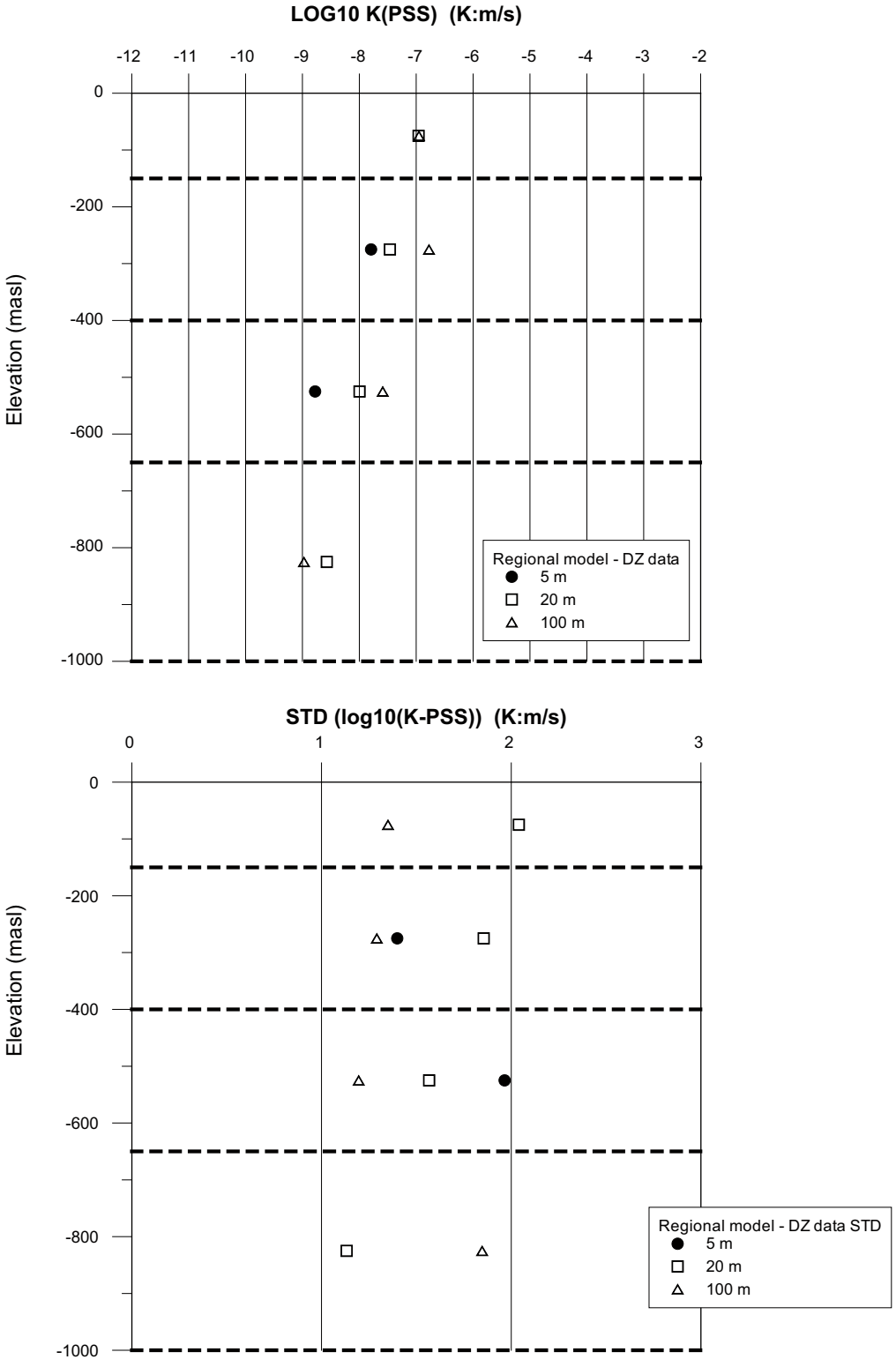

Figure 9-66. *Results for all data samples in test scales 100, 20 and 5 m. Statistics for depth intervals. Top: mean of log10(K), bottom standard deviation of log10(K). Based on deterministic deformation zone data and regional model volume cf. Appendix 9.*

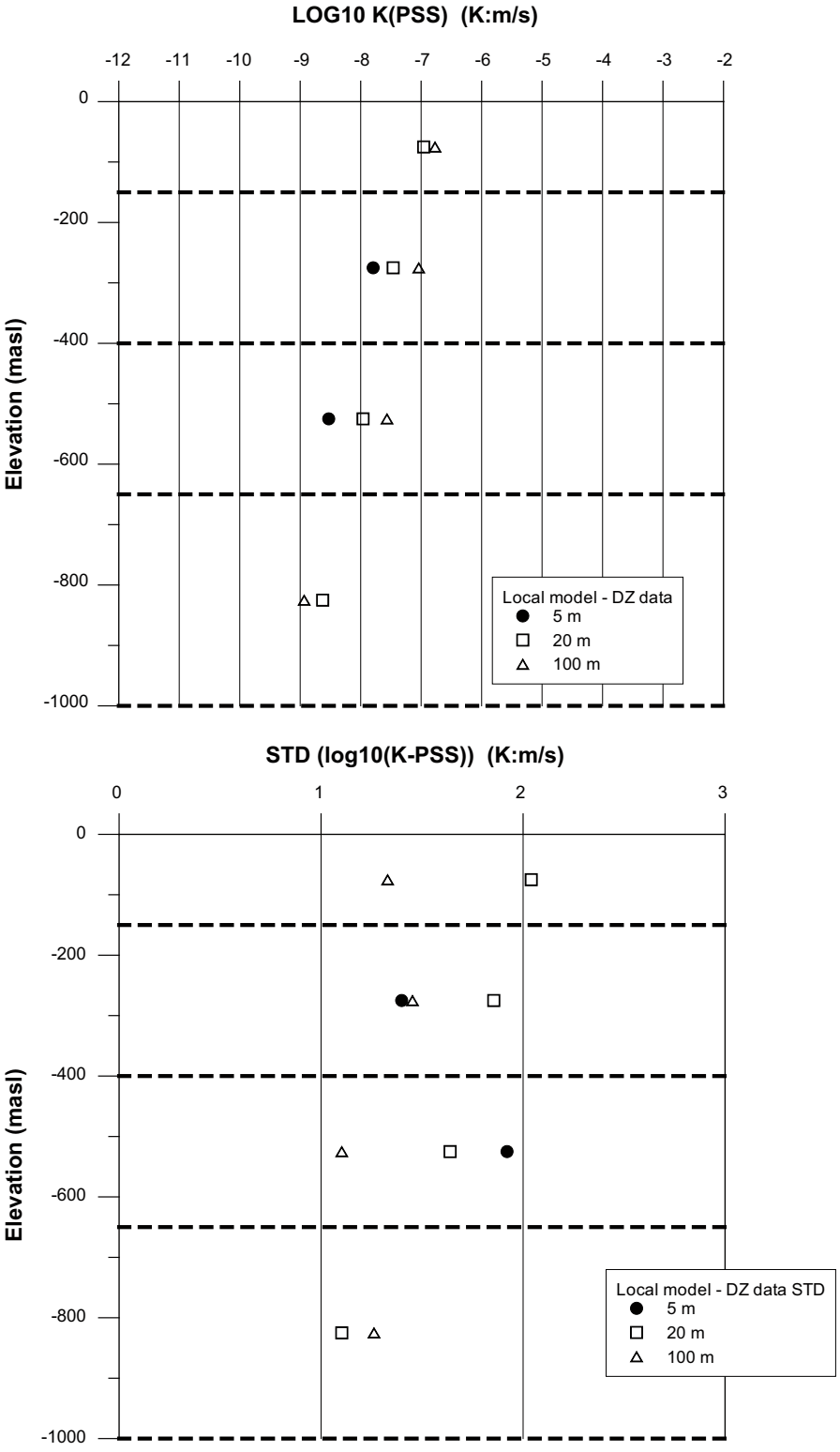

Figure 9-67. *Results for all data samples in test scales 100, 20 and 5 m. Statistics for depth zones. Top: mean of log10(K), bottom standard deviation of log10(K). Based o on deterministic deformation zone data and local model volume cf. Appendix 9.*

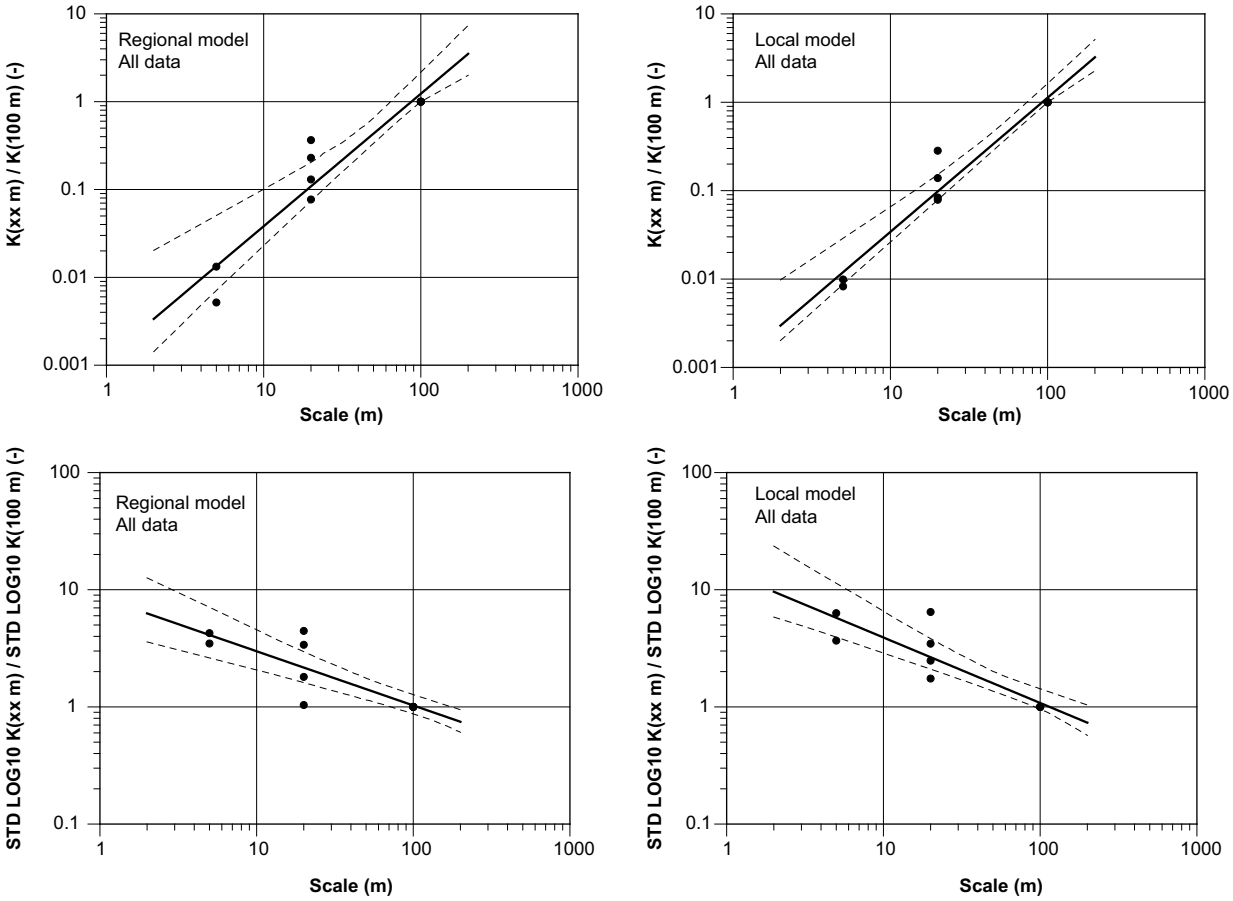

Figure 9-68. *Upscaling models based on test scales 100, 20 and 5 m. Statistics normalised based on values from 100 m test scale. Regional land local model volumes, All data, cf. Figure 9-62 and Figure 9-63.*

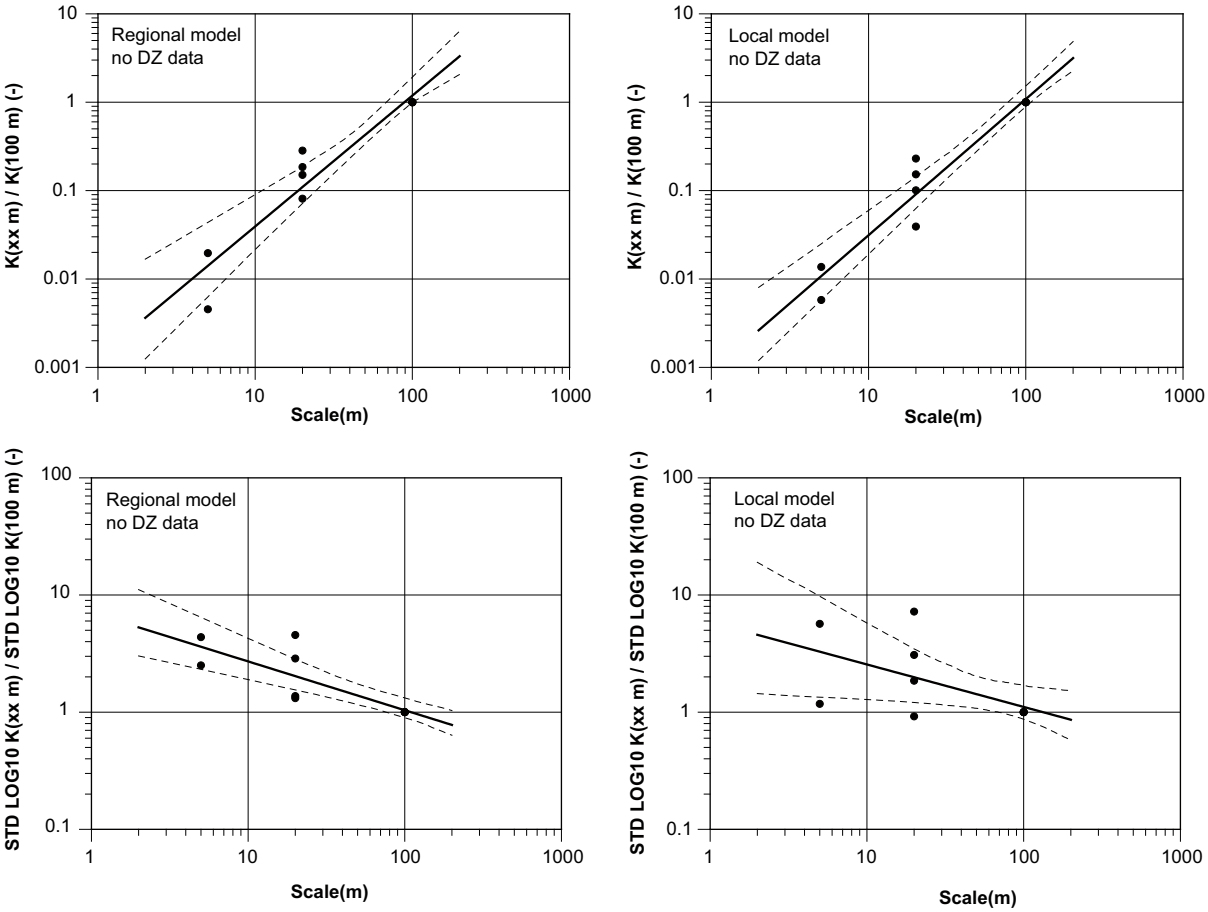

Figure 9-69. *Upscaling models based on test scales 100, 20 and 5 m. Statistics normalised based on values from 100 m test scale. Regional and local model volumes, HRD between HCDs, cf. Figure 9-64 and Figure 9-65.*

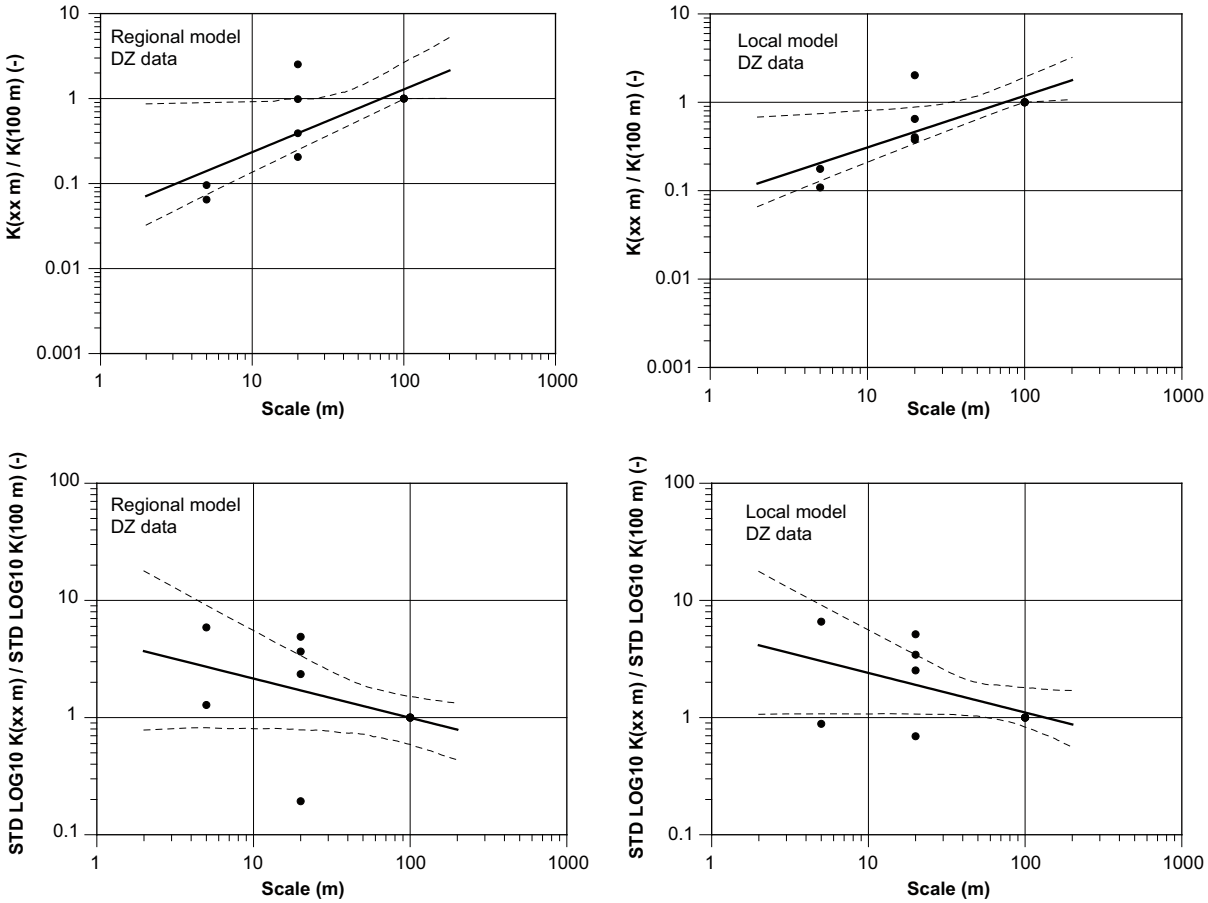

Figure 9-70. *Upscaling models based on test scales 100, 20 and 5 m. Statistics normalized based on values from 100 m test scale. Regional and local model volumes, HCDs, cf. Figure 9-66 and Figure 9-67.*

9.7 Hydraulic conductivity of rock types and sections with crush

The hydraulic conductivity of the rock mass (between the deterministically defined deformation zones) based on PFL-s (5 m section) has been analysed with regards to rock type. The influence of smaller veins of fine-grained granite on the hydraulic conductivity is also studied in this section.

The mapping of the drill cores differentiates between “rock type” and “rock occurence”. The rock type is mapped under “rock type” if the mapped length is > 1 m borehole length and under “rock occurrence” if the mapped length is < 1 m borehole length, the latter for the most part representing subordinate rock types. The rock types, and related rock codes, for “rock types” and “rock occurrences” used in the geological mapping are shown in Table 9-15.

Table 9-15. Igneous rock types in the Laxemar-Simpevarp area and their relative age relationships. The rock codes for each rock type employed by SKB are shown within brackets. Reproduced from /Wahlgren et al. 2008/.

Rock type	Relative age
Dolerite (501027)	Youngest
Götemar and Uthammar granites (521058)	
Fine-grained granite (511058) and pegmatite (501061)	
Fine-grained diorite-gabbro (505102)	
Granite, equigranular (501058)	
Ävrö granite (501044)/Ävrö quartz monzodiorite (501046)	
Quartz monzodiorite (501036)	
Diorite-gabbro (501033)	
Fine-grained dioritoid (501030)	Oldest

The statistics for different subsets of the entire PFL-s data set are shown in Figure 9-72 to Figure 9-75 and Appendix 9. For overview, the geometric means and the confidence intervals for the geometric mean of the different rock types are shown in Figure 9-71. In the latter figure the results based on samples comprising only measurement limit values have been plotted as one value with $K=10^{-14}$ m/s, without any confidence interval, simply to differentiate between the samples where statistics could be evaluated by the fact that some data were indeed above measurement limit. The truth is, of course, that the geometric mean is probably below the measurement limit for PFL-s; $2\cdot10^{-10}$ m/s and nothing else can be stated. For the analysis of rock types two sample types were prepared for each rock type: (1) test sections with dominant rock type corresponding to that being investigated (2) test sections with 100% coverage of the rock type being investigated. In terms of statistics there seems to be only minor differences between these two groups.

The entire sample of 5 m PFL-s measurements comprises 4,036 tests of which 3,379 are associated with rock between deterministic deformation zones. Figure 9-72 and Appendix 9, Table A9-13 shows the statistics for the entire sample of data between HCDs. In this table also results for a subset including all sections with fine-grained granite (511058) are shown, and as can be seen there is hardly any difference between the results for the entire data set and those for the subset including sections with veins of fine-grained granite.

Test sections intersected by a crushed zone are significantly more conductive than sections without a crushed zone, see Appendix 9. There are, in total, 197 PFL-s sections associated with crush (outside HCDs) and of them only 79 are within MDZs defined by geology, cf. Chapter 8 and /Hermanson et al. 2008/ and /Wahlgren et al. 2008/. In terms of transmissivity distribution (geometric mean and standard deviation of Log10(K-PFL-s)) these two groups with crush zones are more or less equitable. This means that data indicate that there may exist quite conductive “hydraulic features” that possibly could be part of features not defined as MDZs by Geology, but of similar size.

Figure 9-73 to Figure 9-75 show examples of distributions of hydraulic conductivity for defined rock types; main rock types being Ävrö granite (501044), quartz monzodiorite (501036) and fine-grained granite (511058). In Appendix 9 the statistics are shown for all rock types. Concerning dolerite (501027) the only data available were from borehole sections intersected by deformation zones, but were still used in the statistical analysis presented here.

The most low-conductive rock types are dolerite (501027) (no data above the measurement limit even though data are from deformation zones) and diorite to gabbro (501033) followed by fine-grained dioritoid (metavolcanite, volcanite) (501030) and quartz monzonite (quartz monzonite to monzodiorite, equigranular to weakly porphyritic)(501036).

The most conductive rock type is generally fine-grained granite (granite, fine- to medium-grained) (511058) but in one depth interval fine-grained diorite-gabbro (mafic rock, fine-grained) (505102) shows similar geometric mean hydraulic conductivity (K), cf. Figure 9-71.

Ävrö granite (granite to quartz monzodiorite, generally porphyritic) (501044) generally shows a geometric mean K that is 3–8 times smaller than that for fine-grained granite (even greater difference below –650 m).

There are rather few test sections with granite, (equi-granular granite, medium- to coarse-grained) (501058) but it appears that this rock type has properties similar to the Ävrö granite.

There are hardly any data for pegmatite (501061) so its hydraulic properties cannot be judged with certainty, 4 of 5 measurements being below the measurement limit.

The variability in statistics for diffent depth intervals is high for fine-grained diorite-gabbro (mafic rock, fine-grained) (505102). The uppermost depth zone shows similar properties as Ävrö granite, with a very low conductivity in the depth interval –150 to –400 m, high as the fine-grained granite in the depth interval –400 to –650 m and similar properties to Ävrögranite below –650 m.

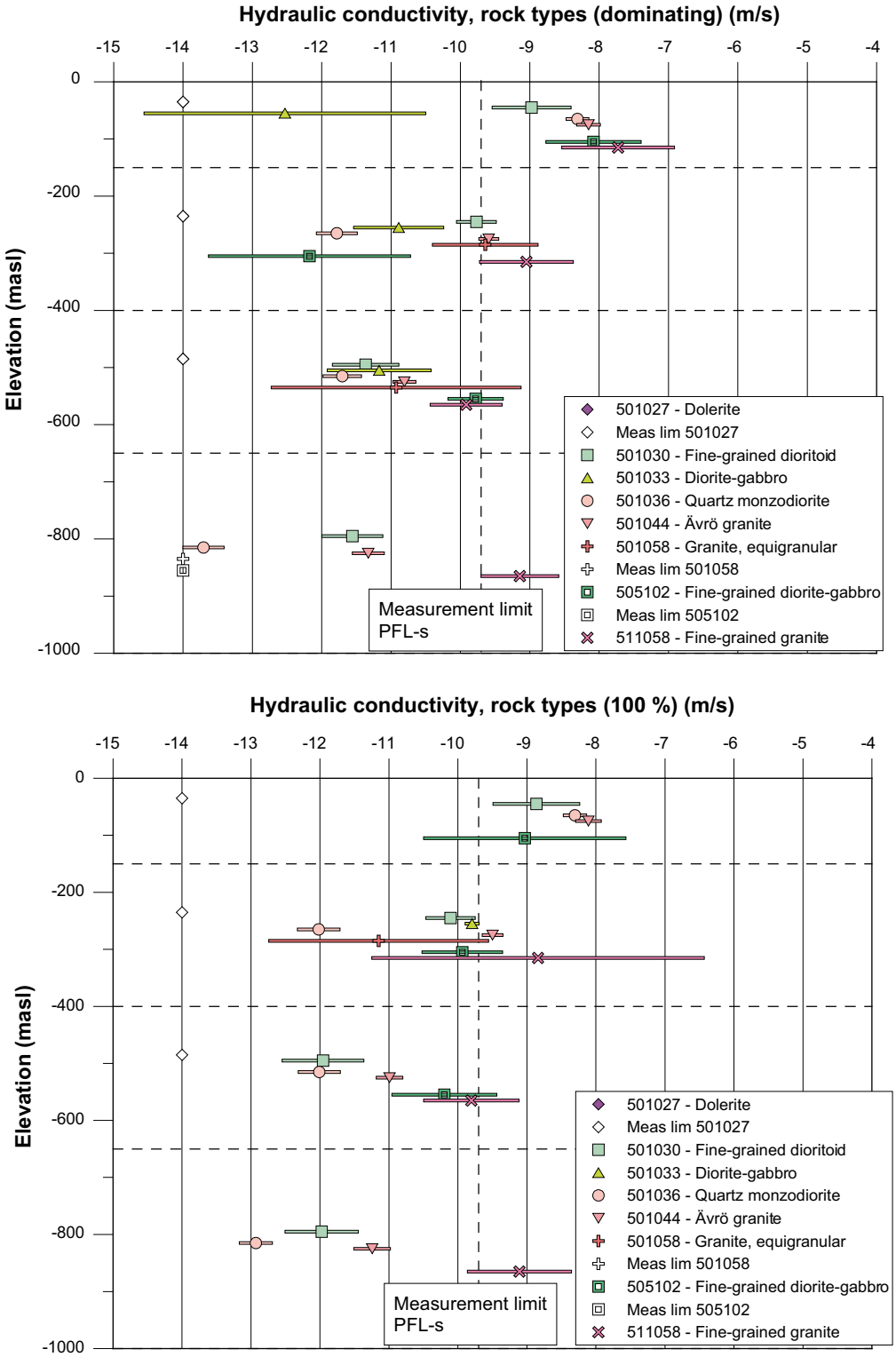

Figure 9-71. *Geometric mean hydraulic conductivity, with 95% confidence interval for geometric mean (length of horizontal line), for rock types. Test scale 5 m. Method PFL-s. Data for rock between the deformation zones. Top: Statistics based on tests sections with the given rock type dominating. Bottom: Statistics based on tests sections with 100% of the the given rock type within the test section.*

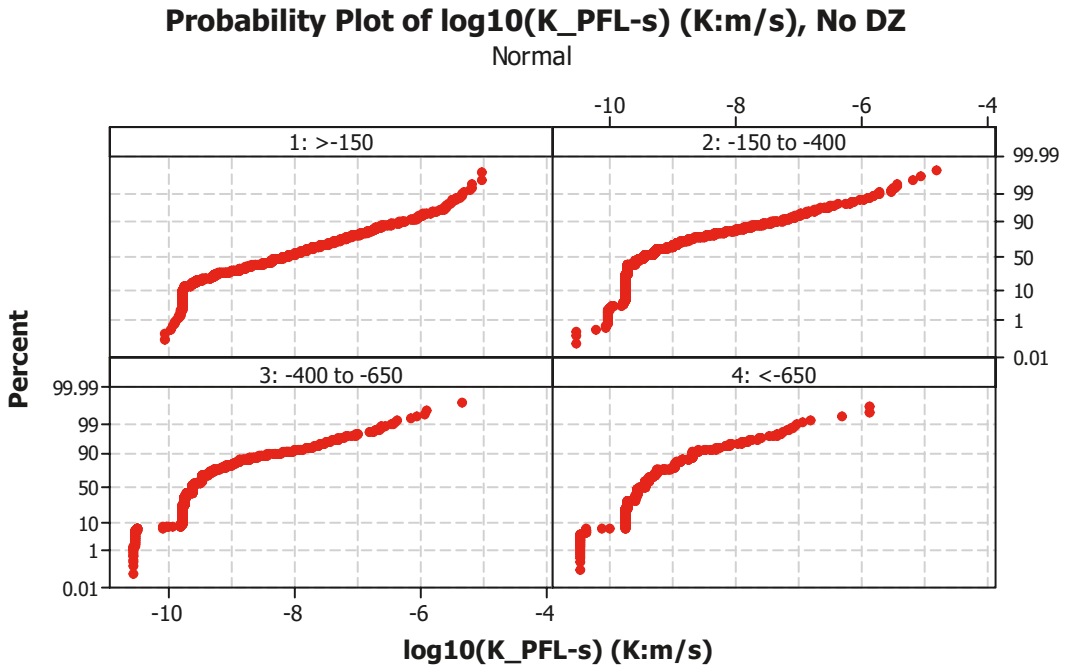

Panel variable: Elev-class_0

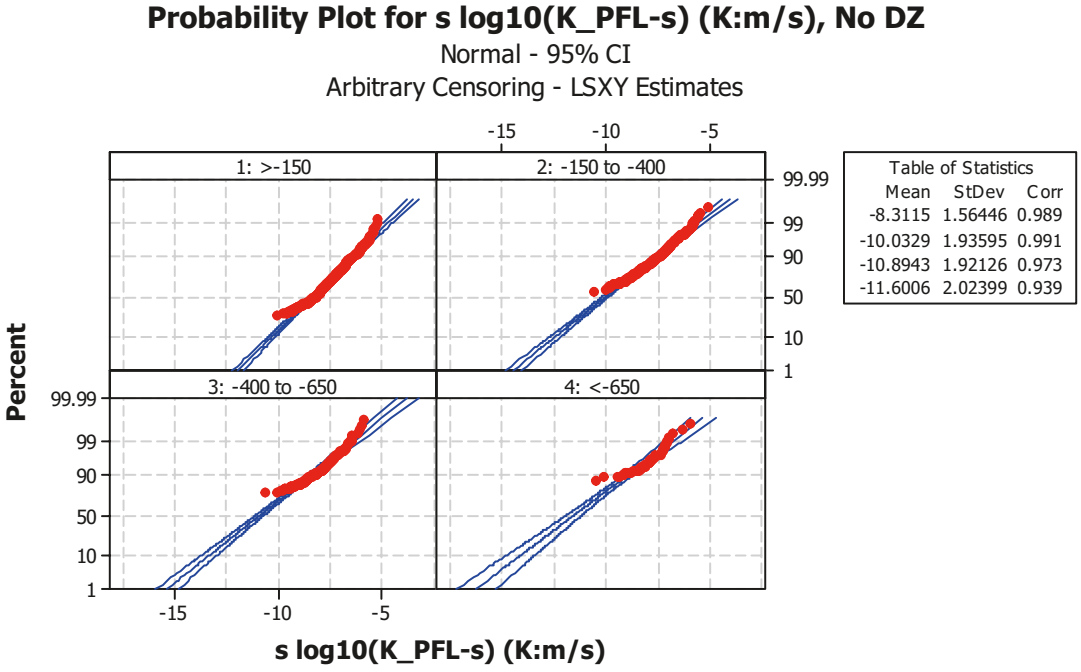

Panel variable: Elev-class_0

Figure 9-72. *Probability plots of hydraulic conductivity data for rock inbetween interpreted deterministic deformation zones. Test scale 5 m. Method PFL-s. Top: probability plots of all data. Bottom: Estimation of distribution taking the censored data into account.*

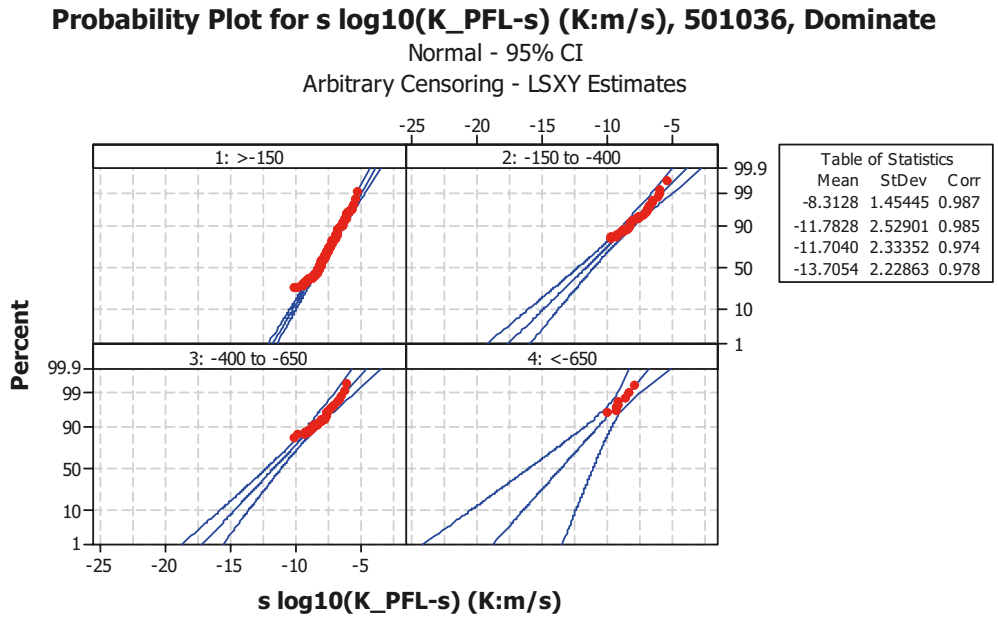

Panel variable: Elev-class_0

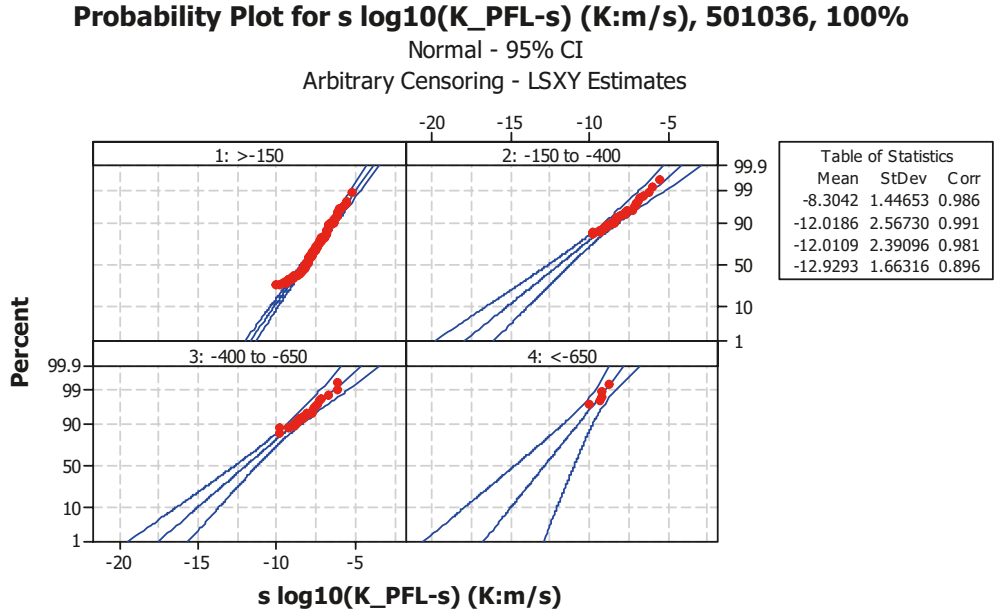

Panel variable: Elev-class_0

Figure 9-73. *Probability plots of hydraulic conductivity data for rock inbetween interpreted deterministic deformation zones. Test scale 5 m. Method PFL-s. Data: Quartz monzodiorite (501036). Estimation of distribution taking the censored data into account. Top: probability plots of test sections with dominant rock type 501036. Bottom: probability plots of test sections with 100% rock type 501036.*

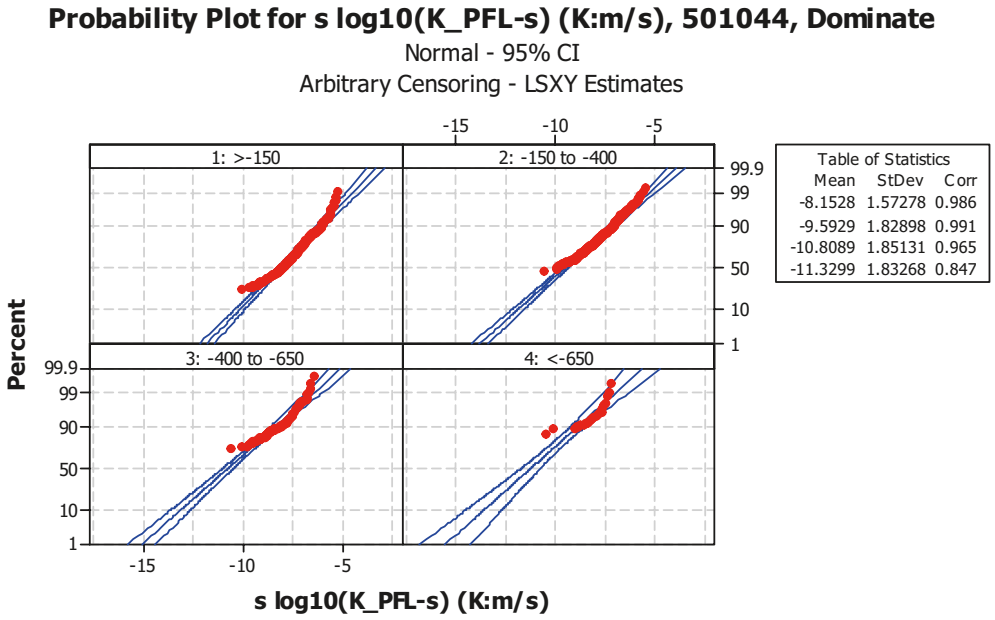

Panel variable: Elev-class_0

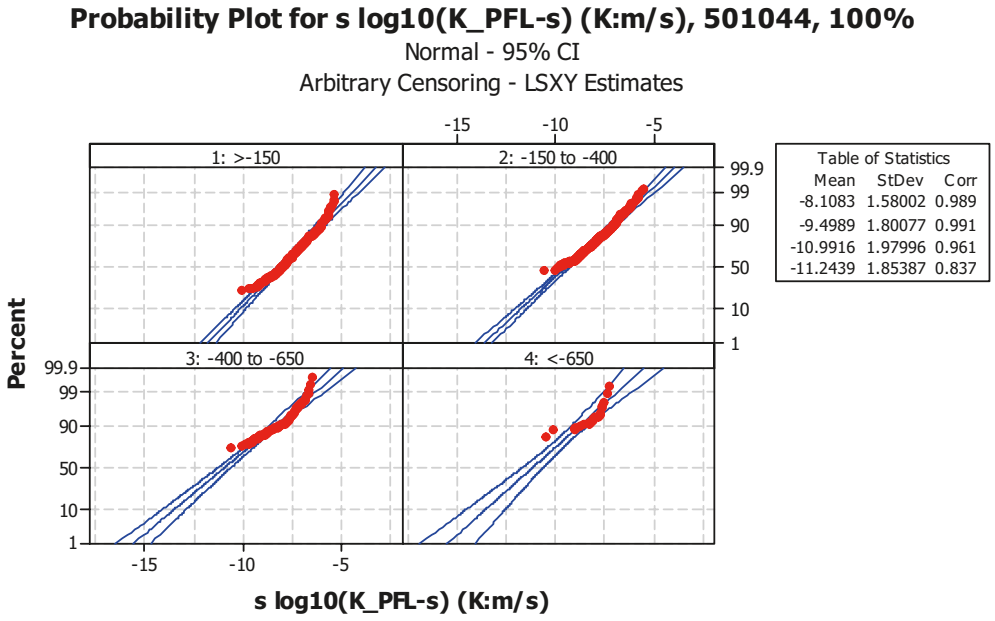

Panel variable: Elev-class_0

Figure 9-74. *Probability plots of hydraulic conductivity data for rock in between interpreted deterministic deformation zones. Data: Ävrö granite (501044). Estimation of distribution taking the censored data into account. Top: probability plots of test sections with the dominant rock type 501044. Bottom: probability plots of test sections with 100% rock type 501044.*

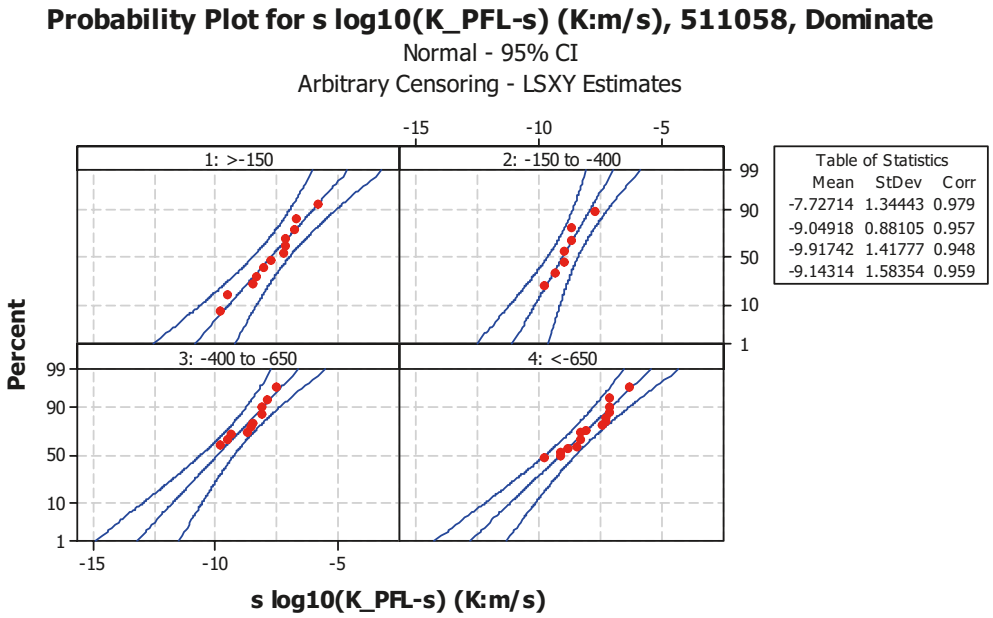

Panel variable: Elev-class_0

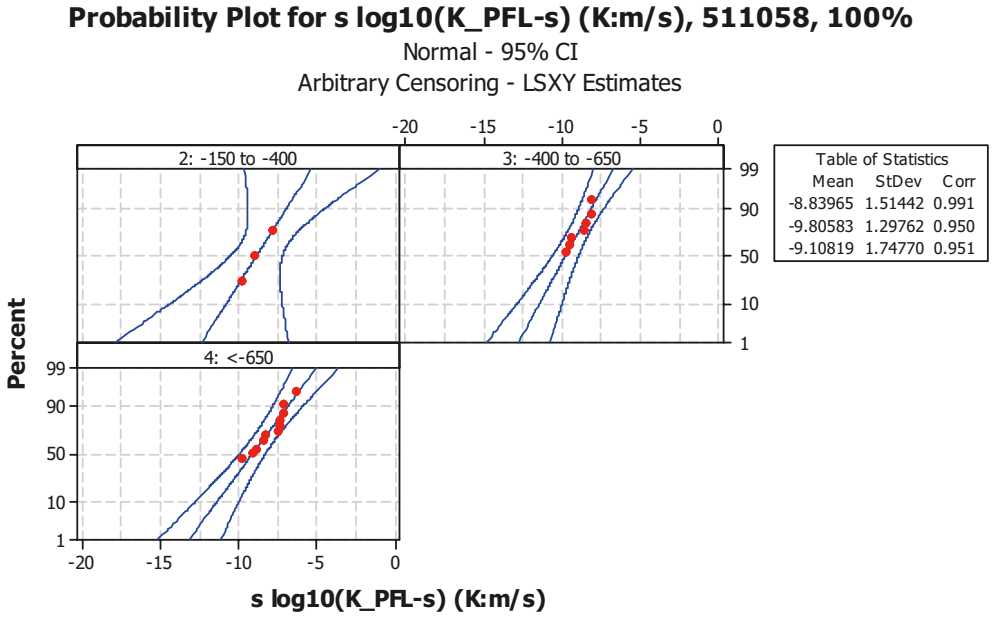

Panel variable: Elev-class_0

Figure 9-75. *Probability plots of hydraulic conductivity data for rock in between interpreted deterministic deformation zones. Data: Fine-grained granite (511058). Estimation of distribution taking the censored data into account. Top: probability plots of test sections with dominant rock type 511058. Bottom: probability plots of test sections with 100% rock type 511058.*

9.8 Hydraulic conductivity in relation to open fractures and crush

As indicated in previous sections, it is the frequency of conductive fractures that controls the expected mean transmissivity over a certain thickness, even though the variability of the number of conductive fractures for a certain transmissivity is large. In this section it is explored whether the frequency (no./m) of open fractures is correlated with the hydraulic conductivity measured with the PFL-s method. All test sections considered in this analysis have a test section length of 5 m with the exception of KLX02, where they are 3 m. In this analysis the total data set is used, including both test sections between and within interpreted deterministic deformation zones (DZ). In Sections 9.1 to 9.5 the statistics of open fractures between deformation zones and in relation to fracture domains are explored in detail.

The following definition of variables applies:

- OPEN_TOTAL: The sum of all open fractures (Certain (C), Probable (P), Possible (Po)) and estimated open fractures within crush zone.
- OPEN_ALL: The sum of all open fractures (Certain (C), Probable (P), Possible (Po)).
- OPEN_CP: The sum of open fractures mapped as Certain (C) or Probable (P). Possible (Po))

In some cases test sections (generally 5 m) including one or seyveral crush zones are studied separately ("sections with crush") and in other cases excluded ("sections without crush").

The frequency of fractures (OPEN_TOTAL, OPEN_ALL and OPEN_CP) and subsets of these groupings are plotted versus hydraulic conductivity (K) of the PFL-s tests in Figure 9-76 to Figure 9-78. As expected there exists a weak positive correlation, with a significant variability, between the number of open fractures for all test sections and test sections with crush zone (with attributed mean frequencies of 40 fractures/m). In Table 9-16 the approximate ranges of open fractures, as can be interpreted from Figure 9-76 through Figure 9-78 are compiled. In test sections with crush zones the fracture frequency is fairly constant in relation to evalauted hydraulic conductivity. This means that there generally exists a higher frequency of open fractures near a crush, which appears consistent with the assumption that a crush may be an indication of a larger structure formed during brittle deformation. As mentioned in Section 5.2.2, possibly a few of the data representing "crush zones" can be attributed to damage during drilling as interpreted by the geological extended single-hole interpretation.

Table 9-16. Approximate range of the mean frequency of open fractures within a hydraulic conductivity range of c. 10^{-11} to 10^{-4} m/s. (See Figure 9-76 to Figure 9-78.)

Category of fractures	All test sections Frequency (m^{-1})	Test sections with crush Frequency (m^{-1})
OPEN_TOTAL	c.1–10	c. 10
OPEN_ALL:	c. 1–6	c. 5
OPEN_CP:	c. 0.5–2	c. 1–2

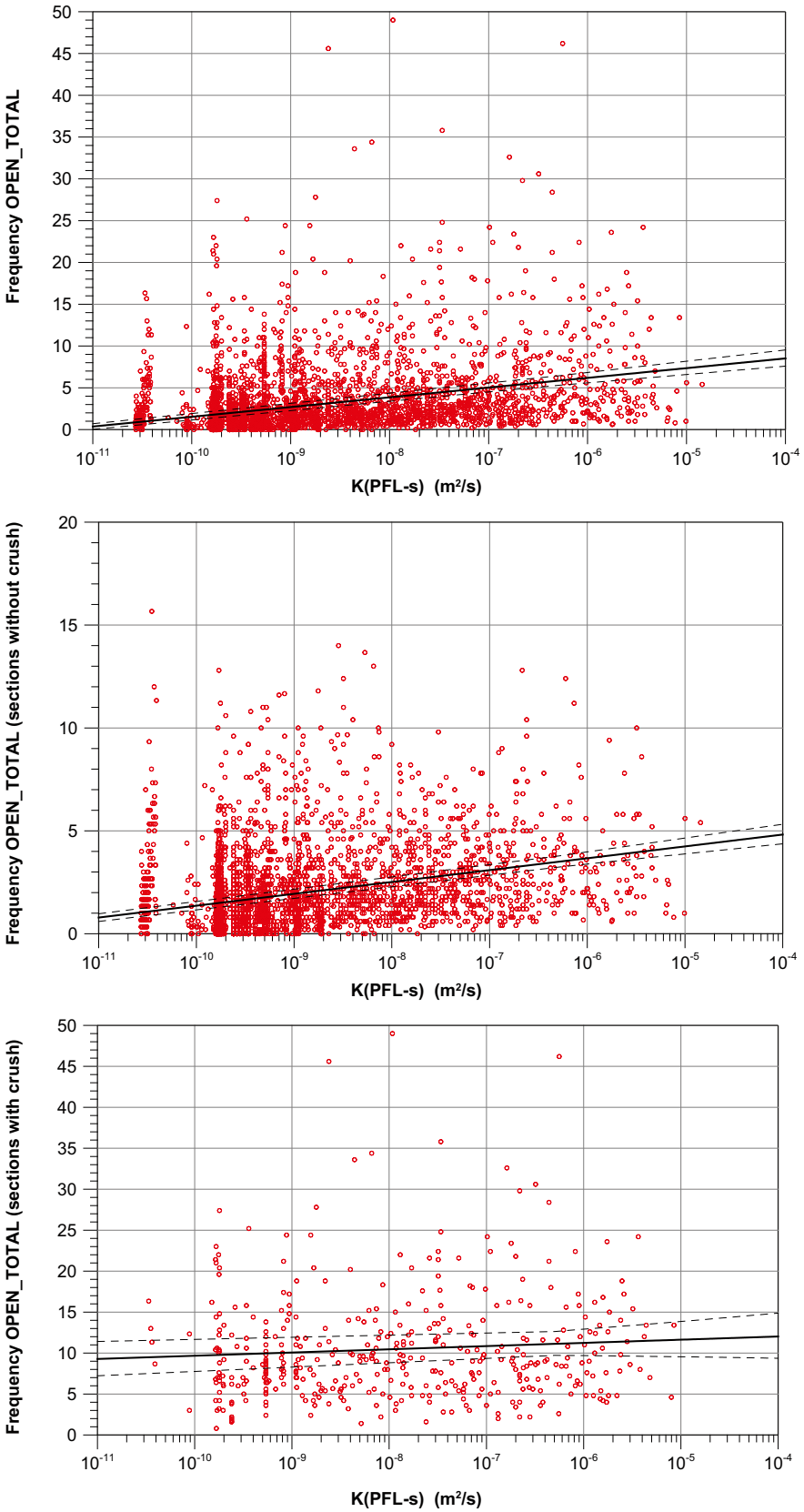

Figure 9-76. *Hydraulic conductivity versus frequency of open fractures: OPEN_TOTAL. Top: all test sections, Middle: sections without crush. Bottom: sections with crush.*

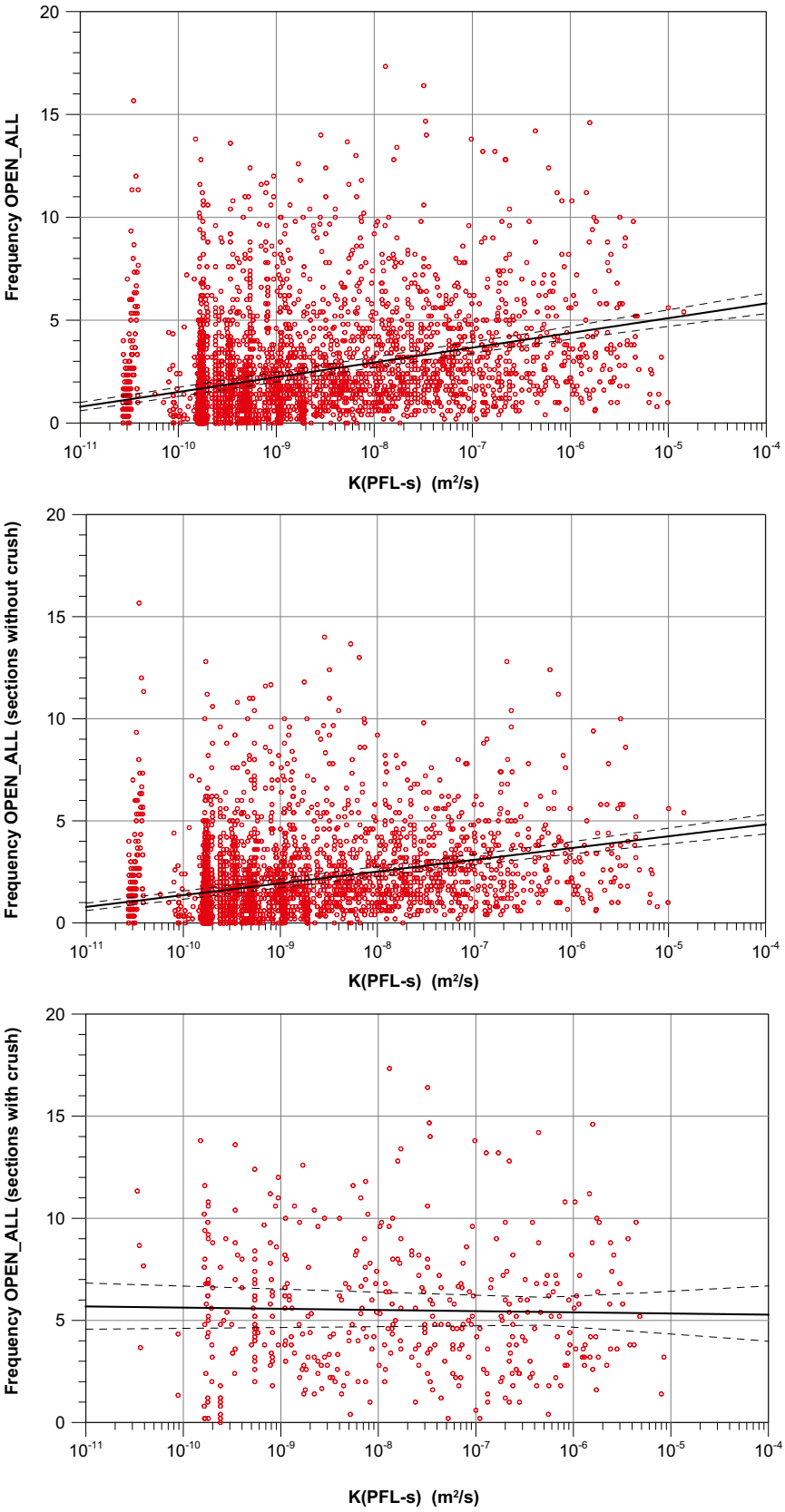

Figure 9-77. *Hydraulic conductivity versus frequency of open fractures: OPEN_ALL. Top: all test sections, Middle: sections without crush. Bottom: sections with crush.*

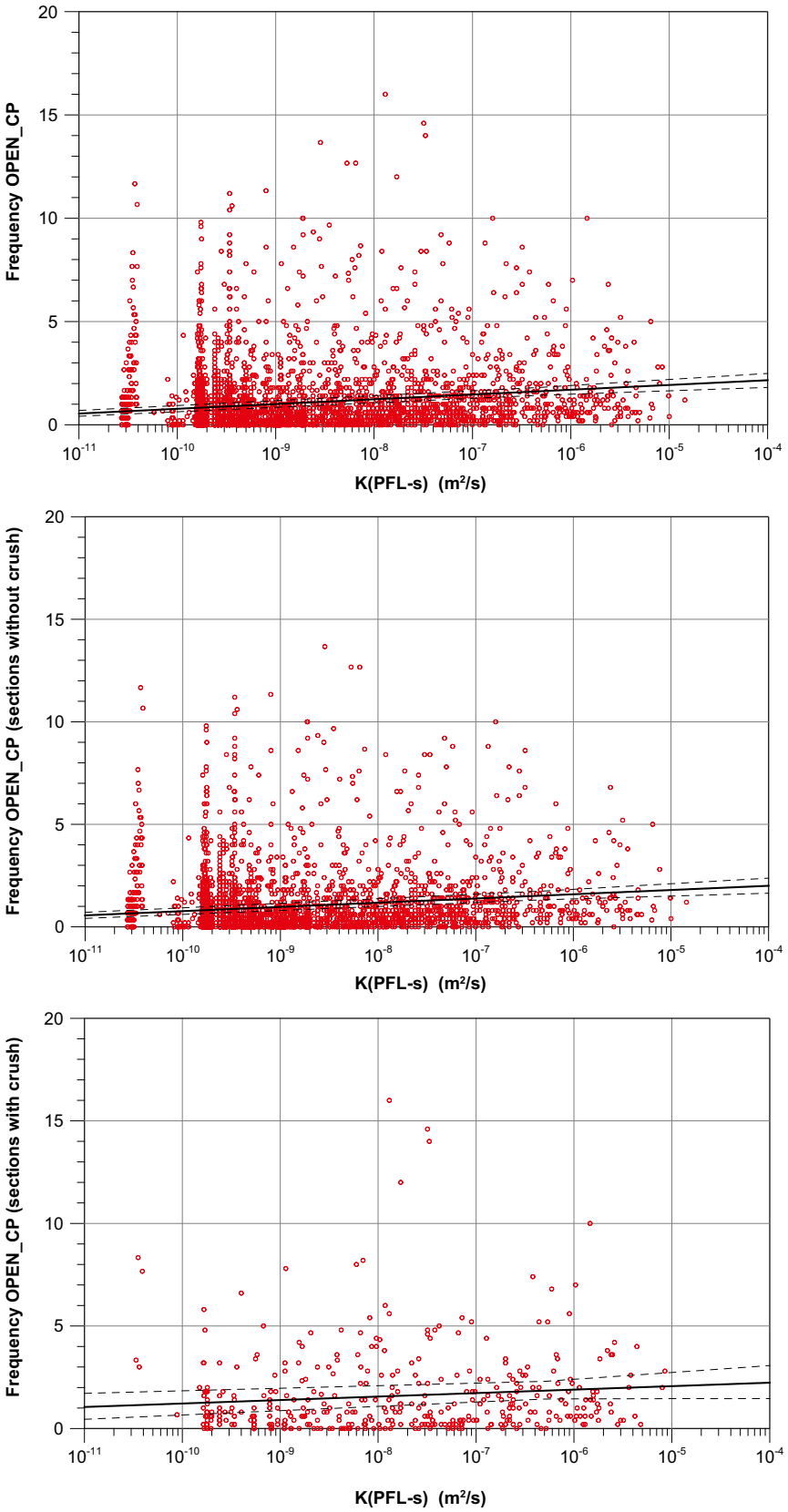

Figure 9-78. *Hydraulic conductivity versus frequency of open fractures: OPEN_CP. Top: all test sections, Middle: sections without crush. Bottom: sections with crush.*

9.9 Specific storage

Specific storage in crystalline rock is generally difficult or virtually impossible to assess from hydraulic tests. However, rough estimates can be obtained from rock mechanical parameters, as outlined in the section below. An alternative approach to estimate the specific storage is to use the relation between hydraulic feature transmissivity and storage coefficent provided in Section 7.6, an established hydrogeological DFN model and subsequent block simulations similar to what is presented in Section 10.6. Such simulations have not been made within the current project but could probably provide a better estimate of specific storage than based on rock mechanical parameters, the latter which probably overestimates the specific storage. There are however no storage coefficient data from tests in the transmissivity range < c. $1 \cdot 10^{-7}$ m^2/s according to Section 7.6. This makes the assessment of the storage coefficient uncertain for low- transmissive features in a hydrogeological DFN model.

9.9.1 Specific storage based on rock mechanical parameters

In /Hakami et al. 2008/ the deformation modulus (E_d) and Poisson's ratios (v) are provided, see Table 9-17 and Table 9-18. Based on these values the bulk compressibility of the porous medium (α) can be calculated as:

$$\alpha = 3 \cdot (1 - v) / E_d \qquad (9\text{-}1)$$

From the literature /e.g. Freeze and Cherry 1979/ α can be expected to be in the range 10^{-8}–10^{-10} Pa^{-1} for fractured rock and in the range 10^{-9}–10^{-11} Pa^{-1} for intact rock. Using the max and min values for E_d and v, the range for α becomes $3 \cdot 10^{-10}$–10^{-11} Pa^{-1} and using mean ±3 std, with min $E_d \geq 1$ and min $v \geq 0$, the range for α becomes $3 \cdot 10^{-9}$–$7 \cdot 10^{-12}$ Pa^{-1}. The values of estimated α for the rock mass representative of the Laxemar local model volume correspond well to the literature values.

The specific storage (S_S) can be estimated as e.g. /Marsily 1986/:

$$S_S = \rho \cdot g \cdot (n \cdot \beta_l + \alpha) \qquad (9\text{-}2)$$

ρ: Fluid density (kg/m^3)

g: Acceleration of gravity (m/s^2)

n: Porosity (–)

β_l: Coefficient of compressibility of the fluid (Pa^{-1})

α: Bulk compressibility of the porous medium (Pa^{-1})

Assuming a water temperature of 10°C (β_l=$4.8 \cdot 10^{-10}$ Pa^{-1}, ρ=999.7 kg/m^3), g=9.81 m/s^2 and a porosity range n=0.001–0.03, it can be shown that the influence of α has the greatest impact on S_S. Table 9-19 and Figure 9-79 present the calculated ranges for S_S.

As α is dependent on, among other things, fracture frequency, S_S is likely to be correlated to hydraulic conductivity K. As shown in Chapter 7 and 8 the mean P_{10}-corr for PFL-f features is c. 0.3 to 2.4 for HCDs and MDZs, respectively, and in Table 9-14 it was previously shown that P10-corr for PFL-f features was c. 0.000 to 0.8 for rock between HCDs. Taking the estimated thicknesses of the HCDs into account and the presented relation of storage coefficient S=f(T), see Section 7.6, it is possible to roughly estimate the relationship between K and S_S (although with a large variation), with $S_S \approx 10^{-5}$ 1/m for $K \approx 10^{-4}$ m/s. As shown in Chapter 4, the matrix hydraulic conductivity is in the range 10^{-14}–10^{-12} m/s and according to Section 9.6 the lower range of the estimated hydraulic conductivity is c. 10^{-12}–10^{-10} m/s, it is reasonable to use the relation shown in Table 9-20 and Figure 9-80 for a approximate estimation of S_S based on K.

Section 7.6 indicates that the hydraulic diffusivity is c. 0.2 for T=$1 \cdot 10^{-9}$ m^2/s and c. 12 for T=$1 \cdot 10^{-3}$ m^2/s. Figure 9-80 indicates hydraulic diffusivity is c. 0.0003 for K=$1 \cdot 10^{-10}$ m/s and c. 10 for K=$1 \cdot 10^{-4}$ m/s. It seems that the estimate based on the rock mechanical parameters possibly generates too high specific storage parameters for low values of hydraulic conductivity.

Table 9-17. Deformation modulus for various subdivisions of the Laxemar bedrock; fracture domains with MDZ excluded (FSMxxxx), minor deformation zones (MDZ), deterministic deformation zones interpreted in boreholes but without lineament (Other DZs) , deterministic deformation zones interpreted in boreholes and lineaments (ZSMEW007A, ZSMEW0946A etc). Compiled from /Hakami et al. 2008, cf. Tables 5-11, 5-12, 5-13 and 5-14 therein/.

Object	E_d Min (GPa)	E_d Mean (GPa)	E_d Max (GPa)	E_d Std (GPa)
FSM_C, FSM_W, FSM_NE006	39	59	79	10
FSM_N, FSM_EW007	22	50	78	14
MDZ	10	40.6	66.1	20.8
Other DZ	10	37.6	72.3	20.2
ZSMEW007A	16.8	42	77.9	16.7
ZSMEW0946A	18.2	29.8	52.9	14.5
ZSMNE107A	12.1	30.3	66.1	12.8
ZSMNE942A	10.9	38.9	54.4	12.2
ZSMEW042A	10	38.7	59.5	23.9

Table 9-18. Poisson's ratio for various subdivisions of the Laxemar bedrock; fracture domains with MDZ excluded (FSMxxxx), minor deformation zones (MDZ), deterministic deformation zones interpreted in boreholes but without lineament (Other DZs) , deterministic deformation zones interpreted in boreholes and lineaments (ZSMEW007A, ZSMEW0946A etc). Compiled from /Hakami et al. 2008, cf. Tables 5-11, 5-12, 5-13 and 5-14 therein/.

Object	v Min (–)	v Mean (–)	v Max (–)	v Std (–)
FSM_C, FSM_W, FSM_NE006	0.24	0.3	0.36	0.03
FSM_N, FSM_EW007	0.24	0.3	0.36	0.03
MDZ	0.2	0.14	0.24	0.08
Other DZ	0	0.12	0.24	0.08
ZSMEW007A	0.04	0.11	0.21	0.04
ZSMEW0946A	0.05	0.09	0.15	0.05
ZSMNE107A	0.04	0.1	0.24	0.05
ZSMNE942A	0.02	0.12	0.19	0.04
ZSMEW042A	0	0.14	0.21	0.21

Table 9-19. Estimated specific storage S_S for various subdivisions of the Laxemar bedrock; fracture domains with MDZ excluded (FSMxxxx), minor deformation zones (MDZ), deterministic deformation zones interpreted in boreholes but without lineament (Other DZs) , deterministic deformation zones interpreted in boreholes and lineaments (ZSMEW007A, ZSMEW0946A etc). The maximum and minimum values for S_S are based on results using the maximum and minimum values for α, E_d and n.

Object	S_s Min(2) (m^{-1})	S_s Min(1) (m^{-1})	S_s Mean (m^{-1})	S_s Max(1) (m^{-1})	S_s Max(2) (m^{-1})
FSM_C, FSM_W, FSM_NE006	7.74E–08	1.09E–07	2.72E–07	5.34E–07	7.30E–07
FSM_N, FSM_EW007	7.51E–08	1.10E–07	3.08E–07	8.37E–07	2.27E–06
MDZ	7.33E–08	2.36E–07	5.95E–07	1.91E–06	2.96E–05
Other DZ	8.86E–08	2.16E–07	6.68E–07	3.08E–06	2.96E–05
EW007A	1.77E–07	2.24E–07	6.19E–07	1.75E–06	2.96E–05
EW0946A	2.13E–07	3.94E–07	8.83E–07	1.60E–06	2.96E–05
NE107A	2.19E–07	2.36E–07	8.50E–07	2.38E–06	2.96E–05
NE942A	2.07E–07	3.40E–07	6.48E–07	2.73E–06	1.29E–05
EW042A	6.87E–08	2.92E–07	6.20E–07	3.08E–06	2.96E–05

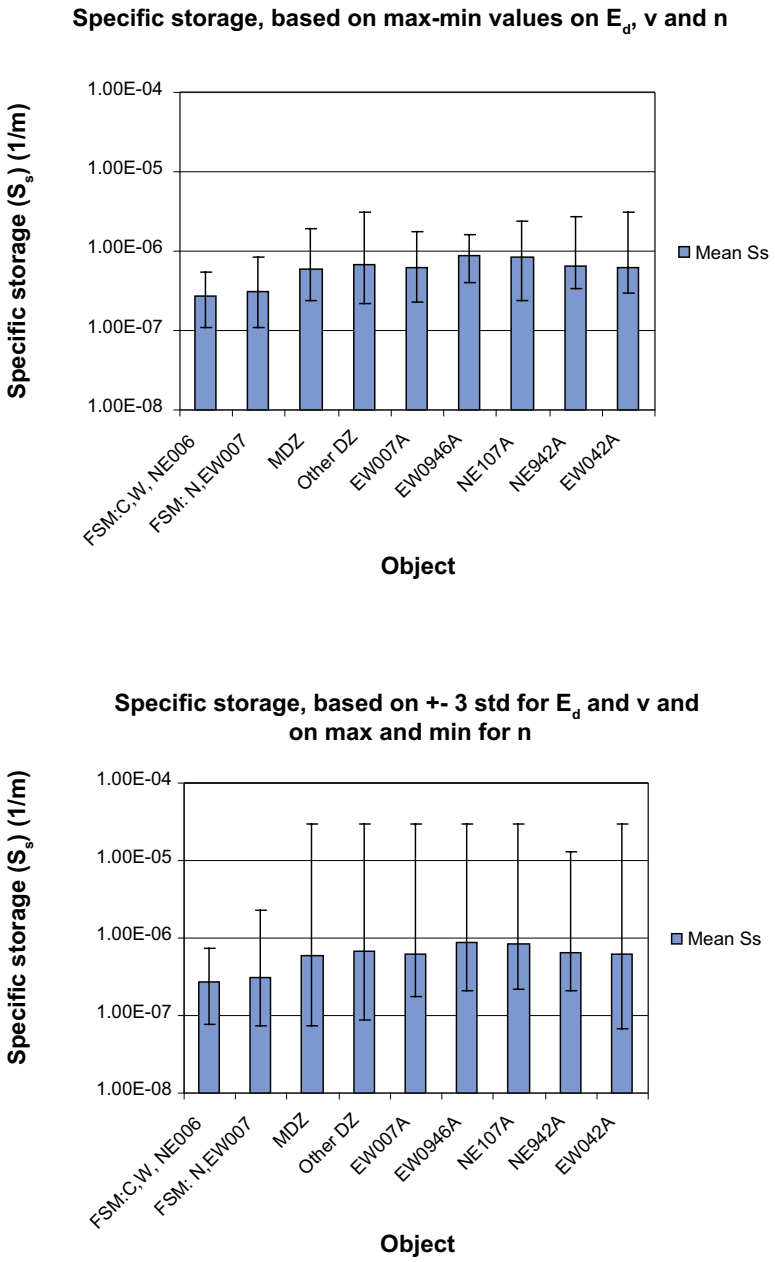

Figure 9-79. *Specific storage S_S within various subdivisions of the Laxemar bedrock; fracture domains with MDZ excluded (FSMxxxx), minor deformation zones (MDZ), deterministic deformation zones interpreted in boreholes but without lineament (Other DZs) , deterministic deformation zones interpreted in boreholes and lineaments (ZSMEW007A, ZSMEW0946A etc). The error bars indicate two different estimates of the maximum and minimum for S_S.*

Table 9-20. Relationship between *K* and S_s valid for bedrock between deterministic deformation zones (S_S=a·K^B) as shown in Figure 9-80.

Model ID	Object	Data type	Coeff. a	Coeff. B
HRD-KSs1	HRD	Specific Storage coefficient as function of hydraulic conductivity in the bedrock between deterministic deformation zones	1e–4	0.25

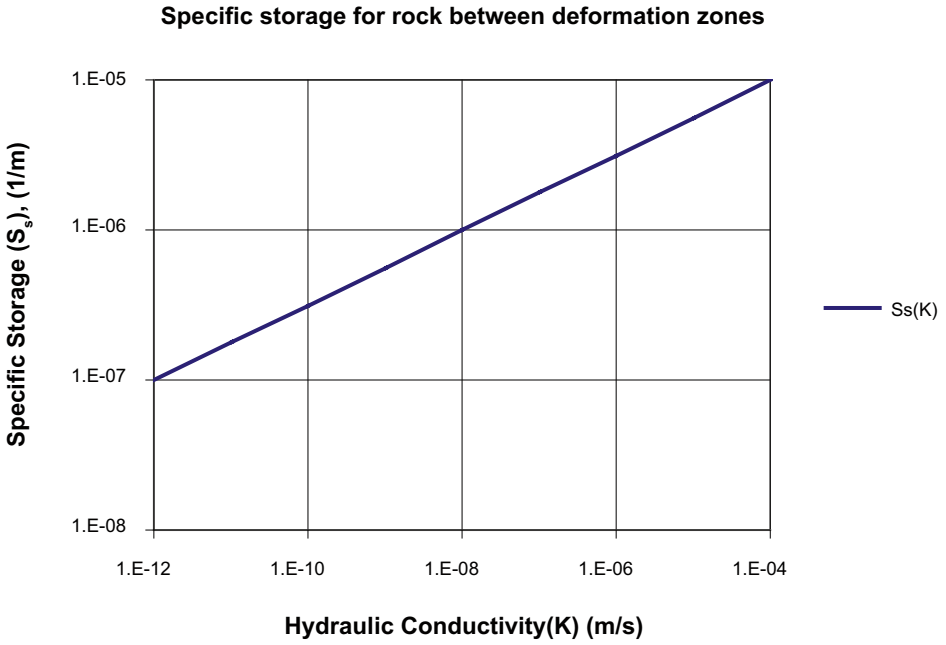

Figure 9-80. *Established approximate correlation between* K *and* Ss *for Laxemar rock between deformation zones based on interpreation of rock mechanical and hydraogeological data in Section 9.9.1.*

9.10 Comparison of hydraulic conductivity data in Äspö and Laxemar

PSS tests were performed in tests scales 3, 30 and 100 m during the site investigation program preceding the construction of the Äspö HRL. During site investigation for a geological repository in the Laxemar-Simpevarp area the test scales have been 5, 20 and 100 m. In Appendix 9, Section A.9.2, test results from surface drilled cored boreholes at Äspö HRL on test scales 3 and 30 m are compared with corresponding test results from Laxemar in HRD_C, HRD_W and HRD_EW007, south of deformation zone ZSM_EW007, on test scales 5 and 20 m. Data plotted include both data from HRDs and HCDs.

The overall conclusion is that the hydraulic conductivity within depth zone –150 to –400 m is slightly lower in Laxemar compared with Äspö and lower within depth zone –400 to –650 m in Laxemar compared with Äspö.

Below –650 m the hydraulic conductivity in Laxemar is possibly lower than in Äspö, but the number data points are limited at both sites. Above elevation –150 m the data are too scarce to enable any firm conclusion.

10 Hydrogeological DFN modelling

The objectives of this chapter are to:

- Explain the methodology used to parameterise a hydrogeological DFN model for each of the defined hydraulic rock domains (HRDs) and for each depth zone based primarily on data from PFL measurements.
- Demonstrate the performance of the derived models in reproducing defined hydraulic characteristics of the bedrock.
- Present the recommended hydrogeological DFN parameterisation for each HRD and depth zone.

10.1 Background and overview of work performed

The Laxemar 1.2 geological DFN /Hermanson et al. 2005/ provided definitions of the geometrical characteristics of the DFN such as fracture set hard sectors and orientation distributions, as well as some suggestions for fracture size distributions. The hydrogeological DFN modelling /Hartley et al. 2006/ considered aspects of the intensity of open fractures, fracture network connectivity and groundwater flow. Hydraulic rock domains were defined on the basis of preliminary definitions of rock domains. A limited number of boreholes had been completed within in each rock domain for model version Laxemar 1.2, and so /Hartley et al. 2006/ used data from individual boreholes to calibrate a hydrogeological DFN model for each HRD. KLX04 was used for the Ävrö granite (rock domain RSMA01), and KLX03 for the quartz monzodirite (rockdomain RSMM01). The rock was divided into two depth zones: above and below –300 masl for the purposes of the hydrogeological DFN modelling. A further hydraulic depth zone was suggested in the regional groundwater flow modelling of the palaeo-hydrogeology to calibrate bedrock properties against hydrochemistry data which implied an order of magnitude reduction in transmissivity below –600 masl. /Follin et al. 2006/ used data from KLX04 to investigate issues of fracture connectivity and concluded that even when fracture occurrence is generated using a Poisson point process, the subset of connected fractures can still form a fractal spatial distribution, depending on fracture intensity and size parameters. Alternative transmissivity relationships between fracture size and transmissivity were recommended as part of the hydrogeological DFN uncertainty analysis (see /Hartley et al. 2006/), but there was insufficient data to discern any clear difference in transmissivity between the fracture sets.

As part of the Laxemar 2.1 hydrogeological pre-modelling exercises, /Hartley et al. 2007/ developed a hydrogeological DFN model of the near-surface Ävrö granite based on a series of 5 closely spaced vertical and inclined boreholes centred on KLX09, cf. Figure 3-1. As well as enhancing the methodology to consider PFL-based interference tests in addition to single-hole tests, the use of inclined boreholes gave much better resolution of the hydraulic properties of the subvertical sets and implied that the fractures of the NW set were more extensive and generally of higher transmissivity. It suggested that the interference tests offered some possibility to determine a relationship between fracture size and transmissivity, with the NW set interpreted as having a strong correlation between size and transmissivity, while other orientations were weakly correlated.

As seen in Chapter 4 a far larger amount of data are available for the SDM-Site Laxemar modelling based on data freeze Laxmar 2.3, with each hydraulic rock domain being characterised by several boreholes. The hydrogeological DFN methodology has been developed and tested for a similar application in the Forsmark 2.2 modelling /Follin et al. 2007b/ for the 3 main defined fracture domains (FFM).

The SDM-Site Laxemar geological DFN model was developed in parallel to this work, and was therefore not available as a direct input to the hydrogeological DFN. For this reason, the set classifications and fracture orientation distributions were determined as part of hydrogeologcial DFN modelling. Likewise, in the absence of guidance from an updated geological DFN, the distribution of fracture sizes for potential water-conducting fractures had to be derived independently and then compared with the size distribution interpreted in the geological DFN for all fractures, cf. Section 10.10.

Here, a power-law distribution for size was assumed and combinations of the location parameter r_0 and shape parameter k_r were calibrated based on simulations of fracture connectivity relative to the frequency of flowing features detected by PFL hydraulic tests. The underlying principle is simple:

$$P_{10,all} \geq P_{10,open} \geq P_{10,cof} \geq P_{10,PFL} \quad (10\text{-}1)$$

where $P_{10,cof}$ denotes the frequency of "connected open fractures", the key property of any hydrogeological DFN model, and $P_{10,open}$ denotes the frequency of "potentially water-conducting fractures", cf. Figure 10-1. This procedure ensures that the size distribution models used are self-consistent in predicting the total frequency of all potentially water-conducting fractures observed in the boreholes, and the subset of those fractures that form open channels connected to the fracture network. It should be noted that the size distribution for all fractures and the subset of potentially water-conducting fractures are not necessarily the same, or even correlated. Consistent with Equation (10-1), one can insist that the hydrogeologcial DFN fractures be a subset of geological DFN fractures on any scale, and this is one physical constraint that the two independently derived DFN models should satisfy for consistency. This consistency check is made in Section 10.10.

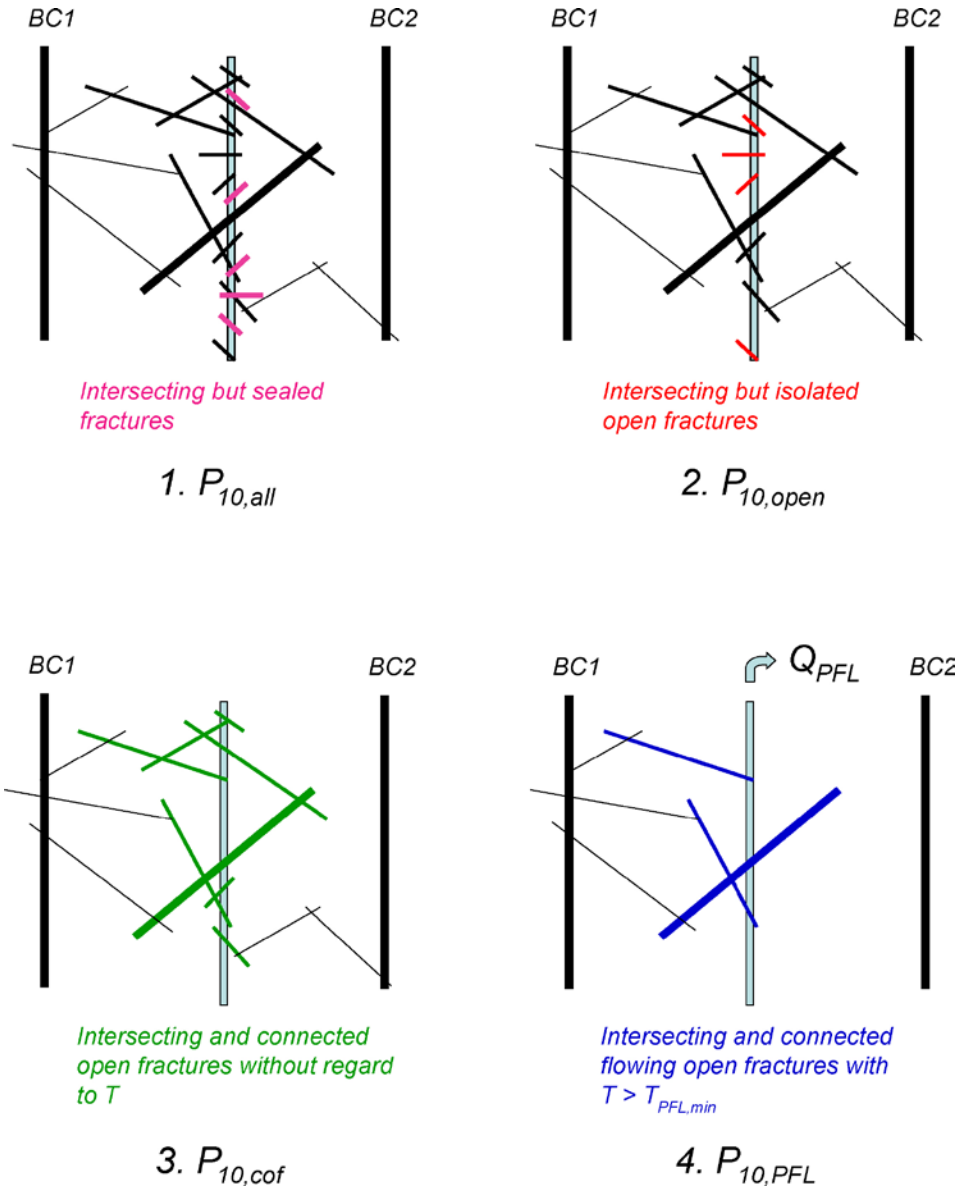

Figure 10-1. *P_{10} all is the frequency of all fractures intersecting the borehole, $P_{10,open}$ the frequency of all open fractures, $P_{10,cof}$ of "all connected open fractures" and $P_{10,PFL}$ of all interconnected, open, flowing fractures that have a transmissivity greater than c. $1 \cdot 10^{-9}$ m^2/s. BC means boundary condition. Reproduced from /Follin et al. 2007b/.*

The above approach is essentially a geometrical one used to identify appropriate initial choices for pairs of (r_0, k_r) power-law size parameters. The model is stochastic, and so a Monte-Carlo approach is used in sampling a number of realisations, and comparing the mean intensity of the modelled connected open fractures in a borehole to the mean intensity of flowing features detected by PFL within a specified rock subdivision (i.e. HRD and depth zone). Then, by performing flow simulations of the inflows into a borehole, again based on a Monte-Carlo approach (i.e. multiple realisations), the choice of size parameters may be refined and transmissivities assigned to match the measured distribution of interpreted transmissivities. The quality of the match is quantified in terms of 4 comparisons of the model and measurements for each rock subdivision:

- The shape of the distribution of inflows divided by drawdown (quantified by comparing the histograms over the ensemble of realisations of inflow/drawdown using a bin size of a half order of magnitude and calculating the correlation coefficient of the 2 histograms as well as visual inspection).
- The total flow to the borehole interval (calculated as an arithmetic average over the realisations – arithmetic mean is used as it best captures the maximum observed and simulated inflows).
- The inflow to 100 m borehole intervals (calculated as geometric mean over the realisations, as well as standard deviation – since this is how the PSS data are collated).
- Statistics of the inflows divided by drawdown for each fracture set.

The hydrogeological DFN parameterisation is determined for HRD_EW007, HRD_N, HRD_W and HRD_C and for each of the four depth zones (see Section 9.3.5 for examples of the parameters that define the hydrogeological DFN). In each case, alternative relationships between fracture size and transmissivity including a direct correlation, a semi-correlation and uncorrelated model are considered.

In summary, the methodology used here in deriving the hydrogeological DFN is principally driven by the Laxemar 2.3 data obtained for open fractures and PFL-f features, along with geological concepts of fracture domains and the deformation zone model. These inputs to the modelling were finalised during the present study, and so the majority of input to this hydrogeological DFN study will not change. Therefore, it is anticipated that the SDM-Site Laxemar geological DFN will have limited bearing on the results and conclusions of the present study. It is noteworthy that the SDM-Site Laxemar geological DFN model treats all fractures, sealed as well as open, and has made use of both fractures gathered on outcrops and fractures intersections with boreholes. In contrast, the hydrogeological DFN model focuses solely on open (and partly-open) fractures as observed in cored boreholes at depth, although there are some logged borehole sections close to the surface. This distinction is necessary for the hydrogeological DFN since it is not possible to hydraulically test outcrop fractures, rather the focus is on fractures in deep boreholes which is more pertinent to flow conditions at repository depth.

10.2 Conceptual model development

10.2.1 Model recipients

The hydrogeological DFN model delivery is defined by a conceptual model and stochastic prescription for the parameters to be used in making simulations of flow and transport through the fracture system between the defined deformation zones. The hydrogeological DFN defines the properties of the hydraulic rock domain component of the overall hydrogeological model. The recipients of this model include:

- Internal users with SDM modelling such as
  - Hydrogeological modelling of regional groundwater flow and transport.
  - Description of bedrock transport processes and properties.
  - Surface systems modelling with an exchange between the soil and bedrock.
- External users such as
  - In safety assessments, quantification of groundwater flow pathways, and calculation of inflows during the “Open repository” phase.
  - In repository design, for guiding choices of layouts and grouting strategies.

10.2.2 Definitions

Here, some of the concepts and terminology used in the hydrogeological DFN modelling are defined.

Fracture classification

Each one of the fractures mapped in the drill cores are classified according to a range of different properties and characteristics. One main classification used in this study is an indication of whether the fracture corresponds with some void space in the borehole core indicating a potential contribution to flow:

- *Sealed fractures* – fractures mapped in the core that are judged to be sealed in the bedrock.
- *Open fractures* – fractures mapped in the core that are judged to be open in the bedrock.
- *Partly-open fractures* – fractures mapped in the core that are judged to have open channels but do not break the core.

The term "*All fractures*" will be used here to denote fractures which are sealed, open or partly open, whereas "*Open fractures*" will be used to denote only those fractures which are either open or partly-open. The numbers of partly-open fractures is generally very small, only 0.4% of all fractures.

Another key classification used in this study is:

- PFL-f feature – either a fracture which is judged to be the most likely to be associated with an observed flowing feature in a PFL-f hydraulic test, or a feature which combines several flowing features within one of local minor deformation zones or local major deformation zones.

Conceptually, it is assumed that open fractures form potential conduits for groundwater flow, whether they actually provide paths for flow depending on their connectivity and transmissivity. The PFL-f features represent a sub-set of the open fractures that are both connected to a wider network and have a transmissivity above a threshold which will give flow measurable by the PFL-f method.

Fracture size distribution

One of the most difficult characteristics of fractures to measure directly in the sub-surface rock is fracture size. Fracture trace-length can be measured on outcrops for fractures on the scale of metres to tens of metres, and data are available for lineaments on the scale of 1 km to several kilometres, but this leaves a gap between the scales. (The minimum lineament length mapped in Laxemar is around 1 km). A widely used assumption is one of a continuous scale of fracturing that spans all scales in a continuous manner which can be described by a power-law relationship between fracture intensity and fracture size. The parameters for a power-law distribution for fractures of different sizes, measured in terms of the radius of a disc, are the shape parameter (k_r) and the location parameter (r_0). The distribution, $f(r)$, is often defined only in a truncated range, between r_{min} and r_{max}.

$$f(r) = \frac{k_r r_0^{k_r}}{r^{k_r+1}} \qquad (10\text{-}2)$$

where $r_{max} \geq r \geq r_{min} \geq r_0$, $r_0 > 0$, and $k_r > 0$.

The outcrop and lineament fracture size data can be used to derive measures of fracture intensity by using so called area-normalised intensity plots to combine structural data gathered on different scales of observation so as to guide the choice of fracture size parameters. Fracture intensity is also measured along core-drilled boreholes, which gives another scale of measurement resolution. Small scale fractures generally show up well on the surfaces of a cored rock cylinder, so it is possible to observe fractures on the scale of the borehole diameter, 0.076 m. Figure 10-2 illustrates the fracture size windows measured by each of the fracture characterisation techniques used in SKB's site investigations.

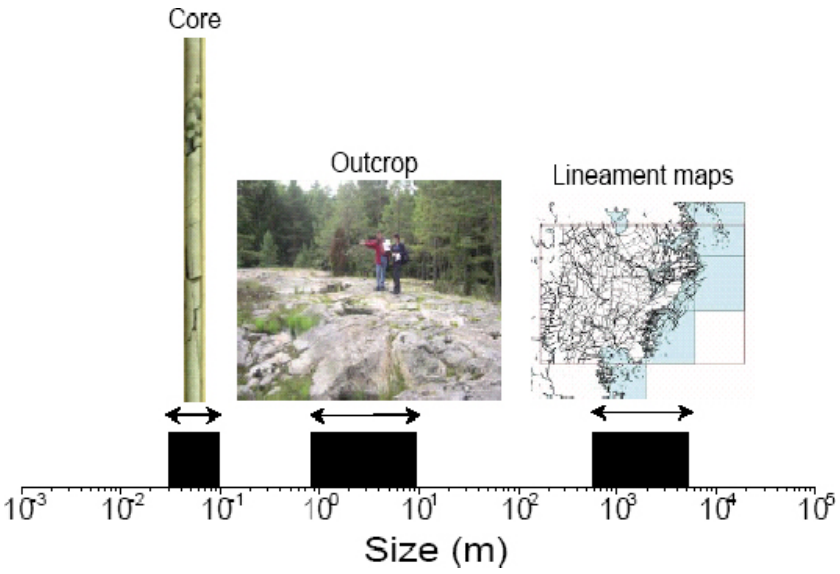

Figure 10-2. *Three scales of fracture trace observations. Outcrop fracture and Lineament trace lengths are used for the construction of a fracture size model in the geological DFN. In this study, the fracture size model are modified to honour fracture intensity data from core and hydraulic tests in boreholes /from Follin et al. 2006/.*

Typically in the geological DFN modelling, the fracture size parameters are determined from combining fracture intensity data for deformation zones, outcrop maps and borehole cores. Such models are developed based on all fractures mapped in the cores and outcrop without consideration for the flow characteristics of the interpreted fracture system.

In this study, the fracture size distribution only those those fractures that contribute to the hydrogeological system are of interest, i.e. open fractures and PFL-f feature fractures. Clearly this will be a sub-set of all fractures, but the parameter distributions of this sub-set do not necessarily display a simple relationship to those for all fractures derived in geological DFN models. Since the distribution of fracture sizes for open fractures cannot be measured directly methods were developed for calibrating the size distribution of open fractures based on characteristics such as the observed intensity of PFL-f feature fractures. This indicates the connectivity of the fracture system which is strongly dependent on the fracture size distribution given the measured intensity of open fractures.

Fracture intensity

The intensity of fracturing can be measured and expressed in several ways usually depending on the method by which fractures are mapped. The main measures of intensity are defined as:

- P_{10} – average fracture frequency along a borehole or scan-line.
- P_{21} – average fracture trace length per unit area, e.g. on an outcrop or lineament map.
- P_{32} – average fracture area per unit volume of rock.

The first two of these are used commonly to collate field data since they can be computed readily. However, both are subject to bias introduced by the orientation in which a measurement is made relative to the orientation of fractures. Hence, the process of Terzaghi correction /Terzaghi 1965/ is used (see Section 9.3 and Figure 9-2).

The third measure, P_{32}, is an unbiased fracture intensity statistic, although it is obviously difficult, if not impossible, to measure in the field directly. Still, it is used to parameterise and characterise fracture intensity in models because of its independence from the definition of orientations. In practice, P_{32} can be approximated by $P_{10,corr}$ and adjusted if necessary by calibration against numerical simulations.

For the power-law size distribution it is useful to be able to calculate the P_{32} fracture intensity associated with different ranges of fracture size using the following formulae. If $P_{32}[r > r_0]$ denotes the fracture surface area of all fractures greater than the location parameter, r_0, the following relation applies:

$$P_{32}[r > r_1] = P_{32}[r > r_0]\left(\frac{r_1}{r_0}\right)^{(2-k_r)} \tag{10-3}$$

where $P_{32}[r > r_1]$ is the fracture surface area of all fractures r greater than the size r_1. From a modelling point of view, it is necessary to decide the size range $[r_{min}, r_{max}]$ that will be used in the numerical simulations and, equally important, the intensity value $P_{32}[r > r_0]$ that corresponds to the smallest value of the underlying data set. For fractures in the size interval $[r_{min}, r_{max}]$, the fracture intensity of a DFN model is given by:

$$P_{32}[r_{min}, r_{max}] = P_{32}[r > r_0]\left(\frac{(r_{min})^{(2-k_r)} - (r_{max})^{(2-k_r)}}{(r_0)^{(2-k_r)}}\right) \tag{10-4}$$

In modelling a hydrogeological DFN, it is important to quantify both the geometrical connectivity of the network and the transmissivity distribution of fractures that conduct flow. Figure 10-3 illustrates the concept of fracture connectivity and flow as modelled in a borehole. Here, N_{OPEN} is the number of all open fractures seen in the borehole section; N_{COF} is the number of open connected fractures; and N_{PFL} is the number of PFL-f feature fractures observed with flow above the detection limit, typically corresponding to a transmissivity above about 10^{-9} m^2/s. Then the corresponding measures of fracture intensity would be:

- $P_{10} = N_{OPEN} / D$
- $P_{10,cof} = N_{COF} / D$
- $P_{10,PFL} = N_{PFL} / D$

where D is the length of borehole section mapped.

10.3 Fracture set definitions

The same fracture sets were used for all the hydraulic rock domains (See Section 9.3.1) based on the hard sector definitions defined in Table 9-2. All model parameters were defined separately for each fracture set, and the calibration of fracture size and flow parameters was performed on the basis of these individual sets.

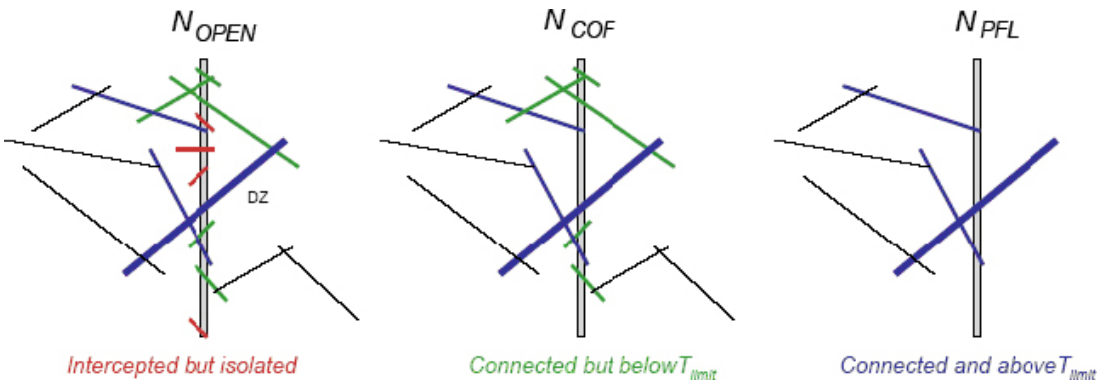

Figure 10-3. *The definition of N_{OPEN}, N_{COF} and N_{PFL} for open fractures. T_{limit} denotes the lower measurement limit for transmissivity, which is typically around 10^{-9} m^2/s for the Posiva Flow Log (PFL-f), from /Follin et al. 2005/.*

Within each hydraulic rock domain and each fracture set, the distribution of fracture orientation was approximated by a univariate Fisher distribution characterised by a mean plunge and trend, together with a Fisher concentration parameter. The parameters were obtained by fitting the distribution to the PFL-f features within each set separately. The four HRDs were analysed separately, but were not further divided by depth. The fitting was done using the stereographic methods with Terzaghi weighting. The resulting parameters are given in Table 10-1. Note that set names refer to the direction of the pole, not the mean fracture plane. This is opposite to the convention used in geological DFN in which the sets are denoted according to mean strike orientation.

10.4 Simulations of fracture geometry

10.4.1 Modelling approach

In previous hydrogeological DFN studies of Laxemar, data have only been available for a handful of boreholes, and so it was appropriate to develop hydrogeological DFN models based on explicit models of each one of a small number of boreholes. For the SDM-Site Laxemar modelling, firstly it is impractical to construct individual hydrogeological DFN models for each of the core drilled boreholes with PFL-f data, and secondly the analysis of Chapter 9 concludes that the key characteristic of flowing fractures are described by the defined hydraulic rock domains and depth zones. Hence, the hydrogeological DFN models are developed for each of the 4 defined HRDs, each separated into the same 4 depth zones. To characterise statistics for each HRD, data are pooled over several boreholes for the same HRD and depth zone. Therefore, models are developed based on statistics homogenised over the HRD and depth zone, so as to derive models that capture the overall characteristic of each HRD.

The methodology for deriving a hydrogeological DFN model for each fracture domain involves the following steps:

1. Perform DFN simulations of open fractures based on the orientation models in Table 10-1 and based on several different power-law models for fracture size to check the simulated fracture frequency in boreholes for each set.
2. Use the open fracture models to perform connectivity analyses to test the simulated frequency of potential flow channels for each of the fracture size models and assess which best reproduce the frequency of PFL-f features measured in the boreholes.
3. Based on step 2, optimise the choice of power-law size parameters for each set to give a frequency of connected fractures consistent with the frequency of PFL-f features measured in the boreholes, and consider uncertainties in the intensity and size of open fractures.
4. Using the power-law size parameters from step3, perform DFN flow simulations to calibrate hydraulic parameters and possible relationships between fracture size and transmissivity. The parameters are derived for each set, each depth zone and each HRD. A direct correlation between fracture size and transmissivity is considered, as well as alternatives based on a semi-correlation and a completely uncorrelated model (the semi-correlated model is taken as the base case).

Table 10-1. The parameters of the Fisher distributions for the orientation of the mean pole of the fracture sets for each defined hydraulic rock domain. (Set name defined by the approximate strike of the set.)

Set	(Trend, plunge), Fisher concentration			
	HRD_C	HRD_EW007	HRD_N	HRD_W
ENE	(155.1, 3.4) 9.6	(162.8, 1.4) 10.7	(342.2, 0.2) 15.8	(340.3, 1.2) 15
WNW	(204, 1.6) 12.0	(25.3, 0.2) 16.4	(209.8, 1.6) 14.6	(208.9, 2.2) 10.9
N-S	(270.2, 8.4) 7.8	(88.9, 3.9) 8.8	(271.3, 3.8) 10.3	(272.8, 12) 11.5
SubH	(46.3, 84.7) 12.0	(138.7, 81.3) 9.7	(238.9, 81.5) 12.7	(277.1, 84.3) 11.1

The sensitivities quantified as part of steps 1) and 2) to the magnitude of the shape parameter k_r and the location parameter r_0 are quantified based on the following four different combinations of k_r and r_0 to illustrate the importance of these parameters in determining the nature of network connectivity and flow prior to seeking optimised parameters that best match the field-data as part of step 3):

a) Small k_r and r_0, (2.6 and 0.038 m).
b) Large k_r and r_0, (2.9 and 0.282 m).
c) Large k_r and small r_0, (2.9 and 0.038 m).
d) Small k_r and large r_0, (2.6 and 0.282 m).

The above combinations have been selected from previous size distributions used in hydrogeological DFN models of either Forsmark or Laxemar (e.g. /Hartley et al. 2006, Follin et al. 2007b/) to give an estimate of the possible parameters. It is worth noting that the geological DFN Base case (BMU) has a range in k_r of 2.8–3.31 (and a range in r_0 of 0.08 m to 0.59 m). This is steeper than the cases listed above, which is reasonable because it is expected that larger fractures are more likely to be open and so the subset of open fractures contains a higher proportion of larger fractures.

For each HRD, 10 realisations of the hyrogeological DFN were simulated in a suitable domain containing a linear representation of a vertical borehole. Ten realisations were used since the model set up essentially represents the idealised conditions surrounding one borehole, and simulations of 10 such boreholes is commensurate with the number of boreholes drilled in each HRD. Ideally, one would simulate 100s of such boreholes and randomly choose groups of 10, say, and use these to quantify both the mean and uncertainty in the predicted statistics for 10 boreholes, but this would be a far greater undertaking. That is, the main benefit of doing far more realisations would be to quantify the expected uncertainty given the finite data available, and hence set appropriate margins for the calibration, rather than in obtaining statistical convergence of predictions.

An example is shown in Figure 10-4. The model extended 400 m in each of the horizontal directions and between elevations 100 masl to –1,100 masl. The simulated borehole was 1,000 m long, inserted through the middle of the model, between elevations 0 masl and –1,000 masl. The lateral model extension of 400 m was chosen as an approximate average horizontal spacing between the regional deterministic deformation zones in the local-scale model. The borehole geometry was chosen to represent the deep core drilled boreholes which are typically 1 km long and cased in the upper 100 m. In this way, the results are expected to approximate those for a much larger model domain in which transmissive subvertical deformation zones were inserted regularly at a 400 m spacing to provide connectivity and fixed head boundary conditions. This idealised vertical column model is used since it allows a generic stochastic hydrogeological DFN model to be developed for each HRD. Simulations results in this section are analysed in terms of the fracture intersections simulated with the borehole in the depth zones 0 to –150 masl, –150 to –400 masl, –400 to –650 masl, and –650 to –1,000 masl. However, for the data, the top depth zone is interpreted as ground surface to –150 masl, and the bottom is interpreted as any borehole intersection below –650 masl.

For practical reasons, the centres of fractures with radius $r=r_0$ to $r=2.26$ m are generated only within a cylinder of radius 2.83 m around the vertical borehole (2.83 m was chosen because the fractures generated in ConnectFlow were squares not circles), while the centres of fractures with radius $r=2.26$ m to 564 m were generated in a region 500 m larger in each direction than the model domain. Therefore, the centres of large fractures of radius up to 564 m could be generated outside the model domain, but their part extending into the model domain would be included in the model, while their part outside would be removed. It is necessary to generate fracture centres in a larger region than model domain whenever the maximum fracture size is comparable or large relative to the model domain size, as here. This is the case because the size range of stochastic fractures (i.e. up to the minimum size for detetministically modelled deformation zones) is similar to the average spacing between the interpreted deformation zones in the local model area.

The methodology described here for obtaining the power-law distribution parameters ensures that the intensity of connected open fractures predicted by the model is on average consistent with the intensity of PFL-f features. The methodology therefore, requires that transmissivity assigned to the generated connected open fractures are predominantly above the detection limit fro the PFL-f method, i.e. $T > 10^{-9}$ m^2/s. Generally, the intensity of PFL-f features in Laxemar is much lower

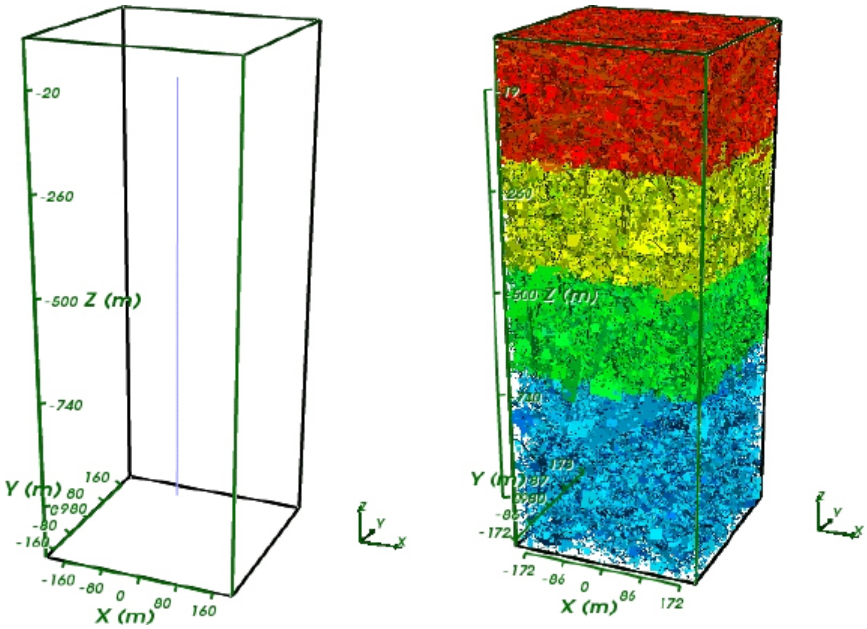

Figure 10-4. *Example of a DFN model used in the calibration. The right picture shows all the fractures and the left just the domain and central vertical borehole. The fractures are coloured according to the depth zone in which their centres are generated.*

than intensity of OPO fractures. Our conceptual model assumes that this is primarily a result of the majority of open fractures having limited hydraulic connectivity rather than transmissivity. This then drives an appropriate choice of power-law fracture size distribution to give a sparsity of the connected network consistent with the intensity of PFL-features. If the PFL method had a lower detection limit, then the intensity of PFL-features would be higher, and so a different slope would result. However, based on the assumption that fracture connectivity is the key characteristic controlling the intensity of flowing features, then Appendix 8, Section A.8.2, demonstrates that the proportion of connected open fractures with flows below the PFL detection limits is likely to be small, and so the sensitivity to the PFL detection limit on the model calibration is not considered to be large.

10.4.2 Fracture intensity

The other key input to hydrogeological DFN simulations apart from fracture set orientations is the intensity of open fractures defined in terms of P_{32}. Since P_{32} is based on a volume sample, then it is not dependent on a sample direction as with P_{10} and P_{21} – it is unbiased. However, it is not readily measured directly. In practice, P_{32} can be estimated from $P_{10,corr}$ and adjusted if necessary by calibration against numerical simulations. The values used in the simulations are given in Table 10-2.

Because of the variations in borehole orientation, all calibration of the models was performed on the basis of comparing Terzaghi corrected P_{10} values of open fractures and PFL-f features with the equivalent simulated fracture intensities from the model. Because of the uncertainty in using the geological indicators of open fractures according to their confidence (see Section 9.3.3), two alternative models were considered where open fracture intensity was calculated based on either open or partially-open (OPO) fractures or on open and partially-open with either certain or probable confidence (OPO-CP) fractures. Eventually after several iterations of the DFN flow model, it was found using OPO fractures as the basis for the hydrogeological DFN gave the most realistic hydraulic properties compared to a case where the hydrogeological DFN was restricted to OPO-CP fractures. Hence, the OPO case was taken as the base case, and as the OPO-CP case was treated as a variant. The geometric characteristics of the OPO case were found to have a preferential effect on the matching process. The OPO case has higher fracture intensity, but in order to match the PFL flow-anomaly data, has shorter fractures compared to the OPO-CP case.

Table 10-2. Average fracture intensity, P_{32}, of open fractures for all depths for each fracture set and hydraulic rock domain, based on the OPO fractures, or OPO-CP fractures in brackets.

Depth zone (masl)	Set	Estimated P_{32} (m^2/m^3) based on OPO (OPO-CP) fractures			
		HRD_C	HRD_EW007	HRD_N	HRD_W
–150 to 0	ENE	0.52 (0.29)	0.55 (0.28)	0.41 (0.16)	0.44 (0.13)
	WNW	0.95 (0.61)	1.01 (0.58)	0.92 (0.55)	0.61 (0.26)
	N-S	0.54 (0.27)	0.33 (0.16)	0.46 (0.23)	0.54 (0.21)
	SubH	1.2 (0.63)	1.72 (0.82)	1.35 (0.45)	1.03 (0.43)
–400 to –150	ENE	0.47 (0.26)	0.6 (0.32)	0.41 (0.14)	0.28 (0.16)
	WNW	0.55 (0.3)	1.15 (0.67)	0.54 (0.32)	0.38 (0.18)
	N-S	0.63 (0.39)	0.54 (0.32)	0.39 (0.11)	0.4 (0.16)
	SubH	0.71 (0.24)	0.82 (0.3)	1.28 (0.38)	0.5 (0.18)
–650 to –400	ENE	0.38 (0.16)	0.69 (0.39)	0.26 (0.14)	0.17 (0.07)
	WNW	0.74 (0.35)	1.43 (0.55)	0.36 (0.29)	0.33 (0.1)
	N-S	0.47 (0.23)	0.64 (0.32)	0.25 (0.17)	0.3 (0.16)
	SubH	0.58 (0.18)	0.92 (0.29)	0.41 (0.24)	0.38 (0.12)
–1,000 to –650	ENE	0.46 (0.2)	0.33 (0.15)	0.35 (0.19)	0.12 (0.01)
	WNW	0.73 (0.34)	0.89 (0.39)	0.45 (0.26)	0.09 (0.02)
	N-S	0.25 (0.12)	0.21 (0.13)	0.08 (0.06)	0.14 (0.05)
	SubH	0.35 (0.14)	0.80 (0.26)	0.07 (0.05)	0.65 (0.16)

The intensities of open fractures are specified in the model for each depth zone and for each fracture set as given in Table 10-2. The reasons for the choice of base case are elaborated further within this chapter.

10.4.3 Consistency check

The first step in the modelling was a consistency check, i.e. to check that the geometrical parameters (intensity in Table 10-2 and orientation distributions in Table 10-1) for each fracture set can be used in DFN simulations of open fractures that yield on average the measured fracture intensity, $P_{10,corr}$, for OPO fractures (or OPO-CP, as a variant). As with previous hydrogeological DFN studies (e.g. /Hartley et al. 2007, Follin et al. 2007b/), the base set of four generic cases suggested in Section 10.4.1 was used initially to illustrate sensitivities to the power-law size parameters.

Figure 10-5 presents comparisons of the generated and measured Terzaghi corrected fracture intensities (for the individual fracture sets and for all sets combined) based on an ensemble over 10 realisations of the hydrogeological DFN for HRD_C. As can be seen, the fracture intensities for the generated realisations are in good agreement with the measured values, and there is little difference between the different size distributions used. In fact, the differences between the cases just indicate the level of statistical convergence using 10 realisations since the intensity of the generated fractures seen along a scan-line representation of the borehole should not depend on the size distribution used. The size distribution does however have a strong effect on connectivity, as will be seen later. The intensities for the generated realisations are slightly lower than the measured intensities for some subvertical sets, but the difference is less than about 14%, which is considered acceptable relative to the variability in intensity between boreholes, the uncertainty in correcting for the borehole trajectories many of which are inclined, and the number of realisations performed. A maximum Terzaghi weight of 7 was used in this analysis as discussed in Section 9.2. Increasing this maximum weight might have improved the match, but then the corrected intensity might have become overly sensitive to the contribution from a few fractures near-parallel to the borehole. An alternative way of improving the match is to increase the P_{32} of the open fractures to correct for the difference between model and the data. This was not done for this study given the small magnitude of the discrepancies.

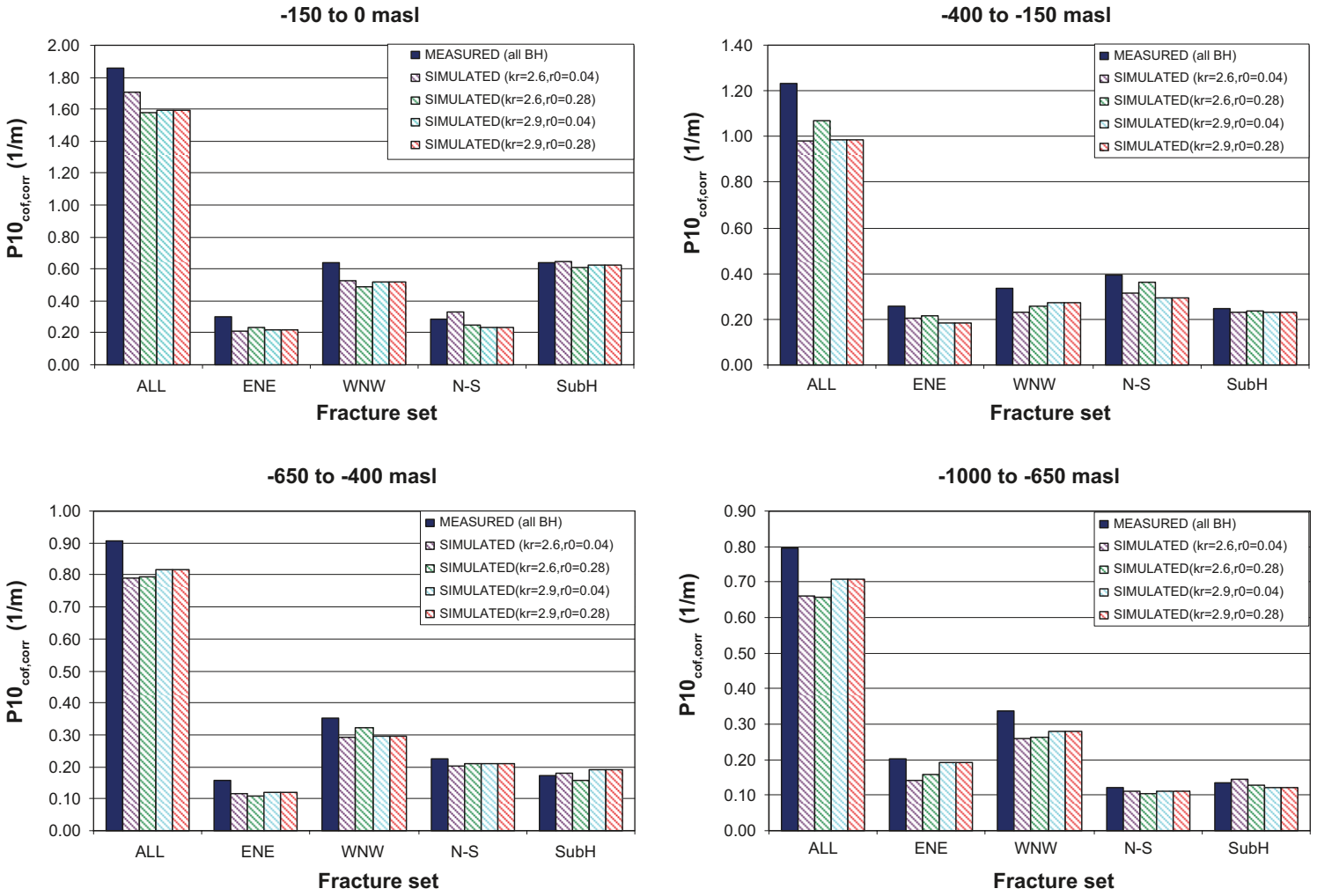

Figure 10-5. *Comparisons by depth of the generated and measured fracture intensities ($P_{10,corr}$) in a borehole for each fracture set and for all sets for the different fracture size models considered for hydraulic rock domain HRD_C (The results shown here are for fracture intensity based on OPO-CP fractures).*

10.4.4 Calibration of fracture intensity and connectivity

The next step in the analysis was to perform connectivity analyses and then determine the fracture intensities (Terzaghi corrected) for connected open fractures, $P_{10,cof,corr}$, which may potentially form flowing features. This is done to derive appropriate choices for the size distributions of open fractures.

The approach is to generate a realisation of all open fractures within the specified domain without any borehole present initially. A connectivity analysis is then performed. This is done by first identifying all the intersections between any two fractures and between a fracture and a boundary of the domain, and then fractures that either have no connection via the network to a boundary of the domain, or ones that have only one intersection (i.e. a dead-end) are removed. Hence, what remain are the open connected fracture system under *in situ* conditions, i.e. without any enhancements to connectivity that may occur locally around a borehole. Only at this stage is a vertical borehole inserted through the remaining connected network to obtain the intensity of connected open fractures. This procedure avoids retaining, and counting, fractures that form isolated or dead-end connections with the borehole. However, it also excludes new local connections with the fracture network created when the borehole is dilled. The borehole is inserted after the connectivity analysis so as to calculate the *in situ* intensity of connected open fractures. The potential contribution of the borehole to connectivity is analysed in Section 10.5 and Appendix 8.

An example of a connectivity analysis is shown in Figure 10-6 for HRD_C. The left hand picture shows all the fractures on a vertical slice and the right hand picture shows the effect of removing isolated and dead-end fractures.

This demonstrates how small fractures tend to not contribute to connectivity and are far less likely to form potential flow paths, leaving areas of rock through which there is little flow or no flow. This effect becomes more exaggerated for parts of the rock with low intensity of open fractures, as are found at greater depth.

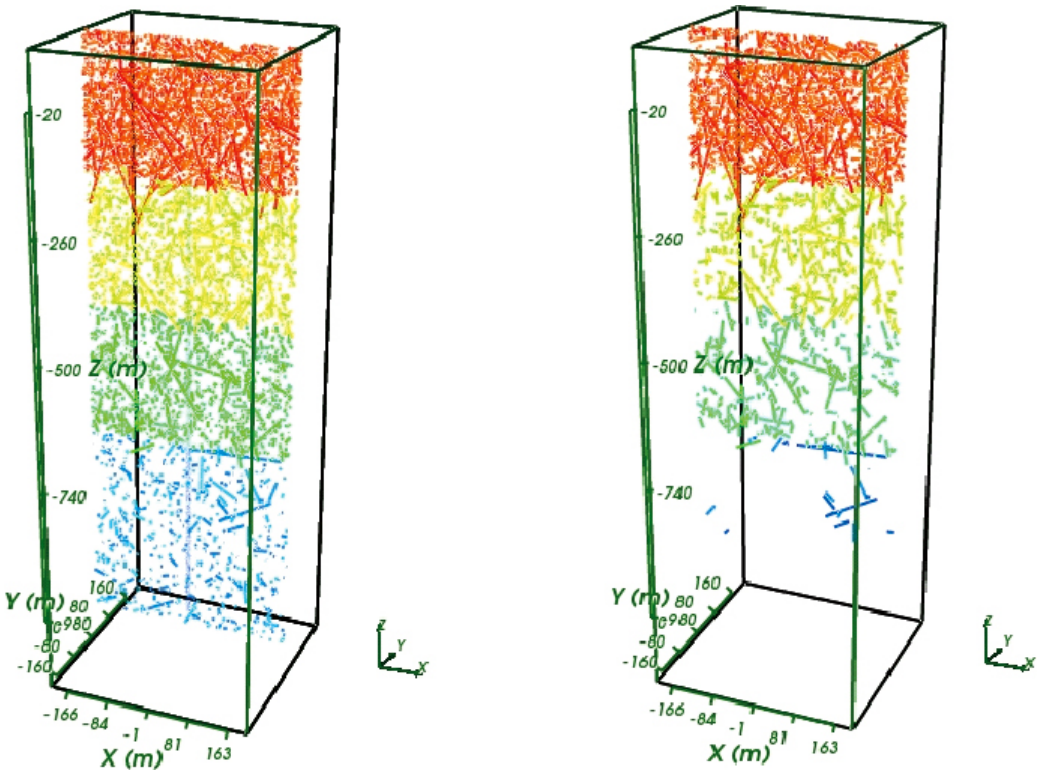

Figure 10-6. *Example of connectivity analysis shown on a vertical (E-W) slice through a DFN simulation of open fractures (this example uses OPO-CP fractures) in HRD_C. Left: a slice through the open fractures generated prior to any connectivity analysis. Right: the same model slice after isolated fractures and dead-ends are removed. The fractures are coloured according to the depth zone in which their centres are generated.*

Initially for Step 2, as described in Section 10.4.1, the sensitivity of fracture connectivity to the power-law size parameters are quantified by considering 4 initial guesses for possible combinations of k_r and r_0 as specified in Section 10.4.1. The results are shown in Figure 10-7 for the fracture intensities of simulated connected open fractures for the individual fracture sets, and all sets combined, are compared with the measured fracture intensities for PFL-f features for HRD_C. These results demonstrate how sensitive connectivity can be to the size parameters, and therefore the fracture size parameters can be quite tightly constrained on the basis of matching the connected open fracture intensity to the of detected flowing feature. For HRD_C, no single initial distribution gave the best match for all sets, the combination of k_r=2.6 and r_0=0.038 m tends to give the best match for ENE and N-S sets and sometimes subH, and k_r=2.9 with r_0=0.28 m tends to give the best match for the WNW set. The case with k_r=2.9 and r_0=0.038 m gives no flowing connections, and the combination k_r=2.6 with r_0=0.28 m gives the most connections. Interestingly, k_r=2.6 and r_0=0.038 m under-predicts the connectivity above –650 masl by about a factor 2–3, but is about right below –650 masl, suggesting that k_r should be less than 2.6 in the upper bedrock and then increase to about 2.6. A physical interpretation of this is that the extent of open fractures, or the open channels within fractures, is generally shorter at depth. Since the OPO or OPO-CP fracture intensities also decrease with depth, the implication is that a less connected network will result at depth as consistent with the PFL data.

Because there are two parameters defining the size distribution and only a single constraint in calibration, i.e. the intensity of PFL-f features, then that calibration is non-unique. Therefore, in order to scope the range of possible size distributions, two quite opposite approaches to calibrate the size parameters were followed: in one case r_0 was fixed at 0.038 m (i.e. the borehole radius that is a definite lower limit for radius of the mapped open fractures) and k_r varied to match the PFL data; and in the other k_r was held fixed and r_0 varied. Also, the geological DFN analysis of outcrops implies an upper limit on r_0 of generally no more than about 0.1–1.5 m /La Pointe et al. 2008/, depending on fracture domain. It is worth noting that if k_r is set to less than around 2.2 then Equation 10-4 predicts a significant fraction of the total open fracture intensity in fractures above the size limit prescribed for stochastic fractures, i.e. $r > 564$ m, implying a large part of stochastic fracture network are sufficiently large that they should have been mapped as deterministic features. Hence, to avoid this conceptual inconsistency a lower limit on k_r was set at 2.2, and so there are additional physical constraints on both r_0 and k_r. For the case when r_0 was fixed at 0.038 m and k_r varied, sometimes a value of k_r less than 2.2 would have been required to achieve a match in the upper depth zones. In such instances, k_r was held at 2.2 and r_0 was increased instead. Assuming that the smallest open fractures are of a similar radius to that of the borehole, then the results presented here suggest that values of $k_r > 2.9$ give rise to models that have too few connections. Hence, this study is limited to values of k_r in the range 2.2 to 2.9, although it is recognised that large values of k_r are plausible when coupled to a higher minimum fracture size, r_0. Further refinements to the choices of size parameters were considered in the flow modelling to account for the role of transmissivity has in determining the number of measured inflows, above the constraints imposed by fracture connectivity described in Section 10.5. These two different approaches to determine optimal size distribution parameters were demonstrated using a hydrogeological DFN based on OPO fractures. For OPO fractures, the case with k_r fixed and r_0 varying had k_r set to 2.9. Likewise, variants of the hydrogeological DFN based on OPO-CP fractures were considered to give up to 4 alternative geometrical parameter definitions. For OPO-CP fractures, the case with k_r fixed and r_0 varying had k_r set to 2.7. Here in the main report, results are presented only for HRD_C. Corresponding plots for other HRD appear in Appendix 6.

A comparison of the simulated intensities of connected open fractures for each of the 4 geometrical cases considered, and the PFL-f feature intensity for each set and depth zone in HRD_C is shown in Figure 10-8. Again, the margin of matching is considered acceptable relative to the variability in intensity between boreholes, the uncertainty in correcting for the borehole trajectories many of which are inclined, and the sensitivity of the results given the number of realisations performed. This margin is relatively large in the lowermost interval as the data are very sparse and the matching is reduced to comparing very small numbers of simulated and detected fractures. The parameters for the models based on OPO fractures are listed in Table 10-3. As an alternative model, the parameters for the model based on OPO-CP fractures are listed in Table 10-4. In each case, the parameters were chosen to give good matches between $P_{10,cof,corr}$ and $P_{10,PFL,corr}$ for each fracture set and hydraulic rock domain, assuming that transmissivity of the open connected fractures are above the detection limit for PFL-f method. It was felt important to give alternative models that reflect the uncertainty in interpreting the hydrogeological DFN model. These models provide an initial guess for the fracture size parameters to be used in Step 4 when matching the flow-rates measured by PFL.

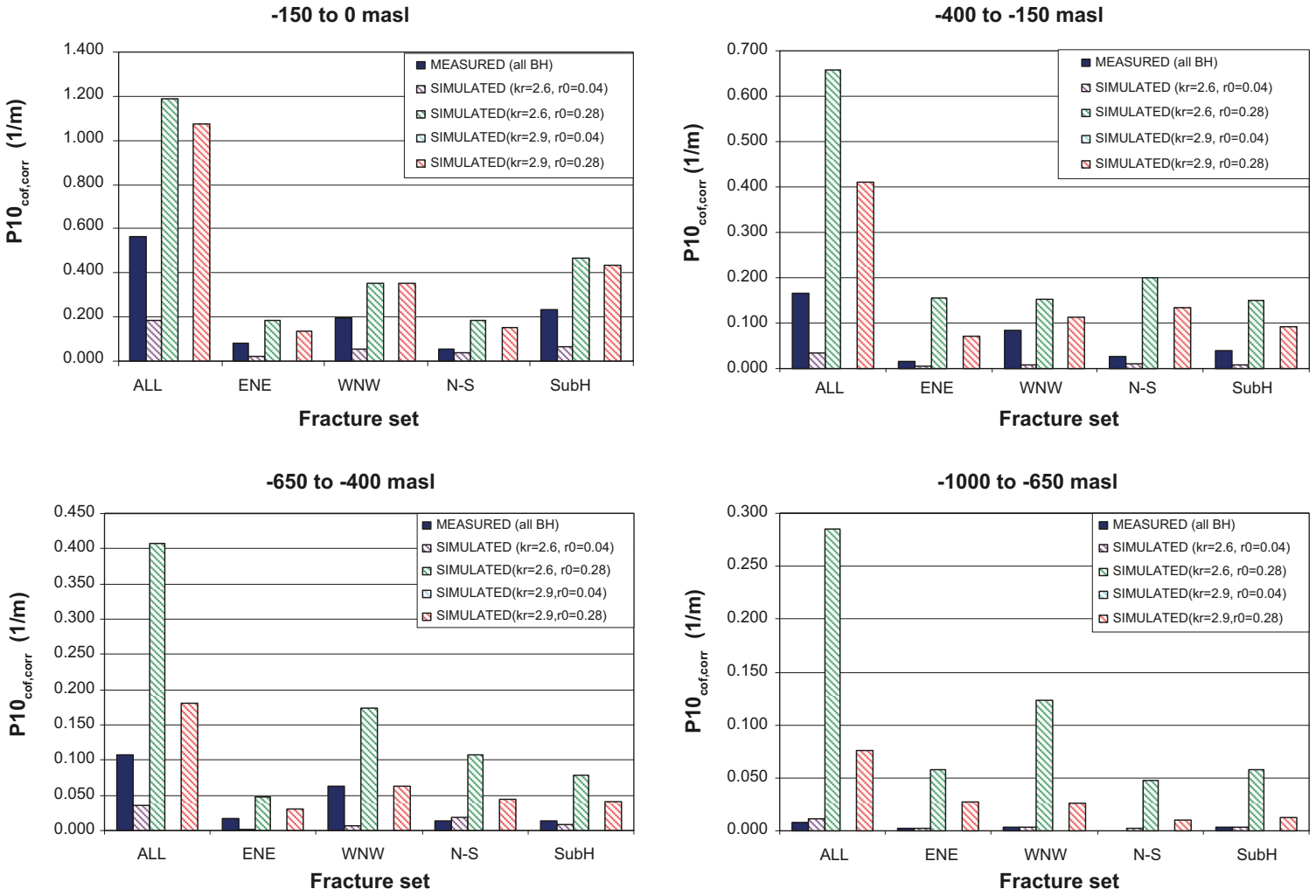

Figure 10-7. *Comparison of the Terzaghi corrected connected open fracture intensities, $P_{10,cof,corr}$ for the individual fracture sets with the measured fracture intensities for PFL-f features for rock domains HRD_C. The 4 generic base case power-law size models are used here and the fracture statistics are based on OPO-CP fractures.*

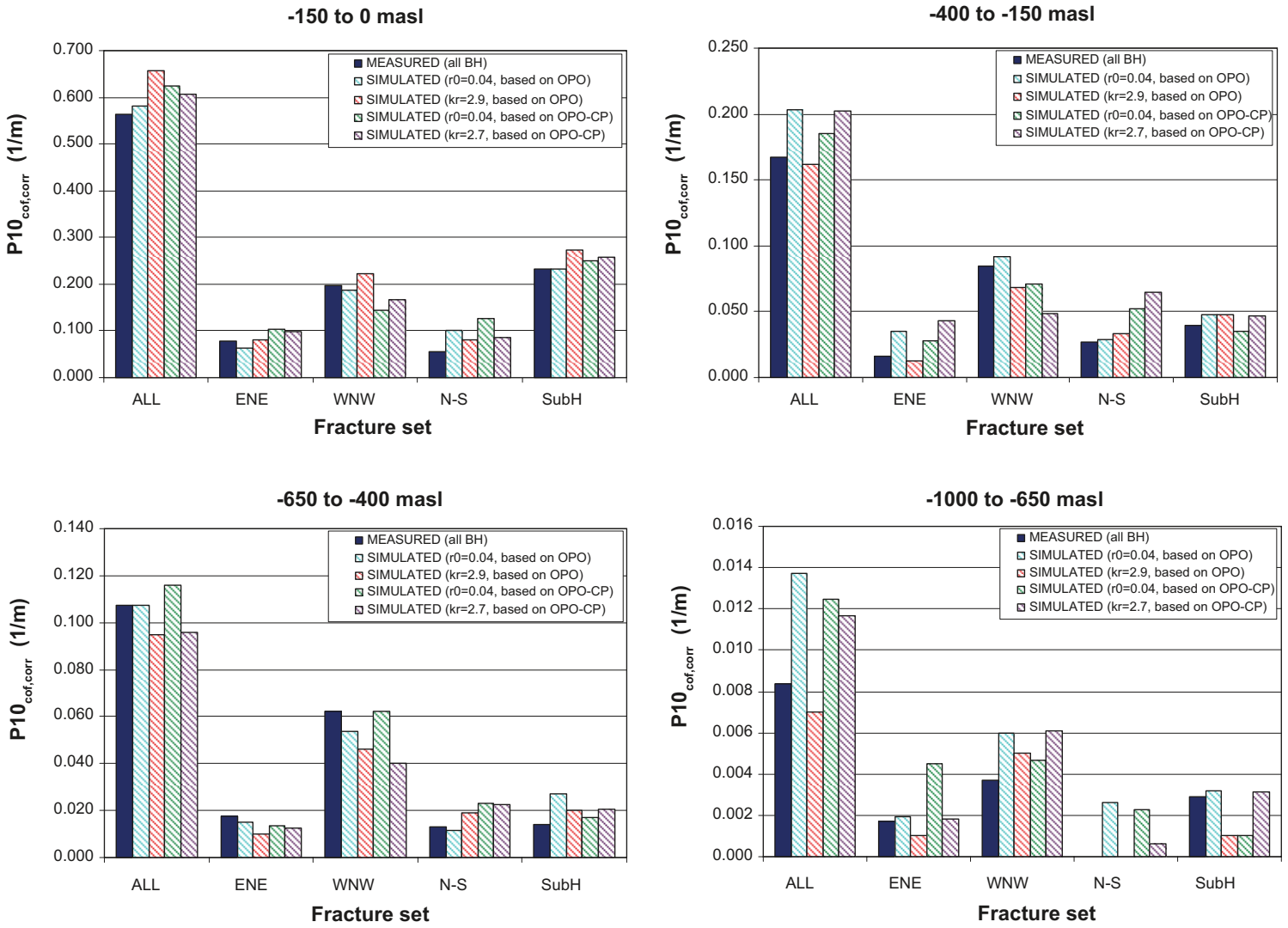

Figure 10-8. *Comparison of the Terzaghi corrected connected open fracture intensities, $P_{10,cof,corr}$ for the individual fracture sets with the measured fracture intensities for PFL-f features for HRD_C. Four geometrical fracture models were considered: k_r fixed with r_0 varying or r_0 fixed with k_r varying, and an input P_{32} based on $P_{10,corr}$ of OPO fractures; r_0 fixed with k_r varying or r_0 fixed with k_r varying, and an input P_{32} based on $P_{10,corr}$ of OPO-CP fractures. A reasonable match is obtained in each case.*

Table 10-3. Two examples of pairs of power-law distribution parameters for fracture size that gave good predictions of flowing fracture frequency for fracture set and each hydraulic rock domain. The estimated open fracture intensity was based on OPO fractures. (See Table 10-2 for the associated open fracture intensities).

Depth zone (masl)	Set	HRD_C Fracture radius models power-law (k_r, r_0)		HRD_EW007 Fracture radius models power-law (k_r, r_0)		HRD_N Fracture radius models power-law (k_r, r_0)		HRD_W Fracture radius models power-law (k_r, r_0)	
–150 to 0	ENE	(2.7, 0.038)	(2.9, 0.07)	(2.7, 0.038)	(2.9, 0.038)	(2.5, 0.038)	(2.9, 0.09)	(2.7, 0.038)	(2.9, 0.038)
	WNW	(2.5, 0.038)	(2.9, 0.13)	(2.4, 0.038)	(2.9, 0.17)	(2.3, 0.038)	(2.9, 0.20)	(2.5, 0.038)	(2.9, 0.11)
	N-S	(2.7, 0.038)	(2.9, 0.05)	(2.7, 0.038)	(2.9, 0.06)	(2.55, 0.038)	(2.9, 0.08)	(2.65, 0.038)	(2.9, 0.08)
	SubH	(2.7, 0.038)	(2.9, 0.07)	(2.75, 0.038)	(2.9, 0.05)	(2.7, 0.038)	(2.9, 0.05)	(2.55, 0.038)	(2.9, 0.11)
–400 to –150	ENE	(2.8, 0.038)	(2.9, 0.038)	(2.8, 0.038)	(2.9, 0.05)	(2.8, 0.038)	(2.9, 0.038)	(2.7, 0.038)	(2.9, 0.13)
	WNW	(2.4, 0.038)	(2.9, 0.20)	(2.4, 0.038)	(2.9, 0.15)	(2.3, 0.038)	(2.9, 0.19)	(2.5, 0.038)	(2.9, 0.23)
	N-S	(2.85, 0.038)	(2.9, 0.06)	(2.75, 0.038)	(2.9, 0.07)	(2.8, 0.038)	(2.9, 0.09)	(2.9, 0.038)	(2.9, 0.038)
	SubH	(2.8, 0.038)	(2.9, 0.05)	(2.8, 0.038)	(2.9, 0.05)	(2.8, 0.038)	(2.9, 0.06)	(2.7, 0.038)	(2.9, 0.10)
–650 to –400	ENE	(2.75, 0.038)	(2.9, 0.09)	(2.95, 0.038)	(2.9, 0.038)	(2.6, 0.038)	(2.9, 0.18)	(2.6, 0.038)	(2.9, 0.038)
	WNW	(2.5, 0.038)	(2.9, 0.17)	(2.65, 0.038)	(2.9, 0.10)	(2.4, 0.038)	(2.9, 0.32)	(2.6, 0.038)	(2.9, 0.22)
	N-S	(2.85, 0.038)	(2.9, 0.05)	(2.95, 0.038)	(2.9, 0.038)	(2.6, 0.038)	(2.9, 0.14)	(2.6, 0.038)	(2.9, 0.26)
	SubH	(2.85, 0.038)	(2.9, 0.038)	(2.95, 0.038)	(2.9, 0.038)	(2.6, 0.038)	(2.9, 0.07)	(2.65, 0.038)	(2.9, 0.13)
–1,000 to –650	ENE	(2.85, 0.038)	(2.9, 0.05)	(2.95, 0.038)	(2.9, 0.038)	(2.55, 0.038)	(2.9, 0.18)	(2.8, 0.038)	(2.9, 0.05)
	WNW	(2.75, 0.038)	(2.9, 0.08)	(2.9, 0.038)	(2.9, 0.038)	(2.35, 0.038)	(2.9, 0.40)	(2.8, 0.038)	(2.9, 0.05)
	N-S	(2.95, 0.038)	(2.9, 0.038)	(2.85, 0.038)	(2.9, 0.11)	(2.55, 0.038)	(2.9, 0.038)	(2.8, 0.038)	(2.9, 0.35)
	SubH	(2.9, 0.038)	(2.9, 0.05)	(2.95, 0.038)	(2.9, 0.038)	(2.55, 0.038)	(2.9, 0.038)	(2.8, 0.038)	(2.9, 0.038)

Table 10-4. Two examples of pairs of power-law distribution parameters for fracture size that gave good predictions of flowing fracture frequency for fracture set and each hydraulic rock domain. The estimated open fracture intensity was based on OPO-CP fractures. (See Table 10-2, bracketed values, for the associated open fracture intensities).

Depth zone (masl)	Set	HRD_C Fracture radius models power-law		HRD_EW007 Fracture radius models power-law		HRD_N Fracture radius models power-law		HRD_W Fracture radius models power-law	
		(k_r, r_0)	(k_r, r_0)	(k_r, r_0)	(k_r, r_0)	(k_r, r_0)	(k_r, r_0)	(k_r, r_0)	(k_r, r_0)
–150 to 0	ENE	(2.3, 0.038)	(2.7, 0.14)	(2.2, 0.038)	(2.7, 0.16)	(2.2, 0.15)	(2.7, 0.3)	(2.2, 0.2)	(2.7, 0.35)
	WNW	(2.3, 0.038)	(2.7, 0.14)	(2.2, 0.15)	(2.7, 0.2)	(2.2, 0.15)	(2.7, 0.4)	(2.2, 0.3)	(2.7, 0.45)
	N-S	(2.3, 0.038)	(2.7, 0.14)	(2.2, 0.038)	(2.7, 0.16)	(2.2, 0.15)	(2.7, 0.3)	(2.2, 0.2)	(2.7, 0.35)
	SubH	(2.3, 0.038)	(2.7, 0.14)	(2.2, 0.038)	(2.7, 0.15)	(2.2, 0.15)	(2.7, 0.25)	(2.2, 0.3)	(2.7, 0.35)
–400 to –150	ENE	(2.55, 0.038)	(2.7, 0.12)	(2.4, 0.038)	(2.7, 0.15)	(2.2, 0.038)	(2.7, 0.4)	(2.5, 0.038)	(2.7, 0.2)
	WNW	(2.3, 0.038)	(2.7, 0.2)	(2.2, 0.15)	(2.7, 0.2)	(2.2, 0.12)	(2.7, 0.4)	(2.3, 0.038)	(2.7, 0.3)
	N-S	(2.55, 0.038)	(2.7, 0.12)	(2.4, 0.038)	(2.7, 0.15)	(2.2, 0.038)	(2.7, 0.4)	(2.5, 0.038)	(2.7, 0.1)
	SubH	(2.55, 0.038)	(2.7, 0.12)	(2.4, 0.038)	(2.7, 0.15)	(2.2, 0.08)	(2.7, 0.3)	(2.4, 0.038)	(2.7, 0.2)
–650 to –400	ENE	(2.5, 0.038)	(2.7, 0.11)	(2.6, 0.038)	(2.7, 0.07)	(2.35, 0.038)	(2.7, 0.25)	(2.4, 0.038)	(2.7, 0.2)
	WNW	(2.3, 0.038)	(2.7, 0.2)	(2.3, 0.038)	(2.7, 0.17)	(2.35, 0.038)	(2.7, 0.25)	(2.2, 0.038)	(2.7, 0.5)
	N-S	(2.5, 0.038)	(2.7, 0.11)	(2.6, 0.038)	(2.7, 0.07)	(2.4, 0.038)	(2.7, 0.15)	(2.3, 0.038)	(2.7, 0.3)
	SubH	(2.5, 0.038)	(2.7, 0.11)	(2.6, 0.038)	(2.7, 0.07)	(2.4, 0.038)	(2.7, 0.25)	(2.3, 0.038)	(2.7, 0.4)
–1,000 to –650	ENE	(2.8, 0.038)	(2.7, 0.038)	(2.7, 0.038)	(2.7, 0.038)	(2.3, 0.038)	(2.7, 0.2)	(2.5, 0.038)	(2.7, 0.15)
	WNW	(2.7, 0.038)	(2.7, 0.05)	(2.7, 0.038)	(2.7, 0.038)	(2.3, 0.038)	(2.7, 0.35)	(2.5, 0.038)	(2.7, 0.15)
	N-S	(2.8, 0.038)	(2.7, 0.038)	(2.7, 0.038)	(2.7, 0.038)	(2.3, 0.038)	(2.7, 0.2)	(2.5, 0.038)	(2.7, 0.15)
	SubH	(2.6, 0.038)	(2.7, 0.038)	(2.7, 0.038)	(2.7, 0.038)	(2.3, 0.038)	(2.7, 0.2)	(2.5, 0.038)	(2.7, 0.15)

The implication of this method to calibrate the fracture size parameters is that flow is restricted to certain size ranges of fractures, generally the larger ones as they are more likley to make connections. The implication of this method is that fracture intensity and size parameters are the key governing parameters for the spatial distribution of flow, although transmissivity also has a role to play. The size distribution of connected open fractures is considered in Section 10.4.5.

When it comes to constructing hydrogeological models on the regional-scale, the hydrogeological DFN model will be formed by applying the hydrogeological DFN parameterisations within the appropriate sub-divisions of the model based on the hydraulic rock domains, and including representations of the HCDs. Recommendations for how this is done are made in Section 10.8. At this stage it is illustrative to show how the choice of geometrical model parameters, mainly the power-law size parameters, affects fracture connectivity with the Laxemar model volume. Figure 10-9 shows examples of the connected fractures after removal of isolated and dead-end fractures on vertical slices, N-S and ESE through an example of the hydrogeological DFN within the Laxemar model volume (The base case with an intensity based on OPO fractures and r_0 fixed is used in this demonstration). The slices show the marked decrease in the intensity of connected fractures at depth, and the slightly higher intensity in the uppermost interval (above –150 masl) and also the lower intensity at intermediate depths in HRD_W (and to a lesser extent in HRD_C) compared to the other HRDs.

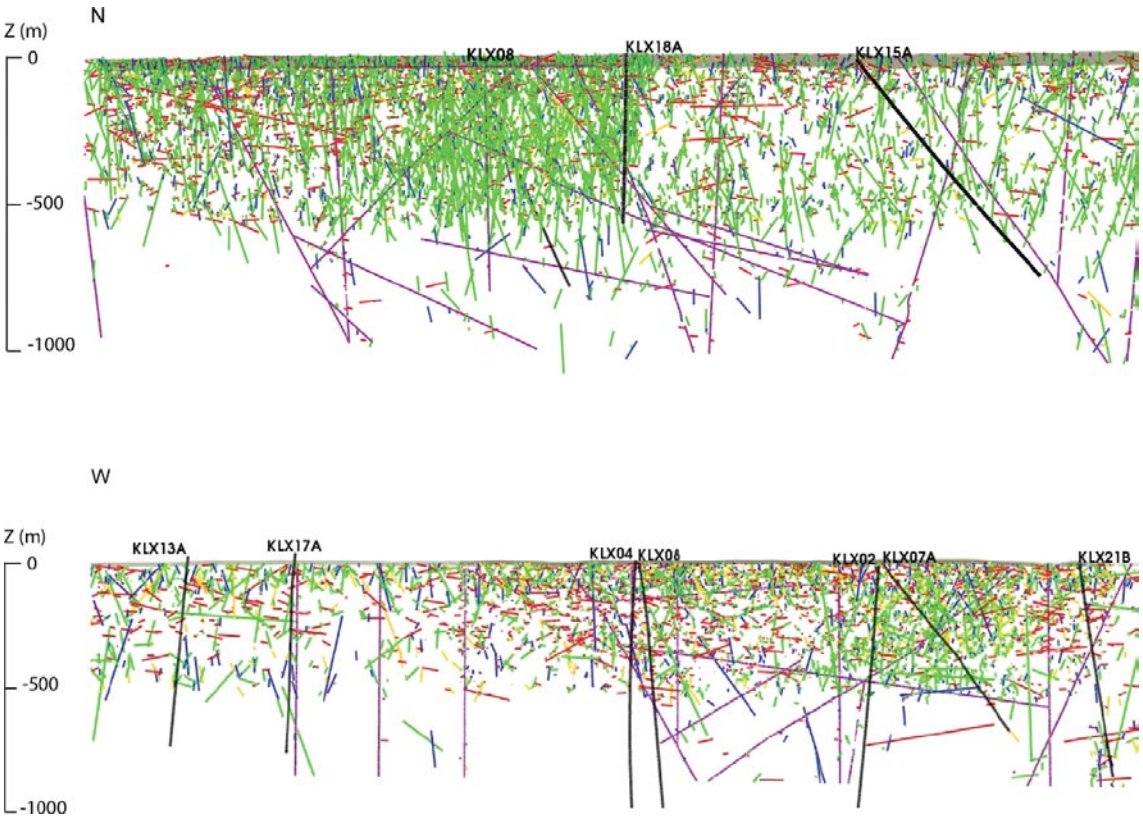

Figure 10-9. *Traces of connected OPO fractures on the N-S Section A and the WNW-ESE Section B (see Figure 10-10) through a regional- scale hydrogeological DFN simulation. The fractures are coloured according to orientation set (ENE – blue, WNW – green, N-S – yellow, subH – red). The HCD are shown in purple together with core drilled boreholes in the close proximity of the vertical section.*

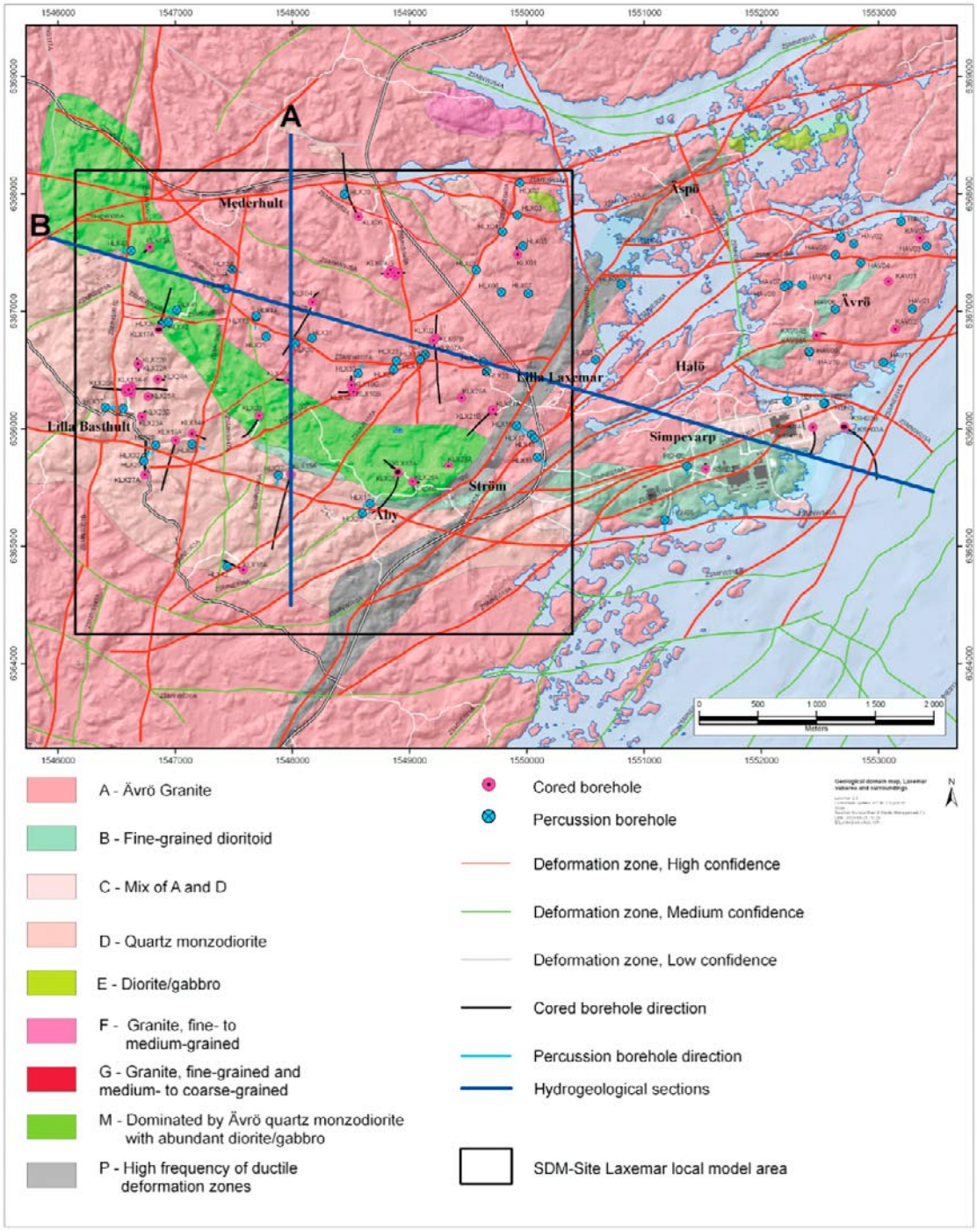

Figure 10-10. *Sections A and B (blue lines) correspond to hydrogeological sections used in Figure 10-9.*

10.4.5 Uncertainties associated with the fracture size models

Fracture connectivity and the spatial distribution of connected open fractures, and hence flowing fractures, are most most sensitive to open fracture intensity, P_{32}, and open fracture size distribution, i.e. the parameters k_r and r_0 for a power-law distribution. Fracture orientation plays a role, but is generally of secondary importance. Given the information available, these 3 parameters cannot be uniquely determined, but Section 10.4.4 shows how combinations of the parameters can be constrained by calibration on the PFL-f data. Here, the implications for the nature of the connected open fracture networks that result from this calibration process are considered, the consistency between them, and in consequence the level of robustness in predicting the spatial distribution of flowing features that might be expected.

Obviously long fractures are more likely to be connected than short fractures, and so the distribution of fracture sizes after the removal of isolated fractures can be quite different to the fracture size distribution for all potentially open fractures. This is demonstrated in Figure 10-11 and Figure 10-12. Figure 10-11 compares the distribution of fracture intensity against fracture size for 3 model quantities:

- P_{32} as specified input in the model (HRD_C, OPO, r_0 fixed).
- $P_{10,corr}$ of simulated open fractures intersected by a vertical borehole (ensemble of 10 realisations).
- $P_{10,corr}$ of connected open fractures simulated in a vertical borehole (ensemble of 10 realisations).

Plots are shown for each of the 4 depth zones. Above –150 masl only some fractures smaller than about 3 m radius are removed. By –400 masl to –650 masl some fractures less than about 30 m are removed as isolated, and below –650 masl fractures up to 100 m are removed. These plots give an indication of what size of fractures contribute to flow in the network.

Figure 10-12 shows a comparison of $P_{10,corr}$ of connected open fractures in a vertical borehole for the 3 geometrical alternatives derived by simulations of fracture connectivity for each of the 4 depth zones:

- Potential open fracture intensity based on OPO-CP fractures and r_0 fixed, k_r calibrated.
- Potential open fracture intensity based on OPO fractures and r_0 fixed, k_r calibrated.
- Potential open fracture intensity based on OPO fractures and k_r fixed, r_0 calibrated.

Each of these 3 models are viable alternatives for explaining the occurrence of open fractures observed in the core logging and the occurrence of PFL flow-f features seen in the hydraulic testing. However, Figure 10-12 reveals that these cases give rise to subtly different fracture networks in how connected fracture intensity is distributed over fracture sizes. The case based on OPO-CP fractures and r_0 fixed has a lower intensity of connected small fractures than the other 2 cases, but has a higher intensity of connected large fractures. The cases based on OPO fracture intensity appear more similar and have a steeper slope in the intensity of open fractures, as they use a higher value of k_r. The case based on OPO fractures and k_r fixed has the fewest long connected fractures. The consequence is that all 3 cases can be calibrated to the PFL-f data seen in boreholes, but flow in the network is concentrated in longer fractures for the OPO-CP, fixed r_0 case than the other cases. Later in this chapter it is shown how this characteristic affects some properties of the resulting hydrogeological DFN models such as the scale dependence of hydraulic conductivity, in particular the hydraulic conductivity on the 100 m scale. The implication is that the parameterisation of open fracture intensity and fracture size distribution are uncertain, and the PFL-f data can only be used to identify possible parameter combinations, with the consequences of the choice these parameters might only becoming apparent in regional-scale groundwater flow models (e.g. predicting large-scale interference tests, groundwater heads, and palaeo-hydrogeology).

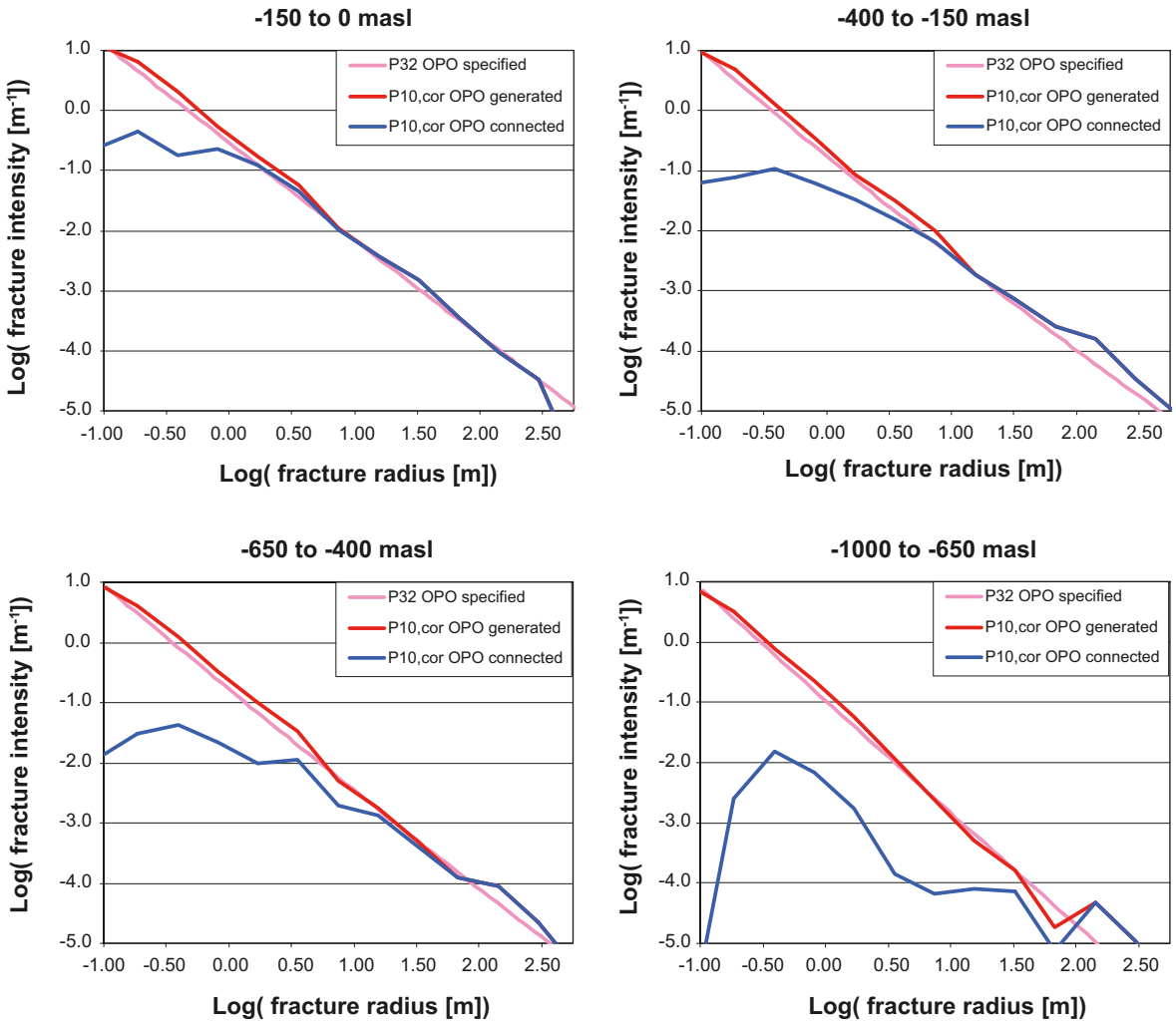

Figure 10-11. *Distributions of fracture intensity (PDF) as a function of fracture radius for the 4 depth zones used in the modelling for the HRD_C for fracture intensity based on OPO fractures and with the r_0 fixed at 0.038 m. The pink line shows the specified distribution of P_{32}; the red curve shows the mean simulated $P_{10,corr}$ in a vertical borehole for 10 realisation; the blue curve shows the simulated $P_{10,corr}$ of connected open fractures.*

Another characteristic of the generated fracture networks that can be investigated is the spatial variability in fracture intensity, or clustering. One way of measuring this is to consider how the number of fractures intersecting a chosen borehole length interval varies between intervals. This can be done both for the data by considering the actual fracture numbers observed in boreholes, and for the model by considering several realisations. Here, a 50 m borehole interval was used, as in Section 9.3, and Terzaghi weighted counts summed over all sets were used to mitigate against borehole trajectory bias. The cumulative frequency of Terzaghi weighted fracture counts per 50 m borehole interval were calculated for each of the 4 depth zones separately. For the data, boreholes from HRD_C and HRD_W were combined to give a reasonable degree of statitical significance. For the model, the appropriate 50 m intervals within 10 realisations of 1 km boreholes were used for a model of HRD_C based on OPO fracture intensity and the r_0 fixed fracture size variant. This was done for both OPO fractures, as shown in Figure 10-13, and for connected open fractures, as shown in Figure 10-14.

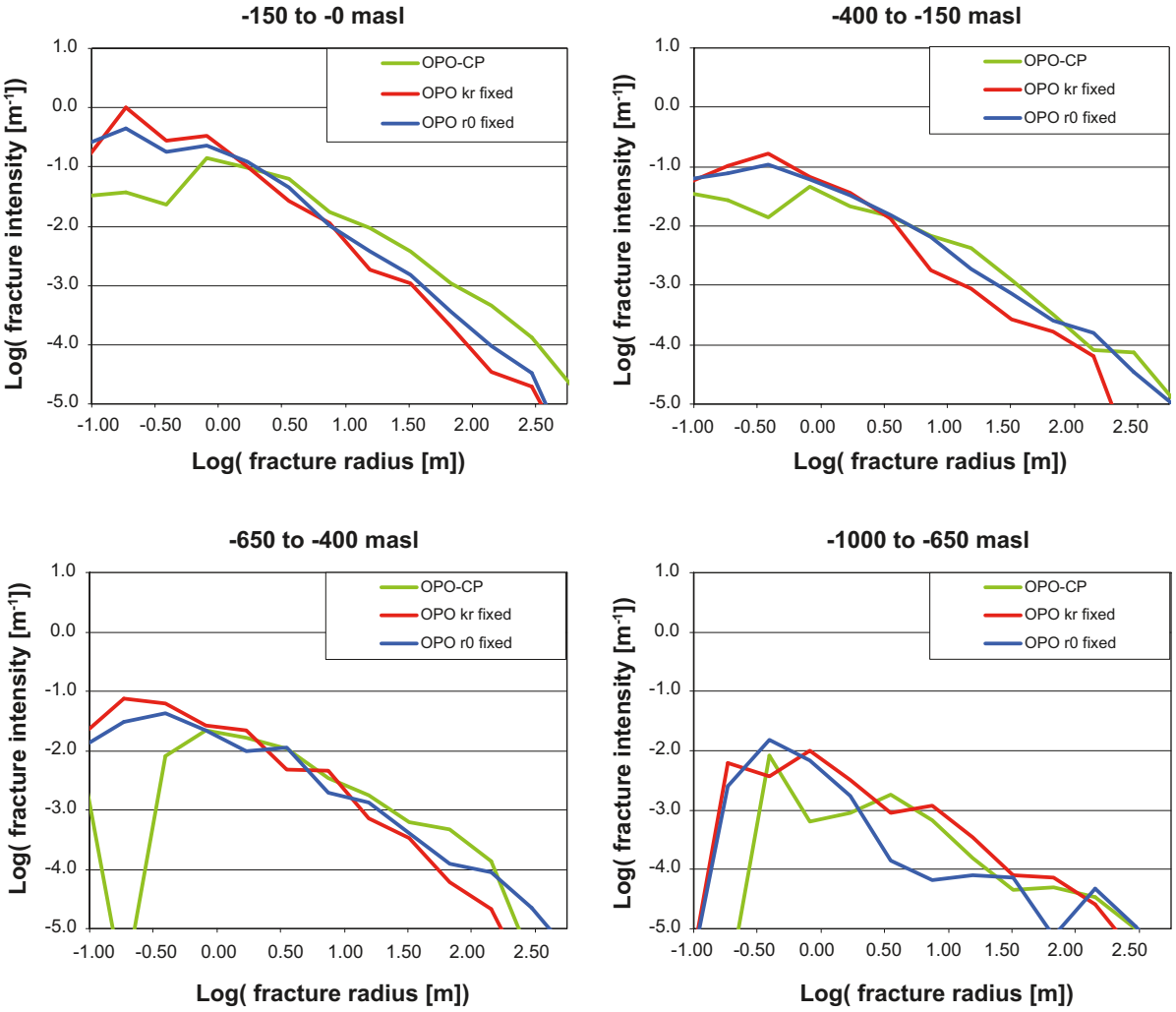

Figure 10-12. *Distributions (PDF) of connected open fracture intensity, $P_{10,corn}$, as a function of fracture radius for the 3 size variants and the 4 depth zones used in the modelling for the HRD_C for. The green curve is the case based on OPO-CP fractures; the red curve is the k_r fixed variant, with intensity based on OPO fractures; and the blue curve is the variant with r_0 fixed, with intensity based on OPO fractures.*

From Figure 10-13 it is clear that generating the open fracture network based on average fracture intensity results in less spatial variability in fracture intensity than is evident from the borehole data. This is no surprise, as the model is based on a homogenisation of fracture intensity within a depth zone and HRD, and hence is unable to reproduce the observed variability. More interestingly though is the comparison for connected open fractures (based on PFL-f features for the borehole data) shown in Figure 10-14, which demonstrates a high level of consistency between the spatial variability in the intensity of this subset of the fractures. This would suggest the clustering of flowing fractures is reproduced by the model, at least on the 50 m interval considered, which provides reassurance that the hydrogeological DFN model is reproducing some of the variability observed in the flowing feature network as well as mean values. However, considering these 2 figures together suggests that the use of a power-law fracture size distribution that allows the model to mimic the observed variability in detected flowing feature intensity, whereas in reality spatial variations in the intensity of open fractures will also give rise to variability in PFL feature intensity. Therefore, the models may require slightly shallower slopes of k_r (i.e. more variability in fracture size) in order to compensate for the homogenisation of fracture intensity.

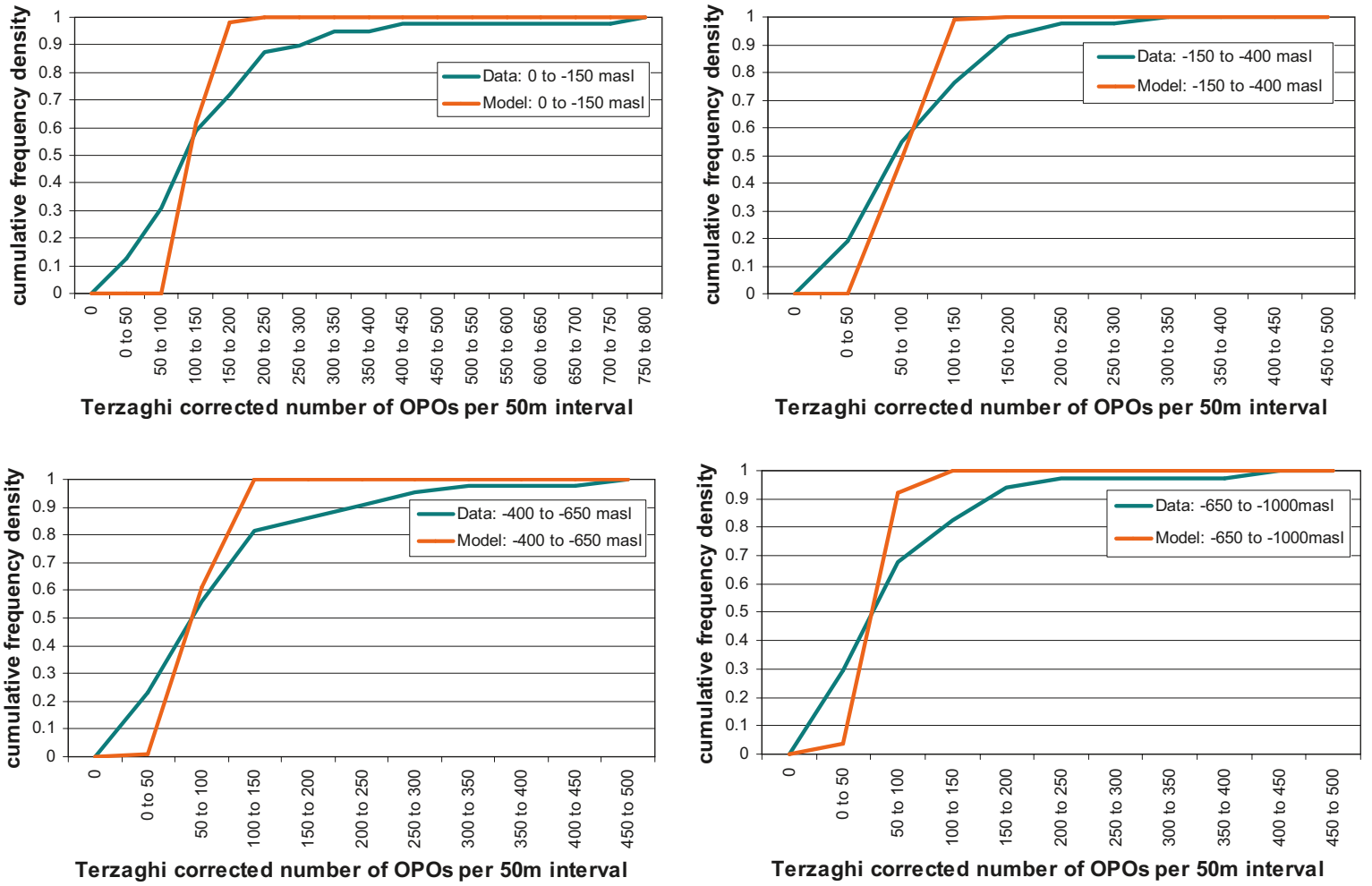

Figure 10-13. *Comparison of distributions (CDFs) of Terzaghi corrected open fracture count within 50 m borehole intervals between the borehole intervals within both HRD_C and HRD_W combined, and the results of 10 realisations of HRD_C based on the OPO, r_0 fixed model. The results for each of the 4 depth zones are shown with a wider range of counts considered for the more fractured upper depth zone.*

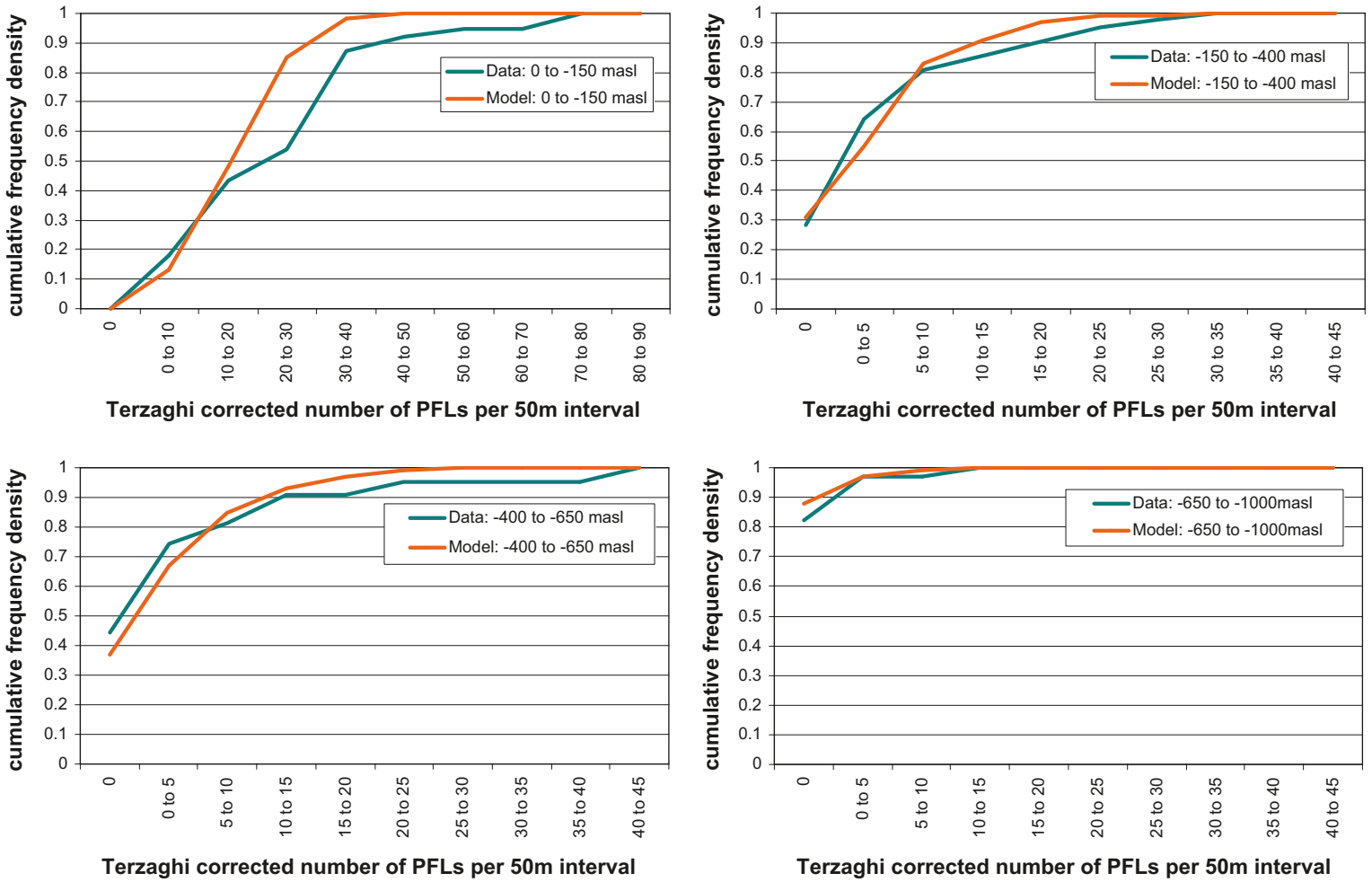

Figure 10-14. *Comparison of distributions (CDFs) of Terzaghi corrected connected open fracture count within 50 m borehole intervals between the borehole intervals within both HRD_C and HRD_W combined (based on PFL-f features) and the results of 10 realisations of HRD_C based on the OPO, r_0 fixed model. The results for each of the 4 depth zones are shown with a wider range of counts considered for the more fractured upper depth zone.*

10.5 Simulation of Posiva Flow Log (PFL-f) tests

10.5.1 Modelling approach

The final stage of modelling is to account for the role of fracture transmissivity in determining both the intensity of flowing features detected by PFL and the magnitudes of inflows measured in the boreholes as they are pumped. It is important at this point to recollect what is actually measured with the PFL-f method. For each PFL-f feature identified, the change in flux (inflow) and head (drawdown) after several days of pumping relative to conditions prior to pumping are calculated. A transmissivity value is interpreted for the PFL-f feature based on an assumed radius of influence of 20 m. The choice of 20 m reflects that tests are performed over several days, and hence should represent an effective transmissivity of the whole fracture intersected, and possibly adjoining parts of the network, but 20 m is otherwise arbitrary. Consequently, the interpreted values of transmissivity should not be viewed as necessarily the transmissivity of an individual fracture, or the transmissivity of the fracture local to the borehole intersect. They are more indicative of the effective transmissivity over a larger scale. This remark influences the way in which the PFL-f data are used in the hydrogeological DFN modelling.

The geometrical model configuration used in the flow simulations is largely the same as for the connectivity simulations described in Section 10.4.4. There are 2 minor differences. Firstly, the generation of open fractures and connectivity analysis is performed with the boreholes present. The connectivity analysis removes all isolated fractures and fractures part of a dead-end (recursively removing those fractures with only one intersect), but retains all fractures connected to a borehole. Some of the fractures retained at the borehole may provide new connections between the borehole and the wider connected network that would otherwise be dead-ends in the absence of a borehole, and hence would form additional flowing features. Such fractures are generally short and may form a cloud of dead-end fractures surrounding an extensive connected open fracture which only becomes hydraulically active once boreholes and tunnels are created. This potentially increases the number of connected open fractures simulated in the flow simulations relative to Section 10.4.4. Other fractures connected to the borehole, might be either single fractures or apert of a local cluster isolated from the wider network, but will have zero inflow for steady-state flow calculations. (The slight difference in approach compared to Section 10.4.4 was necessary due to the current functionality of ConnectFlow). The second difference, was to discard fractures smaller than 0.28 m radius, otherwise running multiple realisations became very time consuming. Such small fractures generally do not contribute significantly to connectivity or flow. The flow boundary conditions configuration has zero head imposed on the vertical sides and top, a uniform 10 m drawdown in the vertical borehole, and hence there is an inflow at every fracture intersection with borehole.

The hydrogeological DFN is parameterised in terms of the transmissivity of individual fractures, and may depend on the size of the fracture according to which transmissivity model is used. Steady-state DFN flow simulations of the PFL-f test configuration are used to predict the distribution of inflows to the boreholes. The idealised boundary conditions used are zero head on the top and vertical boundaries, and a drawdown of 10 m along the whole 1 km of borehole. In the field, the drawdown is typically 10 m near the top, but gradually decreases, and hence the normalised flow-rate of flux, Q, divided by drawdown, s, is used for the comparison of inflows. Again, 10 realisations are performed for each simulation case.

In order to investigate variations with depth, the calculated values of flow rates, Q/s, and the measurements from PFL-f, are both divided according to the 4 depth zones and then used as ensembles to compare the distribution between modelled and measured results. Four main calibration targets are used to quantify how well the model simulates the data:

1. A histogram of the distribution of flow-rates, Q/s, is compared with a bin size of half an order of magnitude. (The comparison of the shape of this histogram is quantified by calculating the correlation coefficient between numbers of PFL-f features within each bin).
2. The total flow to the borehole, sum of Q/s (calculated as arithmetic average over the realisations).
3. The inflow to 100 m borehole intervals (calculated as geometric mean over the realisations, as well as standard deviation).

4. The numbers of PFL-f features associated with each fracture set and the distribution of *Q/s*, for each set. This distribution is quantified in terms of the mean, plus/minus 1 standard deviation, minimum and maximum of Log(*Q/s*).

Each of these is compared for each depth zone. For the data, statistics are calculated over the ensemble of measurements made in all boreholes for intervals within each depth zone. The statistics (such as total flow and numbers of PFL-f features) are then rescaled according to the thickness of the depth zone divided by the total length of borehole sections measured within that depth zone. For the model, ensemble statistics are calculated over the 10 realisations. Hence the statistical variability between realisations is used as an analogue of the spatial variability between boreholes. For measures 1, 2 and 4, the comparison is made with statistics based on the PFL-f data. For measure 3, the geometric mean for the data is taken over the 100 m PSS data in intervals not intersected by major deformation zones, cf. Section 9.6. However, based on the good correlation between PSS 100 m packer data and the sum of PFL-f inflows over the equivalent intervals shown in Figure 9-53, this should be equivalent to comparing with the sum of PFL-f inflows over 100 m intervals.

Since the model considers only a vertical borehole, while the data contains many inclined boreholes, then efforts were made to use Terzaghi weighting of the calibration targets wherever appropriate and practicable. This was done to mitigate against bias in comparing the simulation of inflows to vertical boreholes with measurements in inclined boreholes, which has particular relevance to Laxemar with the hydraulic importance of the WNW set. Hence, in calibration targets 1, 2 and 4 above, any counts of inflows, Q/s, were weighted by the Terzaghi weight of the associated fracture (according to the angle made between the fracture and the borehole). For example, in calibration target 4, the Terzaghi weighted count of PFL-f features were compared, which is consistent with the connectivity calibration of Section 10.4.4.

A final comparison with data was made against hydraulic data from the short interval PSS tests, which largely used a 5 m interval. These were only available for elevations between about –300 masl and –700 masl (i.e. spanning depth zones 3 and 4), and for fewer boreholes than PFL. As a smaller sample size, this data was only as a confirmatory comparison of the calibrated models. To make a comparison, the simulated flows, *Q/s*, were equated to transmissivity and summed over 5 m intervals to compare with the Moye interpretation of the PSS tests, and histograms of modelled and measured distributions compared. As an extra comparison, the number of 5 m intervals within each depth zone that had no detectable flow was calculated and placed on the far left of the histograms as a measure of the sparsity of flowing features.

The parameterisation of the hydrogeological DFN model is non-unique as a number of decisions have to be made in setting it up, including the relationship of transmissivity to fracture size, the fracture size distribution and the interpretation of fracture intensity for potentially open fractures. The various options are listed below.

Three models for the relationship of the fracture transmissivity to fracture size are considered – uncorrelated, semi-correlated and correlated. The uncorrelated and correlated models are two extremes, but a semi-correlated model, somewhere in between, is included as it is likely to be more physically realistic. The definitions of these models are explained in Table 10-5. The non-uniqueness of the fracture size distribution is addressed by performing variants based on Table 10-3 and Table 10-4, i.e. a case where r_0 is held constant, a case where k_r is held constant, and alternatives where the hydrogeological DFN is based on either all OPO fractures or restricted to only OPO-CP fractures.

Table 10-5. The 3 fracture transmissivity to size relationships considered as alternative parameterisations of flow in the hydrogeological DFN model (where μ: mean log10(T), σ: standard deviation of log10(T), $N(0,1)$: Standard normal distribution r: feature radius, a, b: constants).

Type	Description	Relationship	Parameters
Semi-correlated (SC)	Log-normal distribution about a correlated mean	$Log_{10}T = Log_{10}(a \times r^b) + \sigma N(0,1)$	(a , b, σ)
Uncorrelated (UC)	Log-normal distribution about a specified mean	$Log_{10}T = \mu + \sigma N(0,1)$	(10^{μ} , σ)
Correlated (C)	Power-law relationship	$T = a \times r^b$	(a , b)

Each of these possible parameterisations is physically plausible, and it is not clear *a priori* which is likely to best reproduce the observed data. However, in order to obtain a compromise between calibrating models that represent all of the possible valid hydrogeological DFN parameterisations and restricting the number of variants to a pragmatic number, a subset of the possible models was chosen. The variants chosen are described in Table 10-6. The significance of the colour coding relates to the reporting of the variants. For the variants coloured red, the comparison between model and measurements as well as their final parameterisation are given in the main body of this section. For those coloured blue, only the final parameterisations are given in this section, with the flow comparison given in Appendix 6. For those coloured black, only the final parameterisation is given here. As can be seen, special emphasis has been placed on HRD_C since this corresponds to a majority of the potential repository volume.

10.5.2 Hydrogeological DFN calibration of hydraulic rock domain HRD_C

The parameters for each of the variants that gave the best match to the observations (the 'calibrated model') for HRD_C are listed in Table 10-7 for the case with fixed r_0 size model, open fracture intensity based on OPO fractures, and 3 different transmissivity models; Table 10-8 is for the variant with open fracture intensity based on OPO-CP fractures; and Table 10-9 is for the variant with OPO fractures and the k_r fixed size model. The same fracture size distribution was used for each of the variants on fracture transmissivity versus size model. The parameters recommended for the semi-correlated (SC), uncorrelated (UC) and correlated (C) model are given in the far right column. It was possible to discern some difference in transmissivity between fracture sets, but the key difference for hydraulics comes in the size distributions with the WNW generally being longer – lower k_r or higher r_0.

The quality of the match to the observed distributions of PFL-f and PSS flows for the HRD_C base case with a semi-correlated transmissivity, r_0 fixed, and open fracture P_{32} based on OPO fractures is illustrated in Figure 10-15 through Figure 10-19. Figure 10-15 shows the histograms of flow-rates, Q/s, which indicates the shape of the distribution of flows. These are in good agreement to the eye. The agreement in the shape of the distributions was also quantified by calculating the correlation coefficient between the numbers of PFL-f features across the histogram bin (1/2 order of magnitude in flow-rate) in Table 10-10. Our objective was to achieve correlation coefficients above 0.75, which is the case in the upper 3 depth zones. Sometimes this was not possible for sub-divisions of the rock for which there were too few measurements to give a coherent distribution of Q/s to match against.

Table 10-6. Description of the variants chosen for the DFN flow modelling. The colouring reflects the degree of reporting of each variant: Red ones are fully reported; Blue ones are mainly reported in Appendix 6; for the black ones, only the recommended parameters are given.

HRD	P_{32}	Fracture distribution parameters	Transmissivity model
HRD_C	$P_{10,opo}$	r_0 = 0.038, k_r varies	Semi-correlated
HRD_C	$P_{10,opo\text{-}cp}$	r_0 = 0.038, k_r varies	Semi-correlated
HRD_C	$P_{10,opo}$	r_0 = 0.038, k_r varies	Correlated
HRD_C	$P_{10,opo}$	r_0 = 0.038, k_r varies	Uncorrelated
HRD_C	$P_{10,opo}$	r_0 varies, k_r = 2.9	Semi-correlated
HRD_EW007	$P_{10,opo}$	r_0 = 0.038, k_r varies	Semi-correlated
HRD_EW007	$P_{10,opo\text{-}cp}$	r_0 = 0.038, k_r varies	Semi-correlated
HRD_EW007	$P_{10,opo}$	r_0 = 0.038, k_r varies	Correlated
HRD_EW007	$P_{10,opo}$	r_0 = 0.038, k_r varies	Uncorrelated
HRD_N	$P_{10,opo}$	r_0 = 0.038, k_r varies	Semi-correlated
HRD_N	$P_{10,opo\text{-}cp}$	r_0 = 0.038, k_r varies	Semi-correlated
HRD_N	$P_{10,opo}$	r_0 = 0.038, k_r varies	Correlated
HRD_N	$P_{10,opo}$	r_{00} = 0.038, k_r varies	Uncorrelated
HRD_W	$P_{10,opo}$	r_0 = 0.038, k_r varies	Semi-correlated
HRD_W	$P_{10,opo\text{-}cp}$	r_0 = 0.038, k_r varies	Semi-correlated
HRD_W	$P_{10,opo}$	r_0 = 0.038, k_r varies	Correlated
HRD_W	$P_{10,opo}$	r_0 = 0.038, k_r varies	Uncorrelated

This was the case for the deepest depth zone (below –650 masl) in HRD_C. The correlation coefficients of the distributions are given in Table 10-7. The lower correlation coefficient below –650 masl was considered acceptable given the very sparse data at these depths (see Figure 10-15, bottom right).

Table 10-7. Description of the calibrated hydrogeological DFN input parameters for HRD_C with fixed r_0=0.038 m and intensity of open fractures based OPO.

Depth zone (masl)	Set	Orientation set pole: (trend, plunge), conc.	Fracture radius model power-law (k_r, r_0)	Intensity P_{32} (m^2/m^3) of open fractures	Transmissivity model T (m^2/s) See Table 10-5
–150 to 0	ENE	(155.1,3.4), 9.6	(2.6, 0.038)	0.52	SC: ($6\cdot10^{-8}$, 0.5, 0.4) UC: ($2\cdot10^{-7}$, 0.6) C: ($2\cdot10^{-8}$, 0.9)
	WNW	(204,1.6), 12	(2.5, 0.038)	0.95	SC: ($2\cdot10^{-7}$, 0.6, 0.7) UC: ($1\cdot10^{-5}$, 0.9) C: ($5\cdot10^{-8}$, 1.1)
	N-S	(270.2,8.4), 7.8	(2.7, 0.038)	0.54	SC: ($2\cdot10^{-7}$, 0.6, 0.5) UC: ($1\cdot10^{-7}$, 0.7) C: ($6\cdot10^{-8}$, 1.2)
	SubH	(46.3,84.7), 12	(2.7, 0.038)	1.20	SC: ($1.5\cdot10^{-7}$, 0.7, 0.7) UC: ($3\cdot10^{-7}$, 0.8) C: ($6\cdot10^{-8}$, 1.0)
–400 to –150	ENE	(155.1,3.4), 9.6	(2.85, 0.038)	0.47	SC: ($1\cdot10^{-6}$, 0.7, 0.7) UC: ($2\cdot10^{-7}$, 0.7) C: ($5\cdot10^{-8}$, 1.4)
	WNW	(204,1.6), 12	(2.45, 0.038)	0.55	SC: ($8\cdot10^{-8}$, 0.3, 0.1) UC: ($3\cdot10^{-7}$, 0.6) C: ($2\cdot10^{-9}$, 1.3)
	N-S	(270.2,8.4), 7.8	(2.85, 0.038)	0.63	SC: ($1\cdot10^{-7}$, 0.7, 0.7) UC: ($2\cdot10^{-7}$, 0.4) C: ($3\cdot10^{-8}$, 1.0)
	SubH	(46.3,84.7), 12	(2.85, 0.038)	0.71	SC: ($1.5\cdot10^{-7}$, 0.8, 0.9) UC: ($8\cdot10^{-7}$, 1.4) C: ($3\cdot10^{8}$, 1.1)
–650 to –400	ENE	(155.1,3.4), 9.6	(2.8, 0.038)	0.38	SC: ($5\cdot10^{-7}$, 0.5, 0.5) UC: ($2\cdot10^{-6}$, 0.8) C: ($3\cdot10^{-8}$, 0.7)
	WNW	(204,1.6), 12	(2.5, 0.038)	0.74	SC: ($2\cdot10^{-8}$, 0.6, 0.4) UC: ($1\cdot10^{-7}$, 0.9) C: ($3\cdot10^{-9}$, 0.9)
	N-S	(270.2,8.4), 7.8	(2.9, 0.038)	0.47	SC: ($1\cdot10^{-8}$, 0.4, 0.4) UC: ($8\cdot10^{-8}$, 0.4) C: ($1\cdot10^{-8}$, 0.5)
	SubH	(46.3,84.7), 12	(2.9, 0.038)	0.58	SC: ($3\cdot10^{-7}$, 0.6, 0.6) UC: ($2\cdot10^{-6}$, 0.9) C: ($1.5\cdot10^{-7}$, 0.9)
–1,000 to –650	ENE	(155.1,3.4), 9.6	(2.9, 0.038)	0.46	SC: ($5\cdot10^{-9}$, 0.6, 0.4) UC: ($1\cdot10^{-8}$, 0.4) C: ($5\cdot10^{-9}$, 0.6)
	WNW	(204,1.6), 12	(2.8, 0.038)	0.73	SC: ($5\cdot10^{-8}$, 0.6, 0.4) UC: ($5\cdot10^{-7}$, 0.4) C: ($5\cdot10^{-8}$, 0.6)
	N-S	(270.2,8.4), 7.8	(2.95, 0.038)	0.25	SC: ($5\cdot10^{-9}$, 0.6, 0.4) UC: ($1\cdot10^{-8}$, 0.4) C: ($5\cdot10^{-9}$, 0.6)
	SubH	(46.3,84.7), 12	(2.95, 0.038)	0.35	SC: ($1\cdot10^{-7}$, 0.6, 0.4) UC: ($2\cdot10^{-7}$, 0.4) C: ($1\cdot10^{-7}$, 0.6)

Table 10-8. Description of the calibrated hydrogeological DFN input parameters for HRD_C with fixed r_0=0.038 m (where k_r > 2.2) and intensity of open fractures based OPO-CP.

Depth zone (masl)	Set	Orientation set pole: (trend, plunge), conc.	Fracture radius model power-law (k_r, r_0)	Intensity P_{32} (m^2/m^3) of open fractures	Transmissivity model T (m^2/s) See Table 10-5
–150 to 0	ENE	(155.1,3.4), 9.6	(2.3, 0.038)	0.29	SC: ($1.5\cdot10^{-8}$, 0.5, 0.4)
	WNW	(204,1.6), 12	(2.3, 0.05)	0.61	SC: ($4\cdot10^{-8}$, 0.7, 0.7)
	N-S	(270.2,8.4), 7.8	(2.4, 0.038)	0.27	SC: ($2\cdot10^{-8}$, 0.6, 0.5)
	SubH	(46.3,84.7), 12	(2.35, 0.038)	0.63	SC: ($4\cdot10^{-8}$, 0.7, 0.7)
–400 to –150	ENE	(155.1,3.4), 9.6	(2.65, 0.038)	0.26	SC: ($5\cdot10^{-8}$, 0.8, 0.8)
	WNW	(204,1.6), 12	(2.3, 0.08)	0.30	SC: ($8\cdot10^{-9}$, 0.5, 0.3)
	N-S	(270.2,8.4), 7.8	(2.7, 0.038)	0.39	SC: ($3\cdot10^{-9}$, 0.5, 0.3)
	SubH	(46.3,84.7), 12	(2.55, 0.038)	0.24	SC: ($1.5\cdot10^{-8}$, 0.8, 1.1)
–650 to –400	ENE	(155.1,3.4), 9.6	(2.5, 0.038)	0.16	SC: ($1\cdot10^{-8}$, 0.7, 0.7)
	WNW	(204,1.6), 12	(2.3, 0.038)	0.35	SC: ($3\cdot10^{-9}$, 0.4, 0.4)
	N-S	(270.2,8.4), 7.8	(2.5, 0.038)	0.23	SC: ($1\cdot10^{-9}$, 0.4, 0.3)
	SubH	(46.3,84.7), 12	(2.55, 0.038)	0.18	SC: ($3\cdot10^{-8}$, 0.7, 0.5)
–1,000 to –650	ENE	(155.1,3.4), 9.6	(2.8, 0.038)	0.20	SC: ($5\cdot10^{-9}$, 0.7, 0.4)
	WNW	(204,1.6), 12	(2.7, 0.038)	0.34	SC: ($1\cdot10^{-8}$, 0.7, 0.4)
	N-S	(270.2,8.4), 7.8	(2.8, 0.038)	0.12	SC: ($5\cdot10^{-9}$, 0.7, 0.4)
	SubH	(46.3,84.7), 12	(2.65, 0.038)	0.14	SC: ($1\cdot10^{-8}$, 0.7, 0.4)

Table 10-9. Description of the calibrated hydrogeogical DFN input parameters for HRD_C for fixed k_r = 2.9 and intensity of open fractures based OPO.

Depth zone (masl)	Set	Orientation set pole: (trend, plunge), conc.	Fracture radius model power-law (k_r, r_0)	Intensity P_{32} (m^2/m^3) of open fractures	Transmissivity model T (m^2/s) See Table 10-5
–150 to 0	ENE	(155.1,3.4), 9.6	(2.9, 0.07)	0.52	SC: ($1\cdot10^{-6}$, 0.5, 0.4)
	WNW	(204,1.6), 12	(2.9, 0.13)	0.95	SC: ($2\cdot10^{-6}$, 0.7, 0.5)
	N-S	(270.2,8.4), 7.8	(2.9, 0.05)	0.54	SC: ($7\cdot10^{-7}$, 0.5, 0.3)
	SubH	(46.3,84.7), 12	(2.9, 0.07)	1.20	SC: ($1.2\cdot10^{-6}$, 0.8, 0.2)
–400 to –150	ENE	(155.1,3.4), 9.6	(2.9, 0.038)	0.47	SC: ($1\cdot10^{-6}$, 0.8, 0.6)
	WNW	(204,1.6), 12	(2.9, 0.20)	0.55	SC: ($3\cdot10^{-7}$, 0.8, 0.5)
	N-S	(270.2,8.4), 7.8	(2.9, 0.06)	0.63	SC: ($8\cdot10^{-7}$, 0.6, 0.5)
	SubH	(46.3,84.7), 12	(2.9, 0.05)	0.71	SC: ($1.2\cdot10^{-6}$, 0.8, 0.7)
–650 to –400	ENE	(155.1,3.4), 9.6	(2.9, 0.09)	0.38	SC: ($1\cdot10^{-6}$, 0.6, 0.6)
	WNW	(204,1.6), 12	(2.9, 0.17)	0.74	SC: ($4\cdot10^{-6}$, 0.4, 0.2)
	N-S	(270.2,8.4), 7.8	(2.9, 0.05)	0.47	SC: ($1\cdot10^{-7}$, 0.2, 0.1)
	SubH	(46.3,84.7), 12	(2.9, 0.038)	0.58	SC: ($1\cdot10^{-6}$, 0.9, 0.4)
–1,000 to –650	ENE	(155.1,3.4), 9.6	(2.9, 0.05)	0.46	SC: ($5\cdot10^{-9}$, 0.6, 0.3)
	WNW	(204,1.6), 12	(2.9, 0.08)	0.73	SC: ($2\cdot10^{-8}$, 0.6, 0.3)
	N-S	(270.2,8.4), 7.8	(2.9, 0.038)	0.25	SC: ($3\cdot10^{-9}$, 0.6, 0.3)
	SubH	(46.3,84.7), 12	(2.9, 0.05)	0.35	SC: ($7\cdot10^{-8}$, 0.6, 0.3)

Table 10-10. Correlation coefficients for the shape of histograms of Q/s across the bins shown in Figure 10-15 for the semi-correlated transmissivity model with r_0 fixed and open fracture intensity based on OPO for HRD_C.

Depth zone (masl)	Correlation coefficient for distribution of *Q/s* between model and PFL
–150 to 0	0.92
–400 to –150	0.82
–650 to –400	0.77
–1,000 to –650	0.18

The equivalent comparison with the PSS data for depth zones 2 and 3 are shown in Figure 10-16. The simulated and measured distributions of *Q/s* are similar between –400 masl to –150 masl, although the model predicts a small percentage of intervals with high flow-rates, about 1% above $3 \cdot 10^{-6}$ m^2/s, which is thought to be a consequence of the model being calibrated on the larger number of measurements available in the PFL-f data; and fewer simulated intervals with flow rates < 10^{-8} m^2/s, which is likely to have resulted from the model being matched to the PFL-f data that tends to record fewer flow-rates around and below 10^{-9} m^2/s. The numbers of 5 m intervals without any flow shown on the far left of the graphs is similar, 39 intervals per 250 m (i.e. 78%) for the model and 31 (i.e. 62%) for the PSS data. For the interval –650 masl to –400 masl, the number of low flow rates is under in the model and predicts 42 5 m intervals without flow per 250 m of boreholes (i.e. 84%) compared to 31 (i.e. 62%) for the PSS data. The differences at low flow-rates may be influenced by the effect mentioned in Section 9.4.1, i.e. the PSS method measuring flow in single fractures or isolated networks due to its short duration, while the PFL-f method only measures flow in the connected network that can still provide inflows after several days of pumping.

In Figure 10-17 bar and whisker plots are used to represent the variability in flow-rate for individual sets as well as displaying the number of PFL-f features (Terzaghi weighted) per depth zone of the borehole for each set. These plots were used to guide refinement of the transmissivity models for individual sets and for each depth zone. As a result, hydraulic anisotropy and depth trends could be reproduced in the modelling to a reasonable degree. The derived parameterisation suggests the following features:

- the WNW tends to be more extensive (lower k_r),
- transmissivity of fractures decreases only gradually with depth,
- the variability in transmissivity tends to decrease with depth.

Figure 10-18 confirms the agreement in total flow-rate. This calibration target is highly dependent on the far right-hand tail of the transmissivity distribution generated.

The calibration against the geometric mean of total flow-rates, *Q/s*, to 100 m borehole sections shown in Figure 10-19 depends on a slightly larger portion of right-hand side of the distributions shown in Figure 10-15. Roughly, it depends on the part of the *Q/s* distribution where the values are high and the frequency is at least 1 inflow per 100 m. The match achieved is reasonable in the sense that the modelled mean is generally with the 95% uncertainty limits in the mean based on the PSS data. The model predicts slightly higher values (half order of magnitude) than the data in depth zones between –150 masl and –650 masl. This is considered to be acceptable given the 100 m PSS data set is no more than about 10 measurements.

It was possible to find parameters for each of the three relationships between transmissivity and fracture size that would give an acceptable match to observations. Correlation coefficients > 0.8 were achieved for all variants above –400 masl, and > 0.73 between –400 and –650 masl. Below –650 masl, the data do not follow a coherent distribution to match, and so only the numbers of inflows and total flow were considered in the matching at these depths. Because the different types of relationship are parameterised in different ways, it is not easy to compare the different relationships. Figure 10-20 illustrates the ranges of transmissivity obtained for the different relationships for the sub-horizontal set in HRD_C. Not surprisingly, although the distributions are different and parameterised in different ways, the ranges of transmissivities that each relationship produces are fairly similar for the fracture sizes of interest, particularly for the ~10–100 m fractures, which are probably the features that mainly determine the connectivity, and hence the features carrying the flow. An additional check on the plausibility of the chosen transmissivity parameters was to calculate the maximum transmissivity that would be expected for a stochastic fracture and ensure this did not significantly exceed the maximum transmissivity measured in the deterministically interpreted deformation zones (HCD). The maximum transmissivity was calculated based on the size of the largest stochastic fracture, r=564 m, for the correlated and semi-correlated models, and adding 2 standard deviations for the semi-correlated and uncorrelated models. This was satisfied for all HRD and variants, and ensures that when the hydrogeological DFN model is applied on the regional scale, then no anomalously high transmissivities are generated compared to field data.

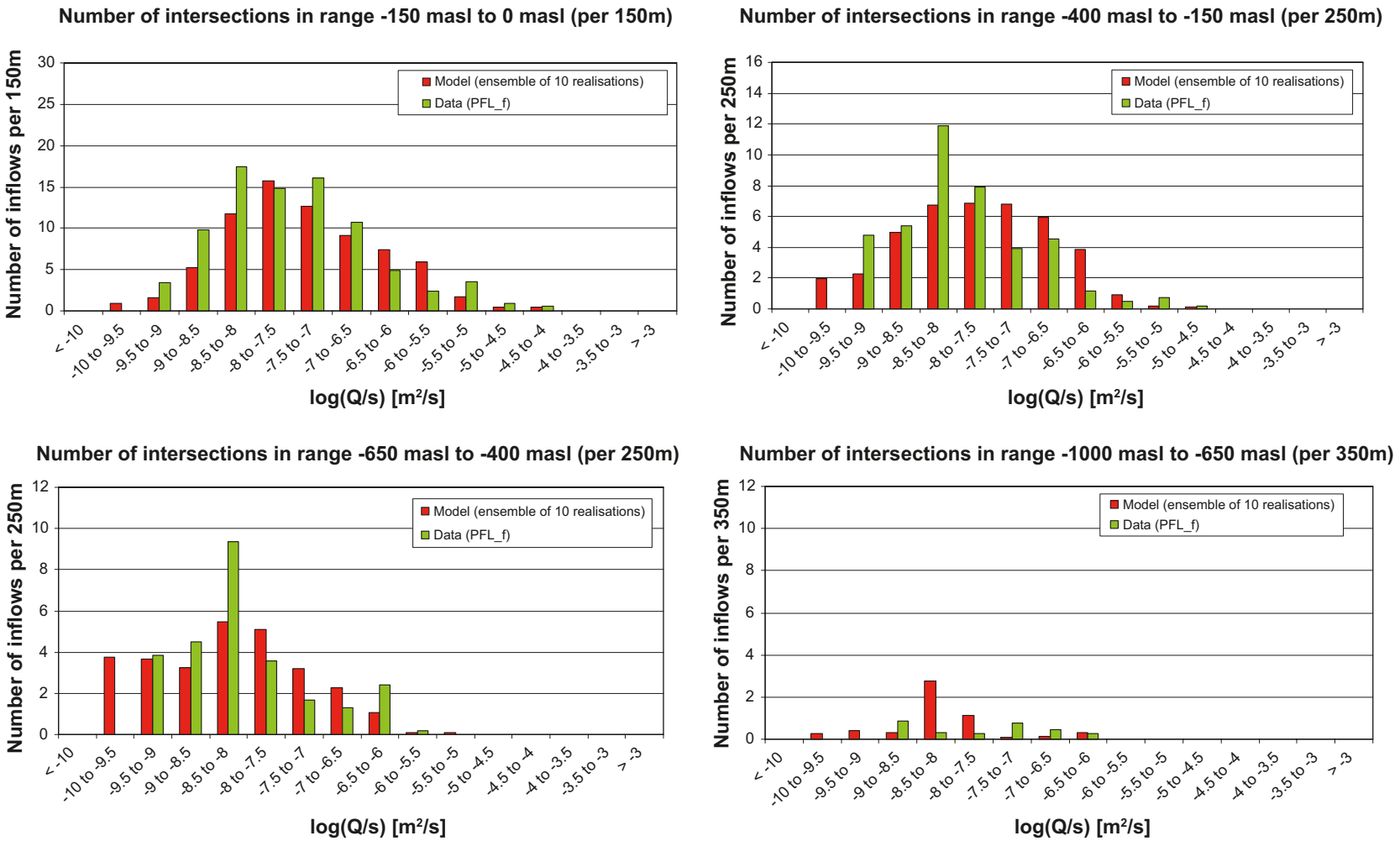

Figure 10-15. *Histogram comparing the distribution of the magnitude of inflows divided by drawdown, Q/s, at abstraction boreholes in HRD_C. The model has a semi-correlated transmissivity, with r_0 fixed and open fracture intensity based on OPO fractures (see Table 10-7 for parameter values). The PFL-f measurements are treated as ensemble over all boreholes sections within HRD_C. The simulations represent the combined results of 10 realisations of the hydrogeological DFN model. The numbers of intersections are Terzaghi weighted and normalised to the length of borehole which is provided in the heading of each graph.*

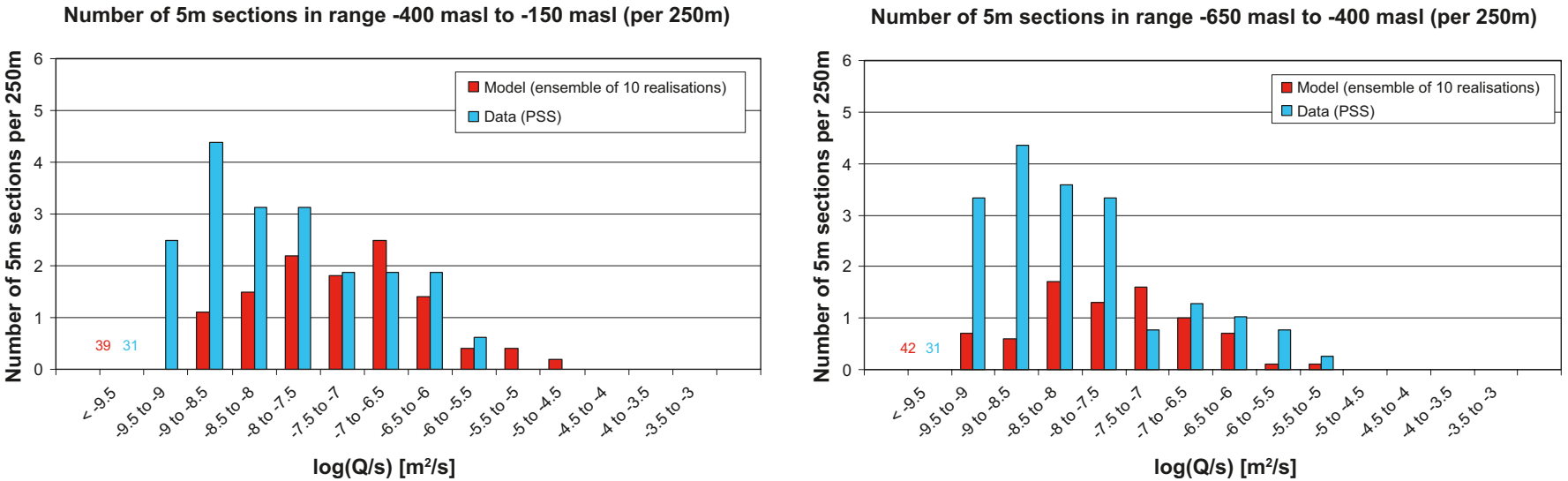

Figure 10-16. *Histogram comparing the distribution of the magnitude of inflows divided by drawdown, Q/s, in 5 m sections at abstraction boreholes in HRD_C. The model has a semi-correlated transmissivity, with r_0 fixed and open fracture intensity based on OPO fractures. The PFL-f measurements are treated as ensemble over all boreholes sections within HRD_C. The simulations represent the combined results of 10 realisations of the hydrogeological DFN model. The numbers of intersections are normalised to the length of borehole which is provided in the heading of each graph.*

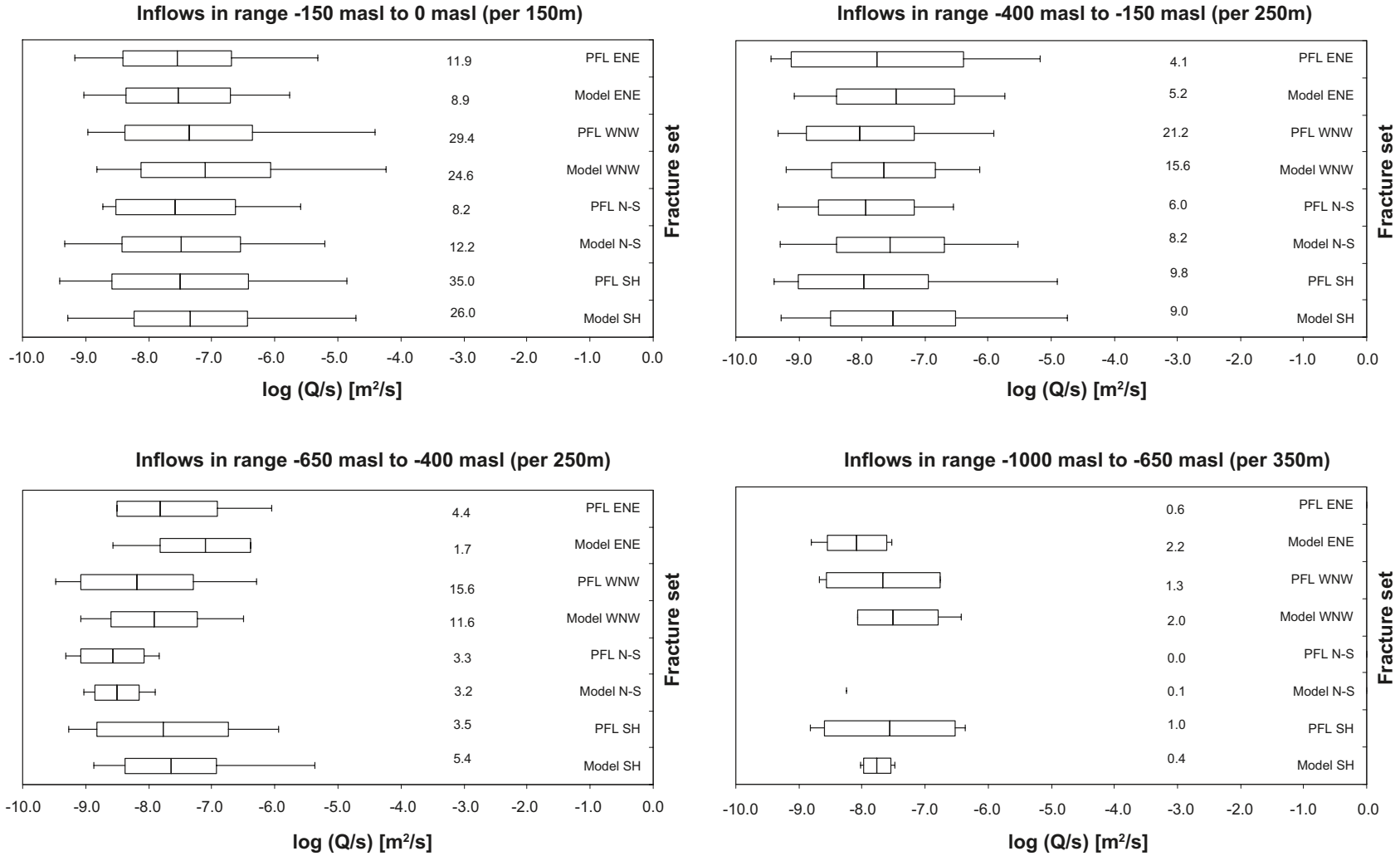

Figure 10-17. *Bar and whisker plots comparing statistics taken over each fracture set for the individual inflows, Q/s, for the PFL-f data from borehole sections within HRD_C against statistics for an ensemble over 10 realisations of the hydrogeological DFN model. The model has a semi-correlated transmissivity, with r_0 fixed and P_{32} based on OPO fractures. The centre of the bar indicates the mean value, the ends of the bar indicate ±1 standard deviation, the error bars indicate the minimum and maximum values and the value is the number of flowing features above the PFL-f detection limit per borehole section. For the data statistics are taken over the identified flow-features within each set. For the model, statistics are taken over the fractures generated within each set and over 10 realisations. The numbers of fractures are Terzaghi weighted and normalised to the length specified in the respective graph heading.*

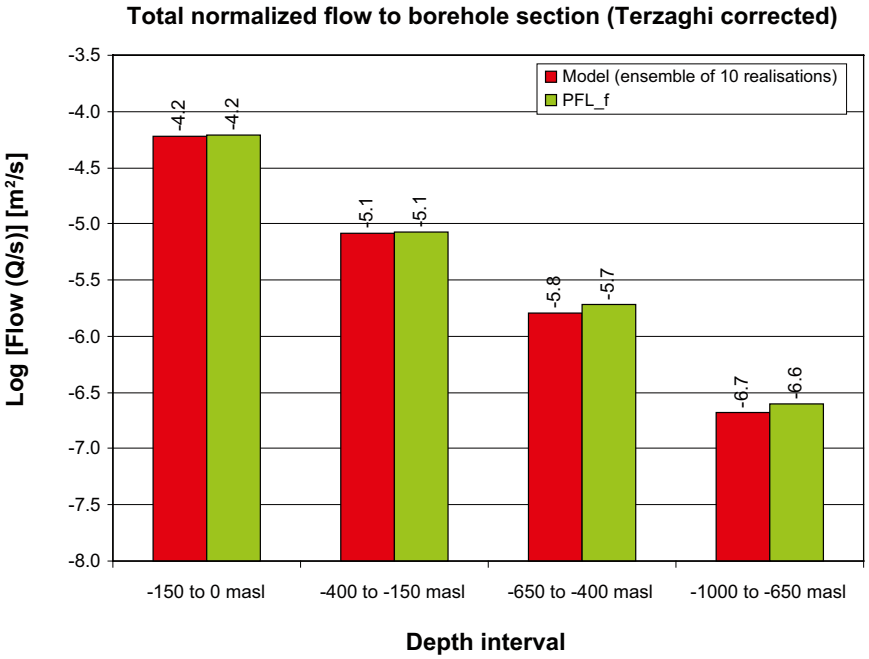

Figure 10-18. *Comparison of the sum of individual flows, Q/s, for the PFL-f data from borehole sections within HRD_C against the hydrogeological DFN model. The model has a semi-correlated transmissivity, with r_0 fixed and open fracture intensity based on OPO fractures. For the model, the arithmetic mean is taken over 10 realisations. The flows are Terzaghi weighted and normalised to the borehole length indicated by the range on the horizontal axis.*

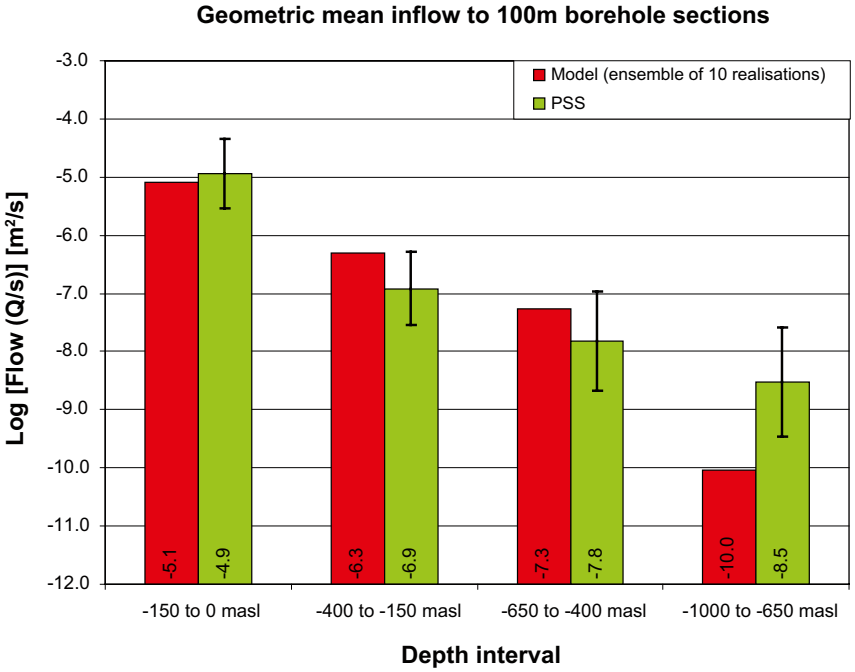

Figure 10-19. *Comparison of the geometric mean of total flows, Q/s, to 100 m borehole intervals for the PSS data from borehole sections within HRD_C against the hydrogeological DFN model. The model has a semi-correlated transmissivity, with r_0 fixed and open fracture intensity based on OPO fractures. For the data, the geometric mean is shown as well as the 95% confidence interval in the mean. For the model, the mean value of total flow is taken over 10 realisations.*

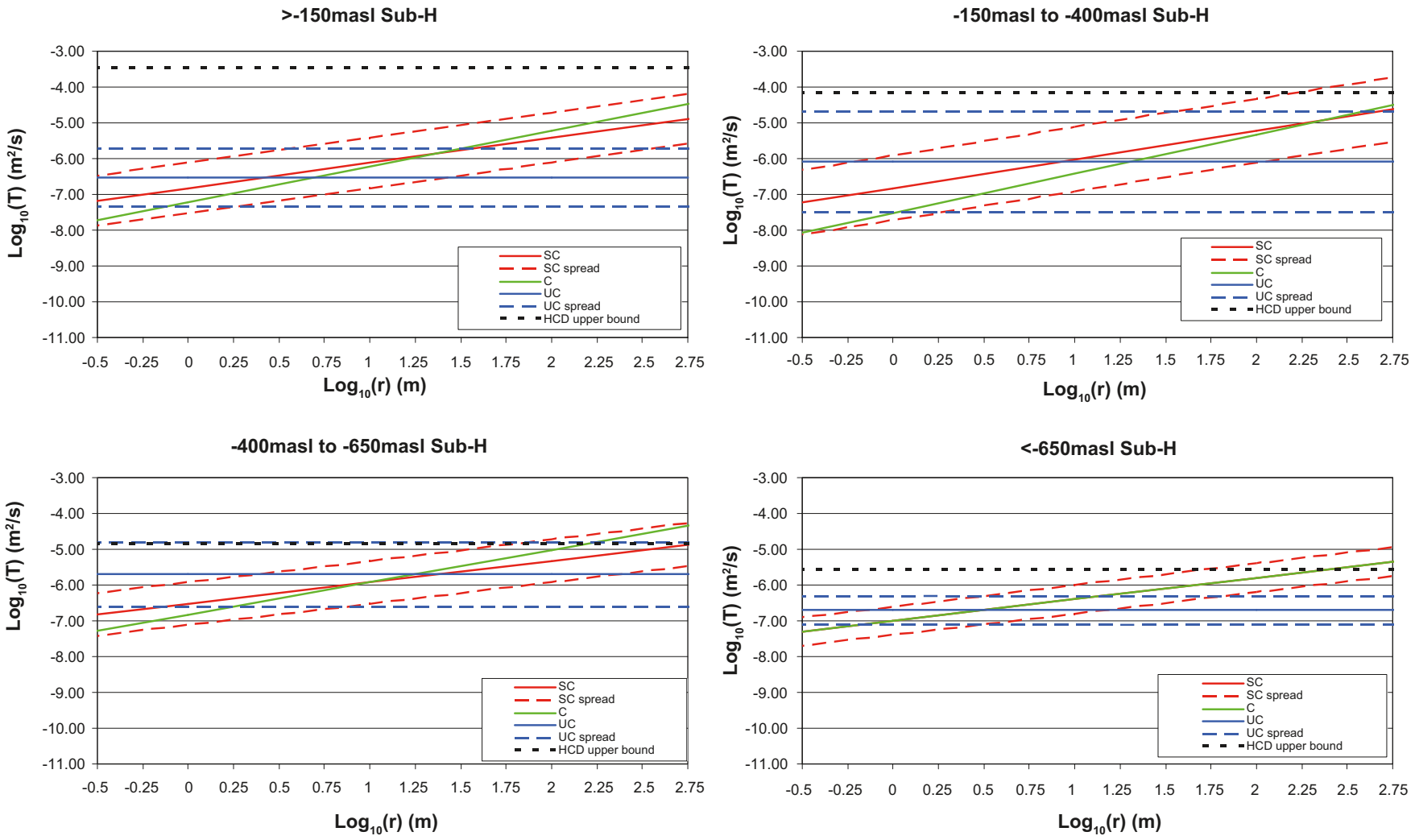

Figure 10-20. *Comparison of the relationships between fracture transmissivity and fracture size in each depth zone for HRD_C. The plots are for the calibrated model with r_0=0.038 m and open fracture intensity based on OPO fractures. The plots show the central trend for each relationship together with lines at 1 standard deviation above and below the central trend. The dashed black line indicates the maximum value measured in the deterministically interpreted deformation zones (HCD).*

The calibration of the transmissivity variants and the variants that use open fracture intensity based on OPO-CP fractures is presented in Appendix 6. The correlation coefficients associated with the matching of the *Q/s* histograms, exemplified in Figure 10-15, for the base case and each variant are given in Table 10-11. Generally, the agreement is within the target, 0.8, apart from the lowermost depth zone, and for depths of –650 to –400 masl for the uncorrelated variant as it was difficult to reproduce the shape of the histogram for this model. The overall similarity of correlation coefficients between variants demonstrates that a consistent level of match to the data was achieved for each variant. The minor differences between variants should not be over-interpreted, especially in the deeper depth zones, since distributions based on a finite number of samples are compared (on the order of 10 boreholes versus 10 model realisations).

10.5.3 Hydrogeological DFN calibration of hydraulic rock domain HRD_W

An illustration of the results of the flow calibration for HRD_W is also given here since it forms part of the candidate volume. The hydrogeological DFN parameterisations for the geometrical model that uses OPO fractures for the open fracture intensity and has r_0 fixed for each of the transmissivities models are given in Table 10-12. For the variant with open fracture intensity based on OPO-CP fractures, the parameters are given in Table 10-13.

For the case where fracture intensity is based on OPO-CP fracturing, Table 10-13 shows that r_0 had to be increased significantly above 0.038 m in the top depth zone to avoid having to make $k_r < 2.2$, which tends to create unrealistic proportions of large fractures. This was also the case for HRD_N and HRD_EW007. The effect of using small values of k_r is that it results in large fractures dominating the flow, which as a consequence effects how the hydraulic properties of block volumes scales with size as will be seen in Section 10.6. It was also found to be more difficult to match the total flow rate and the geometric mean flow-rates to 100 m borehole sections below –150 masl when small values of k_r were used. These factors lead to the case where fracture intensity is based on OPO fractures being selected as probably the more realistic to be recommended as a base case.

An illustration of the calibration of a hydrogeogical DFN model for HRD_W is given for the case with r_0 fixed, open fracture intensity based on OPO and a semi-correlated model in Figure 10-21 through Figure 10-25. The match is good for the top depth zone, but was more difficult for the other depth zones due to the skewed shape of the measured flows with a long tail towards higher transmissivities. This is reflected in the lower correlation coefficients of the histogram matches given in Table 10-14 for all 4 variants considered for HRD_W, and shows the match is more difficult to achieve than for HRD_C. Part of the problem in matching HRD_W compared to HRD_C may simply be that there is less data to define a coherent distribution of the hydraulic characteristics of the HRD. Below –650 masl there is only one PFL-f feature, and so it was not appropriate to try and fit a distribution. Instead the size and transmissivity parameters were taken from the bottom depth zone of HRD_C. Figure 10-23 demonstrates the matching for individual sets. The subhorizontal set tends to be responsible for the high flow rates, with WNW also giving a high contribution above –400 masl.

Table 10-11. Correlation coefficients for the shape of histograms of *Q/s* across the bins shown in Figure 10-15 for the 5 variants considered for HRD_C.

Depth zone (masl)	Correlation coefficient for distribution of *Q/s* between model and PFL				
	OPO, r_0 fixed, SC	OPO, r_0 fixed, UC	OPO, r_0 fixed, C	OPO-CP, r_0 fixed, SC	OPO-CP, k_r fixed, SC
–150 to 0	0.92	0.82	0.93	0.91	0.86
–400 to –150	0.82	0.94	0.80	0.90	0.85
–650 to –400	0.77	0.79	0.90	0.73	0.89
–1,000 to –650	0.18	0.72	0.80	0.43	0.56

Table 10-12. Description of the calibrated hydrogeological DFN input parameters for HRD_W with fixed r_0=0.038 m and open fracture intensity based on OPO.

Depth zone (masl)	Set	Orientation set pole: (trend, plunge), conc.	Fracture radius model power-law (k_r, r_0)	Intensity P_{32} (m^2/m^3) of open fractures	Transmissivity model T (m^2/s) See Table 10-5
–150 to 0	ENE	(340.3,1.2), 15	(2.65, 0.038)	0.44	SC: ($5\cdot10^{-8}$, 0.7, 0.7) UC: ($8\cdot10^{-8}$, 1.1) C: ($4\cdot10^{-8}$, 1.2)
	WNW	(208.9,2.2), 10.9	(2.5, 0.038)	0.61	SC: ($1\cdot10^{-7}$, 0.8, 0.6) UC: ($6\cdot10^{-7}$, 1.1) C: ($3\cdot10^{-8}$, 1.3)
	N-S	(272.8,12), 11.5	(2.65, 0.038)	0.54	SC: ($1.5\cdot10^{-7}$, 0.7, 0.7) UC: ($4\cdot10^{-7}$, 1.0) C: ($2\cdot10^{-8}$, 1.0)
	SubH	(277.1,84.3), 11.1	(2.55, 0.038)	1.03	SC: ($1.5\cdot10^{-7}$, 0.7, 0.9) UC: ($1\cdot10^{-6}$, 0.9) C: ($1.5\cdot10^{-7}$, 1.0)
–400 to –150	ENE	(340.3,1.2), 15	(2.65, 0.038)	0.28	SC: ($1\cdot10^{-7}$, 0.5, 0.2) UC: ($1\cdot10^{-6}$, 0.4) C: ($3\cdot10^{-7}$, 0.5)
	WNW	(208.9,2.2), 10.9	(2.5, 0.038)	0.38	SC: ($3\cdot10^{-7}$, 0.5, 0.6) UC: ($6\cdot10^{-7}$, 0.8) C: ($1\cdot10^{-8}$, 1.0)
	N-S	(272.8,12), 11.5	(2.9, 0.038)	0.40	SC: ($1\cdot10^{-8}$, 0.5, 0.5) UC: ($1\cdot10^{-8}$, 0.5) C: ($2\cdot10^{-9}$, 0.5)
	SubH	(277.1,84.3), 11.1	(2.7, 0.038)	0.50	SC: ($1\cdot10^{-7}$, 0.7, 1.0) UC: ($1.5\cdot10^{-6}$, 1.4) C: ($8\cdot10^{-8}$, 1.2)
–650 to –400	ENE	(340.3,1.2), 15	(2.8, 0.038)	0.17	SC: ($3\cdot10^{-9}$, 0.6, 0.5) UC: ($2\cdot10^{-9}$, 0.5) C: ($1\cdot10^{-9}$, 0.6)
	WNW	(208.9,2.2), 10.9	(2.55, 0.038)	0.33	SC: ($3\cdot10^{-8}$, 0.6, 0.5) UC: ($2\cdot10^{-7}$, 0.3) C: ($2\cdot10^{-8}$, 0.7)
	N-S	(272.8,12), 11.5	(2.55, 0.038)	0.30	SC: ($3\cdot10^{-8}$, 0.4, 0.4) UC: ($2\cdot10^{-7}$, 0.3) C: ($1\cdot10^{-8}$, 0.6)
	SubH	(277.1,84.3), 11.1	(2.65, 0.038)	0.38	SC: ($5\cdot10^{-7}$, 0.4, 1.0) UC: ($1.5\cdot10^{-5}$, 1.2) C: ($1.2\cdot10^{-7}$, 1.2)
–1,000 to –650	ENE	(340.3,1.2), 15	(2.9, 0.038)	0.12	SC: ($5\cdot10^{-9}$, 0.6, 0.4) UC: ($1\cdot10^{-8}$, 0.6) C: ($5\cdot10^{-9}$, 0.6)
	WNW	(208.9,2.2), 10.9	(2.8, 0.038)	0.09	SC: ($5\cdot10^{-8}$, 0.6, 0.4) UC: ($5\cdot10^{-8}$, 0.6) C: ($5\cdot10^{-8}$, 0.6)
	N-S	(272.8,12), 11.5	(2.95, 0.038)	0.14	SC: ($5\cdot10^{-9}$, 0.6, 0.4) UC: ($1\cdot10^{-8}$, 0.6) C: ($5\cdot10^{-9}$, 0.6)
	SubH	(277.1,84.3), 11.1	(2.95, 0.038)	0.65	SC: ($1\cdot10^{-7}$, 0.6, 0.4) UC: ($8\cdot10^{-7}$, 0.6) C: ($1\cdot10^{-7}$, 0.6)

Table 10-13. Description of the calibrated hydrogeological DFN input parameters for HRD_W with fixed r_0=0.038 m (where k_r > 2.2) and open fracture intensity based on OPO-CP.

Depth zone (masl)	Set	Orientation set pole: (trend, plunge), conc.	Fracture radius model power-law (k_r, r_0)	Intensity P_{32} (m^2/m^3) of open fractures	Transmissivity model T (m^2/s) See Table 10-5
–150 to 0	ENE	(340.3,1.2), 15	(2.2, 0.2)	0.13	SC: ($2\cdot10^{-8}$, 0.7, 0.5)
	WNW	(208.9,2.2), 10.9	(2.2, 0.3)	0.26	SC: ($3\cdot10^{-8}$, 0.9, 0.6)
	N-S	(272.8,12), 11.5	(2.2, 0.2)	0.21	SC: ($2\cdot10^{-8}$, 0.7, 0.5)
	SubH	(277.1,84.3), 11.1	(2.2, 0.15)	0.43	SC: ($4\cdot10^{-8}$, 0.7, 0.7)
–400 to –150	ENE	(340.3,1.2), 15	(2.5, 0.038)	0.16	SC: ($6\cdot10^{-9}$, 0.5, 0.3)
	WNW	(208.9,2.2), 10.9	(2.3, 0.038)	0.18	SC: ($1\cdot10^{-8}$, 0.7, 0.7)
	N-S	(272.8,12), 11.5	(2.5, 0.038)	0.16	SC: ($5\cdot10^{-9}$, 0.5, 0.3)
	SubH	(277.1,84.3), 11.1	(2.4, 0.038)	0.18	SC: ($8\cdot10^{-9}$, 1, 0.8)
–650 to –400	ENE	(340.3,1.2), 15	(2.5, 0.038)	0.07	SC: ($6\cdot10^{-9}$, 0.5, 0.3)
	WNW	(208.9,2.2), 10.9	(2.2, 0.038)	0.10	SC: ($8\cdot10^{-9}$, 0.6, 0.3)
	N-S	(272.8,12), 11.5	(2.3, 0.038)	0.16	SC: ($6\cdot10^{-9}$, 0.5, 0.3)
	SubH	(277.1,84.3), 11.1	(2.35, 0.038)	0.12	SC: ($\cdot10^{-8}$, 1, 0.4)
–1,000 to –650	ENE	(340.3,1.2), 15	(2.8, 0.038)	0.01	SC: ($5\cdot10^{-9}$, 0.7, 0.4)
	WNW	(208.9,2.2), 10.9	(2.7, 0.038)	0.02	SC: ($1\cdot10^{-8}$, 0.7, 0.4)
	N-S	(272.8,12), 11.5	(2.8, 0.038)	0.05	SC: ($5\cdot10^{-9}$, 0.7, 0.4)
	SubH	(277.1,84.3), 11.1	(2.65, 0.038)	0.16	SC: ($1\cdot10^{-8}$, 0.7, 0.4)

Table 10-14. Correlation coefficients for the shape of histograms of *Q/s* across the bins shown in Figure 10-21 for the 4 variants considered for HRD_W.

Depth zone (masl)	Correlation coefficient for distribution of *Q/s* between model and PFL			
	OPO, r_0 fixed, SC	OPO, r_0 fixed, UC	OPO, r_0 fixed, C	OPO-CP, r_0 fixed, SC
–150 to 0	0.91	0.91	0.94	0.80
–400 to –150	0.64	0.69	0.57	0.77
–650 to –400	0.58	0.64	0.75	0.63

The total flow rates are in good agreement as shown in Figure 10-24, as are the geometric mean flow rates for 100 m borehole intervals. The confidence intervals in the mean 100 m PSS data are large below –150 masl for HRD_W than HRD_C due to a greater variability.

The calibration of the OPO-CP variant is demonstrated in Appendix 6, Section A.6.3, and the two transmissivity variants for the OPO case. Comparisons of the three different transmissivity models as a function of fracture size for the geometrical case with open fracture intensity based on OPO fractures for each depth zone are shown in Figure 10-26. Table 10-14 reveals that a similar level of calibration in terms of the shapes of the *Q/s* distribution was achieved in all variants. A good match was achieved for the top depth zone where data is plentiful, but was more difficult in the depth zones beneath –150 masl. The correlation coefficients in the shape of the inflow distribution between data and model were generally lower than was achieved for HRD_C, and hence there is more uncertainty in the hydrogeological DFN for HRD_W below –150 masl compared to HRD_C.

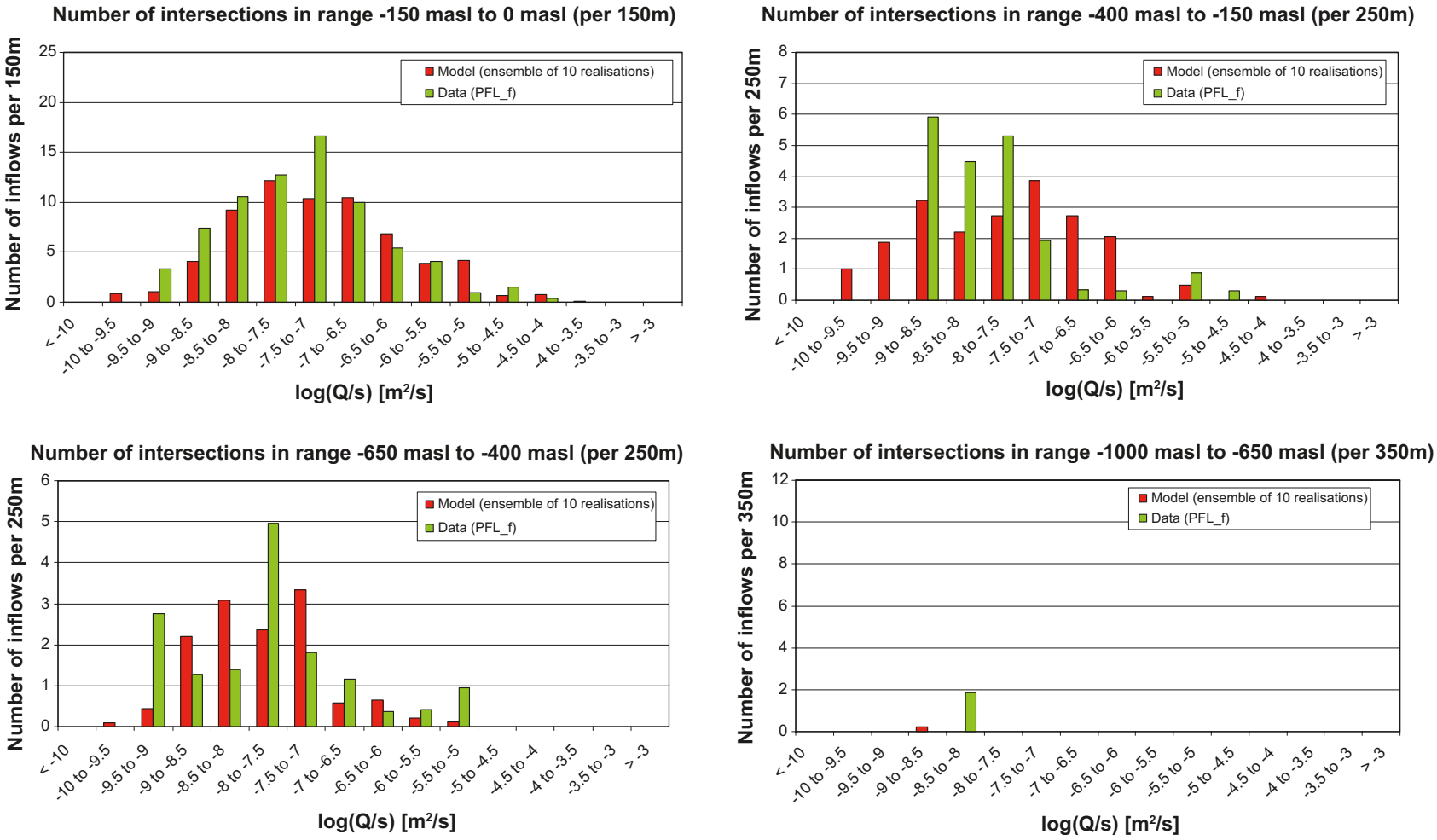

Figure 10-21. *Histograms comparing the distribution of the magnitude of inflows divided by drawdown, Q/s, at abstraction boreholes in HRD_W. The model has a semi-correlated transmissivity, with r_0 fixed and open fracture intensity based on OPO fractures. The PFL-f measurements are treated as ensemble over all boreholes sections within HRD_W. The simulations represent the combined results of 10 realisations of the hydrgeological DFN model. The numbers of intersections are Terzaghi weighted and normalised to the length of borehole which is provided in the heading of each graph.*

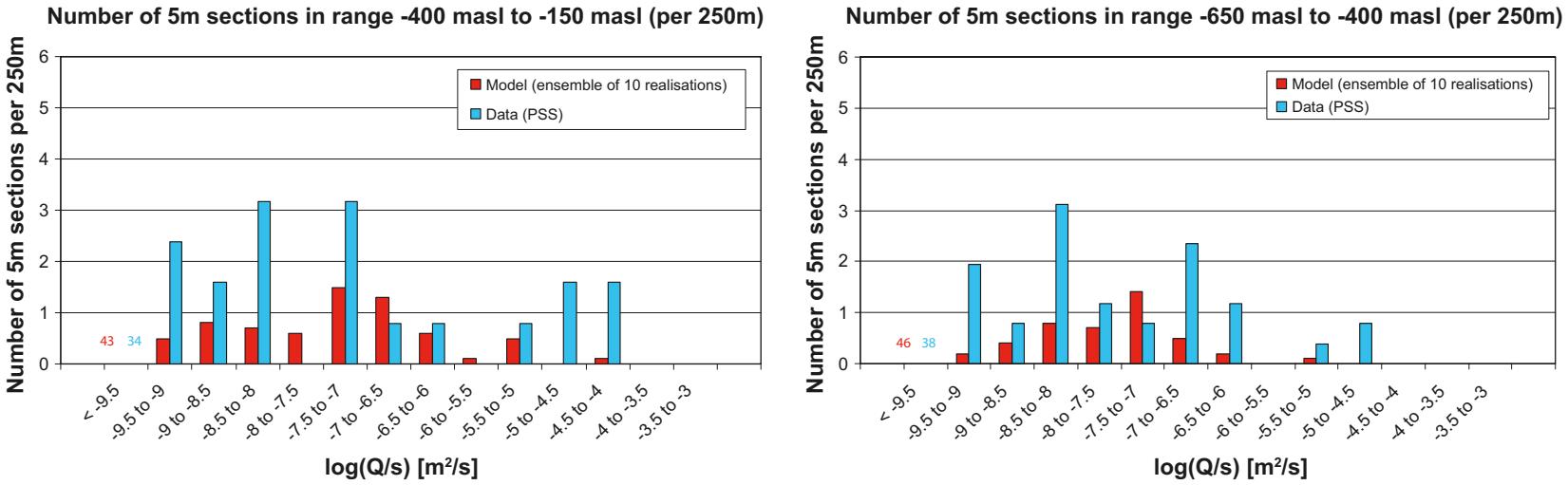

Figure 10-22. *Histograms comparing the distribution of the magnitude of inflows divided by drawdown, Q/s, in 5 m sections at abstraction boreholes in HRD_W. The model has a semi-correlated transmissivity, with r_0 fixed and open fracture intensity based on OPO fractures. The PFL-f measurements are treated as ensemble over all boreholes sections within HRD_W. The simulations represent the combined results of 10 realisations of the hydrogeological DFN model. The numbers of intersections are normalised to the length of borehole in the heading of each graph.*

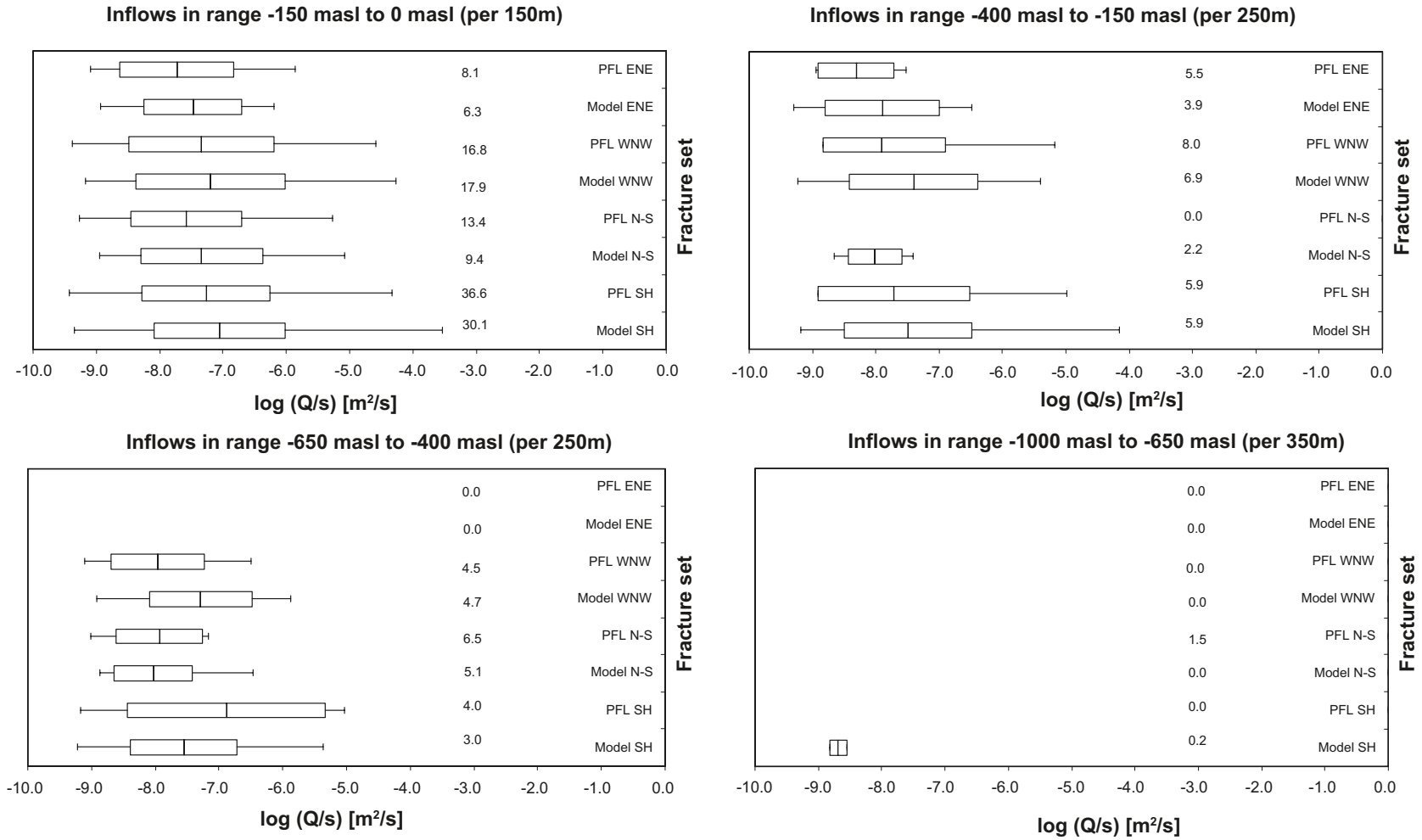

Figure 10-23. *Bar and whisker plots comparing statistics taken over each fracture set for the individual inflows, Q/s, for the PFL-f data from borehole sections within HRD_W against statistics for an ensemble over 10 realisations of the hydrogeological DFN model. The model has a semi-correlated transmissivity, with r_0 fixed and open fracture intensity based on OPO fractures. The centre of the bar indicates the mean value, the ends of the bar indicate ±1 standard deviation, the error bars indicate the minimum and maximum values and the value is the number of flowing features above the PFL-f detection limit per borehole section. For the data statistics are taken over the identified flow-features within each set. For the model, statistics are taken over the fractures generated within each set and over 10 realisations. The numbers of fractures are Terzaghi weighted and normalised to the length specified in the respective graph heading.*

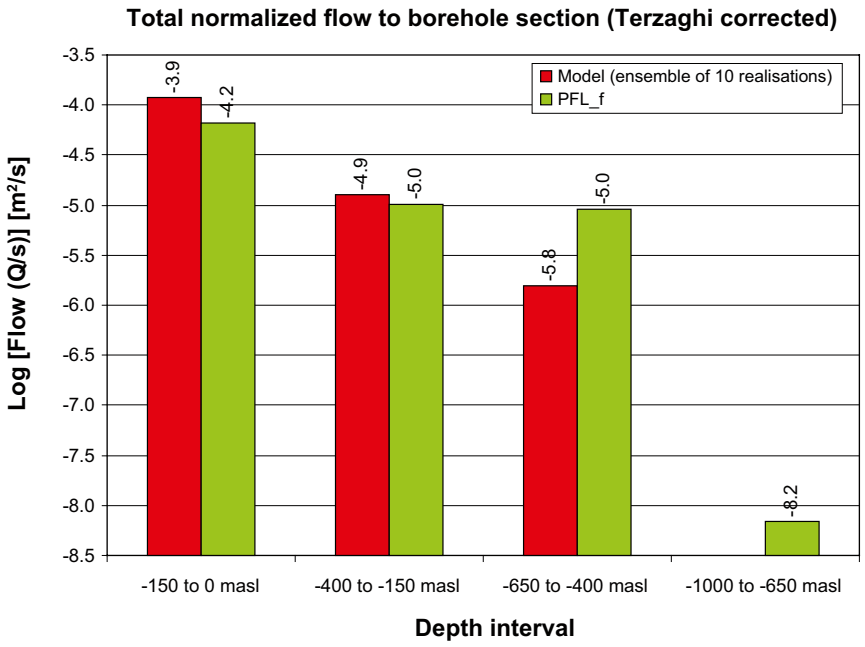

Figure 10-24. *Comparison of the sum of individual flows, Q/s, for the PFL-f data from borehole sections within HRD_W against the hydrogeological DFN model. The model has a semi-correlated transmissivity, with r_0 fixed and open fracture intensity based on OPO fractures. For the model, the arithmetic mean is taken over 10 realisations. The flows are Terzaghi weighted and normalised to the borehole length indicated by the range on the horizontal axis.*

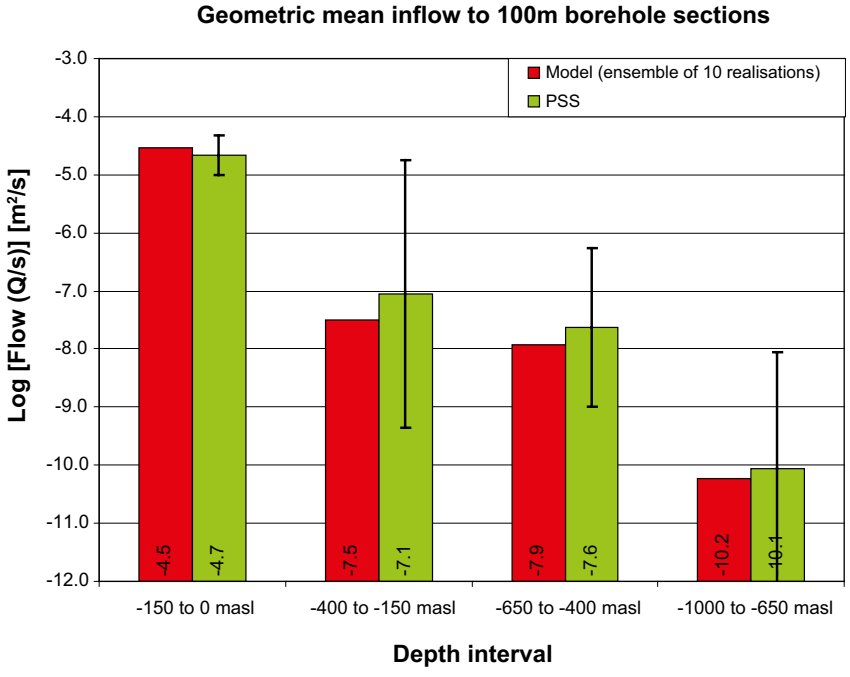

Figure 10-25. *Comparison of the geometric mean of total flows, Q/s, to 100 m borehole intervals for the PSS data from borehole sections within HRD_W against the hydrogeological model. The model has a semi-correlated transmissivity, with r_0 fixed and open fracture intensity based on OPO fractures. For the data, the geometric mean is shown as well as the 95% confidence interval in the mean. For the model, the mean value of total flow is taken over 10 realisations.*

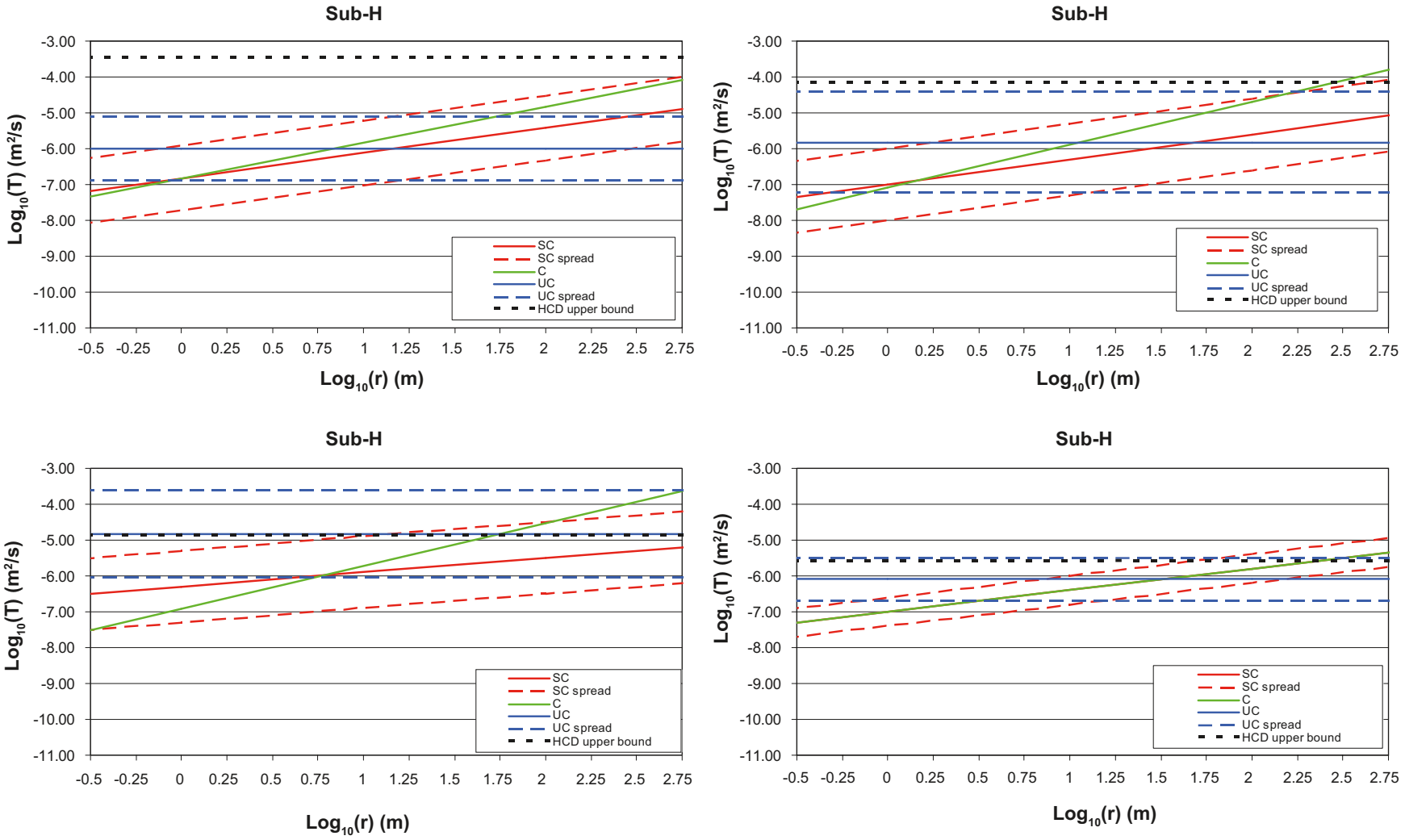

Figure 10-26. *Comparison of the relationships between fracture transmissivity and fracture size for HRD_W. The plots are for the calibrated model with r_0=0.038 m and with open fracture intensity based on OPO fractures. The plots show the central trend for each relationship together with lines at 1 standard deviation above and below the central trend. The dashed black line indicates the maximum value measured in the deterministically interpreted deformation zones (HCD).*

10.5.4 Hydrogeological DFN calibration of hydraulic rock domains HRD_EW007 and HRD_N

Only part of hydraulic rock domains HRD_EW007 may fall within the repository candidate area, while HRD_N is outside repository candidate area. Hence, the details of the model calibration for these HRD are described in Appendix 6 and only the hydrogeological DFN parameterisation is given here in the main text.

The parameters for the geometrical model which estimates open fracture intensity from OPO fractures and r_0 fixed and 3 different transmissivity models are given for HRD_EW007 in Table 10-15. The HRD_EW007 variant that uses OPO-CP fractures to estimate open fracture intensity is given in Table 10-16. The results of calibrating the model are described in Appendix 6, Section A.6.4.

Table 10-15. Description of the calibrated hydrogeological DFN input parameters for HRD_EW007 with fixed r_0=0.038 m and open fracture intensity based on OPO.

Depth zone (masl)	Set	Orientation set pole: (trend, plunge), conc.	Fracture radius model power-law (k_r, r_0)	Intensity P_{32} (m^2/m^3) of open fractures	Transmissivity model T (m^2/s) See Table 10-5
–150 to 0	ENE	(162.8,1.4), 10.7	(2.70, 0.038)	0.55	SC: ($1\cdot10^{-7}$, 0.4, 0.4) UC: ($3\cdot10^{-7}$, 0.6) C: ($1\cdot10^{-7}$, 0.4)
	WNW	(25.3,0.2), 16.4	(2.3, 0.038)	1.01	SC: ($1\cdot10^{-7}$, 0.4, 0.4) UC: ($3\cdot10^{-7}$, 0.6) C: ($1\cdot10^{-7}$, 0.4)
	N-S	(88.9,3.9), 8.8	(2.65, 0.038)	0.33	SC: ($1\cdot10^{-6}$, 0.4, 0.4) UC: ($3\cdot10^{-6}$, 0.6) C: ($1\cdot10^{-6}$, 0.4)
	SubH	(138.7,81.3), 9.7	(2.75, 0.038)	1.72	SC: ($3\cdot10^{-7}$, 0.5, 0.5) UC: ($1.5\cdot10^{-6}$, 0.7) C: ($1.5\cdot10^{-7}$, 0.8)
–400 to –150	ENE	(162.8,1.4), 10.7	(2.8, 0.038)	0.60	SC: ($6\cdot10^{-8}$, 0.6, 0.6) UC: ($1\cdot10^{-6}$, 0.9) C: ($6\cdot10^{-8}$, 0.8)
	WNW	(25.3,0.2), 16.4	(2.35, 0.038)	1.15	SC: ($2\cdot10^{-8}$, 0.6, 0.6) UC: ($8\cdot10^{-8}$, 0.8) C: ($2\cdot10^{-8}$, 0.6)
	N-S	(88.9,3.9), 8.8	(2.6, 0.038)	0.54	SC: ($1.5\cdot10^{-7}$,0.7,0.7) UC: ($2\cdot10^{-6}$, 1.1) C: ($1.5\cdot10^{-7}$, 0.9)
	SubH	(138.7,81.3), 9.7	(2.8, 0.038)	0.82	SC: ($8\cdot10^{-8}$, 0.7, 0.9) UC: ($2\cdot10^{-7}$, 1.1) C: ($8\cdot10^{-8}$, 0.7)
–650 to –400	ENE	(162.8,1.4), 10.7	(2.95, 0.038)	0.69	SC: ($3\cdot10^{-8}$, 0.4, 0.4) UC: ($3\cdot10^{-8}$, 0.6) C: ($3\cdot10^{-8}$, 0.4)
	WNW	(25.3,0.2), 16.4	(2.50, 0.038)	1.43	SC: ($1\cdot10^{-7}$, 0.3, 0.3) UC: ($2\cdot10^{-7}$, 0.5) C: ($1\cdot10^{-7}$, 0.3)
	N-S	(88.9,3.9), 8.8	(2.95, 0.038)	0.64	SC: ($3\cdot10^{-7}$, 0.4, 0.4) UC: ($1\cdot10^{-6}$, 0.6) C: ($3\cdot10^{-7}$, 0.4)
	SubH	(138.7,81.3), 9.7	(2.95, 0.038)	0.92	SC: ($3\cdot10^{-8}$, 0.6, 0.4) UC: ($1\cdot10^{-7}$, 0.8) C: ($3\cdot10^{-8}$, 0.6)
–1,000 to –650	ENE	(162.8,1.4), 10.7	(2.9, 0.038)	0.33	SC: ($5\cdot10^{-9}$, 0.6, 0.4) UC: ($1\cdot10^{-8}$, 0.6) C: ($5\cdot10^{-9}$, 0.6)
	WNW	(25.3,0.2), 16.4	(2.8, 0.038)	0.89	SC: ($5\cdot10^{-8}$, 0.6, 0.4) UC: ($5\cdot10^{-8}$, 0.6) C: ($5\cdot10^{-8}$, 0.6)
	N-S	(88.9,3.9), 8.8	(2.95, 0.038)	0.21	SC: ($5\cdot10^{-9}$, 0.6, 0.4) UC: ($1\cdot10^{-8}$, 0.6) C: ($5\cdot10^{-9}$, 0.6)
	SubH	(138.7,81.3), 9.7	(2.95, 0.038)	0.80	SC: ($1\cdot10^{-7}$, 0.6, 0.4) UC: ($8\cdot10^{-7}$, 0.6) C: ($1\cdot10^{-7}$, 0.6)

Table 10-16. Description of the calibrated hydrogeological DFN input parameters for HRD_EW007 with fixed r_0=0.038 m (where k_r > 2.2) and open fracture intensity based on OPO-CP.

Depth zone masl)	Set	Orientation set pole: (trend, plunge), conc.	Fracture radius model power-law (k_r, r_0)	Intensity P_{32} (m^2/m^3) of open fractures	Transmissivity model T (m^2/s) See Table 10-5
–150 to 0	ENE	(340.3,1.2), 15	(2.2, 0.038)	0.28	SC: ($3\cdot10^{-8}$, 0.5, 0.4)
	WNW	(208.9,2.2), 10.9	(2.2, 0.3)	0.58	SC: ($3\cdot10^{-8}$, 0.5, 0.4)
	N-S	(272.8,12), 11.5	(2.2, 0.038)	0.16	SC: ($3\cdot10^{-7}$, 0.5, 0.4)
	SubH	(277.1,84.3), 11.1	(2.4, 0.038)	0.82	SC: ($1\cdot10^{-7}$, 0.7, 0.5)
–400 to –150	ENE	(340.3,1.2), 15	(2.4, 0.038)	0.32	SC: ($5\cdot10^{-8}$, 0.6, 0.6)
	WNW	(208.9,2.2), 10.9	(2.2, 0.15)	0.67	SC: ($1\cdot10^{-8}$, 0.7, 0.5)
	N-S	(272.8,12), 11.5	(2.4, 0.038)	0.32	SC: ($8\cdot10^{-8}$, 0.7, 0.7)
	SubH	(277.1,84.3), 11.1	(2.5, 0.038)	0.30	SC: ($5\cdot10^{-8}$, 0.6, 0.7)
–650 to –400	ENE	(340.3,1.2), 15	(2.6, 0.038)	0.39	SC: ($1\cdot10^{-8}$, 0.5, 0.4)
	WNW	(208.9,2.2), 10.9	(2.3, 0.038)	0.55	SC: ($4\cdot10^{-8}$, 0.4, 0.4)
	N-S	(272.8,12), 11.5	(2.7, 0.038)	0.32	SC: ($6\cdot10^{-8}$, 0.5, 0.4)
	SubH	(277.1,84.3), 11.1	(2.65, 0.038)	0.29	SC: ($\cdot10^{-8}$, 0.7, 0.4)
–1,000 to –650	ENE	(340.3,1.2), 15	(2.8, 0.038)	0.15	SC: ($5\cdot10^{-9}$, 0.7, 0.4)
	WNW	(208.9,2.2), 10.9	(2.7, 0.038)	0.39	SC: ($1\cdot10^{-8}$, 0.7, 0.4)
	N-S	(272.8,12), 11.5	(2.8, 0.038)	0.13	SC: ($5\cdot10^{-9}$, 0.7, 0.4)
	SubH	(277.1,84.3), 11.1	(2.65, 0.038)	0.26	SC: ($1\cdot10^{-8}$, 0.7, 0.4)

The quality of the match for each of the four cases considered for HRD_EW007 is quantified in Table 10-17. The matches are generally good, with correlation coefficients above 0.75. Again, the model was only calibrated for the three depth zones above –650 masl as there is only one identified PFL-f feature in HRD_EW007 below this depth. This makes it impossible to determine a stochastic model in this depth zone, and so the size and transmissivity parameters are taken from HRD_C. The correlation coefficients achieved for HRD_EW007 were generally as good as HRD_C suggesting reasonable confidence in the hydrogeological DFN above –650 masl.

The parameters for the geometrical model which estimates open fracture intensity from OPO fractures and r_0 fixed and three different transmissivity models are given for HRD_N in Table 10-18. The HRD_N variant that uses OPO-CP fractures to estimate open fracture intensity is given in Table 10-19. The calibration of the model is described in Appendix 6, Section A.6.5. The quality of the match for each of the four cases considered for HRD_N is quantified in Table 10-20. The matches are good for the top two depth zones, but poorer below –400 masl due to the sparsity of PFL-f features to match against. At elevations between –400 masl to –650 masl the measured distribution is very flat with a gap in the middle around 10^{-7} m^2/s (see Appendix 6, Section A.6.5), which is particularly hard to simulate. Again, the gap in the data could be an artefact of the sparsity of data in this rock subdivision. Reasonable confidence can be placed in the hydrogeological DFN for HRD_N above –400 masl.

Hence, parameterisations of the hydrogeological DFN has been derived for each of the four HRD defined within the Laxemar local model volume. The recommended base case model has fracture intensity based on OPO fractures, and there are two variants to scope uncertainties; the description of transmissivity and its relation to size, along with one geometrical variant that derives intensity of open fractures based on OPO-CP which when calibrated has a lower overall fracture intensity, but more extensive fractures.

Table 10-17. Correlation coefficients for the shape of histograms of *Q/s* across the bins shown in Figure 10-15 for the four variants considered for HRD_EW007.

Depth zone (masl)	Correlation coefficient for distribution of *Q/s* between model and PFL			
	OPO, r_0 fixed, SC	OPO, r_0 fixed, UC	OPO, r_0 fixed, C	OPO-CP, r_0 fixed, SC
–150 to 0	0.80	0.82	0.78	0.83
–400 to –150	0.96	0.98	0.95	0.90
–650 to –400	0.99	0.91	0.90	0.85

Table 10-18. Description of the calibrated hydrogeological DFN input parameters for HRD_N with fixed r_0=0.038 m and open fracture intensity based on OPO.

Depth zone (masl)	Set	Orientation set pole: (trend, plunge), conc.	Fracture radius model power-law (k_r, r_0)	Intensity P_{32} (m^2/m^3) of open fractures	Transmissivity model T (m^2/s) See Table 10-5
–150 to 0	ENE	(342.2,0.2), 15.8	(2.5, 0.038)	0.41	SC: ($1\cdot10^{-7}$, 0.6, 0.6) UC: ($3\cdot10^{-7}$, 0.7) C: ($1\cdot10^{-7}$, 0.7)
	WNW	(209.8,1.6), 14.6	(2.3, 0.038)	0.92	SC: ($2\cdot10^{-7}$, 0.7, 0.8) UC: ($2\cdot10^{-6}$, 0.8) C: ($4\cdot10^{-7}$, 0.9)
	N-S	(271.3,3.8), 10.3	(2.5, 0.038)	0.46	SC: ($1\cdot10^{-7}$, 0.7, 1.0) UC: ($5\cdot10^{-7}$, 1.1) C: ($1\cdot10^{-7}$, 0.9)
	SubH	(238.9,81.5), 12.7	(2.7, 0.038)	1.35	SC: ($2\cdot10^{-7}$, 0.7, 1.0) UC: ($6\cdot10^{-7}$, 1.2) C: ($2\cdot10^{-7}$, 0.9)
–400 to –150	ENE	(342.2,0.2), 15.8	(2.8, 0.038)	0.41	SC: ($1\cdot10^{-7}$, 0.6, 0.8) UC: ($1\cdot10^{-6}$, 1.0) C: ($1\cdot10^{-7}$, 0.6)
	WNW	(209.8,1.6), 14.6	(2.4, 0.038)	0.54	SC: ($2\cdot10^{-7}$, 0.6, 0.6) UC: ($2\cdot10^{-6}$, 0.8) C: ($3\cdot10^{-7}$, 0.7)
	N-S	(271.3,3.8), 10.3	(2.8, 0.038)	0.39	SC: ($1\cdot10^{-7}$, 0.4, 0.4) UC: ($3\cdot10^{-7}$, 0.6) C: ($1\cdot10^{-7}$, 0.4)
	SubH	(238.9,81.5), 12.7	(2.75, 0.038)	1.28	SC: ($3\cdot10^{-7}$, 0.6, 0.6) UC: ($3\cdot10^{-6}$, 1.0) C: ($2\cdot10^{-7}$, 0.9)
–650 to –400	ENE	(342.2,0.2), 15.8	(2.6, 0.038)	0.26	SC: ($1\cdot10^{-7}$, 0.5, 0.7) UC: ($6\cdot10^{-6}$, 1.1) C: ($2\cdot10^{-7}$, 0.8)
	WNW	(209.8,1.6), 14.6	(2.4, 0.038)	0.36	SC: ($1\cdot10^{-7}$, 0.5, 0.5) UC: ($3\cdot10^{-7}$, 0.7) C: ($2\cdot10^{-7}$, 0.5)
	N-S	(271.3,3.8), 10.3	(2.6, 0.038)	0.25	SC: ($5\cdot10^{-8}$, 0.3, 0.3) UC: ($2\cdot10^{-7}$, 0.5) C: ($5\cdot10^{-8}$, 0.3)
	SubH	(238.9,81.5), 12.7	(2.7, 0.038)	0.41	SC: ($5\cdot10^{-8}$, 0.4, 0.4) UC: ($5\cdot10^{-8}$, 0.3) C: ($3\cdot10^{-8}$, 0.4)
–1,000 to –650	ENE	(342.2,0.2), 15.8	(2.9, 0.038)	0.35	SC: ($5\cdot10^{-9}$, 0.6, 0.4) UC: ($1\cdot10^{-8}$, 0.6) C: ($5\cdot10^{-9}$, 0.6)
	WNW	(209.8,1.6), 14.6	(2.8, 0.038)	0.45	SC: ($5\cdot10^{-8}$, 0.6, 0.4) UC: ($5\cdot10^{-8}$, 0.6) C: ($5\cdot10^{-8}$, 0.6)
	N-S	(271.3,3.8), 10.3	(2.95, 0.038)	0.08	SC: ($5\cdot10^{-9}$, 0.6, 0.4) UC: ($1\cdot10^{-8}$, 0.6) C: ($5\cdot10^{-9}$, 0.6)
	SubH	(238.9,81.5), 12.7	(2.95, 0.038)	0.07	SC: ($1\cdot10^{-7}$, 0.6, 0.4) UC: ($8\cdot10^{-7}$, 0.6) C: ($1\cdot10^{-7}$, 0.6)

Table 10-19. Description of the calibrated hydrogeological DFN input parameters for HRD_N with fixed r_0=0.038 m (where k_r > 2.2) and open fracture intensity based on OPO-CP.

Depth zone (masl)	Set	Orientation set pole: (trend, plunge), conc.	Fracture radius model power-law (k_r, r_0)	Intensity P_{32} (m^2/m^3) of open fractures	Transmissivity model T (m^2/s) See Table 10-5
–150 to 0	ENE	(342.2,0.2), 15.8	(2.2, 0.15)	0.16	SC: ($4\cdot10^{-8}$, 0.6, 0.7)
	WNW	(209.8,1.6), 14.6	(2.2, 0.2)	0.55	SC: ($1.5\cdot10^{-7}$, 0.7,0.7)
	N-S	(271.3,3.8), 10.3	(2.2, 0.15)	0.23	SC: ($8\cdot10^{-8}$, 0.7, 0.6)
	SubH	(238.9,81.5), 12.7	(2.2, 0.06)	0.45	SC: ($1\cdot10^{-7}$, 0.7, 0.7)
–400 to –150	ENE	(342.2,0.2), 15.8	(2.3, 0.038)	0.14	SC: ($6\cdot10^{-8}$, 0.7, 0.5)
	WNW	(209.8,1.6), 14.6	(2.2, 0.12)	0.32	SC: ($6\cdot10^{-8}$, 0.7, 0.7)
	N-S	(271.3,3.8), 10.3	(2.2, 0.038)	0.11	SC: ($3\cdot10^{-8}$, 0.6, 0.4)
	SubH	(238.9,81.5), 12.7	(2.2, 0.06)	0.38	SC: ($6\cdot10^{-8}$, 0.8, 0.7)
–650 to –400	ENE	(342.2,0.2), 15.8	(2.35, 0.038)	0.14	SC: ($5\cdot10^{-8}$, 0.7, 0.7)
	WNW	(209.8,1.6), 14.6	(2.35, 0.038)	0.29	SC: ($4\cdot10^{-8}$, 0.6, 0.7)
	N-S	(271.3,3.8), 10.3	(2.45, 0.038)	0.17	SC: ($1\cdot10^{-8}$, 0.4, 0.4)
	SubH	(238.9,81.5), 12.7	(2.7, 0.038)	0.24	SC: ($1\cdot10^{-8}$, 0.6, 0.4)
–1000 to –650	ENE	(342.2,0.2), 15.8	(2.8, 0.038)	0.19	SC: ($5\cdot10^{-9}$, 0.7, 0.4)
	WNW	(209.8,1.6), 14.6	(2.7, 0.038)	0.26	SC: ($1\cdot10^{-8}$, 0.7, 0.4)
	N-S	(271.3,3.8), 10.3	(2.8, 0.038)	0.06	SC: ($5\cdot10^{-9}$, 0.7, 0.4)
	SubH	(238.9,81.5), 12.7	(2.65, 0.038)	0.05	SC: ($1\cdot10^{-8}$, 0.7,0.4)

Table 10-20. Correlation coefficients for the shape of histograms of *Q/s* across the bins shown in Figure 10-15 for the four variants considered for HRD_N.

Depth zone (masl)	Correlation coefficient for distribution of *Q/s* between model and PFL			
	OPO, r_0 fixed, SC	OPO, r_0 fixed, UC	OPO, r_0 fixed, C	OPO-CP, r_0 fixed, SC
–150 to 0	0.95	0.94	0.92	0.94
–400 to –150	0.84	0.89	0.79	0.81
–650 to –400	0.59	0.75	0.34	0.67

10.5.5 Comparison of KLX27A data versus hydrogeological DFN model for HRD_W

KLX27A is a core-drilled borehole in the south-west corner of Laxemar. It is approximately 645 m long, inclined northwards, starting in HRD_C, crossing the ZSMNW042A deformation zone, and ending in HRD_W. About 408 m of the borehole is in HRD_W (excluding major deformation zones). Data from KLX27A were excluded from the data used to develop and calibrate the hydrogeological DFN model of HRD_W, and therefore it may potentially be used to compare predictions of the hydrogeological DFN model with the hydraulic properties observed in relevant parts of KLX27A. This intended as a partial validation of the hydrogeogical DFN, but it also gives an indication of the predictability of the hydraulic fracturing over the types of length scales typical of boreholes, a few hundreds of metres. Only the sections of boreholes in HRD_W were used for the comparison, and so the validation only strictly applies to HRD_W. The comparison is presented in Appendix 10, and the results are summarised in Chapter 11.

10.6 Block modelling for testing scale issues

10.6.1 Approach

The parameters derived in Section 10.5 are intended for use in modelling flow and transport using a DFN concept. However, a significant part of the hydrogeological modelling within the SDM uses equivalent porous continuum medium (ECPM) modelling based on upscaling of an underlying DFN model, and hence it is interesting to evaluate what kind of block scale hydraulic conductivities the hydrogeological DFN model implies. For heterogeneous fracture systems block scale properties have a strong dependence on the block scale considered. On the scale of a deposition hole, a few metres, the properties depend heavily on the intensity and transmissivity distribution of individual fractures, whereas bulk flows on scales of hundreds of metres are controlled by a network system of fractures, and hence is more homogenised. Since the PSS measurements are made on borehole interval scales of 5 m, 20 m and 100 m, these 3 scales are used to study the scale effect and aid comparison with measured data.

For the SDM-Site Laxemar regional-scale groundwater flow modelling, ECPM models will be constructed of the site, probably using elements of 20–40 m size in the local-scale and about 100 m in the regional-scale model. To derive hydraulic properties for such a model it will be necessary to construct a regional-scale hydrogeological DFN. Typically, it is necessary to truncate the fracture size distribution at some lower limit, as it is usually only feasible to work with DFN models of not more than a few tens of millions of fractures. Hence, another objective of studying block-scale ECPM properties is to determine appropriate truncation limits on the size of fractures generated that will not have a significant effect on the upscaled properties.

The upscaling methodology produces a directional hydraulic conductivity tensor, fracture kinematic porosity and other transport properties (such as the connected fracture surface area per unit volume). In ConnectFlow a flux-based upscaling method is used that requires several flow calculations through a DFN model in different directions.

Figure 10-27 shows an illustration of how flow is calculated in a DFN model (a 2D network is shown for simplicity). To calculate equivalent hydraulic conductivity for the block shown, the flux through the network is calculated for a linear head gradient in each of the axial directions. Due to the variety of connections across the network, several flow-paths are possible, and may result in cross-flows non-parallel to the head gradient. Cross-flows are a common characteristic of DFN models and can be approximated in an ECPM by an anisotropic hydraulic conductivity. In 3D, ConnectFlow uses six components to characterise the symmetric hydraulic conductivity tensor. Using the DFN flow simulations, the fluxes through each face of the block are calculated for each head gradient direction. The hydraulic conductivity tensor is then derived by a least-squares fit to these flux responses for the fixed head gradients. Other authors /La Pointe 1995/ have only considered the components of the equivalent hydraulic conductivity parallel to the coordinate axes using a head difference between opposite faces and no-flow on the other faces. This leads to a poor representation of blocks in which the network connections, and hence flow, are mostly between adjacent faces rather than between opposite faces. The effective hydraulic conductivity assigned to such blocks may be essentially zero, even though the flow-paths through the block may contribute significantly to the overall flow through the network.

In 3D, the blocks have to be hexahedra (cuboids), but the upscaling method can be applied to an array of sub-blocks within a much larger DFN domain by performing the upscaling on each sub-block in sequence. The upscaling method is typically used in one of two ways:

- To obtain the statistical distribution of hydraulic conductivity on a given block scale a DFN model is generated for a much larger domain, and then ECPM properties are calculated for an array of sub-blocks of equal size and shape to give an ensemble of properties. (This method is used to obtain the results described here).
- To obtain an ECPM model for a local- or regional-scale grid, a DFN model is generated within the grid domain, and the upscaling is performed within each grid element to derive the ECPM properties element by element.

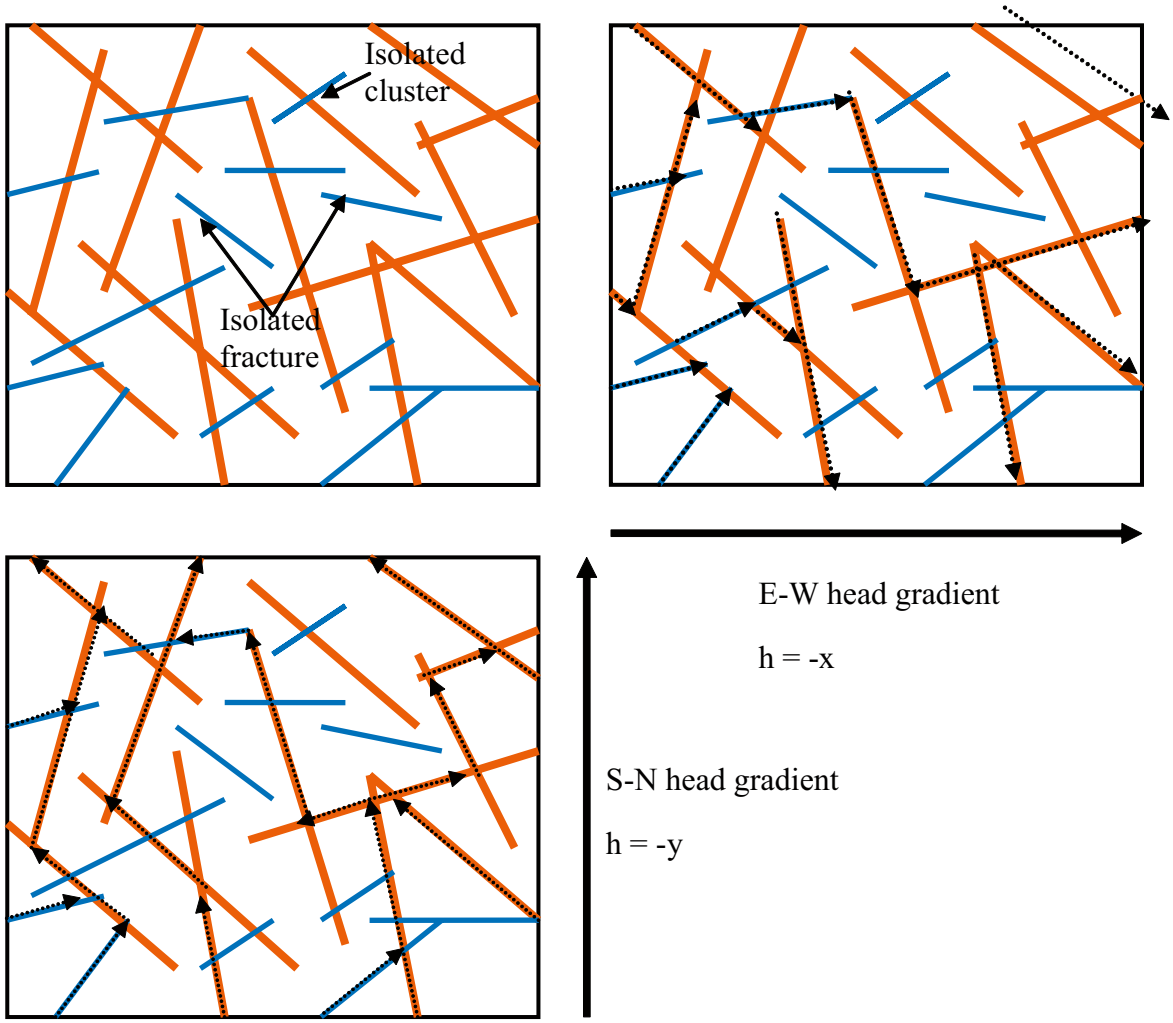

Figure 10-27. *2D illustration of flow through a network of fractures. A random network of fractures with variable length and transmissivity is shown top left (orange fractures are large transmissivity, blue are low). Top right: flow-paths for a linear head gradient E-W decreasing along the x-axis. Bottom left: flow-paths through the network for a linear head gradient S-N decreasing along the y-axis.*

A detailed description of the upscaling method to calculate the ECPM hydraulic conductivity tensor is given in /Jackson et al. 2000/. Briefly, the method can be summarised by the following steps:

- Define a sub-block within a DFN model.
- Identify the fractures that are either completely inside or cut the block.
- Calculate the connections between these fractures and their connection to the faces of the block.
- Remove isolated fractures and isolated fracture clusters, and dead-end fractures if specified.
- Specify a linear head gradient parallel to each coordinate axis on all the faces of the block.
- Calculate the flow through the network and the flux through each face of the block for each axial head gradient.
- Fit a symmetric anisotropic hydraulic conductivity tensor that best fits (least-squares) the flux response of the network.
- Fracture kinematic porosity is calculated as the sum (over all fractures that are connected on the scale of the block) of fracture area within the block multiplied by the transport aperture of the fracture (A preliminary relation was used: $e_t = 0.705\ T^{0.404}$ based on tests performed by SKB. A compilation of tracer tests is planned to be made by SKB that will provide a broader view on some transport parameters /Hjerne et al. 2009/. Alternatives to the preliminary model used are shown in Section 7.7).

One important aspect of this approach is that the properties are calculated on a particular scale, that of the blocks, and that a connectivity analysis of the network is performed only on the scale of the block. Bulk flows across many blocks will depend on the correlation and variability of properties between blocks.

One refinement of the upscaling methodology is to simulate flow through a slightly larger domain than the block size required for the ECPM properties, but then calculate the flux responses through the correct block size. The reason for this is to avoid over-prediction of hydraulic conductivity from flows through fractures that just cut the corner of the block but that are unrepresentative of flows through the *in situ* fracture network. This method is illustrated in Figure 10-28. The area around the block is known as a 'guard-zone', and an appropriate choice for its thickness is about a fracture radius of the fractures that give the largest contribution to the block (i.e. the largest that have an intensity greater than or equal to 1/block size). The problem is most significant in sparse heterogeneous networks in which the flux through the network of fractures is affected by 'bottlenecks' through low transmissivity fractures, and is quite different to the flux through single fractures.

10.6.2 Upscaling results for the OPO semi-correlated case

The calculation of upscaled properties focussed on the base case model parameterised in Section 10.5. A sensitivity study was limited mainly to the hydraulic domains associated with the repository volume, i.e. –650 masl to –400 masl for HRD_C, HRD_W and HRD_EW007. For each block scale of interest, fractures were generated within a volume 12 times the size of the block, which was then sub-divided into a 9 by 9 by 9 matrix of contiguous blocks and the ECPM properties calculated for each of these 729 blocks into total. This provided an ensemble over which block property statistics were collated. For each of the blocks, the domain used for the flow simulation was expanded to 3 times the size of the block, but only the flux through the central volume equal to the required block size was used to calculate the equivalent hydraulic properties, for the reason illustrated in Figure 10-28.

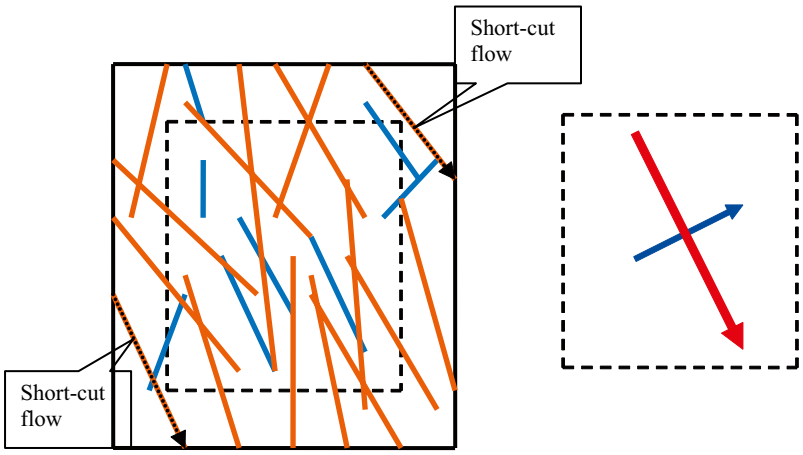

Figure 10-28. *2D sketch of how block-scale hydraulic conductivity can be over-estimated using a linear head gradient by high transmissivity fractures that cut across a corner of the block. By simulating flow through a larger domain, but only calculating the flux through the required block size (dashed block) then fluxes more consistent with flow through an in situ network are obtained. The ECPM hydraulic conductivities are then calculated for the dashed block to give principal components (right). The red arrow is the maximum component, blue the minimum.*

Firstly, detailed statistics are provided including percentiles and analysis of anisotropy for the HRD and depth zone relevant to the repository at 5 m, 20 m and 100 m scales. Secondly, more concise summary tables are presented for all 4 HRD and each depth zone at 5 m, 20 m and 100 m scales. Results for the bottom depth zone, below –650 masl are only given for HRD_C since this is only domain for which the hydraulic DFN was calibrated at these depths.

An example of results for HRD_C using the case where open fracture intensity is based on OPO fractures and the semi-correlated transmissivity model is shown in Figure 10-29 and Table 10-21 for the 3 different block sizes. Figure 10-29 shows the hydraulic conductivity for the axial directions, and the strike of maximum horizontal hydraulic conductivity plotted as frequency over the number of blocks out of a total of 729 blocks. The scale dependence is apparent. For 100 m blocks, the geometric mean is highest, around $2 \cdot 10^{-9}$ m/s, and only moderately heterogeneous with a standard deviation of about 0.7 orders of magnitude. For 20 m blocks, the geometric mean is similar, but the heterogeneity increases significantly such that only 67% of blocks percolate (using a threshold of 10^{-11} m/s) and standard deviation is about 1.0 orders of magnitude. For 5 m, only about 66% of the blocks percolate (for a threshold of 10^{-11} m/s, which decreases to about 50% for a threshold of 10^{-10} m/s, and compares with about 40% measured of 5 m PSS intervals suggested in Figure 10-16) and the geometric mean of those that do is about $3 \cdot 10^{-10}$ m/s, and the standard deviation is about 1.4 orders of magnitude. For all scales there is a clear WNW anisotropy. The vertical hydraulic conductivity is similar to the maximum horizontal due to the hydraulic dominance of sub-vertical WNW fracturing. North-south vertical hydraulic conductivity is about a factor one third to a half of east-west.

The computational cost of the calculations can be reduced significantly by neglecting the smaller fractures. Although the density of fractures increases with decreasing fracture size, the smaller fractures tend to be less well-connected and, for the semi-correlated and correlated models, tend to be less transmissive. Therefore, neglecting the smaller fractures may only involve a small approximation. A study of the effect of the minimum fracture size considered in the calculations was carried out for the 20 m and 100 m blocks and the results are shown in Table 10-21. For the semi-correlated model the results are stable as long as r_{min} is less than about an eighth of the block size. Note that the 100 m block scale gives a geometric mean hydraulic conductivity of $2 \cdot 10^{-9}$ m/s compared with PSS 100 interval data with geometric mean $2 \cdot 10^{-10}$ m/s (with 95% confidence range for geometric mean: $2 \cdot 10^{-11}$ –$1 \cdot 10^{-9}$ m/s) for HRD_C between –650 masl to –400 masl, and $3 \cdot 10^{-9}$ m/s for sum(T)/L based on PFL-f data given in Table 9-12.

Kinematic porosity has less scale dependence, and the apparent increase for smaller blocks shown in Table 10-21 is probably more an effect of the truncation of fracture size, r_{min}, in the fractures generated. It is about $1 \cdot 10^{-3}$ when all small open fractures are included, but is reduced by a factor of about 8 if fracture sizes are truncated at 5.6 m. Hence, the effect of truncation on kinematic porosity needs to be considered in the regional-scale groundwater flow modelling.

Hydraulic properties for HRD_W are given in Table 10-22 for the case with open fracture intensity based on OPO fractures and a semi-correlated transmissivity. (The sensitivity to different minimum fracture radius were not considered for HRD_W). The geometric mean hydraulic conductivity is also about $1.5 \cdot 10^{-9}$ m/s, for 100 m blocks, which compares with $2 \cdot 10^{-10}$ m/s for the geometric mean of the PSS 100 m interval data (with 95% confidence range for geometric mean: $1 \cdot 10^{-11}$ –$5 \cdot 10^{-9}$ m/s) in HRD_W and $3 \cdot 10^{-8}$ m/s for sum(T)/L based on PFL-f data given in Table 9-12. The standard deviation is higher than HRD_C, 1.0 order of magnitude. For 20 m, only 51% of blocks percolate and the geometric mean is also $1.5 \cdot 10^{-9}$ m/s with standard deviation 1.3 orders of magnitude. For 5 m blocks, only 14% of blocks percolate (cf. about 25% of 5 m PSS intervals in Figure 10-22), and the geometric mean is $6 \cdot 10^{-11}$ m/s. Hence, the model confirms that flowing fractures are sparser in HRD_W than HRD_C, but the standard deviation of transmissivity is slightly higher in HRD_W than HRD_C. Kinematic porosity is about $7 \cdot 10^{-4}$.

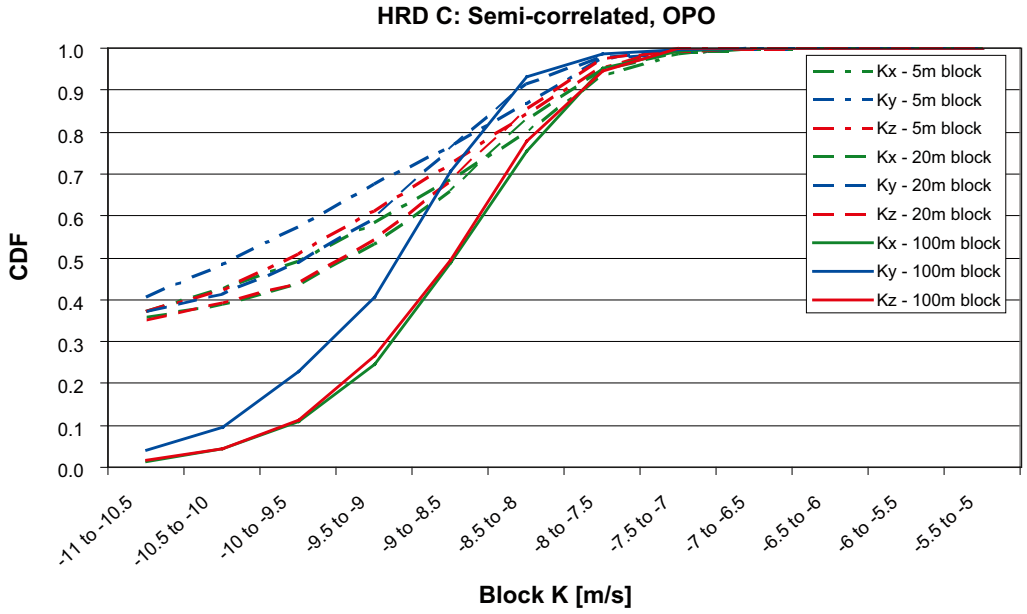

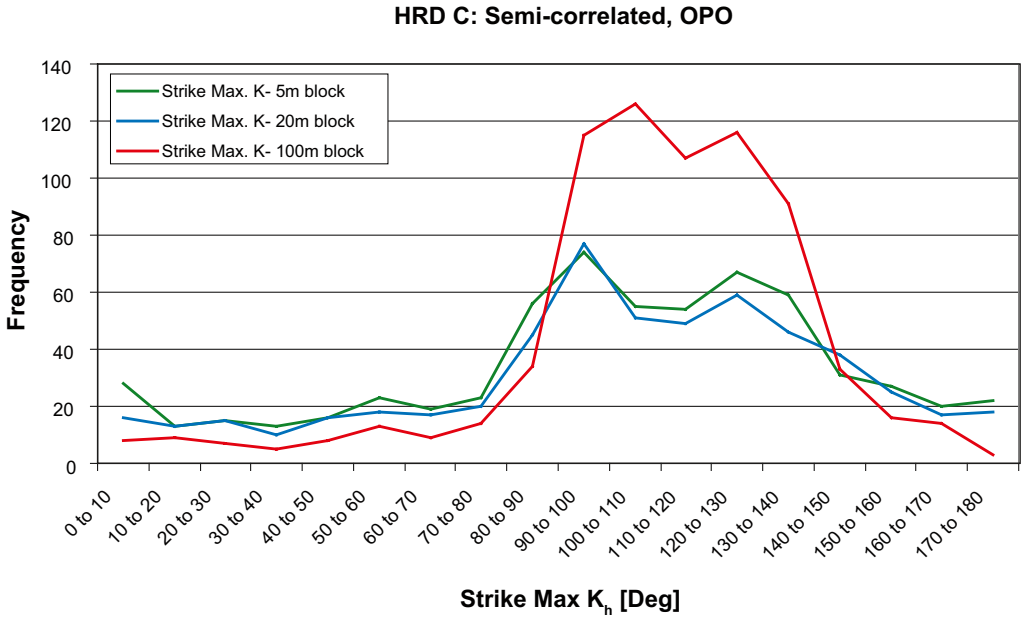

Figure 10-29. *Ensemble statistics for the upscaled hydraulic conductivities for the HRD_C for elevations –150 masl to –400 masl for the case with open fracture intensity based on OPO and the semi-correlated transmissivity model. Top: a comparison of the cumulative distribution of K_x (E-W), K_y (N-S) and K_z (vertical) hydraulic conductivity for block scales of 5 m, 20 m and 100 m. Bottom: a comparison of the strike of maximum horizontal hydraulic conductivity for block scales of 5 m, 20 m and 100 m.*

Hydraulic properties for HRD_EW007 are given in Table 10-23 for the case with open fracture intensity based on OPO fractures and a semi-correlated transmissivity. The geometric mean hydraulic conductivity is also about $8 \cdot 10^{-9}$ m/s, for 100 m blocks, which compares with $4 \cdot 10^{-9}$ m/s for the geometric mean of the PSS 100 m interval data (with 95% confidence range for geometric mean: $3 \cdot 10^{-10}$ – $5 \cdot 10^{-8}$ m/s) in HRD_EW007 and $1 \cdot 10^{-8}$ m/s for sum(T)/L based on PFL-f data given in Table 9-12. The standard deviation is lower than HRD_C, 0.3 orders of magnitude. For 20 m, 99% of blocks percolate and the geometric mean is also about $1 \cdot 10^{-8}$ m/s with standard deviation 0.8 orders of magnitude. For 5 m blocks, 88% of blocks percolate (cf. about 64% of 5 m PSS intervals), and the geometric mean is $1 \cdot 10^{-9}$ m/s. Hence, HRD_EW007 is about 4 times more conductive than HRD_C and is less heterogeneous. Kinematic porosity is about $2 \cdot 10^{-3}$.

For the other depths intervals, a more concise format of hydraulic properties are presented in terms of the % of blocks that percolate, mean and median and the standard deviation of the geometric mean conductivity, as well as mean and standard deviation in kinematic porosity are given for each HRD in Table 10-24 through Table 10-27.

Table 10-21. Details of upscaled properties for HRD_C for elevations –400 masl to –650 masl for the case with open fracture intensity based on OPO fractures and the semi-correlated transmissivity model for 5 m, 20 m and 100 m blocks.

Scale	r_{min} [m]	Log10(K_{eff}) [m/s] 10-percentile	25-percentile	50-percentile	75-percentile	90-percentile	Mean	1 s.d.
5	0.11	N/A	N/A	–9.55	–8.49	–7.80	–9.27	1.41
20	2.3	N/A	N/A	–9.21	–8.37	–8.02	–8.89	1.04
100	5.6	–9.68	–9.13	–8.61	–8.17	–7.89	–8.70	0.70
20	1.1	N/A	–9.70	–8.47	–7.90	–7.21	–8.44	1.04
100	14	–10.32	–9.40	–8.73	–8.25	–7.93	–8.82	0.85

Scale	r_{min} [m]	Mean Log10(K_x) [m/s]	Mean Log10(K_y) [m/s]	Mean Log10(K_z) [m/s]	% of blocks that percolate
5	0.11	–8.71	–9.13	–8.85	66%
20	2.3	–8.77	–9.08	–8.83	67%
100	5.6	–8.58	–8.98	–8.60	99%
20	1.1	–7.89	–8.26	–8.12	83%
100	14	–9.25	–9.65	–9.24	93%

Scale	r_{min} [m]	Median Log10(K_x) [m/s]	Median Log10(K_y) [m/s]	Median Log10(K_z) [m/s]	Median ratio K_{hmax}/K_{hmin}	Median ratio K_{hmax}/K_z	Strike of K_{hmax} (by eye)
5	0.11	–9.46	–9.90	–9.55	9.84	1.62	90–150
20	2.3	–9.12	–9.43	–9.20	5.34	1.06	90–150
100	5.6	–8.47	–8.84	–8.49	6.35	1.25	90–150
20	1.1	–8.35	–8.76	–8.40	6.83	1.49	90–150
100	14	–8.61	–8.95	–8.59	7.56	1.22	90–140

Scale	r_{min} [m]	Log10(kinematic porosity) [–] 10-percentile	25-percentile	50-percentile	75-percentile	90-percentile	Mean	1 s.d.
5	0.11	–3.04	–3.03	–3.01	–3.00	–2.98	–3.01	0.02
20	2.3	–3.84	–3.79	–3.74	–3.69	–3.64	–3.74	0.08
100	5.6	–3.97	–3.95	–3.91	–3.87	–3.84	–3.91	0.05
20	1.1	–3.73	–3.68	–3.61	–3.54	–3.47	–3.60	0.10
100	14	–4.21	–4.17	–4.11	–4.06	–4.01	–4.11	0.08

Table 10-22. Details of upscaled properties for HRD_W for elevations –400 masl to –650 masl for the case with open fracture intensity based on OPO fractures and the semi-correlated transmissivity model for 5 m, 20 m and 100 m blocks.

Scale	r_{min}	Log10(K_{eff}) [m/s]						
	[m]	10-percentile	25-percentile	50-percentile	75-percentile	90-percentile	Mean	1 s.d.
5	0.11	N/A	N/A	N/A	N/A	–10.32	–10.25	1.11
20	2.3	N/A	N/A	–10.67	–8.54	–7.94	–8.78	1.26
100	5.6	–10.14	–9.44	–8.84	–8.05	–7.58	–8.79	1.03

Scale	r_{min} [m]	Mean Log10(K_x) [m/s]	Mean Log10(K_y) [m/s]	Mean Log10(K_z) [m/s]	% of blocks that percolate
5	0.11	N/A	N/A	N/A	14%
20	2.3	–8.72	–8.73	–8.89	51%
100	5.6	–8.78	–8.69	–8.90	97%

Scale	r_{min} [m]	Median Log10(K_x) [m/s]	Median Log10(K_y) [m/s]	Median Log10(K_z) [m/s]	Median ratio K_{hmax}/K_{hmin}	Median ratio K_{hmax}/K_z	Strike of K_{hmax} (by eye)
5	0.11	N/A	N/A	N/A	N/A	1.00	N/A
20	2.3	–10.84	–10.78	–10.99	2.56	1.00	N/A
100	5.6	–8.86	–8.75	–8.82	4.40	1.96	100–180

Scale	r_{min}	Log10(kinematic porosity) [–]						
	[m]	10-percentile	25-percentile	50-percentile	75-percentile	90-percentile	Mean	1 s.d.
5	0.11	–3.19	–3.17	–3.15	–3.13	–3.11	–3.15	0.03
20	2.3	–3.89	–3.84	–3.78	–3.70	–3.62	–3.75	0.13
100	5.6	–3.98	–3.95	–3.90	–3.85	–3.79	–3.89	0.08

Table 10-23. Details of upscaled properties for HRD_EW007 for elevations –400 masl to –650 masl for the case with open fracture intensity based on OPO fractures and the semi-correlated transmissivity model for 5 m, 20 m and 100 m blocks.

Scale	r_{min}	Log10(K_{eff}) [m/s]						
	[m]	10-percentile	25-percentile	50-percentile	75-percentile	90-percentile	Mean	1 s.d.
5	0.11	–11.43	–9.66	–8.69	–8.16	–7.80	–8.89	1.09
20	2.3	–8.77	–8.23	–7.86	–7.57	–6.74	–7.89	0.83
100	5.6	–8.53	–8.31	–8.07	–7.91	–7.78	–8.12	0.29

Scale	r_{min} [m]	Mean Log10(K_x) [m/s]	Mean Log10(K_y) [m/s]	Mean Log10(K_z) [m/s]	% of blocks that percolate
5	0.11	–8.18	–8.62	–8.26	88%
20	2.3	–7.53	–7.73	–7.40	99%
100	5.6	–8.01	–8.42	–7.93	100%

Scale	r_{min} [m]	Median Log10(K_x) [m/s]	Median Log10(K_y) [m/s]	Median Log10(K_z) [m/s]	Median ratio K_{hmax}/K_{hmin}	Median ratio K_{hmax}/K_z	Strike of K_{hmax} (by eye)
5	0.11	–8.61	–8.98	–8.62	9.72	1.49	80–150
20	2.3	–7.73	–8.10	–7.67	8.74	1.11	90–150
100	5.6	–7.98	–8.38	–7.88	6.27	1.02	110–150

Scale	r_{min}	Log10(kinematic porosity) [–]						
	[m]	10-percentile	25-percentile	50-percentile	75-percentile	90-percentile	Mean	1 s.d.
5	0.11	–2.84	–2.83	–2.82	–2.81	–2.80	–2.82	0.02
20	2.3	–3.51	–3.46	–3.41	–3.34	–3.31	–3.41	0.07
100	5.6	–3.73	–3.71	–3.69	–3.67	–3.65	–3.69	0.03

Table 10-24. Summary of upscaled properties for HRD_C for each depth zone for the case with open fracture intensity based on OPO fractures and the semi-correlated transmissivity model for 5 m, 20 m and 100 m blocks.

HRD_C		Depth zone 1: 0 to –150 masl					
Scale	r_{min} [m]	% active	Log10(K_{eff}) [m/s]			Log10(phi) [–]	
			Mean	Median	1 s.d.	Mean	1 s.d.
5	0.11	98%	–7.72	–7.65	1.08	–2.64	0.038
20	2.3	100%	–7.05	–7.07	0.86	–3.06	0.15
100	5.6	100%	–6.99	–7.03	0.36	–3.33	0.038
HRD_C		**Depth zone 2: –150 to –400 masl**					
Scale	r_{min} [m]	% active	Log10(K_{eff}) [m/s]			Log10(phi) [–]	
			Mean	Median	1 s.d.	Mean	1 s.d.
5	0.11	44%	–9.65	–12.11	1.52	–2.87	0.02
20	2.3	76%	–8.41	–8.51	1.09	–3.52	0.10
100	5.6	100%	–7.85	–8.32	1.29	–3.48	0.09
HRD_C		**Depth zone 3: –400 to –650 masl**					
Scale	r_{min} [m]	% active	Log10(K_{eff}) [m/s]			Log10(phi) [–]	
			Mean	Median	1 s.d.	Mean	1 s.d.
5	0.11	66%	–9.27	–9.55	1.41	–3.01	0.02
20	2.3	67%	–8.89	–9.21	1.04	–3.74	0.08
100	5.6	99%	–8.70	–8.61	0.70	–3.91	0.05
HRD_C		**Depth zone 4: < –650 masl**					
Scale	r_{min} [m]	% active	Log10(K_{eff}) [m/s]			Log10(phi) [–]	
			Mean	Median	1 s.d.	Mean	1 s.d.
100	5.6	32%	–9.65	N/A	1.45	–4.45	0.08

Table 10-25. Summary of upscaled properties for HRD_W for each depth zone for the case with open fracture intensity based on OPO fractures and the semi-correlated transmissivity model for 5 m, 20 m and 100 m blocks.

HRD_W		Depth zone 1: 0 to –150 masl					
Scale	r_{min} [m]	% active	Log10(K_{eff}) [m/s]			Log10(phi) [–]	
			Mean	Median	1 s.d.	Mean	1 s.d.
5	0.11	94%	–7.85	–7.92	1.40	–2.72	0.06
20	2.3	100%	–6.81	–6.83	0.98	–3.00	0.14
100	5.6	100%	–6.79	–6.80	0.39	–3.26	0.038
HRD_W		**Depth zone 2: –150 to –400 masl**					
Scale	r_{min} [m]	% active	Log10(K_{eff}) [m/s]			Log10(phi) [–]	
			Mean	Median	1 s.d.	Mean	1 s.d.
5	0.11	32%	–9.59	N/A	1.34	–3.08	0.03
20	2.3	59%	–8.05	–8.95	1.17	–3.59	0.12
100	5.6	97%	–8.29	–8.19	1.03	–3.75	0.06
HRD_W		**Depth zone 3: –400 to –650 masl**					
Scale	r_{min} [m]	% active	Log10(K_{eff}) [m/s]			Log10(phi) [–]	
			Mean	Median	1 s.d.	Mean	1 s.d.
5	0.11	14%	–10.25	N/A	1.11	–3.15	0.03
20	2.3	51%	–8.78	–10.67	1.26	–3.75	0.13
100	5.6	97%	–8.79	–8.84	1.03	–3.89	0.08

Table 10-26. Summary of upscaled properties for HRD_EW007 for each depth zone for the case with open fracture intensity based on OPO fractures and the semi-correlated transmissivity model for 5 m, 20 m and 100 m blocks.

HRD_EW007		Depth zone 1: 0 to –150 masl					
Scale	r_{min} [m]	% active	Log10(K_{eff}) [m/s]			Log10(phi) [–]	
			Mean	Median	1 s.d.	Mean	1 s.d.
5	0.11	99%	–7.62	–7.49	0.66	–2.58	0.02
20	2.3	100%	–6.92	–6.99	0.58	–3.05	0.06
100	5.6	100%	–7.15	–7.15	0.24	–3.46	0.038
HRD_EW007		**Depth zone 2: –150 to –400 masl**					
Scale	r_{min} [m]	% active	Log10(K_{eff}) [m/s]			Log10(phi) [–]	
			Mean	Median	1 s.d.	Mean	1 s.d.
5	0.11	95%	–8.57	–8.43	1.04	–2.87	0.038
20	2.3	100%	–7.31	–7.52	0.92	–3.20	0.12
100	5.6	100%	–7.37	–7.39	0.36	–3.58	0.05
HRD_EW007		**Depth zone 3: –400 to –650 masl**					
Scale	r_{min} [m]	% active	Log10(K_{eff}) [m/s]			Log10(phi) [–]	
			Mean	Median	1 s.d.	Mean	1 s.d.
5	0.11	88%	–8.89	–8.69	1.09	–2.82	0.02
20	2.3	99%	–7.89	–7.86	0.83	–3.41	0.07
100	5.6	100%	–8.12	–8.07	0.29	–3.69	0.03

Table 10-27. Summary of upscaled properties for HRD_N for each depth zone for the case with open fracture intensity based on OPO fractures and the semi-correlated transmissivity model for 5 m, 20 m and 100 m blocks.

HRD_N		Depth zone 1: 0 to –150 masl					
Scale	r_{min} [m]	% active	Log10(K_{eff}) [m/s]			Log10(phi) [–]	
			Mean	Median	1 s.d.	Mean	1 s.d.
5	0.11	100%	–7.43	–7.34	0.95	–2.57	0.038
20	2.3	100%	–6.25	–6.30	0.71	–2.82	0.09
100	5.6	100%	–6.15	–6.18	0.28	–2.98	0.038
HRD_N		**Depth zone 2: –150 to –400 masl**					
Scale	r_{min} [m]	% active	Log10(K_{eff}) [m/s]			Log10(phi) [–]	
			Mean	Median	1 s.d.	Mean	1 s.d.
5	0.11	71%	–8.71	–9.16	1.39	–2.75	0.05
20	2.3	95%	–7.44	–7.26	0.93	–3.23	0.09
100	5.6	100%	–7.33	–7.35	0.46	–3.46	0.038
HRD_N		**Depth zone 3: –400 to –650 masl**					
Scale	r_{min} [m]	% active	Log10(K_{eff}) [m/s]			Log10(phi) [–]	
			Mean	Median	1 s.d.	Mean	1 s.d.
5	0.11	27%	–9.64	N/A	1.24	–3.23	0.03
20	2.3	77%	–8.46	–8.49	1.06	–3.69	0.09
100	5.6	100%	–8.29	–8.28	0.55	–3.85	0.038

10.6.3 Upscaling results for the other variants

Upscaling results for HRD C for the variants based on correlated or uncorrelated transmissivity models and OPO fracture intensity are given in Appendix 6, Section A.6.6. These reveal that a correlated or uncorrelated relation between fracture size and transmissivity give similar hydraulic conductivity on the 100 m scale, i.e. $1–2 \cdot 10^{-9}$ m/s. The only significant difference between the transmissivity variants is that the uncorrelated model gives greater variability and less scale dependence, as well as a factor 3 times higher kinematic porosity. This is to be expected since the uncorrelated model can assign high transmissivity to small fractures, and so the frequency of high hydraulic conductivity 5 m intervals is higher than for a correlated model. Hence, the choice of transmissivity model yields similar large scale hydraulic conductivity, as each model is matched to the same underlying data, but the scale dependence is strongest for a correlated model. This is thought to be a consequnce of flow being more focussed on large fractures for the correlated model, and hence for small block volumes the variability in flow between blocks intersected by large fractures and those not becomes very apparent as large variability. The transmissivity model has greatest effect on the kinematic porosity. The case with fracture intensity based on OPO-CP fractures gives similar hydraulic conductivity, a factor 2 lower in the mean and less variability on the 100 m scale compared to the OPO case, and a factor 3 lower on the 20 m scale.

Block property results for the HRD_W variants are given in Appendix 6, Section A.6.7. Again, these show the characteristic of less scale dependence in the geometric mean hydraulic conductivity for the uncorrelated, and the uncorrelated model gives a factor of 5 higher kinematic porosity. The case with fracture intensity based on OPO-CP fractures gives similar hydraulic conductivity, a factor 2 higher in the mean and less variability on the 100 m scale, and a similar mean but still less variability on the 20 m scale. Block property results for the HRD_EW007 variants are given in Appendix 6, Section A.6.8.

There is difference in mean values for HRD_C is are not considered to be particularly significant, especially as it is not reproduced in HRD_W, mainly it thought to be indication of the basic uncertainty in the matching procedure and calculation of block properties that are probably only constraining effective block properties to within a factor 2–3. The lower variability in the OPO-CP case is probably more notable as a characteristic of this variant.

10.6.4 The importance of large fractures in understanding the block properties of different model variants

As shown in Appendix 6, Section A.6.6 to Appendix 6, Section A.6.8, and noted in the section above, OPO-CP variants gave block scale hydraulic conductivities with less spatial variability than the OPO variants, despite being calibrated to the same measured data. This section considers one possible explanation for the difference in terms of the different fracture size distributions that were used.

If a fracture spans a 20 m or 100 m block then it is amongst the largest in the fracture size distribution (assuming a power-law fracture size distribution) and is likely to have a higher than average transmissivty (assuming a correlated or semi-correlated transmissivity model). Since the fracture spans the block there are no impediments to flow across that block and this single fracture is likely to contribute to a greater hydraulic conductivity (in that particular direction) compared to a block where flow is through a network of smaller, less transmissive fractures. It is therefore expect the intensity of ‘large’ fractures that span the block to be correlated with a higher average effective block hydraulic conductivity.

In both the OPO and OPO-CP variants the models are calibrated to match the observed PFL-f fracture intensity. Since the fracture intensity of OPO fractures is several times greater than the fracture intensity of OPO-CP fractures, the fracture size distribution must be steeper in the first case (the power law parameters k_r are typically smaller). Depending on the location parameter, $r_{0,}$ this may result in fewer ‘large’ fractures.

Since all models variants are also calibrated to the 100 m PSS data, the mean hydraulic conductivities for 100 m blocks should be comparably, but the variability between blocks will depend on the particular parameterisation.

In order to quantify this effect the number of 'large' fractures within 20 m and 100 m blocks is estimated for both types of model in HRD_C. In the following analysis it is assumed that all of the fractures are connected, and therefore contribute to the flow across a block. To be more precise a 'large' fracture is defined as having a radius r_l such that

$$r_l \geq \frac{l}{\sqrt{\pi}} \tag{10-5}$$

Where l is the length of the side of a block (20 m or 100 m). The expected number of fractures capable of spanning a block is estimated using

$$N \approx P_{32}\left[r > r_l\right] \quad l \tag{10-6}$$

The results of this analysis are shown in Table 10-28. It shows that the number of large fractures is higher for the OPO-CP variant at the 100 m and 20 m block scale for all depth zones, and importantly the number of cross-cutting fractures is around 1 or less below -150 masl for the OPO case, and so the hydraulic conductivity is likely to vary considerably according to whether a large high T fracture happens to cross-cut the block or not, whereas it is generally above 1 for the OPO-CP case, and so most block will contain at least one high T cross-cutting fracture. This is believed to be the cause of the difference in variability between the variants.

10.7 Hydrogeological properties of the near surface bedrock

In this section some brief comments are provided concerning the general characteristics of hydraulic properties of near-surface bedrock by firstly collating the relevant hydraulic measurements, and then considering the block properties predicted for the upper depth zone above –150 masl.

10.7.1 Overview of near-surface hydraulic data

The upper 100 m of the bedrock has been tested in various types of cored boreholes and percussion boreholes with test scales 100 m (PSS and HTHB methods) and PFL-s (5 m test sections) and PFL-f (identification of flowing features). There are no PFL tests available for the c. 5–10 m of the uppermost part of the bedrock, as casing generally makes it impossible to test the rock and also due to the fact that injection of water was not used in most cases, which is needed as generally one applies 10 m drawdown when logging with PFL.

Several hydraulic tests using the different methods indicate that the hydraulic conductivity decreases by depth and that most of this decrease is in the upper 100–200 m of the bedrock. Tests with a 100 m test scale indicate that rock above elevation –150 masl has a geometric mean hydraulic conductivity (K) of about $1 \cdot 10^{-7}$ m/s for the entire data set (HCD+HRD) and also between deformation zones (HRD). For the depth zone –150 to –400 masl, the geometric mean K is about $3.5 \cdot 10^{-8}$ m/s for the entire data set (HCD+HRD) and between deformation zones about $1.7 \cdot 10^{-8}$ m/s (See Chapter 7 and Section 9.6.1).

Table 10-28. Estimated numbers of fractures capable of spanning the block, in 20 m and 100 m blocks for HRD_C.

Model type	Block scale [m]	Depth zone			
		0 to –150 masl	–150 to –400 masl	–400 to –650 masl	< –650
OPO	20	1.92	1.01	0.96	0.26
OPO	100	3.11	1.68	1.57	0.30
OPO-CP	20	5.40	1.93	1.43	0.34
OPO-CP	100	12.53	4.21	2.93	0.50

PFL-s tests with 5 m test scale indicate that rock between deformation zones, and above elevation –150 masl, has a geometric mean hydraulic conductivity of about $5 \cdot 10^{-9}$ m/s for data between deformation zones. For depth interval –150 to –400 masl the geometric mean K is about $9 \cdot 10^{-11}$ m/s for the rock mass between deformation zones.

Similar trends can be seen in PFL-f also. Section 9.3 shows that the frequency of open fractures decreases slightly by depth, but the frequency of flowing fractures with transmissivities > $1 \cdot 10^{-9}$ m^2/s decreases significantly below –50 to –150 masl (the variation is rather large between the different defined HRDs). The total (over all 4 fracture orientation sets) Terzaghi corrected intensities for OPO fractures and for PFL-f for rock above elevation –150 masl are 2.6 to 3.6 and 0.2 to 0.8, respectively, and for depth zone –150 to –400 masl 1.6 to 3.1 and 0.6 to 0.1, respectively.

Section 9.3 also shows that the horizontal set of flowing fractures has a slightly higher intensity above elevation –150 masl compared to deeper levels. Combining this characteristic with relatively low stress levels close to the surface (smaller rock load) at small depths, probably results in a horizontal hydraulic anisotropy of the near-surface rock being significantly higher compared to deeper levels.

10.7.2 Conceptual model of near-surface rock

Based on this, the hydraulic conceptual model of the near-surface bedrock can be summarised as follows:

- Hydraulic conductivity decreases with depth in deformation zones as well in the rock between deformation zones.
- Hydraulic conductivity of deterministic deformation zones can be expected to be about 10 times greater than the surrounding rock.
- The properties are probably anisotropic with the characteristics that the sub-horizontal fractures set possibly has a higher transmissivity compared to the sub-vertical fractures in the upper 50–150 m of the rock, although the WNW is also important. The subhorizontal fracture set becomes less dominant at depths below –50 to –150 masl and with the WNW set taking over in importance.

It is sometimes suggested that the uppermost part of the rock, say the uppermost 5–10 m, is more fractured and permeable due to the influence of the latest glaciation and particularly so on the south-eastern slopes of the rock surface as the glacier moved from NW towards SE. Data that can confirm such a hypothesis are difficult to collect and are presently unavailable. However, some trenches have been excavated and on top of some deformation zones there is a part of the near surface rock that is heavily weathered and fractured /Sohlenius et al. 2006/ that possibly is more conductive than the more intact rock beneath.

10.7.3 Comparison of near-surface block modelling results between the hydrogeological DFN and interference test modelling for KLX09B–F and KLX11A–F

The hydrogeological DFN model derived here is based primarily on analysis of single-hole PFL-f tests. PFL based interference tests have also been performed in KLX09B–F and KLX11B–F which have been used as a basis for developing drill site specific hydrogeological DFN models of the near-surface bedrock. Comparison of the consistency between these models can be achieved by calculating the equivalent block properties for each model. (It is not possible to compare directly the various DFN parameterisations due to differences in the way the models were constructed. For example the fracture set definitions, fracture intensities and fracture set orientation parameters are calculated locally for the interference test DFN parameterisations.) This also provides a quantification of uncertainty in the near-surface bedrock associated with the difference between different types of test, single- versus multi-hole, and between different drill sites. This is a selective comparison as the interference test modelling concerned only the near surface (depth zone 0 to –150 masl) and only a restricted area: KLX09 is in HRD_N and KLX11 is in HRD_W.

The KLX09 interference test modelling is described in a separate report /Hartley et al. 2007/. The KLX11 interference test is described in Appendix 7. For convenience the relevant DFN parameterisations derived from the interference tests are given Table 10-30 and Table 10-31.

The results of the upscaling process are presented in Table 10-29. The proportion of blocks that percolate is 100% for all of the cases presented below. HRD_C, HRD_W and HRD_EW007 show very similar hydraulic conductivities at the two block scales considered, and very similar variability between hydraulic conductivities. HRD_N stands out amongst the other HRDs as having higher hydraulic conductivity (by a factor of around 5).

The upscaling results for the KLX09 interference test DFN should be compared to upscaling results for HRD_N. The block scale hydraulic conductivities resulting from the hydrogeological DFN parameterisation developed for the KLX09B–F interpretation test are significantly higher than those for HRD_N (a factor of about 12 for the 20 m scale), and the variability is much larger (a factor of 3). It can be noted that although the DFN parameterisation for KLX09 is labelled as having a semi-correlated transmissivity model, in fact the transmissivity model varies significantly with set: The ENE, NW and HZ sets are uncorrelated (the 'b' parameter is set to zero), with the NW set also having a very low value for variability.

The upscaling results for the hydrogeological DFN developed on the basis of the KLX11B–F interference test should be compared to upscaling results for HRD_W. Two sets of results are presented from the KLX11 interference modelling: a semi-correlated transmissivity model and an uncorrelated transmissivity model. The semi-correlated model is included as it is most equivalent with the other parameterisations. The uncorrelated model produced the closest match to the interference test data. For 100 m blocks cases the hydraulic conductivities for the hydrogeological DFNs based on KLX11B–F are with a factor of about 3 of the HRD_W values, while the variability is slightly lower than the equivalent results for HRD_W. The most significant difference is at the 20 m block scale for the uncorrelated model where the hydraulic conductivity is a factor of 8 lower than for HRD_W.

Table 10-29. Summary of upscaled properties for depth zone 0 masl to –150 masl for 20 m and 100 m scales. For HRD_C, HRD_W, HRD_N, HRD_EW007, the open fracture intensity is based on OPO fractures and the semi-correlated transmissivity model. For KLX09 and KLX11 the DFN is parameterised in Table 10-30 and Table 10-31, respectively.

HRD	20 m scale		100 m scale	
	50-percentile Log10 K_{eff} [m/s]	1 s.d Log10 K_{eff} [m/s]	50-percentile Log10 K_{eff} [m/s]	1 s.d Log10 K_{eff} [m/s]
HRD_C	–7.07	0.86	–7.03	0.36
HRD_W	–6.83	0.98	–6.80	0.39
HRD_EW007	–6.99	0.58	–7.18	0.24
HRD_N	–6.30	0.71	–6.18	0.28
KLX09. SC	–5.01	1.20	–5.10	1.34
KLX11. SC	–7.59	0.73	–6.39	0.37
KLX11. UC	–7.69	0.57	–7.08	0.29

Table 10-30. Hydrogeological DFN parameters from the KLX09 interference test modelling. The transmissivity parameters are given for each set and the semi-correlated (SC) model.

Fracture set name	Orientation set pole: (trend, plunge), conc.	Fracture radius model power-law (r_0, k_r)	Intensity P_{32} of open fractures	Transmissivity model T (m^2/s) See Table 10-5
S_A (ENE)	(350, 12) 19	(0.038, 2.59)	0.76	SC: ($1 \cdot 10^{-7}$, 0.0, 1.5)
S_B (NS)	(92, 1) 17	(0.038, 2.62)	0.52	SC: ($1 \cdot 10^{-7}$, 0.0, 0.2)
S_C (NW)	(213, 5) 13	(0.12, 2.60)	0.84	SC: ($4 \cdot 10^{-7}$, 1.5, 0.3)
S_df (HZ)	(250, 77) 15	(0.038, 2.60)	1.88	SC: ($7 \cdot 10^{-8}$, 0.0, 1.5)

Table 10-31. Hydrogeological DFN parameters from the KLX11 interference test modelling. The transmissivity parameters are given for each set and the semi-correlated (SC) and uncorrelated (UC) models.

Fracture set name	Orientation set pole: (trend, plunge), conc.	Fracture radius model power-law (r_0, k_r)	Intensity P_{32} of open fractures	Transmissivity model T (m^2/s) See Table 10-5
NNE	(283, 6.5) 13	(0.038, 2.5)	0.23	SC: ($1.5 \cdot 10^{-8}$, 0.7, 1.0) UC: ($1.5 \cdot 10^{-7}$, 1.1)
ENE	(332, 0.5) 21	(0.038, 2.45)	0.18	SC: ($3.0 \cdot 10^{-9}$, 0.7, 1.0) UC: ($3.0 \cdot 10^{-8}$, 1.1)
WNW	(201, 5) 12	(0.038, 2.3)	0.19	SC: ($4.8 \cdot 10^{-9}$, 0.7, 1.0) UC: ($5.1 \cdot 10^{-8}$, 1.1)
NNW	(246, 10) 12	(0.038, 2.3)	0.05	SC: ($2.3 \cdot 10^{-8}$, 0.7, 1.0) UC: ($3.1 \cdot 10^{-8}$, 1.1)
Sub-H	(334, 87) 10	(0.038, 2.2)	0.35	SC: ($2.0 \cdot 10^{-8}$, 0.7, 1.0) UC: ($2.2 \cdot 10^{-7}$, 1.1)

10.8 Recommendations for implementation of hydrogeological DFN in regional groundwater flow models

10.8.1 Hydrogeological DFN models based on FSM (Laxemar model volume)

Within the Laxemar local model volume, the hydraulic properties of the rock between deformation zones are defined in terms of the 4 hydraulic rock domains shown in Figure 10-30, which in turn relate to the geologically defined fracture domains (FSM) shown in Figure 3-11. Therefore, in order to create a hydrogeological DFN model of the Laxemar local model volume, it is first necessary to assign the appropriate HRD to each grid cell within the simulation domain, and then apply the corresponding hydrogeological DFN properties as given in Table 10-7 (HRD_C), Table 10-12 (HRD_W), Table 10-15 (HRD_EW007), and Table 10-18 (HRD_N).

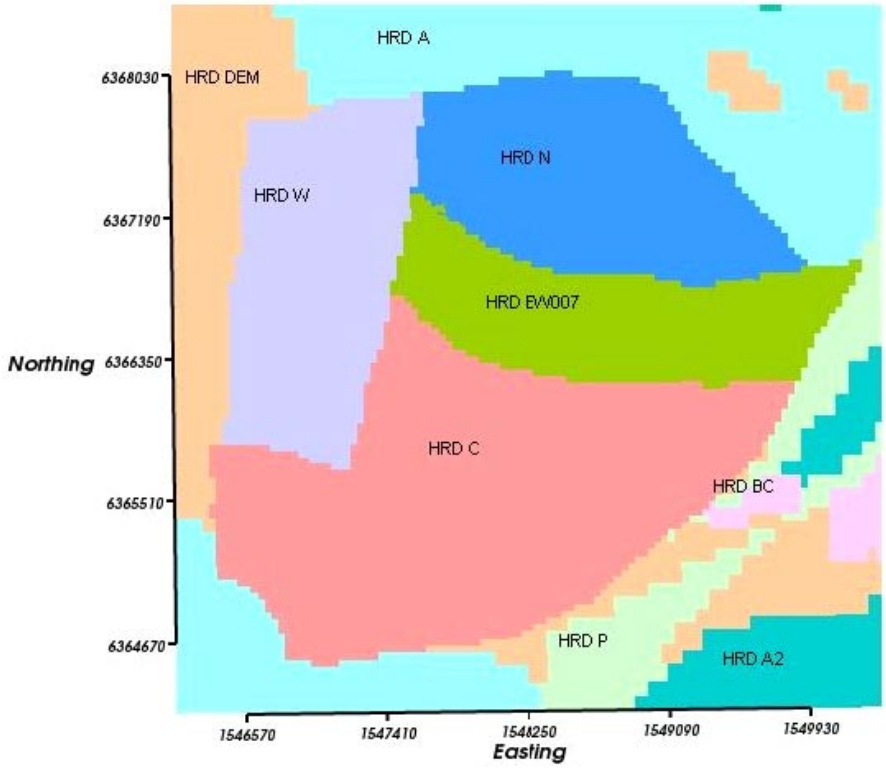

Figure 10-30. Hydraulic rock domain distribution on the top surface of bedrock in vicinity of the local scale hydrogeological model.

10.8.2 Hydrogeological DFN models based on RSM (outside Laxemar local model volume)

The geologically defined fracture domain model is confined to the Laxemar local model volume, while the rock properties outside of this are defined in terms of the rock domains (RSM). The hydrogeological DFN model is derived specifically for the local fracture domains (FSM) rather than the more regionally applicable rock domains (RSM), and hence the extrapolation of the hydrogeological DFN to the regional scale is not straightforward. The approach recommended is to define additional hydraulic rock domains based on the RSM, and then draw analogues between these RSM based HRD and the FSM based HRD for which a hydrogeological DFN model has been parameterised. Six new HRD are defined based on the RSM rock domains (see Figure 10-31):

- HRD_A – corresponds to RSMA01, RSMA02 and RSMBA03 with HRD_A2 excluded (see below).
- HRD_A2 – a sub-domain of RSMA01 and RSMA02 within a rhombus corresponding to the Äspö shear zone.
- HRD_D-E-M – corresponds to RSMD01–07, RSME01–18 and RSMM01.
- HRD_B-C – corresponds to RSMB01–06 and RSMC01–02.
- HRD_F-G – corresponds to RSMF01–03 and RSMG01–02.
- HRD_P – corresponds to RSMP01–02.

Based on the analysis of fracture hydraulic data summarised in Table 9-12 and Table 9-13 for both RSM and FSM it can be concluded that HRD_A (RSMA01) is comparable with HRD_N and HRD_D-E-M (RSMD01 and RSMM01) is comparable with HRD_C. For HRD_A2 it is useful to analyse data from Ävrö boreholes which lie outside the Laxemar model volume considered in Chapter 9. Likewise for HRD_B-C, boreholes from the Simpevarp peninsula can provide guidance.

There is some limited data available outside the Laxemar model volume around Ävrö (KAV01, KAV04A and KAV04B) that can be used to characterise HRD_A2, and on the Simpevarp peninsula (KSH01A and KSH02) that can be used to characterise HRD_BC. A summary of the statistics of PFL-f data for these HRDs is given in Table 10-32 and Table 10-33 that may be compared with the equivalent for the Laxemar model volume given in Table 9-12 and Table 9-13. Based on this comparison, HRD_A2 was assumed analogous to HRD_N in terms of the hydrogeological DFN parameterisation, except the properties below –650 masl were assumed to be the same as those between –650 masl and –400 masl; and HRD_BC was assumed to be analogous to HRD_C.

There is no direct data for HRD_P, but based on its rock type is expected to be analogous to HRD_N, while HRD_F-G is expected to be perhaps 10 times more conductive than HRD_N. In summary, the recommended prescription for assigning hydrogeological DFN properties across the regional scale is described in Table 10-34. The three-dimensional definition of rock domains and fracture domains are available from the geological modelling as files of voxels that describe the spatial extent of each subdomain. The FSM voxels are available on a scale of 20 m resolution, while the RSM are given on

Table 10-32. Summary transmissivity statistics for boreholes outside the Laxemar local model volume of flowing features detected by PFL.

Domain	Depth zone (m)	Sum *T*/ Length (m/s)	Min T (m^2/s)	Max *T* (m^2/s)	Mean log*T*	SD log*T*	Geometric mean (m^2/s)	Length (m)
HRD_A2	50 to –150	1.6E–07	4.2E–10	8.1E–06	–7.5	1.1	3.0E–08	310
(KAV holes)	–150 to –400	1.4E–08	4.2E–10	2.1E–06	–7.9	0.6	1.2E–08	501
	–400 to –650	4.8E–09	2.0E–09	6.9E–07	–7.8	0.4	1.6E–08	362
	–650 to –1,000	2.1E–08	3.7E–09	2.7E–06	–7.3	0.5	5.3E–08	357
HRD_BC	50 to –150	1.9E–08	4.8E–10	6.2E–07	–7.7	1.1	2.1E–08	193
(KSH holes)	–150 to –400	7.2E–09	4.0E–10	1.2E–06	–8.1	0.8	7.4E–09	508
	–400 to –650	4.9E–09	8.6E–10	1.0E–06	–7.8	0.5	1.6E–08	440
	–650 to –1,000	2.3E–09	4.4E–10	5.4E–07	–7.7	0.8	2.1E–08	666

Table 10-33. Summary intensity statistics for boreholes outside the Laxemar local model volume of flowing features detected by PFL.

Domain	Depth zone (m)	Length	Count	PFL $P_{10,corr}$ (m^{-1})	PFL P_{10} (m^{-1})
HRD_A2	50 to –150	310	117	0.807	0.377
(KAV holes)	–150 to –400	501	102	0.583	0.204
	–400 to –650	362	34	0.186	0.094
	–650 to –1,000	357	32	0.138	0.090
HRD_BC	50 to –150	193	28	0.479	0.145
(KSH holes)	–150 to –400	508	44	0.177	0.087
	–400 to –650	440	33	0.133	0.075
	–650 to –1,000	666	17	0.0384	0.026

Table 10-34. Proposed hydraulic property assignment of the regional-scale hydraulic rock domains to be used in SDM regional groundwater flow modelling.

Regional hydraulic rock domain	Suggested hydraulic properties based on hydrogeological DFN
HRD_A	HRD_N
HRD_A2	HRD_N, but rock below –650 masl is the same as –400 masl to –650 masl
HRD_D-E-M	HRD_C
HRD_B-C	HRD_C
HRD_F-G	HRD_N, 10 times higher T
HRD_P	HRD_N

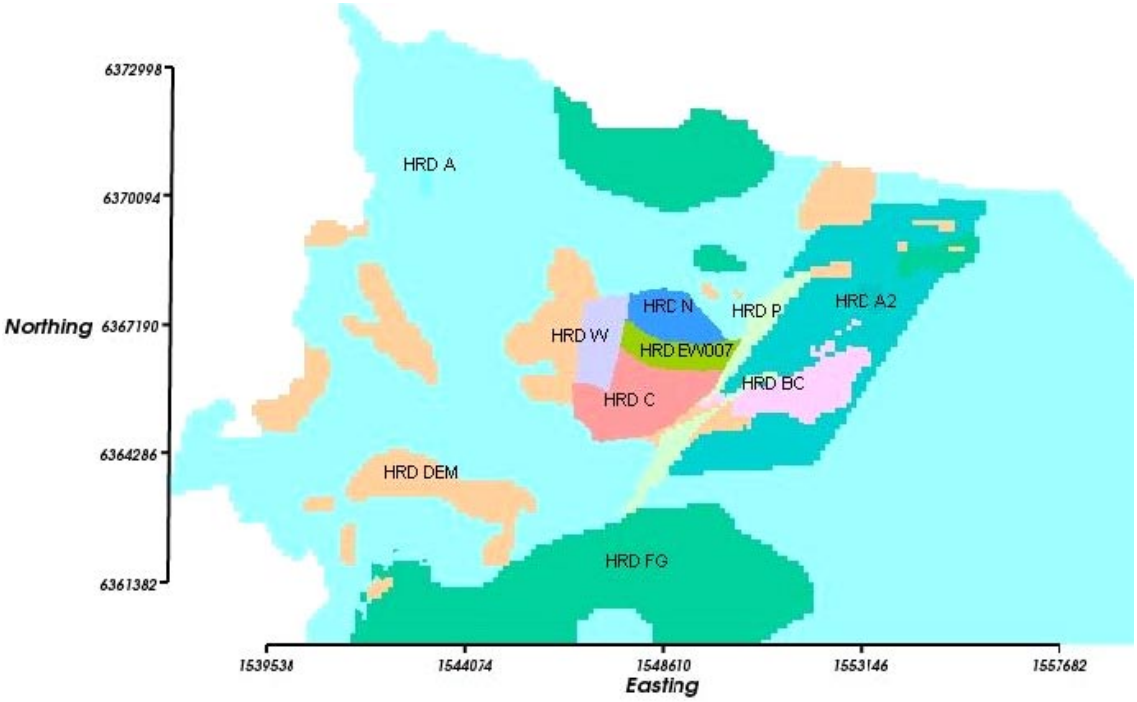

Figure 10-31. Hydraulic rock domain distribution on the top surface of the bedrock in the regional scale hydrogeological model.

a coarser 100 m scale. The distribution of the full set of hydraulic rock domains on the regional scale is shown in Figure 10-31. The apparent increased heterogeneity around the Laxemar subarea simply reflects the abundance of data in this area that has supported a higher resolution of geological and hydrogeological interpretation.

10.9 Analysis of minor deformation zones (MDZ)

In the conceptual model underlying the development of the hydrogeological DFN, each MDZ is considered to be a single feature in the overall distribution of features. MDZs are therefore included in the hydrogeological DFN model as stochastic features. Therefore, within a simulation of the hydrogeological DFN model it is not possible to identify explicitly whether or not a particular feature is a MDZ. However, it is to be expected that the MDZs are probably among the larger features in the size distribution.

The treatment of each MDZ was as follows:

- The features that lie within an MDZ are merged into a single effective hydraulic feature in the statistics that are used to define the hydrogeological DFN model for each HRD, i.e. this single MDZ feature represents the combined effect of their hydrogeological properties.
- Each MDZ is assigned an orientation of the effective planar feature that it represents. All MDZs are assumed to be open for the purposes the calculating P_{10}.
- If an MDZ contains any PFL-f features then it is hydrogeologically significant. It is assigned a transmissivity which is the sum of the transmissivities of the PFL-f features that it contains. It contributes to $P_{10,PFL}$ only as a single feature if it contains 1 or more PFL-f features.
- If an MDZ does not contain any PFL-f features then it will only contribute to P_{10} for open fractures.

Analyses of the properties of the MDZs for HRD_C and HRD_W have been undertaken to quantify the properties and to examine the consistency of the conceptual model. (In Chapter 8 the MDZs in all HRDs were examined, but not in the level of detail as here.)

The first step was to consider whether the MDZs do indeed have hydrogeological significance. The Terzaghi-corrected fracture intensities for different depth zones and fracture sets were calculated for various categories of feature and compared. The categories considered were:

- OPO fractures,
- PFL-f features,
- MDZs, and
- MDZs that (are considered to) have PFL-f features associated with them.

The comparisons for HRD_C and HRD_W are presented in Table 10-35 and Table 10-36 respectively. For HRD_C, the fraction of MDZs that have a PFL-f feature associated with them is about 39%, whereas the fraction of OPO fractures that have a PFL-f feature associated with them is about 7%. For HRD_W, the fraction of MDZs that have a PFL-f feature associated with them is about 69%, whereas the fraction of OPO-CP fractures that have a PFL-f feature associated with them is about 17%. Thus, an MDZ is significantly more likely to have a PFL-f feature associated with it than an OPO fracture (or even an OPO-CP fracture). This strongly supports the view that, overall, MDZs have hydrogeological significance. (For some of the depth zones and fracture sets, the numbers of MDZs and MDZs with associated PFL-f features are very small, so that the statistical significance of this observation is low for these depth zones and sets.)

However, for many depth zones and fracture sets, not all MDZs have a PFL-f feature associated with them. The depth zones and fracture sets in which almost all MDZs do have an associated PFL-f feature are mainly the zones and sets in which there are only a small number of MDZs so the statistical significance of every MDZ having an associated PFL-f feature for these zones and sets may be low.

The next step in the analysis was to consider the implications of the observation that many MDZs do not have an associated PFL-f feature. In the hydrogeological DFN, each feature was taken to have constant transmissivity throughout. Under this interpretation, there are only two reasons why a feature in the hydrogeological DFN does not have a PFL-f feature associated with it:

- Not all MDZs are hydraulically significant (e.g. because their transmssivity is less than the measurement limit for a PFL-f feature, or the zone is too thin to contain a network of connected fractures).
- The feature is not part of the connected network, which, in general, means that the feature is among the smallest features (because the larger features are almost always connected).

For all the calibrated hydrogeological DFN models, the probability that a feature has a transmissivity less than the measurement limit for a PFL-f feature (about 10^{-9} m/s, say) is very low for features larger than say 3 m. Thus, in general, MDZs should be hydrogeologically significant features providing they are connected (assuming they have constant transmissivity throughout).

Further analyses were carried out to consider the sizes of the MDZs. An extreme possibility would be that the MDZs constitute all of the largest features in the distribution of features in the hydrogeological DFN. The range of sizes can be estimated on this basis from the intensities of the different categories of feature given in Table 10-35 and Table 10-36. The results for HRD_C and HRD_W are given in Table 10-37 and Table 10-38, respectively. It should be stressed that the lower ends of the ranges for the sizes of MDZs given in these tables are not necessarily consistent with all the available data, but rather are upper bounds on the lower ends of the ranges, which may, in some cases be shown to be unrealistic by other information. For some of the depth zones and fracture sets, the lower ends of the ranges are on the small side compared to the expected sizes (many tens of metres) of the geological interpreted features corresponding to the MDZs.

If assumed that the MDZs have the minimum radii listed in Table 10-37 and Table 10-38 then from the connectivity analysis described in 10.4.5 it is possible to estimate the proportion of MDZs that would not carry flow because they are not connected to the wider network. This analysis was carried out for HRD_C and the results described in Table 10-39. It confirms that part of the reason for the decrease in proportion of MDZs that have flow measureable by the PFL method is the decrease in intensity with depth that results in diminishing connectivity of water-conducting features. Above –150 masl, the model predicts virtually all MDZs will have flow, as is observed, and then falls to about 20% below –650 masl, as is also the case in the field. Between these depths connectivity only seems to be part of the answer.

Table 10-35. Terzaghi-corrected fracture intensities of features in various categories for HRD_C.

Depth zone (masl)	Set	P10 corrected OPO	P10 corrected PFL	P10 corrected MDZ	P10 corrected MDZ that are PFL	% of OPO that are PFL	% of MDZ that are PFL
0 to –150	ENE	0.52	0.079	0.0040	0.0040	15%	100%
	WNW	0.95	0.196	0.0133	0.0133	21%	100%
	N-S	0.54	0.055	0.0038	0.0038	10%	100%
	SH	1.20	0.233	0.0185	0.0158	19%	85%
–150 to –400	ENE	0.47	0.016	0.0080	0.0024	3%	30%
	WNW	0.55	0.085	0.0022	0.0000	15%	0%
	N-S	0.63	0.027	0.0082	0.0027	4%	33%
	SH	0.71	0.039	0.0182	0.0063	6%	35%
–400 to –650	ENE	0.38	0.017	0.0097	0.0019	5%	20%
	WNW	0.74	0.062	0.0011	0.0000	8%	0%
	N-S	0.47	0.013	0.0074	0.0016	3%	22%
	SH	0.58	0.014	0.0097	0.0030	2%	30%
Below –650	ENE	0.46	0.002	0.0067	0.0000	0%	0%
	WNW	0.73	0.004	0.0014	0.0000	1%	0%
	N-S	0.25	0.000	0.0000	0.0000	0%	
	SH	0.35	0.003	0.0016	0.0007	1%	45%

Table 10-36. Terzaghi-corrected fracture intensities of features in various categories for HRD_W.

Depth zone (masl)	Set	P10 corrected OPO	P10 corrected PFL	P10 corrected MDZ	P10 corrected MDZ that are PFL	% of OPO that are PFL	Fraction of MDZ that are PFL
0 to –150	ENE	0.44	0.054	0.0010	0.0010	12%	1.00
	WNW	0.61	0.121	0.0026	0.0010	20%	0.39
	N-S	0.54	0.091	0.0053	0.0053	17%	1.00
	SH	1.03	0.251	0.0253	0.0198	24%	0.78
–150 to –400	ENE	0.28	0.0388	0.0030	0.0015	17%	0.51
	WNW	0.38	0.066	0.0020	0.0020	17%	1.00
	N-S	0.40	0.060	0.0045	0.0039	15%	0.86
	SH	0.50	0.050	0.0126	0.0087	10%	0.69
–400 to –650	ENE	0.17	0.014	0.0000	0.0071	9%	
	WNW	0.33	0.0384	0.0000	0.0000	13%	
	N-S	0.30	0.0384	0.0059	0.0000	15%	0.00
	SH	0.38	0.0388	0.0207	0.0072	13%	0.35
Below –650	ENE	0.12	0.000	0.0000	0.0000	0%	
	WNW	0.09	0.000	0.0000	0.0000	0%	
	N-S	0.14	0.005	0.0195	0.0054	4%	0.28
	SH	0.65	0.000	0.0000	0.0000	0%	

Table 10-37. Size ranges (ranges of effective radii) inferred for the MDZ on the basis that the largest features correspond to the MDZ for HRD_C.

Depth zone (masl)	Set	Minimum radius (m)	Maximum radius (m)
0 to –150	ENE	73	564
	WNW	81	564
	N-S	37	564
	SH	14	564
–150 to –400	ENE	5	564
	WNW	318	564
	N-S	6	564
	SH	3	564
–400 to –650	ENE	4	564
	WNW	403	564
	N-S	4	564
	SH	4	564
Below –650	ENE	4	564
	WNW	73	564
	N-S	564	564
	SH	11	564

Table 10-38. Size ranges (ranges of effective radii) inferred for the MDZ on the basis that the largest features correspond to the MDZ for HRD_W.

Depth zone (masl)	Set	Minimum radius (m)	Maximum radius (m)
0 to –150	ENE	177	564
	WNW	252	564
	N-S	37	564
	SH	24	564
–150 to –400	ENE	33	564
	WNW	212	564
	N-S	6	564
	SH	7	564
–400 to –650	ENE	564	564
	WNW	564	564
	N-S	33	564
	SH	3	564
Below –650	ENE	564	564
	WNW	564	564
	N-S	0.3	564
	SH	564	564

Table 10-39. Comparison of the proportion of MDZs that carry flow as calculated by a connectivity analysis based on estimated minimum radii and the fraction of MDZs that contain a PFL-f anomaly.

Depth zone (masl)	Proportion of MDZs that carry flow	
	Connectivity analysis	PFL-f data
0 to –150	1.00	0.96
–150 to –400	0.60	0.25
–400 to –650	0.51	0.18
–650 to –1000	0.18	0.15

These findings suggest that not all MDZs are hydraulically significant simply due to the sparsity of fracturing at depth. Other analyses were made to establish whether the geologically identified MDZs would be expected to be hydraulically significant based on various measures of fracture intensity within the zones. This was to consider:

- Is the intensity of open fractures within the MDZ higher than the background rock?
- Is the intensity of PFL-f features within the MDZ higher than the background rock?
- Is the ratio of PFL-f features to OPO fractures within the MDZ higher than the background rock?
- Are the MDZs sufficiently wider to always contain a PFL-f feature?

The first of these questions is addressed by Table 10-40 which confirms that the intensity of open fractures is around 4 times higher in borehole sections within MDZs than in the background rock as a hole. Table 10-41 demonstrates that the intensity of PFLs is also about 4 times higher in MDZs than in the background rock overall. Hence, the MDZs taken all together are more hydraulically significant than the background rock. The next question is whether there is something special hydraulically about the fractures with MDZ? In fact, Table 10-42 shows that the probability an open fracture within the MDZs is a PFL is very similar to that in the background rock. It is also true that the distribution of transmissivities of PFLs within the MDZs is similar to that of the background, and hence there does not seem to be anything special hydraulically about the fractures within the MDZs.

The reason the intensity of PFL fractures within the MDZs is higher than in the background rock is simply because the intensity of open fractures is higher, i.e. they are essentially just a more concentrated version of the background rock. It stands to reason then that thicker MDZs are likely to contain more PFLs, and hence higher transmissivity than thin ones. The distribution of the thickness of MDZs (as measured in boreholes) spans a large range from a few decimetres to 32 m as is shown in Figure 10-32. Since large numbers of MDZs are thinner than 1 m, and the intensity of PFL fractures is about 0.5 m^{-1} overall (see Table 10-41), then such MDZs are unlikely to contain a PFL. In fact, if one divides MDZs according to whether their thickness in less or greater than 1.25 m, then there are 110 MDZs thinner than 1.25 m which contain only 44 PFLs in total, while the 111 MDZs wider than 1.25 m contain 273 PFLs. This would then suggest that in terms of hydraulics, only the MDZs thicker than than about 1.5–2 m, i.e. about a a half, should have been considered as hydraulically significant features.

In conclusion, the seeming contradiction that MDZs are amongst the largest stochastic features, but only 39% contain a flowing feature detected by PFL can be reconciled simply by noting that many of the thin geologically interpreted MDZ are unlikely to be hydraulically significant especially when considering the reduction in fracture connectivity with depth.

Table 10-40. Comparison of fracture intensity P10 for open fractures within the background rock and within MDZs for each HRD and depth zone.

Depth zone (masl)	HRD_C	HRD_EW007	HRD_N	HRD_W	total
	P10 OPO fractures in background rock				
0 to –150	2.192	2.316	1.945	1.603	1.896
–150 to –400	1.286	1.634	1.715	0.904	1.353
–400 to –650	1.224	1.823	0.739	0.726	1.213
–650 to –1,000	0.800	1.280	0.896	0.718	0.843
total	1.260	1.748	1.542	1.133	1.365
	P10 OPO fractures in MDZ				
0 to –150	6.639	6.752	6.898	4.682	5.984
–150 to –400	5.176	6.145	5.276	5.232	5.383
–400 to –650	4.085	5.447	4.449	4.179	4.365
–650 to –1,000	7.205	4.316	N/A	5.643	4.885
total	4.916	5.728	5.955	4.754	5.223

Table 10-41. Comparison of fracture intensity P10 for PFL fractures within the background rock and within MDZs for each HRD and depth zone.

Depth zone (masl)	HRD_C	HRD_EW007	HRD_N	HRD_W	total
	P10 PFL fractures in background rock				
0 to –150	0.309	0.397	0.341	0.290	0.318
–150 to –400	0.080	0.233	0.176	0.029	0.122
–400 to –650	0.039	0.079	0.0385	0.031	0.0388
–650 to –1,000	0.006	0.000	0.051	0.000	0.008
total	0.079	0.175	0.209	0.133	0.131
	P10 PFL fractures in MDZ				
0 to –150	0.601	0.497	1.038	0.763	0.761
–150 to –400	0.497	0.758	0.637	0.450	0.560
–400 to –650	0.185	0.504	0.106	0.280	0.249
–650 to –1,000	0.288	0.077	N/A	0.226	0.131
total	0.344	0.462	0.747	0.543	0.499

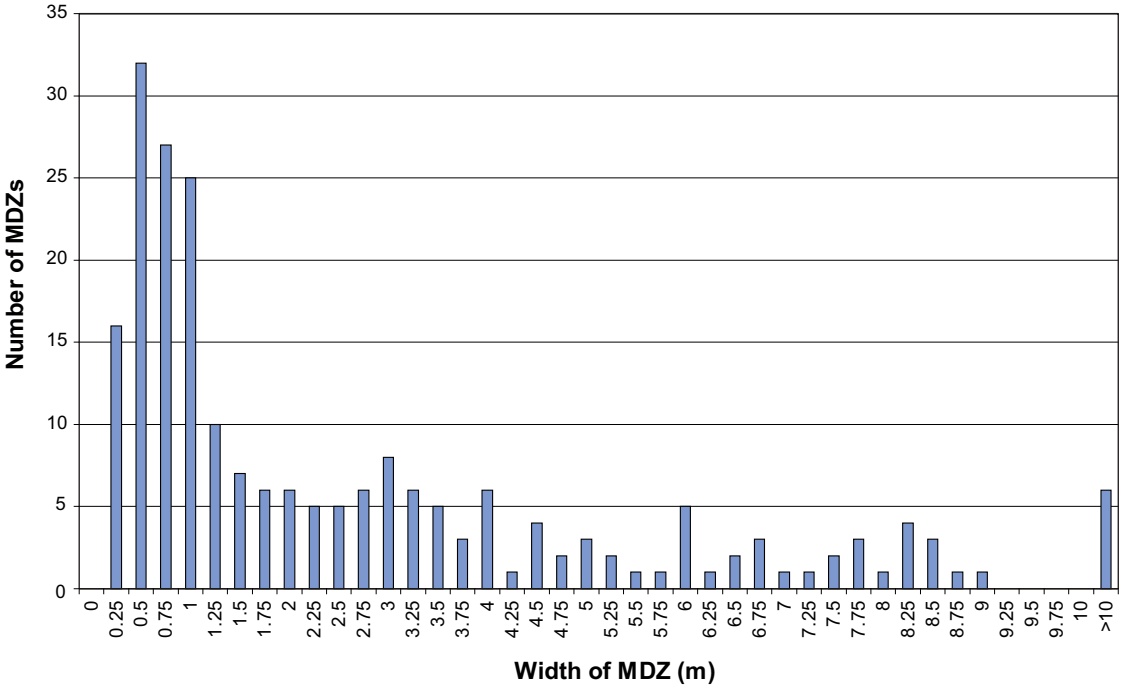

Figure 10-32. *Distribution of the thickness of MDZs.*

Table 10-42. Comparison of the ratio of PFL:OPO fractures within the background rock and within MDZs for each HRD and depth zone.

Depth zone (masl)	HRD_C	HRD_EW007	HRD_N	HRD_W	total
	P10 PFL fractures in background rock				
0 to –150	0.141	0.171	0.175	0.181	0.168
–150 to –400	0.063	0.142	0.102	0.032	0.090
–400 to –650	0.032	0.0383	0.061	0.0383	0.039
–650 to –1,000	0.007	0.000	0.057	0.000	0.010
total	0.063	0.100	0.135	0.117	0.096
	P10 PFL fractures in MDZ				
0 to –150	0.091	0.074	0.151	0.163	0.127
–150 to –400	0.096	0.123	0.121	0.086	0.104
–400 to –650	0.0385	0.092	0.024	0.067	0.057
–650 to –1,000	0.0380	0.018	N/A	0.0380	0.027
total	0.070	0.081	0.125	0.114	0.096

10.10 Comparison of hydrogeological and geological DFN models

The fractures represented by the hydrogeological DFN model represent a sub-set of all fractures – those that are potential water-conducting fractures. The geological DFN represents all fractures, and hence the hydrogeological DFN should be a sub-set of the geological DFN on all scales. Models of the distribution of fracture intensity as a function of fracture size have been derived for the hydrogeological DFN and geological DFN independently, though both assume a power-law size model. To demonstrate that the hydrogeological DFN is a sub-set of the geological DFN on all scales, the distributions of fracture intensity for all fractures (as predicted by the geological DFN), for open fractures (as predicted by the hydrogeological DFN model), and for connected open fractures (as simulated in the connectivity analysis of Section 10.4.4 using the hydrogeological DFN) are compared. This consistency is demonstrated here by comparing the geological DFN Base Model derived from Unlinked traces (BMU) /La Pointe et al. 2008/ for FSM_C with the hydrogeological DFN model derived for HRD_C.

The geological DFN parameter definition is given in Table 10-43. It does not vary with depth, unlike the hydrogeological DFN. This is reasonable since the geological DFN parameterises the size distribution of *all* fractures and their intensity does not have an apparent depth trend (as concluded in /La Pointe et al. 2008/ and verified in Section 9.3.2). This is in contrast to the situation described in section 9.3.4 where there are clear depth trends in the intensities of PFL-f features, and some variation in OPO and OPO-CP fracture intensity. These trends lead to the interpreted depth variation in fracture size distribution parameters in the hydrogeological DFN.

In Figure 10-33 the distribution of total fracture intensity as a function of size is plotted for the geological DFN and hydrogeological DFN from each depth zone. The distribution of intensity for connected open fractures is also shown based on simulating the hydrogeological DFN and identifying the connected fracture network. Ten realisations were considered, and so there is some noise in the calculated distribution. As can be seen, the connected open fractures are a sub-set of the open fractures, which in turn are (generally) a sub-set of all fractures.

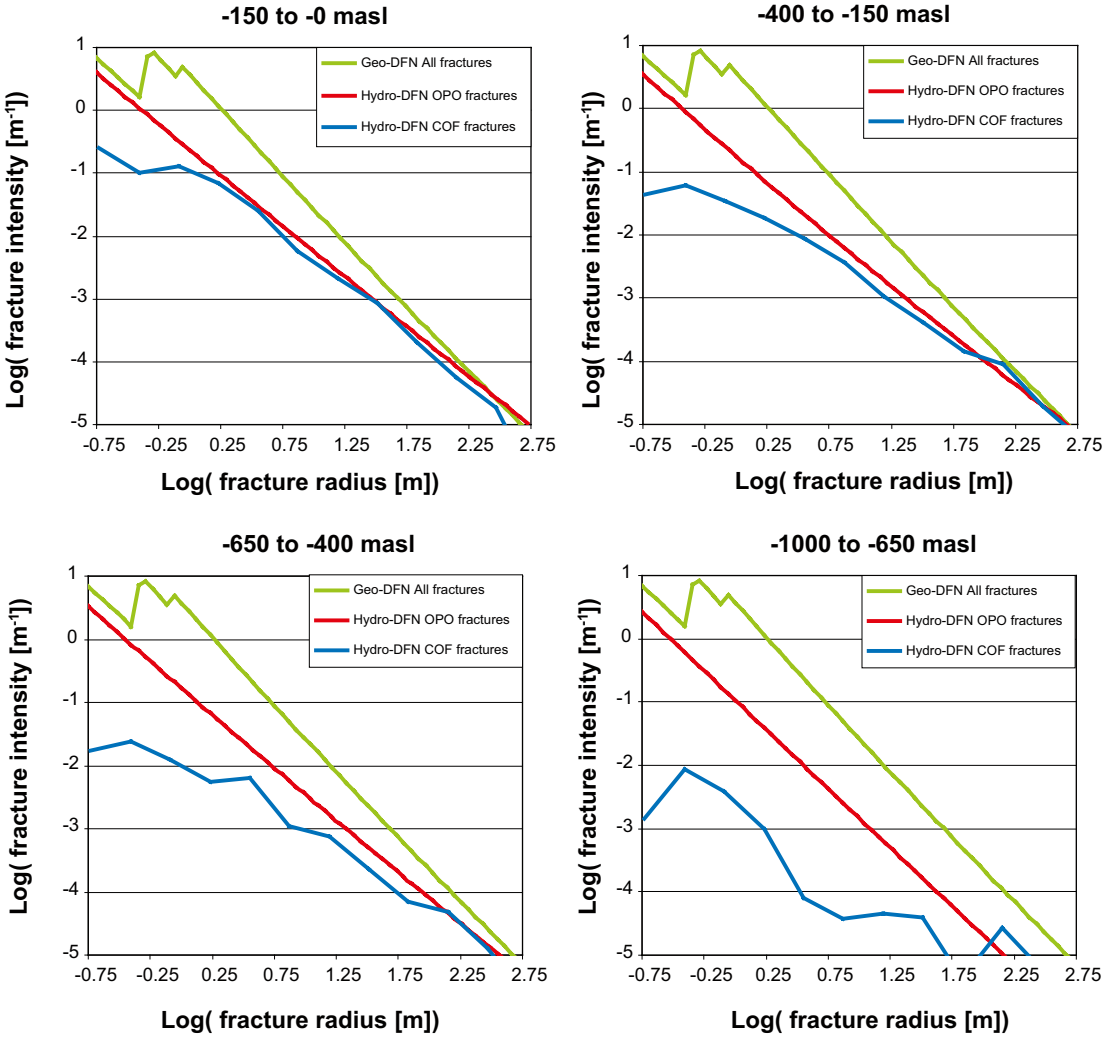

Figure 10-33. *Comparison of the distributions of fracture intensity, P_{32}, versus fracture size for all fractures (as predicted by the geological DFN in green), for open fractures (as predicted by the hydrogeological DFN, OPO case, shown in red), and for simulated open connected fractures using the hydrogeological DFN connectivity analysis (shown in blue). Note that the jagged part of the geological DFN size distribution reflects the use of different r_0 parameters for each set.*

Table 10-43. Definition of geological DFN base model (BMU) for all fractures in FSM_C and all depths derived by /La Pointe et al. 2008/.

Set	Distribution	Fracture intensity P_{32} (m^2/m^3)	k_r	r_0
ENE	Truncated power law	1.72	**3.00**	**0.37**
NS	Truncated power law	2.33	**3.26**	**0.59**
SH	Truncated power law	2.66	**3.31**	**0.33**
WNW	Truncated power law	2.53	**2.80**	**0.08**

In the depth zones 0 to –650 masl the three curves tend to converge, approaching each other around 100 m radius, suggesting a majority of large fractures of this scale are both open and connected. For the depth zone –650 to –1,000 masl the curves for the geological DFN and hydrogeological DFN converge less, suggesting that even large fractures may not conduct flow, which is probably due to the sparisty of fracturing and lower transmissivities at such depths.

A minor exception to the claim that the hydrogeological DFN is a subset of the geological DFN occurs in depth zone 0 to –150 masl for fractures larger than approximately 308 m. The P_{32} for fractures with radii in the range 308 m to 564 m is $8.2 \cdot 10^{-6}$ (m^2/m^3) for the geological DFN compared to $1.3 \cdot 10^{-5}$ (m^2/m^3) for the hydrogeological DFN. This discrepancy, amounting to approximately 60%, is within the known uncertainties in the geological DFN, as quantified in Section 6.2 of /La Pointe et al. 2008/. Of course the hydrogeological DFN parameters are also subject to uncertainties. Examples include the uncertainty in $P_{10,corr}$ for OPO fractures (see Figure 9-42), and particularly the uncertainty in the calibration target; $P_{10,cor}$ for PFL-f features (see Figure 9-43). The calibration process itself has errors that are introduced in order to make the methodology computationally tractable; these are quantified in Appendix 8. In conclusion, this discrepancy is not large enough to undermine the consistency between the geological DFN and hydrogeological DFN models.

For the purposes of testing the robustness of this consistency, the 3 alternative fracture size models for hydrogeological DFN suggested in Table 10-3 and Table 10-4 are also compared with the geological DFN in Figure 10-34. These suggest both variants based on OPO fractures are consistent at all depths, but the variant based on OPO-CP fractures requires far more larger fractures ($r >$ c. 100 m) to achieve sufficient connectivity, than suggested by the geological DFN. Such conceptual inconsistency possibly reduces the plausibility of the case based on OPO-CP fractures as being representative of the fracturing in Laxemar.

The stereonets suggest consistent set specifications between the hydrogeological DFN and geological DFN, cf. Figure 10-35, despite the following differences in how they were calculated: The hydrogeological DFN set definitions are based on PFL-f statistics whereas the geological DFN set definitions are based on statistics for all fractures (including outcrop and borehole data), the fracture set assignments for the data were made differently – the hydrological DFN uses hard set definitions and the geological DFN uses soft set definitions i.e. continuous probability functions for assigning fractures to clusters depending on orientation.

10.11 Summary

DFN flow models of the open fractures (which were taken to correspond to the interpreted OPO fractures or OPO-CP fractures) were set up on the basis of the fracture intensities for the different fracture sets and using power-law distributions for fracture size and calibrated on the measured PFL-f data to obtain hydrogeological DFN model parameterisations for HRD_C, HRD_W, HRD_EW007 and HRD_N.

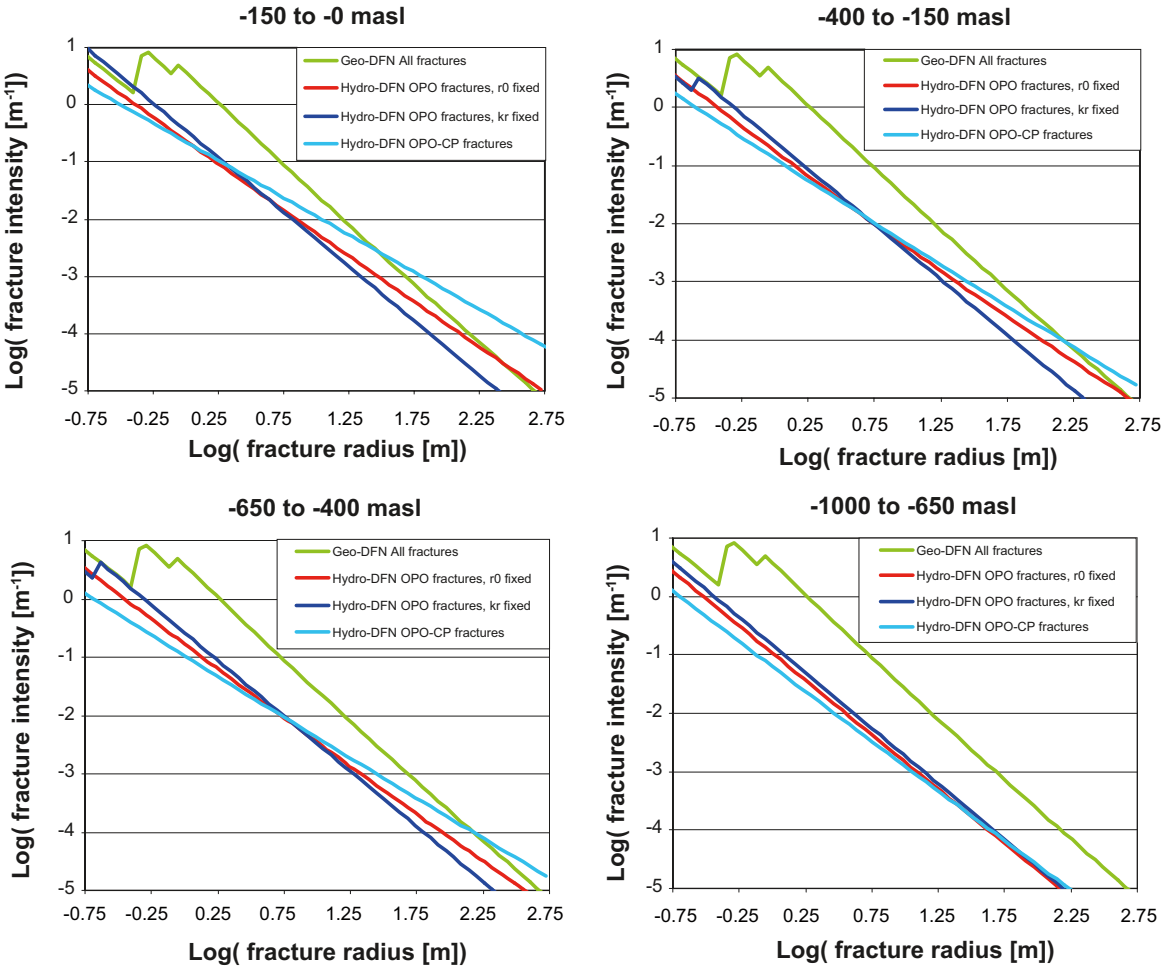

Figure 10-34. *Comparison of the distributions of fracture intensity, P_{32}, versus fracture size for all fractures (as predicted by the geological DFN in green), for open fractures as predicted by the 3 alternative size model derived for the hydrogeological DFN. The OPO case and r_0 fixed is shown in red, the OPO case and k_r fixed is shown in dark blue, and the OPO-CP is shown in light blue. Note that the jagged part of the geological DFN size distribution reflects the use of different r_0 parameters for each set.*

A preliminary calibration of the parameters of the power-law size distribution was carried out to give a match to the overall fracture intensity for PFL-f features (which were taken to correspond to the connected open fractures). The match is not unique: an acceptable match could be obtained for a particular value of the minimum radius in the power-law distribution or for a particular value of the exponent, and presumably for intermediate combinations. The OPO case generally required exponents in the range 2.5 to 2.9, while the OPO-CP case required exponents in the range 2.2 to 2.7. In consequence the OPO-CP case contains a higher number of large fractures on the order of >100 m.

Models for the relationship of the fracture transmissivity to fracture size were then calibrated. Three different types of relationship were considered: a model in which the transmissivity is not correlated to fracture size, a model in which it is partly correlated, and a model in which it is fully correlated. The models were calibrated to match the distributions of transmissivity for the PFL-f features and the distributions of transmissivity from the PSS measurements.

The calibrations were not unique: not only was it possible to calibrate models with the three different types of relationship between transmissivity and fractures size, but it was possible to obtain acceptable matches for more than one parameter set for each type of relationship, and also using statistics based on either OPO or OPO-CP fractures. Both models appear viable given the data available, and it may be speculated that direct evidence to select one above the other may only be revealed when data of a different type is available, for example tunnel wall fracture mapping. However, the choice of geometrical model has an effect on the hydraulic conductivity of block volumes and their

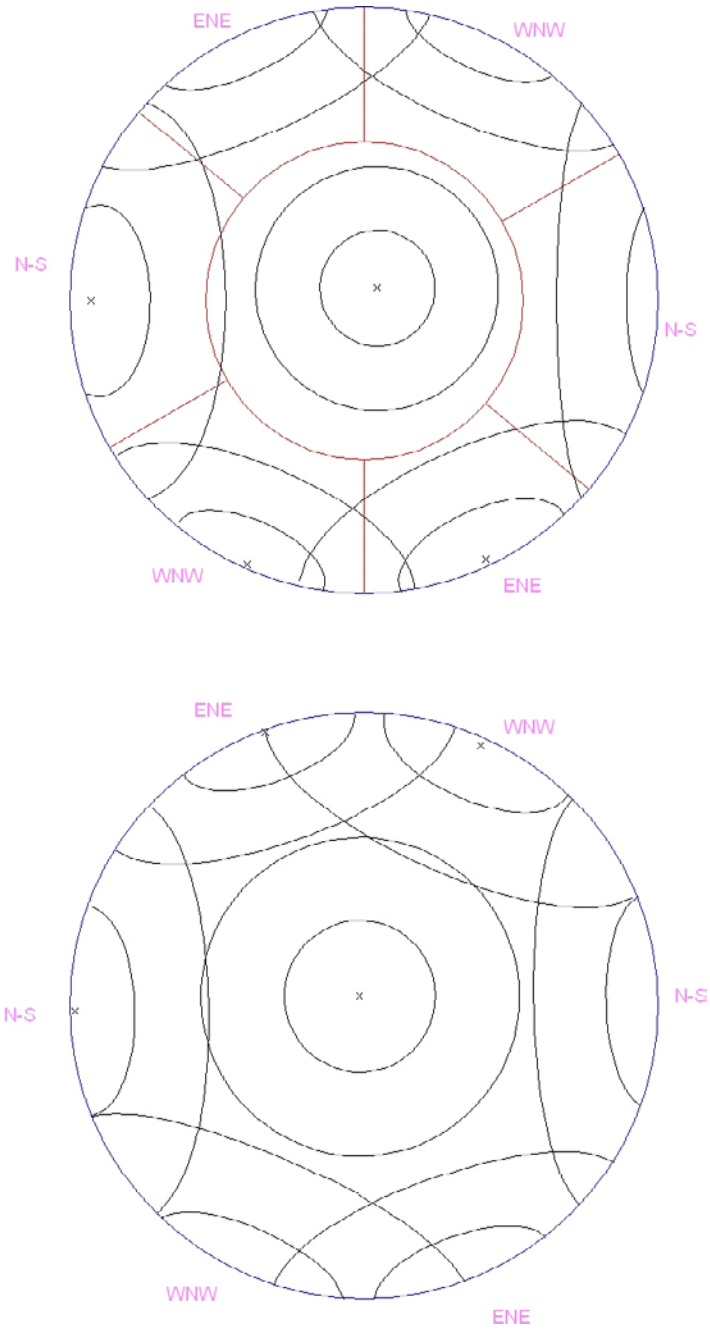

Figure 10-35. *Stereonets comparing the fracture set specifications used in the hydrogeological DFN and geological DFN. For all sets the mean pole is shown as a cross, surrounded by concentration contours containing 63% and 95% of poles. The top stereonet shows the hydrogeological DFN fracture set specification for HRD_C, with the corresponding hard sectors shown in red. The bottom stereonet shows the geological DFN fracture set specification for the base case BMU model (which is the same across all HRDs). The steroenets both use an equal-area, lower-hemisphere projection.*

dependence on the block size. The OPO model generally gives greater heterogeneity in hydraulic conductivity than the OPO-CP model. This a consequence of the OPO-CP model requiring a lower value of k_r, leading to flow taking place in a network of lower intensity, but having more long fractures compared to OPO, and hence most block volumes on the scale of 100 m tend to contain one or more cross-cutting fractures in the OPO-CP case, which is not the case for OPO. The observed dependence of hydraulic conductivity on interval scale given by the PSS 5 m, 20 m and 100 m tests provide some evidence that the lower hydraulic conductivities of the OPO model reflects the site better. Further indirect evidence may come from regional groundwater flow modelling based on these different hydrogeological DFN models.

The upscaled hydraulic conductivity for 100 m block volumes within the candidate area and depth has a geometric mean of about $2 \cdot 10^{-9}$ m/s and a kinematic porosity of about $1 \cdot 10^{-3}$ in HRD_C for the OPO base case with a semi-correlated transmissivity. For the variants, the hydraulic conductivity is similar on the 100 m scale for all variants. For the uncorrelated transmissivity model the mean block hydraulic conductivities showed relatively small variation between the 5 m, 20 m and 100 m scales, whereas hydraulic conductivity generally decreased with scale for all the other transmissivity model, which is consistent with the scale dependence seen in the PSS data This perhaps points to the uncorrelated model being the least consistent with field data. The other variants appear to provide plausible descriptions of the bedrock hydrogeology, and hence it is recommended that the semi-correlated and correlated transmissivity models be considered as well as the OPO and OPO-CP variants be considered in the regional groundwater flow modelling used for confirmatory testing of the conceptual model. If the regional groundwater flow model calibration can guide the hydraulic parameters, then it may eliminate some of the hydrogeological DFN variants, and hence reduce uncertainty.

There are some problems of statistical significance in trying to parameterise some of the hydraulic sub-domains since the numbers of flowing features detected by the PFL method have been divided into very small samples. This is particularly the case below –650 masl, making it necessary to either choose fracture size and transmissivity parameters based on analogues to other rock divisions, or by pooling together all measured flow together below –650 masl. The former approach was used here by using the same transmissivity relationships derived for HRD_C below –650 masl.

11 Summary and conclusions

The current report constitutes one of two reports (Level III) presenting the bedrock hydrogeological description and modelling as part of model version SDM-Site Laxemar. The objective of this first report is to present the parameterisation of the identified deterministic deformation zones (hydraulic conductor domains (HCDs) and the bedrock in between deterministic deformation zones, the so called hydraulic rock domains (HRDs), the parameterisation of the latter being derived from a hydrogeological DFN model. The resulting parameterisation of HRDs is accompanied and preceded by presentation of basic data and various types of explorative and statistical analyses of hydraulic properties and their relationship with various geological model entities, e.g. rock domains, fracture domains and defined depth zones. Similarly, the parameterisation of HCDs is accompanied by analyses of various types of correlations between HCD properties and e.g. the orientation, ductile/ brittle characteristics, thickness and dip of interpreted deterministic deformation zones in Laxemar (and the associated regional model volume).

The bedrock hydraulic properties are assessed by various types of single-hole and multiple hole tests at Laxemar. In total the HRDs are informed by a total of 3,412 PFL-f feature observations, 3,692 PFL-s tests with a test scale of 5 m, and 898/ 775/ 304 PSS evaluated tests sections of test scales 5 m/ 20 m/ 100 m section lengths collected in 46 cored boreholes (NB. not all test types and test scales in all boreholes). The 304 tests of test scale of 100 m also include data from tests in percussion boreholes made with HTHB equipment. Tests in KLX27A are not included as the hydraulic data from the borehole were not available for this evaluation.

The main finding and conclusions of the work performed may be summarised as follows:

Methods for establishing hydraulic properties (Chapter 4)

- Although the two test methods PSS and PFL employ different methodologies for determining hydraulic properties, they provide similar estimates of the transmissivity (and associated hydraulic conductivity) of the bedrock. This gives confidence that no large systematic errors are affecting the results as most data in a cross plot of transmissivities in the range 10^{-9} to 10^{-4} m^2/s show that for the same test sections, T(PSS) is within a factor of 10 of $T(\Sigma T$(PFL-f)) over the corresponding borehole section.
- Over the same bedrock intervals, the PSSs tests (which are short-term tests, transient evaluation method) show more test sections that are conductive (above the measurement limit) compared to the PFL-f (which are performed after long term pumping – only hydraulically and "far-field" connected fractures are involved, stationary evaluation method). Due to the differences in how the test methods operate, the larger proportion of conductive test sections suggested by PSS tests is interpreted as being an indication of potentially compartmentalised portions of the conductive fracture network. However, the PSS method also indicates that these isolated fractures, or clusters of connected fractures, are fairly low-transmissive, transmissivities being in the order of 10^{-8} m^2/s or lower.
- Comparing T(PSS) based on the transient and stationary evaluation methods, respectively, shows that the two methods provide rather similar distributions of transmissivity. However, there is a tendency that the stationary T is slightly higher than the transient T for T below c. 10^{-8} m^2/s but lower above c. 10^{-8} m^2/s.
- Interpreted flow dimensions from transient evaluation of PSS tests are in the order of 2 indicating that radial flow is predominant in the flowing fractures. Still the flow may be channelised but the results indicate that sometimes a network of channels may be involved rather than flow along discrete single channels.
- Laboratory tests show that the matrix hydraulic conductivity is in the range 10^{-16} to 10^{-12} m/s. Laboratory tests of matrix porosity show that the resulting probability distribution is lognormal with geometrical mean values in the range 0.13 to 0.24% for intact core material from the bedrock between deterministically interpreted deformation zones. Notably the matrix porosity of HRD_N is higher but the sample size is small. Intact rock cores sampling the interior of

deterministically interpreted deformation zones have a slightly higher geometric mean porosity; 0.40% than the intact rock. Laboratory tests provide estimates of the effective diffusivity in the range 10^{-14} to 10^{-12} m^2/s.

Hydraulic properties of hydraulic conductor domains (HCD) and local minor deformation zones (MDZ) (Chapters 7 and 8)

- The transmissivities of deterministically interpreted deformation zones and minor deformation zones (determined by summing the transmssisvity of individual features within the zones) tend to decrease with depth, but the statistical distribution parameters (mean log10(*T*) , standard deviation Log10(*T*)) of the individual flowing features within the interpreted zones seem to have more or less the same values irrespective of depth; geometric mean values of c. $2 \cdot 10^{-8}$ to $1 \cdot 10^{-7}$ m^2/s with a standard deviation (Log10(*T*-PFL-f)) between c. 0.5 to 1.
- The total transmissivity of the deterministically interpreted deformation zones tends to increase with zone size. It is suggested that the reason for this is that larger deformation zones generally are thicker and consequently encompass more conductive fractures, and hence show higher total transmissivity.
- To some extent the total transmissivity within the deterministically interpreted deformation zones is also dependent on the orientation of the zones. For zone orientation (strike) groupings; E-W, NW-SE, N-S, NE-SW, as defined by Geology, the E-W group are slightly more conductive (less than an order of magnitude) than the others, based on data from the regional model volume. Using data from the local model volume, the same relation holds for zones larger than 2 km, but it is mainly data from two large deformation zones that affects the statistics, namely zones ZSMEW005 (Äspö shear zone) and ZSMEW002 (Mederhult zone).
- Generally, there are only a few hydraulic tests in individual deterministic deformation zones and only one test in minor deformation zones that quantify the total transmissivity of a given zone within the regional model volume. It is therefore difficult to assess the heterogeneity within a given deformation zone. However, the statistical distribution of the number of flowing fractures (or intensity) and their transmissivity distribution, over the thickness of a deformation zone can be considered as a (local) measure of heterogeneity. The geometric mean P_{10}-corrected (Terzaghi corrected, for approximate estimate of P_{32}) intensity within the deterministically defined deformation zones and minor deformation zones are found to decrease with depth:
  - Deterministically defined deformation zones: c. 0.9 m^{-1} (with a standard deviation of c. 0.6.) near surface and c. 0.4 m^{-1} (with a standard deviation of c. 0.2) within depth zone –400 to –650 m. (Mean zone thickness at borehole intercept: c. 20–40 m).
  - Minor deformation zones: c. 2.1 m^{-1} (with a standard deviation of c. 3.1) near surface and c. 2.4. 1 m^{-1} (with a standard deviation of c. 2.6) within depth zone –400 to –650 m. (Mean zone thickness at borehole intercept: c. 2–3 m).
- There are some cases where several hydraulic tests have been performed in the same deformation zone and at different locations, from which a rough estimate of the variability within the deformation zone can be obtained. The standard deviation (log10(*T*)) for tests made within a specific deterministic deformation zone ranges from 0.4 to 3 with a mean of c.1, based on 24 deformation zones with 2 to 19 (mean 4) observations within the specific deterministic deformation zone. This can be compared with the standard deviation of (log10(*T*)) for all deterministic deformation zones, separated based on elevation depth zones used for the hydrogeological DFN model, which is c. 1.4 for all depth zones (all values based on regional model data).
- Nearly all deterministically defined deformation zones include flowing features with transmissivities greater than the measurement limit for PFL-f; $1 \cdot 10^{-9}$ m^2/s, whereas only c. 60% of the geologically defined minor deformation zones (MDZs) encompass flowing features with transmissivities greater than the measurement limit. This observation suggests that there may be significant heterogeneity within geologically identified MDZs, and this should be further explored as part of the subsequent model testing employing flow modelling.
- MDZs that are judged to be brittle or ductile/brittle can generally be expected to have a conductive feature with a transmissivity (T) > $1 \cdot 10^{-9}$ m^2/s whereas a MDZ judged to be mostly ductile can generally be expected to show no conductive feature with a transmissivity (T) >$1 \cdot 10^{-9}$ m^2/s.

All deterministically defined deformation zone have been judged to be either brittle or ductile/ brittle.

Properties of the bedrock between hydraulic conductor domains (HRD) – based on PFL-s and PSS data (test sections 5, 20 or 100 m) (Chapter 9)

- The depth dependency of the hydraulic conductivity between the deterministically defined deformation zones is similar as for the hydraulic conductivity of the deterministically defined deformation zones. Using the tests made at test scale 100 m, it is noted that the hydraulic conductivity within a deterministically defined deformation zone is c. 10 times larger compared with the rock between the deterministically defined deformation zones.
- The PSS tests on scales 5, 20 and 100 m show a clear scale effect in estimated statistical parameters; mean Log10(K) and standard deviation (Log10(K)). The geometric mean increases c. 100 times going from test scale 5 m to 100 m if the entire sample, including HCDs and HRDs, or only HRDs are considered. A similar behaviour is seen in data representing HCDs but the geometric mean increases c. 10 times going from test scale 5 m to 100 m. This type of behaviour was also noticed by /Rhén et al. 1997/ but the increase was less than that reported here. The reason for the scale dependence seen in the geometric mean is probably that it is more likely that a large high transmissivity feature intersects a large block than a small block.
- The identified rock types (underlying rock domains and fracture domains) exhibit different hydraulic properties.
  - The least-conductive rock types are dolerite (501027) (no data above the measurement limit even though data are from deformations zones, i.e. HCD data) and diorite to gabbro (501033) followed by fine-grained dioritoid (metavolcanite, volcanite) (501030) and quartz monzonite (quartz monzonite to monzodiorite, equigranular to weakly porphyritic) (501036).
  - The most conductive rock type is generally fine-grained granite (granite, fine- to medium-grained) (511058) but in one depth zone fine-grained diorite-gabbro (mafic rock, fine-grained) (505102) shows a similar high geometric mean hydraulic conductivity (K).
  - Ävrö granite (granite to quartz monzodiorite, generally porphyritic) (501044) generally shows a geometric mean hydraulic conductivity that is 3–8 times lower than fine-grained granite (greater difference observed below –650 m).
  - Veins of fine-grained granite (granite, fine- to medium-grained) (511058) do not seem to entail an increase in the hydraulic conductivity. It takes larger bodies of fine-grained granite to increase the hydraulic conductivity, comparable to what is mapped as “rock type” in SICADA.
- Borehole sections mapped as crush generally have a hydraulic conductivity above the measurement limit. Some 50% of all mapped crush zones have one or several PFL-f features associated with crush zones (deterministic deformation zones included).

Properties of the rock between hydraulic conductor domains (HRD) – Analysis of fracture data combined with the PFL-f hydraulic tests (Chapter 9)

- The fracture domains defined by Geology (FSM_N, FSM_W, FSM_C, FSM_EW007, FSM_NE005, FSM_C and FSM_S) and employed in the geological DFN modelling /La Pointe et al. 2008/ have been adopted in the hydrogeological DFN analysis carried out.
- Revised hard sector fracture set definitions have been developed on the basis of the borehole fracture mapping. The revised sets, which are broadly consistent with the subdivisions used in the geological DFN /La Pointe et al. 2008/, consist of WNW, ENE and N-S striking sub-vertical sets and a sub-horizontal set SH.
- The defined hard sectors are applicable for all the various rock subdivisions considered based on either rock domains or fracture domains. Broadly, the WNW set is the most important for flow, followed by the sub-horizontal set SH.

- The fracture intensities for all fractures characterised in the core mapping, and for the various open fractures (OPO and OPO-CP) show little depth dependence, although for the OPO-CP fractures in fracture domain FSM_W, there appears to be a slight decrease in fracture intensity with depth.
- However, for flowing fractures detected by PFL-f, there is a significant decrease in fracture intensity with depth for all rock subdivisions. The intensity is highest above about –150 masl, is somewhat lower at elevations down to about –650 masl, and is considerably lower at depths below about –650 masl.
- On the basis of the above (and depth trends in the geometric mean transmissivity), it was decided to employ four depth zones (defined in terms of elevation for the hydrogeological DFN modelling work).
  - down to –150 masl,
  - –150 masl to –400 masl,
  - –400 masl to –650 masl,
  - below –650 masl.
- When comparing fracture intensity statistics within the same depth zone between the various rock subdivisions, there are not very large differences. The differences are relatively subtle, such as an increased importance of the N-S set in fracture domain FSM_W, and the higher intensity of WNW fractures in fracture domain FSM_EW007. When comparing the fracture intensities within same depth zone between individual boreholes, there is significant spatial variability, but this does not appear to follow any coherent spatial structure.
- The subdivision of bedrock between deterministic deformation zones according to fracture domains was used as the basis for defining an appropriate subdivision for the hydrogeological DFN modelling. The following four hydraulic rock domains (HRDs) basaed on the underlying fracture domains were introduced:
  - HRD_EW007 (corresponding to FSM_EW007),
  - HRD_N (corresponding to FSM_N),
  - HRD_W (corresponding to FSM_W),
  - HRD_C (corresponding to an amalgam of FSM_C, FSM_NE005 and FSM_S).
- It is recommended that the subset of OPO fractures be used as an estimate of intensity of potentially water-conducting fractures, although the correspondence between geological characterisation of the core and hydraulic testing is sufficiently erratic between boreholes to consider, as a variant, a scenario where all OPO-CP fractures are potentially water-conducting.
- There is some correlation between the occurrence of high transmissivity values associated with the WNW and SH sets for all rock subdivisions, and between some high transmissivities of the N-S set in hydraulic rock domain HRD_W.
- Fracture domain FSM_NE005 appears to be the least permeable of the fracture domains, and FSM_N appears to be the most permeable.
- Fracture domain FSM_NE005 appears to be the least permeable of the fracture domains with an arithmetic mean hydraulic conductivity at repository depth in the order of 10^{-9} m/s. FSM_N appears to be the most permeable with an arithmetic mean hydraulic conductivity in the order of 10^{-8} m/s at repository depth. For the hydraulic rock domains: HRD_C has a low arithmetic mean hydraulic conductivity in the order of 10^{-9} m/s at repository depth, HRD_W is about an order of magnitude higher, although the intensity of PFL-f features is lower in HRD_W.

Hydrogeogical DFN model simulations and parameterisation (Chapter 10)

- Fracture size distributions have been derived for each fracture set, depth zone and hydraulic rock domain based on an assumed power-law model described by a shape parameter k_r and a location parameter r_0. The approach used is to model the connectivity of the network taking the fracture orientation model and the intensity of open fractures as input, and to identify the geometrically connected open fractures as seen in a vertical borehole as output. This distribution is then calibrated against the observed fracture intensity of flowing fractures detected by PFL.

- The approach does not yield an unique size distribution. Hence, two alternative models were derived to scope the effect of possible size distributions. Additional physical constraints on the size distributions are: $r_0 > 0.038$ m (the borehole radius) since open fracture by definition cut the diameter of the core, $k_r > \sim 2.2$ to avoid predicting far more large fractures than have been identified as deformation zones. One size model was derived that used an estimate of open fracture intensity based on OPO fractures with r_0=0.038 m, and the other used an open fracture intensity based on only OPO-CP fractures. An alternative approach attempted was to keep k_r fixed and calibrate values of r_0. For OPO fractures k_r=2.9 was used , and k_r=2.7 for OPO-CP fractures.
- It has been demonstrated that these seemingly distinct geometrical models once calibrated against the intensity of PFL-f features all predict quite similar distributions of fracture sizes for the sub-set of connected open fractures. This implies that the methodology provides a strong constraint on the spatial pattern of connected open fractures, and hence the potential water-conducting network.
- These alternative geometrical models were used as the basis for simulating the distributions of inflows divided by drawdown associated with each flowing feature detected by PFL. Using this hydraulic information, the size distributions were refined and model fracture transmissivity parameterised. Three alternative relationships between fracture transmissivity and size were considered: a completely correlated model, a semi-correlated model, and an uncorrelated model.
- The analysis led to several alternative parameterisations of a hydrogeological DFN model.
- The hydrogeological DFN has also been used to calculate block model directional and effective hydraulic conductivity at support scales of 5, 20 and 100 m for most combinations of HRD and depth zone, as well as a sensitivity analysis for the depth zone –400 to –650 masl to consider the hydraulic conductivities implied by the model variants. The results show a prominent maximum hydraulic conductivity oriented about 80–140 degrees for HRD_C, i.e. WNW. This orientation coincides with the current orientation of maximum horizontal stress. This orientation is distinct on all scales, but especially for the 100 m scale.
- Effective block conductivity on the 100 m scale for HRD_C and HRD_W in the depth zone –650 to –400 masl both have a geometric mean of about $1–2 \cdot 10^{-9}$ m/s for the base case model (OPO, semi-correlated), but a greater heterogeneity in HRD_W. The geometric mean for HRD_EW007 is about $8 \cdot 10^{-9}$ m/s and is less heterogeneous than HRD_C.
- The transmissivity model variants and the case based on OPO-CP fractures all give similar mean hydraulic conductivities on the 100 m scale. The OPO-CP case predicts less heterogeneity, while the uncorrelated transmissivity model predicts little variation with scale. However, since the data suggests a reduction in mean hydraulic conductivity with scale, then perhaps a completely uncorrelated model is not a viable scenario.
- The kinematic porosity is about $1 \cdot 10^{-3}$ for both HRD_C and HRD_W (slightly less for HRD_W) and about $2 \cdot 10^{-3}$ for HRD_EW007. It has a strong dependence on the transmissivity model assumed – it increases (by about a factor of 3) when fracture transmissivity is uncorrelated to size.
- It has been demonstrated that the distribution of open fracture sizes derived in the hydrogeological DFN based on OPO fractures is consistently a sub-set of all the distribution of all fractures implied by the geological DFN (which was derived independently) on all scales and at all depths. Hydrogeological DFN based on OPO-CP fractures require more larger fractures than predicted by the geological DFN, and hence are less plausible from a conceptual viewpoint.
- The HRD_C and HRD_W bulk effective hydraulic conductivity (100 m) at repository depth is almost identical to that developed for the hydraulic rock domain HRD(D, E, M) (Quartz monzodiorite, Diorite/gabbro) employed in model version Laxemar 1.2 based on information from KLX03.
- The very similar effective hydraulic conductivity of HRD_W and HRD_C masks some difference in the hydraulic characteristics, a corresponding comparison of intensity $P10_{corr}$ (PFL-f) for the corresponding depth zones shows a $P10_{corr}$ of 0.06 m^{-1} in HRD_W compared with 0.13 m^{-1} in HRD_C, but a higher transmissivity in HRD_W. In the regional groundwater flow modelling this will show up as a greater number of grid elements that have a fracture intensity below the percolation threshold in HRD_W at depth compared to HRD_C.

- The current HRD block properties (100 m) are consistent with the geometric mean PSS 100 m data for HRD_C and HRD_W.
- Examining HRD_C and HRD_W; the intensity of open fractures is overall about 4 times higher in MDZs than in the background rock. However, the ratio of PFL fractures to open fractures in MDZs is similar to that of the backround rock. Hence, provided the MDZ are sufficiently thick, greater than a few metres, then they are likely to contain at least one PFL-f feature just because of the higher intensity and hence connectivity. However, about half of the geologically interpreted MDZ are around a metre or less which are of insufficient width for the increased intensity to take effect on connectivity.
- The appropriateness of the developed hydrogeological DFN model is tested out in regional scale flow models by calibration employing head data, hydrogeochemistry data and data from multi-hole interference tests /Rhén et al. 2008/.

Hydrogeological model uncertainties

There are some problems of statistical significance in trying to parameterise some of the hydraulic sub-domains since the numbers of flowing features detected by the PFL method have been divided into very small samples. This is particularly the case below –650 masl.

There is significant spatial variability between statistics of hydraulic fracture properties between boreholes as is expected for the rather long distances between the boreholes providing the data. For example, within domain HRD_C and HRD_W between depth zone –400 to –650 m all information for the hydrogeological DFN model originates from 13 boreholes (KLX03, KLX05, KLX11A, KLX15A, KLX19A, KLX21B boreholes spanned the entire HRD/depth zone, while KLX02, KLX07A, KLX08,.KLX10, KLX12A, KLX17A, KLX18A partially spanned the HRD/depth zone) covering c. 6 km^2 borehole length. In the absence of any coherent trend for this spatial variability, hydraulic data were collated within a HRD and depth to parameterise the hydrogeological DFN. Hence, the hydrogeological DFN model reproduces the variability of this ensemble of data, but may not predict the variability that may exist within the entire investigation volume.

The comparison made between the model and the validation borehole data from KLX27A, cf. premises in Section 10.5.5 and results in Appendix 10, demonstrates that a number of the observed hydraulic characteristics fall within the predicted variability, but some properties such as the intensity of PFL-f features below –400 m in KLX27A is exceptional. Considering the large spatial variability of PFL-f features occurrence and the use of only one borehole for the comparison, the conditions for a statistically significant comparison cannot be expected. It is therefore not possible to draw stronger conclusions from the comparison, other than that the outcome of KLX27A confirms that HRD_W is characterised by a strong element of heterogeneity and is also probably more difficult to predict than HRD_C.

12 References

Andersson J, Ström A, Almén K-E, Ericsson LO, 2000a. Vilka krav ställer djupförvaret på berget? Geovetenskapliga lämplighetsindikationer och kriterier för lokalisering och platsutvärdering. SKB R-00-15, Svensk Kärnbränslehantering AB.

Andersson P, Ludvigsson J-E, Wass E, Holmqvist M, 2000b. Äspö Hard Rock Laboratory, True Block Scale Project, Tracer test stage. Interference tests, dilutiontests and tracer tests. SKB IPR-00-28, Svensk Kärnbränslehantering AB.

Andersson P, Ludvigsson J-E, Wass E, Holmqvist M, 2001a. Äspö Hard Rock Laboratory, True Block Scale, Detailed characterisation stage, Interference tests and tracer tests PT-1 PT-4. SKB IPR-01-52, Svensk Kärnbränslehantering AB.

Andersson P, Ludvigsson J-E, Wass E, 2001b. Äspö Hard Rock Laboratory, True Block Scale Project, Preliminary characterisation. Combined interference tests and tracer tests. SKB IPR-01-44, Svensk Kärnbränslehantering AB.

Ask H, 2003. Installation of four monitoring wells, SSM000001, SSM000002, SSM000004 and SSM000005 in the Simpevarp subarea. Oskarshamn site investigation. SKB P-03-80, Svensk Kärnbränslehantering AB.

Ask H, Samuelsson L, 2003. Drilling of three flushing water wells, HSH01, HSH02 and HSH03. Oskarshamn site investigation. SKB P-03-114, Svensk Kärnbränslehantering AB.

Ask H, Morosini M, Samuelsson L, Stridsman H, 2003. Drilling of cored borehole KSH01. Oskarshamn site investigation. SKB P-03-113, Svensk Kärnbränslehantering AB.

Ask H, 2004. Drilling and installation of two monitoring wells, SSM 000006 and SSM 000007 in the Simpevarp subarea. Oskarshamn site investigation. SKB P-04-46, Svensk Kärnbränslehantering AB.

Ask H, Samuelsson L, 2004a. Drilling of two flushing water wells, HAV09 and HAV10. Oskarshamn site investigation. SKB P-04-150, Svensk Kärnbränslehantering AB.

Ask H, Samuelsson L, 2004b. Drilling of two percussion boreholes, HLX13 and HLX14. Oskarshamn site investigation. SKB P-04-234, Svensk Kärnbränslehantering AB.

Ask H, Samuelsson L, 2004c. Percussion drilling of borehole HLX20 for investigation of lineament EW002. Oskarshamn site investigation. SKB P-04-236, Svensk Kärnbränslehantering AB.

Ask H, Morosini M, Samuelsson L, Ekström L, 2004a. Drilling of cored borehole KSH02. Oskarshamn site investigation. SKB P-04-151, Svensk Kärnbränslehantering AB.

Ask H, Morosini M, Samuelsson L, Ekström L, Håkansson N, 2004b. Drilling of cored borehole KSH03. Oskarshamn site investigation. SKB P-04-233, Svensk Kärnbränslehantering AB.

Ask H, Samuelsson L, Zetterlund M, 2004c. Percussion drilling of boreholes HLX15, HLX26, HLX27, HLX28, HLX29 and HLX32 for investigation of lineament NW042. Oskarshamn site investigation. SKB P-04-235, Svensk Kärnbränslehantering AB.

Ask H, 2005. Percussion drilling of boreholes HLX36 and HLX37 for investigation of lineament NS001. Oskarshamn site investigation. SKB P-05-275, Svensk Kärnbränslehantering AB.

Ask H, Zetterlund M, 2005. Percussion drilling of boreholes HLX16, HLX17, HLX18 and HLX19. Oskarshamn site investigation. SKB P-05-190, Svensk Kärnbränslehantering AB.

Ask H, Morosini M, Samuelsson L, Ekström L, Håkansson N, 2005a. Drilling of cored borehole KAV04. Oskarshamn site investigation. SKB P-05-25, Svensk Kärnbränslehantering AB.

Ask H, Samuelsson L, Zetterlund M, 2005b. Percussion drilling of boreholes HLX21, HLX22, HLX23, HLX24, HLX25, HLX30, HLX31 and HLX33 for investigation of lineament EW007. Oskarshamn site investigation. SKB P-05-55, Svensk Kärnbränslehantering AB.

Ask H, Morosini M, Samuelsson L, Ekström L, Håkanson N, 2005c. Drilling of cored borehole KLX04. Oskarshamn site investigation. SKB P-05-111, Svensk Kärnbränslehantering AB.

Ask H, Morosini M, Samuelsson L, Ekström L, Håkanson N, 2005d. Drilling of cored borehole KLX03. Oskarshamn site investigation. SKB P-05-167, Svensk Kärnbränslehantering AB.

Ask H, Morosini M, Samuelsson L, Ekström L, Håkanson N, 2005e. Drilling of cored borehole KLX05. Oskarshamn site investigation. SKB P-05-233, Svensk Kärnbränslehantering AB.

Ask H, Morosini M, Samuelsson L, Ekström L, Håkanson N, 2005f. Drilling of cored borehole KLX06. Oskarshamn site investigation. SKB P-05-234, Svensk Kärnbränslehantering AB.

Ask H, 2006a. Core drilling of short boreholes KLX09B, KLX09C, KLX09D, KLX09E and KLX09F for discrete fracture network investigation (DFN). Oskarshamn site investigation. SKB P-06-265, Svensk Kärnbränslehantering AB.

Ask H, 2006b. Core drilling of short boreholes KLX11B, KLX11C, KLX11D, KLX11E and KLX11F for discrete fracture network investigation (DFN). Oskarshamn site investigation. SKB P-06-283, Svensk Kärnbränslehantering AB.

Ask H, 2006c. Percussion drilling of boreholes HLX38, HLX39, HLX40, HLX41, HLX42 and HLX43 for lineament investigation. Oskarshamn site investigation. SKB P-06-291, Svensk Kärnbränslehantering AB.

Ask H, Morosini M, Samuelsson L, Ekström L, Håkanson N, 2006a. Drilling of cored boreholes KLX07A and KLX07B. Oskarshamn site investigation. SKB P-06-14, Svensk Kärnbränslehantering AB.

Ask H, Morosini M, Samuelsson L, Ekström L, Håkanson N, 2006b. Drilling of cored borehole KLX10. Oskarshamn site investigation. SKB P-06-116, Svensk Kärnbränslehantering AB.

Ask H, Morosini M, Samuelsson L, Ekström L, Håkanson N, 2006c. Drilling of cored borehole KLX08. Oskarshamn site investigation. SKB P-06-222, Svensk Kärnbränslehantering AB.

Ask H, Morosini M, Samuelsson L, Ekström L, Håkanson N, 2006d. Drilling of cored borehole KLX12A. Oskarshamn site investigation. SKB P-06-305, Svensk Kärnbränslehantering AB.

Ask H, Morosini M, Samuelsson L, Ekström L, Håkanson N, 2006e. Drilling of cored borehole KLX11A. Oskarshamn site investigation. SKB P-06-306, Svensk Kärnbränslehantering AB.

Ask H, Morosini M, Samuelsson L, Ekström L, Håkanson N, 2007a. Drilling of cored borehole KLX18A. Oskarshamn site investigation. SKB P-07-98, Svensk Kärnbränslehantering AB.

Ask H, Morosini M, Samuelsson L, Ekström L, Håkanson N, 2007b. Drilling of cored borehole KLX20A. Oskarshamn site investigation. SKB P-07-134, Svensk Kärnbränslehantering AB.

Ask H, Morosini M, Samuelsson L, Tiberg L, 2007c. Drilling of cored borehole KLX13A. Oskarshamn site investigation. SKB P-07-195, Svensk Kärnbränslehantering AB.

Ask H, Morosini M, Samuelsson L, Tiberg L, 2007d. Drilling of cored borehole KLX19A. Oskarshamn site investigation. SKB P-07-202, Svensk Kärnbränslehantering AB.

Barker J A, 1988. A generalised radial flow model forhydraulic tests in fractured rock, Water Resour. Res., v. 24, 1796–1804.

Bosson E, 2006. Near-surface hydrogeological model of Laxemar, Open repository – Laxemar 1.2. SKB R-06-66, Svensk Kärnbränslehantering AB.

Caine J S, Evans J P, Forster C B, 1996. Fault zone architecture and permeability structure. Geology 24 (11), 1025–1028.

Crawford J, 2008. Bedrock transport properties Forsmark. Site descriptive modelling. SDM-Site Forsmark. SKB R-08-48, Svensk Kärnbränslehantering AB.

Crawford J, Sidborn M (eds) 2009. Bedrock transport properties Laxemar. Site descriptive modelling. SDM Site Laxemar. SKB R-08-94, Svensk Kärnbränslehantering AB.

Dershowitz W, Winberg A, Hermanson J, Byegård J, Tullborg E-L, Andersson P, Mazurek M, 2003. Äspö Hard Rock Laboratory. Äspö Task Force on modelling of groundwater flow and transport of solutes – Task 6C – A semi-synthetic model of block scale conductive structures at the Äspö HRL. SKB IPR-03-13, Svensk Kärnbränslehantering AB.

Drew D J, Vandergraaf T T, 1989. Construction and operation of a high-pressure radioisotope migration apparatus. Atomic Energy of Canada Limited Technical Record, TR-476.

Earlougher R C, 1977. Advances in Well Test Analysis, Henry L. Doherty Series, 5. SPE, Dallas.

Enachescu C, Böhner J, Rohs S, 2006a. Hydraulic interference tests, pumping borehole KLX07A Subarea Laxemar. Oskarshamn site investigation. SKB P-06-145, Svensk Kärnbränslehantering AB.

Enachescu C, Rohs S, Wolf P, 2006b. Hydraulic injection tests in borehole KLX11A Subarea Laxemar. Oskarshamn site investigation. SKB P-06-201, Svensk Kärnbränslehantering AB.

Enachescu C, Rohs S, van der Wall R, 2006c. Hydraulic injection tests in borehole KLX18A Subarea Laxemar. Oskarshamn site investigation. SKB P-06-225, Svensk Kärnbränslehantering AB.

Enachescu C, Rahm N, 2007. Method evaluation of single hole hydraulic injection tests at site investigations Oskarshamn. Oskarshamn site investigation. SKB P-07-79, Svensk Kärnbränslehantering AB.

Enachescu C, Rohs S, 2007a. Hydraulic injection tests in borehole KLX20A, 2006 Subarea Laxemar. Oskarshamn site investigation. SKB P-07-49, Svensk Kärnbränslehantering AB.

Enachescu C, Rohs S, 2007b. Hydraulic injection tests in borehole KLX13A Subarea Laxemar. Oskarshamn site investigation. SKB P-07-99, Svensk Kärnbränslehantering AB.

Enachescu C, Rohs S, Wolf P, 2007a. Hydraulic injection tests in borehole KLX08, 2006 Subarea Laxemar. Oskarshamn site investigation. SKB P-07-48, Svensk Kärnbränslehantering AB.

Enachescu C, Böhner J, Wolf P, 2007b. Pumping tests and hydraulic injection tests in borehole KLX19A, 2007 Subarea Laxemar. Oskarshamn site investigation. SKB P-07-90, Svensk Kärnbränslehantering AB.

Enachescu C, Böhner J, van der Wall R, 2007c. Hydraulic injection tests in borehole KLX21B Subarea Laxemar. Oskarshamn site investigation. SKB P-07-94, Svensk Kärnbränslehantering AB.

Enachescu C, Rohs S, Wolf P, 2007d. Hydraulic injection tests in borehole KLX16A, 2007 Subarea Laxemar. Oskarshamn site investigation. SKB P-07-120, Svensk Kärnbränslehantering AB.

Enaschescu C, Rohs S, van der Wall R, Wolf P, 2007e. Hydraulic injection tests in borehole KLX15A, 2007 Subarea Laxemar. Oskarshamn site investigation. SKB P-07-192, Svensk Kärnbränslehantering AB.

Enachescu C, van der Wall R, Wolf P, 2007f. Hydraulic Injection Tests in Borehole KLX17A, 2007 Subarea Laxemar. Oskarshamn site investigation. SKB P-07-193, Svensk Kärnbränslehantering AB.

Enachescu C, Roh S, Wolf P, 2007g. Hydraulic interference tests, pumping borehole KLX20A Subarea Laxemar. Oskarshamn site investigation. SKB P-07-39, Svensk Kärnbränslehantering AB.

Enachescu C, Wolf P, Rohs S, van der Wall R, 2007h. Hydraulic interference tests, pumping borehole KLX08 Subarea Laxemar. Oskarshamn site investigation. SKB P-07-18, Svensk Kärnbränslehantering AB.

Enachescu C, Rohs S, van der Wall R, 2008a. Evaluation of hydraulic interference tests, pumping borehole KLX19A Subarea Laxemar. Oskarshamn site investigation. SKB P-08-15, Svensk Kärnbränslehantering AB.

Enachescu C, Rohs S, van der Wall R, Wolf P, Morosini M, 2008b. Evaluation of hydraulic interference tests, pumping borehole KLX27A Subarea Laxemar. Oskarshamn site investigation. SKB P-08-16, Svensk Kärnbränslehantering AB.

Enachescu C, Wolf P, Rohs S, van der Wall R, 2008c. Hydraulic injection tests in borehole KLX27A, 2008 Subarea Laxemar. Oskarshamn site investigation. SKB P-08-27, Svensk Kärnbränslehantering AB.

Enachescu C, Lenné S, Rohs S, van der Wall R, 2008d. Transient evaluation of PFL pumping tests. Subarea Laxemar and Simpevarp. Oskarshamn site investigation, SKB P-08-57, Svensk Kärnbränslehantering AB.

Follin S, Stigsson M, Svensson U, 2005. Variable-density groundwater flow simulations and particle tracking – Numerical modelling using DarcyTools. Preliminary site description Simpevarp subarea – version 1.2. SKB R-05-11, Svensk Kärnbränslehantering AB.

Follin S, Stigsson M, Svensson U, 2006. Hydrogeological DFN modelling using structural and hydraulic data from KLX04, Preliminary site description, Laxemar subarea – version 1.2. SKB R-06-24, Svensk Kärnbränslehantering AB.

Follin S, Johansson P-O, Levén J, Hartley L, Holton D, McCarthy R, Roberts D, 2007a. Updated strategy and test of new concepts for groundwater flow modelling in Forsmark in preparation of site descriptive modelling stage 2.2. SKB R-07-20, Svensk Kärnbränslehantering AB.

Follin S, Levén J, Hartley L, Jackson P, Joyce S, Roberts D, Swift B, 2007b. Hydrogeological characterisation and modelling of deformation zones and fracture domains, Forsmark modelling stage 2.2. SKB R-07-48, Svensk Kärnbränslehantering AB.

Follin S, Johansson P-O, Hartley L, Jackson P, Roberts D, Marsic N, 2007c. Hydrogeological conceptual model development and numerical modelling using CONNECTFLOW. Forsmark modelling stage 2.2. SKB R-07-49, Svensk Kärnbränslehantering AB.

Forsmark T, Wikström M, Forssman I, Rhén I, 2007. Oskarshamn site investigation. Correlation of Posiva Flow Log anomalies to core mapped features in KLX17A, KLX18A, KLX19A, KLX20A, KLX21B. SKB P-07-215, Svensk Kärnbränslehantering AB.

Forssman I, Zetterlund M, Forsmark T, Rhén I, 2005a. Oskarshamn site investigation. Correlation of Posiva Flow Log anomalies to core mapped features in KSH01A, KSH02A and KAV01. SKB P-05-65, Svensk Kärnbränslehantering AB.

Forssman I, Zetterlund M, Forsmark T, Rhén I, 2005b. Oskarshamn site investigation. Correlation of Posiva Flow Log anomalies to core mapped features in KLX02, KLX03, KLX04, KAV04A and KAV04b. SKB P-05-241, Svensk Kärnbränslehantering AB.

Freeze R A, Cherry J A, 1979. Groundwater, Prentice-Hall Inc. London.

Gokall-Norman K, Ludvigson J, 2007. Hydraulic pumping- and interference tests in soil monitoring wells on Laxema, spring of 2007. Oskarshamn site investigation. SKB P-07-173, Svensk Kärnbränslehantering AB.

Gustafsson E, Ludvigson J, 2005. Combined interference test and tracer test between KLX02 and HLX10. Oskarshamn site investigation. SKB P-05-20, Svensk Kärnbränslehantering AB.

Gustavsson E, 2006. Oskarshamn site investigation.Data report from the laboratory investigations of the transport properties of the rock. Data delivery for data freeze Laxemar 2.2. SKB P-06-286, Svensk Kärnbränslehantering AB.

Hakami E, Fredriksson A, Lanaro F, 2008. Rock mechanics Laxemar, Site descriptive modelling SDM-Site Laxemar. SKB R-08-57, Svensk Kärnbränslehantering AB.

Hartley L, Hunter F, Jackson P, McCarthy R, Gylling B, Marsic N, 2006. Regional hydrogeological simulations using CONNECTFLOW. Preliminary site description Laxemar subarea – version 1.2. SKB R-06-23, Svensk Kärnbränslehantering AB.

Hartley L, Jackson P, Joyce S, Roberts D, Shevelan JSwift B, Gylling B, Marsic N, Hermanson J, Öhman J, 2007. Hydrogeological Pre-Modelling Exercises: Assessment of impact of the Äspö Hard Rock Laboratory; Sensitivities of Palaeo-Hydrogeology; Development of a Local Near-Surface Hydro-DFN for KLX09B-F. Site descriptive modelling SDM-Site Laxemar. SKB R-07-57, Svensk Kärnbränslehantering AB.

Harrström J, Ludvigson J, Hjerne C, 2006a. Hydraulic injection tests in borehole KLX12A Subarea Laxemar. Oskarshamn site investigation. SKB P-06-148, Svensk Kärnbränslehantering AB.

Harrström J, Ludvigson J, Hjerne C, 2006b. Single-hole injection tests in borehole KLX10. Oskarshamn site investigation. SKB P-06-182, Svensk Kärnbränslehantering AB.

Harrström J, Walger E, Ludvigson J, Morosini M, 2007. Hydraulic interference tests HLX27, HLX28 and HLX32 , Subarea Laxemar. Oskarshamn site investigation. SKB P-07-186, Svensk Kärnbränslehantering AB.

Hermanson J, Forsberg O, Fox A, La Pointe P, 2005. Statistical model of fractures and deformation zones. Preliminary site description, Laxemar subarea, version 1.2. SKB R-05-45, Svensk Kärnbränslehantering AB.

Hermanson J, Fox A, Öhman J, Rhén I, 2008. Compilation of data used for the analysis of the geological and hydrogeological DFN models. Site Descriptive Modelling. SDM-Site Laxemar. SKB R-08-56, Svensk Kärnbränslehantering AB.

Helsel D R, 2004. Nondetects and Data Analysis: Statistics for Censored Environmental Data, John Wiley & Sons Inc.

Hjerne C, Nordqvist R, Harrström J, 2009 (in prep). Compilation and analyses of results from cross-hole tracer tests with conservative tracers. SKB R-09-28, Svensk Kärnbränslehantering AB.

Holmén J G, 2008. Premodelling of the importance of the location of the upstream hydraulic boundary of a regional flow model of the Laxemar-Simpevarp area. Site descriptive modelling, SDM-Site Laxemar. SKB R-08-60, Svensk Kärnbränslehantering AB.

HydroSOLVE Inc., 2007. AQTESOLV v. 4.5, Reston.

Jackson C P, Hoch A R, Todman S, 2000. Self-consistency of a heterogeneous continuum porous medium representation of a fractured medium. Water Resourc. Res., 36(1), 189–202.

Jensen J L, Lake L W, Corbett P W M, Goggin D J, 2000. Statistics for petroleum engineers and geoscientists, Handbook of Petroleum Exploration and Production, 2, Second ed, Elsevier, Amsterdam.

Johansson T, Adestam L, 2004. Drilling and sampling in soil. Installation of groundwater monitoring wells in the Laxemar area. Oskarshamn site investigation. SKB P-04-317, Svensk Kärnbränslehantering AB.

Kristiansson S, 2006. Oskarshamn site investigation. Difference flow logging of borehole KLX20A. Subarea Laxemar. SKB P-06-183, Svensk Kärnbränslehantering AB.

Kristiansson S, Pöllänen J, Väisäsvaara J, Kyllönen H, 2006. Oskarshamn site investigation. Difference flow logging of borehole , KLX22A–B, KLX23A–B, KLX24A, KLX25A, Subarea Laxemar. SKB P-06-246, Svensk Kärnbränslehantering AB.

Kyllönen H, Leppänen H, 2007. Oskarshamn site investigation. Difference flow logging of borehole KLX19A. Subarea Laxemar. SKB P-07-20, Svensk Kärnbränslehantering AB.

La Pointe P, 1995. Estimation of undiscovered hydrocarbon potential through fractal geometry. Chap. 3, Fractals in Petroleum Geology and Earth Processes, Plenum Press, New York. 35–57.

La Pointe P, Fox A, Hermanson J, Öhman J, 2008. Geological discrete fracture network model for the Laxemar site, Site Descriptive Modelling, SDM-Site Laxemar. SKB R-08-55, Svensk Kärnbränslehantering AB.

Ludvigson J-E, Hansson K, 2002. Methodology study of Posiva difference flow meter in borehole KLX02 at Laxemar. SKB R-01-52, Svensk Kärnbränslehantering AB.

Ludvigson J, Levén J, Jönsson S, 2003. Hydraulic tests and flow logging in borehole HSH03. Oskarshamn site investigation. SKB P-03-56, Svensk Kärnbränslehantering AB.

Ludvigson J, Levén J, Källgården J, Jönsson S, 2004. Single-hole injection tests in borehole KSH02. Oskarshamn site investigation. SKB P-04-247, Svensk Kärnbränslehantering AB.

Ludvigson J-E, Hansson K, Hjerne C, 2007. Method evaluation of single-hole hydraulic injection tests at site investigations in Forsmark, Forsmark site investigation. SKB P-07-80, Svensk Kärnbränslehantering AB.

Marsily G, 1986. Quantitative hydrogeology, Groundwater hydrology for engineers, Academic Press In., New York.

Morosini M, Wass E, 2006. Hydraulic interference and tracer testing of a rock-soil aquifer system between HLX35 and HLX34, SSM000037, SSM000222 and SSM000223. Subarea Laxemar. Oskarshamn site investigation. SKB P-06-151, Svensk Kärnbränslehantering AB.

Morosini M, Jönsson S, 2007. Pump- and interference testing of percussion drilled section of cored boreholes KLX09, KLX11A, KLX12A, KLX13A, KLX18A, KLX19A and KLX39 Subarea Laxemar. Oskarshamn site investigation. SKB P-07-182, Svensk Kärnbränslehantering AB.

Morosini M, Ludvigson J-E, Walger E, 2009. Hydraulic characterisation of deformation zone EW007, Subarea Laxemar. Oskarshamn site investigation. SKB P-05-193, Svensk Kärnbränslehantering AB.

Moye D G, 1967. Diamond drilling for foundation exploration, Civil Eng. Trans. Inst. Eng. Australia, p. 95–100

Olsson T, Stanfors R, Sigurdsson, O, Erlström M,2006. Oskarshamn site investigation, Identification and characterisation of minor deformation zones based on lineament interpretaition. SKB P-06-282, Svensk Kärnbränslehantering AB.

Pöllänen J, Sokolnicki M, 2004. Oskarshamn site investigation – Difference flow measurements in borehole KAV04A and KAV04B. SKB P-04-216, Svensk Kärnbränslehantering AB.

Pöllänen J, 2007a. Oskarshamn site investigation. Difference flow logging of borehole, KLX28 and KLX29A, Subarea Laxemar. SKB P-07-17, Svensk Kärnbränslehantering AB.

Pöllänen J, 2007b. Oskarshamn site investigation. Difference flow logging of borehole KLX17A. Subarea Laxemar. SKB P-07-34

Pöllänen J, 2007c. Oskarshamn site investigation. Difference flow logging of borehole, KLX26A and KLX26B, Subarea Laxemar. SKB P-07-72, Svensk Kärnbränslehantering AB.

Pöllänen J, Sokolnicki M, Väisäsvaara J, 2007. Oskarshamn site investigation. Difference flow logging of borehole KLX15A. Subarea Laxemar. SKB P-07-176, Svensk Kärnbränslehantering AB.

Pöllänen J, Pekkanen J, Väisäsvaara J, 2008. Oskarshamn site investigation. Difference flow logging of borehole, KLX27A, Subarea Laxemar. SKB P-08-22, Svensk Kärnbränslehantering AB.

Rahm N, Enachescu C, 2004a. Oskarshamn site investigation, Hydraulic testing of percussion drilled lineament boreholes on Ävrö and Simpevarp, 2004 Subarea Simpevarp. SKB P-04-287, Svensk Kärnbränslehantering AB.

Rahm N, Enachescu C, 2004b. Hydraulic injection tests in borehole KLX02, 2003. Subarea Laxemar. Oskarshamn site investigation. SKB P-04-288, Svensk Kärnbränslehantering AB.

Rahm N, Enachescu C, 2004c. Hydraulic injection tests in borehole KSH01A, 2003/2004. Subarea Simpevarp. Oskarshamn site investigation. SKB P-04-289, Svensk Kärnbränslehantering AB.

Rahm N, Enachescu C, 2004d. Hydraulic injection tests in borehole KSH03A, 2004. Subarea Simpevarp. Oskarshamn site investigation. SKB P-04-290, Svensk Kärnbränslehantering AB.

Rahm N, Enachescu C, 2004e. Hydraulic injection tests in borehole KAV04A, 2004. Subarea Simpevarp. Oskarshamn site investigation. SKB P-04-291, Svensk Kärnbränslehantering AB.

Rahm N, Enachescu C, 2004f. Hydraulic injection tests in borehole KLX04, 2004. Subarea Laxemar. Oskarshamn site investigation. SKB P-04-292, Svensk Kärnbränslehantering AB.

Rahm N, Enachescu C, 2005a. Pumping tests and hydraulic injection tests in borehole KLX06, 2005. Subarea Laxemar. Oskarshamn site investigation. SKB P-05-184, Svensk Kärnbränslehantering AB.

Rahm N, Enachescu C, 2005b. Hydraulic injection tests in borehole KLX03, 2005. Subarea Laxemar. Oskarshamn site investigation. SKB P-05-192, Svensk Kärnbränslehantering AB.

Rahm N, Enachescu C, 2005c. Hydraulic injection tests in borehole KLX05, 2005. Subarea Laxemar. Oskarshamn site investigation. SKB P-05-222, Svensk Kärnbränslehantering AB.

Rahm N, Enachescu C, 2005d. Hydraulic injection tests in borehole KLX07A, 2005 Laxemar. Oskarshamn site investigation. SKB P-05-273, Svensk Kärnbränslehantering AB.

Rahm N, Enachescu C, 2005e. Pumping tests and water sampling in borehole KLX04, 2004. Subarea Laxemar. Oskarshamn site investigation. SKB P-05-16, Svensk Kärnbränslehantering AB.

Rhén I (ed), Gustafson G, Stanfors R, Wikberg P, 1997. Äspö HRL – Geoscientific evaluation 1997/5. Models based on site characterization 1986–1995. SKB TR 97-06, Svensk Kärnbränslehantering AB.

Rhén I, Follin S, Hermanson J, 2003. Hydrological Site Descriptive Model – a strategy for its development during Site Investigations. SKB R-03-08, Svensk Kärnbränslehantering AB.

Rhén I, Forsmark T, Forsman I, Zetterlund M, 2006. Hydrogeological single-hole interpretation of KLX02, KLX03, KLX04, KAV04A and KAV04b, Preliminary site description, Laxemar subarea – version 1.2. SKB R-06-21, Svensk Kärnbränslehantering AB.

Rhén I, Forsmark T, Hartley L, Joyce S, Roberts D, Gylling B, Marsic N, 2009. Bedrock Hydrogeolology: model testing and synthesis, Site descriptive modelling, SDM-Site Laxemar. SKB R-08-91, Svensk Kärnbränslehantering AB.

Rohs S, 2006. Flow logging in boreholes HLX21, HLX35 and HLX38 Subarea Laxemar. Oskarshamn site investigation. SKB P-06-147, Svensk Kärnbränslehantering AB.

Rohs S, van der Wall R, Wolf P, 2006. Flow logging in boreholes HLX14, HLX20, HLX27, HLX28, HLX32, HLX33, HLX37, HLX39 and HLX43 Subarea Laxemar. Oskarshamn site investigation. SKB P-06-319, Svensk Kärnbränslehantering AB.

Rouhiainen P, 2000. Äspö Hard Rock Laboratory – Difference flow measurements in borehole KLX02 at Laxemar. SKB IPR-01-06, Svensk Kärnbränslehantering AB.

Rouhiainen P, Pöllänen J, 2003a. Oskarshamn site investigation – Difference flow measurements in borehole KSH01A at Simpevarp. SKB P-03-70, Svensk Kärnbränslehantering AB.

Rouhiainen P, Pöllänen J, 2003b. Oskarshamn site investigation – Difference flow measurements in borehole KSH02 at Simpevarp. SKB P-03-110, Svensk Kärnbränslehantering AB.

Rouhiainen P, Pöllänen J, 2004. Oskarshamn site investigation – Difference flow measurements in borehole KAV01 at Ävrö. SKB P-04-213, Svensk Kärnbränslehantering AB.

Rouhiainen P, Sokolnicki M, 2005. Oskarshamn site investigation. Difference flow logging of borehole KLX04. Subarea Laxemar. SKB P-05-68, Svensk Kärnbränslehantering AB.

Rouhiainen P, Pöllänen J, Sokolnicki M, 2005. Oskarshamn site investigation. Difference flow logging of borehole KLX03. Subarea Laxemar. SKB P-05-67, Svensk Kärnbränslehantering AB.

Selnert E, Byegård J, Widestrand H, 2007 (in prep). Oskarshamn Site investigation. Laboratory measurements within the site investigation programme for the Transport properties of the rock. Final report. SKB P-07-179, Svensk Kärnbränslehantering AB.

Selnert E, Byegård J, Widestrand H, Carlsten S, Döse C, Tullborg E-L, 2009 (in prep). Bedrock Transport Properties, Data Evaluation and Retardation Model, Site descriptive modelling, SDM-Site Laxemar. SKB R-08-100, Svensk Kärnbränslehantering AB.

Sigurdsson O, Ekström L, 2005. Percussion drilling of boreholes HSH04, HSH05, HSH06, HAV11, HAV12, HAV13 and HAV14. Oskarshamn site investigation. SKB P-05-194, Svensk Kärnbränslehantering AB.

Sigurdsson O, Ask H, Zetterlund M, 2005. Percussion drilling of boreholes HLX34 and HLX35. Oskarshamn site investigation. SKB P-05-237, Svensk Kärnbränslehantering AB.

SKB, 2002. Simpevarp – site descriptive model version 0. SKB R-02-35, Svensk Kärnbränslehantering AB.

SKB, 2004. Preliminary site description Simpevarp area – version 1.1. SKB R-04-25, Svensk Kärnbränslehantering AB.

SKB, 2005a. Preliminary site description. Simpevarp subarea – version 1.2. SKB R-05-08, Svensk Kärnbränslehantering AB.

SKB 2005b. Preliminary safety evaluation for the Simpevarp subarea. Based on data and site descriptions after the initial site investigation stage. SKB TR-05-12, Svensk Kärnbränslehantering AB.

SKB, 2006a. Slutförvar för använt kärnbränsle. Preliminär anläggningsbeskrivning – layout D. Oskarshamn, delområde Simpevarp. SKB R-06-31, Svensk Kärnbränslehantering AB.

SKB, 2006b. Preliminary site description. Laxemar subarea – version 1.2. SKB R-06-10, Svensk Kärnbränslehantering AB.

SKB 2006c. Preliminary safety evaluation for the Laxemar subarea. Based on data and site descriptions after the initial site investigation stage. SKB TR-06-06, Svensk Kärnbränslehantering AB.

SKB, 2006d. Slutförvar för använt kärnbränsle. Preliminär anläggningsbeskrivning – layout D. Oskarshamn, delområde Laxemar. SKB R-06-32, Svensk Kärnbränslehantering AB.

SKB, 2006e. Long-term safety for KBS-3 repositories at Forsmark and Laxemar – a first evaluation. Main Report of the SR-Can project. SKB TR-06-09, Svensk Kärnbränslehantering AB.

SKB, 2006f. Programme for further investigations of bedrock, soil, water and environment in Laxemar subarea. Oskarshamn site investigation. SKB R-06-29, Svensk Kärnbränslehantering AB.

SKB, 2006g. Preliminary site description Laxemar stage 2.1. Feedback for completion of the site investigation including input from safety assessment and repository engineering. SKB R-06-110, Svensk Kärnbränslehantering AB.

SKB, 2007a. Prioritering av platsen för ett slutförvar i Oskarshamn. SKB R-07-21, Svensk Kärnbränslehantering AB.

SKI, 2005. Need for Confirmatory Testing of Upscaled Flow and Transport Models, INSITE Report TRD-05-08, Statens Kärnkraftsinspektion.

Sohlenius G, Bergman T, Snäll S, Lundin L, Lode E, Stendahl J, Riise A, 2006. Soils, Quaternary deposits and bedrock in topographic lineaments situated in the Laxemar subarea. Oskarshamn site investigation. SKB P-06-121, Svensk Kärnbränslehantering AB.

Sokolnicki M, Pöllänen J, 2005. Oskarshamn site investigation. Difference flow logging of borehole KLX08. Subarea Laxemar. SKB P-05-267, Svensk Kärnbränslehantering AB.

Sokolnicki M, Rouhianien P, 2005a. Oskarshamn site investigation. Difference flow logging of borehole KLX06. Subarea Laxemar. SKB P-05-74, Svensk Kärnbränslehantering AB.

Sokolnicki M, Rouhianien P, 2005b. Oskarshamn site investigation. Difference flow logging of borehole KLX05. Subarea Laxemar. SKB P-05-160, Svensk Kärnbränslehantering AB.

Sokolnicki M, Rouhianien P, 2005c. Oskarshamn site investigation. Difference flow logging of borehole KLX07A and KLX07B. Subarea Laxemar. SKB P-05-225, Svensk Kärnbränslehantering AB.

Sokolnicki M, 2006. Oskarshamn site investigation. Difference flow logging of borehole KLX10. Subarea Laxemar. SKB P-06-58, Svensk Kärnbränslehantering AB.

Sokolnicki M, Kristiansson S, 2006. Oskarshamn site investigation. Difference flow logging of borehole KLX18A. Subarea Laxemar. SKB P-06-184, Svensk Kärnbränslehantering AB.

Sokolnicki M, Väisäsvaara J, 2006. Oskarshamn site investigation. Difference flow logging of borehole KLX09B-F. Subarea Laxemar. SKB P-06-199, Svensk Kärnbränslehantering AB.

Sokolnicki M, Kristiansson S, 2007. Oskarshamn site investigation. Difference flow logging of borehole KLX11B-F. Subarea Laxemar. SKB P-07-64, Svensk Kärnbränslehantering AB.

Sokolnicki M, Pöllänen J, 2007. Oskarshamn site investigation. Difference flow logging of borehole KLX21B. Subarea Laxemar. SKB P-07-116, Svensk Kärnbränslehantering AB.

Stigsson M, 2008. Analysis of uncertainty in orientation of fractures coupled to PFL anomalies, Site descriptive modelling, SDM-Site Laxemar. SKB P-08-104, Svensk Kärnbränslehantering AB.

Svensson T, 2004. Pumping tests and flow logging in boreholes KSH03A and HSH02. Oskarshamn site investigation. SKB P-04-212, Svensk Kärnbränslehantering AB.

Svensson T, Ludvisgsson J-E, Walger E, Thur P, Gokall-Norman K, Wass Morosini M, 2007. Combined interference- and tracer test in HLX33, SSM000228, and SSM000229, Subarea Laxemar. Oskarshamn site investigation. SKB P-07-187, Svensk Kärnbränslehantering AB.

Terzhagi R D, 1965. Sources of error in joint surveys, Geotechnique, Vol. 15, pp. 287–304.

Teurneau B, Forsmark T, Forssman I, Rhén I, 2007. Oskarshamn site investigation. Correlation of Posiva Flow Log anomalies to core mapped features in KLX05, KLX06, KLX07A-B and KLX08. SKB P-07-212, Svensk Kärnbränslehantering AB.

Thiem G, 1906. Hydrologische Methoden, J M Gebhardt, Leipsig.

Thur P, Walger E, Ludvigson J-E, 2007. Hydraulic interference in HLX34, HLX27,and HLX42 in the Laxemar subarea. Oskarshamn site investigation. SKB P-07-185, Svensk Kärnbränslehantering AB.

Triumf C-A, 2007. Oskarshamn site investigation, Assessment of probable and possible dolerite dykes in the Laxemar subarea from magnetic total field data and digital elevation models. SKB P-07-223, Svensk Kärnbränslehantering AB.

Vilks, P, 2005. Laboratory program supporting SKB's Long Term Diffusion Experiment, Report No: 06819-REP-01300-10111-R00, Ontario Power Generation.

Vilks, P, 2007a. Rock matrix permeability measurements on core samples from borehole KFM01D. SKB P-07-162, Svensk Kärnbränslehantering AB.

Vilks, P, 2007b. Rock matrix permeability measurements on core samples from borehole KLX03. SKB P-07-204, Svensk Kärnbränslehantering AB.

Väisäsvaara J, 2006. Oskarshamn site investigation. Difference flow logging of borehole KLX14A. Subarea Laxemar. SKB P-06-318, Svensk Kärnbränslehantering AB.

Väisäsvaara J, Pekkanen J, 2006. Oskarshamn site investigation. Difference flow logging of borehole KLX13A. Subarea Laxemar. SKB P-06-245, Svensk Kärnbränslehantering AB.

Väisäsvaara J, Heikkinen P, Kristiansson S, Pöllänen J, 2006a. Oskarshamn site investigation. Difference flow logging of borehole KLX09. Subarea Laxemar. SKB P-06-164, Svensk Kärnbränslehantering AB.

Väisäsvaara J, Heikkinen P, Kristiansson S, Pöllänen J, 2006b. Oskarshamn site investigation. Difference flow logging of borehole KLX12A. Subarea Laxemar. SKB P-06-185, Svensk Kärnbränslehantering AB.

Väisäsvaara J, Leppänen H, Kristiansson S, Pöllänen J, 2006c. Oskarshamn site investigation. Difference flow logging of borehole KLX09G, KLX10B and KLX10C. Subarea Laxemar. SKB P-06-229, Svensk Kärnbränslehantering AB.

Väisäsvaara J, 2007. Oskarshamn site investigation. Difference flow logging of borehole KLX16A. Subarea Laxemar. SKB P-07-87, Svensk Kärnbränslehantering AB.

Väisäsvaara J, Kristiansson S, Sokolnicki M, 2007. Oskarshamn site investigation. Difference flow logging of borehole KLX11A. Subarea Laxemar. SKB P-07-24, Svensk Kärnbränslehantering AB.

Waber H N, Gimmi T , Smellie J A T, deHaller A, 2009. Porewater in the rock matrix, Site descriptive modelling, SDM-Site Laxemar. SKB R-08-112, Svensk Kärnbränslehantering AB.

Wahlgren C-H, Hermanson J, Curtis P, Forssberg O, Triumf C-A, Drake H, Tullborg E-L, 2005. Geological description of rock domains and deformation zones in the Simpevarp and Laxemar subareas. Preliminary site description, Laxemar subarea, version 1.2. SKB P-05-69, Svensk Kärnbränslehantering AB.

Wahlgren C-H, Curtis P, Hermanson J, Forssberg O, Öhman J, Fox A, La Pointe P, Drake H, Triumf C-A, Mattsson H, Thunehed H, Juhlin C, 2008. Geology Laxemar. Site descriptive modelling. SDM-Site Laxemar. SKB-R-08-54, Svensk Kärnbränslehantering AB.

Walger E, Ludvigson J-E, Svensson T, Thur P, Harrström J, 2007. Hydraulic interference in KLX06, KLX14A, KLX15A, KLX16A, KLX17A, KLX18A, KLX19A, KLX21B, KLX22A, KLX22B, KLX23A, KLX23B, KLX26A and KLX26B, Laxemar subarea. Oskarshamn site investigation. SKB P-07-183, Svensk Kärnbränslehantering AB.

Wikström M, Forsmark T, Teurneau B, Forssman I, Rhén I, 2007a. Oskarshamn site investigation. Correlation of Posiva Flow Log anomalies to core mapped features in KLX09, KLX09B–G. KLX10, KLX10B–C and KLX11A–F. SKB P-07-213, Svensk Kärnbränslehantering AB.

Wikström M, Forsmark T, Zetterlund M, Forssman I, Rhén I, 2007b. Oskarshamn site investigation. Correlation of Posiva Flow Log anomalies to core mapped features in KLX12A, KLX13A, KLX14A, KLX15A and KLX16A. SKB P-07-214, Svensk Kärnbränslehantering AB.

Wikström M, Forsmark T, Forssman I, Rhén I, 2007c. Oskarshamn site investigation. Correlation of Posiva Flow Log anomalies to core mapped features in KLX22A–B, KLX23A–B, KLX24A, KLX25A, KLX26A–B, KLX27A, KLX28A and KLX29A. SKB P-07-216, Svensk Kärnbränslehantering AB.

Appendix 1

A.1 Matrix porosity- Related to RSM

Comments to data used

Nine data points, in KSH01, KSH02 and one sample from KLX03, were not represented by an RSM (rock domain) in the received data as it was not specified in p_domain from SICADA. These data were excluded in the analysis below.

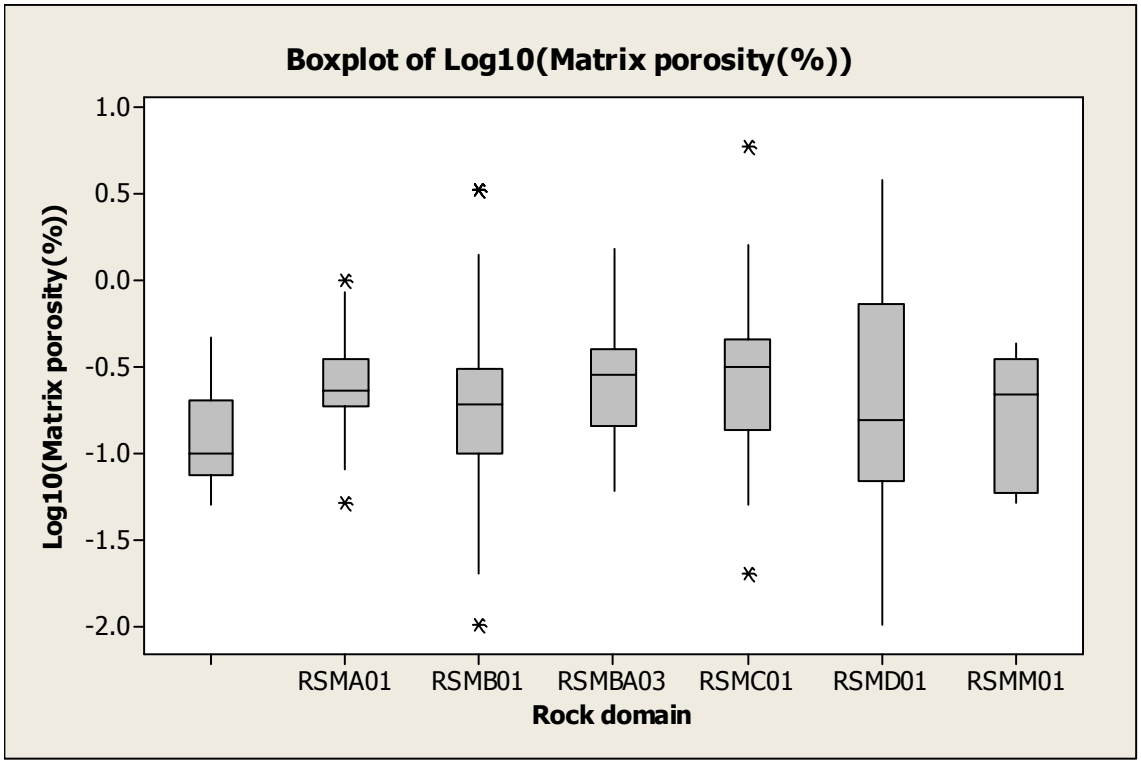
Boxplot of Log10(Matrix porosity(%))
Log10(Matrix porosity(%))
1.0
0.5
0.0
-0.5
-1.0
-1.5
-2.0
RSMA01
RSMB01
RSMBA03
RSMC01
RSMD01
RSMM01
Rock domain

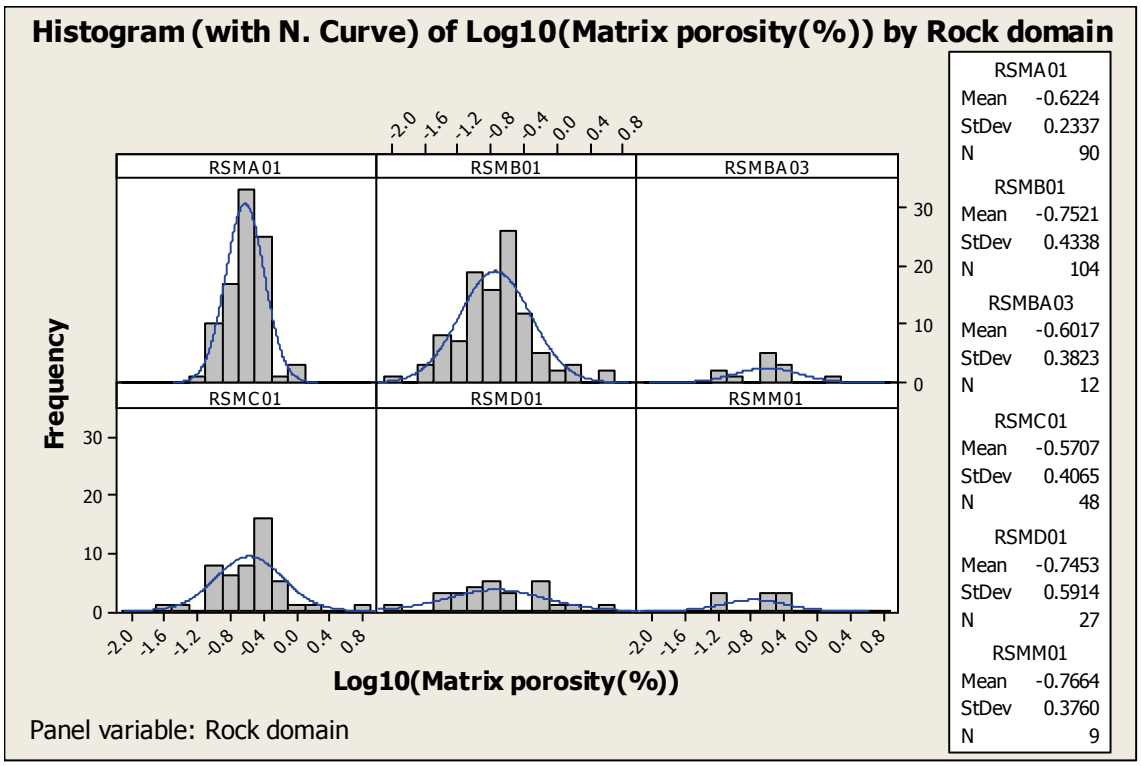
Histogram (with N. Curve) of Log10(Matrix porosity(%)) by Rock domain
RSMA01
RSMB01
RSMBA03
RSMC01
RSMD01
RSMM01
Frequency
Log10(Matrix porosity(%))
Panel variable: Rock domain
RSMA01
Mean -0.6224
StDev 0.2337
N 90
RSMB01
Mean -0.7521
StDev 0.4338
N 104
RSMBA03
Mean -0.6017
StDev 0.3823
N 12
RSMC01
Mean -0.5707
StDev 0.4065
N 48
RSMD01
Mean -0.7453
StDev 0.5914
N 27
RSMM01
Mean -0.7664
StDev 0.3760
N 9

A.2 PFL-f versus geological interpretations

In Section A2.1 hydraulic data is presented in relation to Fracture Domains (FSMxxx) and in Section A2.2 data is presented in relation to Fracture Domains (FSMxxx)

A.2.1 *PFL-f transmissivities versus Modelled Fracture domains and Deformation zones, as well as Geological Extended Single-hole Interpretation(ESHI)*

The geologically modelled Fracture Domains (FSMxxx) and Deformation Zones (ZSMNNxxxx or shorter: NNxxxx) are deterministically in space. The deformation zones found in Geological Extended Single-hole Interpretation (ESHI) are called Possible Deformation zones (DZx) and rock mass is also divided into rock units (RUx). Some of the DZx are modelled deterministically and the remaining are called minor deformation zones (MDZ). FSMxxx, ZSMNNxxxx and MDZ along the borehole are used for further analysis by different disciplines.

In this appendix the transmissivities and orientations of PFL-f features are shown together with modelled fracture domains and deformation zones. The Geological Extended Single-hole Interpretation (ESHI) is also shown to indicate the background information for FSMxxx, ZSMNNxxxx and MDZ as in a few cases it has some significance for the evaluation of hydraulic data. In the plots the borehole length, as documented in the SICADA data base, and the elevation ("level" in the plots) corresponds to the Z coordinate in the RH70/RHB70 system) are shown. The orientations of the PFL-f features are shown as strike/dip.

The pole plots show the Pole Vector, with orientation trend/dip, to each fracture that has a measured PFL-f feature linked to it. Pol plots marked with FSM though formally not coupled to FSM, but nearby FSM used to indicate nearby FSM. Pole plots are shown for:

- PFL-f feature planes in rock between the possible deformation zones defined by ESHI.
- PFL-f feature planes within minor deformation zones (MDZ).
- PFL-f feature planes within deterministic deformation zones (ZSMNNxxx).

In a few cases FSM was not defined in the geological interpretation for the boreholes within the local model, but in the hydrogeological interpretation has these borehole sections linked to nearby FSM to form basis for the hydraulic rock domains (HRD). This relates to KLX02 (RSMBA03 and below 1000m bh length), KLX06 and lower part of KLX20A.

Borehole KLX02.

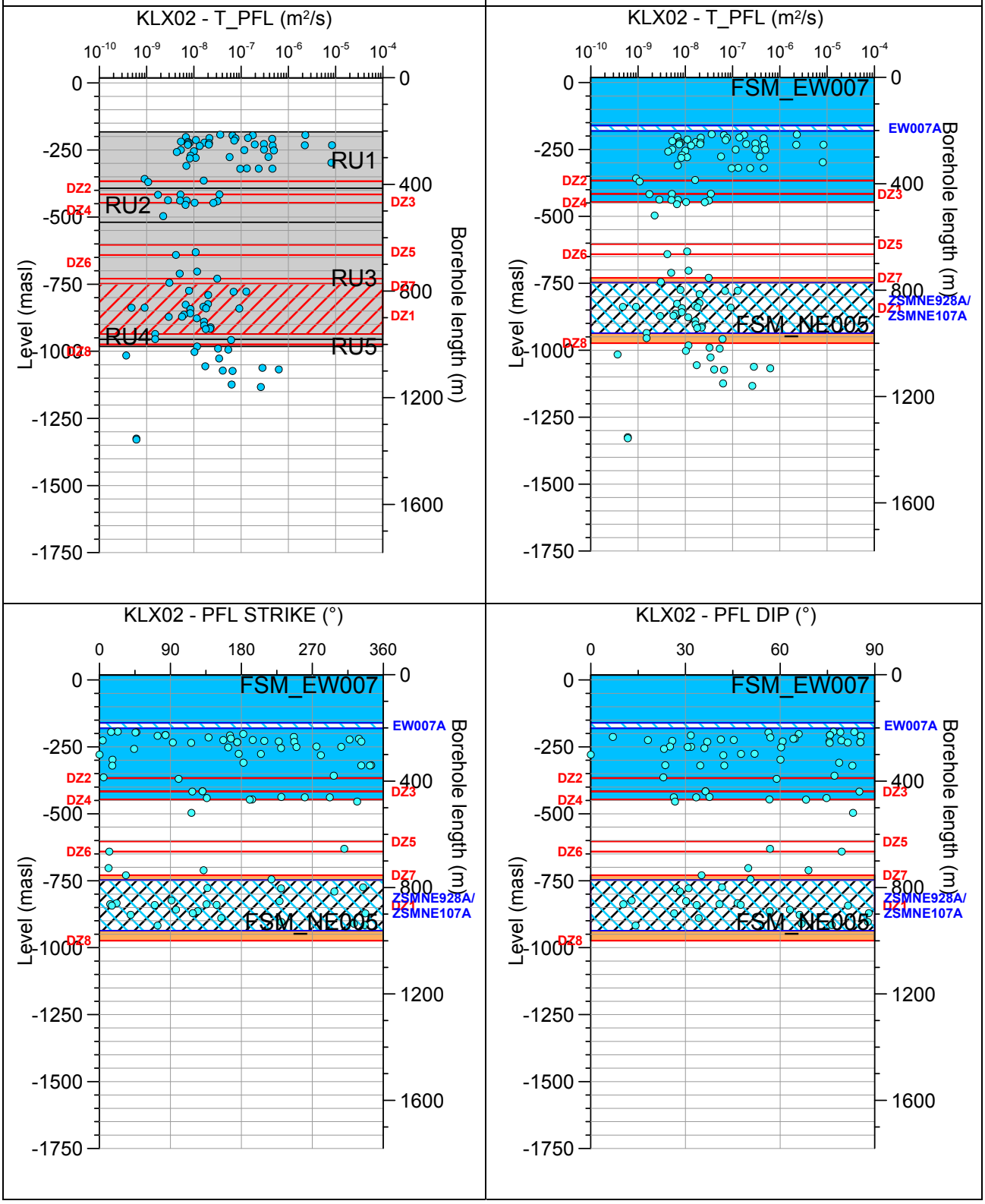

Comment: No fracture domain is currently defined in the mid-part of KLX02 (blank area)

Borehole KLX02. Poles for PFL-f feature planes outside deformation zones.

KLX02, HRD, ELEV.: 0 TO -1000 m

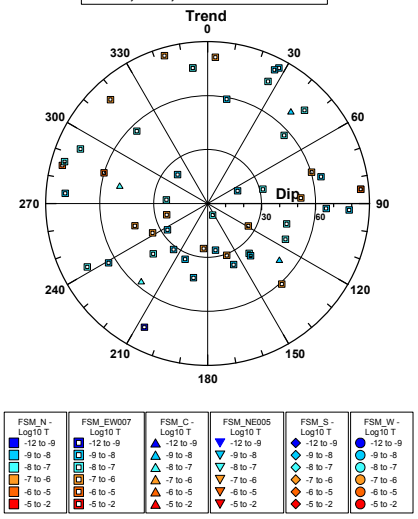

KLX02, HRD, ELEV.: 0 TO -200 m

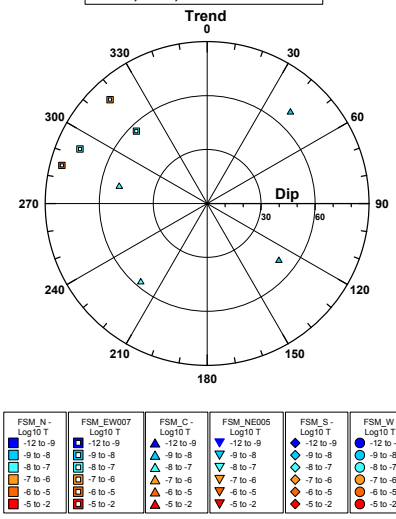

KLX02, HRD, ELEV.: -200 TO -400 m

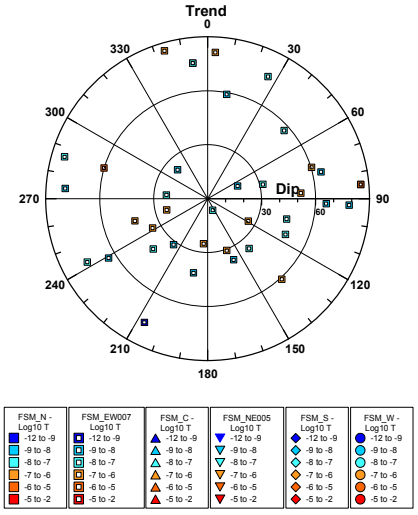

KLX02, HRD, ELEV.: -400 TO -600 m

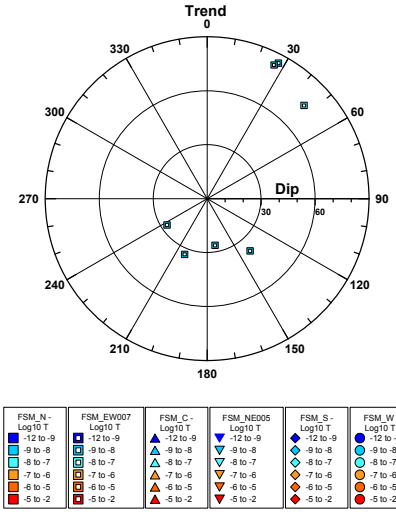

KLX02, HRD, ELEV.: -600 TO -800 m

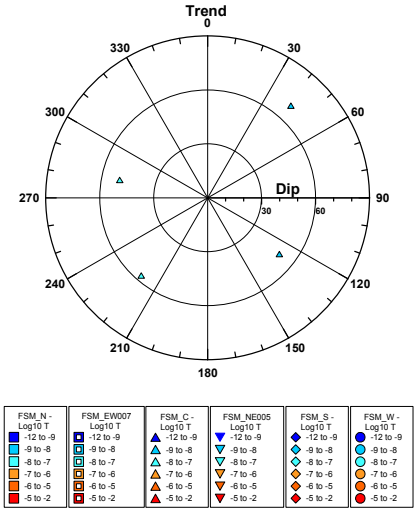

Borehole KLX02. Poles for PFL-f feature planes in possible deformation zones.

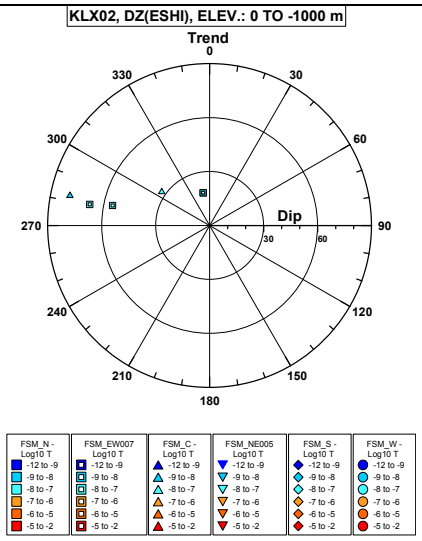

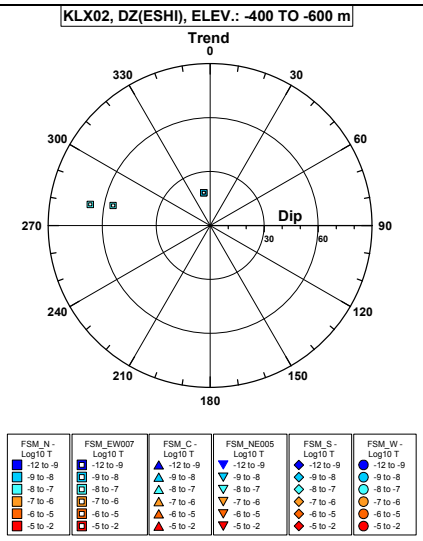

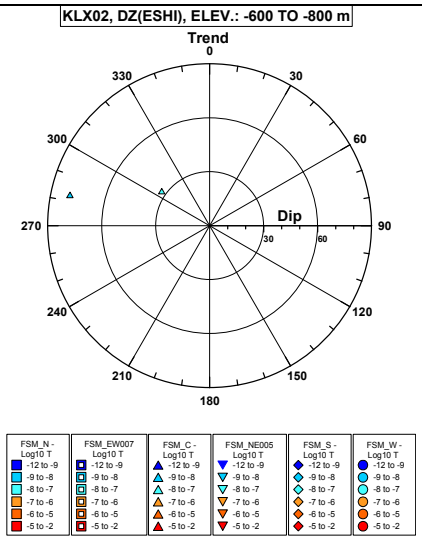

Borehole KLX02. Poles for PFL-f feature planes in deterministically modelled deformation zones.

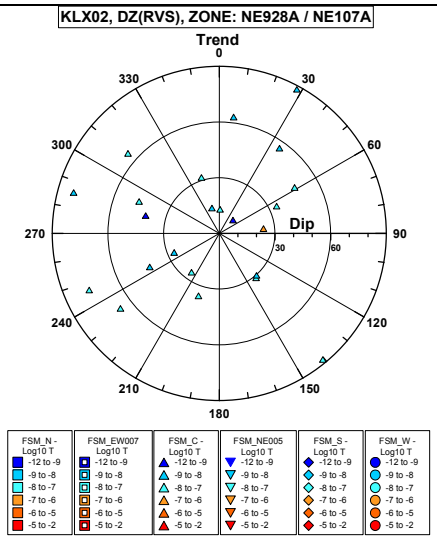

Borehole KLX03.

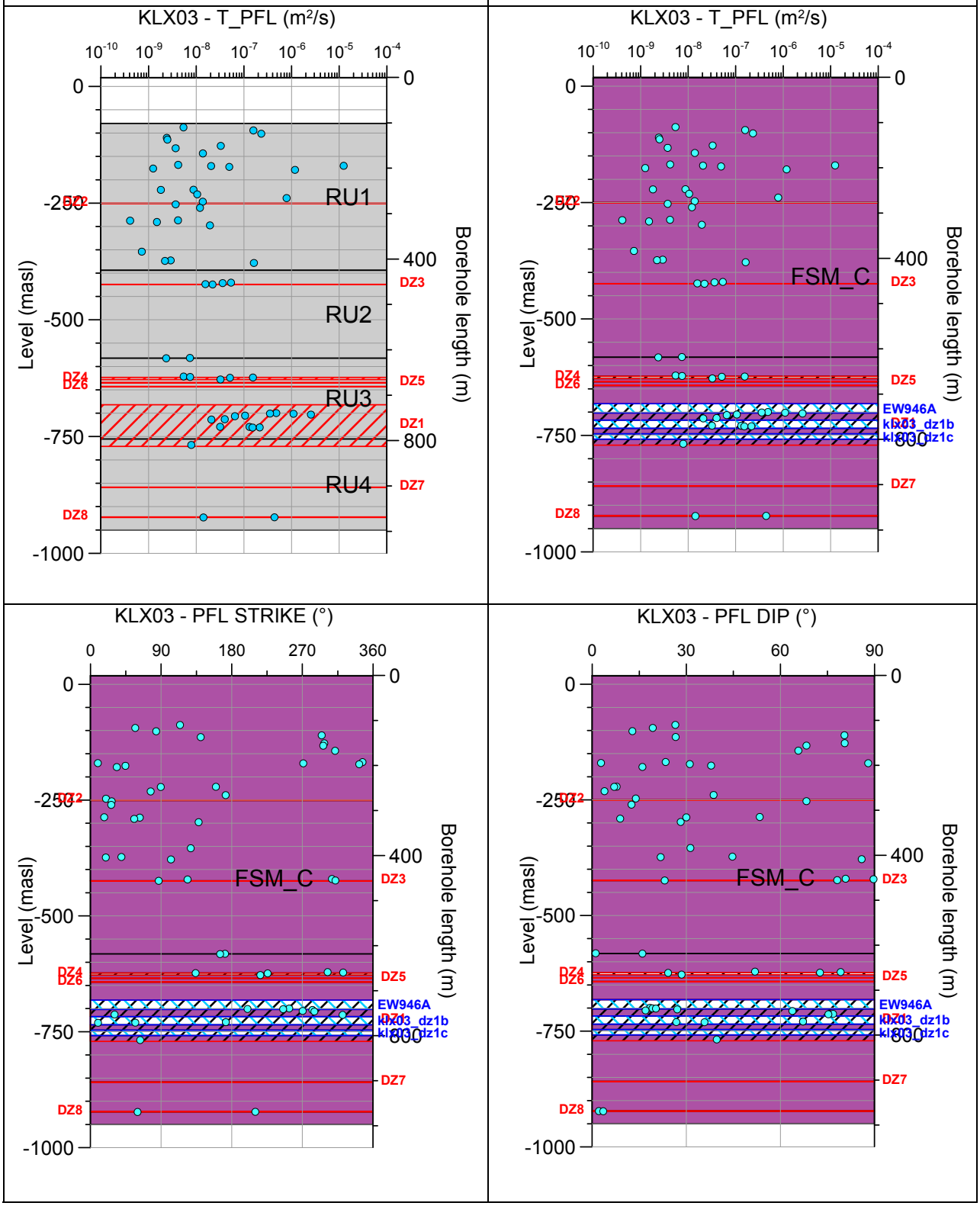

Comment:

Borehole KLX03. Poles for PFL-f feature planes outside deformation zones.

KLX03, HRD, ELEV.: 0 TO -1000 m

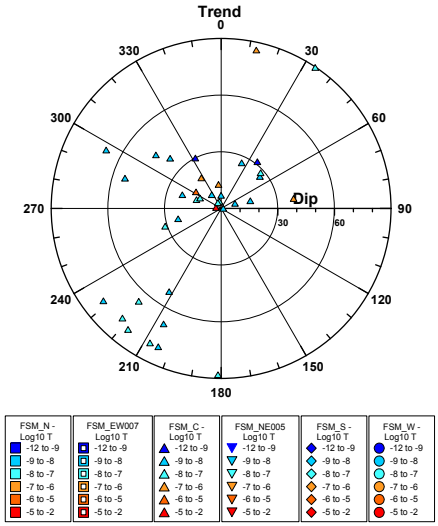

KLX03, HRD, ELEV.: 0 TO -200 m

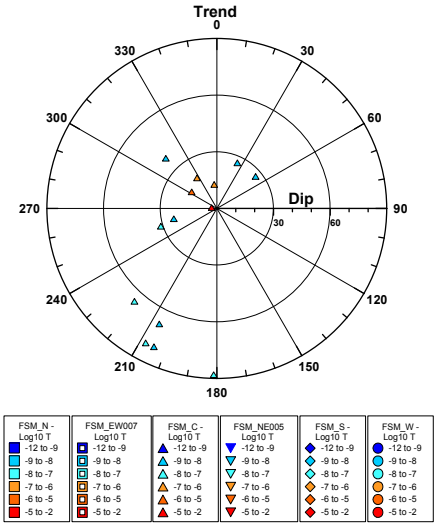

KLX03, HRD, ELEV.: -200 TO -400 m

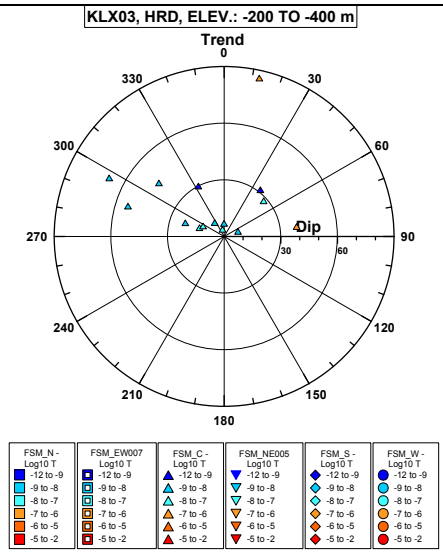

KLX03, HRD, ELEV.: -400 TO -600 m

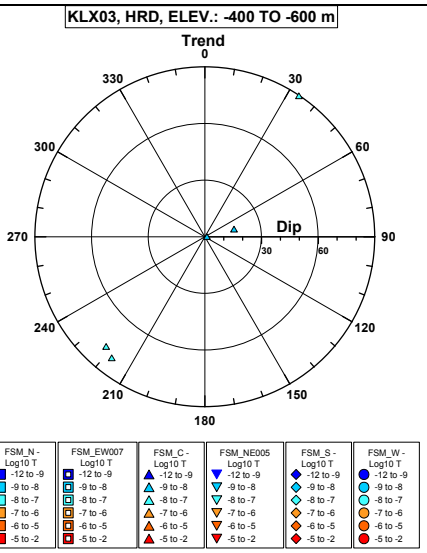

KLX03, HRD, ELEV.: -600 TO -800 m

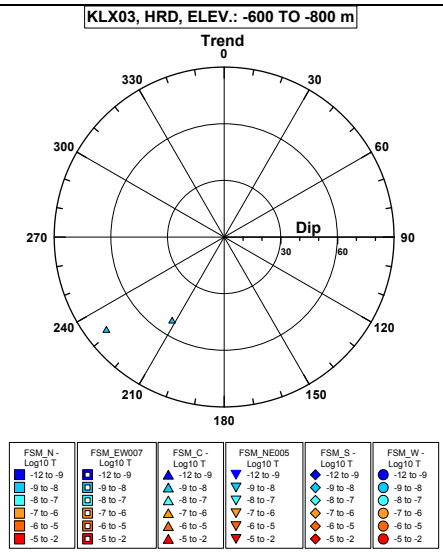

KLX03, HRD, ELEV.: -800 TO -1000 m

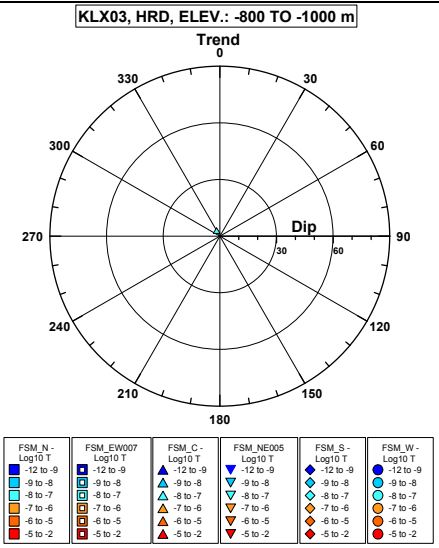

Borehole KLX03. Poles for PFL-f feature planes in possible deformation zones.

KLX03, DZ(ESHI), ELEV.: 0 TO -1000 m

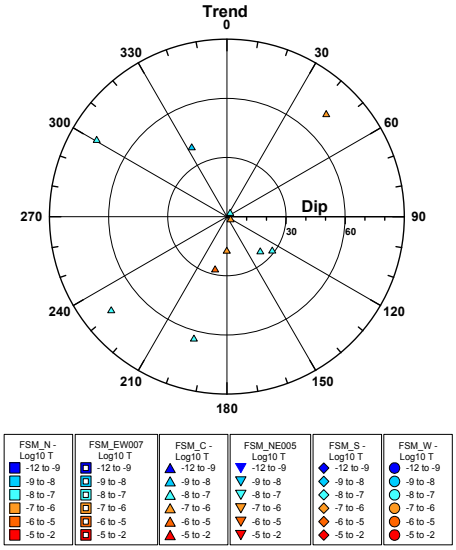

KLX03, DZ(ESHI), ELEV.: -400 TO -600 m

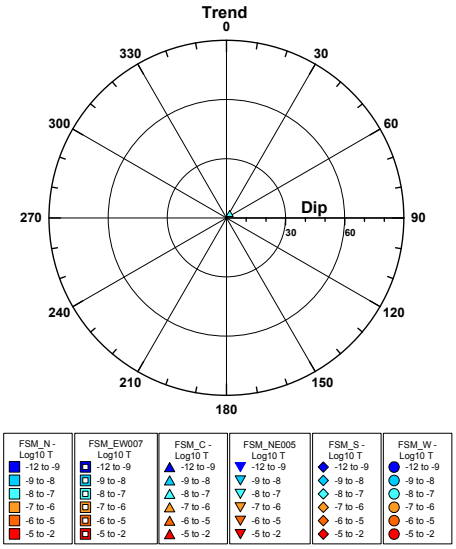

KLX03, DZ(ESHI), ELEV.: -600 TO -800 m

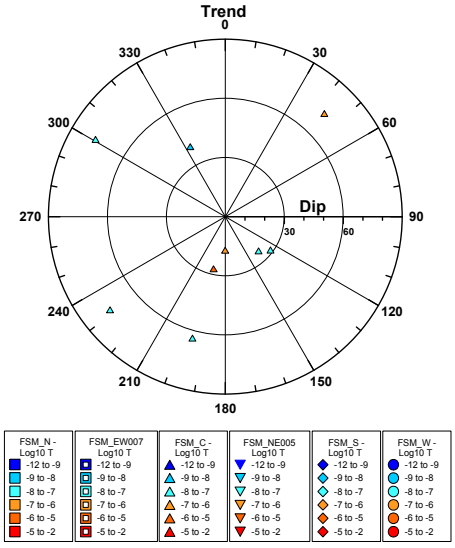

KLX03, DZ(ESHI), ELEV.: -800 TO -1000 m

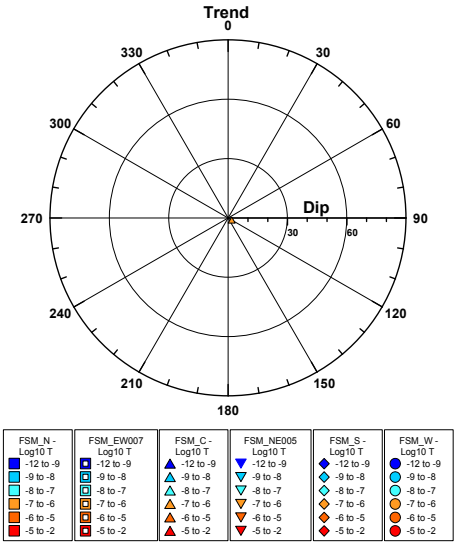

Borehole KLX03. Poles for PFL-f feature planes in deterministically modelled deformation zones.

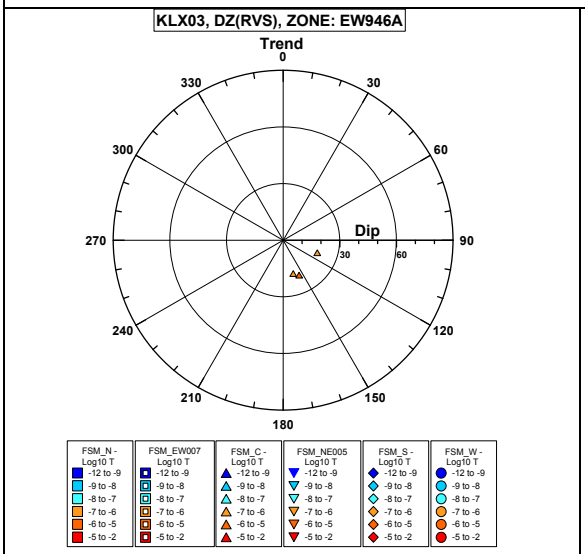

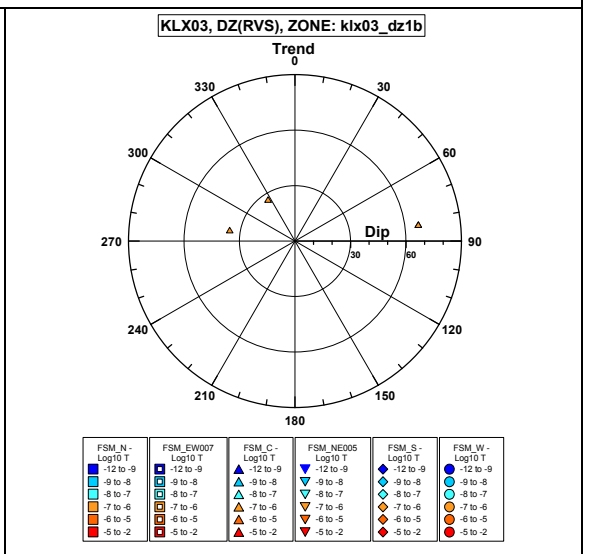

Borehole KLX04.

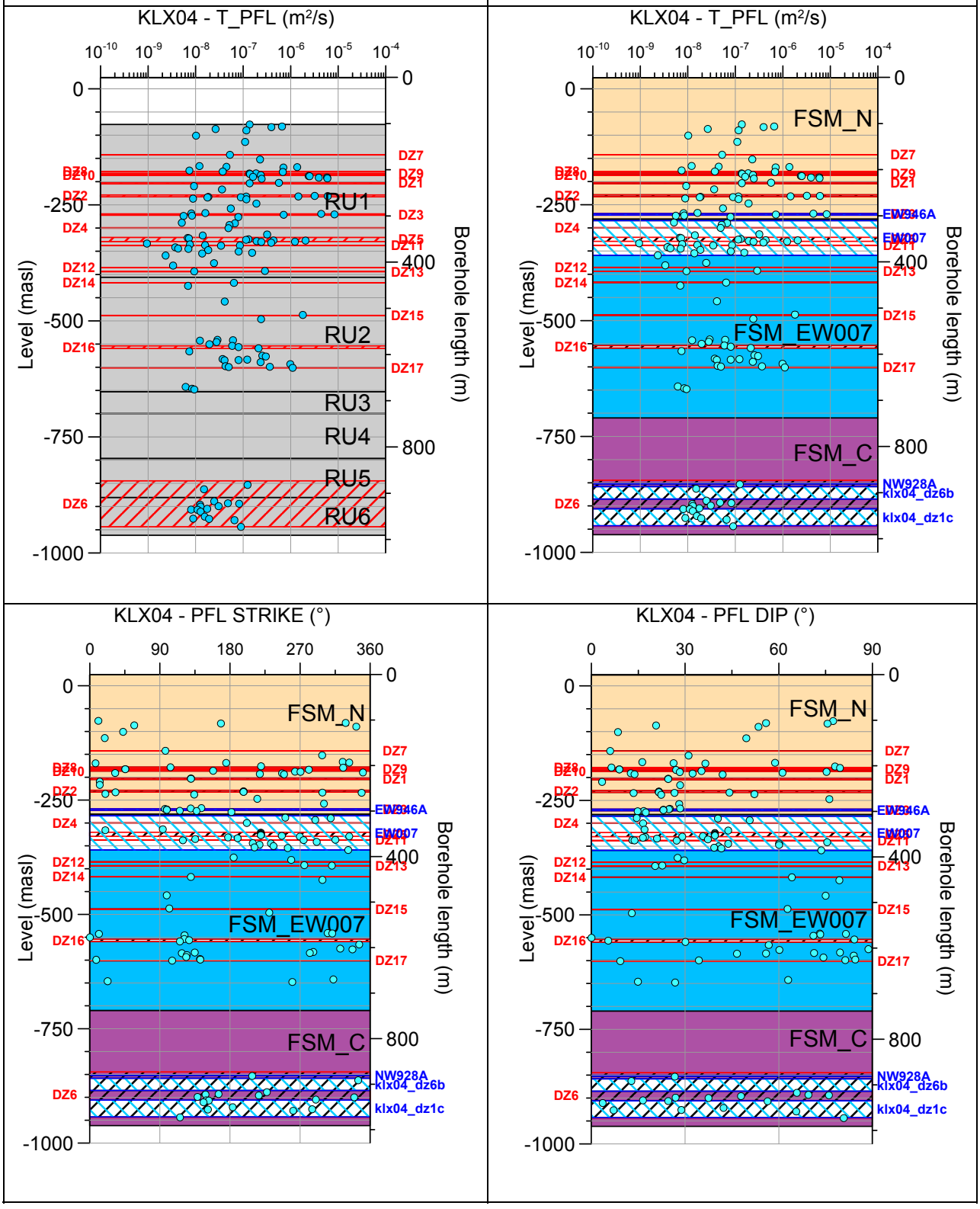

Comment:

Borehole KLX04. Poles for PFL- f feature planes outside deformation zones.

KLX04, HRD, ELEV.: 0 TO -1000 m

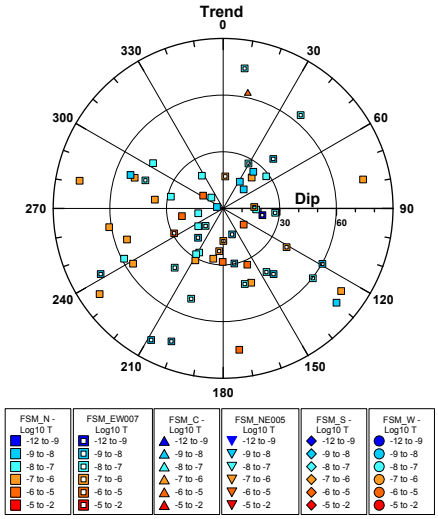

KLX04, HRD, ELEV.: 0 TO -200 m

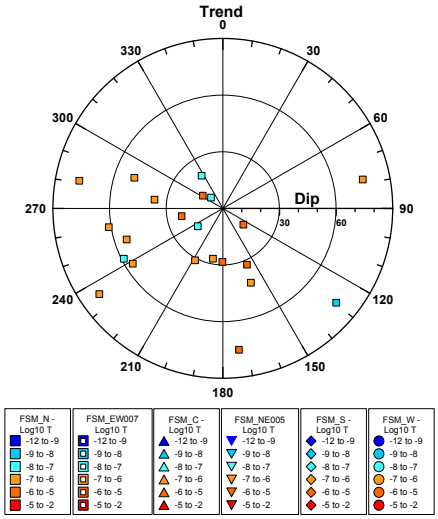

KLX04, HRD, ELEV.: -200 TO -400 m

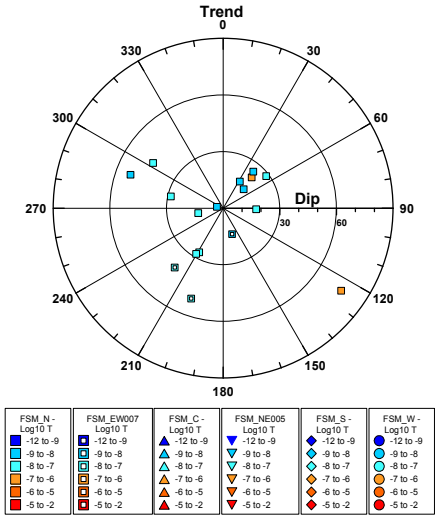

KLX04, HRD, ELEV.: -400 TO -600 m

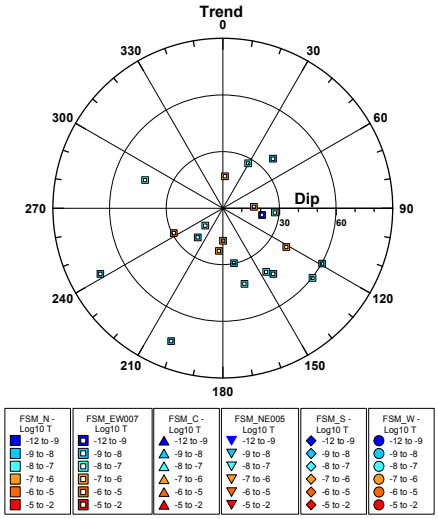

KLX04, HRD, ELEV.: -600 TO -800 m

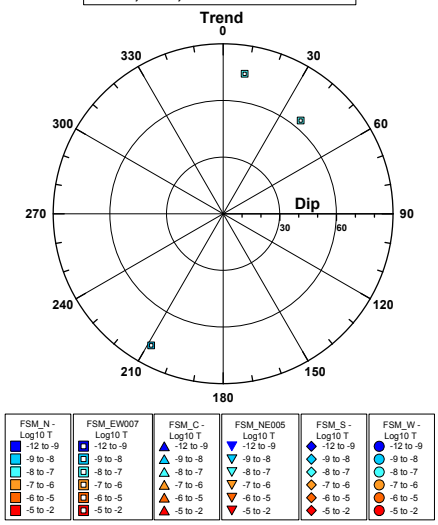

Borehole KLX04. Poles for PFL-f feature planes in possible deformation zones.

KLX04, DZ(ESHI), ELEV.: 0 TO -1000 m

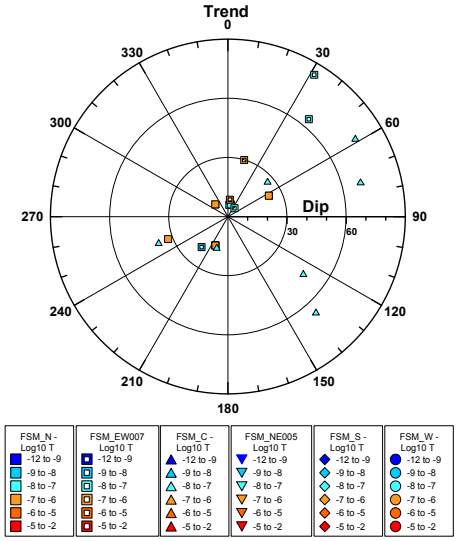

KLX04, DZ(ESHI), ELEV.: 0 TO -200 m

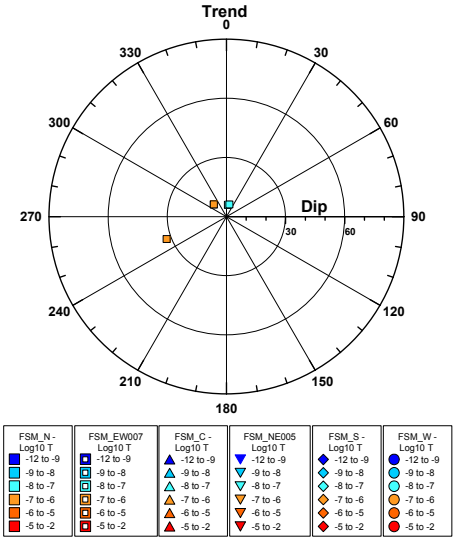

KLX04, DZ(ESHI), ELEV.: -200 TO -400 m

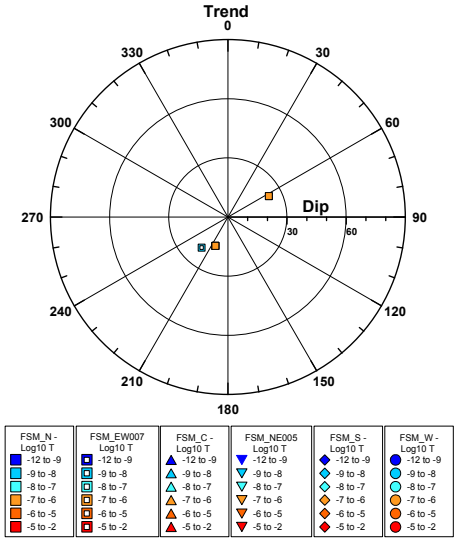

KLX04, DZ(ESHI), ELEV.: -400 TO -600 m

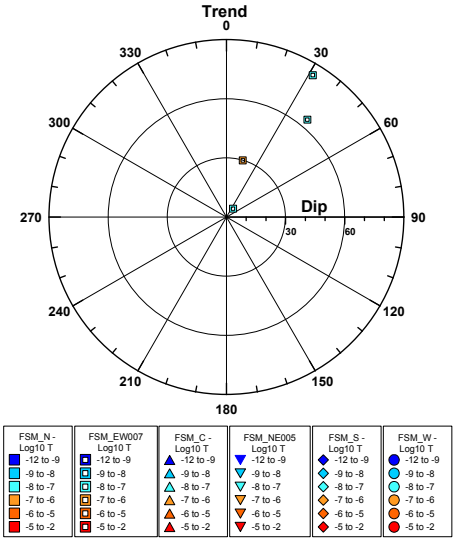

KLX04, DZ(ESHI), ELEV.: -600 TO -800 m

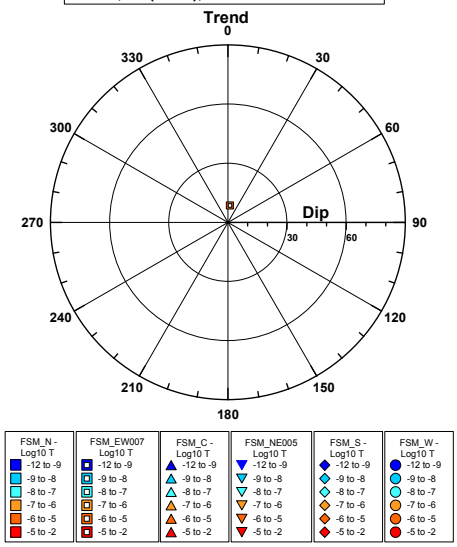

Borehole KLX04. Poles for PFL-f feature planes in deterministically modelled deformation zones.

KLX04, DZ(RVS), ZONE: EW007A

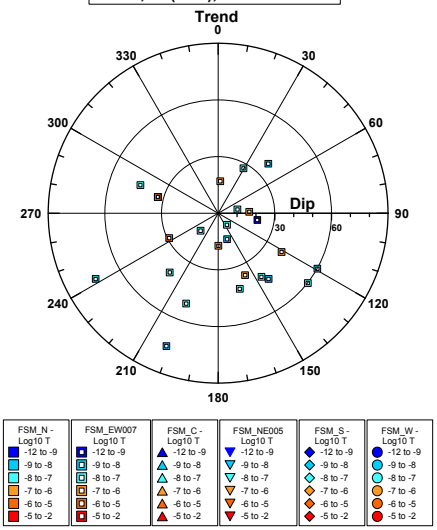

KLX04, DZ(RVS), ZONE: NW928A

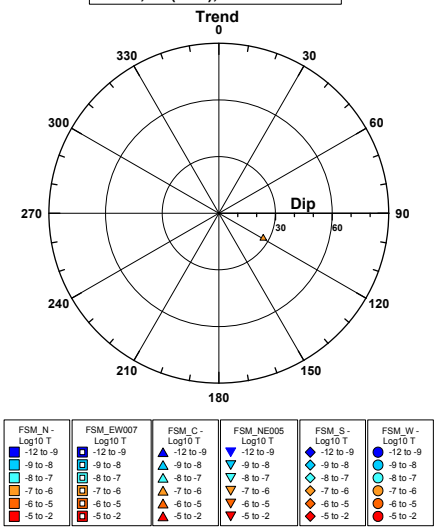

KLX04, DZ(RVS), ZONE: EW946A

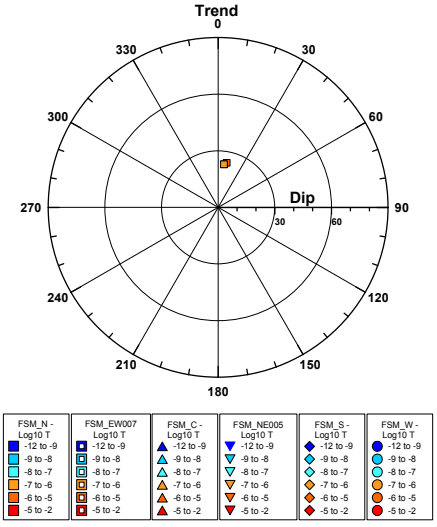

KLX04, DZ(RVS), ZONE: KLX04_DZ6b

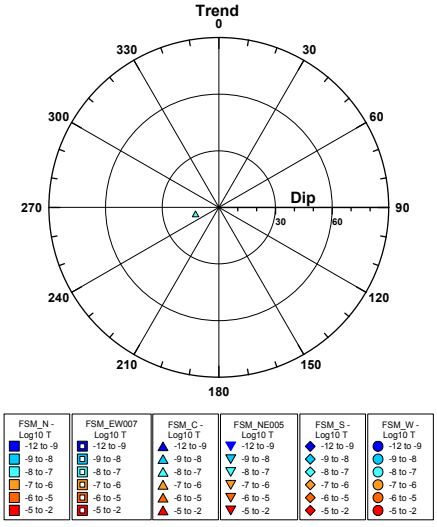

KLX04, DZ(RVS), ZONE: KLX04_DZ6c

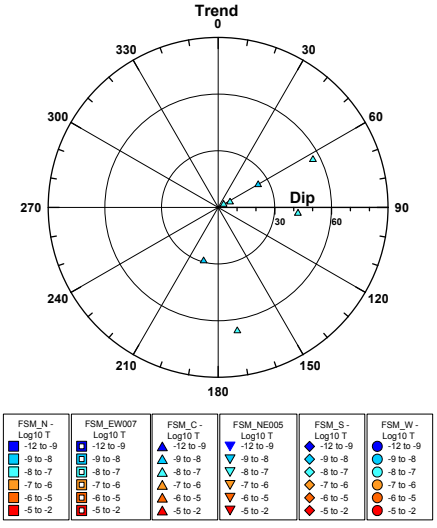

Borehole KLX05.

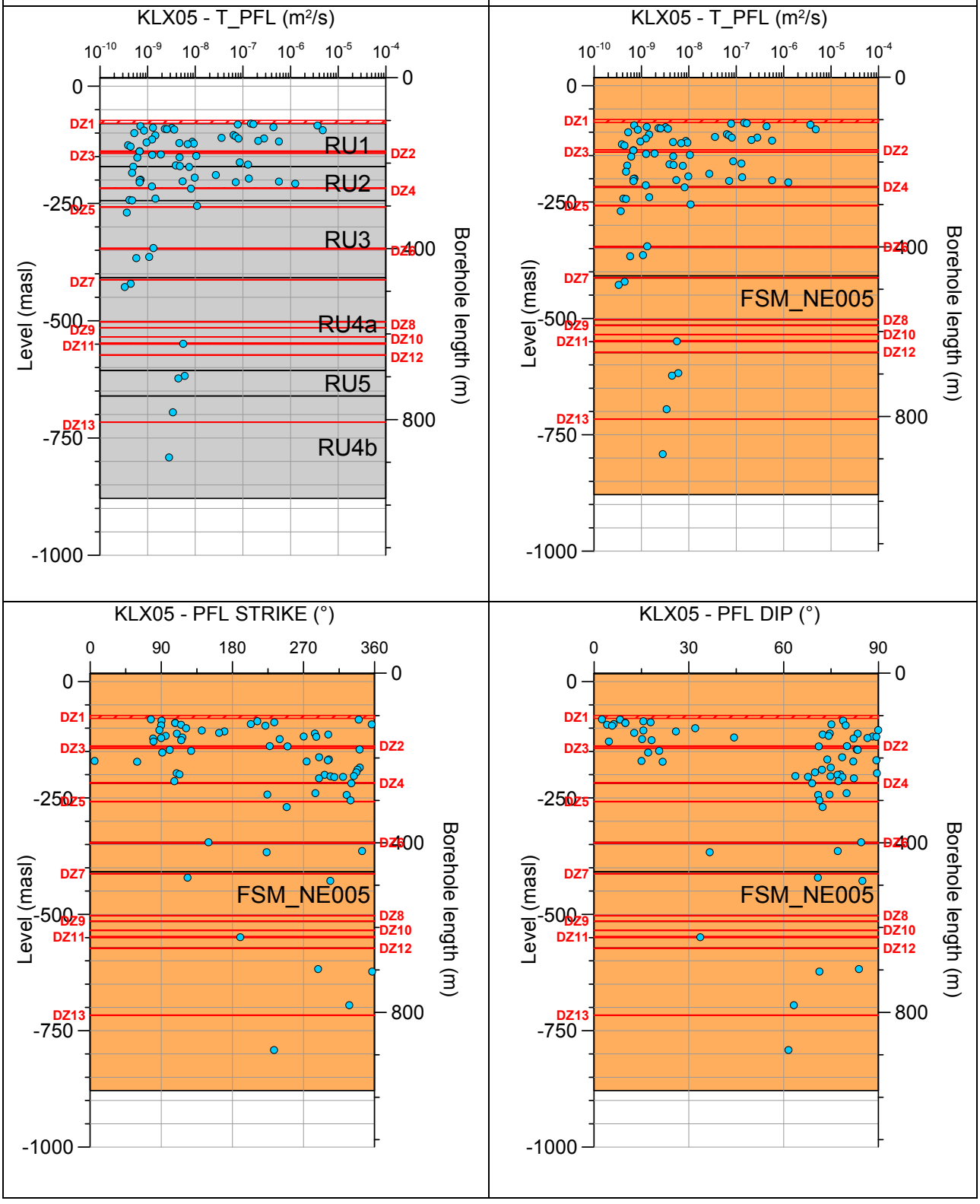

Comment:

Borehole KLX05. Poles for PFL-f feature planes outside deformation zones.

KLX05, HRD, ELEV.: 0 TO -1000 m

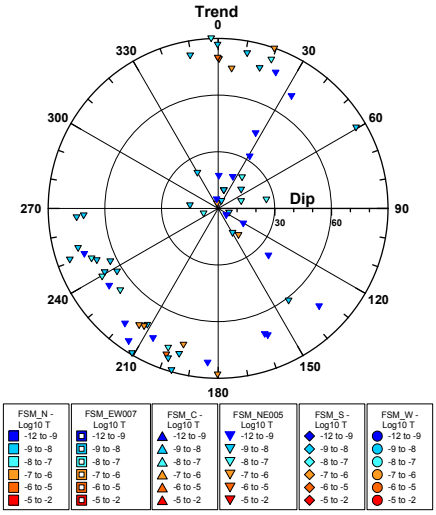

KLX05, HRD, ELEV.: 0 TO -200 m

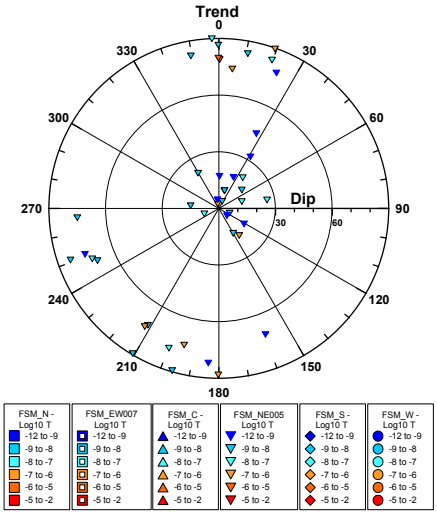

KLX05, HRD, ELEV.: -200 TO -400 m

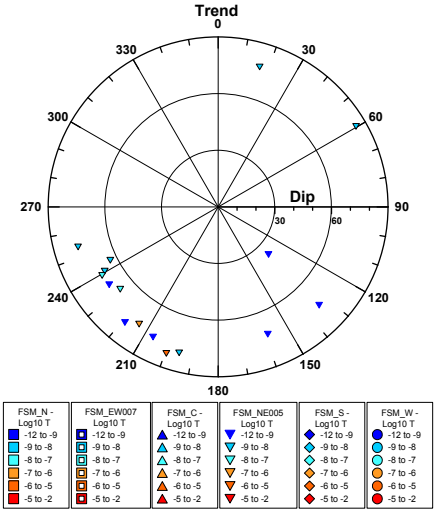

KLX05, HRD, ELEV.: -400 TO -600 m

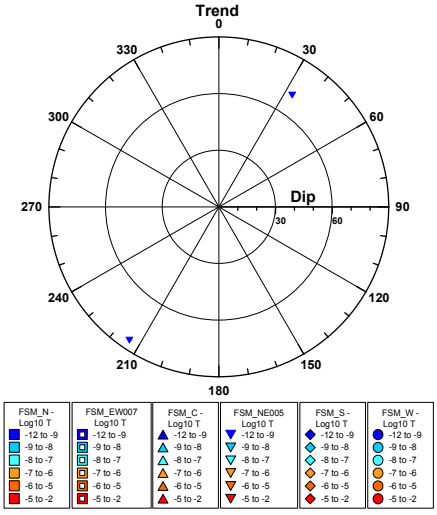

KLX05, HRD, ELEV.: -600 TO -800 m

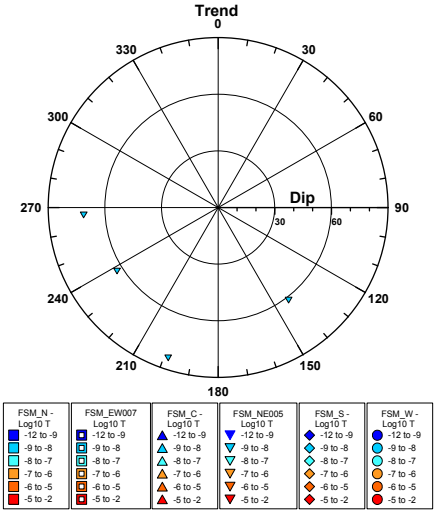

Borehole KLX05. Poles for PFL-f feature planes in possible deformation zones.

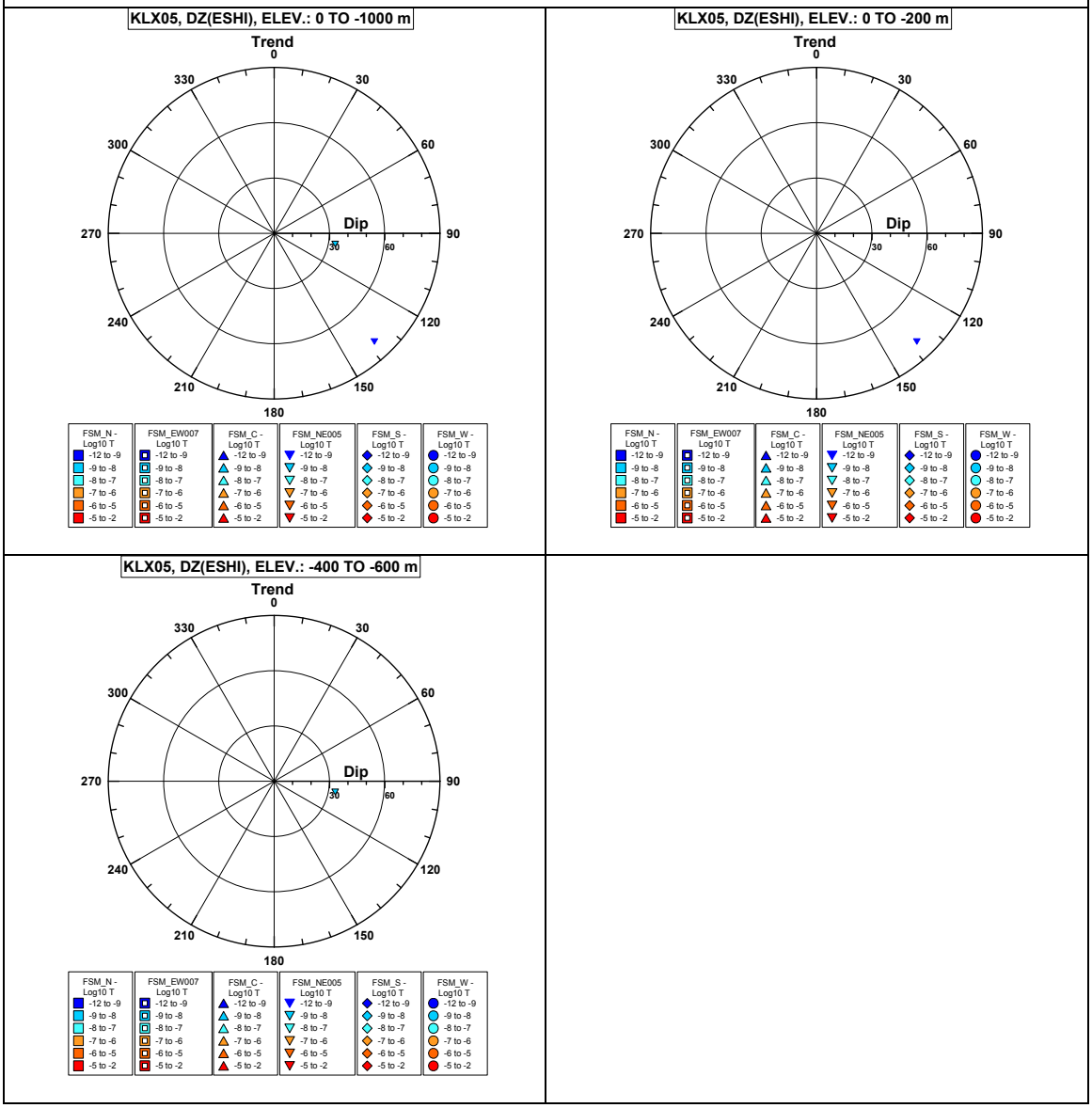

No PFL-f feature planes in deterministically modelled deformation zones exist in KLX05.

Borehole KLX06.

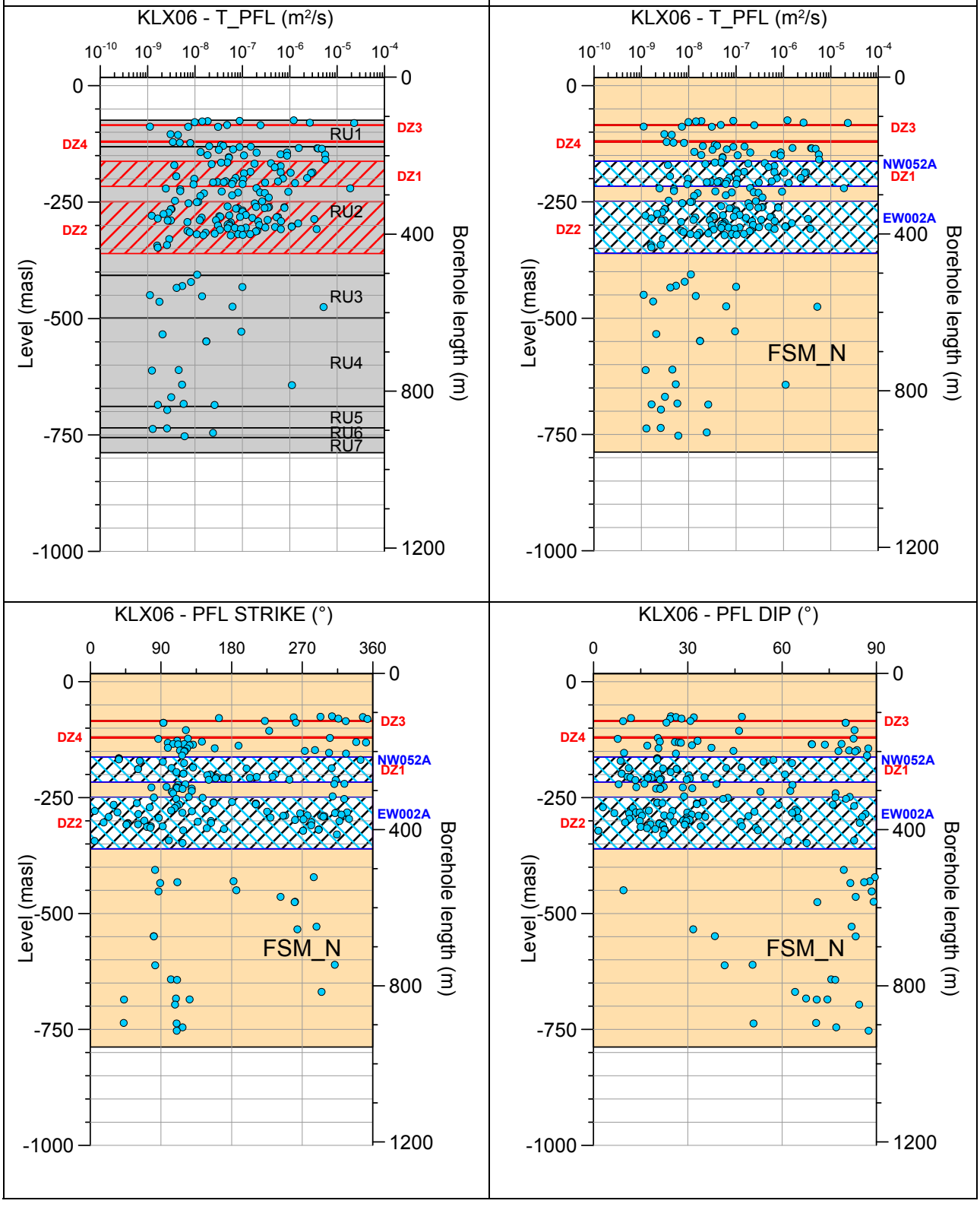

Comment:

Borehole KLX06. Poles for PFL-f feature planes outside deformation zones.

KLX06, HRD, ELEV.: 0 TO -1000 m

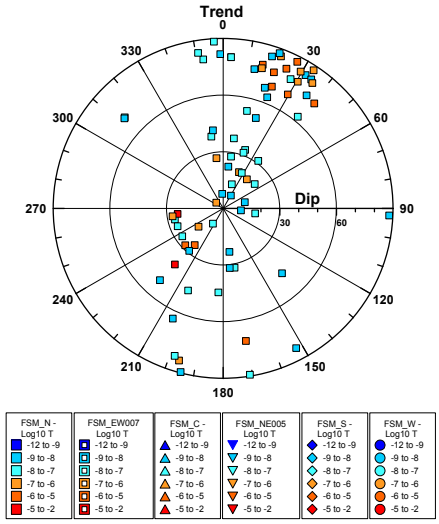

KLX06, HRD, ELEV.: 0 TO -200 m

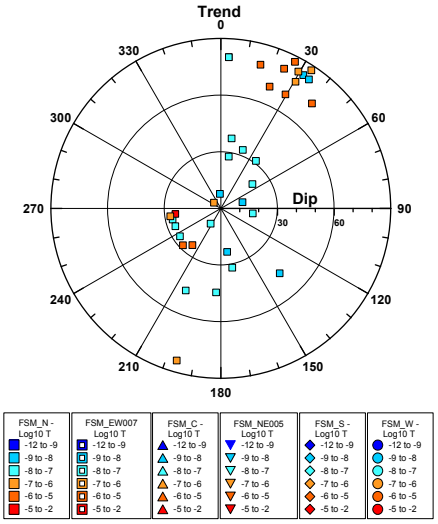

KLX06, HRD, ELEV.: -200 TO -400 m

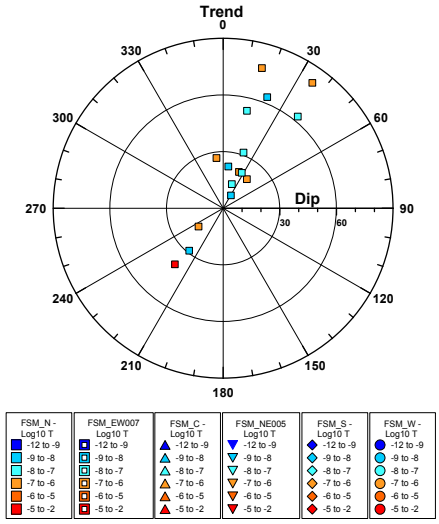

KLX06, HRD, ELEV.: -400 TO -600 m

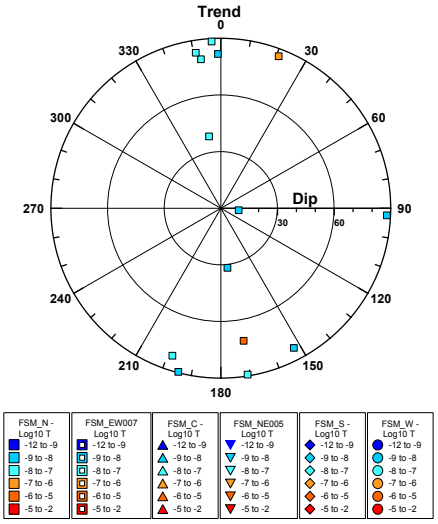

KLX06, HRD, ELEV.: -600 TO -800 m

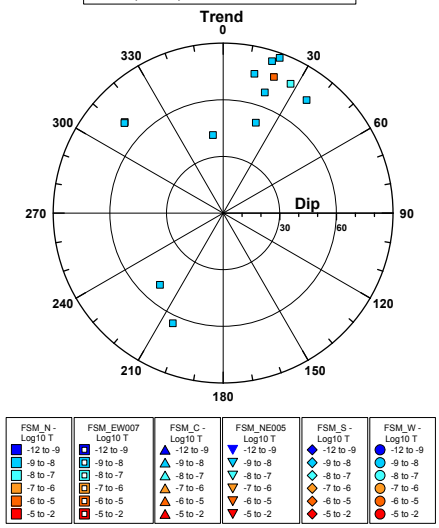

Borehole KLX06. Poles for PFL-f feature planes in possible deformation zones.

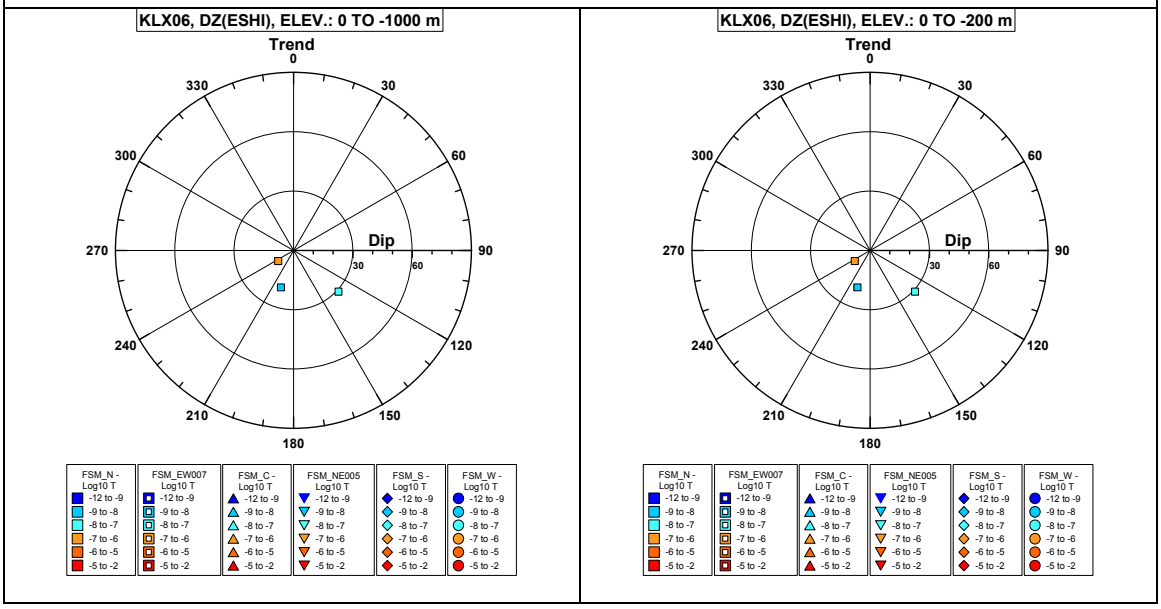

Borehole KLX06. Poles for PFL-f feature planes in deterministically modelled deformation zones.

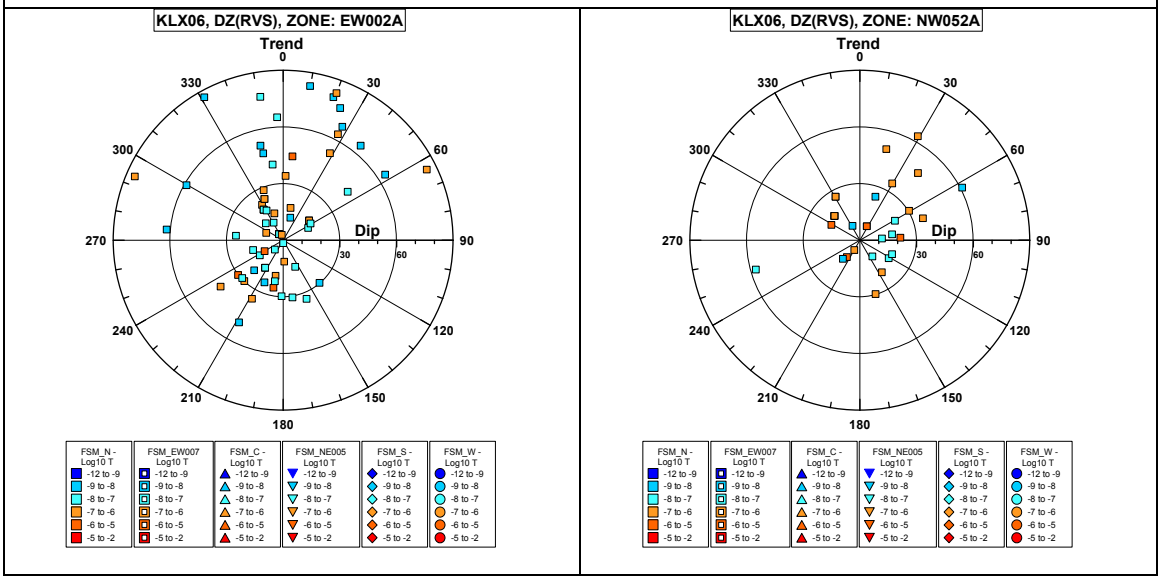

Borehole KLX07A.

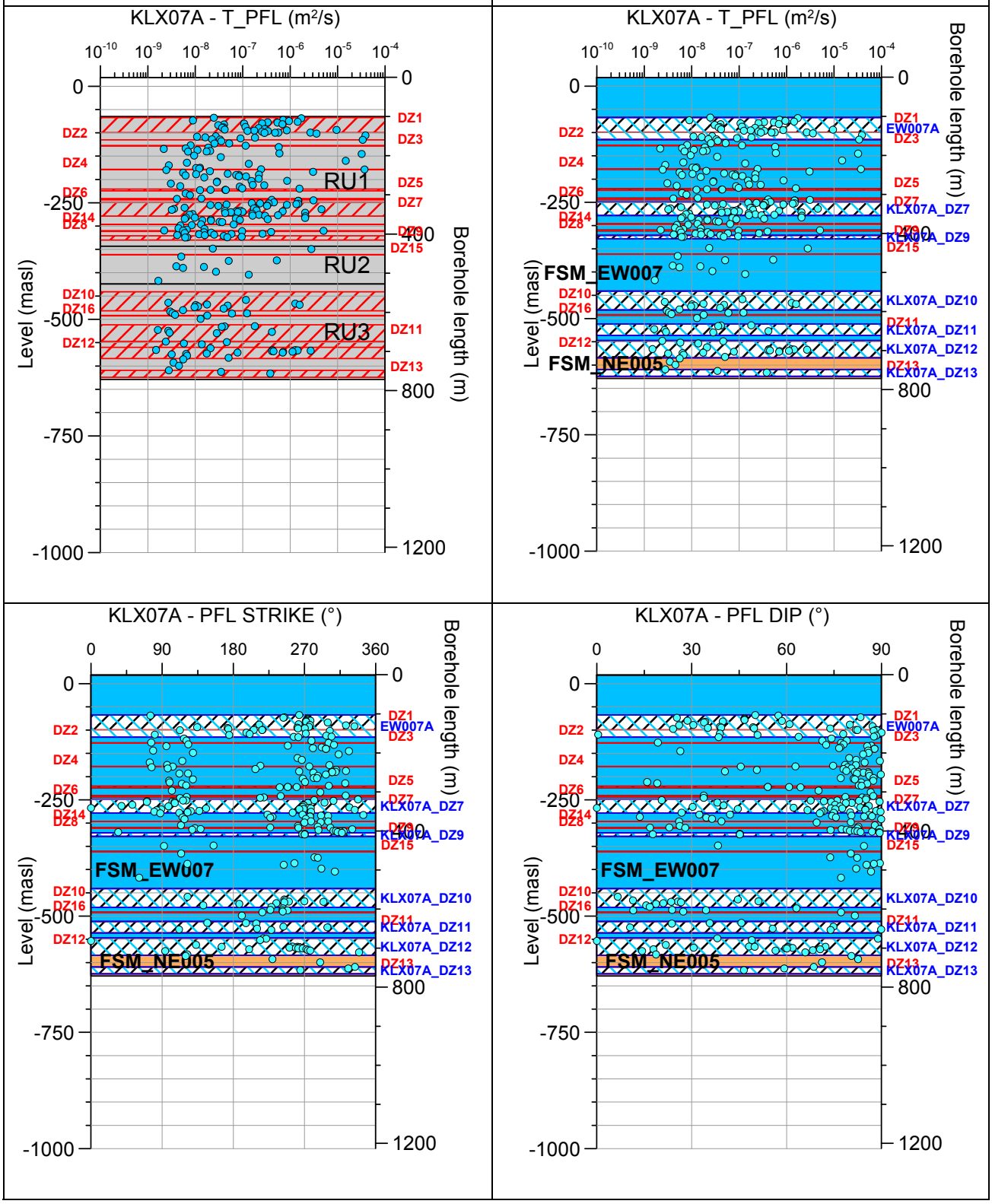

Comment:

Borehole KLX07A. Poles for PFL-f feature planes outside deformation zones.

KLX07A, HRD, ELEV.: 0 TO -1000 m

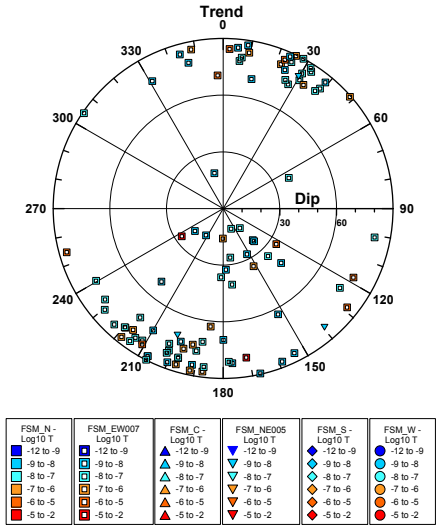

KLX07A, HRD, ELEV.: 0 TO -200 m

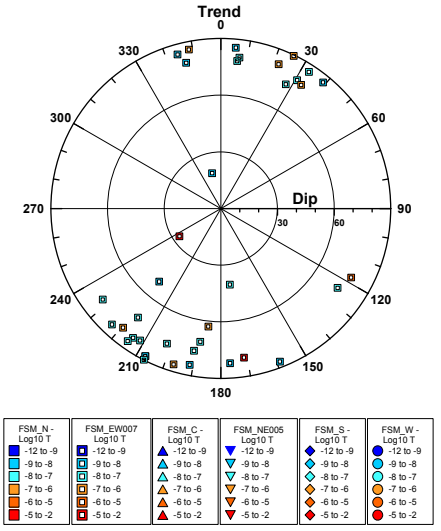

KLX07A, HRD, ELEV.: -200 TO -400 m

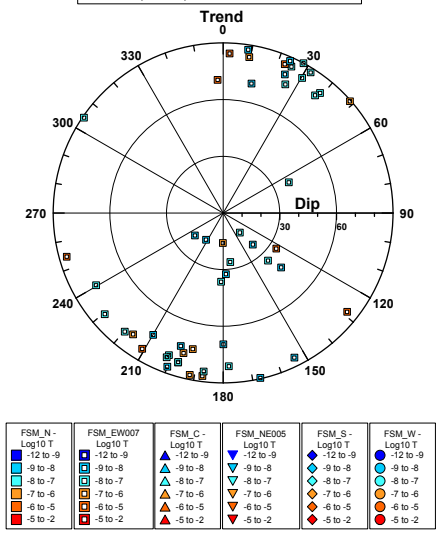

KLX07A, HRD, ELEV.: -400 TO -600 m

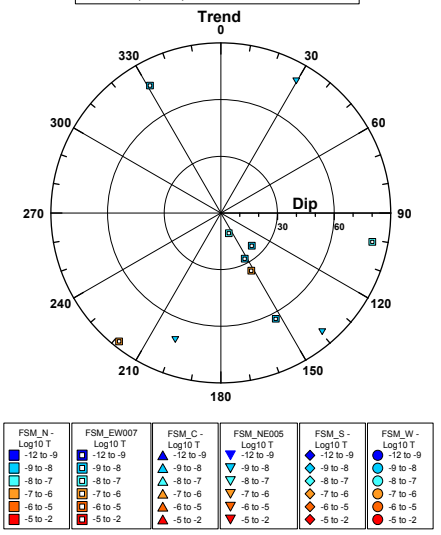

Borehole KLX07A. Poles for PFL-f feature planes in possible deformation zones.

KLX07A, DZ(ESHI), ELEV.: 0 TO -1000 m

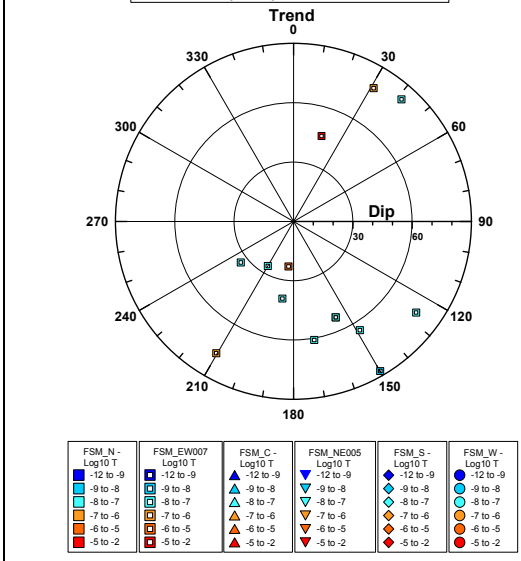

KLX07A, DZ(ESHI), ELEV.: 0 TO -200 m

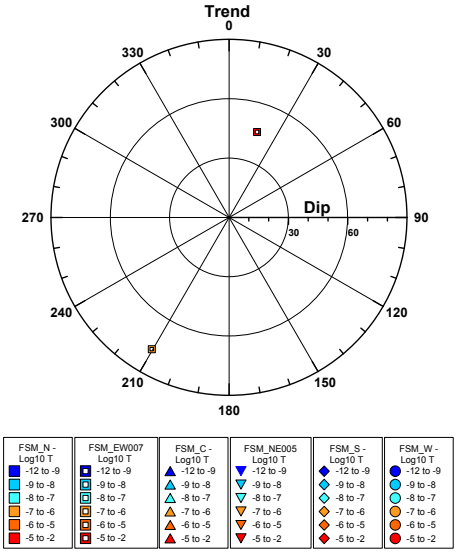

KLX07A, DZ(ESHI), ELEV.: -200 TO -400 m

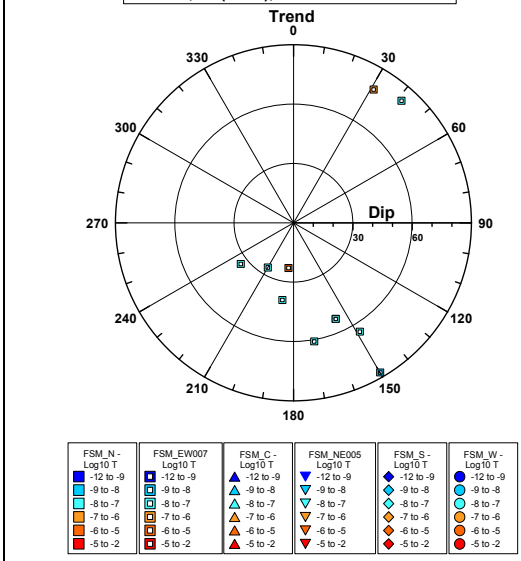

KLX07A, DZ(ESHI), ELEV.: -400 TO -600 m

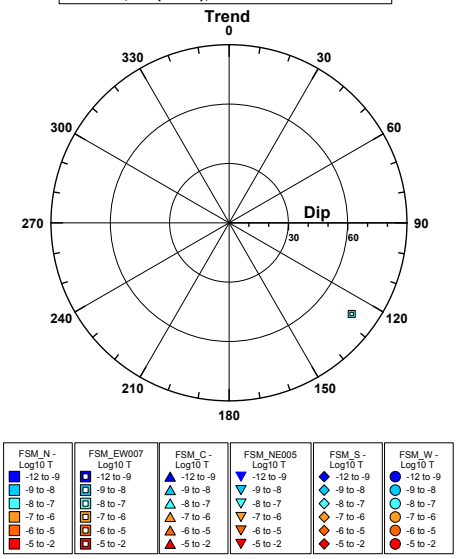

Borehole KLX07A. Poles for PFL-f feature planes in deterministically modelled deformation zones.

KLX07A, DZ(RVS), ZONE: EW007A

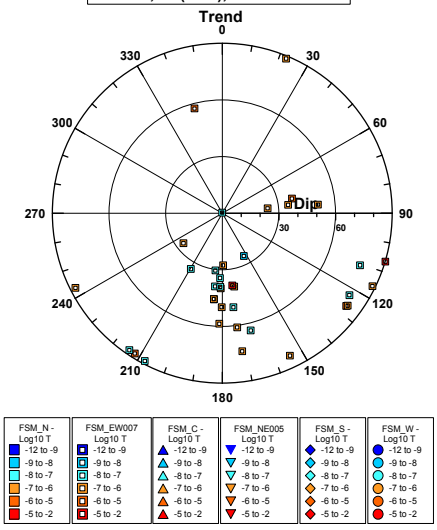

KLX07A, DZ(RVS), ZONE: KLX07A_DZ7

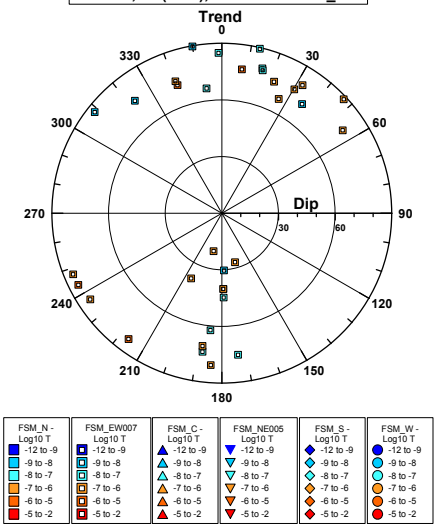

KLX07A, DZ(RVS), ZONE: KLX07A_DZ9

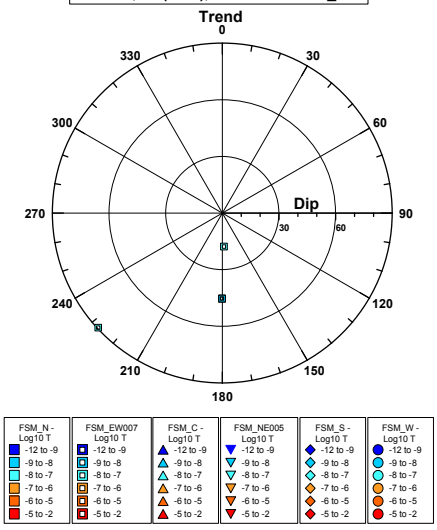

KLX07A, DZ(RVS), ZONE: KLX07A_DZ10

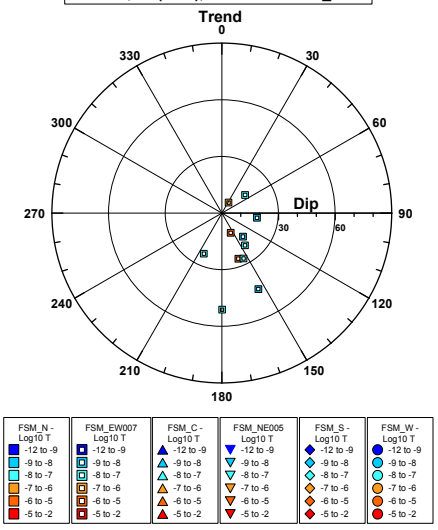

KLX07A, DZ(RVS), ZONE: KLX07A_DZ11

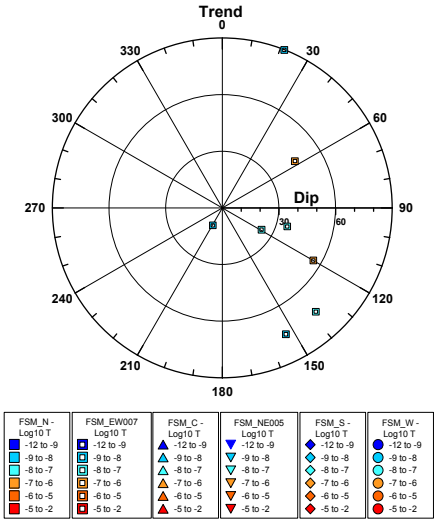

KLX07A, DZ(RVS), ZONE: KLX07A_DZ12

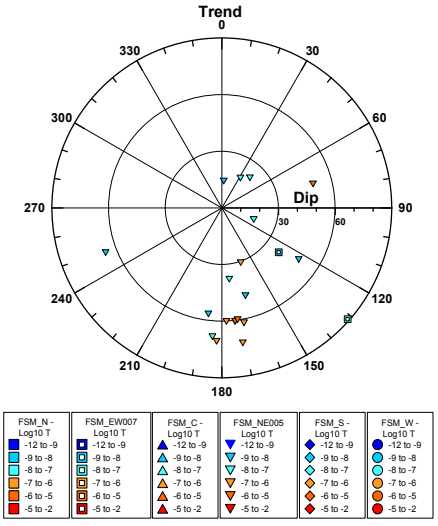

Borehole KLX07A. Poles for PFL-f feature planes in deterministically modelled deformation zones.

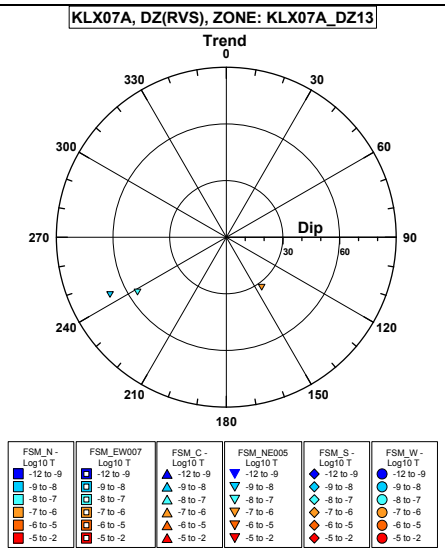

Borehole KLX07B.

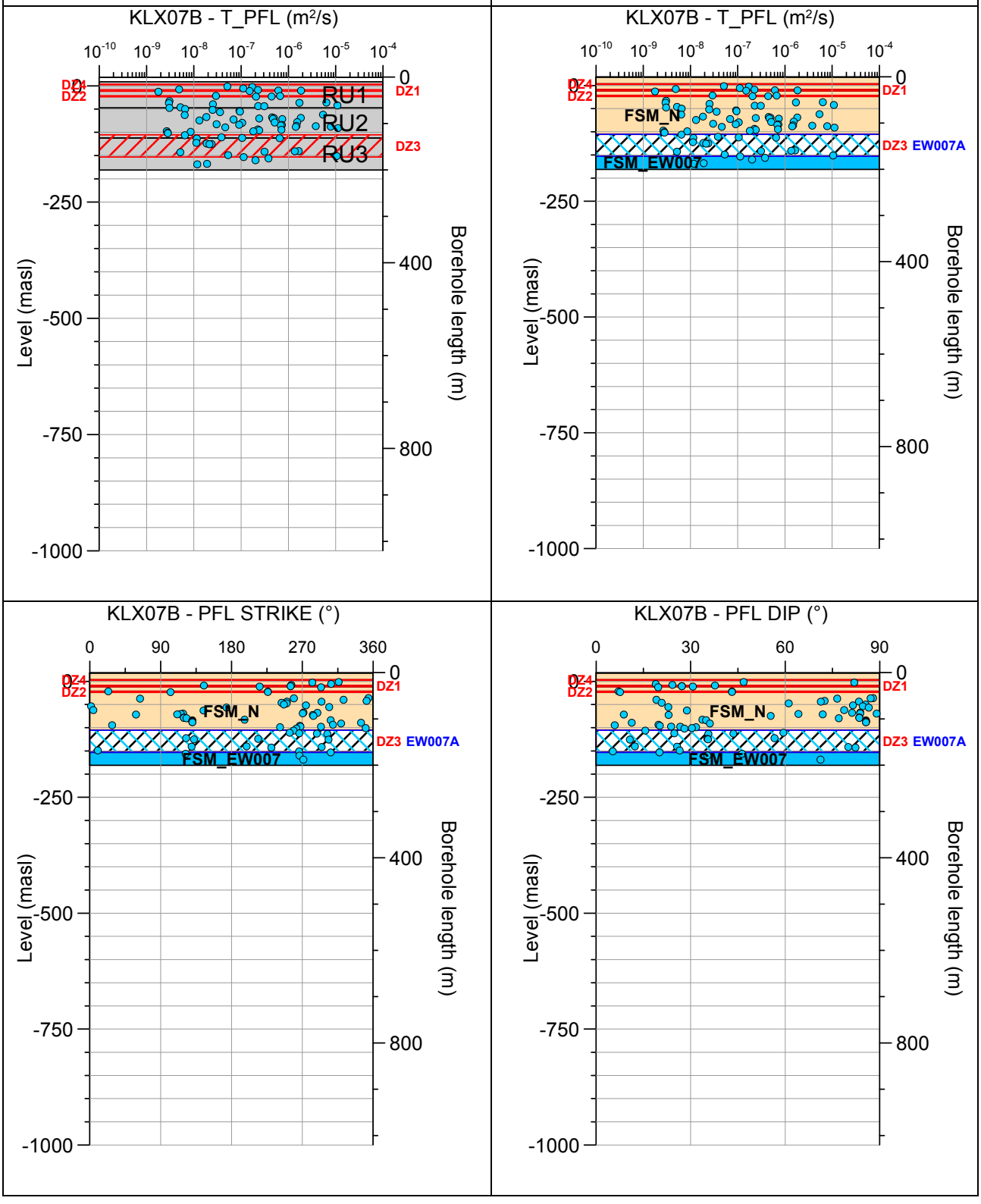

Comment:

Borehole KLX07B. Poles for PFL-f feature planes outside deformation zones.

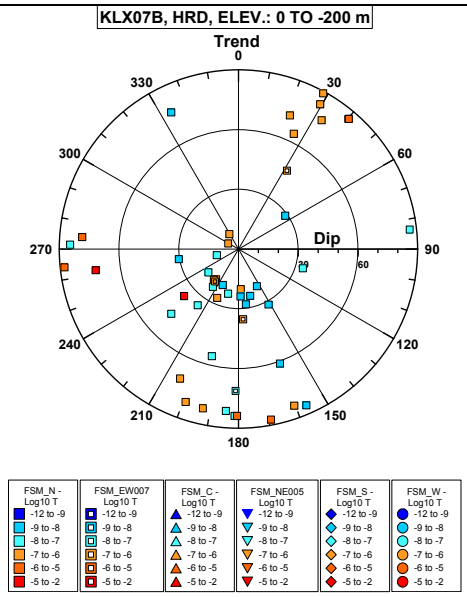

Borehole KLX07B. Poles for PFL-f feature planes in possible deformation zones.

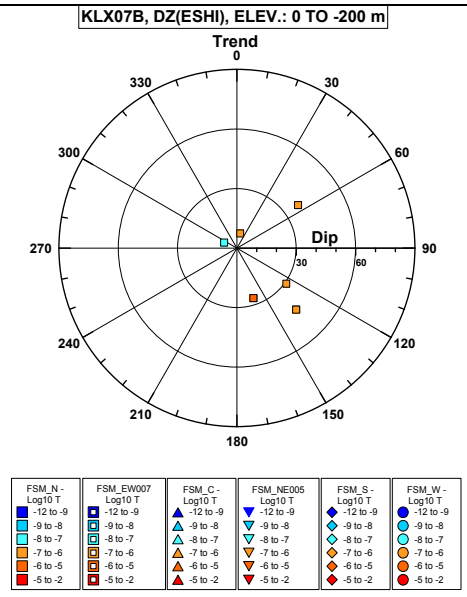

Borehole KLX07B. Poles for PFL-f feature planes in deterministically modelled deformation zones.

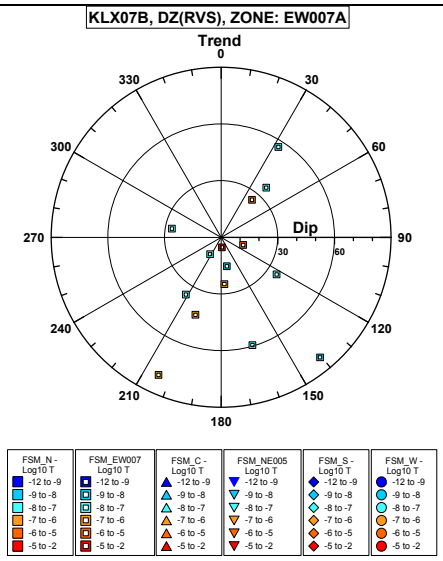

Borehole KLX08.

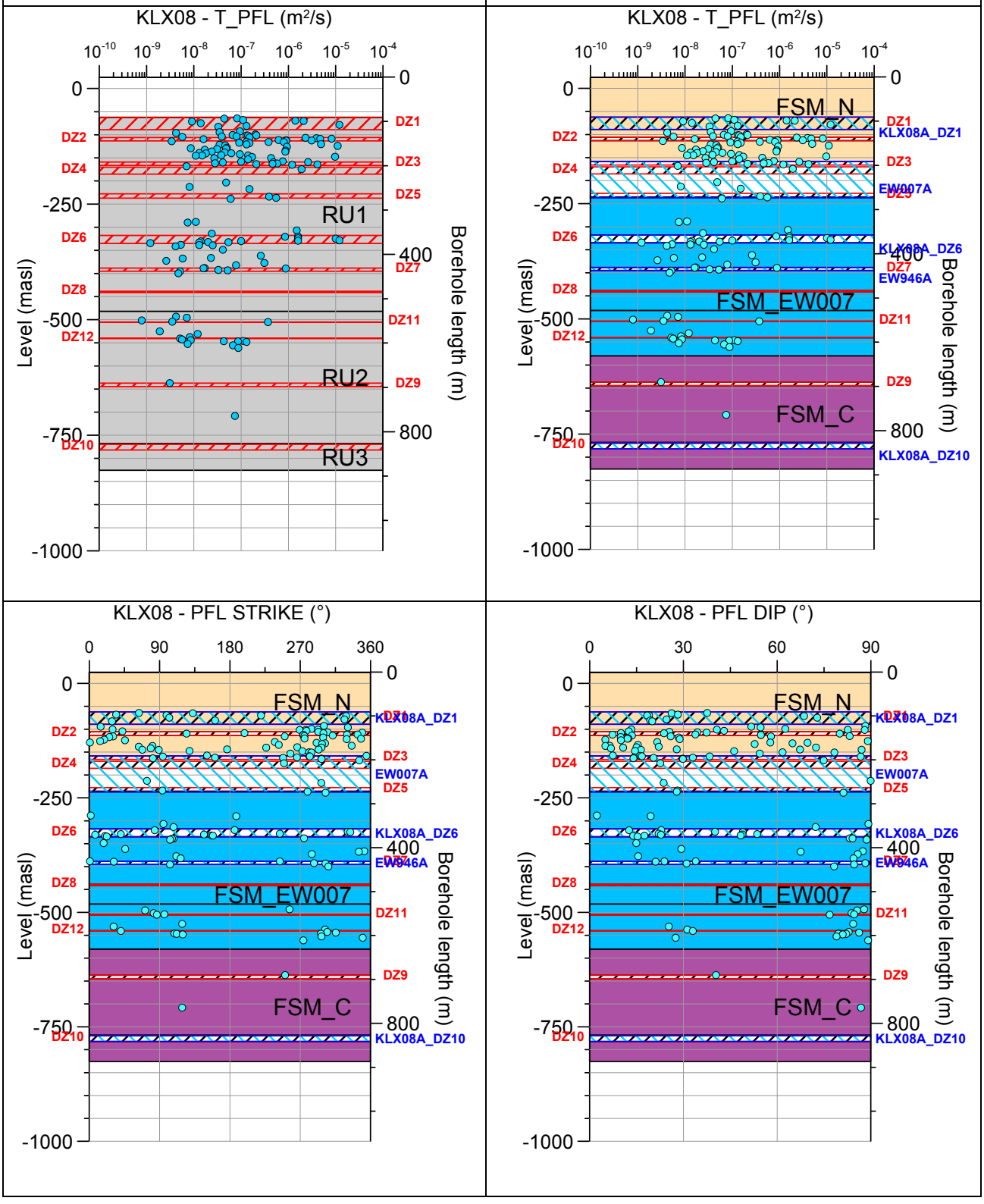

Comment:

Borehole KLX08. Poles for PFL-f feature planes outside deformation zones.

KLX08, HRD, ELEV.: 0 TO -1000 m

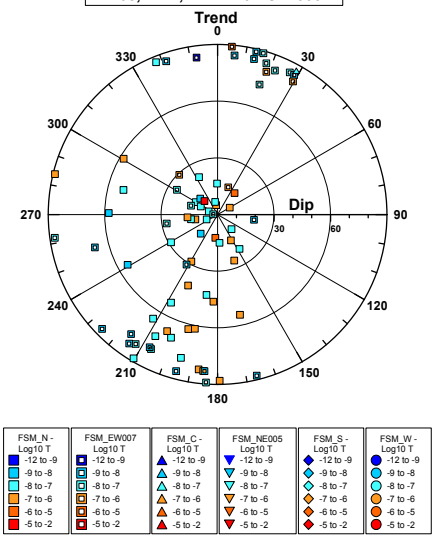

KLX08, HRD, ELEV.: 0 TO -200 m

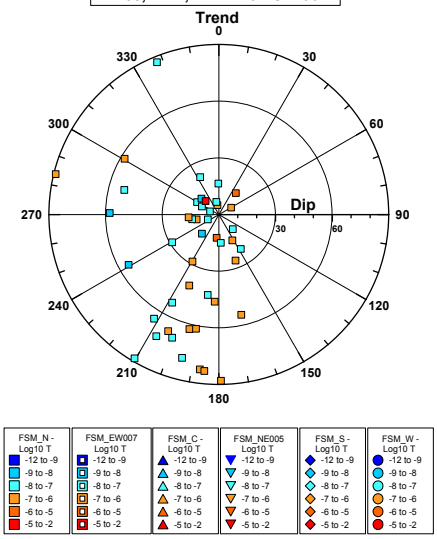

KLX08, HRD, ELEV.: -200 TO -400 m

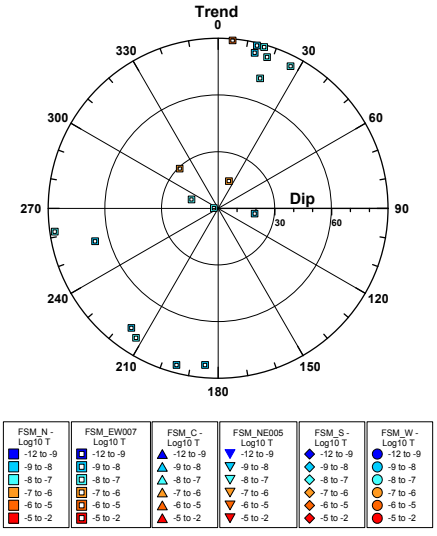

KLX08, HRD, ELEV.: -400 TO -600 m

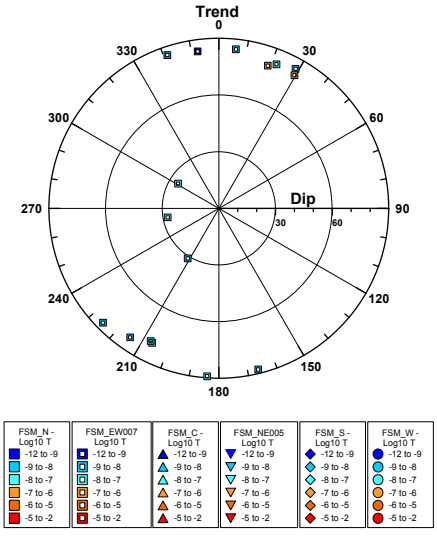

KLX08, HRD, ELEV.: -600 TO -800 m

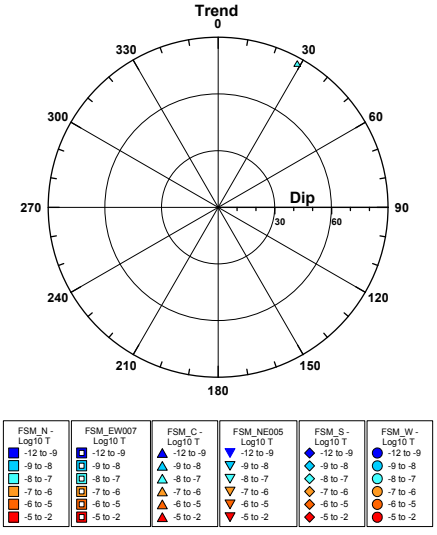

Borehole KLX08. Poles for PFL-f feature planes in possible deformation zones.

KLX08, DZ(ESHI), ELEV.: 0 TO -1000 m

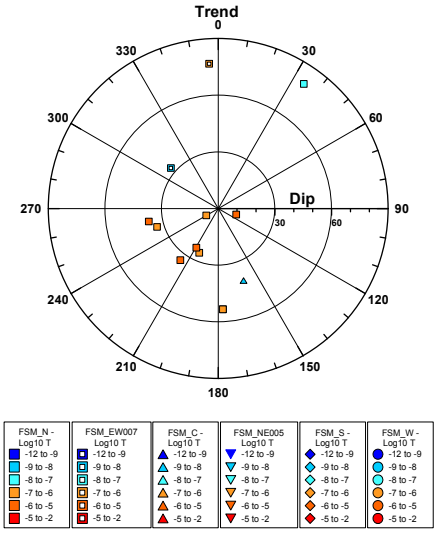

KLX08, DZ(ESHI), ELEV.: 0 TO -200 m

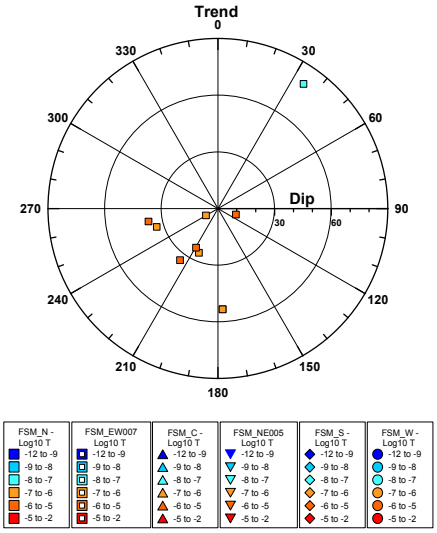

KLX08, DZ(ESHI), ELEV.: -200 TO -400 m

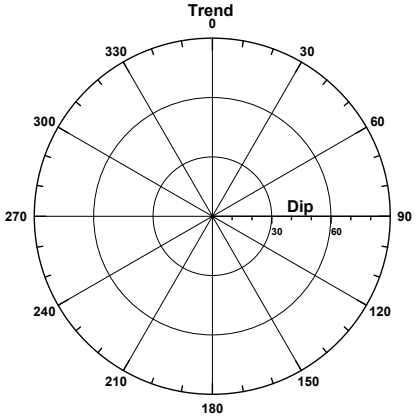

KLX08, DZ(ESHI), ELEV.: -400 TO -600 m

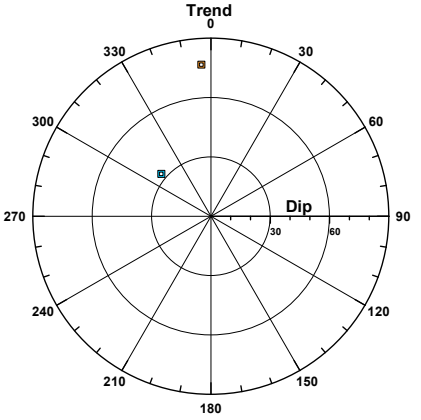

KLX08, DZ(ESHI), ELEV.: -600 TO -800 m

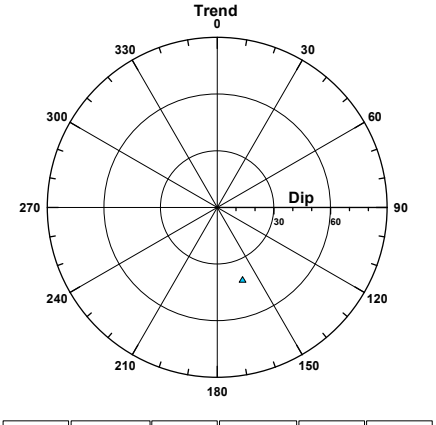

Borehole KLX08. Poles for PFL-f feature planes in deterministically modelled deformation zones.

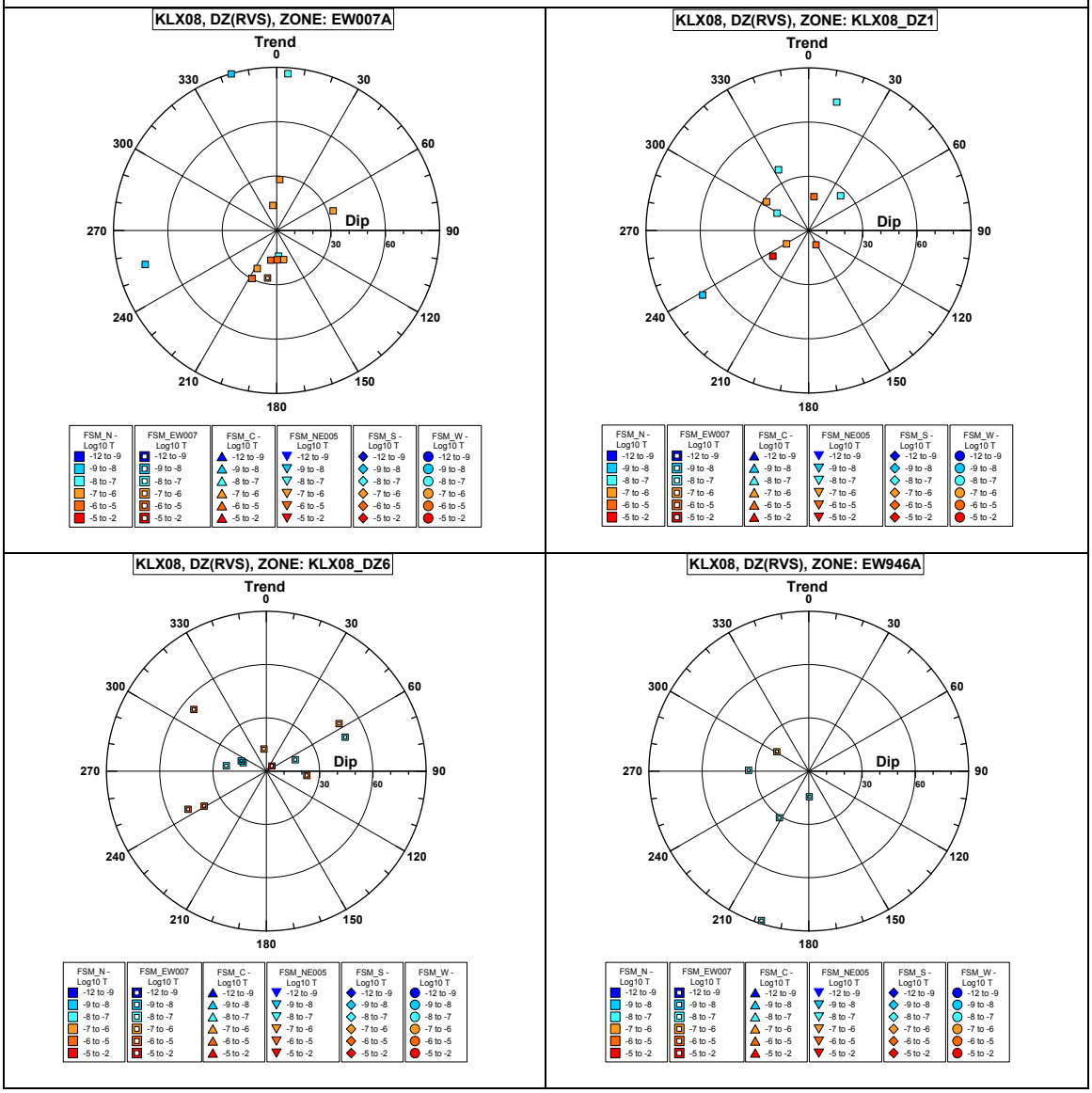

Borehole KLX09.

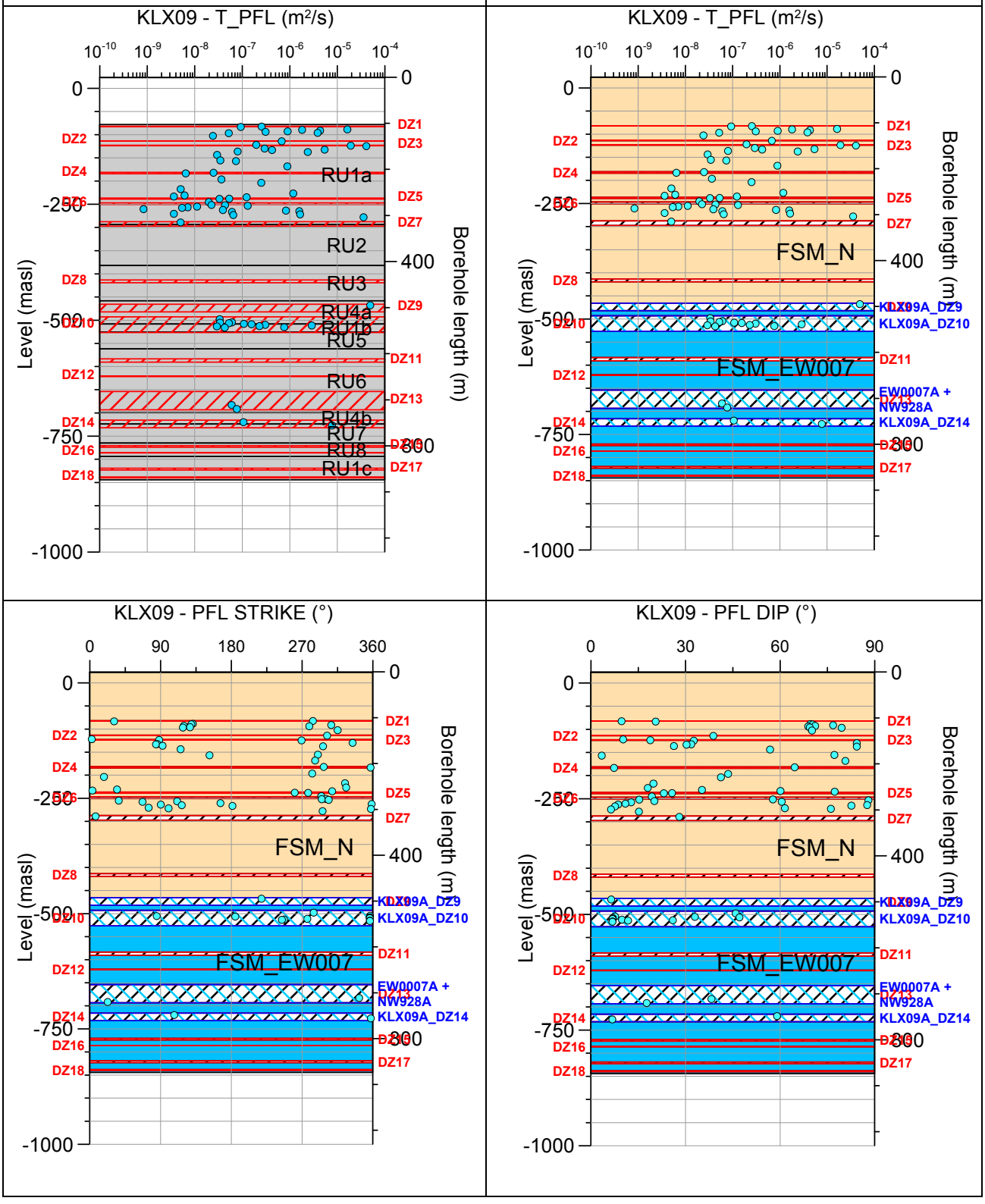

Comment:

Borehole KLX09. Poles for PFL-f feature planes outside deformation zones.

KLX09, HRD, ELEV.: 0 TO -1000 m

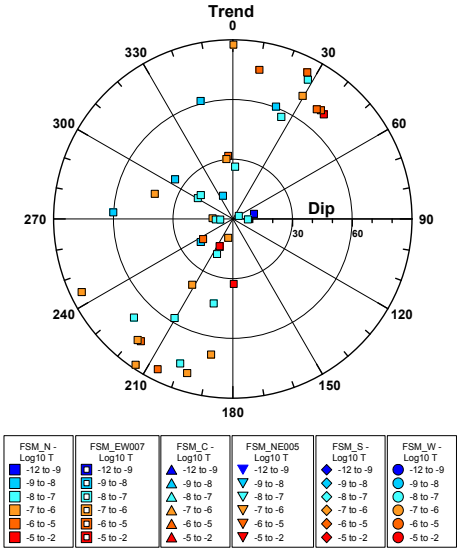

KLX09, HRD, ELEV.: 0 TO -200 m

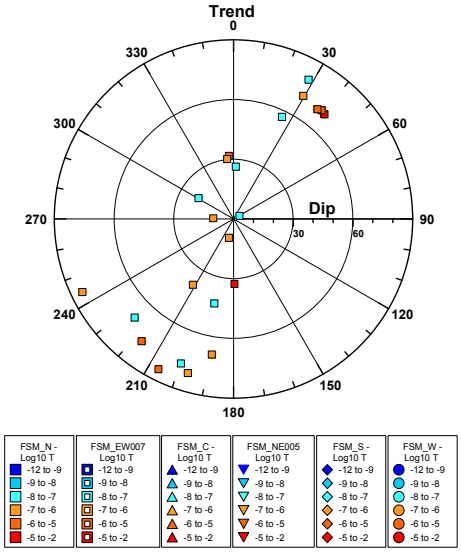

KLX09, HRD, ELEV.: -200 TO -400 m

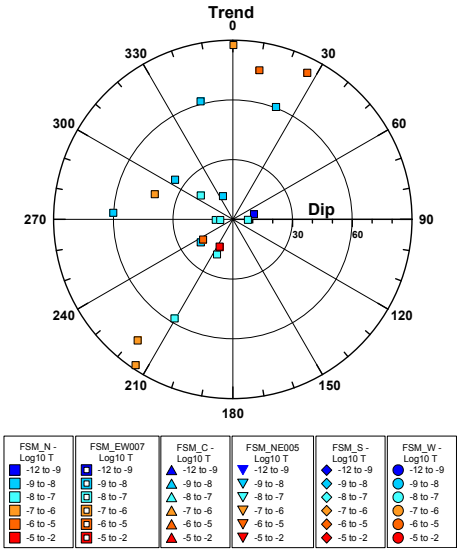

Borehole KLX09. Poles for PFL-f feature planes in possible deformation zones.

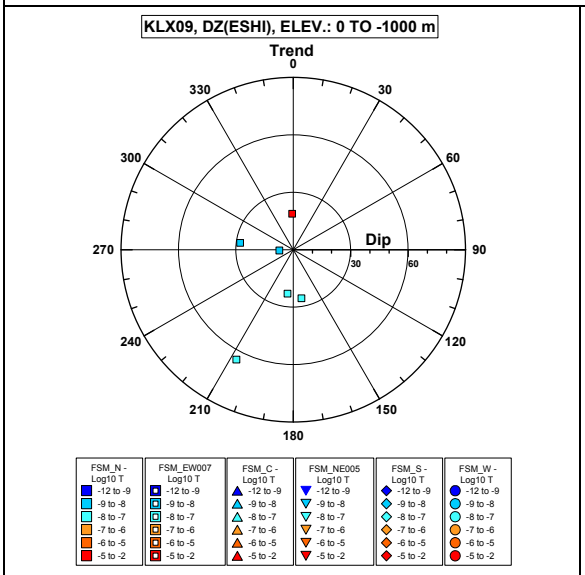

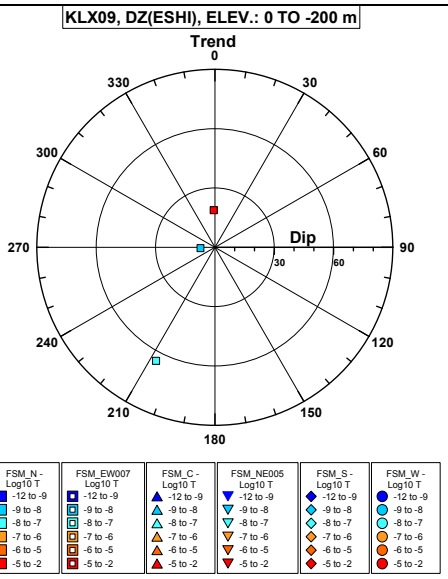

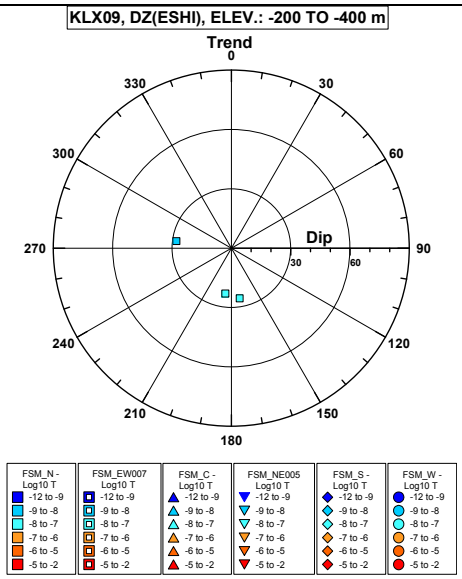

Borehole KLX09. Poles for PFL-f feature planes in deterministically modelled deformation zones.

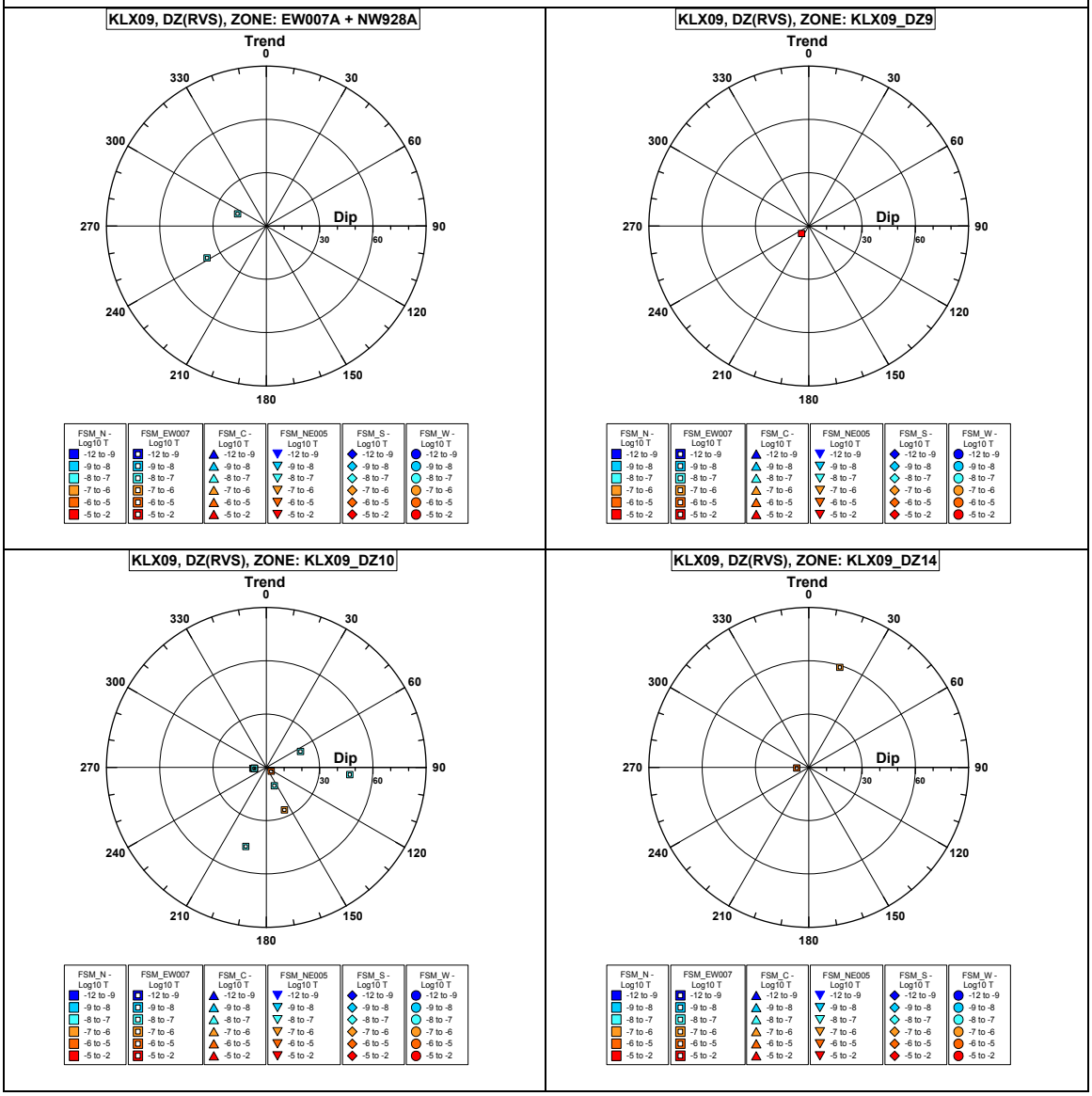

Borehole KLX09B.

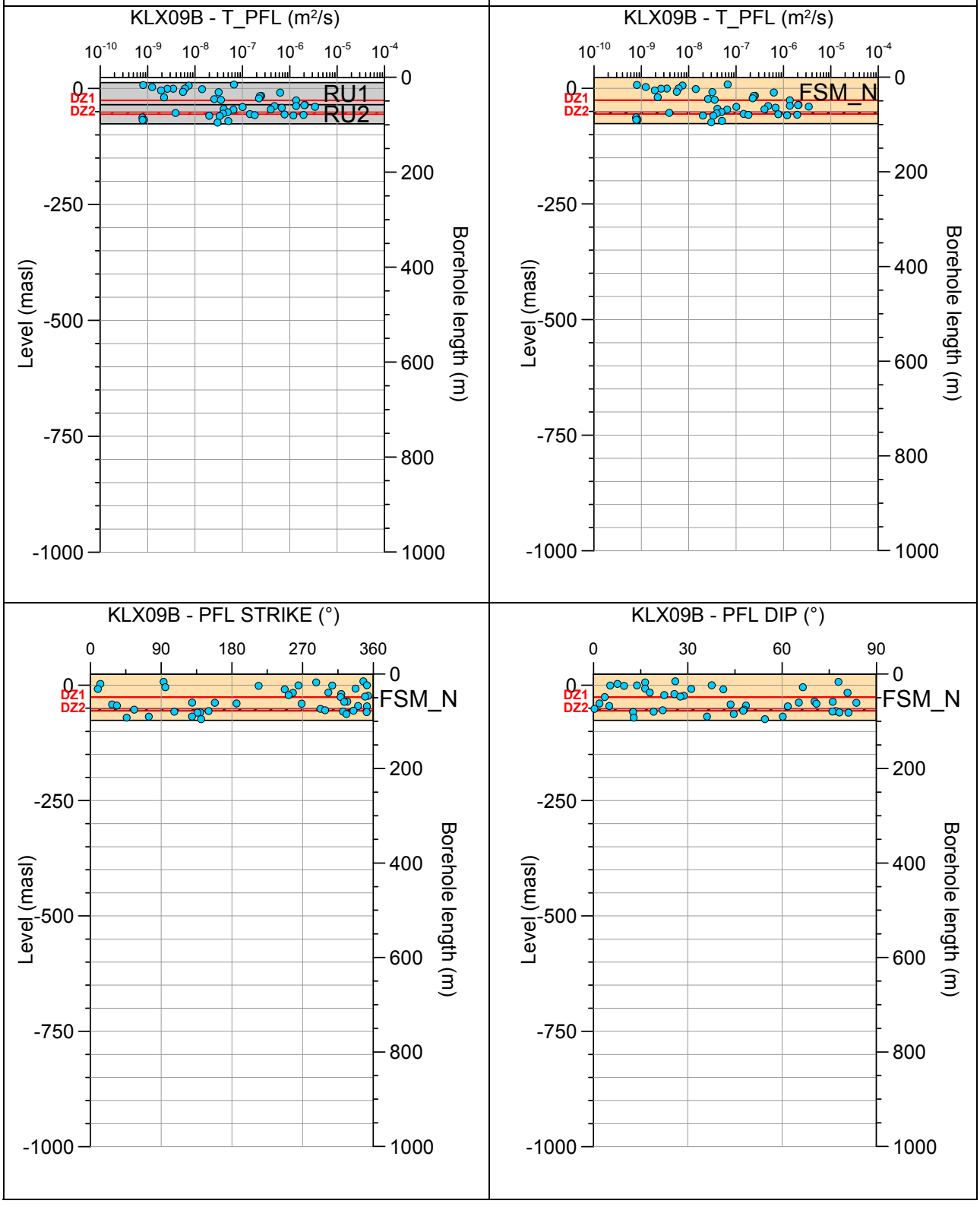

Comment:

Borehole KLX09B. Poles for PFL-f feature planes outside deformation zones.

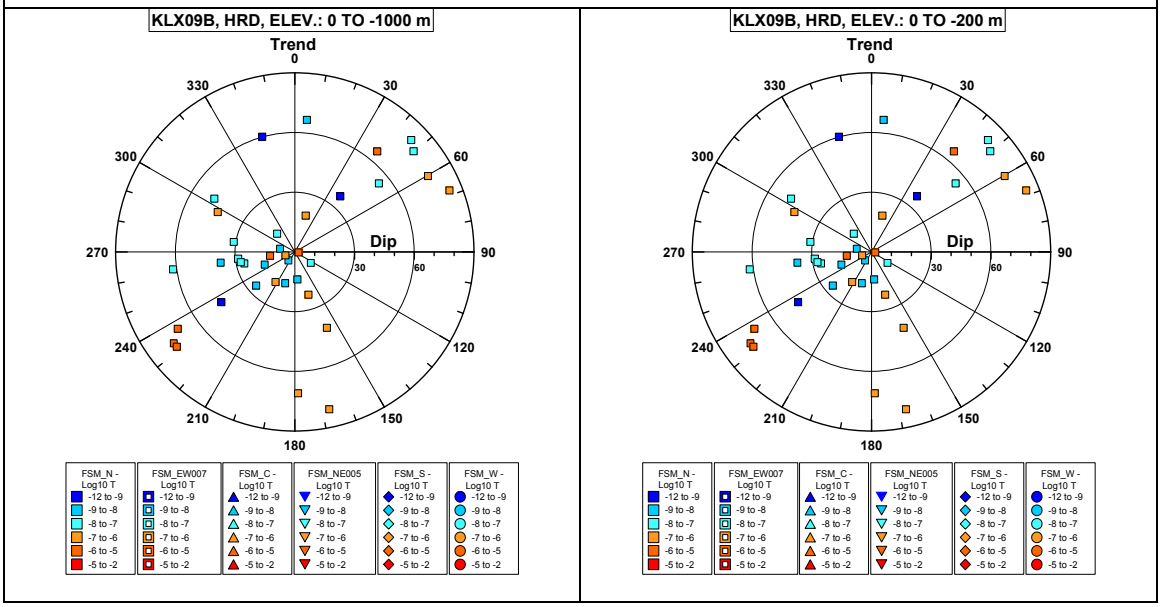

Borehole KLX09B. Poles for PFL-f feature planes in possible deformation zones.

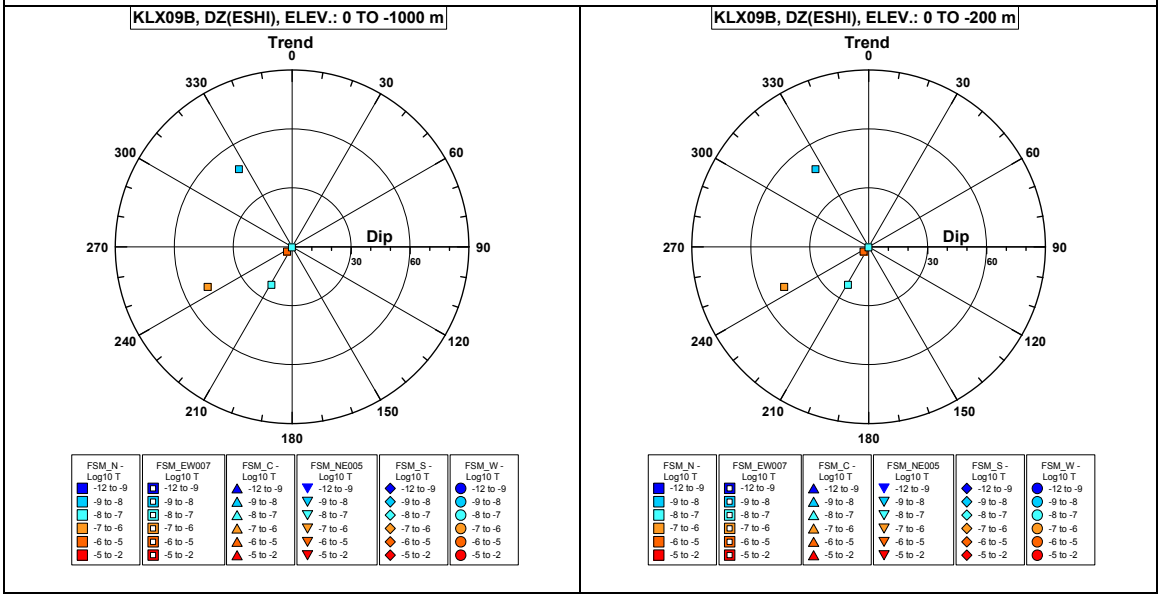

No PFL-f feature planes in deterministically modelled deformation zones exist in KLX09B.

Borehole KLX09C.

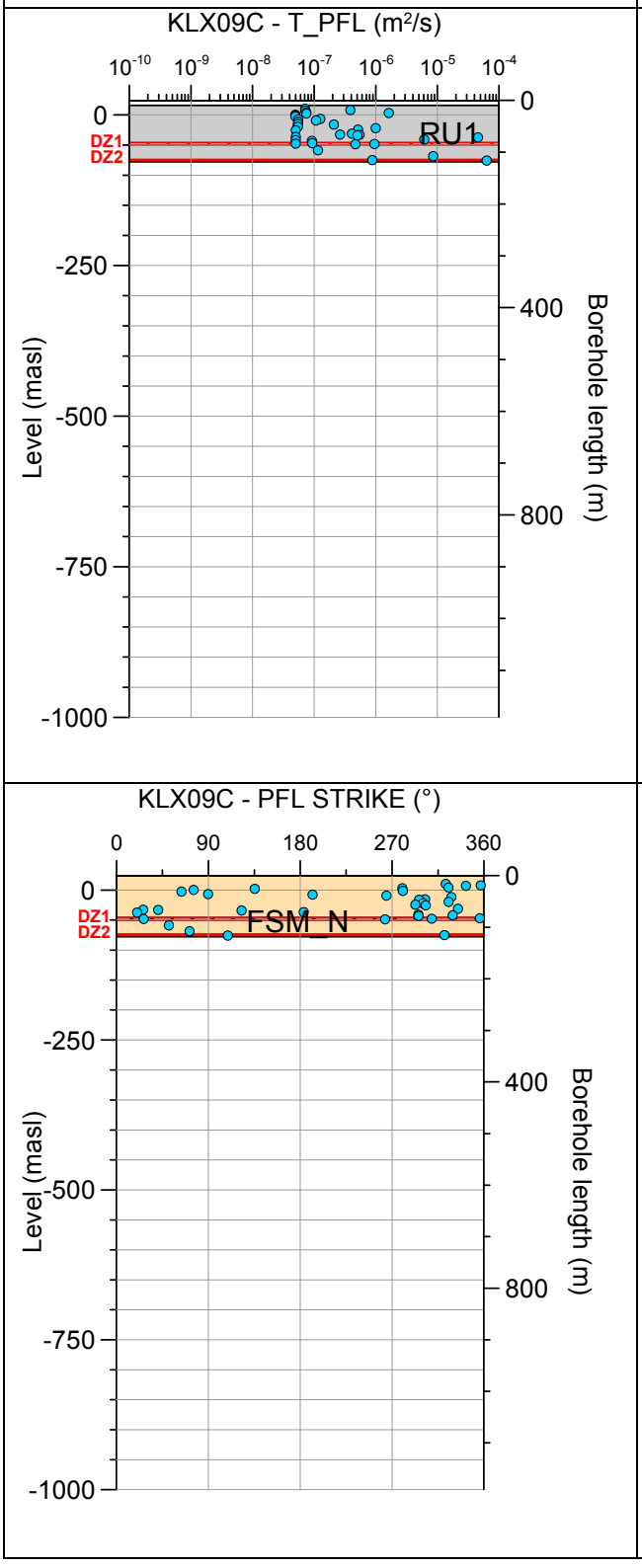

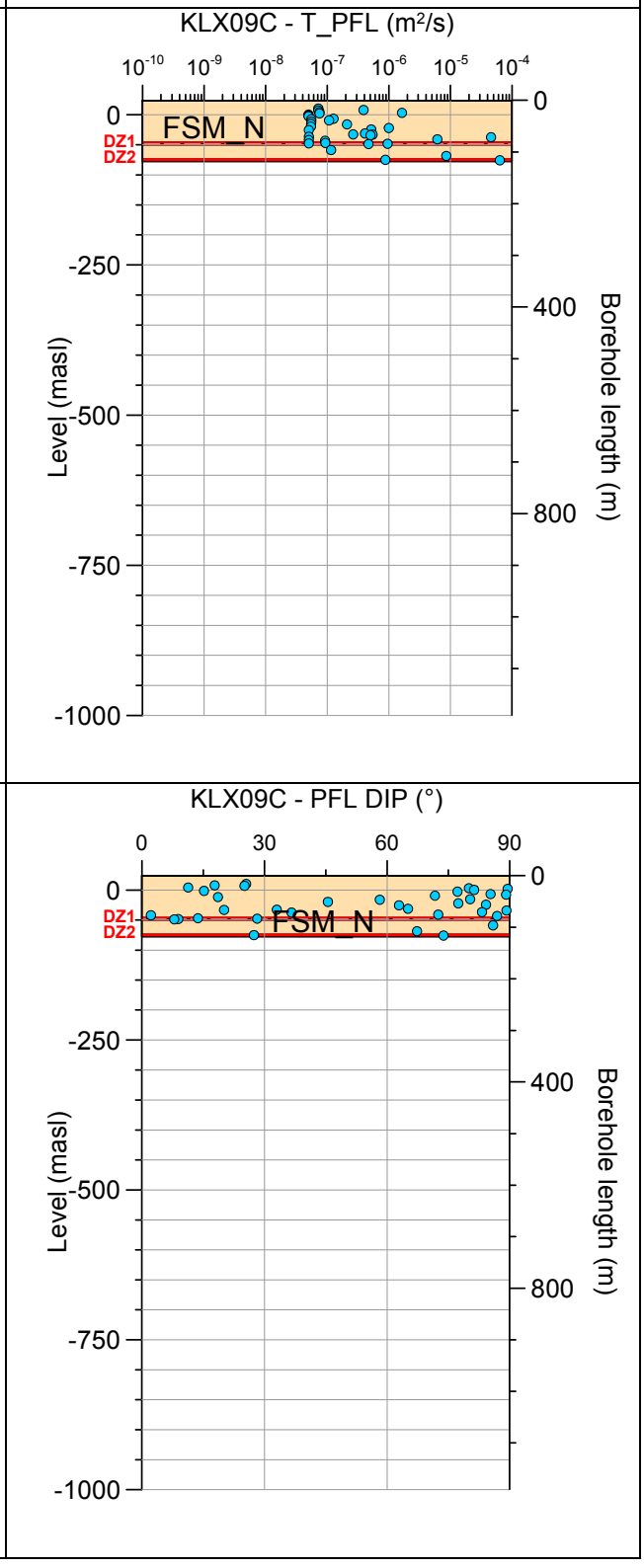

Comment:

Borehole KLX09C. Poles for PFL-f feature planes outside deformation zones.

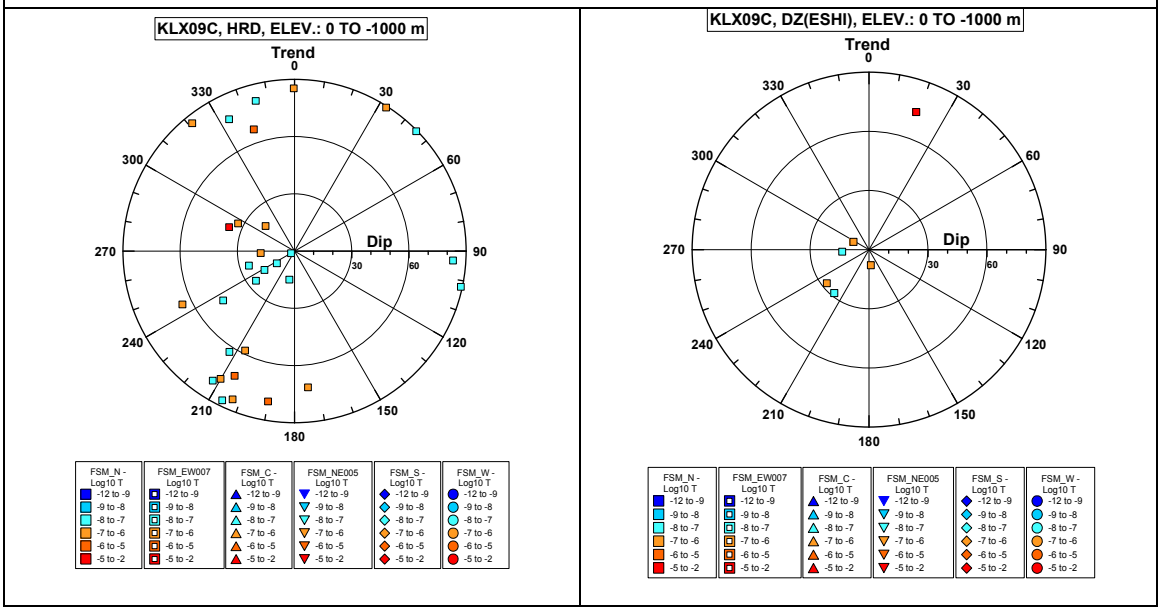

Borehole KLX09C. Poles for PFL-f feature planes in possible deformation zones.

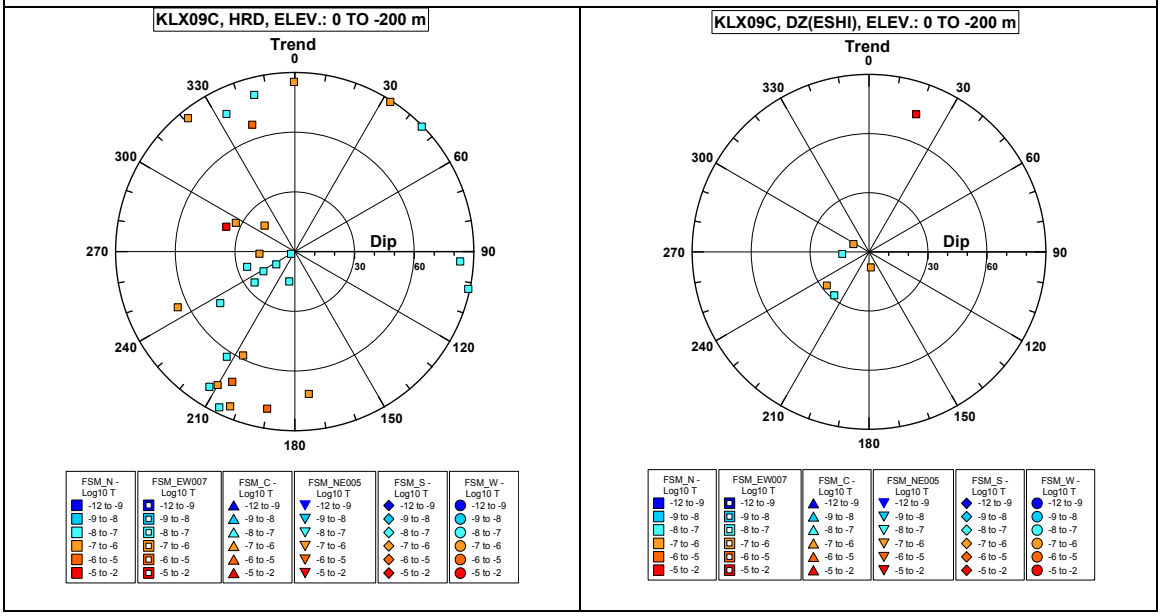

No PFL-f feature planes in deterministically modelled deformation zones exist in KLX09C.

Borehole KLX09D.

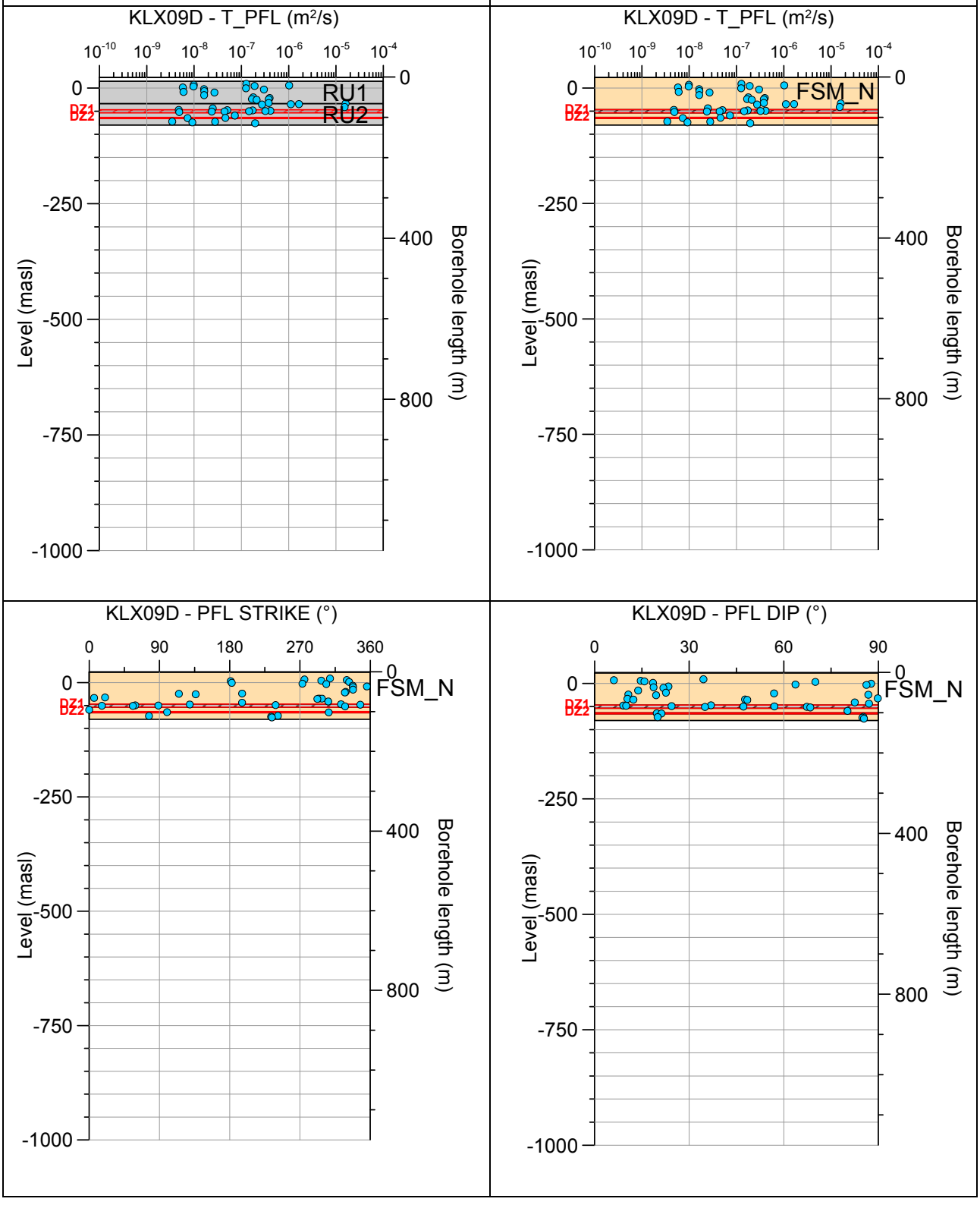

Comment:

Borehole KLX09D. Poles for PFL-f feature planes outside deformation zones.

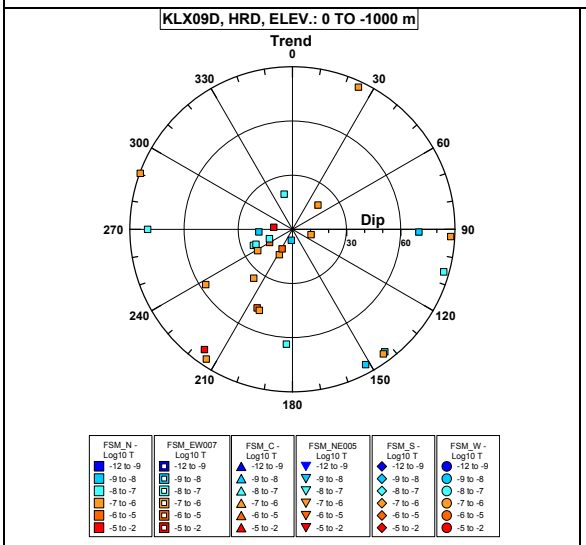

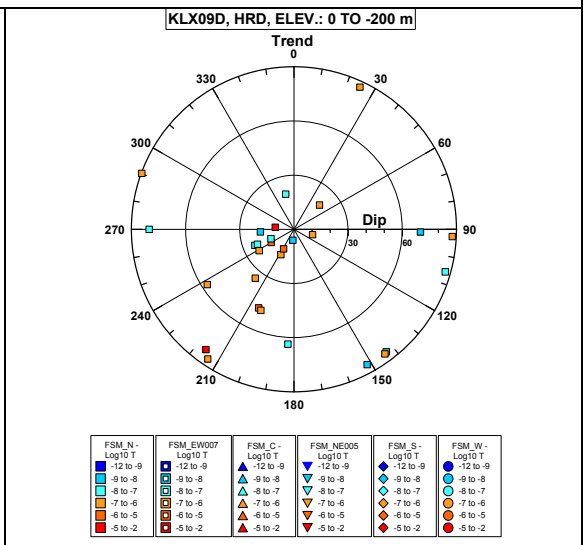

Borehole KLX09D. Poles for PFL-f feature planes in possible deformation zones.

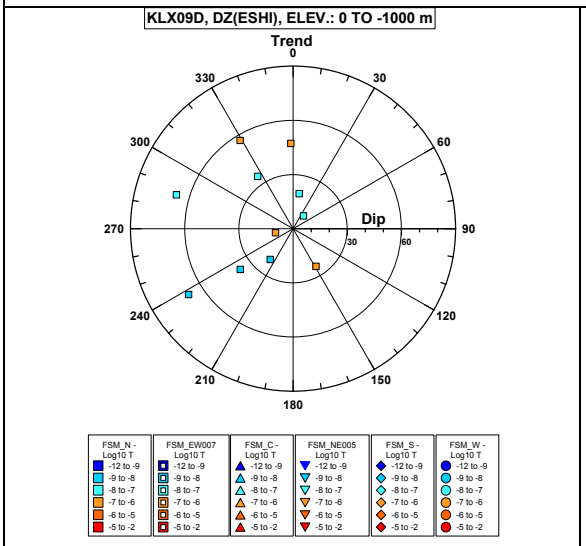

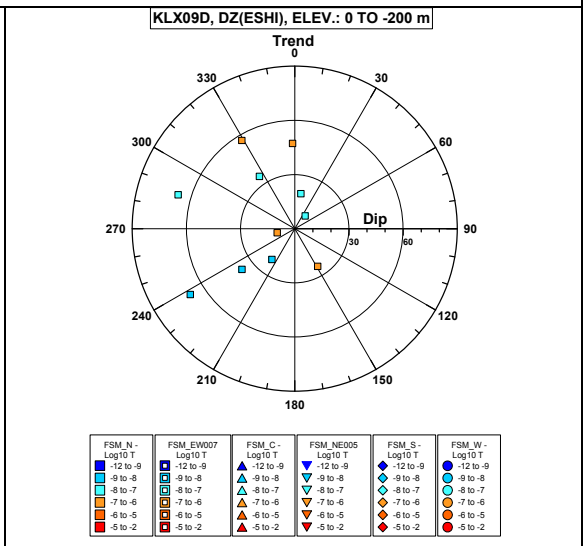

No PFL-f feature planes in deterministically modelled deformation zones exist in KLX09D.

Borehole KLX09E.

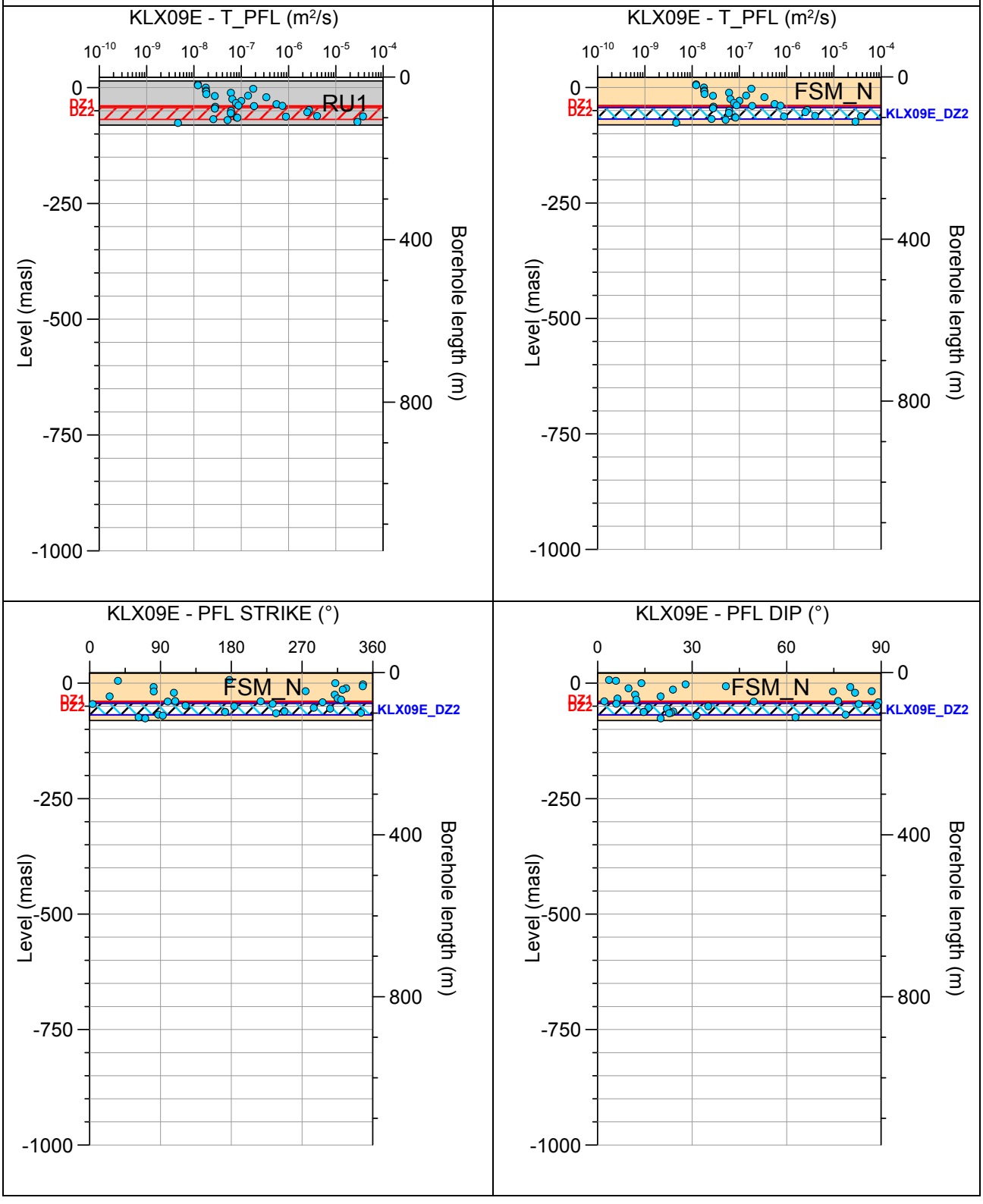

Comment:

Borehole KLX09E. Poles for PFL-f feature planes outside deformation zones.

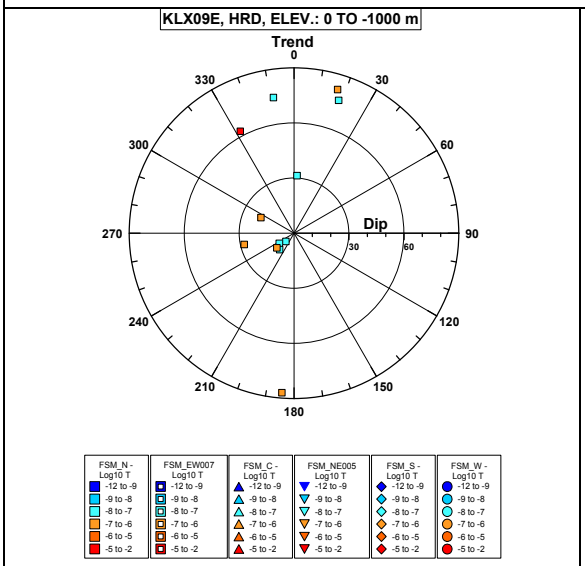

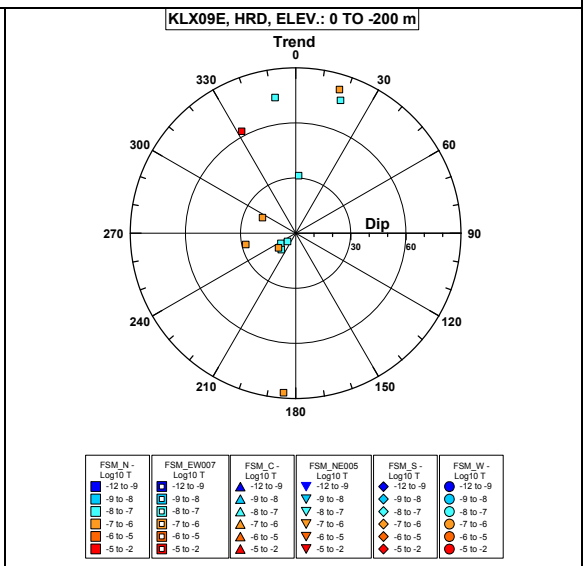

Borehole KLX09E. Poles for PFL-f feature planes in possible deformation zones.

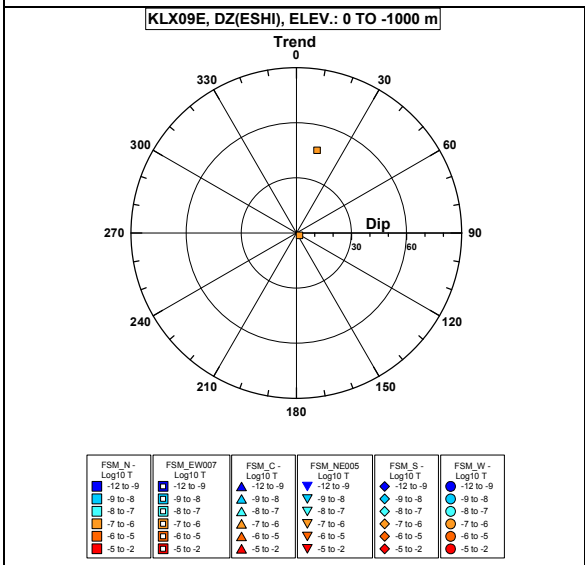

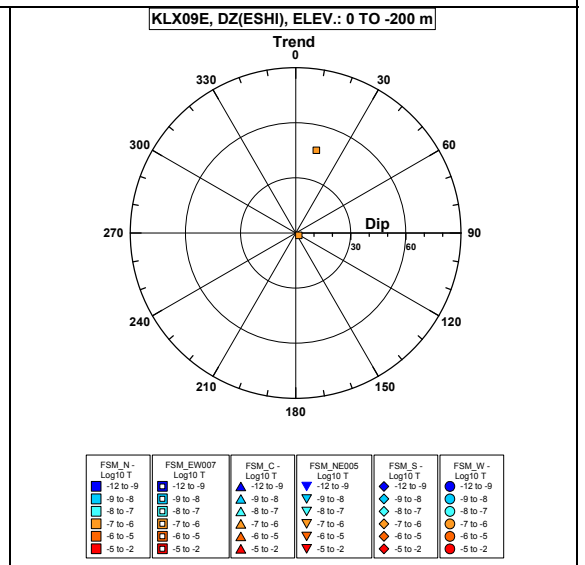

Borehole KLX09E. Poles for PFL-f feature planes in deterministically modelled deformation zones.

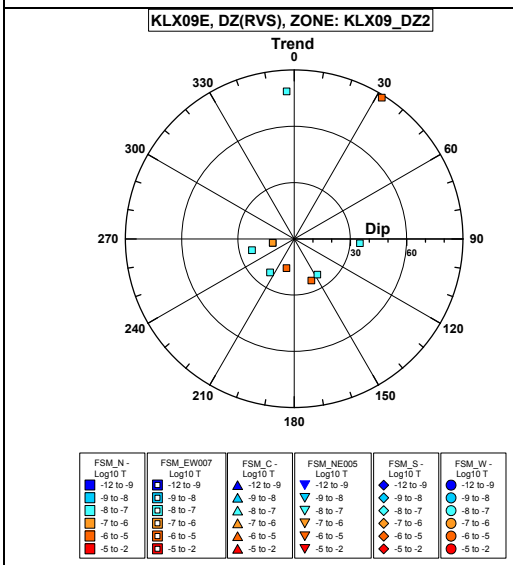

Borehole KLX09F.

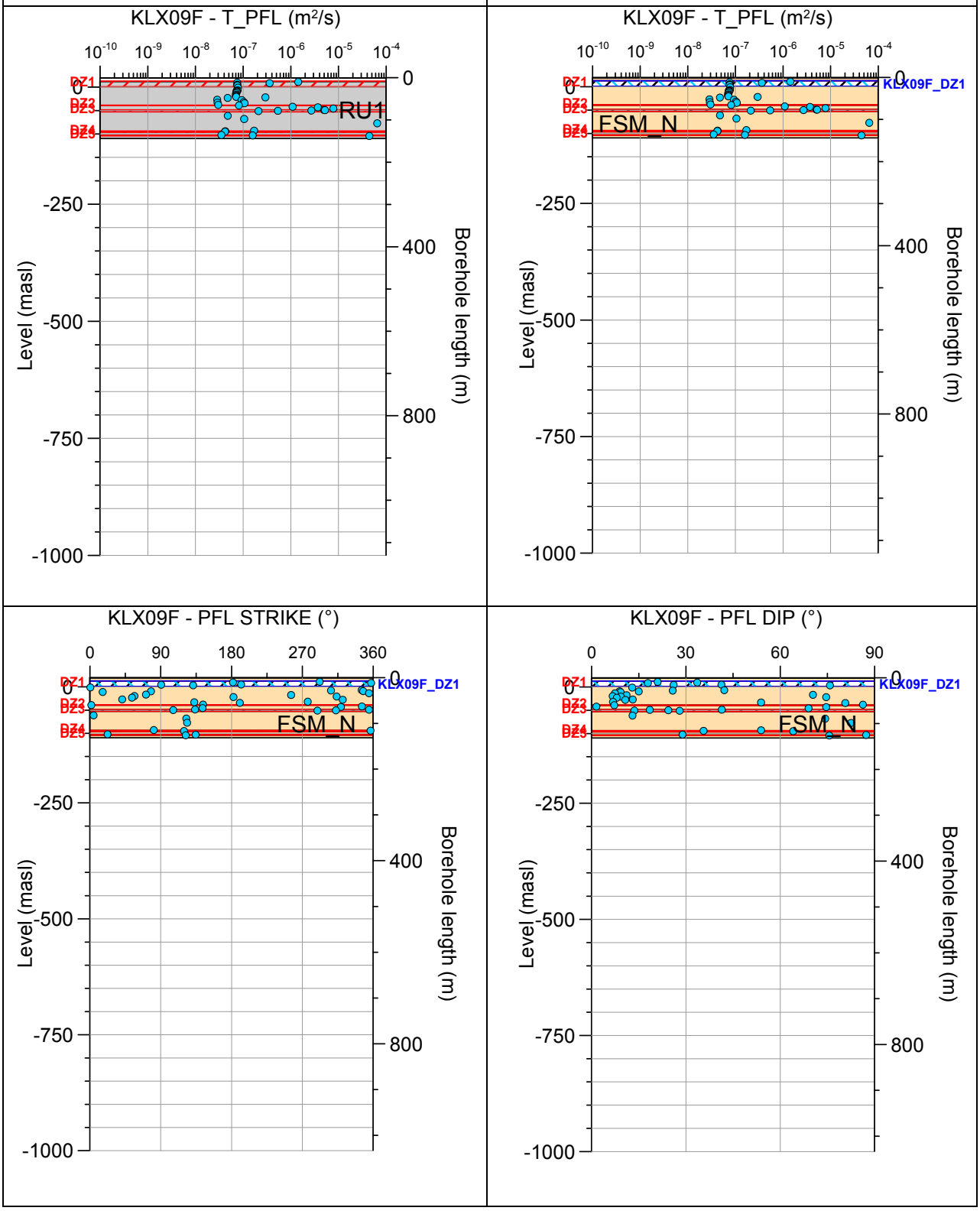

Comment:

Borehole KLX09F. Poles for PFL-f feature planes outside deformation zones.

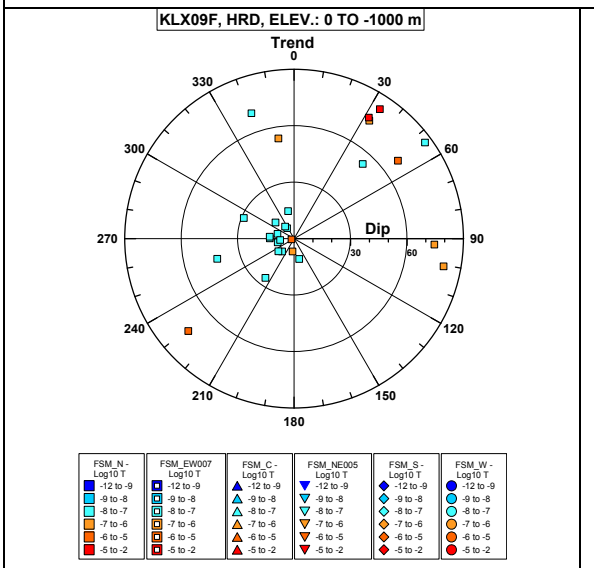

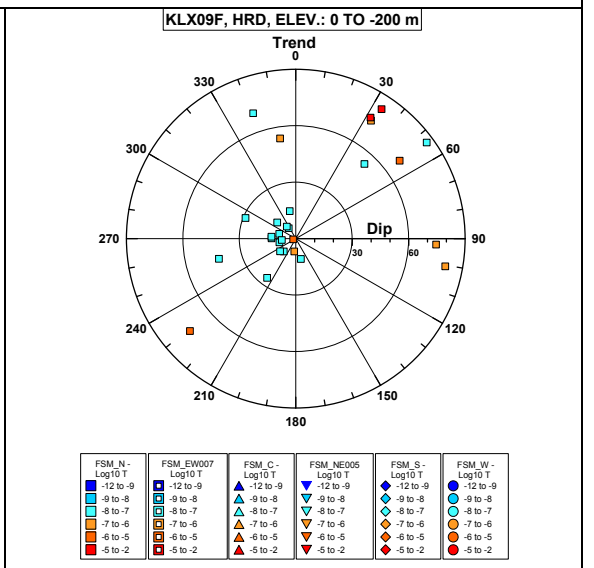

Borehole KLX09F. Poles for PFL-f feature planes in possible deformation zones.

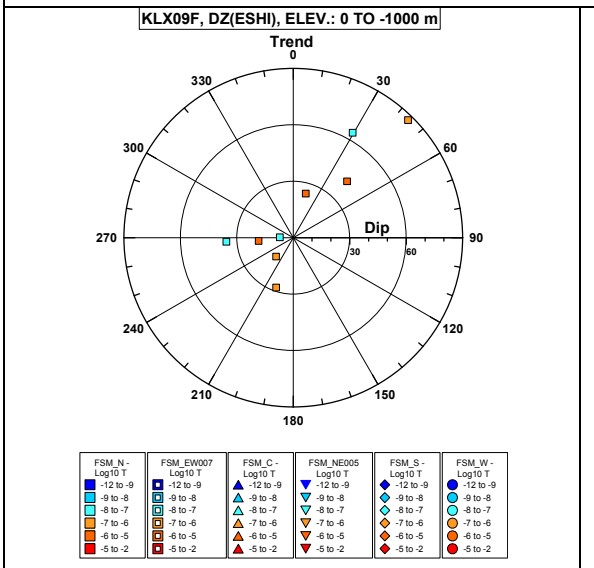

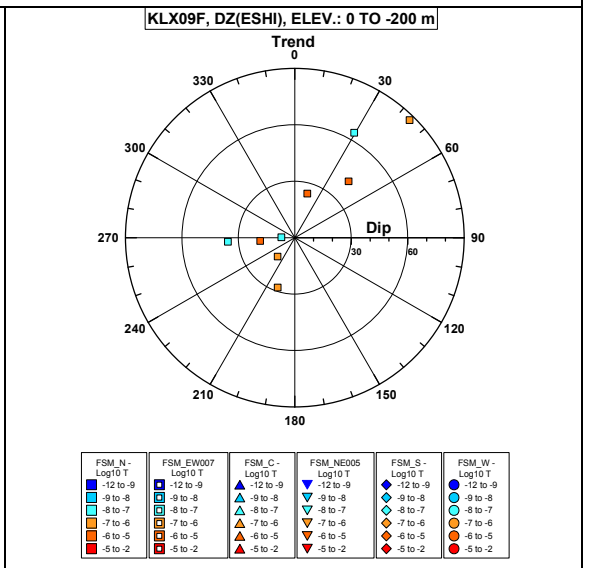

Borehole KLX09F. Poles for PFL-f feature planes in deterministically modelled deformation zones.

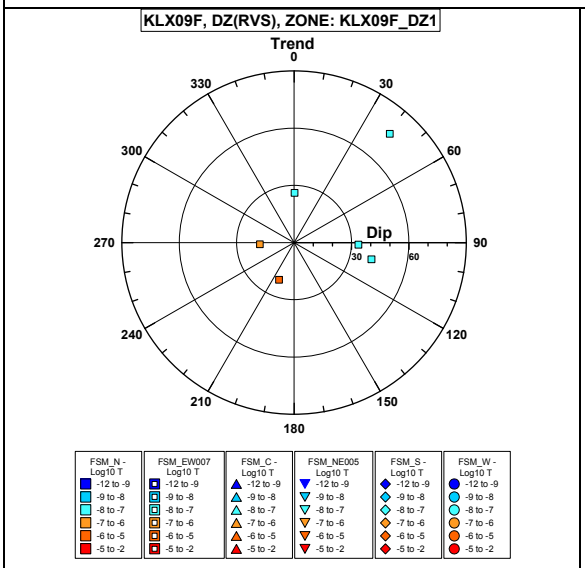

Borehole KLX09G.

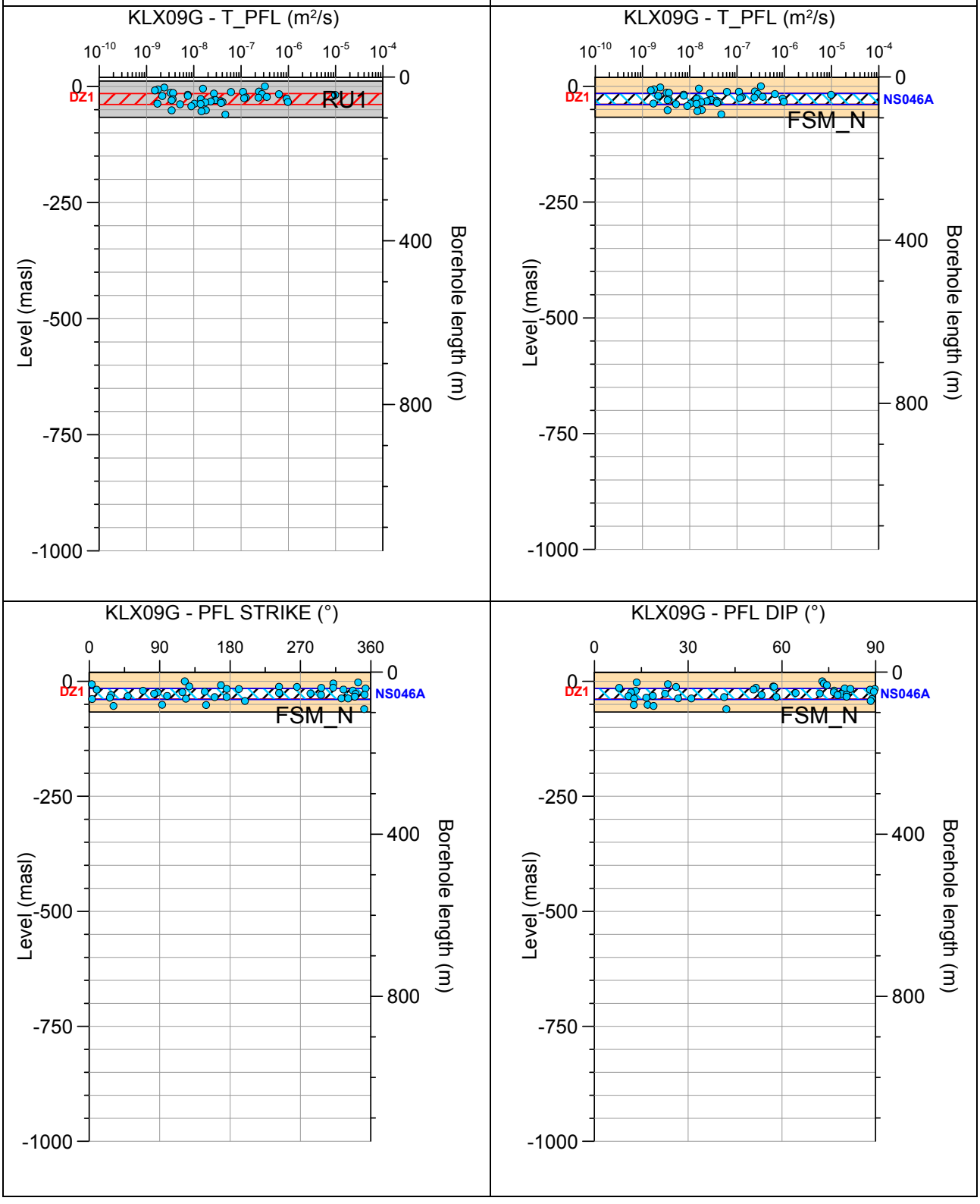

Comment:

Borehole KLX09G. Poles for PFL-f feature planes outside deformation zones.

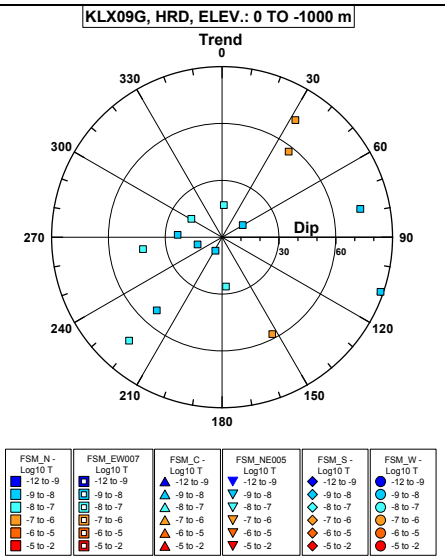

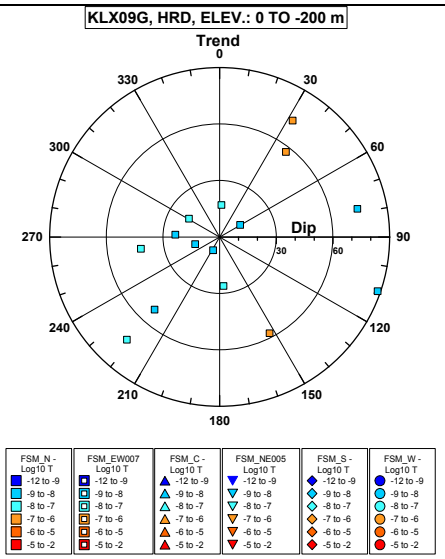

No PFL-f feature planes in possible deformation zones exist in KLX09G.

Borehole KLX09G. Poles for PFL-f feature planes in deterministically modelled deformation zones.

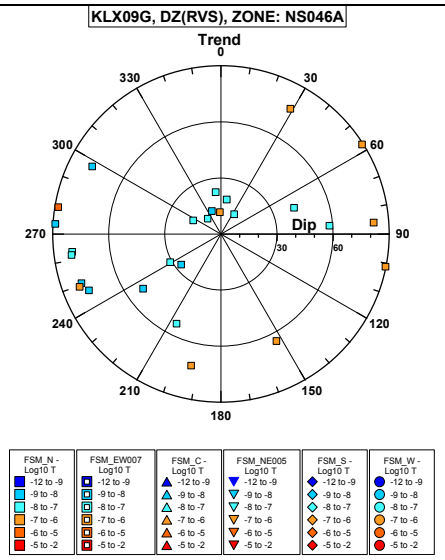

Borehole KLX10.

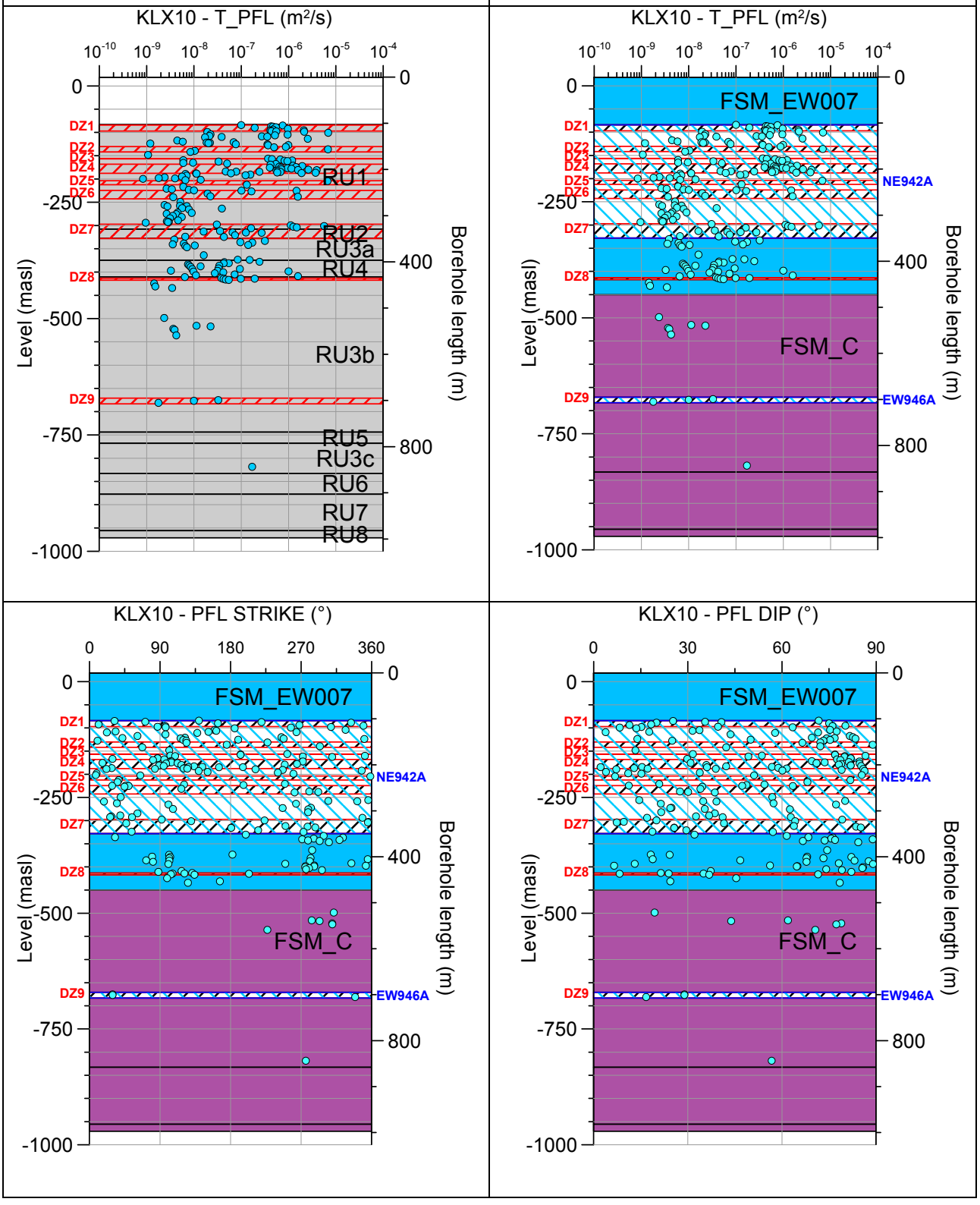

Comment:

Borehole KLX10. Poles for PFL-f feature planes outside deformation zones.

KLX10, HRD, ELEV.: 0 TO -1000 m

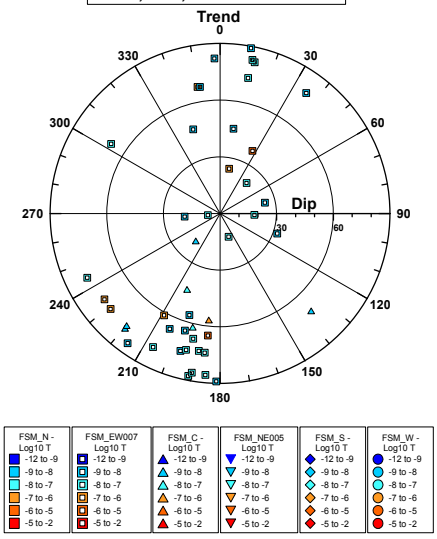

KLX10, HRD, ELEV.: 0 TO -200 m

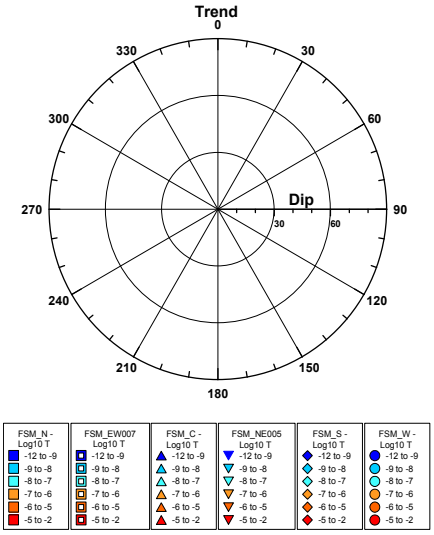

KLX10, HRD, ELEV.: -200 TO -400 m

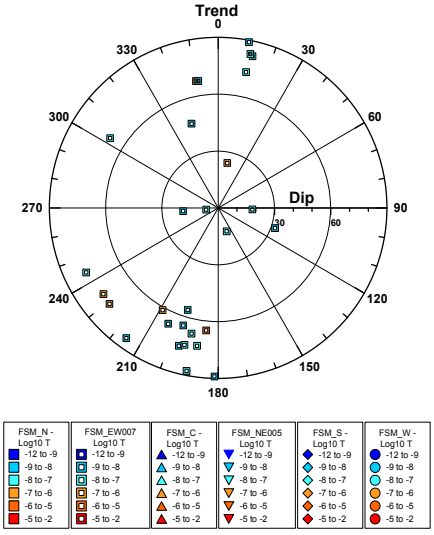

KLX10, HRD, ELEV.: -400 TO -600 m

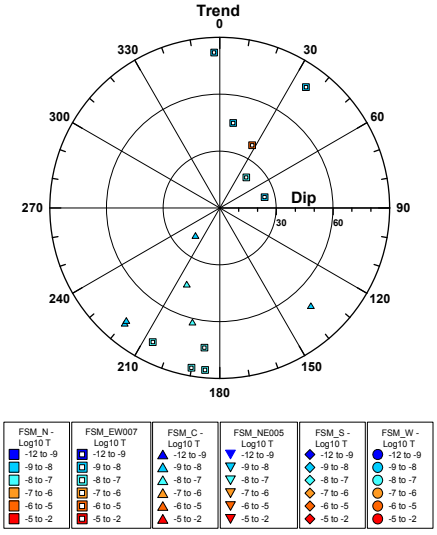

KLX10, HRD, ELEV.: -800 TO -1000 m

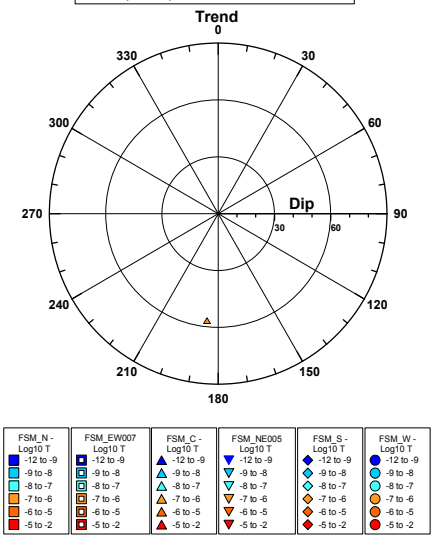

Borehole KLX10. Poles for PFL-f feature planes in possible deformation zones.

KLX10, DZ(ESHI), ELEV.: 0 TO -1000 m

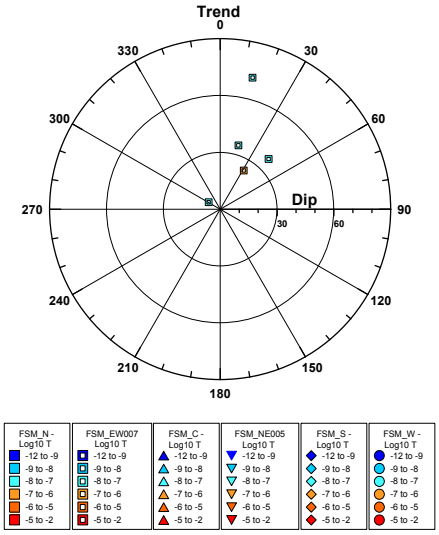

KLX10, DZ(ESHI), ELEV.: 0 TO -200 m

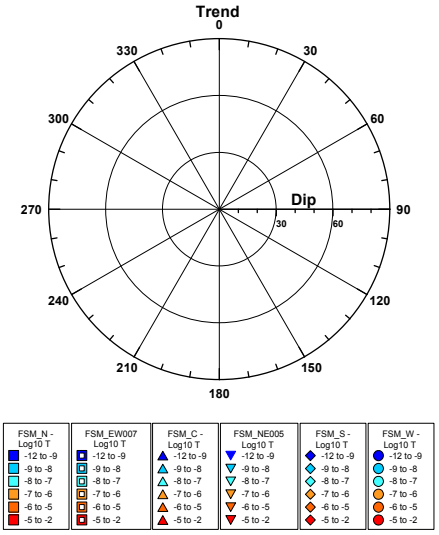

KLX10, DZ(ESHI), ELEV.: -200 TO -400 m

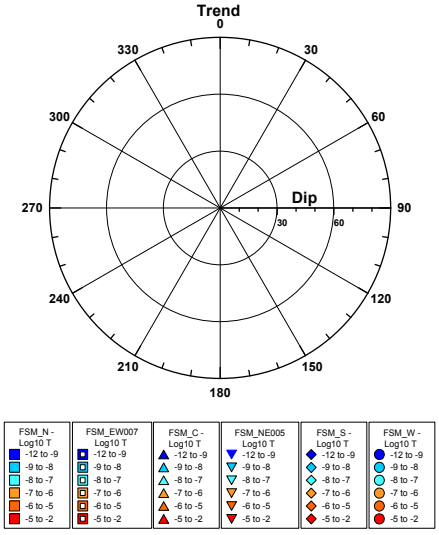

KLX10, DZ(ESHI), ELEV.: -400 TO -600 m

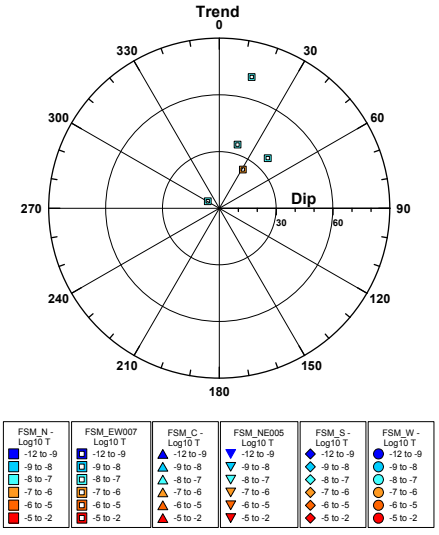

Borehole KLX10. Poles for PFL-f feature planes in deterministically modelled deformation zones.

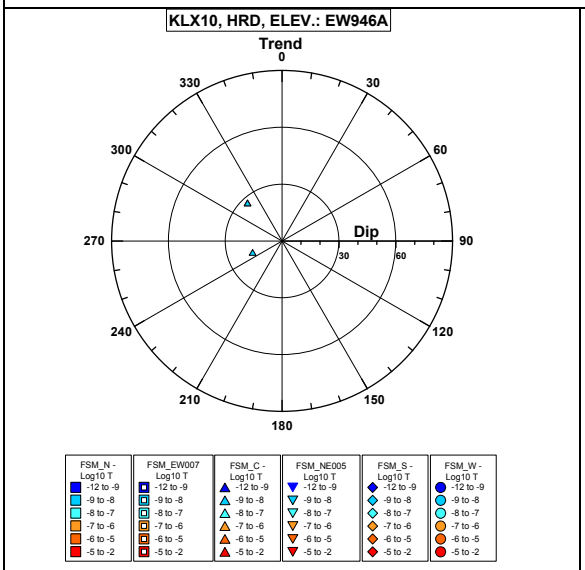

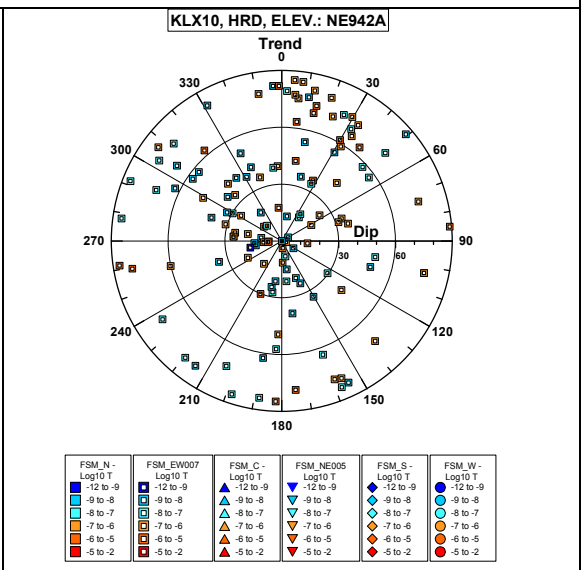

Borehole KLX10B.

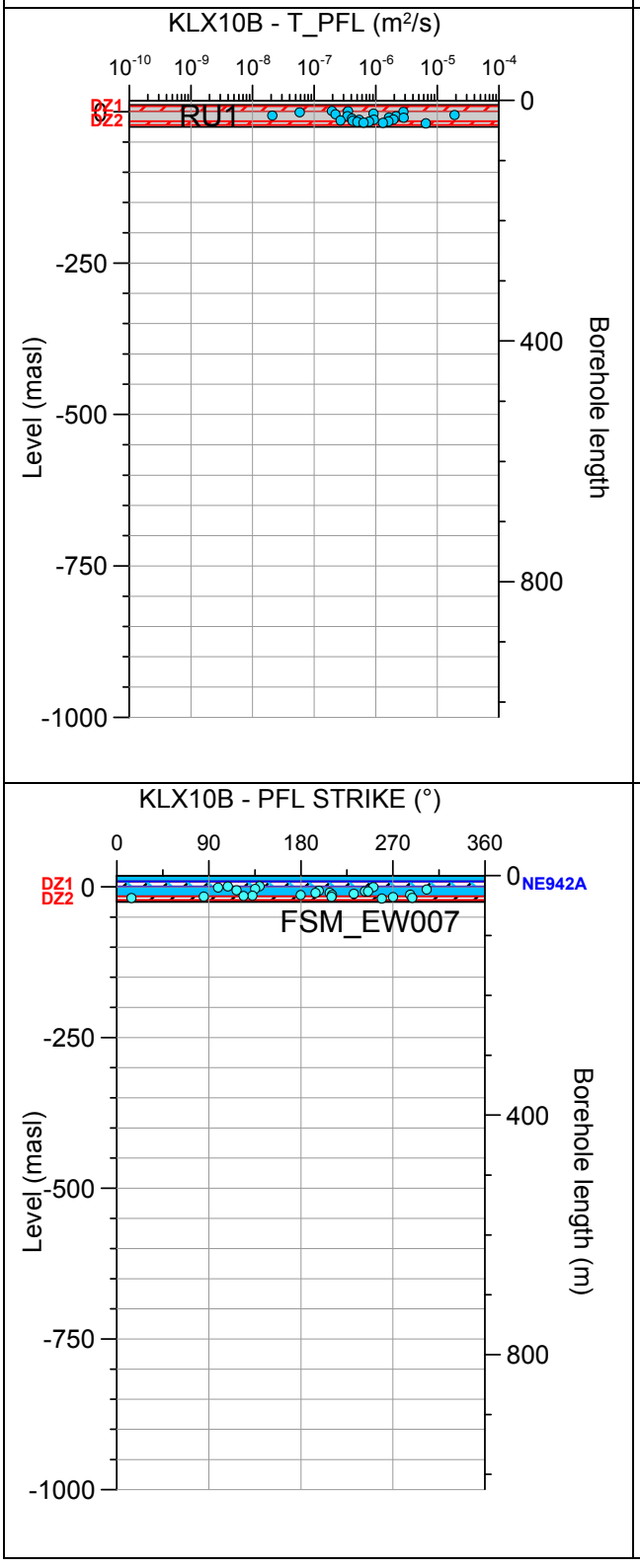

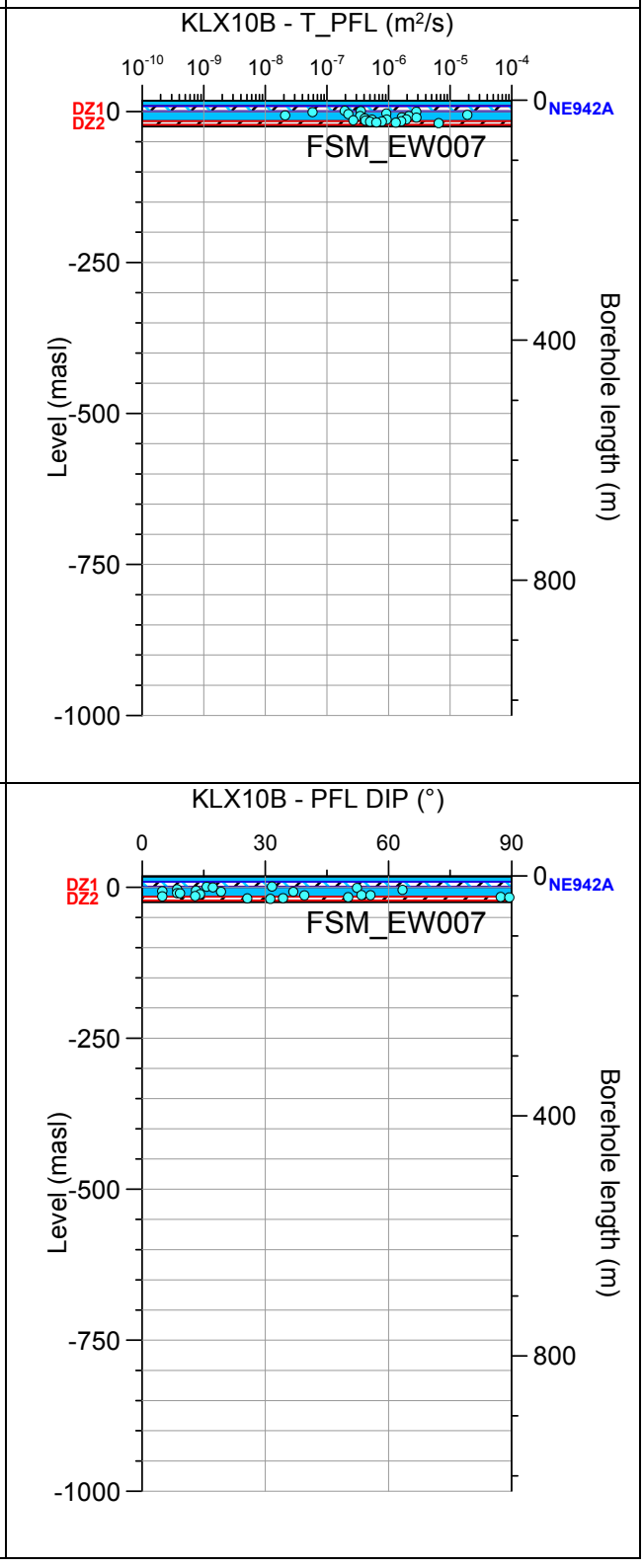

Comment:

Borehole KLX10B. Poles for PFL-f feature planes outside deformation zones.

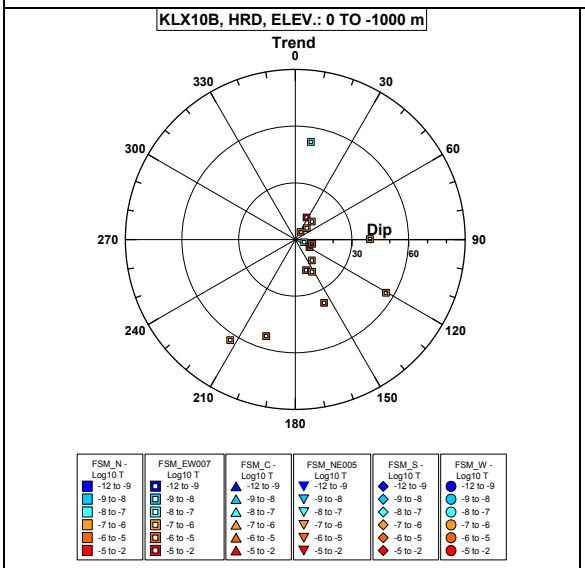

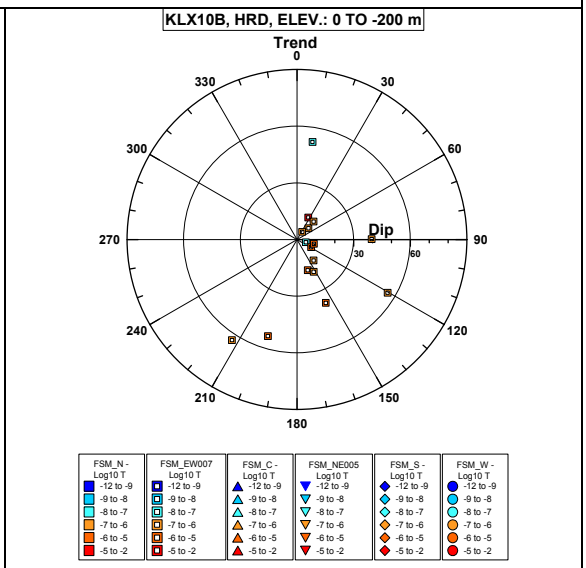

Borehole KLX10B. Poles for PFL-f feature planes in possible deformation zones.

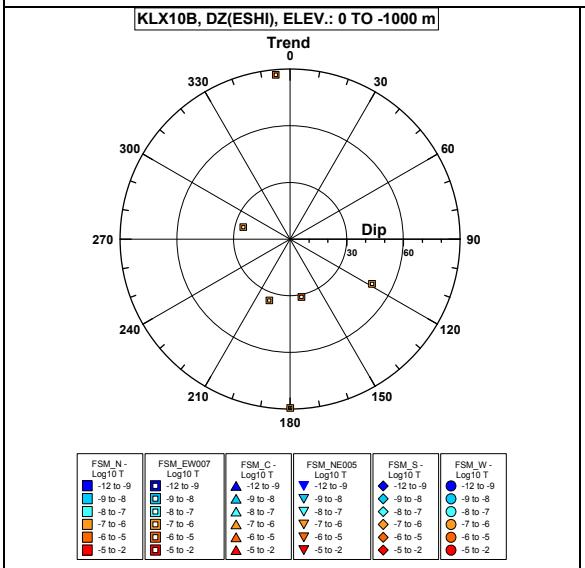

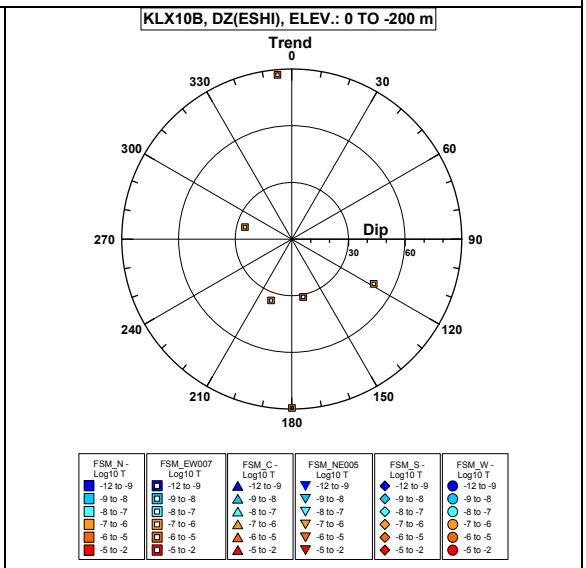

Borehole KLX10B. Poles for PFL-f feature planes in deterministically modelled deformation zones.

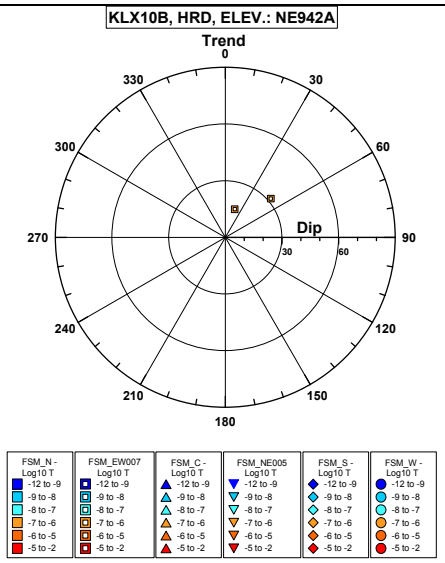

Borehole KLX10C.

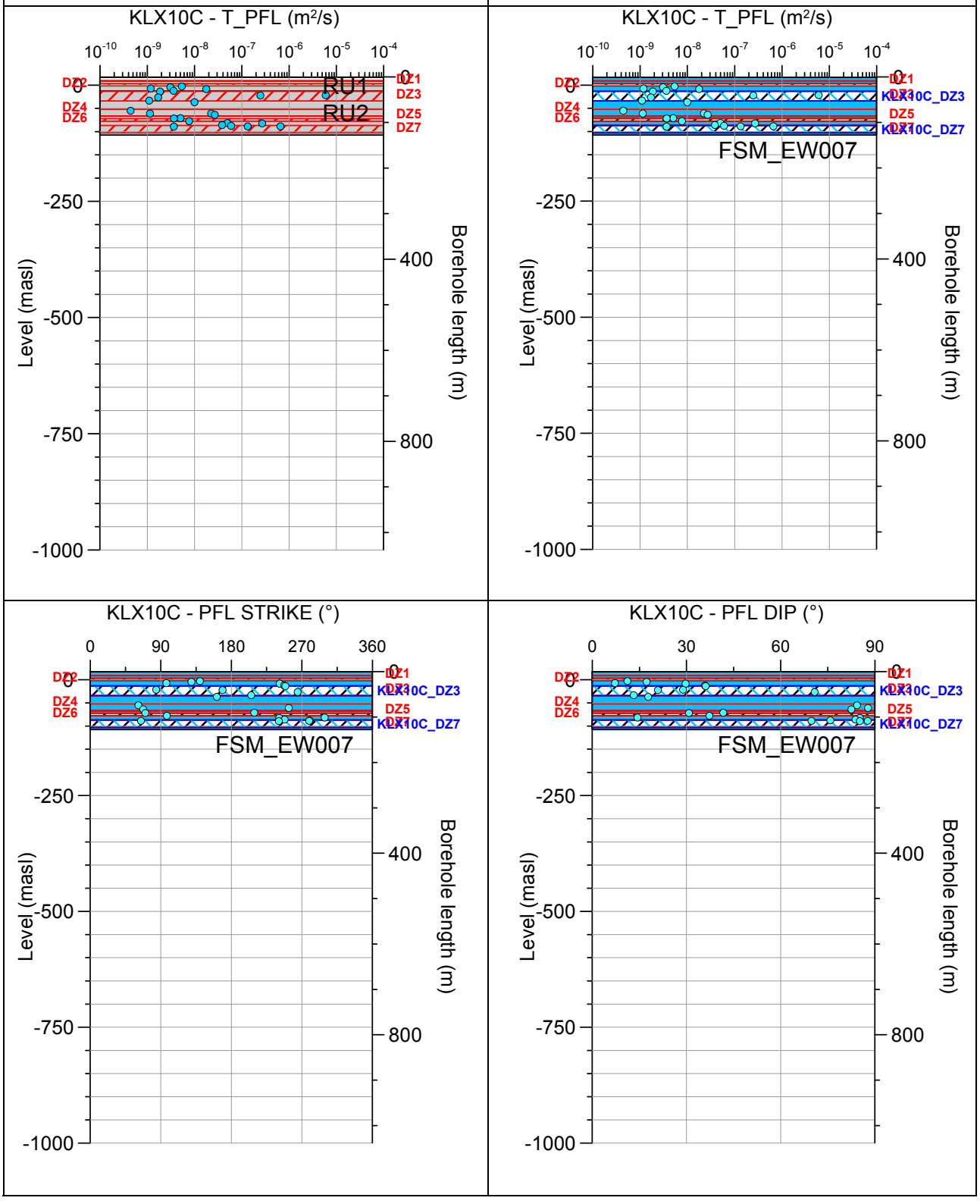

Comment:

Borehole KLX10C. Poles for PFL-f feature planes outside deformation zones.

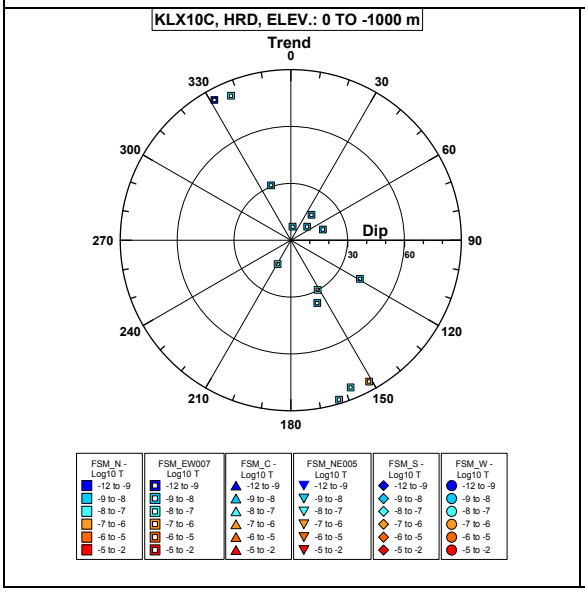

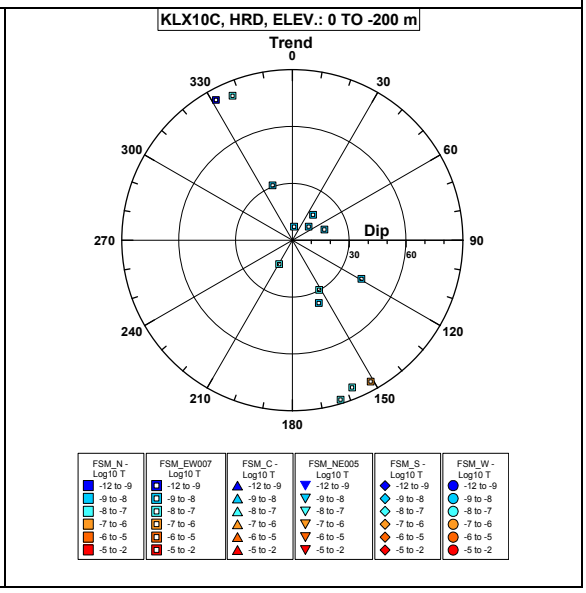

Borehole KLX10C. Poles for PFL-f feature planes in possible deformation zones.

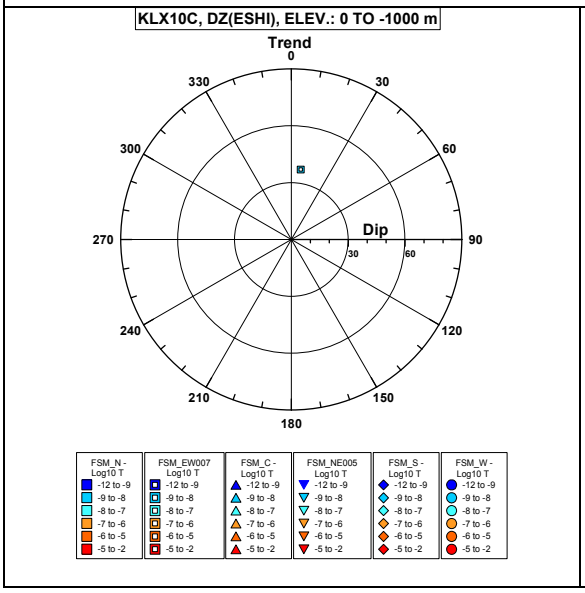

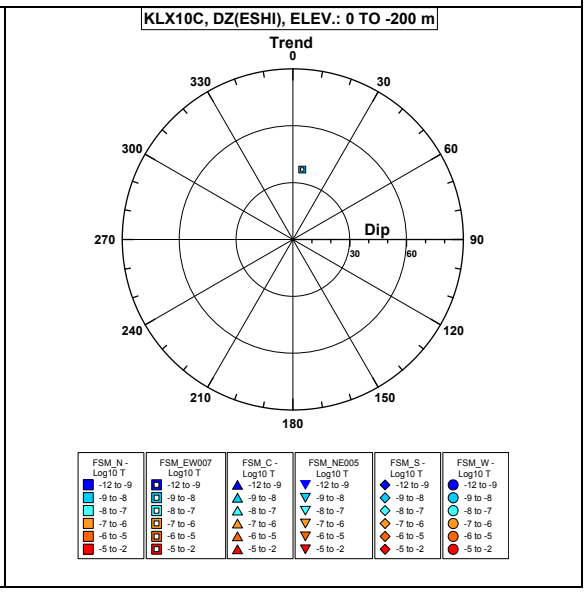

Borehole KLX10C. Poles for PFL-f feature planes in deterministically modelled deformation zones.

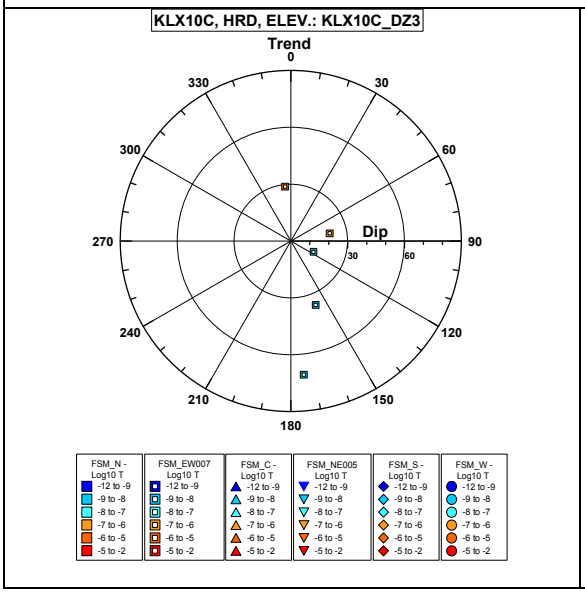

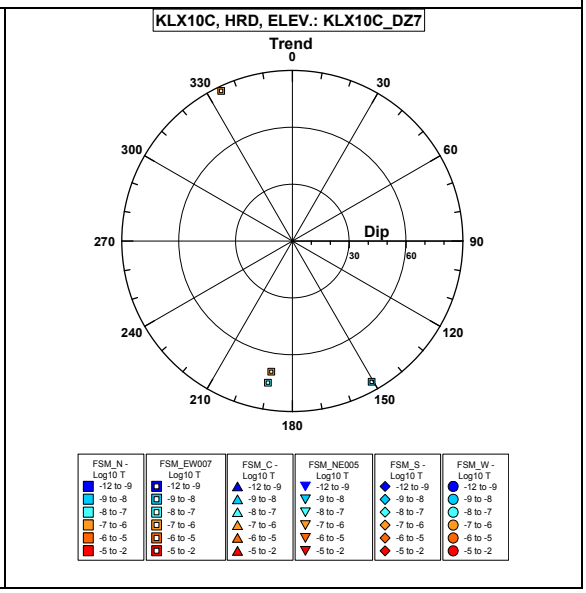

Borehole KLX11A.

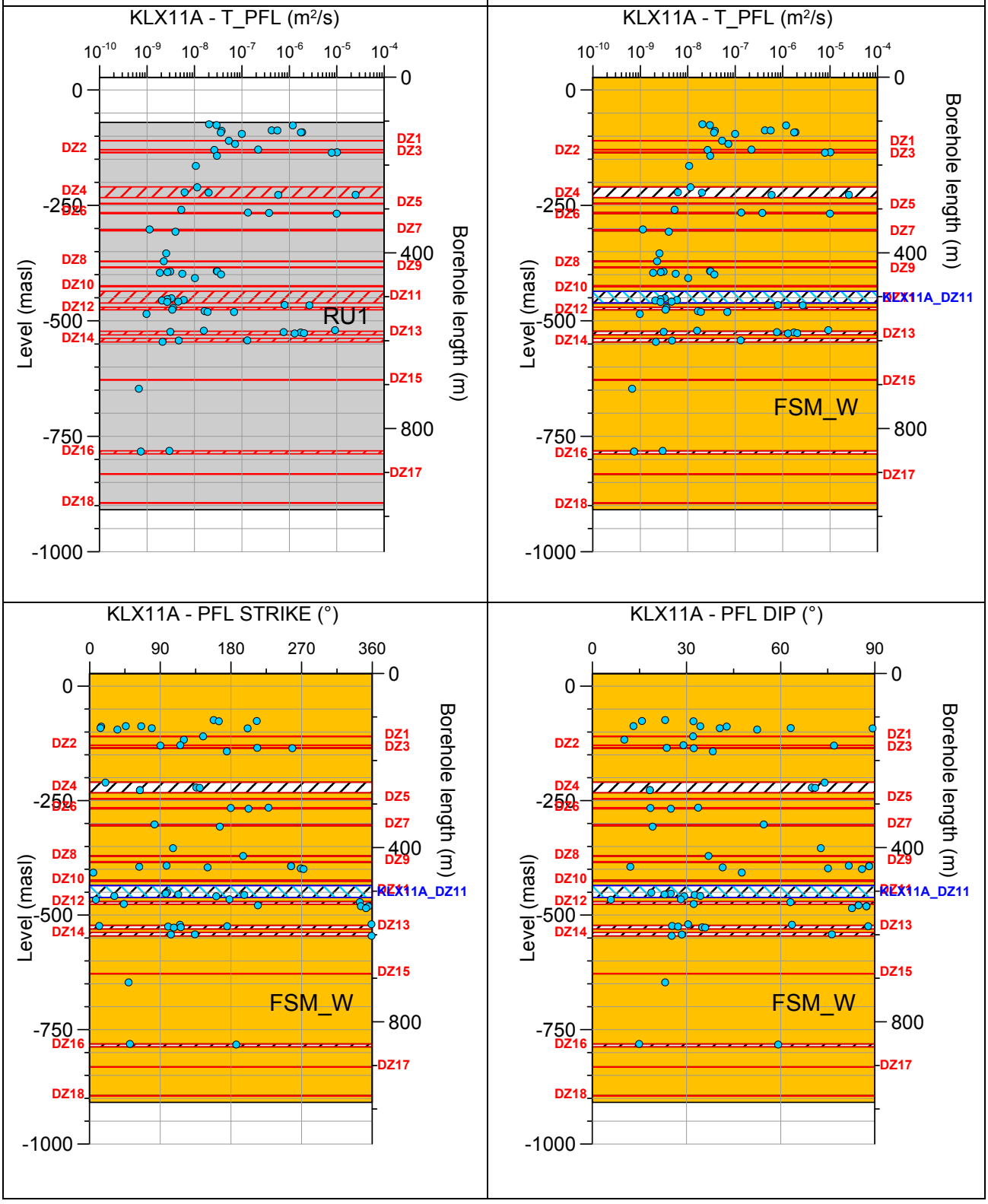

Comment:

Borehole KLX11A. Poles for PFL-f feature planes outside deformation zones.

KLX11A, HRD, ELEV.: 0 TO -1000 m

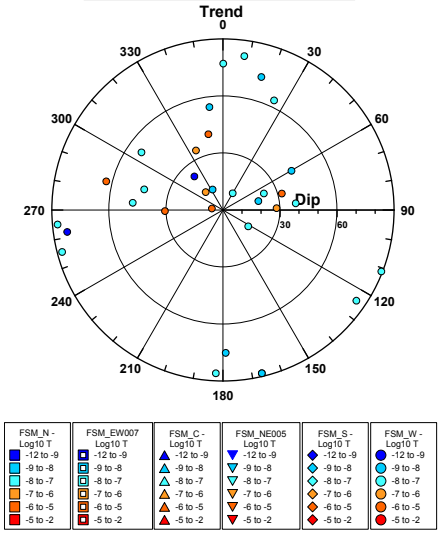

KLX11A, HRD, ELEV.: 0 TO -200 m

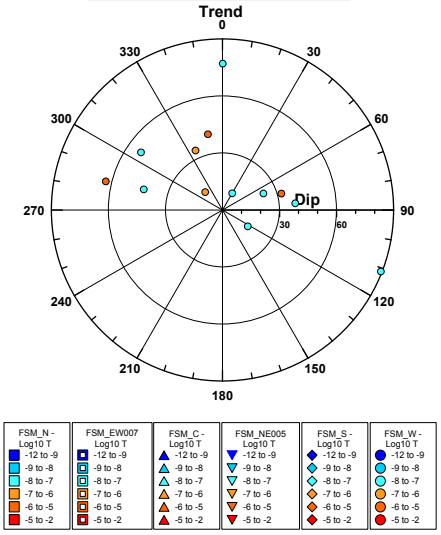

KLX11A, HRD, ELEV.: -200 TO -400 m

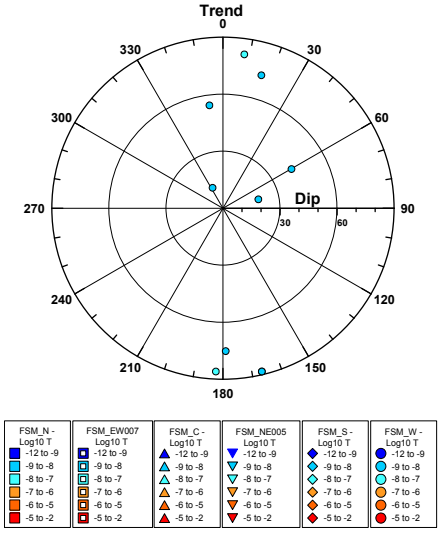

KLX11A, HRD, ELEV.: -400 TO -600 m

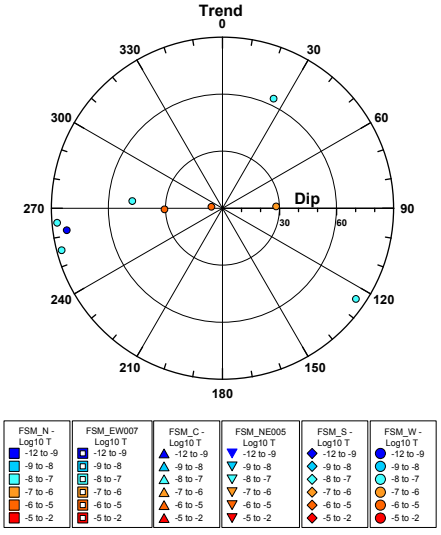

KLX11A, HRD, ELEV.: -600 TO -800 m

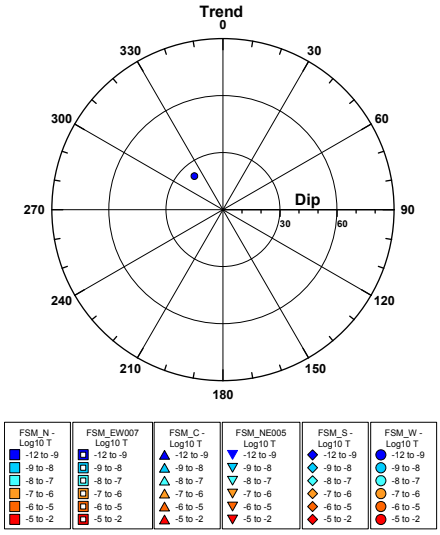

Borehole KLX11A. Poles for PFL-f feature planes in possible deformation zones.

KLX11A, DZ(ESHI), ELEV.: 0 TO -1000 m

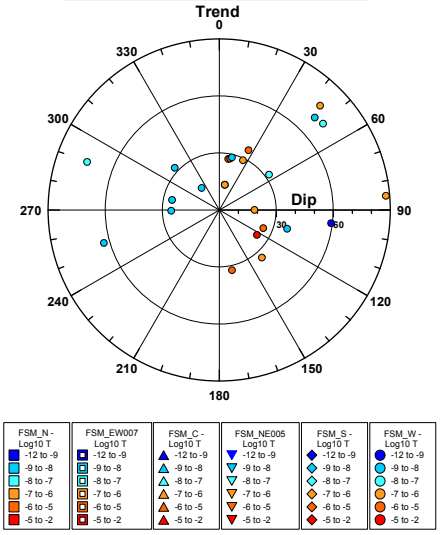

KLX11A, DZ(ESHI), ELEV.: 0 TO -200 m

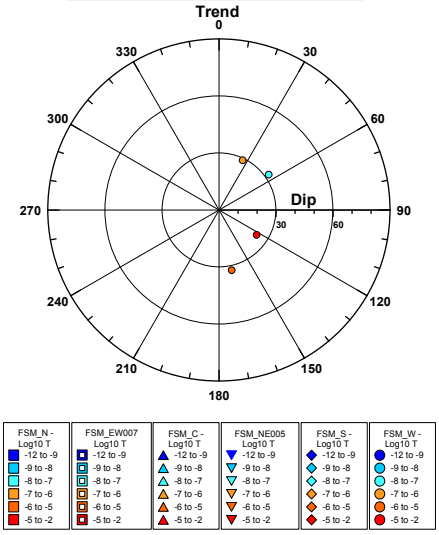

KLX11A, DZ(ESHI), ELEV.: -200 TO -400 m

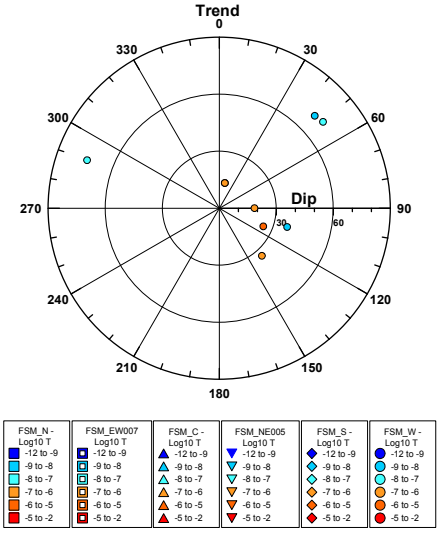

KLX11A, DZ(ESHI), ELEV.: -400 TO -600 m

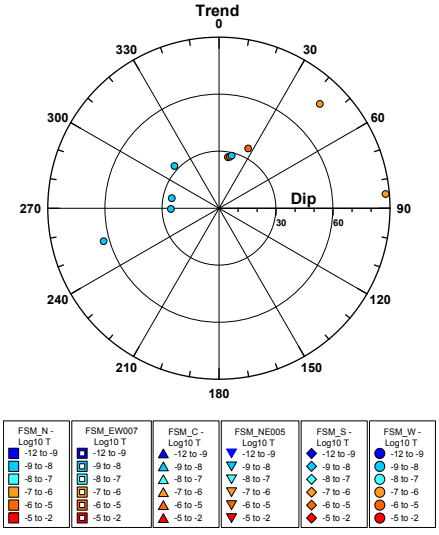

KLX11A, DZ(ESHI), ELEV.: -600 TO -800 m

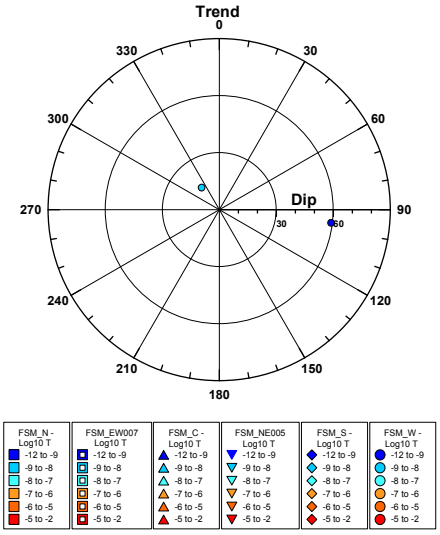

Borehole KLX11A. Poles for PFL-f feature planes in deterministically modelled deformation zones.

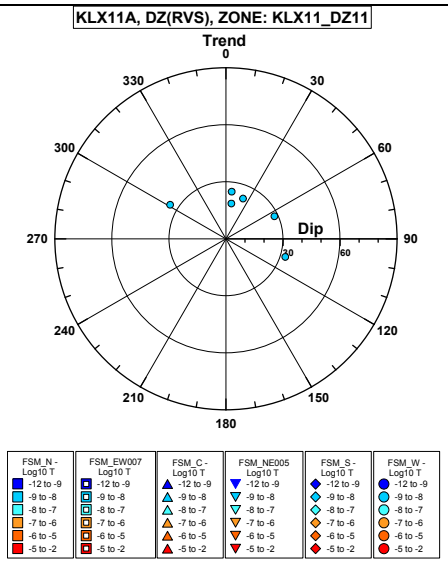

Borehole KLX11B.

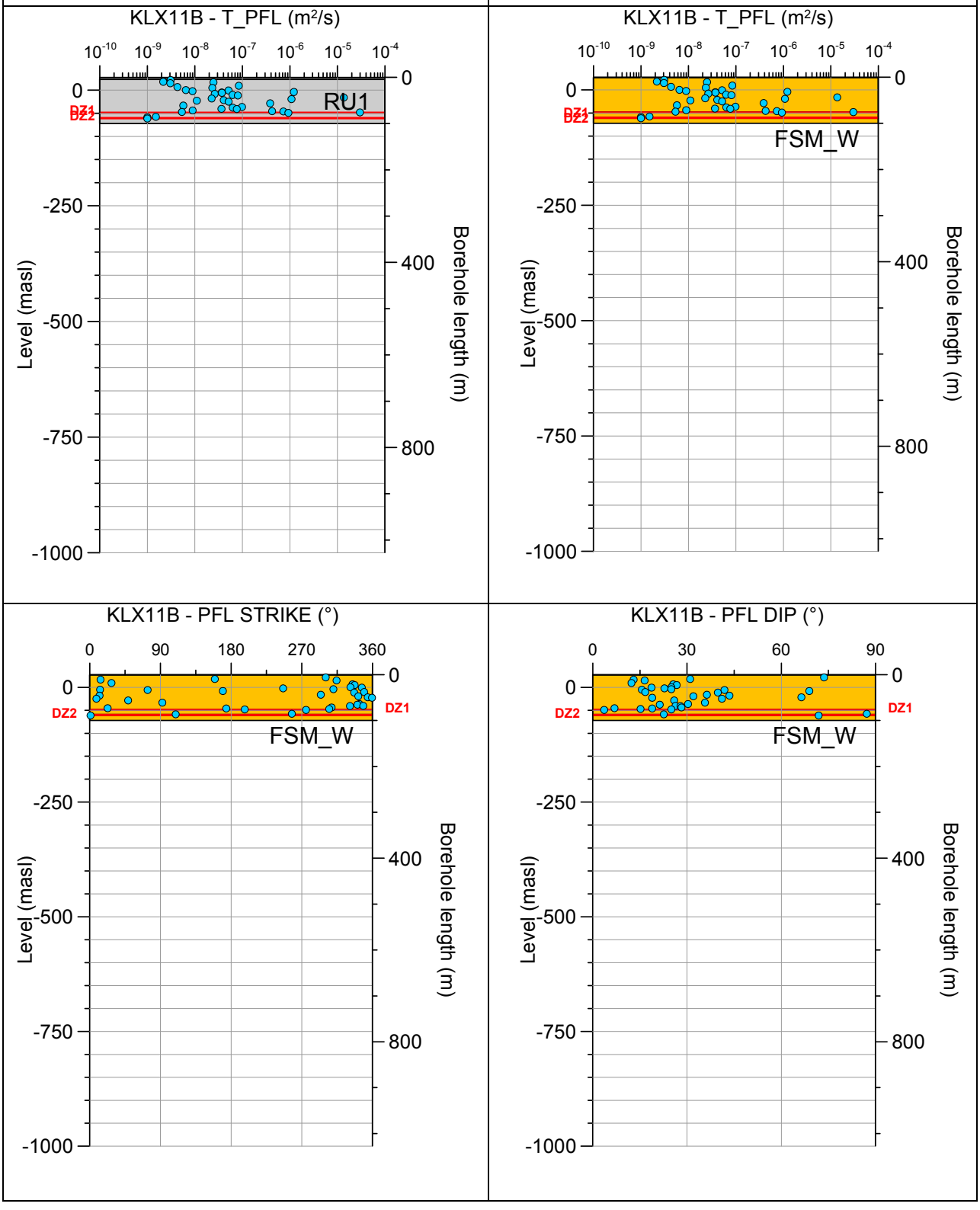

Comment:

Borehole KLX11B. Poles for PFL-f feature planes outside deformation zones.

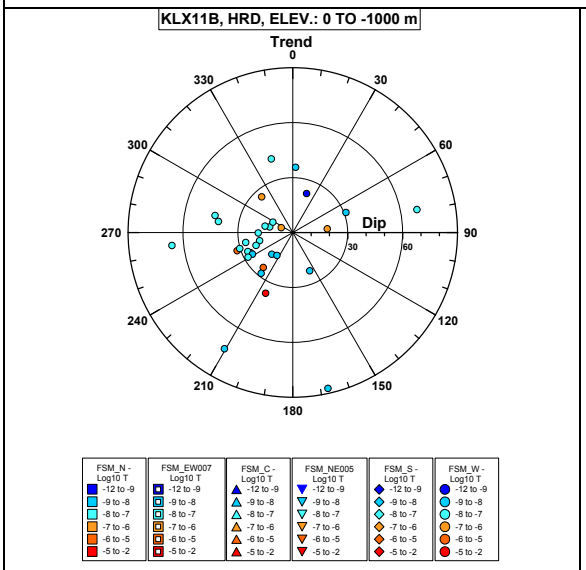

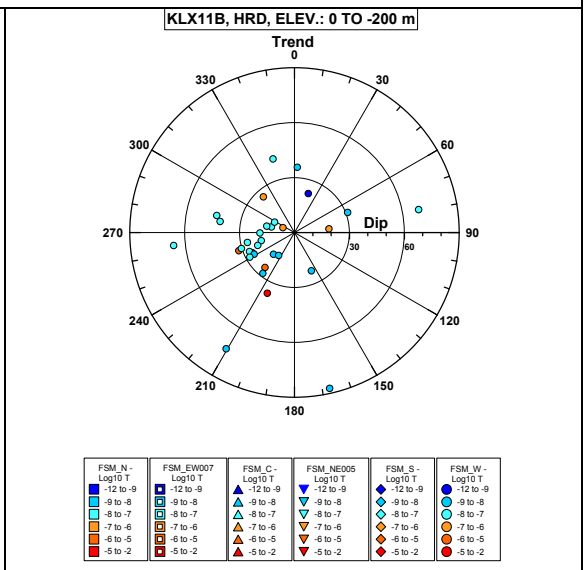

Borehole KLX11B. Poles for PFL-f feature planes in possible deformation zones.

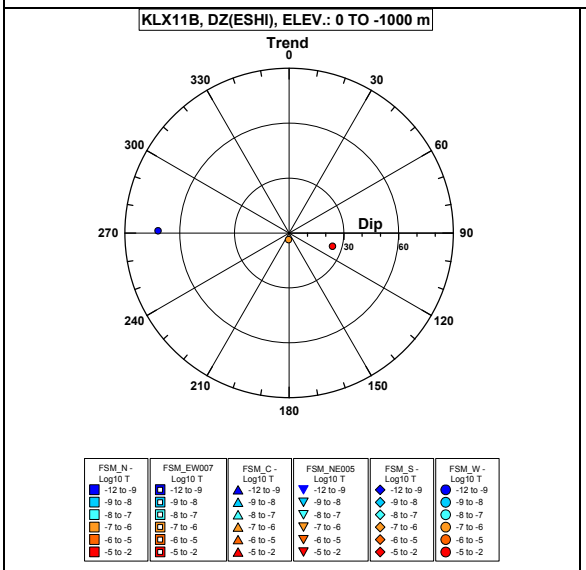

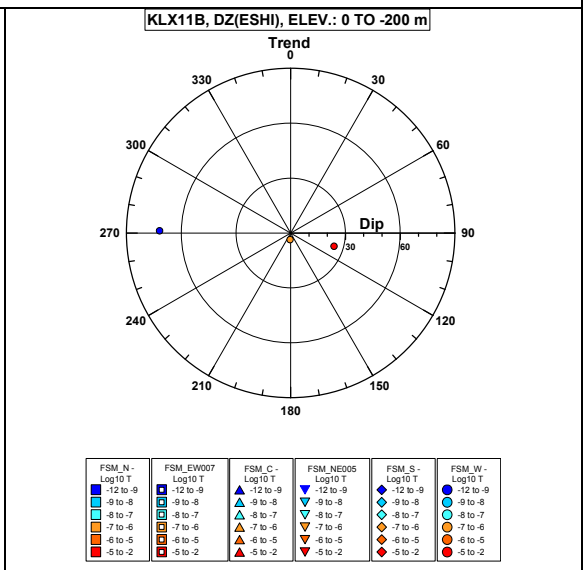

No PFL-f feature planes in deterministically modelled deformation zones exist in KLX11B.

Borehole KLX11C.

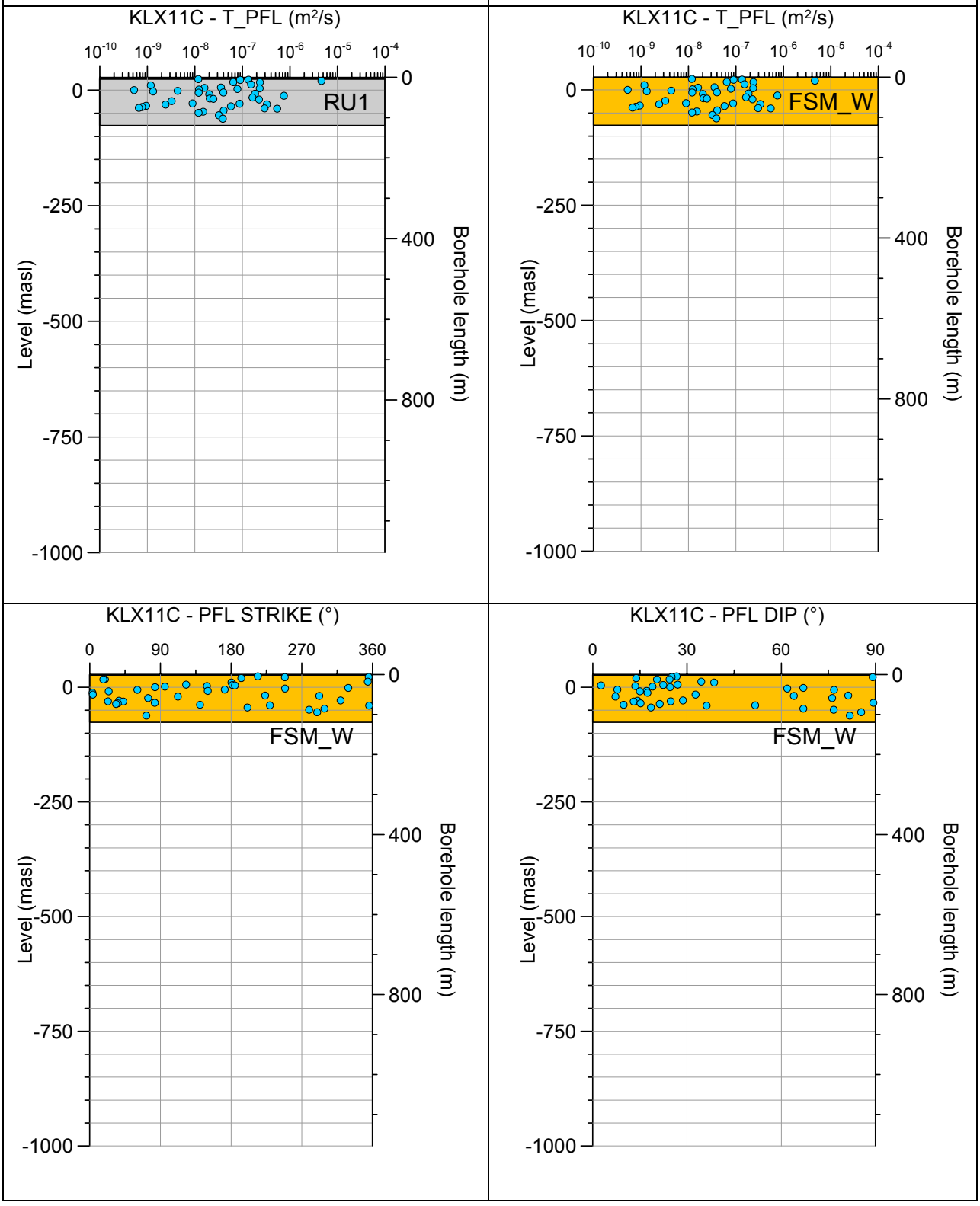

Comment:

Borehole KLX11C. Poles for PFL-f feature planes outside deformation zones.

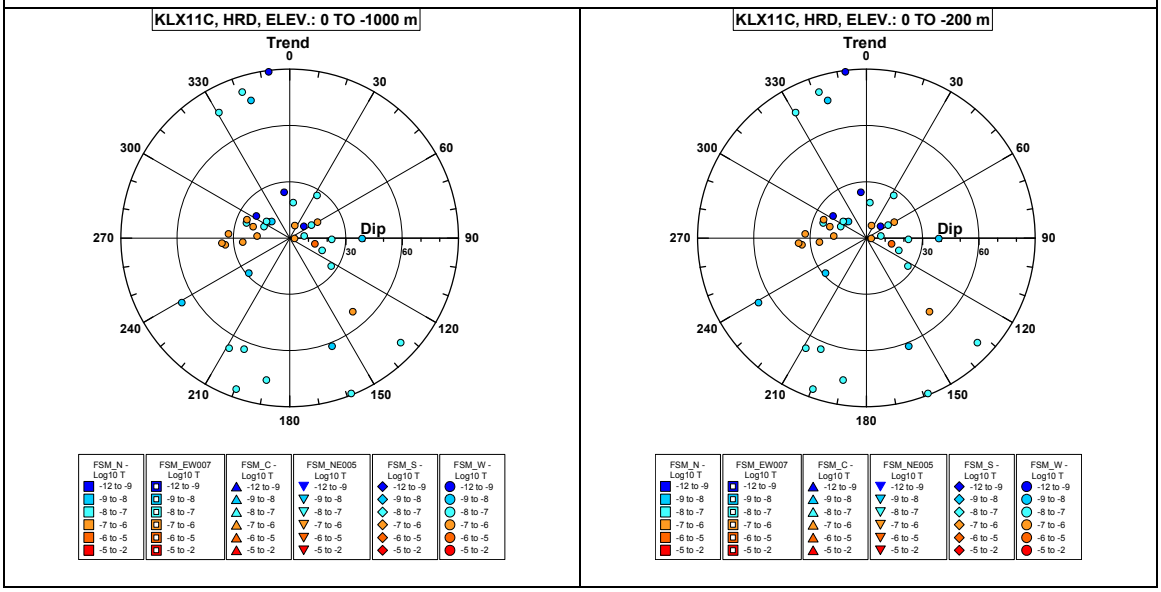

No PFL-f feature planes in possible deformation zones exist in KLX11C.

No PFL-f feature planes in deterministically modelled deformation zones exist in KLX11C.

Borehole KLX11D.

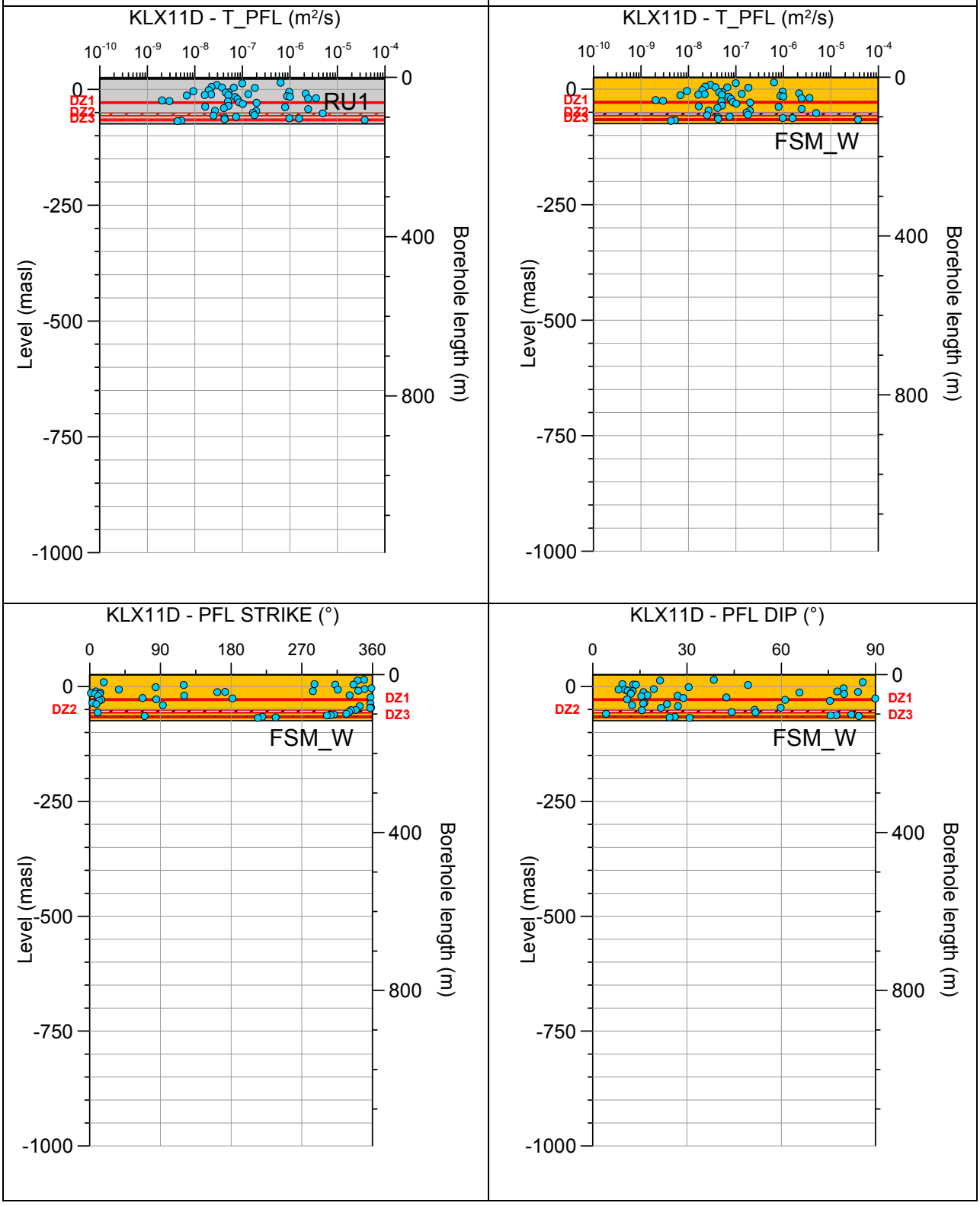

Comment:

Borehole KLX11D. Poles for PFL-f feature planes outside deformation zones.

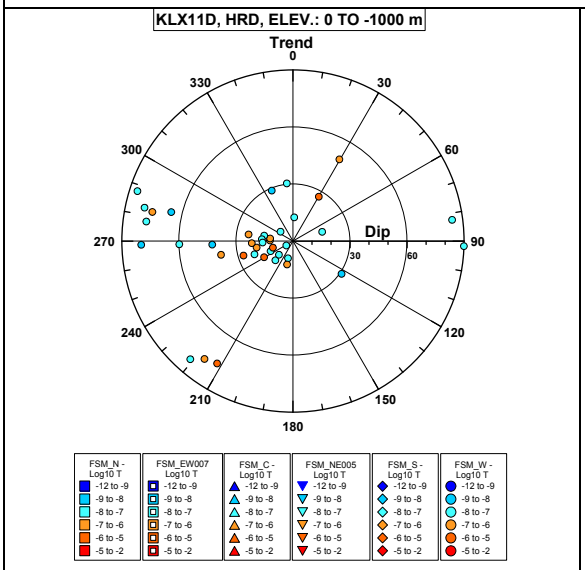

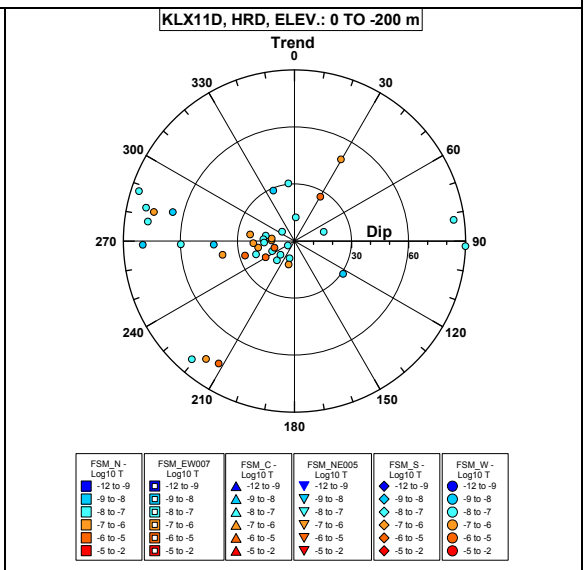

Borehole KLX11D. Poles for PFL-f feature planes in possible deformation zones.

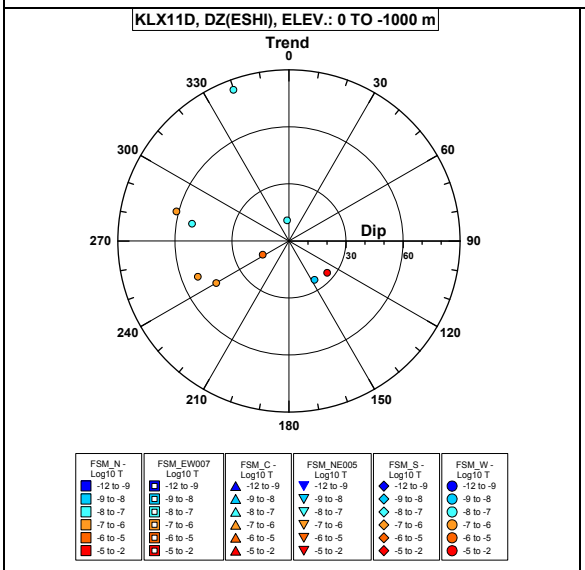

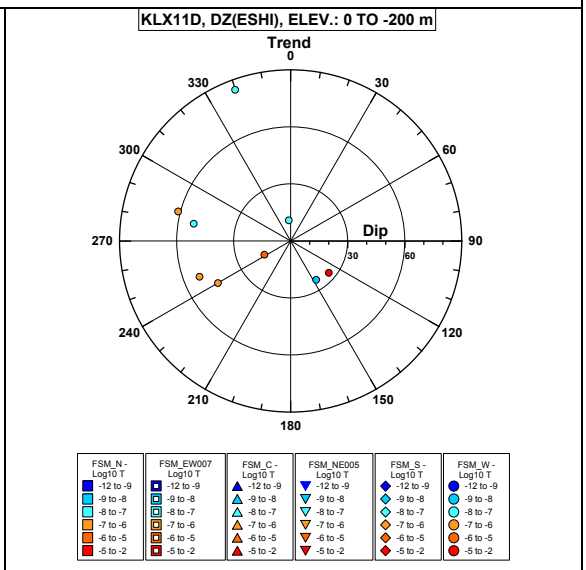

No PFL-f feature planes in deterministically modelled deformation zones exist in KLX11D.

Borehole KLX11E.

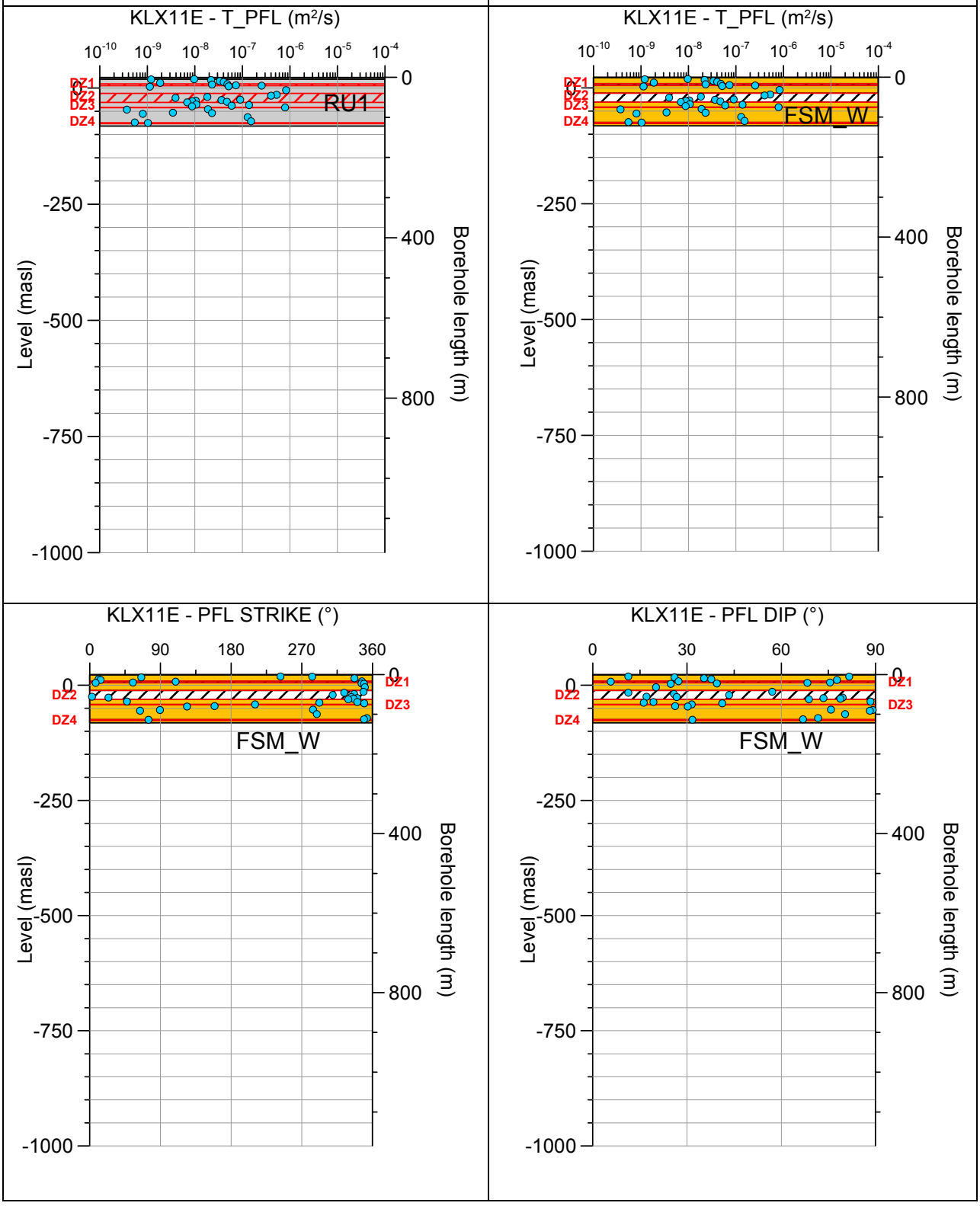

Comment:

Borehole KLX11E. Poles for PFL-f feature planes outside deformation zones.

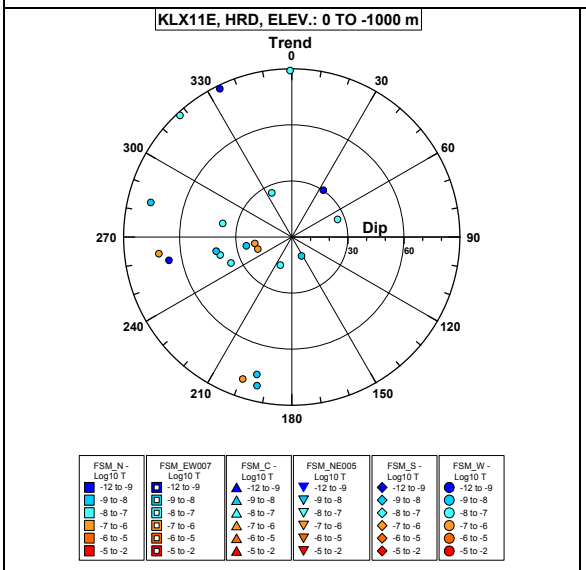

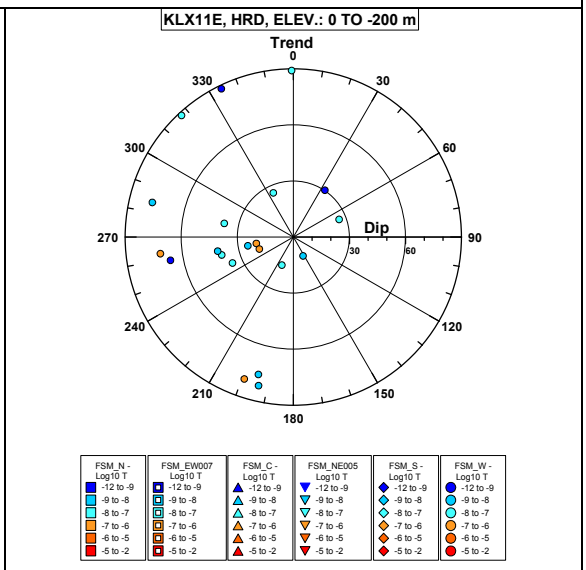

Borehole KLX11E. Poles for PFL-f feature planes in possible deformation zones.

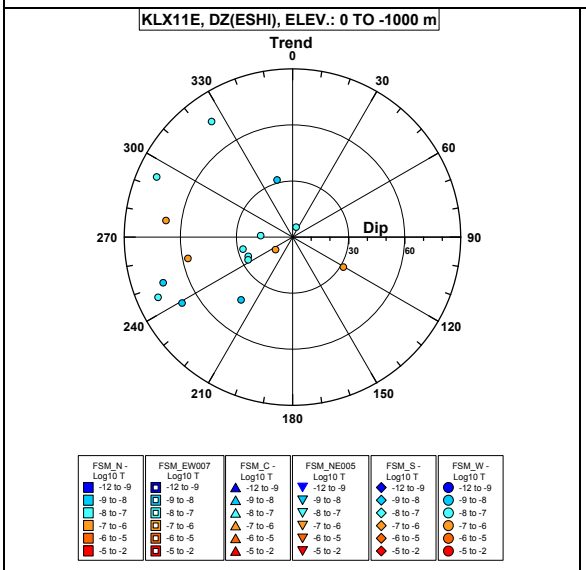

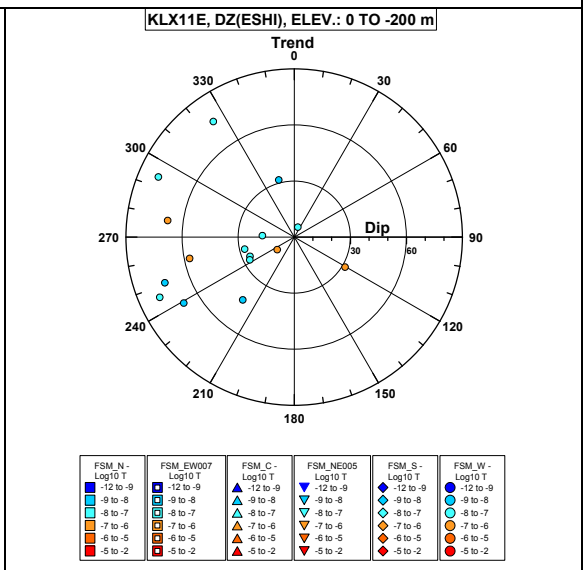

No PFL-f feature planes in deterministically modelled deformation zones exist in KLX05.

Borehole KLX11F.

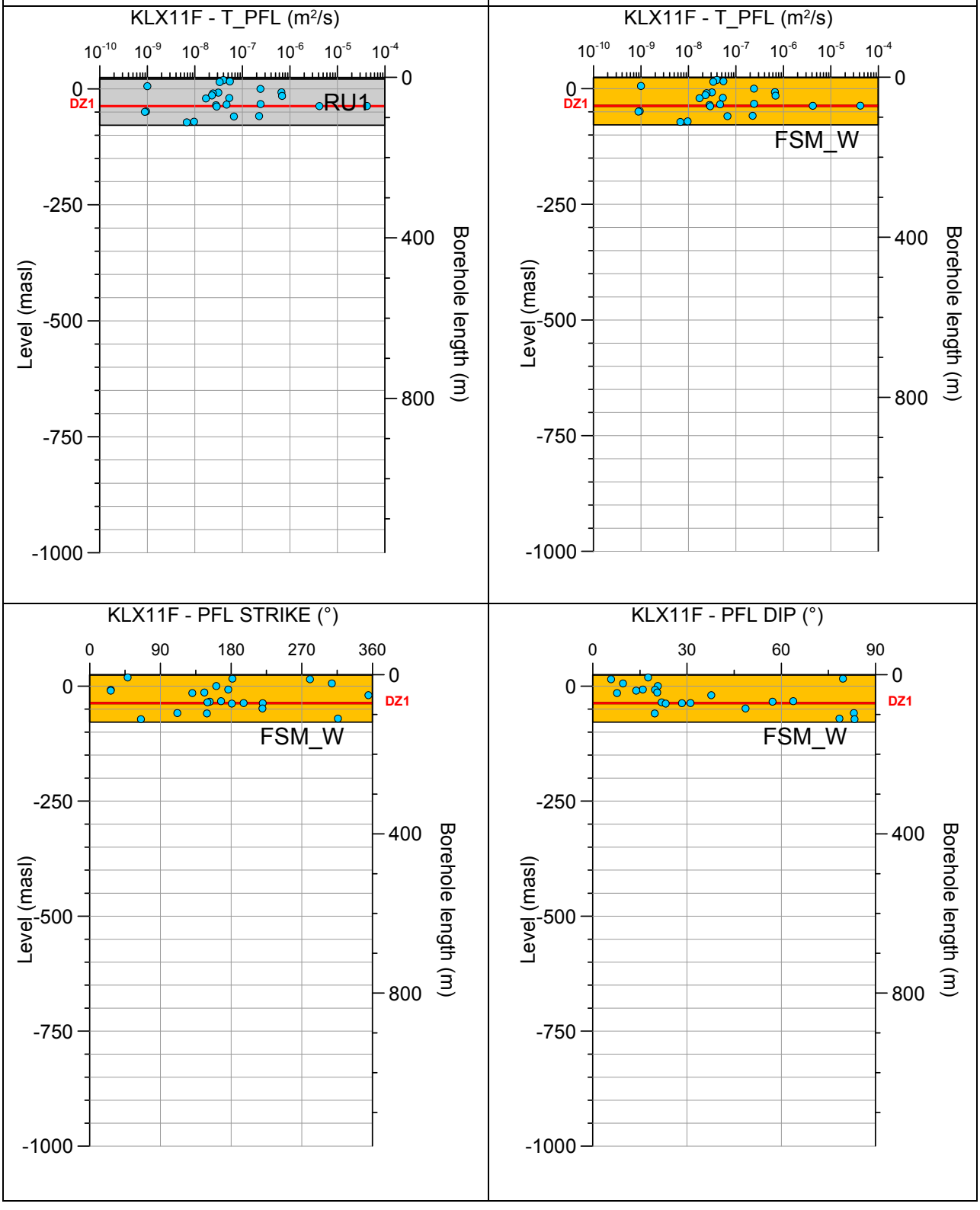

Comment:

Borehole KLX11F. Poles for PFL-f feature planes outside deformation zones.

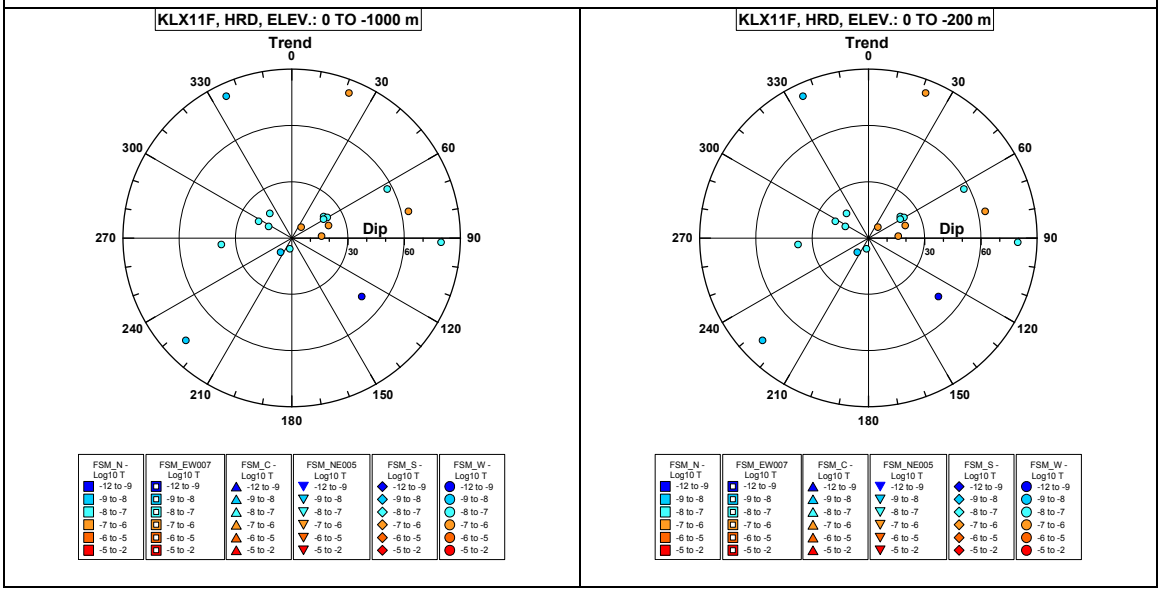

Borehole KLX11F. Poles for PFL-f feature planes in possible deformation zones.

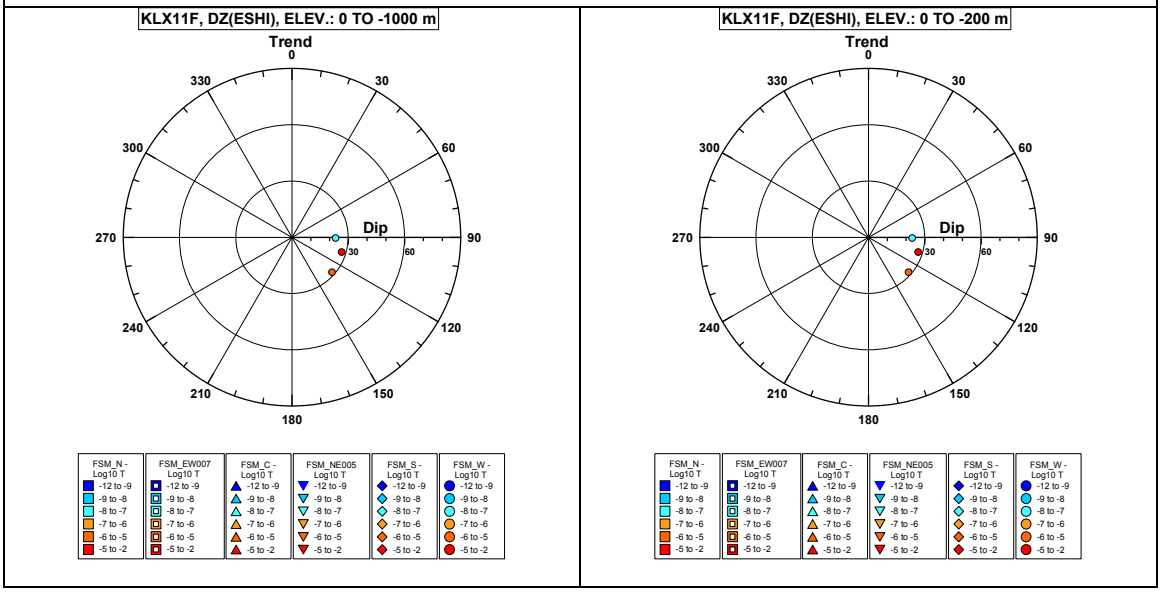

No PFL-f feature planes in deterministically modelled deformation zones exist in KLX11F.

Borehole KLX12A.

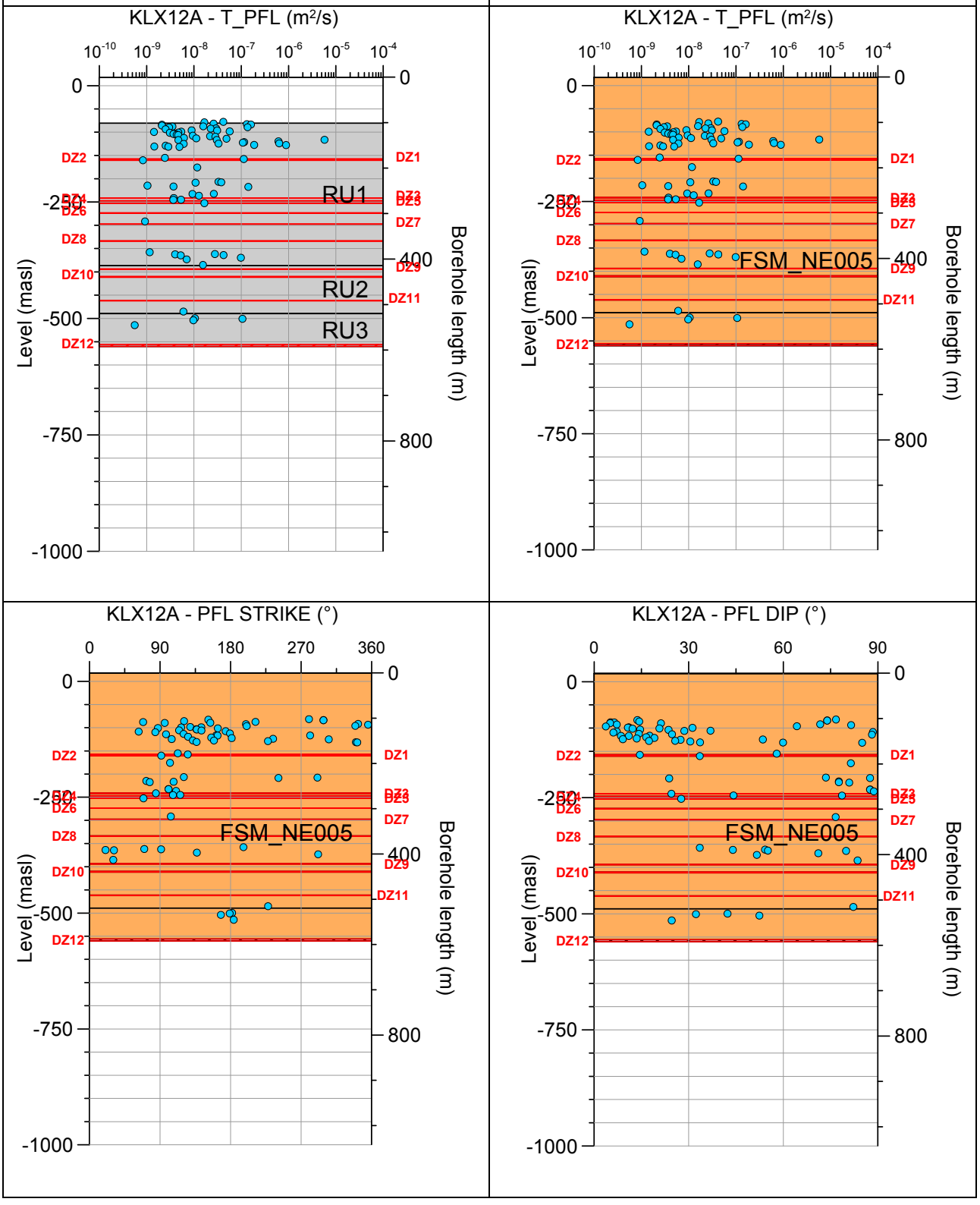

Comment:

Borehole KLX12A. Poles for PFL-f feature planes outside deformation zones.

KLX12A, HRD, ELEV.: 0 TO -1000 m

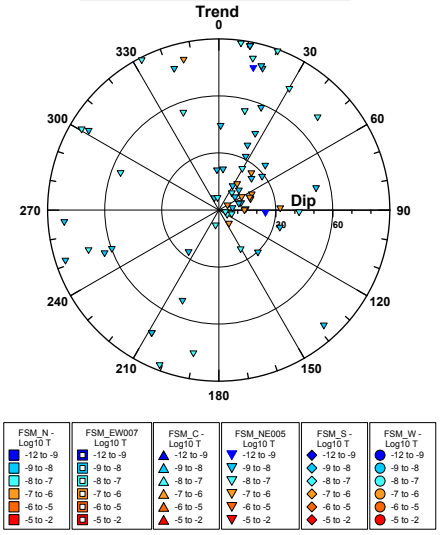

KLX12A, HRD, ELEV.: 0 TO -200 m

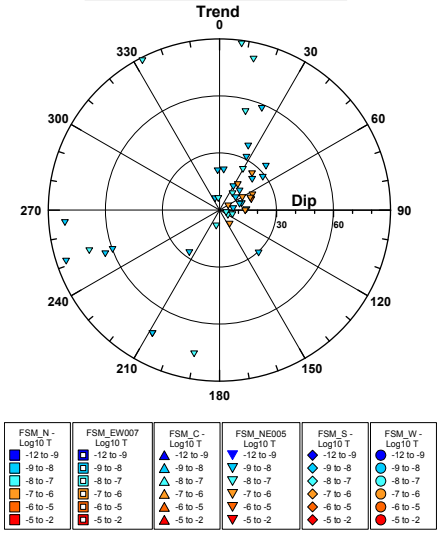

KLX12A, HRD, ELEV.: -200 TO -400 m

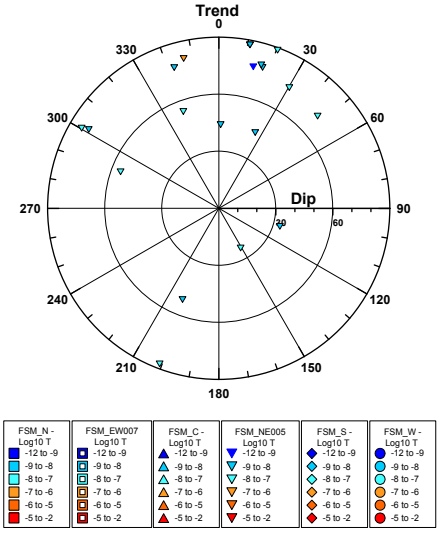

KLX12A, HRD, ELEV.: -400 TO -600 m

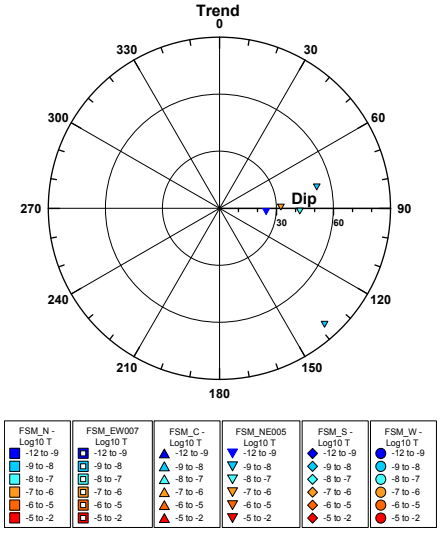

Borehole KLX12A. Poles for PFL-f feature planes in possible deformation zones.

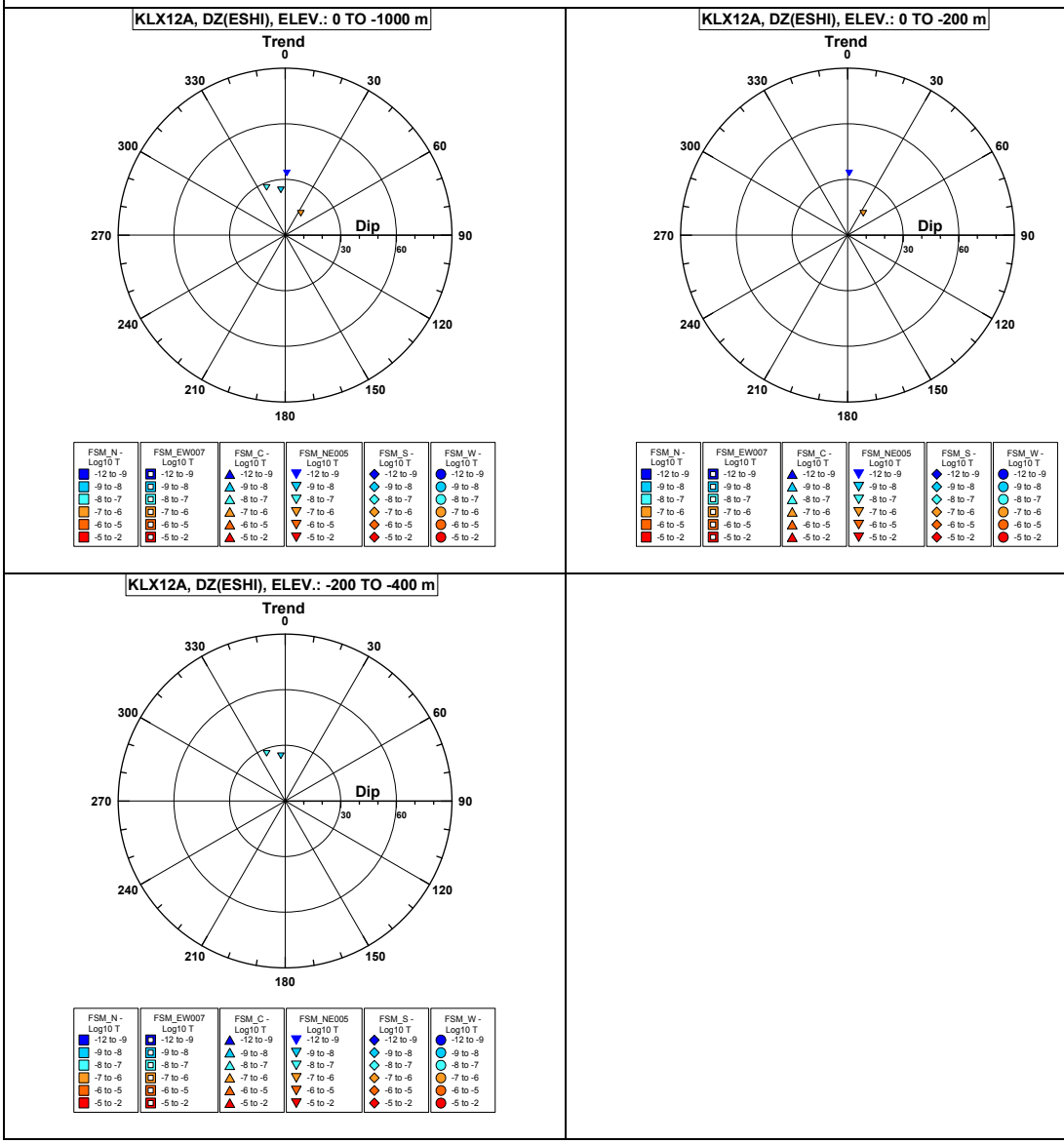

No PFL-f feature planes in deterministically modelled deformation zones exist in KLX12A.

Borehole KLX13A.

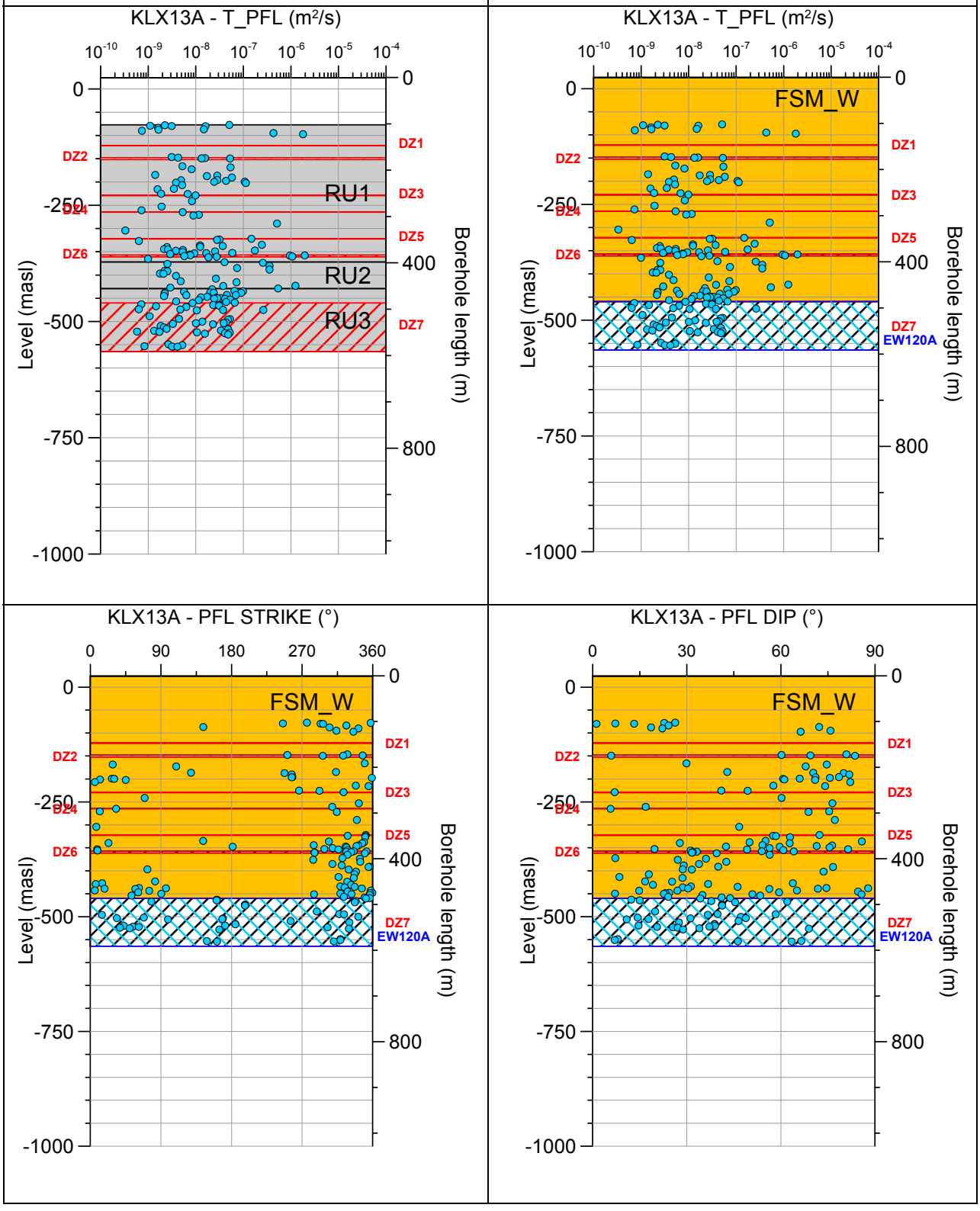

Comment:

Borehole KLX13A. Poles for PFL-f feature planes outside deformation zones.

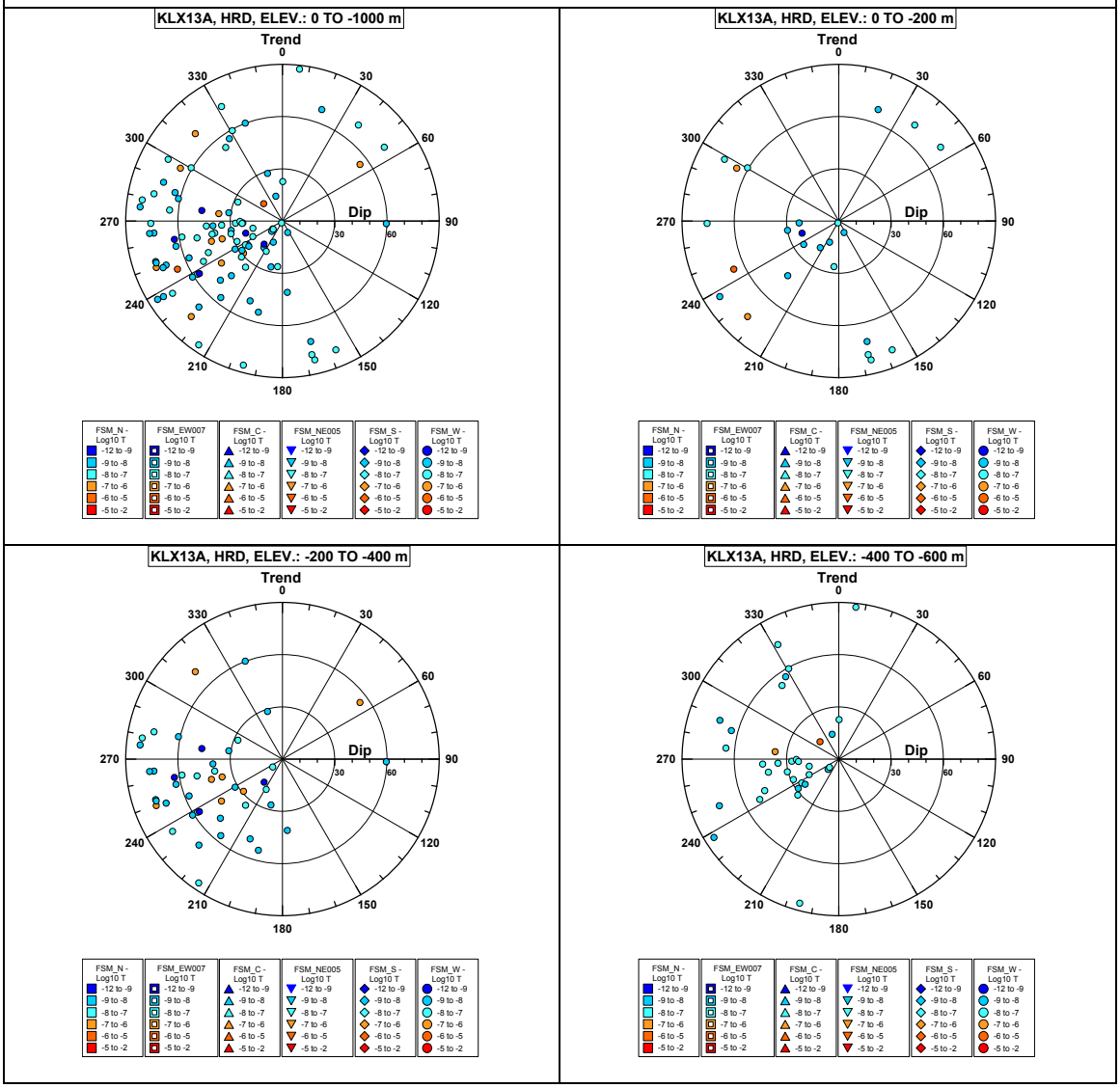

Borehole KLX13A. Poles for PFL-f feature planes in possible deformation zones.

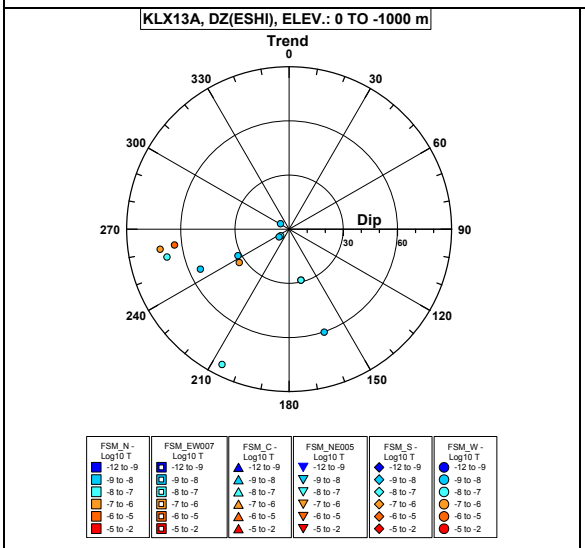

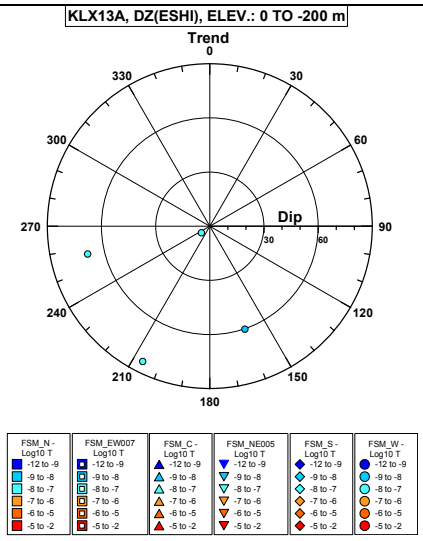

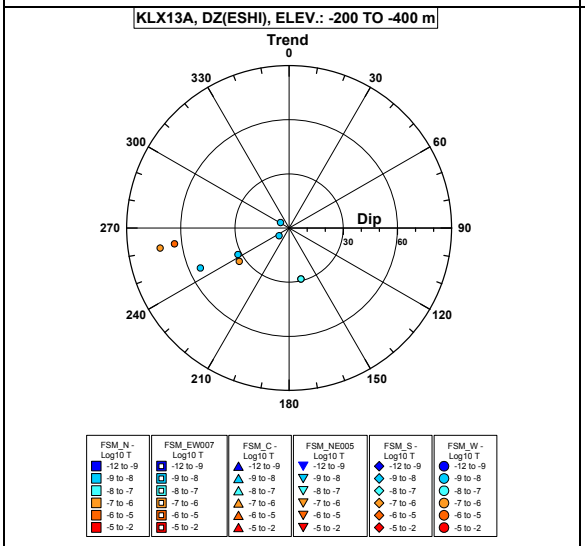

Borehole KLX13A. Poles for PFL-f feature planes in deterministically modelled deformation zones.

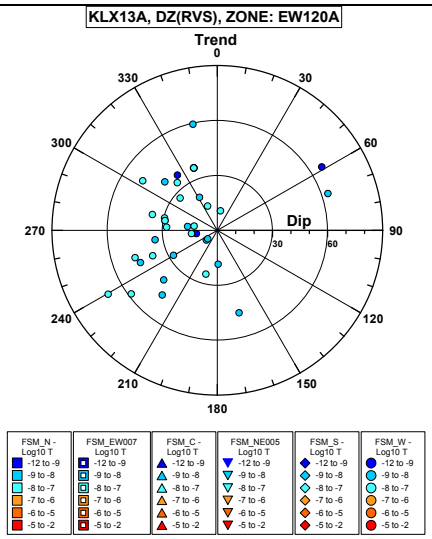

Borehole KLX14A.

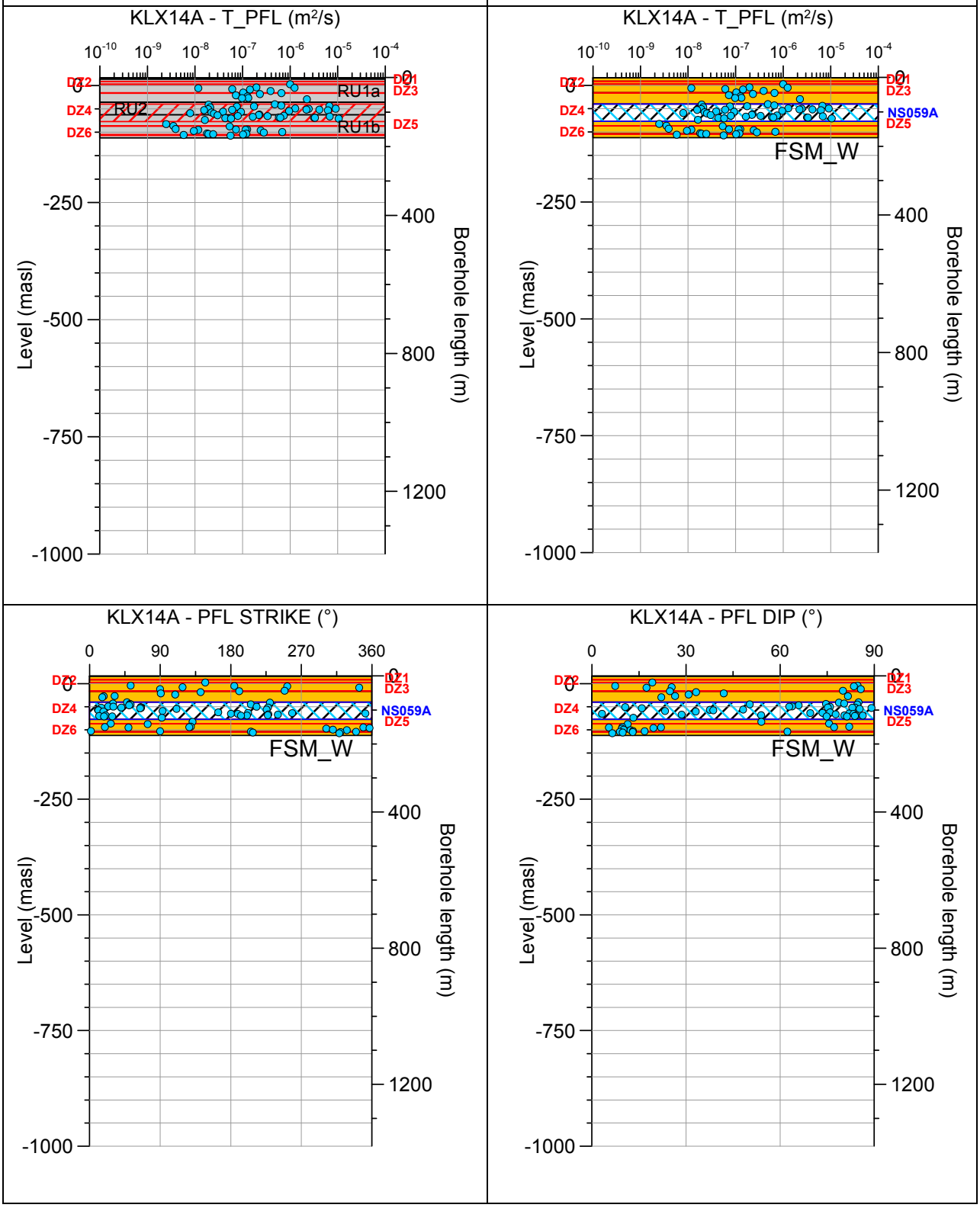

Comment:

Borehole KLX14A. Poles for PFL-f feature planes outside deformation zones.

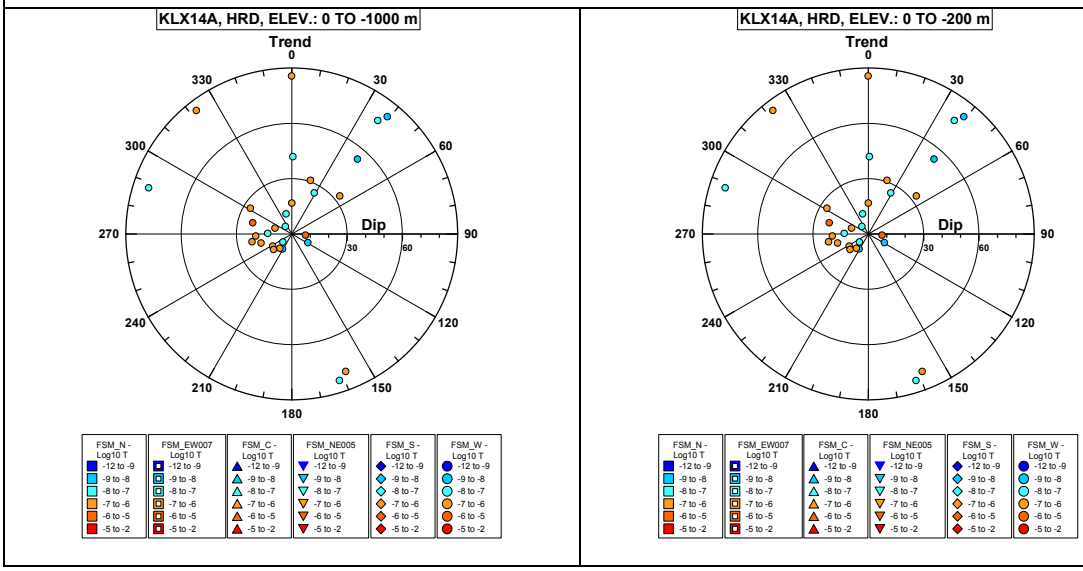

Borehole KLX14A. Poles for PFL-f feature planes in possible deformation zones.

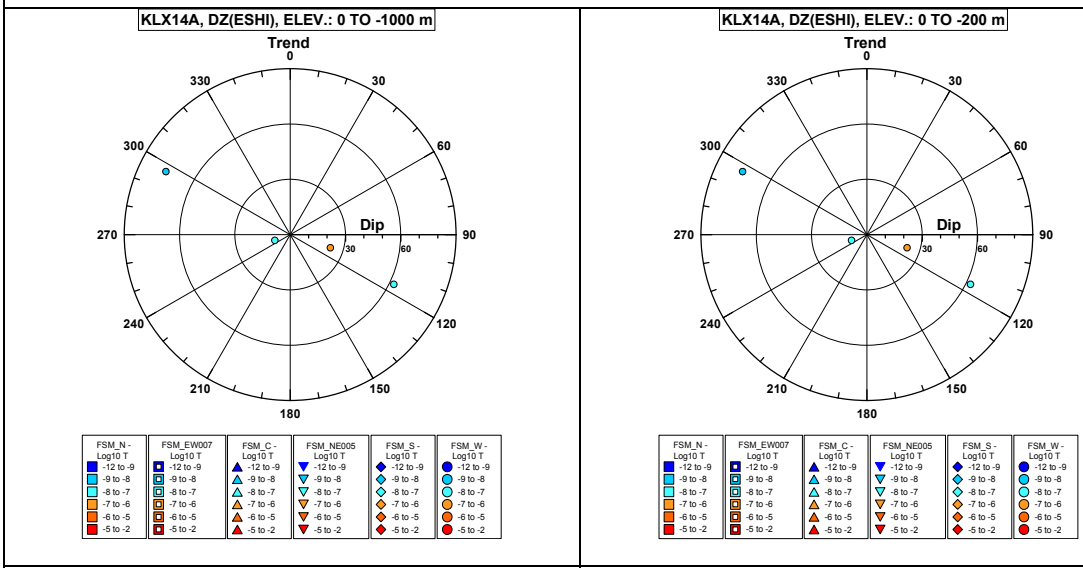

Borehole KLX14A. Poles for PFL-f feature planes in deterministically modelled deformation zones.

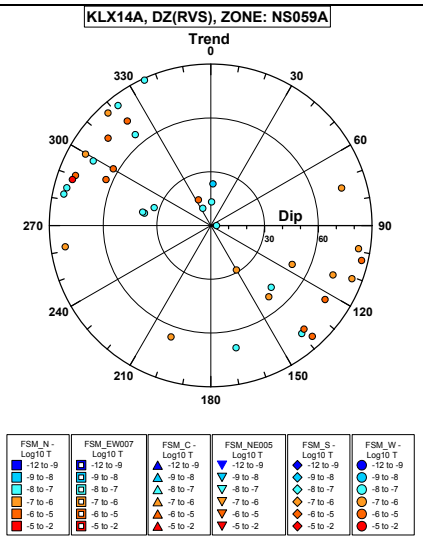

Borehole KLX15A.

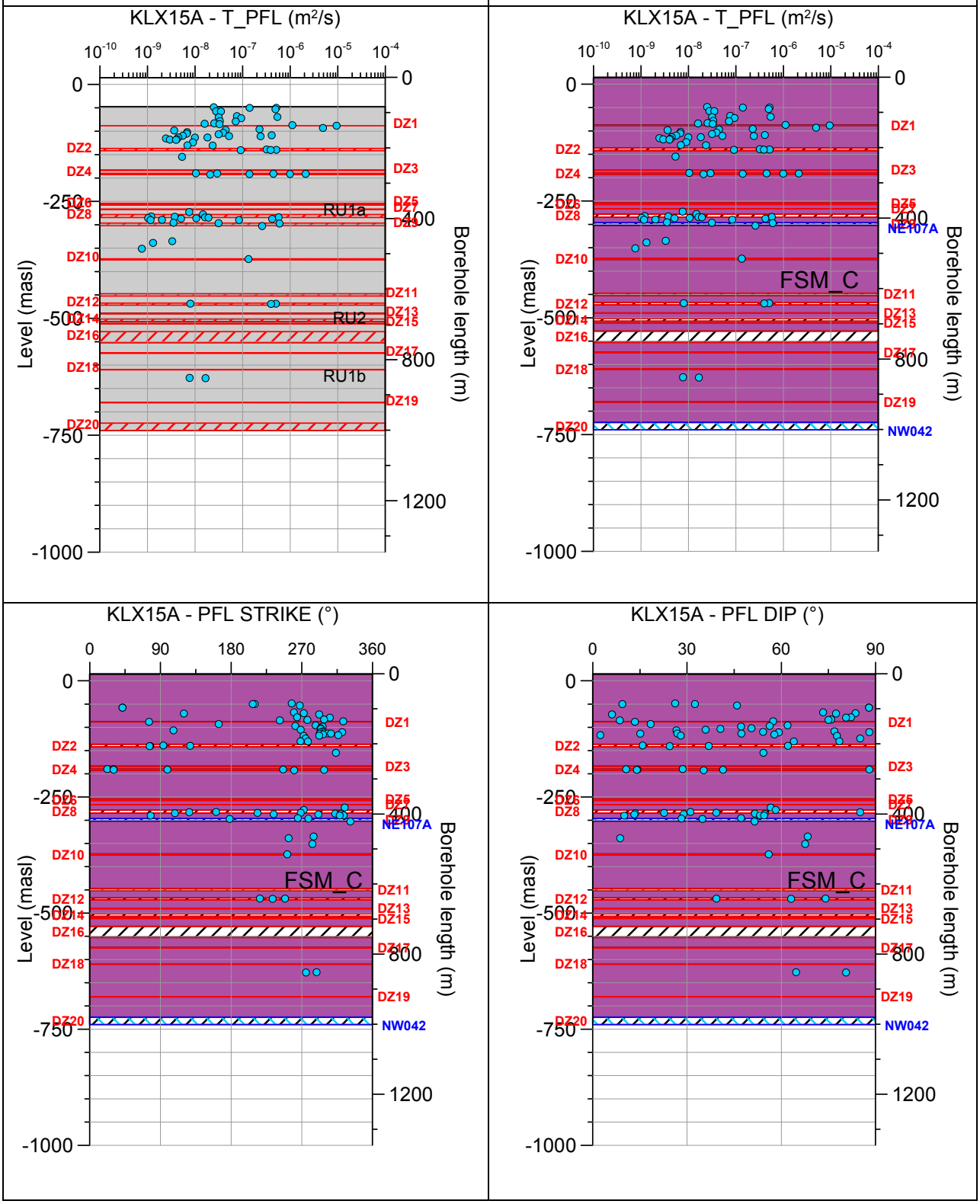

Comment:

Borehole KLX15A. Poles for PFL-f feature planes outside deformation zones.

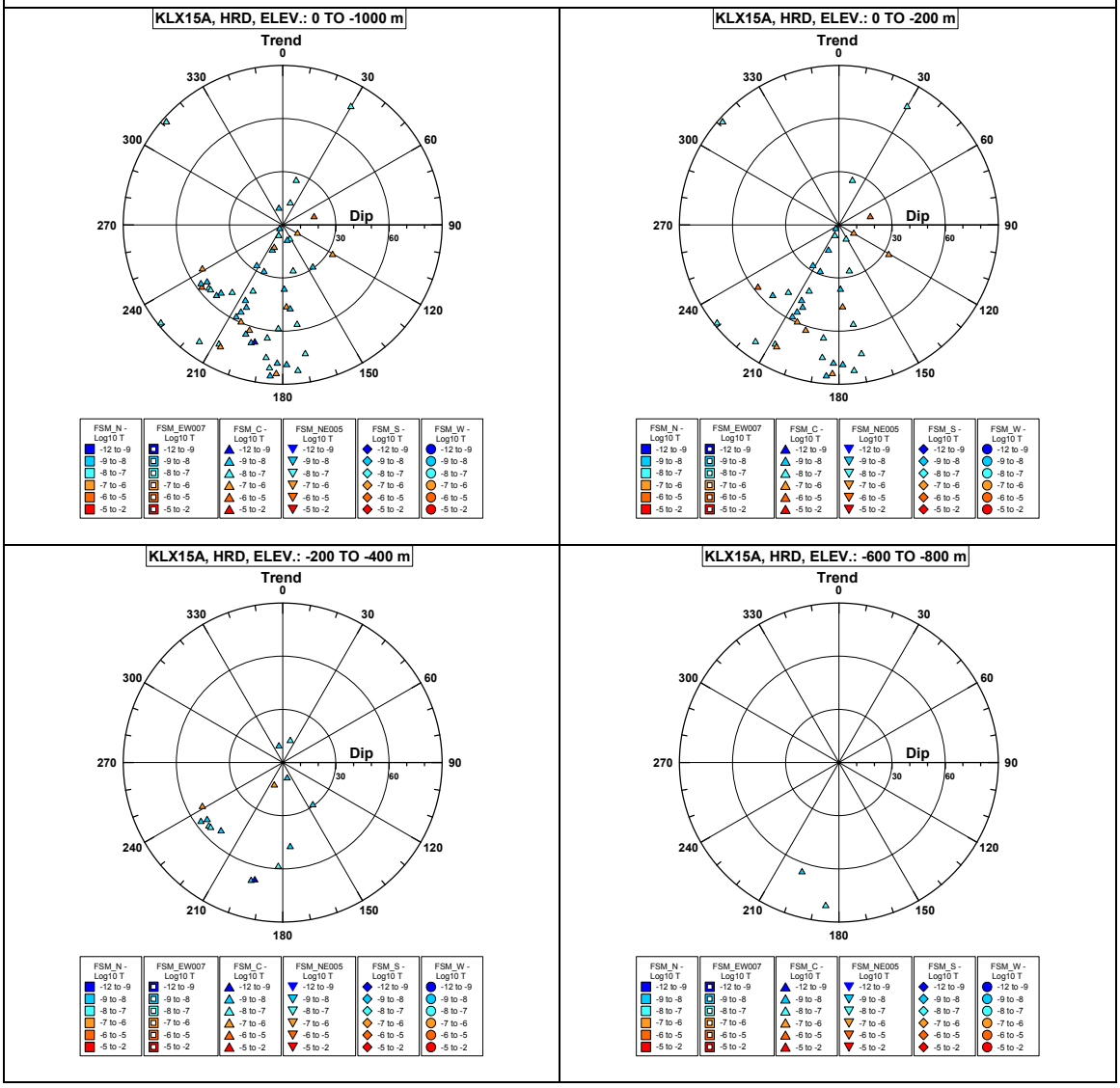

Borehole KLX15A. Poles for PFL-f feature planes in possible deformation zones.

KLX15A, DZ(ESHI), ELEV.: 0 TO -1000 m

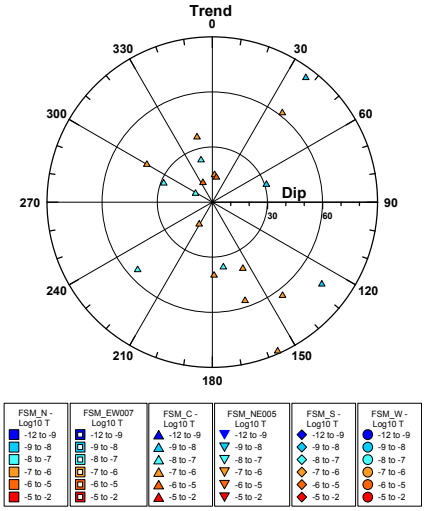

KLX15A, DZ(ESHI), ELEV.: 0 TO -200 m

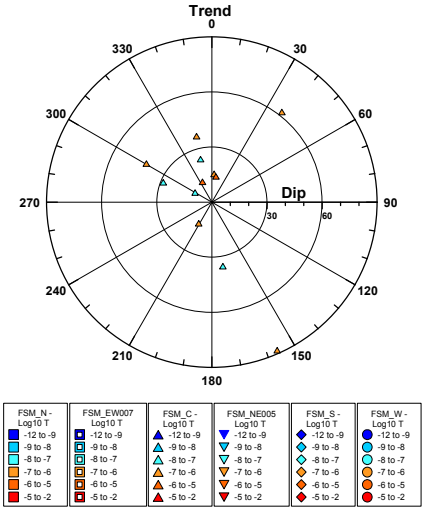

KLX15A, DZ(ESHI), ELEV.: -200 TO -400 m

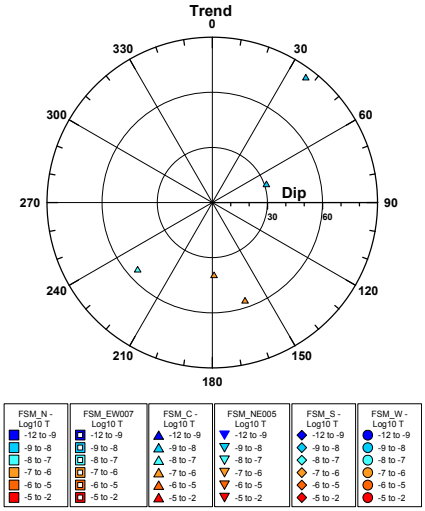

KLX15A, DZ(ESHI), ELEV.: -400 TO -600 m

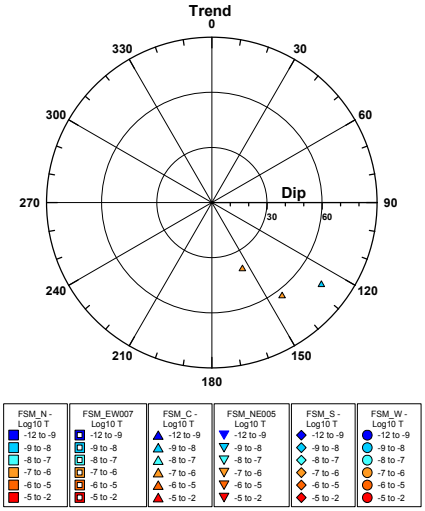

Borehole KLX15A. Poles for PFL-f feature planes in deterministically modelled deformation zones.

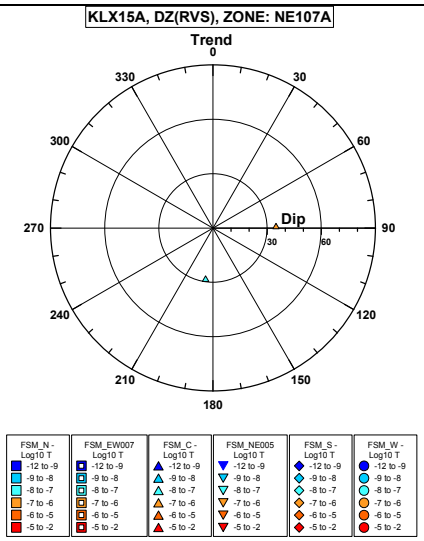

Borehole KLX16A.

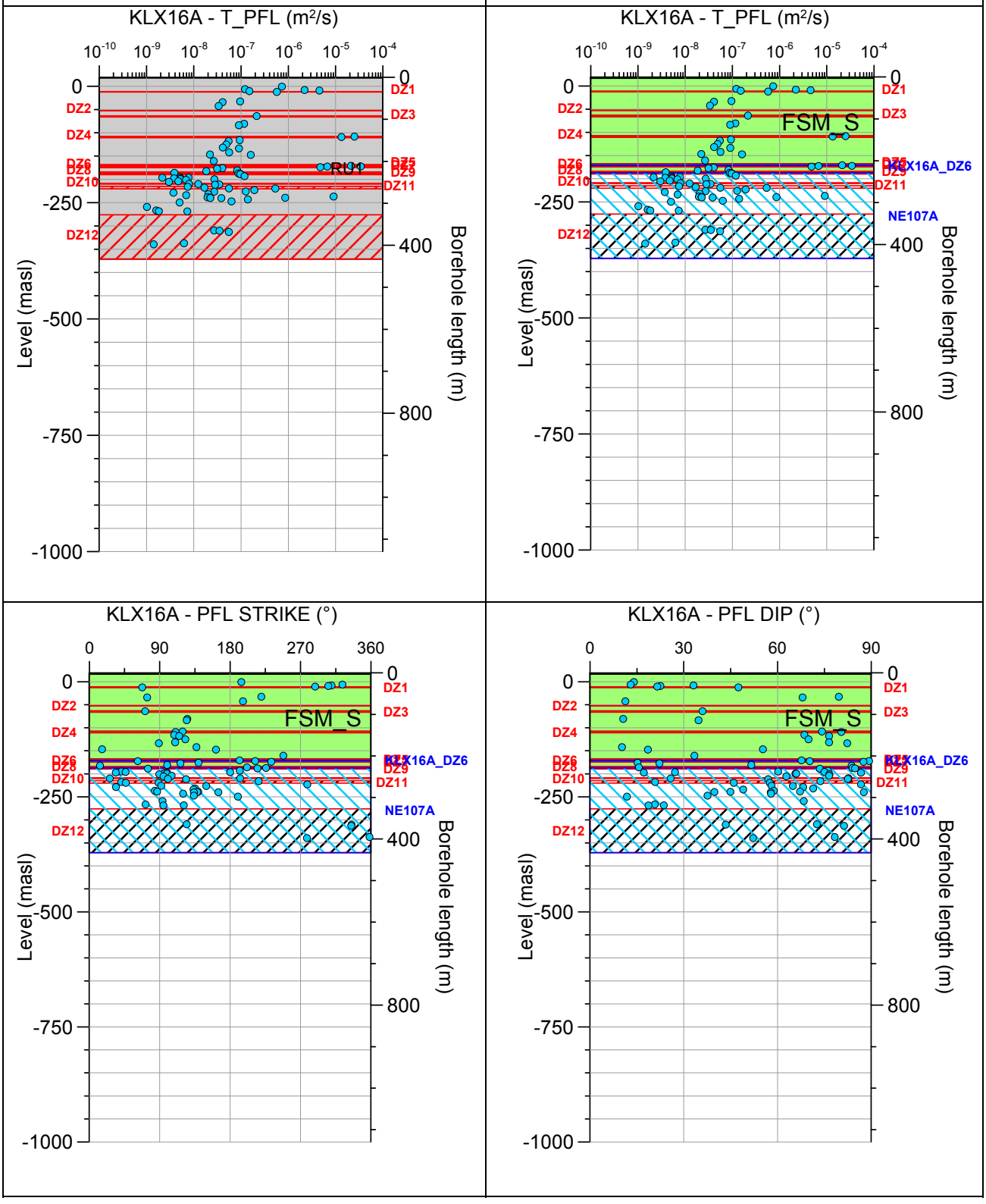

Comment:

Borehole KLX16A. Poles for PFL-f feature planes outside deformation zones.

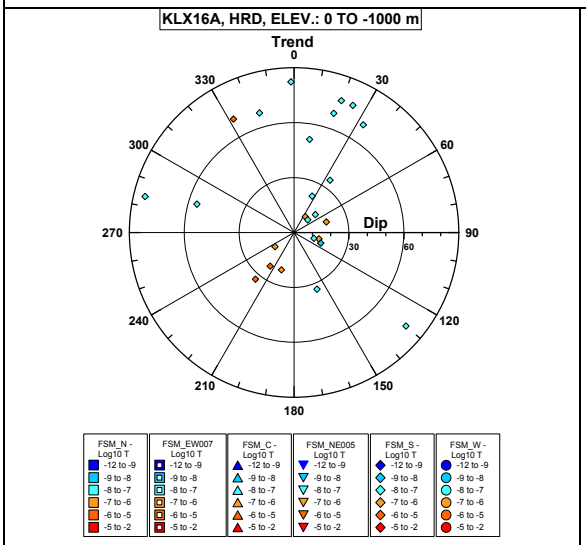

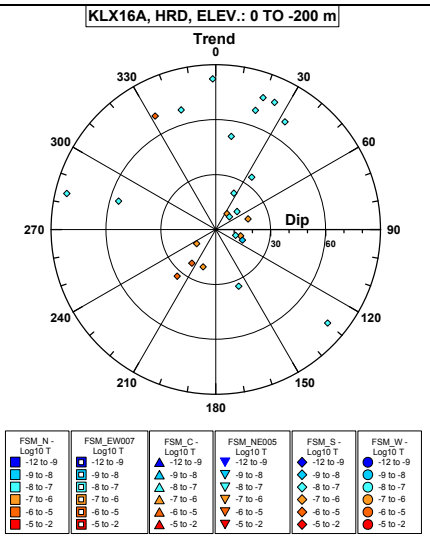

Borehole KLX16A. Poles for PFL-f feature planes in possible deformation zones.

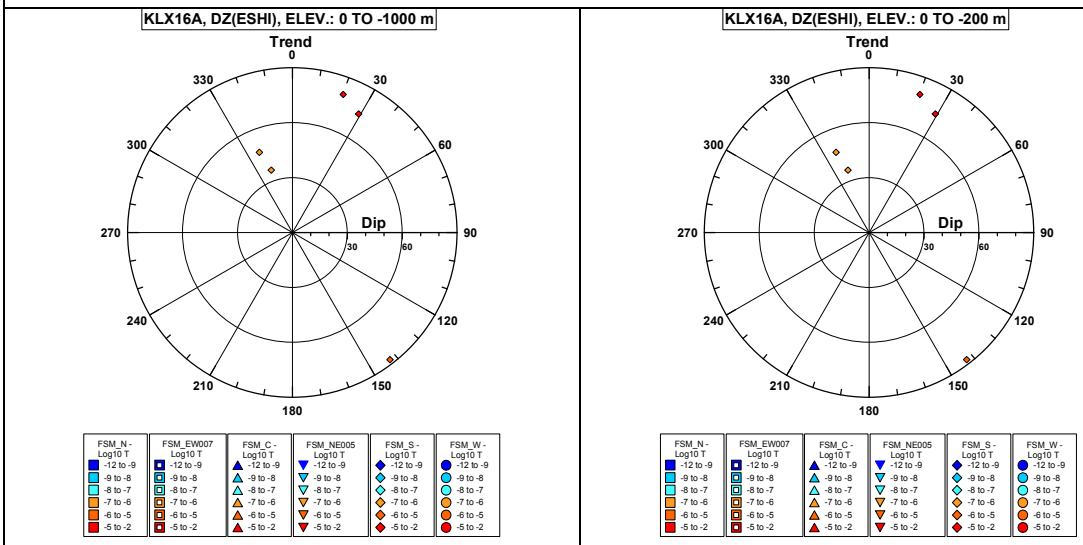

Borehole KLX16A. Poles for PFL-f feature planes in deterministically modelled deformation zones.

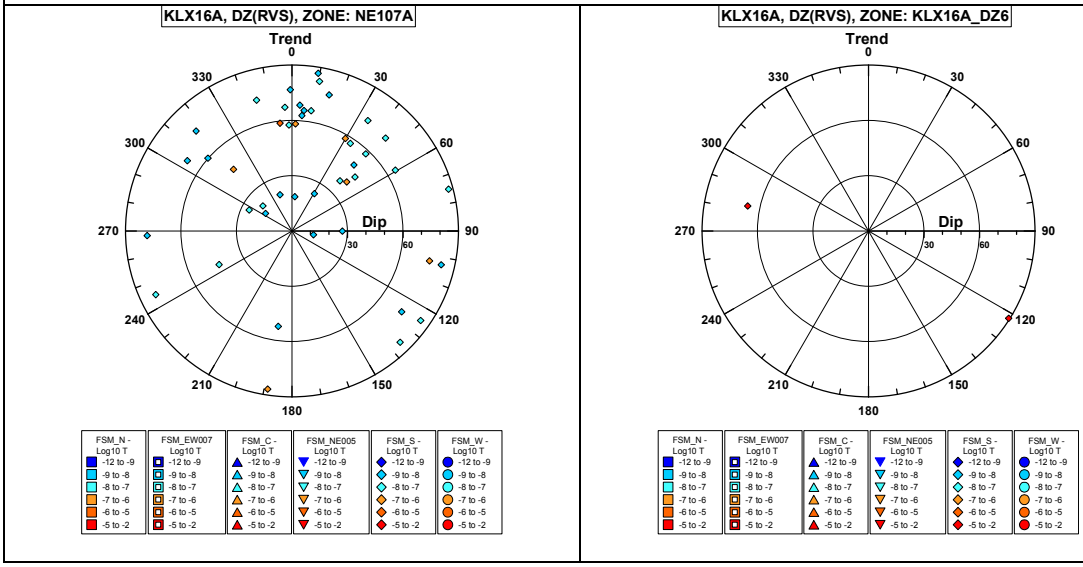

Borehole KLX17A.

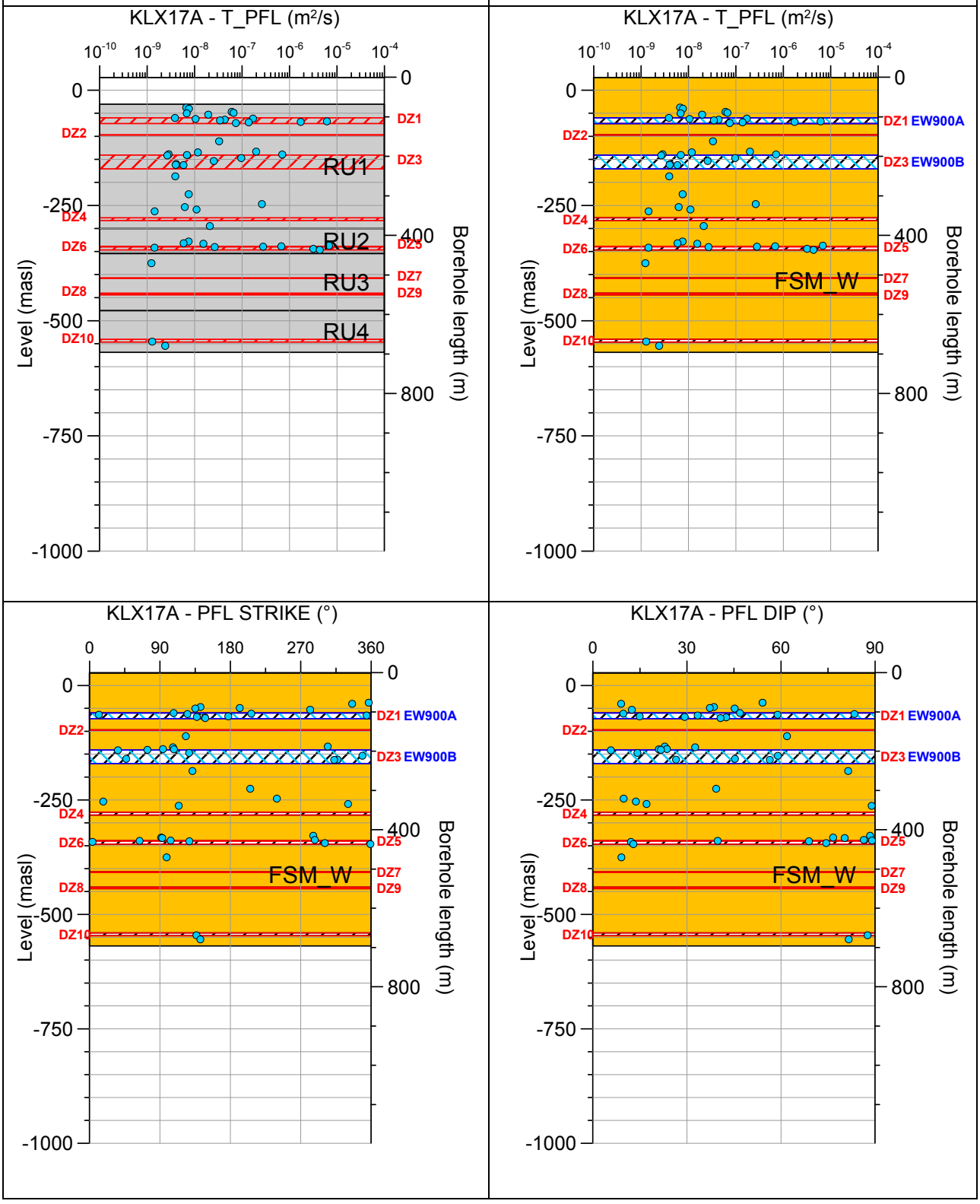

Comment:

Borehole KLX17A. Poles for PFL-f feature planes outside deformation zones.

KLX17A, HRD, ELEV.: 0 TO -1000 m

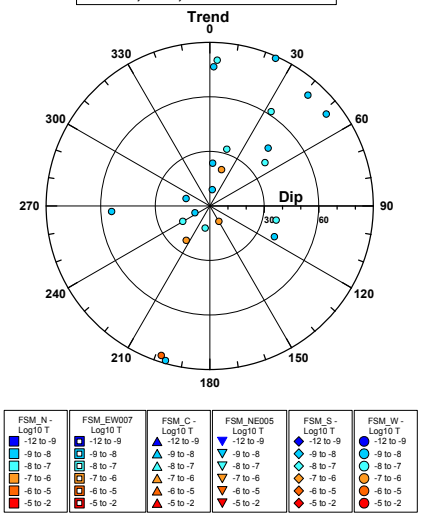

KLX17A, HRD, ELEV.: 0 TO -200 m

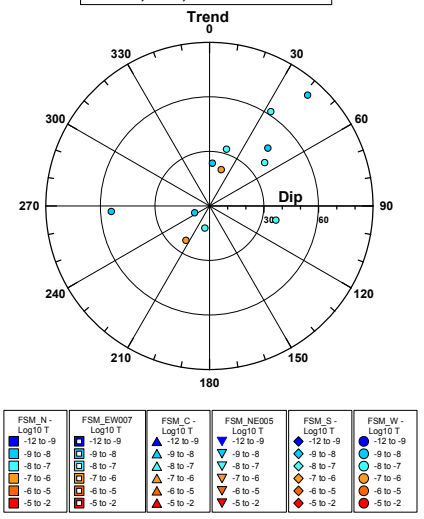

KLX17A, HRD, ELEV.: -200 TO -400 m

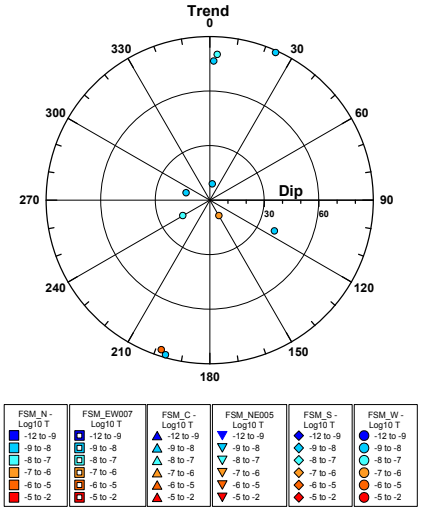

KLX17A, HRD, ELEV.: -400 TO -600 m

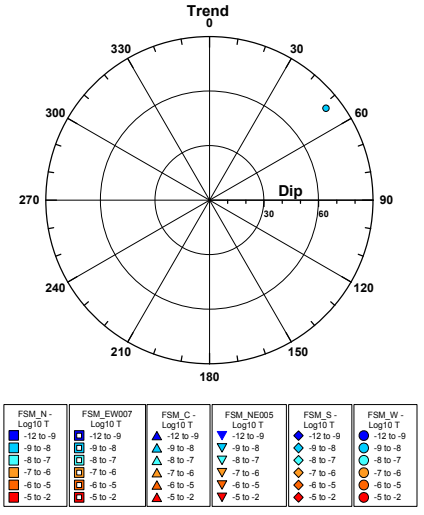

Borehole KLX17A. Poles for PFL-f feature planes in possible deformation zones.

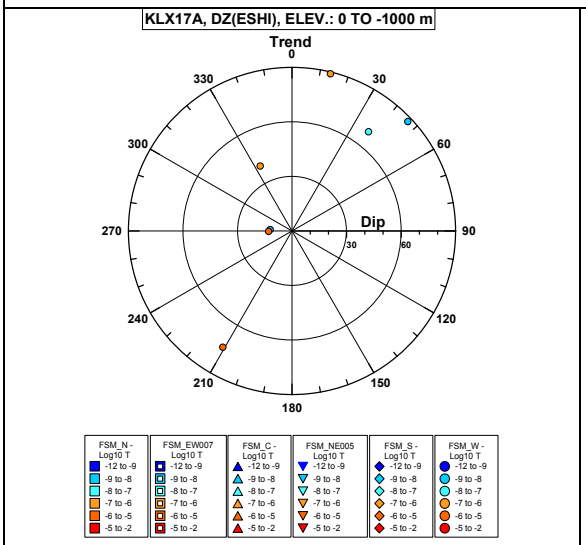

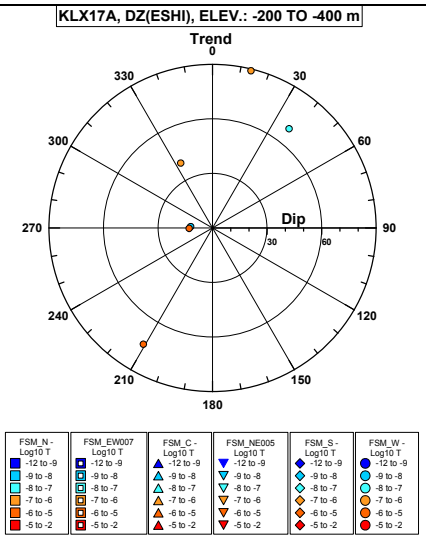

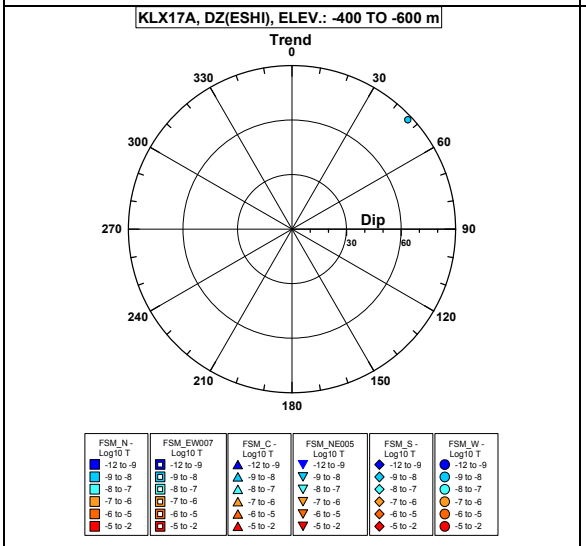

Borehole KLX17A. Poles for PFL-f feature planes in deterministically modelled deformation zones.

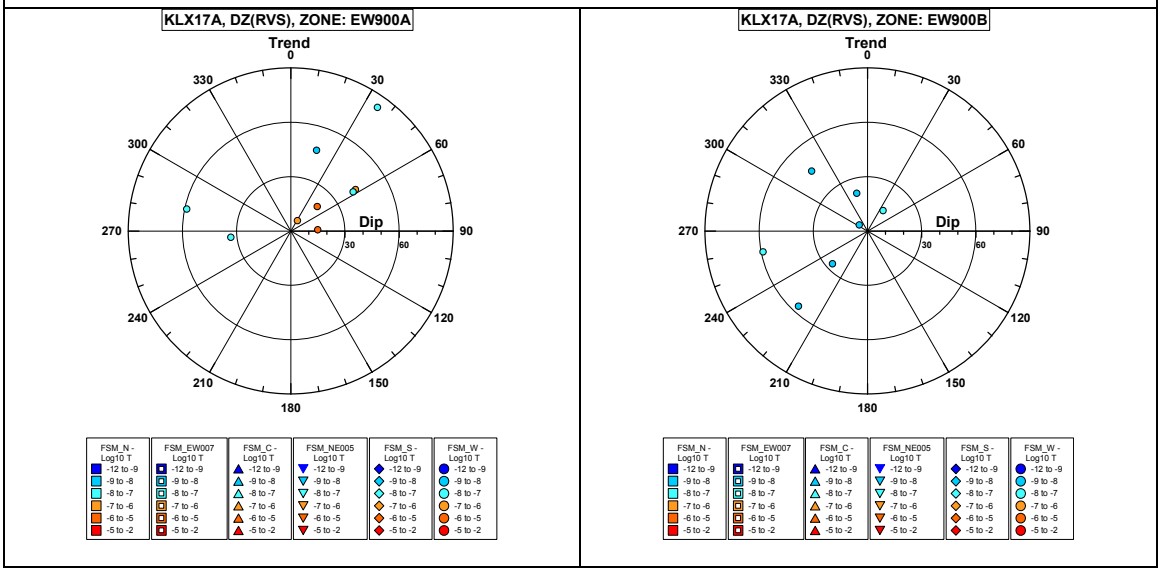

Borehole KLX18A.

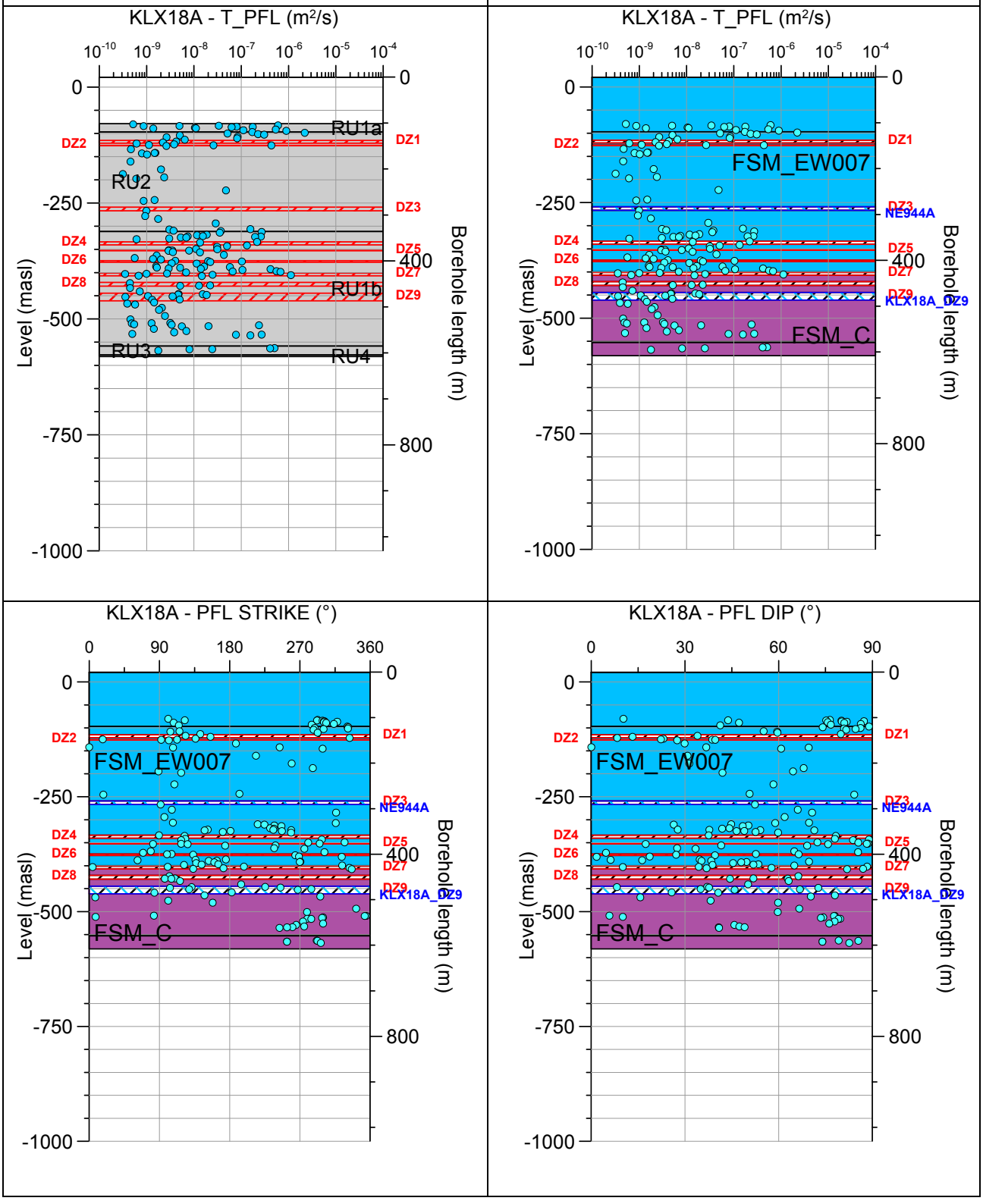

Comment:

Borehole KLX18A. Poles for PFL-f feature planes outside deformation zones.

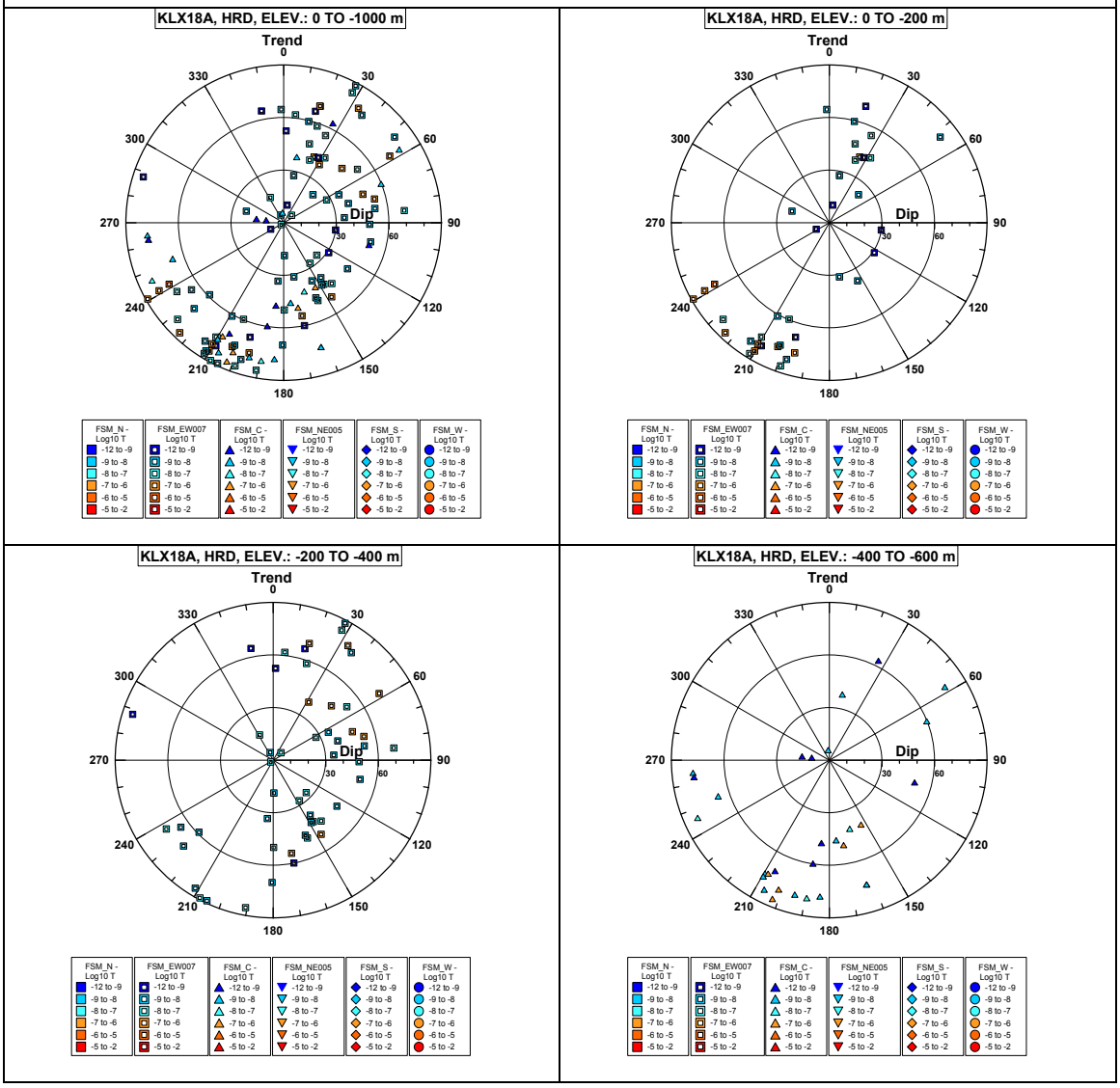

Borehole KLX18A. Poles for PFL-f feature planes in possible deformation zones.

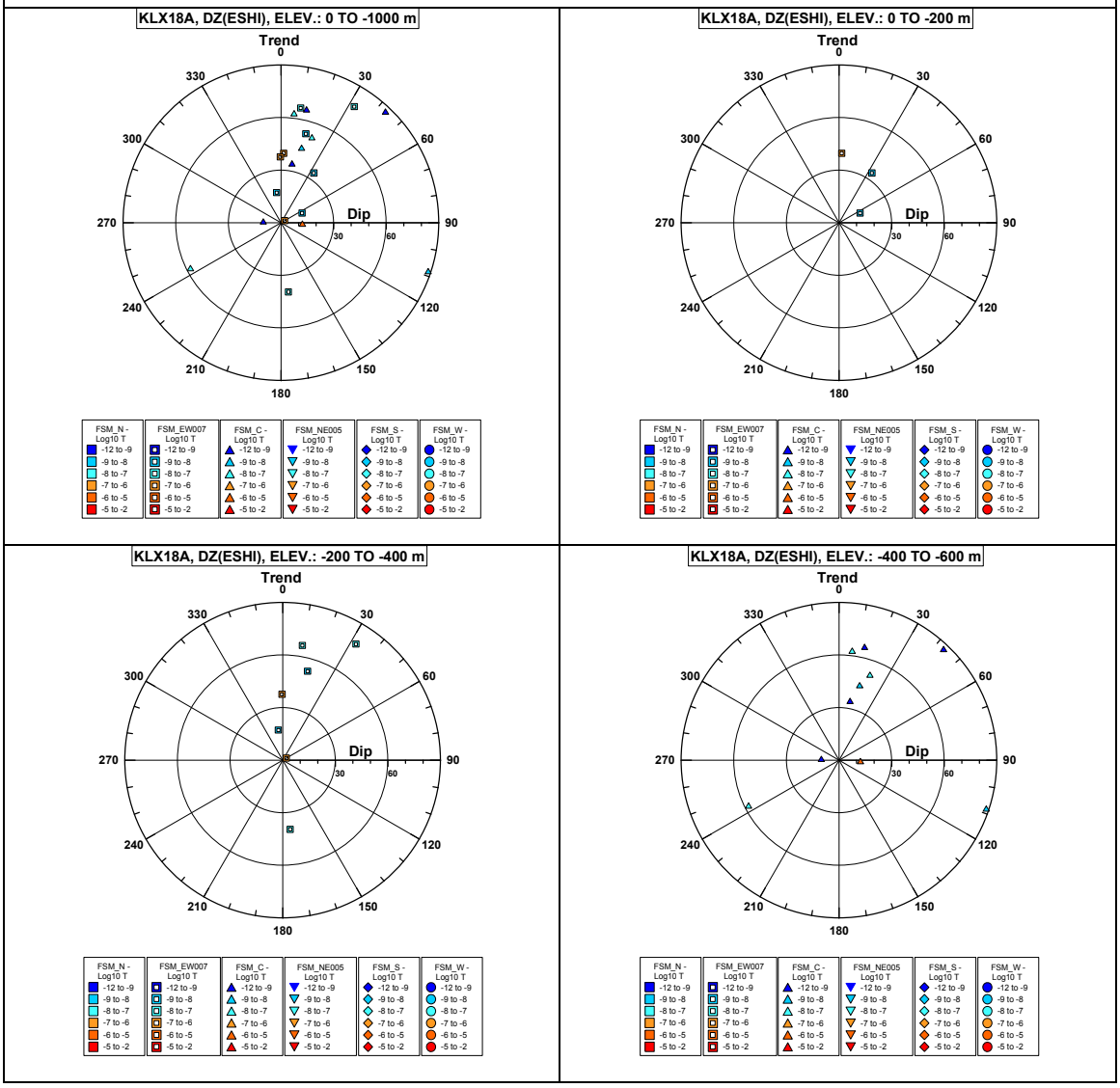

Borehole KLX18A. Poles for PFL-f feature planes in deterministically modelled deformation zones.

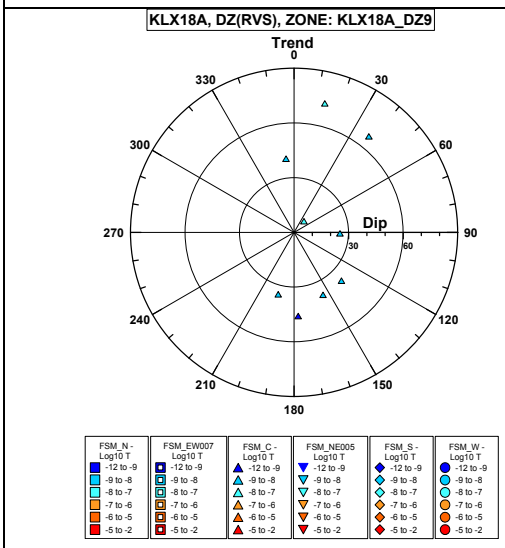

Borehole KLX19A.

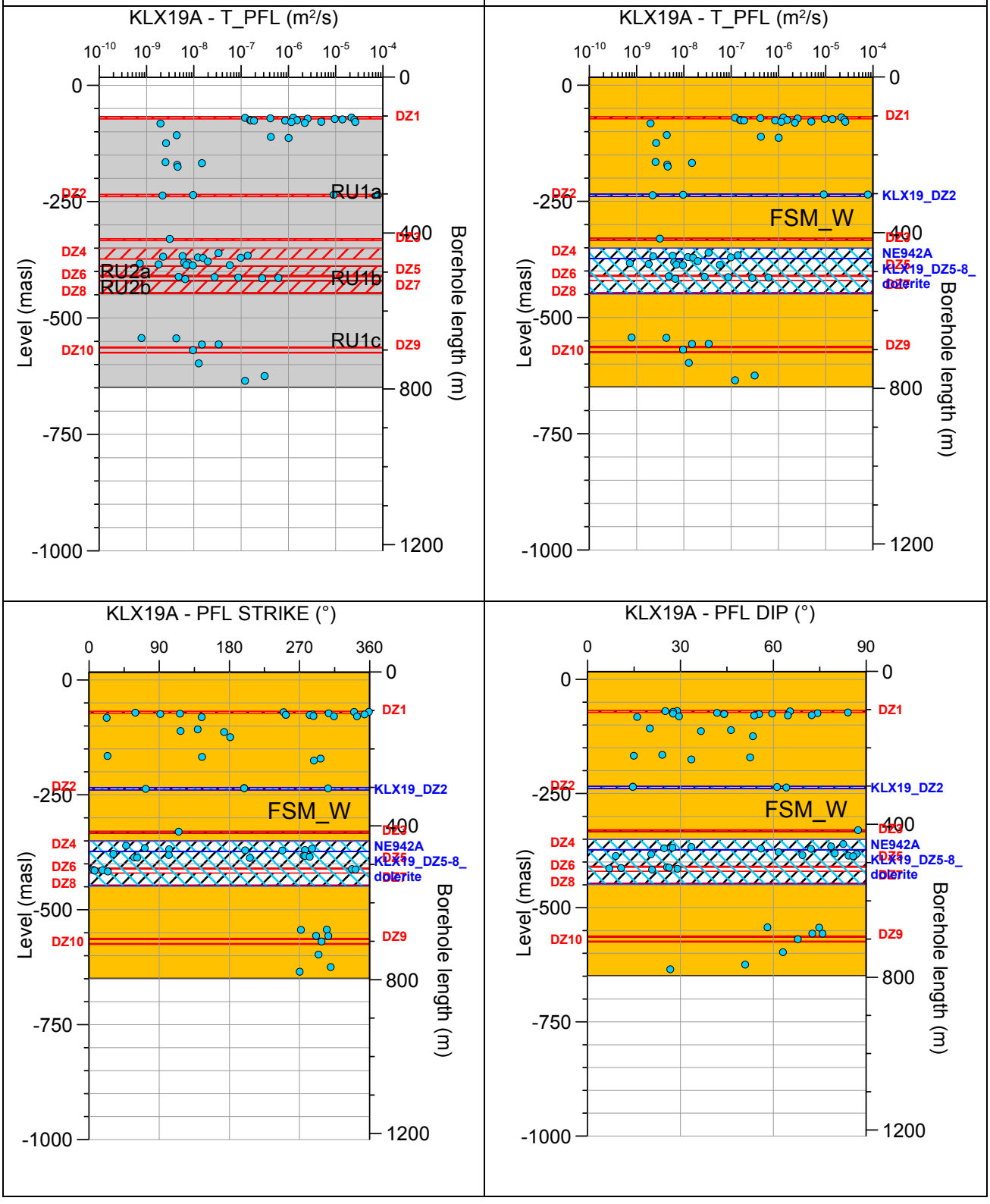

Comment:

Borehole KLX19A. Poles for PFL-f feature planes outside deformation zones.

KLX19A, HRD, ELEV.: 0 TO -1000 m

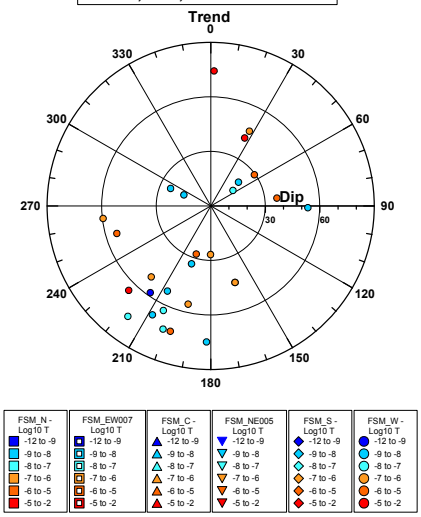

KLX19A, HRD, ELEV.: 0 TO -200 m

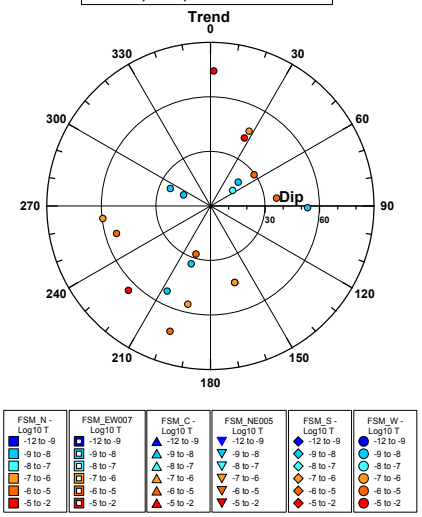

KLX19A, HRD, ELEV.: -400 TO -600 m

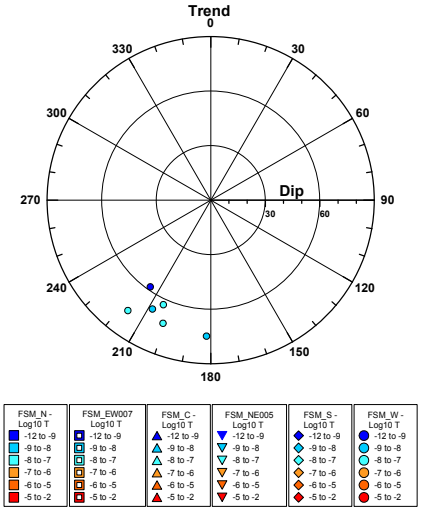

KLX19A, HRD, ELEV.: -600 TO -800 m

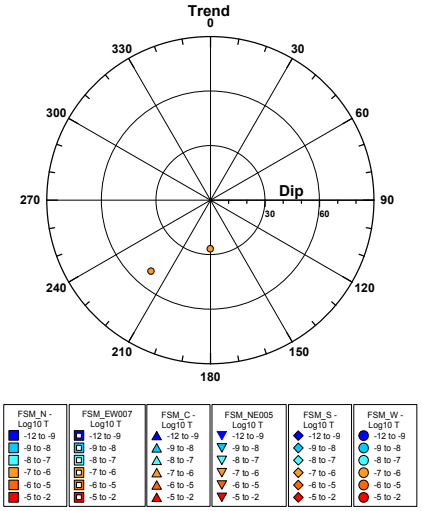

Borehole KLX19A. Poles for PFL-f feature planes in possible deformation zones.

KLX19A, DZ(ESHI), ELEV.: 0 TO -1000 m

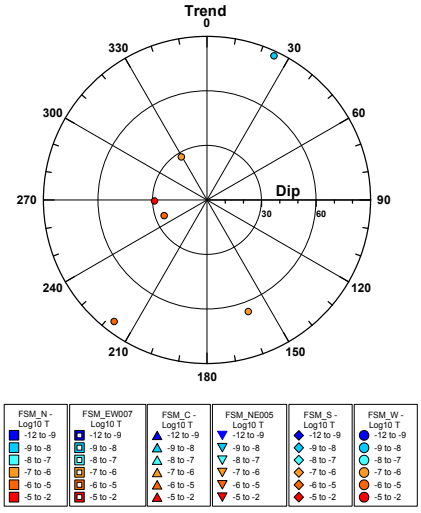

KLX19A, DZ(ESHI), ELEV.: 0 TO -200 m

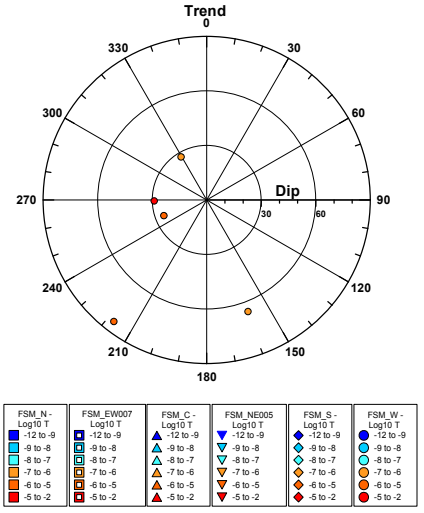

KLX19A, DZ(ESHI), ELEV.: -200 TO -400 m

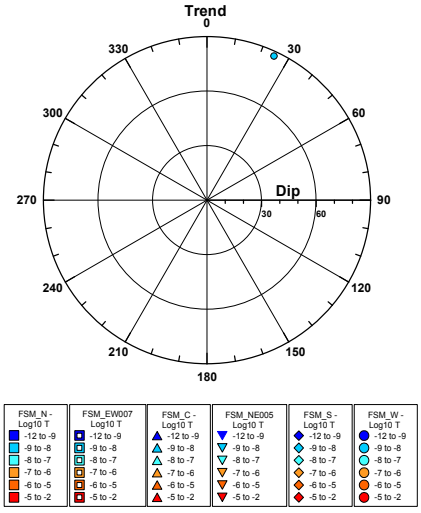

Borehole KLX19A. Poles for PFL-f feature planes in deterministically modelled deformation zones.

KLX19A, DZ(RVS), ZONE: NE942A

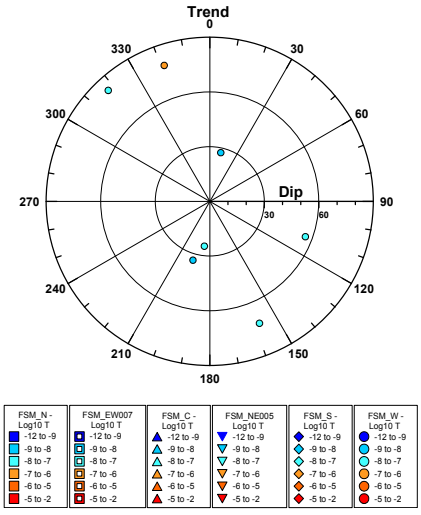

KLX19A, DZ(RVS), ZONE: KLX19_DZ5-8_DOLERITE

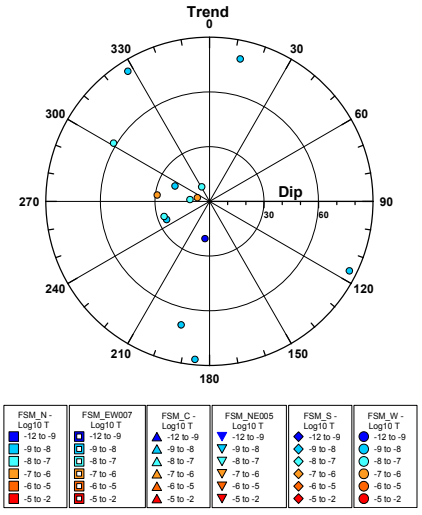

KLX19A, DZ(RVS), ZONE: KLX19_DZ2

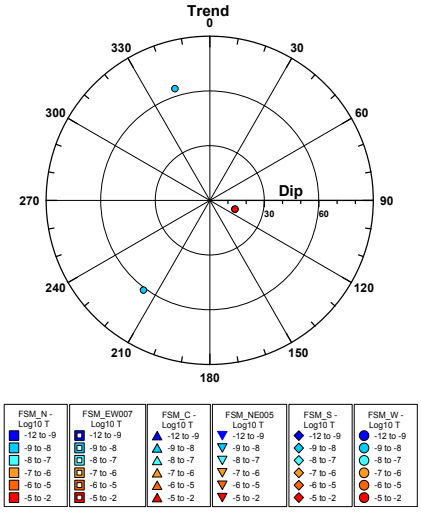

Borehole KLX20A.

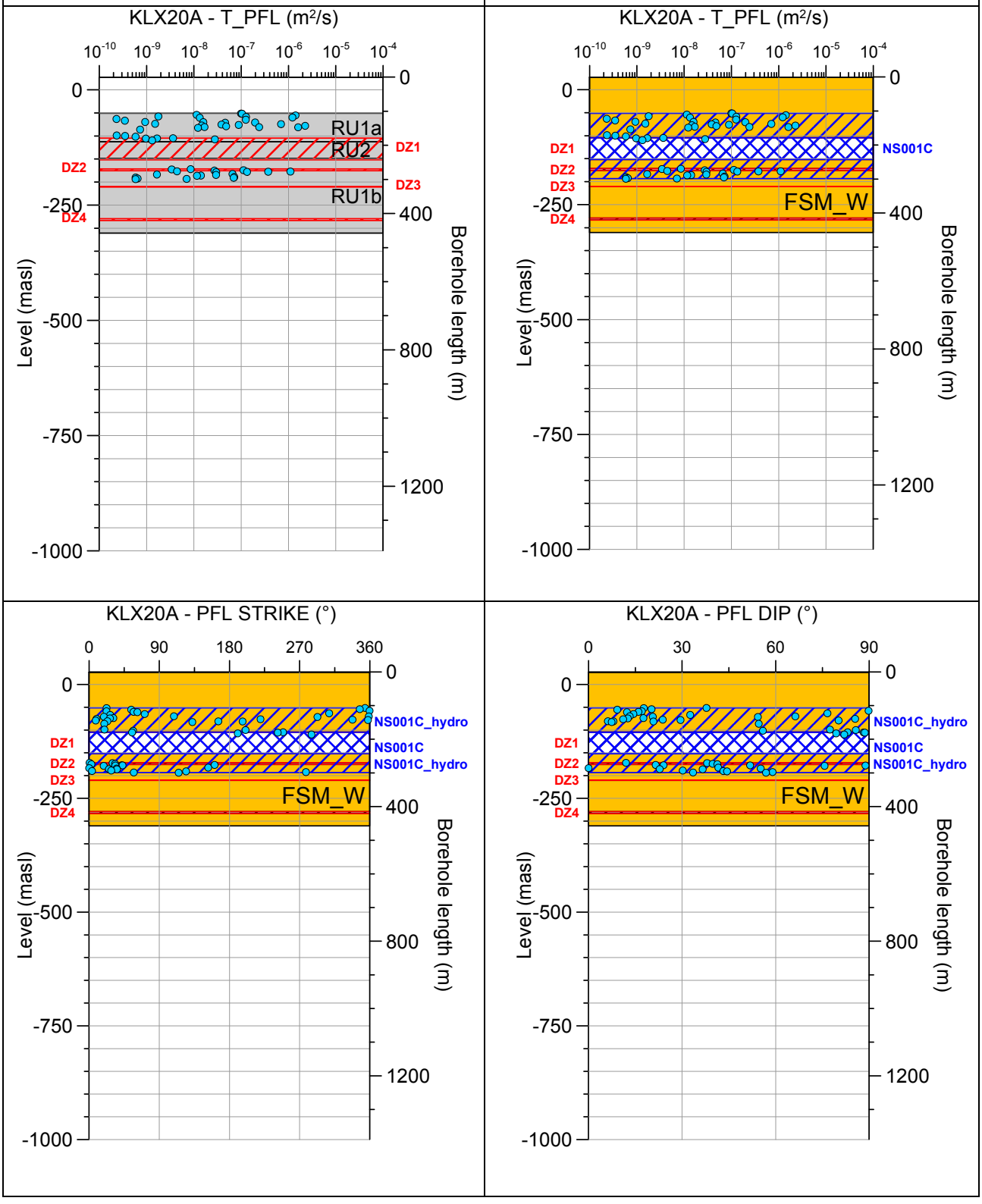

Comment:

Borehole KLX20A. Poles for PFL-f feature planes outside deformation zones.	

Borehole KLX20A. Poles for PFL-f feature planes in possible deformation zones.	

Borehole KLX20A. Poles for PFL-f feature planes in deterministically modelled deformation zones.	
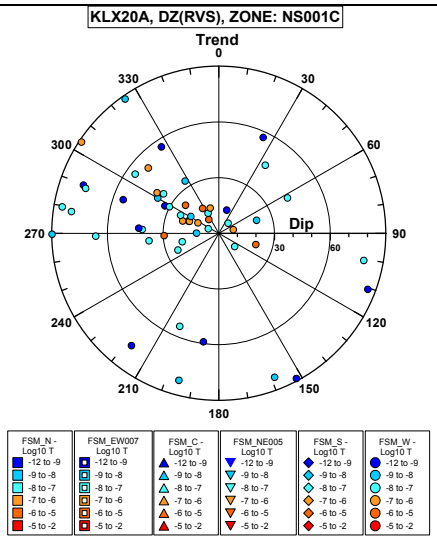	

Borehole KLX21B.

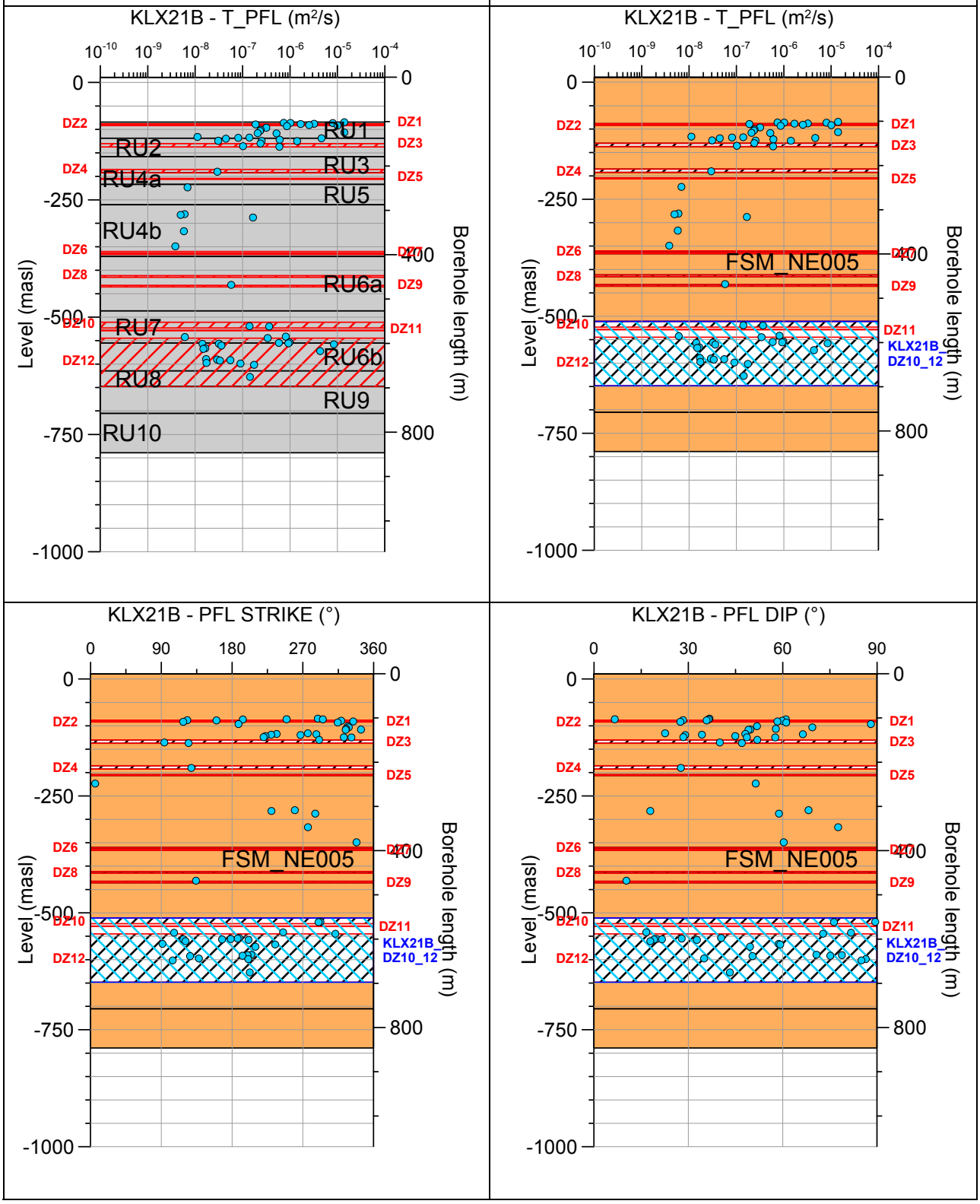

Comment:

Borehole KLX21B. Poles for PFL-f feature planes outside deformation zones.

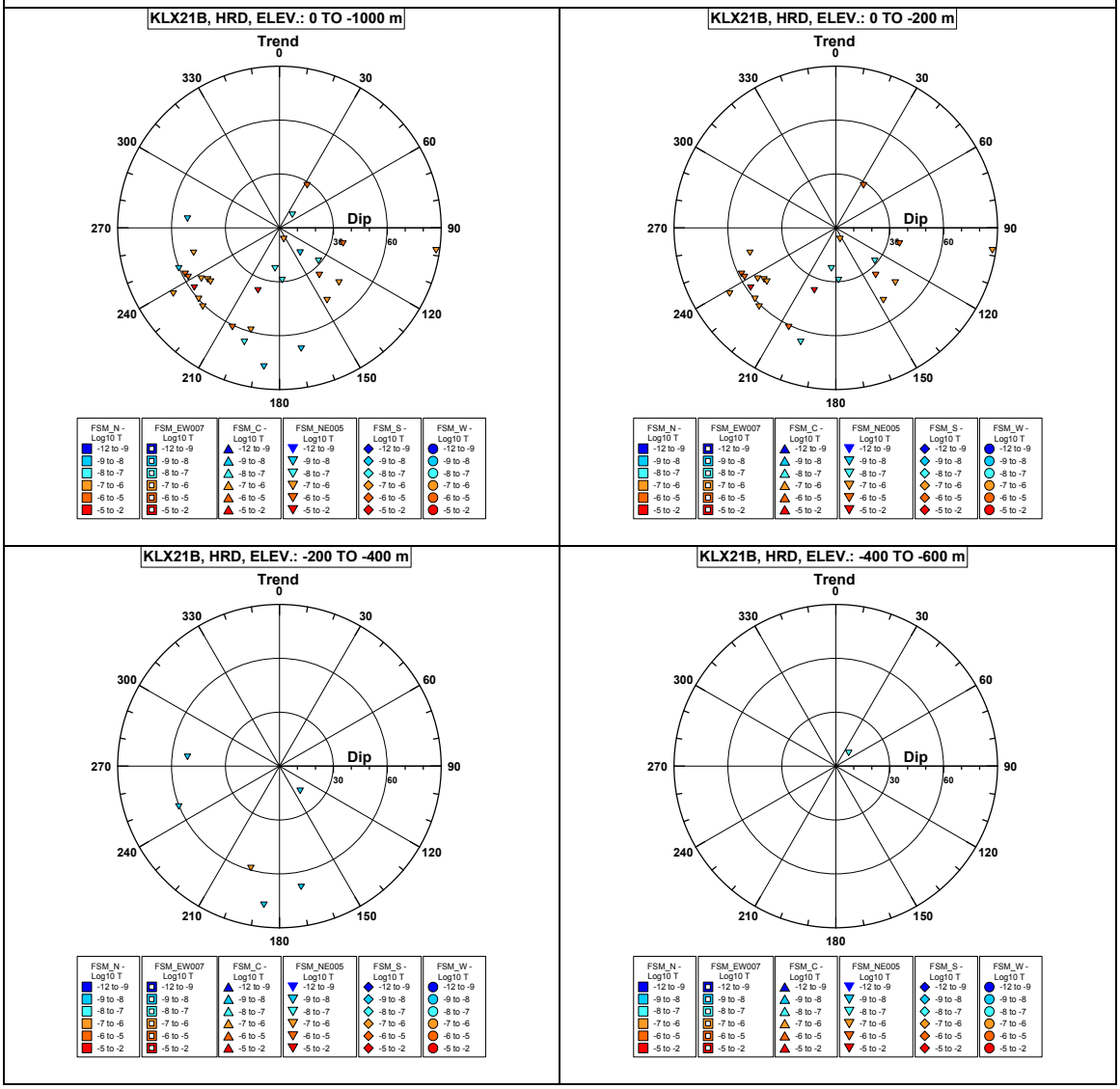

Borehole KLX21B. Poles for PFL-f feature planes in possible deformation zones.

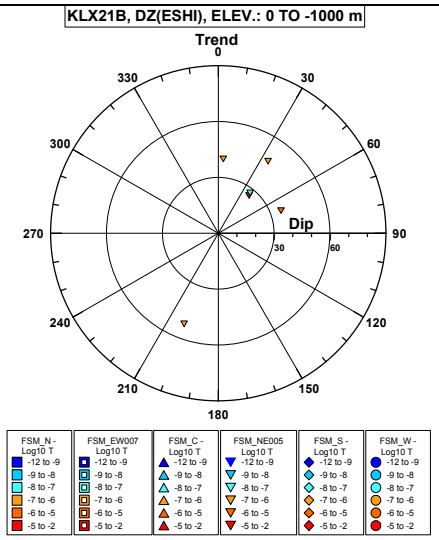

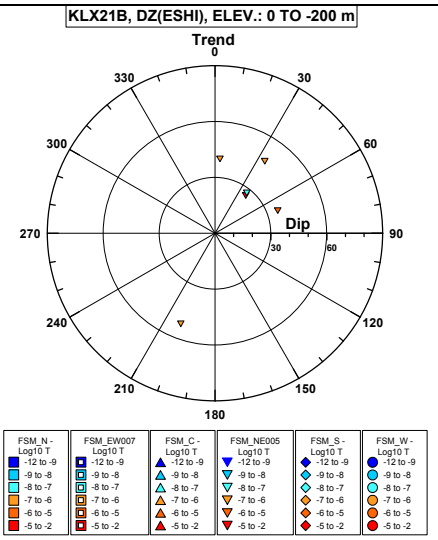

Borehole KLX21B. Poles for PFL-f feature planes in deterministically modelled deformation zones.

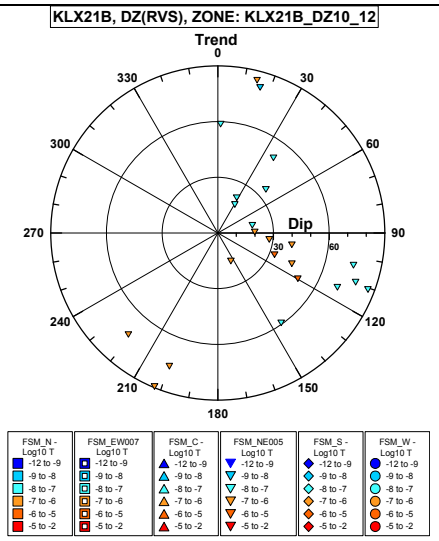

Borehole KLX22A.

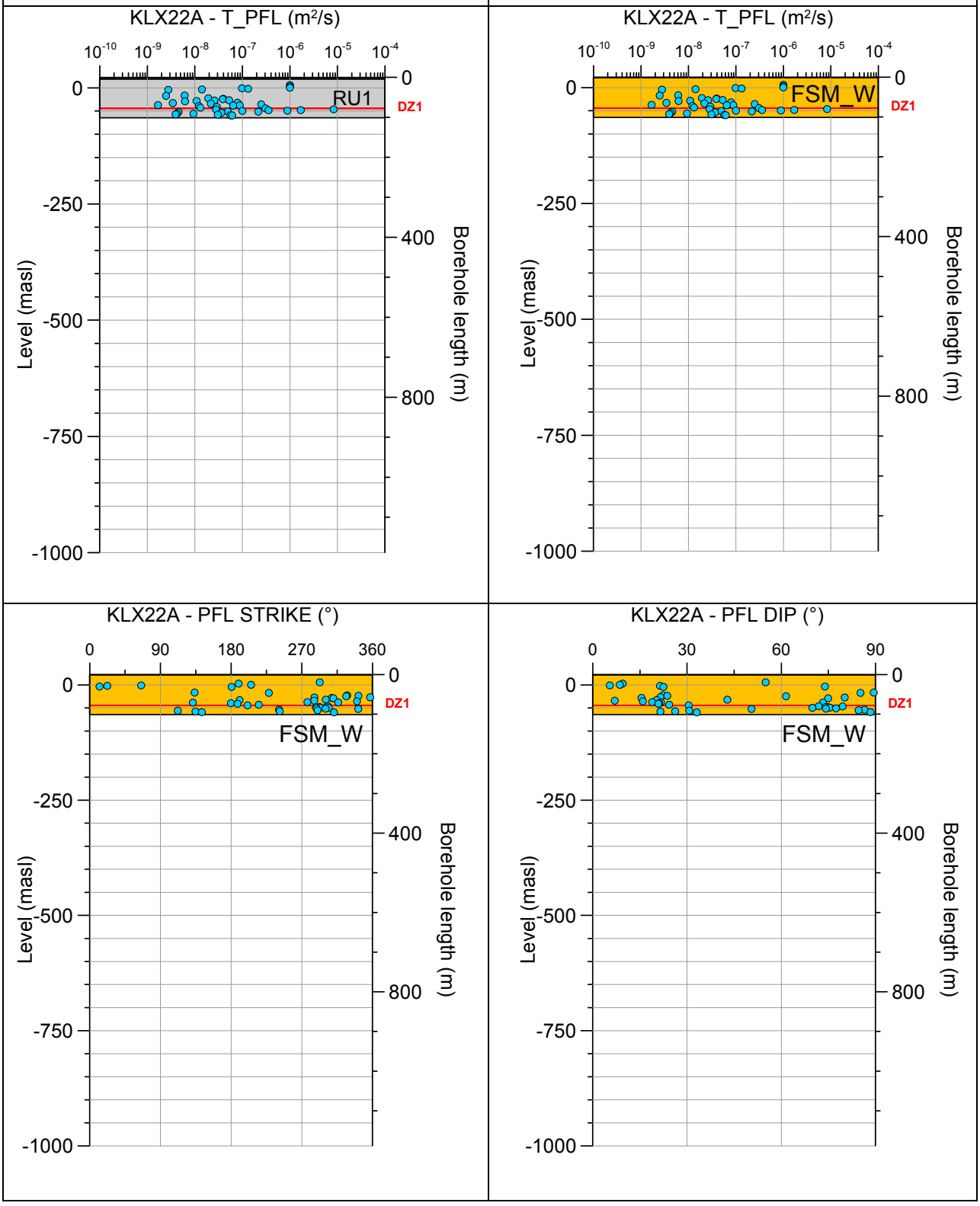

Comment:

Borehole KLX22A. Poles for PFL-f feature planes outside deformation zones.

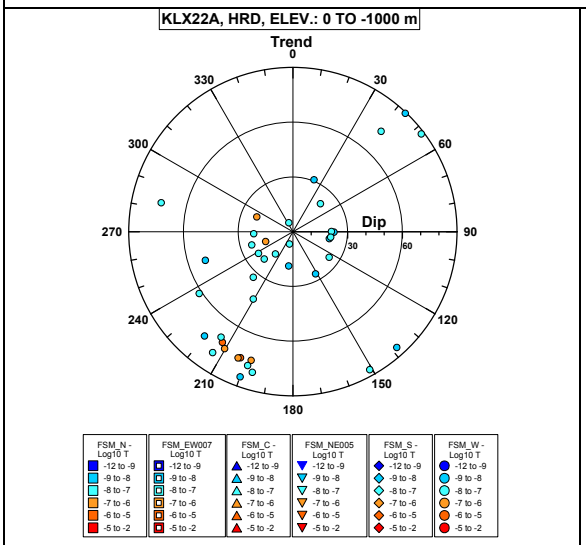

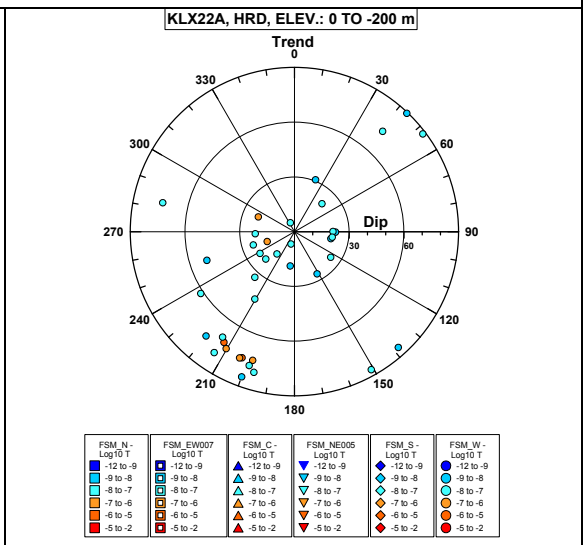

Borehole KLX22A. Poles for PFL-f feature planes in possible deformation zones.

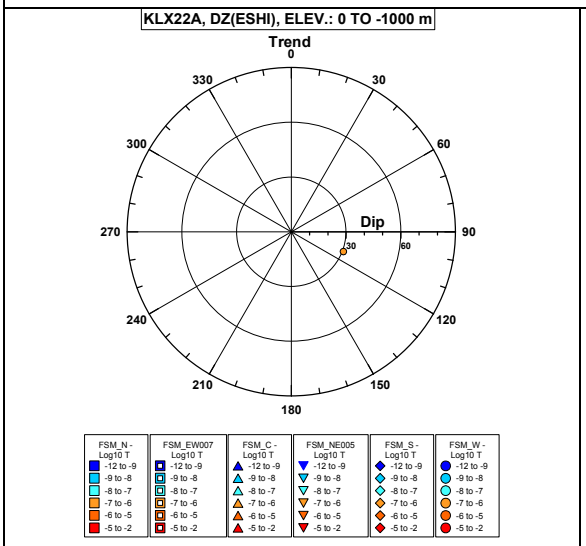

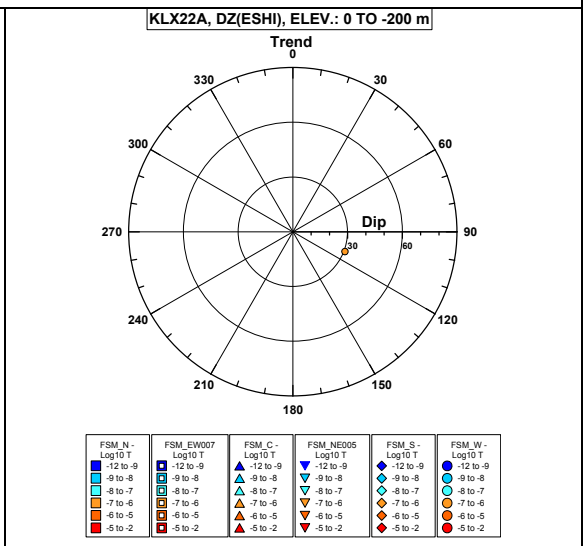

No PFL-f feature planes in deterministically modelled deformation zones exist in KLX22A.

Borehole KLX22B.

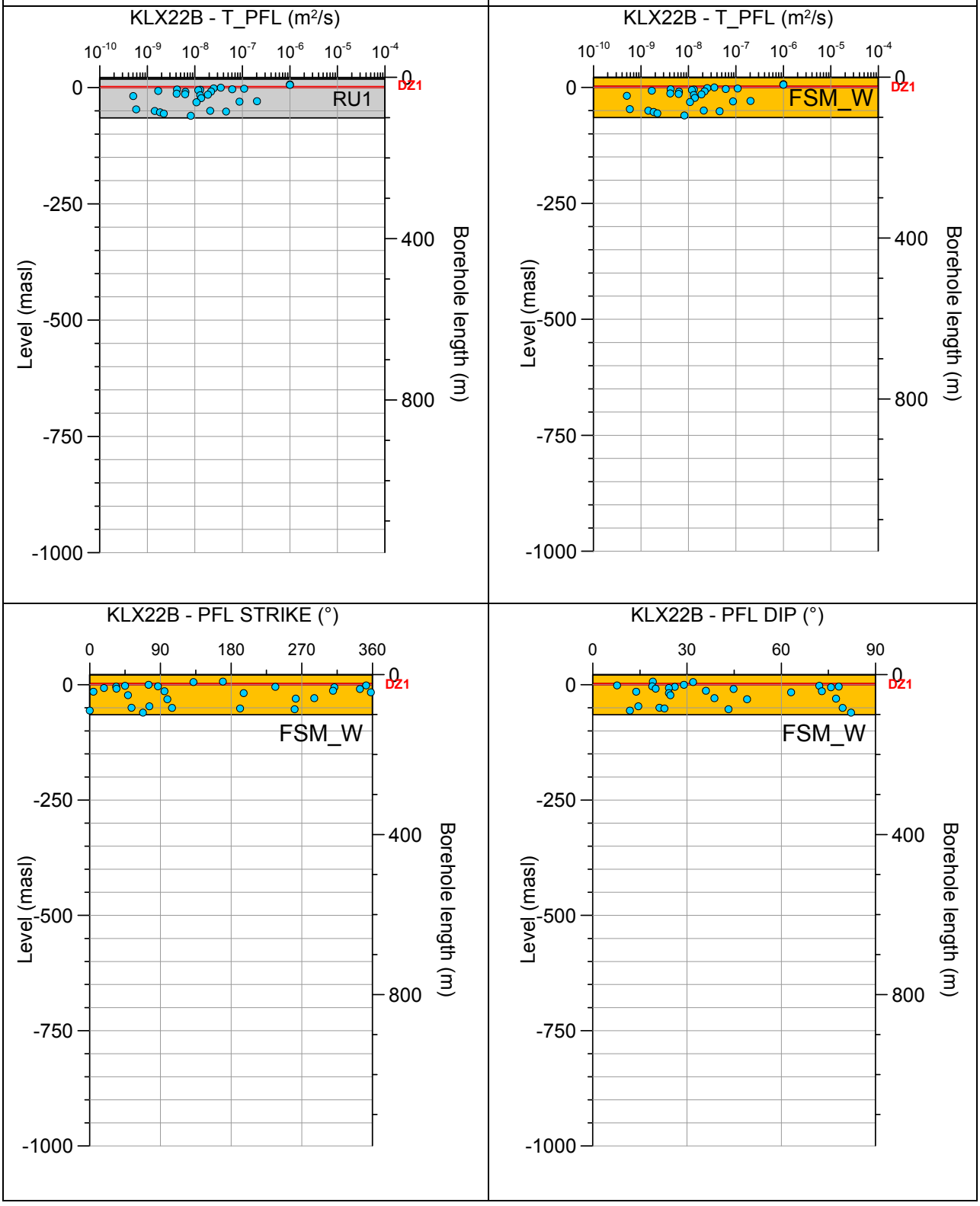

Comment:

Borehole KLX22B. Poles for PFL-f feature planes outside deformation zones.

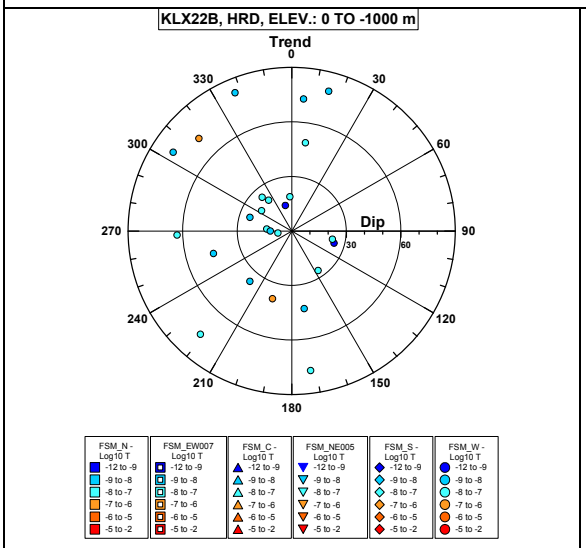

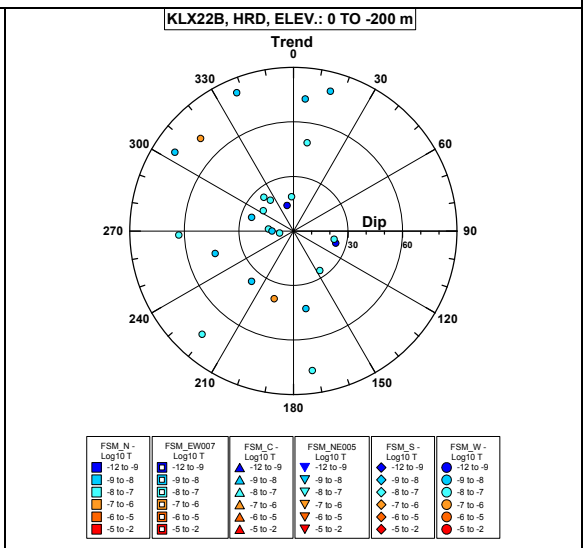

Borehole KLX22B. Poles for PFL-f feature planes in possible deformation zones.

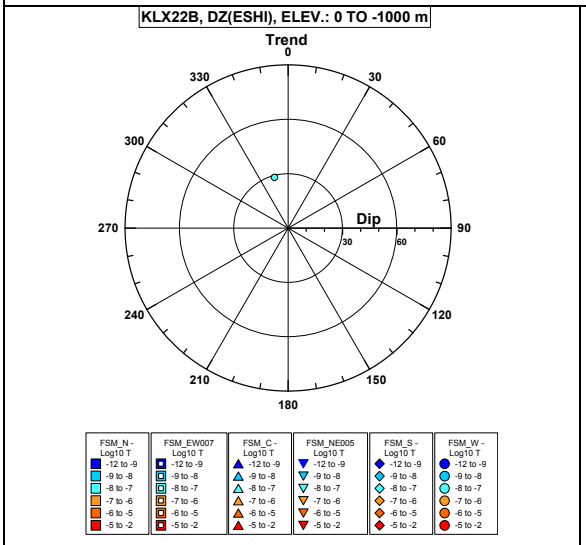

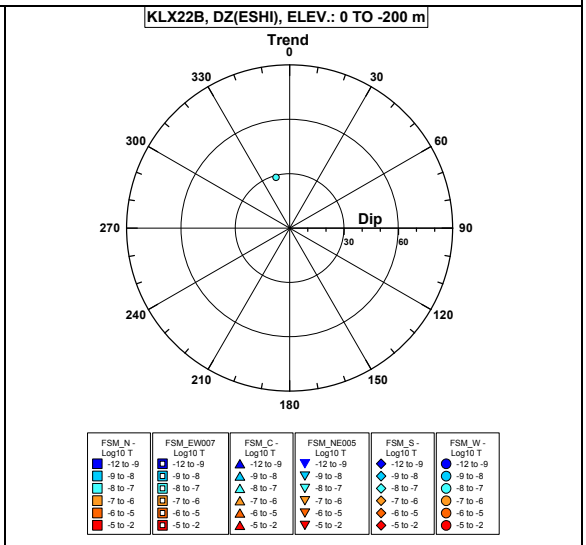

No PFL-f feature planes in deterministically modelled deformation zones exist in KLX22B.

Borehole KLX23A.

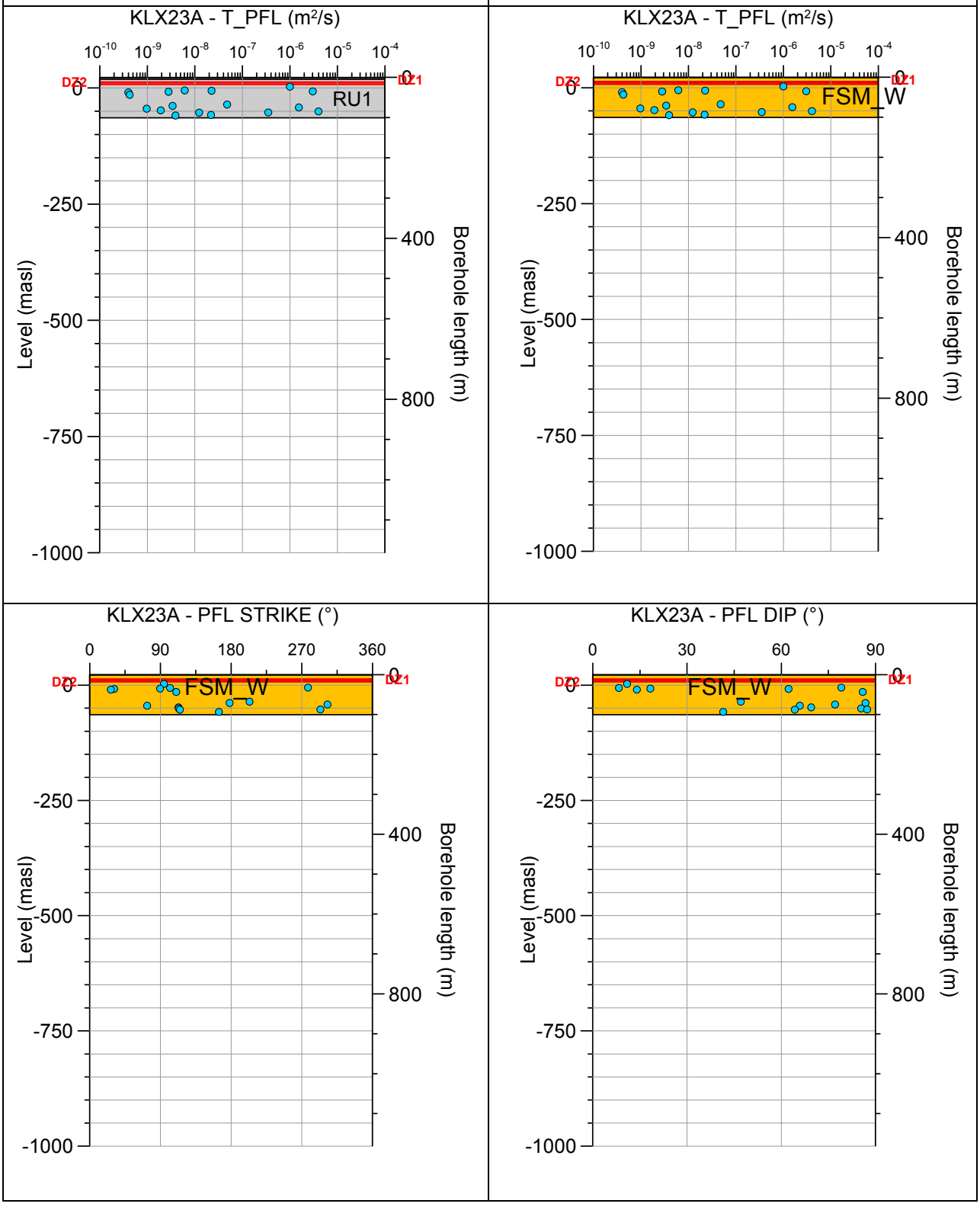

Comment:

Borehole KLX23A. Poles for PFL-f feature planes outside deformation zones.

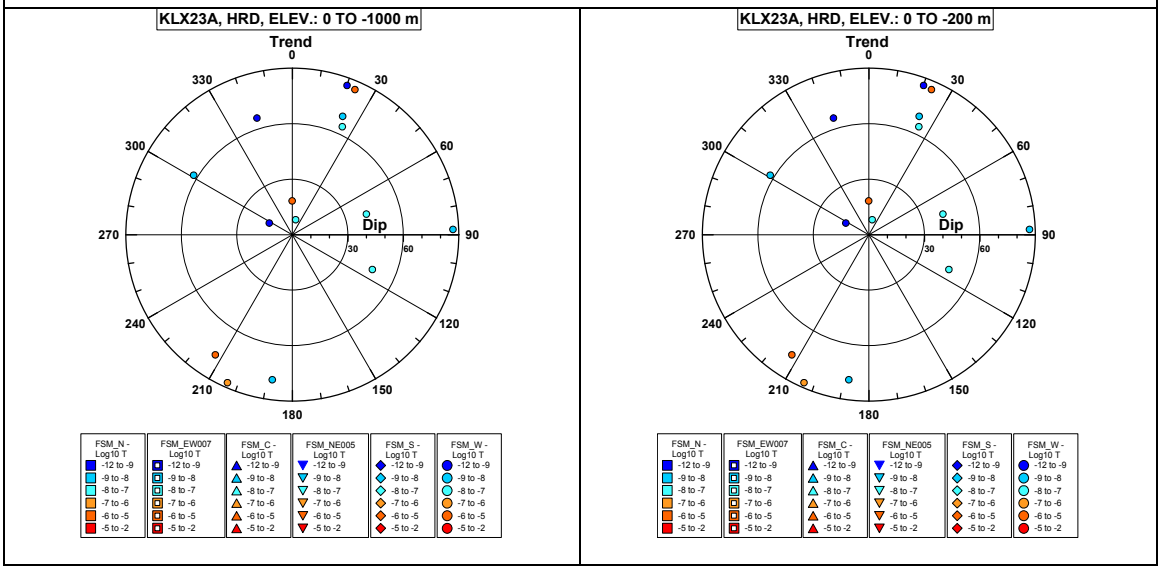

No PFL-f feature planes in possible deformation zones exist in KLX23A.

No PFL-f feature planes in deterministically modelled deformation zones exist in KLX23A.

Borehole KLX23B.

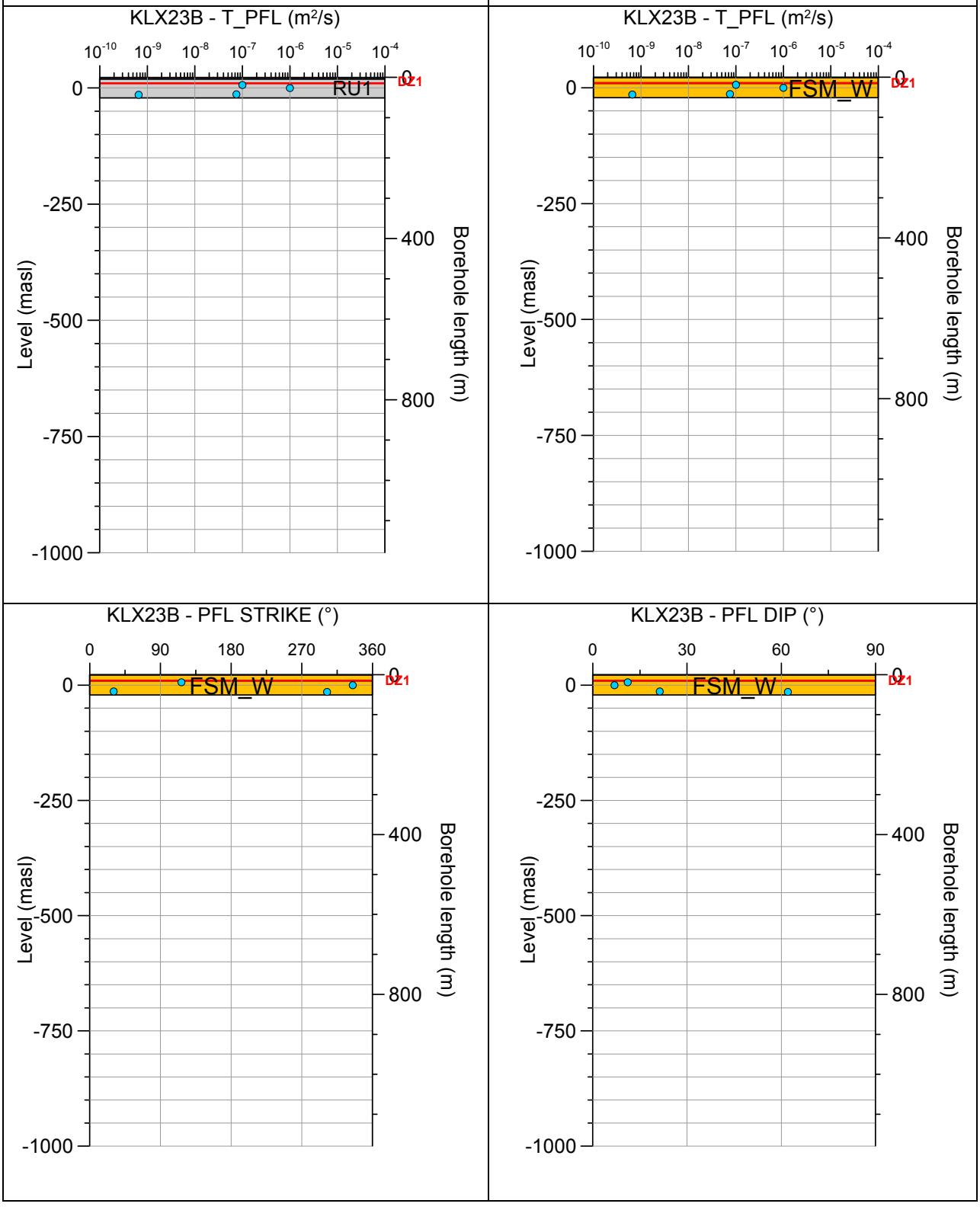

Comment:

Borehole KLX23B. Poles for PFL-f feature planes outside deformation zones.

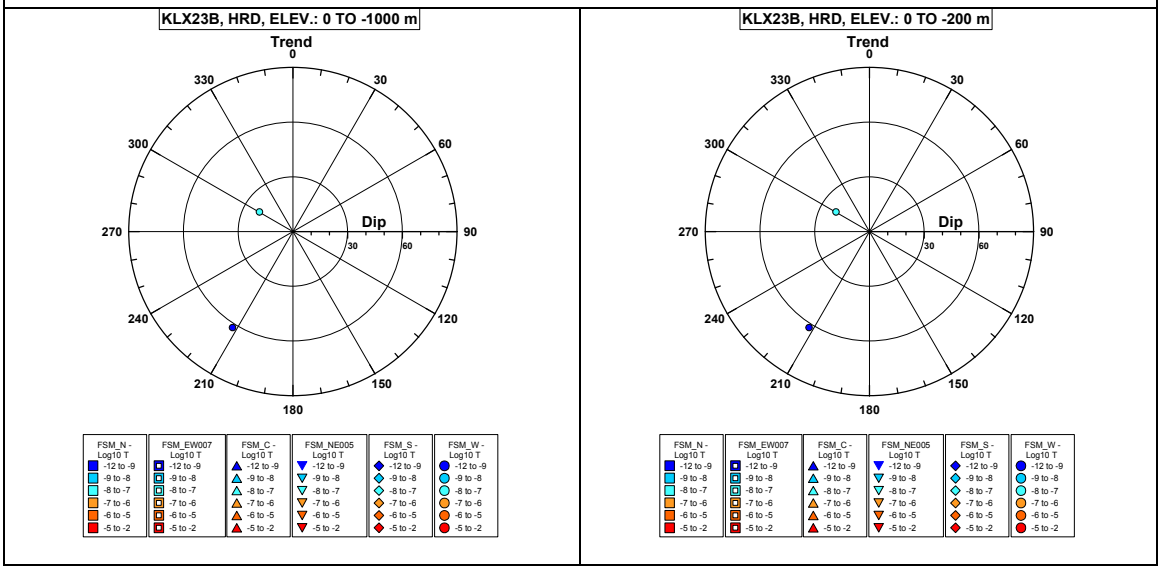

No PFL-f feature planes in possible deformation zones exist in KLX23B.

No PFL-f feature planes in deterministically modelled deformation zones exist in KLX23B.

Borehole KLX24A.

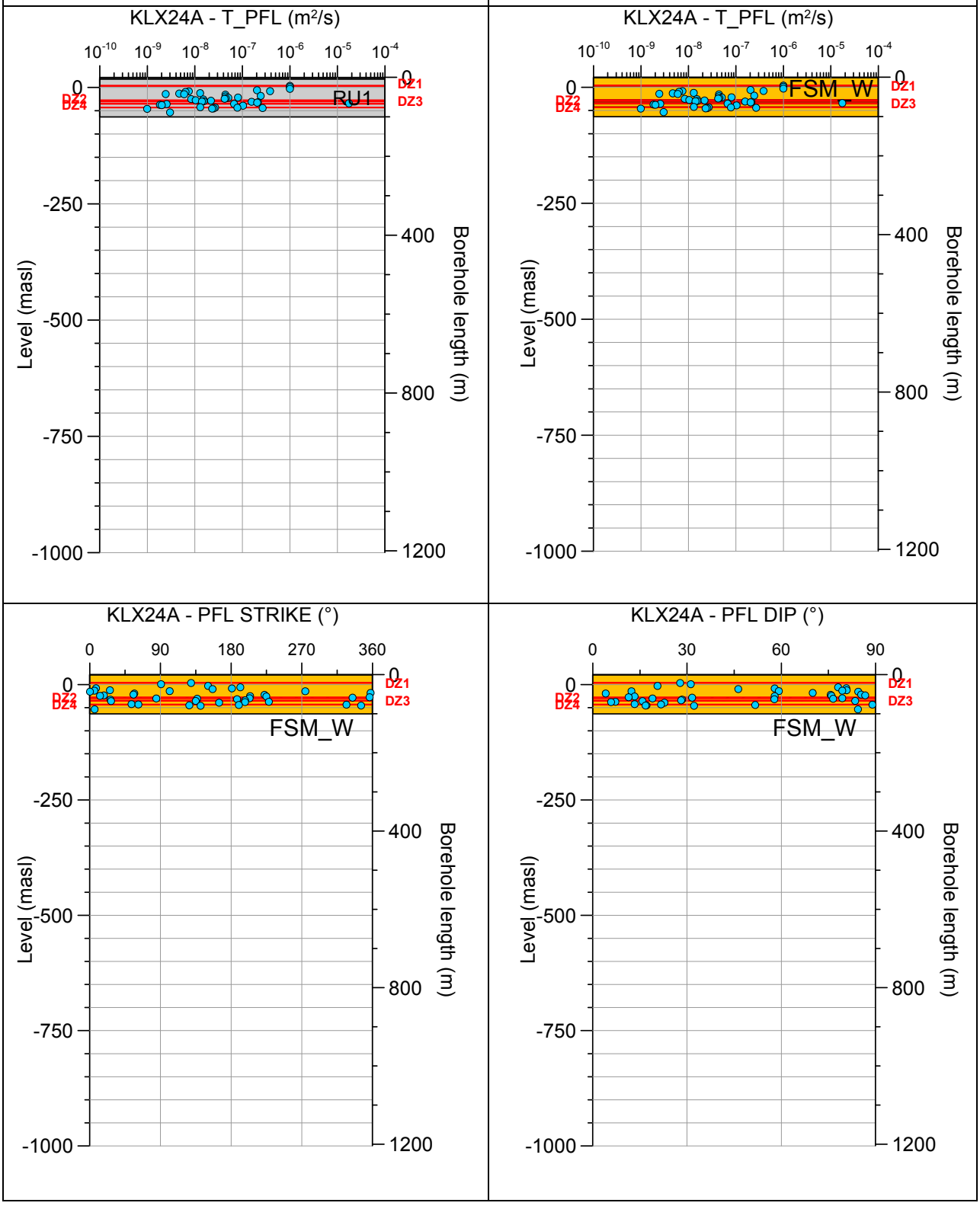

Comment:

Borehole KLX24A. Poles for PFL-f feature planes outside deformation zones.

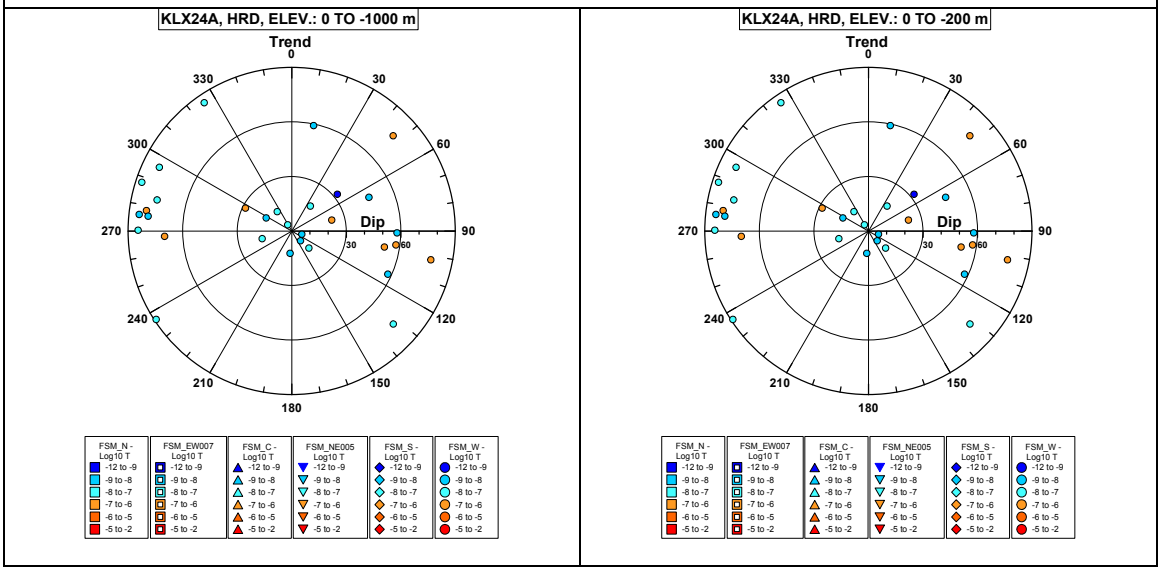

Borehole KLX24A. Poles for PFL-f feature planes in possible deformation zones.

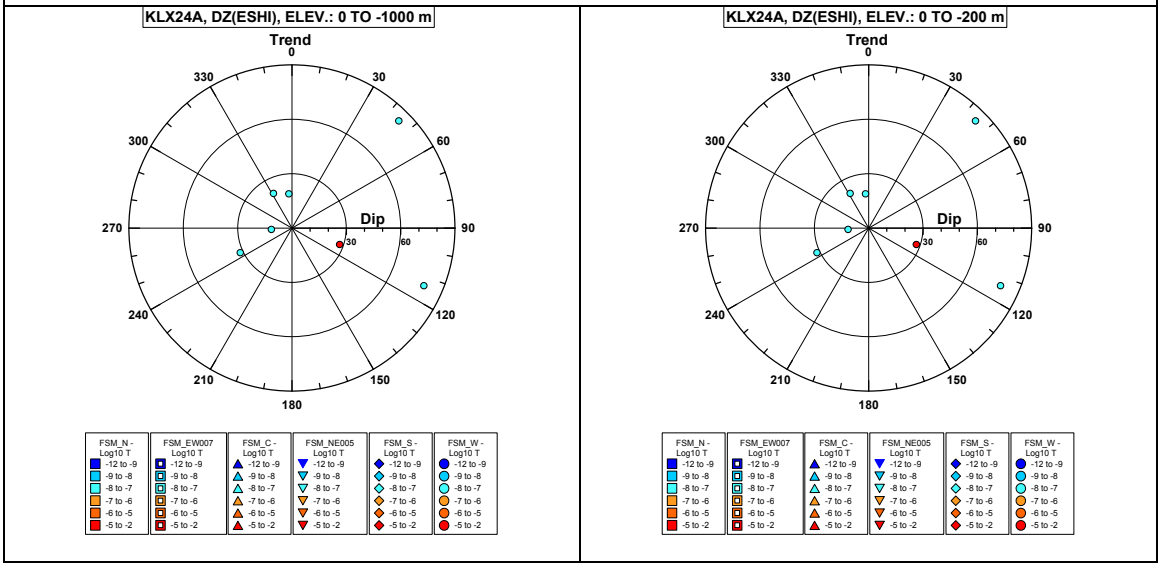

No PFL-f feature planes in deterministically modelled deformation zones exist in KLX24A.

Borehole KLX25A.

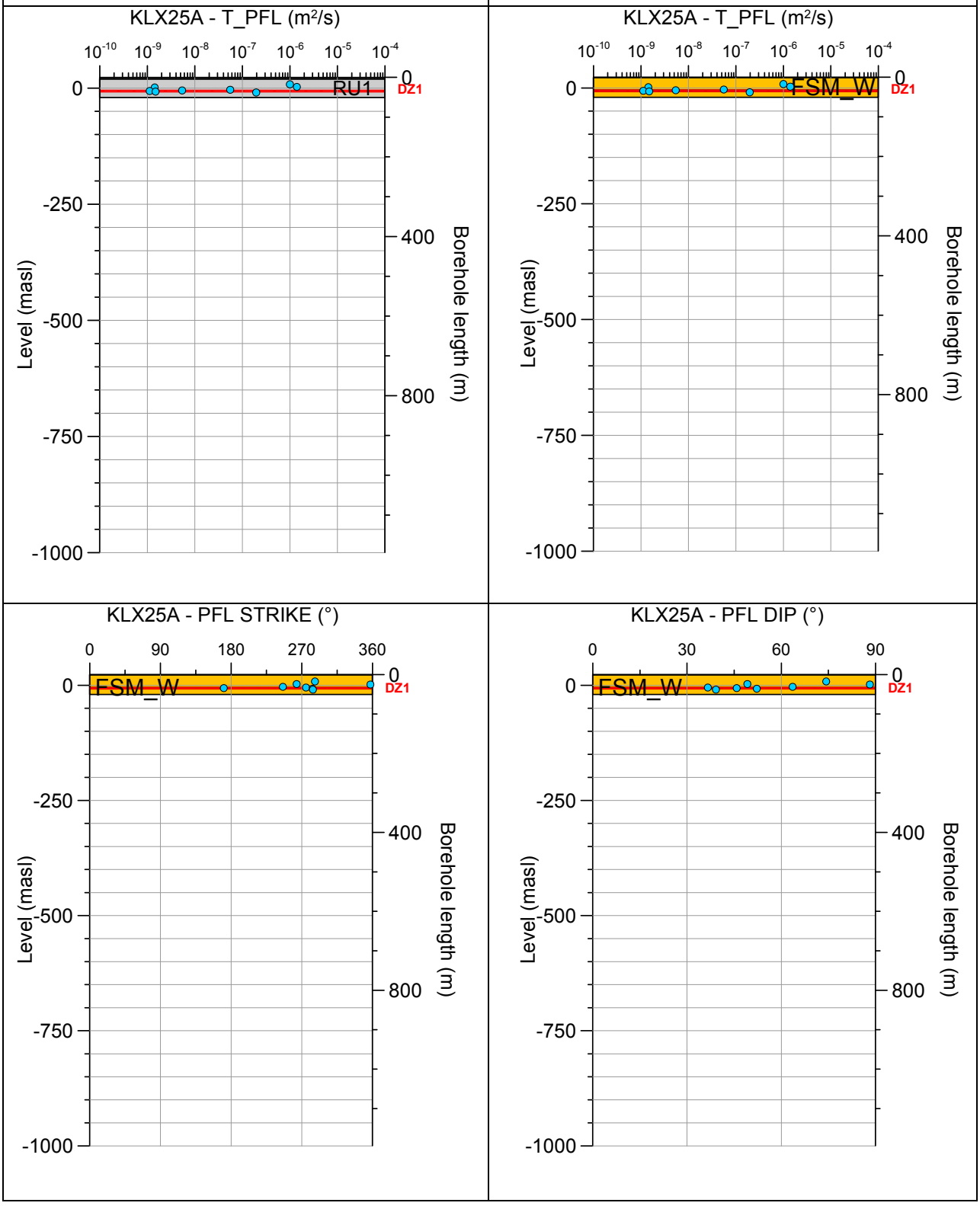

Comment:

Borehole KLX25A. Poles for PFL-f feature planes outside deformation zones.

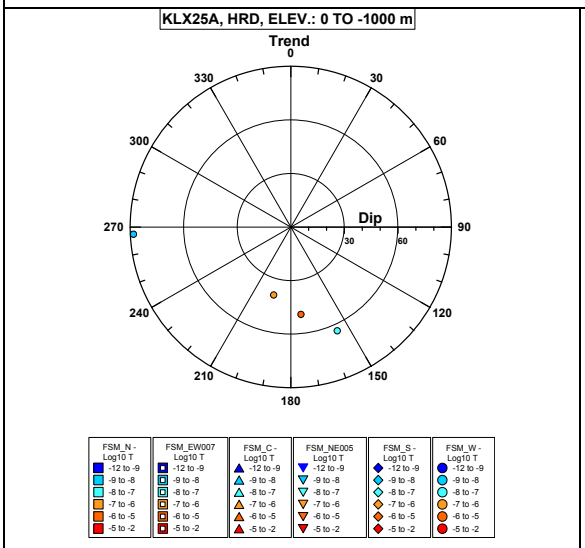

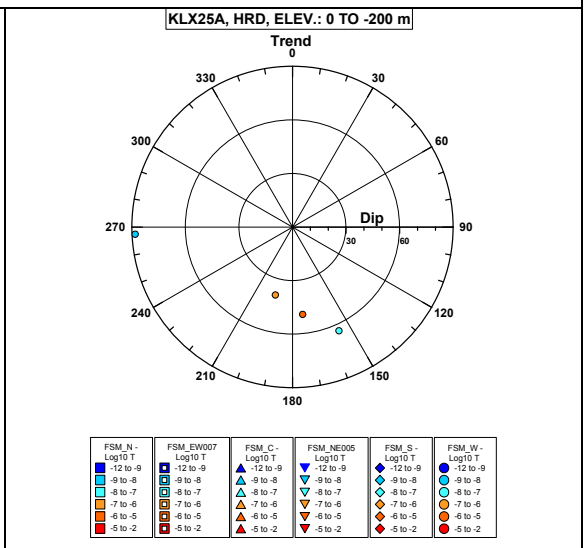

Borehole KLX25A. Poles for PFL-f feature planes in possible deformation zones.

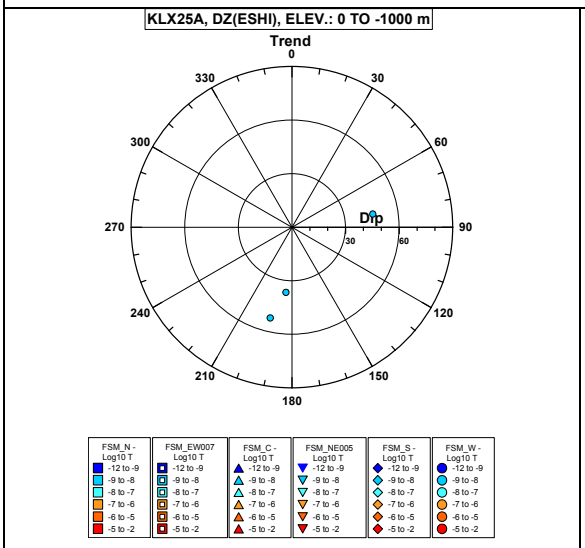

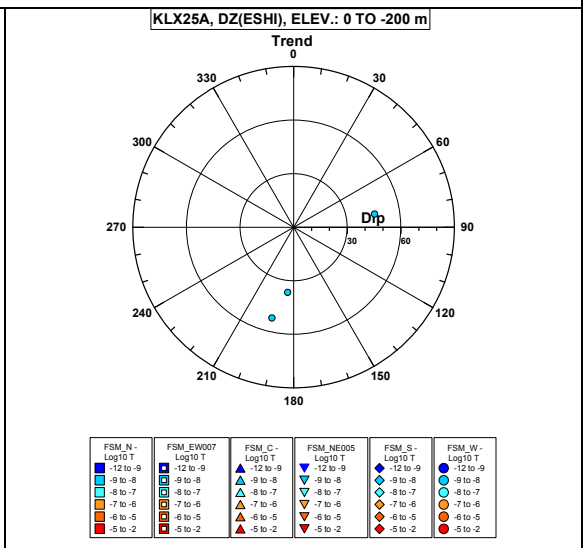

No PFL-f feature planes in deterministically modelled deformation zones exist in KLX25A.

Borehole KLX26A.

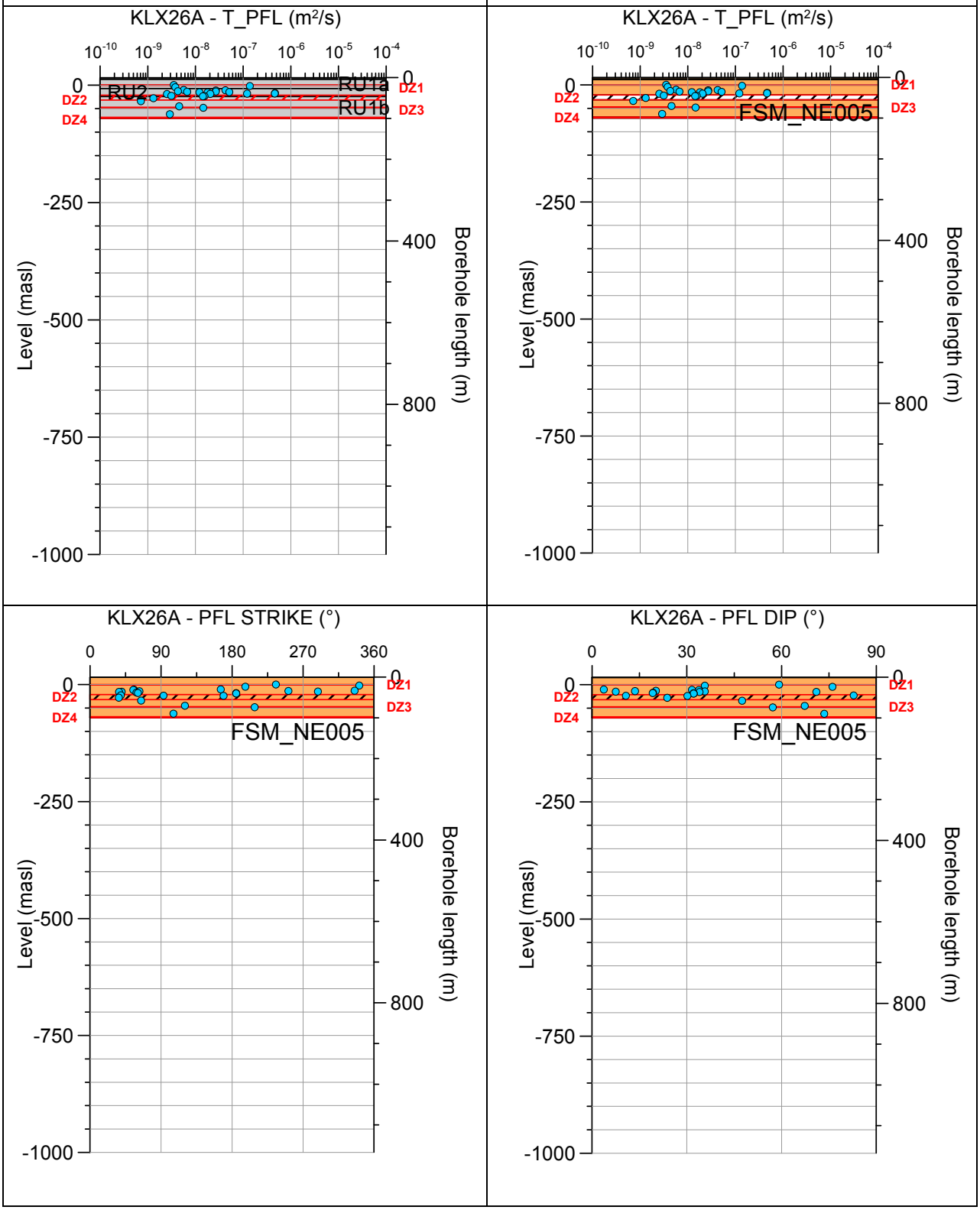

Comment:

Borehole KLX26A. Poles for PFL-f feature planes outside deformation zones.

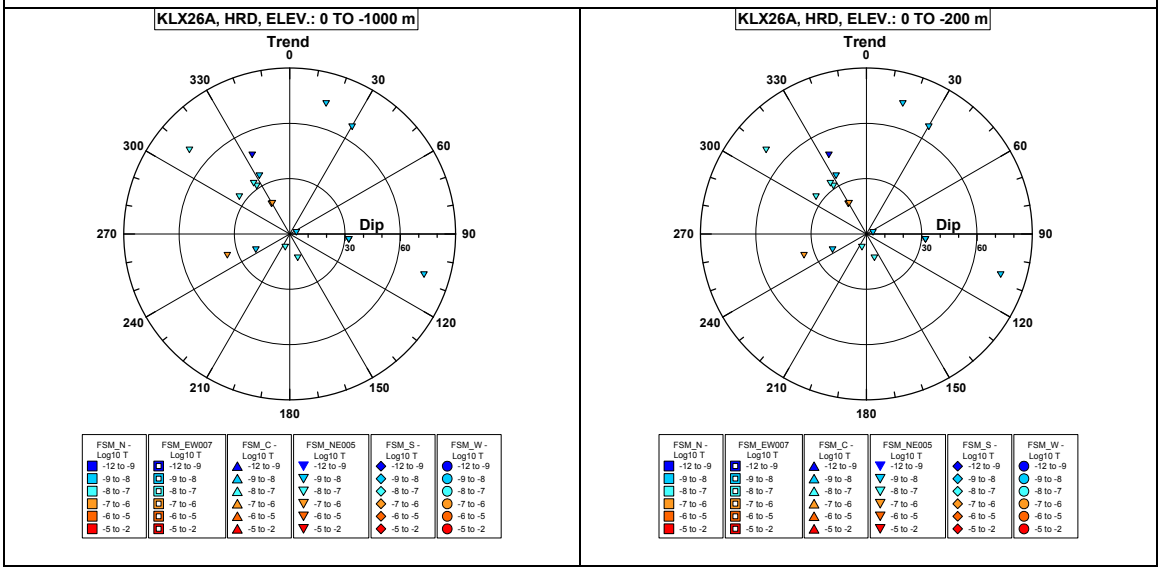

Borehole KLX26A. Poles for PFL-f feature planes in possible deformation zones.

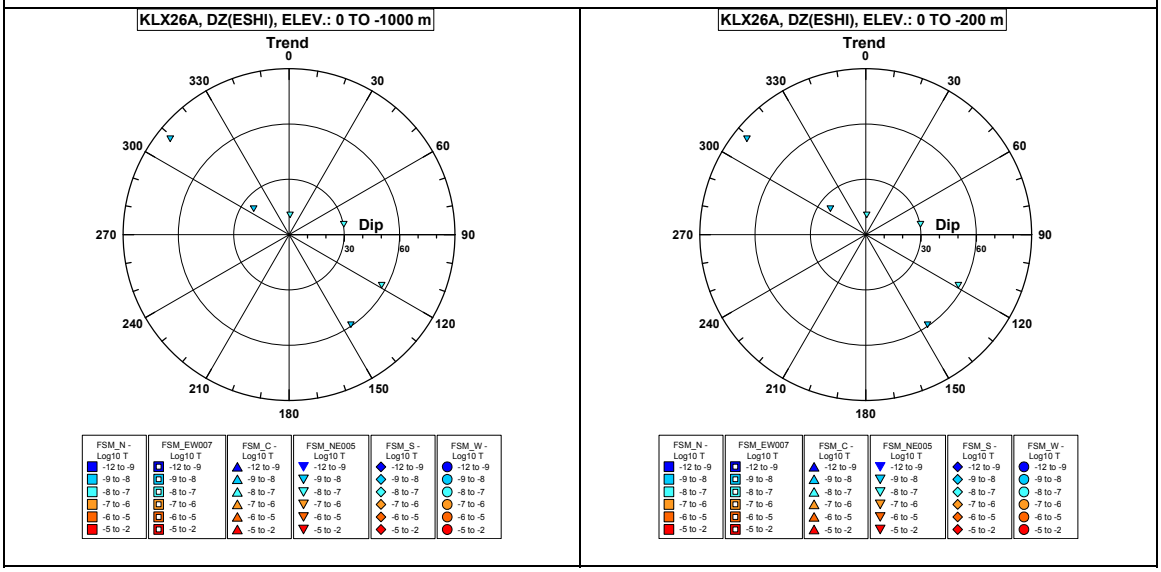

No PFL-f feature planes in deterministically modelled deformation zones exist in KLX26A.

Borehole KLX26B.

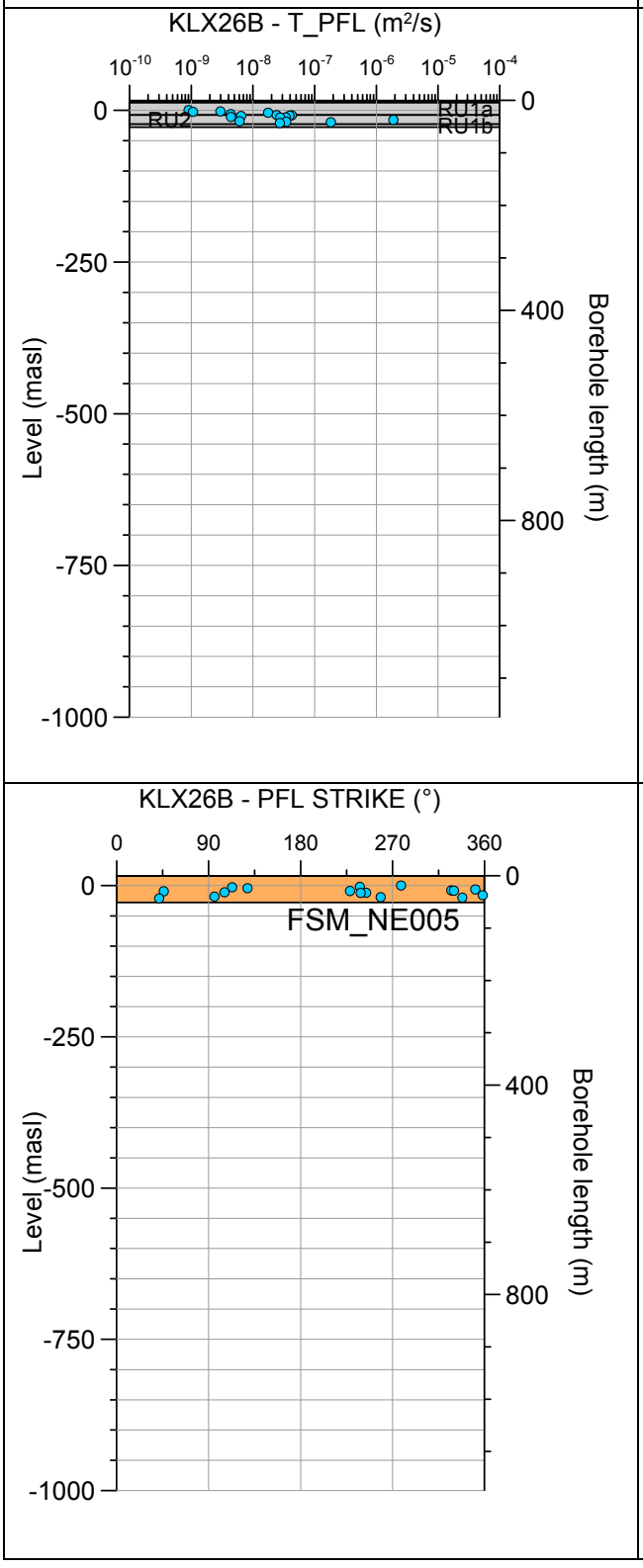

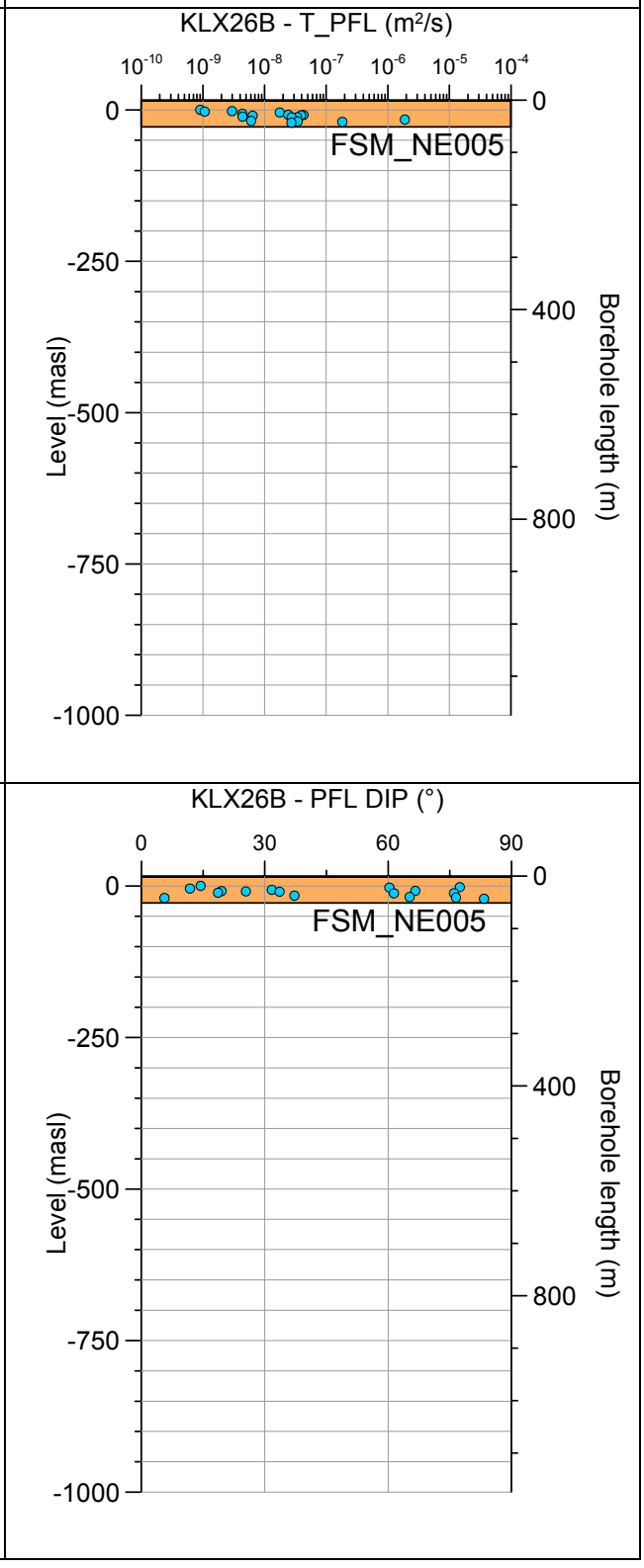

Comment:

Borehole KLX26B. Poles for PFL-f feature planes outside deformation zones.

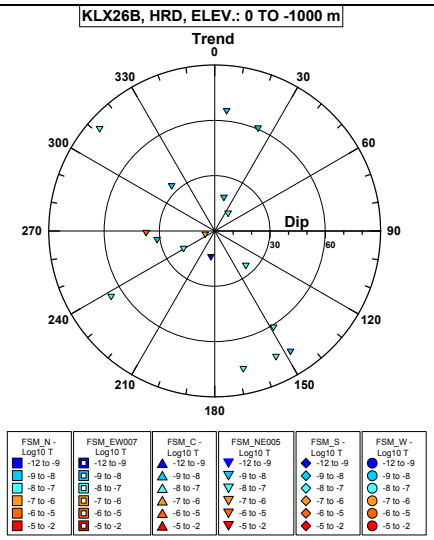

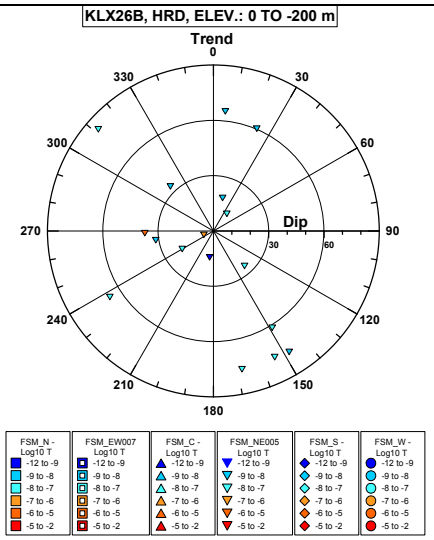

No PFL-f feature planes in possible deformation zones exist in KLX26B.

No PFL-f feature planes in deterministically modelled deformation zones exist in KLX26B.

Borehole KLX27A.

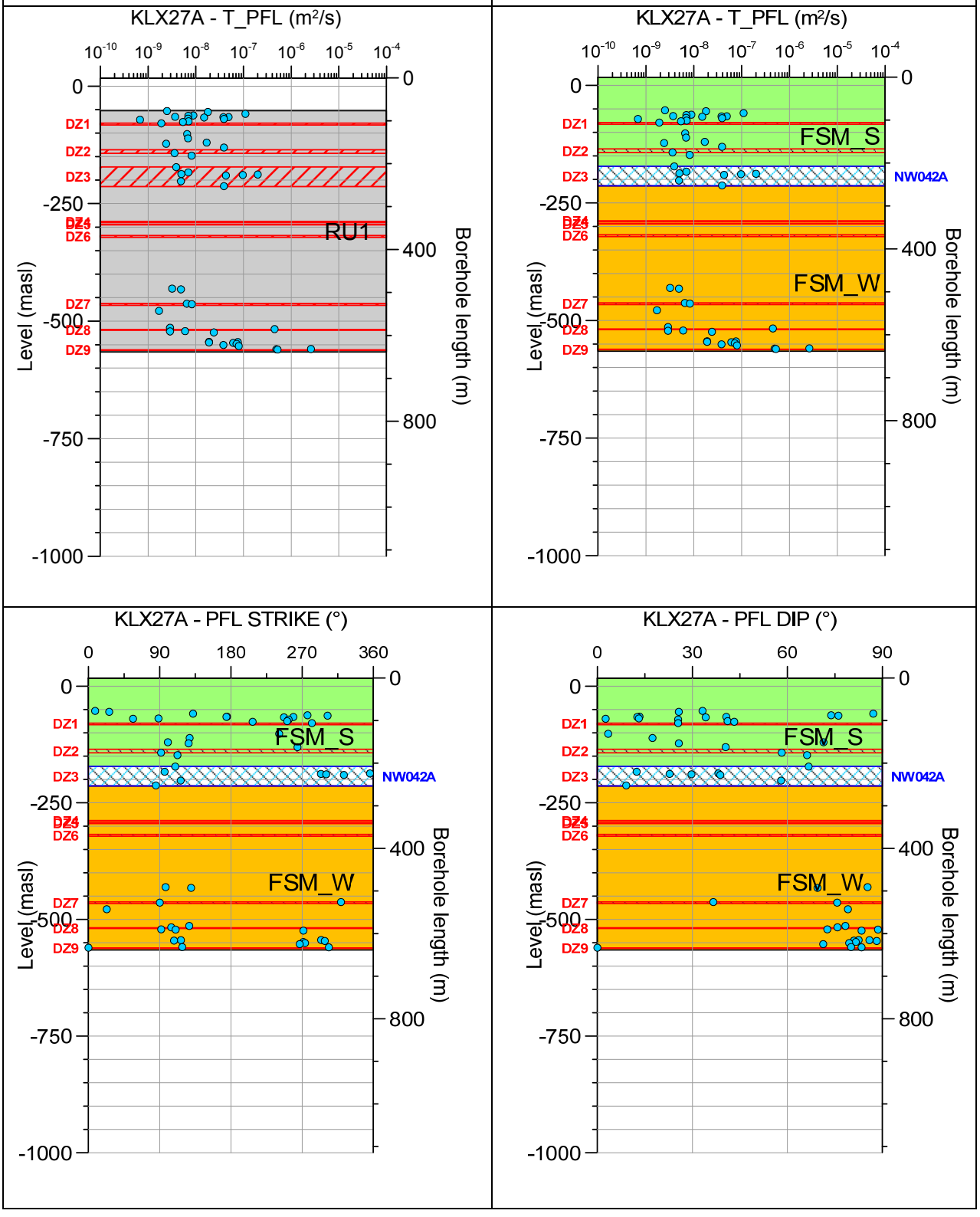

Comment:

Borehole KLX27A. Poles for PFL-f feature planes outside deformation zones.

KLX27A, HRD, ELEV.: 0 TO -1000 m

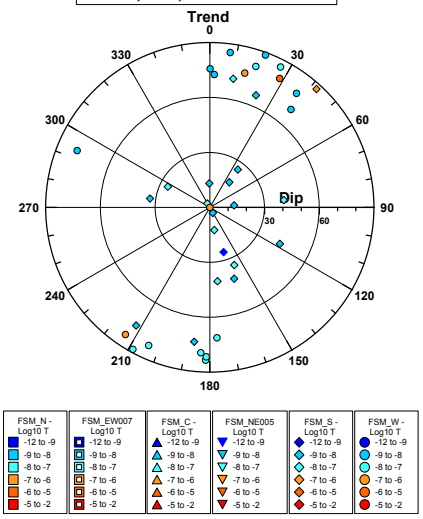

KLX27A, HRD, ELEV.: 0 TO -200 m

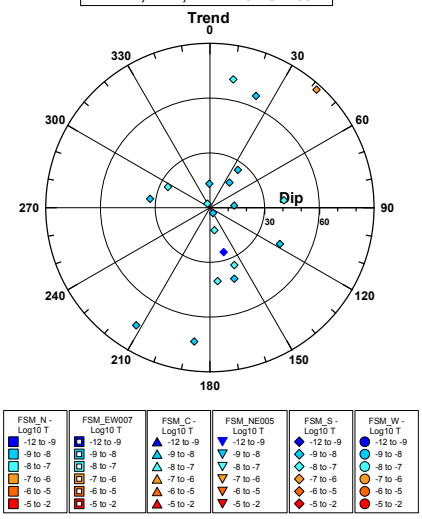

KLX27A, HRD, ELEV.: -400 TO -600 m

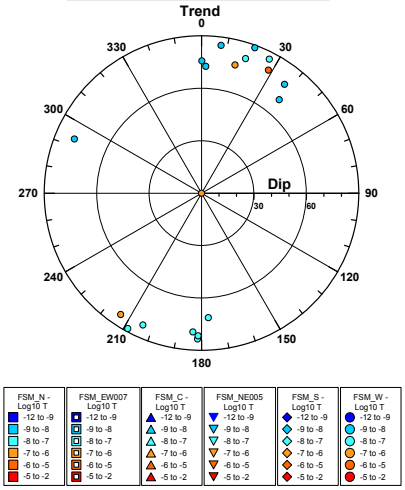

Borehole KLX27A. Poles for PFL-f feature planes in possible deformation zones.

KLX27A, DZ(ESHI), ELEV.: 0 TO -1000 m

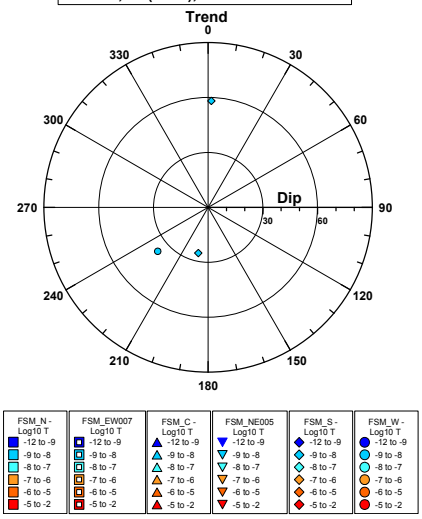

KLX27A, DZ(ESHI), ELEV.: 0 TO -200 m

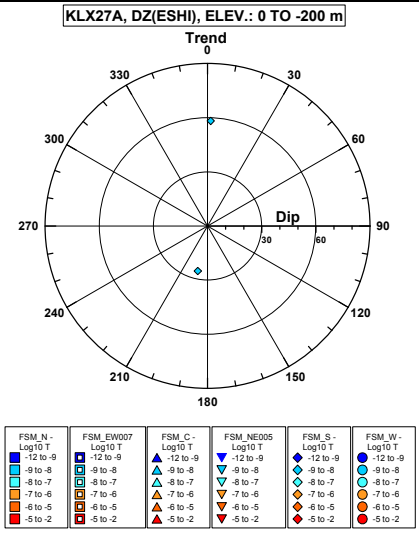

KLX27A, DZ(ESHI), ELEV.: -400 TO -600 m

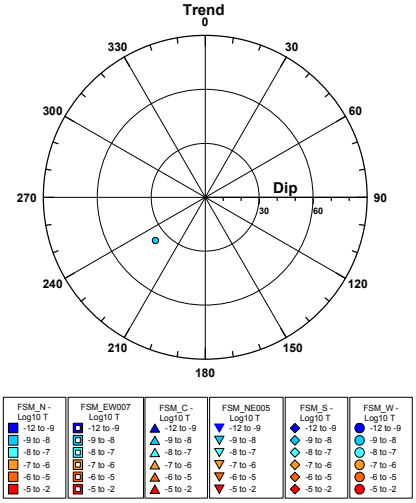

Borehole KLX27A. Poles for PFL-f feature planes in deterministically modelled deformation zones.

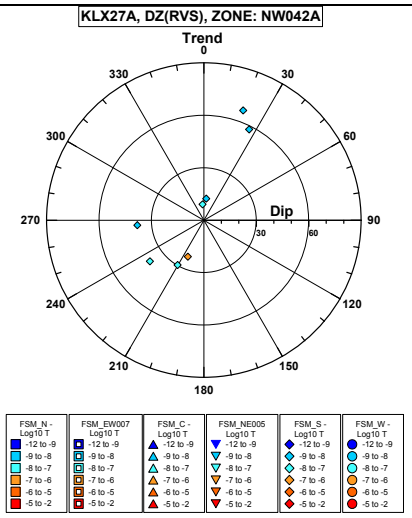

Borehole KLX28A.

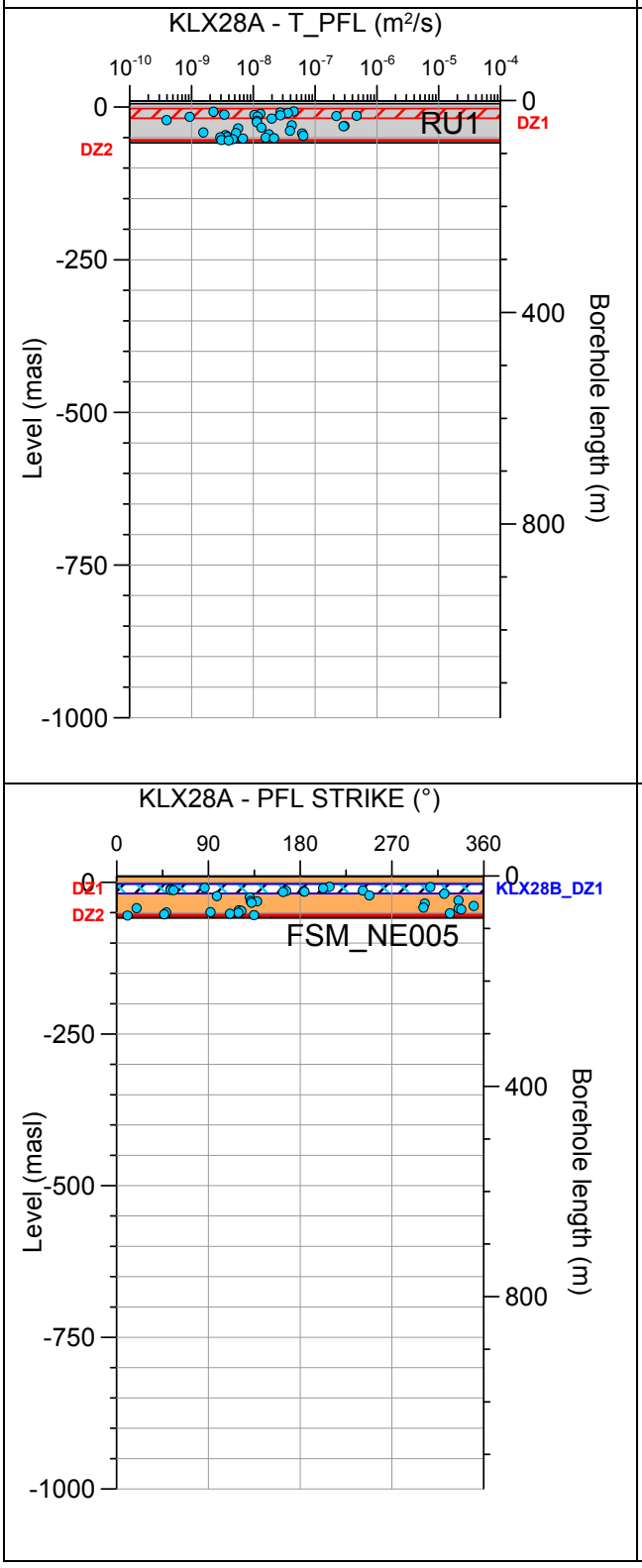

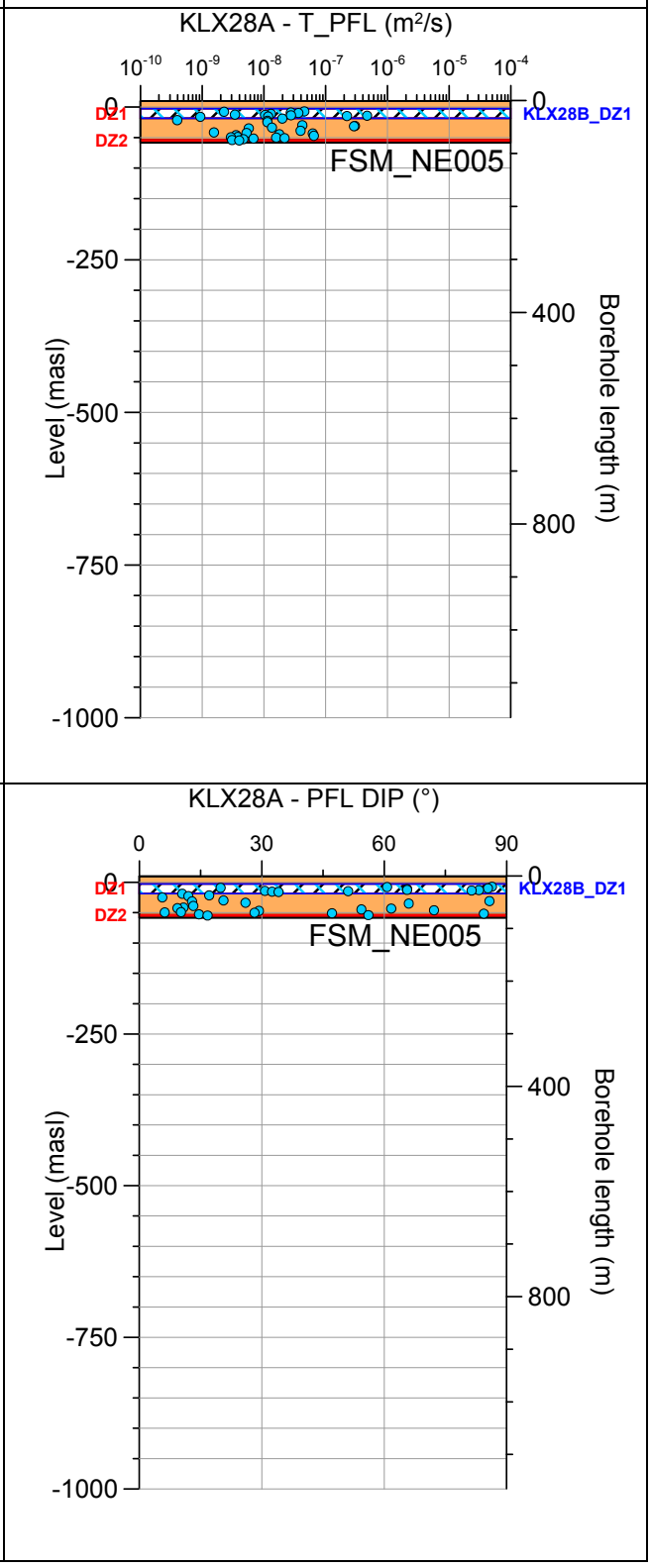

Comment:

Borehole KLX28A. Poles for PFL-f feature planes outside deformation zones.

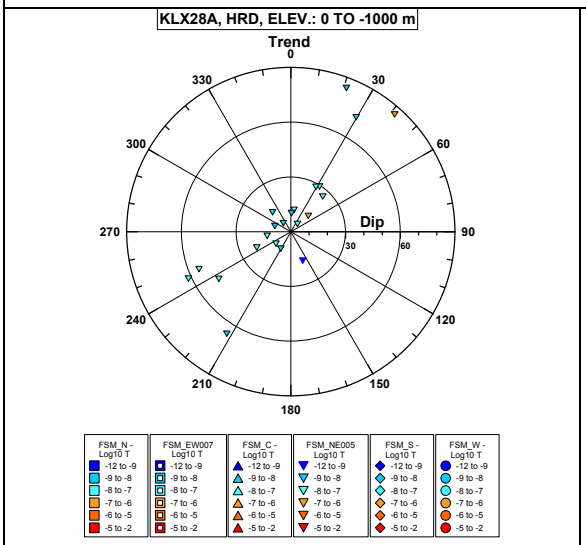

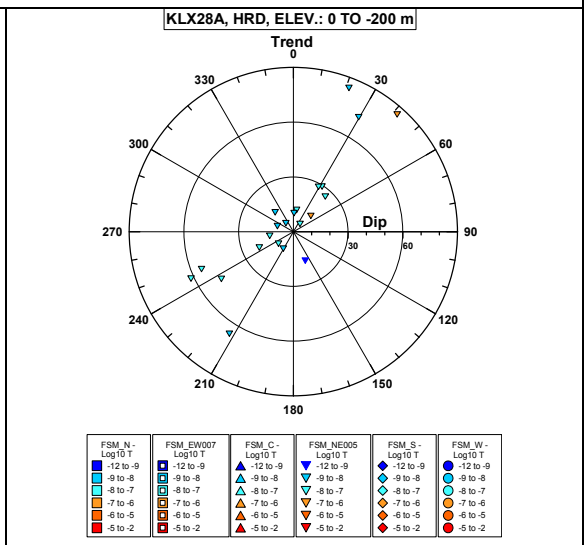

Borehole KLX28A. Poles for PFL-f feature planes in possible deformation zones.

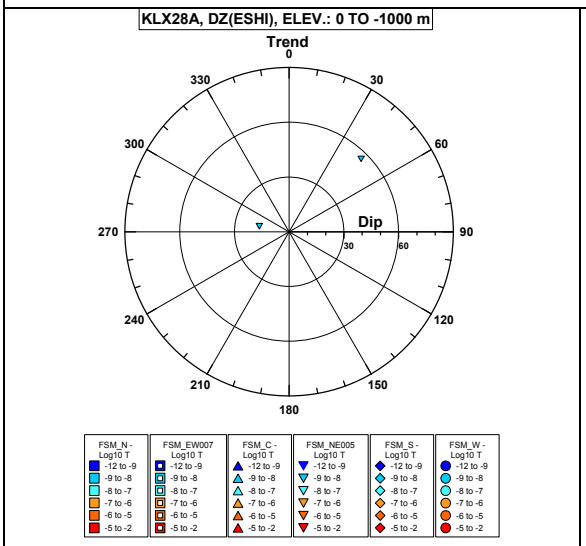

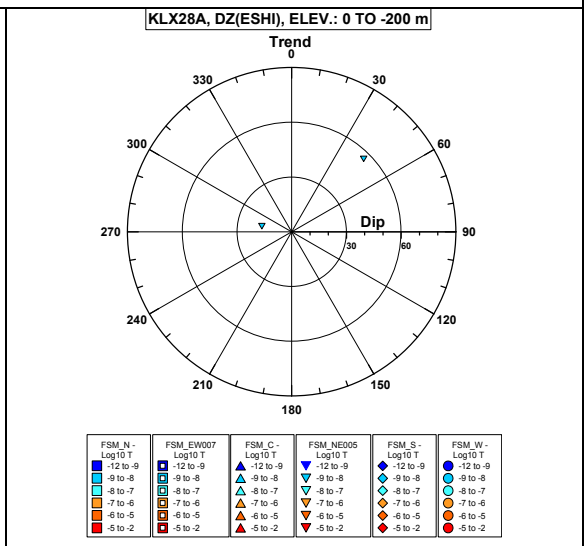

Borehole KLX28A. Poles for PFL-f feature planes in deterministically modelled deformation zones.

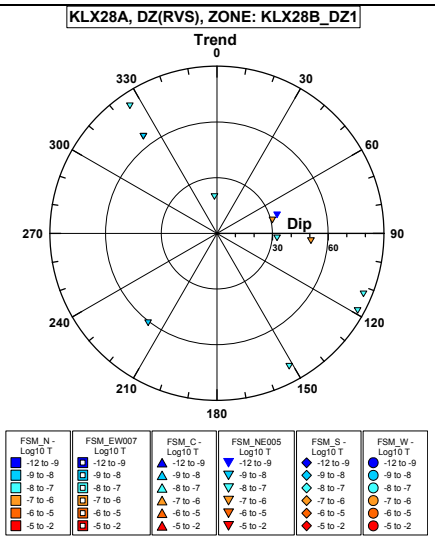

Borehole KLX29A.

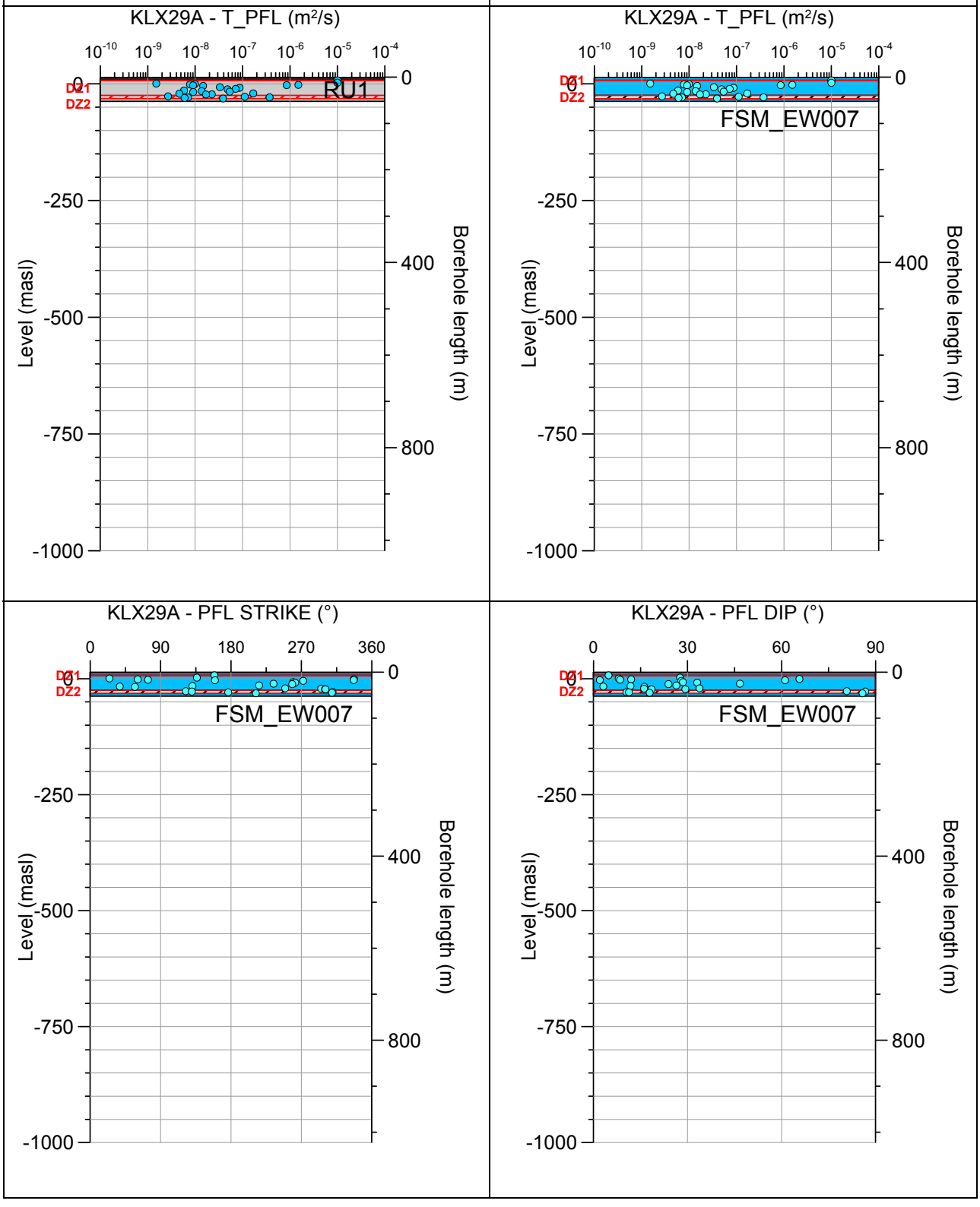

Comment:

Borehole KLX29A. Poles for PFL-f feature planes outside deformation zones.

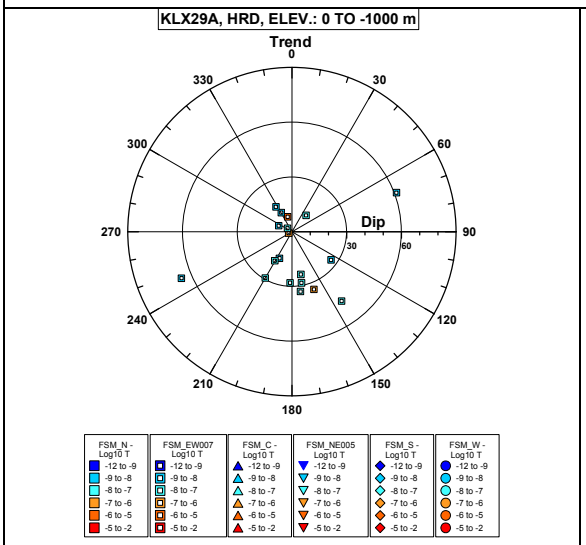

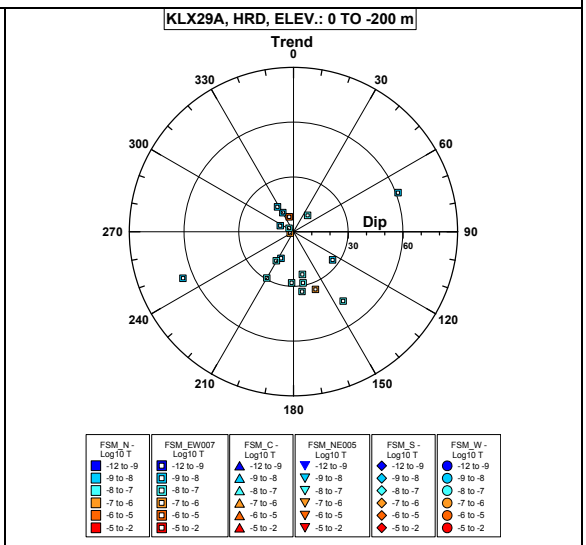

Borehole KLX29A. Poles for PFL-f feature planes in possible deformation zones.

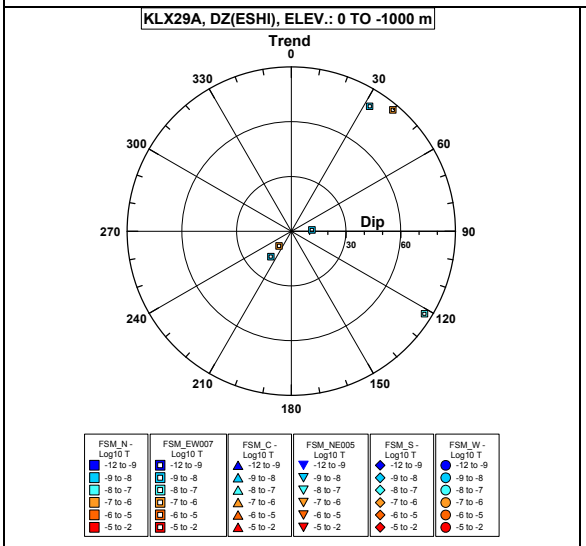

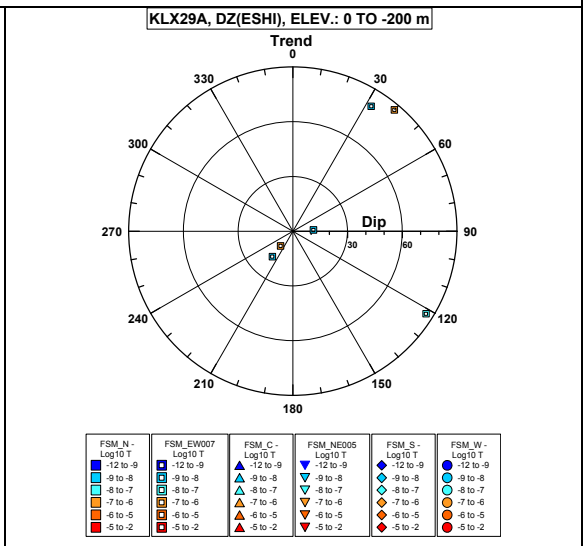

No PFL-f feature planes in deterministically modelled deformation zones exist in KLX29A.

A.2.2 *PFL-f transmissivities versus Modelled Rock domains and Deformation zones, as well as Geological Extended Single-hole Interpretation(ESHI)*

The geologically modelled Rock Domains (RSMxxx, "RDxx"or just "xx" in plots) and Deformation Zones (ZSMNNxxxx or shorter: NNxxxx) are deterministically in space. The deformation zones found in Geological Extended Single-hole Interpretation (ESHI) are called Possible Deformation zones (DZx) and rock mass is also divided into rock units (RUx). Some of the DZx are modelled deterministically and the remaining are called minor deformation zones (MDZ). RSMxxx, ZSMNNxxxx and MDZ along the borehole are used for further analysis by different disciplines.

In this appendix the transmissivities and orientations of PFL-f features are shown together with modelled rock domains and deformation zones. The Geological Extended Single-hole Interpretation (ESHI) is also shown to indicate the background information for RSMxxx, ZSMNNxxxx and MDZ as in a few cases it has some significance for the evaluation of hydraulic data. In the plots the borehole length, as documented in the SICADA data base, and the elevation ("level" in the plots) corresponds to the Z coordinate in the RH70/RHB70 system) are shown. The orientations of the PFL-f features are shown as strike/dip.

The pole plots show the Pole Vector, with orientation trend/dip, to each fracture that has a measured PFL-f feature linked to it. Pol plots marked with RDxx.

- PFL-f feature planes in rock between the possible deformation zones defined by ESHI.
- PFL-f feature planes within minor deformation zones (MDZ).
- PFL-f feature planes within deterministic deformation zones (ZSMNNxxx).

Borehole KLX02.

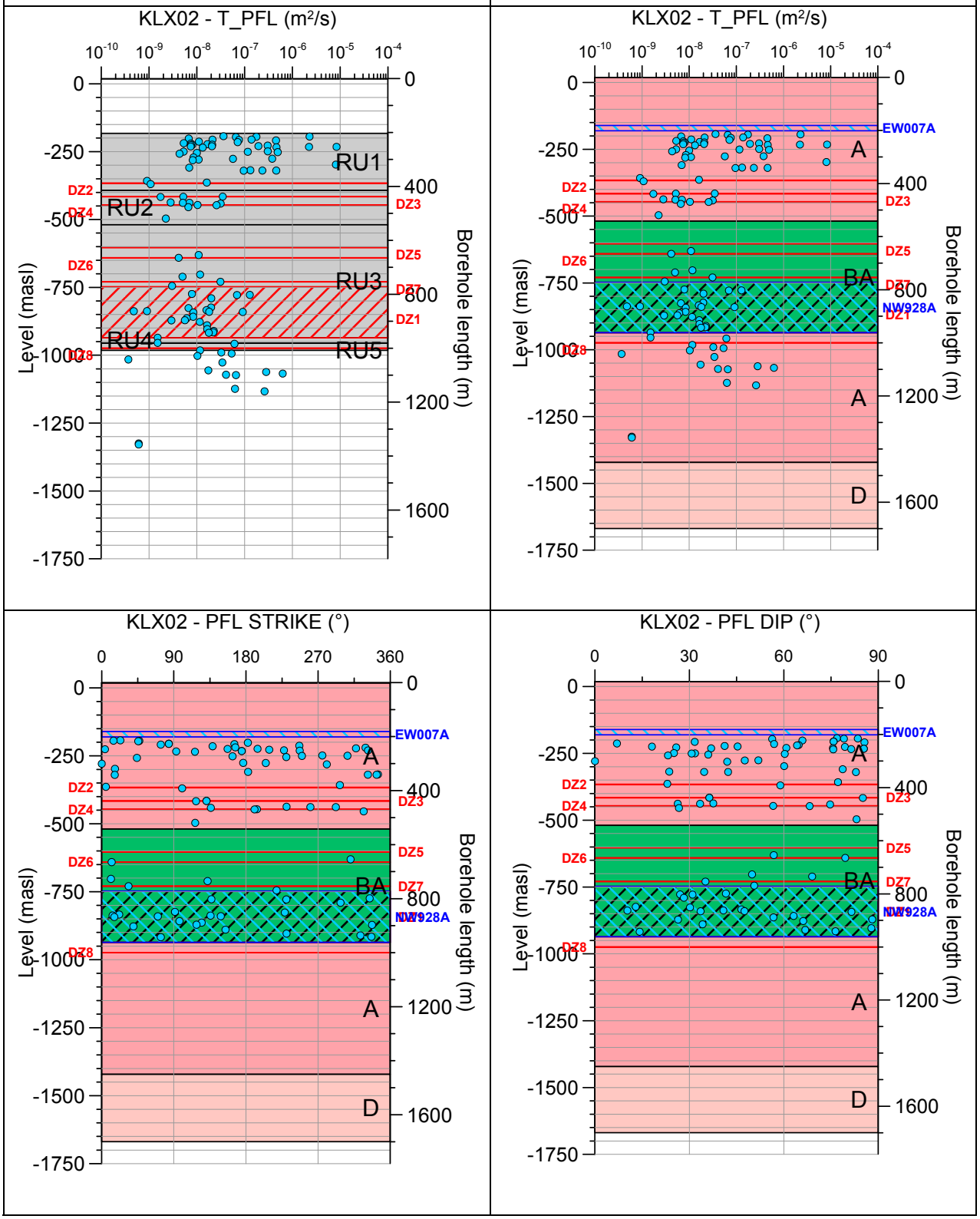

Comment:

Borehole KLX02. Poles for PFL-f feature planes outside deformation zones.

KLX02, HRD, ELEV.: 0 TO -1000 m

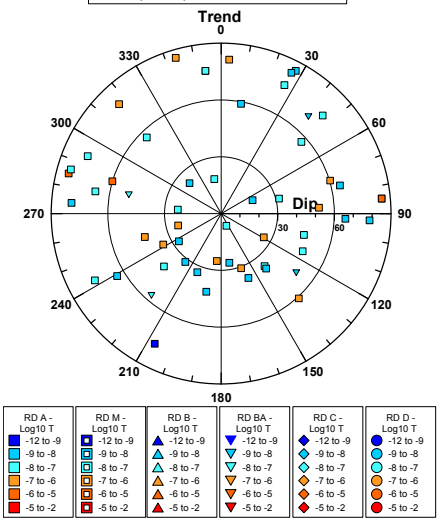

KLX02, HRD, ELEV.: 0 TO -200 m

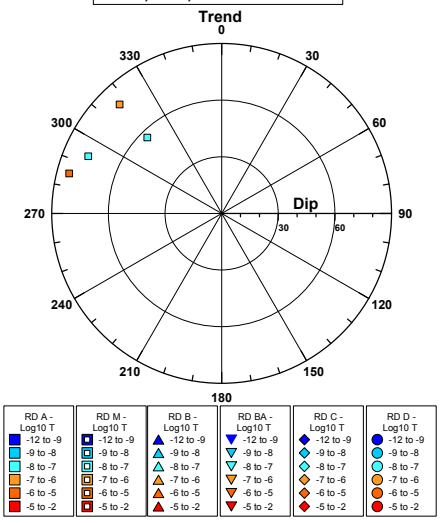

KLX02, HRD, ELEV.: -200 TO -400 m

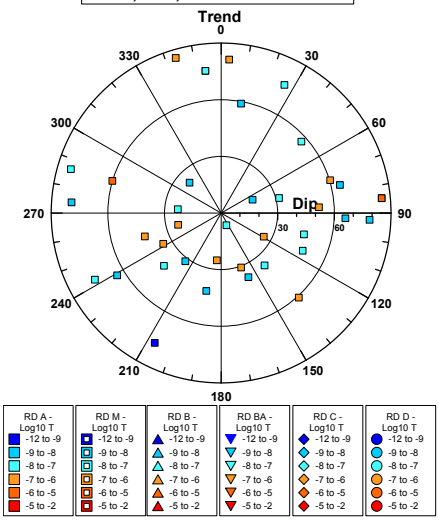

KLX02, HRD, ELEV.: -400 TO -600 m

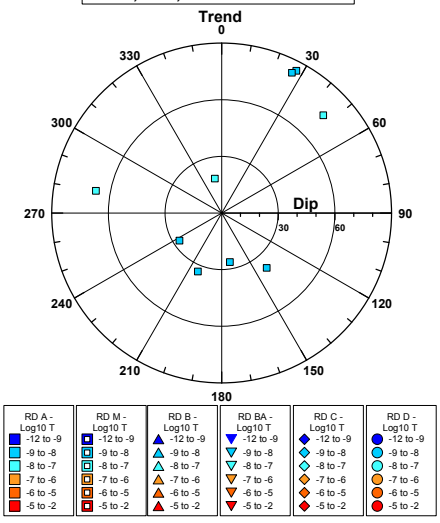

KLX02, HRD, ELEV.: -600 TO -800 m

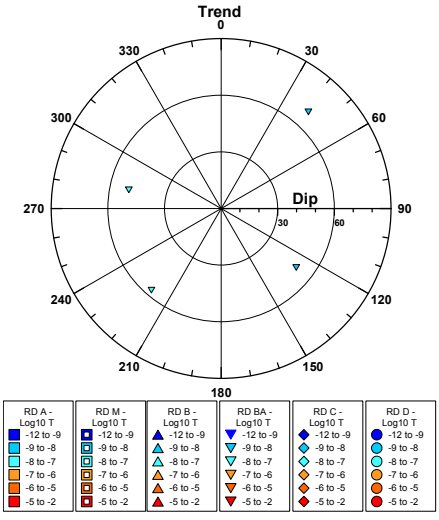

Borehole KLX02. Poles for PFL-f feature planes in possible deformation zones.

KLX02, DZ(ESHI), ELEV.: 0 TO -1000 m

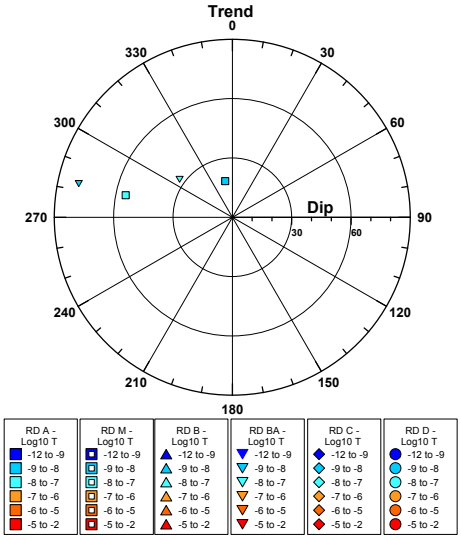

KLX02, DZ(ESHI), ELEV.: -400 TO -600 m

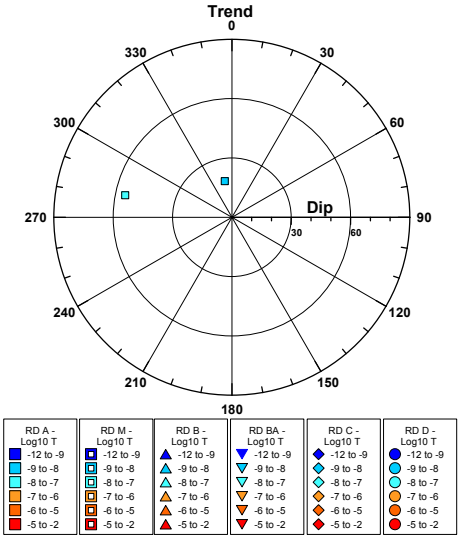

KLX02, DZ(ESHI), ELEV.: -600 TO -800 m

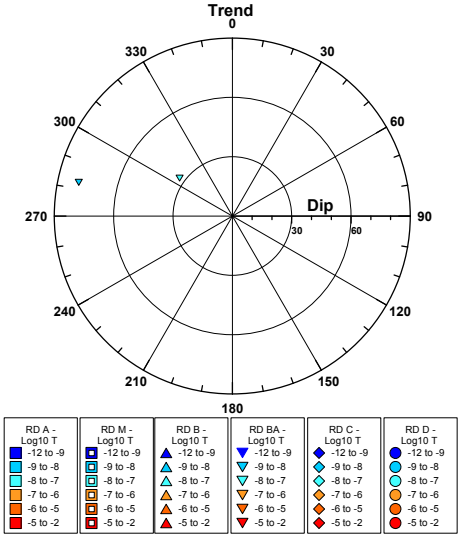

Borehole KLX02. Poles for PFL-f feature planes in deterministically modelled deformation zones.

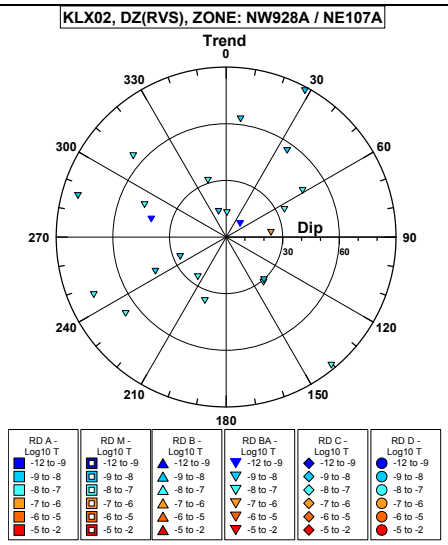

Borehole KLX03.

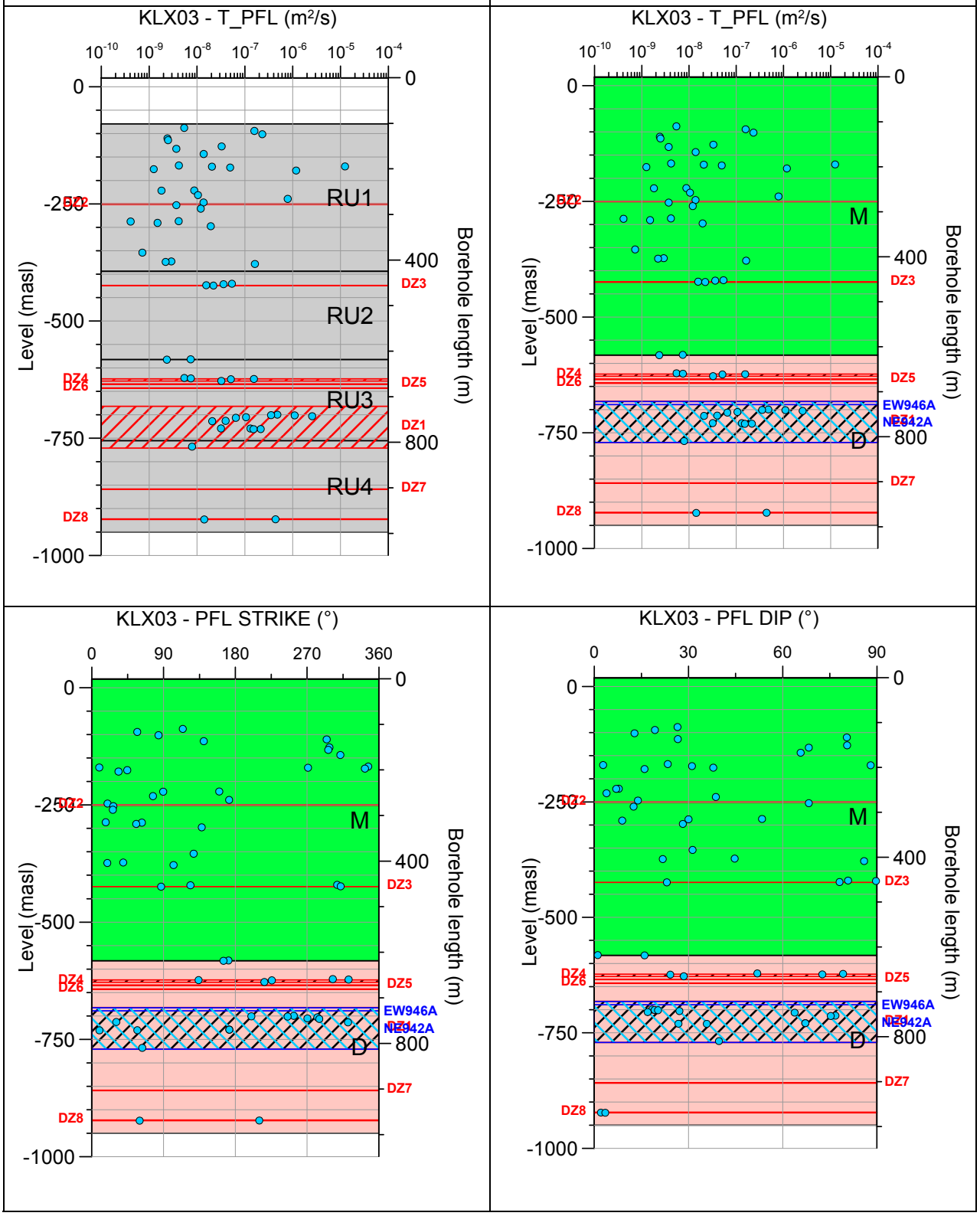

Comment:

Borehole KLX03. Poles for PFL-f feature planes outside deformation zones.

KLX03, HRD, ELEV.: 0 TO -1000 m

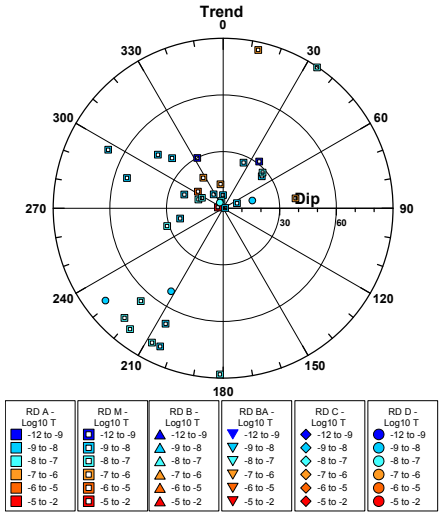

KLX03, HRD, ELEV.: 0 TO -200 m

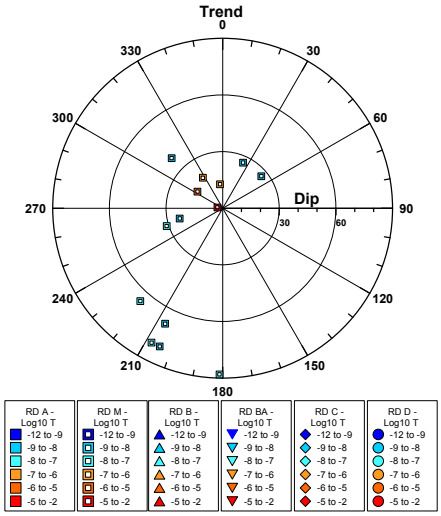

KLX03, HRD, ELEV.: -200 TO -400 m

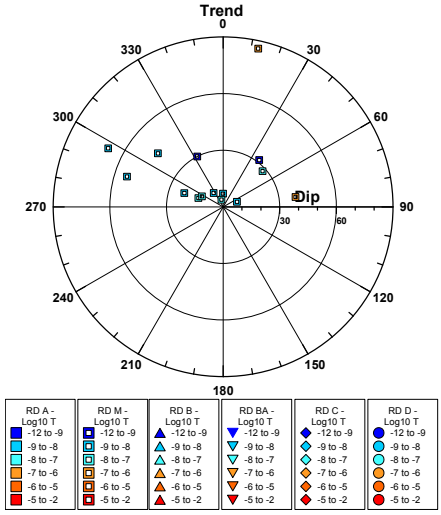

KLX03, HRD, ELEV.: -400 TO -600 m

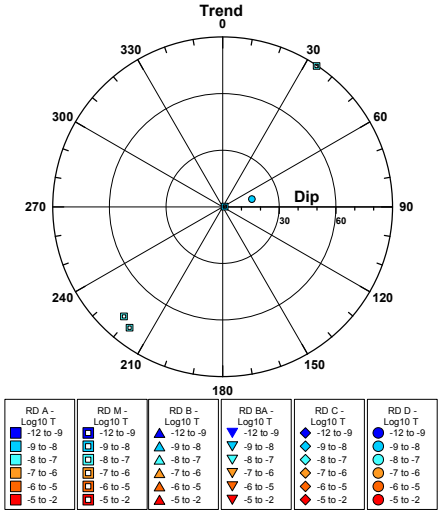

KLX03, HRD, ELEV.: -600 TO -800 m

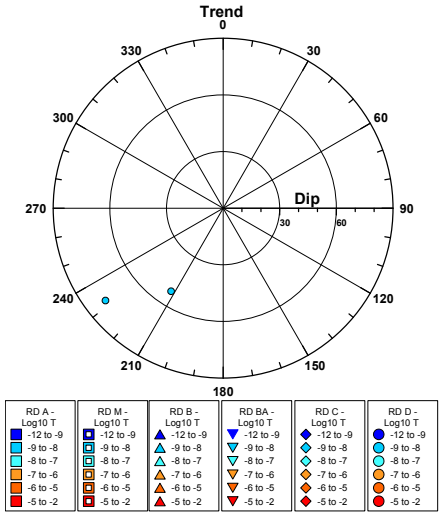

KLX03, HRD, ELEV.: -800 TO -1000 m

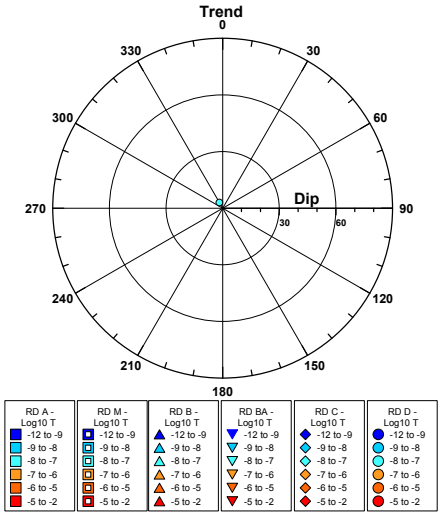

Borehole KLX03. Poles for PFL-f feature planes in possible deformation zones.

KLX03, DZ(ESHI), ELEV.: 0 TO -1000 m

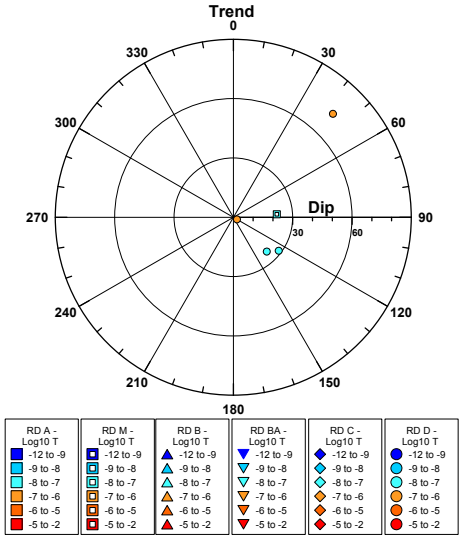

KLX03, DZ(ESHI), ELEV.: -400 TO -600 m

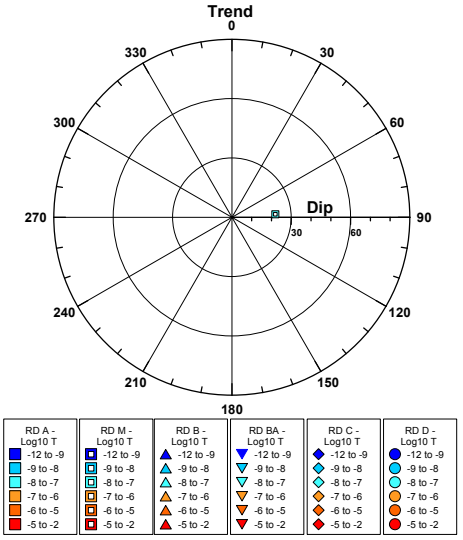

KLX03, DZ(ESHI), ELEV.: -600 TO -800 m

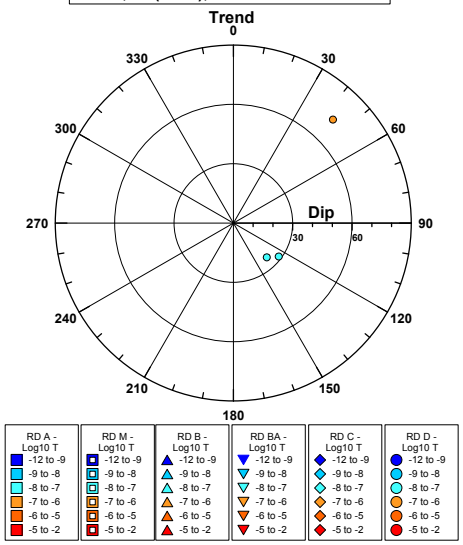

KLX03, DZ(ESHI), ELEV.: -800 TO -1000 m

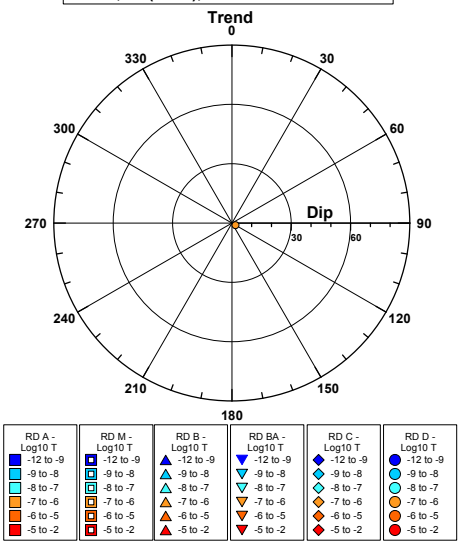

Borehole KLX03. Poles for PFL-f feature planes in deterministically modelled deformation zones.

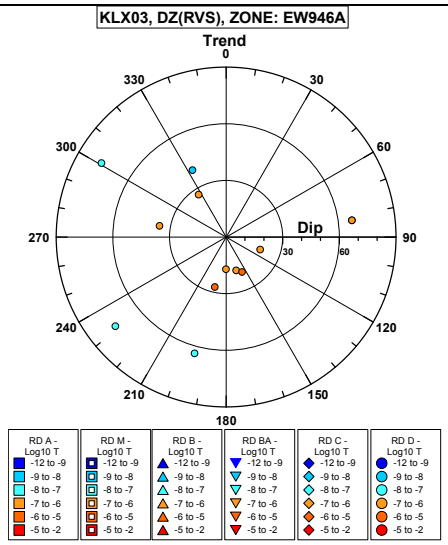

Borehole KLX04.

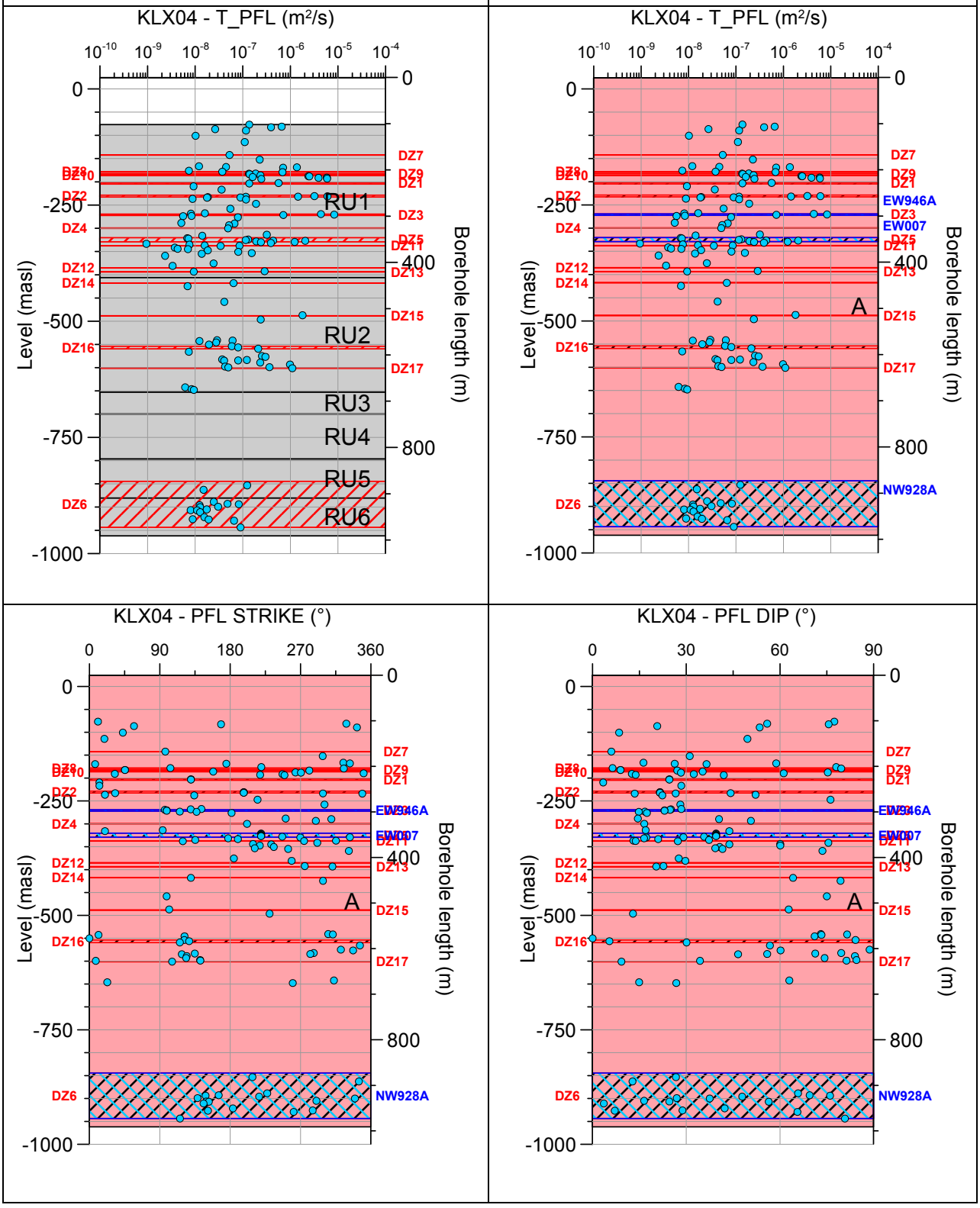

Comment:

Borehole KLX04. Poles for PFL- f feature planes outside deformation zones.

KLX04, HRD, ELEV.: 0 TO -1000 m

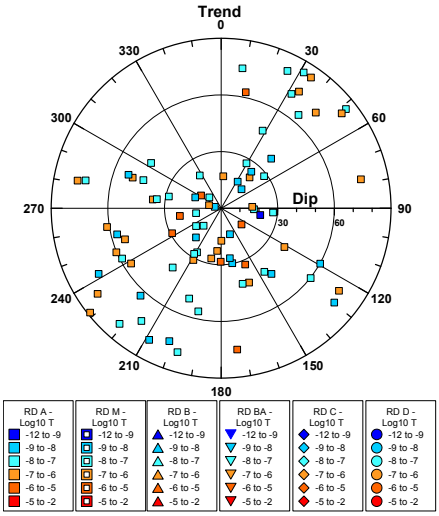

KLX04, HRD, ELEV.: 0 TO -200 m

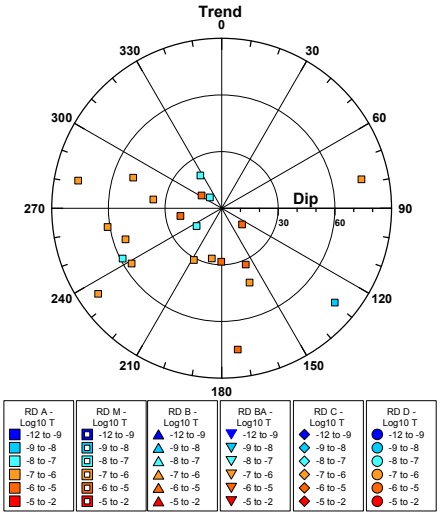

KLX04, HRD, ELEV.: -200 TO -400 m

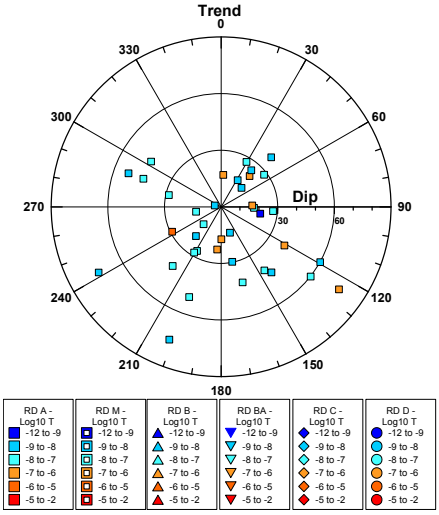

KLX04, HRD, ELEV.: -400 TO -600 m

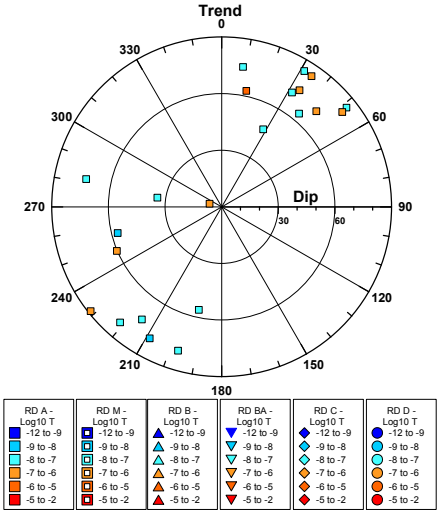

KLX04, HRD, ELEV.: -600 TO -800 m

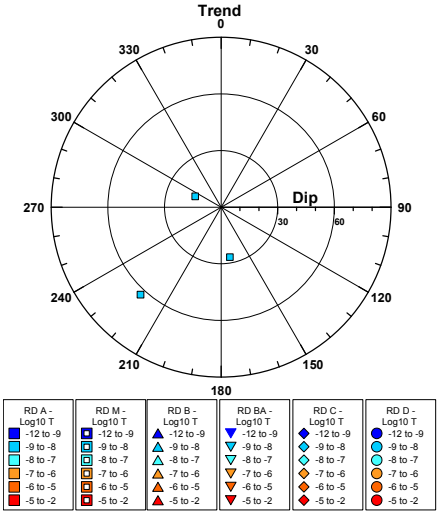

Borehole KLX04. Poles for PFL-f feature planes in possible deformation zones.

KLX04, DZ(ESHI), ELEV.: 0 TO -1000 m

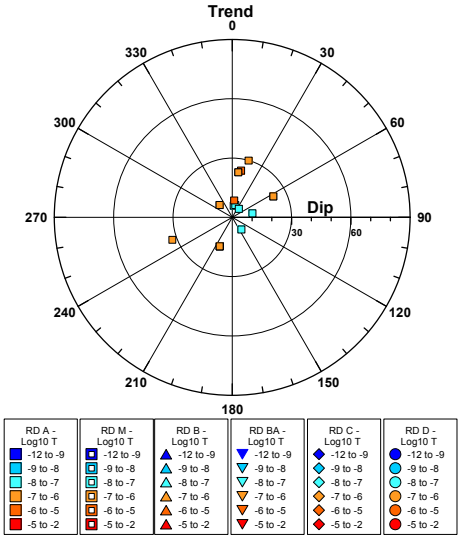

KLX04, DZ(ESHI), ELEV.: 0 TO -200 m

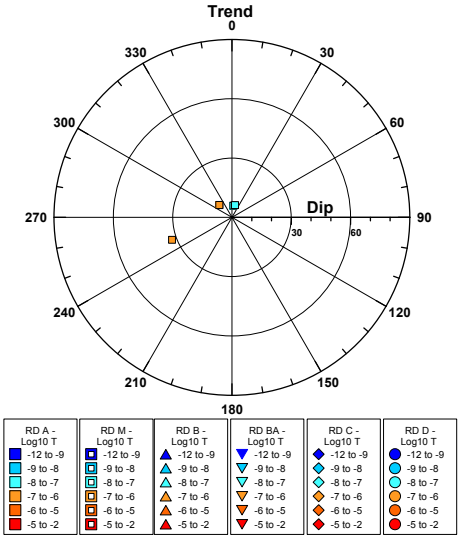

KLX04, DZ(ESHI), ELEV.: -200 TO -400 m

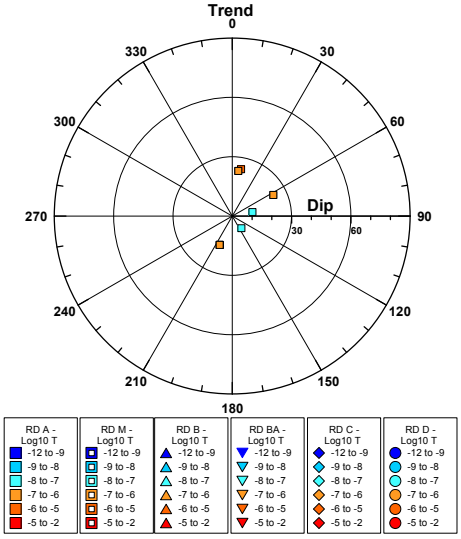

KLX04, DZ(ESHI), ELEV.: -400 TO -600 m

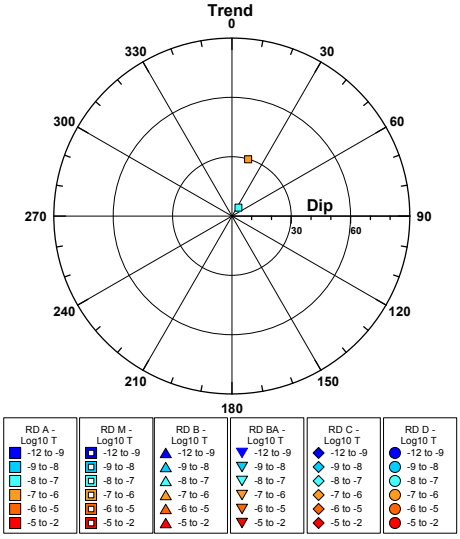

KLX04, DZ(ESHI), ELEV.: -600 TO -800 m

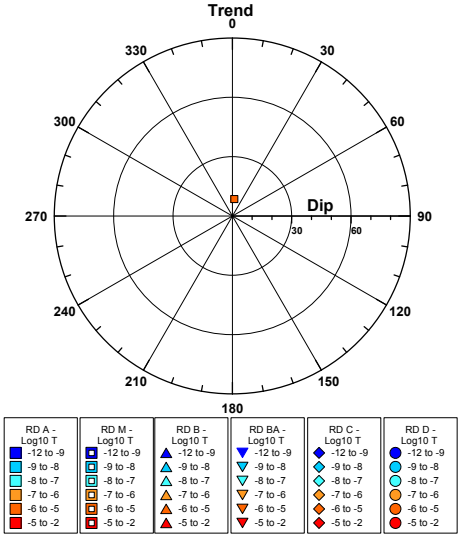

Borehole KLX04. Poles for PFL-f feature planes in deterministically modelled deformation zones.

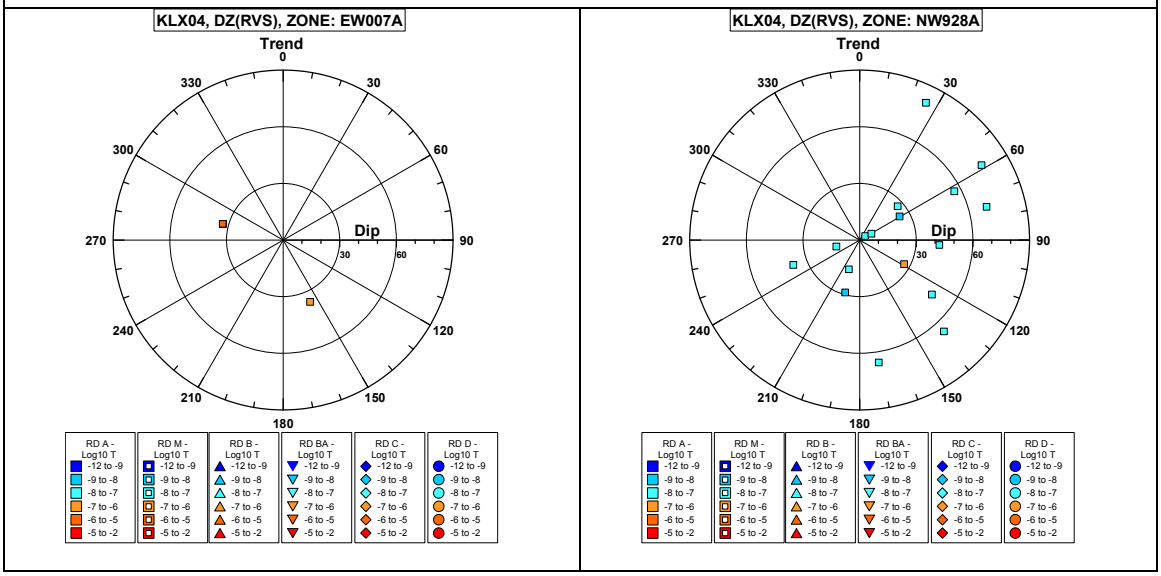

Borehole KLX05.

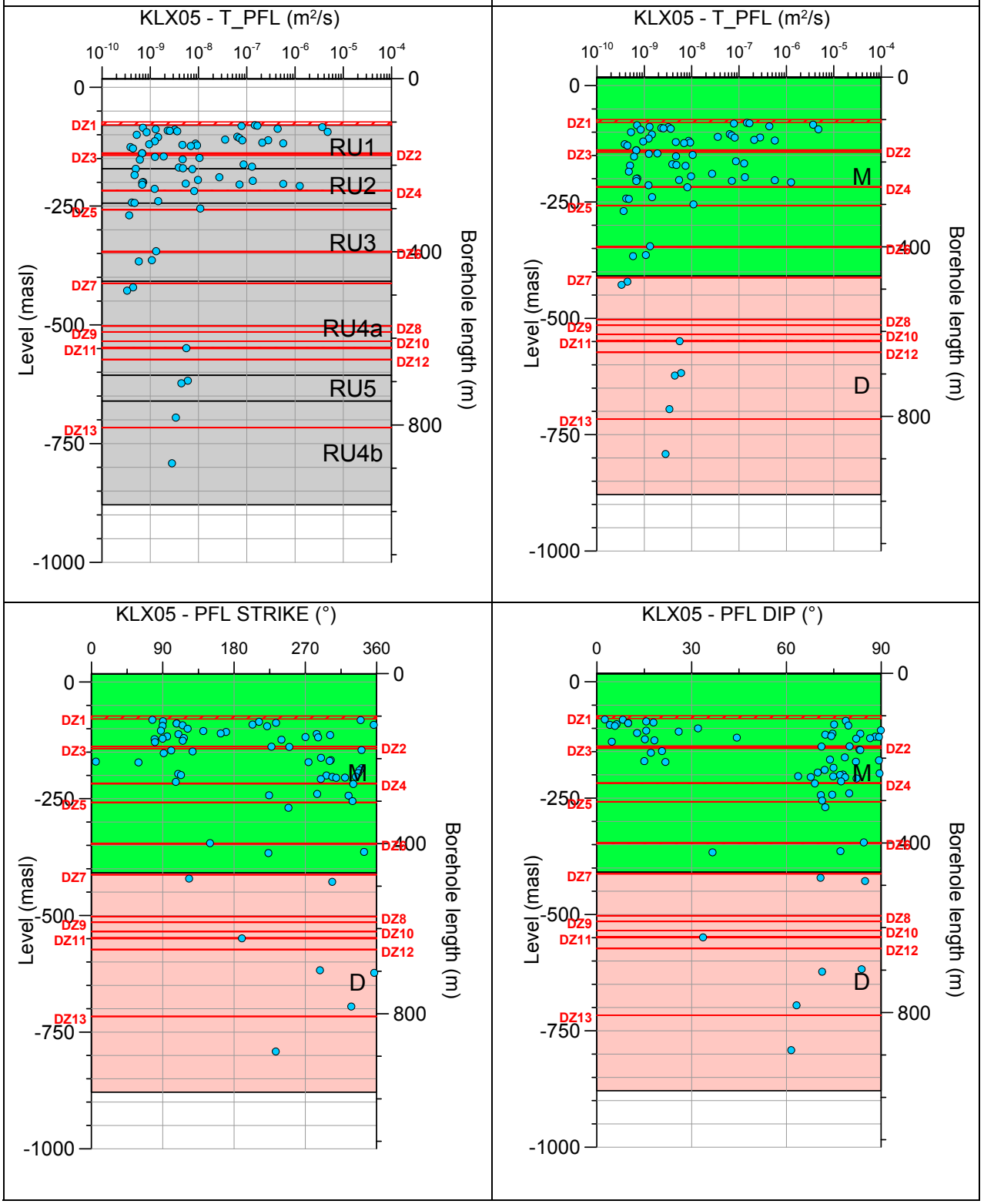

Comment:

Borehole KLX05. Poles for PFL-f feature planes outside deformation zones.

KLX05, HRD, ELEV.: 0 TO -1000 m

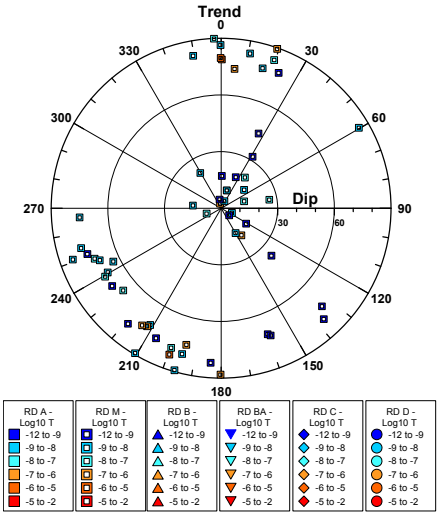

KLX05, HRD, ELEV.: 0 TO -200 m

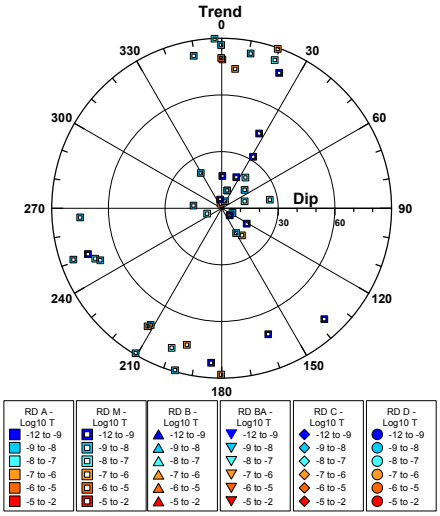

KLX05, HRD, ELEV.: -200 TO -400 m

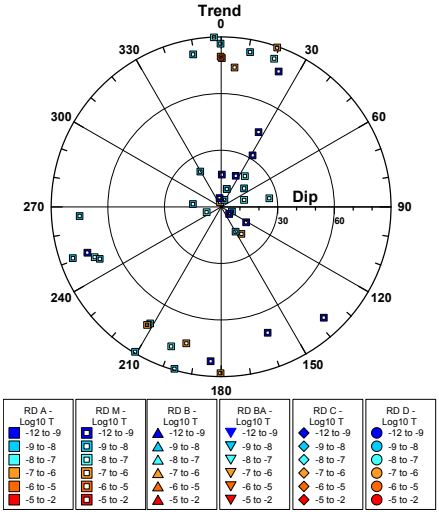

KLX05, HRD, ELEV.: -400 TO -600 m

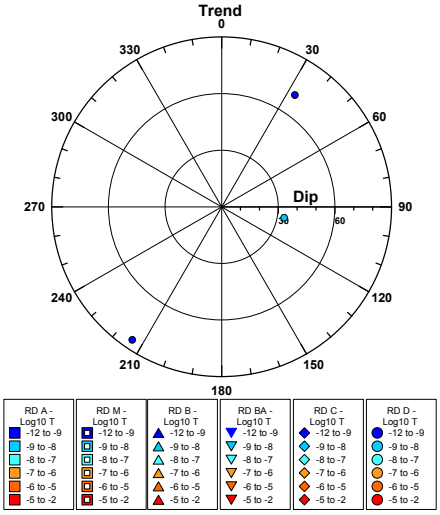

KLX05, HRD, ELEV.: -600 TO -800 m

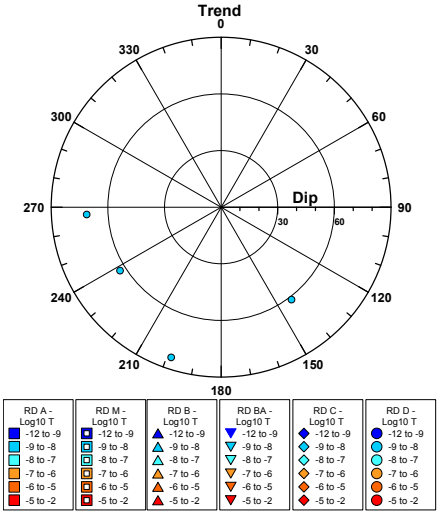

No PFL-f feature planes in possible deformation zones exist in KLX05.

No PFL-f feature planes in deterministically modelled deformation zones exist in KLX05.

Borehole KLX06.

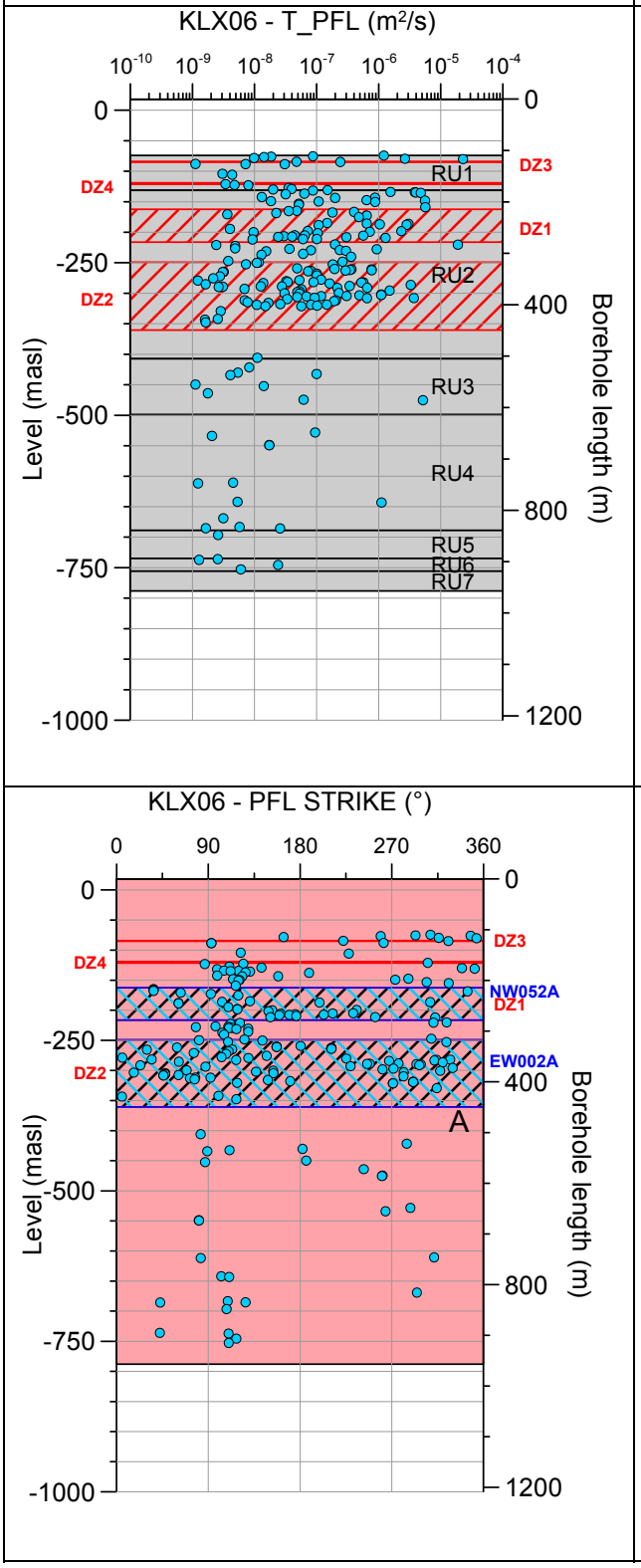

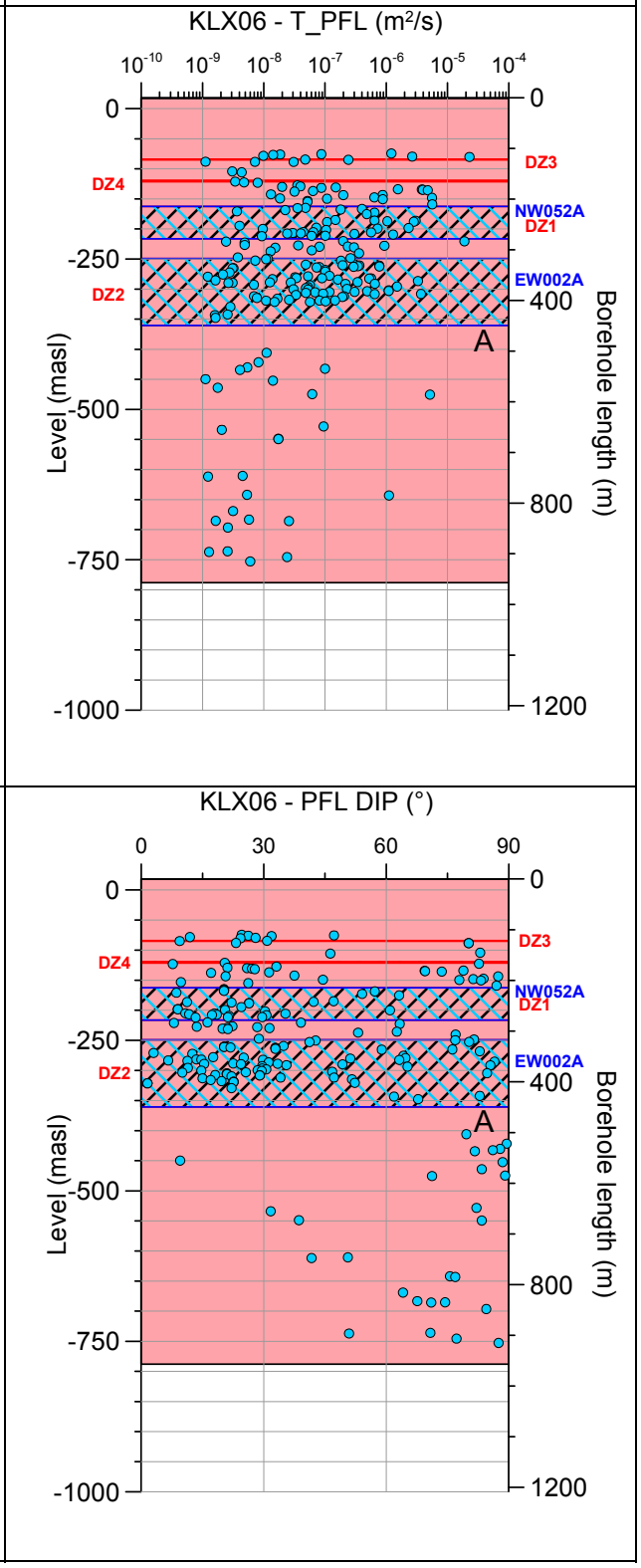

Comment:

Borehole KLX06. Poles for PFL-f feature planes outside deformation zones.

KLX06, HRD, ELEV.: 0 TO -1000 m

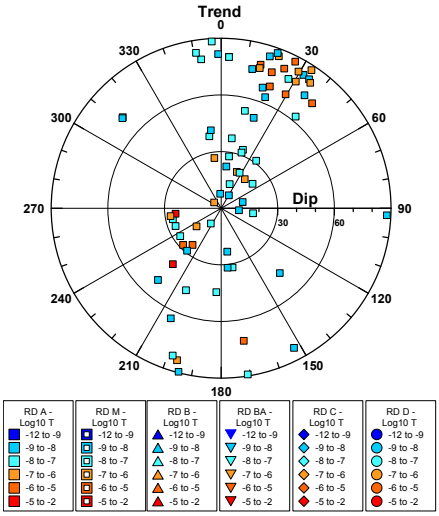

KLX06, HRD, ELEV.: 0 TO -200 m

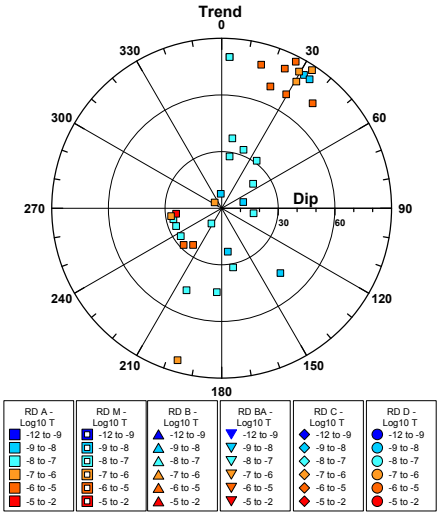

KLX06, HRD, ELEV.: -200 TO -400 m

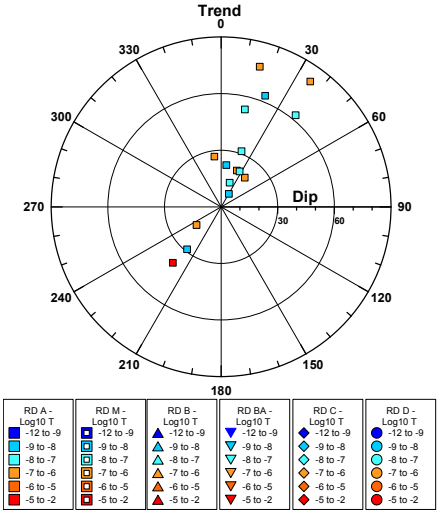

KLX06, HRD, ELEV.: -400 TO -600 m

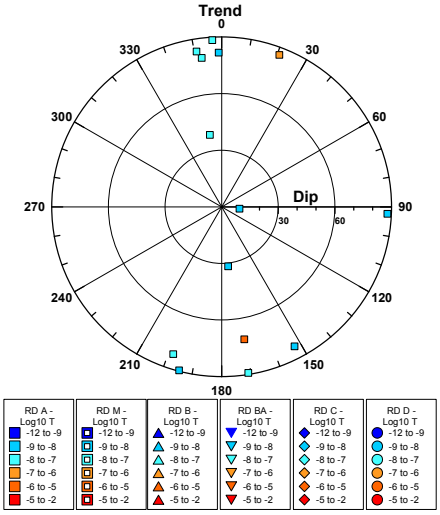

KLX06, HRD, ELEV.: -600 TO -800 m

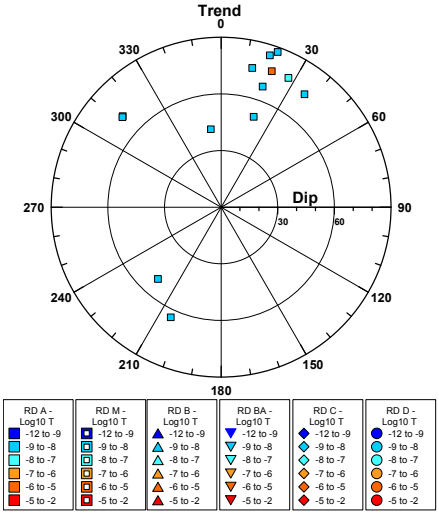

Borehole KLX06. Poles for PFL-f feature planes in possible deformation zones.

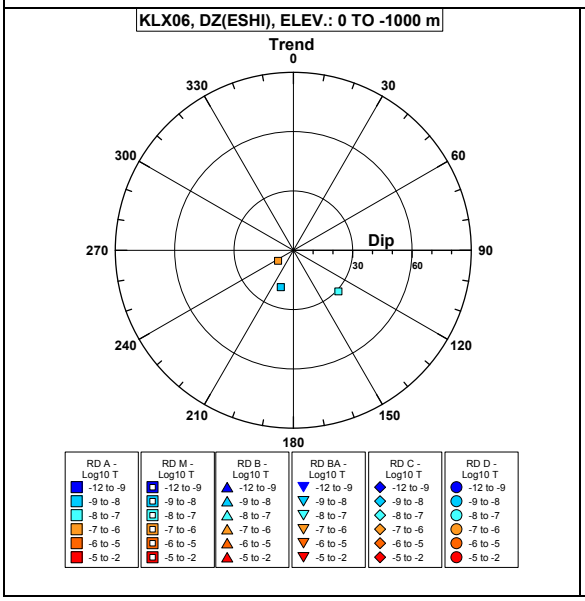

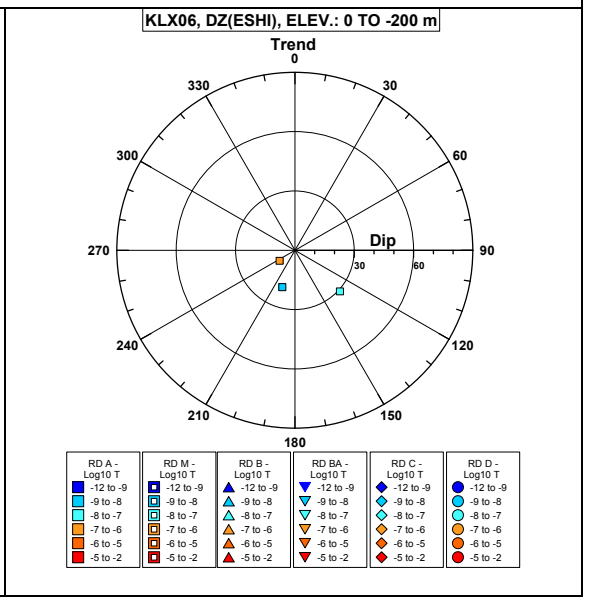

Borehole KLX06. Poles for PFL-f feature planes in deterministically modelled deformation zones.

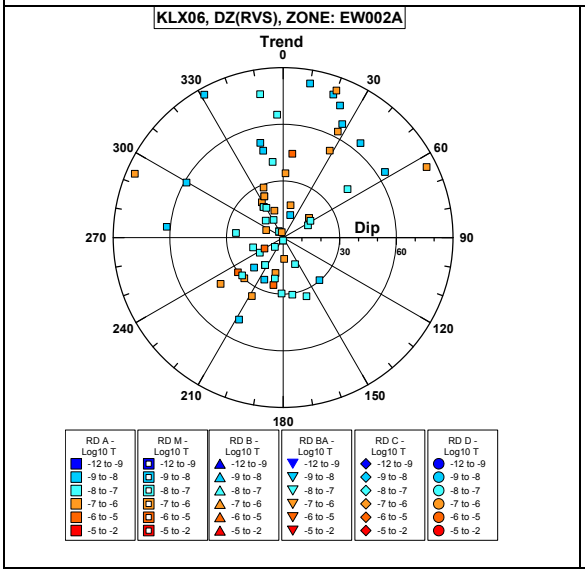

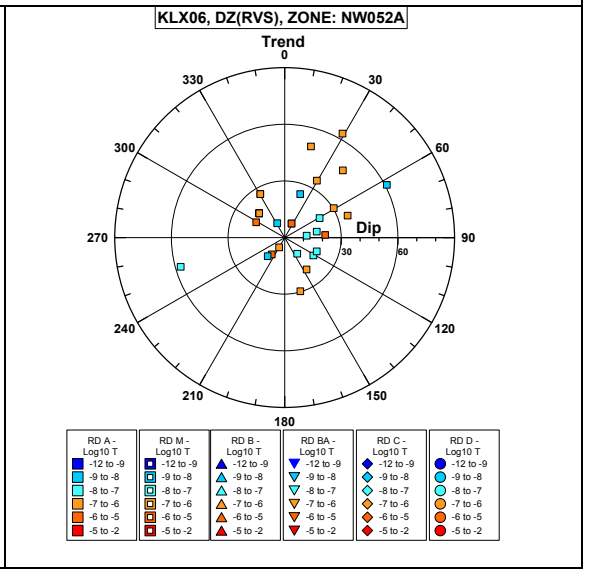

Borehole KLX07A.

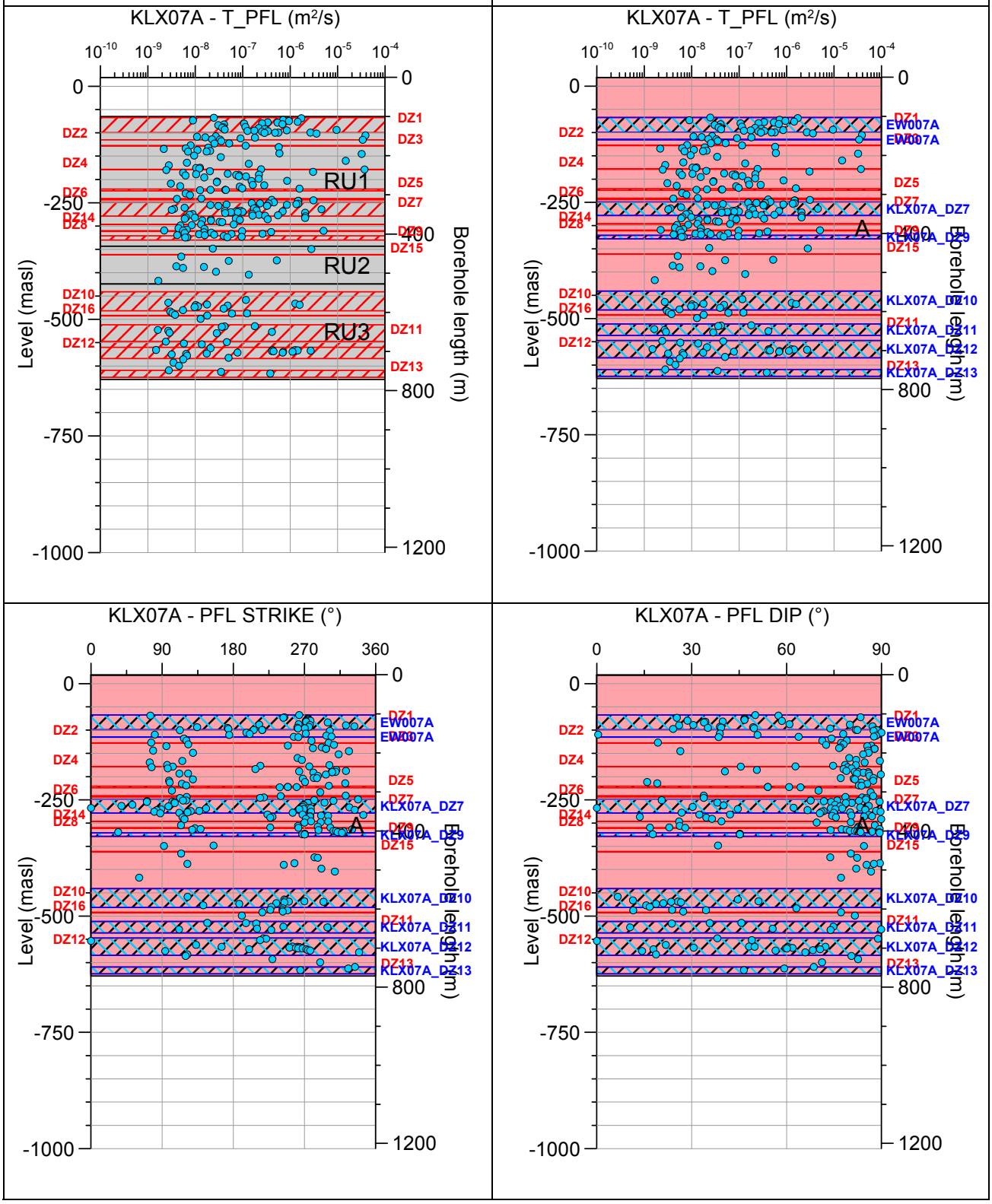

Comment:

Borehole KLX07A. Poles for PFL-f feature planes outside deformation zones.

KLX07A, HRD, ELEV.: 0 TO -1000 m

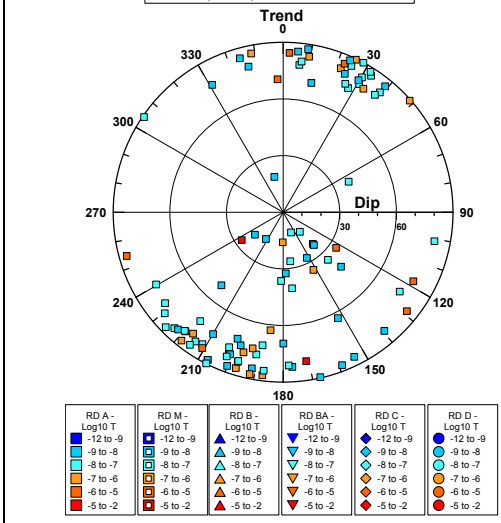

KLX07A, HRD, ELEV.: 0 TO -200 m

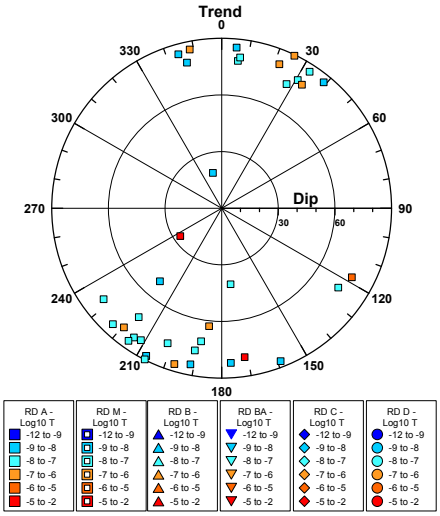

KLX07A, HRD, ELEV.: -200 TO -400 m

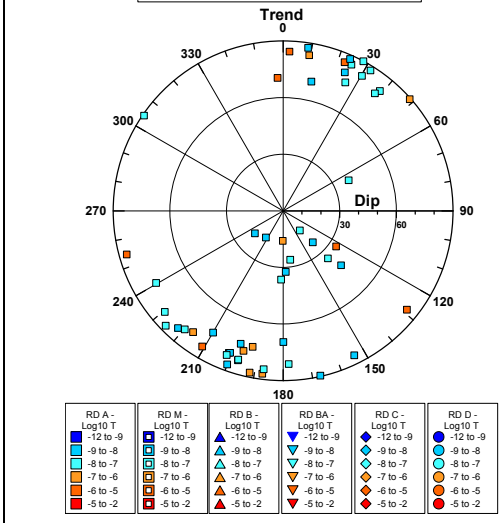

KLX07A, HRD, ELEV.: -400 TO -600 m

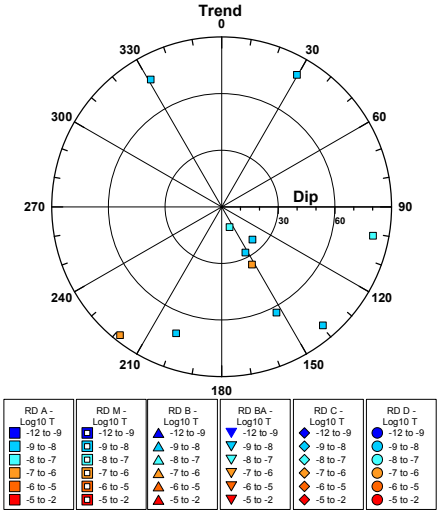

Borehole KLX07A. Poles for PFL-f feature planes in possible deformation zones.

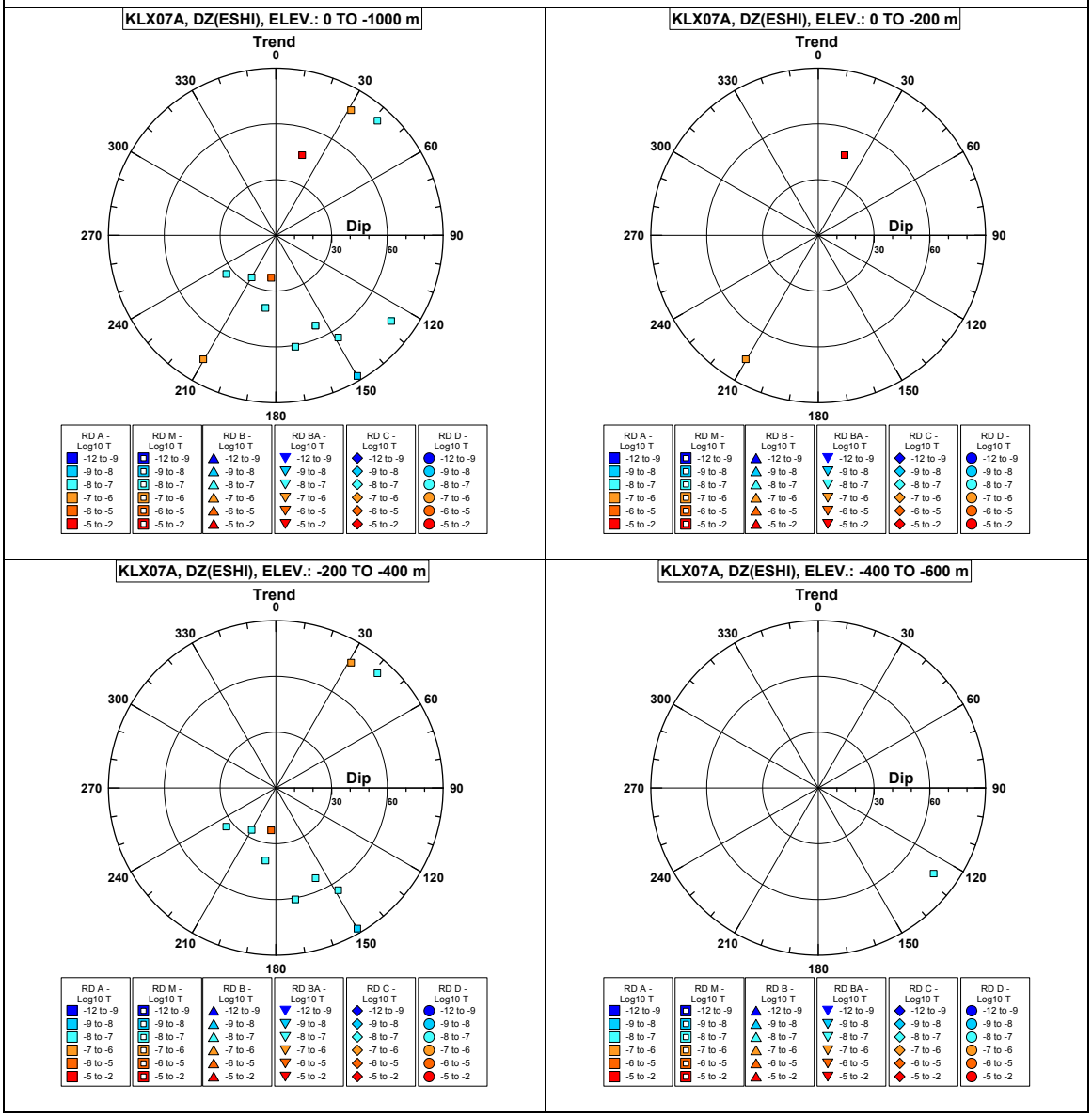

Borehole KLX07A. Poles for PFL-f feature planes in deterministically modelled deformation zones.

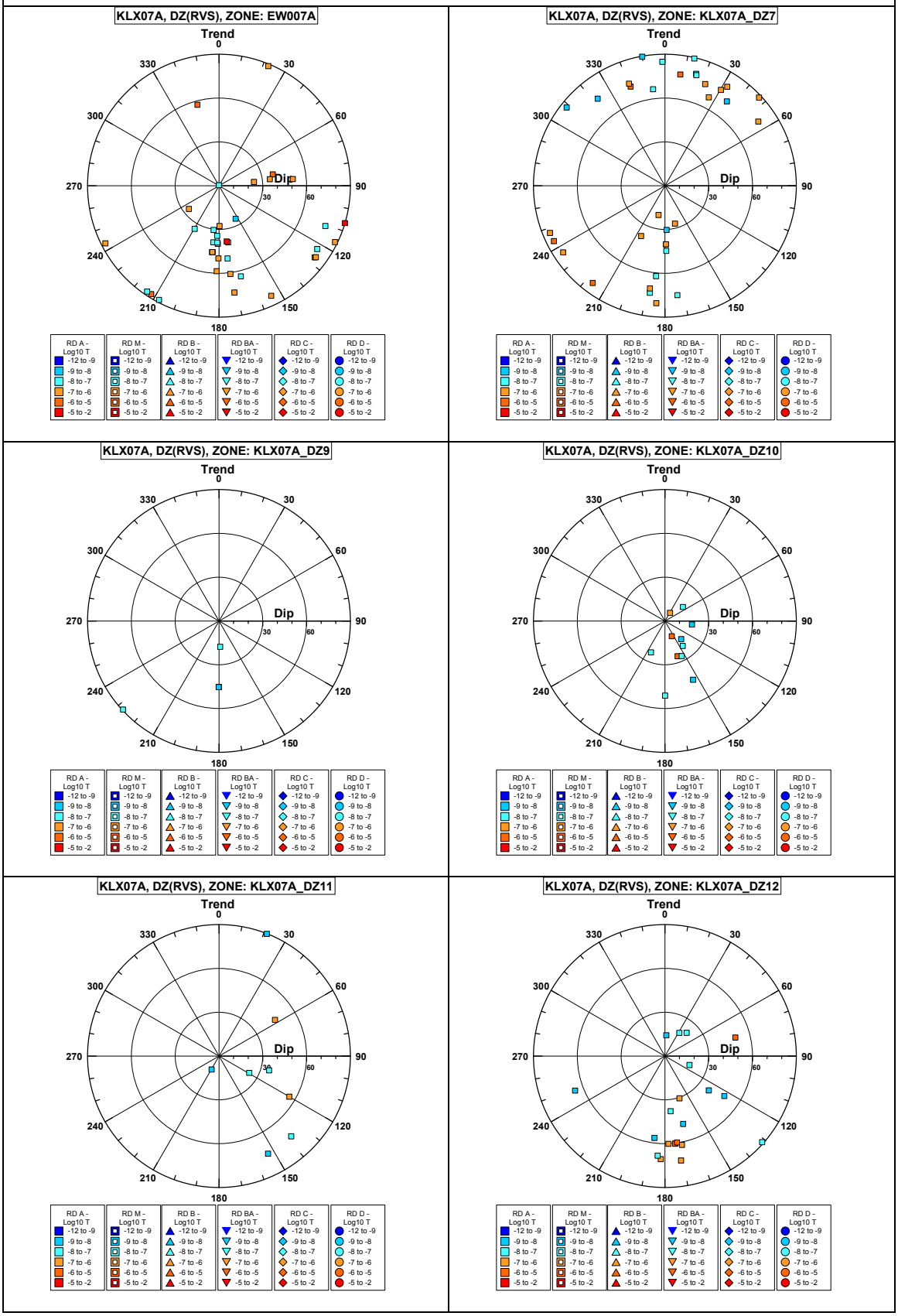

Borehole KLX07A. Poles for PFL-f feature planes in deterministically modelled deformation zones.

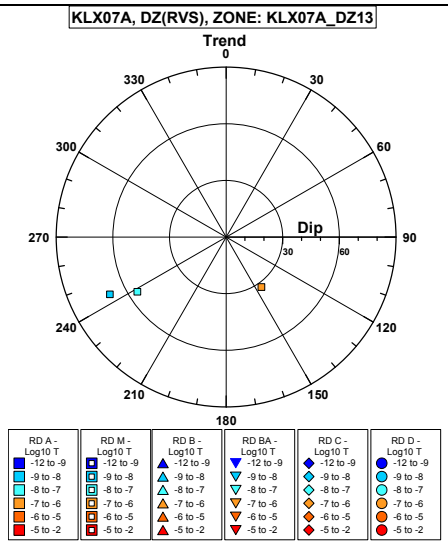

Borehole KLX07B.

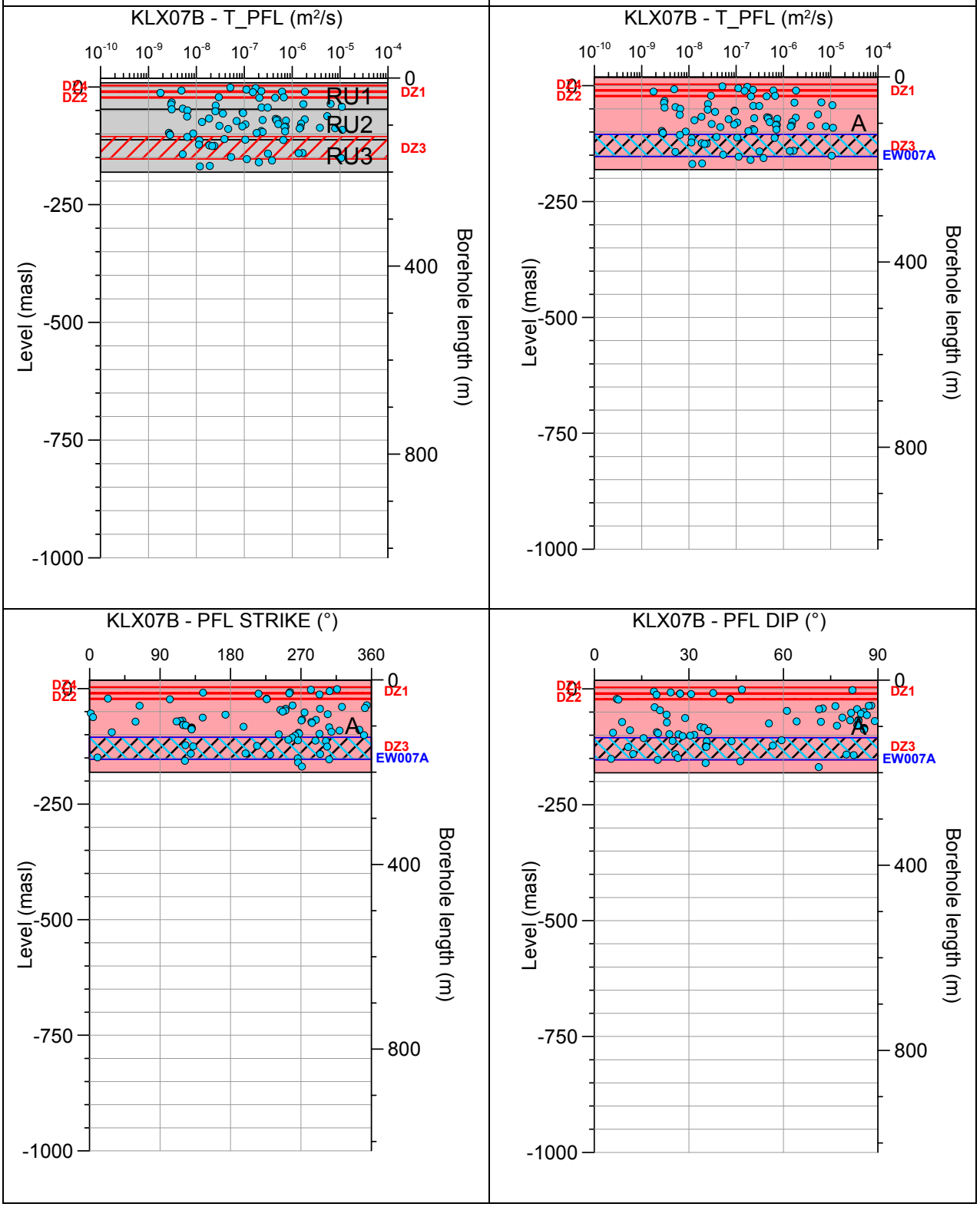

Comment:

Borehole KLX07B. Poles for PFL-f feature planes outside deformation zones.

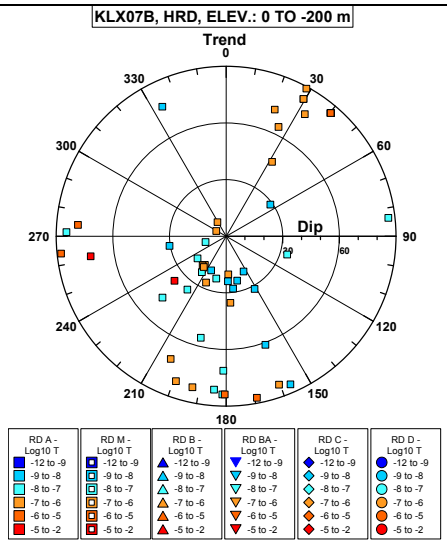

Borehole KLX07B. Poles for PFL-f feature planes in possible deformation zones.

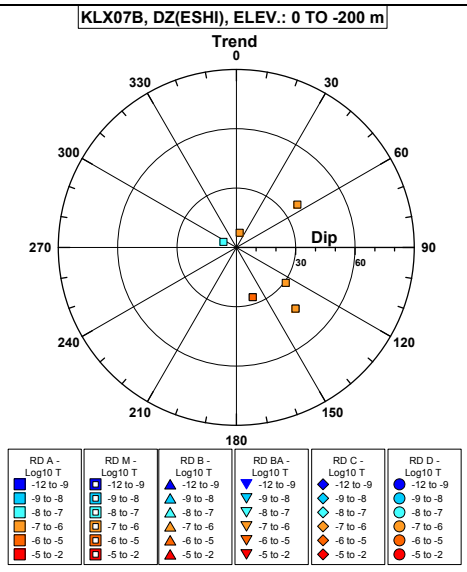

Borehole KLX07B. Poles for PFL-f feature planes in deterministically modelled deformation zones.

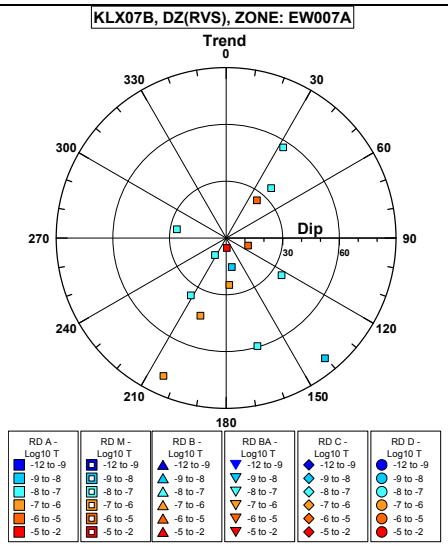

Borehole KLX08.

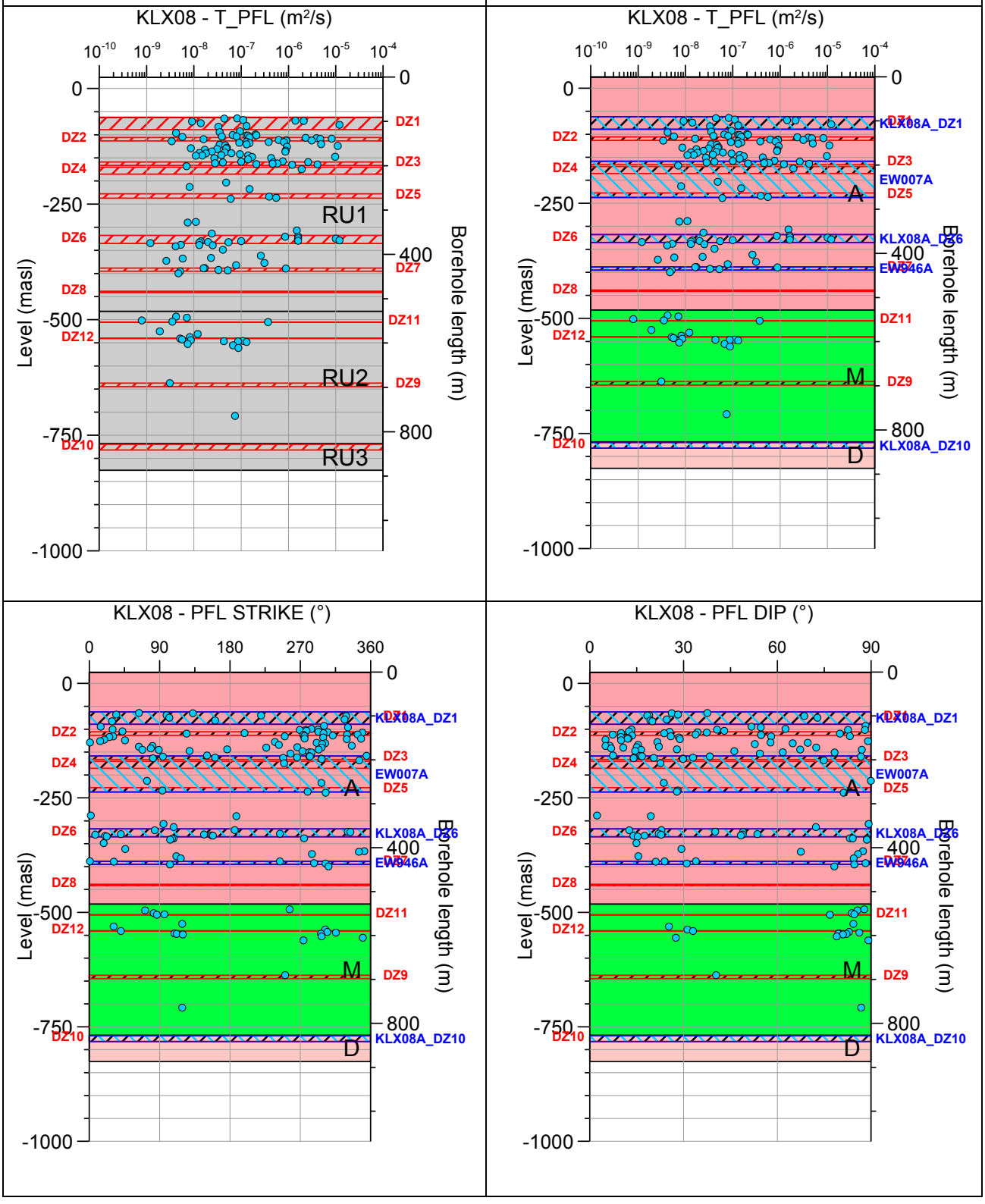

Comment:

Borehole KLX08. Poles for PFL-f feature planes outside deformation zones.

KLX08, HRD, ELEV.: 0 TO -1000 m

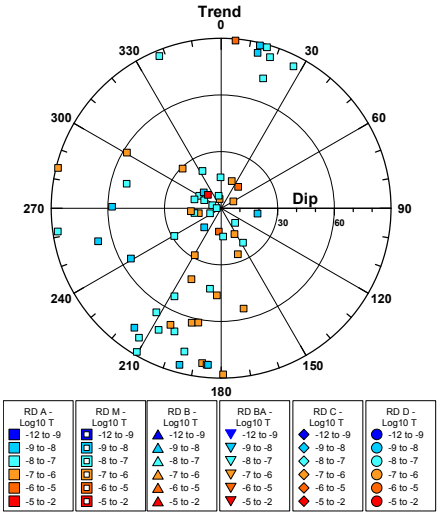

KLX08, HRD, ELEV.: 0 TO -200 m

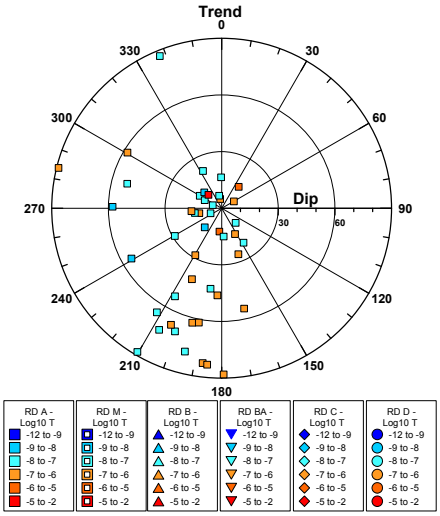

KLX08, HRD, ELEV.: -200 TO -400 m

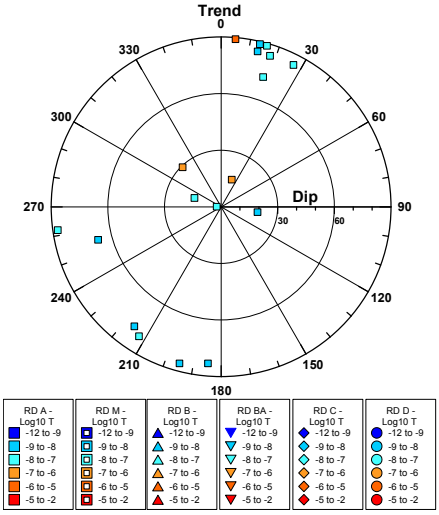

KLX08, HRD, ELEV.: -400 TO -600 m

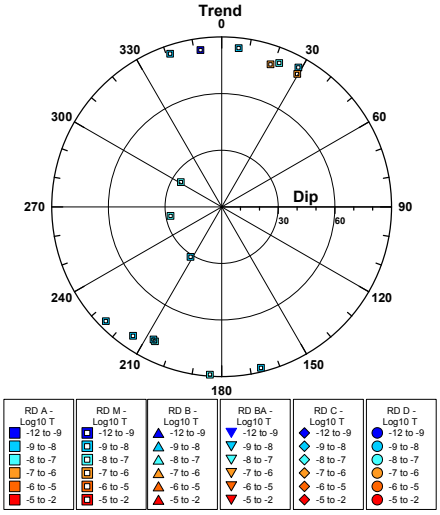

KLX08, HRD, ELEV.: -600 TO -800 m

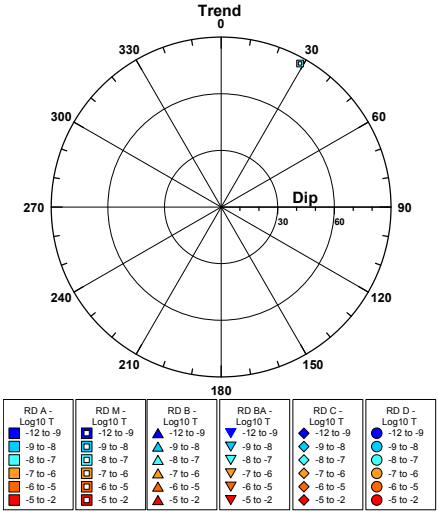

Borehole KLX08. Poles for PFL-f feature planes in possible deformation zones.

KLX08, DZ(ESHI), ELEV.: 0 TO -1000 m

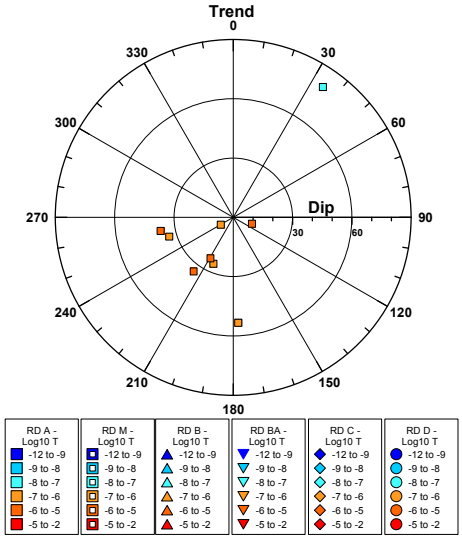

KLX08, DZ(ESHI), ELEV.: 0 TO -200 m

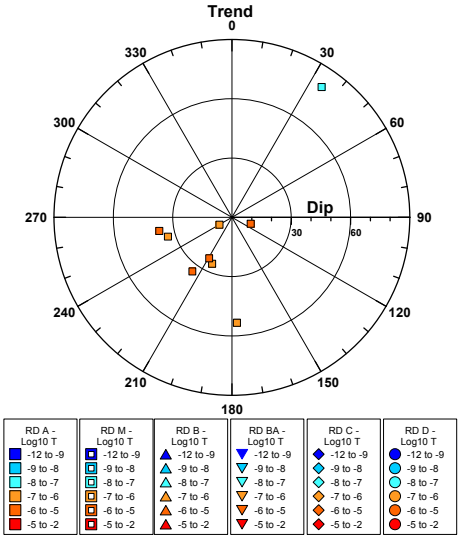

KLX08, DZ(ESHI), ELEV.: -200 TO -400 m

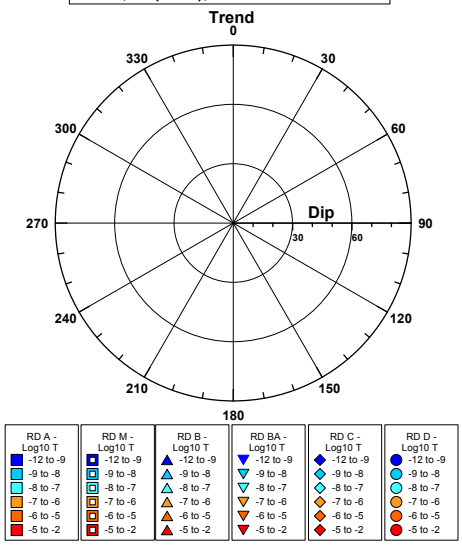

KLX08, DZ(ESHI), ELEV.: -400 TO -600 m

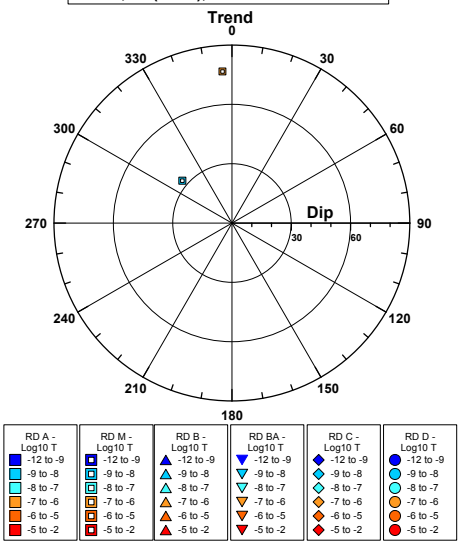

KLX08, DZ(ESHI), ELEV.: -600 TO -800 m

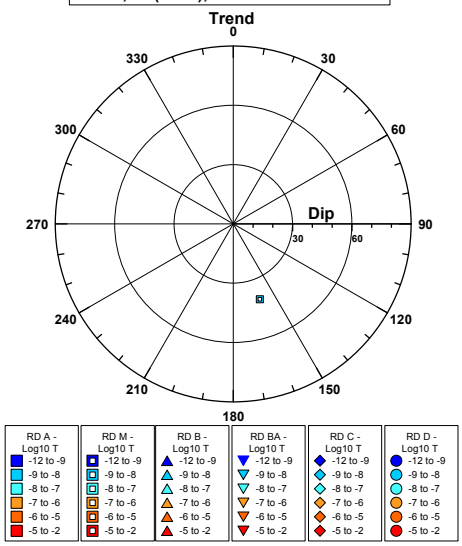

Borehole KLX08. Poles for PFL-f feature planes in deterministically modelled deformation zones.

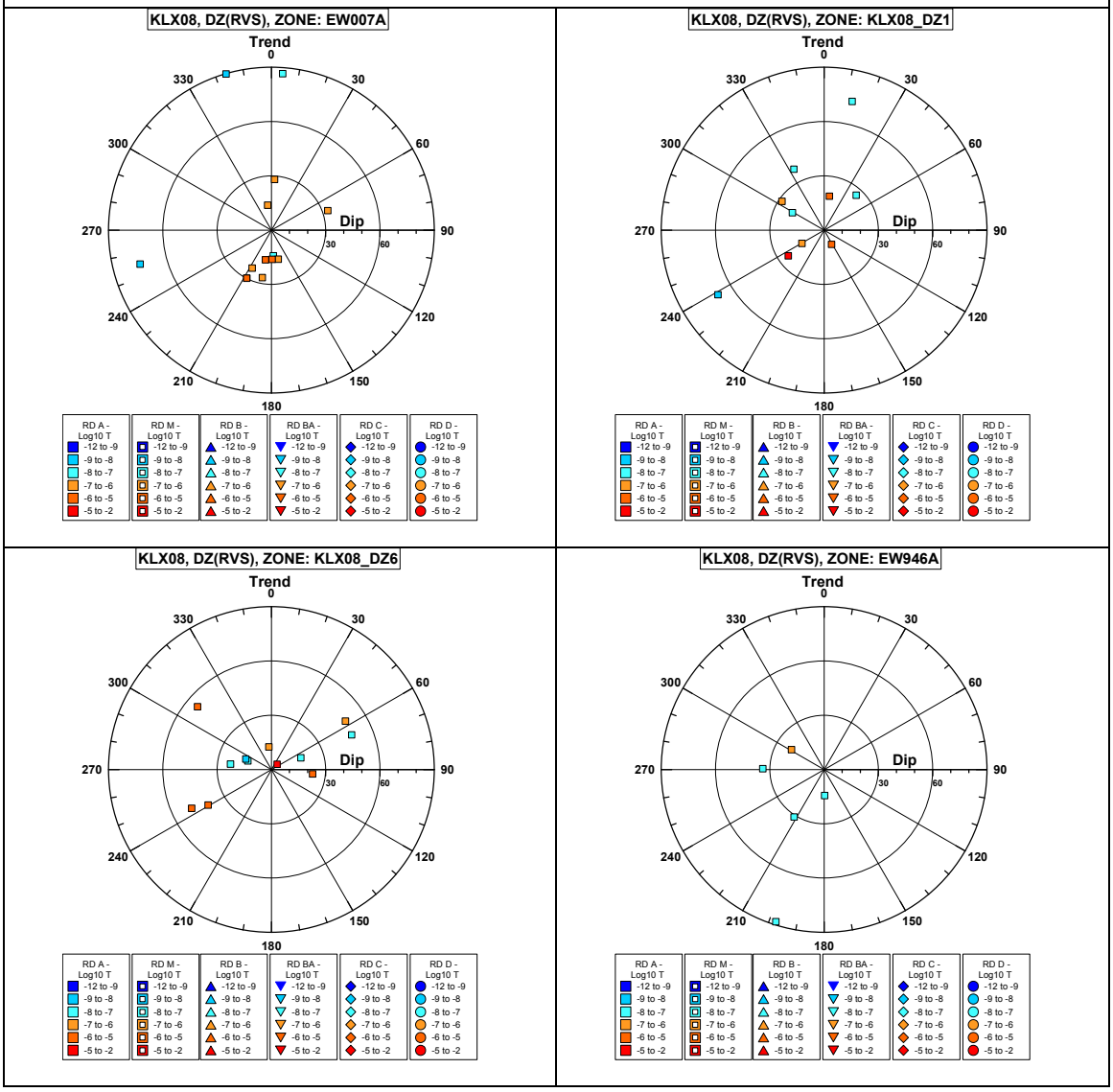

Borehole KLX09.

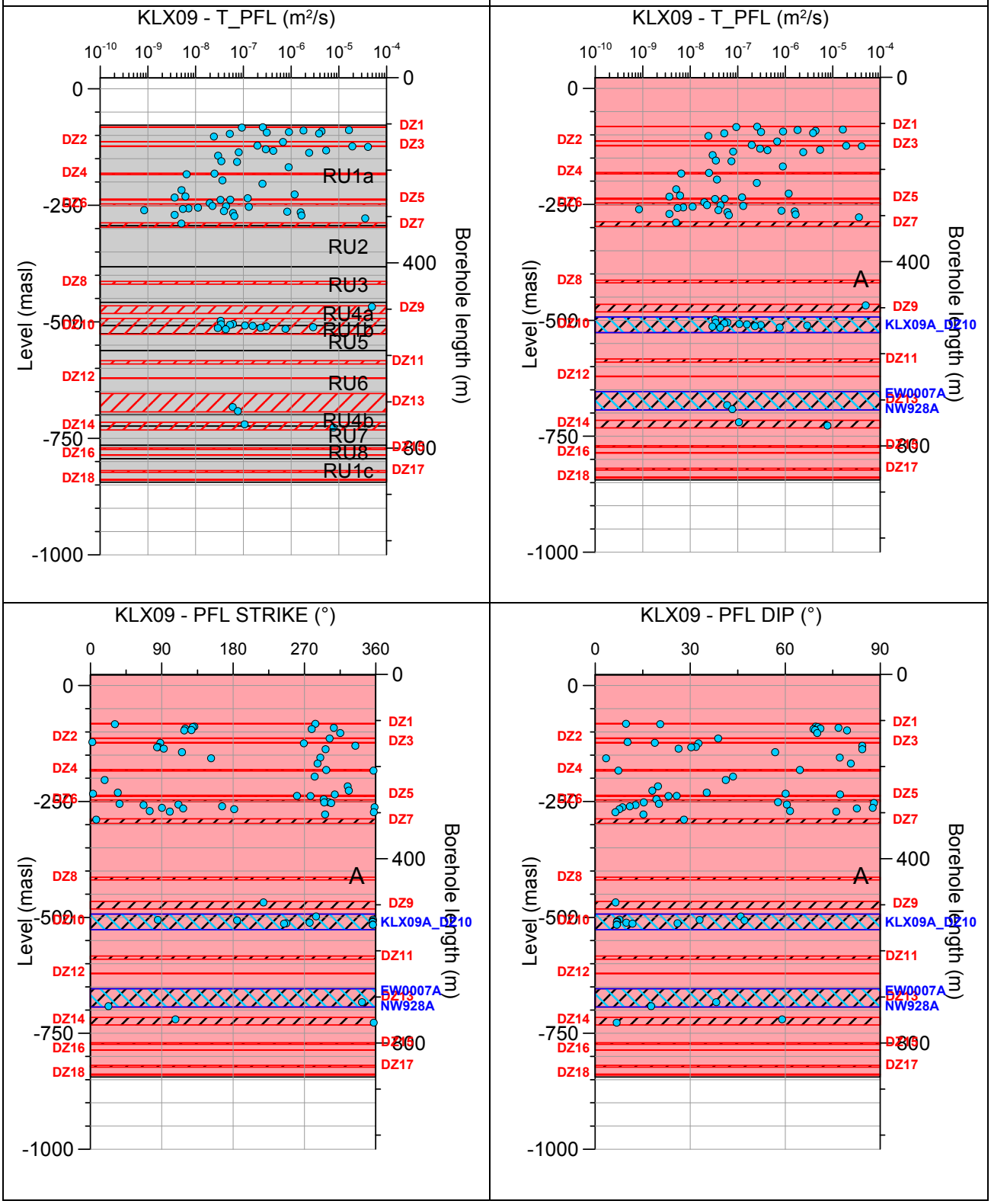

Comment:

Borehole KLX09. Poles for PFL-f feature planes outside deformation zones.

KLX09, HRD, ELEV.: 0 TO -1000 m

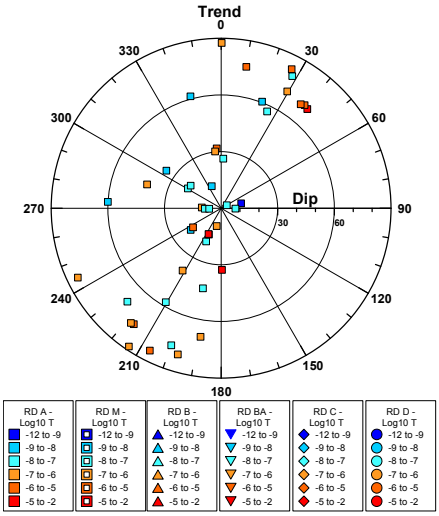

KLX09, HRD, ELEV.: 0 TO -200 m

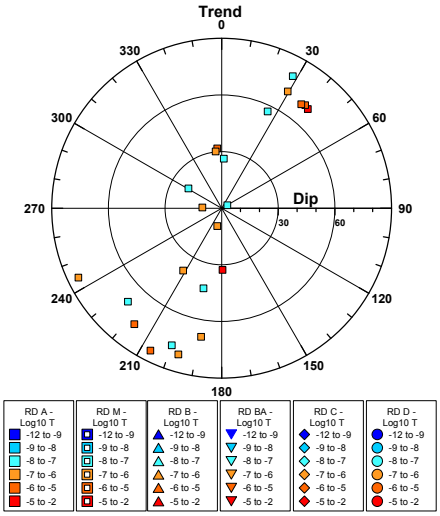

KLX09, HRD, ELEV.: -200 TO -400 m

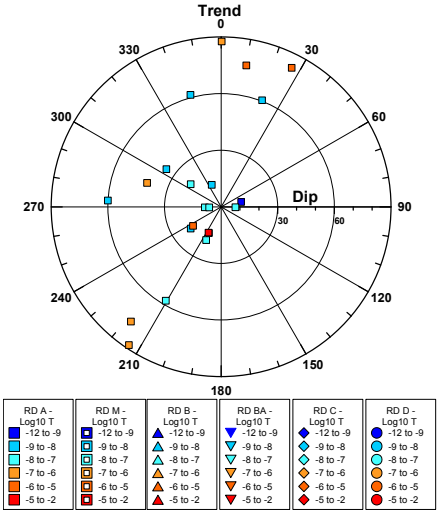

Borehole KLX09. Poles for PFL-f feature planes in possible deformation zones.

KLX09, DZ(ESHI), ELEV.: 0 TO -1000 m

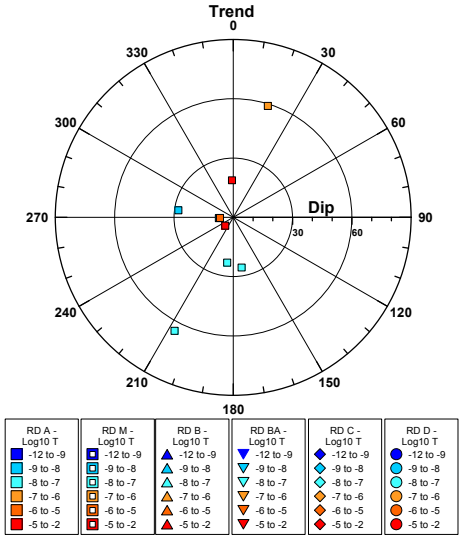

KLX09, DZ(ESHI), ELEV.: 0 TO -200 m

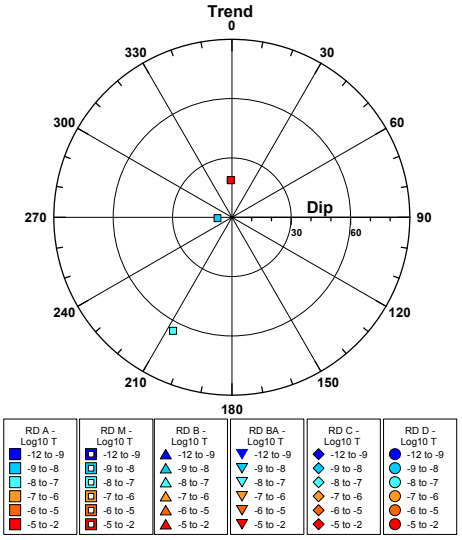

KLX09, DZ(ESHI), ELEV.: -200 TO -400 m

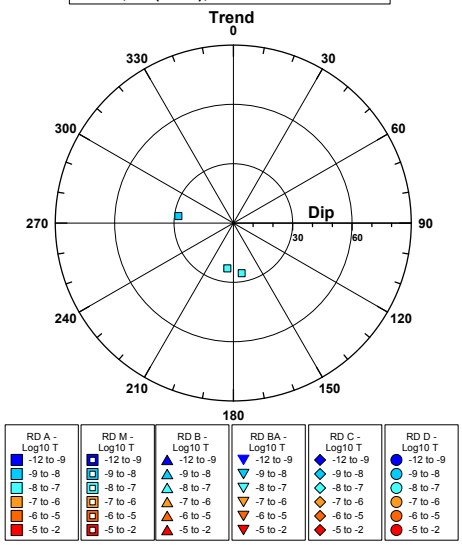

KLX09, DZ(ESHI), ELEV.: -400 TO -600 m

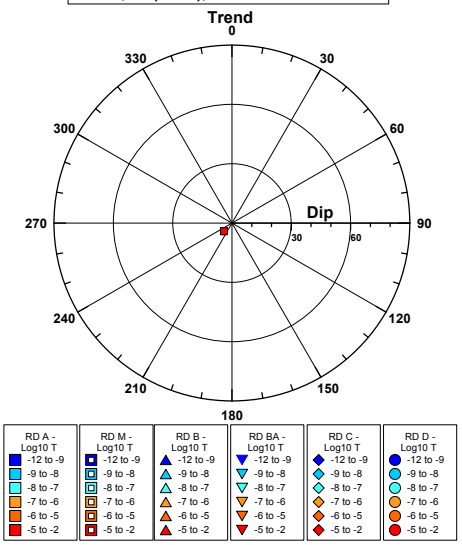

KLX09, DZ(ESHI), ELEV.: -600 TO -800 m

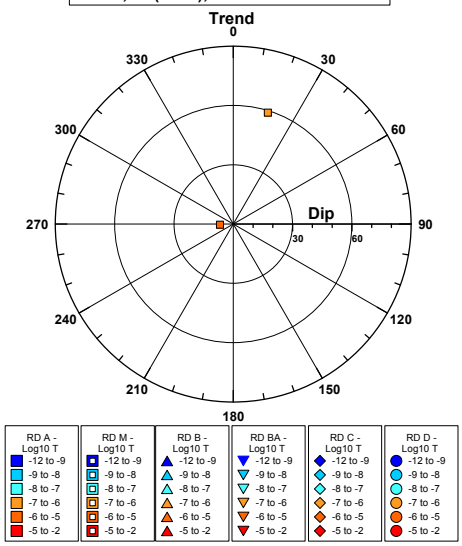

Borehole KLX09. Poles for PFL-f feature planes in deterministically modelled deformation zones.

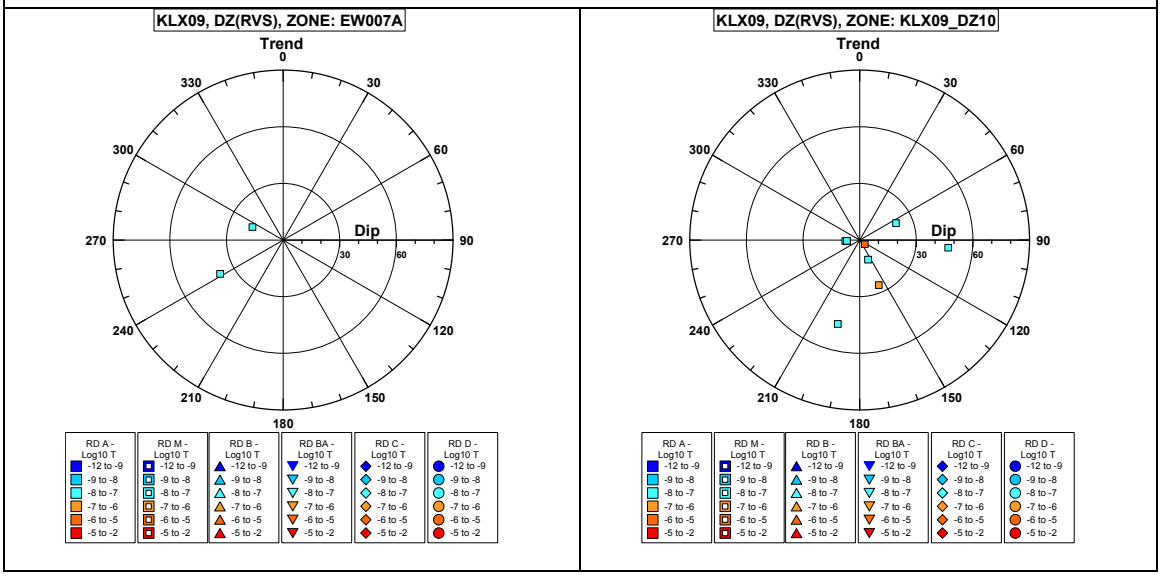

Borehole KLX09B.

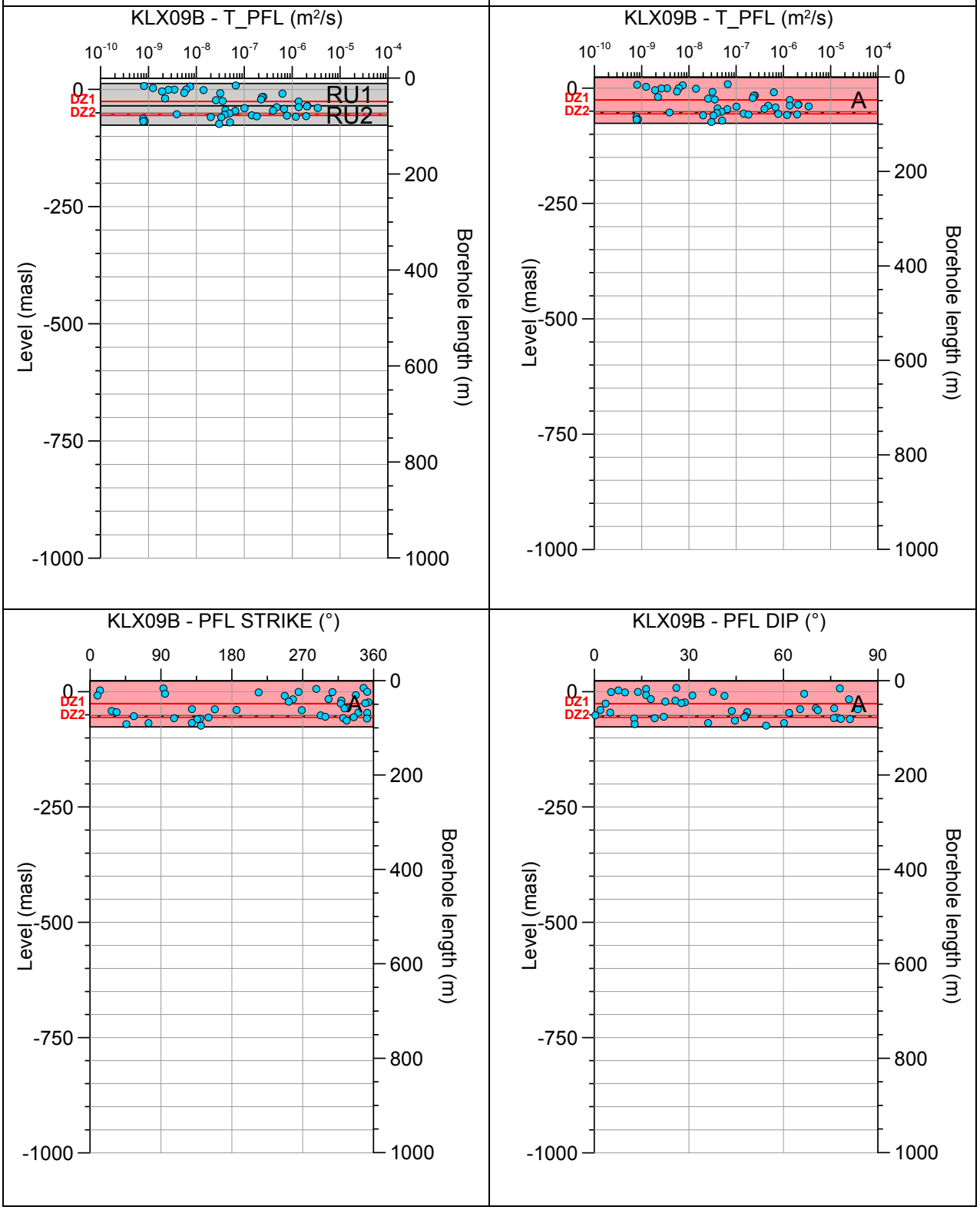

Comment:

Borehole KLX09B. Poles for PFL-f feature planes outside deformation zones.

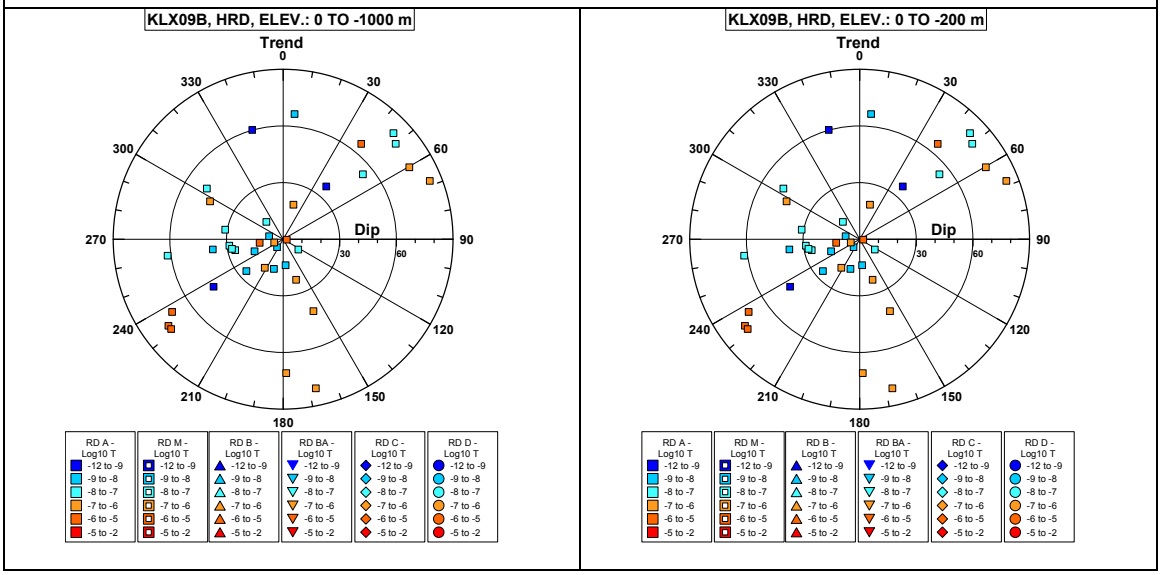

Borehole KLX09B. Poles for PFL-f feature planes in possible deformation zones.

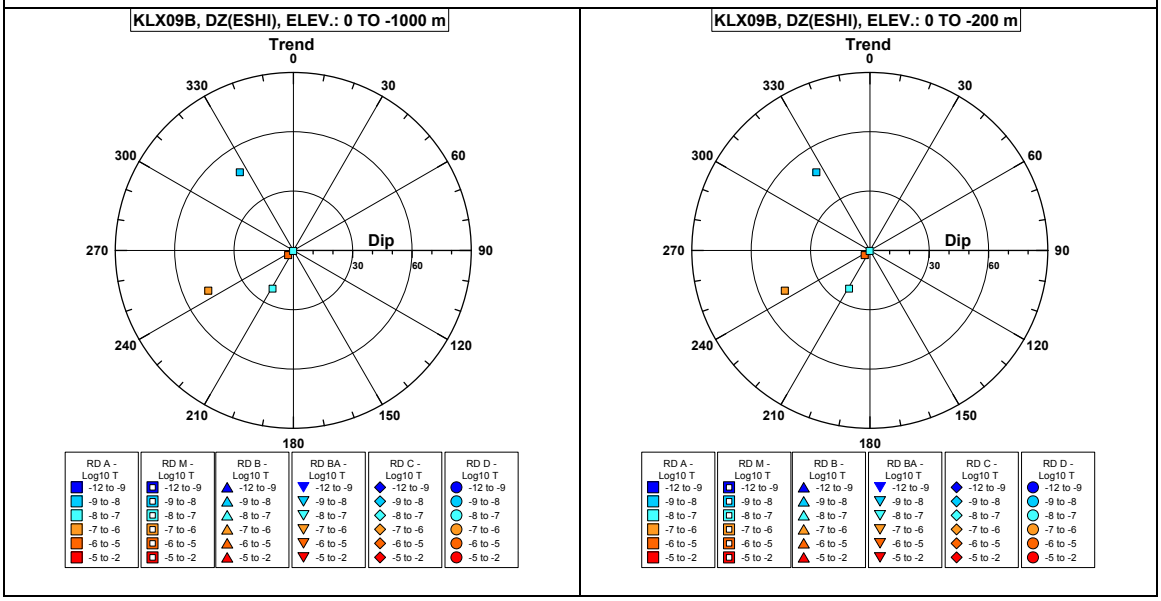

No PFL-f feature planes in deterministically modelled deformation zones exist in KLX09B.

Borehole KLX09C.

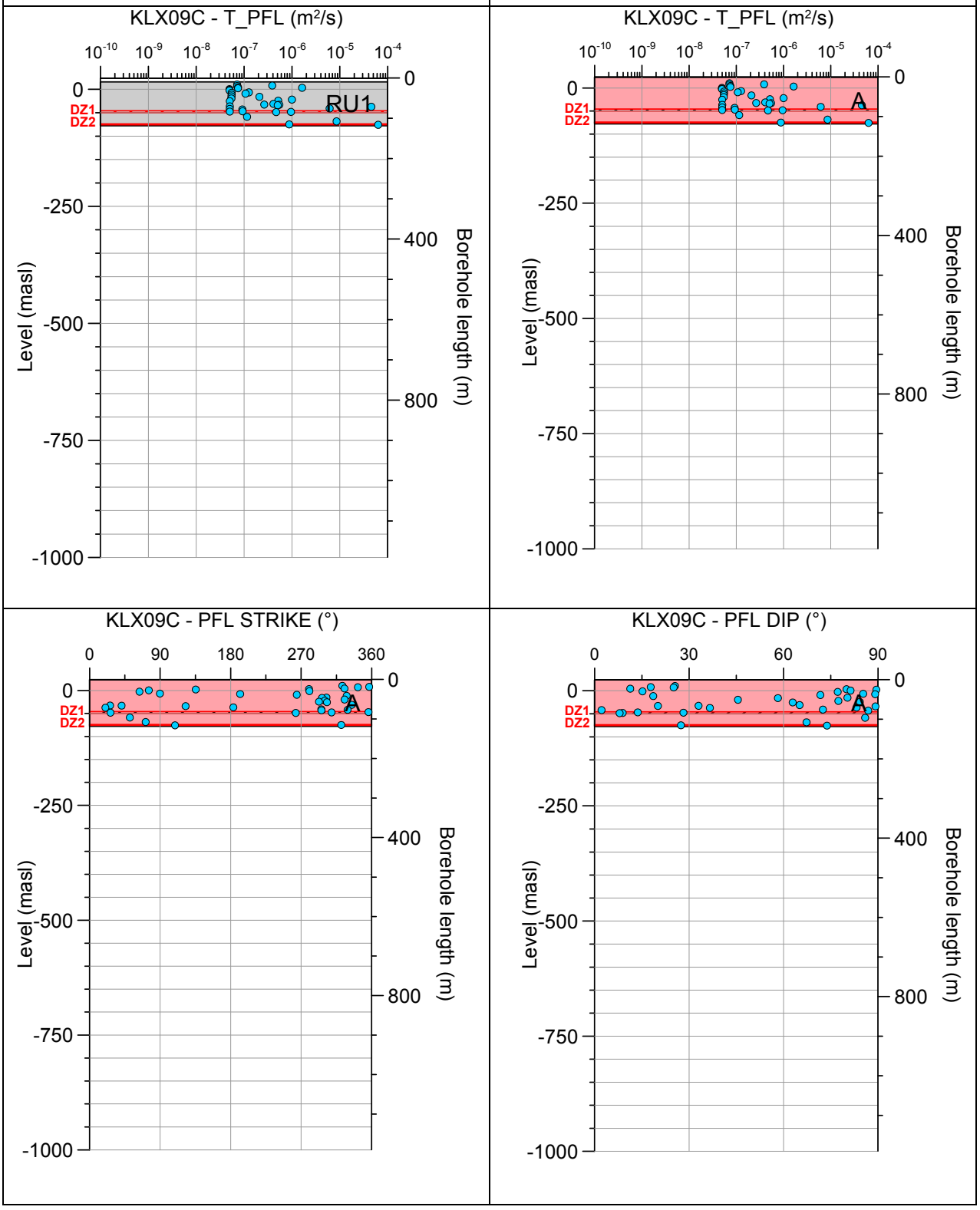

Comment:

Borehole KLX09C. Poles for PFL-f feature planes outside deformation zones.

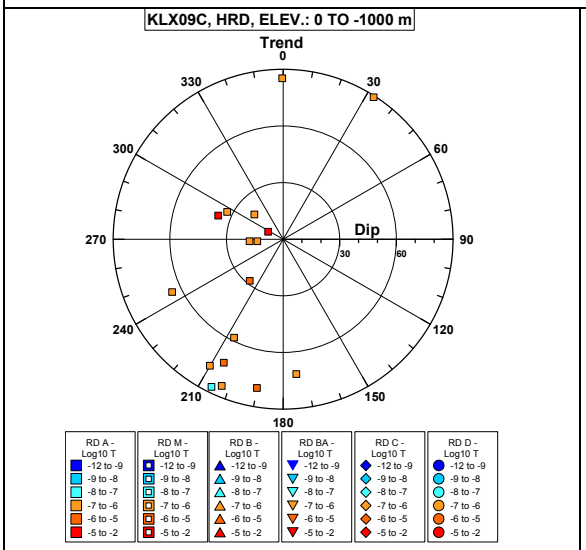

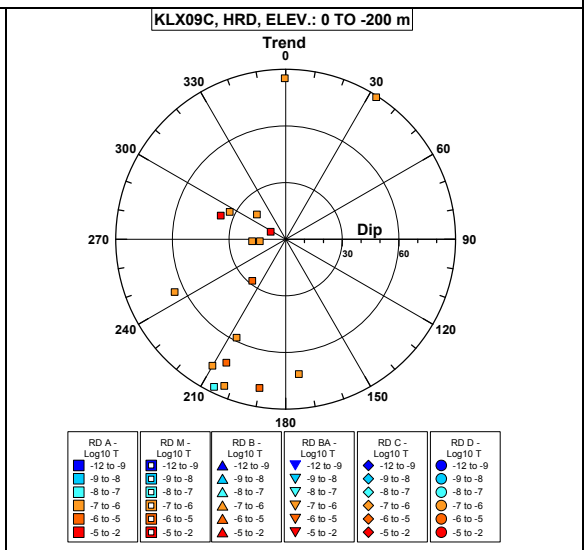

Borehole KLX09C. Poles for PFL-f feature planes in possible deformation zones.

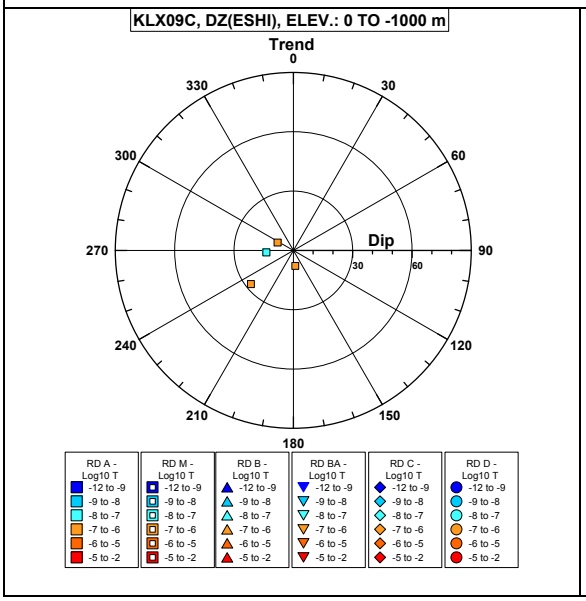

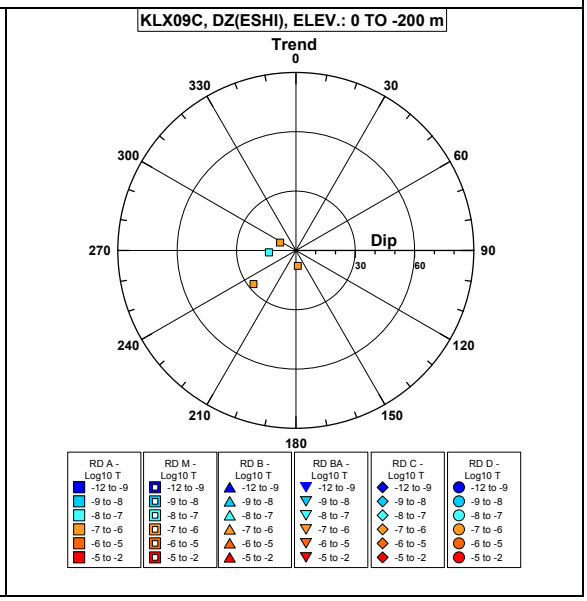

No PFL-f feature planes in deterministically modelled deformation zones exist in KLX09C.

Borehole KLX09D.

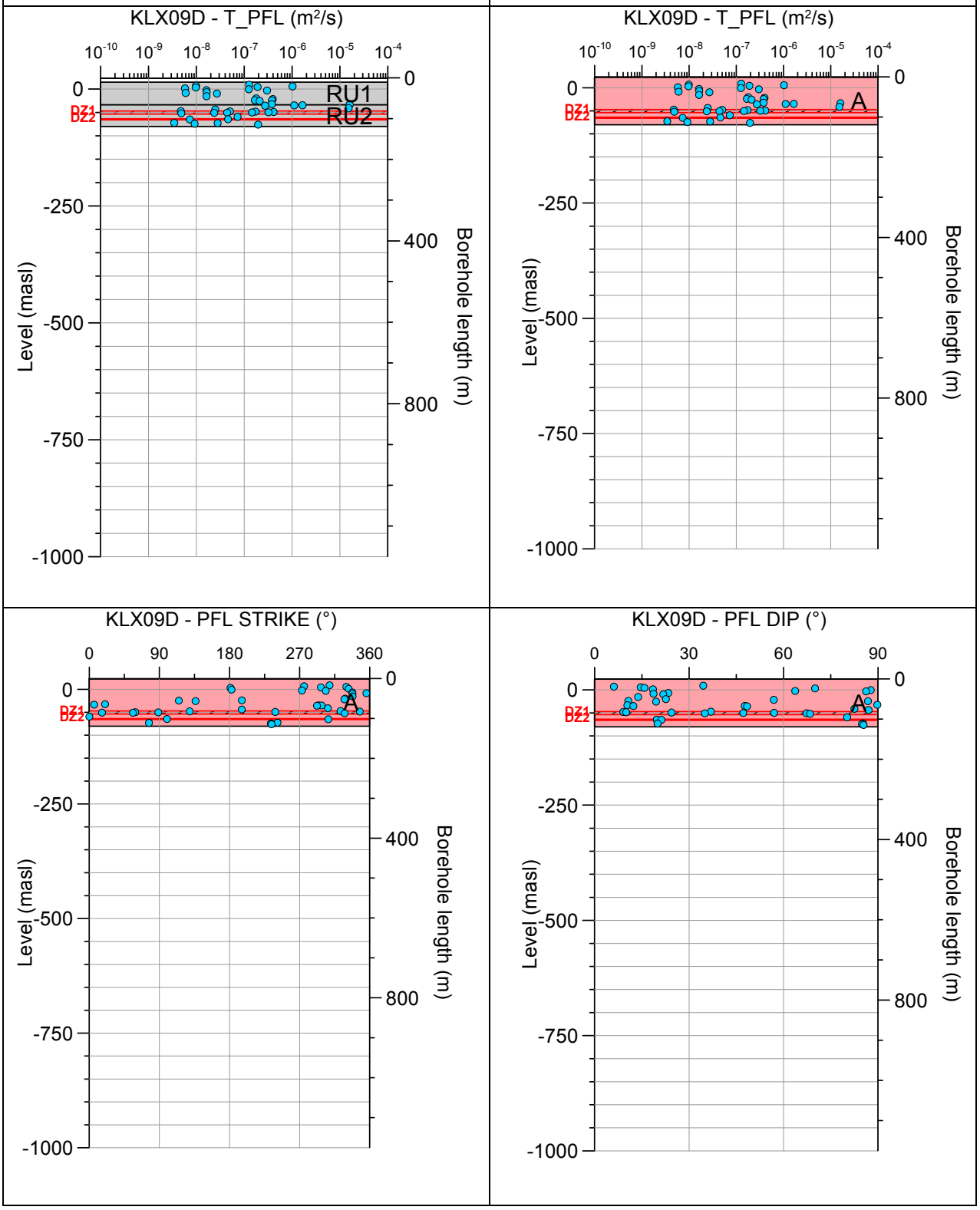

Comment:

Borehole KLX09D. Poles for PFL-f feature planes outside deformation zones.

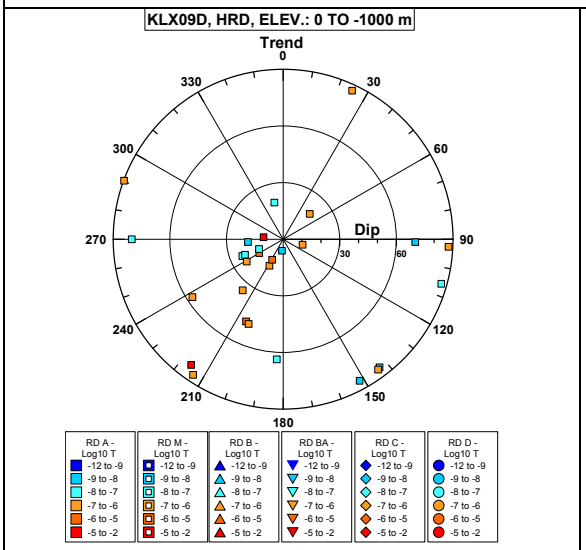

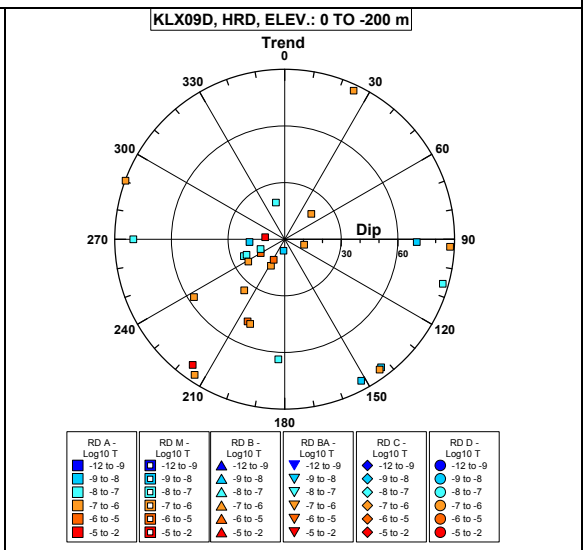

Borehole KLX09D. Poles for PFL-f feature planes in possible deformation zones.

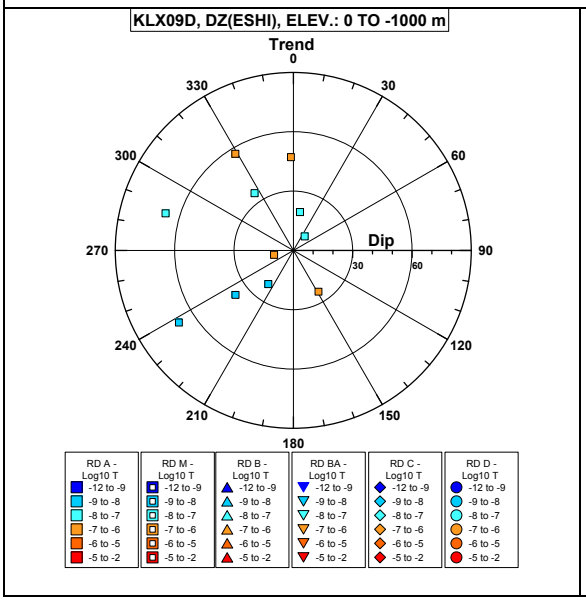

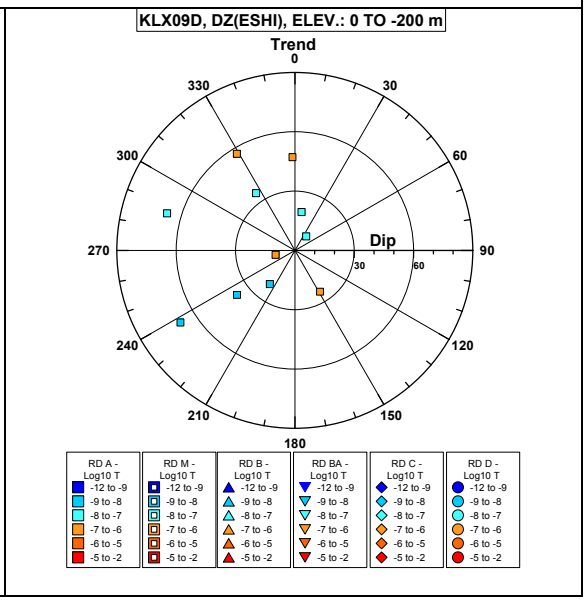

No PFL-f feature planes in deterministically modelled deformation zones exist in KLX09D.

Borehole KLX09E.

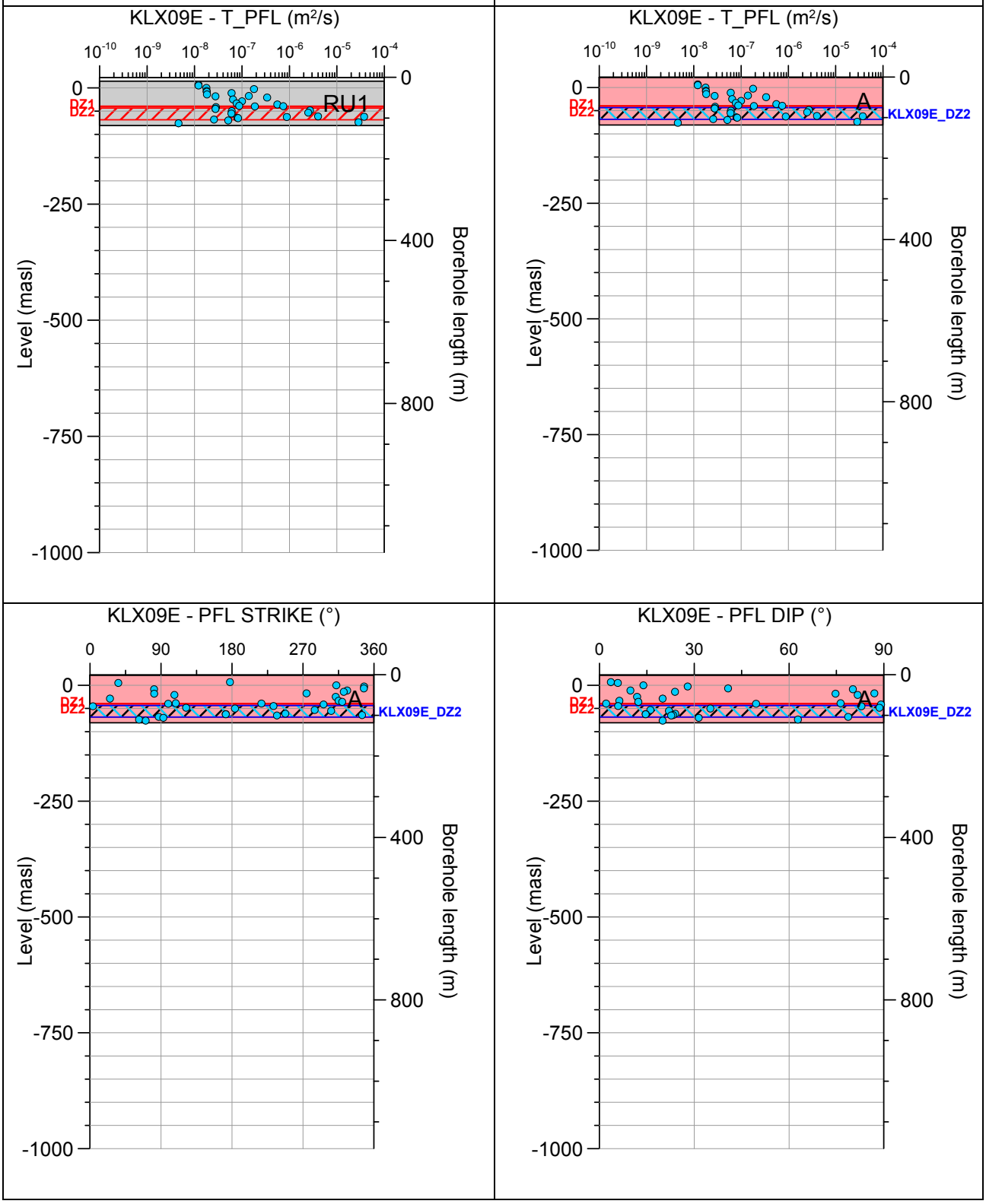

Comment:

Borehole KLX09E. Poles for PFL-f feature planes outside deformation zones.

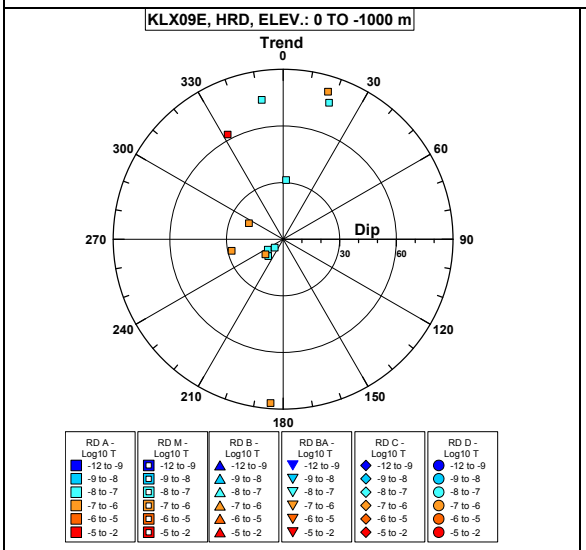

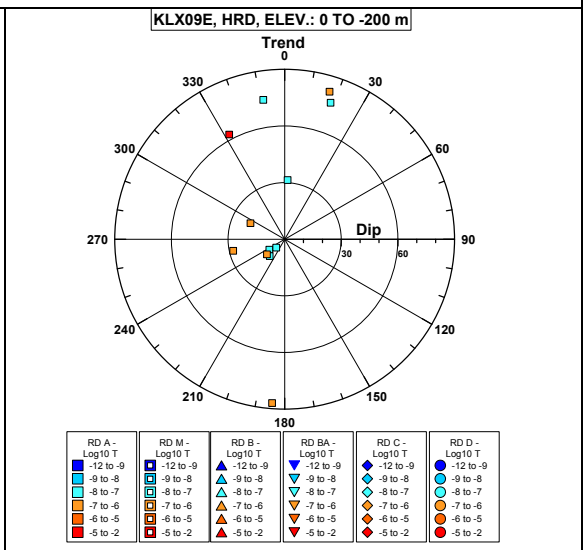

Borehole KLX09E. Poles for PFL-f feature planes in possible deformation zones.

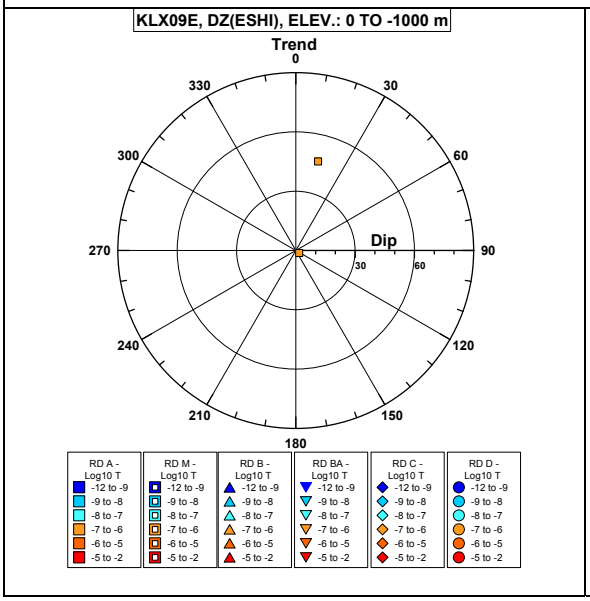

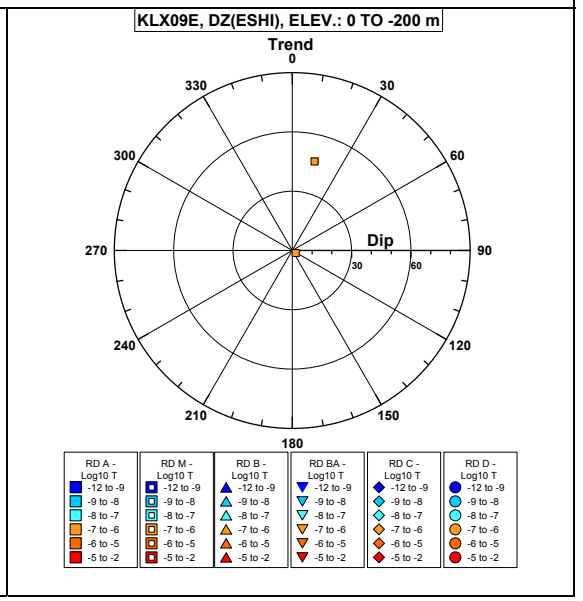

Borehole KLX09E. Poles for PFL-f feature planes in deterministically modelled deformation zones.

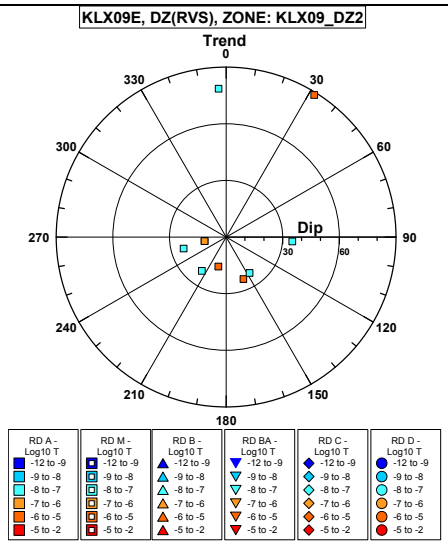

Borehole KLX09F.

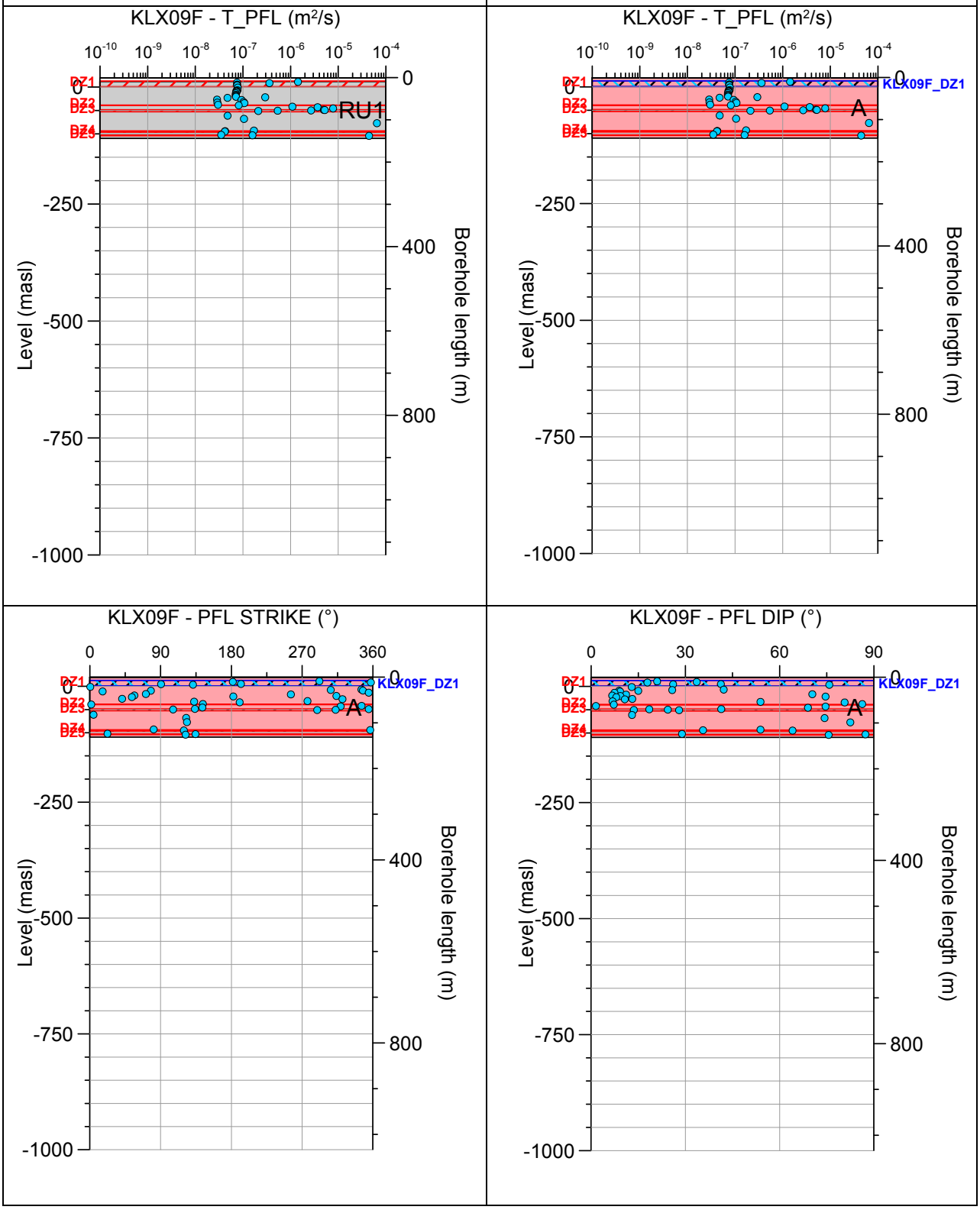

Comment:

Borehole KLX09F. Poles for PFL-f feature planes outside deformation zones.

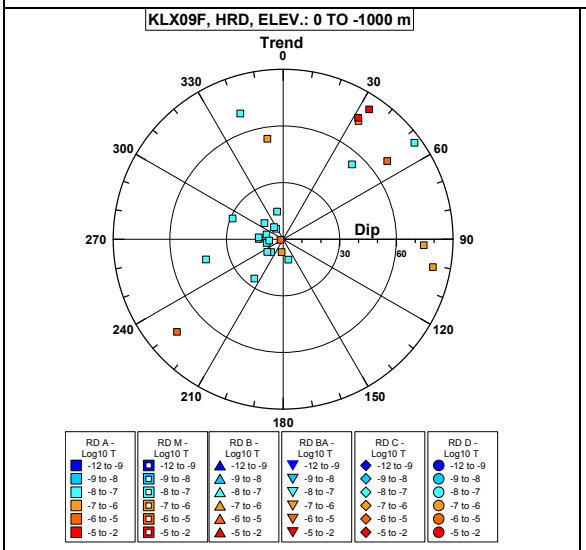

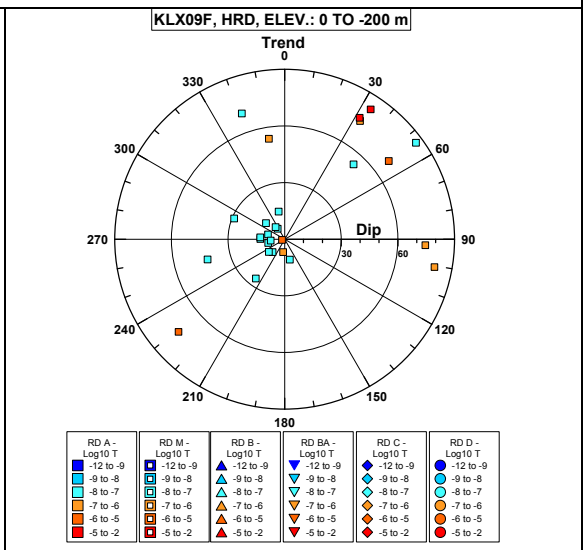

Borehole KLX09F. Poles for PFL-f feature planes in possible deformation zones.

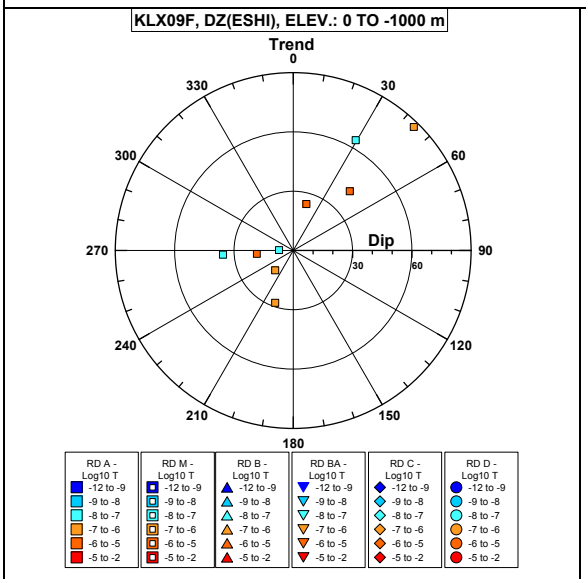

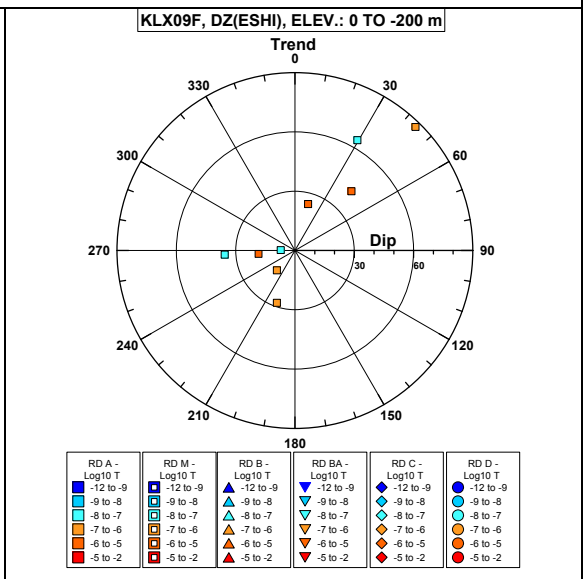

Borehole KLX09F. Poles for PFL-f feature planes in deterministically modelled deformation zones.

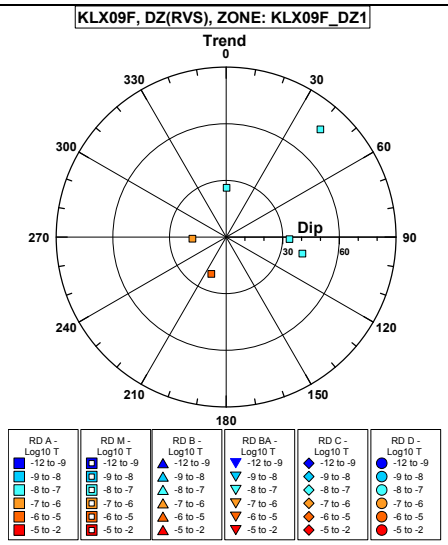

Borehole KLX09G.

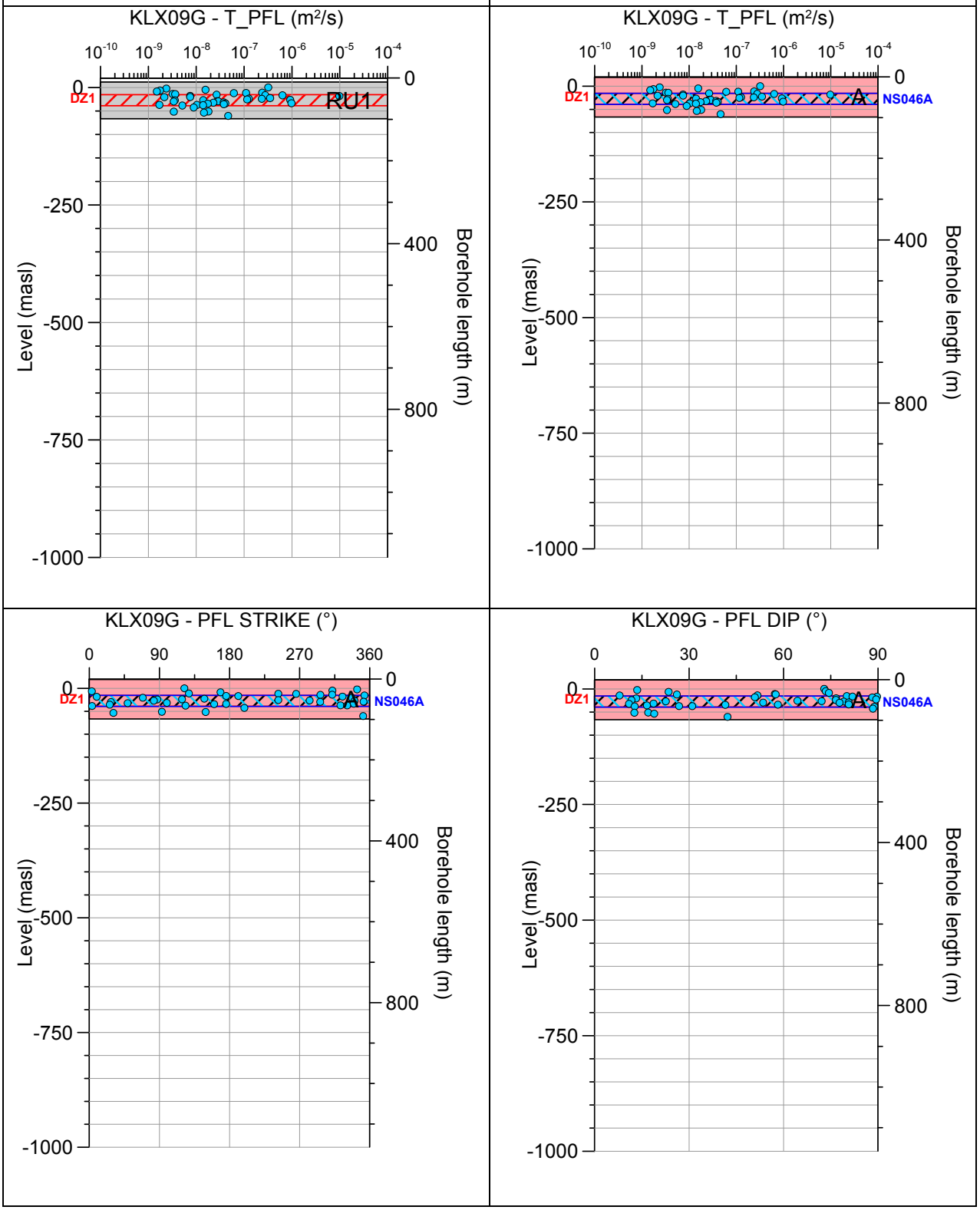

Comment:

Borehole KLX09G. Poles for PFL-f feature planes outside deformation zones.

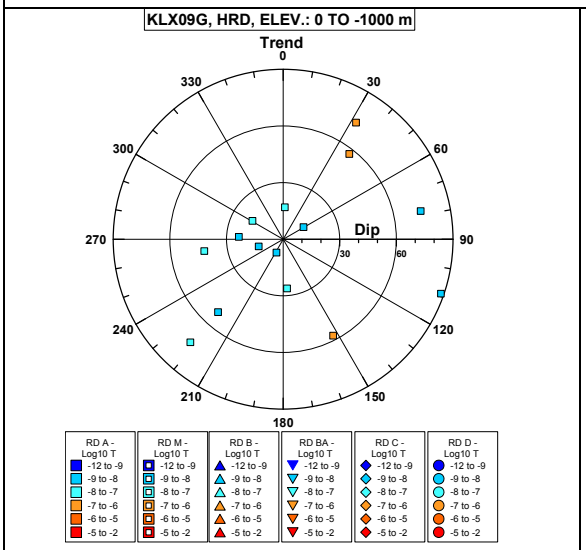

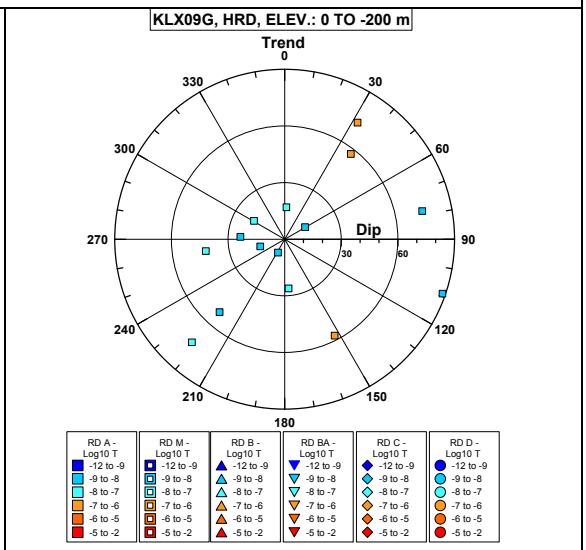

No PFL-f feature planes in possible deformation zones exist in KLX09G.

Borehole KLX09G. Poles for PFL-f feature planes in deterministically modelled deformation zones.

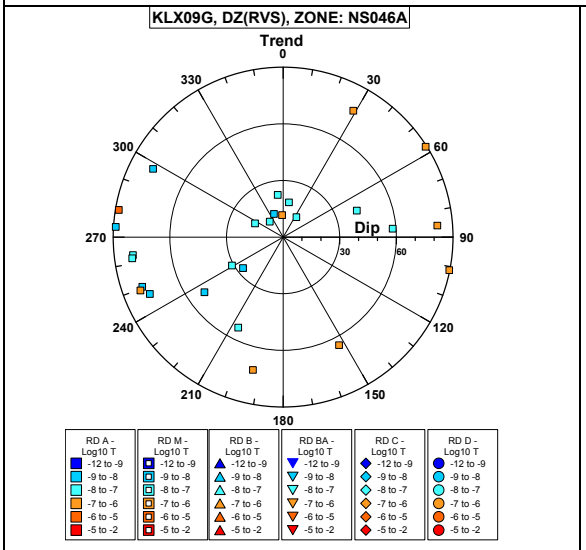

Borehole KLX10.

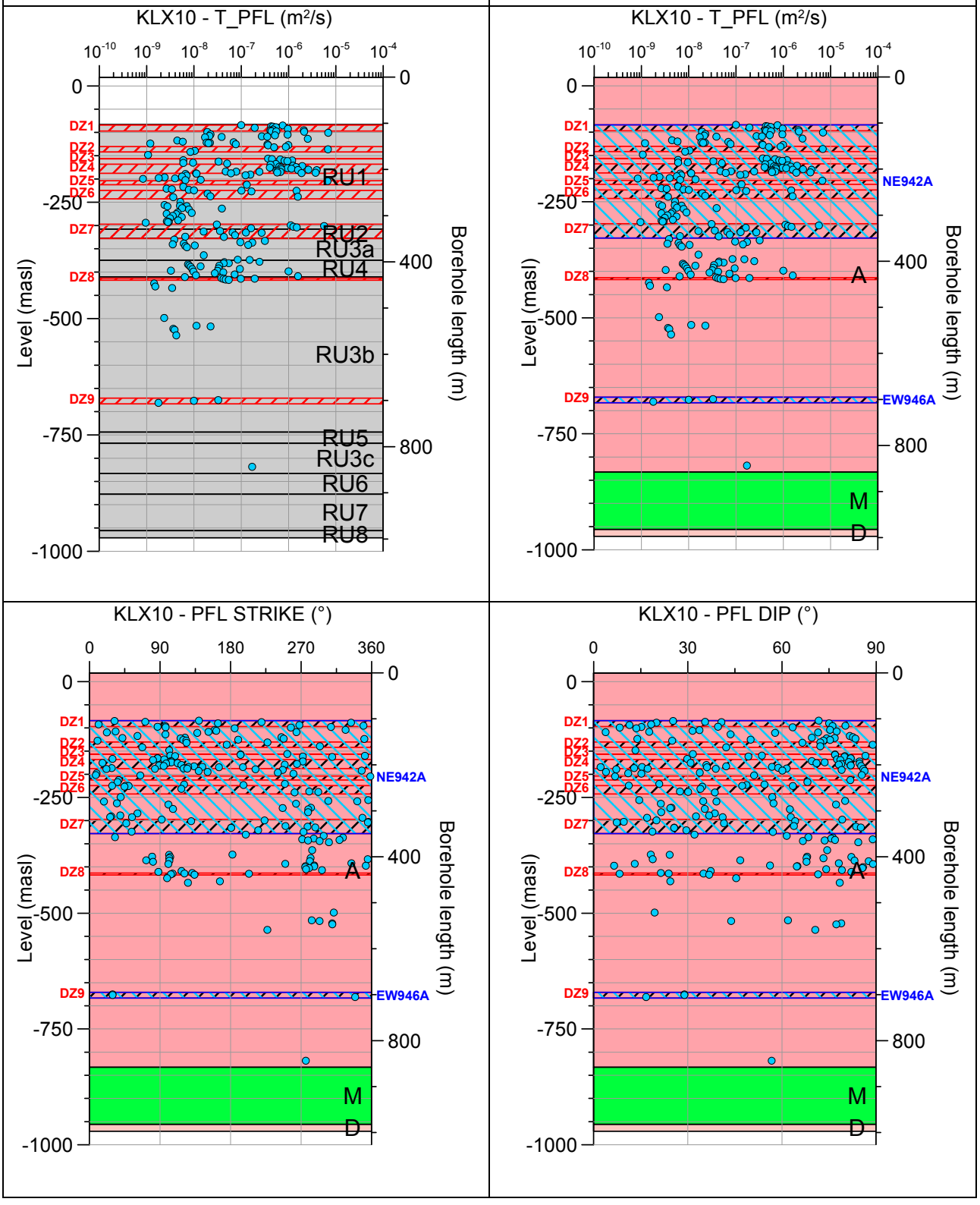

Comment:

Borehole KLX10. Poles for PFL-f feature planes outside deformation zones.

KLX10, HRD, ELEV.: 0 TO -1000 m

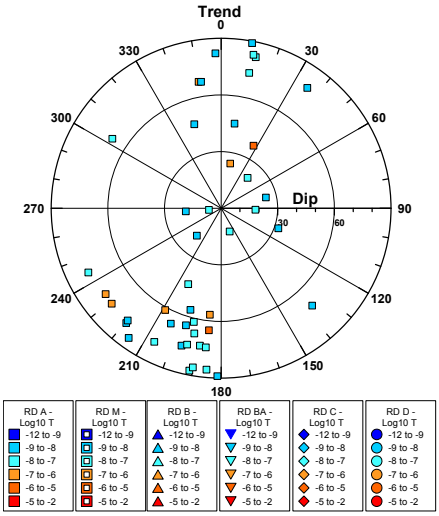

KLX10, HRD, ELEV.: 0 TO -200 m

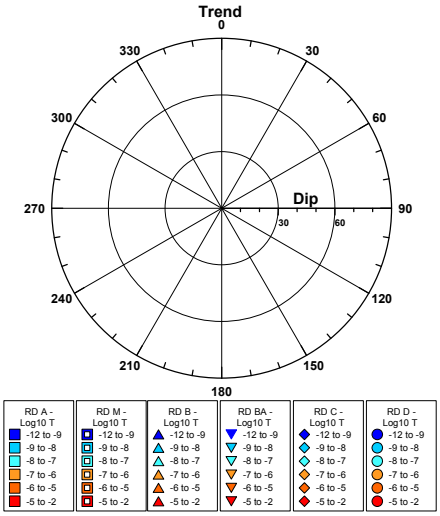

KLX02, HRD, ELEV.: -200 TO -400 m

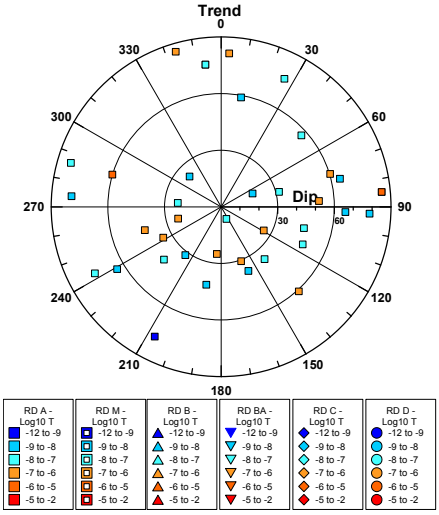

KLX10, HRD, ELEV.: -400 TO -600 m

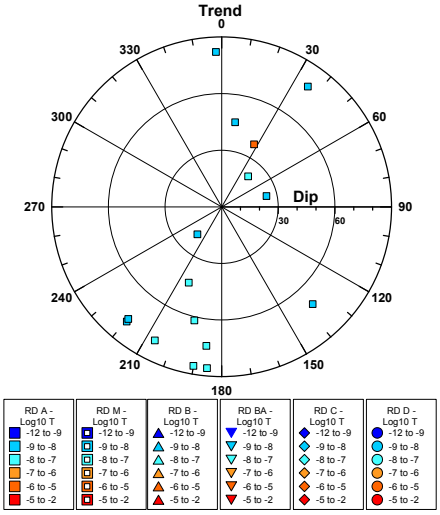

KLX10, HRD, ELEV.: -800 TO -1000 m

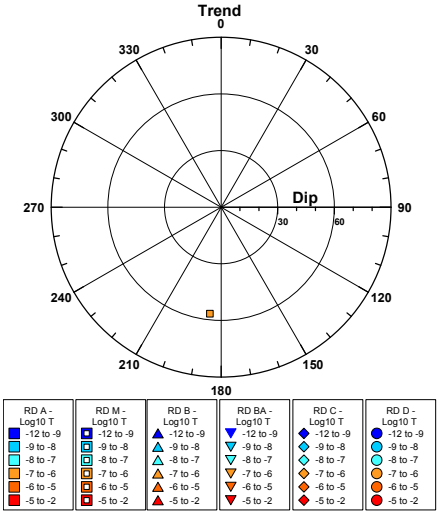

Borehole KLX10. Poles for PFL-f feature planes in possible deformation zones.

KLX10, DZ(ESHI), ELEV.: 0 TO -1000 m

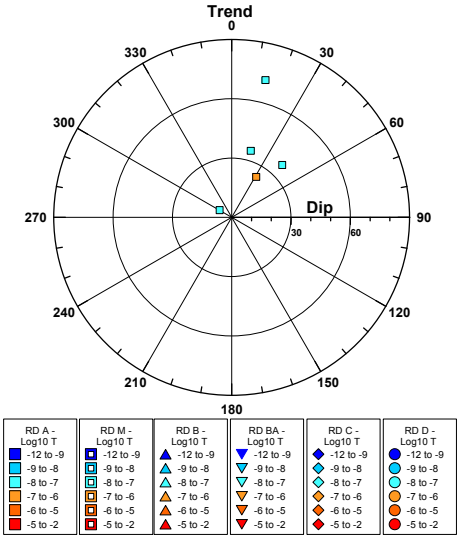

KLX10, DZ(ESHI), ELEV.: 0 TO -200 m

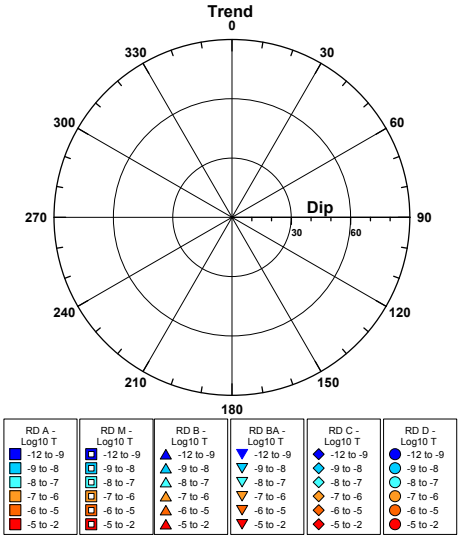

KLX10, DZ(ESHI), ELEV.: -200 TO -400 m

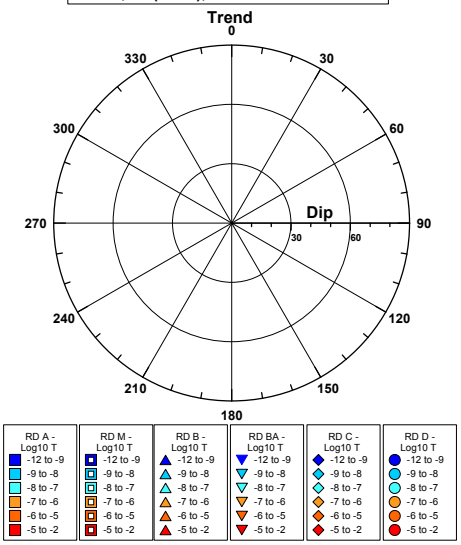

KLX10, DZ(ESHI), ELEV.: -400 TO -600 m

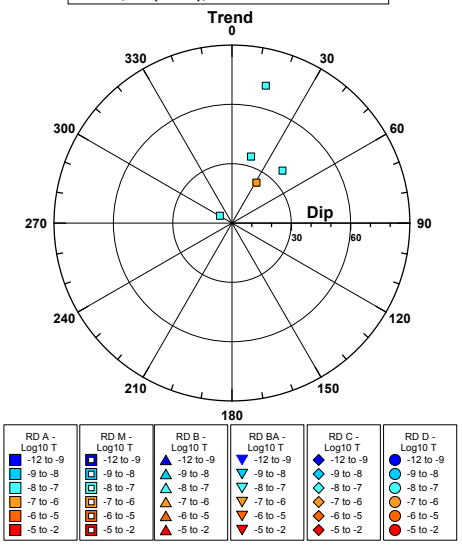

KLX10, DZ(ESHI), ELEV.: -600 TO -800 m

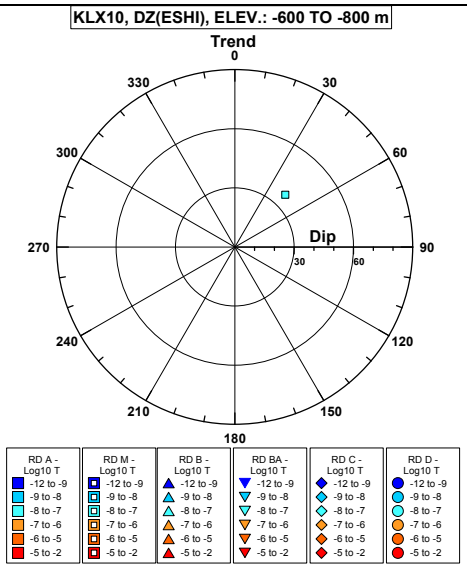

Borehole KLX10. Poles for PFL-f feature planes in deterministically modelled deformation zones.

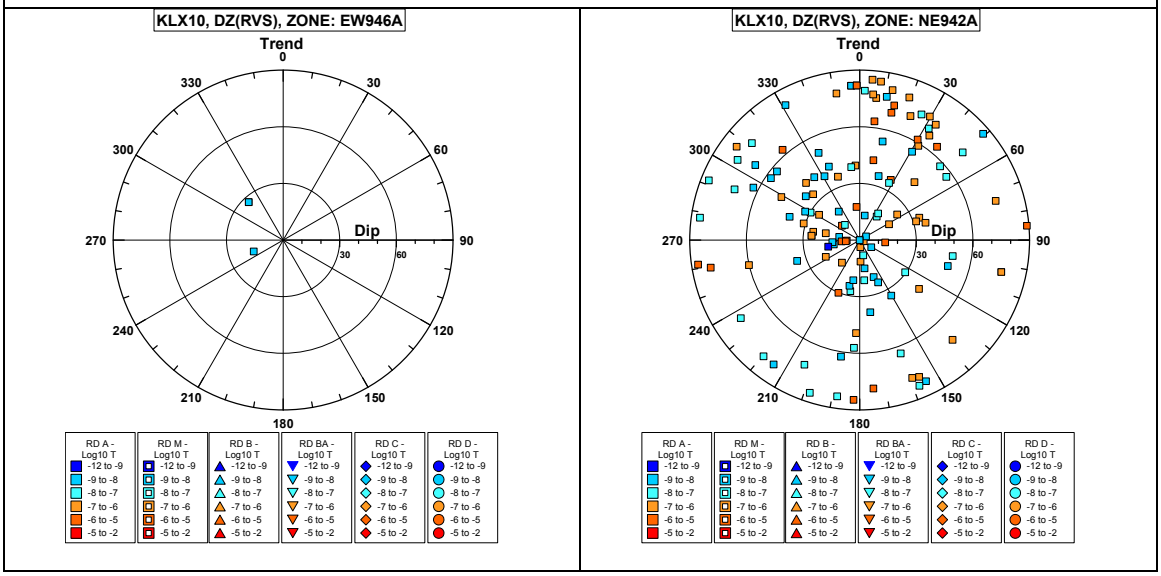

Borehole KLX10B.

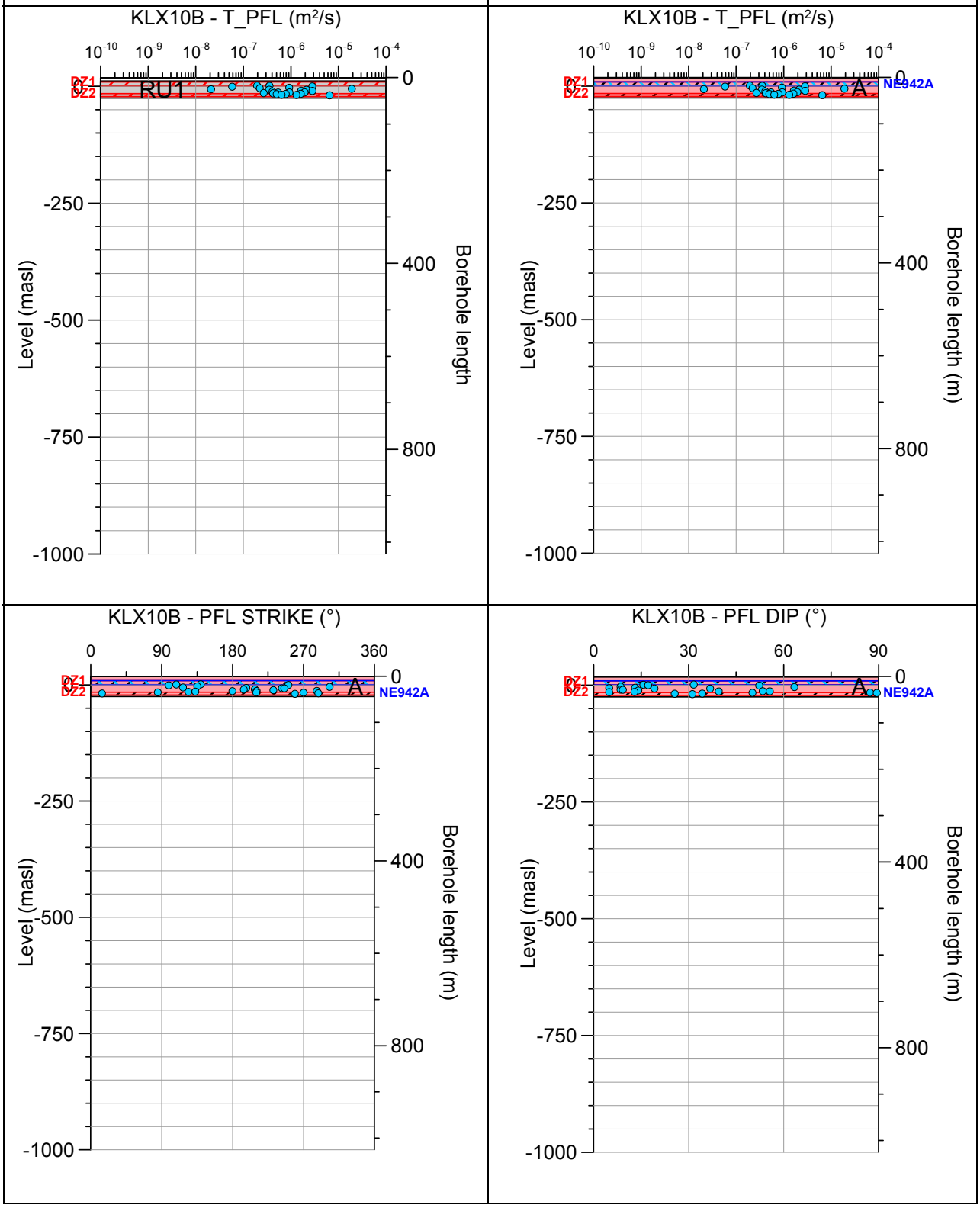

Comment:

Borehole KLX10B. Poles for PFL-f feature planes outside deformation zones.

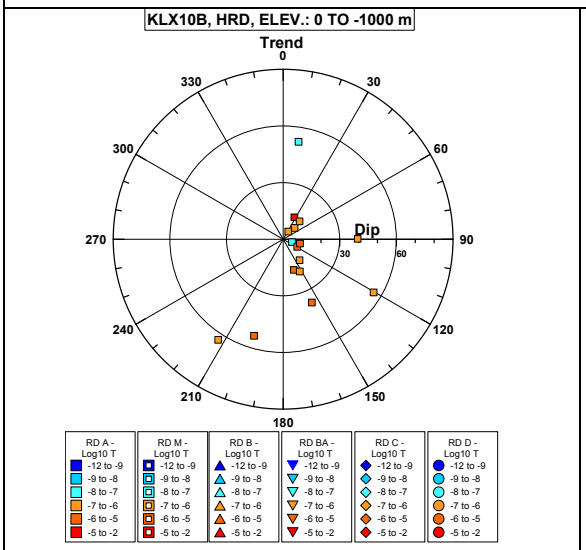

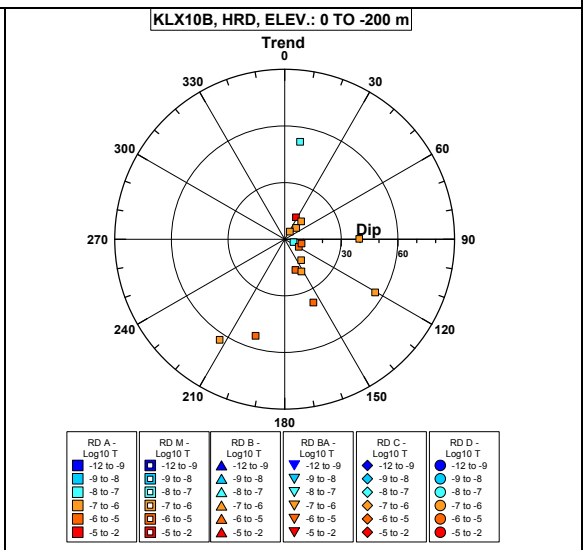

Borehole KLX10B. Poles for PFL-f feature planes in possible deformation zones.

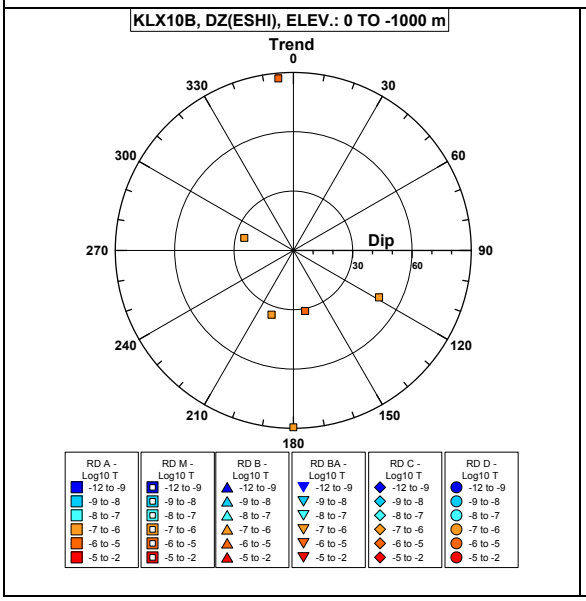

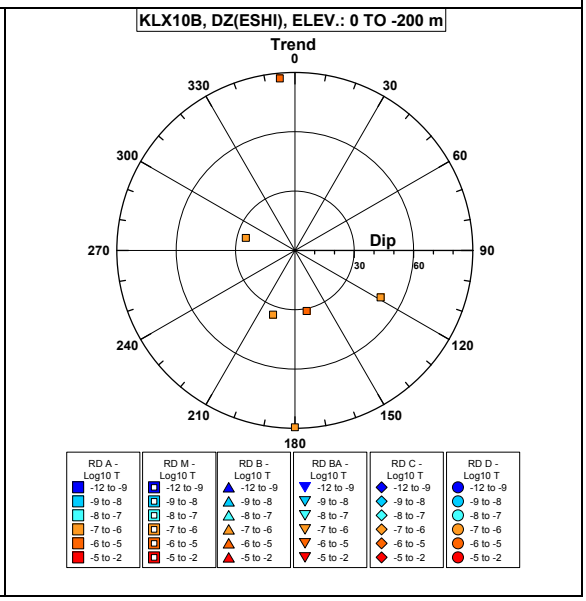

Borehole KLX10B. Poles for PFL-f feature planes in deterministically modelled deformation zones.

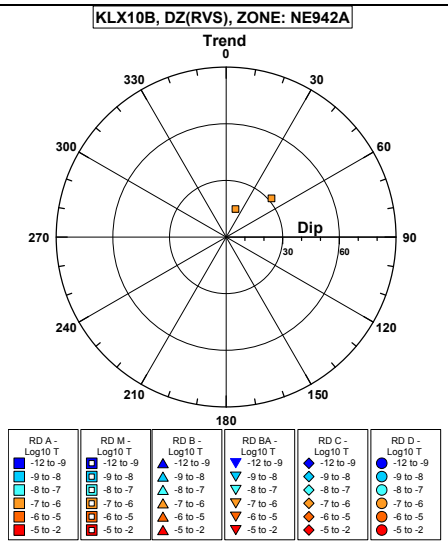

Borehole KLX10C.

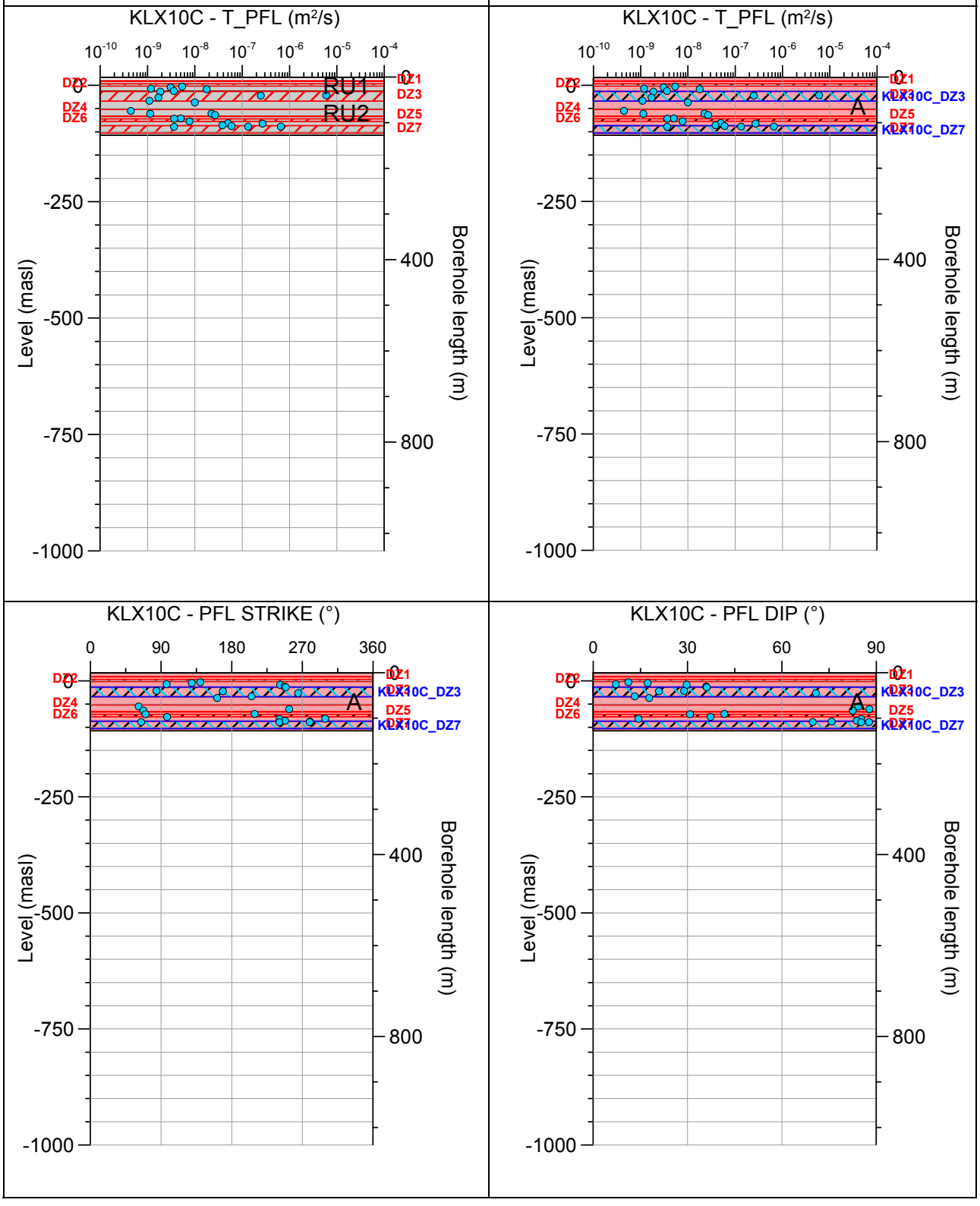

Comment:

Borehole KLX10C. Poles for PFL-f feature planes outside deformation zones.

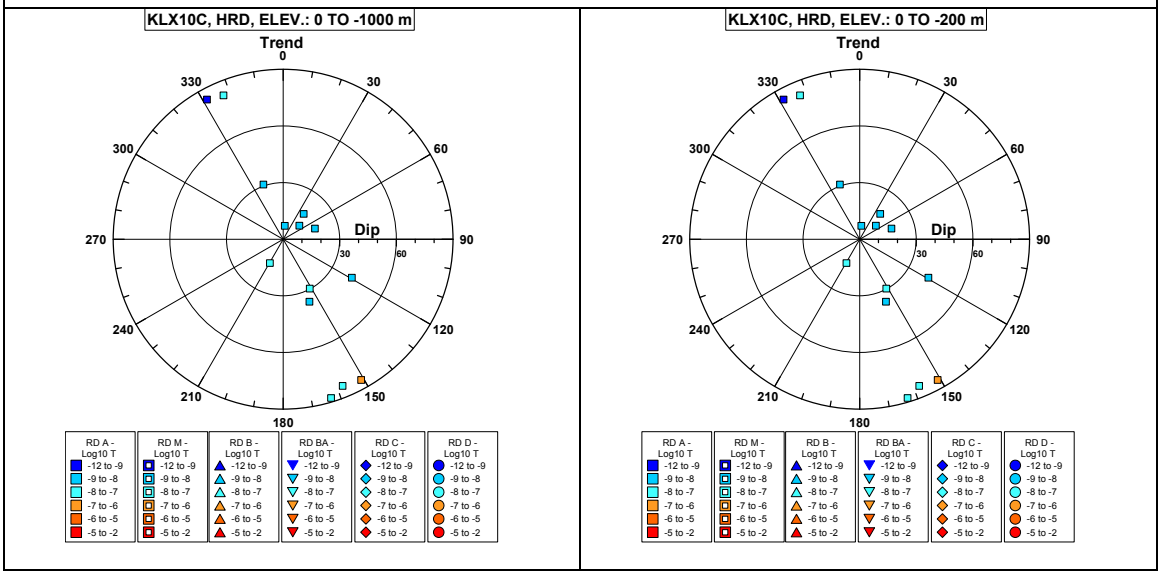

Borehole KLX10C. Poles for PFL-f feature planes in possible deformation zones.

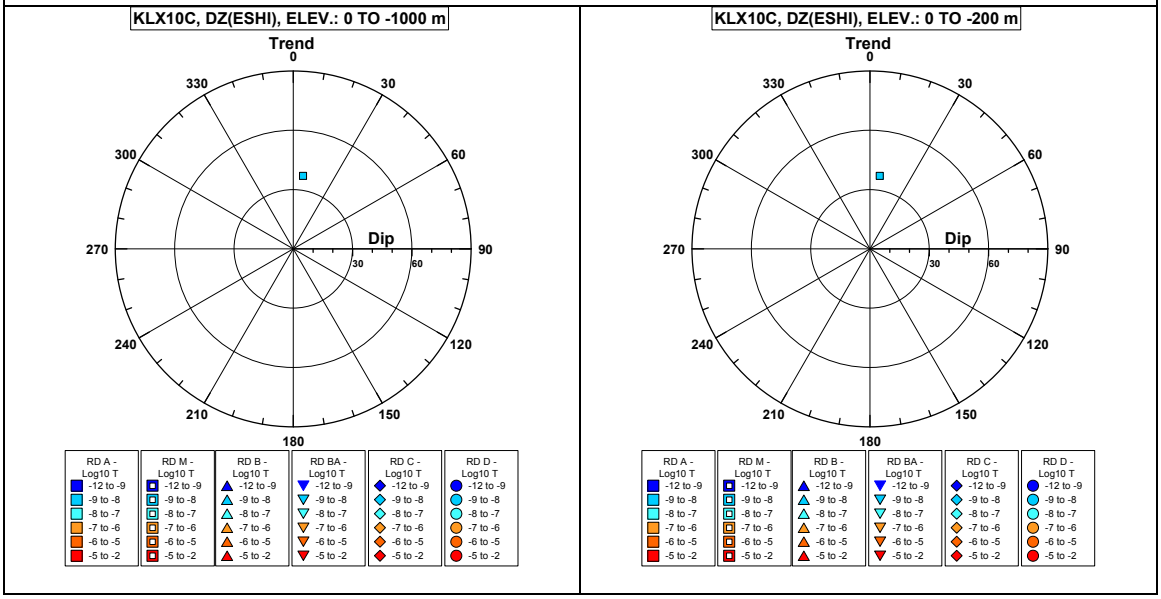

Borehole KLX10C. Poles for PFL-f feature planes in deterministically modelled deformation zones.

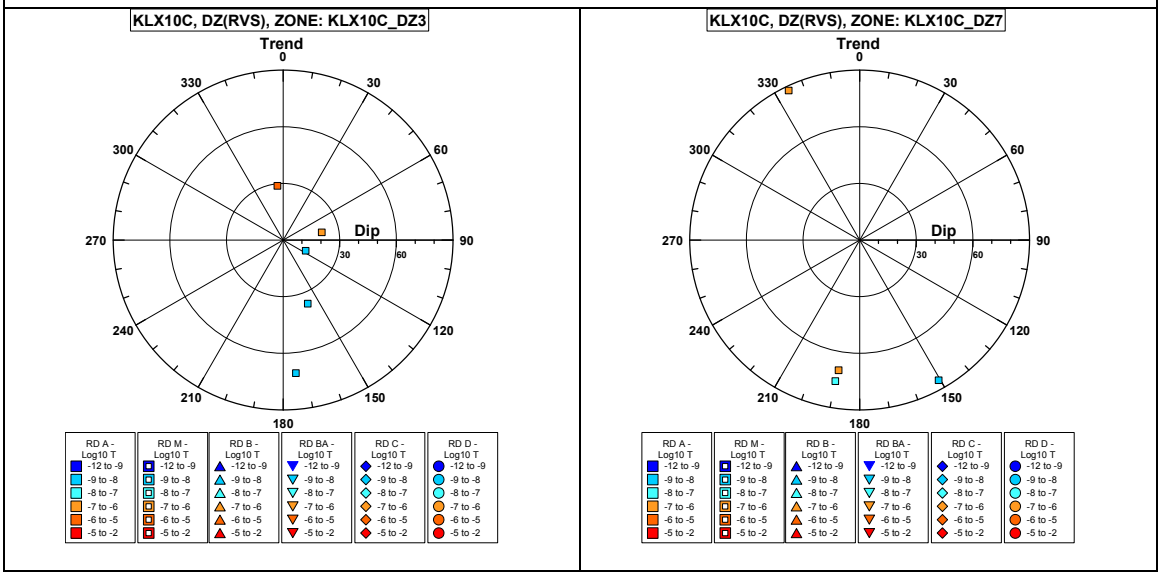

Borehole KLX11A.

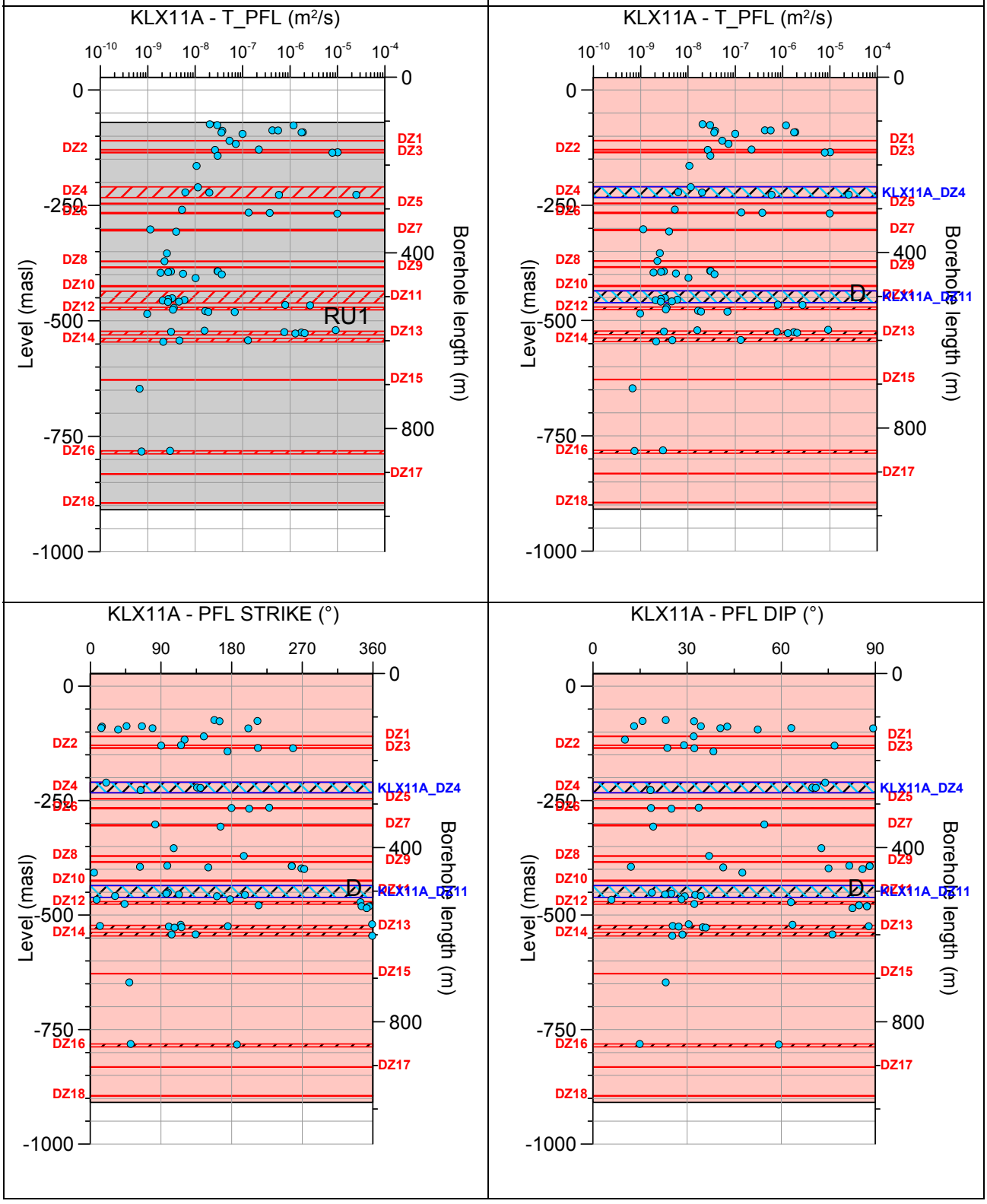

Comment:

Borehole KLX11A. Poles for PFL-f feature planes outside deformation zones.

KLX11A, HRD, ELEV.: 0 TO -1000 m

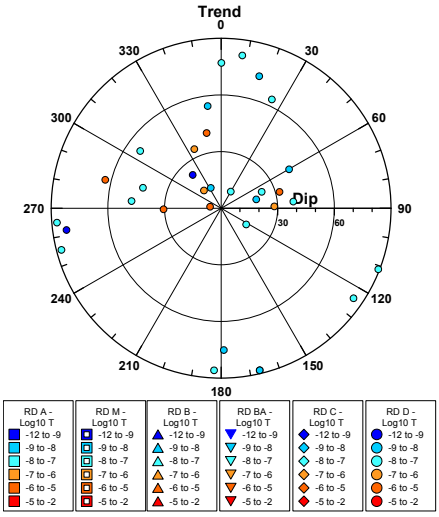

KLX11A, HRD, ELEV.: 0 TO -200 m

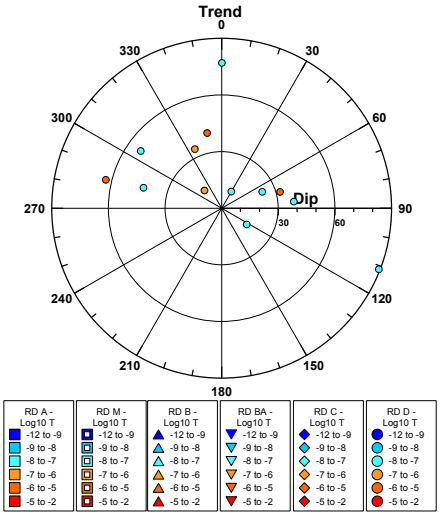

KLX11A, HRD, ELEV.: -200 TO -400 m

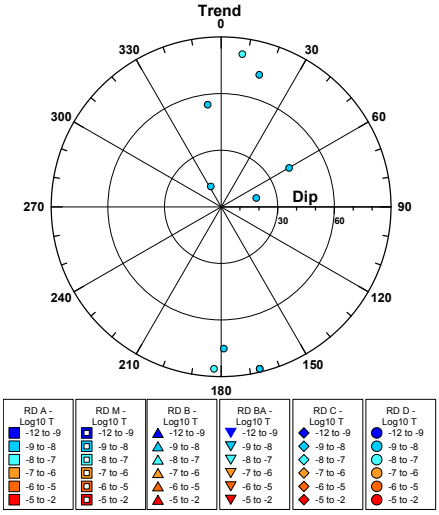

KLX11A, HRD, ELEV.: -400 TO -600 m

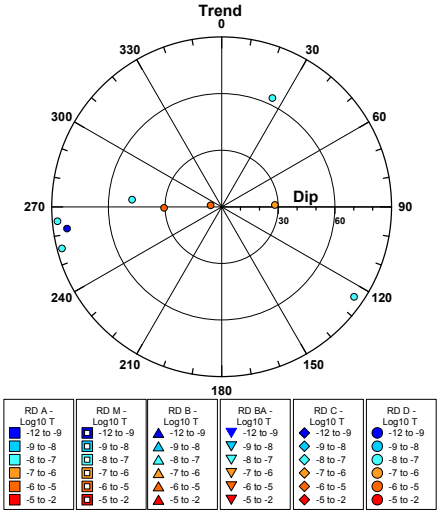

KLX11A, HRD, ELEV.: -600 TO -800 m

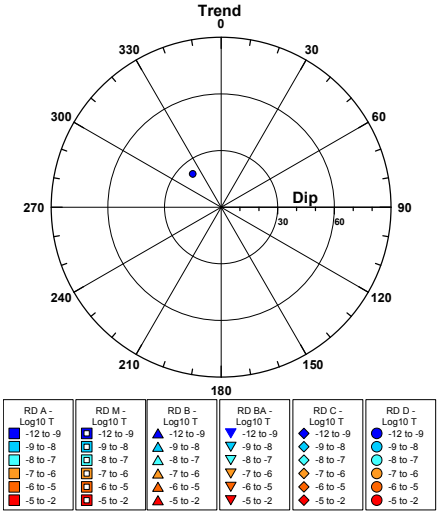

Borehole KLX11A. Poles for PFL-f feature planes in possible deformation zones.

KLX11A, DZ(ESHI), ELEV.: 0 TO -1000 m

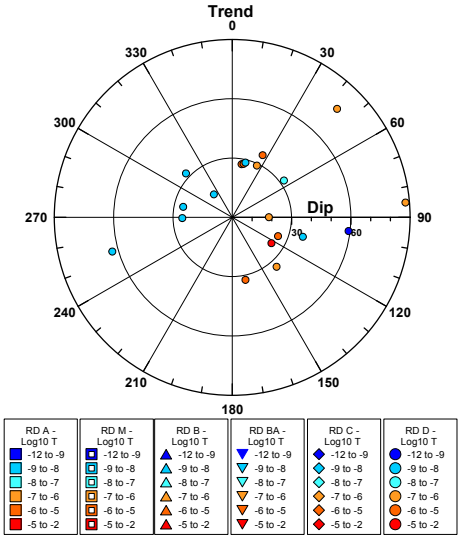

KLX11A, DZ(ESHI), ELEV.: 0 TO -200 m

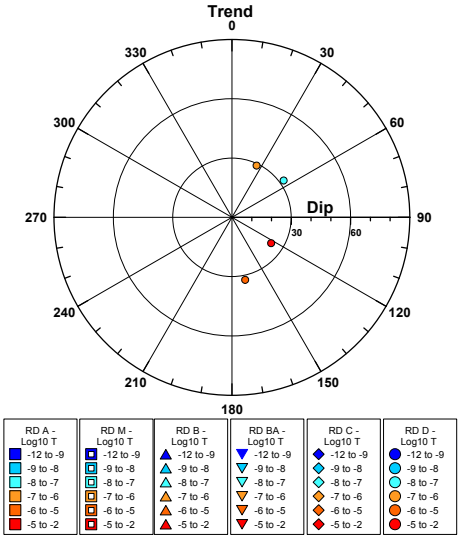

KLX11A, DZ(ESHI), ELEV.: -200 TO -400 m

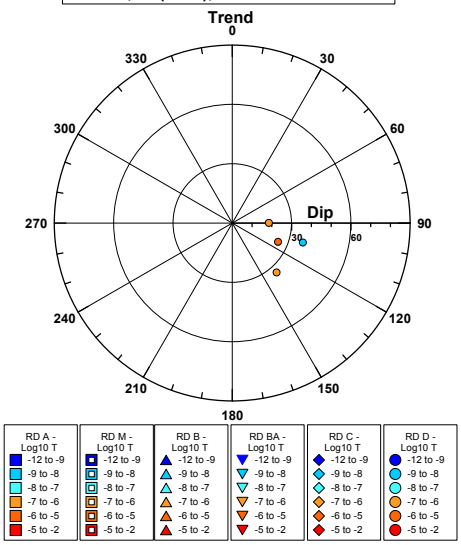

KLX11A, DZ(ESHI), ELEV.: -400 TO -600 m

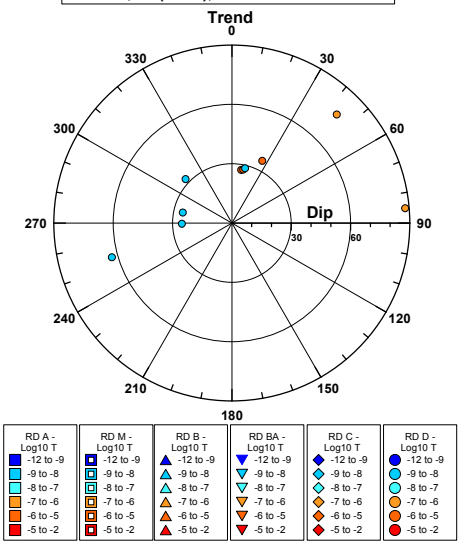

KLX11A, DZ(ESHI), ELEV.: -600 TO -800 m

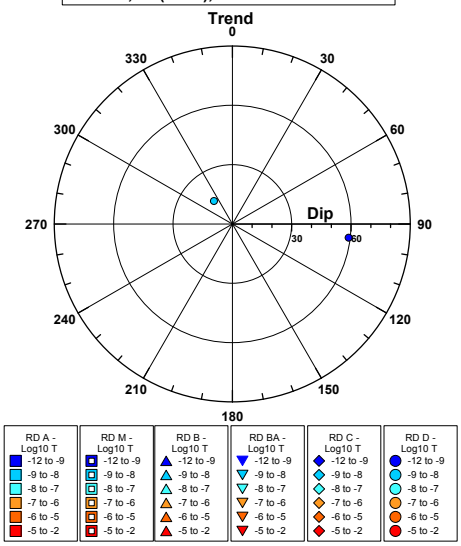

Borehole KLX11A. Poles for PFL-f feature planes in deterministically modelled deformation zones.

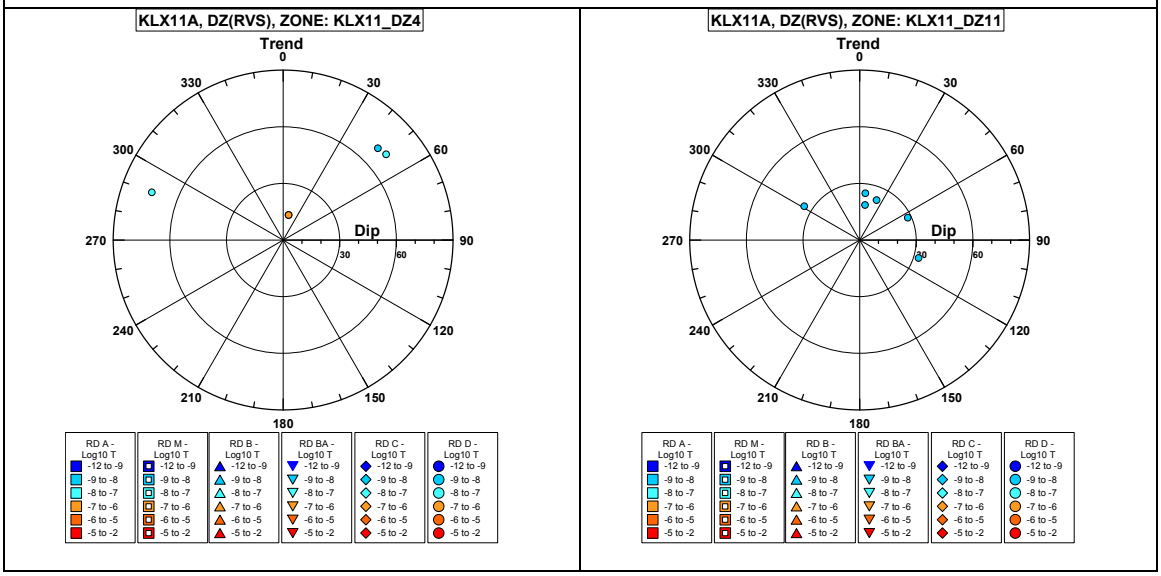

Borehole KLX11B.

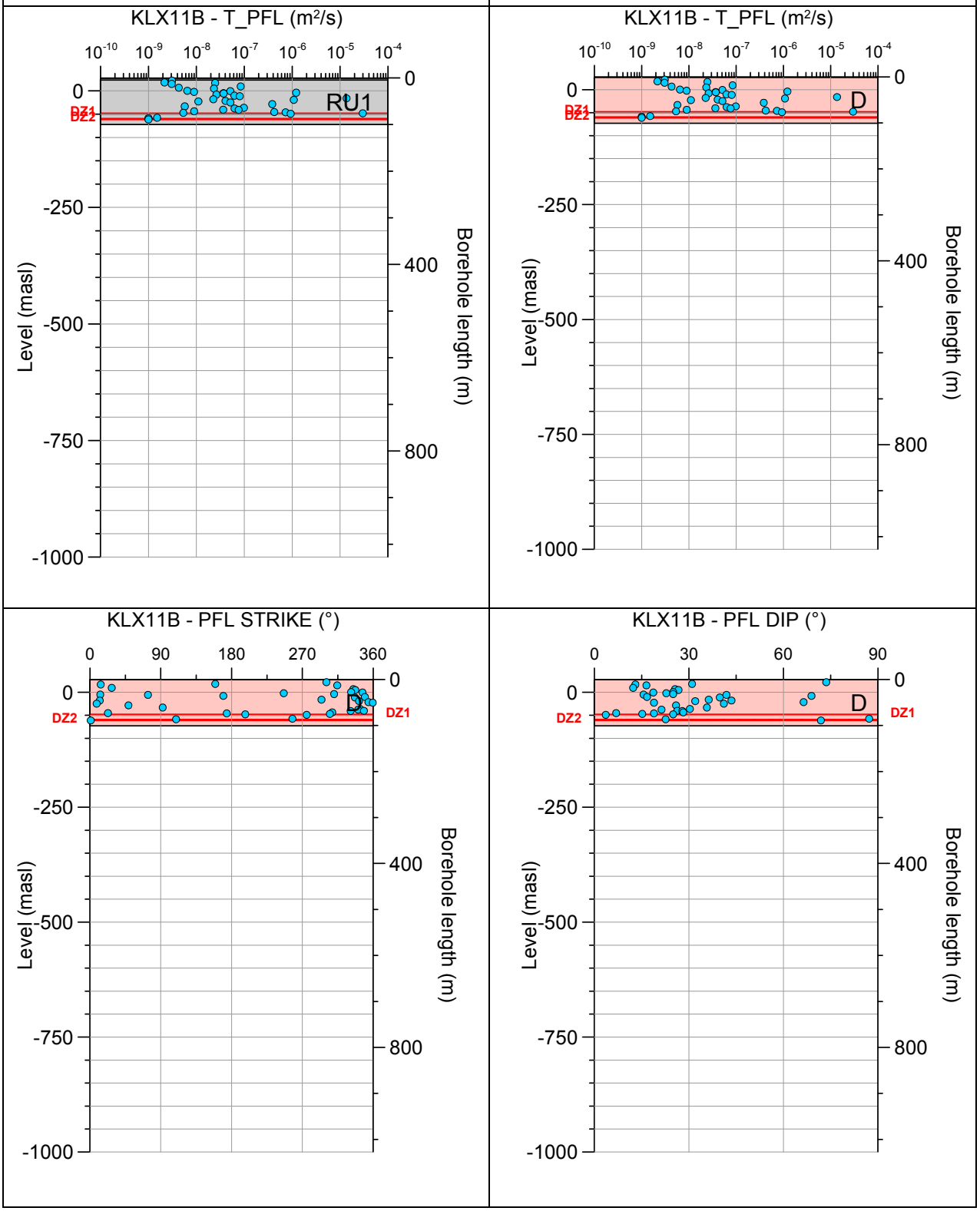

Comment:

Borehole KLX11B. Poles for PFL-f feature planes outside deformation zones.

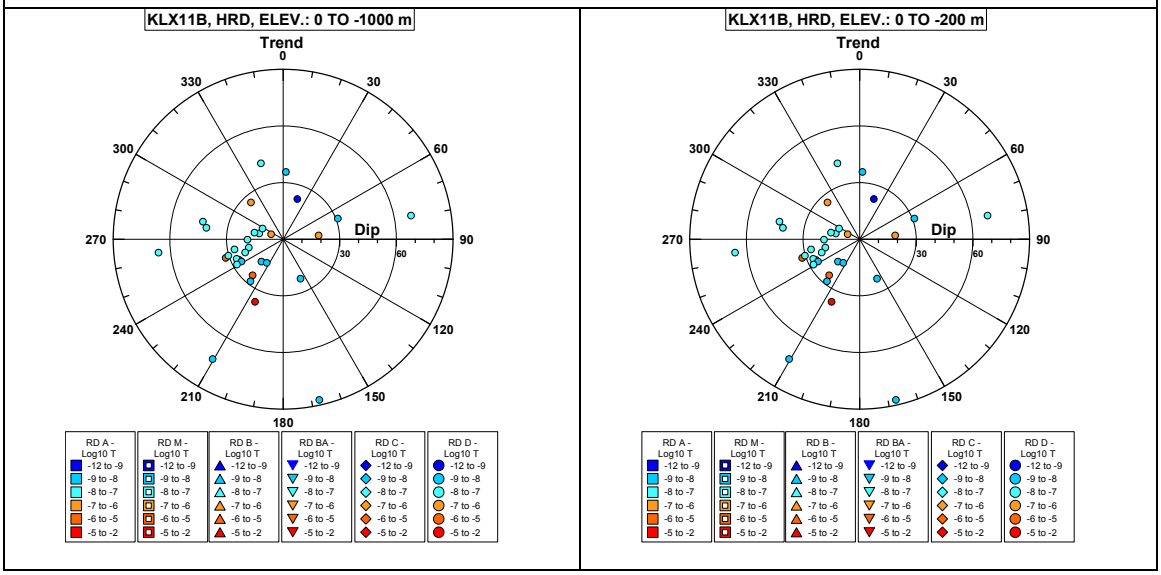

Borehole KLX11B. Poles for PFL-f feature planes in possible deformation zones.

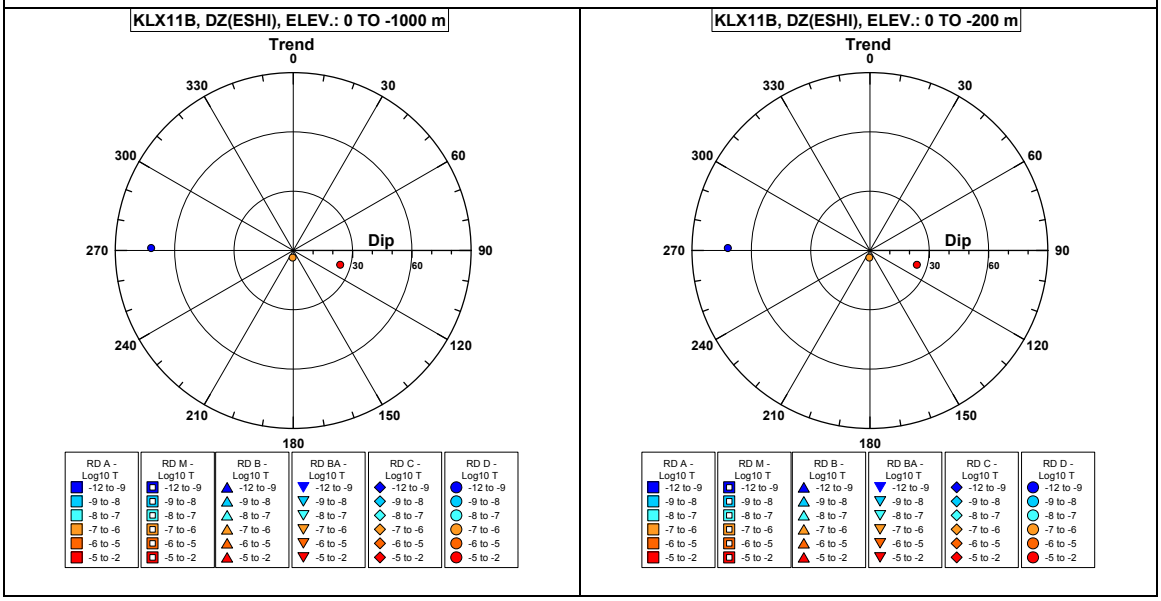

No PFL-f feature planes in deterministically modelled deformation zones exist in KLX11B.

Borehole KLX11C.

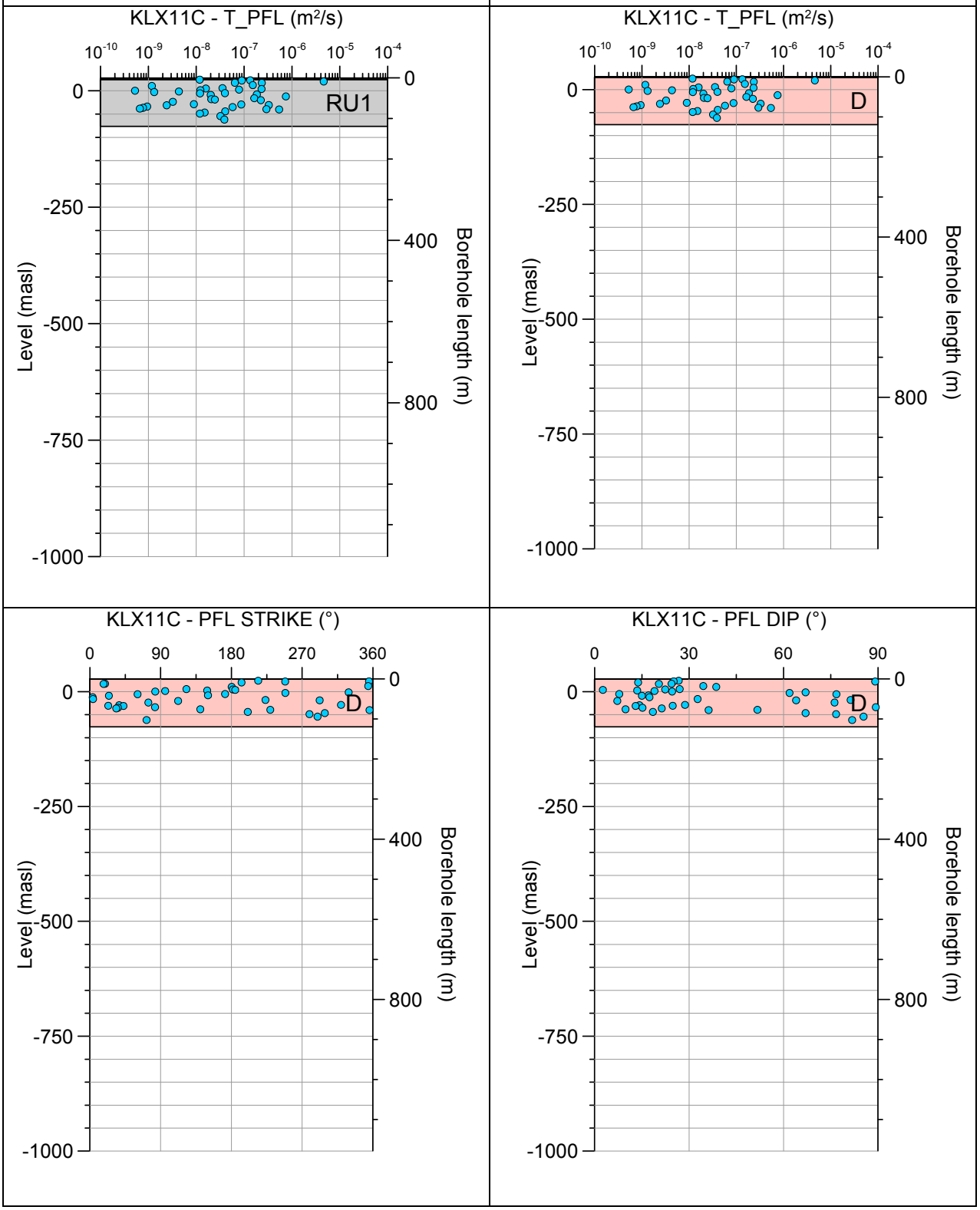

Comment:

Borehole KLX11C. Poles for PFL-f feature planes outside deformation zones.

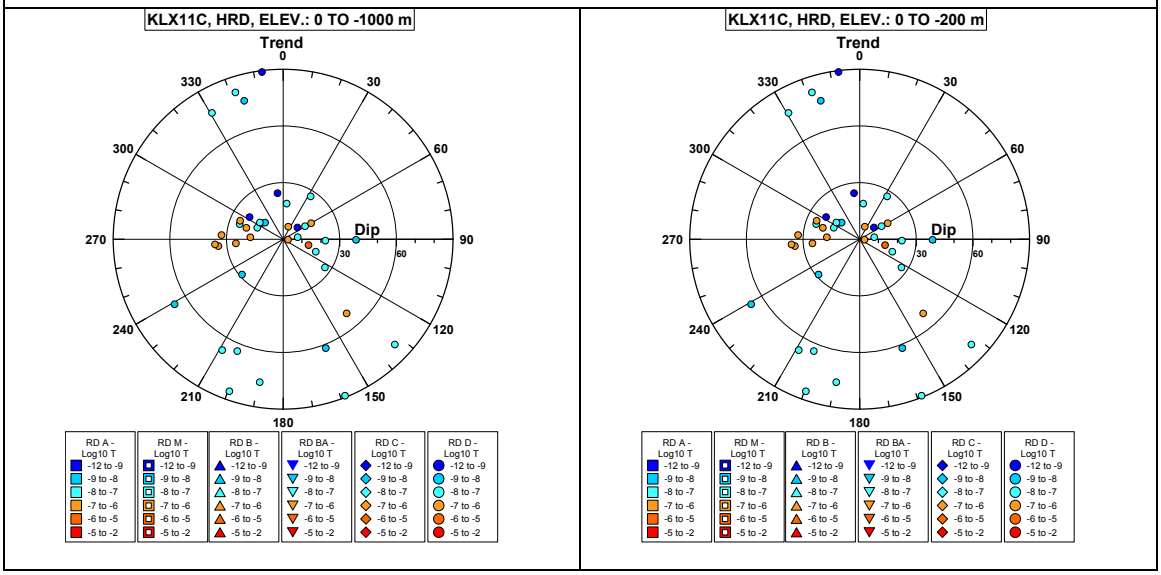

No PFL-f feature planes in possible deformation zones exist in KLX11C.

No PFL-f feature planes in deterministically modelled deformation zones exist in KLX11C.

Borehole KLX11D.

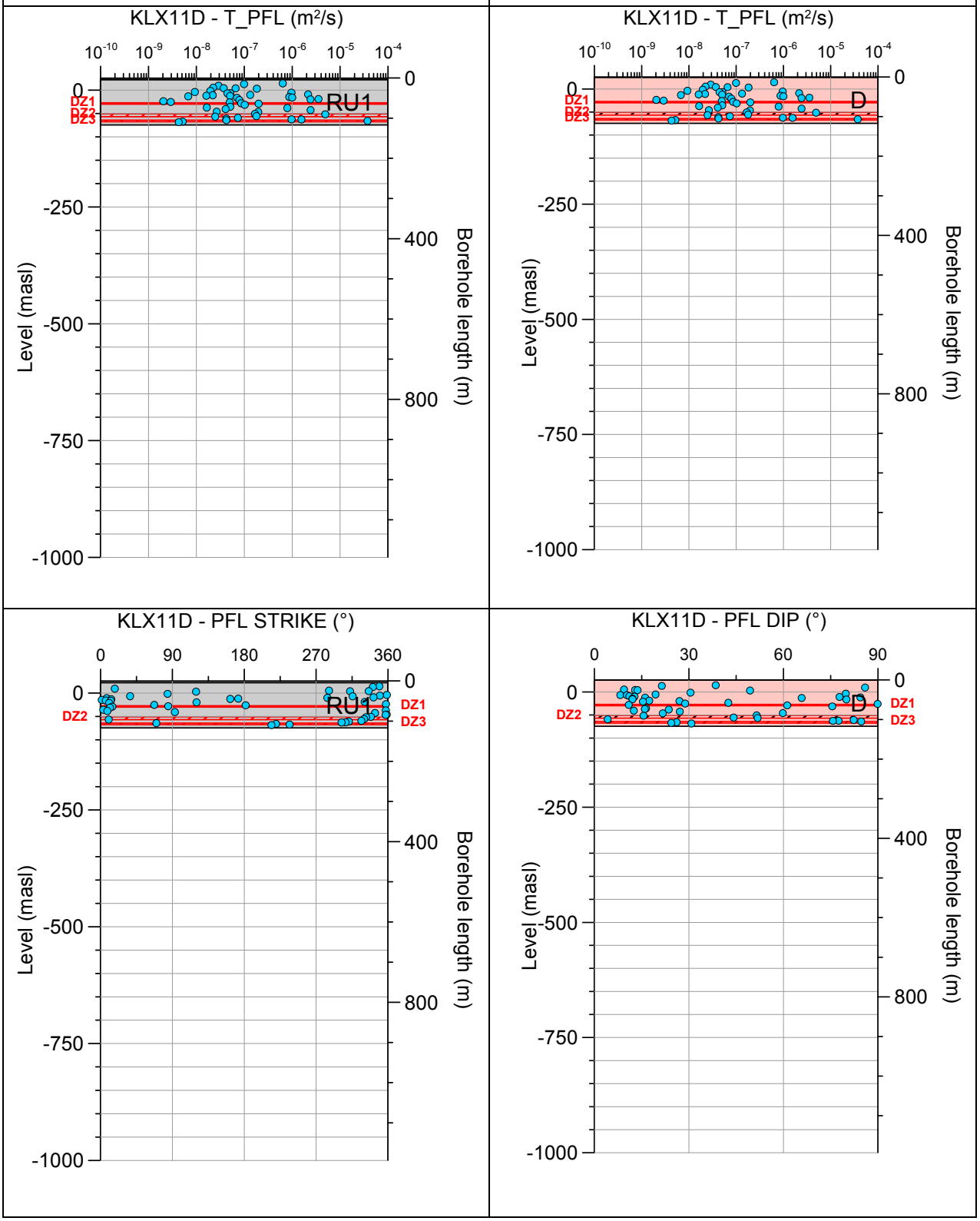

Comment:

Borehole KLX11D. Poles for PFL-f feature planes outside deformation zones.

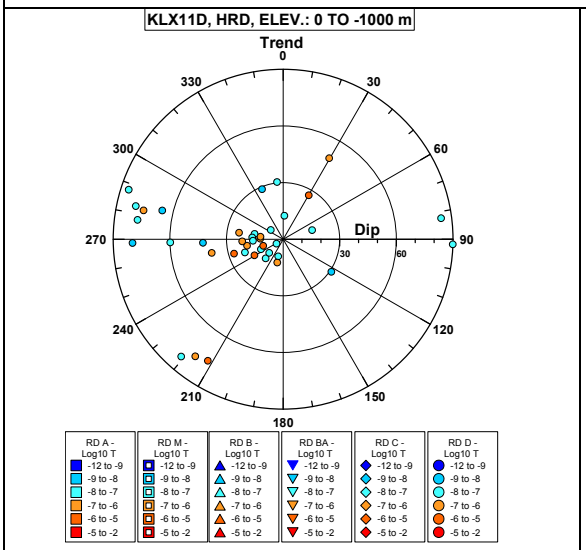

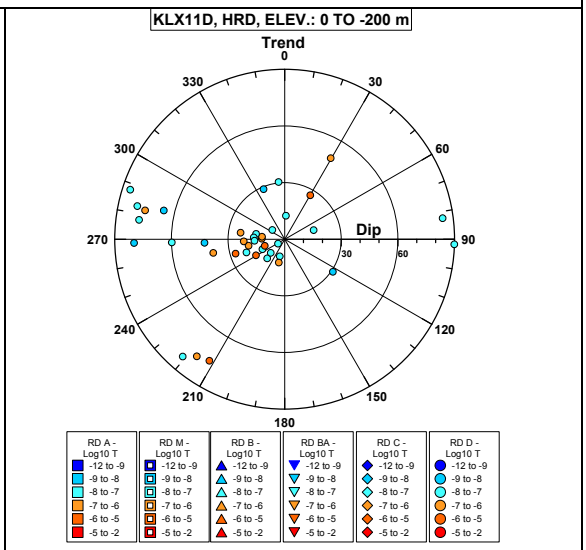

Borehole KLX11D. Poles for PFL-f feature planes in possible deformation zones.

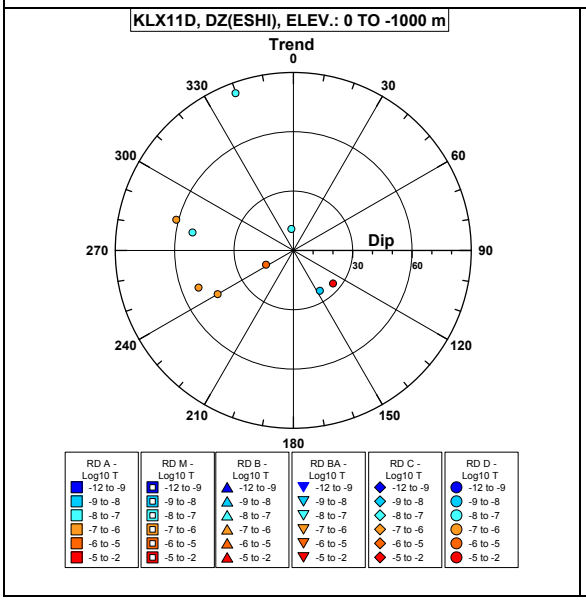

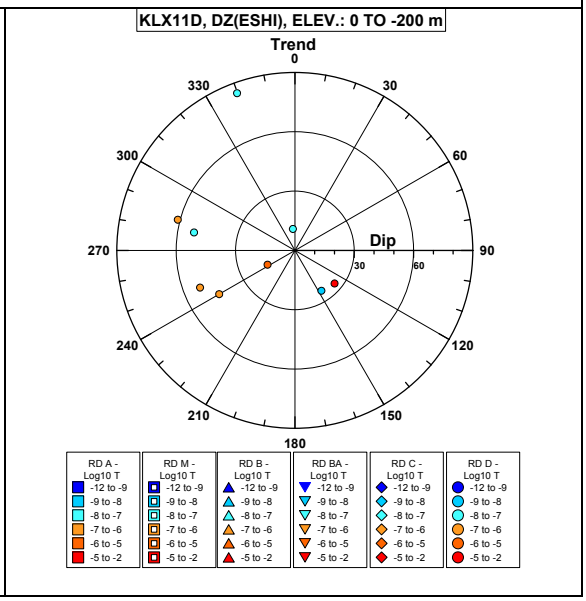

No PFL-f feature planes in deterministically modelled deformation zones exist in KLX11D.

Borehole KLX11E.

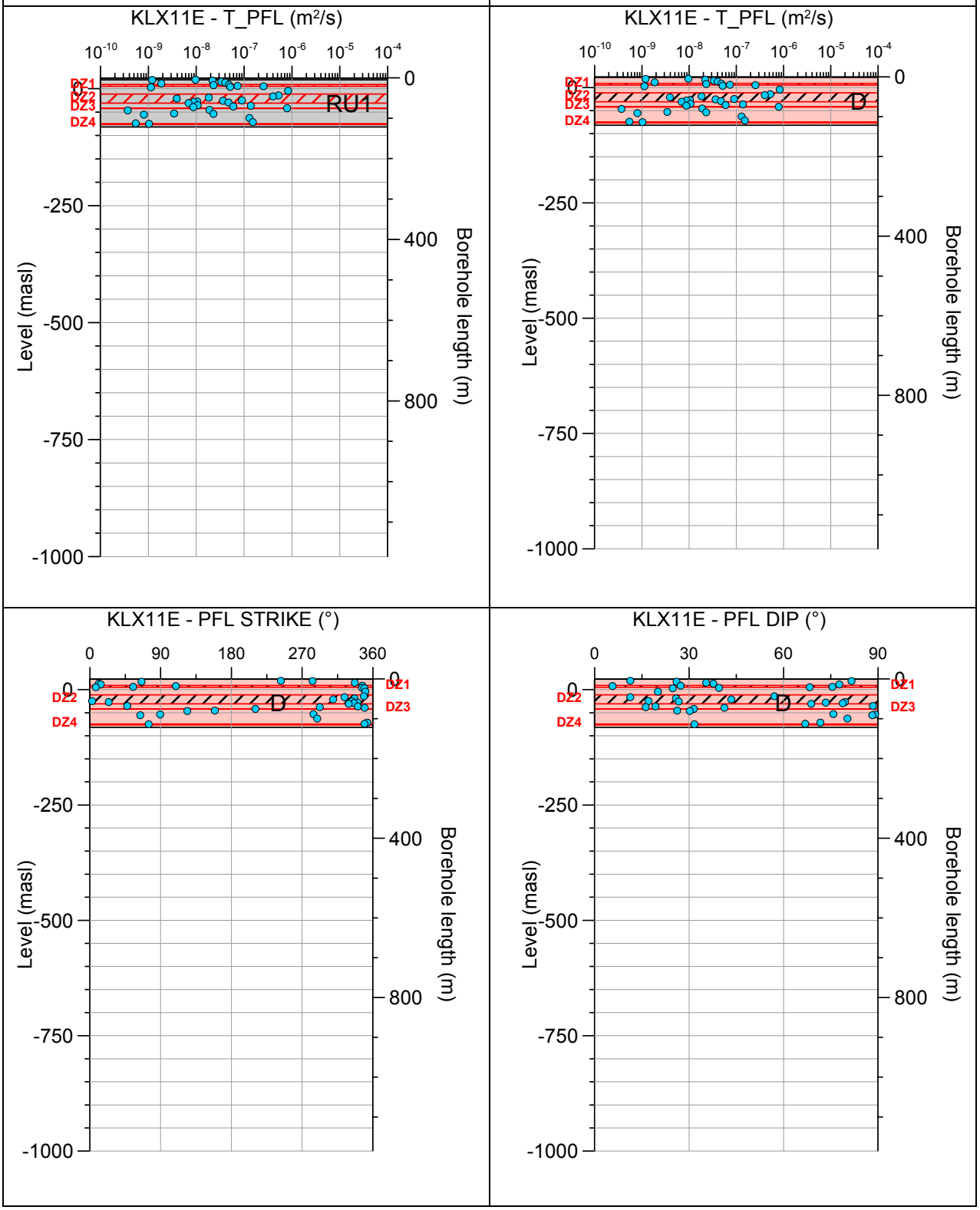

Comment:

Borehole KLX11E. Poles for PFL-f feature planes outside deformation zones.

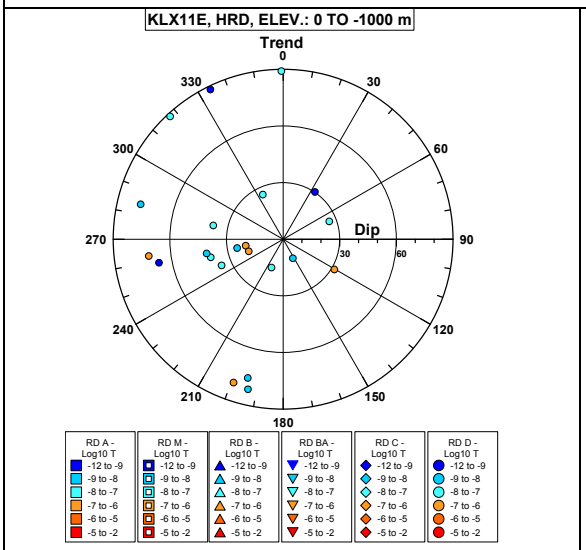

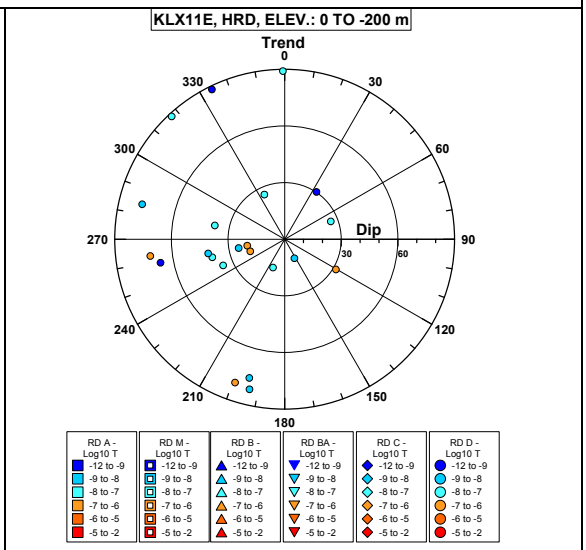

Borehole KLX11E. Poles for PFL-f feature planes in possible deformation zones.

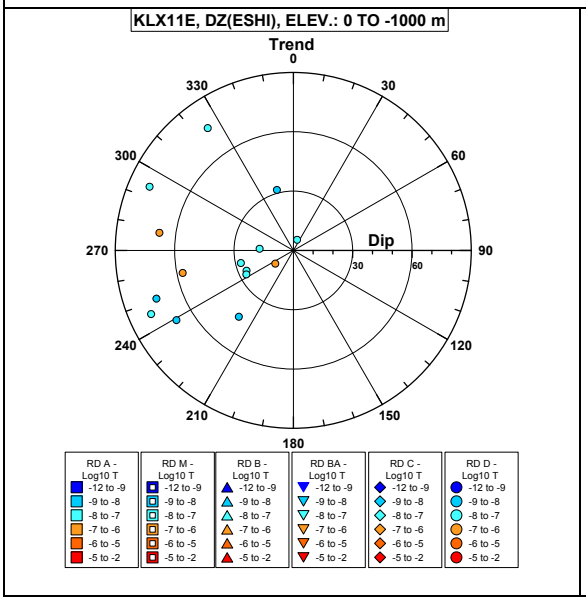

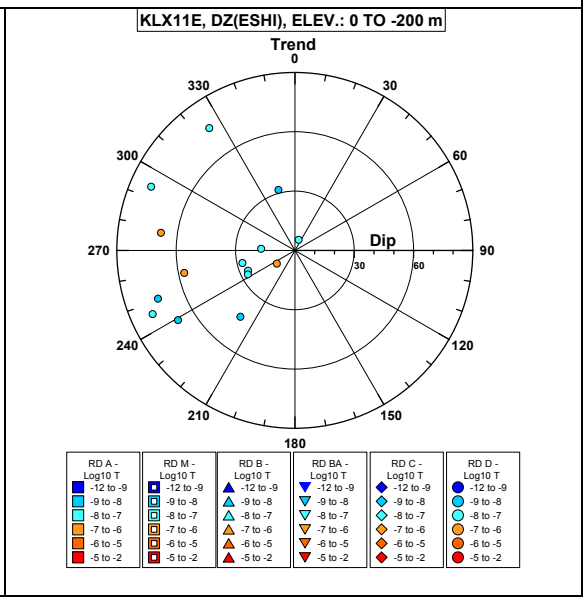

No PFL-f feature planes in deterministically modelled deformation zones exist in KLX11E.

Borehole KLX11F.

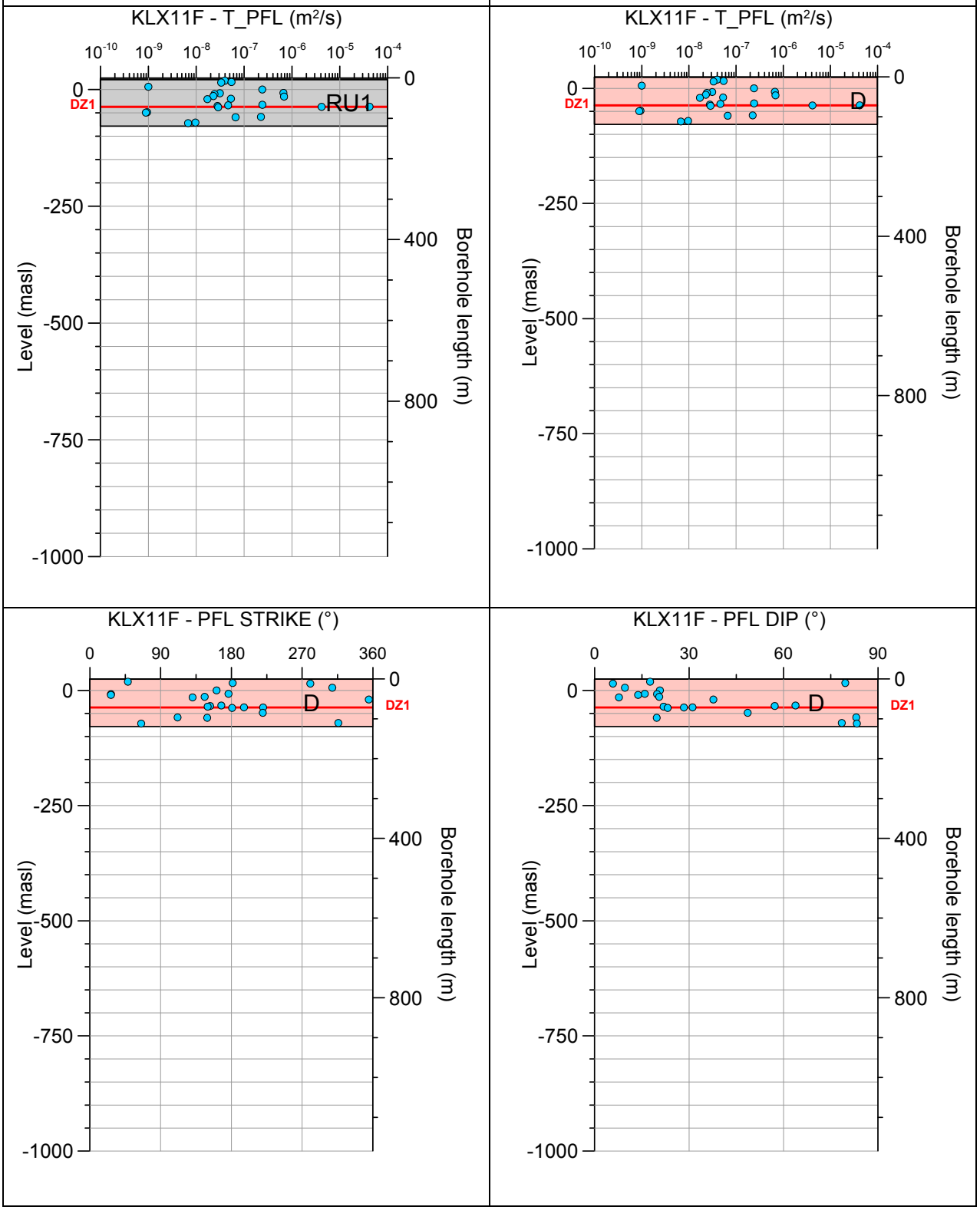

Comment:

Borehole KLX11F. Poles for PFL-f feature planes outside deformation zones.

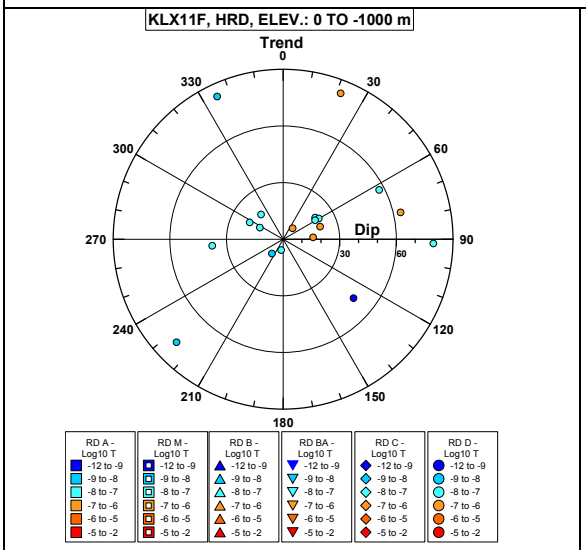

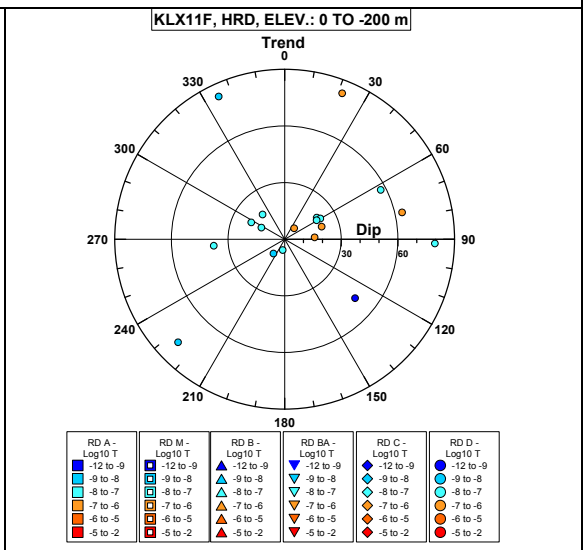

Borehole KLX11F. Poles for PFL-f feature planes in possible deformation zones.

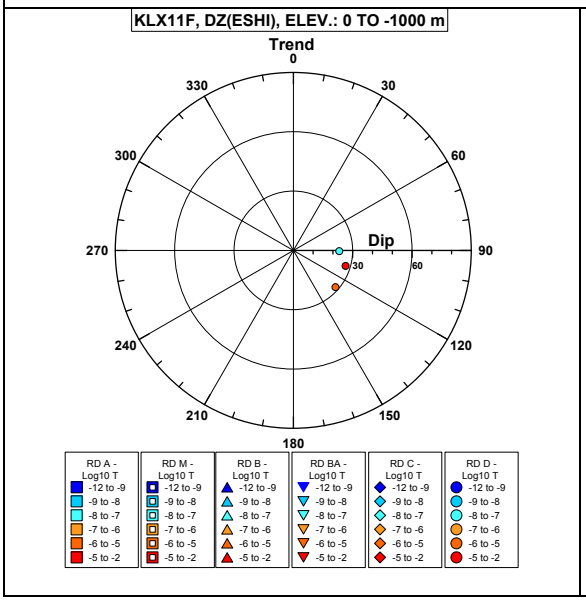

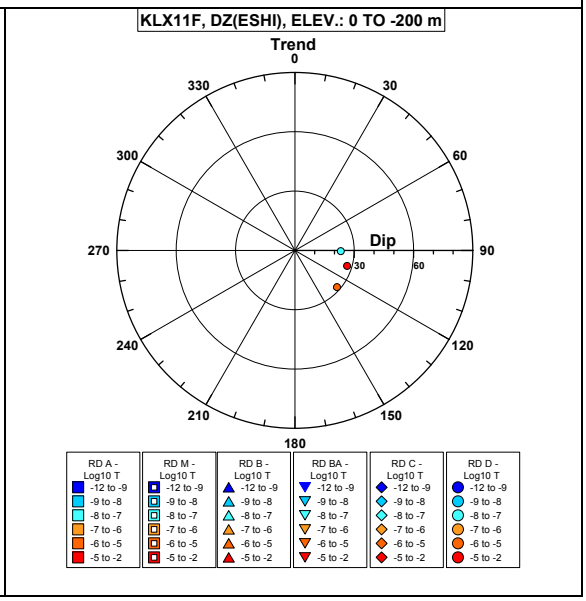

No PFL-f feature planes in deterministically modelled deformation zones exist in KLX11F.

Borehole KLX12A.

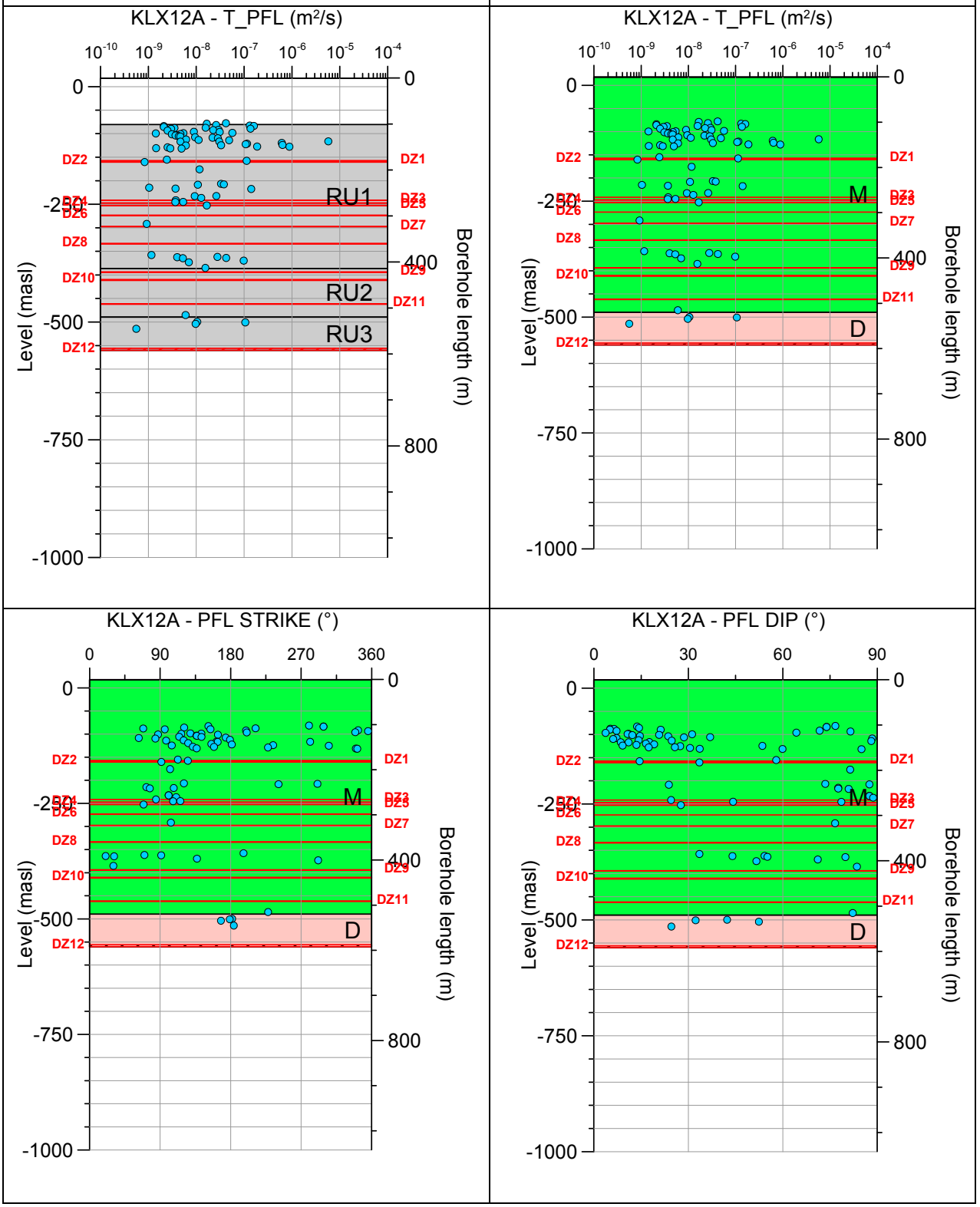

Comment:

Borehole KLX12A. Poles for PFL-f feature planes outside deformation zones.

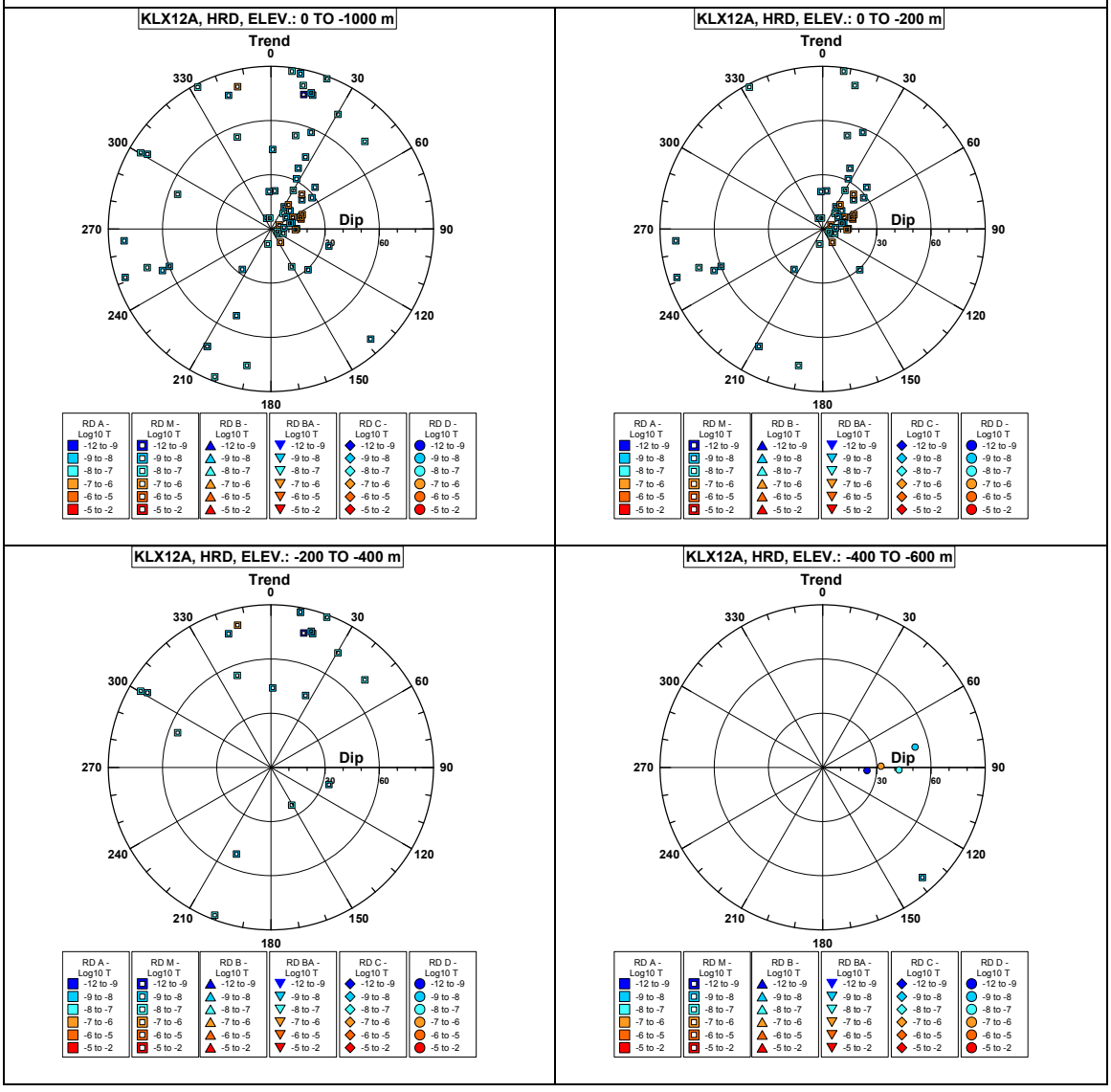

Borehole KLX12A. Poles for PFL-f feature planes in possible deformation zones.

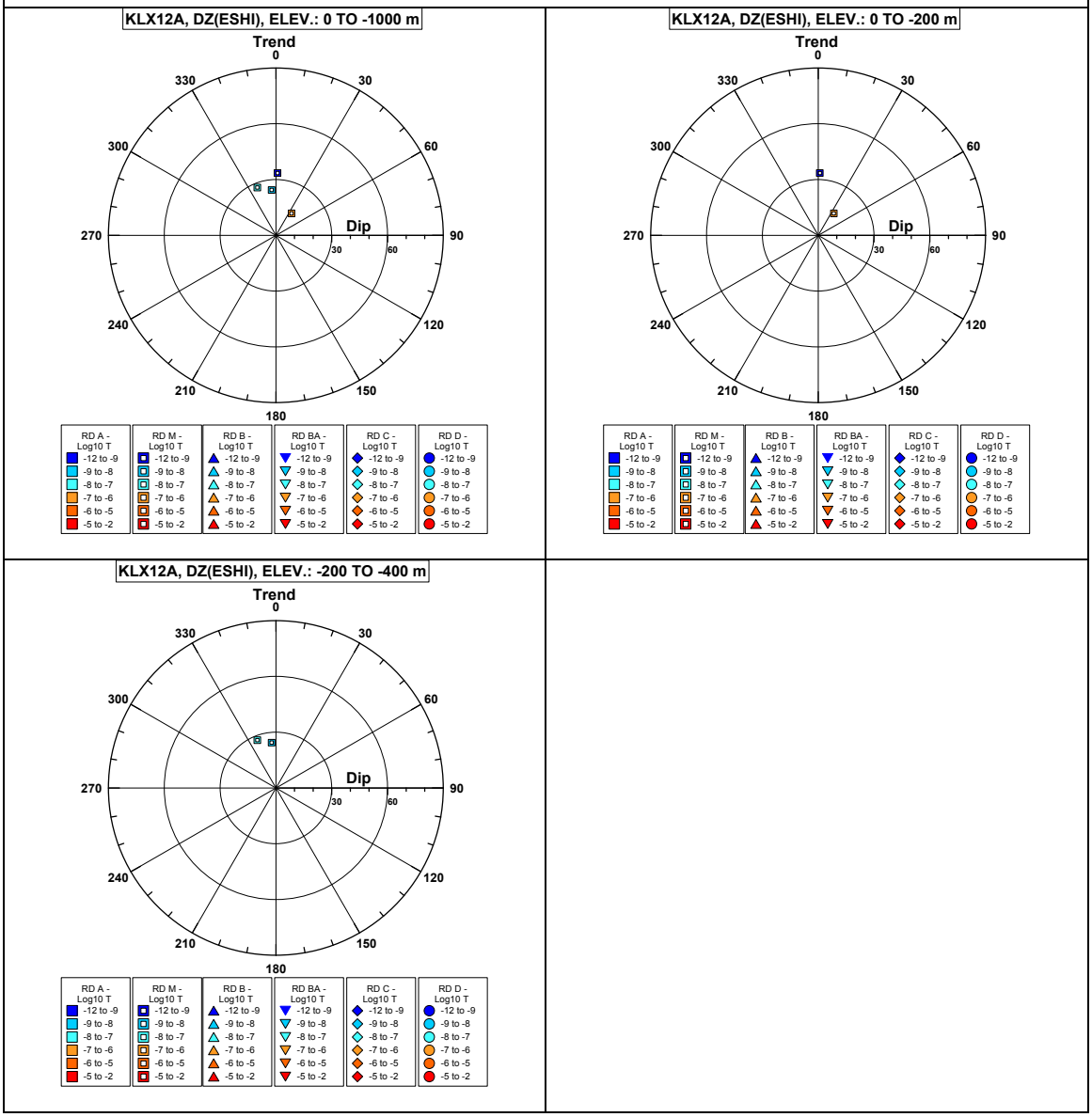

No PFL-f feature planes in deterministically modelled deformation zones exist in KLX12A.

Borehole KLX13A.

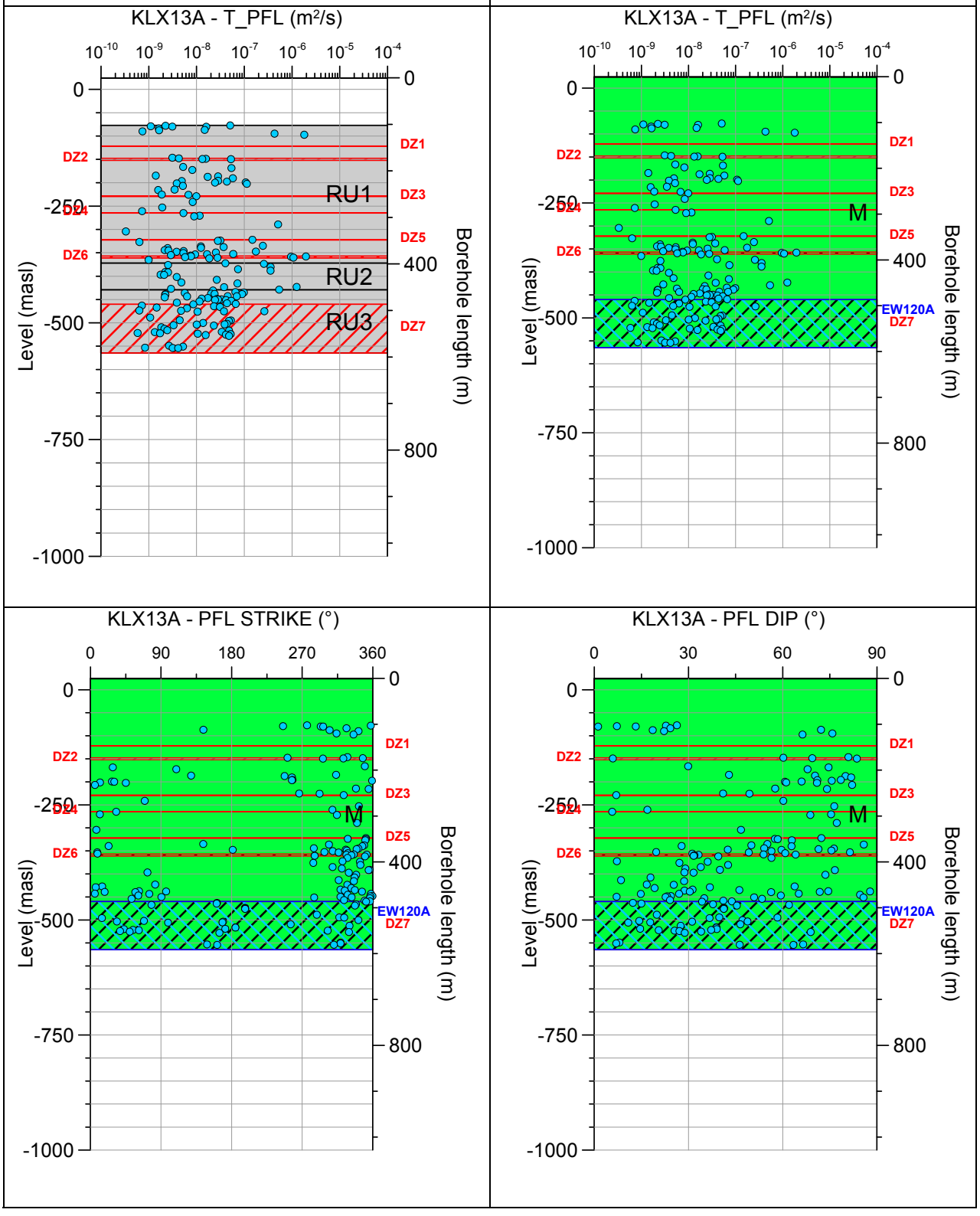

Comment:

Borehole KLX13A. Poles for PFL-f feature planes outside deformation zones.

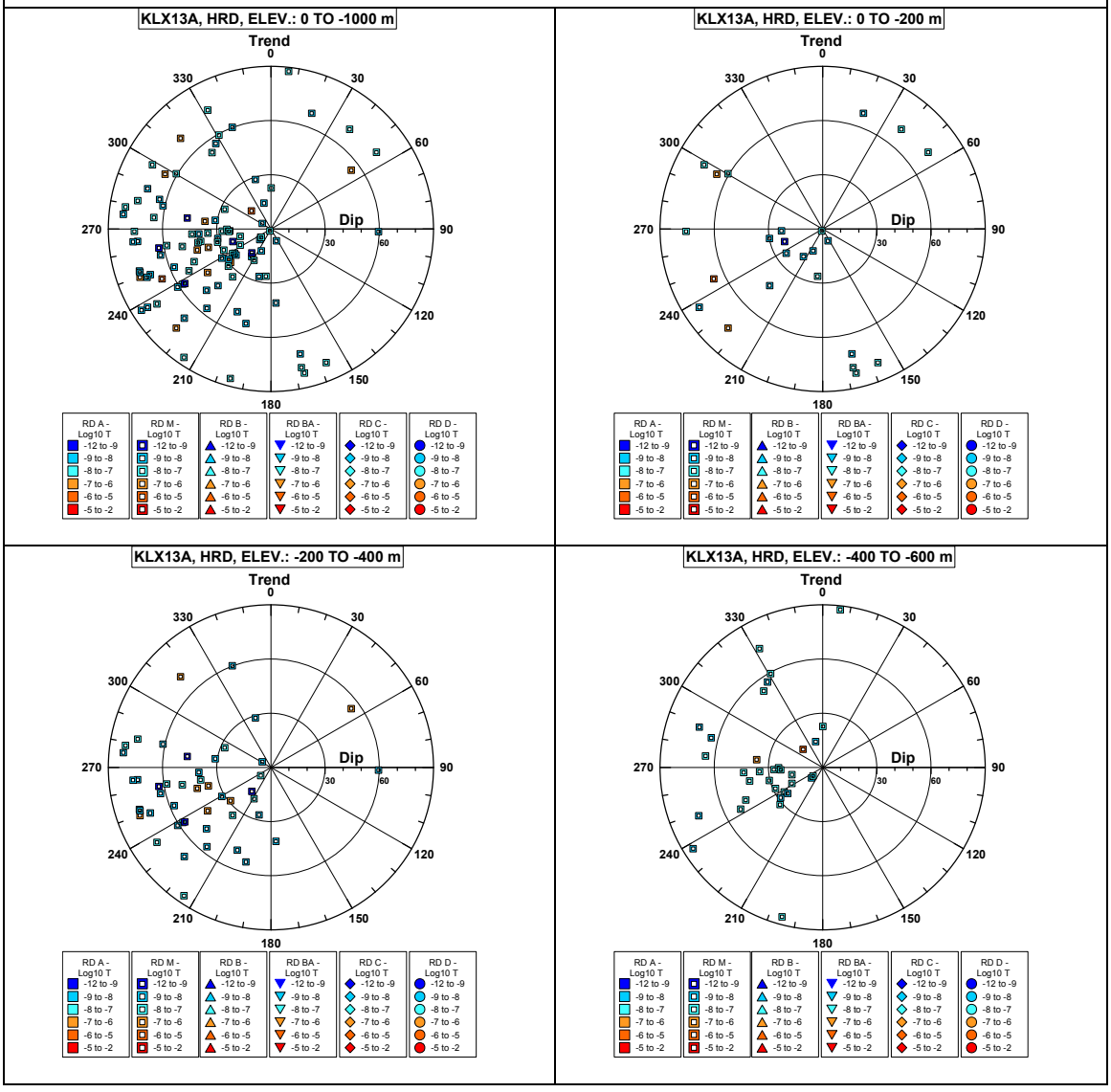

Borehole KLX13A. Poles for PFL-f feature planes in possible deformation zones.

KLX13A, DZ(ESHI), ELEV.: 0 TO -1000 m

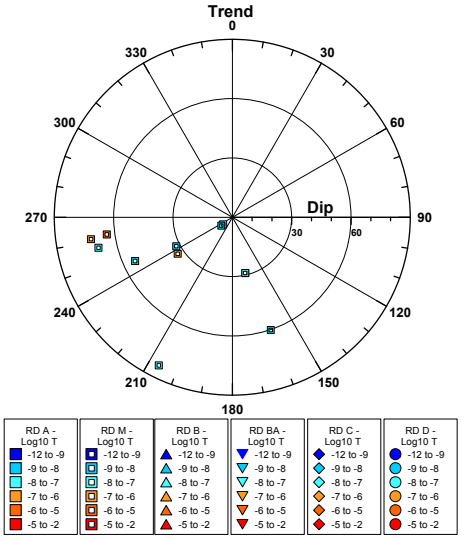

KLX13A, DZ(ESHI), ELEV.: 0 TO -200 m

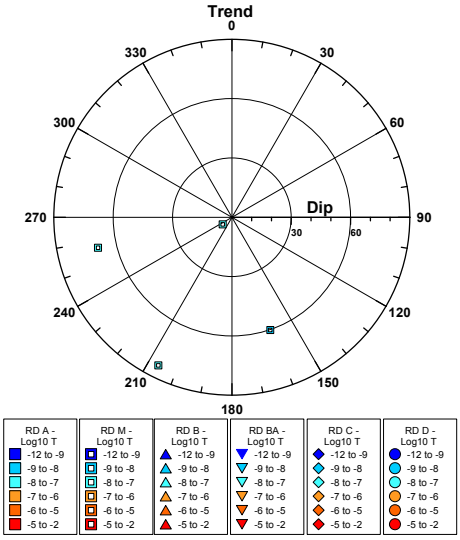

KLX13A, DZ(ESHI), ELEV.: -200 TO -400 m

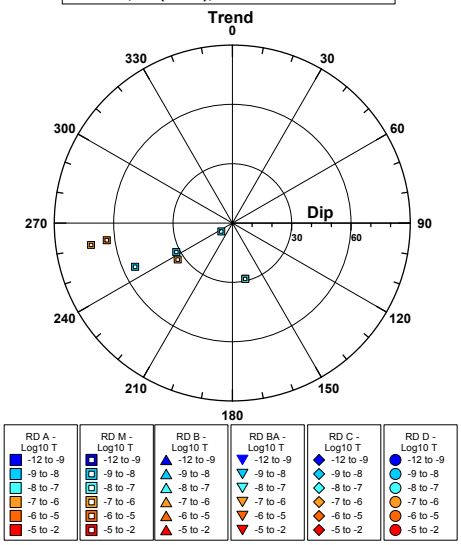

Borehole KLX13A. Poles for PFL-f feature planes in deterministically modelled deformation zones.

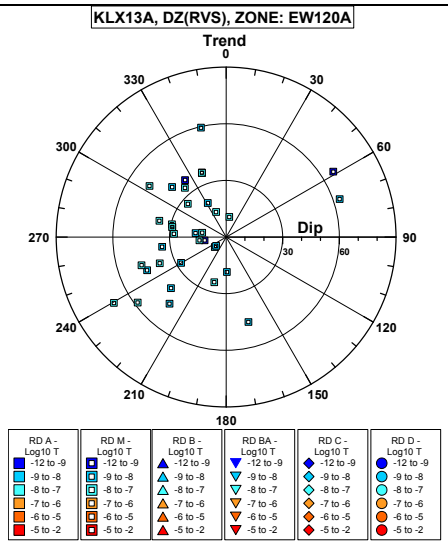

Borehole KLX14A.

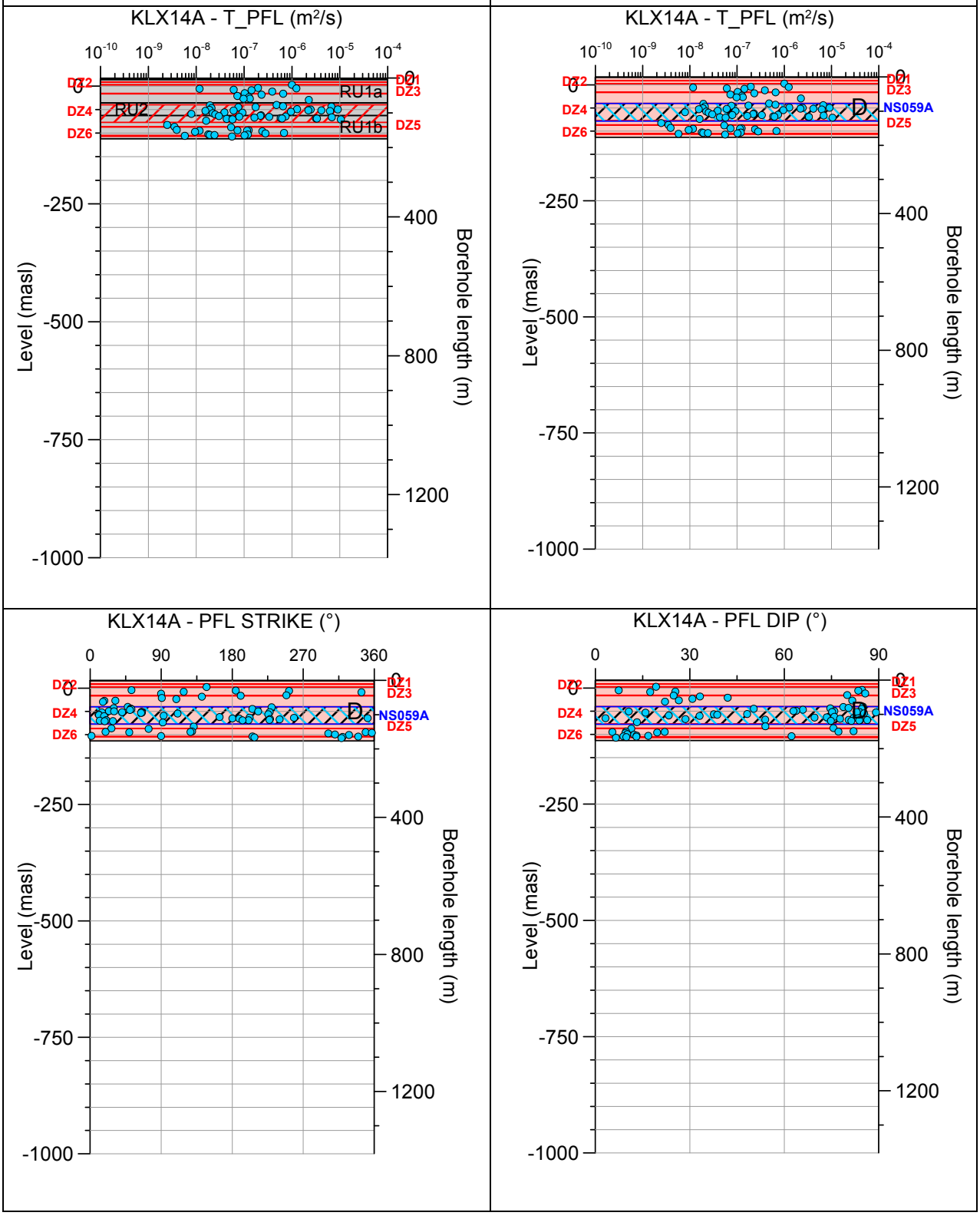

Comment:

Borehole KLX14A. Poles for PFL-f feature planes outside deformation zones.

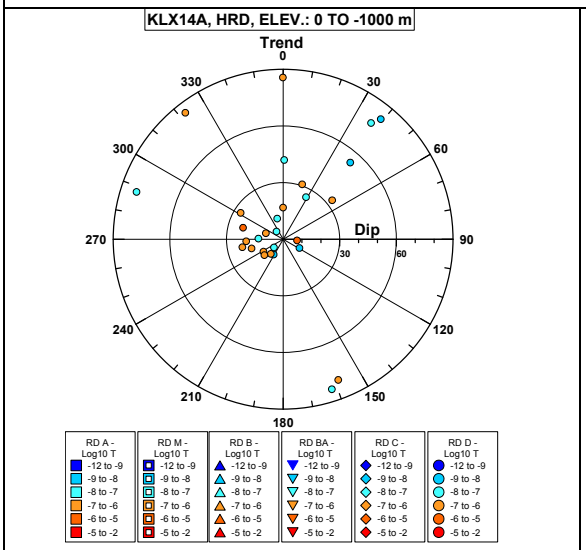

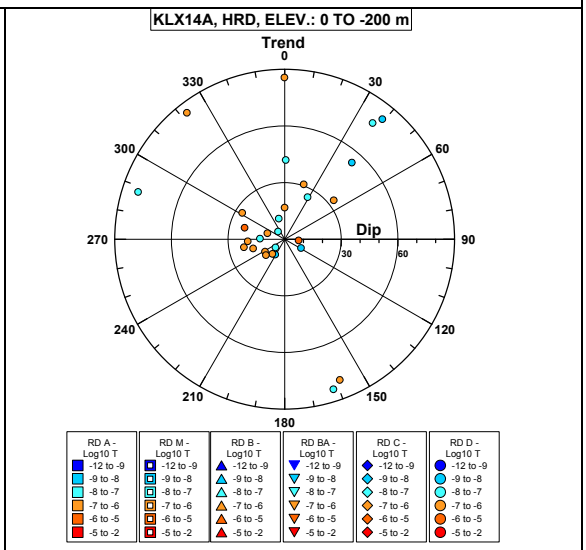

Borehole KLX14A. Poles for PFL-f feature planes in possible deformation zones.

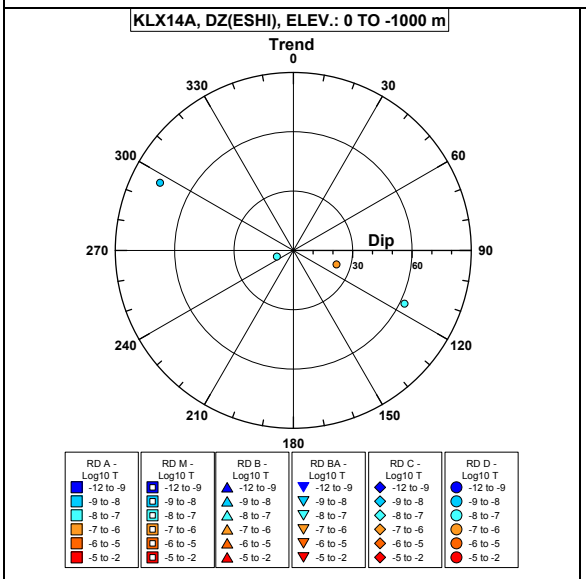

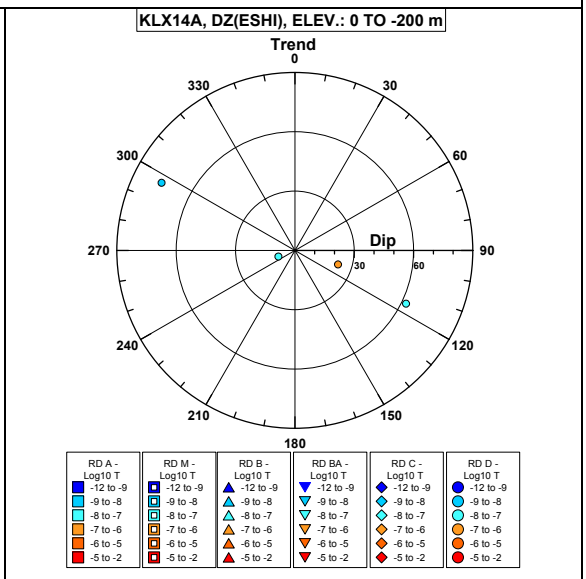

Borehole KLX14A. Poles for PFL-f feature planes in deterministically modelled deformation zones.

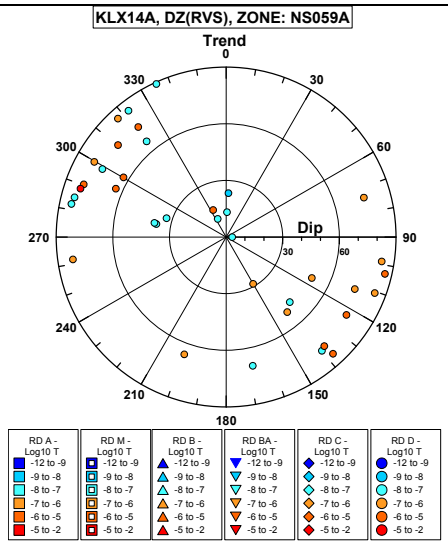

Borehole KLX15A.

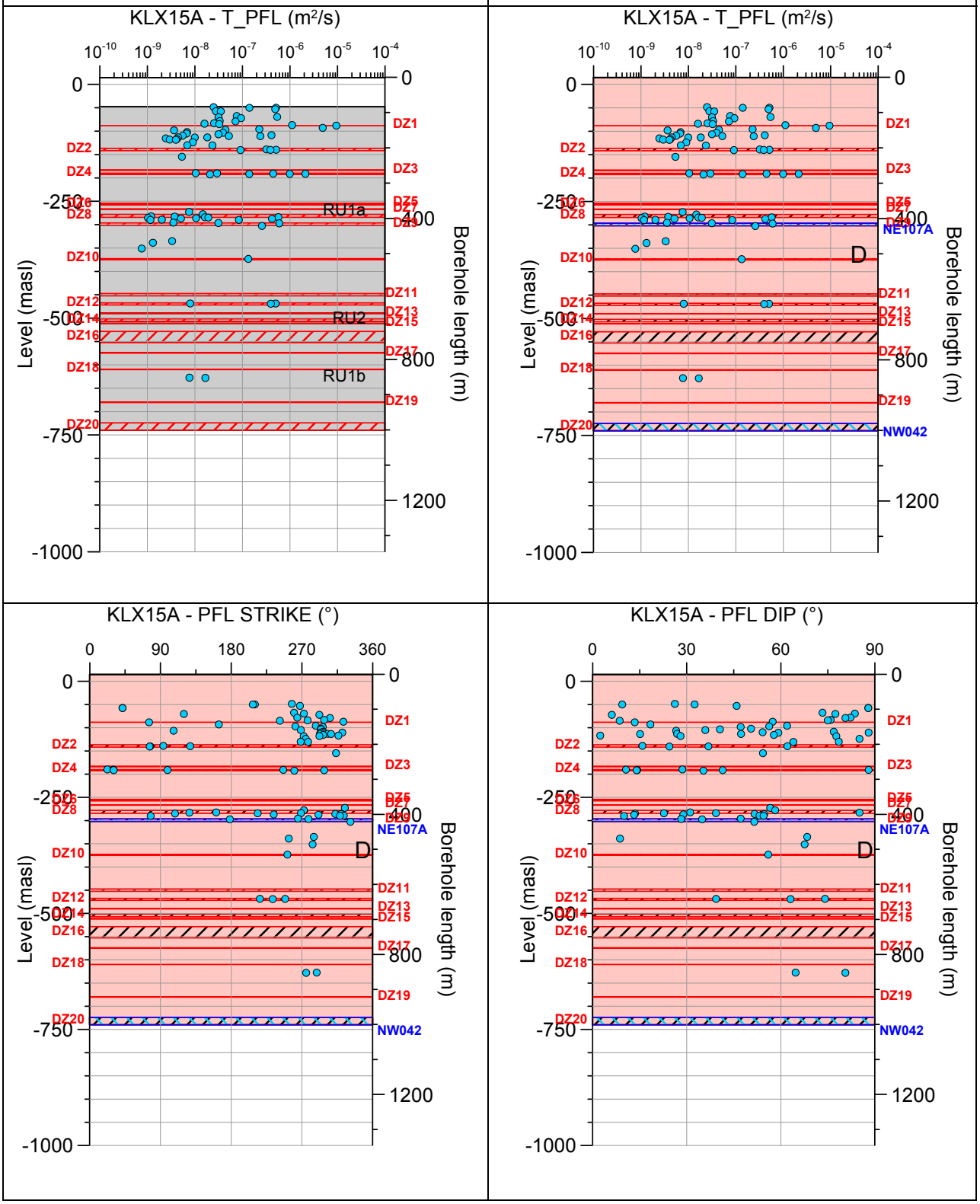

Comment:

Borehole KLX15A. Poles for PFL-f feature planes outside deformation zones.

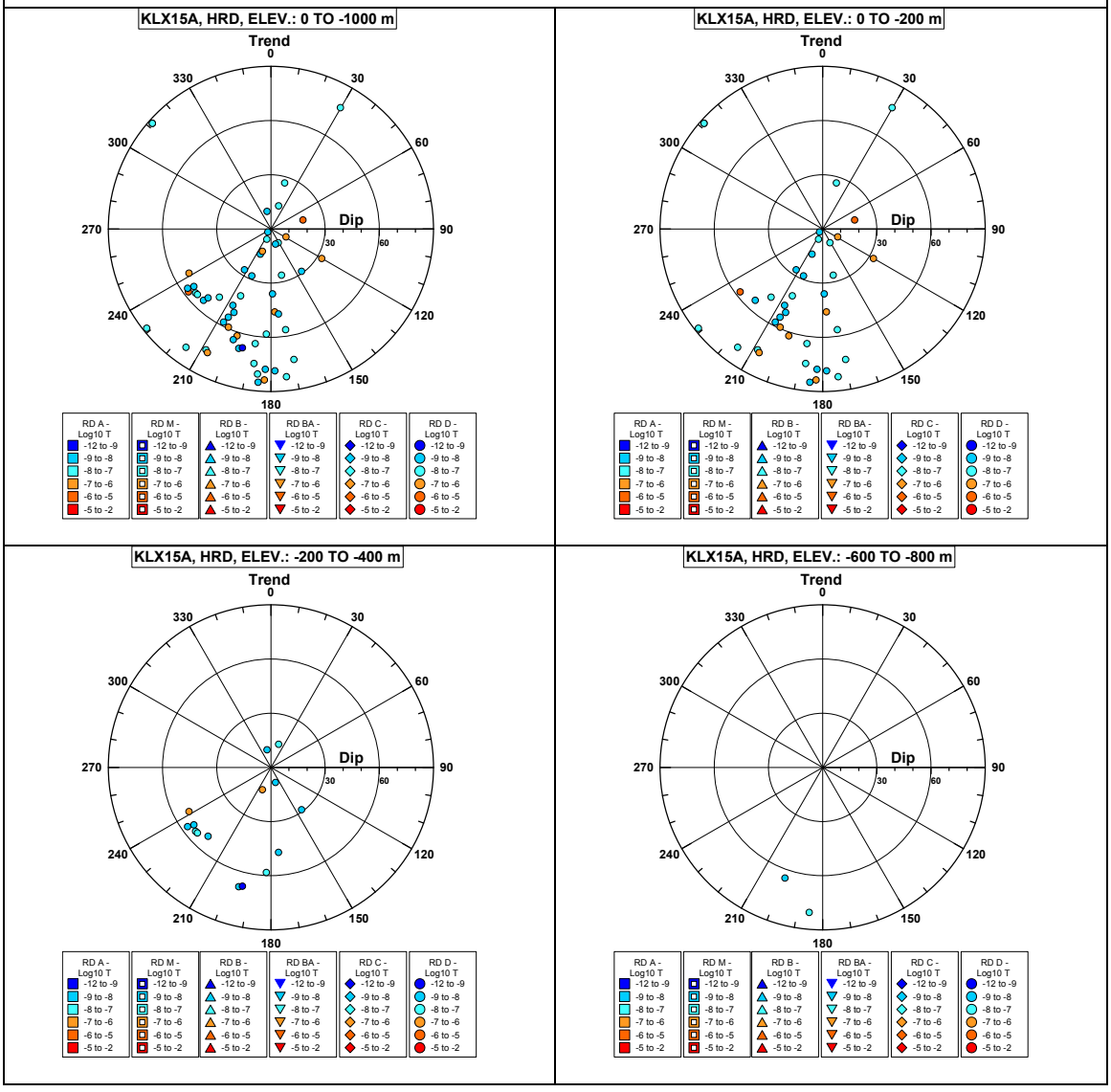

Borehole KLX15A. Poles for PFL-f feature planes in possible deformation zones.

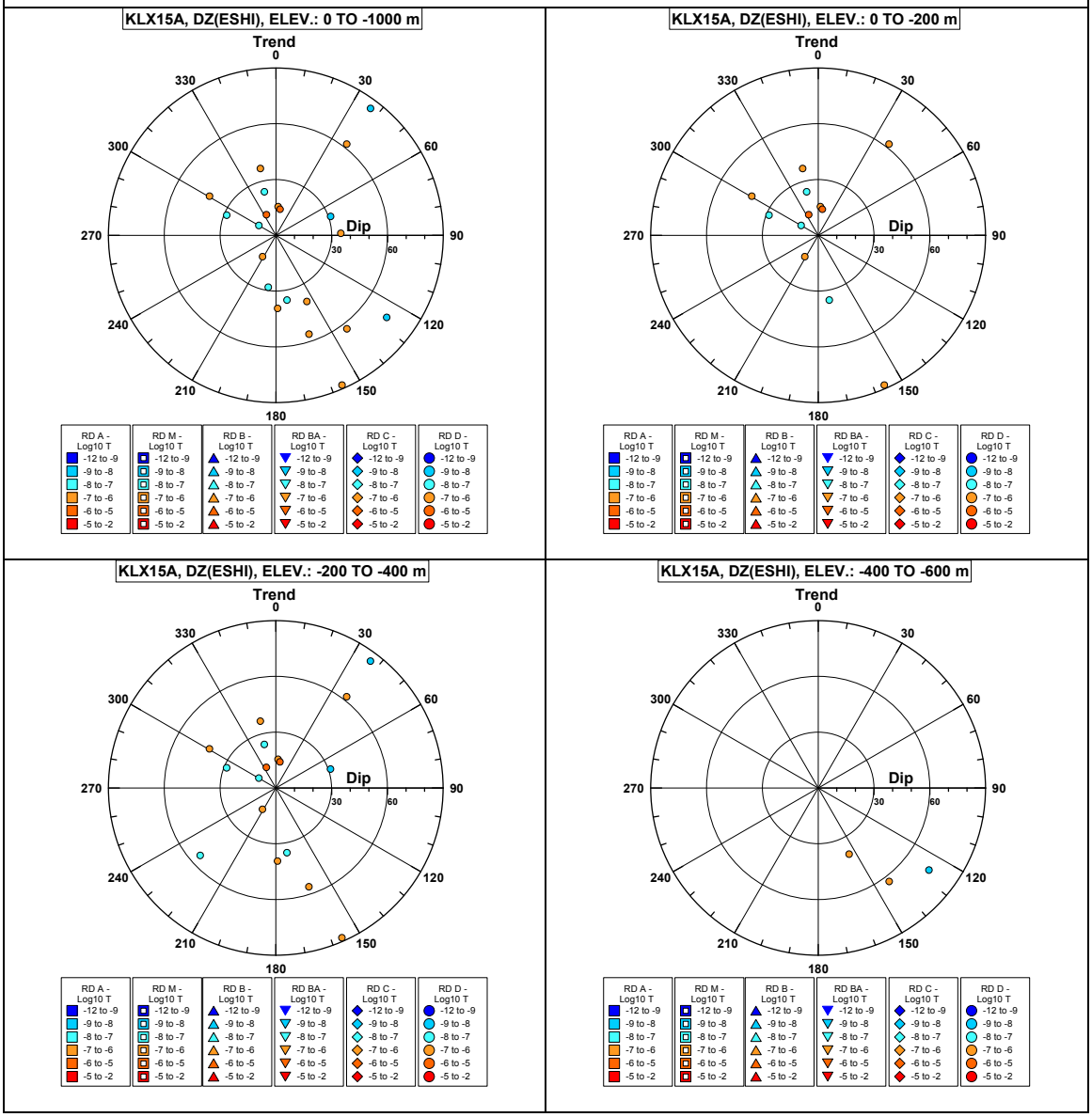

Borehole KLX15A. Poles for PFL-f feature planes in deterministically modelled deformation zones.

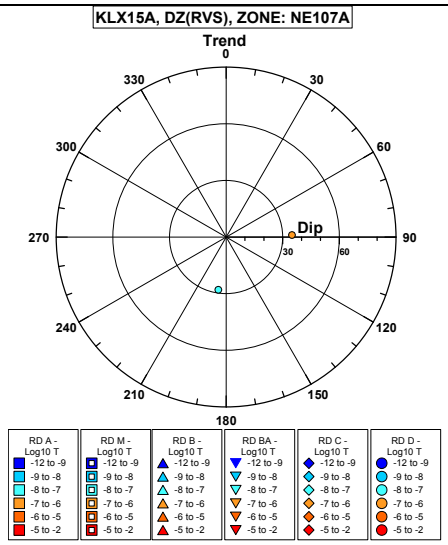

Borehole KLX16A.

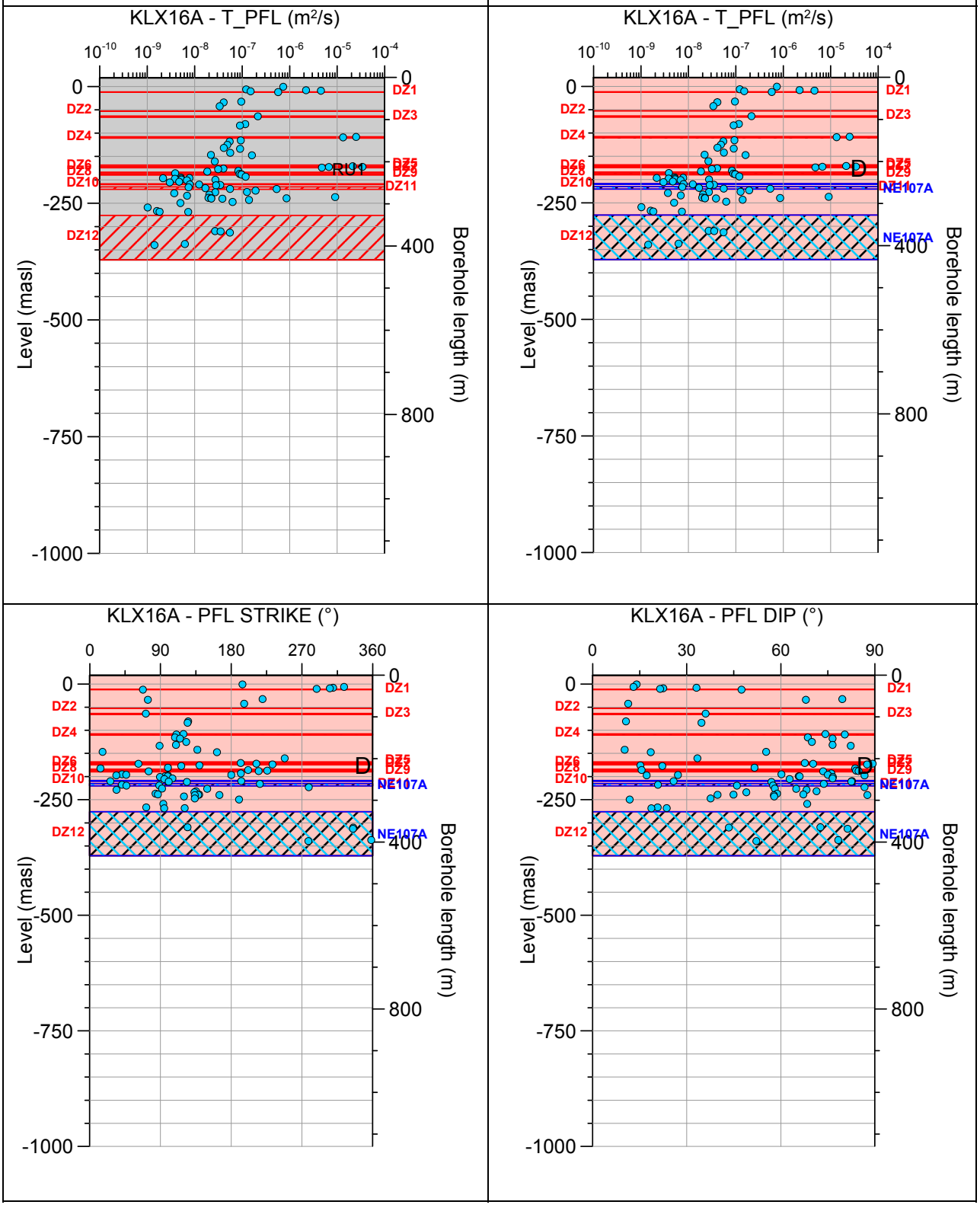

Comment:

Borehole KLX16A. Poles for PFL-f feature planes outside deformation zones.

KLX16A, HRD, ELEV.: 0 TO -1000 m

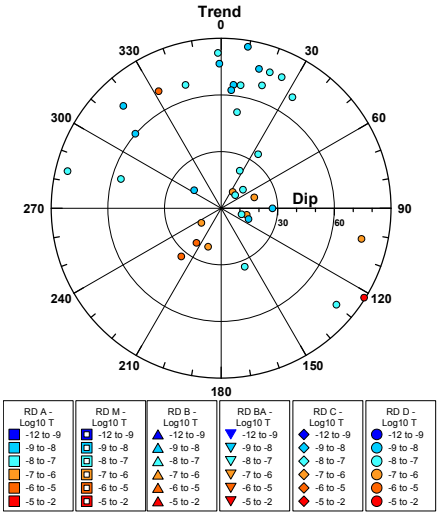

KLX16A, HRD, ELEV.: 0 TO -200 m

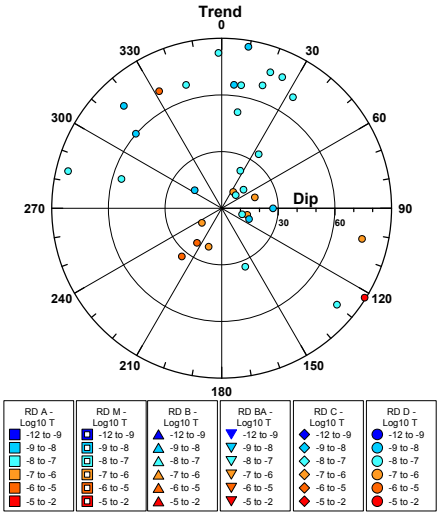

KLX16A, HRD, ELEV.: -200 TO -400 m

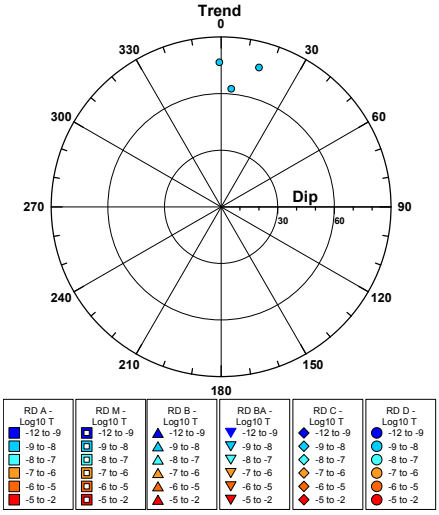

Borehole KLX16A. Poles for PFL-f feature planes in possible deformation zones.

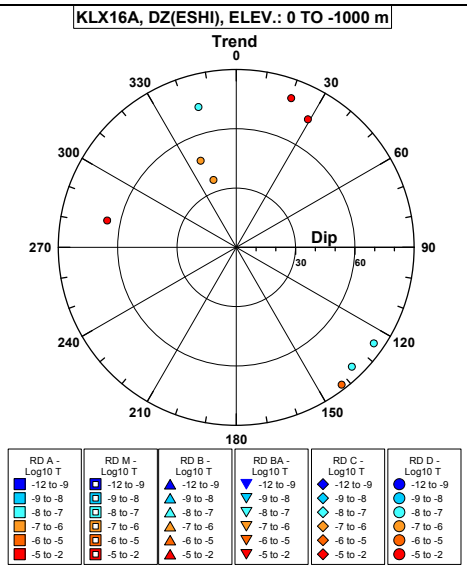

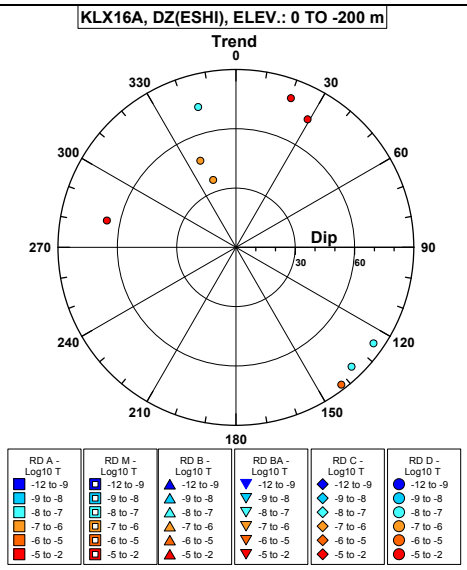

Borehole KLX16A. Poles for PFL-f feature planes in deterministically modelled deformation zones.

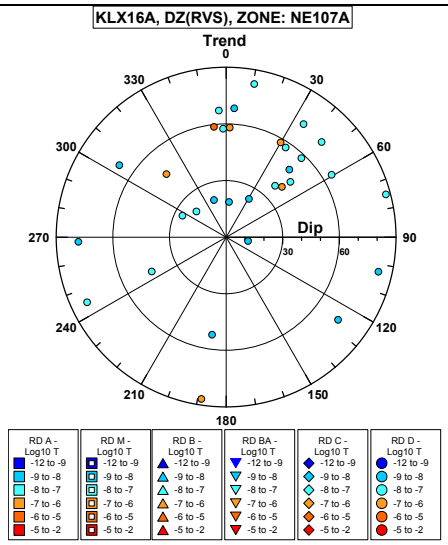

Borehole KLX17A.

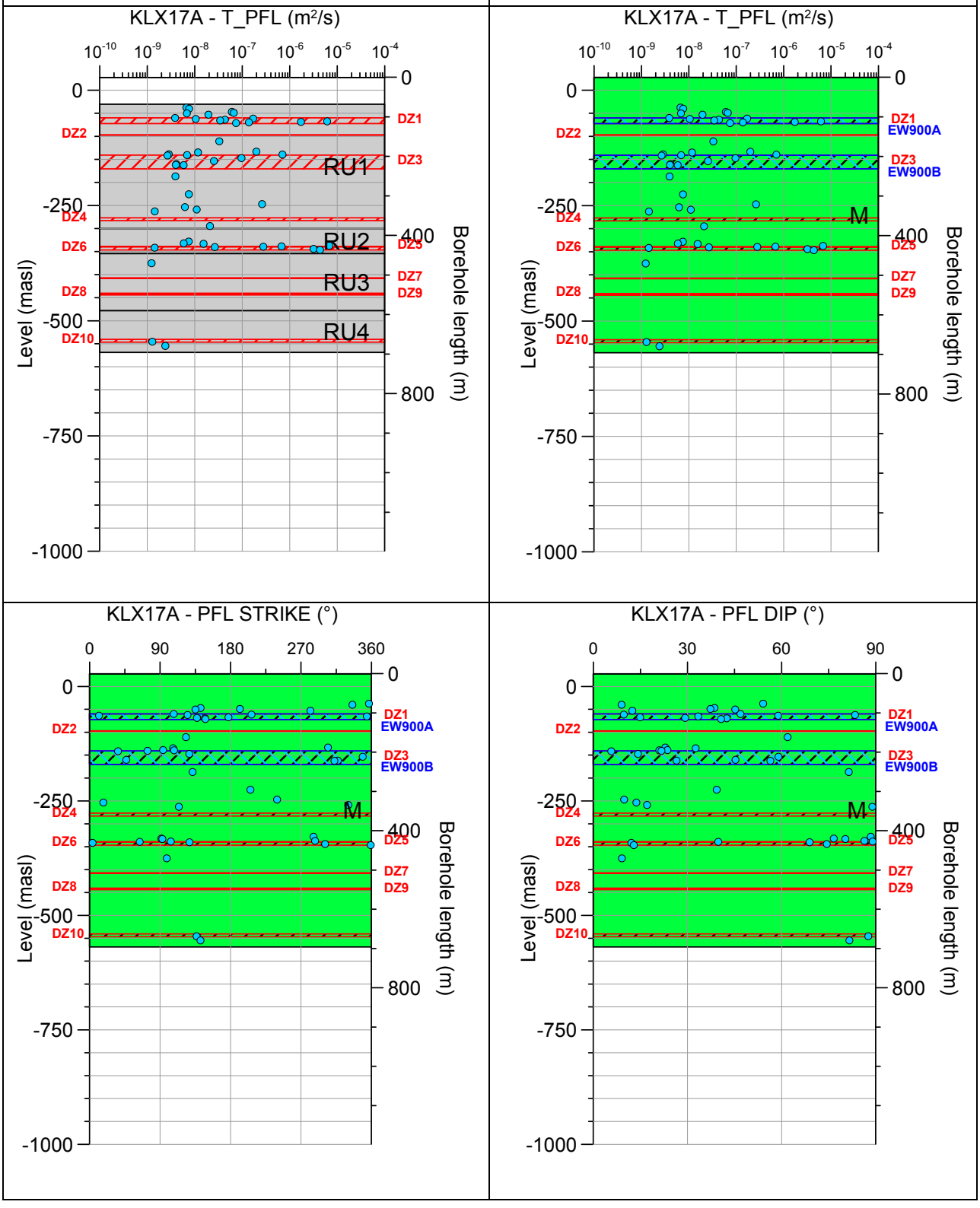

Comment:

Borehole KLX17A. Poles for PFL-f feature planes outside deformation zones.

KLX17A, HRD, ELEV.: 0 TO -1000 m

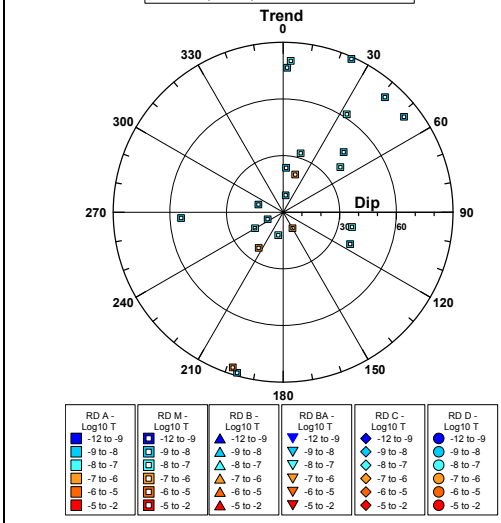

KLX17A, HRD, ELEV.: 0 TO -200 m

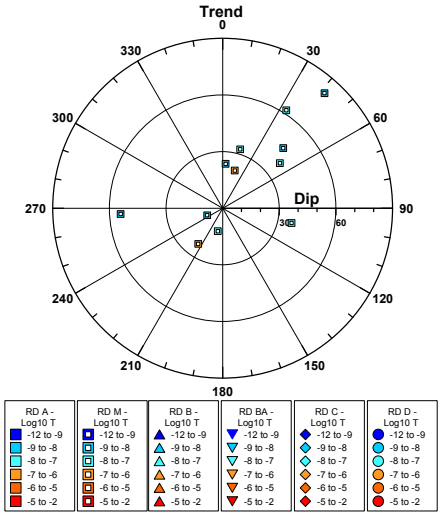

KLX17A, HRD, ELEV.: -200 TO -400 m

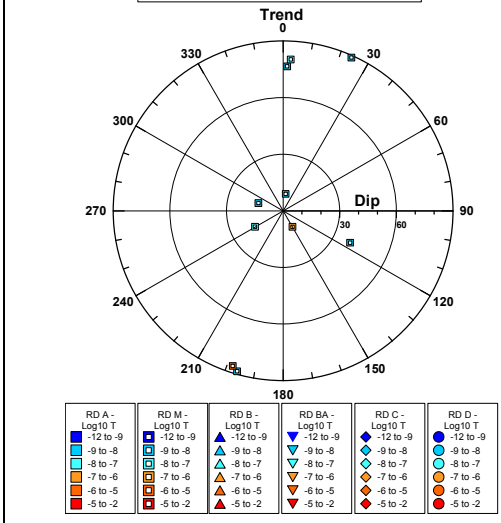

KLX17A, HRD, ELEV.: -400 TO -600 m

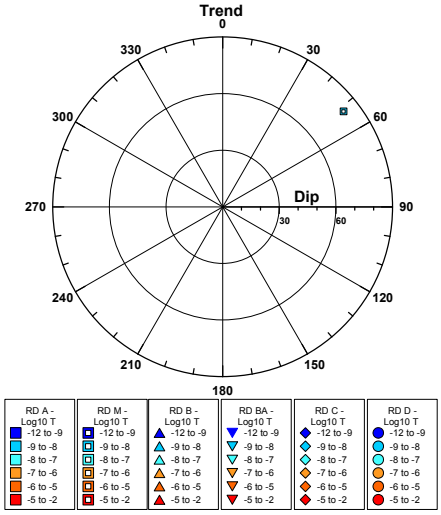

Borehole KLX17A. Poles for PFL-f feature planes in possible deformation zones.

KLX17A, DZ(ESHI), ELEV.: 0 TO -1000 m

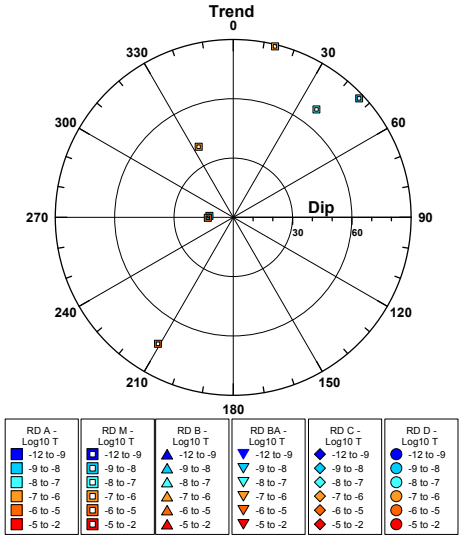

KLX17A, DZ(ESHI), ELEV.: -200 TO -400 m

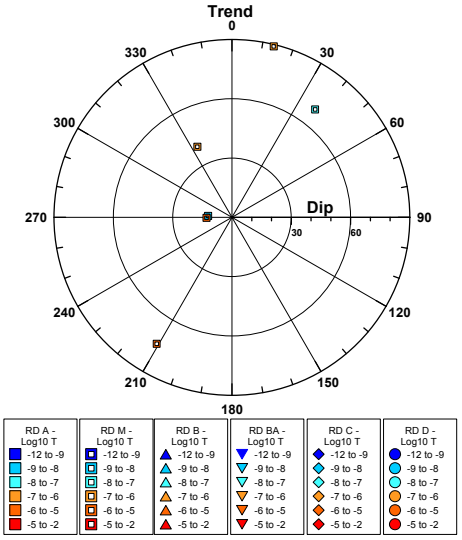

KLX17A, DZ(ESHI), ELEV.: -400 TO -600 m

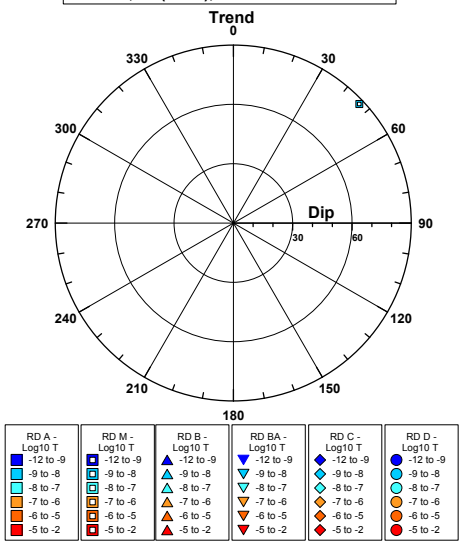

Borehole KLX17A. Poles for PFL-f feature planes in deterministically modelled deformation zones.

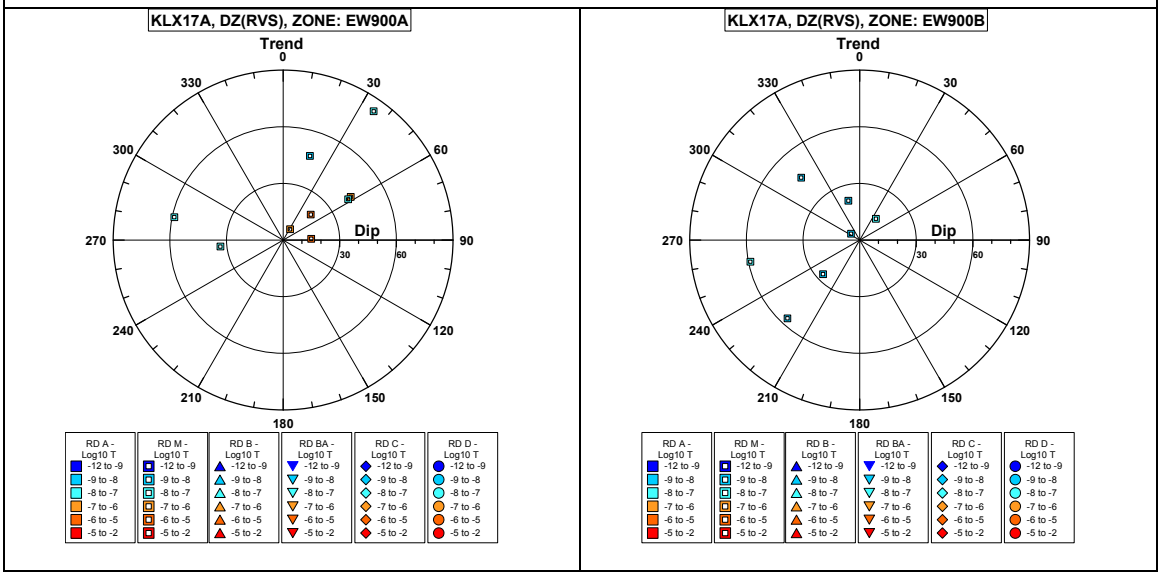

Borehole KLX18A.

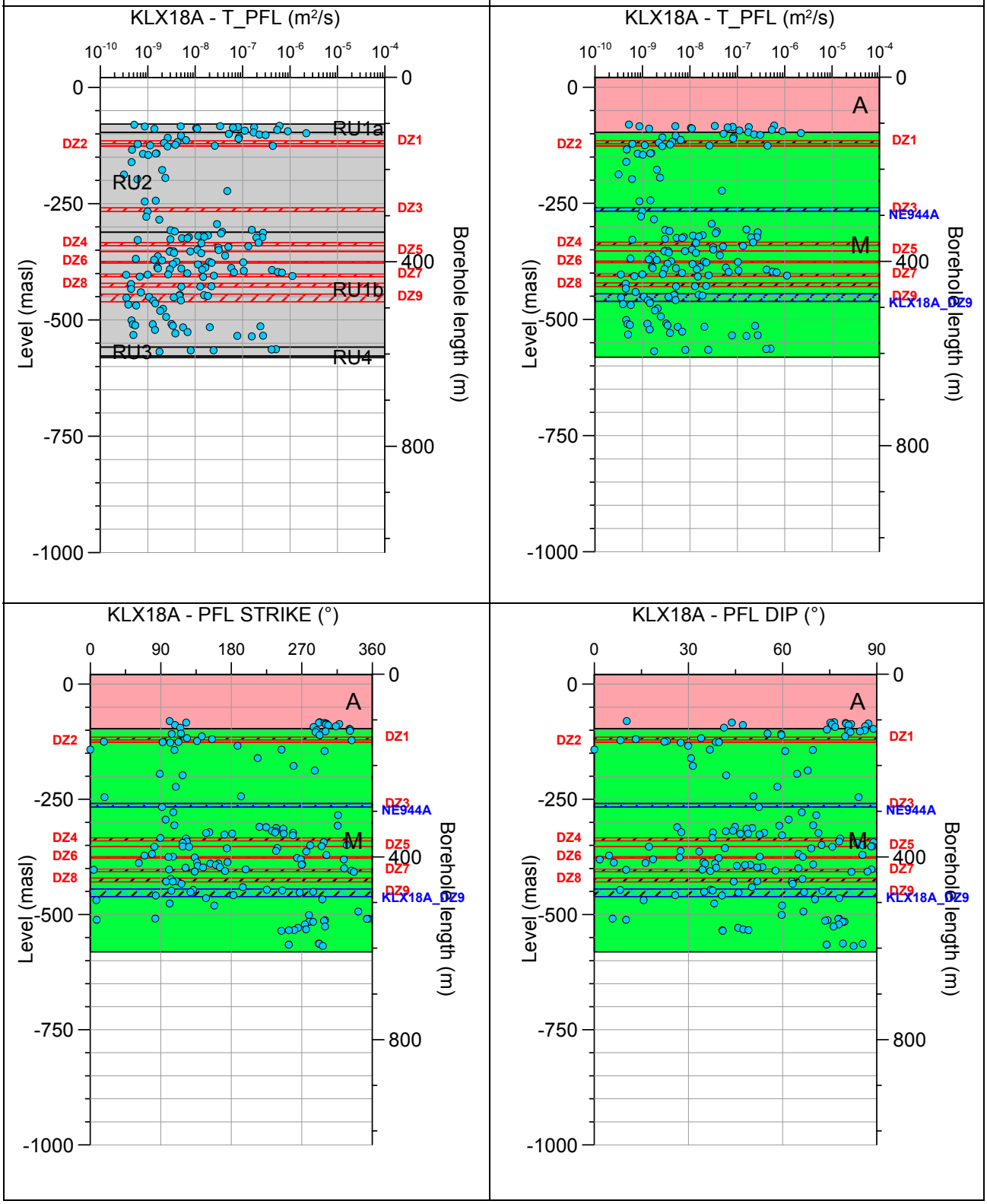

Comment:

Borehole KLX18A. Poles for PFL-f feature planes outside deformation zones.

KLX18A, HRD, ELEV.: 0 TO -1000 m

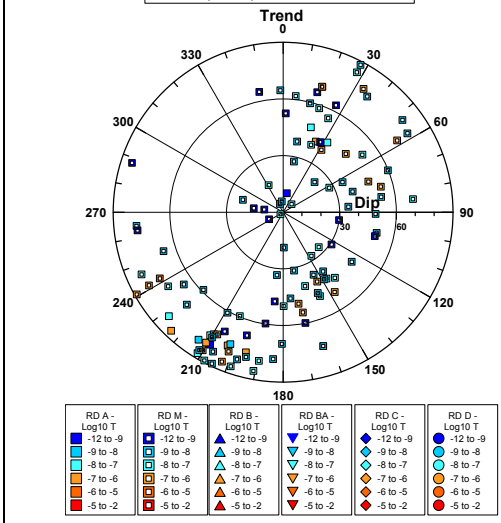

KLX18A, HRD, ELEV.: 0 TO -200 m

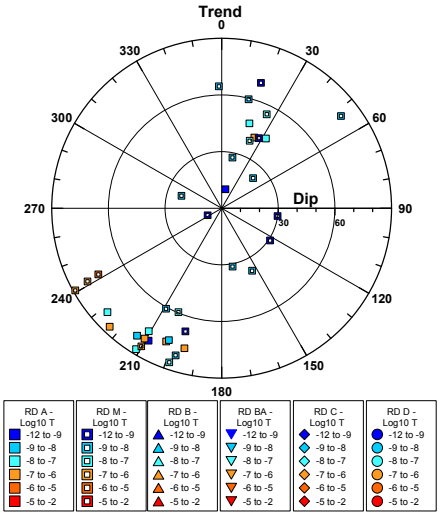

KLX18A, HRD, ELEV.: -200 TO -400 m

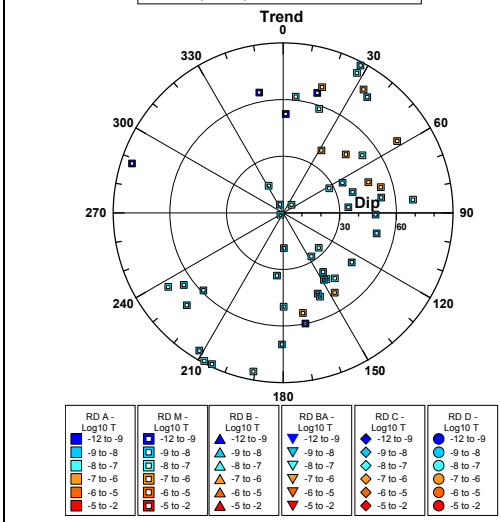

KLX18A, HRD, ELEV.: -400 TO -600 m

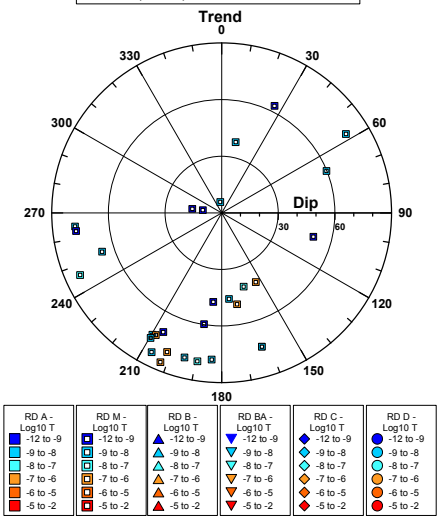

Borehole KLX18A. Poles for PFL-f feature planes in possible deformation zones.

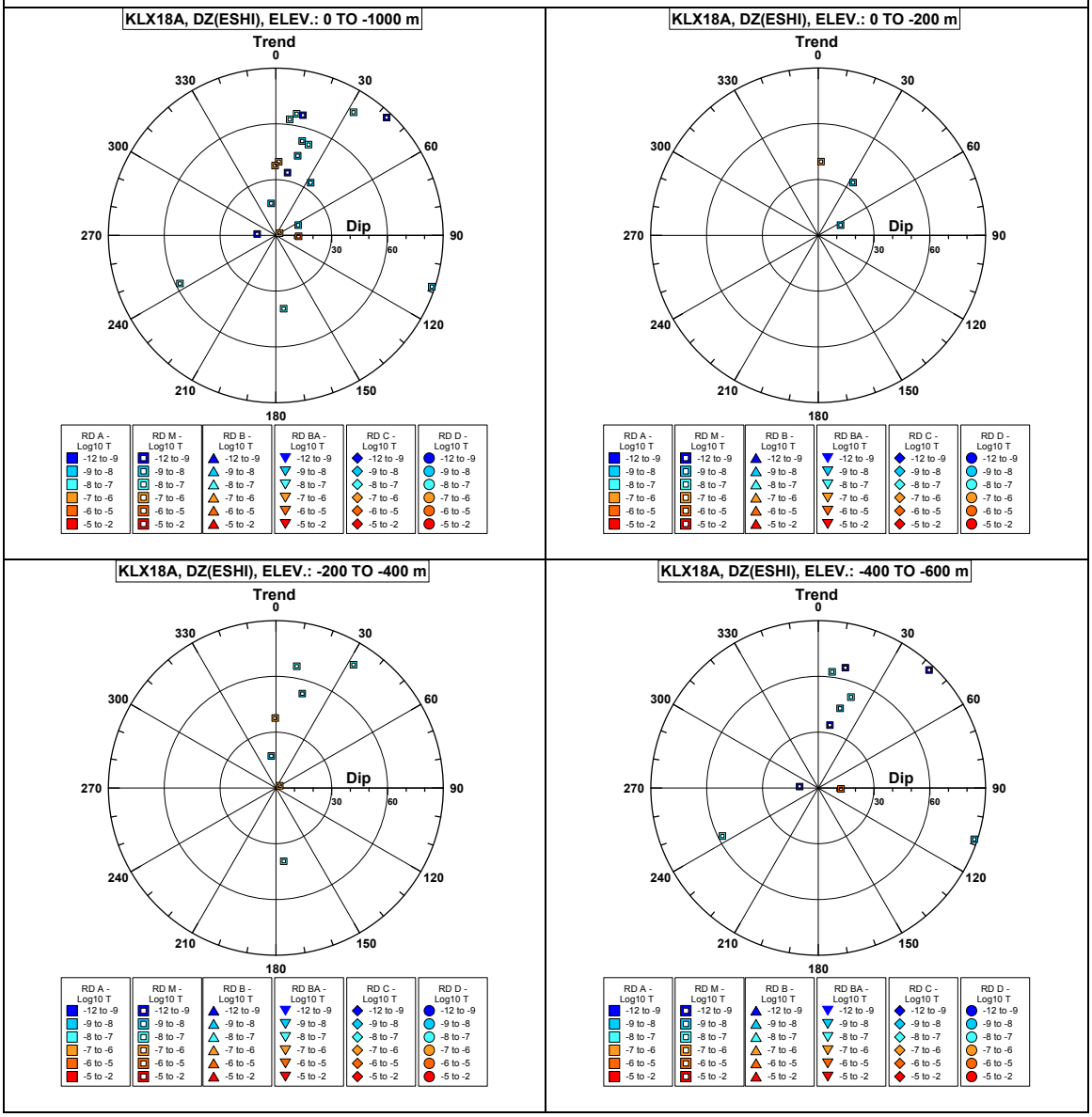

Borehole KLX18A. Poles for PFL-f feature planes in deterministically modelled deformation zones.

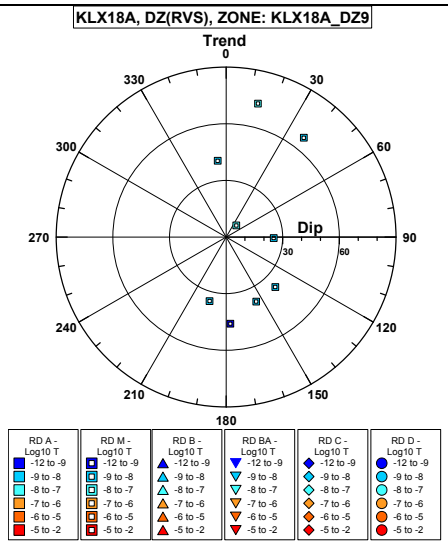

Borehole KLX19A.

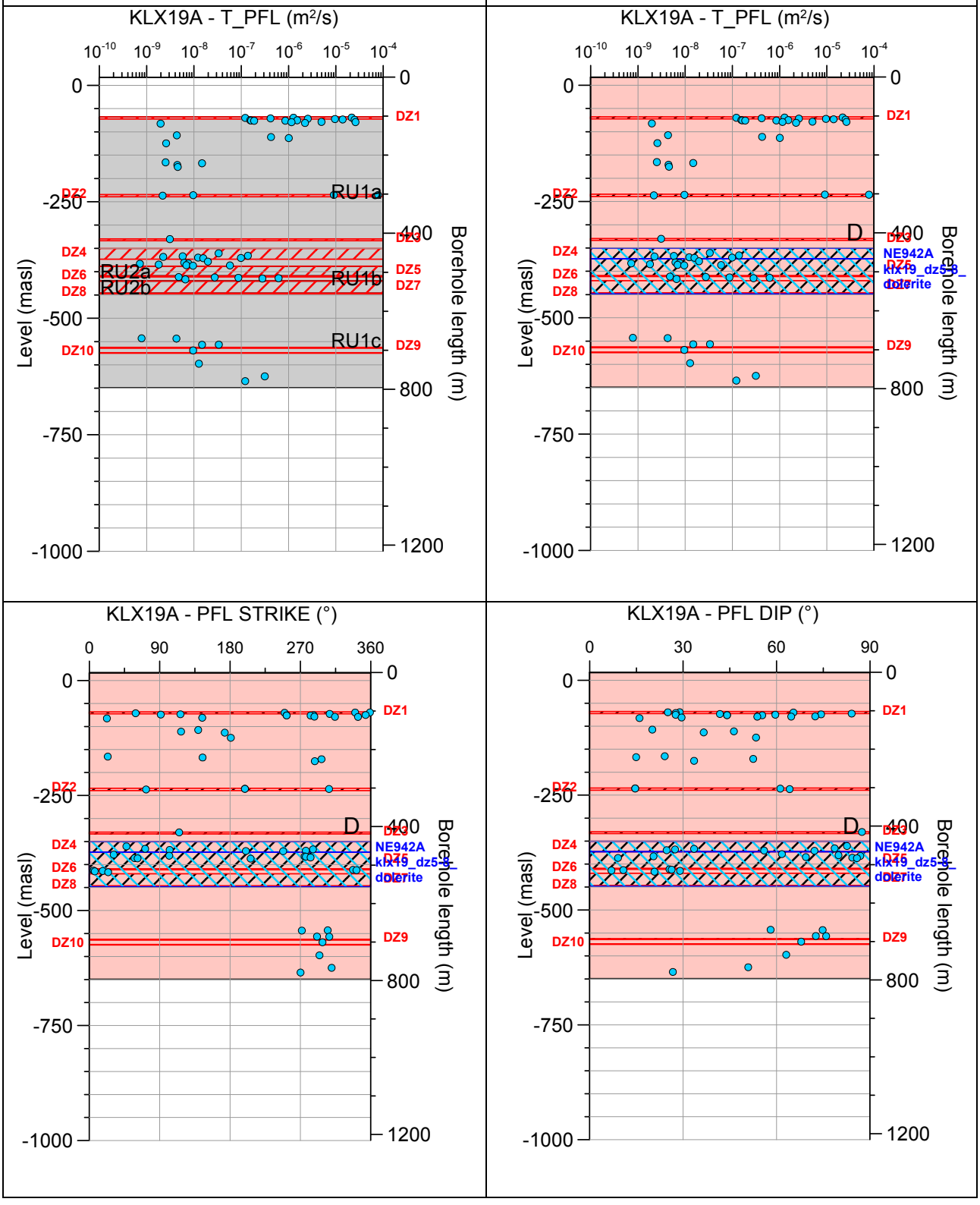

Comment:

Borehole KLX19A. Poles for PFL-f feature planes outside deformation zones.

KLX19A, HRD, ELEV.: 0 TO -1000 m

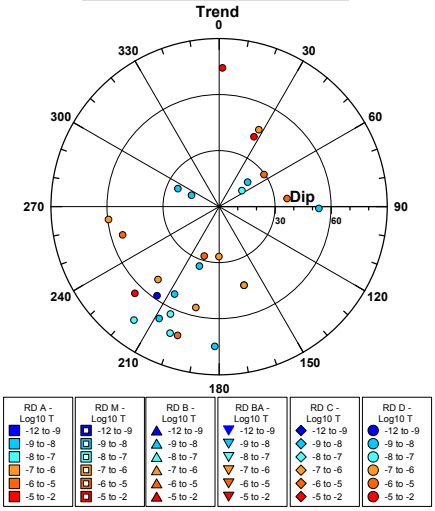

KLX19A, HRD, ELEV.: 0 TO -200 m

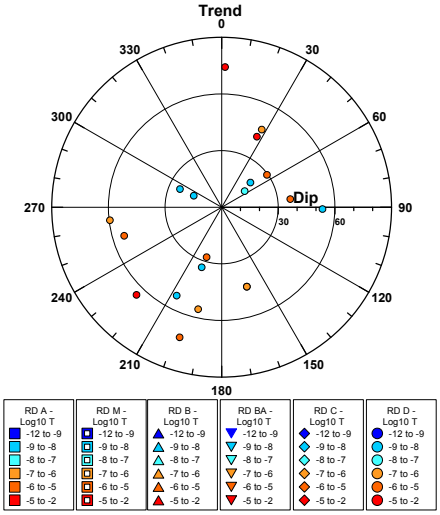

KLX19A, HRD, ELEV.: -200 TO -400 m

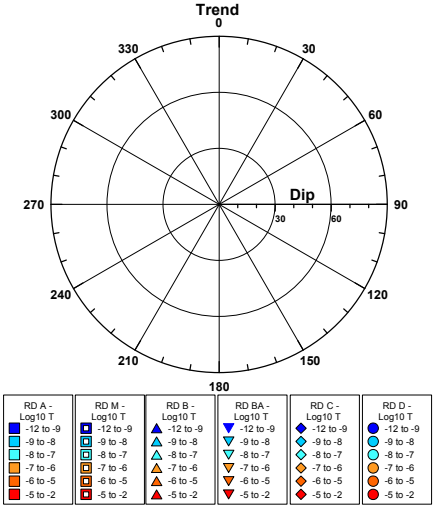

KLX19A, HRD, ELEV.: -400 TO -600 m

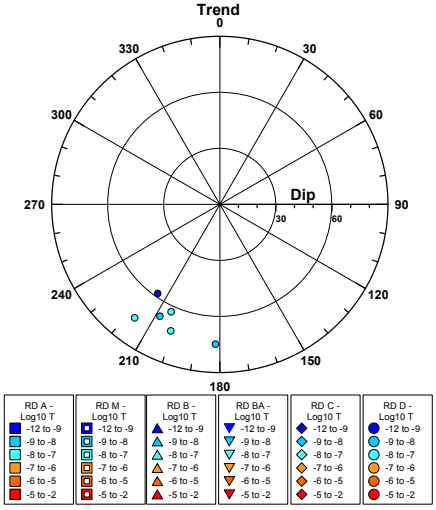

KLX19A, HRD, ELEV.: -600 TO -800 m

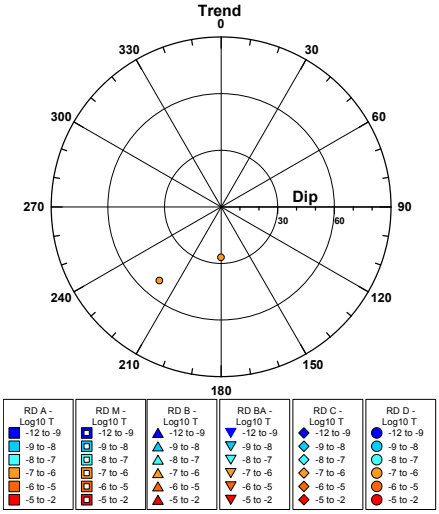

Borehole KLX19A. Poles for PFL-f feature planes in possible deformation zones.

KLX19A, DZ(ESHI), ELEV.: 0 TO -1000 m

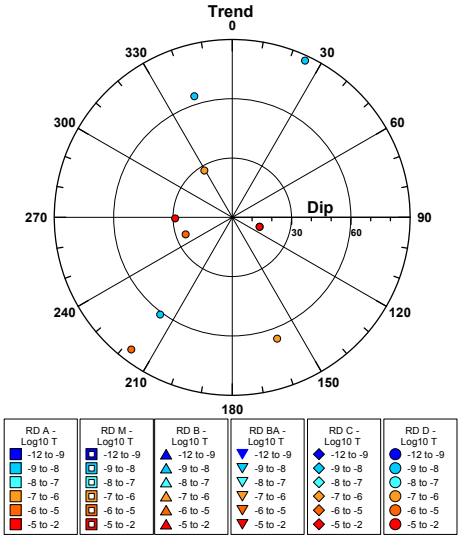

KLX19A, DZ(ESHI), ELEV.: 0 TO -200 m

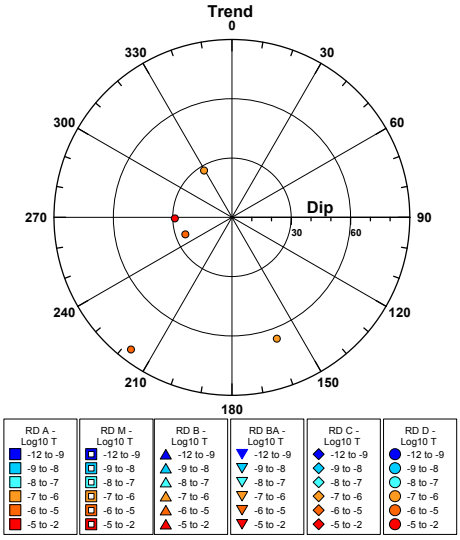

KLX19A, DZ(ESHI), ELEV.: -200 TO -400 m

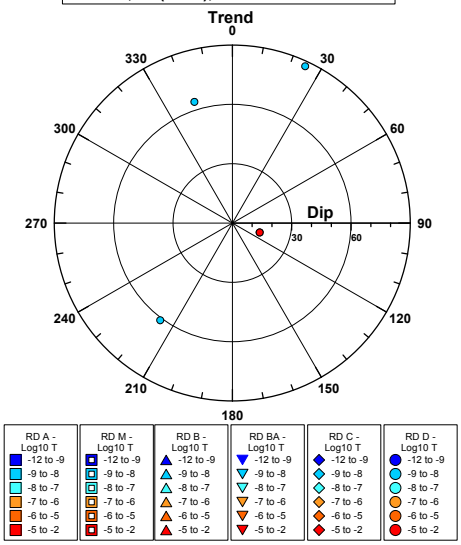

Borehole KLX19A. Poles for PFL-f feature planes in deterministically modelled deformation zones.

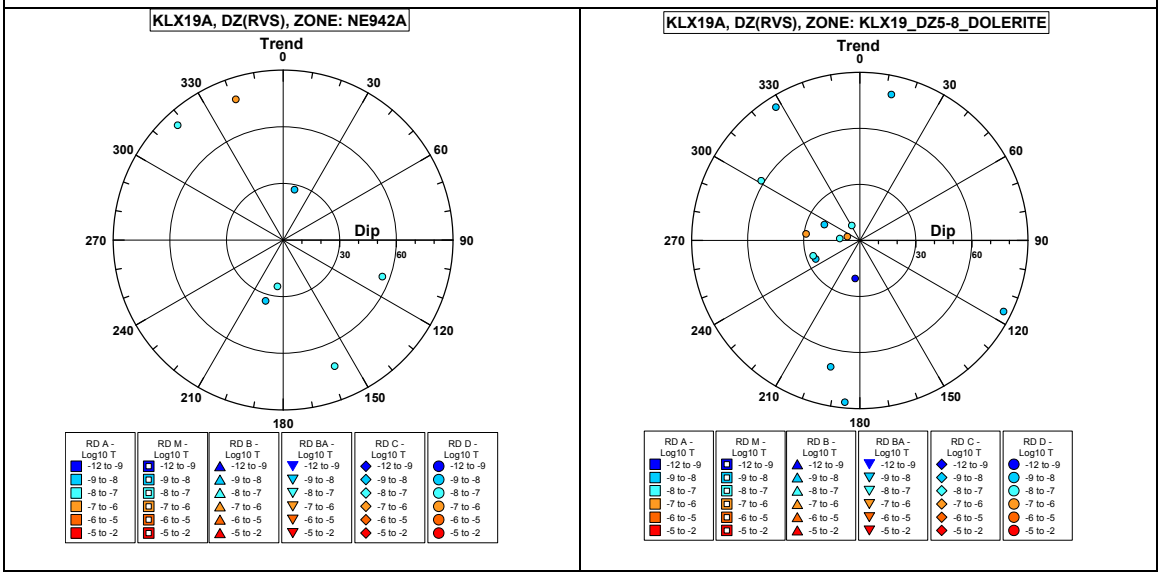

Borehole KLX20A.

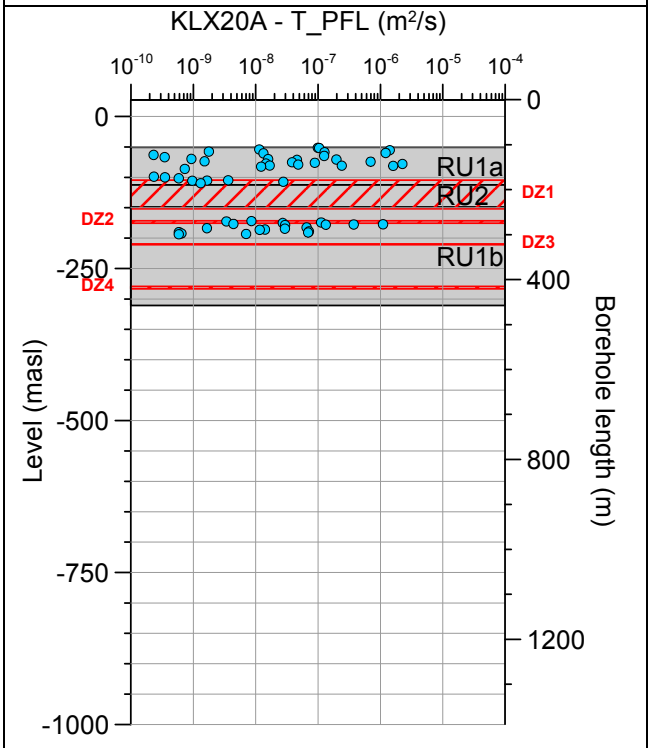

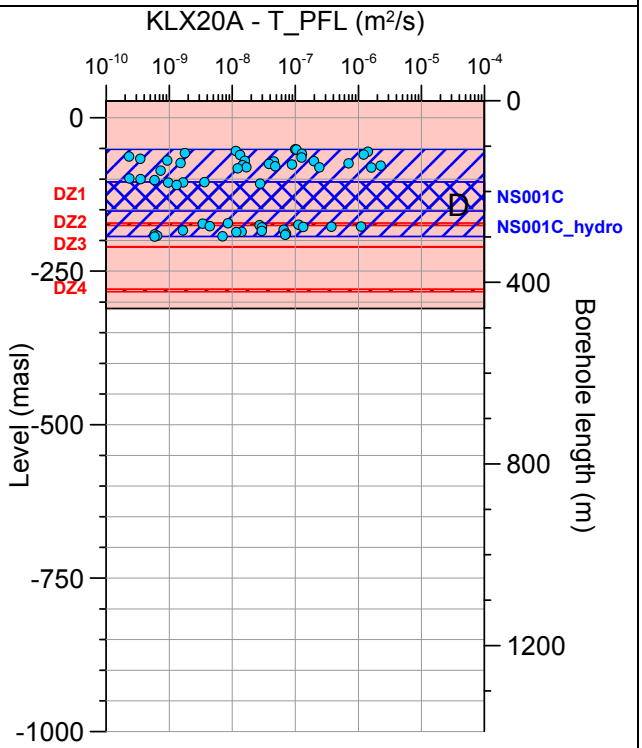

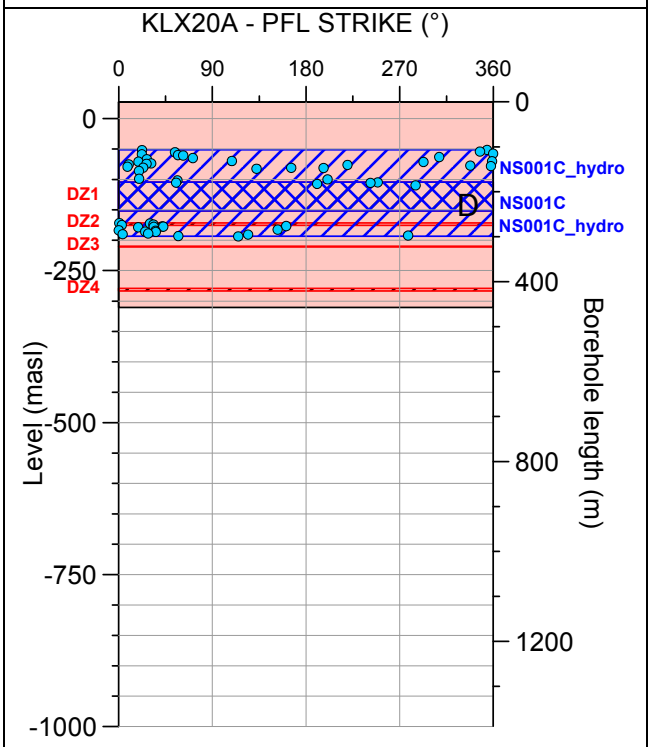

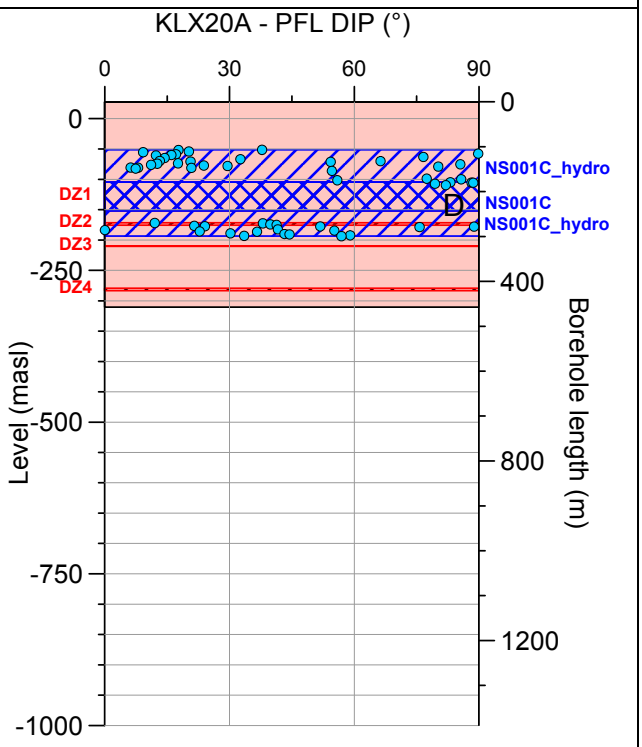

Comment:

Borehole KLX20A. Poles for PFL-f feature planes outside deformation zones.

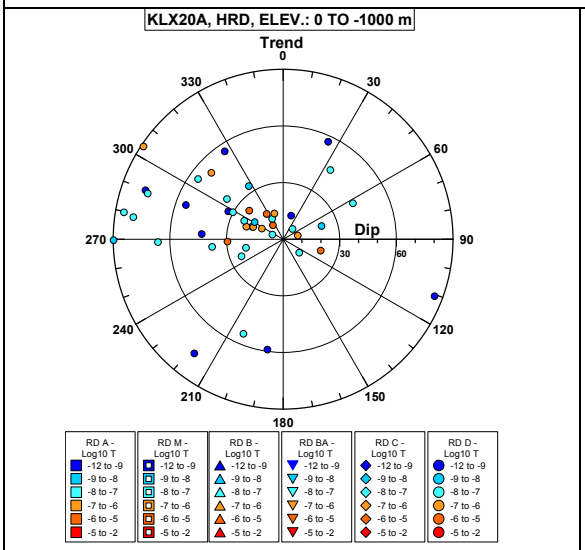

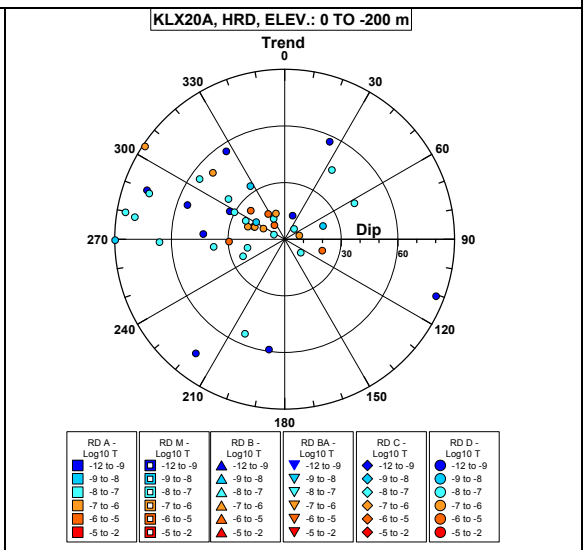

Borehole KLX20A. Poles for PFL-f feature planes in possible deformation zones.

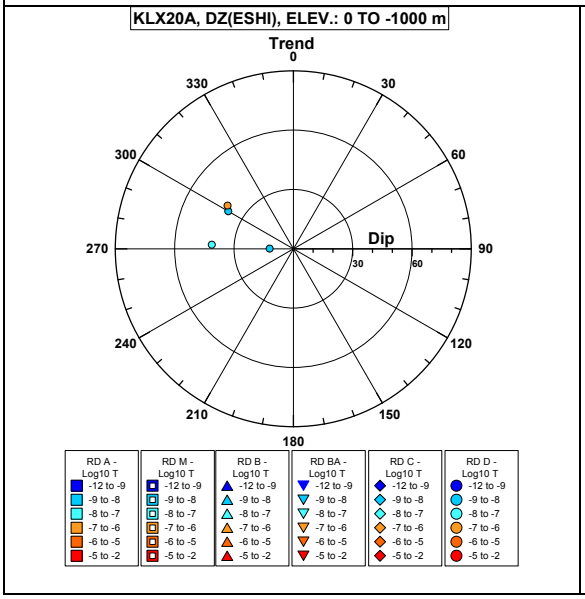

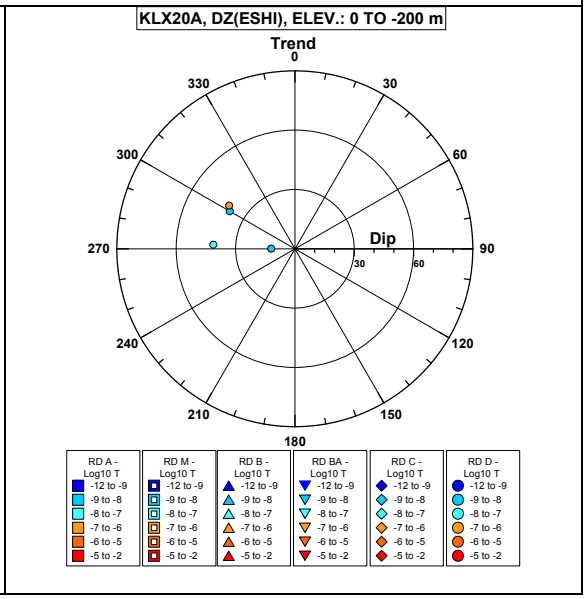

Borehole KLX20A. Poles for PFL-f feature planes in deterministically modelled deformation zones.

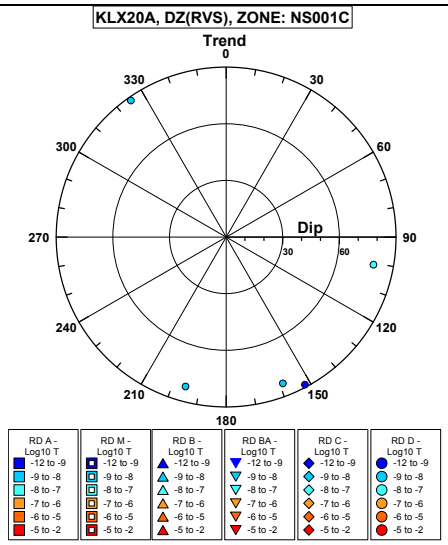

Borehole KLX21B.

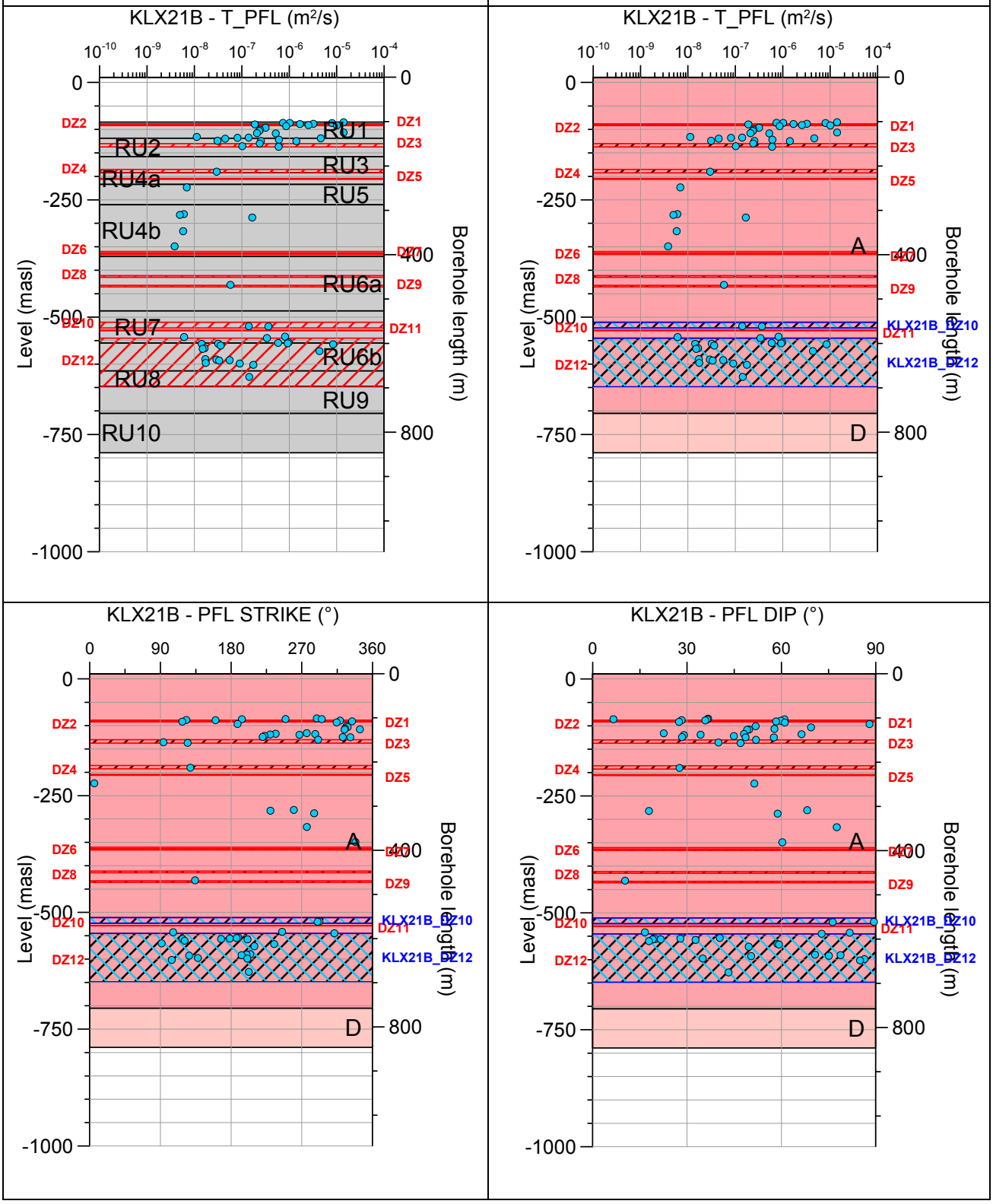

Comment:

Borehole KLX21B. Poles for PFL-f feature planes outside deformation zones.

KLX21B, HRD, ELEV.: 0 TO -1000 m

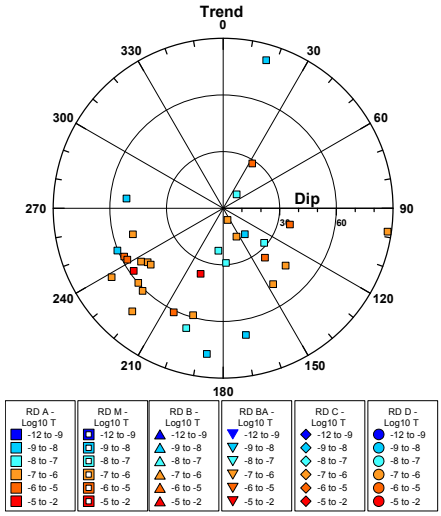

KLX21B, HRD, ELEV.: 0 TO -200 m

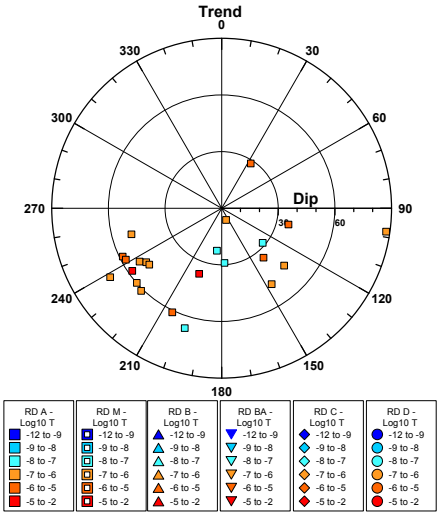

KLX21B, HRD, ELEV.: -200 TO -400 m

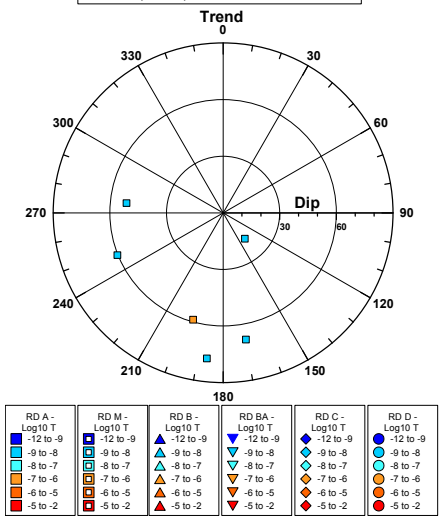

KLX21B, HRD, ELEV.: -400 TO -600 m

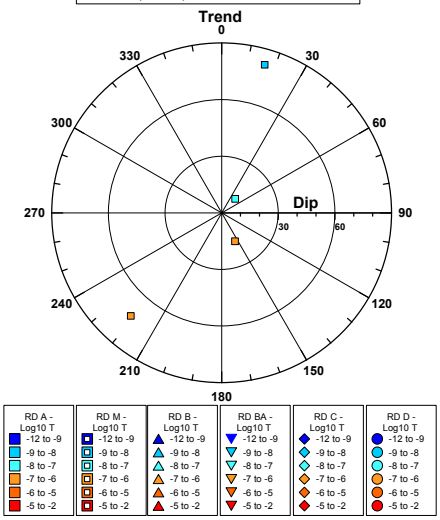

Borehole KLX21B. Poles for PFL-f feature planes in possible deformation zones.

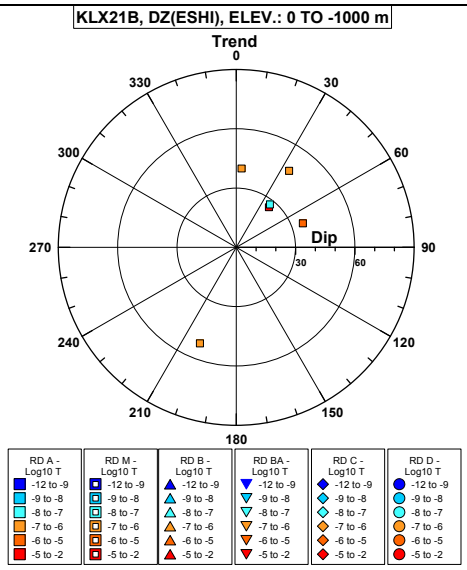

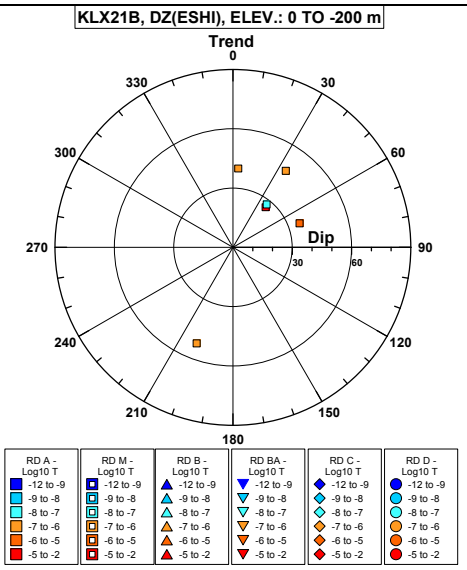

Borehole KLX21B. Poles for PFL-f feature planes in deterministically modelled deformation zones.

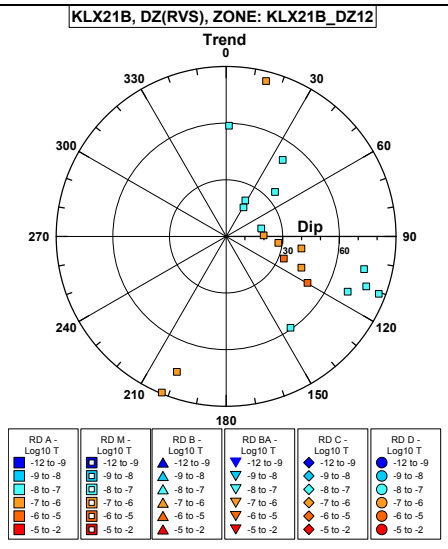

Borehole KLX22A.

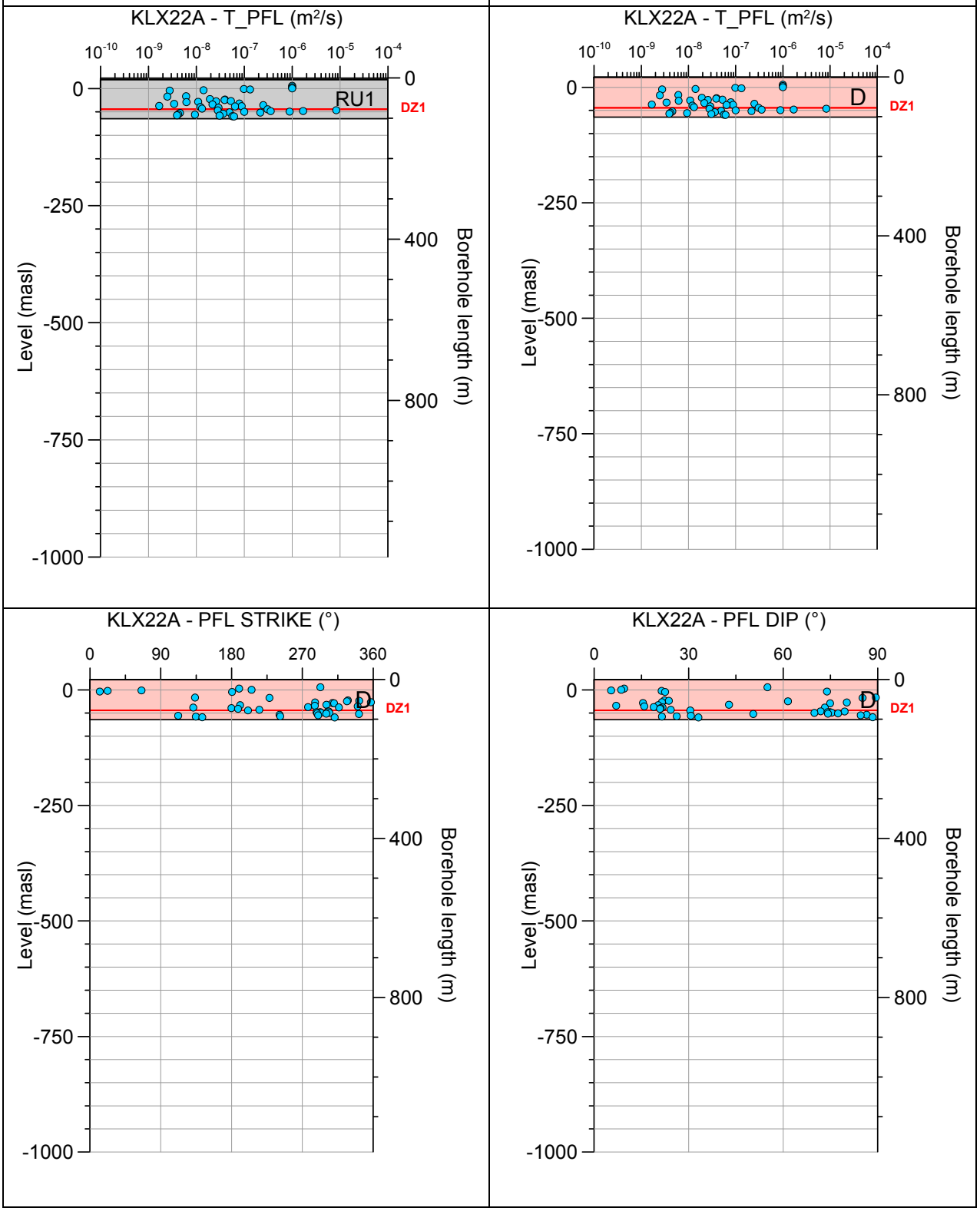

Comment:

Borehole KLX22A. Poles for PFL-f feature planes outside deformation zones.

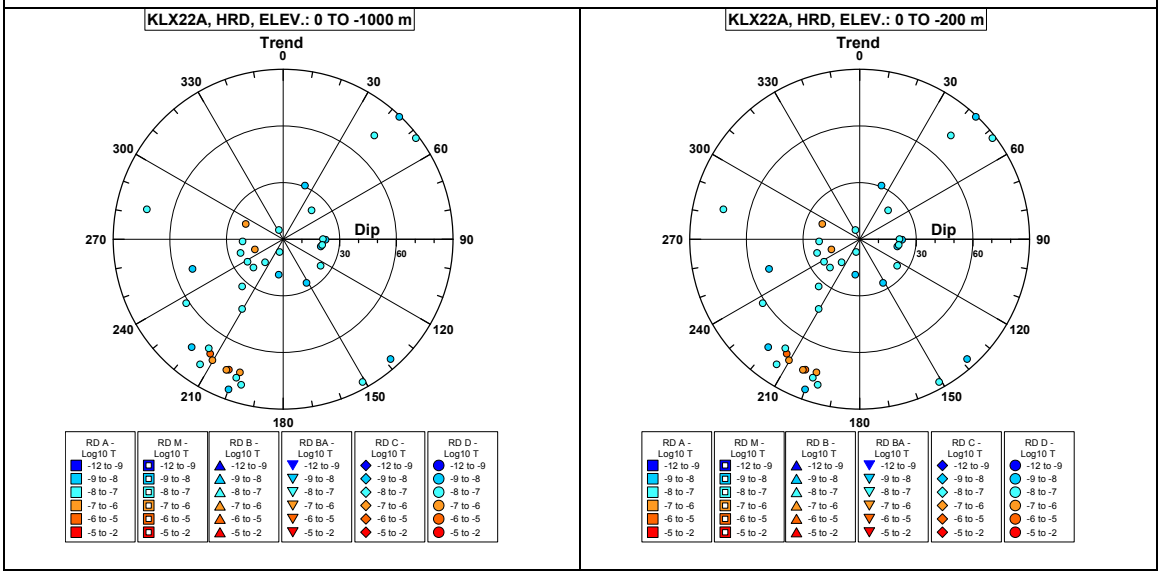

Borehole KLX22A. Poles for PFL-f feature planes in possible deformation zones.

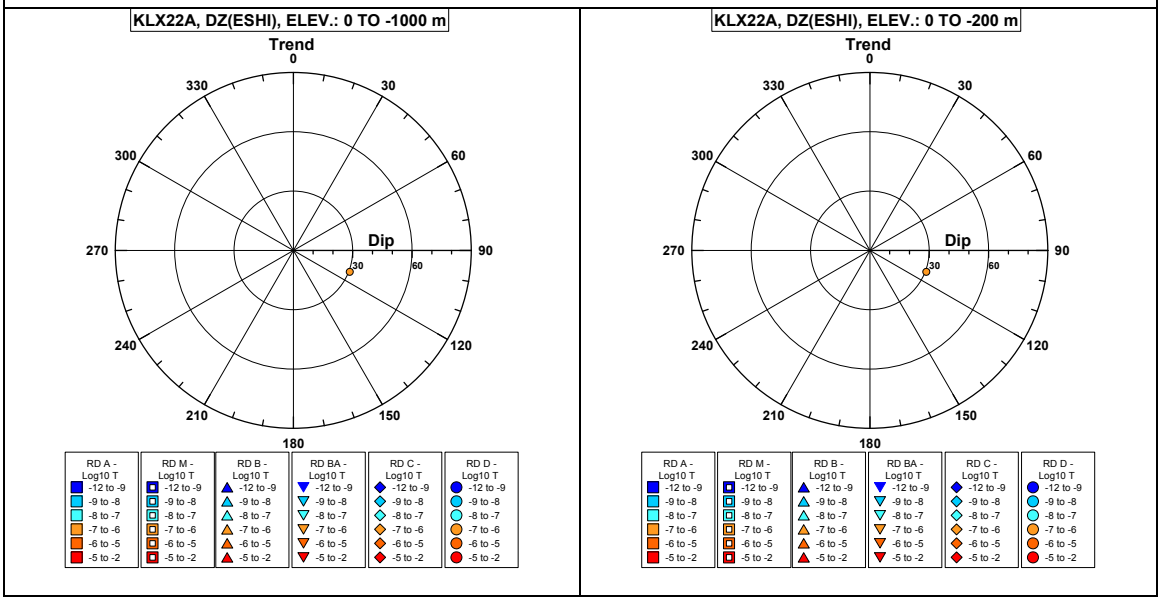

No PFL-f feature planes in deterministically modelled deformation zones exist in KLX22A.

Borehole KLX22B.

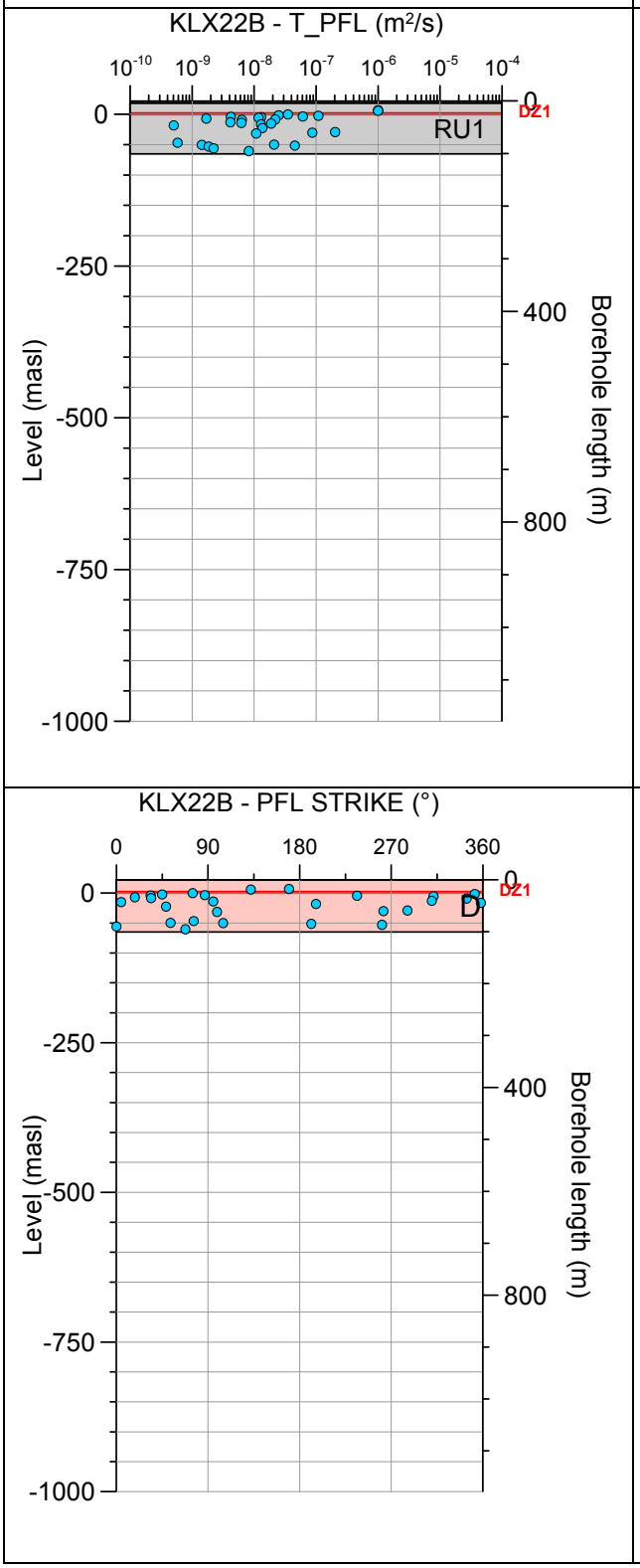

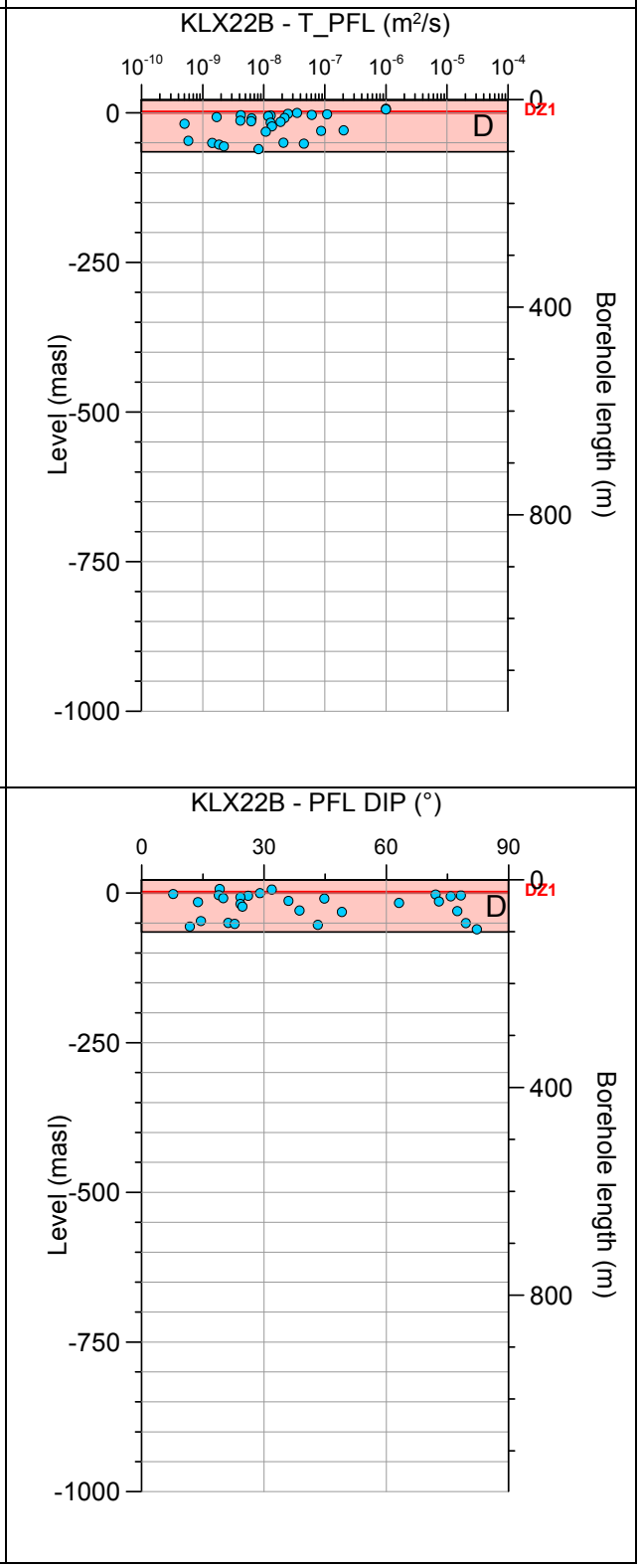

Comment:

Borehole KLX22B. Poles for PFL-f feature planes outside deformation zones.

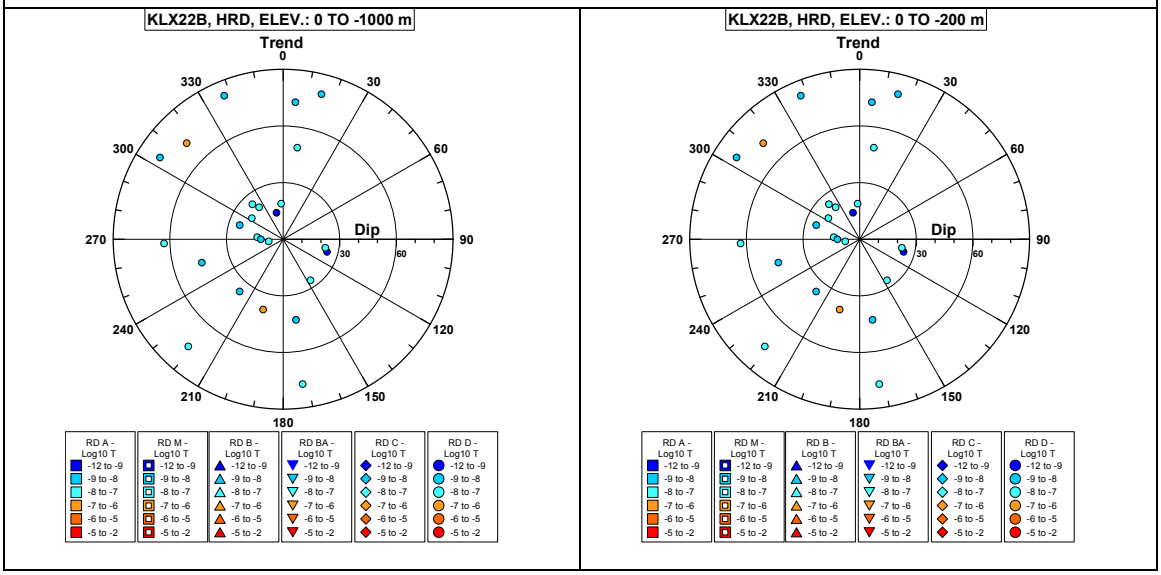

Borehole KLX22B. Poles for PFL-f feature planes in possible deformation zones.

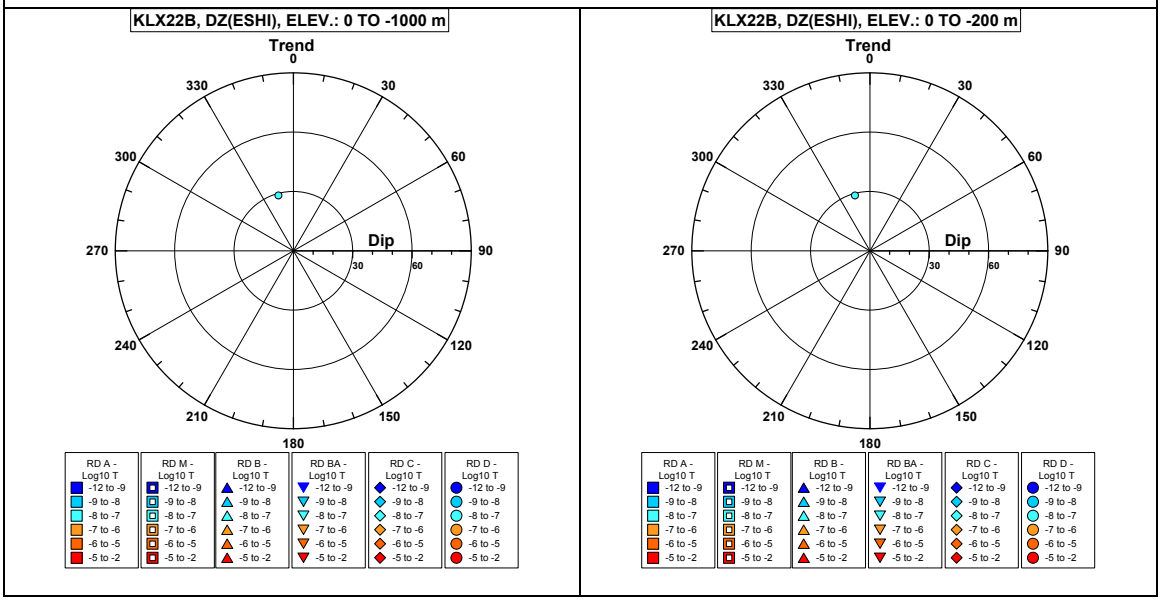

No PFL-f feature planes in deterministically modelled deformation zones exist in KLX22B.

Borehole KLX23A.

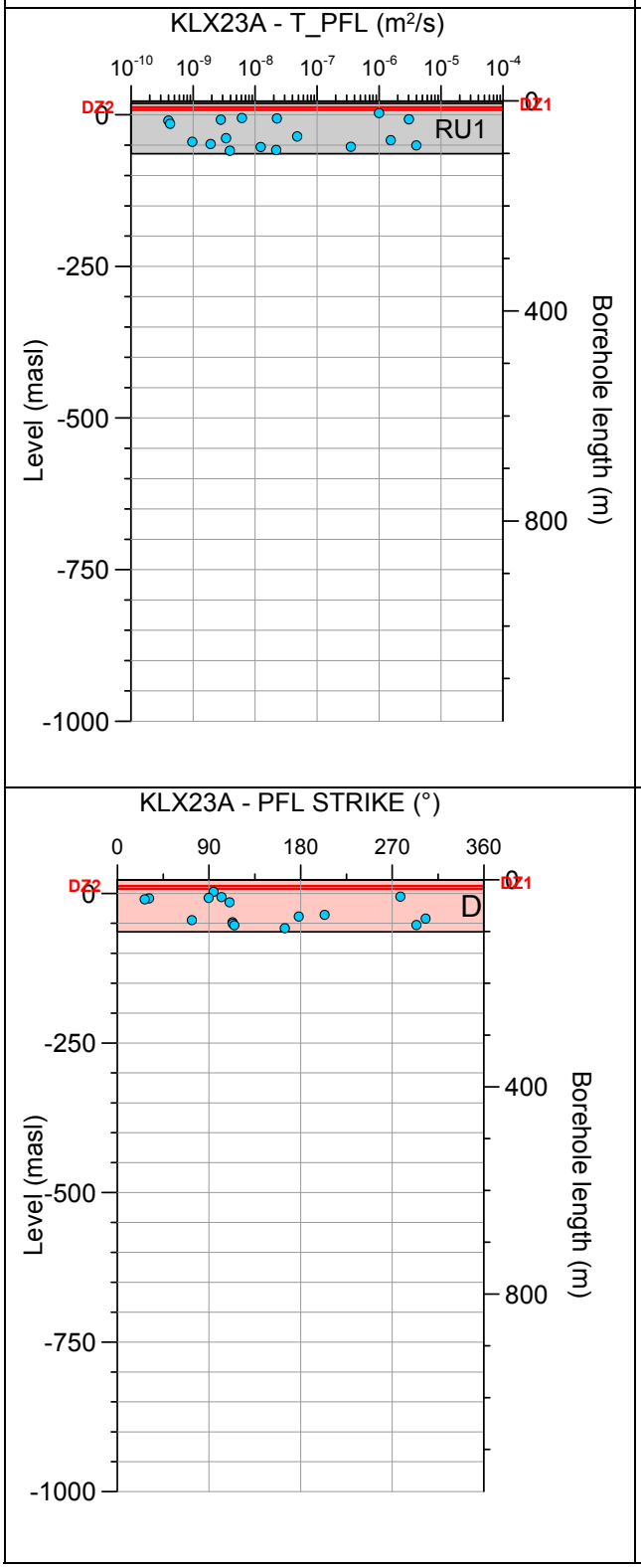

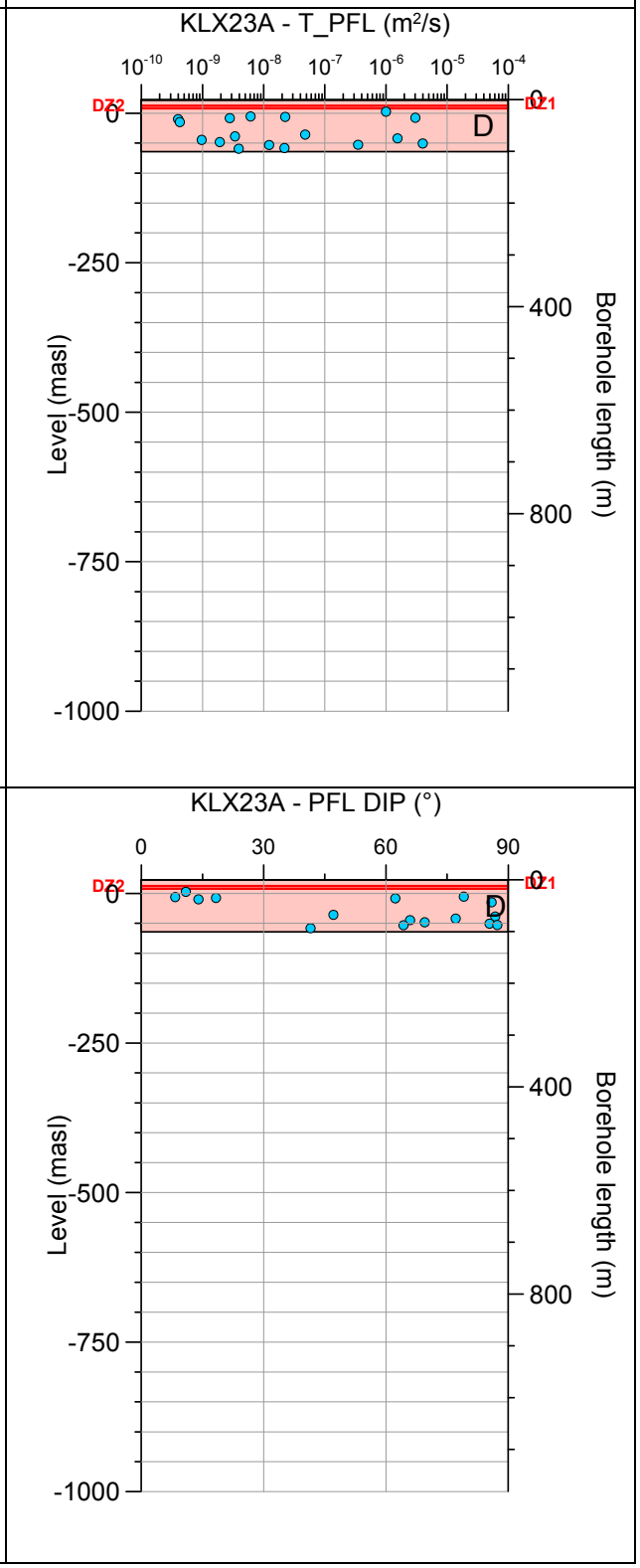

Comment:

Borehole KLX23A. Poles for PFL-f feature planes outside deformation zones.

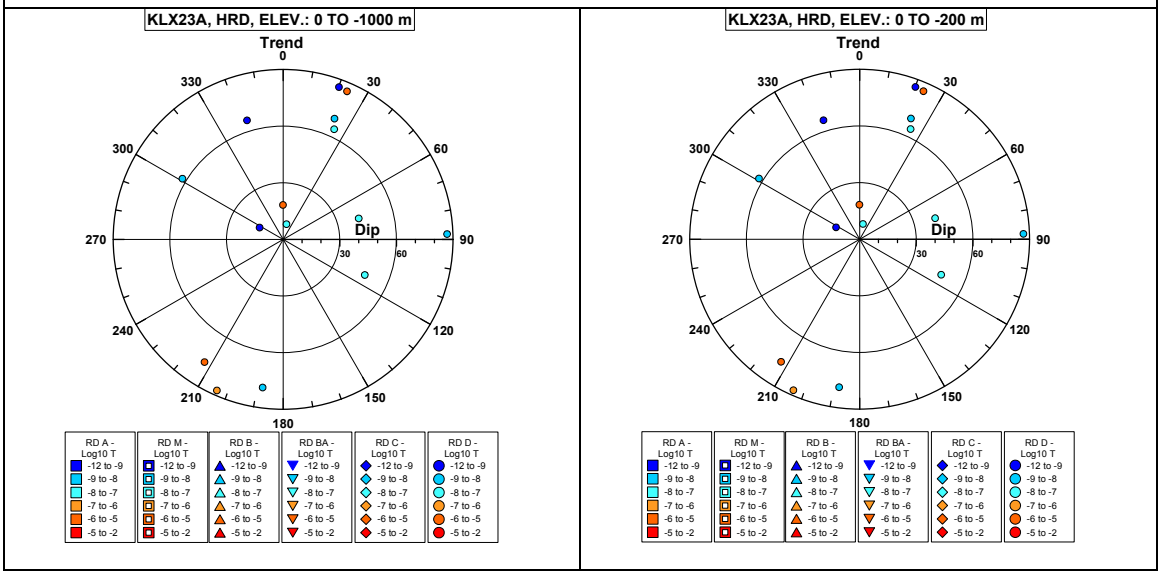

No PFL-f feature planes in possible deformation zones exist in KLX23A.

No PFL-f feature planes in deterministically modelled deformation zones exist in KLX23A.

Borehole KLX23B.

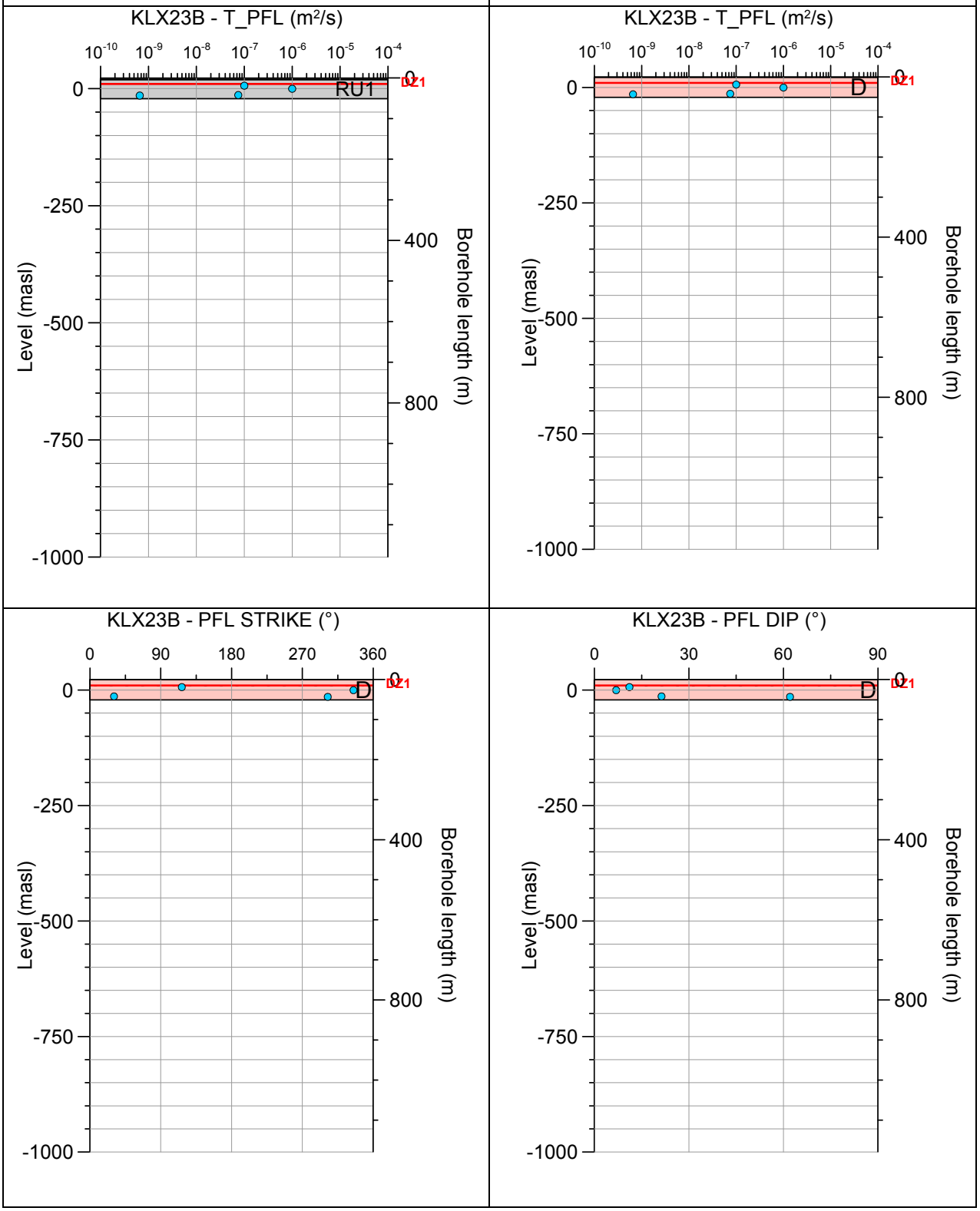

Comment:

Borehole KLX23B. Poles for PFL-f feature planes outside deformation zones.

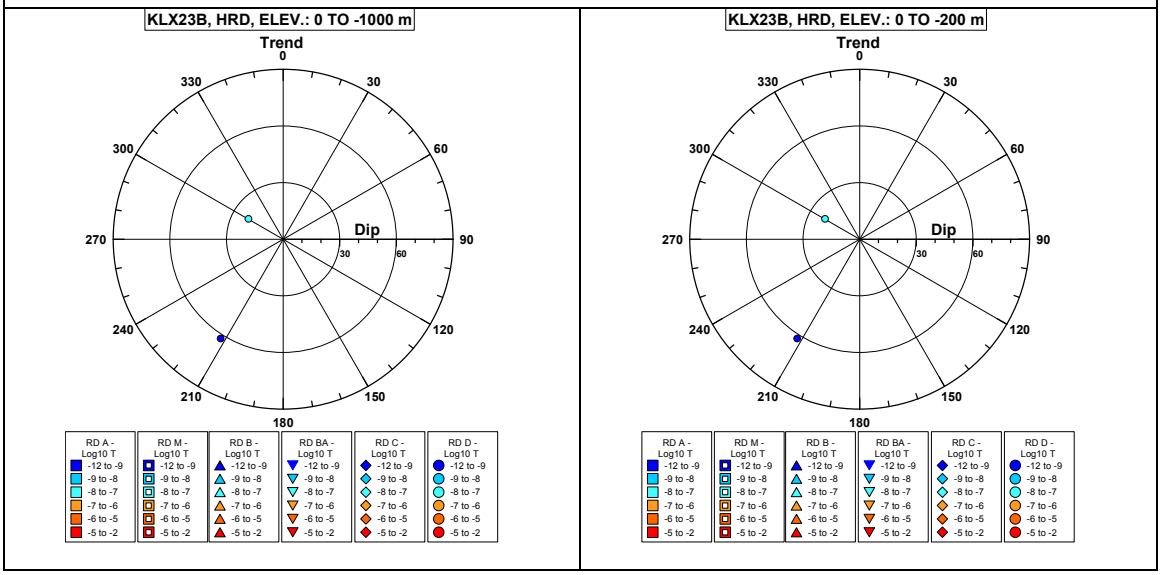

No PFL-f feature planes in possible deformation zones exist in KLX23B.

No PFL-f feature planes in deterministically modelled deformation zones exist in KLX23B.

Borehole KLX24A.

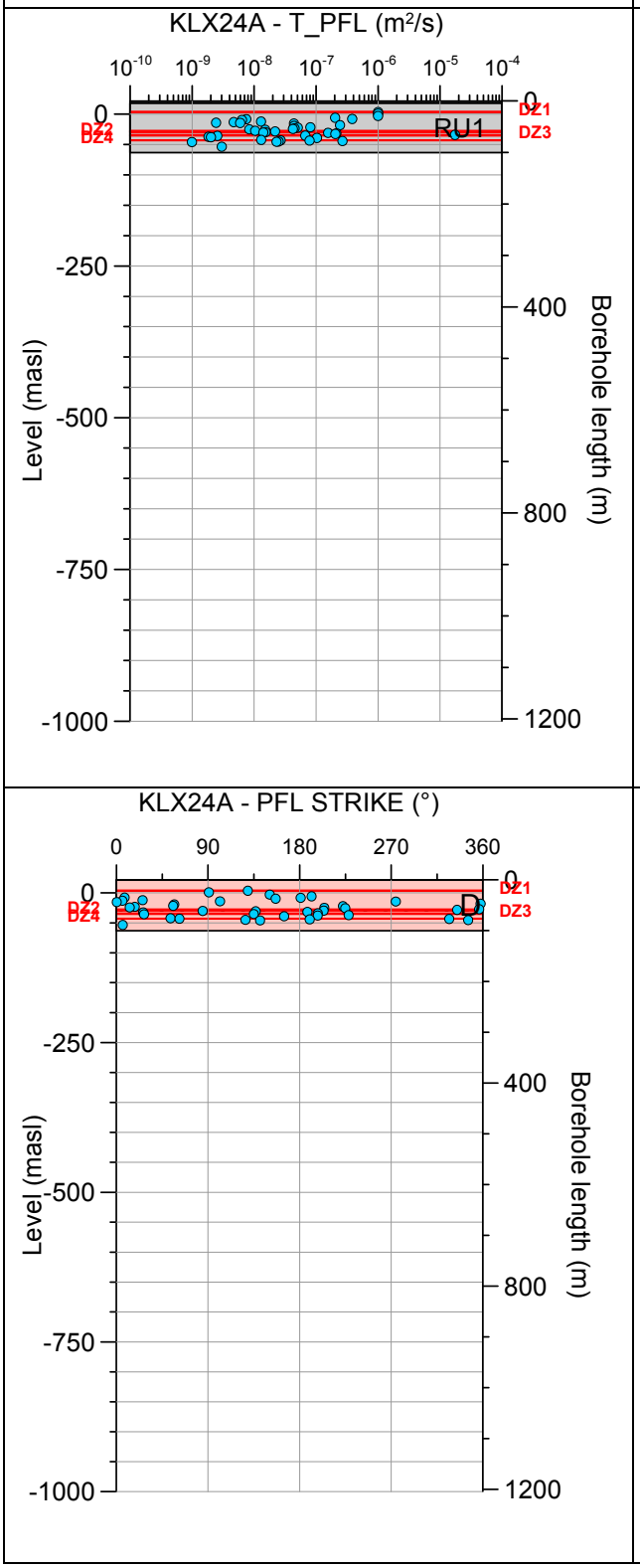

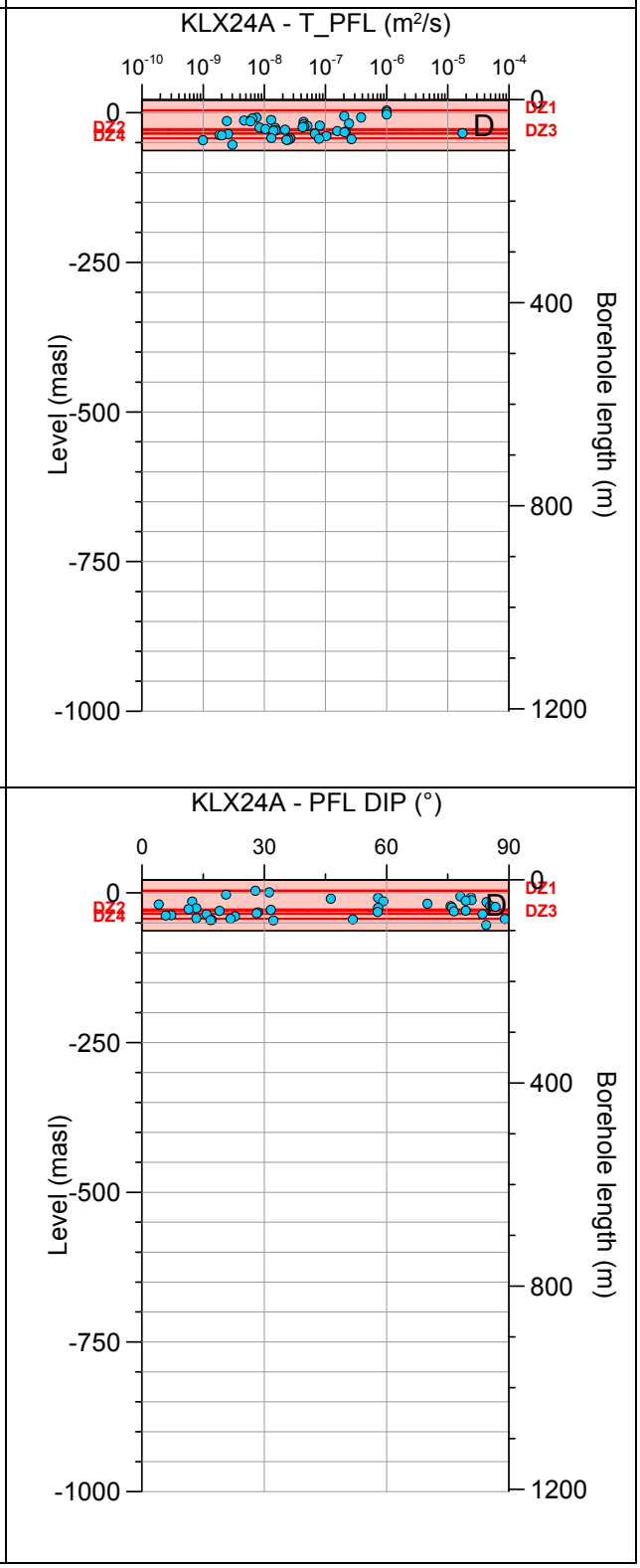

Comment:

Borehole KLX24A. Poles for PFL-f feature planes outside deformation zones.

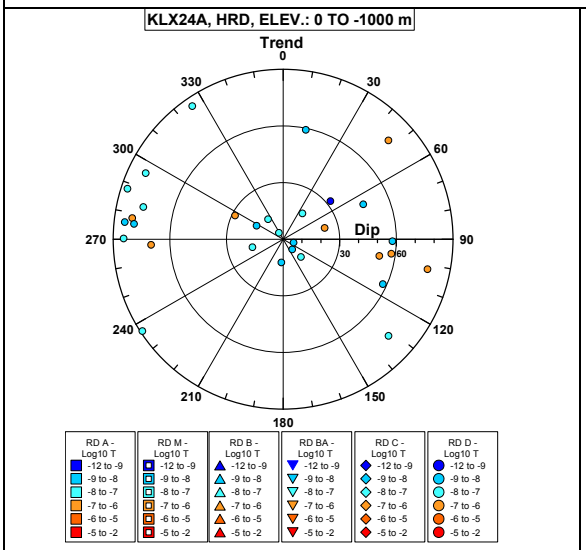

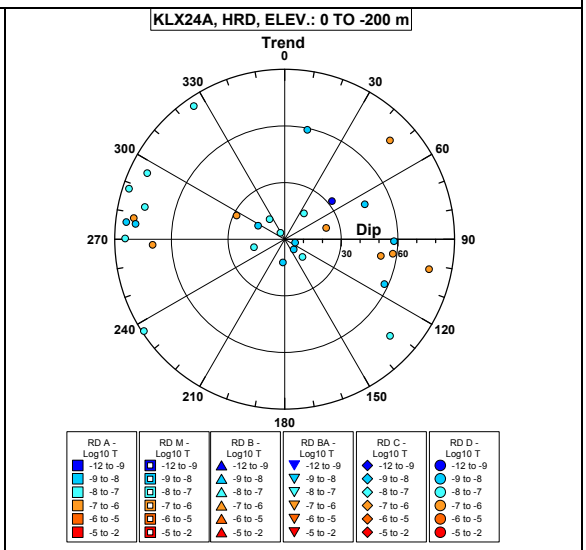

Borehole KLX24A. Poles for PFL-f feature planes in possible deformation zones.

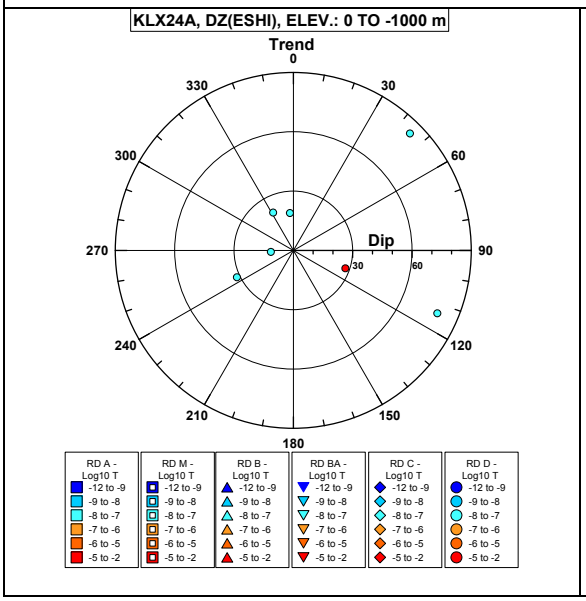

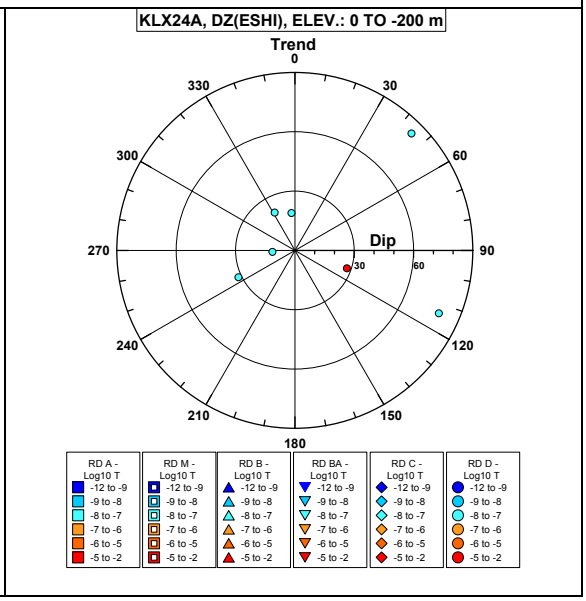

No PFL-f feature planes in deterministically modelled deformation zones exist in KLX24A.

Borehole KLX25A.

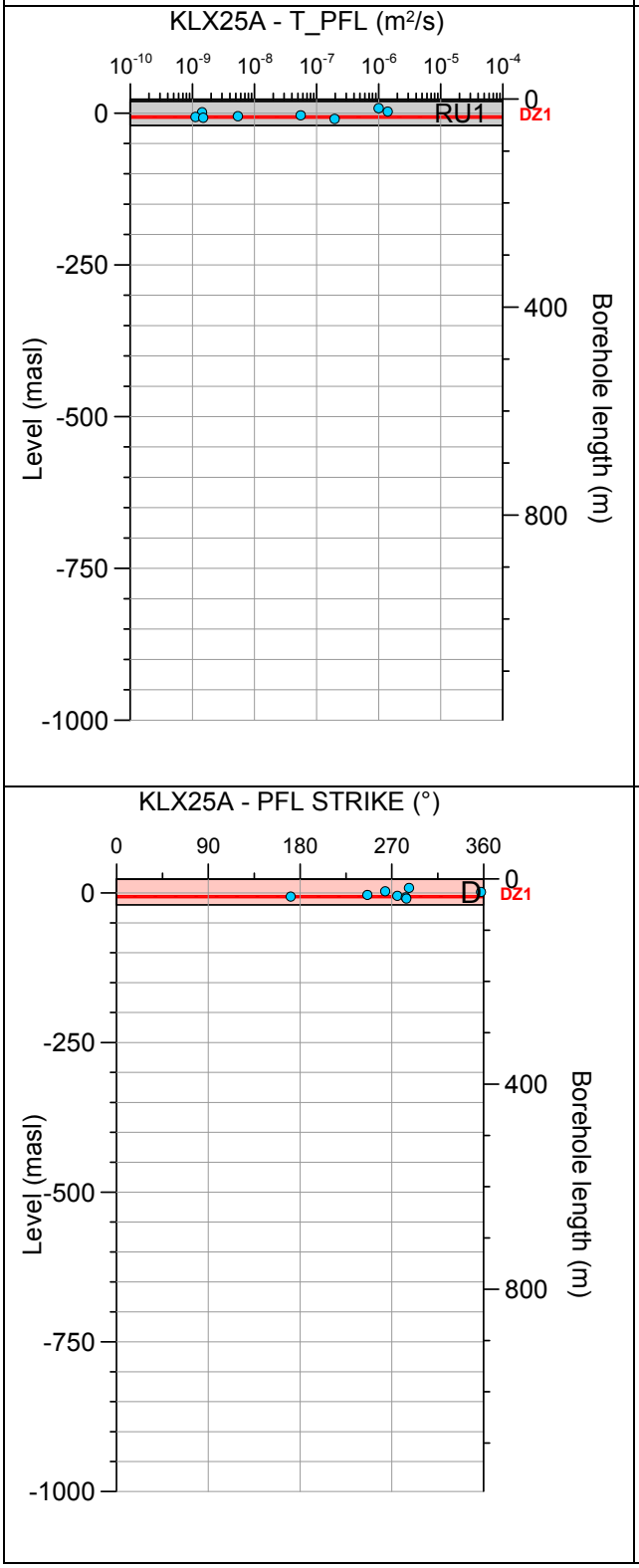

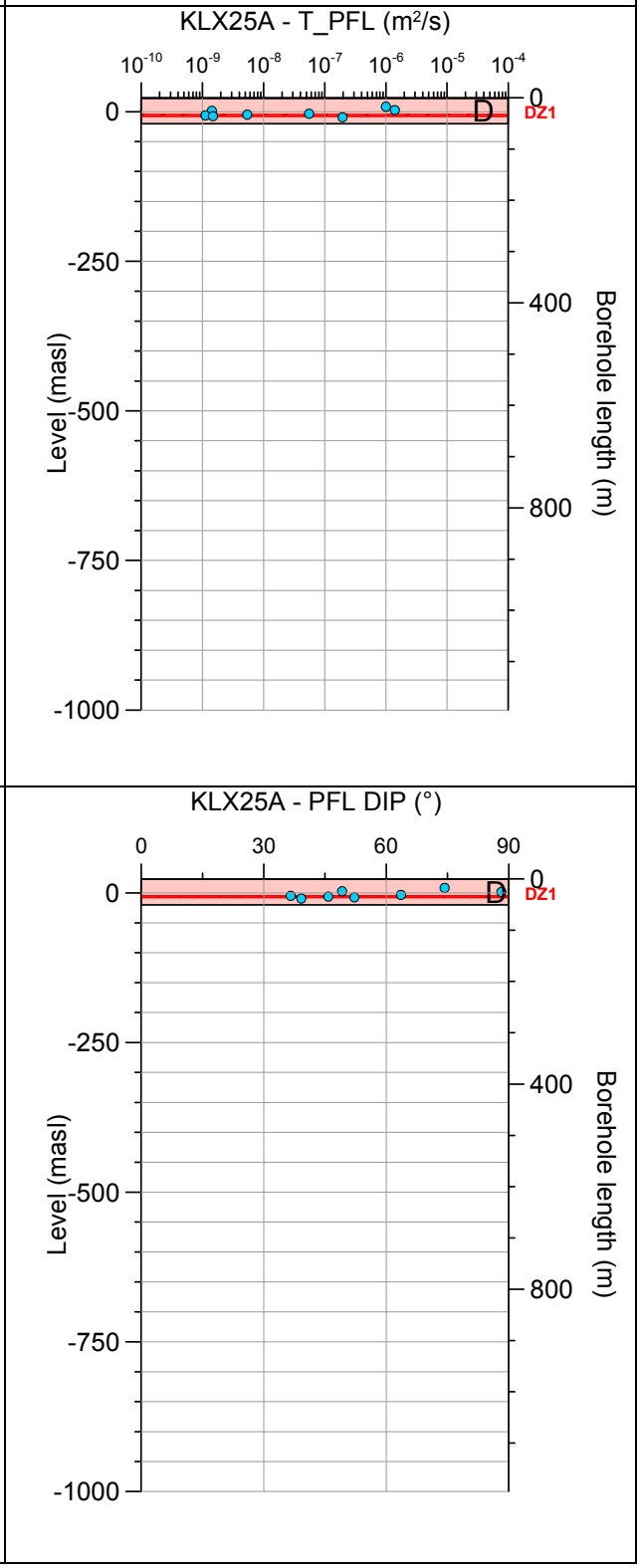

Comment:

Borehole KLX25A. Poles for PFL-f feature planes outside deformation zones.

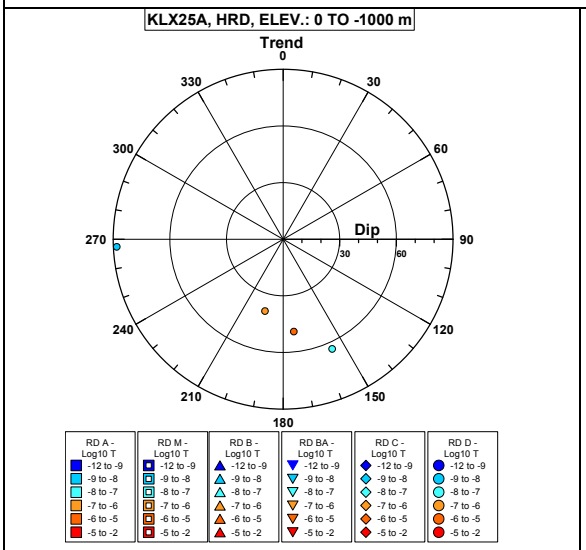

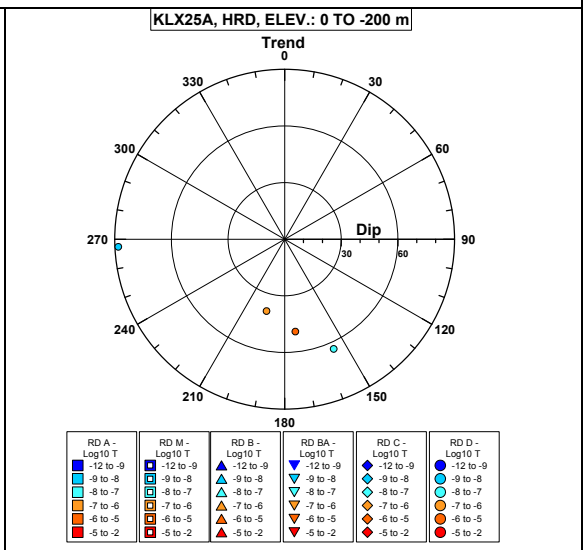

Borehole KLX25A. Poles for PFL-f feature planes in possible deformation zones.

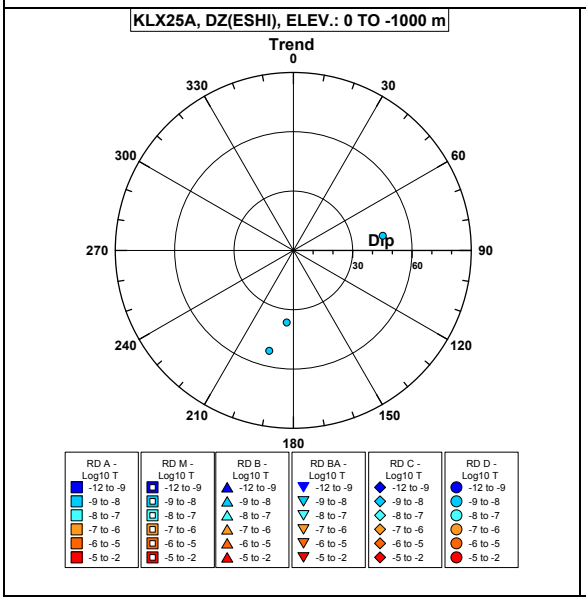

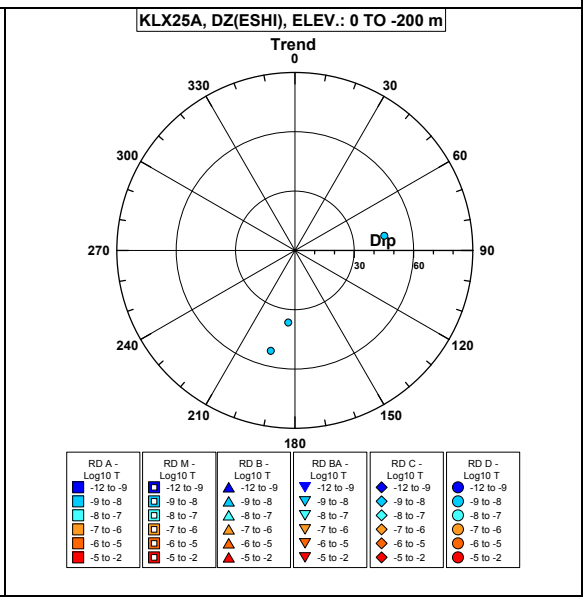

No PFL-f feature planes in deterministically modelled deformation zones exist in KLX25A.

Borehole KLX26A.

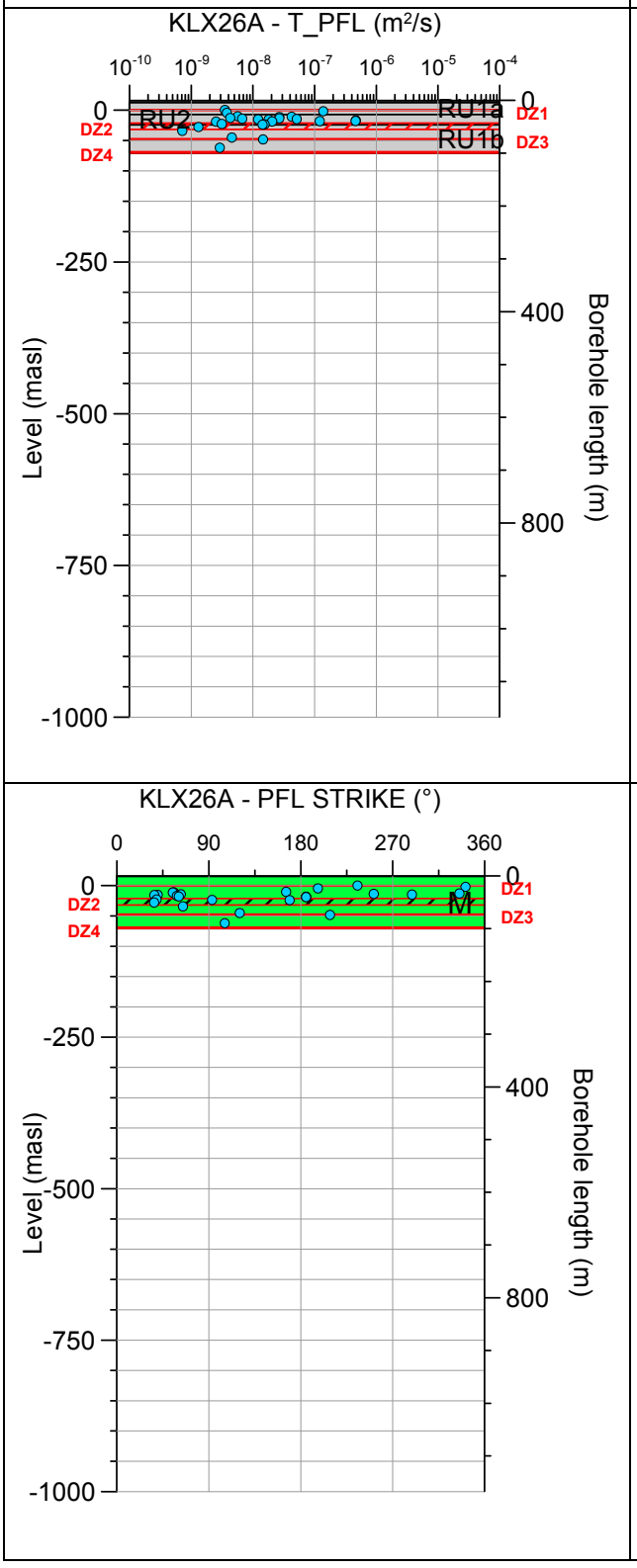

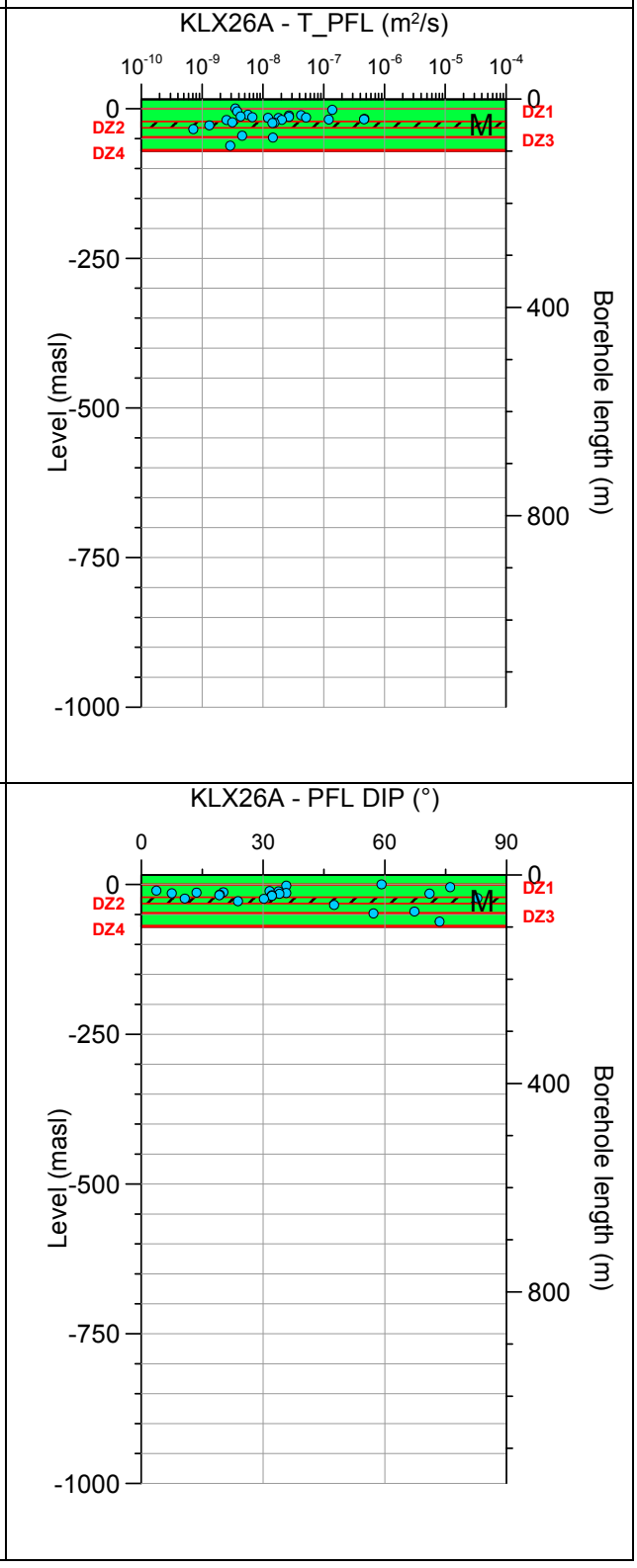

Comment:

Borehole KLX26A. Poles for PFL-f feature planes outside deformation zones.

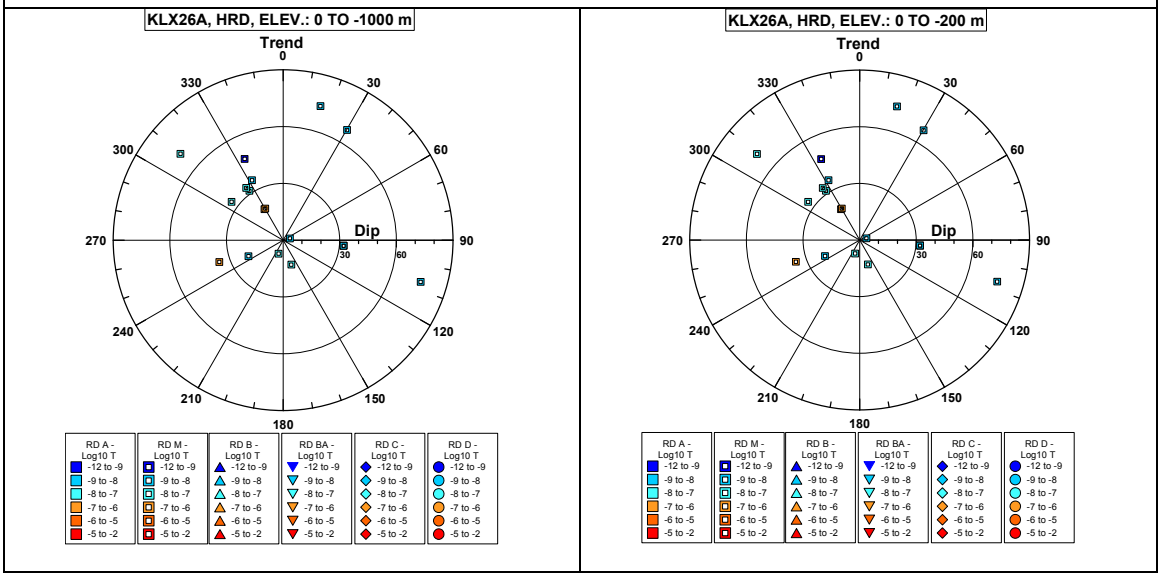

Borehole KLX26A. Poles for PFL-f feature planes in possible deformation zones.

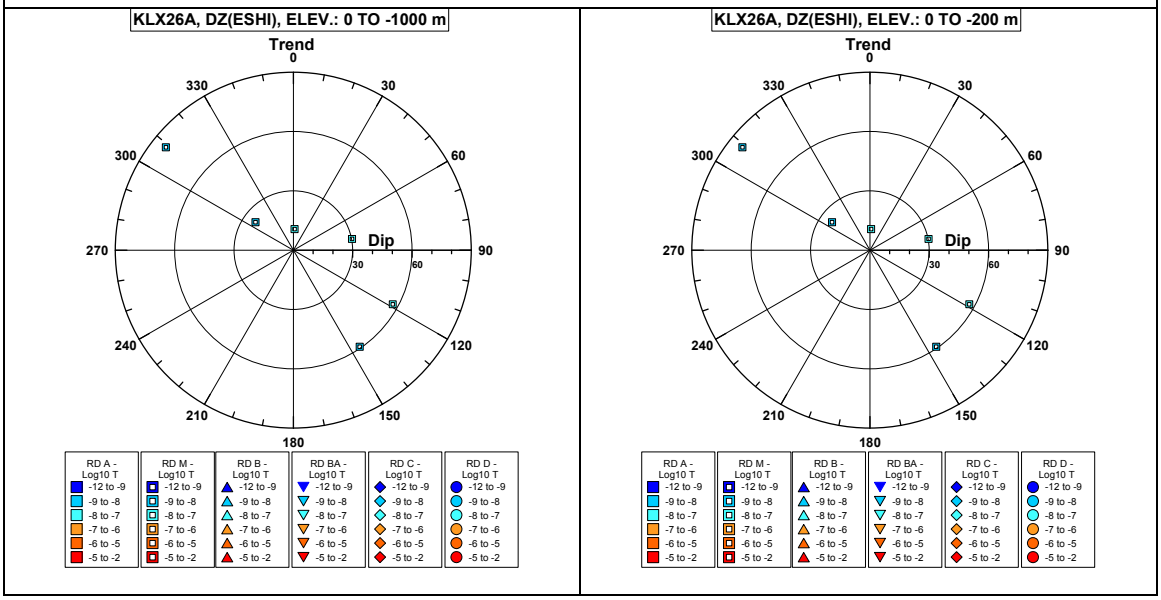

No PFL-f feature planes in deterministically modelled deformation zones exist in KLX26A.

Borehole KLX26B.

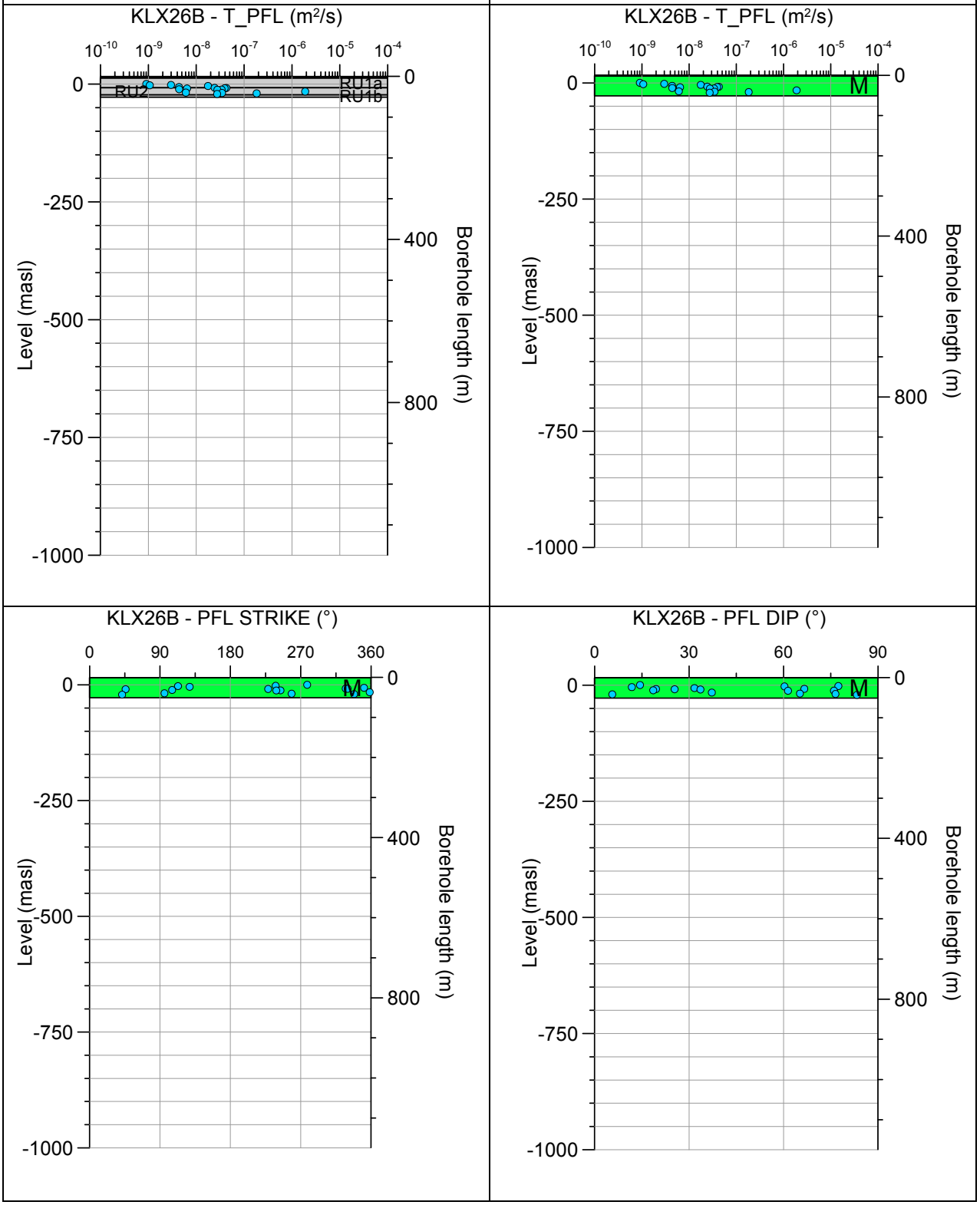

Comment:

Borehole KLX26B. Poles for PFL-f feature planes outside deformation zones.

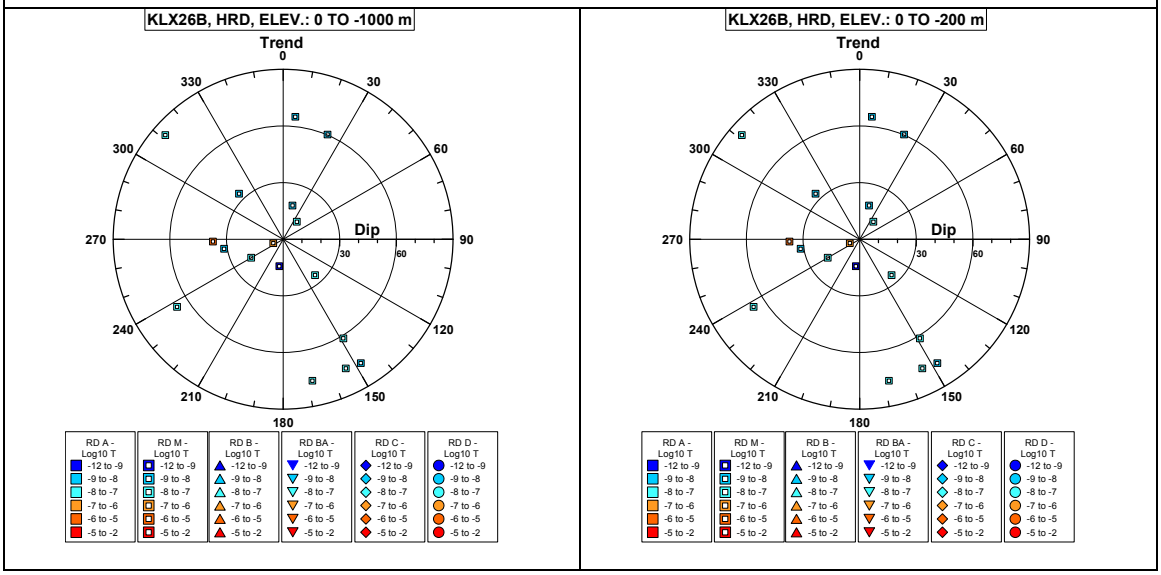

No PFL-f feature planes in possible deformation zones exist in KLX26B.

No PFL-f feature planes in deterministically modelled deformation zones exist in KLX26B.

Borehole KLX27A.

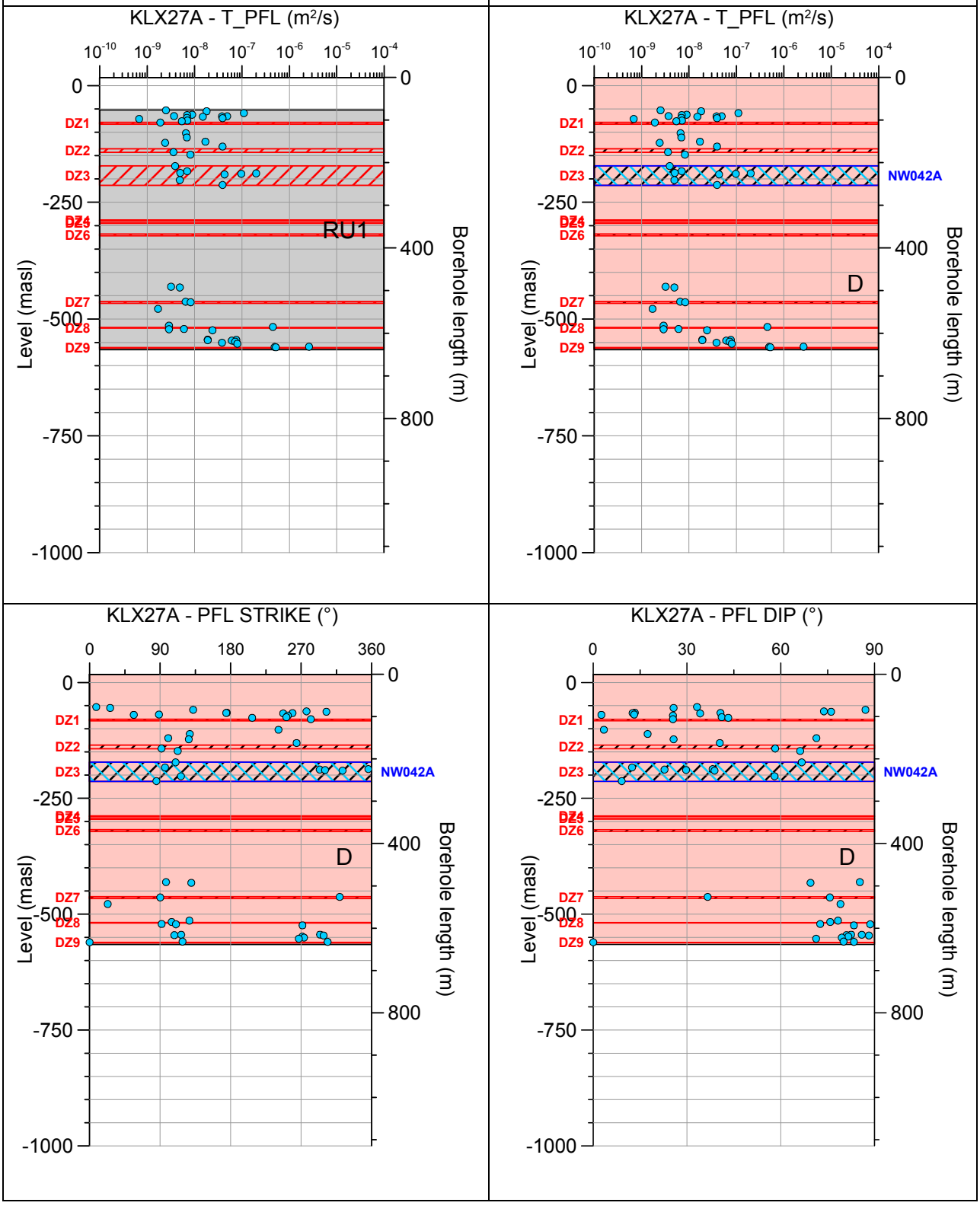

Comment:

Borehole KLX27A. Poles for PFL-f feature planes outside deformation zones.

KLX27A, HRD, ELEV.: 0 TO -1000 m

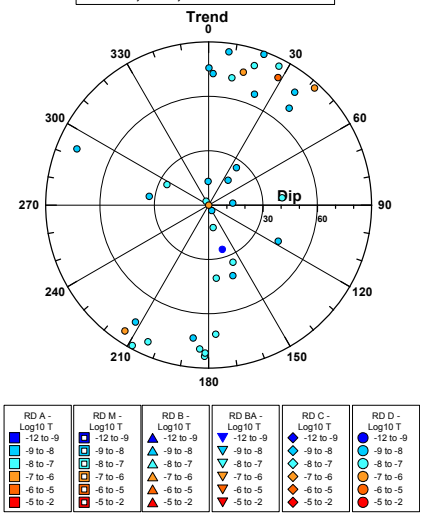

KLX27A, HRD, ELEV.: 0 TO -200 m

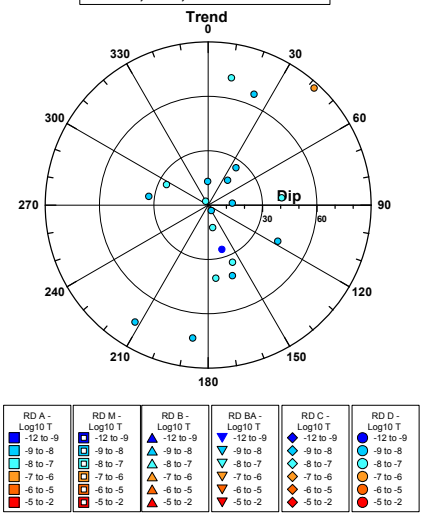

KLX27A, HRD, ELEV.: -400 TO -600 m

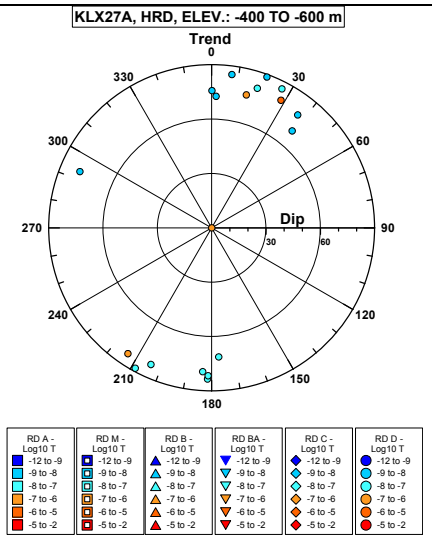

Borehole KLX27A. Poles for PFL-f feature planes in possible deformation zones.

KLX27A, DZ(ESHI), ELEV.: 0 TO -1000 m

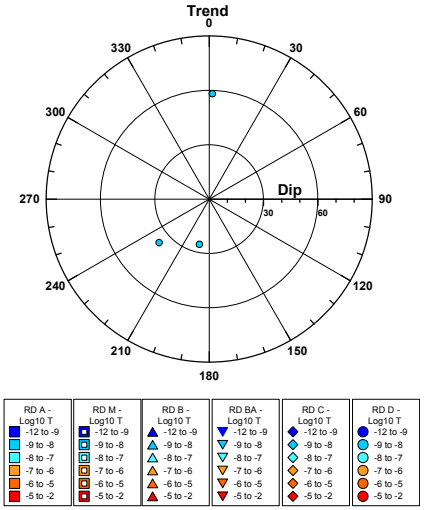

KLX27A, DZ(ESHI), ELEV.: 0 TO -200 m

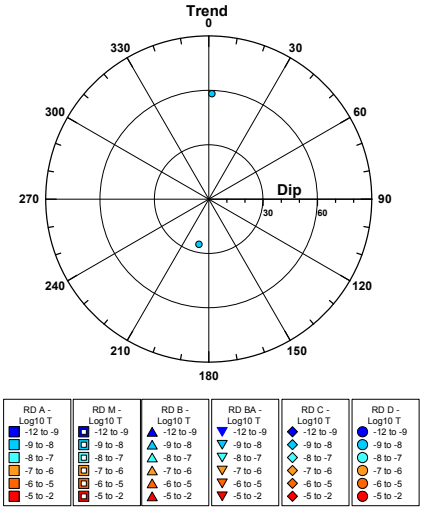

KLX27A, DZ(ESHI), ELEV.: -400 TO -600 m

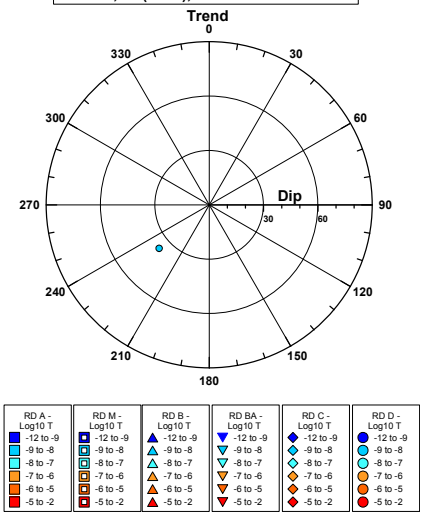

Borehole KLX27A. Poles for PFL-f feature planes in deterministically modelled deformation zones.

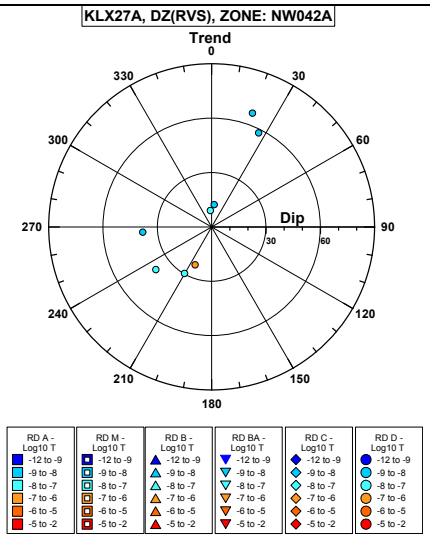

Borehole KLX28A.

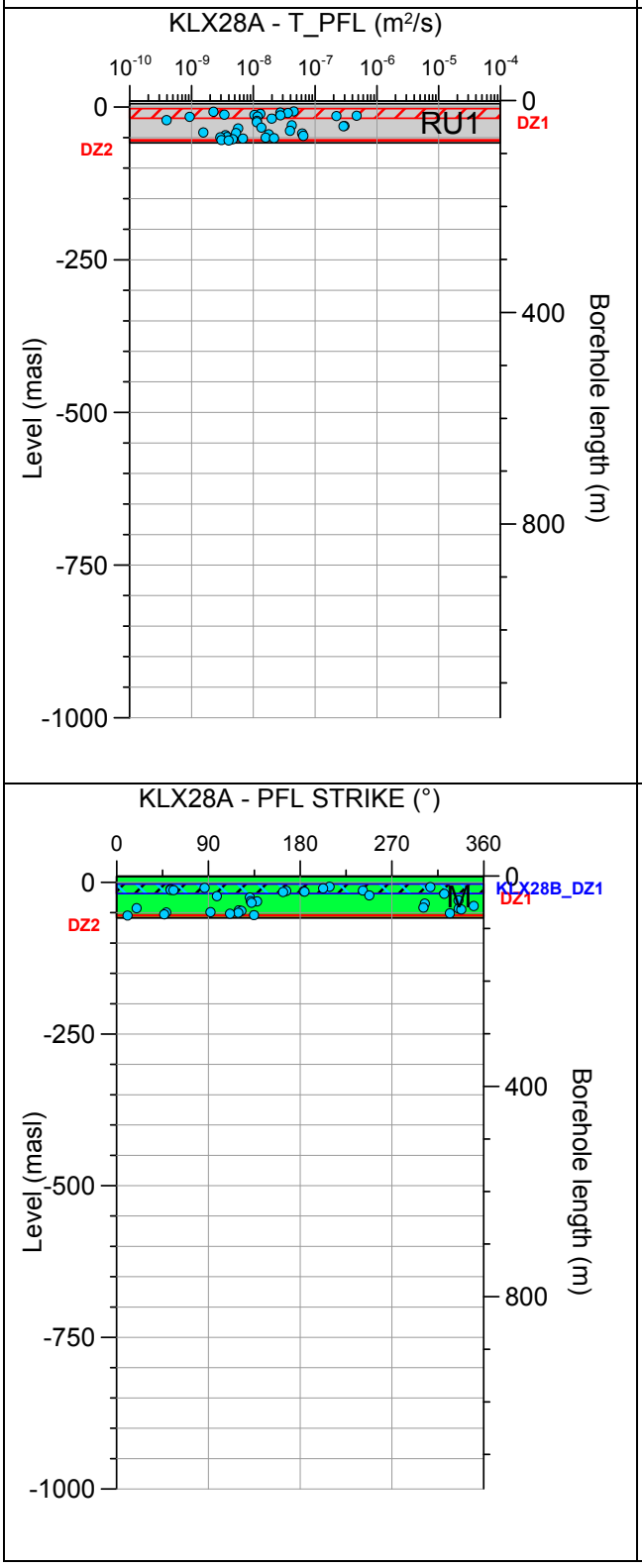

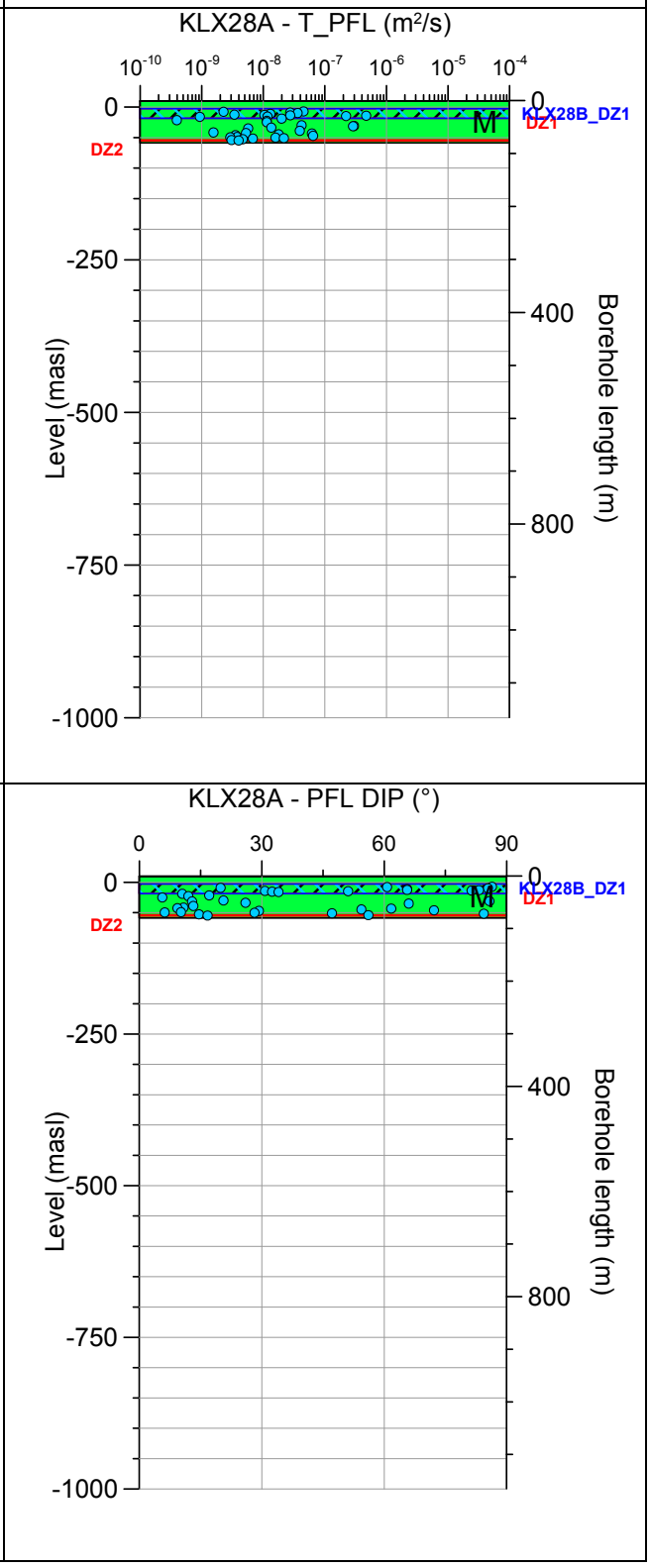

Comment:

Borehole KLX28A. Poles for PFL-f feature planes outside deformation zones.

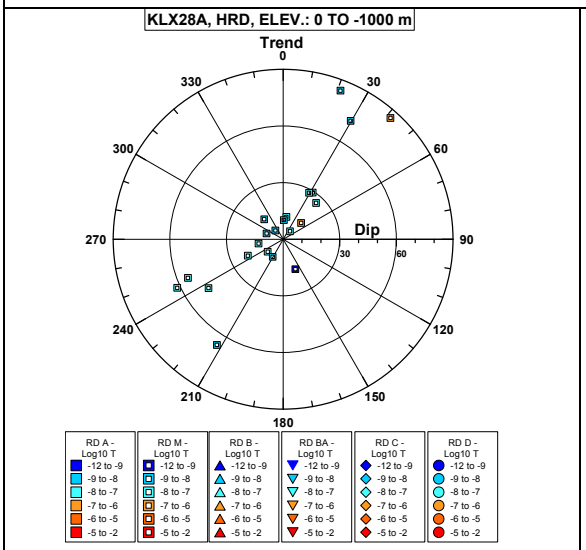

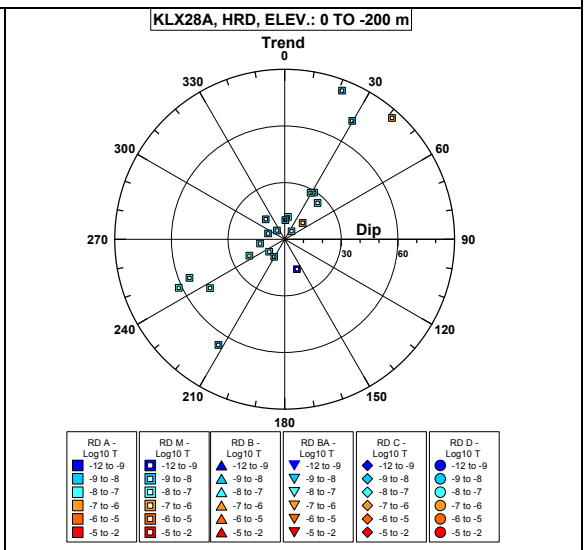

Borehole KLX28A. Poles for PFL-f feature planes in possible deformation zones.

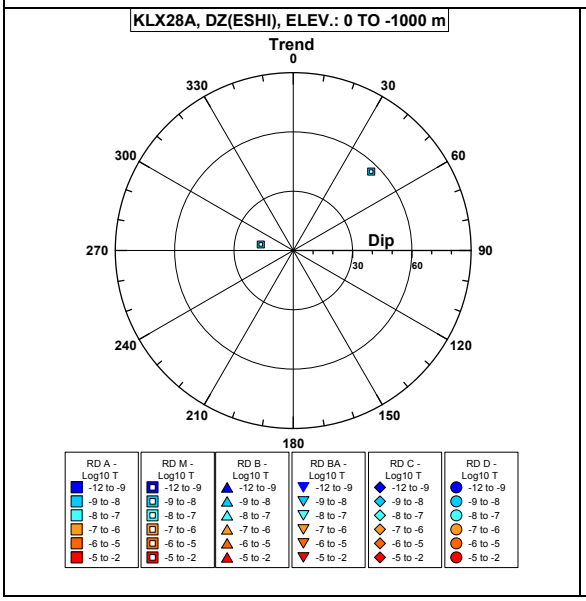

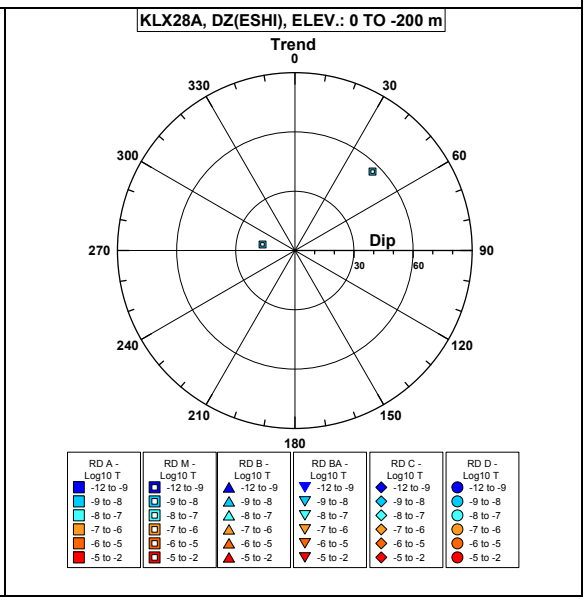

Borehole KLX28A. Poles for PFL-f feature planes in deterministically modelled deformation zones.

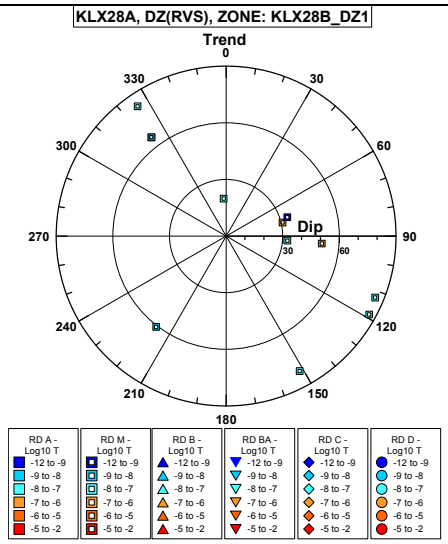

Borehole KLX29A.

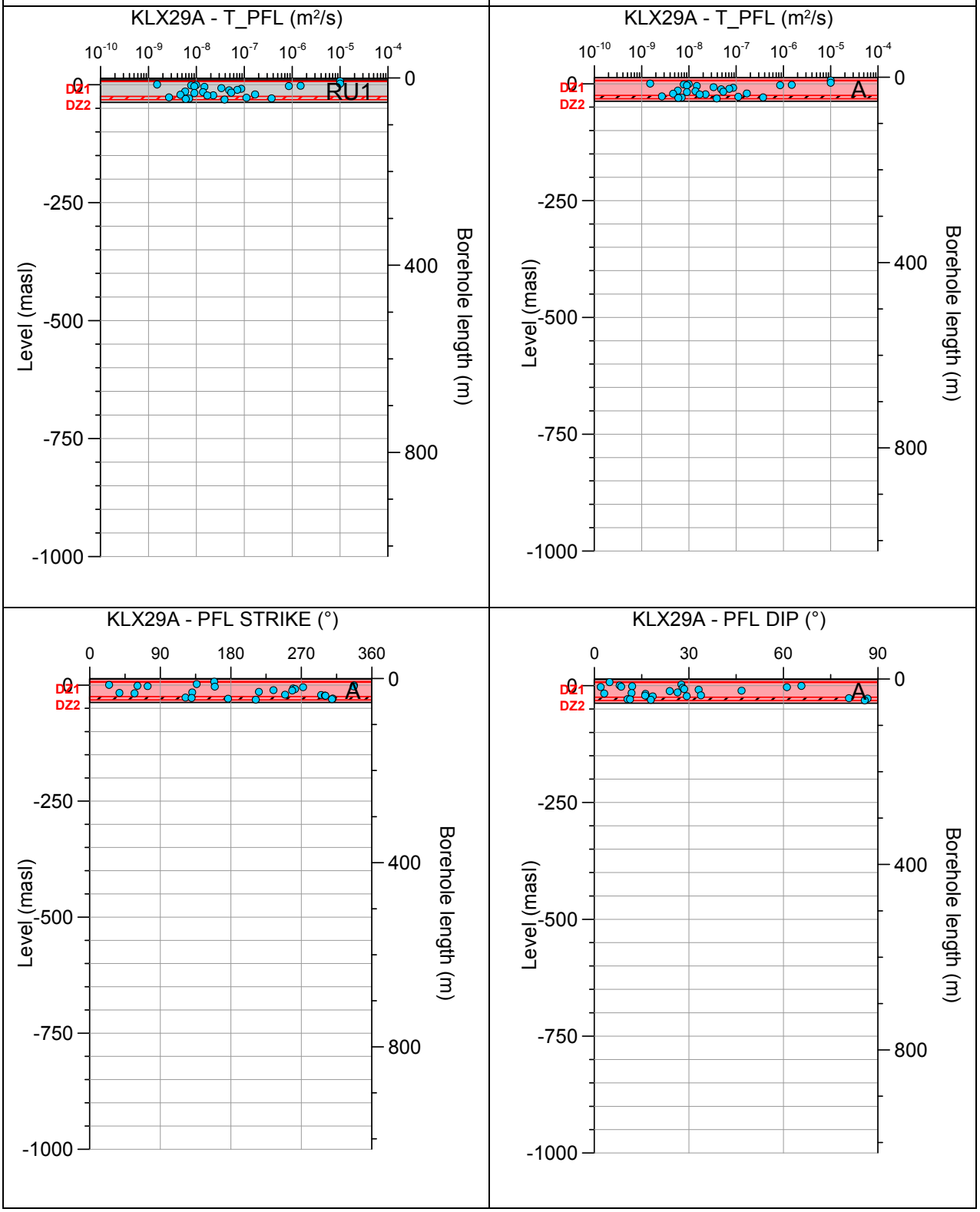

Comment:

Borehole KLX29A. Poles for PFL-f feature planes outside deformation zones.

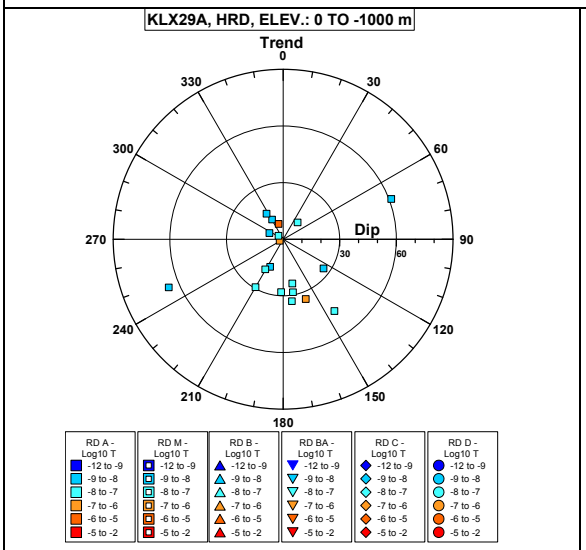

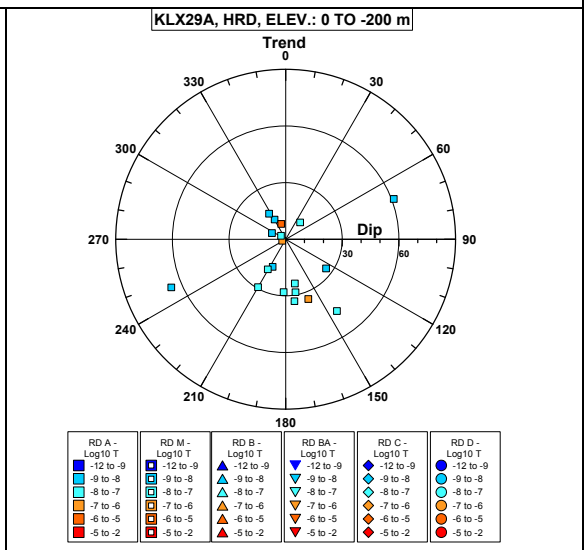

Borehole KLX29A. Poles for PFL-f feature planes in possible deformation zones.

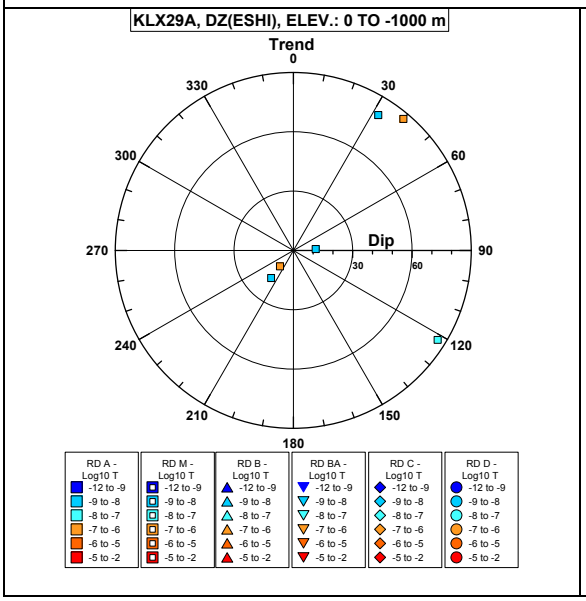

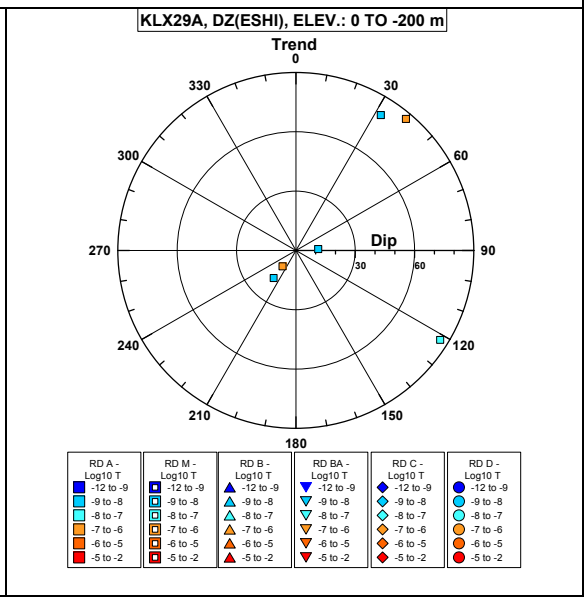

No PFL-f feature planes in deterministically modelled deformation zones exist in KLX29A.

A.3 HCD data

This appendix covers the following:

- Section A3.1: HCD site specific data tabulated
- Section A3.2: HCD statistics
- Section A3.3: Trend functions for HCD with site specific data
- Section A.3.4: PFL-f statistics for HCDs
- Section A.3.5:HCDs defined as compliment to deterministic deformation zones defined by geology

A.3.1 HCD site specific data tabulated

Comments to table

In the table the transmissivities of identified Hydraulic Conductor Domains (HCD) are compiled together with some of the geometrical and other geological information.

HCD_(DZ-group) is the naming used in the hydrogeological modelling . *HCD_(bh-intercept)* shows the HCDs that corresponds to the borehole intercepts of deformation zone segments or in a few cases the possible intercepts of several deformation zones). *HCD_Geol.* shows the correspondence naming in the geological model (indicating that a few HCD are considered MDZ in the geological model).

T-BC is the Best Choice transmissivity estimate for each borehole intercept. *Value type T-BC*= -1 indicates a measurement limit value of the transmissivity and 0 an estimate of the transmissivity. The columns *mean(log10(T-BC))* provides the estimates for each deformation zone with hydraulic data and in cases of several observations for a HCD the standard deviation is also provided; *std(log10(T-BC)).* All these estimates are related to elevation intervals according to the elevation intervals in the HydroDFN model.; *mean elevation class (T-BC) (m*) The elevation or mean elevation if several observations are shown in *mean elevation (T-BC) (m).*

HCD_(DZ-group)	HCD_(bh-intercept)	DZ_Geol.	Active in local model	Geological length (km)	Zone thickness (m)	Maximum thickness (m)	Zone Strike	Zone Dip	Earlier names	Geological length (km)	BH	Target_secup (BH length, m)	Target_seclow (BH length, m)	Target_sec-length (BH length, m)	Elevation (T-secup)	Elevation (T-seclow)	Elevation (mid-sec)	Geol. DZ-orientation group (NE-SW/ N-S/ NW-SE/ E-W/ Subh)	DZ-Char (D/DB/B)	Valu type T-BC	T-BC (m^2/s)	log10(T-BC) (T: m^2/s)	Sample size tot of T-BC	Sample size in elevation interval of T-BC	mean(log10(T-BC))	std(log10(T-BC))	mean elevation (T-BC) (m)	mean elevation class (T-BC) (m)
HLX28_DZ1	HLX28_DZ1	HLX28_DZ1	X	>1	10	10	180	20		>1	HLX28	75	89	14	-50	-61	-55	N-S	B	0	3.62E-04	-3.44	3	3	-4.78	1.39	-85	-75
HLX28_DZ1	HLX28_DZ1	HLX28_DZ1	X		10		180	20			HLX32	104	114	10	-75	-83	-79	N-S	B	0	2.03E-05	-4.69						
HLX28_DZ1	HLX28_DZ1	HLX28_DZ1	X		10		180	20			KLX11A	142	163	21	-109	-129	-119	N-S	B	0	6.19E-07	-6.21						
KLX03_DZ1b	KLX03_DZ1b	KLX03_DZ1b	X	>1	10	10	121	20		>1	KLX03	759	777	18	-717	-735	-726	SubH	B	0	5.19E-07	-6.29	1	1	-6.29		-726	-825
KLX03_DZ1c	KLX03_DZ1c	KLX03_DZ1c	X	>1	10	10	125	13		>1	KLX03	789	801	12	-747	-758	-752	SubH	DB	-1	3.40E-09	-8.47	1	1	-8.47		-752	-825
KLX04_DZ6b	KLX04_DZ6b	KLX04_DZ6b	X	>1	14	14	156	67		>1	KLX04	887	914	27	-858	-885	-872	N-S	B	0	6.88E-08	-7.16	1	1	-7.16		-872	-825
KLX04_DZ6c	KLX04_DZ6c	KLX04_DZ6c	X	>1	30	30	177	42		>1	KLX04	935	972	37	-906	-943	-924	N-S	B	0	3.22E-07	-6.49	1	1	-6.49		-924	-825
KLX07A_DZ10	KLX07A_DZ10	KLX07A_DZ10	X	>1	10	10	225	28		>1	KLX07A	604	655	51	-441	-481	-461	SubH	DB	0	7.83E-06	-5.11	1	1	-5.11		-461	-575
KLX07A_DZ11	KLX07A_DZ11	KLX07A_DZ11	X	>1	30	30	253	35		>1	KLX07A	693	724	31	-512	-536	-524	E-W	B	0	1.47E-06	-5.83	1	1	-5.83		-524	-575
KLX07A_DZ12	KLX07A_DZ12	KLX07A_DZ12	X	>1	47	47	263	41		>1	KLX07A	738	785	47	-547	-584	-566	E-W	B	0	1.78E-05	-4.75	1	1	-4.75		-566	-575
KLX07A_DZ13	KLX07A_DZ13	KLX07A_DZ13	X	>1	10	10	348	65		>1	KLX07A	817	836	19	-609	-624	-617	N-S	DB	0	5.26E-07	-6.28	1	1	-6.28		-617	-575
KLX07A_DZ7	KLX07A_DZ7	KLX07A_DZ7	X	>1	30	30	267	90		>1	KLX07A	347	388	41	-249	-278	-264	E-W	DB	0	1.83E-05	-4.74	1	1	-4.74		-264	-275
KLX07A_DZ9	KLX07A_DZ9	KLX07A_DZ9	X	>1	10	10	253	35		>1	KLX07A	448	459	11	-321	-329	-325	E-W	DB	0	2.05E-07	-6.69	1	1	-6.69		-325	-275
KLX08_DZ1	KLX08_DZ1	KLX08_DZ1	X	>1	27	27	0	18		>1	KLX08	100	131	31	-62	-89	-76	SubH	B	0	2.27E-05	-4.64	1	1	-4.64		-76	-75
KLX08_DZ10	KLX08_DZ10	KLX08_DZ10	X	>1	11	11	79	11		>1	KLX08	925	940	15	-769	-782	-776	SubH	B	-1	1.70E-09	-8.77	1	1	-8.77		-776	-825
KLX08_DZ6	KLX08_DZ6	KLX08_DZ6	X	>1	10	10	296	89		>1	KLX08	396	416	20	-318	-335	-327	NW-SE	B	0	4.30E-05	-4.37	1	1	-4.37		-327	-275
KLX09_DZ10	KLX09_DZ10	KLX09_DZ10	X	>1	25	25	263	37		>1	KLX09	520	554	34	-493	-527	-510	E-W	B	0	6.10E-06	-5.21	1	1	-5.21		-510	-575
KLX09E_DZ2	KLX09E_DZ2	KLX09E_DZ2	X	>1	22	22	295	14		>1	KLX09E	76	105	29	-44	-69	-56	SubH	DB	0	2.39E-05	-4.62	1	1	-4.62		-56	-75
KLX09F_DZ1	KLX09F_DZ1	KLX09F_DZ1	X	>1	14	14	178	19		>1	KLX09F	8	22	14	13	1	7	SubH	B	0	5.33E-07	-6.27	1	1	-6.27		7	-75
KLX10C_DZ3	KLX10C_DZ3	KLX10C_DZ3	X	>1	10	10	300	35		>1	KLX10C	35	59	24	-13	-34	-24	NW-SE	DB	0	6.28E-06	-5.20	1	1	-5.20		-24	-75
KLX10C_DZ7	KLX10C_DZ7	KLX10C_DZ7	X	>1	10	10	323	39		>1	KLX10C	121	140	19	-87	-103	-95	NW-SE	DB	0	1.10E-06	-5.96	1	1	-5.96		-95	-75
KLX11_DZ11	KLX11_DZ11	KLX11_DZ11	X	>1	20	20	65	20		>1	KLX11A	486	513	27	-436	-461	-449	SubH	B	0	3.03E-08	-7.52	1	1	-7.52		-449	-575
KLX18A_DZ9	KLX18A_DZ9	KLX18A_DZ9	X	>1	10	10	95	50		>1	KLX18A	472	489	17	-444	-461	-453	E-W	DB	0	5.31E-08	-7.27	1	1	-7.27		-453	-575

HCD_(DZ-group)	HCD_(bh-intercept)	DZ_Geol.	Active in local model	Geological length (km)	Zone thickness (m)	Maximum thickness (m)	Zone Strike	Zone Dip	Earlier names	Geological length (km)	BH	Target_secup (BH length, m)	Target_seclow (BH length, m)	Target_sec-length (BH length, m)	Elevation (T-secup)	Elevation (T-seclow)	Elevation (mid-sec)	Geol. DZ-orientation group (NE-SW/ N-S/ NW-SE/ E-W/ Subh)	DZ-Char (D/DB/B)	Valu type T-BC	T-BC (m²/s)	log10(T-BC) (T: m²/s)	Sample size tot of T-BC	Sample size in elevation interval of T-BC	mean(log10(T-BC))	std(log10(T-BC))	mean elevation (T-BC) (m)	mean elevation class (T-BC) (m)
klx19_dz5-8_dolerite	klx19_dz5-8_dolerite	MDZ	X	>1	10		185	81		>1	KLX19A	464	555	91	-373	-449	-411	N-S		0	1.59E-06	-5.80	1	1	-5.80		-411	-575
KLX21B_DZ10_2	KLX21B_DZ10_2	KLX21B_DZ10_12	X	>1	10	10	192	80		>1	KLX21B	559	707	148	-511	-648	-580	N-S	DB	0	2.55E-05	-4.59	1	1	-4.59		-580	-575
KLX28_DZ1	KLX28_DZ1	KLX28_DZ1	X	>1	10		182	33		>1	KLX28A	14	33	19	-2	-19	-10	N-S		0	5.83E-07	-6.23	1	1	-6.23		-10	-75
ZSMEW002A	ZSMEW002A	ZSMEW002A	X	30	100	200	90	65		30	HLX02	0	132	132	9	-109	-50	E-W	DB	0	2.20E-06	-5.66	4	3	-5.05	0.53	-85	-75
ZSMEW002A	ZSMEW002A	ZSMEW002A	X		100		90	65			KLX06	297	425	128	-67	-137	-102	E-W	DB	0	2.10E-05	-4.68						
ZSMEW002A	ZSMEW002A	ZSMEW002A	X		100		90	65			HLX20	90	170	80	-67	-137	-102	E-W	DB	0	1.52E-05	-4.82						
ZSMEW002A	ZSMEW002A	ZSMEW002A	X		100		90	65	Mederhult zone		KAS03	280	480	200	-269	-468	-368	E-W	DB	0	5.40E-06	-5.27		1	-5.27		-368	-275
ZSMEW007A	ZSMEW007A	ZSMEW007A	X	3.3	80	80	281	44		3.3	HLX25	6	80	74	15	-48	-17	E-W	B	0	2.05E-04	-3.69	19	14	-3.96	0.81	-51	-75
ZSMEW007A	ZSMEW007A	ZSMEW007A	X		80		281	44			HLX33	0	70	70	12	-49	-18	E-W	B	0	2.18E-04	-3.66						
ZSMEW007A	ZSMEW007A	ZSMEW007A	X		80		281	44			HLX23	6	80	74	10	-52	-21	E-W	B	0	1.45E-04	-3.84						
ZSMEW007A	ZSMEW007A	ZSMEW007A	X		80		281	44			HLX30	9	80	71	4	-59	-27	E-W	B	0	5.60E-05	-4.25						
ZSMEW007A	ZSMEW007A	ZSMEW007A	X		80		281	44			HLX10	0	85	85	12	-67	-28	E-W	B	0	3.02E-04	-3.52						
ZSMEW007A	ZSMEW007A	ZSMEW007A	X		80		281	44			HLX21	18	24	6	-5	-66	-36	E-W	B	0	3.45E-04	-3.46						
ZSMEW007A	ZSMEW007A	ZSMEW007A	X		80		281	44			HLX13	29	103	74	-7	-69	-38	E-W	B	0	3.48E-07	-6.46						
ZSMEW007A	ZSMEW007A	ZSMEW007A	X		80		281	44			HLX24	0	150	150	13	-108	-48	E-W	B	0	6.78E-04	-3.17						
ZSMEW007A	ZSMEW007A	ZSMEW007A	X		80		281	44			HLX31	50	100	50	-31	-75	-53	E-W	B	0	1.23E-04	-3.91						
ZSMEW007A	ZSMEW007A	ZSMEW007A	X		80		281	44			HLX14	44	116	72	-24	-90	-57	E-W	B	0	1.44E-04	-3.84						
ZSMEW007A	ZSMEW007A	ZSMEW007A	X		80		281	44			HLX22	9	163	154	2	-119	-58	E-W	B	0	3.06E-04	-3.51						
ZSMEW007A	ZSMEW007A	ZSMEW007A	X		80		281	44			KLX07A	105	168	63	-67	-115	-91	E-W	B	0	1.06E-04	-3.97						
ZSMEW007A	ZSMEW007A	ZSMEW007A	X		80		281	44			HLX35	110	152	42	-78	-112	-95	E-W	B	0	3.70E-04	-3.43						
ZSMEW007A	ZSMEW007A	ZSMEW007A	X		80		281	44			KLX07B	124	172	48	-105	-153	-129	E-W	B	0	1.95E-05	-4.71						
ZSMEW007A	ZSMEW007A	ZSMEW007A	X		80		281	44			KLX02	180	200	20	-161	-181	-171	E-W	B	0	6.20E-05	-4.21		3	-4.68	0.44	-230	-275
ZSMEW007A	ZSMEW007A	ZSMEW007A	X		80		281	44			KLX08	211	300	89	-158	-235	-197	E-W	B	0	1.64E-05	-4.78						
ZSMEW007A	ZSMEW007A	ZSMEW007A	X		80		281	44			KLX04	310	385	75	-284	-359	-322	E-W	B	0	8.69E-06	-5.06						
ZSMEW007A	ZSMEW007A + ZSMNW928A	ZSMEW007A + ZSMNW928A	X		80		281	44	Reflector N, ZSMNW928A		KLX09	682	722	40	-654	-693	-674	E-W	B	0	2.12E-07	-6.67		2	-5.75	1.31	-832	-825

HCD_(DZ-group)	HCD_(bh-intercept)	DZ_Geol.	Active in local model	Geological length (km)	Zone thickness (m)	Maximum thickness (m)	Zone Strike	Zone Dip	Earlier names	Geological length (km)	BH	Target_secup (BH length, m)	Target_seclow (BH length, m)	Target_sec-length (BH length, m)	Elevation (T-secup)	Elevation (T-seclow)	Elevation (mid-sec)	Geol. DZ-orientation group (NE-SW/ N-S/ NW-SE/ E-W/ Subh)	DZ-Char (D/DB/B)	Valu type T-BC	T-BC (m^2/s)	log10(T-BC) (T: m^2/s)	Sample size tot of T-BC	Sample size in elevation interval of T-BC	mean(log10(T-BC))	std(log10(T-BC))	mean elevation (T-BC) (m)	mean elevation class (T-BC) (m)
ZSMEW007A	ZSMEW007A	ZSMEW007A	X		80		281	44			KLX01	1000	1020	20	-981	-1001	-991	E-W	B	0	1.50E-05	-4.82						
ZSMEW009A	ZSMEW009A	ZSMEW009A		1.7	12	20	85	76		1.7	HAS14				-22	-22	-22	E-W	DB	0	2.50E-05	-4.60	4	3	-4.94	0.43	-36	-75
ZSMEW009A	ZSMEW009A	ZSMEW009A			12		85	76			HAS21				-33	-33	-33	E-W	DB	0	1.60E-05	-4.80						
ZSMEW009A	ZSMEW009A	ZSMEW009A			12		85	76			KAS06				-53	-53	-53	E-W	DB	0	3.80E-06	-5.42						
ZSMEW009A	ZSMEW009A	ZSMEW009A			12		85	76			TASA				-196	-196	-196	E-W	DB	0	1.40E-05	-4.85		1	-4.85		-196	-275
ZSMEW013A	ZSMEW013A	ZSMEW013A	X	4.4	45	50	85	90		4.4	HLX03	0	100	100	10	-82	-36	E-W	DB	0	2.80E-06	-5.55	4	3	-6.36	1.63	-56	-75
ZSMEW013A	ZSMEW013A	ZSMEW013A	X		45		85	90			HAS01	0	100	100	6	-82	-38	E-W	DB	0	5.80E-09	-8.24						
ZSMEW013A	ZSMEW013A	ZSMEW013A	X		45		85	90			KAS04	87	158	71	-63	-124	-93	E-W	DB	0	5.00E-06	-5.30						
ZSMEW013A	ZSMEW013A	ZSMEW013A	X		45		85	90	EW1A		KA1755A	180	230	50	-342	-342	-342	E-W	DB	0	5.00E-05	-4.30		1	-4.30		-342	-275
ZSMEW014A	ZSMEW014A	ZSMEW014A	X	1.2	10	30	100	90		1.2	HLX02	0	132	132	9	-109	-50	E-W	DB	0	2.20E-06	-5.66	1	1	-5.66		-50	-75
ZSMEW038A	ZSMEW038A	ZSMEW038A		3.2	10	10	90	90		3.2	HAV05				-17	-17	-17	E-W	DB	0	1.10E-06	-5.96	4	1	-5.96		-17	-75
ZSMEW038A	ZSMEW038A	ZSMEW038A			10		90	90			TASA				-163	-163	-163	E-W	DB	0	1.58E-03	-2.80		3	-3.23	0.38	-177	-275
ZSMEW038A	ZSMEW038A	ZSMEW038A			10		90	90			KBH02				-175	-175	-175	E-W	DB	0	4.32E-04	-3.36						
ZSMEW038A	ZSMEW038A	ZSMEW038A			10		90	90			KAS09				-193	-193	-193	E-W	DB	0	2.90E-04	-3.54						
ZSMEW120A	ZSMEW120A	ZSMEW120A	X	1.2	50	60+	80	64		1.2	KLX13A	488	593	105	-460	-565	-512	E-W	DB	0	1.44E-06	-5.84	1	1	-5.84		-512	-575
ZSMEW900	ZSMEW900A	ZSMEW900A	X	0.9	25	30	92	57		0.9	HLX39	75	85	10	-37	-46	-41	E-W	DB	0	1.48E-04	-3.83	4	3	-4.23	0.69	-55	-75
ZSMEW900	ZSMEW900B	ZSMEW900B	X		25		106	78			HLX39	0	199	199	27	-144	-59	E-W	DB	0	1.48E-04	-3.83						
ZSMEW900	ZSMEW900A	ZSMEW900A	X		25		92	57	ZSMEW005A or 7A		KLX17A	100	114	14	-60	-72	-66	E-W	DB	0	9.55E-06	-5.02						
ZSMEW900	ZSMEW900B	ZSMEW900B	X		25		106	78			KLX17A	193	227	34	-141	-171	-156	E-W	DB	0	8.55E-07	-6.07		1	-6.07		-156	-275
ZSMEW946A	ZSMEW946A	ZSMEW946A	X	1.5	10	20	80	23		1.5	KLX04	295	298	3	-269	-272	-271	SubH	DB	0	2.11E-05	-4.68	5	1	-4.68		-271	-275
ZSMEW946A	ZSMEW946A	ZSMEW946A	X		10		80	23			KLX18A	580	582	2	-551	-553	-552	SubH	DB	-1	8.70E-10	-9.06		1	-9.06		-552	-575
ZSMEW946A	ZSMEW946A	ZSMEW946A	X		10		80	23			KLX10	698	706	8	-675	-683	-679	SubH	DB	0	1.77E-07	-6.75		3	-5.96	0.78	-700	-825
ZSMEW946A	ZSMEW946A	ZSMEW946A	X		10		80	23	Reflector M		KLX03	727	743	16	-682	-702	-692	SubH	DB	0	6.28E-06	-5.20						
ZSMEW946A	ZSMEW946A	ZSMEW946A	X		10		80	23			KLX08	478	486	8	-1063	-395	-729	SubH	DB	0	1.21E-06	-5.92						
ZSMNE004A	ZSMNE004A	ZSMNE004A	X	>15	150	650	50	90		>15	TASA	302	334	32	-44	-44	-44	NE-SW	DB	0	2.80E-06	-5.55	2	2	-5.98	0.61	-80	-75
ZSMNE004A	ZSMNE004A	ZSMNE004A	X		150		50	90	ZSMEW005		HLX19	139	154	15	-110	-123	-117	NE-SW	DB	0	3.88E-07	-6.41						

HCD_(DZ-group)	HCD_(bh-intercept)	DZ_Geol.	Active in local model	Geological length (km)	Zone thickness (m)	Maximum thickness (m)	Zone Strike	Zone Dip	Earlier names	Geological length (km)	BH	Target_secup (BH length, m)	Target_seclow (BH length, m)	Target_sec-length (BH length, m)	Elevation (T-secup)	Elevation (T-seclow)	Elevation (mid-sec)	Geol. DZ-orientation group (NE-SW/ N-S/ NW-SE/ E-W/ Subh)	DZ-Char (D/DB/B)	Valu type T-BC	T-BC (m^2/s)	log10(T-BC) (T: m^2/s)	Sample size tot of T-BC	Sample size in elevation interval of T-BC	mean(log10(T-BC))	std(log10(T-BC))	mean elevation (T-BC) (m)	mean elevation class (T-BC) (m)
									4A																			
ZSMNE005A	ZSMNE005A	ZSMNE005A	X	16	250	300	60	90		16	HLX17			0	-32	-32	-32	NE-SW	DB	0	1.17E-07	-6.93	9	3	-6.06	2.19	-87	-75
ZSMNE005A	ZSMNE005A	ZSMNE005A	X		250		60	90			HLX16			0	-108	-108	-108	NE-SW	DB	0	2.09E-08	-7.68						
ZSMNE005A	ZSMNE005A	ZSMNE005A	X		250		60	90			HLX09			0	-120	-120	-120	NE-SW	DB	0	2.70E-04	-3.57						
ZSMNE005A	ZSMNE005A	ZSMNE005A	X		250		60	90			KAS04	131	437	306	-188	-188	-188	NE-SW	DB	0	2.40E-05	-4.62						
ZSMNE005A	ZSMNE005A	ZSMNE005A	X		250		60	90			KA1751 A	110	114	4	-246	-246	-246	NE-SW	DB	0	2.60E-05	-4.59						
ZSMNE005A	ZSMNE005A	ZSMNE005A	X		250		60	90			KA1754 A	90	115	25	-278	-278	-278	NE-SW	DB	0	4.20E-06	-5.38						
ZSMNE005A	ZSMNE005A	ZSMNE005A	X		250		60	90	Äspö shear zone; EW1b		KA1755 A	95	140	45	-293	-293	-293	NE-SW	DB	0	4.90E-05	-4.31						
ZSMNE005A	ZSMNE005A	ZSMNE005A	X		250		60	90			KA3590 G02	19	30	11	-465	-465	-465	NE-SW	DB	0	1.90E-07	-6.72		1	-6.72		-465	-575
ZSMNE005A	ZSMNE005A	ZSMNE005A	X		250		60	90			KAS12	19	286	267	-849	-849	-849	NE-SW	DB	0	3.40E-05	-4.47		1	-4.47		-849	-825
ZSMNE006A	ZSMNE006A	ZSMNE006A	X	2.1	130	130	215	65	NE1	2.1	HLX08			0	-85	-85	-85	NE-SW	DB	0	4.58E-05	-4.34	12	4	-3.42	0.63	-110	-75
ZSMNE006A	ZSMNE006A	ZSMNE006A	X		130		215	65			KAS14	51	91	40	-96	-96	-96	NE-SW	DB	0	9.60E-04	-3.02						
ZSMNE006A	ZSMNE006A	ZSMNE006A	X		130		215	65			KAS09	50	112	62	-116	-116	-116	NE-SW	DB	0	1.00E-03	-3.00						
ZSMNE006A	ZSMNE006A	ZSMNE006A	X		130		215	65			KA1061	198	209	11	-143	-143	-143	NE-SW	DB	0	4.80E-04	-3.32						
ZSMNE006A	ZSMNE006A	ZSMNE006A	X		130		215	65			KAS11	156	220	64	-177	-177	-177	NE-SW	DB	0	4.10E-04	-3.39		5	-3.58	0.46	-211	-275
ZSMNE006A	ZSMNE006A	ZSMNE006A	X		130		215	65			TASA	1240	1325	85	-177	-177	-177	NE-SW	DB	0	4.13E-04	-3.38						
ZSMNE006A	ZSMNE006A	ZSMNE006A	X		130		215	65			KA1131 B	173	203	30	-184	-184	-184	NE-SW	DB	0	4.00E-05	-4.40						
ZSMNE006A	ZSMNE006A	ZSMNE006A	X		130		215	65			KBH02	667	706	39	-192	-192	-192	NE-SW	DB	0	4.32E-04	-3.36						
ZSMNE006A	ZSMNE006A	ZSMNE006A	X		130		215	65			KAS16	380	430	50	-324	-324	-324	NE-SW	DB	0	4.20E-04	-3.38						
ZSMNE006A	ZSMNE006A	ZSMNE006A	X		130		215	65			KAS08	537	601	64	-412	-412	-412	NE-SW	DB	0	1.30E-04	-3.89		2	-4.34	0.64	-417	-575
ZSMNE006A	ZSMNE006A	ZSMNE006A	X		130		215	65			KAS07	497	602	105	-422	-422	-422	NE-SW	DB	0	1.60E-05	-4.80						
ZSMNE006A	ZSMNE006A	ZSMNE006A	X		130		215	65			KAS02	806	914	108	-821	-821	-821	NE-SW	DB	0	2.50E-04	-3.60		1	-3.60		-821	-825
ZSMNE012A	ZSMNE012A	ZSMNE012A	X	5.6	120	120	60	45		5.6	HMJ01	0	46	46	-18	-18	-18	NE-SW	DB	0	3.34E-04	-3.48	12	9	-4.70	1.21	-78	-75
ZSMNE012A	ZSMNE012A	ZSMNE012A	X		120		60	45			HAV13	0	142	142	2	-119	-59	NE-SW	DB	0	3.47E-07	-6.46						
ZSMNE012A	ZSMNE012A	ZSMNE012A	X		120		60	45			HAV12	51	127	76	-34	-99	-67	NE-SW	DB	0	1.06E-04	-3.97						

HCD_(DZ-group)	HCD_(bh-intercept)	DZ_Geol.	Active in local model	Geological length (km)	Zone thickness (m)	Maximum thickness (m)	Zone Strike	Zone Dip	Earlier names	Geological length (km)	BH	Target_secup (BH length, m)	Target_seclow (BH length, m)	Target_sec-length (BH length, m)	Elevation (T-secup)	Elevation (T-seclow)	Elevation (mid-sec)	Geol. DZ-orientation group (NE-SW/ N-S/ NW-SE/ E-W/ Subh)	DZ-Char (D/DB/B)	Valu type T-BC	T-BC (m^2/s)	log10(T-BC) (T: m^2/s)	Sample size tot of T-BC	Sample size in elevation interval of T-BC	mean(log10(T-BC))	std(log10(T-BC))	mean elevation (T-BC) (m)	mean elevation class (T-BC) (m)
ZSMNE012A	ZSMNE012A	ZSMNE012A	X		120		60	45			HLX18	16	181	165	-9	-149	-79	NE-SW	DB	0	4.58E-05	-4.34						
ZSMNE012A	ZSMNE012A	ZSMNE012A	X		120		60	45			HLX18	16	181	165	-11	-149	-80	NE-SW	DB	0	1.30E-05	-4.89						
ZSMNE012A	ZSMNE012A	ZSMNE012A	X		120		60	45			KBH02	140	194	54	-76	-92	-84	NE-SW	DB	0	3.00E-05	-4.52						
ZSMNE012A	ZSMNE012A	ZSMNE012A	X		120		60	45			HLX17	0	202	202	3	-176	-86	NE-SW	DB	0	1.17E-07	-6.93						
ZSMNE012A	ZSMNE012A	ZSMNE012A	X		120		60	45			TASA	827		-827	-113	-113	-113	NE-SW	DB	0	1.27E-04	-3.90						
ZSMNE012A	ZSMNE012A	ZSMNE012A	X		120		60	45	includes NW004A		HAV02	90	150	60	-84	-144	-114	NE-SW	DB	0	1.40E-04	-3.85						
ZSMNE012A	ZSMNE012A	ZSMNE012A	X		120		60	45			KAV03	164	232	68	-155	-223	-189	NE-SW	DB	0	6.91E-04	-3.16		1	-3.16		-189	-275
ZSMNE012A	ZSMNE012A	ZSMNE012A	X		120		60	45			KAV01	400	580	180	-386	-566	-476	NE-SW	DB	0	2.55E-05	-4.59		1	-4.59		-476	-575
ZSMNE012A	ZSMNE012A	ZSMNE012A	X		120		60	45			KAV04A	840	900	60	-827	-887	-857	NE-SW	DB	0	1.72E-06	-5.76		1	-5.76		-857	-825
ZSMNE015A	ZSMNE015A	ZSMNE015A		1.9	10	15	50	70		1.9	KSH01A				-936	-936	-936	NE-SW	DB	0	3.90E-09	-8.41	1	1	-8.41		-936	-825
ZSMNE024A	ZSMNE024A	ZSMNE024A		>15	80	100	225	52		>15	HAV11	124	180	56	-105	-153	-129	NE-SW	DB	0	3.85E-04	-3.41	5	1	-3.41		-129	-75
ZSMNE024A	ZSMNE024A	ZSMNE024A			80		225	52			KSH03A	162	275	113	-132	-228	-180	NE-SW	DB	0	3.64E-04	-3.44		1	-3.44		-180	-275
ZSMNE024A	ZSMNE024A	ZSMNE024A			80		225	52			KSH01A	540	631	91	-520	-608	-564	NE-SW	DB	0	1.43E-06	-5.84		1	-5.84		-564	-575
ZSMNE024A	ZSMNE024A	ZSMNE024A			80		225	52			KAV01	680	757	77	-665	-743	-704	NE-SW	DB	0	1.00E-08	-8.00		2	-8.50	0.71	-831	-825
ZSMNE024A	ZSMNE024A	ZSMNE024A			80		225	52			KAV04A	940	1004	64	-926	-990	-958	NE-SW	DB	0	1.00E-09	-9.00						
ZSMNE031A	ZSMNE031A	ZSMNE031A		4.2 (15 ++)	15	20	215	52		4.2(15+ +)	KSH03A				-240	-240	-240	NE-SW	B	0	1.58E-04	-3.80	2	1	-3.80		-240	-275
ZSMNE031A	ZSMNE031A	ZSMNE031A			15		215	52			KSH01A				-668	-668	-668	NE-SW	B	0	8.60E-09	-8.07		1	-8.07		-668	-825
ZSMNE040A	ZSMNE040A	ZSMNE040A	X	1.6	20	20	30	90		1.6	HLX01	0	100	100	9	-78	-35	NE-SW	DB	0	9.00E-05	-4.05	2	2	-6.14	2.96	-42	-75
ZSMNE040A	ZSMNE040A	ZSMNE040A	X		20		30	90			HLX04	0	125	125	10	-108	-49	NE-SW	DB	0	5.89E-09	-8.23						
ZSMNE107A	ZSMNE107A	ZSMNE107A	X	3.1	35	40	225	80		3.1	HLX10	0	85	85	12	-67	-28	NE-SW	DB	0	3.02E-04	-3.52	4	1	-3.52		-28	-75
ZSMNE107A	ZSMNE107A	ZSMNE107A	X		35		225	80			KLX16A	228	434	206	-187	-371	-279	NE-SW	DB	0	1.31E-05	-4.88		1	-4.88		-279	-275
ZSMNE107A	ZSMNE107A	ZSMNE107A	X		35		225	80			KLX15A	711	744	33	-529	-553	-541	NE-SW	DB	0	8.40E-09	-8.08		1	-8.08		-541	-575
ZSMNE107A	ZSMNE107A + ZSMNE928A	ZSMNE107A + ZSMNE928A	X		35		225	80	Reflector N, ZSMNW928A		KLX02	770	960	190	-747	-936	-842	NE-SW	DB	0	6.30E-07	-6.20		1	-6.20		-842	-825
ZSMNE942A	ZSMNE942A	ZSMNE942A	X	2.5	15	50	246	88		2.5	KLX10B	0	20	20	9	1	5	NE-SW	DB	0	4.91E-07	-6.31	4	2	-5.07	1.75	-46	-75
ZSMNE942A	ZSMNE942A	ZSMNE942A	X		15		246	88			HLX23	124	150	26	-87	-108	-98	NE-SW	DB	0	1.45E-04	-3.84						

HCD_(DZ-group)	HCD_(bh-intercept)	DZ_Geol.	Active in local model	Geological length (km)	Zone thickness (m)	Maximum thickness (m)	Zone Strike	Zone Dip	Earlier names	Geological length (km)	BH	Target_secup (BH length, m)	Target_seclow (BH length, m)	Target_sec-length (BH length, m)	Elevation (T-secup)	Elevation (T-seclow)	Elevation (mid-sec)	Geol. DZ-orientation group (NE-SW/ N-S/ NW-SE/ E-W/ Subh)	DZ-Char (D/DB/B)	Valu type T-BC	T-BC (m^2/s)	log10(T-BC) (T: m^2/s)	Sample size tot of T-BC	Sample size in elevation interval of T-BC	mean(log10(T-BC))	std(log10(T-BC))	mean elevation (T-BC) (m)	mean elevation class (T-BC) (m)
ZSMNE942A	ZSMNE942A	ZSMNE942A	X		15		246	88			KLX10	103	349	246	-84	-328	-206	NE-SW	DB	0	8.79E-05	-4.06		2	-5.24	1.68	-284	-275
ZSMNE942A	ZSMNE942A	ZSMNE942A	X		15		246	88			KLX19A	437	464	27	-350	-373	-362	NE-SW	DB	0	3.74E-07	-6.43						
ZSMNE944A	ZSMNE944A	ZSMNE944A	X	1.2	10	20	58	75		1.2	HLX31	129	130	1	-101	-104	-103	NE-SW	DB	0	1.23E-04	-3.91	2	1	-3.91		-103	-75
ZSMNE944A	ZSMNE944A	ZSMNE944A	X		10		58	75			KLX18A	284	292	8	-259	-267	-263	NE-SW	DB	0	3.22E-09	-8.49		1	-8.49		-263	-275
ZSMNS001C hydr	ZSMNS001C hydr	ZSMNS001C	X	10.9 (A-E)	45	80	187	81		10.9 (A-E)	HLX43	32	82	50	-1	-40	-20	N-S	DB	0	1.43E-04	-3.84	3	3	-4.40	0.54	-82	-75
ZSMNS001C_ hydr	ZSMNS001C_ hydr	ZSMNS001C	X		45	80	187	81			HLX37	122	147	25	-88	-108	-98	N-S	DB	0	3.68E-05	-4.43						
ZSMNS001C_ hydr	ZSMNS001C_ hydr	ZSMNS001C	X		130	80	187	81			KLX20A	102	290	188	-104	-152	-128	N-S	DB	0	1.19E-05	-4.92						
ZSMNS017B	ZSMNS017B	ZSMNS017B		2.1	20	100	335	83		2.1	HA1960 A				-267	-267	-267	N-S	DB	0	8.60E-05	-4.07	9	8	-4.24	1.48	-277	-275
ZSMNS017B	ZSMNS017B	ZSMNS017B			20		335	83			SA1997 A				-272	-272	-272	N-S	DB	0	1.10E-04	-3.96						
ZSMNS017B	ZSMNS017B	ZSMNS017B			20		335	83			SA2009 A				-273	-273	-273	N-S	DB	0	2.20E-08	-7.66						
ZSMNS017B	ZSMNS017B	ZSMNS017B			20		335	83			SA2025B				-276	-276	-276	N-S	DB	0	2.10E-04	-3.68						
ZSMNS017B	ZSMNS017B	ZSMNS017B			20		335	83			SA2074B				-281	-281	-281	N-S	DB	0	1.30E-03	-2.89						
ZSMNS017B	ZSMNS017B	ZSMNS017B			20		335	83			KA2048 B				-282	-282	-282	N-S	DB	0	1.00E-04	-4.00						
ZSMNS017B	ZSMNS017B	ZSMNS017B			20		335	83			SA2090B				-283	-283	-283	N-S	DB	0	7.00E-04	-3.15						
ZSMNS017B	ZSMNS017B	ZSMNS017B			20		335	83			SA2109B				-285	-285	-285	N-S	DB	0	2.90E-05	-4.54						
ZSMNS017B	ZSMNS017B	ZSMNS017B			20		335	83			KC0045F				-439	-439	-439	N-S	DB	0	1.10E-04	-3.96		1	-3.96		-439	-575
ZSMNS046A	ZSMNS046A	ZSMNS046A	X	2.1	20	30	170	90		2.1	KLX09G	40	68	28	-15	-39	-27	N-S	DB	0	1.33E-05	-4.88	1	1	-4.88		-27	-75
ZSMNS059A	ZSMNS059A	ZSMNS059A	X	4.8	50	80	192	88		4.8	HLX38	23	67	44	-9	-45	-27	N-S	DB	0	1.16E-04	-3.94	3	3	-3.84	0.49	-60	-75
ZSMNS059A	ZSMNS059A	ZSMNS059A	X		50		192	88			KLX14A	75	125	50	-40	-77	-59	N-S	DB	0	5.31E-05	-4.27						
ZSMNS059A	ZSMNS059A	ZSMNS059A	X		50		192	88			HLX35	116	142	26	-83	-104	-94	N-S	DB	0	4.82E-04	-3.32						
ZSMNS947A	ZSMNS947A	ZSMNS947A	X	1.8	20	25	178	90		1.8	HLX42	116	153	37	-85	-115	-100	N-S	DB	0	4.30E-05	-4.37	1	1	-4.37		-100	-75
ZSMNW025A	ZSMNW025A	ZSMNW025A		1.9	10	15	110	90		1.9	HSH04A				-119	-119	-119	NW-SE	B	0	9.60E-04	-3.02	2	1	-3.02		-119	-75
ZSMNW025A	ZSMNW025A	ZSMNW025A			10		110	90			HSH01A				-170	-170	-170	NW-SE	B	0	1.85E-07	-6.73		1	-6.73		-170	-275
ZSMNW042A	ZSMNW042A	ZSMNW042A	X	8.3	40	50	105	55		8.3	HLX26	50	80	30	-36	-61	-48	NW-SE	DB	0	1.00E-08	-8.00	4	2	-6.35	2.34	-50	-75

HCD_(DZ-group)	HCD_(bh-intercept)	DZ_Geol.	Active in local model	Geological length (km)	Zone thickness (m)	Maximum thickness (m)	Zone Strike	Zone Dip	Earlier names	Geological length (km)	BH	Target_secup (BH length, m)	Target_seclow (BH length, m)	Target_sec-length (BH length, m)	Elevation (T-secup)	Elevation (T-seclow)	Elevation (mid-sec)	Geol. DZ-orientation group (NE-SW/ N-S/ NW-SE/ E-W/ Subh)	DZ-Char (D/DB/B)	Valu type T-BC	T-BC (m^2/s)	log10(T-BC) (T: m^2/s)	Sample size tot of T-BC	Sample size in elevation interval of T-BC	mean(log10(T-BC))	std(log10(T-BC))	mean elevation (T-BC) (m)	mean elevation class (T-BC) (m)
ZSMNW042A	ZSMNW042A	ZSMNW042A	X		40		105	55			HLX32	20	130	110	-6	-96	-51	NW-SE	DB	0	2.03E-05	-4.69						
ZSMNW042A	ZSMNW042A	ZSMNW042A	X		40		105	55			KLX27A	209	255	46	-172	-214	-193	NW-SE	DB	0	1.94E-07	-6.71		1	-6.71		-193	-275
ZSMNW042A	ZSMNW042A	ZSMNW042A	X		40		105	55			KLX15A	978	1000	22	-724	-740	-732	NW-SE	DB	0	8.26E-08	-7.08		1	-7.08		-732	-825
ZSMNW052A	ZSMNW052A	ZSMNW052A	X	1.1	15	20	116	90		1.1	KLX06	200	260	60	-163	-216	-189	NW-SE	B	0	1.59E-05	-4.80	1	1	-4.80		-189	-275
ZSMNW928A	ZSMEW007A + ZSMNW928A	ZSMEW007A + ZSMNW928A	X	1.5	10	100	120	28		1.5	KLX09	682	722	40	-654	-693	-674	SubH	B	0	2.12E-07	-6.67	3	3	-6.97	0.95	-789	-825
ZSMNW928A	ZSMNE107A + ZSMNE928A	ZSMNE107A + ZSMNE928A	X		10		120	28	Reflector N, ZSMNW928A		KLX02	770	960	190	-747	-936	-842	SubH	B	0	6.30E-07	-6.20						
ZSMNW928A	ZSMNW928A	ZSMNW928A	X		10		120	28			KLX04	879	881	2	-850	-852	-851	SubH	B	-1	9.40E-09	-8.03						
klx09_dz9	klx09_dz9	MDZ	X	>1	6.2		230	64		>1	KLX09	492	509	17	-465	-482	-474	NE-SW	B	0	4.93E-05	-4.31	1	1	-4.31		-474	-575
klx09_dz14	klx09_dz14	MDZ	X	>1	9		193	50		>1	KLX09	745	761	17	-716	-732	-724	N-S	B	0	7.84E-06	-5.11	1	1	-5.11		-724	-825
klx16_dz6	klx16_dz6	MDZ	X	>1	0.7		21	72		>1	KLX16A	210	211	1	-171	-172	-171	N-S	DB	0	5.52E-05	-4.26	1	1	-4.26		-171	-275
klx19_dz2	klx19_dz2	MDZ	X	>1	4.2		262	73		>1	KLX19A	298	304	6	-234	-239	-237	E-W	B	0	8.70E-05	-4.06	1	1	-4.06		-237	-275

High confidence in existence, Geology

Medium confidence in existence, Geology

Hydro re-defined thickness of geological deterministic DZ

Hydro defined deterministic HCD

Hydro nameing of geol- DZ groups

A.3.2 HCD statistics

Comments to figures

The figures shown cover the regional model data(“All data”) and local model data (Lx All data”) and only main statistical fits are shown. Corresponding tabulated data can be found in Chapter 7, Table 7-4 and base for regression models shown in tables 7-6 and 7-7.

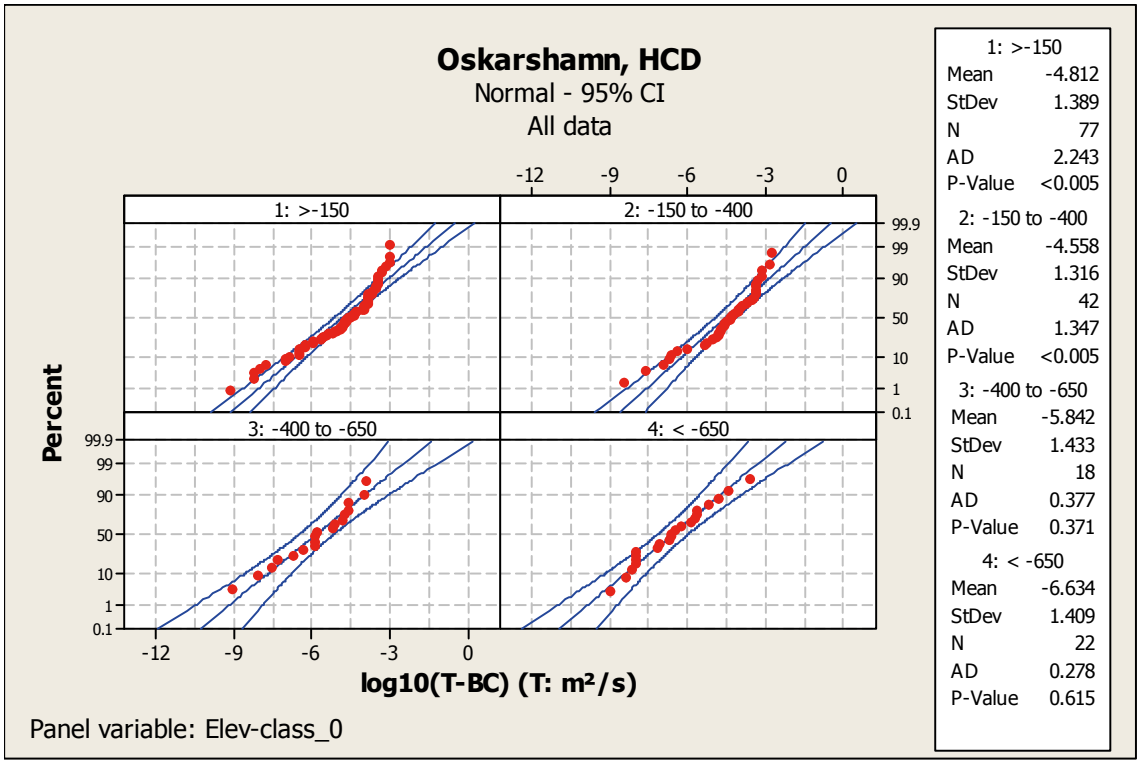
Oskarshamn, HCD
Normal - 95% CI
All data
1: >-150
2: -150 to -400
3: -400 to -650
4: < -650
Percent
log10(T-BC) (T: m²/s)
Panel variable: Elev-class_0
1: >-150
Mean -4.812
StDev 1.389
N 77
AD 2.243
P-Value <0.005
2: -150 to -400
Mean -4.558
StDev 1.316
N 42
AD 1.347
P-Value <0.005
3: -400 to -650
Mean -5.842
StDev 1.433
N 18
AD 0.377
P-Value 0.371
4: < -650
Mean -6.634
StDev 1.409
N 22
AD 0.278
P-Value 0.615

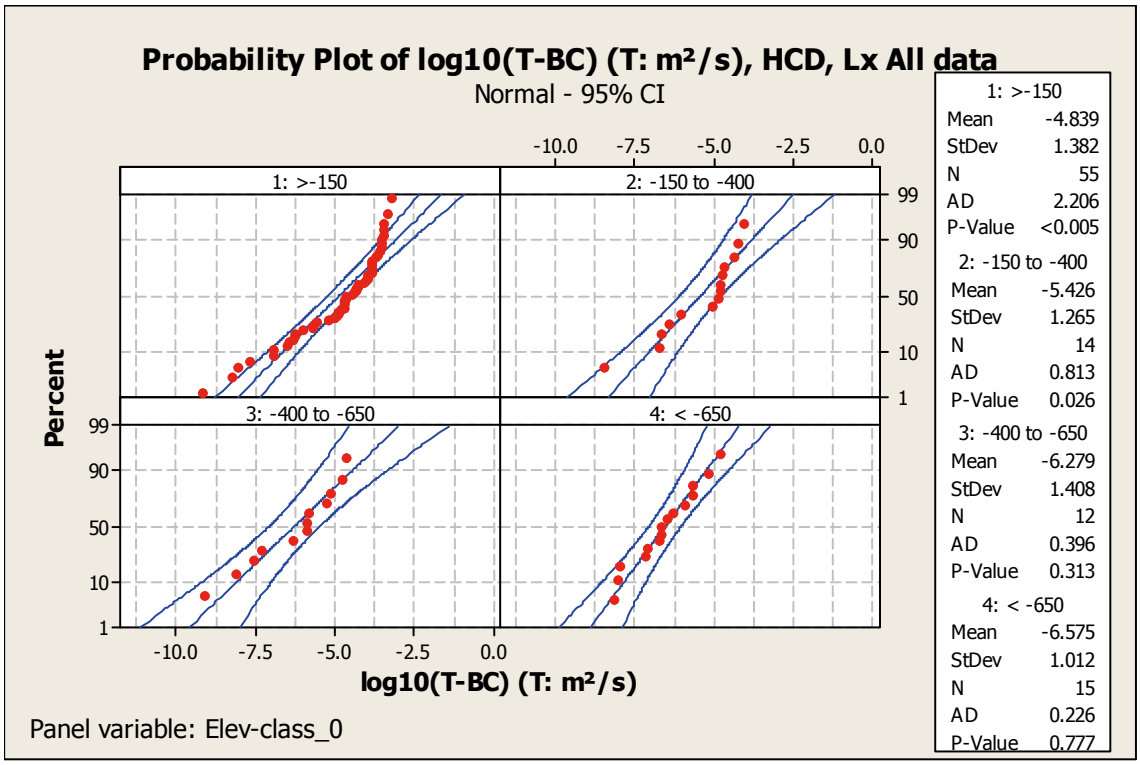
Probability Plot of log10(T-BC) (T: m²/s), HCD, Lx All data
Normal - 95% CI
1: >-150
2: -150 to -400
3: -400 to -650
4: < -650
Percent
log10(T-BC) (T: m²/s)
Panel variable: Elev-class_0
1: >-150
Mean -4.839
StDev 1.382
N 55
AD 2.206
P-Value <0.005
2: -150 to -400
Mean -5.426
StDev 1.265
N 14
AD 0.813
P-Value 0.026
3: -400 to -650
Mean -6.279
StDev 1.408
N 12
AD 0.396
P-Value 0.313
4: < -650
Mean -6.575
StDev 1.012
N 15
AD 0.226
P-Value 0.777

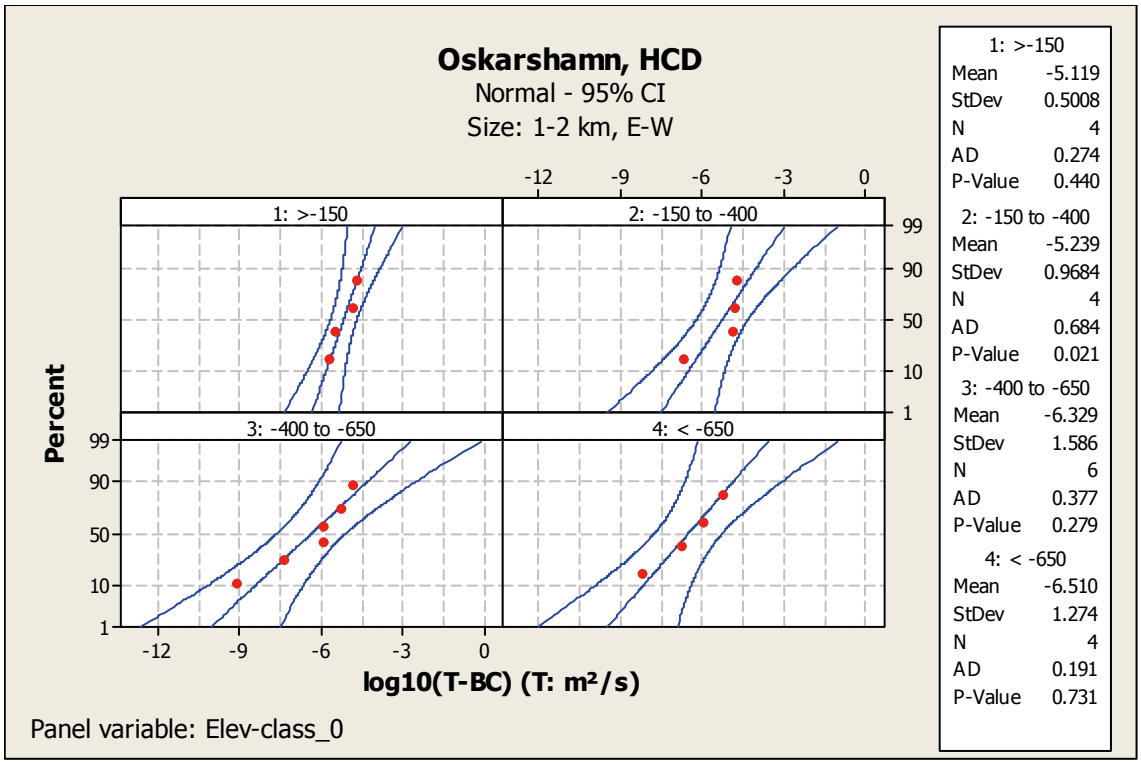
Oskarshamn, HCD
Normal - 95% CI
Size: 1-2 km, E-W
1: >-150
2: -150 to -400
3: -400 to -650
4: < -650
Percent
log10(T-BC) (T: m²/s)
Panel variable: Elev-class_0
1: >-150
Mean -5.119
StDev 0.5008
N 4
AD 0.274
P-Value 0.440
2: -150 to -400
Mean -5.239
StDev 0.9684
N 4
AD 0.684
P-Value 0.021
3: -400 to -650
Mean -6.329
StDev 1.586
N 6
AD 0.377
P-Value 0.279
4: < -650
Mean -6.510
StDev 1.274
N 4
AD 0.191
P-Value 0.731

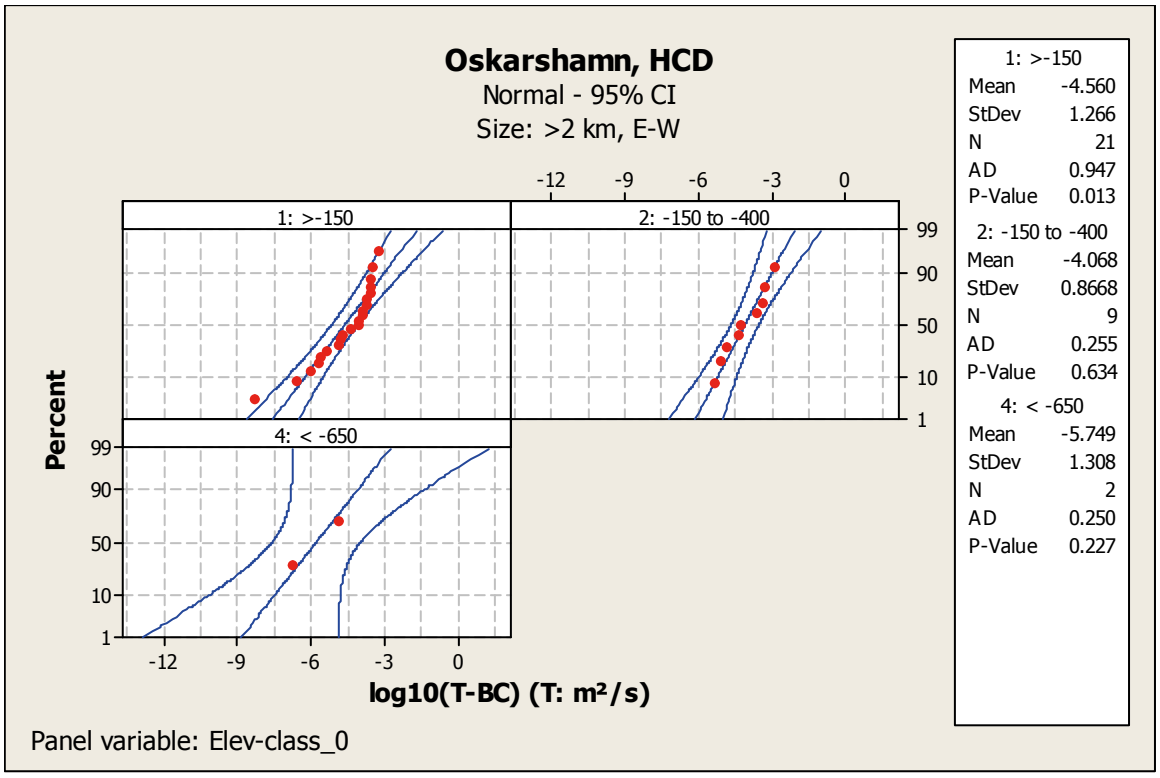
Oskarshamn, HCD
Normal - 95% CI
Size: >2 km, E-W
1: >-150
2: -150 to -400
4: < -650
Percent
log10(T-BC) (T: m²/s)
Panel variable: Elev-class_0
1: >-150
Mean -4.560
StDev 1.266
N 21
AD 0.947
P-Value 0.013
2: -150 to -400
Mean -4.068
StDev 0.8668
N 9
AD 0.255
P-Value 0.634
4: < -650
Mean -5.749
StDev 1.308
N 2
AD 0.250
P-Value 0.227

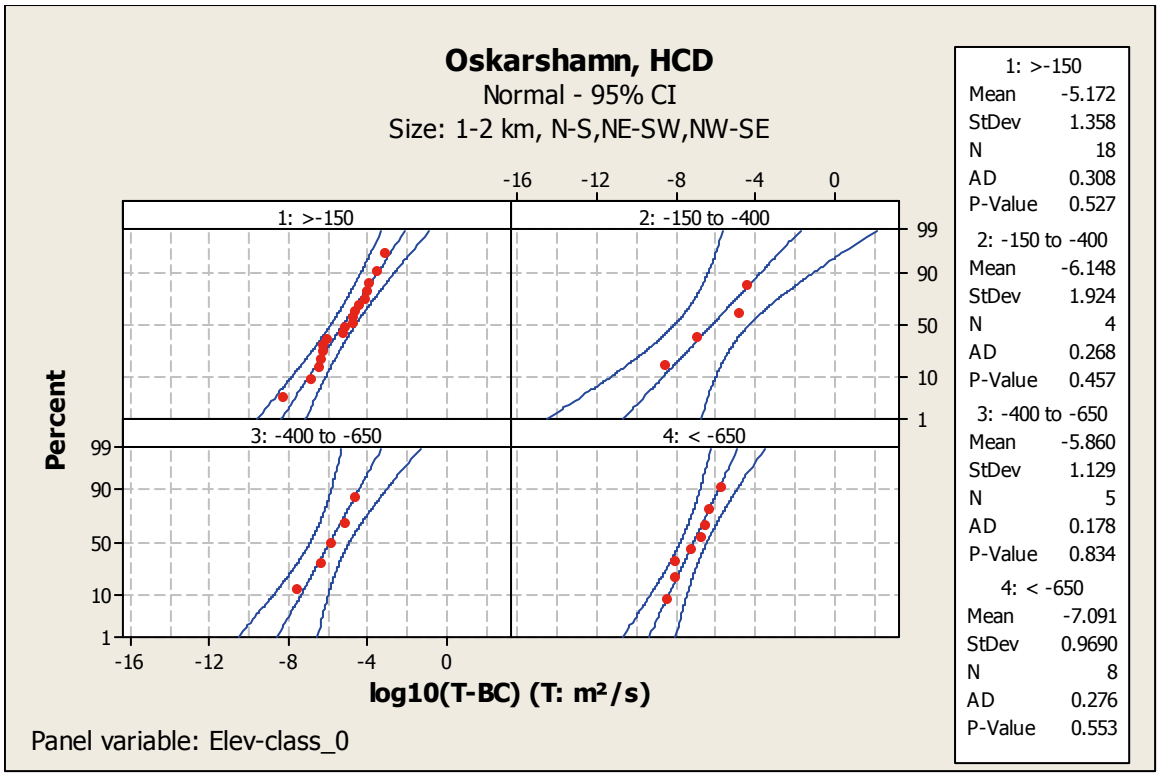
Oskarshamn, HCD
Normal - 95% CI
Size: 1-2 km, N-S,NE-SW,NW-SE
1: >-150
2: -150 to -400
3: -400 to -650
4: < -650
Percent
log10(T-BC) (T: m²/s)
Panel variable: Elev-class_0
1: >-150
Mean -5.172
StDev 1.358
N 18
AD 0.308
P-Value 0.527
2: -150 to -400
Mean -6.148
StDev 1.924
N 4
AD 0.268
P-Value 0.457
3: -400 to -650
Mean -5.860
StDev 1.129
N 5
AD 0.178
P-Value 0.834
4: < -650
Mean -7.091
StDev 0.9690
N 8
AD 0.276
P-Value 0.553

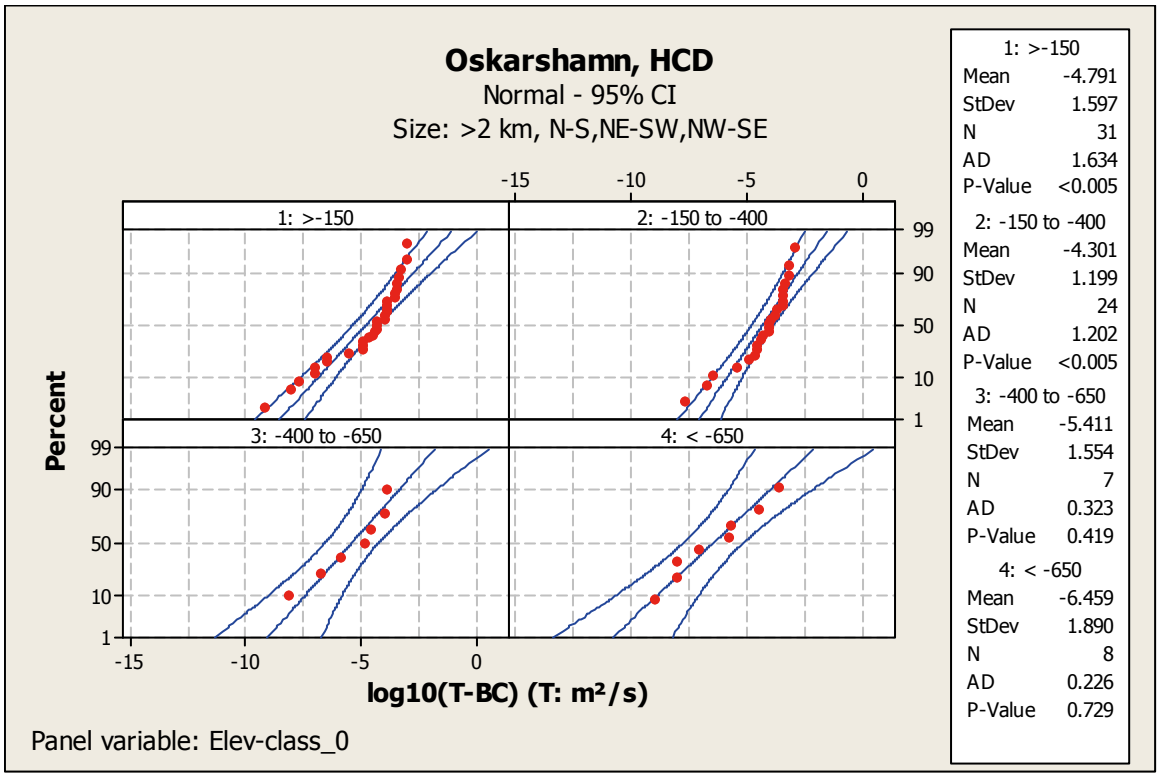
Oskarshamn, HCD
Normal - 95% CI
Size: >2 km, N-S,NE-SW,NW-SE
1: >-150
2: -150 to -400
3: -400 to -650
4: < -650
Percent
log10(T-BC) (T: m²/s)
Panel variable: Elev-class_0
1: >-150
Mean -4.791
StDev 1.597
N 31
AD 1.634
P-Value <0.005
2: -150 to -400
Mean -4.301
StDev 1.199
N 24
AD 1.202
P-Value <0.005
3: -400 to -650
Mean -5.411
StDev 1.554
N 7
AD 0.323
P-Value 0.419
4: < -650
Mean -6.459
StDev 1.890
N 8
AD 0.226
P-Value 0.729

A.3.3 Trend functions for HCD with site specific data

Comments to figures and table

In this appendix transmissivity-elevation trend functions are shown on the format:

Below the trend function: Log10 (T-HCD) = a + B * Z is used for the deformation zones (T: m^2/s). Z: Elevation in m (masl) (Z defined positive up).

For HCD with comment "Uncertain“, the suggested trend functions for DZ without hydraulic tests should be used.

HCD	a	B	Comment
HLX28_DZ1	-4,578	0,002405	Uncertain
ZSMEW002A	-4,848	0,002405	Uncertain
ZSMEW007A	**-3.996**	**0.002158**	
ZSMEW009A	-4,852	0,002405	Uncertain
ZSMEW013A	-6,230	0,002405	Uncertain
ZSMEW038A	-2,808	0,002405	Uncertain
ZSMEW900	-4,093	0,002405	Uncertain
ZSMEW946	**-4.210**	**0.004638**	
ZSMNE004A	-5,789	0,002405	Uncertain
ZSMNE005A	-5.267	0.002120	Uncertain
ZSMNE006A	**-3.017**	**0.003104**	
ZSMNE012A	**-3673**	**0.002209**	
ZSMNE024A	**-2.234**	**0.007197**	
ZSMNE031A	-1409	0.009965	Uncertain
ZSMNE040A	-6,038	0,002405	Uncertain
ZSMNE107A	-4.095	0.003426	Uncertain
ZSMNE942A	**-4,559**	**0,002405**	
ZSMNE944A	-5,760	0,002405	Uncertain
ZSMNS001	-4,203	0,002405	Uncertain
ZSMNS017B	**-3,240**	**0,002405**	
ZSMNS059A	-3,698	0,002405	Uncertain
ZSMNW025A	-4,527	0,002405	Uncertain
ZSMNW042A	-6,227	0,002405	Alt 1, Uncertain
ZSMNW042A	-6.398	0.000973	Alt 2 ,Uncertain
ZSMNW928A	-4,900	0,002405	Uncertain

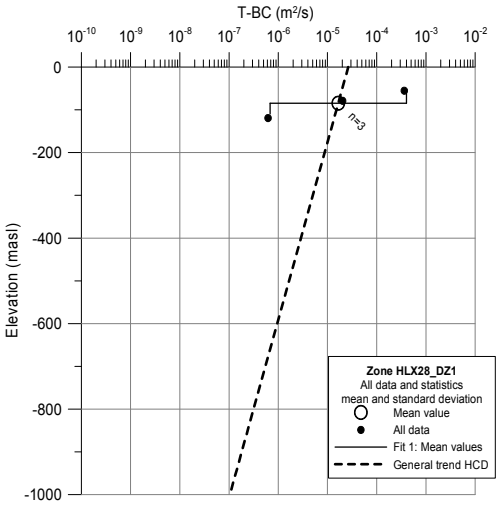
T-BC (m²/s)
Elevation (masl)
n=3
Zone HLX28_DZ1
All data and statistics
mean and standard deviation
Mean value
All data
Fit 1: Mean values
General trend HCD

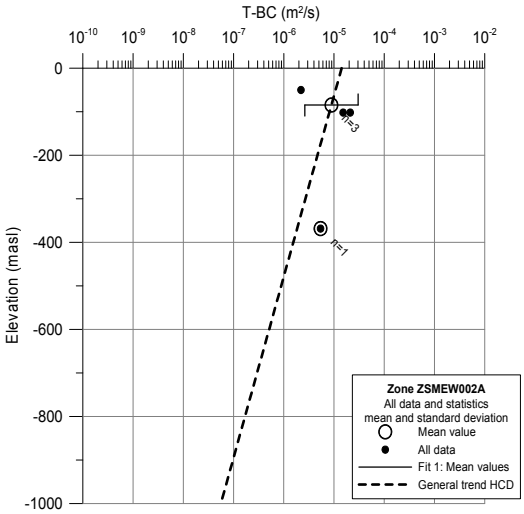
T-BC (m²/s)
Elevation (masl)
n=3
n=1
Zone ZSMEW002A
All data and statistics
mean and standard deviation
Mean value
All data
Fit 1: Mean values
General trend HCD

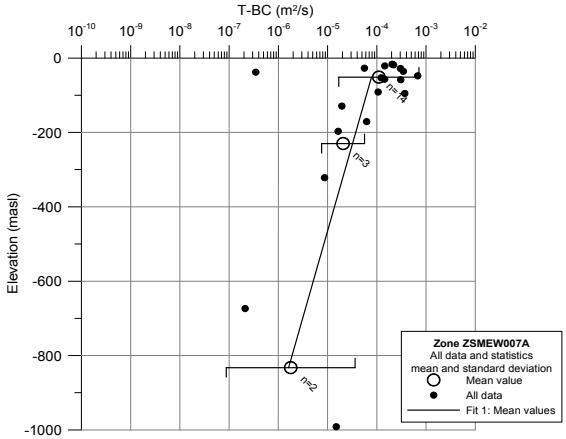
T-BC (m²/s)
Elevation (masl)
n=4
n=3
n=2
Zone ZSMEW007A
All data and statistics
mean and standard deviation
Mean value
All data
Fit 1: Mean values

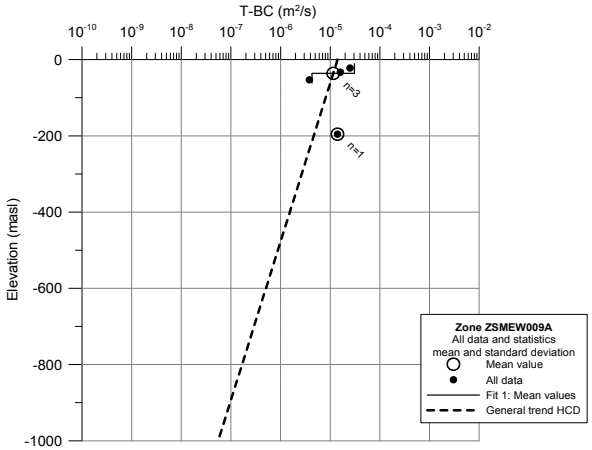
T-BC (m²/s)
Elevation (masl)
n=3
n=1
Zone ZSMEW009A
All data and statistics
mean and standard deviation
Mean value
All data
Fit 1: Mean values
General trend HCD

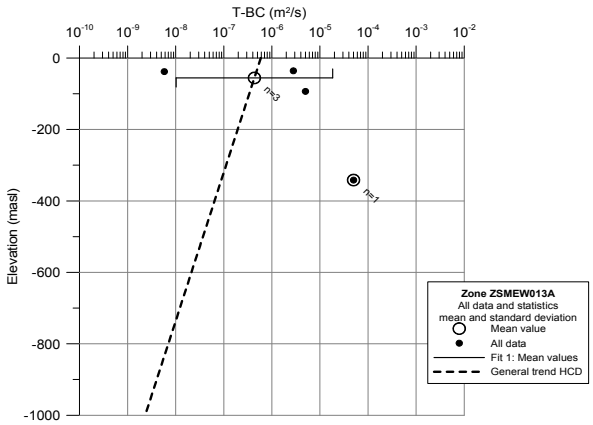
T-BC (m²/s)
Elevation (masl)
n=3
n=1
Zone ZSMEW013A
All data and statistics
mean and standard deviation
Mean value
All data
Fit 1: Mean values
General trend HCD

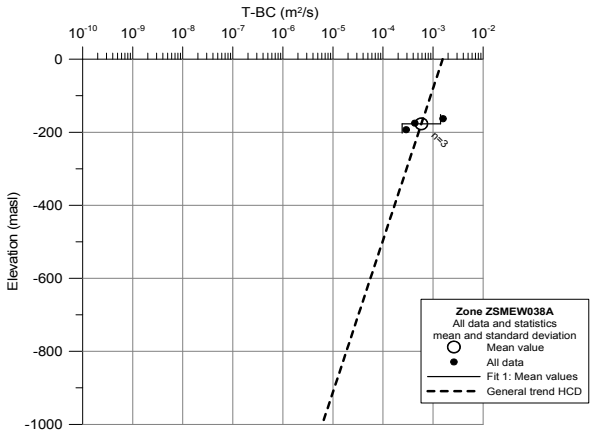
T-BC (m²/s)
Elevation (masl)
n=3
Zone ZSMEW038A
All data and statistics
mean and standard deviation
Mean value
All data
Fit 1: Mean values
General trend HCD

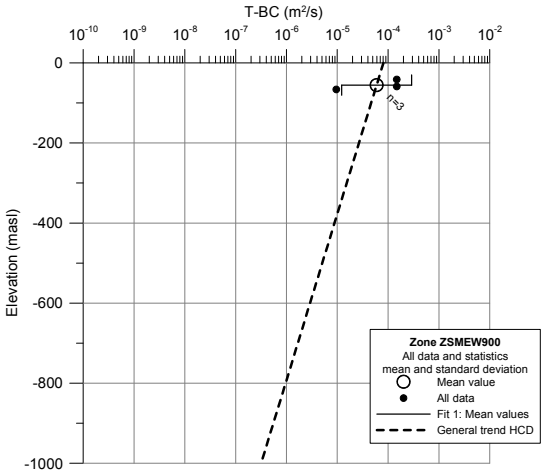
T-BC (m²/s)
Elevation (masl)
n=3
Zone ZSMEW900
All data and statistics
mean and standard deviation
Mean value
All data
Fit 1: Mean values
General trend HCD

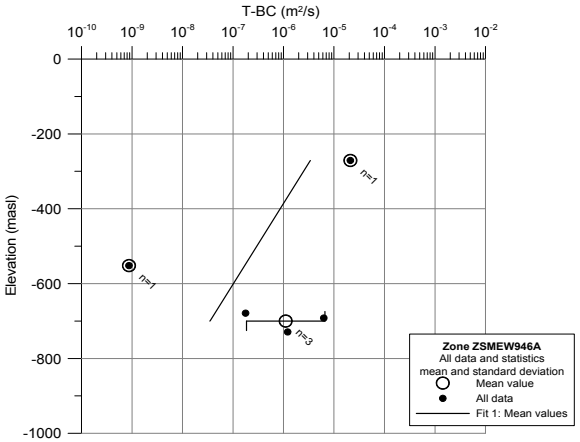
T-BC (m²/s)
Elevation (masl)
n=1
n=1
n=3
Zone ZSMEW946A
All data and statistics
mean and standard deviation
Mean value
All data
Fit 1: Mean values

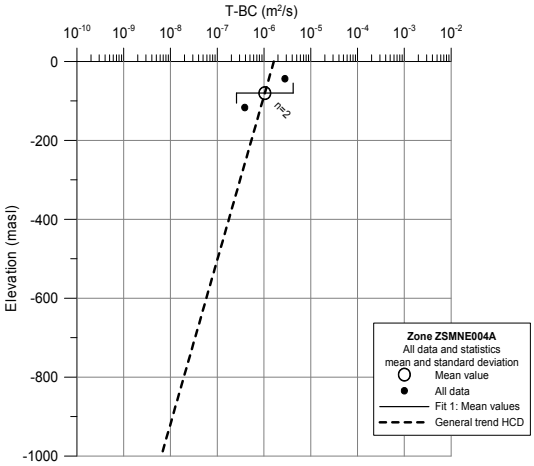
T-BC (m²/s)
Elevation (masl)
n=2
Zone ZSMNE004A
All data and statistics
mean and standard deviation
Mean value
All data
Fit 1: Mean values
General trend HCD

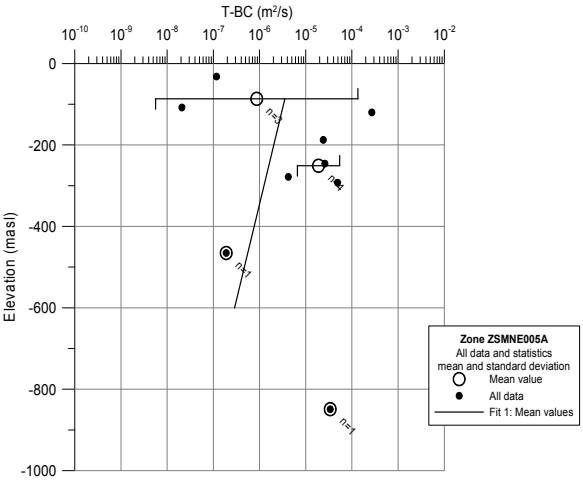
T-BC (m²/s)
Elevation (masl)
n=3
n=4
n=1
n=1
Zone ZSMNE005A
All data and statistics
mean and standard deviation
Mean value
All data
Fit 1: Mean values

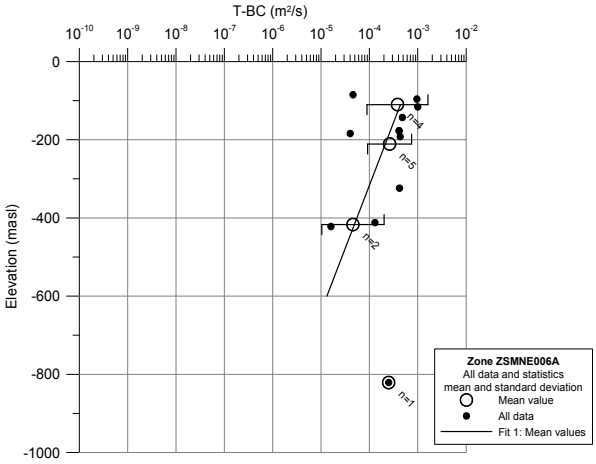
T-BC (m²/s)
Elevation (masl)
n=4
n=5
n=2
n=1
Zone ZSMNE006A
All data and statistics
mean and standard deviation
Mean value
All data
Fit 1: Mean values

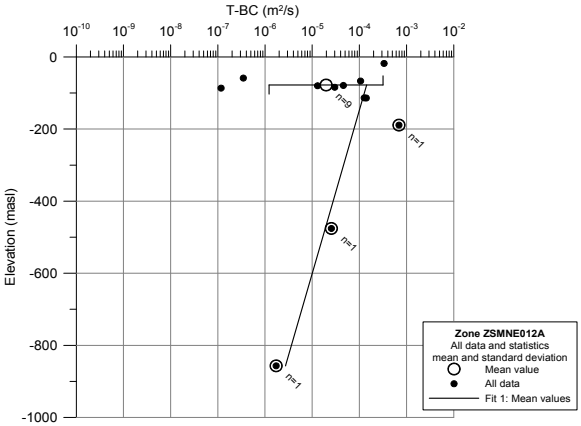
T-BC (m²/s)
Elevation (masl)
n=9
n=1
n=1
n=1
Zone ZSMNE012A
All data and statistics
mean and standard deviation
Mean value
All data
Fit 1: Mean values

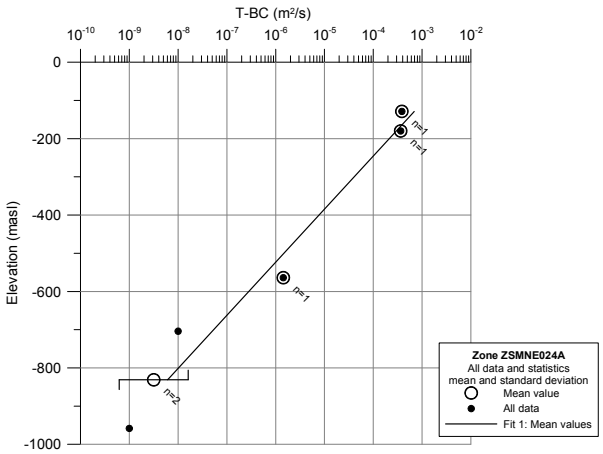
T-BC (m²/s)
Elevation (masl)
n=1
n=1
n=1
n=2
Zone ZSMNE024A
All data and statistics
mean and standard deviation
Mean value
All data
Fit 1: Mean values

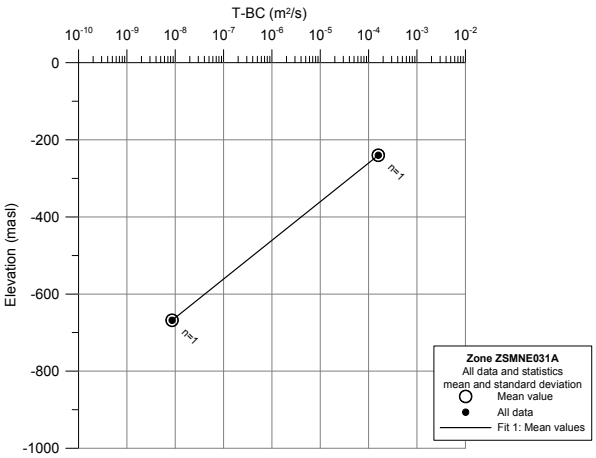
T-BC (m²/s)
Elevation (masl)
n=1
n=1
Zone ZSMNE031A
All data and statistics
mean and standard deviation
Mean value
All data
Fit 1: Mean values

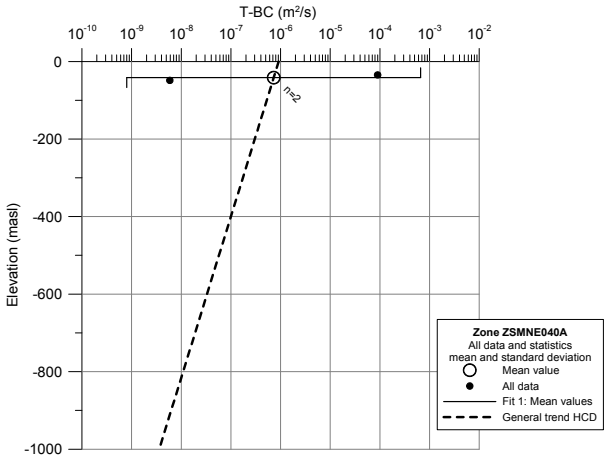
T-BC (m²/s)
Elevation (masl)
n=2
Zone ZSMNE040A
All data and statistics
mean and standard deviation
Mean value
All data
Fit 1: Mean values
General trend HCD

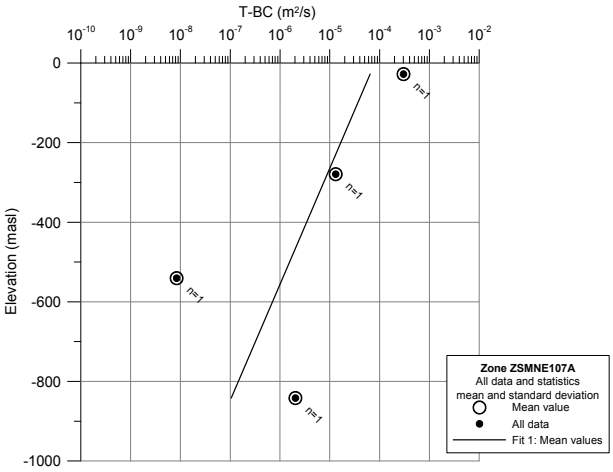
T-BC (m²/s)
Elevation (masl)
n=1
n=1
n=1
n=1
Zone ZSMNE107A
All data and statistics
mean and standard deviation
Mean value
All data
Fit 1: Mean values

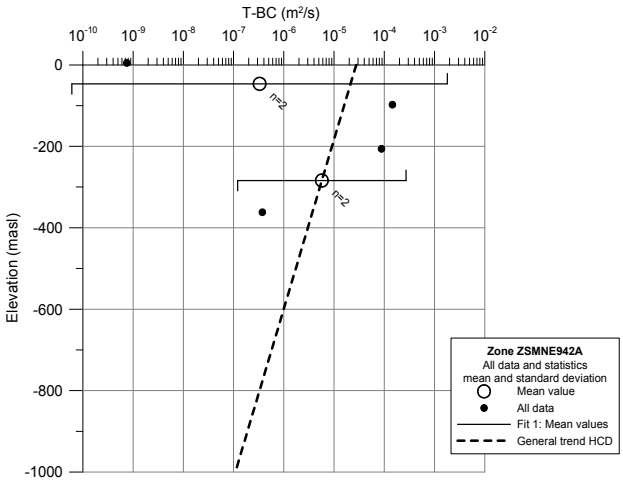
T-BC (m²/s)
Elevation (masl)
n=2
n=2
Zone ZSMNE942A
All data and statistics
mean and standard deviation
Mean value
All data
Fit 1: Mean values
General trend HCD

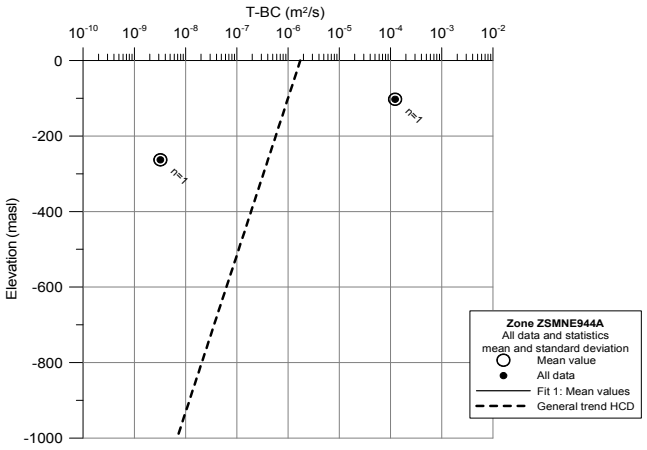
T-BC (m²/s)
Elevation (masl)
n=1
n=1
Zone ZSMNE944A
All data and statistics
mean and standard deviation
Mean value
All data
Fit 1: Mean values
General trend HCD

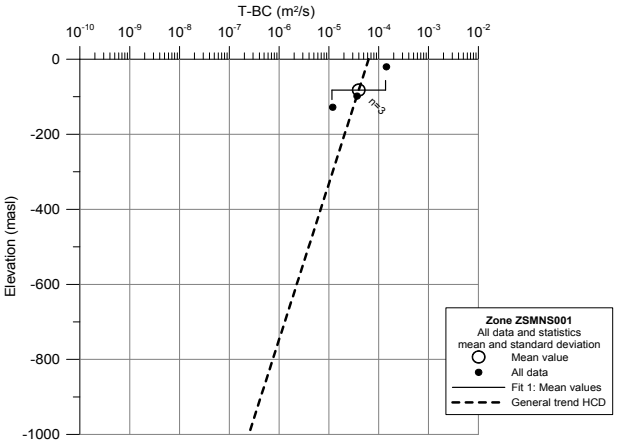
T-BC (m²/s)
Elevation (masl)
ns=3
Zone ZSMNS001
All data and statistics
mean and standard deviation
Mean value
All data
Fit 1: Mean values
General trend HCD

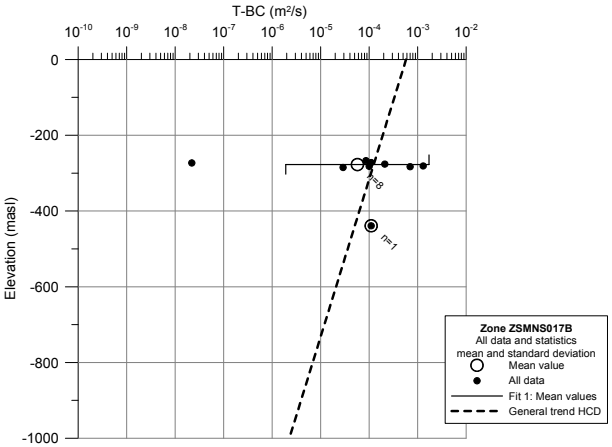
T-BC (m²/s)
Elevation (masl)
ns=8
ns=1
Zone ZSMNS017B
All data and statistics
mean and standard deviation
Mean value
All data
Fit 1: Mean values
General trend HCD

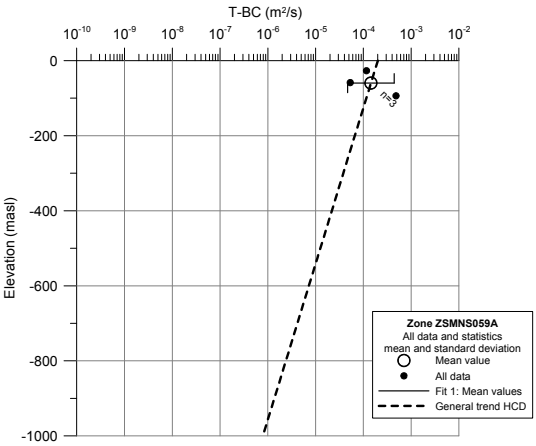
T-BC (m²/s)
Elevation (masl)
ns=3
Zone ZSMNS059A
All data and statistics
mean and standard deviation
Mean value
All data
Fit 1: Mean values
General trend HCD

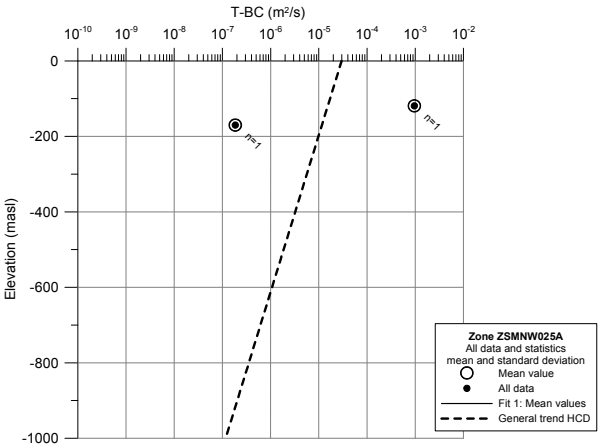
T-BC (m²/s)
Elevation (masl)
ns=1
ns=1
Zone ZSMNW025A
All data and statistics
mean and standard deviation
Mean value
All data
Fit 1: Mean values
General trend HCD

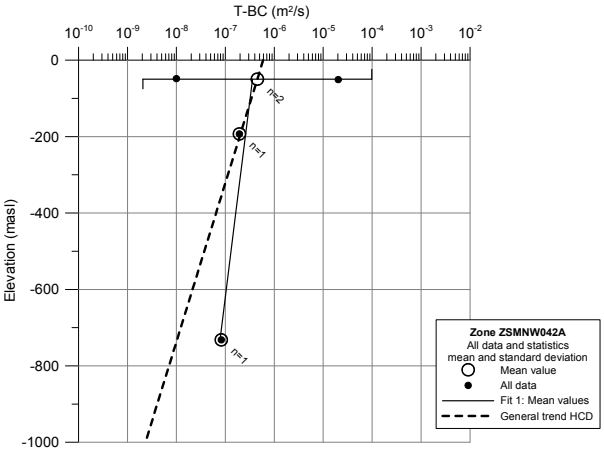
T-BC (m²/s)
Elevation (masl)
ns=2
ns=1
ns=1
Zone ZSMNW042A
All data and statistics
mean and standard deviation
Mean value
All data
Fit 1: Mean values
General trend HCD

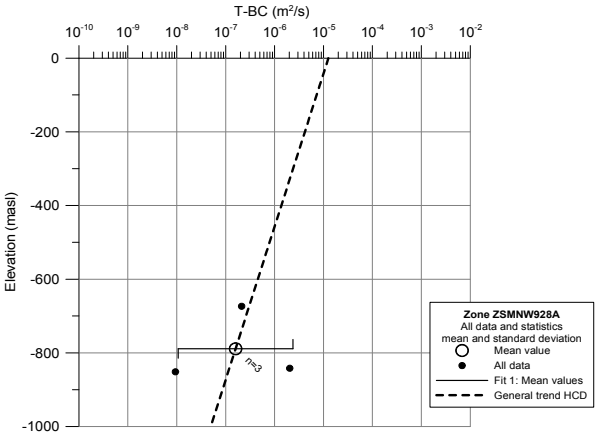
T-BC (m²/s)
Elevation (masl)
ns=3
Zone ZSMNW928A
All data and statistics
mean and standard deviation
Mean value
All data
Fit 1: Mean values
General trend HCD

A.3.4 PFL-f statistics for HCDs

Comments to figures

The table covers local model area, except for borehole KLX27A, and shows for the Hydraulic Conductor Domains (HCD, the statistics of PFL-f within HCDs and includes the following columns:

- *Bh-ID*: Borehole name.
- *HCD*: HCD identification.
- *Certainty*: Judgement of the HCD existence based on the geological interpretation of the deformation zones.
- *Z type*: Zone type grouped into main character: Brittle, Ductile/brittle or Brittle.
- *Strike/dip*: Orientation of HCD.
- *From length, To length:* Borehole section for the HCD
- *Bh-length(HCD)*: Lengths of individual HCDs (with PFL-f features) along the borehole.
- *HCD-thickness at bh*: Estimated true thickness of individual HCDs (with PFL-f features).
- *N-PFL-f*: Number of PFL-f features within individual HCDs.
- *N-corr-PFL-f*: Number of PFL-f features, Terzaghi corrected due to PFL-f features orientations, within individual HCDs.
- *P10 (PFL-f)* and *P10-corr(PFL-f)*: Intensity of PFL-f features within a HCD. N-PFL-f and N-corr-PFL-f divided by HCD length along the borehole, for each individual HCD.
- *T(sum T-PFL-f)*: **Sum of T-PFL-f**, where T-PFL-f is the **transmissivity of individual PFL-f features** within a HCD (sum T-PFL-f= total transmissivity of a HCD).
- *log10 (sum T-PFL-f)*: **Log10(sum T-PFL-f)**, where T-PFL-f is the **transmissivity of individual PFL-f features** within a HCD (sum T-PFL-f= total transmissivity of a HCD).
- *Mean T-PFL-f*: Arithmetic mean of T-PFL-f within each HCD, where T-PFL-f is the **transmissivity of individual PFL-f features** within a HCD.
- *10^(Mean log10(T-PFL-f))*: Anti-log of the calculated values for Mean log10(T-PFL-f) shown below.
- *Mean log10(T-PFL-f)*: Arithmetic mean of log10(T-PFL-f)) within each HCD, where T-PFL-f is the **transmissivity of individual PFL-f features** within a HCD.

- *Std log10(T-PFL-f)*: Standard deviation of log10(T-PFL-f) within each HCD, where T-PFL-f is the **transmissivity of individual PFL-f features** within a HCD.

- *Elevation-class_0:* Depth grouping parameter.

- *Elevation HCD*: Elevation for the HCD.

Bh-ID	HCD	Certainty	Z type	Strike (degr.)	Dip (degr.)	From length (m)	To length (m)	Bh-length (HCD) (m)	HCD thickness at bh (m)	N PFL-f (-)	N PFL-f-corr (-)	P10 (PFL-f) (1/m)	P10corr (PFL-f) (1/m)	T (sum T-PFL-f) (m^2/s)	log10 (sum T-PFL-f) (T:m^2/s)	Mean T PFL-f (m^2/s)	10^(Mean log10(T-PFL-f)) (m^2/s)	Mean log10(T-PFL-f) (T:m^2/s)	Std log10(T-PFL-f) (T:m^2/s)	Elev-class_0 (m)	ELEVATION MDZ (m)
KLX09F	KLX09F_DZ1	High conf.	B	178	19	8	22	14	14	6	8	0.43	0.58	2.09E-06	-5.68	3.48E-07	1.60E-07	-6.80	0.54	1: >-150	7.10
KLX10B	ZSMNE942A	High conf.	DB	246	88	0	20	20	15	2	3	0.22	0.34	5.48E-07	-6.26	2.74E-07	2.62E-07	-6.58	0.18	1: >-150	0.98
KLX28A	KLX28A_DZ1	High conf.	NA	182	33	14.4	33.1	18.7	13	12	39	0.64	2.11	8.68E-07	-6.06	7.23E-08	1.83E-08	-7.74	0.78	1: >-150	-12.00
KLX10C	KLX10C_DZ3	High conf.	DB	300	35	35	59	24	10	5	11	0.21	0.46	6.20E-06	-5.21	1.24E-06	2.20E-08	-7.66	1.67	1: >-150	-23.58
KLX09G	ZSMNS046A	High conf.	DB	170	90	40	68	28	20	27	62	0.96	2.23	1.37E-05	-4.86	5.08E-07	4.03E-08	-7.39	0.92	1: >-150	-27.52
KLX09E	KLX09E_DZ2	High conf.	DB	295	14	76	105	29	22	12	21	0.41	0.72	4.80E-05	-4.32	4.00E-06	2.94E-07	-6.53	1.07	1: >-150	-56.80
KLX14A	ZSMNS059A	High conf.	DB	192	88	75	125	50	50	38	80	0.76	1.60	6.16E-05	-4.21	1.62E-06	2.70E-07	-6.57	0.95	1: >-150	-57.57
KLX17A	ZSMEW900A	High conf.	DB	92	57	100	114	14	25	9	12	0.64	0.87	8.32E-06	-5.08	9.25E-07	1.01E-07	-7.00	1.01	1: >-150	-65.63
KLX08	KLX08_DZ1	High conf.	B	0	18	100	131	31	27	10	17	0.32	0.56	1.63E-05	-4.79	1.63E-06	1.54E-07	-6.81	1.02	1: >-150	-72.52
KLX10C	KLX10C_DZ7	High conf.	DB	323	39	121	140	19	10	4	13	0.21	0.67	8.51E-07	-6.07	2.13E-07	6.59E-08	-7.18	0.94	1: >-150	-88.73
KLX07A	ZSMEW007A	High conf.	B	281	44	105	168.3	63.3	80	39	64	0.62	1.01	9.92E-05	-4.00	2.54E-06	2.39E-07	-6.62	0.89	1: >-150	-92.49
KLX20A	ZSMNS001C_hydr	High conf.	DB	187	81	102	290	188	130	55	92	0.29	0.49	1.05E-05	-4.98	1.90E-07	1.64E-08	-7.79	1.10	1: >-150	-115.61
KLX07B	ZSMEW007A	High conf.	B	281	44	124	172	48	80	15	25	0.31	0.52	1.48E-05	-4.83	9.85E-07	8.10E-08	-7.09	1.00	1: >-150	-127.82
KLX17A	ZSMEW900B	High conf.	DB	106	78	193	227	34	25	7	17	0.21	0.51	1.45E-07	-6.84	2.07E-08	8.86E-09	-8.05	0.55	2: -150 to -400	-152.58
KLX16A	klx16_dz6	High conf.	DB	21	72	209.95	210.92	0.97	0.7	1	1	1.03	1.39	2.12E-05	-4.67	2.12E-05	2.12E-05	-4.67	NA	2: -150 to -400	-171.56
KLX08	ZSMEW007A	High conf.	B	281	44	211	300	89	80	16	23	0.18	0.25	1.27E-05	-4.89	7.97E-07	2.31E-07	-6.64	0.85	2: -150 to -400	-181.48
KLX10	ZSMNE942A	High conf.	DB	246	88	103	349	246	15	137	383	0.56	1.56	8.35E-05	-4.08	6.09E-07	7.60E-08	-7.12	1.07	2: -150 to -400	-190.86
KLX06	ZSMNW052A	High conf.	B	116	90	200	260	60	15	31	39	0.52	0.66	1.53E-05	-4.81	4.95E-07	1.26E-07	-6.90	0.81	2: -150 to -400	-192.09
KLX16A	ZSMNE107A	High conf.	DB	225	80	228	434	206	35	46	117	0.22	0.57	4.17E-04	-3.38	9.06E-06	1.97E-08	-7.71	0.79	2: -150 to -400	-232.27

Bh-ID	HCD	Certainty	Z type	Strike (degr.)	Dip (degr.)	From length (m)	To length (m)	Bh-length (HCD) (m)	HCD thickness at bh (m)	N PFL-f (-)	N PFL-f-corr (-)	P10 (PFL-f) (1/m)	P10corr (PFL-f) (1/m)	T (sum T-PFL-f) (m^2/s)	log10 (sum T-PFL-f) (T:m^2/s)	Mean T PFL-f (m^2/s)	10^(Mean log10(T-PFL-f)) (m^2/s)	Mean log10(T-PFL-f) (T:m^2/s)	Std log10(T-PFL-f) (T:m^2/s)	Elev-class_0 (m)	ELEVATION MDZ (m)
KLX19A	klx19_dz2	High conf.	B	262	73	298.35	304.2	5.85	4.2	4	11	0.68	1.82	8.70E-05	-4.06	2.17E-05	3.49E-07	-6.46	2.22	2: -150 to -400	-235.91
KLX07A	KLX07A_DZ7	High conf.	DB	267	90	347	388	41	30	35	68	0.85	1.67	1.54E-05	-4.81	4.40E-07	1.25E-07	-6.90	0.77	2: -150 to -400	-263.97
KLX04	ZSMEW946A	High conf.	DB	80	23	295	298	3	10	3	3	1.00	1.05	1.34E-05	-4.87	4.48E-06	2.97E-06	-5.53	0.55	2: -150 to -400	-270.68
KLX06	ZSMEW002A	High conf.	DB	90	65	297	425	128	100	73	107	0.57	0.84	2.00E-05	-4.70	2.75E-07	5.39E-08	-7.27	0.88	2: -150 to -400	-291.75
KLX15A	ZSMNE107A	High conf.	DB	225	80	711	744	33	35	2	3	0.06	0.09	6.27E-07	-6.20	3.14E-07	1.36E-07	-6.87	0.91	2: -150 to -400	-296.95
KLX07A	KLX07A_DZ9	High conf.	DB	253	35	448	459	11	10	5	6	0.45	0.56	1.95E-07	-6.71	3.90E-08	2.36E-08	-7.63	0.54	2: -150 to -400	-323.32
KLX08	KLX08_DZ6	High conf.	B	296	89	396	416	20	10	12	22	0.60	1.09	2.80E-05	-4.55	2.33E-06	2.14E-07	-6.67	1.28	2: -150 to -400	-328.25
KLX04	ZSMEW007A	High conf.	B	281	44	310	385	75	80	29	46	0.39	0.61	5.73E-06	-5.24	1.98E-07	3.91E-08	-7.41	0.85	2: -150 to -400	-329.12
KLX19A	ZSMNE942A	High conf.	DB	246	88	437	464	27	15	7	17	0.26	0.62	3.06E-07	-6.51	4.37E-08	1.96E-08	-7.71	0.64	2: -150 to -400	-367.66
KLX08	ZSMEW946A	High conf.	DB	80	23	478	486	8	10	5	6	0.63	0.80	1.00E-06	-6.00	2.00E-07	5.28E-08	-7.28	0.72	2: -150 to -400	-390.45
KLX19A	klx19_dz5-8_dolerite	Medium conf.	NA	185	81	464.1	554.63	90.53	10	14	29	0.15	0.32	1.13E-06	-5.95	8.07E-08	1.58E-08	-7.80	0.81	2: -150 to -400	-396.60
KLX18A	KLX18A_DZ9	High conf.	DB	95	50	472	489	17	10	9	16	0.53	0.95	5.44E-08	-7.26	6.05E-09	3.36E-09	-8.47	0.55	3: -400 to -650	-451.19
KLX11A	KLX11_DZ11	High conf.	B	65	20	486	513	27	20	6	7	0.22	0.26	2.11E-08	-7.68	3.52E-09	3.29E-09	-8.48	0.17	3: -400 to -650	-455.33
KLX09	KLX09_DZ9	High conf.	B	230	64	492.38	509.05	16.67	6.2	1	1	0.06	0.06	4.93E-05	-4.31	4.93E-05	4.93E-05	-4.31	NA	3: -400 to -650	-467.79
KLX07A	KLX07A_DZ10	High conf.	B	253	35	693	724	31	30	11	13	0.22	0.25	3.12E-06	-5.51	2.84E-07	3.60E-08	-7.44	0.91	3: -400 to -650	-469.89
KLX13A	ZSMEW120A	High conf.	DB	80	64	488	593.32	105.32	50	39	52	0.37	0.49	9.00E-07	-6.05	2.31E-08	7.96E-09	-8.10	0.68	3: -400 to -650	-504.72
KLX09	KLX09_DZ10	High conf.	B	263	37	520	554	34	25	12	13	0.35	0.39	4.71E-06	-5.33	3.93E-07	1.23E-07	-6.91	0.62	3: -400 to -650	-509.14
KLX07A	KLX07A_DZ11	High conf.	B	263	41	738	785	47	47	8	12	0.26	0.40	7.06E-07	-6.15	8.83E-08	2.11E-08	-7.68	0.89	3: -400 to -650	-522.26
KLX07A	KLX07A_DZ12	High conf.	DB	348	65	817	836	19	10	21	28	0.45	0.60	9.47E-06	-5.02	4.51E-07	6.98E-08	-7.16	1.06	3: -400 to -650	-566.46
KLX21B	klx21b_dz10_12	High conf.	DB	192	80	559	707	148	10	23	67	0.16	0.45	1.75E-05	-4.76	7.63E-07	1.14E-07	-6.94	0.85	3: -400 to -650	-567.84
KLX07A	KLX07A_DZ13	High conf.	DB	225	28	604	654.7	50.7	10	3	5	0.16	0.24	4.19E-07	-6.38	1.40E-07	3.33E-08	-7.48	1.07	3: -400 to -650	-613.14
KLX10	ZSMEW946A	High conf.	DB	80	23	698	706	8	10	3	3	0.38	0.40	4.44E-08	-7.35	1.48E-08	8.34E-09	-8.08	0.64	4: <-650	-677.64

Bh-ID	HCD	Certainty	Z type	Strike (degr.)	Dip (degr.)	From length (m)	To length (m)	Bh-length (HCD) (m)	HCD thickness at bh (m)	N PFL-f (-)	N PFL-f-corr (-)	P10 (PFL-f) (1/m)	P10corr (PFL-f) (1/m)	T (sum T-PFL-f) (m^2/s)	log10 (sum T-PFL-f) (T:m^2/s)	Mean T PFL-f (m^2/s)	10^(Mean log10(T-PFL-f)) (m^2/s)	Mean log10(T-PFL-f) (T:m^2/s)	Std log10(T-PFL-f) (T:m^2/s)	Elev-class_0 (m)	ELEVATION MDZ (m)
KLX09	ZSMEW007A + ZSMNW928A	High conf.	B	281	44	682	722	40	80	2	2	0.05	0.05	1.36E-07	-6.87	6.82E-08	6.76E-08	-7.17	0.08	4: <-650	-687.21
KLX03	ZSMEW946A	High conf.	DB	80	23	727	743	16	10	3	3	0.19	0.20	1.93E-06	-5.71	6.44E-07	5.70E-07	-6.24	0.26	4: <-650	-700.47
KLX09	KLX09_DZ14	High conf.	B	193	50	744.5	761	16.5	9	2	3	0.12	0.19	7.84E-06	-5.11	3.92E-06	9.05E-07	-6.04	1.32	4: <-650	-723.46
KLX03	klx03_dz1b	High conf.	B	121	20	759	777	18	10	4	13	0.22	0.69	5.30E-07	-6.28	1.32E-07	1.08E-07	-6.97	0.37	4: <-650	-729.75
KLX02	ZSMNE107A + ZSMNE928A	High conf.	DB	225	80	770	960	190	35	23	51	0.12	0.27	5.19E-07	-6.28	2.26E-08	1.08E-08	-7.96	0.58	4: <-650	-852.99
KLX04	ZSMNW928A	Medium conf.	B	120	28	879	881	2	10	1	1	0.50	0.55	1.24E-07	-6.91	1.24E-07	1.24E-07	-6.91	NA	4: <-650	-853.27
KLX04	KLX04_DZ6b	High conf.	B	177	42	935	972	37	30	1	1	0.04	0.04	1.50E-08	-7.82	1.50E-08	1.50E-08	-7.82	NA	4: <-650	-862.70
KLX04	KLX04_DZ6c	High conf.	B	156	67	887	914	27	14	7	10	0.19	0.26	1.41E-07	-6.85	2.01E-08	1.53E-08	-7.82	0.31	4: <-650	-918.28

(1): ZSMNE107A + ZSMNE928A. Certainty, Z.type, Strike, dip, HCD thickness estimates refers to ZSMNE107A

(2): ZSMEW007A + ZSMNW928A: Certainty,, Z.type, Strike, dip, HCD thickness estimates refers to ZSMEW007A

(3): klx19_dz5-8_dolerite: Certainty, based on hydrogeological judgement.

A.3.5 HCDs defined as compliment to deterministic deformation zones defined by geology

A.3.5.1. Background

Traditionally, a strict honouring of the geological definitions of deterministic deformation zones and minor deformation zones (MDZ) has been obeyed in the hydrogeological modelling at Laxemar. However, several independent observations made during calibration and tests with hydraulic models at Laxemar have indicated a need to recalibrate the HydroDFN. The changes/fixes include an identified need to remove a small number of PFL data points, ”outliers”, from the calibration. This position based on HydroDFN performance in the regional flow modelling, and the shapes and properties of the distributions in the HydroDFN model.

The availability and relative abundance of multiple attributes of calibration in the hydrogeological modelling open up for the possibility to argue for introduction of objects (HCDs), corresponding to the above outliers, which do not fall strictly within the geological definitions for deterministic DZs (and subsequently for deterministic HCDs) employed in the Laxemar geological modelling:

- Size L>1000 m
- Thickness $2b \geq 10$ m

In the following, argumentation for definition of additional HCDs based on hydrogeological considerations is put forward.

Geological reasoning

The length-size relationship employed at Laxemar can be regarded as a guide, not a strict rule. Hence we may have structures of hydraulic significance (identified PFLs) with thicknesses less than 10 m, that in fact may/should belong to the HCD domain.

An introduction of ”HCDs outside the geological classification scheme” as indicated above may, under certain conditions, be justified. However, under **no** circumstance can a HCD be introduced without a direct coupling to a geological structure, with a well-defined location and geometry in the borehole. Furthermore, there should exist a underlying important hydrogeological reason for introducing such a HCD. Two cases can be considered:

- Hydraulic data and tests indicate that the geological structure acts as a local hydraulic barrier.
- The measured transmissivity is high (comparable with HCDs) of the geological structure, which implies that the structure also may be large.

A.3.5.2. Data

The transmissivities of the 4 new HCDs (klx09_dz9, klx09_dz14, klx16_dz6 and klx19_dz2) are shown in Figure A3-1 together with other HCDs and MDZs in the loc model volume. The location of HCD-H (in relation to HRDs) are:

KLX09, elev. -468m and -723m (HRD_N/HRD_EW007)

KLX16, elev. -171m, (HRD_C)

KLX19, elev. -236m, (HRD_W)

MDZ without PFL-f (MDZ_0) have been assigned $T=10^{-10}$ m^2/s

Transmissivities of HCD-H are high within depth zones compared to other MDZ:s ar as can be seen these new HCDs have transmissivities in the range of what the rest of HCDs have. Details of the 4 new HCDs are shown in Figure A3-2 through Figure A3

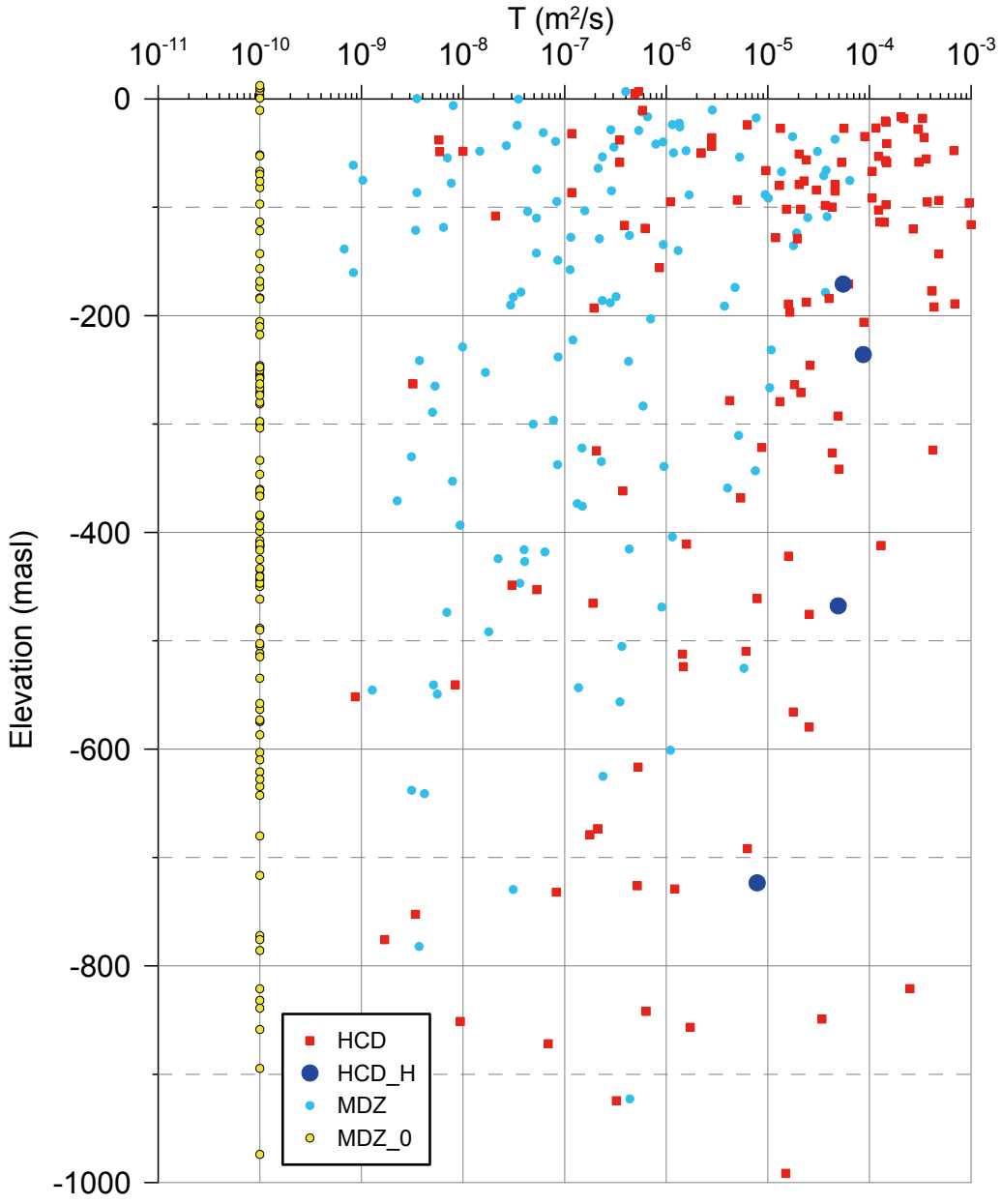

Figure A3-1. *Transmissivity distribution by elevation for HCDs, MDZ and the four new HCDs (called HCD_H in the plot).*

KLX09 – bh-length: 494.8m

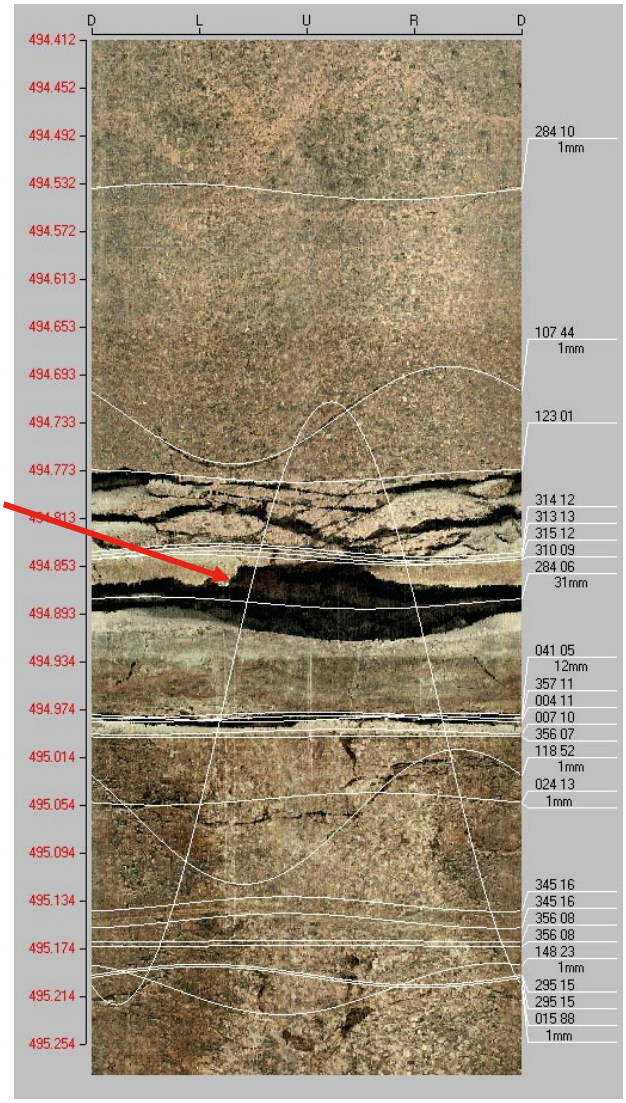

Figure A3-2. *KLX09 – bh-length: 494.8m. One PFL-f within MDZ (ESHI:DZ9, bh-length: 492.4-509m)*

One PFL-f within MDZ (ESHI:DZ9, bh-length: 492.4-509m):

- PFL-f and MDZ near (ca 10m from DZ) deterministic DZ KLX09_dz10 (bh length 520-554m) that has similar orientation as the MDZ
- HRD_N
- MDZ Geometry
    - True thickness: 6.2m
    - Strike/dip: 320/26
- MDZ transmissivity: 4.93E-5 m^2/s

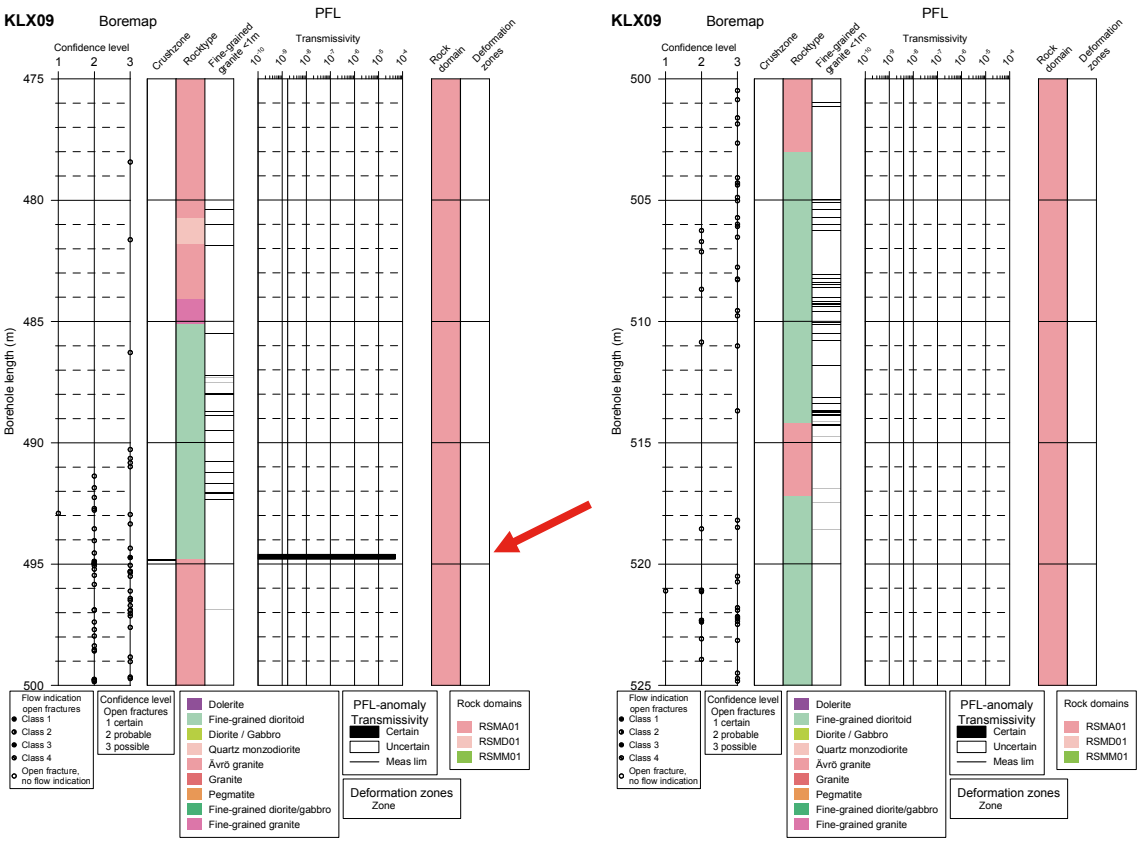

Figure A3-3. *KLX09 – bh-length: 494.8m. One PFL-f within MDZ (ESHI:DZ9, bh-length: 492.4-509m)*

KLX09 – bh-length: 752.3m

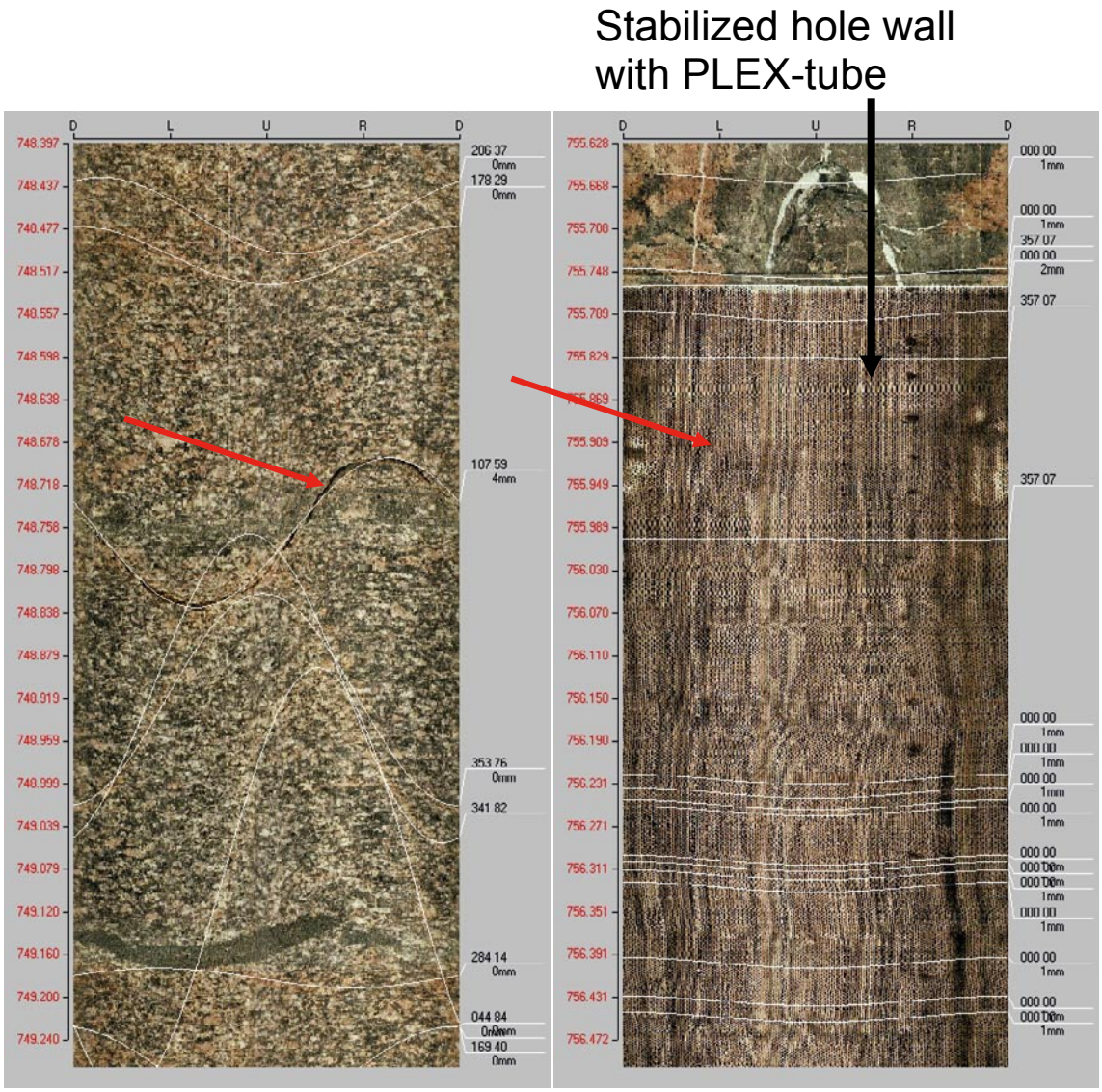

Figure A3-4. *KLX09 – bh-length: 752.3m. Two PFL-f within MDZ (ESHI:DZ14, bh-length: 744.5-761m)*

Two PFL-f within MDZ (ESHI:DZ14, bh-length: 744.5-761m):

- ZSMEW007A + ZSMNW928A are geologically defined within 682-722 m bh-length and with strike/dip 281/44 , 120/28 respectively
- HRD_EW007
- MDZ Geometry
    - True thickness: 9m
    - Strike/dip: 193/50
- MDZ transmissivity: 7.84E-6 m^2/s

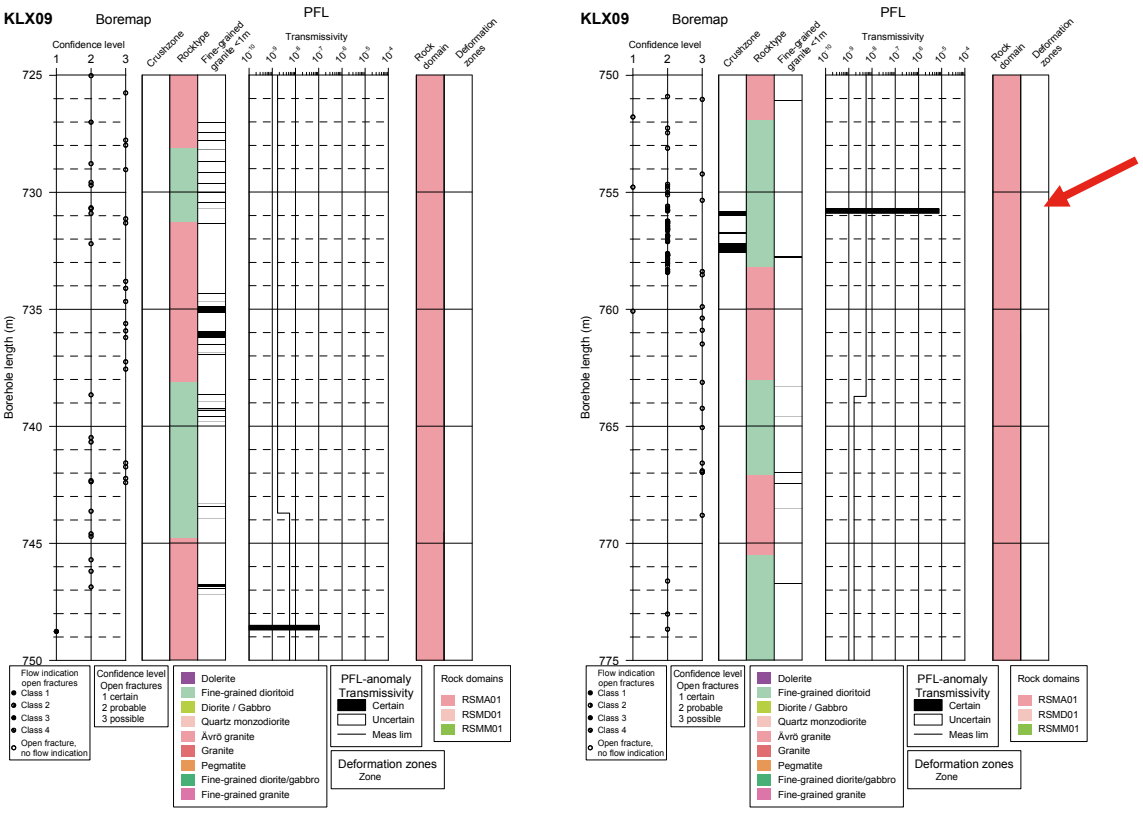

Figure A3-5. *KLX09 – bh-length: 752.3m. Two PFL-f within MDZ (ESHI:DZ14, bh-length: 744.5-761m)*

KLX16A – bh-length: 210m

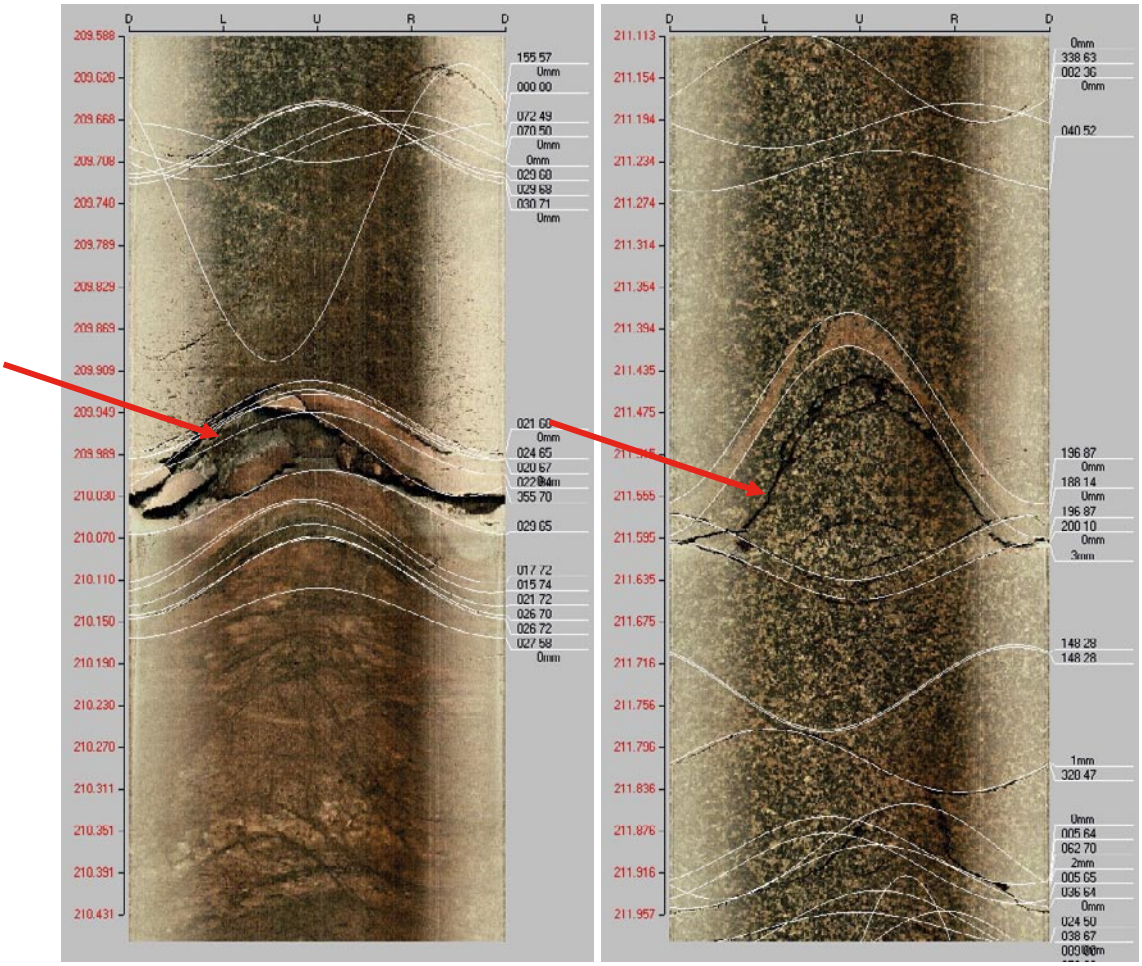

Figure A3-6. *KLX16A – bh-length: 210m. Two PFL-f, one within and one very close to MDZ (ESHI:DZ6, bh-length: 209.95-210.92m)*

Two PFL-f, one within and one very close to MDZ (ESHI:DZ6, bh-length: 209.95-210.92m):

- PFL-f and MDZ DZ6 near (ca 19m from DZ) deterministic DZ NE107A (bh section 228.2-433.55m) that has similar orientation as the MDZ DZ6.
- MDZ DZ6 may be a splay from NE107A
- Several other thin MDZ:s in bh section 207-225m
- HRD_C
- MDZ DZ6 Geometry
    - True thickness: 0.7m
    - Strike/dip: 21/72
- MDZ DZ6 transmissivity: 5.52E-5 m^2/s

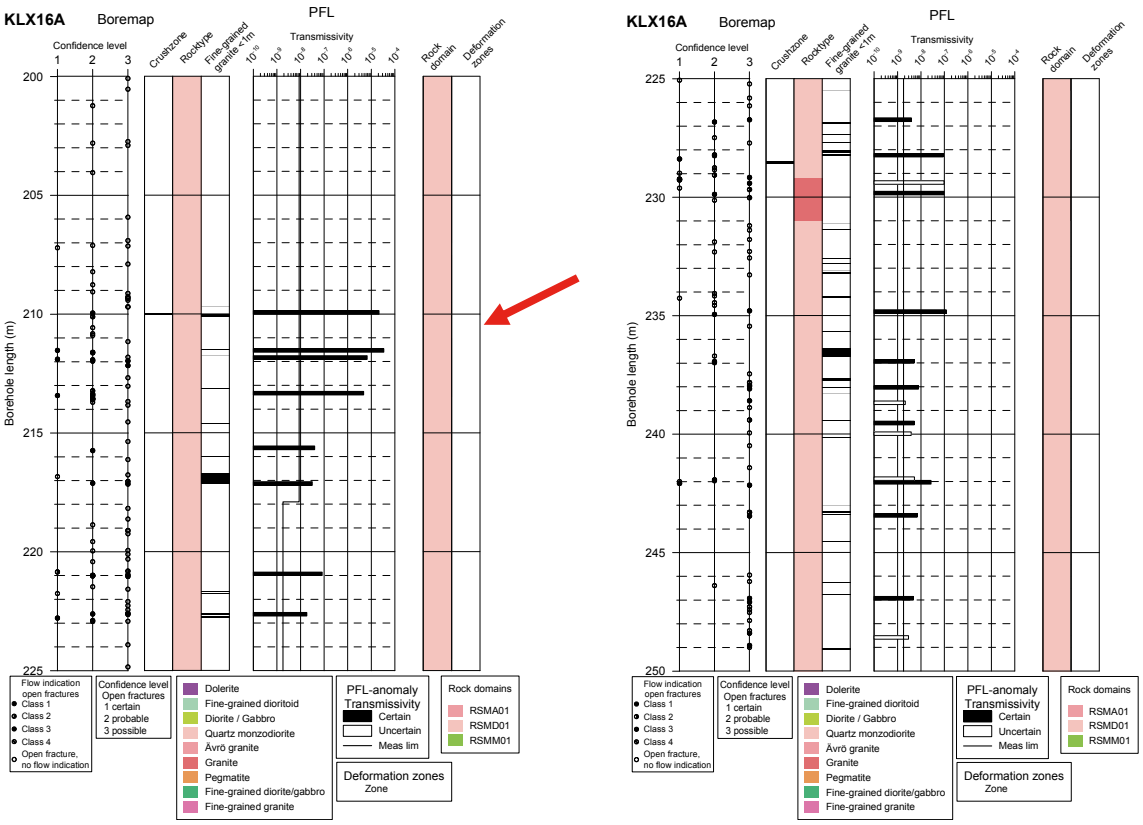

Figure A3-7. *KLX16A – bh-length: 210m. Two PFL-f, one within and one very close to MDZ (ESHI:DZ6, bh-length: 209.95-210.92m)*

KLX19A – bh-length: 299.5m

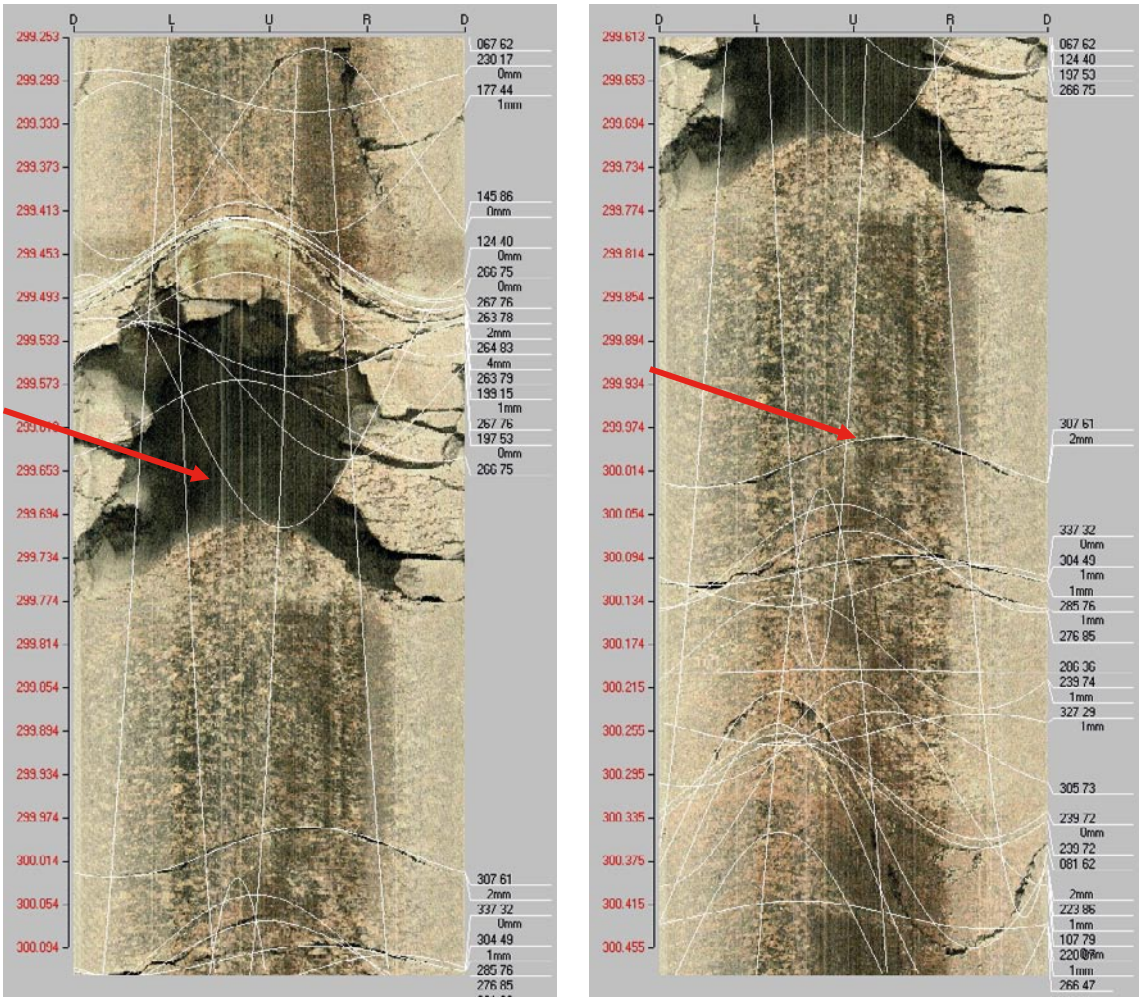

Figure A3-8. *KLX19A – bh-length: 299.5m. Four PFL-f within MDZ (ESHI:DZ2, bh-length: 298.35-304.2m)*

Four PFL-f within MDZ (ESHI:DZ2, bh-length: 298.35-304.2m):

- The MDZ can possibly be explained as a splay from ZSMNE042A due responses seen in an interference test pumping HLX28
- HRD_W
- MDZ Geometry
    - True thickness: 4.2m
    - Strike/dip: 262/73
- MDZ transmissivity: 8.70E-5 m^2/s

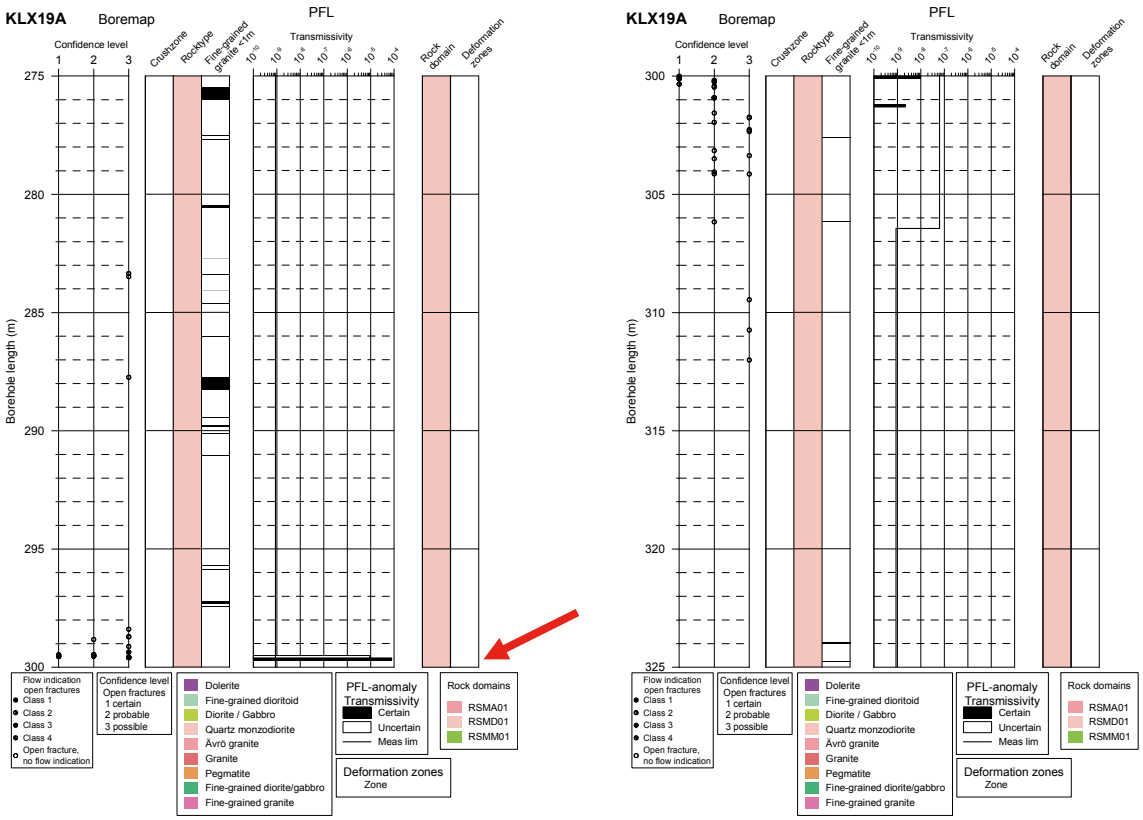

Figure A3-9. *KLX19A – bh-length: 299.5m. Four PFL-f within MDZ (ESHI:DZ2, bh-length: 298.35-304.2m)*

A.3.5.3. Concluding facts and remarks

In Table A3-1 the transmissivity estimates by PFL-f and PFL-s for the new HCDs are shown. A few main points about these featues, initially called “outliers”:

- Outliers show clear coupling to geological structures of well defined location and geometry, and in all cases to a MDZ identified by Geology
- Locations (depth-wise) :
  - Two MDZ:s above repository depth (KLX16A, KLX19A)
  - One MDZ at repository depth (KLX09)
  - One MDZ below repository depth (KLX09)
- Location (in relation to HRDs) :
  - KLX09 (HRD_N/HRD_EW007)
  - KLX16 (HRD_C)
  - KLX19 (HRD_W)

Table A3-1. Transmissivity estimates for HCDs based on sum of PFL-f or PFL-s.

HCD	T (Sum T-PFL-f)	T (Sum T-PFL-s)
	T: m^2/s	T: m^2/s
klx09_dz9	4.93E-05	2.40E-05
klx09_dz14	7.84E-06	6.62E-06
klx16_dz6	5.52E-05	5.30E-06
klx19_dz2	8.70E-05	7.20E-05

Concluding remarks

- The modelling and model testing sequence from HydroDFN to regional groundwater flow modelling (including calibration to steady-state natural groundwater head, interference tests and current hydrogeochemistry through paleohydrogeological simulations) has successively revealed imperfections in the HydroDFN model parameterisation but also provided new insight in upscaling methodology of HydroDFN models to continuum models.

- The imperfections found in the HydroDFN models could be considerably reduced, using the present calibration methodology, by introducing four new deterministic HCDs defined by Hydrogeology that are defined by four of the MDZs with the highest measured transmissivities, being comparable with the transmissivities of deterministic HCDs.

- The MDZs selected to become additional HCDs do not fulfil the geological classification criteria employed by geology to interpret deterministic deformation zones only seen in the boreholes, but as they all have a high transmissivity relative to all other MDZs and show transmissivities comparable to that of HCDs (within each depth zone). Hence, it is reasonable to regard them as HCDs in the continued hydrogeological modelling.

- One of the existing HCDs, apart from being highly transmissive, was earlier found to be likely associated with a hydraulic barrier (hydraulic data indicated this) but did not fulfil the geological criteria to define it as being a deterministic zone (HCD-H: klx19_dz5-8_dolerite) – introduced in June'08.

A.3.5.4. Depth trendfunctions for HCDs

In Figure A3-10 the figure from Chapter 7 showing data and trend function for HCDs are shown together with the four new HCDs; klx09_dz9, klx09_dz14, klx16_dz6, klx19_dz2 that are not part of the numbers of observations, geometric means or trend function. Considering the regional data, the new HCDs transmissivities are close to the geometric mean of elevation interval -150 to -400m and the transmissivities for the other two new HCDs of the elevation intervals -400 to -650 and below -650m are among the higher values but as there are 18 and 22 samples within these intervals, respectively, the trend functions for depth trends shown in Sections 7.4-7.5 will not change much.

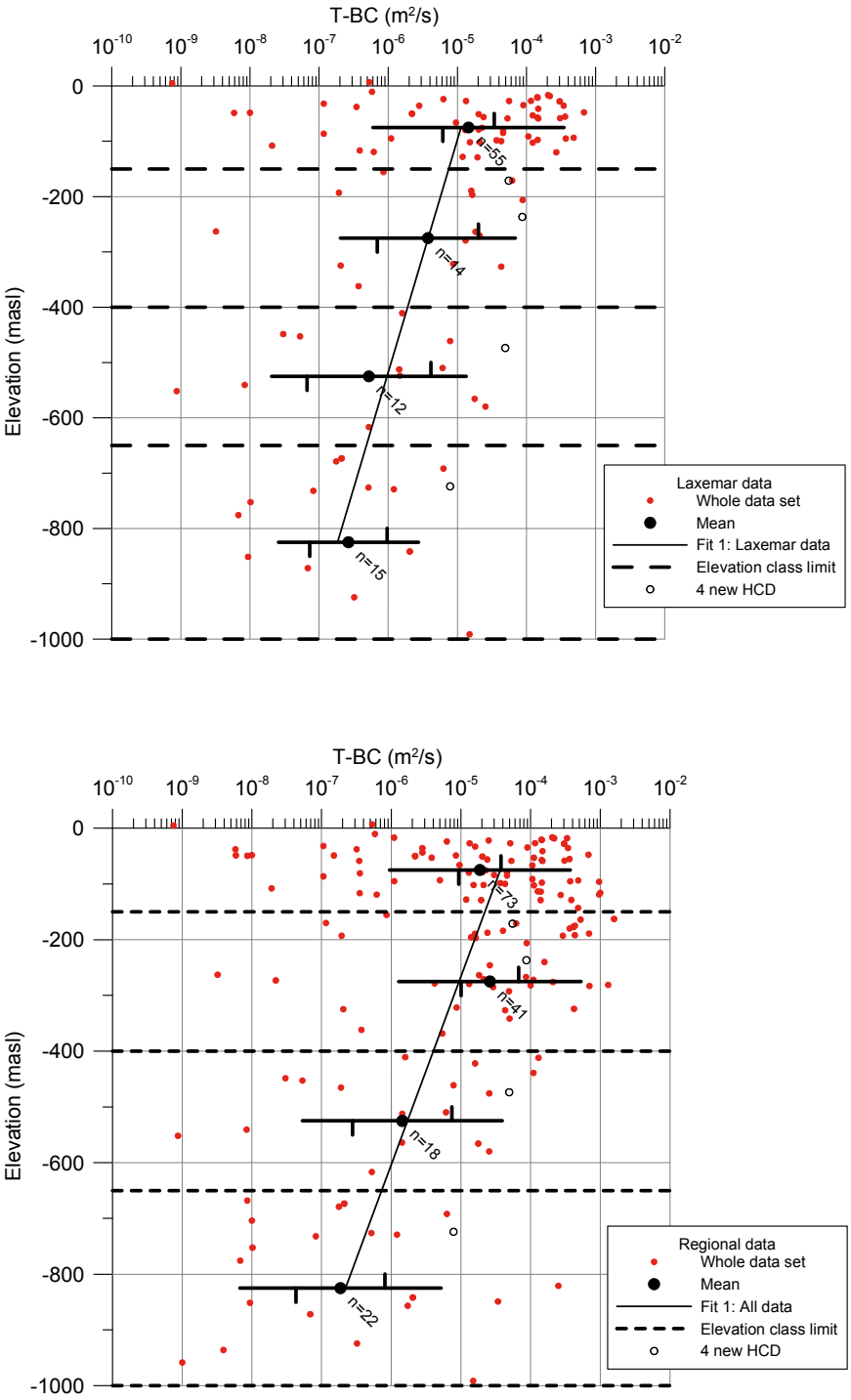

Figure A3-10. *Deformation zone transmissivity (T) versus elevation as presented in Chapter 7: For elevation intervals the number of observations (n) for elevation intervals, geometric mean T, confidence limits for mean log10(T)(vertical bars on horizontal line) and ±1 standard deviation log10(T)(entire horizontal line) are plotted. The line is fitted to the 4 Geometric mean values of data shown in Chapter 7. The four new HCDs are indicated as circles in the plot and are not part of the numbers geometric means or trend function. Top: regional model volume, Bottom: Local model volume.*

A.3.6 HCD general trend functions

The trend functions for HCDs were updated summer 2009 and as the changes were so small it was not considered necessary to re-run regional groundwater simulations based on parameters shown in Table A3-2. The difference between the trend functions in Table A3-2 and Table 7-6 is shown in Figure A3-11 and Figure A3-12. The number of E-W deformation zones with size < 2 km are only 7 and NW-SE,N-S,NE-SW size < 2 km are only 13 deformation zones. The difference between the trend functions for these short and few (compared to all deformation zones) deformation zones has no significant impact on the overall behaviour of the flow model. The differences between the other trend-functions are very small as can be seen in the figures.

Table A3-2. Trend models for transmissivity in HCDs. Data from regional scale model volume. Models used for the regional flow model reported in /Rhén et al. 2009/

Model ID	Depth trend model	Obj.	Data type	Coeff. a	Coeff. B	Corr, coeff. r^2
DZ-R-19	Exp	HCD	T (1). Regional data, Zone E-W size < 2 km	-4.910	0.00209	0.88
DZ-R-20	Exp	HCD	T (1). Regional data, Zone E-W size > 2 km	-4.049	0.00190	0.73
DZ-R-21	Exp	HCD	T (1). Regional data, Zone NW-SE,N-S,NE-SW size < 2 km	-5.137	0.00219	0.80
DZ-R-22	Exp	HCD	T (1). Regional data, Zone NW-SE,N-S,NE-SW size > 2 km	-4.157	0.00255	0.79

T(1): Total transmissivity within a HCD. X=(T_BC). Regression based on mean values of log10(T_BC) for depth zones (4 data points).

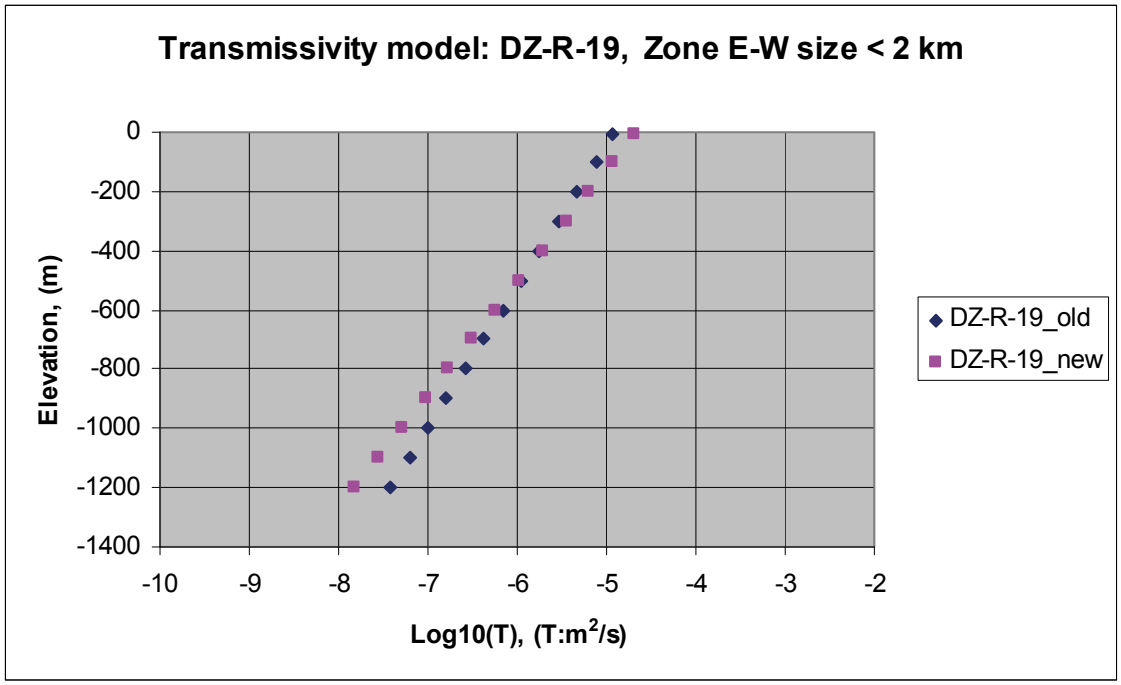

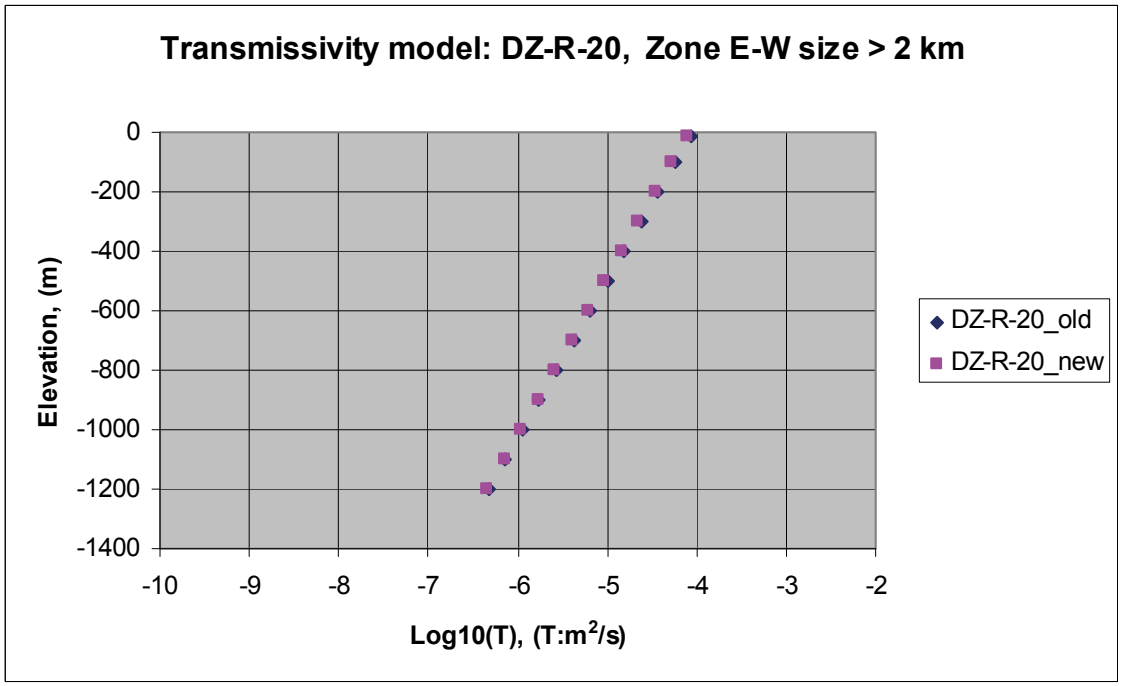

Figure A3-11. *Trend models for transmissivity in HCDs. Data from regional scale model volume. Models used for the regional flow model reported in /Rhén et al. 2009/ compared to models shown in Section 7.5.*

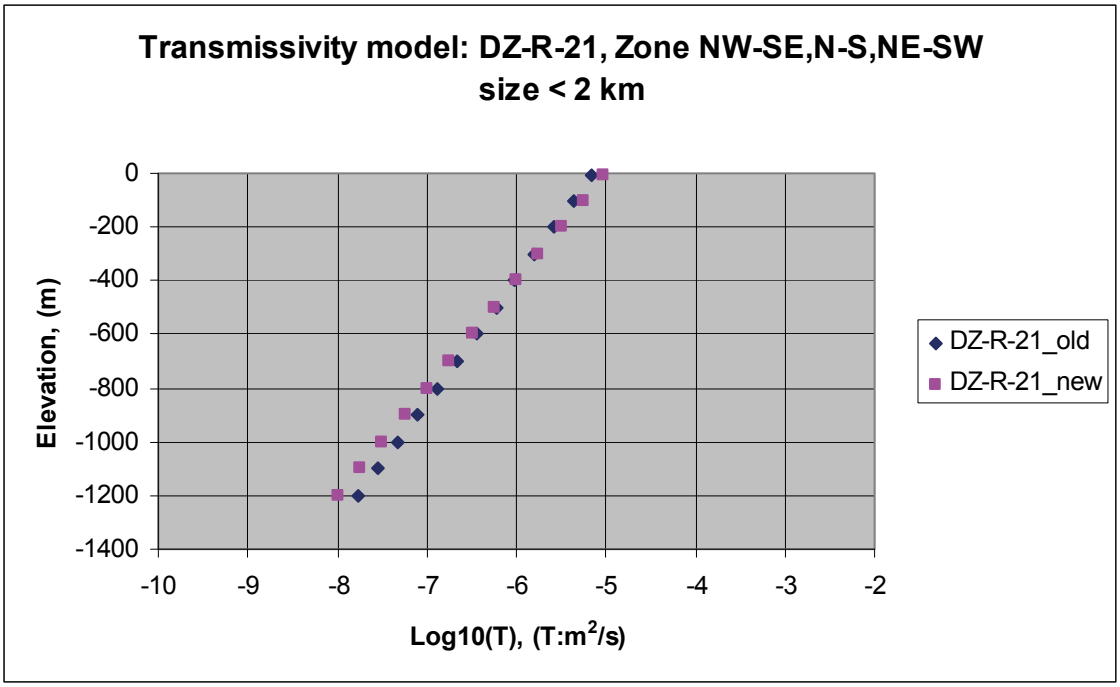

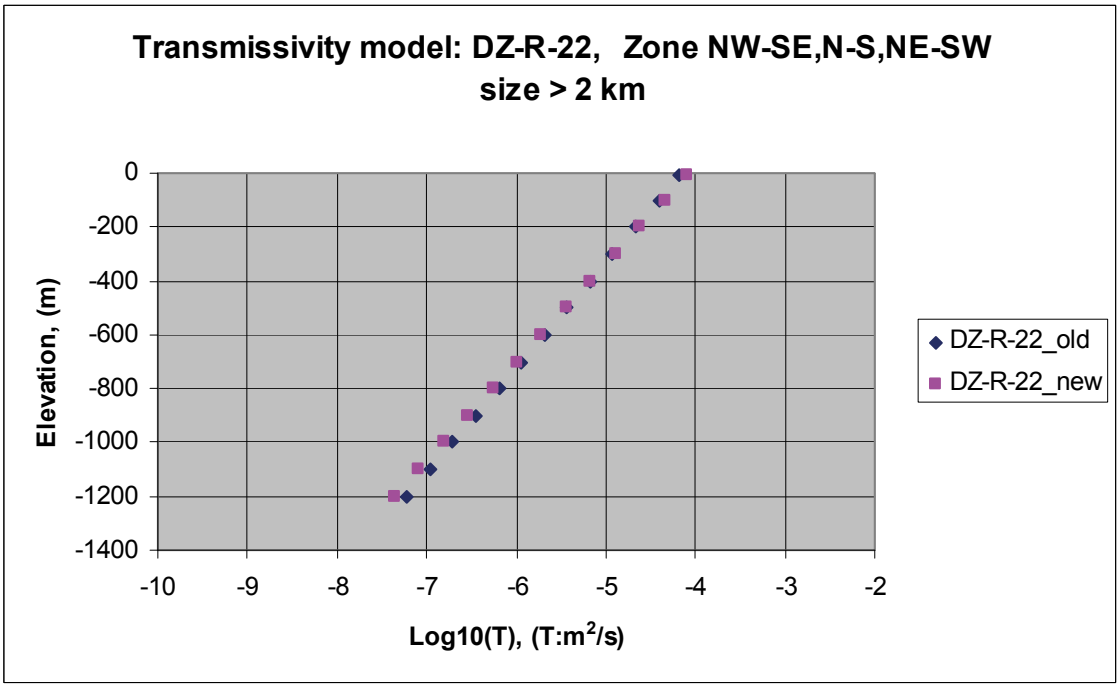

Figure A3-12. *Trend models for transmissivity in HCDs. Data from regional scale model volume. Models used for the regional flow model reported in /Rhén et al. 2009/ compared to models shown in Section 7.5.*

A.4 PFL-f statistics for MDZs

Comments to figures

The table covers local model area, except for borehole KLX27A, and shows for the minor deformation zones (MDZ), the statistics of PFL-f within the MDZs and includes the following columns:

- *Bh-ID*: Borehole name.
- *ESHI-DZ*: DZ identification, together with Bh-ID, in the geological single hole interpretation.
- *Certainty*: Judgement of the MDZ existence.
- *Z type:* Zone type grouped into main character: Brittle, Ductile/brittle or Brittle.
- *Strike/dip*: Orientation of MDZ.
- *From length, To length*: Borehole section for the MDZ
- *Bh-length(MDZ)*: Lengths of individual MDZs (with PFL-f features) along the borehole.
- *MDZ-thickness at bh*: Estimated true thickness of individual MDZs (with PFL-f features).
- *N-PFL-f*: Number of PFL-f features within individual MDZs.
- *N-corr-PFL-f*: Number of PFL-f features, Terzaghi corrected due to PFL-f features orientations, within individual MDZs.
- *P10 (PFL-f)* and *P10-corr(PFL-f)*: Intensity of PFL-f features within a MDZ. N-PFL-f and N-corr-PFL-f divided by MDZ length along the borehole, for each individual MDZ.
- *T(sum T-PFL-f)*: **Sum of T-PFL-f**, where T-PFL-f is the **transmissivity of individual PFL-f features** within a MDZ (sum T-PFL-f= total transmissivity of a MDZ).
- *log10 (sum T-PFL-f)*: **Log10(sum T-PFL-f)**, where T-PFL-f is the **transmissivity of individual PFL-f features** within a MDZ (sum T-PFL-f= total transmissivity of a MDZ).
- *Mean T-PFL-f*: Arithmetic mean of T-PFL-f within each MDZ, where T-PFL-f is the **transmissivity of individual PFL-f features** within a MDZ.
- *10^(Mean log10(T-PFL-f))*: Anti-log of the calculated values for Mean log10(T-PFL-f) shown below.

- *Mean log10(T-PFL-f)*: Arithmetic mean of log10(T-PFL-f)) within each MDZ, where T-PFL-f is the **transmissivity of individual PFL-f features** within a MDZ.

- *Std log10(T-PFL-f)*: Standard deviation of log10(T-PFL-f) within each MDZ, where T-PFL-f is the **transmissivity of individual PFL-f features** within a MDZ.

- *Elevation-class_0:* Depth grouping parameter.

- *Elevation MDZ*: Elevation for the MDZ.

Bh-ID	ESHI-DZ	Certainty	Z type	Strike (degr.)	Dip (degr.)	From length (m)	To length (m)	Bh-length/ MDZ (m)	MDZ thickness at bh (m)	N PFL-f (-)	N PFL-f-corr (-)	P10 (PFL-f) (1/m)	P10corr (PFL-f) (1/m)	T (sum T-PFL-f) (m^2/s)	log10 (sum T-PFL-f) (T:m^2/s)	Mean T PFL-f (m^2/s)	10^(Mean log10(T-PFL-f)) (m^2/s)	Mean log10(T-PFL-f) (T:m^2/s)	Std log10(T-PFL-f) (T:m^2/s)	Elev-class_0 (m)	ELEVATION MDZ (m)
KLX11E	DZ1	Uncertain	Brittle	334	33	15.56	20.05	4.5	3.2	4	5.61	0.891	1.249	3.98E-07	-6.40	9.96E-08	6.74E-08	-7.17	0.44	1: >-150	6.84
KLX24A	DZ1	Probable	Brittle	142	28	19.75	21.2	1.5	1.3	1	1.09	0.690	0.753	NA	NA	NA	NA	NA	NA	1: >-150	3.53
KLX14A	DZ2	Probable	Brittle	155	18	17.83	18.3	0.5	0.4	1	1.16	2.128	2.474	NA	NA	NA	NA	NA	NA	1: >-150	2.43
KLX26A	DZ1	Probable	Ductile/brittle	238	65	17.45	18.1	0.7	0.4	1	1.42	1.538	2.177	3.51E-09	-8.45	3.51E-09	3.51E-09	-8.45	NA	1: >-150	0.32
KLX22B	DZ1	Very uncertain	Brittle	75	29	22	25	3	3	1	1.00	0.333	0.333	3.51E-08	-7.45	3.51E-08	3.51E-08	-7.45	NA	1: >-150	-0.15
KLX25A	DZ1	Uncertain	Ductile/brittle	275	60	32.1	35.66	3.6	2.8	3	3.66	0.843	1.028	8.01E-09	-8.10	2.67E-09	2.08E-09	-8.68	0.36	1: >-150	-6.14
KLX07B	DZ1	Probable	Brittle	254	20	27	30	3	2.9	4	4.60	1.333	1.532	2.84E-06	-5.55	7.10E-07	4.44E-07	-6.35	0.49	1: >-150	-10.19
KLX16A	DZ1	Probable	Ductile/brittle	68	47	33.8	34.25	0.5	0.4	1	1.19	2.222	2.638	5.72E-07	-6.24	5.72E-07	5.72E-07	-6.24	NA	1: >-150	-12.03
KLX14A	DZ3	Probable	Ductile/brittle	230	35	42.07	43.35	1.3	1.2	1	1.05	0.781	0.823	6.55E-07	-6.18	6.55E-07	6.55E-07	-6.18	NA	1: >-150	-16.44
KLX10B	DZ2	Probable	Brittle	192	62	39.2	46.6	7.4	4.3	6	8.81	0.811	1.190	7.68E-06	-5.11	1.28E-06	8.31E-07	-6.08	0.40	1: >-150	-17.53
KLX07B	DZ2	Probable	Brittle	225	47	39.7	42	2.3	1.7	4	4.62	1.739	2.010	1.34E-06	-5.87	3.36E-07	2.05E-07	-6.69	0.60	1: >-150	-22.38
KLX11E	DZ2	Probable	Ductile	236	35	39	61.42	22.4	9.6	10	26.80	0.446	1.195	1.15E-06	-5.94	1.15E-07	3.29E-08	-7.48	0.73	1: >-150	-23.66
KLX26A	DZ2	Probable	Ductile/brittle	182	76	42.6	54.8	12.2	8.5	4	7.10	0.328	0.582	3.41E-08	-7.47	8.54E-09	5.48E-09	-8.26	0.52	1: >-150	-24.40
KLX09B	DZ1	Probable	Brittle	300	21	49.14	49.65	0.5	0.5	1	1.00	1.961	1.964	1.36E-06	-5.87	1.36E-06	1.36E-06	-5.87	NA	1: >-150	-25.78
KLX11D	DZ1	Probable	Brittle	3	67	61.93	65.36	3.4	2.8	2	2.34	0.583	0.683	2.85E-07	-6.55	1.42E-07	1.31E-07	-6.88	0.26	1: >-150	-28.46
KLX29A	DZ2	Very uncertain	Brittle	253	9	44.05	52.4	8.4	6.5	6	14.58	0.719	1.746	5.36E-07	-6.27	8.94E-08	2.38E-08	-7.62	0.83	1: >-150	-29.14
KLX24A	DZ2	Uncertain	Ductile/brittle	80	10	56.75	60.25	3.5	2.8	4	6.24	1.143	1.784	6.16E-08	-7.21	1.54E-08	1.49E-08	-7.83	0.13	1: >-150	-31.12
KLX24A	DZ3	Certain	Ductile/brittle	219	34	64.65	66.6	1.9	1.9	2	3.49	1.026	1.788	1.75E-05	-4.76	8.73E-06	1.08E-06	-5.97	1.71	1: >-150	-34.79
KLX11F	DZ1	Probable	Brittle	200	28	69.6	72	2.4	2.4	3	3.07	1.250	1.277	4.59E-05	-4.34	1.53E-05	1.71E-06	-5.77	1.62	1: >-150	-37.20
KLX09F	DZ2	Probable	Brittle	12	17	67.9	68.75	0.8	0.6	1	1.28	1.176	1.500	8.15E-08	-7.09	8.15E-08	8.15E-08	-7.09	NA	1: >-150	-39.15
KLX09E	DZ1	Probable	Brittle	113	83	71.2	72.35	1.1	0.6	2	2.28	1.739	1.984	9.28E-07	-6.03	4.64E-07	3.71E-07	-6.43	0.42	1: >-150	-39.71
KLX11E	DZ3	Uncertain	Brittle	171	37	74.11	74.53	0.4	0.3	1	1.87	2.381	4.458	7.91E-07	-6.10	7.91E-07	7.91E-07	-6.10	NA	1: >-150	-41.70
KLX24A	DZ4	Probable	Brittle	68	13	75.25	75.75	0.5	0.4	1	1.51	2.000	3.030	2.67E-08	-7.57	2.67E-08	2.67E-08	-7.57	NA	1: >-150	-43.09
KLX22A	DZ1	Certain	Ductile/brittle	183	38	76.9	77.22	0.3	0.2	1	1.23	3.125	3.833	3.06E-07	-6.51	3.06E-07	3.06E-07	-6.51	NA	1: >-150	-44.43
KLX09C	DZ1	Probable	Ductile/brittle	300	19	81.3	86.3	5	4.6	4	4.73	0.800	0.947	1.56E-06	-5.81	3.91E-07	2.13E-07	-6.67	0.60	1: >-150	-47.79

Bh-ID	ESHI-DZ	Certainty	Z type	Strike (degr.)	Dip (degr.)	From length (m)	To length (m)	Bh-length/ MDZ (m)	MDZ thickness at bh (m)	N PFL-f (-)	N PFL-f-corr (-)	P10 (PFL-f) (1/m)	P10corr (PFL-f) (1/m)	T (sum T-PFL-f) (m^2/s)	log10 (sum T-PFL-f) (T:m^2/s)	Mean T PFL-f (m^2/s)	10^(Mean log10(T-PFL-f)) (m^2/s)	Mean log10(T-PFL-f) (T:m^2/s)	Std log10(T-PFL-f) (T:m^2/s)	Elev-class_0 (m)	ELEVATION MDZ (m)
KLX26A	DZ3	Probable	Ductile/brittle	217	67	72.3	73.95	1.7	1.2	1	1.16	0.606	0.700	1.46E-08	-7.84	1.46E-08	1.46E-08	-7.84	NA	1: >-150	-48.22
KLX11B	DZ1	Probable	Brittle	197	25	75.18	76.87	1.7	1.5	2	2.10	1.183	1.244	3.07E-05	-4.51	1.54E-05	5.26E-06	-5.28	1.07	1: >-150	-48.47
KLX09D	DZ1	Uncertain	Ductile/brittle	4	11	81.4	89.52	8.1	7.6	9	11.81	1.108	1.454	1.18E-06	-5.93	1.31E-07	5.41E-08	-7.27	0.72	1: >-150	-49.70
KLX09B	DZ2	Certain	Ductile/brittle	336	23	74.55	79.3	4.8	4.4	4	5.05	0.842	1.063	2.36E-07	-6.63	5.89E-08	3.21E-08	-7.49	0.66	1: >-150	-53.46
KLX11D	DZ2	Probable	Brittle	15	81	90.44	97.7	7.3	5	4	4.33	0.551	0.596	5.28E-06	-5.28	1.32E-06	2.45E-07	-6.61	0.95	1: >-150	-53.60
KLX28A	DZ2	Uncertain	Ductile/brittle	135	56	74	76.1	2.1	0.3	2	8.24	0.952	3.925	7.03E-09	-8.15	3.52E-09	3.48E-09	-8.46	0.08	1: >-150	-54.40
KLX11B	DZ2	Probable	Brittle	352	63	86.3	88.7	2.4	1.1	1	3.20	0.417	1.334	8.30E-10	-9.08	8.30E-10	8.30E-10	-9.08	NA	1: >-150	-61.22
KLX16A	DZ3	Very uncertain	Brittle	96	18	90.89	93.72	2.8	2.6	1	1.10	0.353	0.389	2.14E-07	-6.67	2.14E-07	2.14E-07	-6.67	NA	1: >-150	-63.96
KLX09D	DZ2	Very uncertain	Brittle	51	9	101.15	104	2.8	2.5	2	2.40	0.702	0.842	5.32E-08	-7.27	2.66E-08	1.83E-08	-7.74	0.56	1: >-150	-64.98
KLX11D	DZ3	Probable	Brittle	130	17	106.67	110.6	3.9	2.7	3	6.72	0.763	1.709	3.74E-05	-4.43	1.25E-05	2.01E-07	-6.70	2.02	1: >-150	-65.70
KLX09F	DZ3	Probable	Ductile/brittle	312	13	79.45	84.4	5	3.8	5	6.72	1.010	1.357	1.36E-05	-4.87	2.73E-06	1.51E-06	-5.82	0.62	1: >-150	-67.14
KLX19A	DZ1	Very uncertain	Brittle	225	24	100.42	105.76	5.3	4.7	6	8.30	1.124	1.555	3.55E-05	-4.45	5.92E-06	1.80E-06	-5.75	0.84	1: >-150	-70.83
KLX11E	DZ4	Probable	Brittle	78	71	112.48	114.8	2.3	1.8	1	1.00	0.431	0.431	1.03E-09	-8.99	1.03E-09	1.03E-09	-8.99	NA	1: >-150	-74.99
KLX09C	DZ2	Probable	Brittle	322	27	114.85	117	2.2	1.9	2	5.74	0.930	2.671	6.41E-05	-4.19	3.20E-05	7.44E-06	-5.13	1.31	1: >-150	-75.28
KLX10C	DZ6	Probable	Brittle	108	38	103.5	110.1	6.6	6.4	1	1.01	0.152	0.153	7.67E-09	-8.12	7.67E-09	7.67E-09	-8.12	NA	1: >-150	-77.68
KLX06	DZ3	Certain	Brittle	247	10	112.7	113.9	1.2	1	2	2.92	1.667	2.436	2.90E-07	-6.54	1.45E-07	1.07E-07	-6.97	0.50	1: >-150	-84.73
KLX14A	DZ5	Probable	Brittle	28	78	138.1	138.9	0.8	0.4	1	2.02	1.250	2.526	3.51E-09	-8.45	3.51E-09	3.51E-09	-8.45	NA	1: >-150	-86.42
KLX15A	DZ1	Certain	Ductile/brittle	102	8	130.15	130.36	0.2	0.1	1	1.52	4.762	7.258	9.41E-06	-5.03	9.41E-06	9.41E-06	-5.03	NA	1: >-150	-88.25
KLX21B	DZ1	Probable	Brittle	136	34	105.27	105.73	0.5	0.3	1	1.75	2.174	3.813	1.68E-06	-5.77	1.68E-06	1.68E-06	-5.77	NA	1: >-150	-88.56
KLX21B	DZ2	Probable	Brittle	128	43	108.37	108.82	0.4	0.2	1	1.46	2.222	3.246	1.01E-05	-5.00	1.01E-05	1.01E-05	-5.00	NA	1: >-150	-91.55
KLX09F	DZ4	Probable	Brittle	319	30	133.1	136.2	3.1	1.7	2	4.60	0.645	1.485	8.39E-08	-7.08	4.20E-08	4.19E-08	-7.38	0.00	1: >-150	-94.66
KLX09F	DZ5	Probable	Brittle	134	84	144.32	145.07	0.8	0.3	1	2.96	1.333	3.948	1.58E-07	-6.80	1.58E-07	1.58E-07	-6.80	NA	1: >-150	-103.19
KLX14A	DZ6	Probable	Ductile	72	4	162.07	163.82	1.8	1.2	2	2.66	1.143	1.520	4.33E-08	-7.36	2.17E-08	2.15E-08	-7.67	0.07	1: >-150	-103.88
KLX16A	DZ4	Probable	Brittle	112	69	139.9	143	3.1	1.1	2	9.72	0.645	3.136	3.83E-05	-4.42	1.92E-05	1.82E-05	-4.74	0.19	1: >-150	-108.57
KLX08	DZ2	Probable	Brittle	328	29	150.32	159	8.7	8.3	10	12.88	1.152	1.484	2.47E-05	-4.61	2.47E-06	1.02E-06	-5.99	0.82	1: >-150	-109.49
KLX11A	DZ1	Certain	Ductile/brittle	169	28	142.25	142.9	0.7	0.6	1	1.06	1.538	1.635	5.28E-08	-7.28	5.28E-08	5.28E-08	-7.28	NA	1: >-150	-109.88
KLX18A	DZ1	Probable	Ductile/brittle	147	29	137.8	143.9	6.1	4.9	2	2.38	0.328	0.390	6.42E-09	-8.19	3.21E-09	3.05E-09	-8.52	0.20	1: >-150	-118.51
KLX06	DZ4	Certain	Brittle	292	30	151.43	154	2.6	1.6	1	1.35	0.389	0.525	3.42E-09	-8.47	3.42E-09	3.42E-09	-8.47	NA	1: >-150	-121.17

Bh-ID	ESHI-DZ	Certainty	Z type	Strike (degr.)	Dip (degr.)	From length (m)	To length (m)	Bh-length/ MDZ (m)	MDZ thickness at bh (m)	N PFL-f (-)	N PFL-f-corr (-)	P10 (PFL-f) (1/m)	P10corr (PFL-f) (1/m)	T (sum T-PFL-f) (m^2/s)	log10 (sum T-PFL-f) (T:m^2/s)	Mean T PFL-f (m^2/s)	10^(Mean log10(T-PFL-f)) (m^2/s)	Mean log10(T-PFL-f) (T:m^2/s)	Std log10(T-PFL-f) (T:m^2/s)	Elev-class_0 (m)	ELEVATION MDZ (m)
KLX09	DZ3	Probable	Brittle	102	18	147	148	1	0.9	1	1.07	1.000	1.065	1.92E-05	-4.72	1.92E-05	1.92E-05	-4.72	NA	1: >-150	-123.56
KLX18A	DZ2	Probable	Ductile/brittle	103	39	148.6	149.4	0.8	0.6	1	1.32	1.250	1.646	4.34E-07	-6.36	4.34E-07	4.34E-07	-6.36	NA	1: >-150	-125.95
KLX07A	DZ3	Uncertain	Brittle	295	7	184.8	185.4	0.6	0.5	1	1.49	1.667	2.477	1.15E-07	-6.94	1.15E-07	1.15E-07	-6.94	NA	1: >-150	-127.68
KLX11A	DZ2	Probable	Ductile/brittle	134	37	162.75	163.26	0.5	0.5	1	1.11	1.961	2.179	2.20E-07	-6.66	2.20E-07	2.20E-07	-6.66	NA	1: >-150	-129.03
KLX21B	DZ3	Certain	Ductile/brittle	114	42	150	157.8	7.8	3.8	3	5.62	0.385	0.721	9.36E-07	-6.03	3.12E-07	2.44E-07	-6.61	0.38	1: >-150	-134.43
KLX11A	DZ3	Probable	Ductile/brittle	238	41	168.7	169.9	1.2	1	2	2.23	1.667	1.856	1.79E-05	-4.75	8.95E-06	8.87E-06	-5.05	0.08	1: >-150	-135.36
KLX05	DZ2	NA	Brittle	NA	NA	173.82	173.92	0.1	0	1	2.45	10.000	24.481	6.77E-10	-9.17	6.77E-10	6.77E-10	-9.17	NA	1: >-150	-138.53
KLX15A	DZ2	Certain	Ductile/brittle	83	20	193.14	199.7	6.6	3.5	4	13.47	0.610	2.054	1.31E-06	-5.88	3.27E-07	2.76E-07	-6.56	0.33	1: >-150	-139.87
KLX04	DZ7	Uncertain	Brittle	97	6	167	167.4	0.4	0.4	1	1.00	2.500	2.500	5.27E-08	-7.28	5.27E-08	5.27E-08	-7.28	NA	1: >-150	-142.27
KLX13A	DZ2	Certain	Brittle	33	36	173.2	177.45	4.3	3.5	4	9.53	0.941	2.243	8.58E-08	-7.07	2.14E-08	1.47E-08	-7.83	0.45	1: >-150	-148.81
KLX12A	DZ1	NA	Ductile	NA	NA	182.5	183.2	0.7	0	1	1.07	1.429	1.532	1.13E-07	-6.95	1.13E-07	1.13E-07	-6.95	NA	2: -150 to -400	-157.60
KLX12A	DZ2	NA	Ductile	NA	NA	185.4	185.7	0.3	0	1	1.11	3.333	3.693	8.33E-10	-9.08	8.33E-10	8.33E-10	-9.08	NA	2: -150 to -400	-160.27
KLX16A	DZ7	Very uncertain	Ductile/brittle	49	75	213.33	213.88	0.5	0.3	1	2.83	1.818	5.143	4.75E-06	-5.32	4.75E-06	4.75E-06	-5.32	NA	2: -150 to -400	-173.90
KLX04	DZ8	Probable	Brittle	30	25	203.35	203.75	0.4	0.4	1	1.00	2.500	2.500	3.71E-08	-7.43	3.71E-08	3.71E-08	-7.43	NA	2: -150 to -400	-178.28
KLX07A	DZ4	Very uncertain	Brittle	180	60	252.5	253.1	0.6	0.3	1	7.00	1.667	11.667	3.69E-05	-4.43	3.69E-05	3.69E-05	-4.43	NA	2: -150 to -400	-178.56
KLX04	DZ9	Probable	Brittle	45	9	207.35	207.75	0.4	0.4	2	2.02	5.000	5.041	3.21E-07	-6.49	1.61E-07	1.58E-07	-6.80	0.10	2: -150 to -400	-182.41
KLX09	DZ4	Certain	Brittle	280	29	206	209	3	2.6	2	3.07	0.667	1.023	3.12E-08	-7.51	1.56E-08	1.26E-08	-7.90	0.41	2: -150 to -400	-182.78
KLX04	DZ10	Probable	Brittle	6	37	211.1	211.75	0.7	0.5	1	1.23	1.538	1.892	2.35E-07	-6.63	2.35E-07	2.35E-07	-6.63	NA	2: -150 to -400	-186.04
KLX21B	DZ4	Probable	Brittle	237	25	209.08	216.82	7.7	6.8	1	1.51	0.129	0.195	2.94E-08	-7.53	2.94E-08	2.94E-08	-7.53	NA	2: -150 to -400	-190.20
KLX15A	DZ4	Uncertain	Brittle	302	14	262.35	265.79	3.4	3.1	7	10.90	2.035	3.169	3.74E-06	-5.43	5.35E-07	1.35E-07	-6.87	0.89	2: -150 to -400	-191.14
KLX04	DZ1	Probable	Brittle	163	43	227	230	3	2.3	2	2.13	0.667	0.711	7.02E-07	-6.15	3.51E-07	2.78E-07	-6.56	0.44	2: -150 to -400	-203.05
KLX11A	DZ4	NA	Ductile/brittle	15	81	247.67	272	24.3	3.7	5	12.83	0.206	0.527	2.55E-05	-4.59	5.10E-06	1.15E-07	-6.94	1.51	2: -150 to -400	-221.75
KLX07A	DZ5	Probable	Brittle	244	57	308	313	5	4.6	4	4.32	0.800	0.864	1.20E-07	-6.92	3.01E-08	2.66E-08	-7.58	0.26	2: -150 to -400	-222.49

Bh-ID	ESHI-DZ	Certainty	Z type	Strike (degr.)	Dip (degr.)	From length (m)	To length (m)	Bh-length/ MDZ (m)	MDZ thickness at bh (m)	N PFL-f (-)	N PFL-f-corr (-)	P10 (PFL-f) (1/m)	P10corr (PFL-f) (1/m)	T (sum T-PFL-f) (m^2/s)	log10 (sum T-PFL-f) (T:m^2/s)	Mean T PFL-f (m^2/s)	10^(Mean log10(T-PFL-f)) (m^2/s)	Mean log10(T-PFL-f) (T:m^2/s)	Std log10(T-PFL-f) (T:m^2/s)	Elev-class_0 (m)	ELEVATION MDZ (m)
KLX13A	DZ3	Probable	Ductile/brittle	151	25	254.9	255.6	0.7	0.6	1	1.00	1.429	1.429	9.88E-09	-8.01	9.88E-09	9.88E-09	-8.01	NA	2: -150 to -400	-228.82
KLX04	DZ2	Probable	Brittle	313	18	254	258	4	3.7	4	4.30	1.000	1.076	1.08E-05	-4.97	2.70E-06	1.34E-06	-5.87	0.75	2: -150 to -400	-231.55
KLX09	DZ5	Probable	Brittle	334	11	261.8	264	2.2	2.2	2	2.21	0.909	1.006	8.61E-08	-7.06	4.31E-08	4.19E-08	-7.38	0.14	2: -150 to -400	-238.12
KLX12A	DZ3	Certain	Ductile	67	26	270.7	271.05	0.4	0.3	1	1.04	2.857	2.984	3.73E-09	-8.43	3.73E-09	3.73E-09	-8.43	NA	2: -150 to -400	-241.43
KLX07A	DZ6	Probable	Brittle	239	30	335.6	340	4.4	4.1	3	5.23	0.682	1.188	4.26E-07	-6.37	1.42E-07	2.82E-08	-7.55	1.04	2: -150 to -400	-242.17
KLX12A	DZ5	Certain	Ductile	100	20	282	282.4	0.4	0.4	1	1.03	2.500	2.583	1.66E-08	-7.78	1.66E-08	1.66E-08	-7.78	NA	2: -150 to -400	-252.37
KLX13A	DZ4	Certain	Ductile	237	32	291	291.3	0.3	0.3	1	1.01	3.333	3.362	5.31E-09	-8.27	5.31E-09	5.31E-09	-8.27	NA	2: -150 to -400	-264.95
KLX11A	DZ6	Certain	Ductile/brittle	210	34	306.22	308.78	2.6	2.4	3	3.12	1.172	1.219	1.04E-05	-4.98	3.48E-06	7.91E-07	-6.10	0.98	2: -150 to -400	-266.52
KLX15A	DZ8	Uncertain	Ductile/brittle	130	28	377.84	386	8.2	3.2	4	6.31	0.490	0.774	5.91E-07	-6.23	1.48E-07	1.43E-08	-7.85	1.16	2: -150 to -400	-283.42
KLX09	DZ7	Very uncertain	Brittle	357	12	313	323.2	10.2	10.2	1	1.07	0.098	0.105	5.02E-09	-8.30	5.02E-09	5.02E-09	-8.30	NA	2: -150 to -400	-289.12
KLX07A	DZ14	Probable	Brittle	268	37	413.4	413.73	0.3	0.3	2	2.12	6.061	6.416	7.76E-08	-7.11	3.88E-08	2.92E-08	-7.54	0.49	2: -150 to -400	-296.44
KLX07A	DZ8	Probable	Brittle	270	43	432.6	434.5	1.9	1.9	2	3.38	1.053	1.781	5.16E-06	-5.29	2.58E-06	7.01E-07	-6.15	1.21	2: -150 to -400	-310.58
KLX13A	DZ5	Uncertain	Ductile/brittle	348	61	348.75	349.5	0.8	0.4	1	2.47	1.333	3.298	1.48E-07	-6.83	1.48E-07	1.48E-07	-6.83	NA	2: -150 to -400	-322.11
KLX19A	DZ3	Certain	Brittle	107	89	412.15	416.9	4.8	2.6	1	1.98	0.211	0.417	3.10E-09	-8.51	3.10E-09	3.10E-09	-8.51	NA	2: -150 to -400	-330.23
KLX18A	DZ4	Probable	Ductile/brittle	134	13	359.6	366.2	6.6	6.2	2	8.27	0.303	1.253	2.30E-07	-6.64	1.15E-07	5.40E-08	-7.27	0.85	2: -150 to -400	-334.56
KLX17A	DZ5	Probable	Ductile/brittle	64	40	422.75	423.67	0.9	0.8	2	2.99	2.174	3.246	9.49E-07	-6.02	4.75E-07	4.32E-07	-6.36	0.27	2: -150 to -400	-339.11
KLX17A	DZ6	Certain	Ductile	69	15	423.67	431.76	8.1	7.5	4	7.68	0.494	0.949	7.54E-06	-5.12	1.88E-06	1.51E-07	-6.82	1.69	2: -150 to -400	-343.15
KLX18A	DZ5	Probable	Brittle	92	18	378.6	378.85	0.3	0.2	1	1.05	4.000	4.208	7.88E-09	-8.10	7.88E-09	7.88E-09	-8.10	NA	2: -150 to -400	-352.73
KLX13A	DZ6	Probable	Brittle	336	33	384	388.2	4.2	3.8	6	7.80	1.429	1.858	4.01E-06	-5.40	6.69E-07	1.16E-07	-6.94	1.16	2: -150 to -400	-359.05
KLX11A	DZ8	Probable	Brittle	90	39	417.26	418.1	0.8	0.6	1	1.06	1.190	1.263	2.25E-09	-8.65	2.25E-09	2.25E-09	-8.65	NA	2: -150 to -400	-370.83
KLX15A	DZ10	Uncertain	Ductile/brittle	89	84	502.5	505.6	3.1	1.7	1	1.13	0.323	0.365	1.33E-07	-6.88	1.33E-07	1.33E-07	-6.88	NA	2: -150 to -400	-373.45

Bh-ID	ESHI-DZ	Certainty	Z type	Strike (degr.)	Dip (degr.)	From length (m)	To length (m)	Bh-length/ MDZ (m)	MDZ thickness at bh (m)	N PFL-f (-)	N PFL-f-corr (-)	P10 (PFL-f) (1/m)	P10corr (PFL-f) (1/m)	T (sum T-PFL-f) (m^2/s)	log10 (sum T-PFL-f) (T:m^2/s)	Mean T PFL-f (m^2/s)	10^(Mean log10(T-PFL-f)) (m^2/s)	Mean log10(T-PFL-f) (T:m^2/s)	Std log10(T-PFL-f) (T:m^2/s)	Elev-class_0 (m)	ELEVATION MDZ (m)
KLX18A	DZ6	Probable	Ductile/brittle	49	14	401	404.2	3.2	3.2	4	6.79	1.250	2.121	1.49E-07	-6.83	3.73E-08	2.07E-08	-7.68	0.58	2: -150 to -400	-375.82
KLX04	DZ13	Certain	Brittle	77	31	419.62	419.95	0.3	0.3	1	1.11	3.030	3.357	9.35E-09	-8.03	9.35E-09	9.35E-09	-8.03	NA	2: -150 to -400	-393.37
KLX18A	DZ7	Certain	Ductile/brittle	103	35	428	434	6	4.8	6	18.86	1.000	3.143	1.15E-06	-5.94	1.92E-07	5.09E-09	-8.29	1.32	3: -400 to -650	-404.18
KLX10	DZ8	Probable	Brittle	142	29	435	439.2	4.2	3.5	5	8.36	1.190	1.991	4.33E-07	-6.36	8.66E-08	7.26E-08	-7.14	0.28	3: -400 to -650	-415.30
KLX02	DZ3	Probable	Brittle	57	52	436.1	436.9	0.8	0.5	2	2.05	2.500	2.563	4.00E-08	-7.40	2.00E-08	1.35E-08	-7.87	0.58	3: -400 to -650	-415.99
KLX04	DZ14	Probable	Brittle	349	17	443.8	444	0.2	0.2	1	1.94	5.000	9.714	6.40E-08	-7.19	6.40E-08	6.40E-08	-7.19	NA	3: -400 to -650	-418.07
KLX03	DZ3	Probable	Brittle	4	22	457.2	457.6	0.4	0.4	1	1.04	2.500	2.606	2.21E-08	-7.66	2.21E-08	2.21E-08	-7.66	NA	3: -400 to -650	-424.27
KLX18A	DZ8	Uncertain	Ductile/brittle	223	43	448.35	456.55	8.2	5.1	4	8.14	0.488	0.993	4.04E-08	-7.39	1.01E-08	5.02E-09	-8.30	0.75	3: -400 to -650	-426.88
KLX02	DZ4	Certain	Brittle	11	62	466.6	468.25	1.6	0.8	2	4.25	1.212	2.579	3.62E-08	-7.44	1.81E-08	1.64E-08	-7.79	0.28	3: -400 to -650	-446.91
KLX15A	DZ12	Certain	Brittle	225	71	629.1	634.94	5.8	3.3	3	4.69	0.514	0.803	9.03E-07	-6.04	3.01E-07	1.16E-07	-6.93	1.01	3: -400 to -650	-468.90
KLX11A	DZ12	NA	NA	NA	NA	522.85	528.66	0	0	2	8.21	0.344	1.413	6.94E-09	-8.16	3.47E-09	3.47E-09	-8.46	0.01	3: -400 to -650	-473.82
KLX07A	DZ16	Probable	Brittle	264	38	667.95	669	1	1	1	1.74	0.952	1.659	1.79E-08	-7.75	1.79E-08	1.79E-08	-7.75	NA	3: -400 to -650	-491.72
KLX08	DZ11	Very uncertain	Brittle	303	33	614.45	615	0.5	0.5	1	4.70	1.818	8.550	3.66E-07	-6.44	3.66E-07	3.66E-07	-6.44	NA	3: -400 to -650	-505.18
KLX11A	DZ13	Probable	Brittle	171	15	577.9	586.16	8.3	8.2	5	7.66	0.605	0.927	5.81E-06	-5.24	1.16E-06	4.03E-07	-6.39	1.19	3: -400 to -650	-525.36
KLX08	DZ12	Very uncertain	Brittle	65	25	655.3	656.15	0.9	0.6	1	1.48	1.176	1.741	5.12E-09	-8.29	5.12E-09	5.12E-09	-8.29	NA	3: -400 to -650	-540.76
KLX11A	DZ14	Certain	Ductile	153	25	593.9	602.27	8.4	8.2	3	4.82	0.358	0.576	1.37E-07	-6.86	4.56E-08	1.09E-08	-7.96	0.95	3: -400 to -650	-543.30
KLX17A	DZ10	Uncertain	Brittle	8	39	662.29	670	7.7	4.6	1	1.96	0.130	0.254	1.28E-09	-8.89	1.28E-09	1.28E-09	-8.89	NA	3: -400 to -650	-545.53
KLX05	DZ11	Uncertain	Ductile/brittle	204	60	626.73	629.43	2.7	1	1	1.55	0.370	0.574	5.57E-09	-8.25	5.57E-09	5.57E-09	-8.25	NA	3: -400 to -650	-549.20
KLX04	DZ16	Probable	Brittle	279	18	580.7	586.2	5.5	5.1	3	7.28	0.545	1.323	3.50E-07	-6.46	1.17E-07	9.98E-08	-7.00	0.29	3: -400 to -650	-556.42
KLX04	DZ17	Probable	Brittle	115	6	627.56	628.5	0.9	0.9	1	1.00	1.064	1.068	1.10E-06	-5.96	1.10E-06	1.10E-06	-5.96	NA	3: -400 to -650	-601.04
KLX03	DZ4	Uncertain	Brittle	326	28	662	667.1	5.1	4.9	3	9.30	0.588	1.824	2.38E-07	-6.62	7.94E-08	6.34E-08	-7.20	0.35	3: -400 to -650	-625.03
KLX08	DZ9	Probable	Brittle	248	59	769	778	9	6.3	1	1.17	0.111	0.129	3.12E-09	-8.51	3.12E-09	3.12E-09	-8.51	NA	3: -400 to	-637.96

Bh-ID	ESHI-DZ	Certainty	Z type	Strike (degr.)	Dip (degr.)	From length (m)	To length (m)	Bh-length/ MDZ (m)	MDZ thickness at bh (m)	N PFL-f (-)	N PFL-f-corr (-)	P10 (PFL-f) (1/m)	P10corr (PFL-f) (1/m)	T (sum T-PFL-f) (m^2/s)	log10 (sum T-PFL-f) (T:m^2/s)	Mean T PFL-f (m^2/s)	10^(Mean log10(T-PFL-f)) (m^2/s)	Mean log10(T-PFL-f) (T:m^2/s)	Std log10(T-PFL-f) (T:m^2/s)	Elev-class_0 (m)	ELEVATION MDZ (m)
																				-650	
KLX02	DZ6	Very uncertain	Brittle	43	30	662.5	663.4	0.9	0.8	1	4.98	1.111	5.535	4.17E-09	-8.38	4.17E-09	4.17E-09	-8.38	NA	3: -400 to -650	-641.08
KLX02	DZ7	Certain	Brittle	80	34	751.55	752.25	0.7	0.6	1	1.15	1.429	1.644	3.12E-08	-7.51	3.12E-08	3.12E-08	-7.51	NA	4: <-650	-729.54
KLX11A	DZ16	Probable	Ductile/brittle	184	67	853	860	7	4.8	2	2.47	0.286	0.352	3.69E-09	-8.43	1.84E-09	1.48E-09	-8.83	0.43	4: <-650	-782.14
KLX03	DZ8	Probable	Brittle	334	13	969.3	970.5	1.2	1.2	1	1.03	0.833	0.861	4.38E-07	-6.36	4.38E-07	4.38E-07	-6.36	NA	4: <-650	-922.71

A.5 Additional fracture analysis

A.5.1 Analysis of rock domains

Stereographic density plots for each of the Rock Domains RSMA01, RSMD01 and RSMM01 are presented in Figure A-5-1 through Figure A-5-3.

A summary of the numbers of fractures according to the different categories defined in Section 11.3.2 are given in Table A-5-1 through Table A-5-3.

Overall summary plots of Terzaghi corrected fracture intensity for various categories of fractures within each of the Rock Domains RSMA01, RSMD01 and RSMM01 are presented in Figure A-5-4 through Figure A-5-6.

The variations of Terzaghi corrected intensities of OPO fractures and PFL features according to elevation are shown in Figure A-5-7 to Figure A-5-12 in Rock Domains RSMA01, RSMD01 and RSMM01. The fracture intensity of PFL features is further broken down by set in Figure A-5-13 to Figure A-5-15.

Figure A-5-16 to Figure A-5-18 show the variation of the Terzaghi-corrected fracture intensities for OPO fractures and PFL features for the rock domains in relation to (the surface expression of) the geological structure. As can be seen, there is little evidence of any systematic structure in the variation of the fracture intensities with position. However, the number of points involved is probably too small to draw significant conclusions. One factor affecting the apparent variation in the fracture intensity for PFL features in particular is the difference in the borehole lengths, which because of the decreasing trend in intensity of PFL features with depth (see Section 9.3.4) means different boreholes have a different bias according to their depth of completion. For example, the intensity in a short borehole corresponds to the higher intensity found near the surface, whereas the intensity a deep borehole is an average of the higher intensity near the surface and the lower intensity at depth.

Profiles of the Terzaghi corrected intensities of OPO fractures and PFL features according to depth zone for the rock domains are given in Figure A-5-19 through Figure A-5-24.

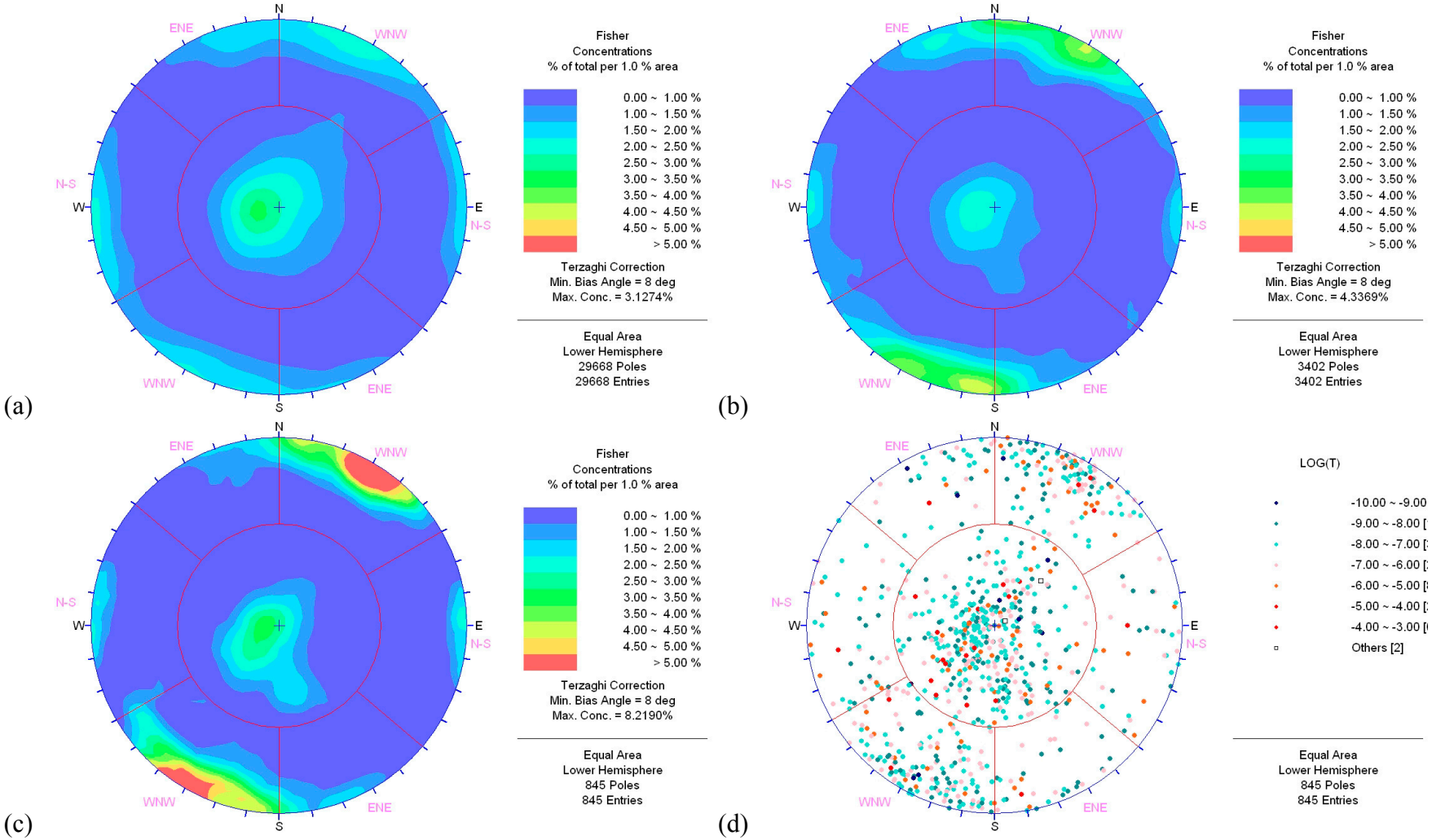

Figure A-5-1. *Stereonets for RSMA01: (a), (b), (c) Terzaghi-corrected intensity for all fractures, OPO-CP fractures and PFL features. (d) poles for PFL features (coloured by transmissivity).*

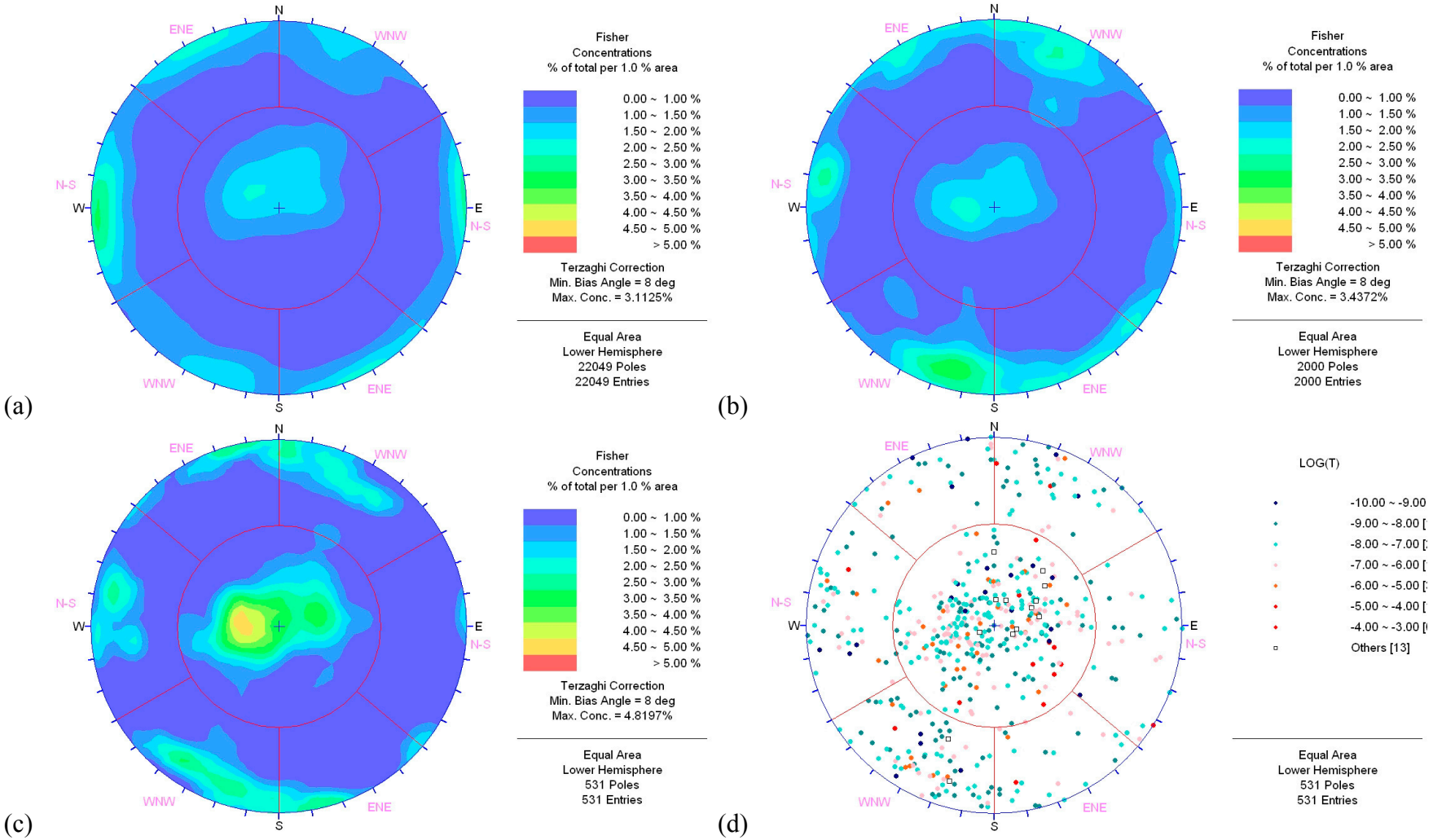

Figure A-5-2. *Stereonets for RSMD01: (a), (b), (c) Terzaghi-corrected intensity for all fractures, OPO-CP fractures and PFL features. (d) poles for PFL features (coloured by transmissivity).*

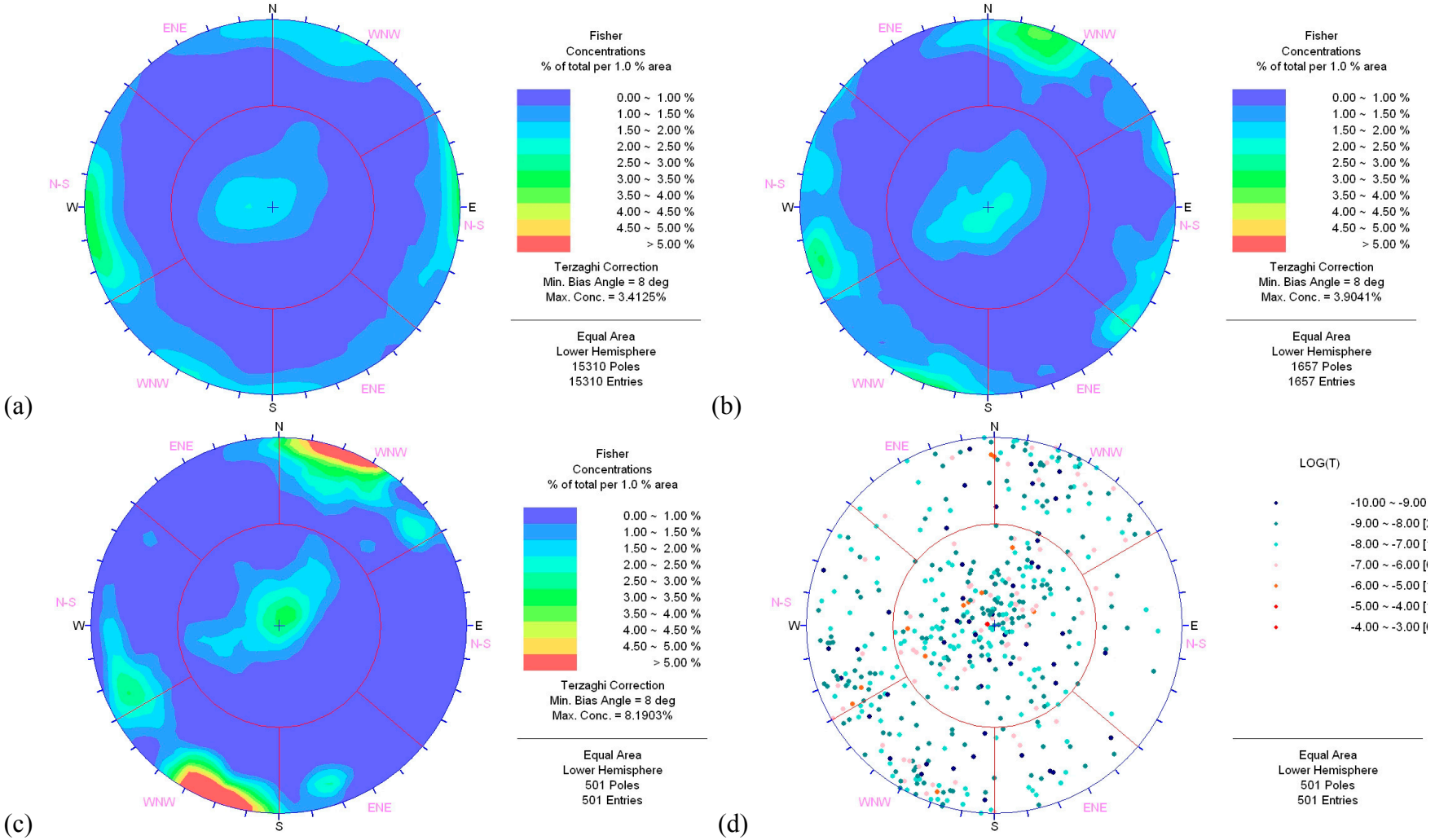

Figure A-5-3. *Stereonets for RSMM01: (a), (b), (c) Terzaghi-corrected intensity for all fractures, OPO-CP fractures and PFL features. (d) poles for PFL features (coloured by transmissivity).*

Table A-5-1. Numbers of fractures in each category for each borehole for the fully characterised sections of Rock Domain RSMA01 excluding identified regional = and major local deformation zones.

	Number					
	All	**OPO**	**OPO-CP**	**OPO-C**	**PFL**	**MDZ**
KLX02	790	497	345	345	56	4
KLX04	4089	1138	175	73	95	15
KLX06	3458	535	350	70	81	2
KLX07A	3618	834	530	50	111	8
KLX07B	664	228	96	31	59	2
KLX08	1829	629	260	139	66	2
KLX09	3254	913	386	57	49	16
KLX09B	475	144	39	3	41	2
KLX09C	613	188	73	16	32	2
KLX09D	624	207	65	32	32	2
KLX09E	582	150	37	11	21	1
KLX09F	735	197	80	30	32	4
KLX09G	395	79	34	2	14	
KLX10	2614	806	224	57	47	1
KLX10B	197	74	49	12	17	1
KLX10C	676	161	53	16	16	4
KLX18A	1183	428	168	29	91	5
KLX21B	3152	715	328	85	37	10
KLX29A	311	118	79	25	22	2
Total	**29259**	**8041**	**3371**	**1083**	**919**	**83**

Table A-5-2. Numbers of fractures in each category for each borehole for the fully characterised sections of Rock Domain RSMD01 excluding identified regional = and major local deformation zones.

	Number					
	All	**OPO**	**OPO-CP**	**OPO-C**	**PFL**	**MDZ**
KLX03	1546	104	34	7	5	5
KLX05	1977	151	100	18	7	7
KLX08	278	73	24			
KLX10	24	9	3			
KLX11A	4259	627	229	36	44	16
KLX11B	351	124	33	5	36	2
KLX11C	433	125	38	8	41	
KLX11D	481	135	64	20	43	3
KLX11E	450	134	30	11	25	4
KLX11F	347	95	25	9	22	1
KLX12A	385	133	34	6	4	1
KLX14A	712	276	150	25	33	4
KLX15A	4343	1327	690	136	62	18
KLX16A	1725	473	223	65	41	9
KLX19A	1427	3187	109	22	30	5
KLX20A	604	138	41	2		2
KLX21B	595	114	26	1		
KLX22A	586	216	69	17	43	1
KLX22B	520	177	39	5	28	1
KLX23A	139	41	25	7	17	
KLX23B	34	15	4	1	4	
KLX24A	619	254	86	22	37	4
KLX25A	199	57	15	6	6	1
Total	**22034**	**5116**	**2298**	**429**	**529**	**84**

Table A-5-3. Numbers of fractures in each category for each borehole for the fully characterised sections of Rock Domain RSMM01 excluding identified regional and major local deformation zones.

	Number					
	All	**OPO**	**OPO-CP**	**OPO-C**	**PFL**	**MDZ**
KLX03	1873	315	61	15	34	2
KLX05	1395	145	112	23	64	5
KLX08	1173	431	132	57	20	3
KLX10	443	69	19			
KLX12A	2454	956	380	59	71	11
KLX17A	3499	666	280	43	27	8
KLX18A	1295	375	89	14	38	2
KLX26A	543	249	122	18	22	3
KLX26B	220	167	26	10	17	
KLX28A	269	106	55	2	23	1
Total	**13164**	**3479**	**1276**	**241**	**316**	**35**

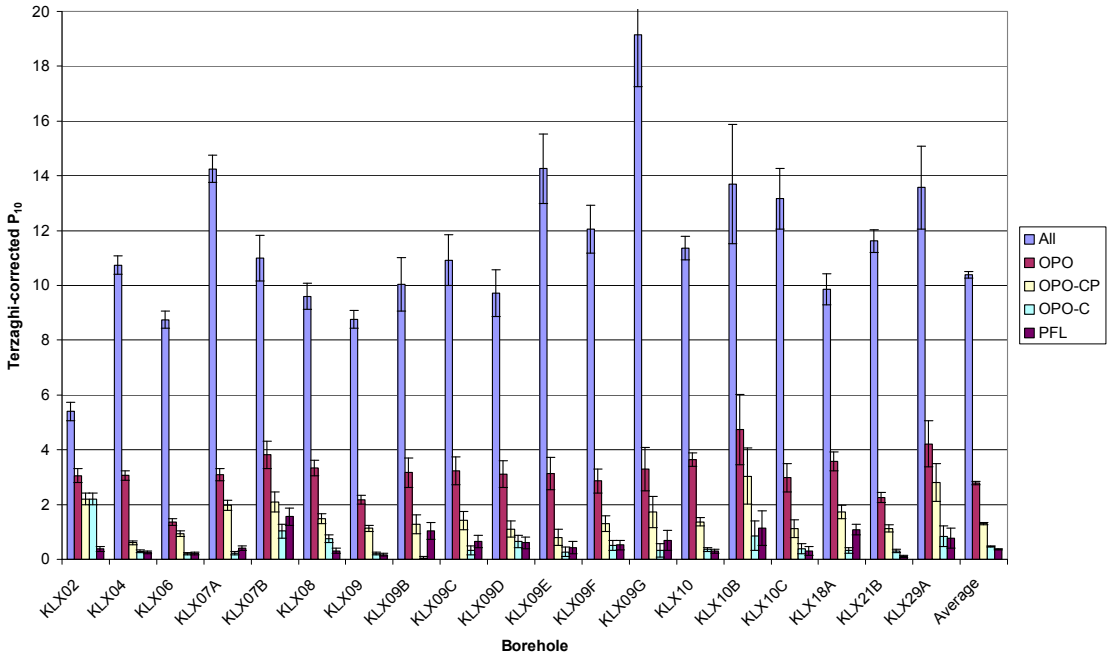

Figure A-5-4. *Comparison of the Terzaghi–corrected fracture intensities for the different categories for fully characterised sections of boreholes penetrating Rock Domain RSMA01.*

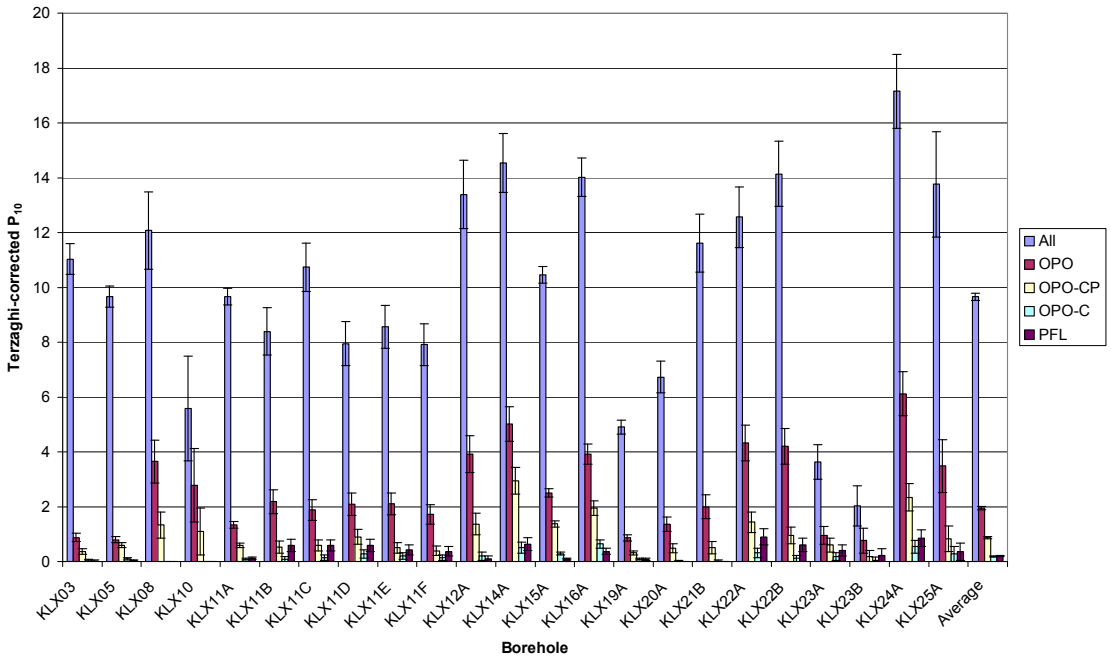

Figure A-5-5. *Comparison of the Terzaghi–corrected fracture intensities for the different categories for fully characterised sections of boreholes penetrating Rock Domain RSMD01.*

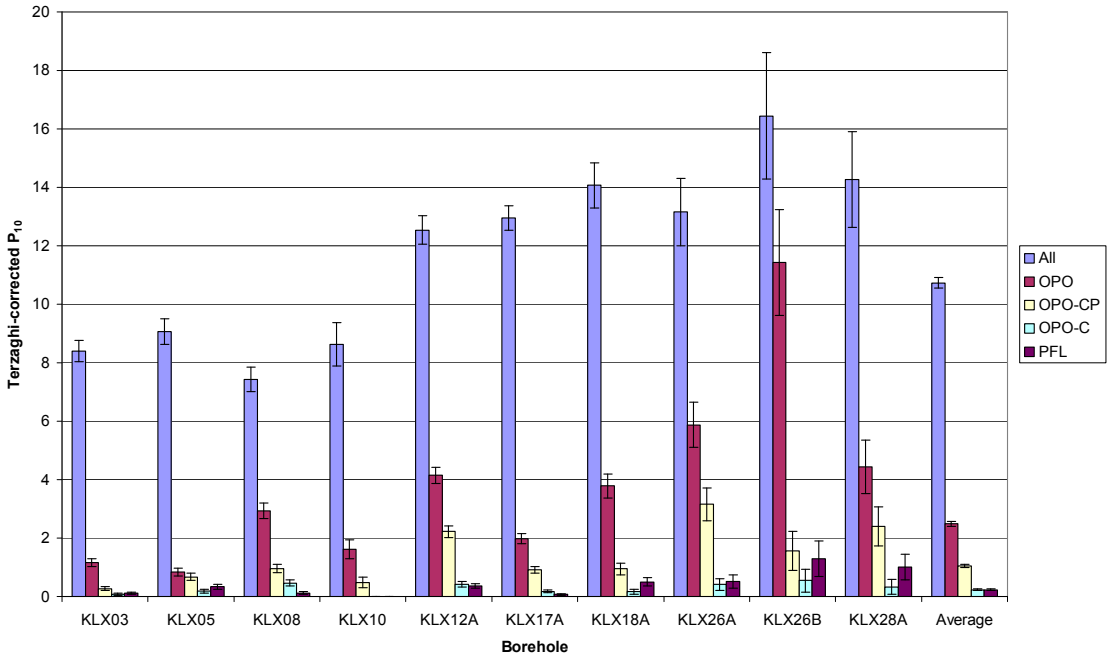

Figure A-5-6. *Comparison of the Terzaghi–corrected fracture intensities for the different categories for fully characterised sections of boreholes penetrating Rock Domain RSMM01.*

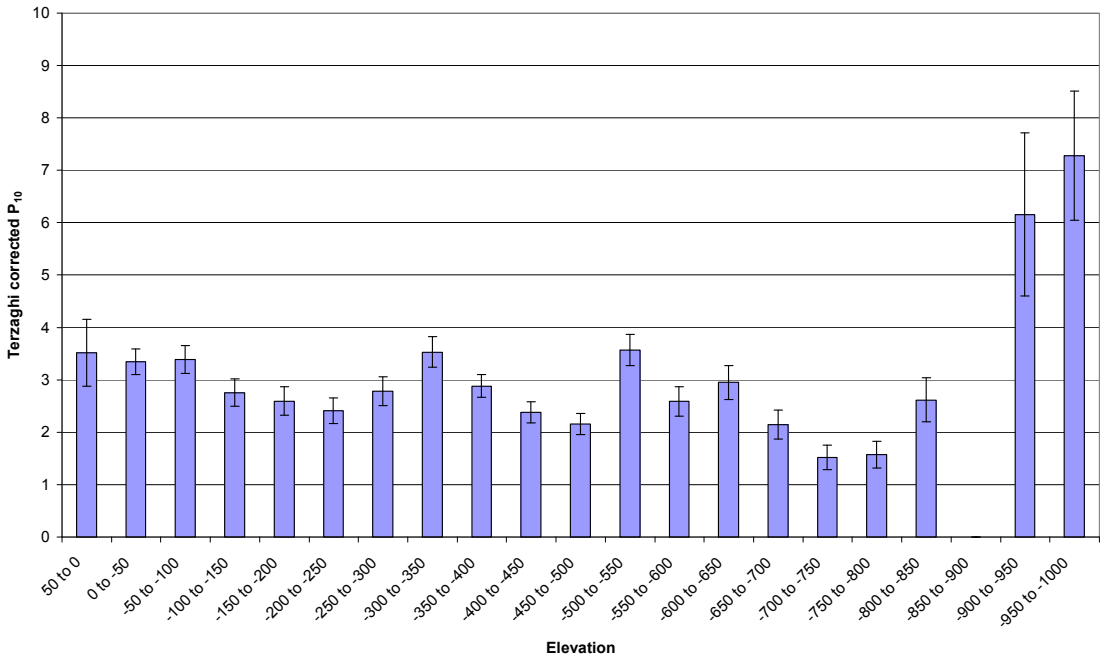

Figure A-5-7. *Variation of the Terzaghi-corrected fracture intensity for OPO fractures with elevation (masl) for the fully characterised sections of boreholes penetrating Rock Domain RSMA01.*

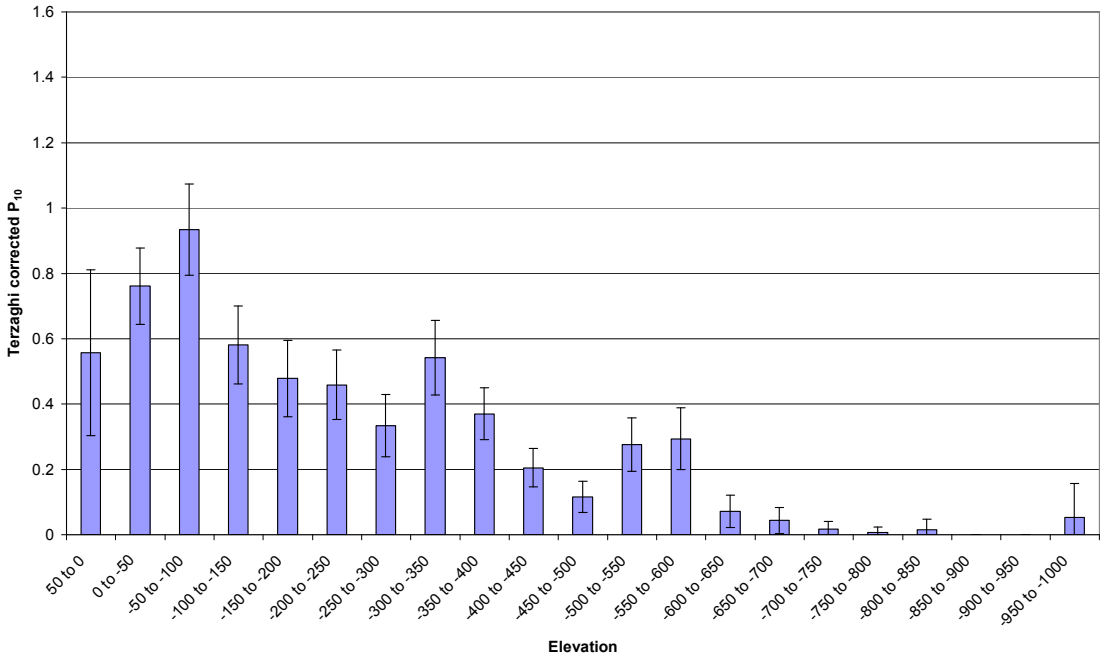

Figure A-5-8. *Variation of the Terzaghi-corrected fracture intensity for PFL features with elevation (masl) for the fully characterised sections of boreholes penetrating Rock Domain RSMA01.*

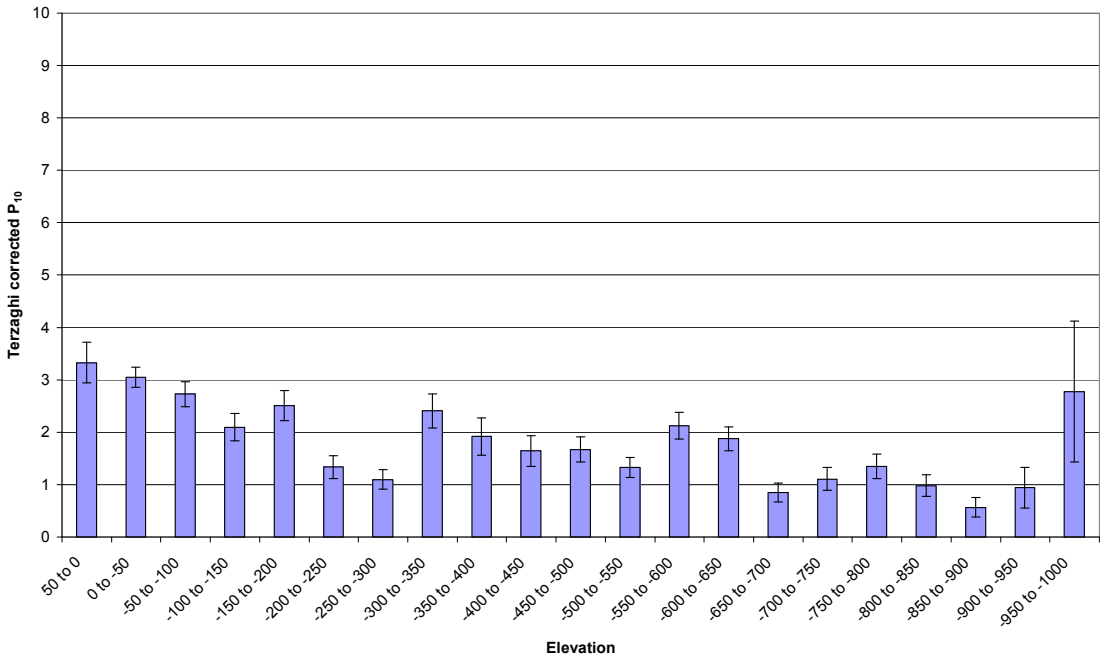

Figure A-5-9. *Variation of the Terzaghi-corrected fracture intensity for OPO fractures with elevation (masl) for the fully characterised sections of boreholes penetrating Rock Domain RSMD01.*

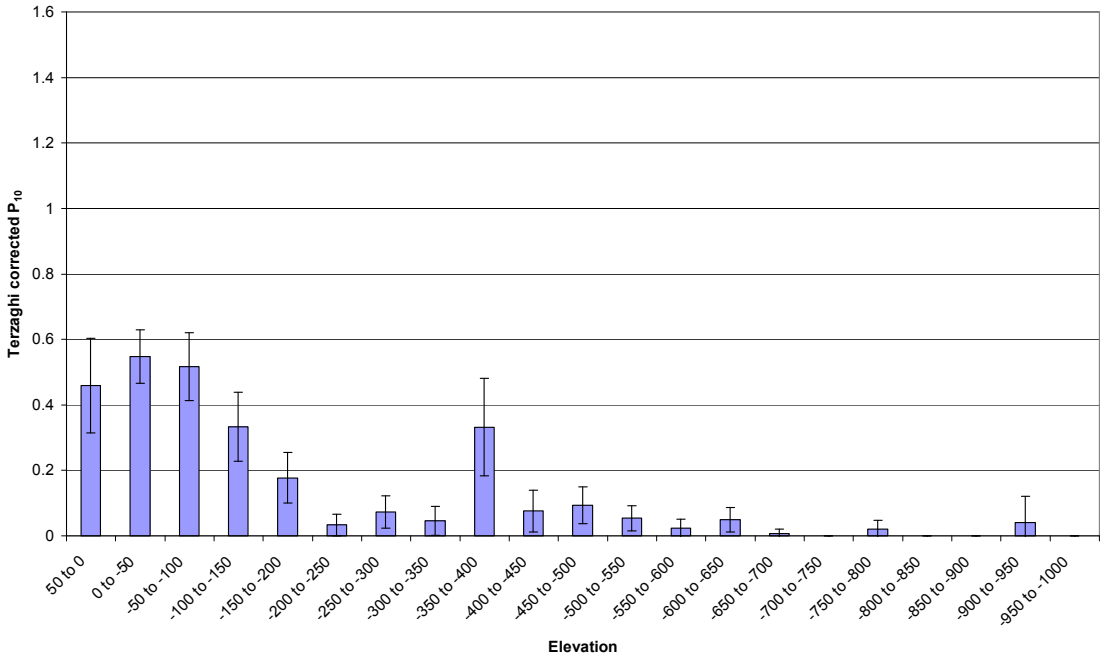

Figure A-5-10. *Variation of the Terzaghi-corrected fracture intensity for PFL features with elevation (masl) for the fully characterised sections of boreholes penetrating Rock Domain RSMD01.*

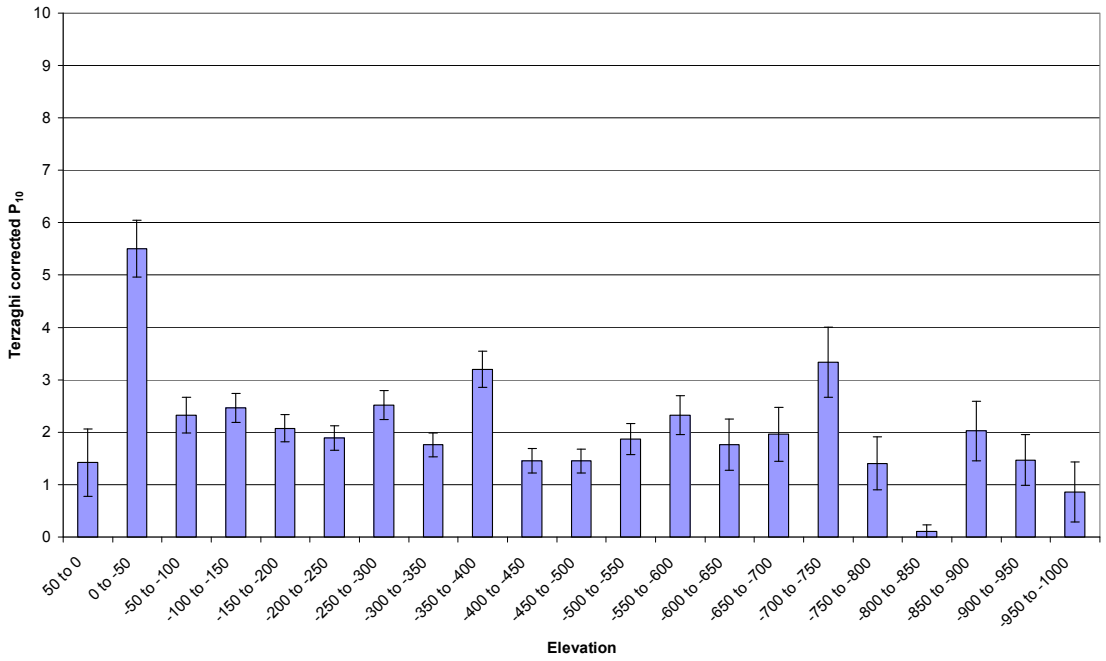

Figure A-5-11. *Variation of the Terzaghi-corrected fracture intensity for OPO fractures with elevation (masl) for the fully characterised sections of boreholes penetrating Rock Domain RSMM01.*

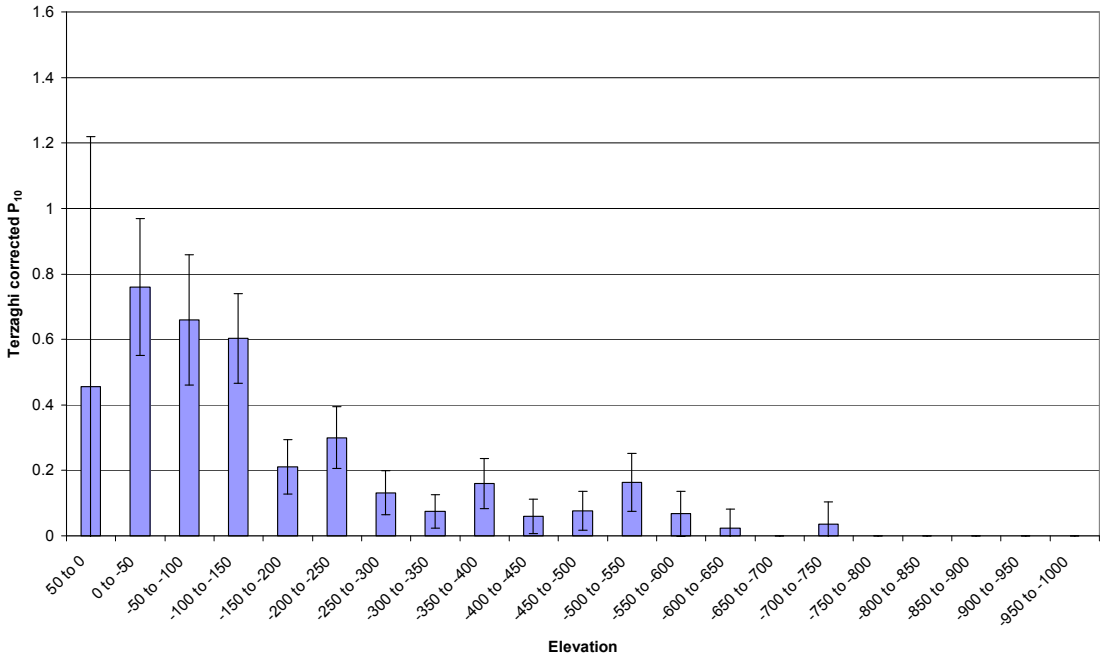

Figure A-5-12. *Variation of the Terzaghi-corrected fracture intensity for PFL features with elevation (masl) for the fully characterised sections of boreholes penetrating Rock Domain RSMM01.*

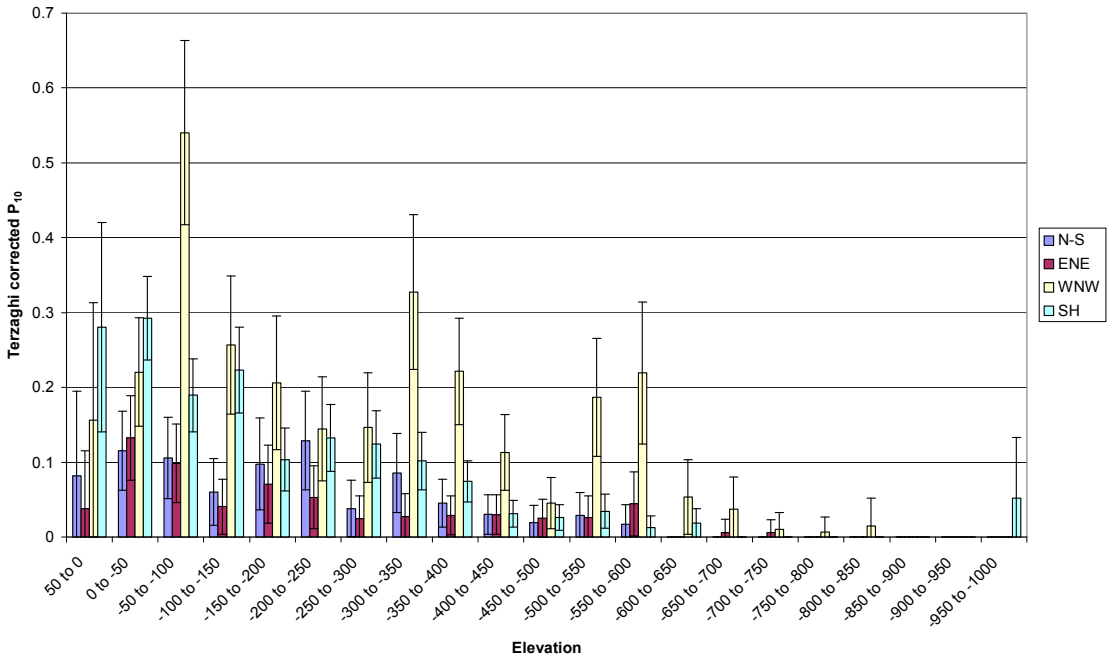

Figure A-5-13. *Variation of the Terzaghi-corrected fracture intensity for PFL features with elevation (masl) and fracture set for the fully characterised sections of boreholes penetrating Rock Domain RSMA01.*

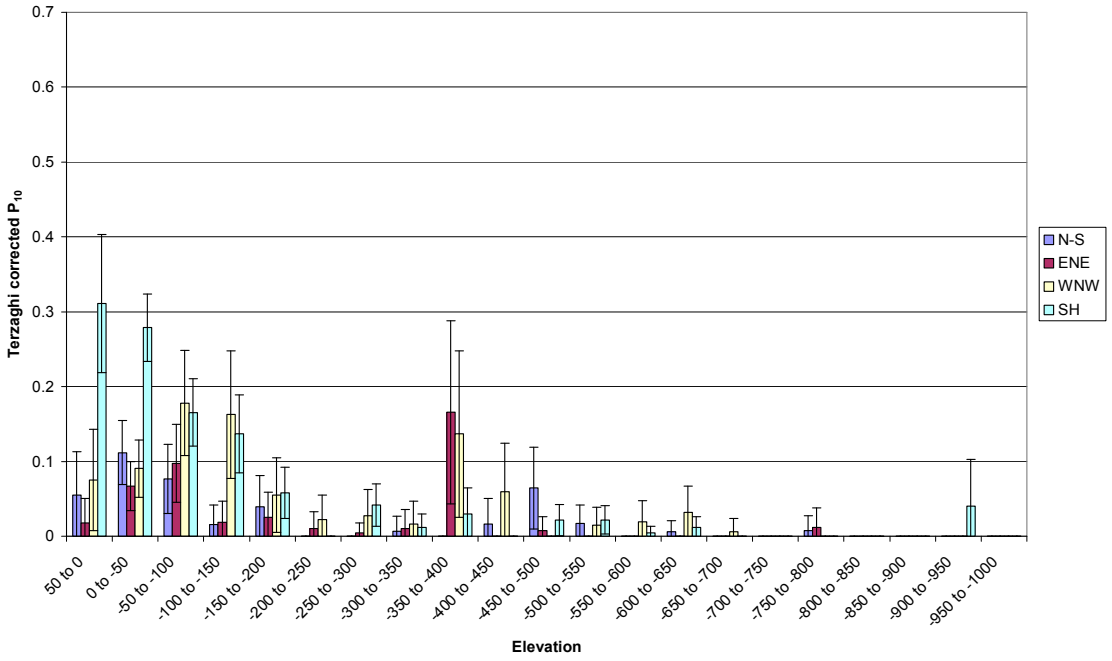

Figure A-5-14. *Variation of the Terzaghi-corrected fracture intensity for PFL features with elevation (masl) and fracture set for the fully characterised sections of boreholes penetrating Rock Domain RSMD01.*

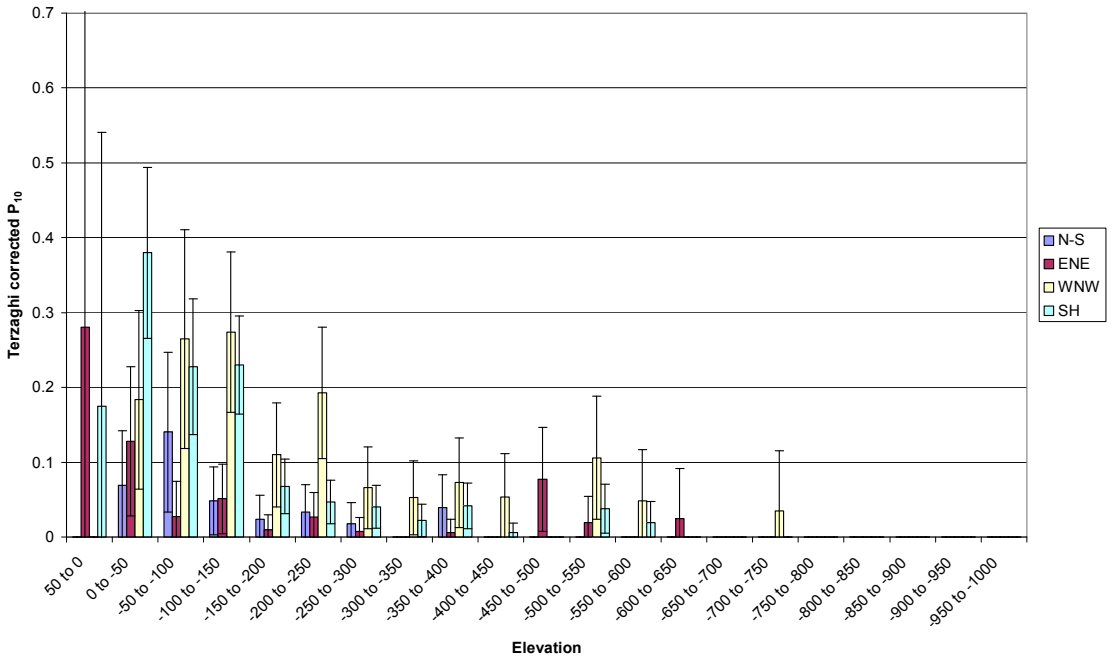

Figure A-5-15. *Variation of the Terzaghi-corrected fracture intensity for PFL features with elevation (masl) and fracture set for the fully characterised sections of boreholes penetrating Rock Domain RSMM01.*

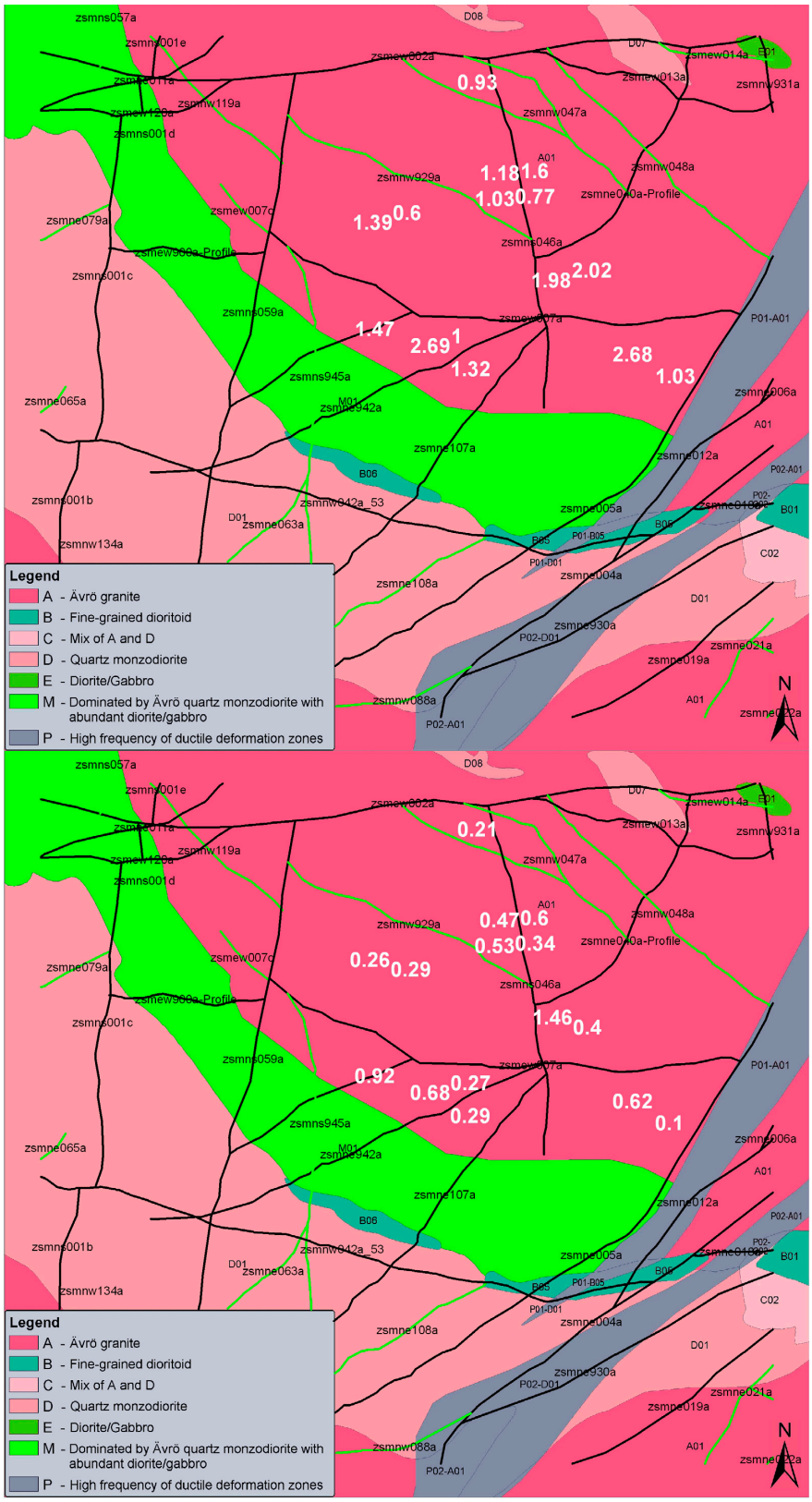

Figure A-5-16. *Variation of the Terzaghi-corrected fracture intensity for OPO-CP (top) and PFL (bottom) fractures for rock domain RSMA01 with position and in relation to (the surface expression of) the geological structure. (A value of 0 indicates that the rock domain is not present in the borehole.)*

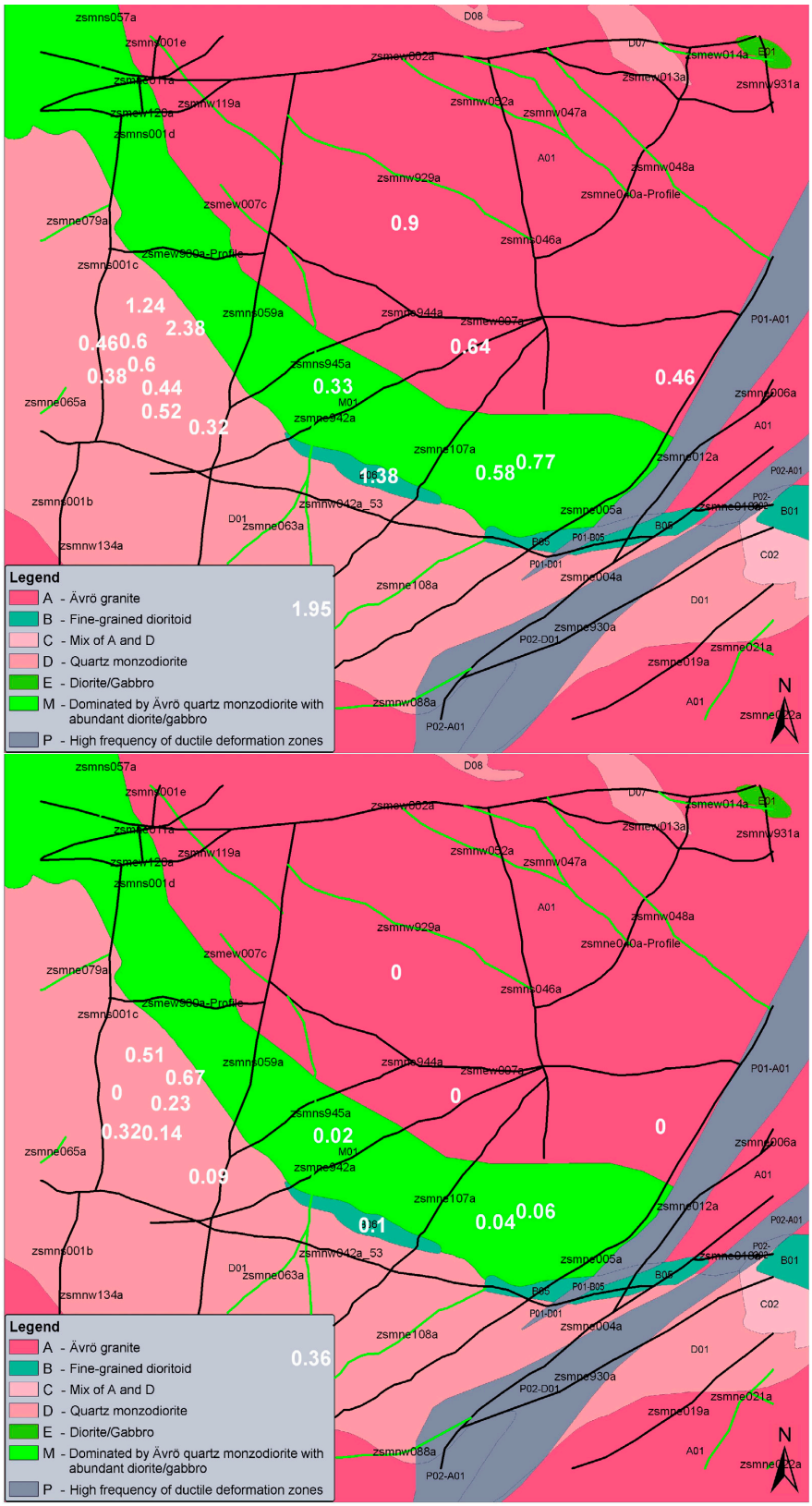

Figure A-5-17. *Variation of the Terzaghi-corrected fracture intensity for OPO-CP (top) and PFL (bottom) fractures for rock domain RSMD01 with position and in relation to (the surface expression of) the geological structure. (A value of 0 indicates that the rock domain is not present in the borehole.)*

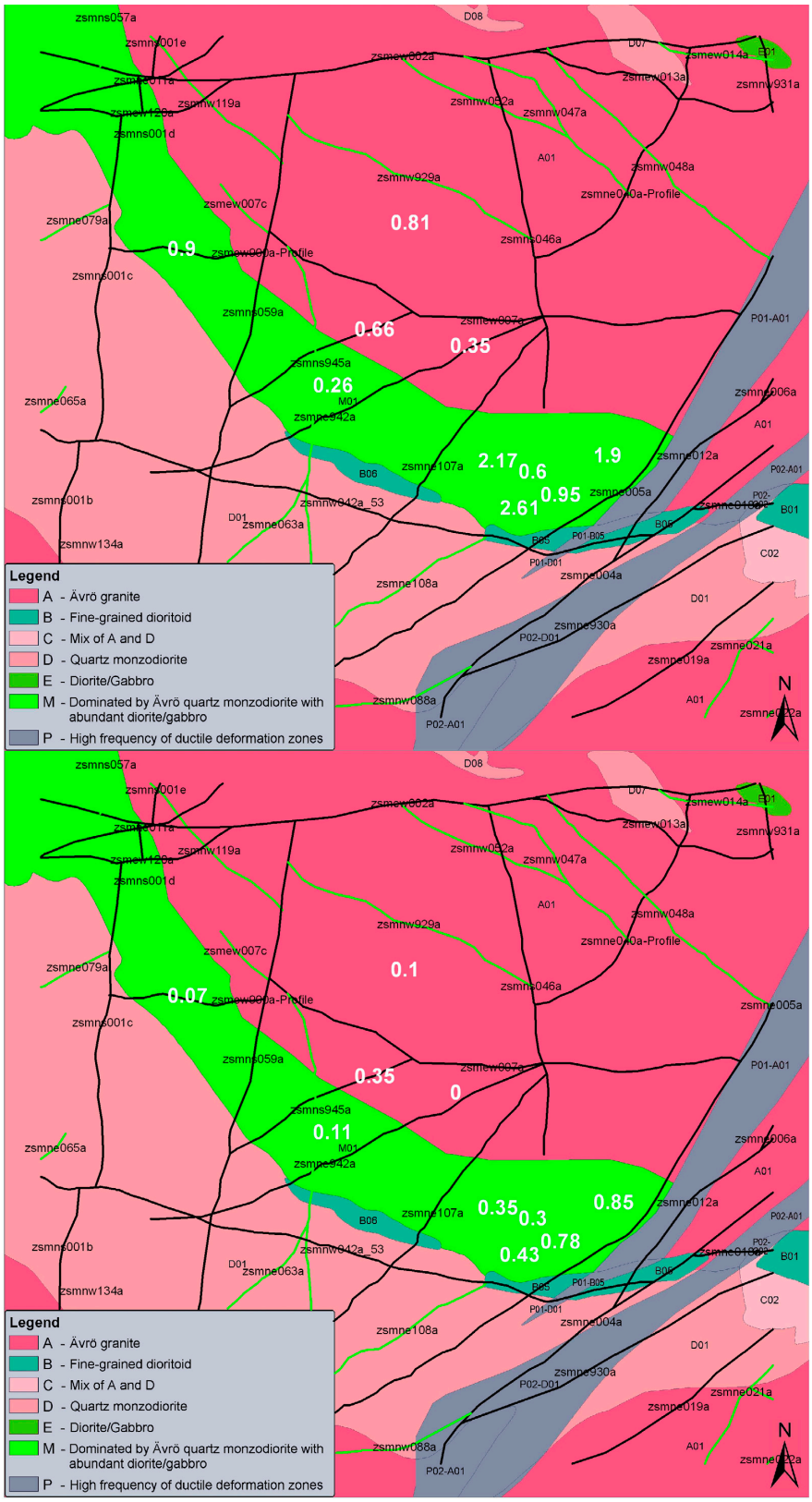

Figure A-5-18. *Variation of the Terzaghi-corrected fracture intensity for OPO-CP fractures for rock domain RSMM01 with position and in relation to (the surface expression of) the geological structure. (A value of 0 indicates that the rock domain is not present in the borehole.)*

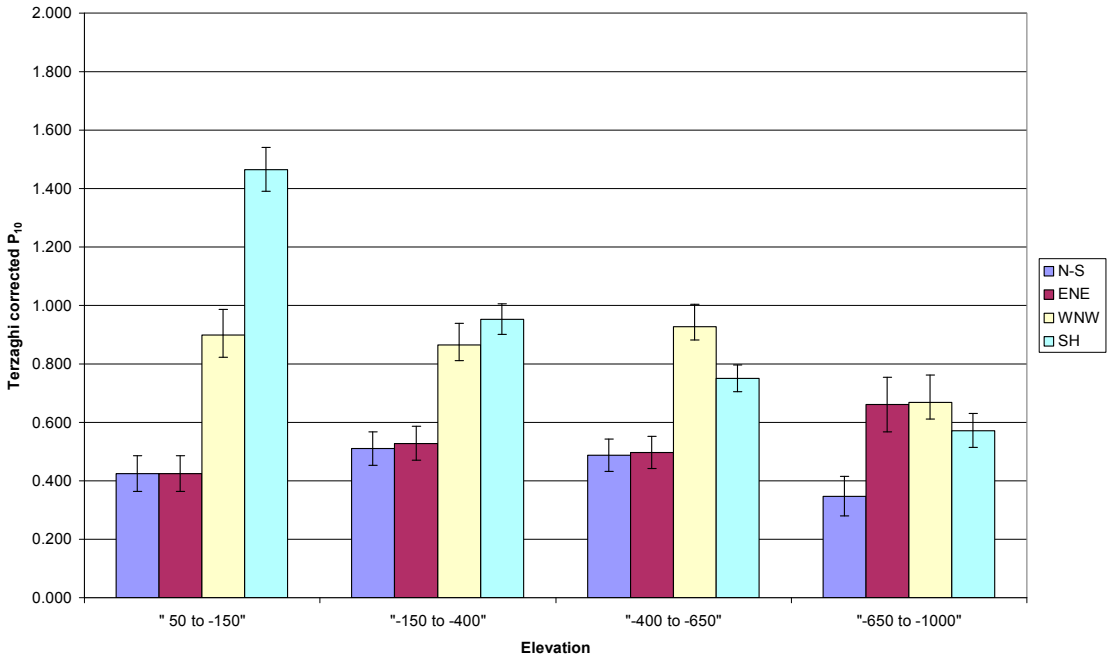

Figure A-5-19. *Variation of the Terzaghi-corrected fracture intensity for OPO fractures with depth zone for the fully characterised sections of boreholes penetrating Rock Domain RSMA01.*

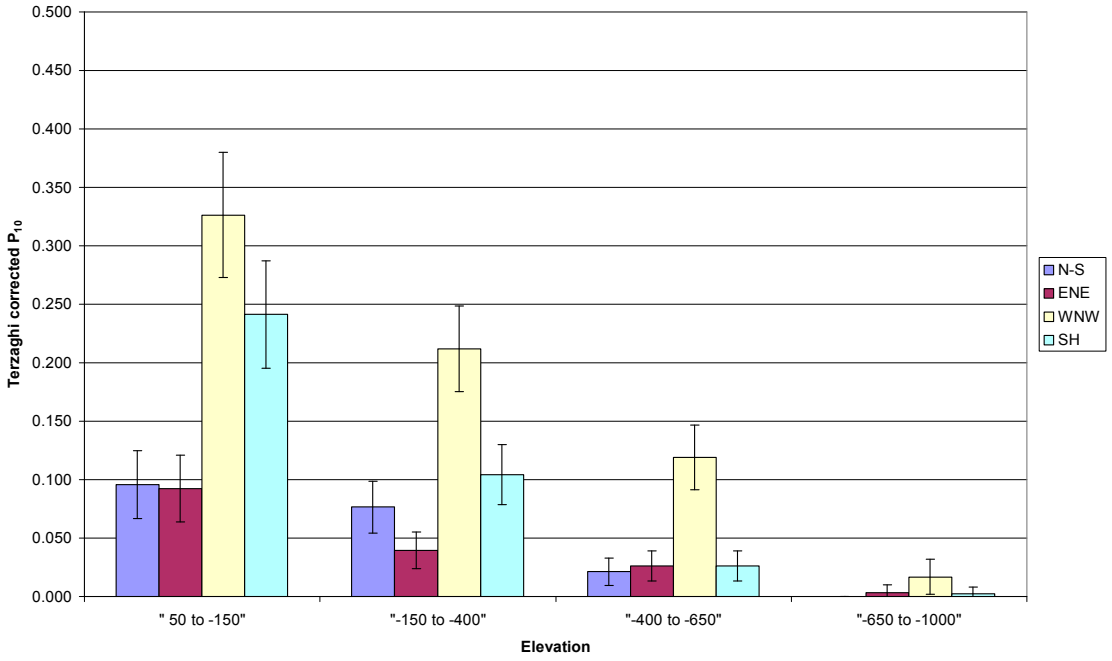

Figure A-5-20. *Variation of the Terzaghi-corrected fracture intensity for PFL features with depth zone for the fully characterised sections of boreholes penetrating Rock Domain RSMA01.*

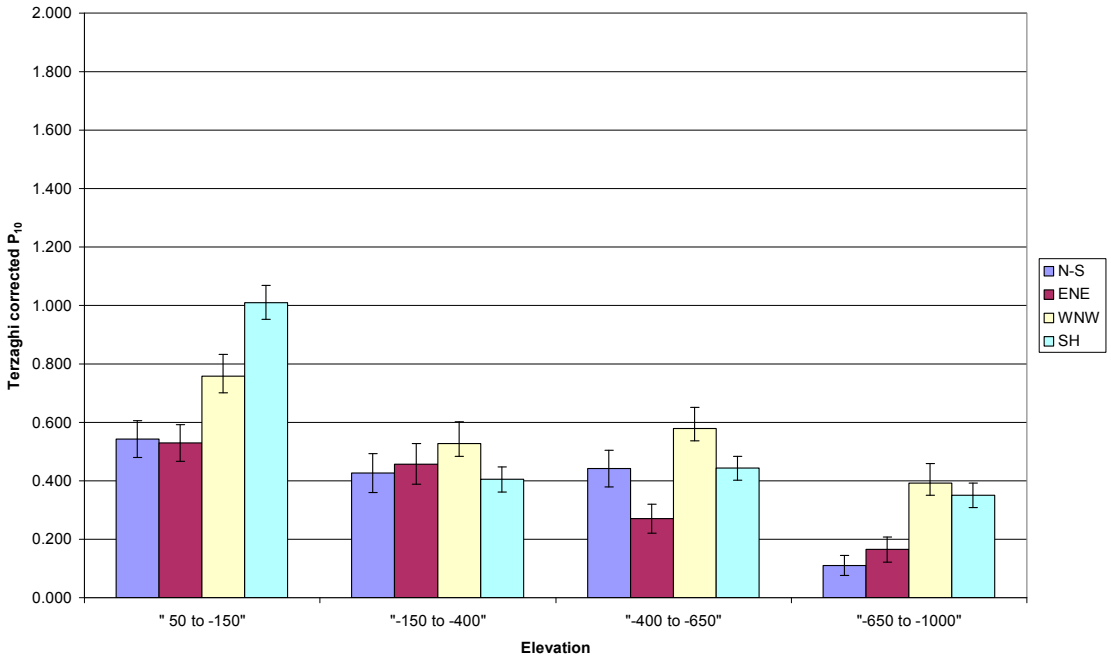

Figure A-5-21. *Variation of the Terzaghi-corrected fracture intensity for OPO fractures with depth zone for the fully characterised sections of boreholes penetrating Rock Domain RSMD01.*

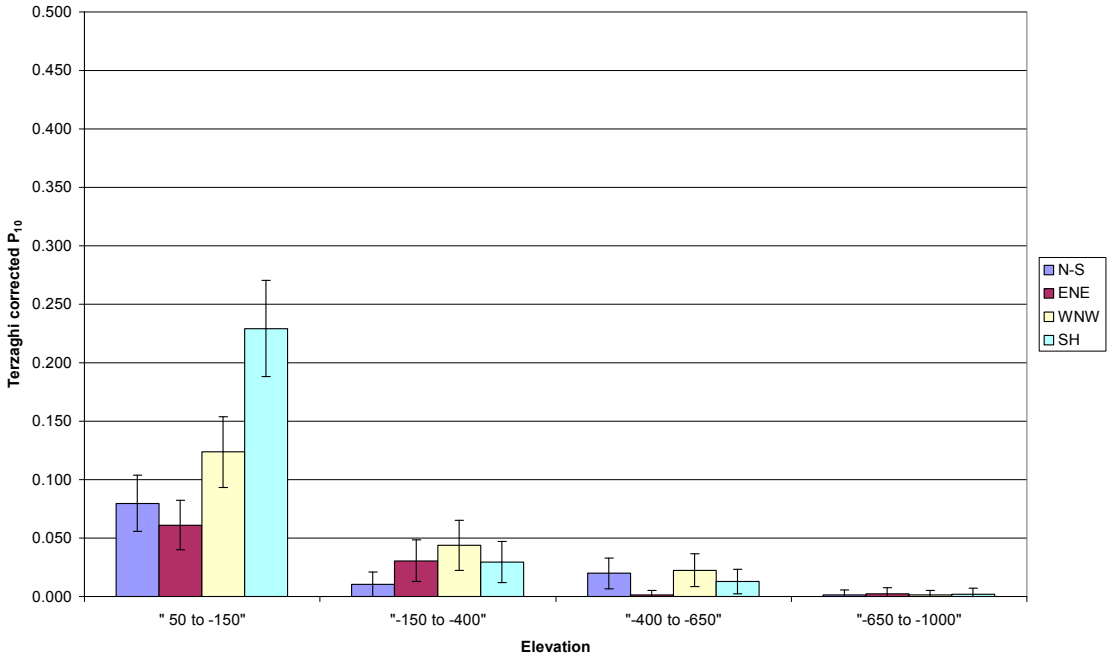

Figure A-5-22. *Variation of the Terzaghi-corrected fracture intensity for PFL features with depth zone for the fully characterised sections of boreholes penetrating Rock Domain RSMD01.*

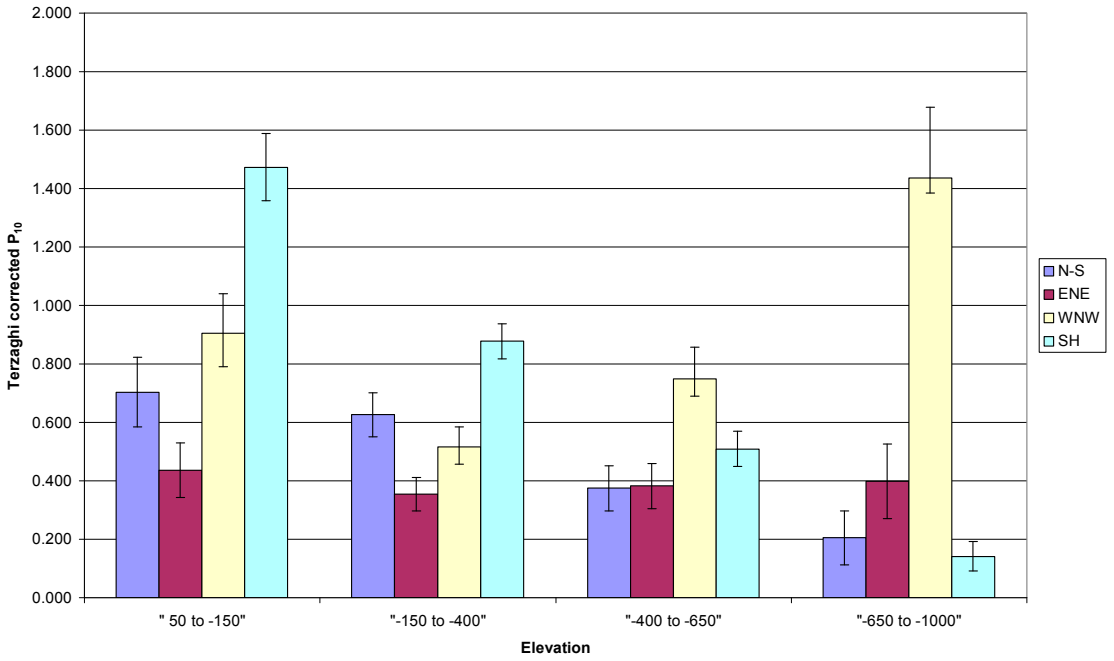

Figure A-5-23. *Variation of the Terzaghi-corrected fracture intensity for OPO fractures with depth zone for the fully characterised sections of boreholes penetrating Rock Domain RSMM01.*

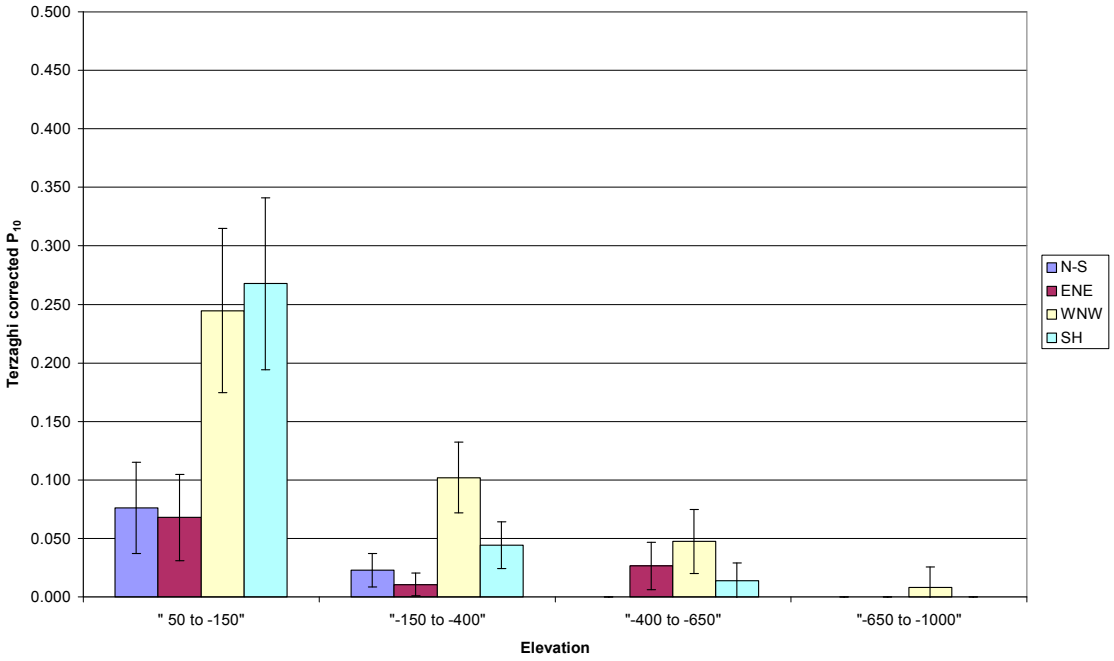

Figure A-5-24. *Variation of the Terzaghi-corrected fracture intensity for PFL features with depth zone for the fully characterised sections of boreholes penetrating Rock Domain RSMM01.*

A.5.2 Indicative error bars

In the plots of fracture intensity shown above and in Sections 9.3.2 to 9.3.5, indicative error bars are shown to give an idea of the statistical errors. The error bars correspond to 2 standard deviations either side of the central value. For a normal distribution with a known variance, this range is close to a 95% confidence interval for the mean. The distributions in question are not normal, but for long lengths of borehole intersected by many fractures, the distributions will be approximately normal from the law of large numbers. However, a precise statistical significance is not attached to the error bars. Rather they are simply used to give a visual indication of the relative magnitudes of the errors

The standard deviations were estimated from the available data on the basis that the fractures are randomly distributed in space i.e. are not clustered, that is correspond to independent samples from a simple Poisson distribution, and have distributions of size and orientation that are independent and independent of position. In this case, it can be shown that, for example, for circular fractures the expectation (mean) of the number of fractures intersected by a vertical borehole of length L is given by

$$n = \int_0^{\infty} dr \int_0^{2\pi} d\phi \int_0^{\pi/2} d\theta \sin\theta \rho D_r(r) D_{\theta\phi}(\theta,\phi) \pi r^2 \cos\theta L$$

where r is fracture radius, θ is fracture azimuth, ϕ is fracture dip, ρ is fracture density, $D_r(r)$ gives the distribution of fracture radius and $D_{\theta\phi}(\theta,\phi)$ gives the distribution of fracture orientation s over orientation.

Corresponding to this, the mean uncorrected fracture intensity is given by

$$P_{10} = \frac{n}{L}$$

It can also be shown that the variance of the number of fractures intersected by the borehole is given by n, and equivalently, the variance of the uncorrected fracture intensity is given by

$$\frac{n}{L^2} = \frac{P_{10}}{L}$$

Further, it can be shown that the mean Terzaghi-corrected fracture intensity (allowing if required, for an upper limit on the Terzaghi correction) is given by

$$P_{10,corr} = \frac{n}{L}\bar{\tau} = P_{10}\bar{\tau}$$

where $\bar{\tau}$ is the mean Terzaghi correction over the orientation distribution, and the variance of the Terzaghi-corrected fracture intensity is given by

$$\frac{n}{L^2}\bar{\tau}^2 + \frac{n}{L^2}\sigma_\tau^2 = P_{10,corr}\frac{\bar{\tau}}{L}\left(1 + \frac{\sigma_\tau^2}{\bar{\tau}^2}\right)$$

where σ_τ^2 is the variance of the Terzaghi correction over the orientation distribution.

For the fracture sets considered and with the Terzaghi correction limited to a maximum value of 7, the term involving σ_τ^2 is relatively small, and so the variance can be approximated by

$$P_{10,corr}\frac{\bar{\tau}}{L}.$$

The discussion above has considered the case of a vertical borehole. It was assumed that the last result also holds for measurements in a suite of boreholes of varying orientation, and the mean Terzaghi correction was estimated from the Terzaghi corrections for all fractures, and further, for simplicity, an approximate value of 1.2 was used for the Sub-Horizontal set and an approximate value of 2.7 was used for the other sets.

A.5.3 Traceability of data used fracture analysis

In this Appendix, the sources of the data used in the anlyses leading to the development of the HydroDFN are listed for Quality Assurance purposes. The various files listed are copies of corresponding files that were stored on ProjectPlace at the time a file was downloaded, and the directory structure closely mimics that used in ProjectPlace at that time.

Boreholes to be analysed

Manually input

Sections of boreholes to be analysed (fully characterised sections in the terminology of Section 11)

P:\SKB\ProjectPlace\HydroNet\Site-descriptive modelling\Exchange of data\L2.3_HydroDFN_ID96\Bh-length-for-statistics_071217\Bh-length-for-statistics_071217\PFL-s_meas-sec_KLX02-29.xls; worksheet: KLX

Fracture set definitions

Derived on basis of analysis of stereographic plots of fractures, MDZs and PFL anomalies and manually input.

Fracture data

P:\SKB\ProjectPlace\HydroNet\Site-descriptive modelling\Exchange of data\L2.3_HydroDFN_ID96\Boremap-data_071217\ Boremap-data_071217

p_fract_core_eshi_001_071113red.xls worksheet: Bearb0

p_fract_core_eshi_002_071113red.xls worksheet: Bearb0

p_fract_core_eshi_003_071113red.xls worksheet: Bearb0

These provide the fracture data for groups of boreholes.

See also Read-me_Boremap data_071217.doc

Note that the ROCK DOMAIN, DEFORMATION ZONE and DZ UNIT columns from these spreadsheets were not used. Rather this information was obtained by comparison with the rock domain and fracture domain data.

Rock unit, Fracture domain and deformation zone data

P:\SKB\ProjectPlace\HydroNet\Site-descriptive modelling\Exchange of data\L2.3_HydroDFN_ID96\RD-FD-DZ-MDZ-data_update_p-domain_080517\p_domain_080417.xls

MDZ data

P:\SKB\ProjectPlace\HydroNet\Site-descriptive modelling\Exchange of data\L2.3_HydroDFN_ID96\MDZ-data_update-control_080516\MDZ-hydro-prop_080505.xlss; worksheet: Bearb

Crush data

This was not used in the analysis because it was considered that all of the crush zones to be taken into account had been included in the DZ.

PFL data

P:\SKB\ProjectPlace\HydroNet\Site-descriptive modelling\Exchange of data\L2.3_HydroDFN_ID96\PFl-L-data_update_080206\PFl-L-data_update_080206\p_anomaly_pfl_eshi_080206.xls: Bearb (4)

A.6 Additional fracture modelling results

A.6.1 Calibration of fracture size models

The calibration of size distributions based on connectivity analyses (see Section 12.4.4) for HRD_EW007, HRD_N and HRD_W are shown in Figure A-6-1, Figure A-6-2 and Figure A-6-3, respectively.

A.6.2 Calibration of Hydro-DFN for HRD_C variants

The calibration of the HRD_C variant with r_0 fixed, open fracture intensity based on OPO fractures and a correlated model of fracture transmissivity is presented in Figure Figure A-6-4through Figure A-6-7.

The calibration of the HRD_C variant with r_0 fixed, open fracture intensity based on OPO fractures and an uncorrelated model of fracture transmissivity is presented in Figure A-6-8 through Figure A-6-11.

The calibration of the HRD_C variant with r_0 fixed, open fracture intensity based on OPO-CP fractures and a semi-correlated model of fracture transmissivity is presented in Figure A-6-12 through Figure A-6-15.

The calibration of the HRD_C variant with k_r fixed (2.9), open fracture intensity based on OPO fractures and a semi-correlated model of fracture transmissivity is presented in Figure A-6-16 through Figure A-6-19.

A.6.3 Calibration of Hydro-DFN for HRD_W variants

The calibration of the HRD_W variant with r_0 fixed, open fracture intensity based on OPO-CP fractures and a semi-correlated model of fracture transmissivity is presented in Figure A-6-20 through Figure A-6-23.

A.6.4 Calibration of Hydro-DFN for HRD_EW007

The calibration of the HRD_EW007 base case with r_0 fixed, open fracture intensity based on OPO fractures and a semi-correlated model of fracture intensity is presented in Figure A-6-24 through Figure A-6-28.

A.6.5 Calibration of Hydro-DFN for HRD_N

The calibration of the HRD_EW007 base case with r_0 fixed, open fracture intensity based on OPO fractures and a semi-correlated model of fracture intensity is presented in Figure A-6-28 through Figure A-6-33.

A.6.6 Block properties for variants in HRD_C

Calculated block properties, hydraulic conductivities and kinematic porosities, are given in Table A-6-1 through Table A-6-3 for the HRD_C variants with a correlated and uncorrelated transmissivity for open fracture intensity based on OPO fractures, and a semi-correlated model of fracture transmissivity for open fracture intensity based on OPO-CP fractures.

A.6.7 Block properties for variants in HRD_W

Calculated block properties, hydraulic conductivities and kinematic porosities, are given in Table A-6-4 through Table A-6-6 for the HRD_W variants with a correlated and uncorrelated transmissivity for open fracture intensity based on OPO fractures, and a semi-correlated model of fracture transmissivity for open fracture intensity based on OPO-CP fractures.

A.6.8 Block properties for variants in HRD_EW007

Calculated block properties, hydraulic conductivities and kinematic porosities, are given in Table A-6-7 through Table A-6-9 for the HRD_EW007 variants with a correlated and uncorrelated transmissivity for open fracture intensity based on OPO fractures, and a semi-correlated model of fracture transmissivity for open fracture intensity based on OPO-CP fractures.

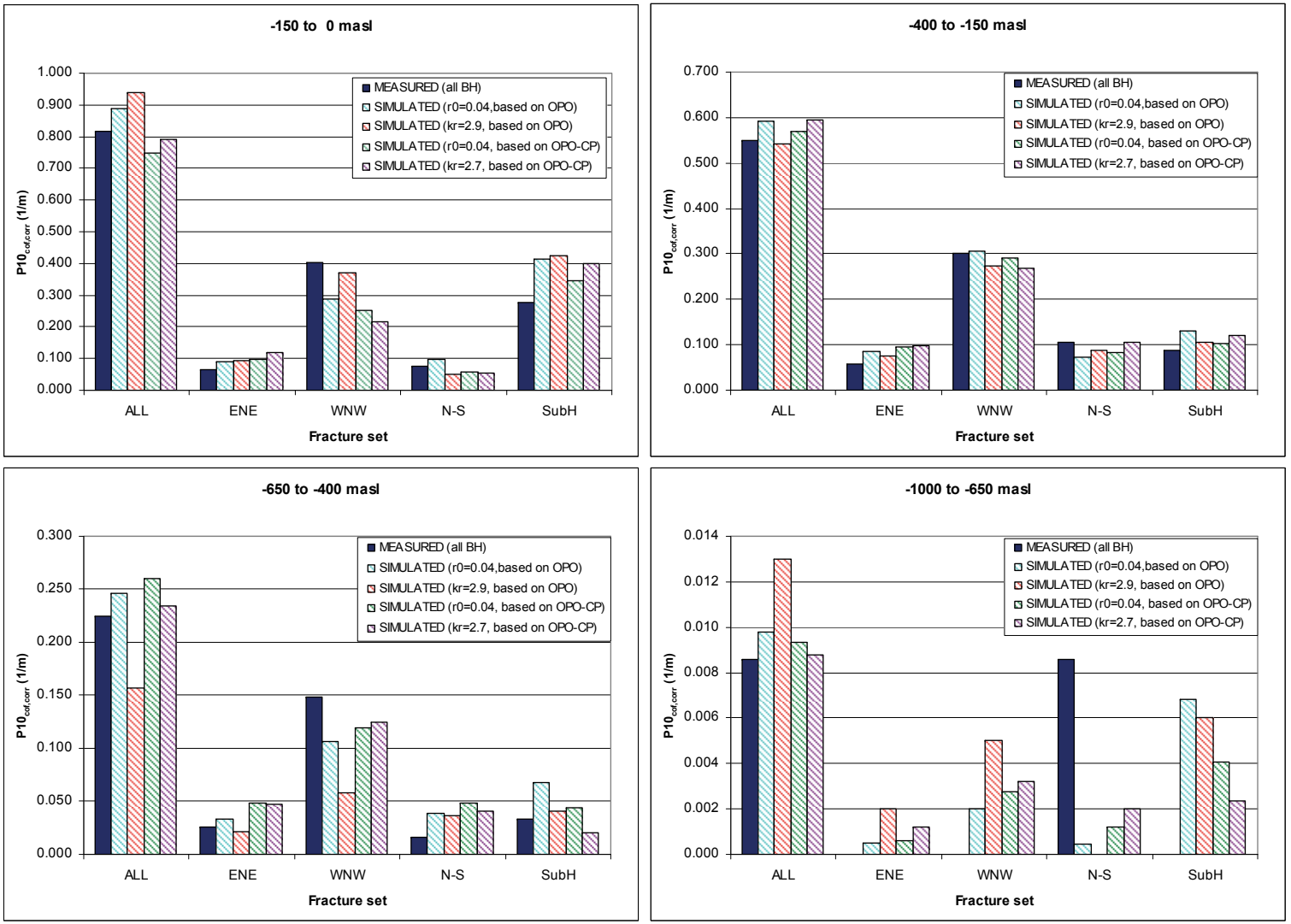

Figure A-6-1. *Comparison of the Terzaghi corrected connected open fracture intensities, $P_{10,cof,corr}$ for the individual fracture sets with the measured fracture intensities for PFL-anomalies for HRD_EW007. Four geometrical fracture models were considered: k_r fixed with r_0 varying or r_0 fixed with k_r varying, and an input P_{32} based on $P_{10,opo}$; r_0 fixed with k_r varying or r_0 fixed with k_r varying, and an input P_{32} based on $P_{10,opo\text{-}cp}$. A reasonable match is obtained in each case.*

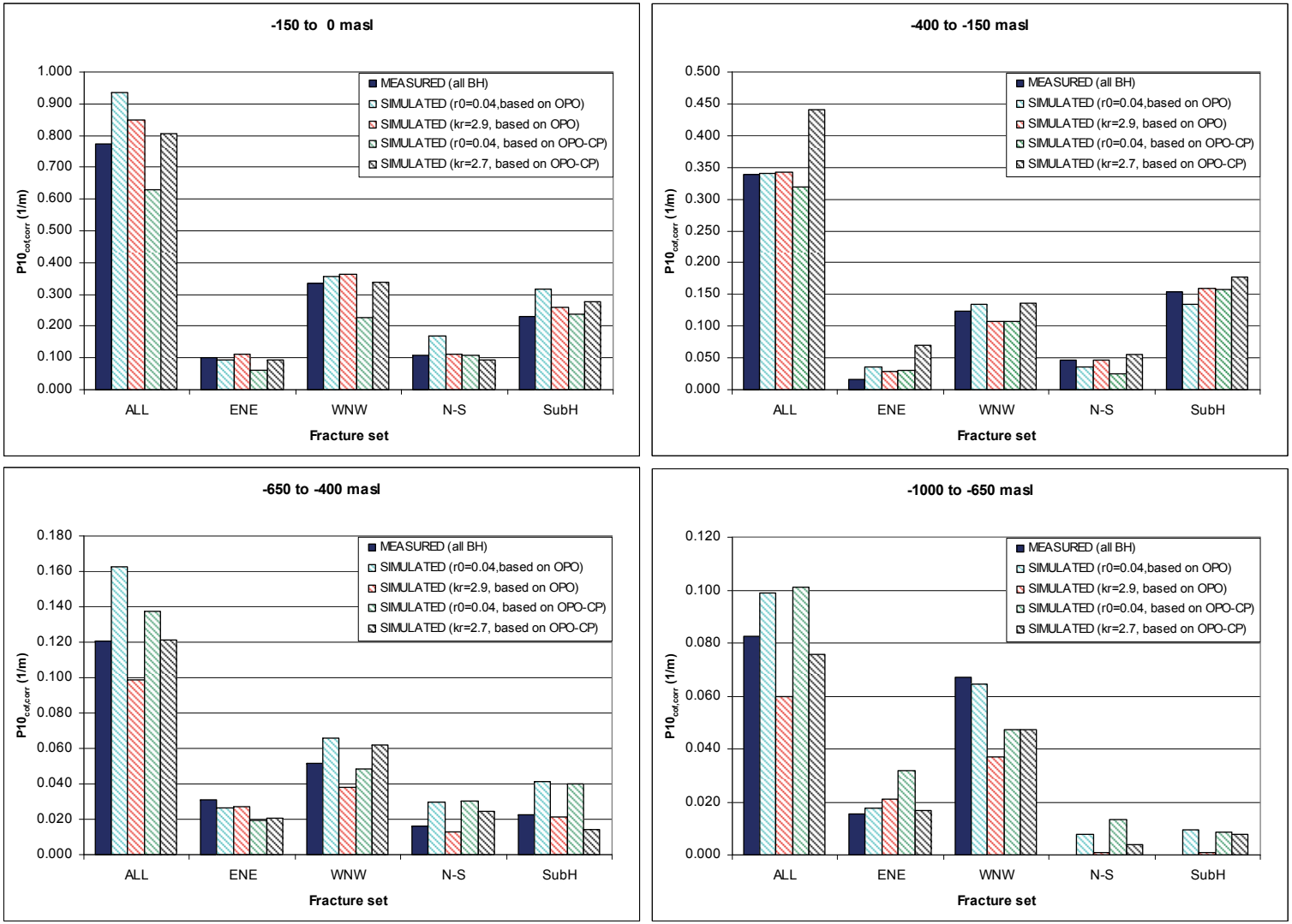

Figure A-6-2. *Comparison of the Terzaghi corrected connected open fracture intensities, $P_{10,cof,corr}$ for the individual fracture sets with the measured fracture intensities for PFL-anomalies for HRD_N. Four geometrical fracture models were considered: k_r fixed with r_0 varying or r_0 fixed with k_r varying, and an input P_{32} based on $P_{10,opo}$; r_0 fixed with k_r varying or r_0 fixed with k_r varying, and an input P_{32} based on $P_{10,opo\text{-}cp}$. A reasonable match is obtained in each case.*

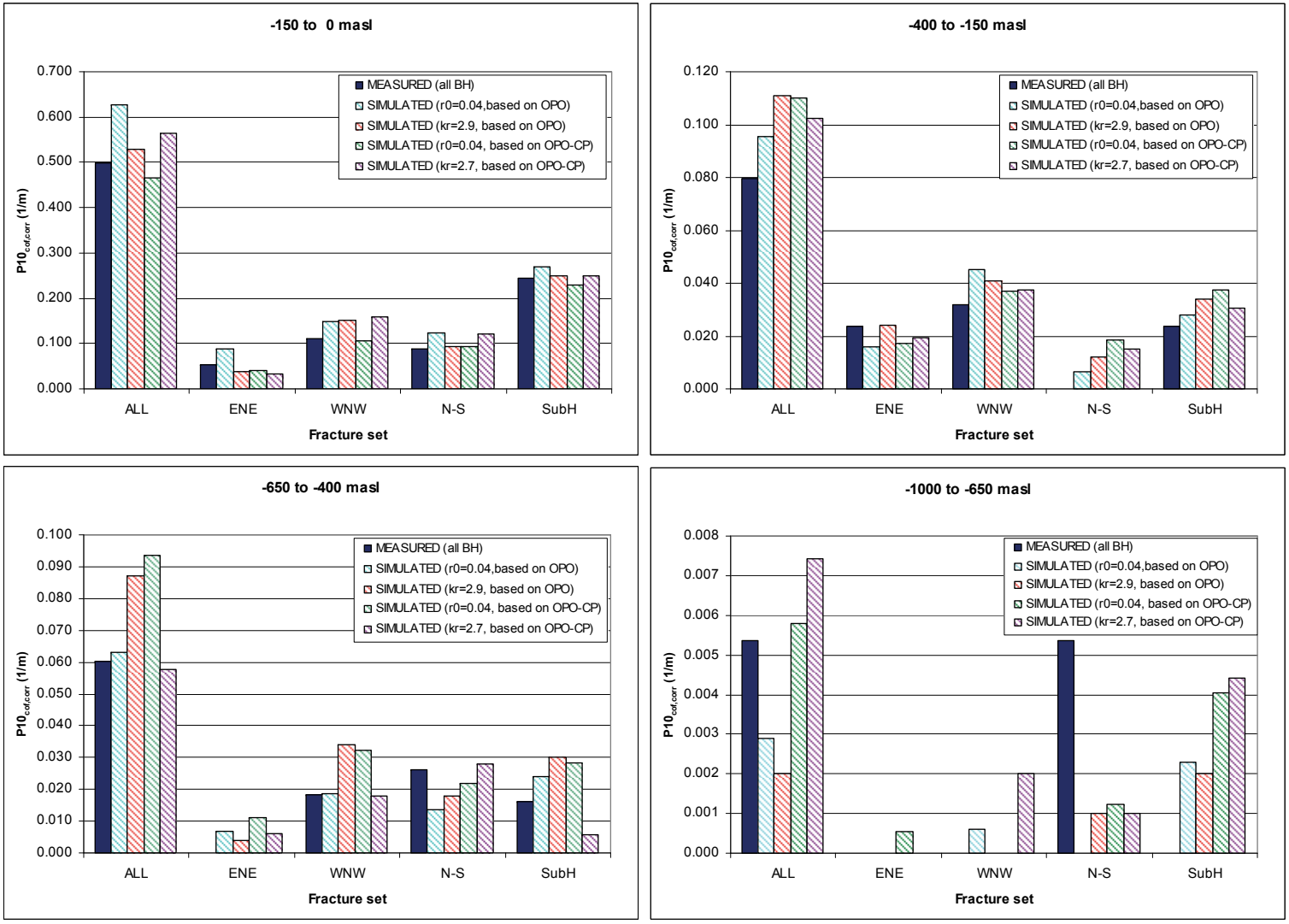

Figure A-6-3. *Comparison of the Terzaghi corrected connected open fracture intensities, $P_{10,cof,corr}$ for the individual fracture sets with the measured fracture intensities for PFL-anomalies for HRD_W. Four geometrical fracture models were considered: k_r fixed with r_0 varying or r_0 fixed with k_r varying, and an input P_{32} based on $P_{10,opo}$; r_0 fixed with k_r varying or r_0 fixed with k_r varying, and an input P_{32} based on $P_{10,opo\text{-}cp}$. A reasonable match is obtained in each case.*

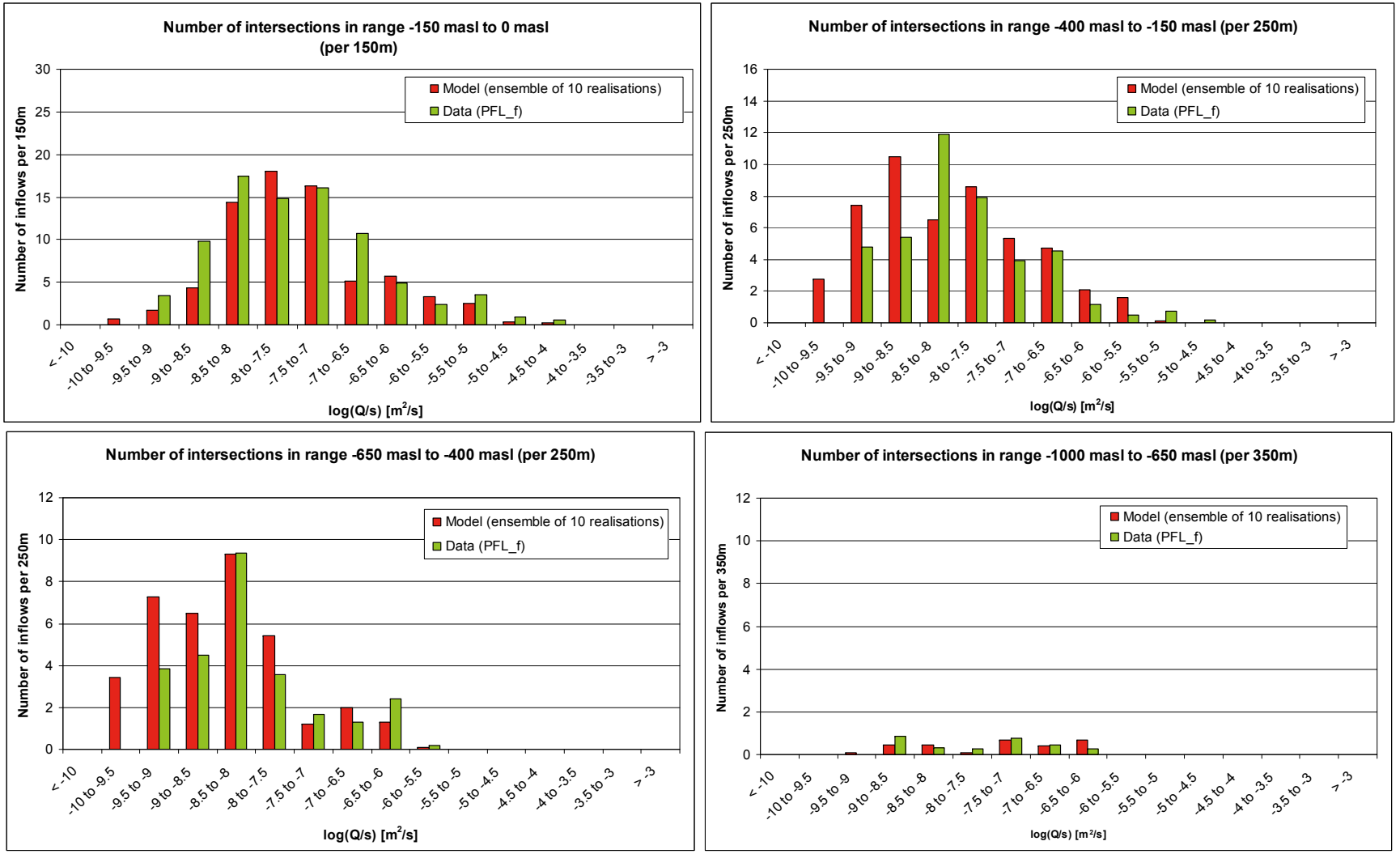

Figure A-6-4. *Histograms comparing the distribution of the magnitude of inflows divided by drawdown, Q/s, at abstraction boreholes in HRD_C. The model has a correlated transmissivity, with r_0 fixed and open fracture intensity based on OPO fractures. The PFL-f measurements are treated as ensemble over all boreholes sections within HRD_C. The simulations represent the combined results of 10 realisations of the Hydro-DFN model. The numbers of intersections are Terzaghi weighted and normalised to the length of borehole which is provided in the heading of each graph.*

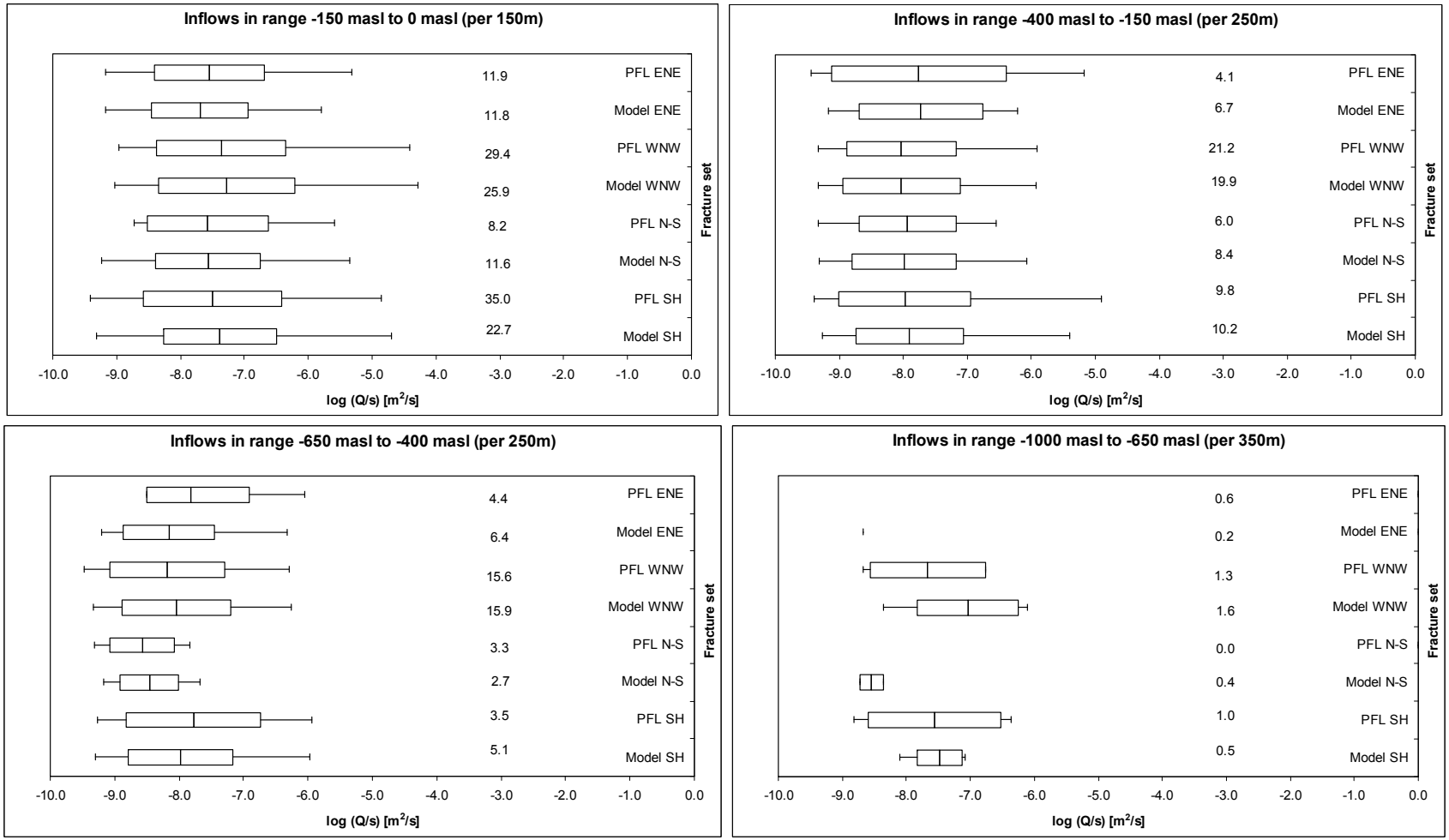

Figure A-6-5. *Bar and whisker plots comparing statistics taken over each fracture set for the individual inflows, Q/s, for the PFL-f data from borehole sections within HRD_C against statistics for an ensemble over 10 realisations of the Hydro-DFN model. The model has a correlated transmissivity, with r_0 fixed and open fracture intensity based on OPO fractures. The centre of the bar indicates the mean value, the ends of the bar indicate ±1 standard deviation, and the error bars indicate the minimum and maximum values. For the data statistics are taken over the identified flow-anomalies within each set. For the model, statistics are taken over the fractures generated within each set and over 10 realisations. The numbers of fractures are Terzaghi weighted and normalised to the length specified in the respective graph heading.*

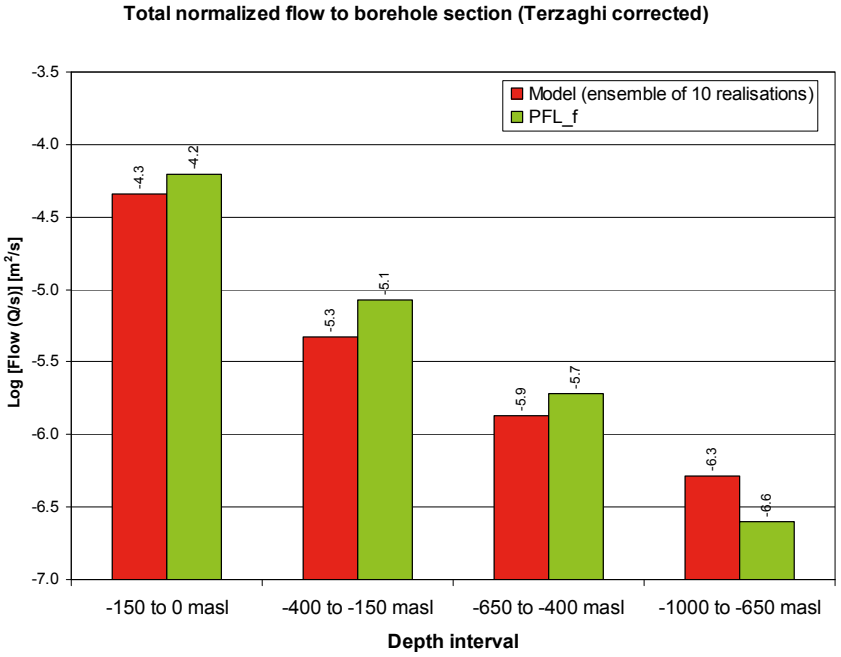

Figure A-6-6. *Comparison of the Terzaghi weighted sum of individual flows, Q/s, for the PFL-f data from borehole sections within HRD_C against the Hydro-DFN model. The model has a correlated transmissivity, with r_0 fixed and open fracture intensity based on OPO fractures. For the model, the arithmetic mean is taken over 10 realisations. The flows are Terzaghi weighted and normalised to the borehole length indicated by the range on the horizontal axis.*

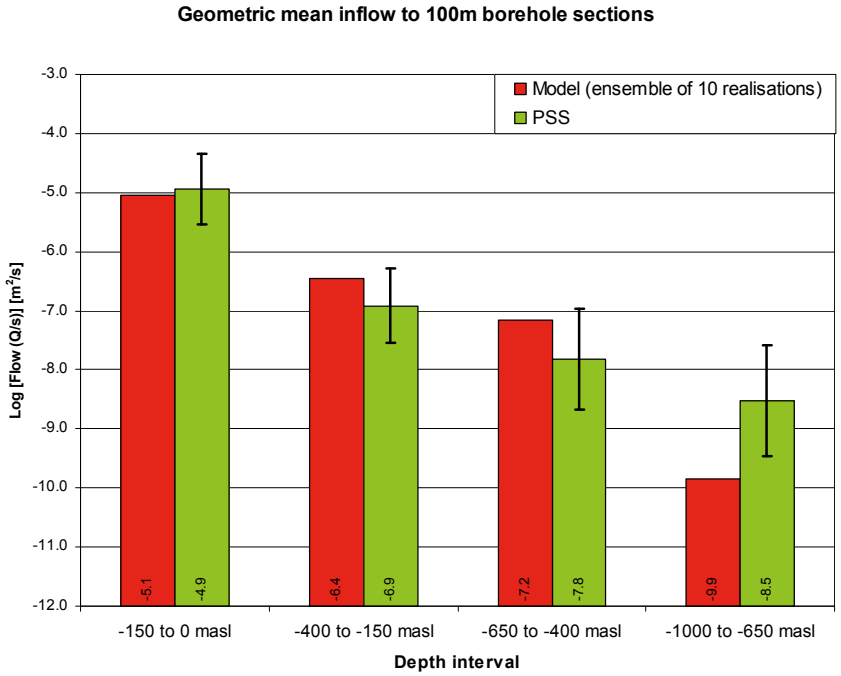

Figure A-6-7. *Comparison of the geometric mean of total flows, Q/s, to 100m borehole intervals for the PSS data from borehole sections within HRD_C against the Hydro-DFN model. The model has a correlated transmissivity, with r_0 fixed and open fracture intensity based on OPO fractures. For the data, the geometric mean is shown as well as the 95% confidence interval in the mean. For the model, the mean value of total flow is taken over 10 realisations.*

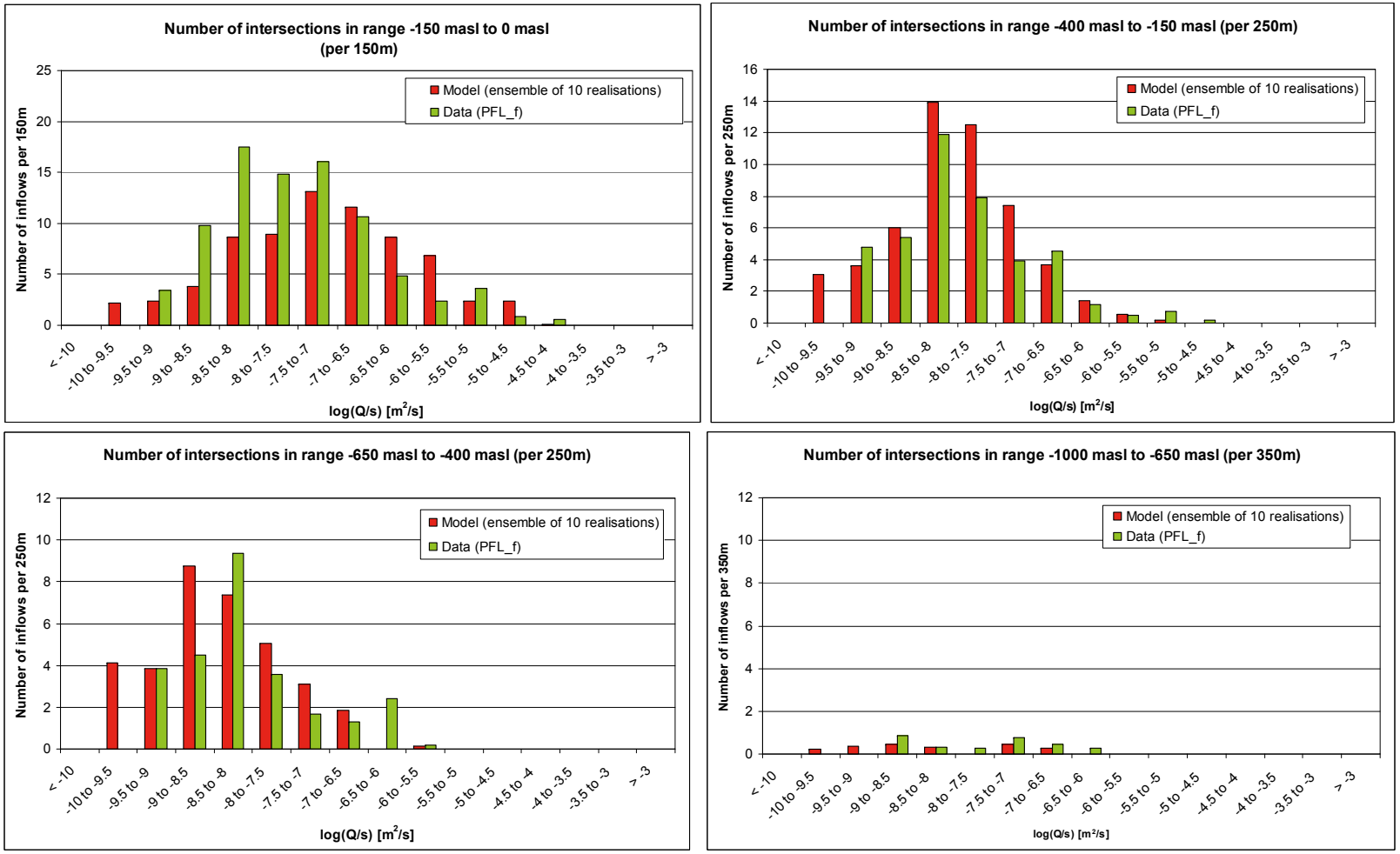

Figure A-6-8. *Histograms comparing the distribution of the magnitude of inflows divided by drawdown, Q/s, at abstraction boreholes in HRD_C. The model has an uncorrelated transmissivity, with r_0 fixed and open fracture intensity based on OPO fractures. The PFL-f measurements are treated as ensemble over all boreholes sections within HRD_C. The simulations represent the combined results of 10 realisations of the Hydro-DFN model. The numbers of intersections are Terzaghi weighted and normalised to the length of borehole which is provided in the heading of each graph.*

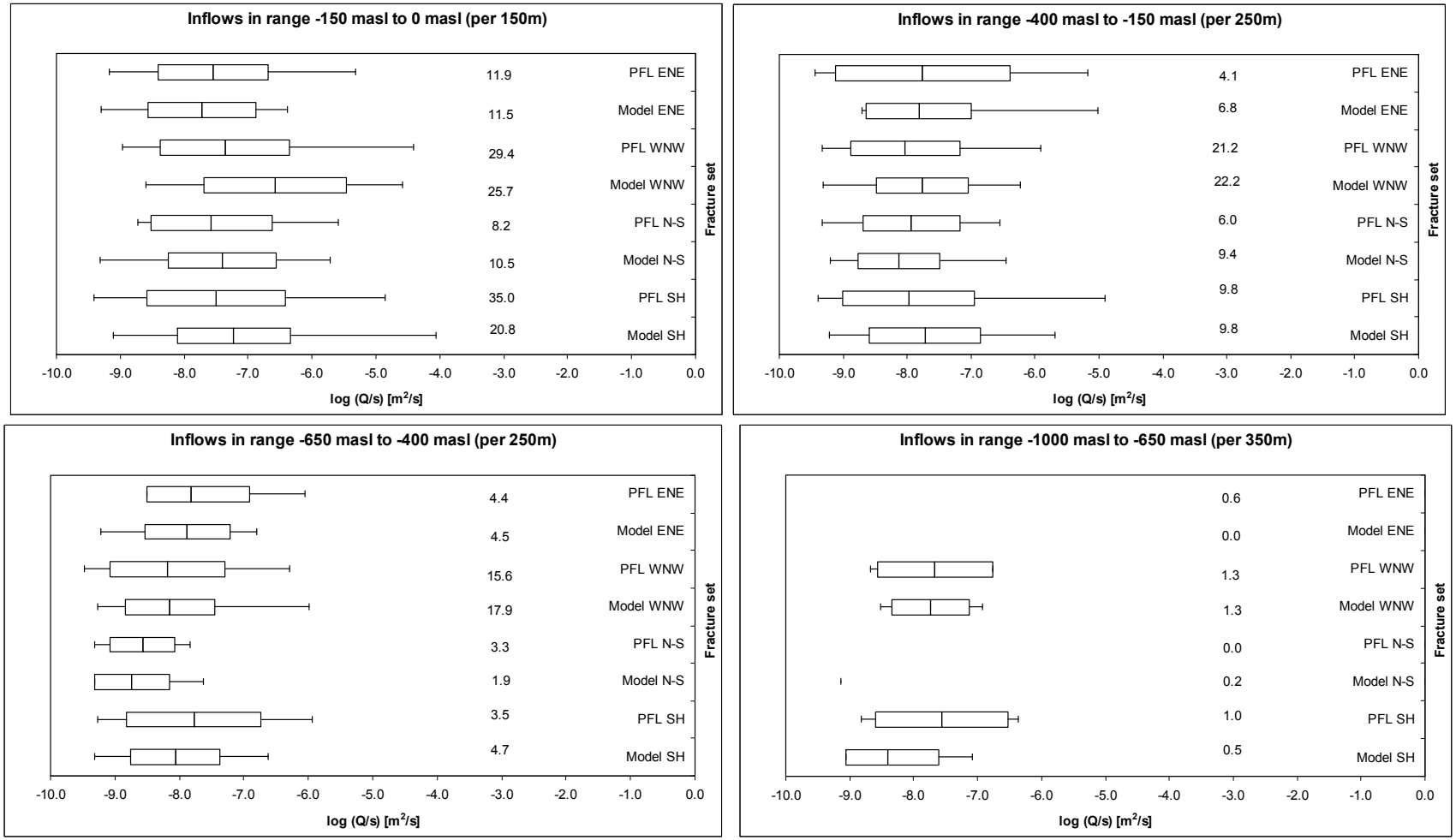

Figure A-6-9. *Bar and whisker plots comparing statistics taken over each fracture set for the individual inflows, Q/s, for the PFL-f data from borehole sections within HRD_C against statistics for an ensemble over 10 realisations of the Hydro-DFN model. The model has an uncorrelated transmissivity, with r_0 fixed and open fracture intensity based on OPOP fractures. The centre of the bar indicates the mean value, the ends of the bar indicate ±1 standard deviation, and the error bars indicate the minimum and maximum values. For the data statistics are taken over the identified flow-anomalies within each set. For the model, statistics are taken over the fractures generated within each set and over 10 realisations. The numbers of fractures are Terzaghi weighted and normalised to the length specified in the respective graph heading.*

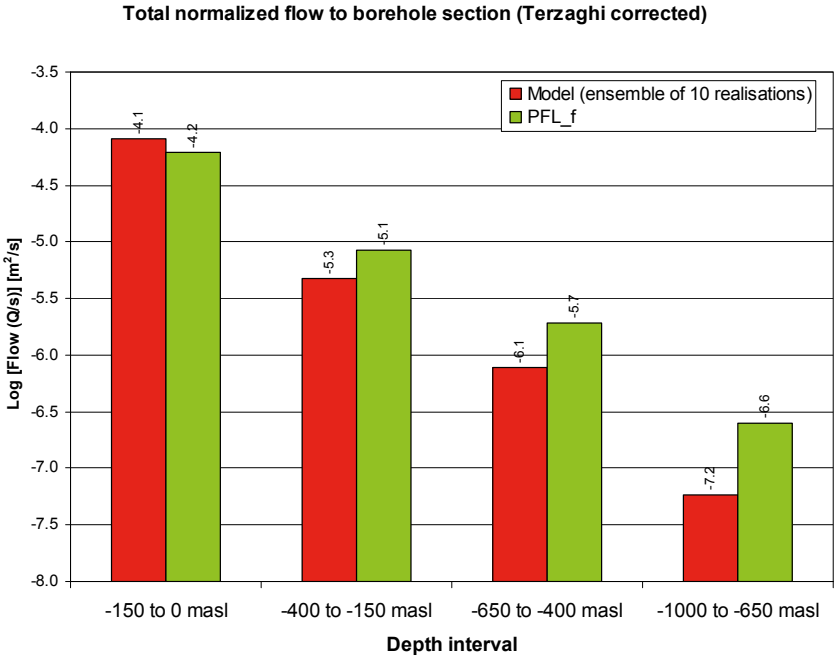

Figure A-6-10. *Comparison of the Terzaghi weighted sum of individual flows, Q/s, for the PFL-f data from borehole sections within HRD_C against the Hydro-DFN model. The model has an uncorrelated transmissivity, with r_0 fixed and open fracture intensity based on OPO fractures. For the model, the arithmetic mean is taken over 10 realisations. The flows are Terzaghi weighted and normalised to the borehole length indicated by the range on the horizontal axis.*

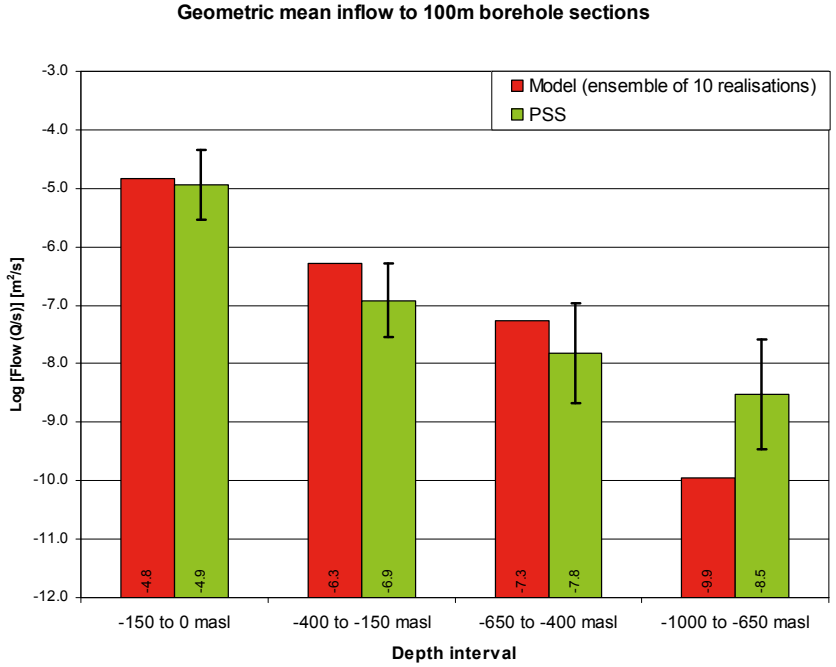

Figure A-6-11. *Comparison of the geometric mean of total flows, Q/s, to 100m borehole intervals for the PSS data from borehole sections within HRD_C against the Hydro-DFN model. The model has an uncorrelated transmissivity, with r_0 fixed and open fracture intensity based on OPO fractures. For the data, the geometric mean is shown as well as the 95% confidence interval in the mean. For the model, the mean value of total flow is taken over 10 realisations.*

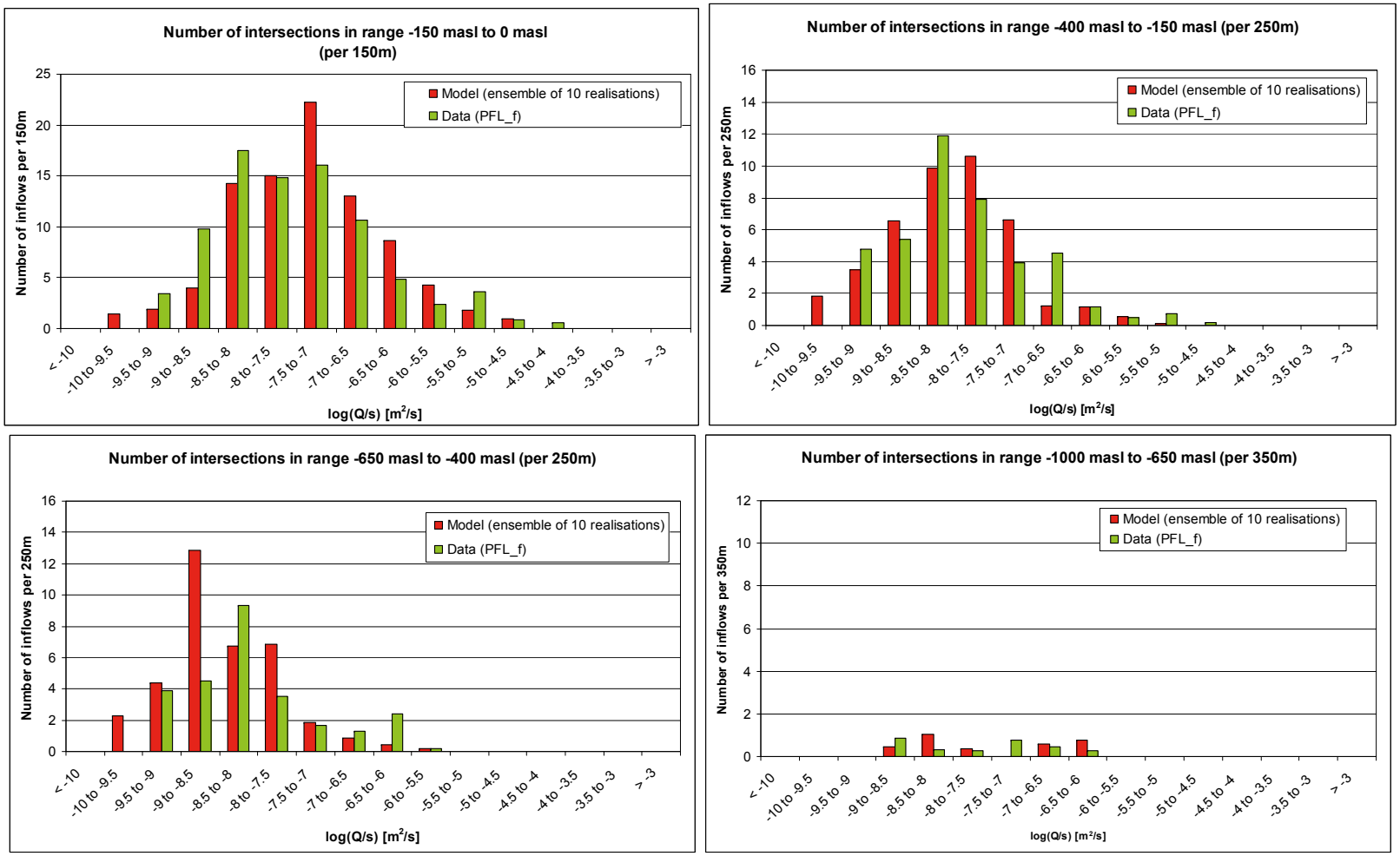

Figure A-6-12. *Histograms comparing the distribution of the magnitude of inflows divided by drawdown, Q/s, at abstraction boreholes in HRD_C. The model has a semi-correlated transmissivity, with r_0 fixed and open fracture intensity based on OPO-CP fractures. The PFL-f measurements are treated as ensemble over all boreholes sections within HRD_C. The simulations represent the combined results of 10 realisations of the Hydro-DFN model. The numbers of intersections are Terzaghi weighted and normalised to the length of borehole which is provided in the heading of each graph.*

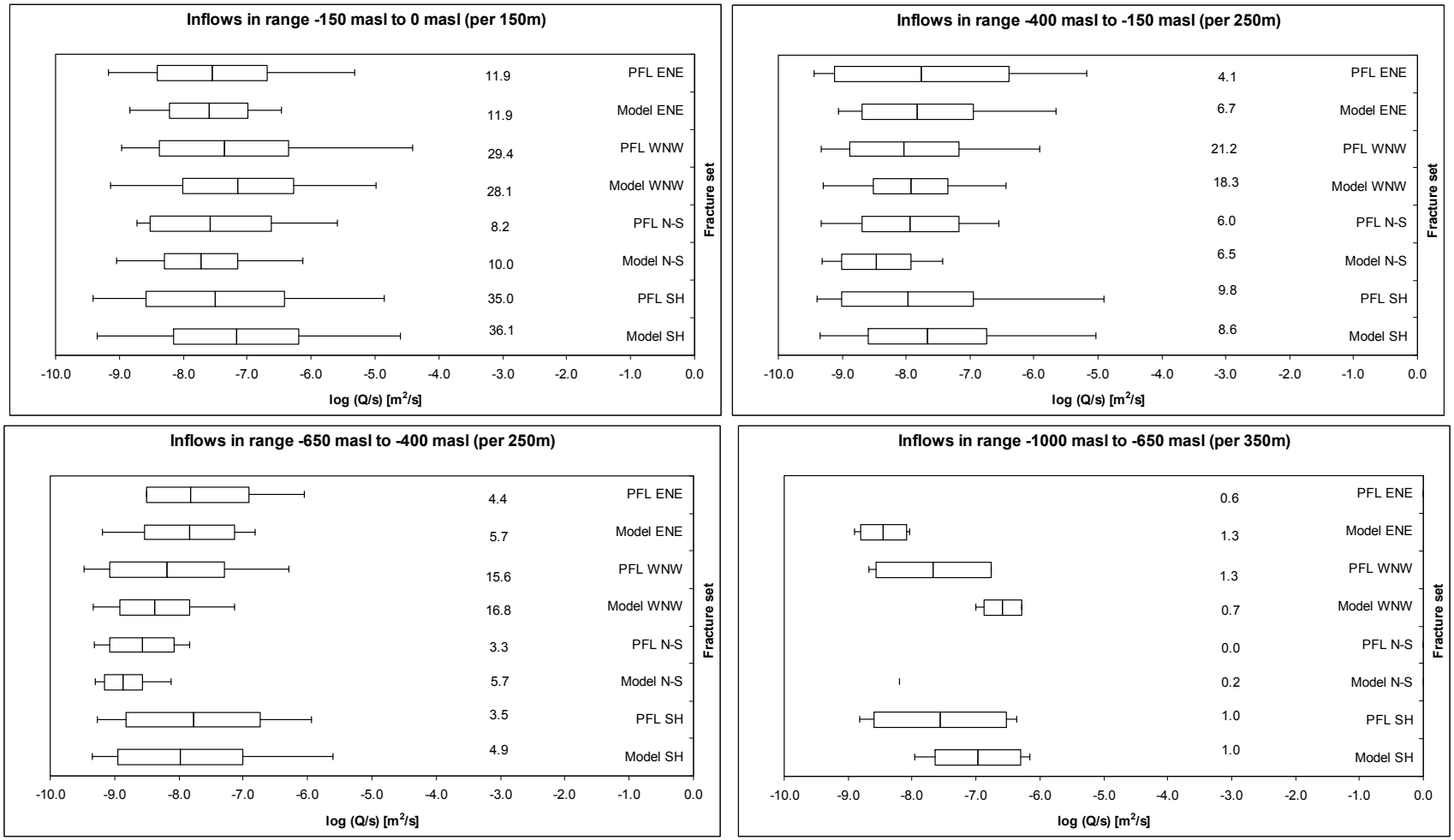

Figure A-6-13. *Bar and whisker plots comparing statistics taken over each fracture set for the individual inflows, Q/s, for the PFL-f data from borehole sections within HRD_C against statistics for an ensemble over 10 realisations of the Hydro-DFN model. The model has a semi-correlated transmissivity, with r_0 fixed and open fracture intensity based on OPO fractures. The centre of the bar indicates the mean value, the ends of the bar indicate ±1 standard deviation, and the error bars indicate the minimum and maximum values. For the data statistics are taken over the identified flow-anomalies within each set. For the model, statistics are taken over the fractures generated within each set and over 10 realisations. The numbers of fractures are Terzaghi weighted and normalised to the length specified in the respective graph heading.*

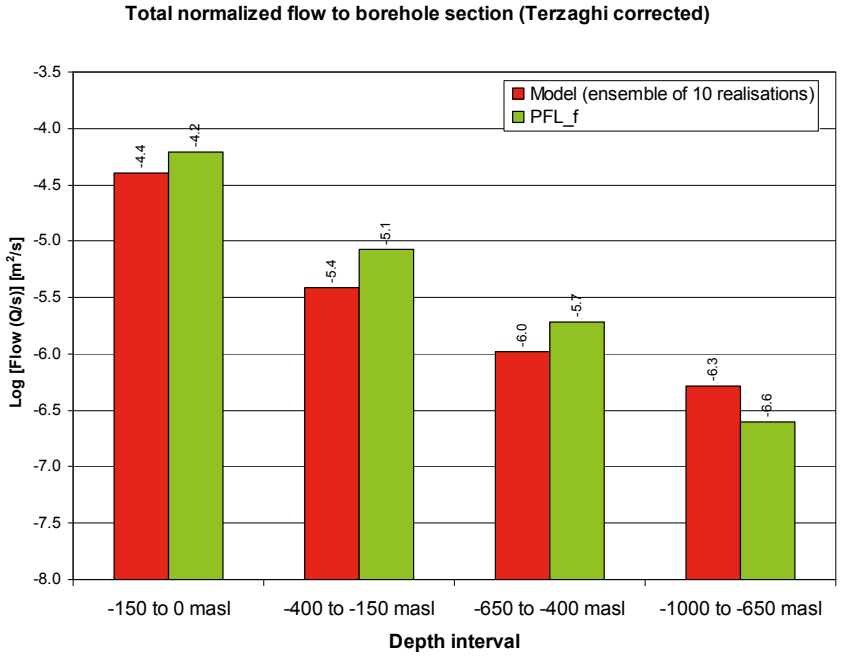

Figure A-6-14. *Comparison of the Terzaghi weighted sum of individual flows, Q/s, for the PFL-f data from borehole sections within HRD_C against the Hydro-DFN model. The model has a semi-correlated transmissivity, r_0 fixed and open fracture intensity based on OPO-CP fractures. For the model, the arithmetic mean is taken over 10 realisations. The flows are Terzaghi weighted and normalised to the borehole length indicated by the range on the horizontal axis.*

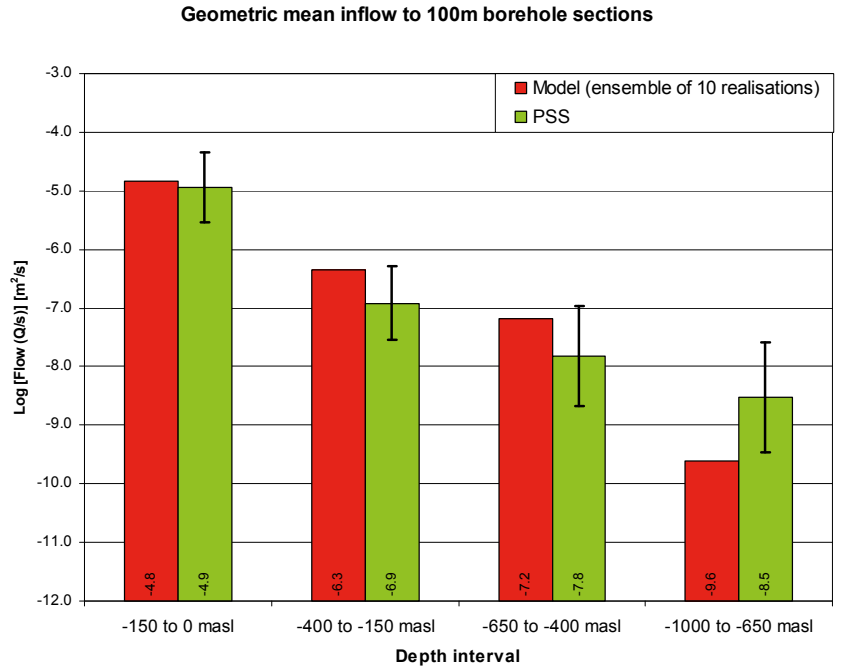

Figure A-6-15. *Comparison of the geometric mean of total flows, Q/s, to 100m borehole intervals for the PSS data from borehole sections within HRD_C against the Hydro-DFN model. The model has a semi-correlated transmissivity, r_0 fixed and open fracture intensity based on OPO-CP fractures. For the data, the geometric mean is shown as well as the 95% confidence interval in the mean. For the model, the mean value of total flow is taken over 10 realisations.*

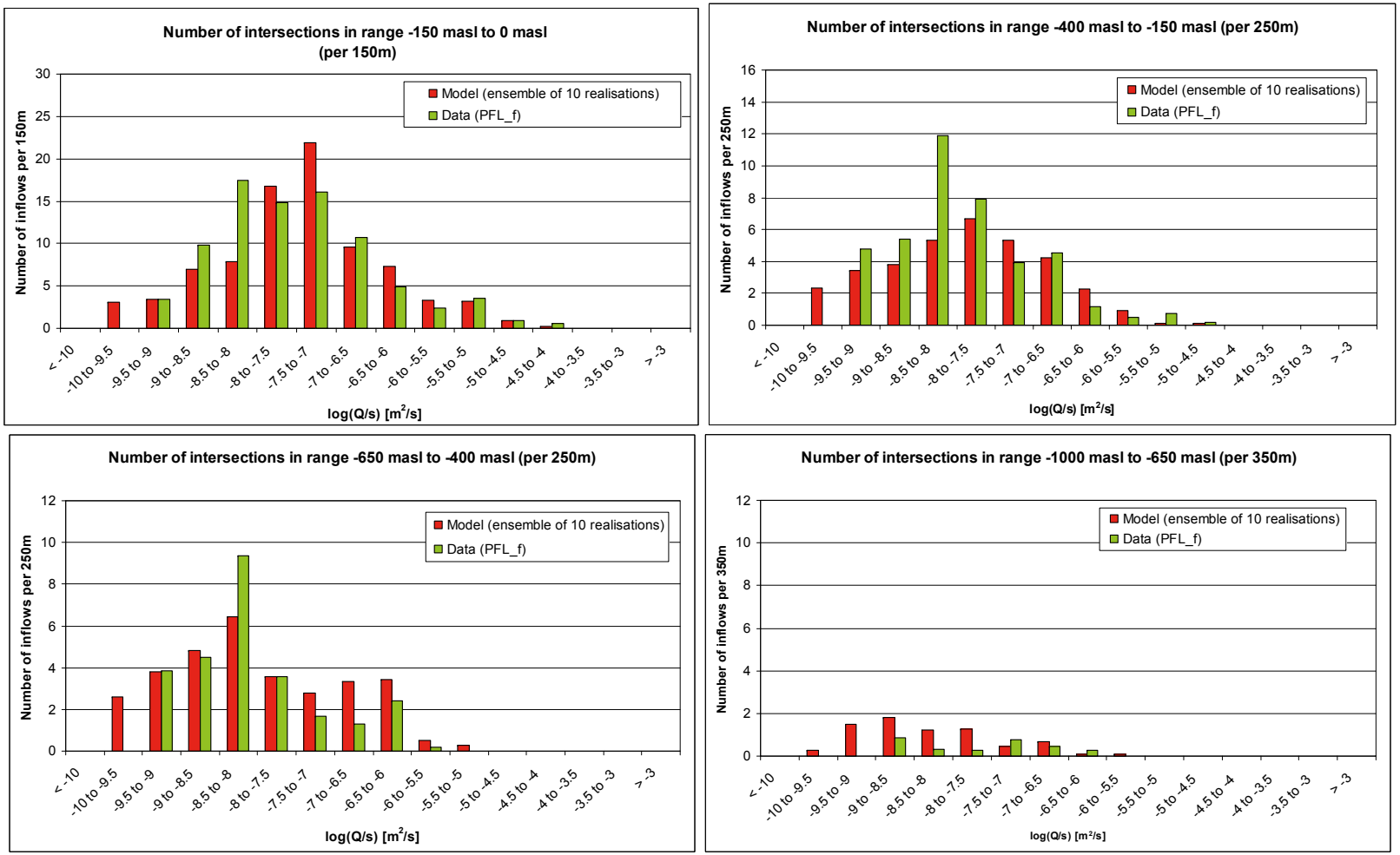

Figure A-6-16. *Histograms comparing the distribution of the magnitude of inflows divided by drawdown, Q/s, at abstraction boreholes in HRD_C. The model has a semi-correlated transmissivity, k_r fixed and open fracture intensity based on OPO fractures. The PFL-f measurements are treated as ensemble over all boreholes sections within HRD_C. The simulations represent the combined results of 10 realisations of the Hydro-DFN model. The numbers of intersections are Terzaghi weighted and normalised to the length of borehole which is provided in the heading of each graph.*

HRD_C, semi-correlated transmissivity, r_0 fixed, P_{32} based on OPO fractures.

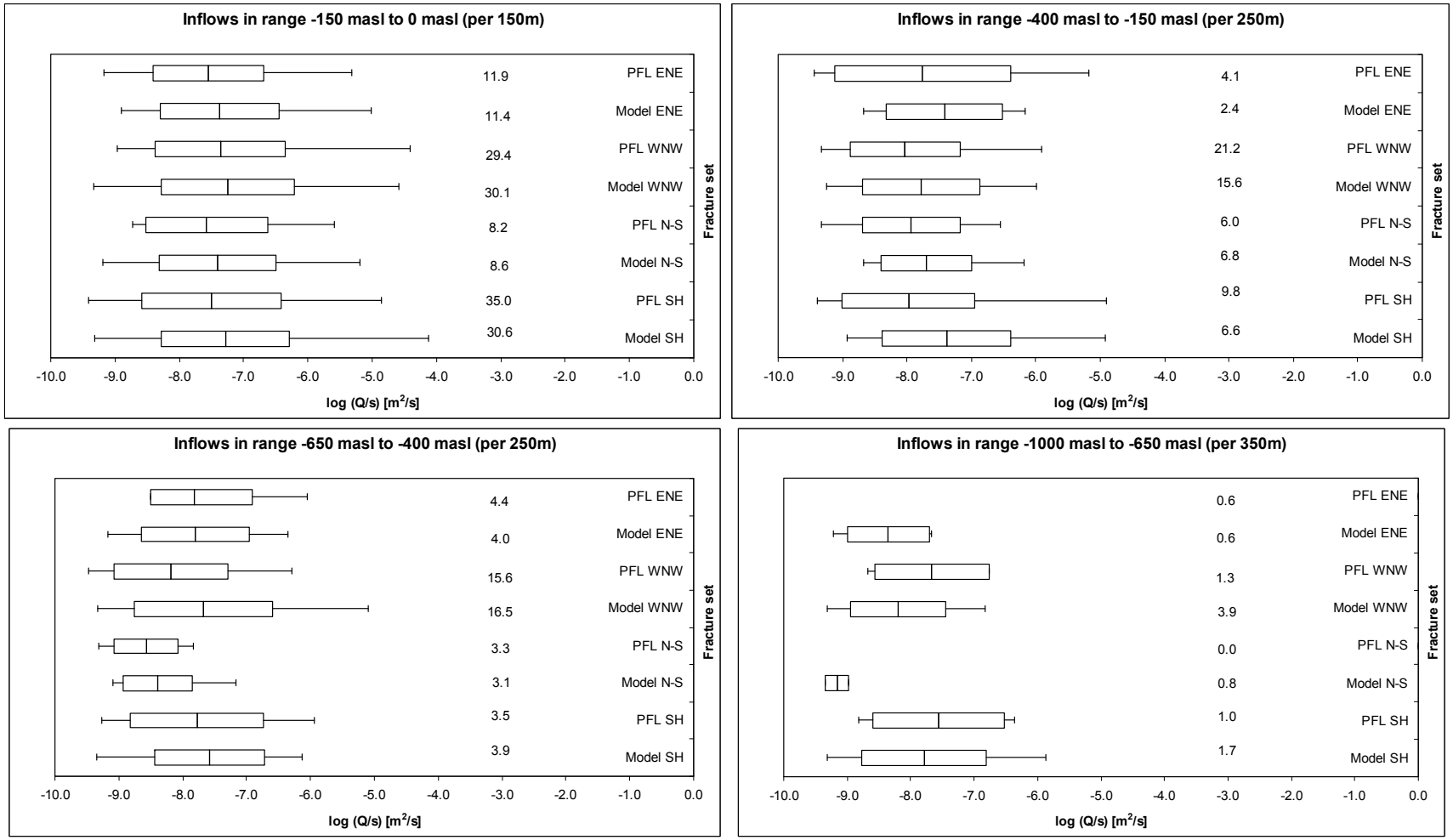

Figure A-6-17. *Bar and whisker plots comparing statistics taken over each fracture set for the individual inflows, Q/s, for the PFL-f data from borehole sections within HRD_C against statistics for an ensemble over 10 realisations of the Hydro-DFN model. The model has a semi-correlated transmissivity, with k_r fixed and open fracture intensity based on OPO fractures. The centre of the bar indicates the mean value, the ends of the bar indicate ±1 standard deviation, and the error bars indicate the minimum and maximum values. For the data statistics are taken over the identified flow-anomalies within each set. For the model, statistics are taken over the fractures generated within each set and over 10 realisations. The numbers of fractures are Terzaghi weighted and normalised to the length specified in the respective graph heading.*

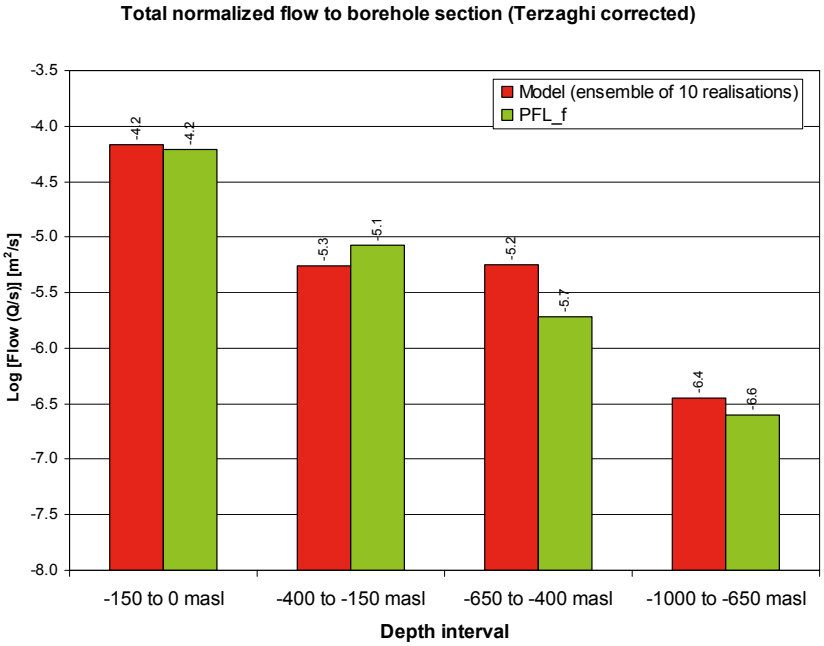

Figure A-6-18. *Comparison of the Terzaghi weighted sum of individual flows, Q/s, for the PFL-f data from borehole sections within HRD_C against the Hydro-DFN model. The model has a semi-correlated transmissivity, k_r fixed and open fracture intensity based on OPO fractures. For the model, the arithmetic mean is taken over 10 realisations. The flows are Terzaghi weighted and normalised to the borehole length indicated by the range on the horizontal axis.*

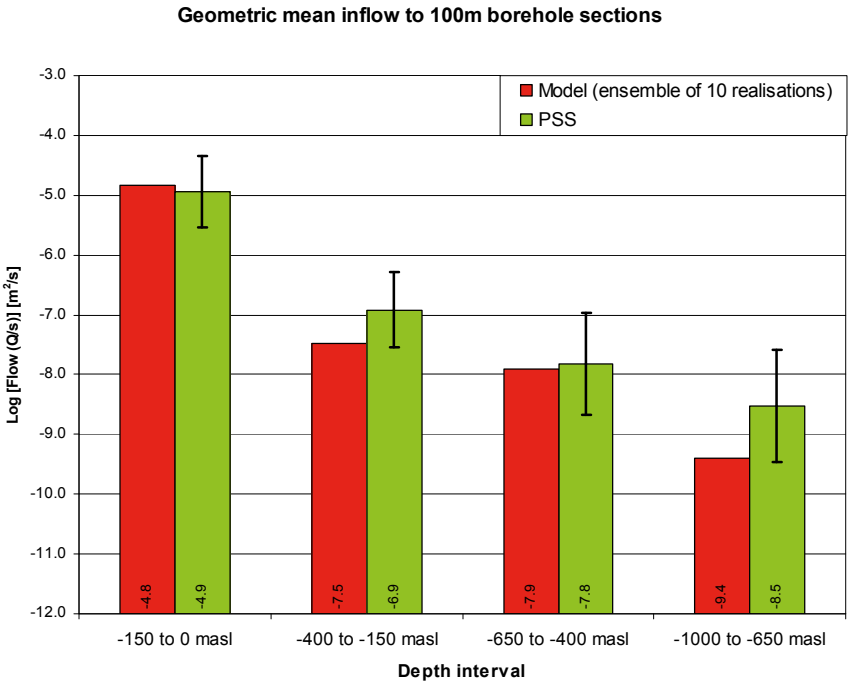

Figure A-6-19. *Comparison of the geometric mean of total flows, Q/s, to 100m borehole intervals for the PSS data from borehole sections within HRD_C against the Hydro-DFN model. The model has a semi-correlated transmissivity, k_r fixed and open fracture intensity based on OPO fractures. For the data, the geometric mean is shown as well as the 95% confidence interval in the mean. For the model, the mean value of total flow is taken over 10 realisations.*

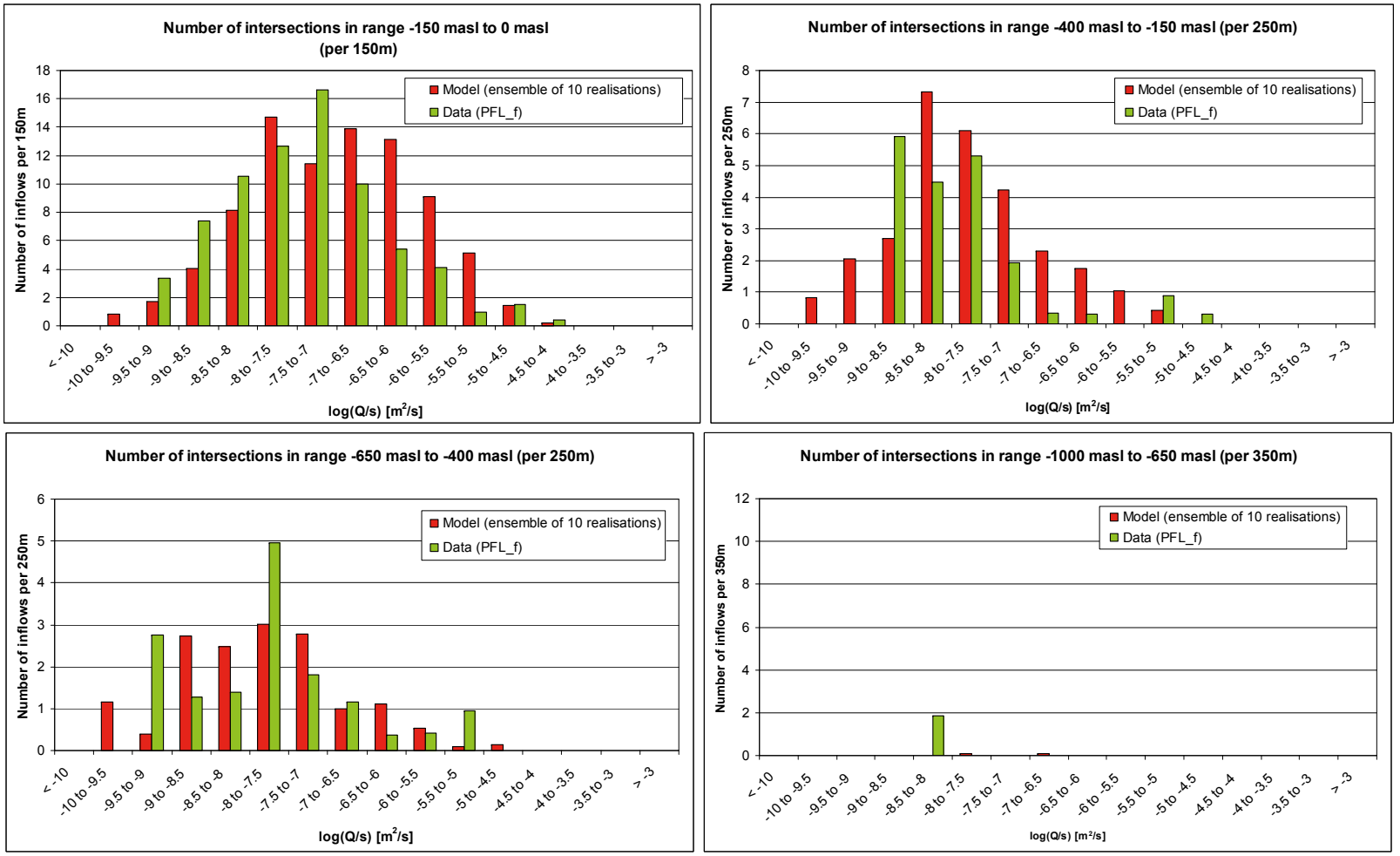

Figure A-6-20. *Histogram comparing the distribution of the magnitude of inflows divided by drawdown, Q/s, at abstraction boreholes in HRD_W. The model has a semi-correlated transmissivity, r_0 fixed and open fracture intensity based on OPO-CP fractures. The PFL-f measurements are treated as ensemble over all boreholes sections within HRD_W. The simulations represent the combined results of 10 realisations of the Hydro-DFN model. The numbers of intersections are Terzaghi weighted and normalised to the length of borehole which is provided in the heading of each graph.*

HRD_C, semi-correlated transmissivity, r_0 fixed, P_{32} based on OPO fractures.

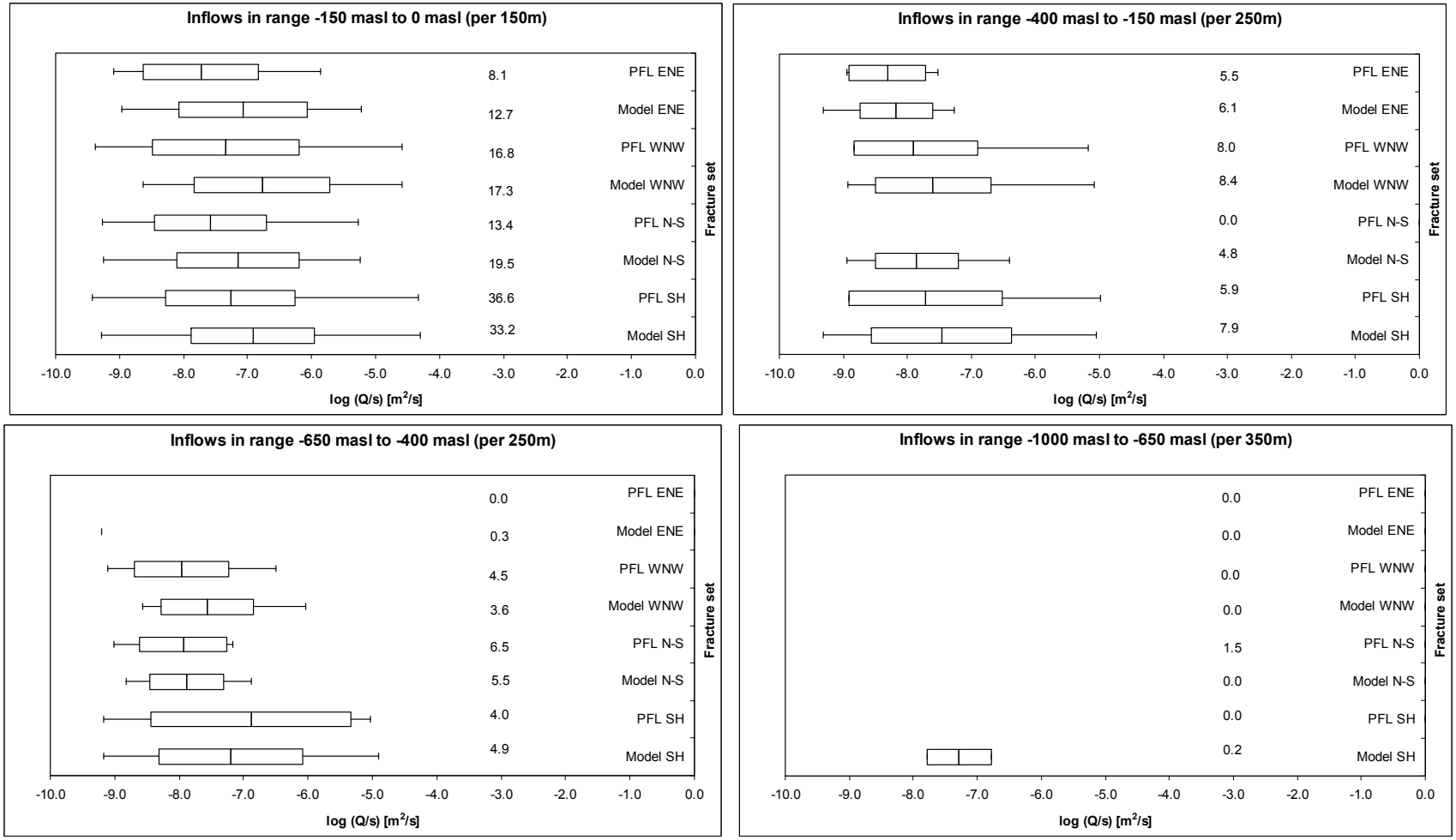

Figure A-6-21. *Bar and whisker plots comparing statistics taken over each fracture set for the individual inflows, Q/s, for the PFL-f data from borehole sections within HRD_W against statistics for an ensemble over 10 realisations of the Hydro-DFN model. The model has a semi-correlated transmissivity, with r_0 fixed and P_{32} based on OPO-CP fractures. The centre of the bar indicates the mean value, the ends of the bar indicate ±1 standard deviation, and the error bars indicate the minimum and maximum values. For the data statistics are taken over the identified flow-anomalies within each set. For the model, statistics are taken over the fractures generated within each set and over 10 realisations. The numbers of fractures are Terzaghi weighted and normalised to the length specified in the respective graph heading.*

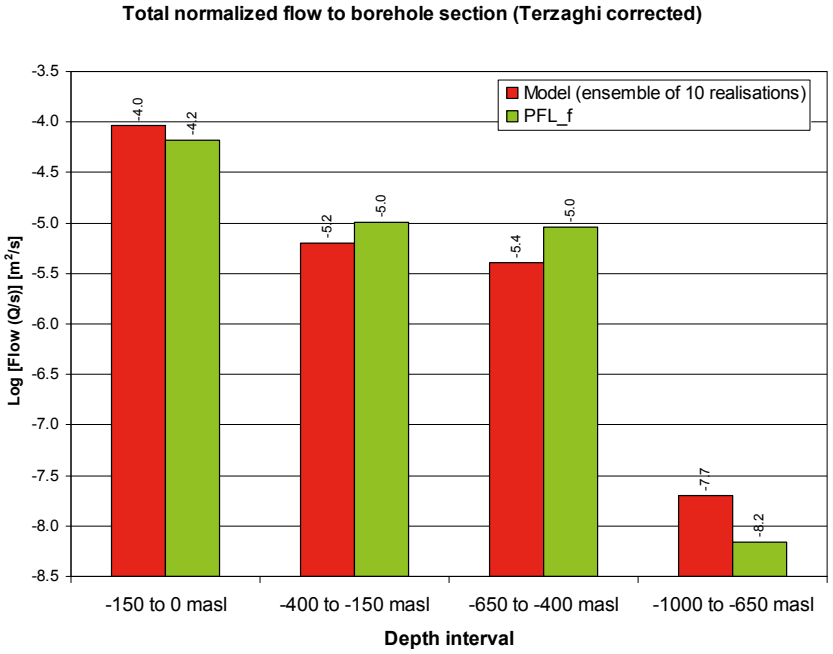

Figure A-6-22. *Comparison of the Terzaghi weighted sum of individual flows, Q/s, for the PFL-f data from borehole sections within HRD_W against the Hydro-DFN model. The model has a semi-correlated transmissivity, r_0 fixed and open fracture intensity based on OPO-CP fractures. For the model, the arithmetic mean is taken over 10 realisations. The flows are Terzaghi weighted and normalised to the borehole length indicated by the range on the horizontal axis.*

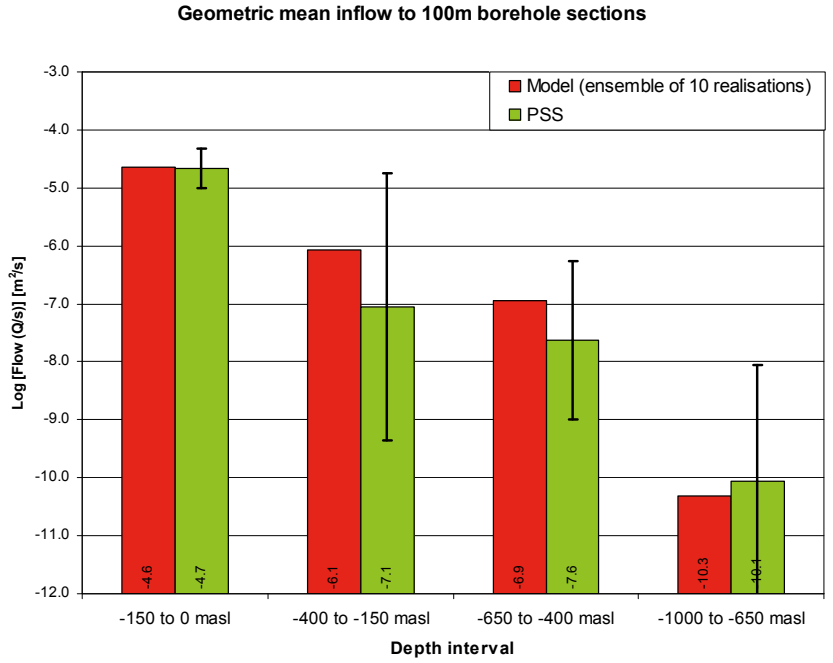

Figure A-6-23. *Comparison of the geometric mean of total flows, Q/s, to 100m borehole intervals for the PSS data from borehole sections within HRD_W against the Hydro-DFN model. The model has a semi-correlated transmissivity, r_0 fixed and open fracture intensity based on OPO-CP fractures. For the data, the geometric mean is shown as well as the 95% confidence interval in the mean. For the model, the mean value of total flow is taken over 10 realisations.*

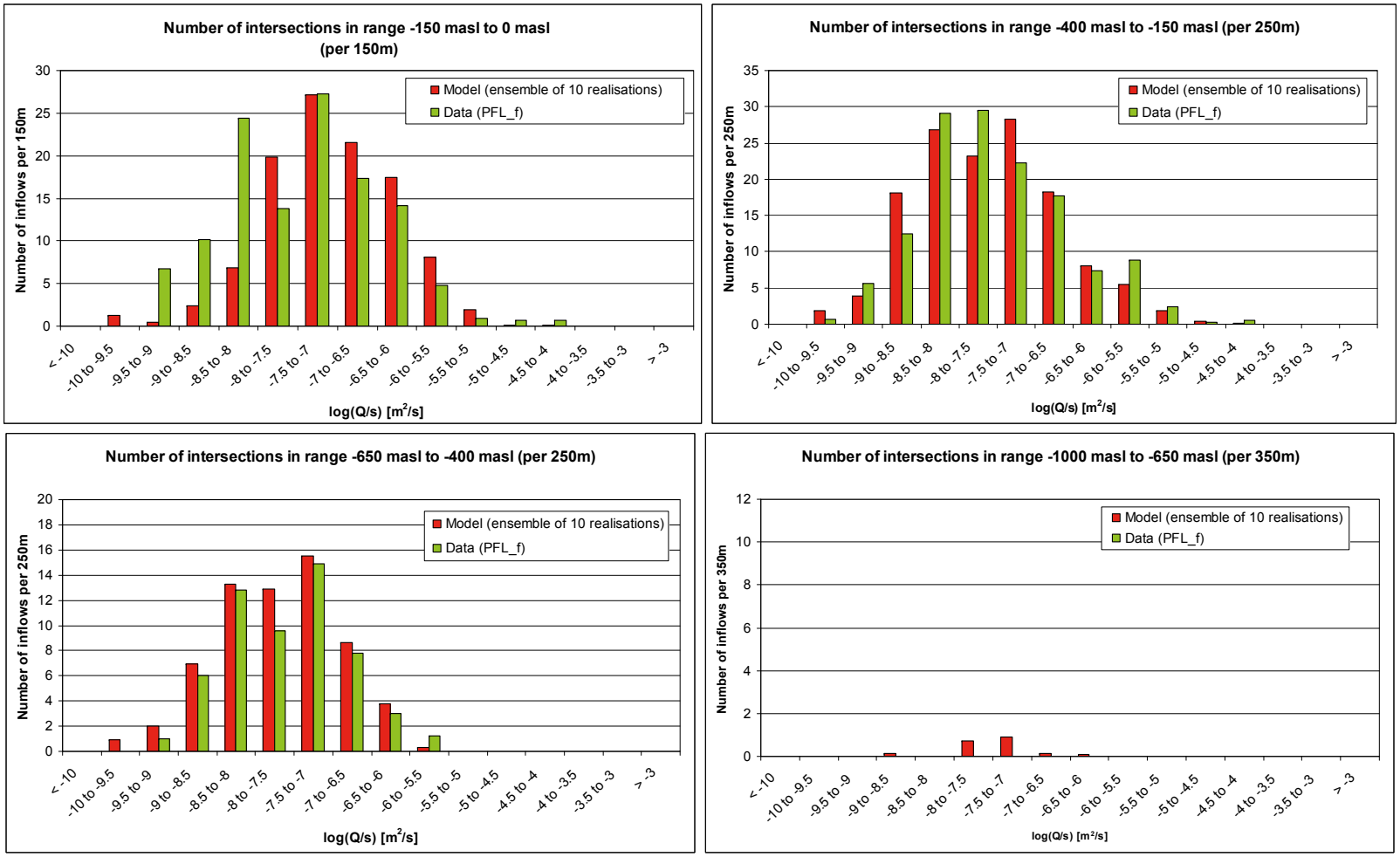

Figure A-6-24. *Histograms comparing the distribution of the magnitude of inflows divided by drawdown, Q/s, at abstraction boreholes in HRD_EW007. The model has a semi-correlated transmissivity, with r_0 fixed and open fracture intensity based on OPO fractures. The PFL-f measurements are treated as ensemble over all boreholes sections within HRD_EW007. The simulations represent the combined results of 10 realisations of the Hydro-DFN model. The numbers of intersections are Terzaghi weighted and normalised to the length of borehole which is provided in the heading of each graph.*

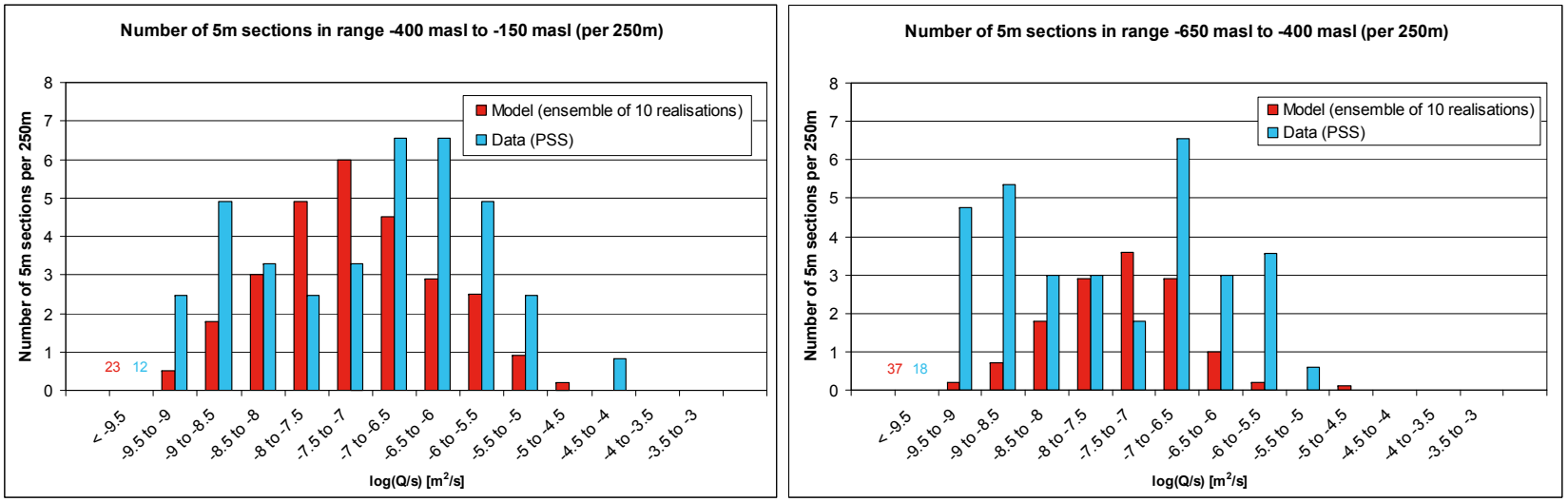

Figure A-6-25. *Histograms comparing the distribution of the magnitude of inflows divided by drawdown, Q/s, in 5m sections at abstraction boreholes in HRD_EW007. The model has a semi-correlated transmissivity, with r_0 fixed and and open fracture intensity based on OPO fractures. The PFL-f measurements are treated as ensemble over all boreholes sections within HRD_EW007. The simulations represent the combined results of 10 realisations of the Hydro-DFN model. The numbers of intersections are normalised to the length of borehole in the heading of each graph.*

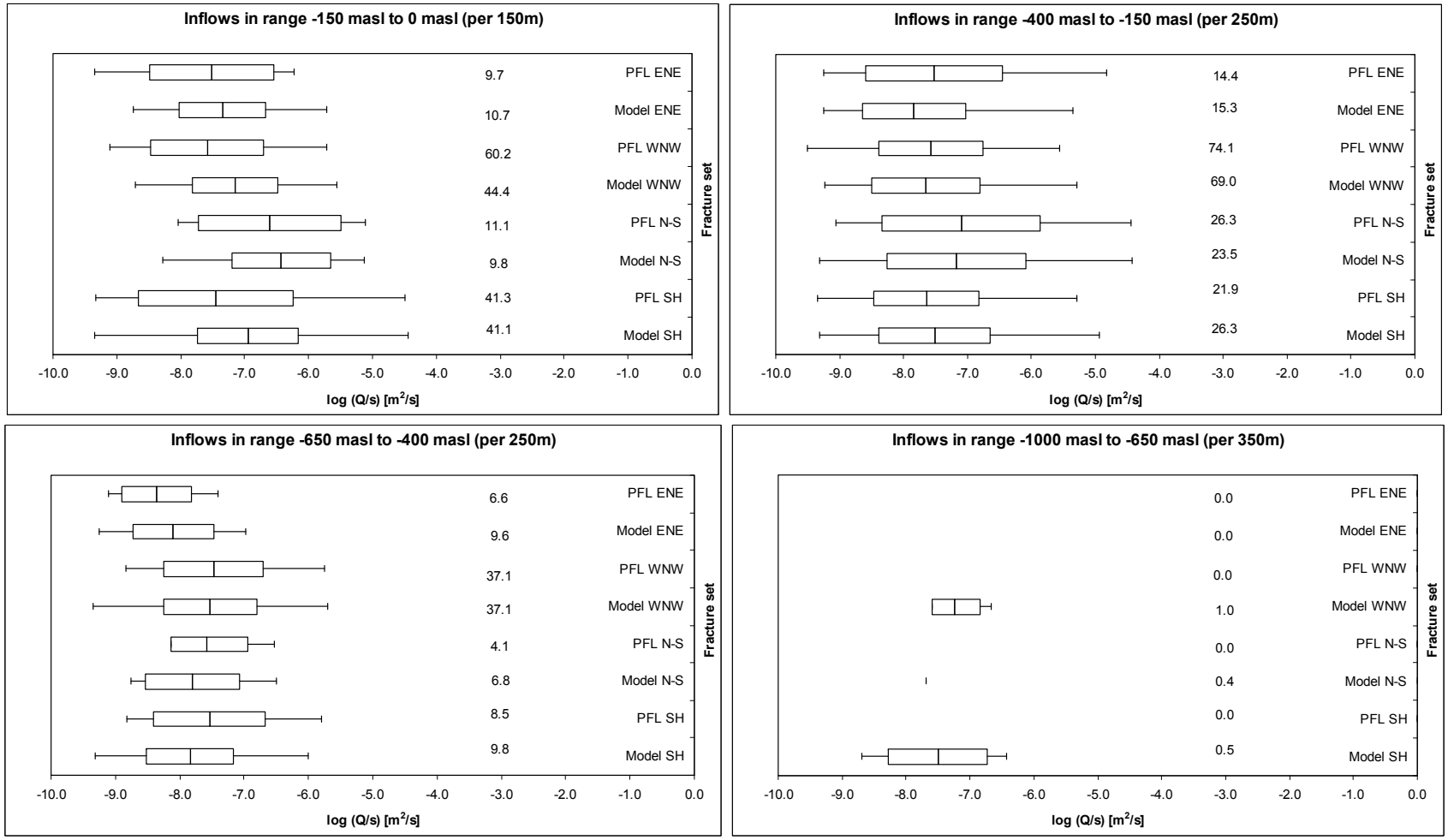

Figure A-6-26. *Bar and whisker plots comparing statistics taken over each fracture set for the individual inflows, Q/s, for the PFL-f data from borehole sections within HRD_EW007 against statistics for an ensemble over 10 realisations of the Hydro-DFN model. The model has a semi-correlated transmissivity, r_0 fixed and open fracture intensity based on OPO fractures. The centre of the bar indicates the mean value, the ends of the bar indicate ±1 standard deviation, and the error bars indicate the minimum and maximum values. For the data, statistics are taken over the identified flow-anomalies within each set. For the model, statistics are taken over the fractures generated within each set and over 10 realisations. The numbers of fractures are Terzaghi weighted and normalised to the length specified in the respective graph heading.*

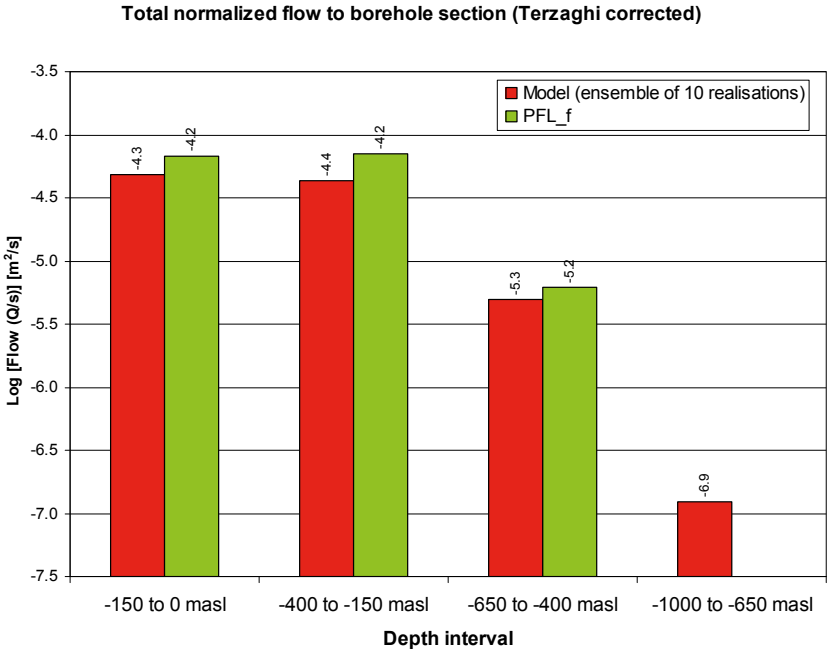

Figure A-6-27. *Comparison of the sum of individual flows, Q/s, for the PFL-f data from borehole sections within HRD_EW007 against the Hydro-DFN model. The model has a semi-correlated transmissivity, r_0 fixed and open fracture intensity based on OPO fractures. For the model, the arithmetic mean is taken over 10 realisations. The flows are Terzaghi weighted and normalised to the borehole length indicated by the range on the horizontal axis.*

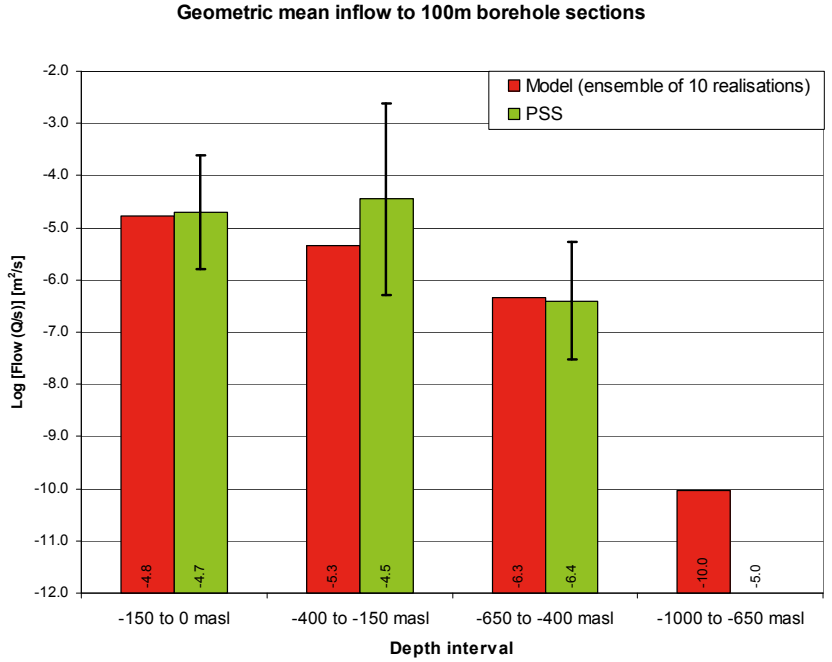

Figure A-6-28*. Comparison of the geometric mean of total flows, Q/s, to 100m borehole intervals for the PSS data from borehole sections within HRD_EW007 against the Hydro-DFN model. The model has a semi-correlated transmissivity, r_0 fixed and open fracture intensity based on OPO fractures. For the data, the geometric mean is shown as well as the 95% confidence interval in the mean. For the model, the mean value of total flow is taken over 10 realisations.*

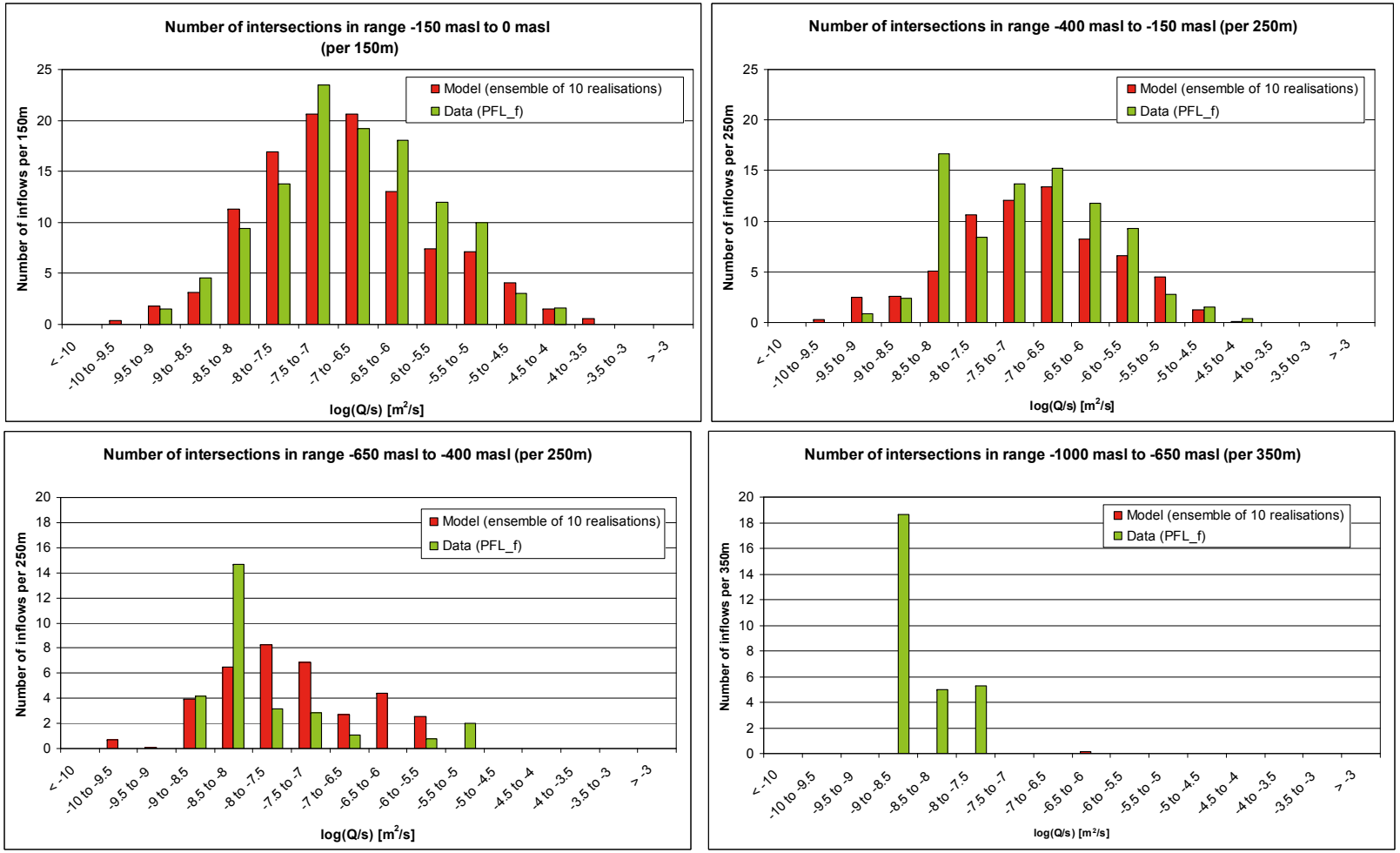

Figure A-6-29. *Histogram comparing the distribution of the magnitude of inflows divided by drawdown, Q/s, at abstraction boreholes in HRD_N. The model has a semi-correlated transmissivity, r_0 fixed and open fracture intensity based on OPO fractures. The PFL-f measurements are treated as ensemble over all boreholes sections within HRD_N. The simulations represent the combined results of 10 realisations of the Hydro-DFN model. The numbers of intersections are Terzaghi weighted and normalised to the length of borehole which is provided in the heading of each graph.*

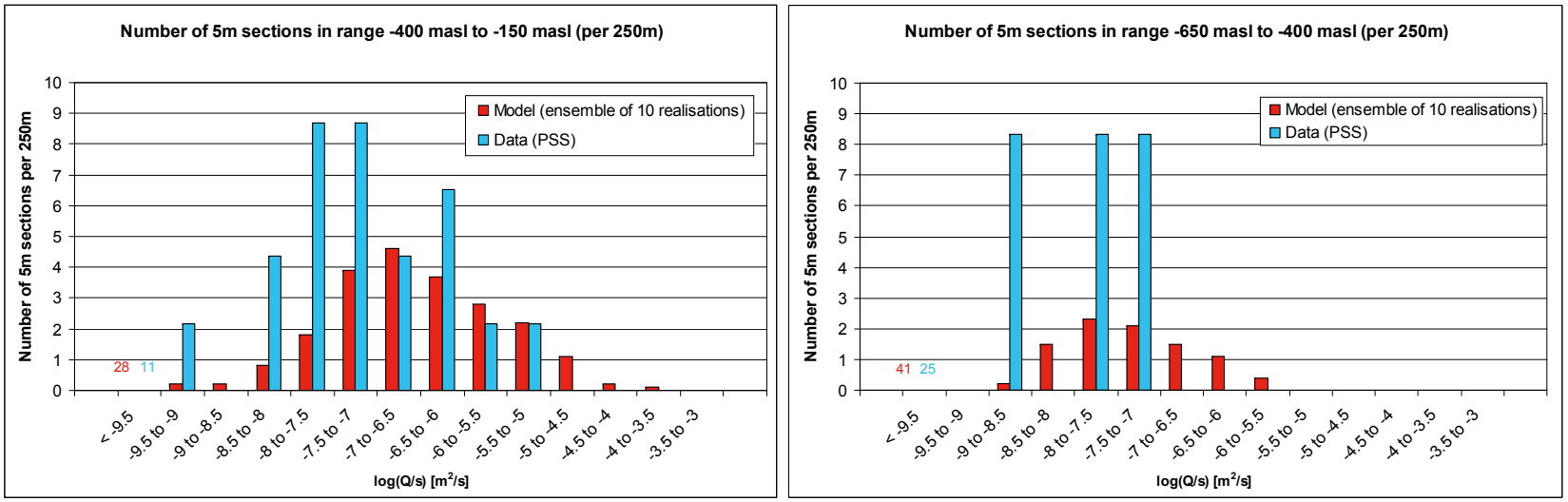

Figure A-6-30. *Histogram comparing the distribution of the magnitude of inflows divided by drawdown, Q/s, in 5m sections at abstraction boreholes in HRD_N. The model has a semi-correlated transmissivity, r_0 fixed and open fracture intensity based on OPO fractures. The PFL-f measurements are treated as ensemble over all boreholes sections within HRD_N. The simulations represent the combined results of 10 realisations of the Hydro-DFN model. The numbers of intersections are normalized to the length of borehole in the heading of each graph.*

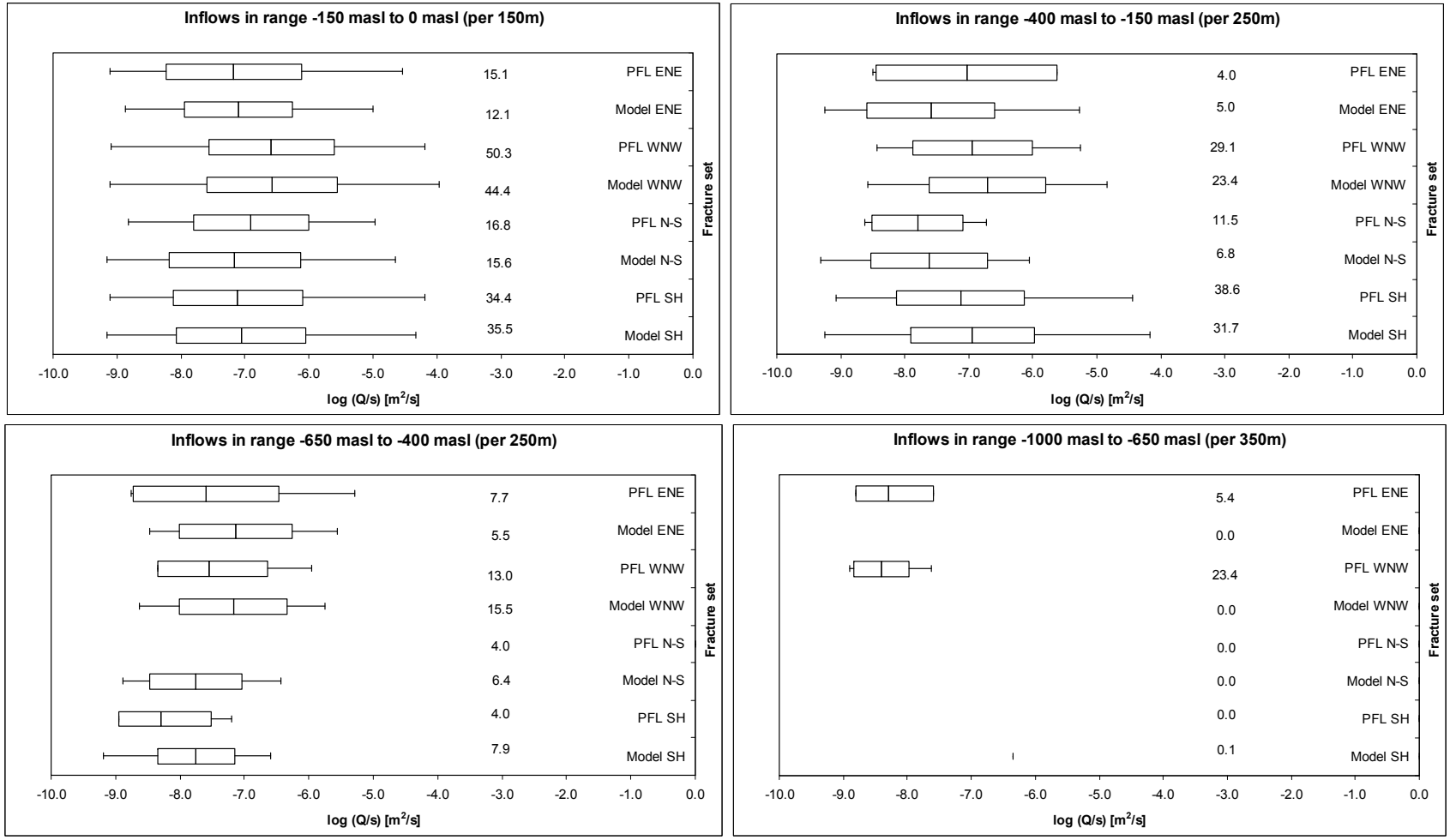

Figure A-6-31. *Bar and whisker plots comparing statistics taken over each fracture set for the individual inflows, Q/s, for the PFL-f data from borehole sections within HRD_N against statistics for an ensemble over 10 realisations of the Hydro-DFN model. The model has a semi-correlated transmissivity, with r_0 fixed and P_{32} on OPO fractures. The centre of the bar indicates the mean value, the ends of the bar indicate ±1 standard deviation, and the error bars indicate the minimum and maximum values. For the data statistics are taken over the identified flow-anomalies within each set. For the model, statistics are taken over the fractures generated within each set and over 10 realisations. The numbers of fractures are Terzaghi weighted and normalised to the length specified in the respective graph heading.*

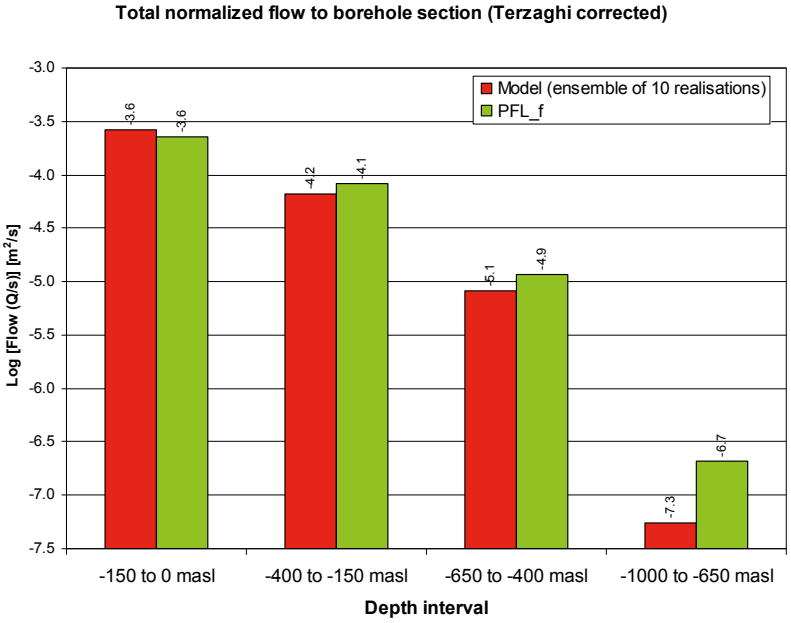

Figure A-6-32. *Comparison of the sum of individual flows, Q/s, for the PFL-f data from borehole sections within HRD_N against the Hydro-DFN model. The model has a semi-correlated transmissivity, r_0 fixed and open fracture intensity based on OPO fractures. For the model, the arithmetic mean is taken over 10 realisations. The flows are Terzaghi weighted and normalised to the borehole length indicated by the range on the horizontal axis.*

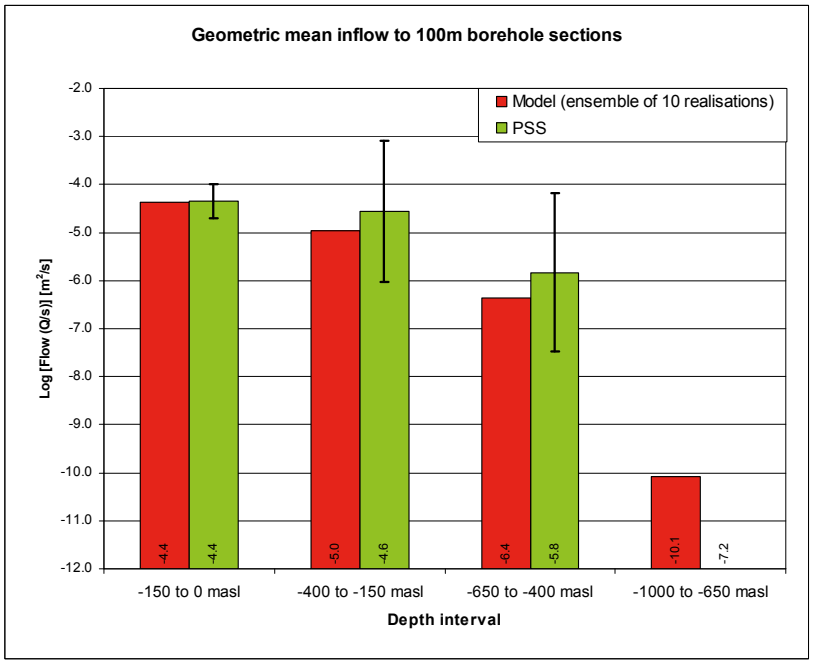

Figure A-6-33. *Comparison of the geometric mean of total flows, Q/s, to 100m borehole intervals for the PSS data from borehole sections within HRD_N against the Hydro-DFN model. The model has a semi-correlated transmissivity, r_0 fixed and open fracture intensity based on OPO fractures. For the data, the geometric mean is shown as well as the 95% confidence interval in the mean. For the model, the mean value of total flow is taken over 10 realisations.*

Table A-6-1. Summary of upscaled properties for HRD_C for elevations –400 masl to –650 masl for the case with open fracture intensity based OPO and the correlated transmissivity model for 5 m, 20 m and 100 m blocks.

Scale (m)	r_{min} (m)	Log10(K_{eff}) [m/s]						
		10-percentile	25-percentile	50-percentile	75-percentile	90-percentile	Mean	1 s.d.
5	0.11	N/A	N/A	N/A	-10.03	-8.36	-9.61	1.37
20	2.3	N/A	N/A	-9.22	-7.99	-7.37	-8.65	1.21
100	5.7	-9.96	-9.42	-8.92	-8.44	-8.14	-8.98	0.77

Scale (m)	r_{min} (m)	Mean (Log10(K_x)) [m/s]	Mean (Log10(Ky)) [m/s]	Mean (Log10(Kz)) [m/s]	% active
5	0.11	-11.82	-12.10	-11.97	34%
20	2.3	-8.37	-8.68	-8.52	70%
100	5.7	-8.88	-9.31	-8.94	97%

Scale (m)	r_{min} (m)	Median (Log10(K_x)) [m/s]	Median (Log10(Ky)) [m/s]	Median (Log10(Kz)) [m/s]	Median ratio K_{hmax}/K_{hmin}	Median ratio K_{hmax}/K_z	Strike of K_{hmax} (by eye)
5	0.11	-13.83	-14.12	-13.90	12.74	1.70	90 - 150
20	2.3	-9.05	-9.31	-9.07	4.65	1.22	90 - 150
100	5.7	-8.74	-9.17	-8.78	7.28	1.25	90 - 140

Scale (m)	r_{min} (m)	Log10(phi) [-]						
		10-percentile	25-percentile	50-percentile	75-percentile	90-percentile	Mean	1 s.d.
5	0.11	-3.38	-3.36	-3.34	-3.31	-3.29	-3.33	0.04
20	2.3	-4.07	-3.99	-3.84	-3.73	-3.62	-3.84	0.17
100	5.7	-4.15	-4.12	-4.08	-4.02	-3.98	-4.07	0.06

Table A-6-2. Summary of upscaled properties for HRD_C for elevations –400 masl to –650 masl for the case with open fracture intensity based OPO and the uncorrelated transmissivity model for 5 m, 20 m and 100 m blocks.

Scale (m)	r_{min} (m)	Log10(K_{eff}) [m/s]						
		10-percentile	25-percentile	50-percentile	75-percentile	90-percentile	Mean	1 s.d.
5	0.11	N/A	N/A	N/A	-9.08	-6.42	-8.80	1.99
20	2.3	N/A	N/A	-9.03	-7.57	-6.89	-8.45	1.41
100	5.7	-10.11	-9.49	-8.94	-8.49	-8.08	-9.03	0.86

Scale (m)	r_{min} (m)	Mean (Log10(K_x)) [m/s]	Mean (Log10(Ky)) [m/s]	Mean (Log10(Kz)) [m/s]	% active
5	0.11	-10.55	-10.86	-10.70	41%
20	2.3	-8.12	-8.45	-8.26	71%
100	5.7	-8.91	-9.37	-8.97	97%

Scale (m)	r_{min} (m)	Median (Log10(K_x)) [m/s]	Median (Log10(Ky)) [m/s]	Median (Log10(Kz)) [m/s]	Median ratio K_{hmax}/K_{hmin}	Median ratio K_{hmax}/K_z	Strike of K_{hmax} (by eye)
5	0.11	-13.04	-13.17	-12.86	12.65	1.73	N/A
20	2.3	-8.95	-9.28	-8.98	4.70	1.18	N/A
100	5.7	-8.80	-9.26	-8.85	7.74	1.33	90 - 150

Scale (m)	r_{min} (m)	Log10(phi) [-]						
		10-percentile	25-percentile	50-percentile	75-percentile	90-percentile	Mean	1 s.d.
5	0.11	-2.57	-2.55	-2.54	-2.51	-2.50	-2.53	0.03
20	2.3	-3.65	-3.60	-3.50	-3.41	-3.34	-3.50	0.12
100	5.7	-3.88	-3.86	-3.84	-3.81	-3.78	-3.83	0.04

Table A-6-3. Summary of upscaled properties for HRD_C for elevations –400 masl to –650 masl for the case with open fracture intensity based OPO-CP and the semi-correlated transmissivity model for 5 m, 20 m and 100 m blocks.

Scale (m)	r_{min} (m)	Log10(K_{eff}) [m/s]						
		10-percentile	25-percentile	50-percentile	75-percentile	90-percentile	Mean	1 s.d.
5	0.11	N/A	N/A	N/A	-10.86	-9.68	-10.53	1.04
20	2.3	N/A	-10.82	-9.66	-9.07	-8.59	-9.52	0.96
100	5.7	-9.70	-9.43	-9.15	-8.73	-8.30	-9.08	0.54

Scale (m)	r_{min} (m)	Mean (Log10(K_x)) [m/s]	Mean (Log10(Ky)) [m/s]	Mean (Log10(Kz)) [m/s]	% active
5	0.11	-14.68	-14.87	-14.58	27%
20	2.3	-9.07	-9.44	-9.23	78%
100	5.7	-8.96	-9.17	-9.10	100%

Scale (m)	r_{min} (m)	Median (Log10(K_x)) [m/s]	Median (Log10(Ky)) [m/s]	Median (Log10(Kz)) [m/s]	Median ratio K_{hmax}/K_{hmin}	Median ratio K_{hmax}/K_z	Strike of K_{hmax} (by eye)
5	0.11	-23.00	-23.00	-23.00	6.54	1.00	90 - 150
20	2.3	-9.52	-9.88	-9.61	6.04	1.28	90 - 150
100	5.7	-9.03	-9.27	-9.14	3.00	1.48	90 - 140

Scale (m)	r_{min} (m)	Log10(phi) [-]						
		10-percentile	25-percentile	50-percentile	75-percentile	90-percentile	Mean	1 s.d.
5	0.11	-3.82	-3.80	-3.78	-3.76	-3.74	-3.78	0.04
20	2.3	-4.22	-4.16	-4.11	-4.02	-3.90	-4.08	0.14
100	5.7	-4.24	-4.22	-4.18	-4.15	-4.08	-4.18	0.06

Table A-6-4. Summary of upscaled properties for HRD_W for elevations –400 masl to –650 masl for the case with open fracture intensity based OPO and the correlated transmissivity model for 5 m, 20 m and 100 m blocks.

Scale (m)	r_{min} (m)	Log10(K_{eff}) [m/s]						
		10-percentile	25-percentile	50-percentile	75-percentile	90-percentile	Mean	1 s.d.
5	0.11	N/A	N/A	N/A	-8.93	-8.00	-9.16	1.49
20	2.3	N/A	N/A	-9.45	-8.15	-7.18	-8.52	1.27
100	5.7	-10.28	-9.43	-8.76	-8.12	-7.39	-8.76	1.06

Scale (m)	r_{min} (m)	Mean (Log10(K_x)) [m/s]	Mean (Log10(Ky)) [m/s]	Mean (Log10(Kz)) [m/s]	% active
5	0.11	-16.19	-16.16	-16.19	41%
20	2.3	-8.00	-8.16	-8.42	61%
100	5.7	-8.76	-8.70	-8.92	95%

Scale (m)	r_{min} (m)	Median (Log10(K_x)) [m/s]	Median (Log10(Ky)) [m/s]	Median (Log10(Kz)) [m/s]	Median ratio K_{hmax}/K_{hmin}	Median ratio K_{hmax}/K_z	Strike of K_{hmax} (by eye)
5	0.11	-18.24	-18.65	-18.34	5.84	1.27	N/A
20	2.3	-9.53	-9.58	-9.48	3.53	1.18	N/A
100	5.7	-8.71	-8.67	-8.76	6.24	2.07	N/A

Scale (m)	r_{min} (m)	Log10(phi) [-]						
		10-percentile	25-percentile	50-percentile	75-percentile	90-percentile	Mean	1 s.d.
5	0.11	-3.53	-3.49	-3.42	-3.35	-3.29	-3.42	0.09
20	2.3	-3.95	-3.88	-3.77	-3.62	-3.49	-3.74	0.17
100	5.7	-4.00	-3.96	-3.91	-3.84	-3.75	-3.89	0.10

Table A-6-5. Summary of upscaled properties for HRD_W for elevations –400 masl to –650 masl for the case with open fracture intensity based OPO and the uncorrelated transmissivity model for 5 m, 20 m and 100 m blocks.

Scale (m)	r_{min} (m)	Log10(K_{eff}) [m/s]						
		10-percentile	25-percentile	50-percentile	75-percentile	90-percentile	Mean	1 s.d.
5	0.11	N/A	N/A	N/A	-8.45	-7.49	-8.75	1.51
20	2.3	N/A	N/A	-9.78	-8.06	-7.36	-8.65	1.54
100	5.7	-10.28	-9.52	-8.94	-8.43	-7.65	-8.96	1.07

Scale (m)	r_{min} (m)	Mean (Log10(K_x)) [m/s]	Mean (Log10(Ky)) [m/s]	Mean (Log10(Kz)) [m/s]	% active
5	0.11	-15.92	-15.87	-15.90	43%
20	2.3	-8.03	-8.17	-8.45	61%
100	5.7	-8.94	-8.86	-9.08	95%

Scale (m)	r_{min} (m)	Median (Log10(K_x)) [m/s]	Median (Log10(Ky)) [m/s]	Median (Log10(Kz)) [m/s]	Median ratio K_{hmax}/K_{hmin}	Median ratio K_{hmax}/K_z	Strike of K_{hmax} (by eye)
5	0.11	-16.70	-16.77	-17.02	N/A	1.25	N/A
20	2.3	-9.70	-9.84	-9.76	3.62	1.17	N/A
100	5.7	-8.98	-8.86	-8.93	5.58	1.88	N/A

Scale (m)	r_{min} (m)	Log10(phi) [-]						
		10-percentile	25-percentile	50-percentile	75-percentile	90-percentile	Mean	1 s.d.
5	0.11	-2.49	-2.48	-2.46	-2.44	-2.43	-2.46	0.03
20	2.3	-3.41	-3.35	-3.27	-3.17	-3.02	-3.24	0.16
100	5.7	-3.64	-3.61	-3.57	-3.53	-3.49	-3.57	0.06

Table A-6-6. Summary of upscaled properties for HRD_W for elevations –400 masl to –650 masl for the case with open fracture intensity based OPO-CP and the semi-correlated transmissivity model for 5 m, 20 m and 100 m blocks.

Scale (m)	r_{min} (m)	Log10(K_{eff}) [m/s]						
		10-percentile	25-percentile	50-percentile	75-percentile	90-percentile	Mean	1 s.d.
5	0.11	N/A	N/A	N/A	N/A	-9.27	-9.46	1.05
20	2.3	N/A	-10.70	-9.00	-8.37	-7.87	-8.82	0.90
100	5.7	-9.11	-8.84	-8.52	-8.09	-7.53	-8.43	0.62

Scale (m)	r_{min} (m)	Mean (Log10(K_x)) [m/s]	Mean (Log10(Ky)) [m/s]	Mean (Log10(Kz)) [m/s]	% active
5	0.11	-20.29	-20.28	-20.22	18%
20	2.3	-8.28	-8.44	-8.42	76%
100	5.7	-8.39	-8.36	-8.51	100%

Scale (m)	r_{min} (m)	Median (Log10(K_x)) [m/s]	Median (Log10(Ky)) [m/s]	Median (Log10(Kz)) [m/s]	Median ratio K_{hmax}/K_{hmin}	Median ratio K_{hmax}/K_z	Strike of K_{hmax} (by eye)
5	0.11	N/A	N/A	N/A	1.00	1.00	N/A
20	2.3	-9.02	-8.95	-8.92	4.63	1.29	N/A
100	5.7	-8.53	-8.45	-8.55	2.86	1.69	N/A

Scale (m)	r_{min} (m)	Log10(phi) [-]						
		10-percentile	25-percentile	50-percentile	75-percentile	90-percentile	Mean	1 s.d.
5	0.11	-4.07	-4.02	-3.95	-3.87	-3.79	-3.94	0.10
20	2.3	-4.16	-4.08	-4.00	-3.91	-3.83	-4.00	0.12
100	5.7	-4.11	-4.07	-4.01	-3.94	-3.85	-3.99	0.10

Table A-6-7. Summary of upscaled properties for HRD_EW007 for elevations –400 masl to –650 masl for the case with open fracture intensity based OPO and the correlated transmissivity model for 5 m, 20 m and 100 m blocks.

Scale (m)	r_{min} (m)	Log10(K_{eff}) [m/s]						
		10-percentile	25-percentile	50-percentile	75-percentile	90-percentile	Mean	1 s.d.
5	0.11	N/A	-9.57	-8.47	-7.76	-7.31	-8.58	1.15
20	2.3	-9.05	-8.45	-8.00	-7.71	-7.50	-8.15	0.72
100	5.7	-8.43	-8.26	-8.08	-7.96	-7.85	-8.12	0.22

Scale (m)	r_{min} (m)	Mean (Log10(K_x)) [m/s]	Mean (Log10(Ky)) [m/s]	Mean (Log10(Kz)) [m/s]	% active
5	0.11	-7.92	-8.29	-7.92	87%
20	2.3	-7.73	-8.09	-7.70	99%
100	5.7	-7.99	-8.43	-7.93	100%

Scale (m)	r_{min} (m)	Median (Log10(K_x)) [m/s]	Median (Log10(Ky)) [m/s]	Median (Log10(Kz)) [m/s]	Median ratio K_{hmax}/K_{hmin}	Median ratio K_{hmax}/K_z	Strike of K_{hmax} (by eye)
5	0.11	-8.43	-8.73	-8.36	11.00	1.21	90 - 150
20	2.3	-7.92	-8.19	-7.84	8.01	1.16	90 - 150
100	5.7	-7.97	-8.40	-7.90	6.30	1.02	100 - 140

Scale (m)	r_{min} (m)	Log10(phi) [-]						
		10-percentile	25-percentile	50-percentile	75-percentile	90-percentile	Mean	1 s.d.
5	0.11	-2.85	-2.84	-2.83	-2.81	-2.80	-2.83	0.02
20	2.3	-3.54	-3.51	-3.48	-3.43	-3.39	-3.47	0.06
100	5.7	-3.74	-3.72	-3.70	-3.68	-3.66	-3.70	0.03

Table A-6-8. Summary of upscaled properties for HRD_EW007 for elevations -400 masl to -650 masl for the case with open fracture intensity based OPO and the uncorrelated transmissivity model for 5 m, 20 m and 100 m blocks.

Scale (m)	r_{min} (m)	Log10(K_{eff}) [m/s]						
		10-percentile	25-percentile	50-percentile	75-percentile	90-percentile	Mean	1 s.d.
5	0.11	N/A	-9.52	-8.44	-7.45	-7.00	-8.42	1.24
20	2.3	-9.17	-8.58	-8.17	-7.84	-7.59	-8.29	0.68
100	5.7	-8.65	-8.47	-8.28	-8.09	-7.91	-8.28	0.29

Scale (m)	r_{min} (m)	Mean (Log10(K_x)) [m/s]	Mean (Log10(Ky)) [m/s]	Mean (Log10(Kz)) [m/s]	% active
5	0.11	-7.72	-8.10	-7.72	88%
20	2.3	-7.83	-8.27	-7.81	99%
100	5.7	-8.16	-8.59	-8.10	100%

Scale (m)	r_{min} (m)	Median (Log10(K_x)) [m/s]	Median (Log10(Ky)) [m/s]	Median (Log10(Kz)) [m/s]	Median ratio K_{hmax}/K_{hmin}	Median ratio K_{hmax}/K_z	Strike of K_{hmax} (by eye)
5	0.11	-8.31	-8.64	-8.29	12.14	1.21	90 - 150
20	2.3	-8.06	-8.39	-8.00	8.60	1.15	90 - 150
100	5.7	-8.16	-8.59	-8.09	6.75	1.06	100 - 140

Scale (m)	r_{min} (m)	Log10(phi) [-]						
		10-percentile	25-percentile	50-percentile	75-percentile	90-percentile	Mean	1 s.d.
5	0.11	-2.58	-2.57	-2.56	-2.55	-2.54	-2.56	0.02
20	2.3	-3.49	-3.47	-3.43	-3.40	-3.36	-3.43	0.05
100	5.7	-3.72	-3.71	-3.69	-3.68	-3.66	-3.69	0.02

Table A-6-9. Summary of upscaled properties for HRD_EW007 for elevations -400 masl to -650 masl for the case with open fracture intensity based OPO-CP and the semi-correlated transmissivity model for 5 m, 20 m and 100 m blocks.

Scale	L_{min}	Log10(K_{eff}) [m/s]						
		10-percentile	25-percentile	50-percentile	75-percentile	90-percentile	Mean	1 s.d.
5	0.11	N/A	N/A	N/A	-10.86	-9.68	-10.53	1.04
20	2.3	-10.13	-8.96	-8.40	-7.96	-7.69	-8.53	0.85
100	5.7	-8.60	-8.40	-8.19	-8.00	-7.83	-8.21	0.30

Scale	L_{min}	Mean (Log10(K_x)) [m/s]	Mean (Log10(Ky)) [m/s]	Mean (Log10(Kz)) [m/s]	% active
5	0.11	-14.68	-14.87	-14.58	27%
20	2.3	-8.02	-8.29	-8.18	94%
100	5.7	-8.12	-8.45	-8.06	100%

Scale	L_{min}	Median (Log10(K_x)) [m/s]	Median (Log10(Ky)) [m/s]	Median (Log10(Kz)) [m/s]	Median ratio K_{hmax}/K_{hmin}	Median ratio K_{hmax}/K_z	Strike of K_{hmax} (by eye)
5	0.11	N/A	N/A	N/A	6.54	1.00	N/A
20	2.3	-8.32	-8.53	-8.33	4.47	1.40	90 - 150
100	5.7	-8.11	-8.43	-8.04	4.74	1.06	110 - 150

Scale	L_{min}	Log10(phi) [-]						
		10-percentile	25-percentile	50-percentile	75-percentile	90-percentile	Mean	1 s.d.
5	0.11	-3.82	-3.80	-3.78	-3.76	-3.74	-3.78	0.04
20	2.3	-3.80	-3.76	-3.69	-3.62	-3.56	-3.68	0.09
100	5.7	-3.88	-3.86	-3.83	-3.81	-3.78	-3.83	0.04

A.7 KLX11A-F PFL-f interference test - development of a local near-surface hydro-geological DFN

A hydrogeological DFN model for the near surface Ävrö Granite has been developed based on data from one vertical and five inclined boreholes around the KLX11 drill site area. This model integrates core descriptions, borehole image and outcrop data together with hydraulic data from single-hole and multi-hole PFL-f tests.

Fracture set classification and orientation models were provided by a local hydrogeological DFN model. Based on the power-law concept for fracture size distribution parameters have been determined for DFN models consistent with the intensity of fractures observed on the ASM100235 outcrop, the intensity of open and partly open fractures in the core-drilled boreholes, and the frequency of connected fractures that provide the flows seen in the PFL-f tests. At least some of these parameter sets are non-unique.

An analysis of the orientations of PFL-f features suggests the sub-horizontal fractures are responsible for the majority of higher flow-rates. The WNW set is the next most important set. This is reasonable since the sub-horizontal set is the most abundant and the WNW set correlates with the direction of maximum horizontal in-situ stress.

The fracture size distribution parameters were calibrated to obtain a statistical match to the frequency and distribution in magnitudes of flows seen in the PFL-f tests for each fracture set based on numerical DFN simulations of connectivity and flow (using the methodology described in Chapter 10). We found that the best match to the data came with a value of r_0 = 0.04m and values for k_r ranging from 2.5 for the NNE set to 2.2 for the SubH set.

The ultimate models were conditioned, based on several statistics that quantified the nature of flow in both the single-hole and multi-hole PFL-f tests, to give a recommended hydrogeological DFN parameterization. The modelling approach is a stochastic one, focussed on obtaining models that reproduce key statistical characteristics identified in the data, rather than trying to honour very detailed individual features seen within the KLX11 boreholes.

Different relationships between fracture transmissivity and size were considered including direct correlations, semi-correlated and uncorrelated models. Each of these models could describe the single-hole results (both the fracture flow rates and the average head drawdowns), but only the uncorrelated model could also give a good match to the interference test data. This could be interpreted as evidence for spatial heterogeneity in fracture transmissivity for the Sub-H set over length scales smaller that the borehole spacing, either between fractures or within a fracture. These results apply to the top 100m of rock; it is uncertain whether they would be applicable at depth due to the different stress on the rock at lower elevations.

A.7.1 Borehole layout and interpreted data

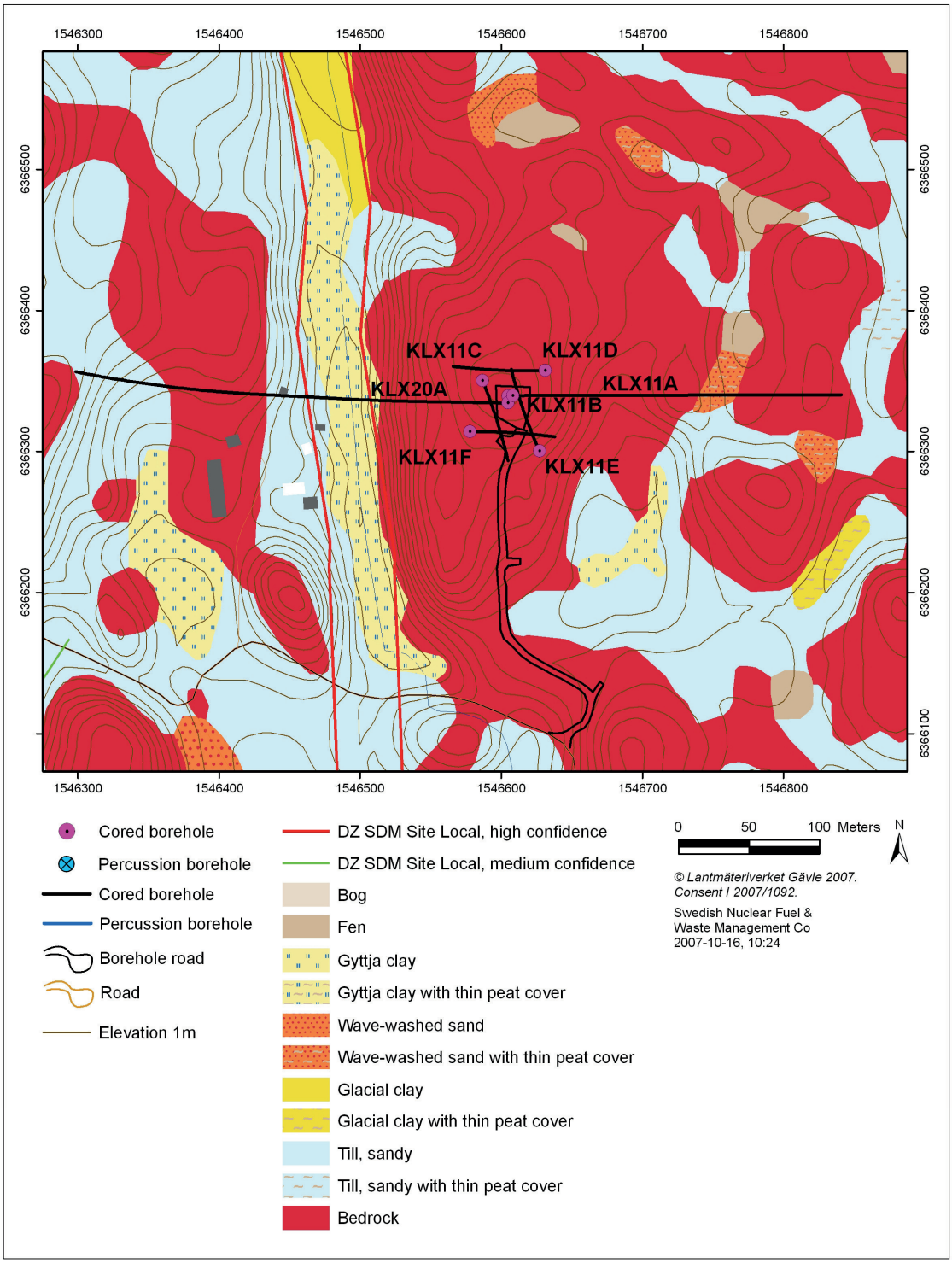

Figure A-7-1. *Layout of the KLX11 boreholes along with the Quaternary deposits map. The borehole KLX20A is not included in this study. The DZ shown with high confidence to the west of the KLX11 site is ZSMNS001C. It was not included in the modelling of the KLX11 tests.*

The boreholes lie in close proximity to one another, as shown in Figure A-7-1. Borehole KLX11B lies in the centre of the region and is vertical. Boreholes KLX11C to KLX11F are inclined and run in different directions (as indicated by the black lines in Figure A-7-1). Boreholes KLX11B to KLX11F are approximately 100 m to 150 m long with casing in the top 13 m to 16 m beneath the surface. Borehole KLX11A is inclined and approximately 900 m long with casing in about the first 100 m. Borehole KLX11A provides mainly geological data and was not involved in the hydraulic tests in the same way as the near-surface boreholes.

The following measured and interpreted data were provided for the KLX11 area:

- Borehole geometries.
- Boremap files, including interpretations of the Posiva Flow Log (PFL) features for boreholes KLX11A to KLX11F.
- Flow rates, freshwater heads and transmissivity values from single-hole tests for boreholes KLX11B to KLX11F.
- Flow rates and drawdowns in observation and pumping boreholes KLX11B to KLX11F.
- Initial and final hydraulic head in the monitored sections of KLX11. Only 3 of the boreholes (KLX11B, KLX11D and KLX11E) were used in the interference tests.
- Data from the ASM100235 outcrop, giving surface P_{21} fracture intensity values.

A.7.2 Fracture sets and orientation

As an initial guide for this choice of hard sectors, the Laxemar 1.2 Geo-DFN /Hermanson et al., 2005/ was used, this was based on an analysis of Laxemar 1.2 outcrop data. The analysis of KLX11A-F was made prior to the update of both the Geo-DFN and hydrogeological DFN for Laxemar 2.3. Therefore, an interim fracture set definition was defined as given in Table A-7-1, which based on a simplification of the hard sectors defined in the Laxemar 1.2 and adjusted for consistency with the fracture orientation data for KLX11A-F. Checks where then made that these sets were appropriate to outcrop data in the vicinity of KLX11A. The outcrop data has previously been analysed in terms of a Geo-DFN based on soft set definitions. In this section we will consider if the outcrop data can be described equally well by the hard sector hydrogeological DFN sets. Cf Section 10.10 for the comparison the hydrogeological DFN and geological DFN set specifications and visualisation.

Table A-7-1. Hard sector hydrogeological DFN definitions of fracture sets.

Identification	Strike description	Trend	Plunge	Dip	Strike
NNE	NNE-SSW	260-310	0-45	45-90	350-360 0-40
ENE	ENE-WSW	310-350	0-45	45-90	40-80
WNW	WNW-ENE	170-230	0-45	45-90	260-320
NNW	NNW-SSE	230-260	0-45	45-90	320-350
Sub-H	Sub-horizontal	0-360	45-90	0-45	0-360

Outcrop data

Unlike the boremap data, outcrop data can provide information on fracture length distributions as well as fracture intensity. In particular, in this report we have considered the ASM100235 outcrop and aimed to model the P_{21} fracture intensity for fractures with lengths of greater than 0.5m. The objective of doing the outcrop analysis is to obtain suitable size parameters for the rock domain around the KLX11 boreholes. The intention was to follow the methodology developed for the KLX09xx interference tests as much as possible.

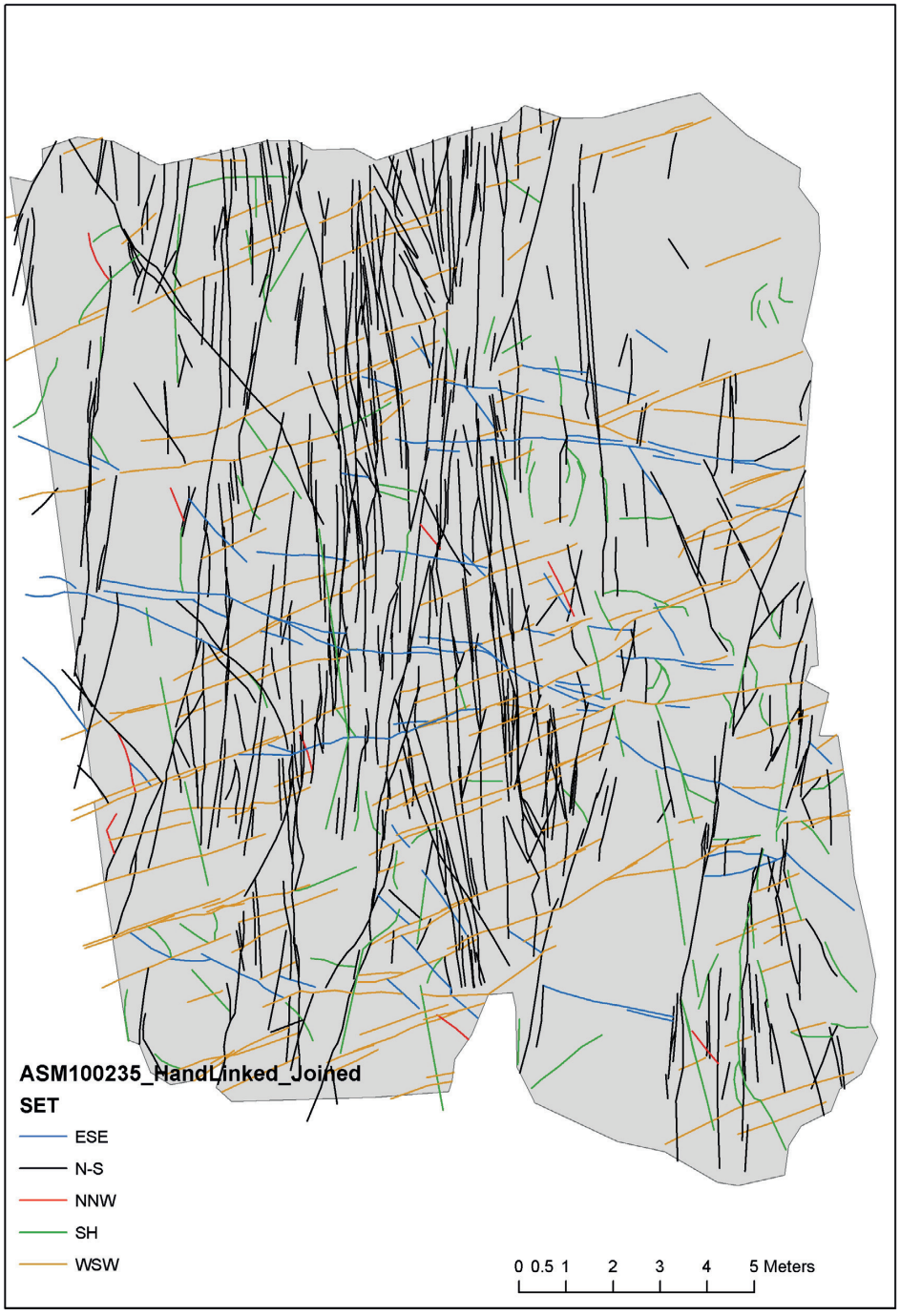

Figure A-7-2. *All fractures mapped on the outcrop ASM100235. The fracture sets are coloured according the Geo-DFN definition of KLX11A-F.*

The ASM100235 outcrop is located in the area were the KLX11 boreholes are drilled and has a surface area of 333 m^2. The location of the outcrop is illustrated in Figure A-7-1. Data on strike, dip, and trace lengths was also available. Based on the data, P_{21} values were calculated for each set as given in Table A-7-2.

The fracture sets were plotted using the tool ArcGIS. This may be seen in Figure A-7-2 as all fracture sets. The trimming of the fractures intersecting the outcrop boundary (grey area) were made in the same tool later on.

Table A-7-2. P_{21} values for outcrop ASM100235 in according to the Geo-DFN for KLX11A-F fracture sets /Hermanson et al., 2008/ (fractures intersecting the outcrop boundary were trimmed against it).

Geo-DFN set	P_{21}, (m/m^2)
ESE	0.20
N-S	1.19
WSW	0.41
NNW	0.03
SubH	0.29
Total	**2.11**

Validity of the fracture sets for the outcrop data

Stereonets for the fracture sets were produced for the fractures identified on the basis of the outcrop data. In Figure A-7-3, all fracture sets are plotted in a polar plot according to the Geo-DFN definitions. In the fracture analysis performed for rock domains RSMA01 and RSMM01 suitable sectors were found for the fractures. This division is here called the hydrogeological DFN fracture set definition. Using this established hydrogeological DFN fracture set definition, the fractures were grouped and P_{21} values are calculated for each set. This may be seen in Table A-7-3.

In Figure A-7-4, a stereonet is shown for all fractures together with the sector division according to the hydrogeological DFN definition. In Figure A-7-4, the fracture intensities are Terzaghi corrected.

Table A-7-3. Calculated P_{21} values for the fractures mapped on outcrop ASM100235 in the hydrogeological DFN sets (cf. Table A-7-2).

Set	P_{21} (m/m^2)
NNE	1.03
ENE	0.38
WNW	0.26
NNW	0.25
SubH	0.26
Total	**2.18**

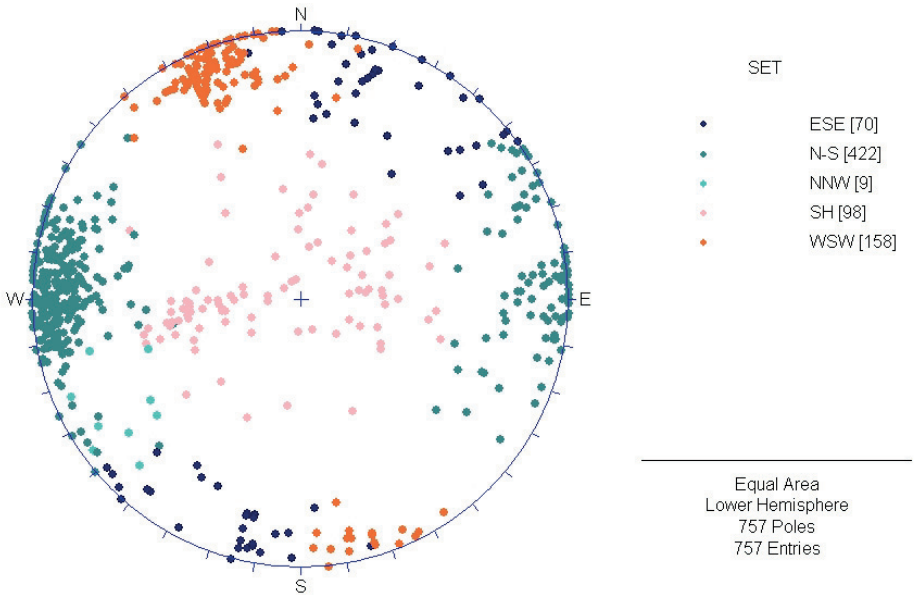

Figure A-7-3. *All fracture sets in the outcrop ASM100235 plotted in a polar plot according Geo-DFN definitions.*

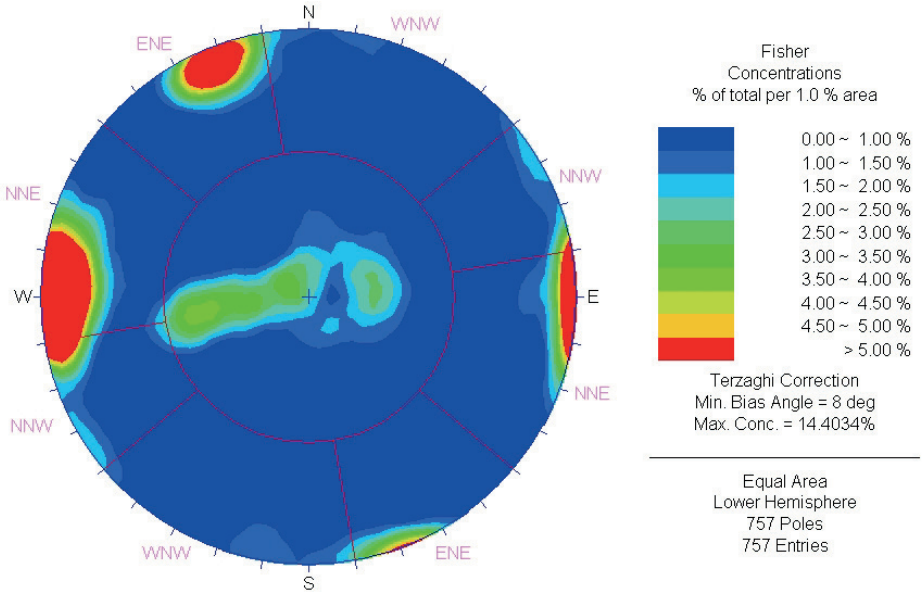

Figure A-7-4. *All fractures in the outcrop ASM100235 according the hard sector hydrogeological DFN definitions. Here the fracture intensities are Terzaghi corrected assuming the outcrop plane is horizontal.*

Validity of the fracture sets for fracture flow

Figure A-7-5 shows a stereonet plot for all fractures taken from KLX11A-F borehole core and image logs. Figure A-7-6 shows a stereonet for only the open and partly-open fractures, and Figure A-7-7 shows only the fractures associated with PFL features identified in the single-hole hydraulic tests. The stereonets seem to indicate that the set definitions provide a useful framework for describing all fractures, for open (and partly-open) fractures and for the PFL features. That is, in all three cases, fracture poles seem to cluster in broadly the same areas.

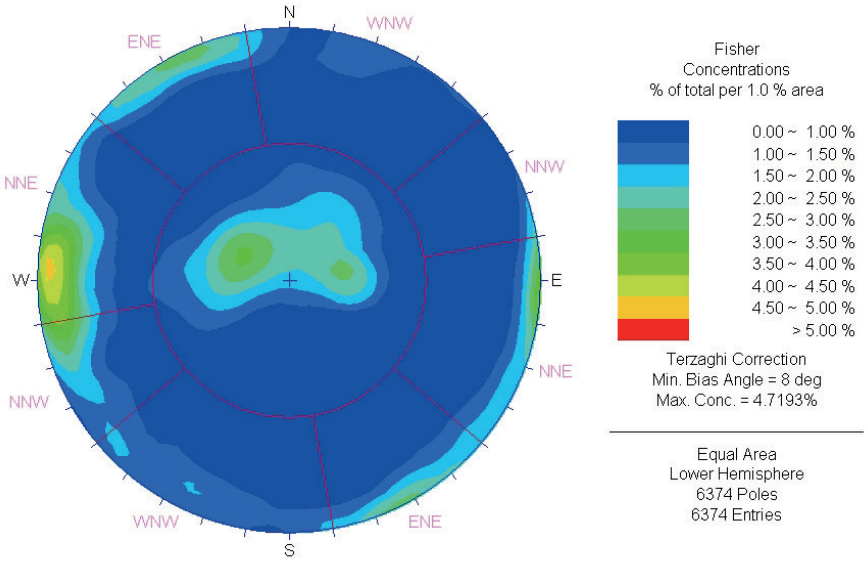

Figure A-7-5. *Stereonets for all fractures intersecting boreholes KLX11A-F.*

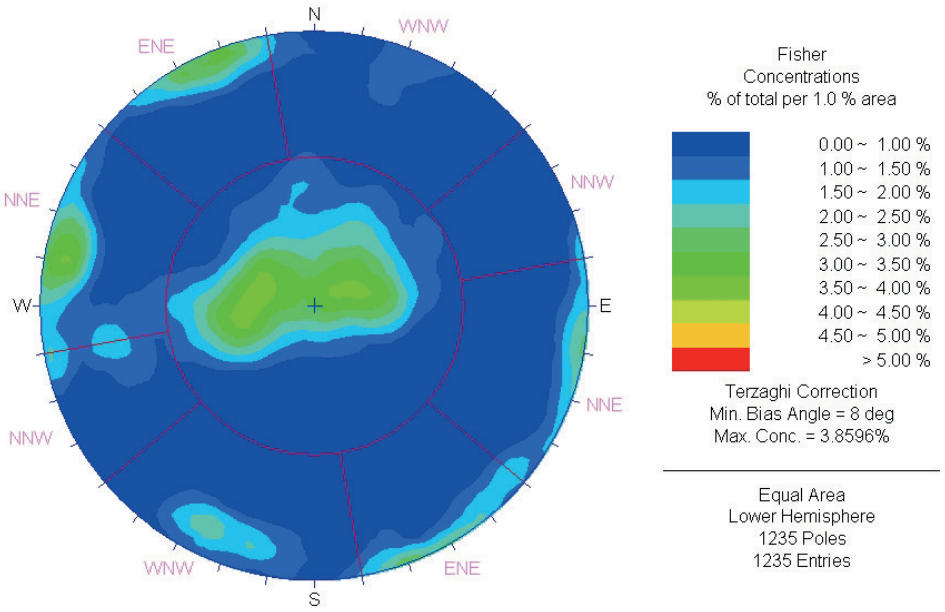

Figure A-7-6. *Stereonets for open and partly open fractures intersecting boreholes KLX11A-F.*

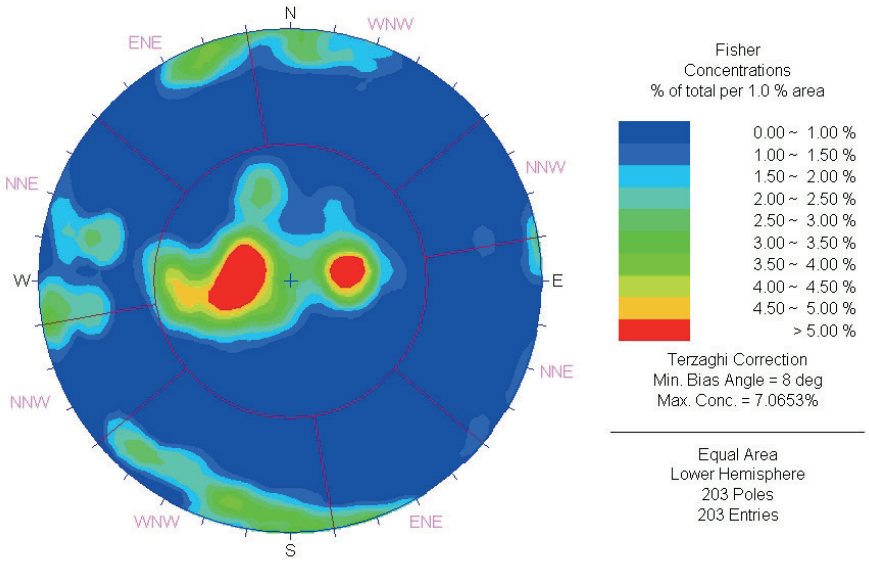

Figure A-7-7. *Stereonet for fractures associated with PFL features intersecting boreholes KLX11A-F.*

Anisotropy in flow

Figure A-7-8 shows the Log_{10}(transmissivity) values in m^2/s for the PFL features interpreted from the single-hole flow tests plotted on a stereonet pole plot. The higher transmissivities, shown by hot colours, tend to correlate with the sub-horizontal set (Sub-H).

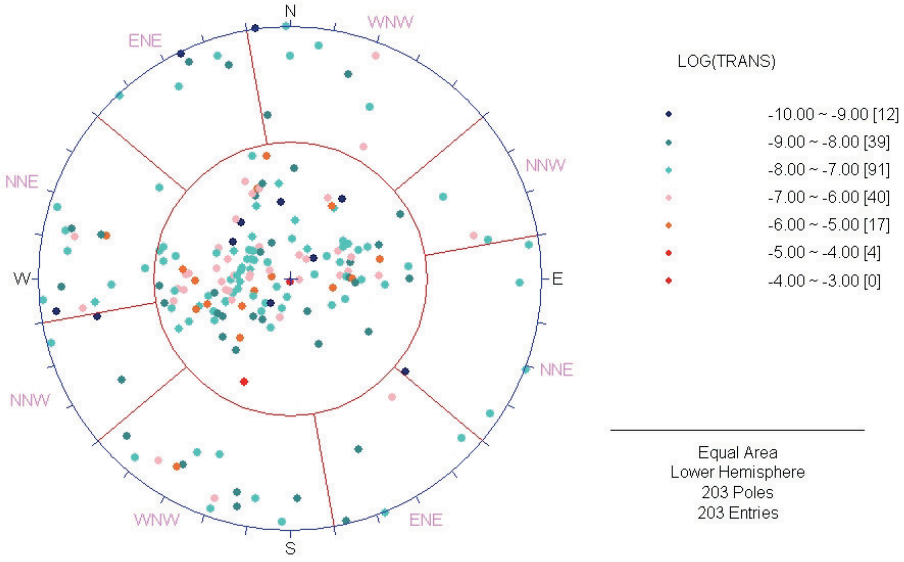

Figure A-7-8. *Symbolic pole plot stereonet showing log(transmissivity) for PFL features intersecting boreholes KLX11A-F. Fracture are coloured by the interpreted Log_{10}(transmissivity) associated with each PFL feature.*

A.7.3 Analysis of fractures in boreholes

The measured KLX11 borehole data was collated and P_{10} calculated by fracture set and by borehole, with a Terzaghi correction (to give $P_{10,corr}$) applied to compensate for the sampling bias of the borehole /Terzaghi, 1965/. These values are given in Table A-7-4, along with the values for boreholes KLX11A to KLX11F combined.

Table A-7-6 shows the percentage of open PFL features according to the certainty with which they were assigned as being open or partly-open. As can be seen the PFL features are almost equally distributed between open fractures that were characterised as certain, probable and possible in the core logging. Therefore, the (Terzaghi corrected) fracture intensities of open or partly open fractures (i.e. equivalent to the OPO case used in Chapter 10), without reference to fracture confidence, were used as the input to subsequent modelling.

Table A-7-4. Calculated $P_{10,corr}$ values for all fractures above -200 masl elevation for each borehole and fracture set with Terzaghi correction applied.

$P_{10,corr}$ [m^{-1}]	NNE	ENE	WNW	NNW	Sub-H
KLX11A	0.96	1.55	3.04	0.79	2.55
KLX11B	0.83	1.28	1.80	1.76	1.93
KLX11C	2.24	3.58	1.75	1.44	1.06
KLX11D	1.03	2.53	1.07	0.79	1.36
KLX11E	1.65	1.52	2.20	1.02	1.63
KLX11F	1.14	3.50	0.64	0.89	0.95
All	1.31	2.32	1.80	1.08	1.61

Table A-7-5. Calculated $P_{10,corr}$ values for fracture sets for all, open and PFL-f features.

$P_{10,corr}$ [m^{-1}]	NNE	ENE	WNW	NNW	Sub-H
All	1.31	2.32	1.80	1.08	1.61
Open + partly open	0.29	0.36	0.30	0.08	0.55
(% of all)	(22.1 %)	(15.5 %)	(16.7%)	(7.4 %)	(34.2 %)
PFL features	0.05	0.05	0.08	0.02	0.17
(% of all)	(3.8 %)	(2.2 %)	(4.4 %)	(1.9 %)	(10.6 %)

Table A-7-6. Percentages of open or partly open PFL-f features by certainty.

PFL features that are:	Open + certain	Open + probable	Open + possible
	26.3 %	35.2 %	38.6 %

A.7.4 Simulations of fracture geometry

As with the approach described in Section 10.4, the initial stage of the modelling was focussed on attempts to simulate the geometry and connectivity of fractures within the KLX11 area. For this part of the study, hydraulic flow was not considered. In order to determine parameter values for the model consistent with the data, three steps were performed in simulating the fracture geometrical parameters: a consistency check that the model is behaving as expected; calibration on outcrop data; and a calibration of $P_{10,corr}$ for connected open fracture generated by the model with $P_{10,corr}$ against the intensities of PFL-f features. The use of outcrop data is justified here since the study is focussed on the near-surface fracturing, and in principle offers sufficient constraints to identify unique fracture size parameters consistent with both outcrop and PFL-f data.

The model domain chosen was centred on borehole KXL11B and was sufficiently large to encompass all the boreholes. The top surface was mapped to the actual topography of the area. This gave a model domain with dimensions of approximately 200 m by 200 m by 200 m. Note that the bottom of KLX11A passes below the bottom of this region, but no measurements outside the model domain are considered for this borehole. In order to avoid reduced fracture intensities at the model boundaries, the fracture generation region extended beyond the model domain. The boreholes were modelled as straight lines. Figure A-7-9 shows the DFN model domain and position of boreholes KLX11A to KLX11F.

The fractures were generated stochastically using specified power-law size distributions. Five sets of fractures were generated based on the hydrogeological DFN (ENE, NNE, WNW, NNW and Sub-H). The orientation parameters for each set are given in Table A-7-7.

Due to the high number of fractures being generated the smallest fractures were only generated in a cylinder around each borehole in order to make the calculations feasible. Figure A-7-9 shows an example of the smaller fractures that were generated around each borehole, coloured by log of transmissivity. In this example, fractures smaller than 2.2m radius (or 4m length) were generated with centres inside cylinders of radius 2.83m centred on the axes of the boreholes. The centres of fractures larger than 2.2m radius were generated throughout the model domain.

Table A-7-7. Basic input data for the fracture geometry simulations. The Trend, Plunge, and Fisher concentration are based on the open fractures with elevation greater than -200 masl recorded from the KLX11 boreholes. The open fracture intensity P_{32} values are based on average $P_{10,corr}$ (average weighted by borehole length) values of the open fractures with elevation greater than -200 masl recorded from the KLX11 boreholes.

Set	Trend	Plunge	Fisher Concentration	Intensity (m^2/m^3) P_{32}
NNE	282.8	6.5	12.7	0.36
ENE	332.4	0.4	20.9	0.29
WNW	201.2	4.8	11.8	0.30
NNW	246.0	10.3	12.0	0.08
SubH	334.0	87.0	10.4	0.17

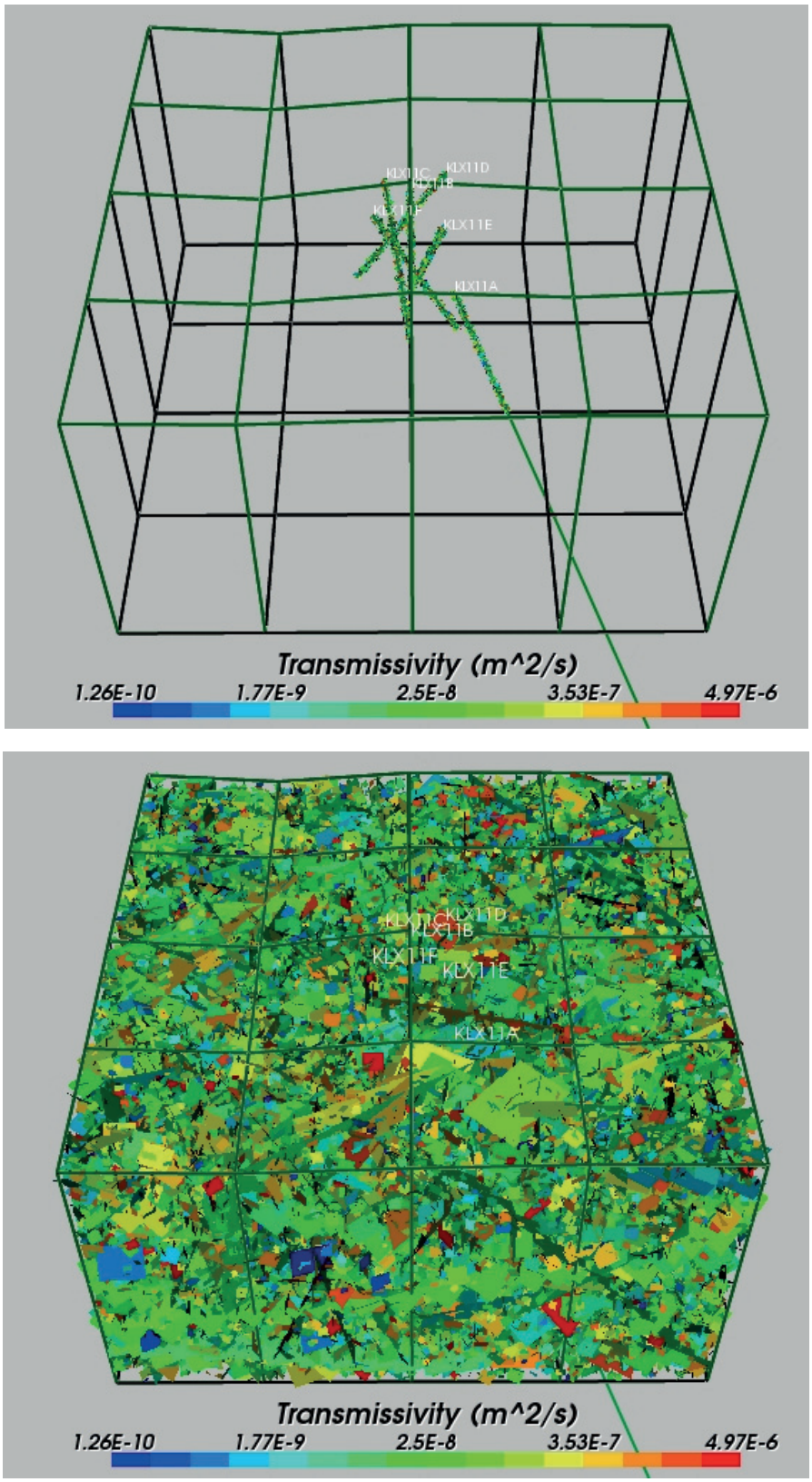

Figure A-7-9. *The model domain used to simulate KLX11A-F. Top: the boreholes and small fractures generated around them down to r=0.038m. Bottom: All fractures generated within the simulation domain. The fractures are coloured by* Log_{10} *transmissivity.*

Consistency check

The first step in the modelling was a consistency check, i.e. to check that the geometrical parameters (intensity in Table A-7-5 and orientation distributions in Table A-7-7) for each fracture set can be used in DFN simulations of open fractures that yield on average the measured fracture intensity, $P_{10,corr}$, for open fractures (cf. Section 10.4.3). The fracture size parameters used are described in Table A-7-8. Figure A-7-10 presents comparisons of the generated and measured fracture intensities (for the individual fracture sets and for all sets combined). As can be seen the fracture intensities for the generated realizations are in good agreement with the measured values. The intensities for the generated realizations are generally lower than the measured intensities but the difference is less than 10%.

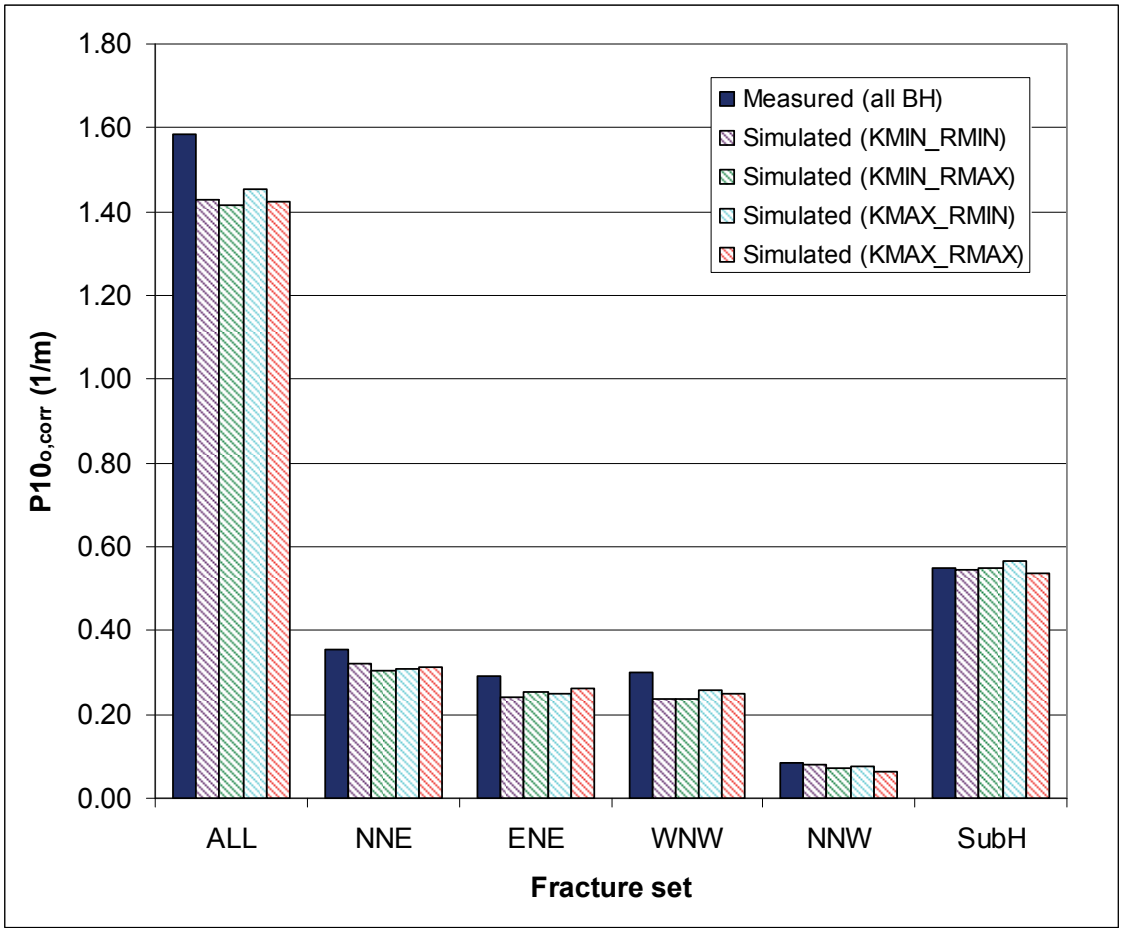

Figure A-7-10. *Comparison of the generated and measured fracture intensities (P10,corr) of open fractures in a borehole for the various fracture sets and for all sets for the different models. The statistics are averaged over all the KLX11A-F boreholes.*

Table A-7-8. Power-law size parameters for OPO fractures by orientation set for each of the initial fracture size model cases considered.

Case	Size parameters	NNE	ENE	WNW	NNW	Sub-H
KMIN_RMIN	r_0	0.04 m	0.04 m	0.04 m	0.04 m	0.04m
	k_r	2.60	2.60	2.60	2.60	2.60
KMIN_RMAX	r_0	0.28 m	0.28 m	0.28 m	0.28 m	0.28 m
	k_r	2.60	2.60	2.60	2.60	2.60
KMAX_RMIN	r_0	0.04 m	0.04 m	0.04 m	0.04 m	0.04m
	k_r	2.90	2.90	2.90	2.90	2.90
KMAX_RMAX	r_0	0.28 m	0.28 m	0.28 m	0.28 m	0.28 m
	k_r	2.90	2.90	2.90	2.90	2.90

Simulations of Outcrop data

The second step is to calibrate against outcrop data which provides additional information about the fracture size distribution of fractures. The aim of this step was to choose fracture size parameters that allow a fit to the P_{21} fracture intensity of fractures with length greater than 0.5m. We aimed to match the total fracture intensity, rather than the fracture intensities for each set.

The model produces fractures of lengths from r_0, 0.038m, up to 560m. As part of the data processing fractures smaller than 0.5m are discarded before the P_{21} value is calculated. The model also requires other input data: the orientation and Fisher concentrations of the fracture sets, and the P_{32} fracture intensity of all fractures. These parameters are described in Table A-7-9. The mapping of outcrops does not discern between open and sealed fractures, and hence to compare with the outcrop data, the model has to simulate all fractures, i.e. open plus sealed. The same orientation parameters are assumed as for the open fractures in Table A-7-7, but fracture intensity is higher. This seems reasonable based on the stereonets for the KLX11 borehole mapping data (Figure A-7-5 and Figure A-7-6). The orientation and Fisher concentration parameters are in any case less important than the P_{32} value and fracture size parameters.

Two suites of variants were considered: In one case r_0 was held constant and k_r varied, and in the other case k_r was held constant and r_0 varied. In each variant, fractures with size less than r=0.28m were neglected in the calculations of outcrop intensity, P21. The parameters used, and the results obtained, are described in Table A-7-10 and Table A-7-11. The basic input data for the simulations are listed in Table A-7-7, with the fracture set orientations and intensities for the Terzaghi corrected open and partly open fractures.

The parameterisation for the fracture size distribution is not unique, with combinations in the ranges (k_r, r_0) = (2.5-2.6, 0.04) and (k_r, r_0) = (2.9, 0.06-0.08) being consistent with the measured outcrop data with reasonable accuracy.

Table A-7-9. Basic input data for the outcrop simulations. The trend, plunge, and Fisher concentration are based on all fractures with elevation greater than -200 masl recorded from the KLX11 boreholes. The relative intensity P_{32} values are equal to the $P_{10,corr}$ values for all fractures with elevation greater than -200 masl recorded from the KLX11 boreholes.

Set	Trend	Plunge	Fisher Concentration	Fracture intensity P_{32} (m^2/m^3)
NNE	282.8	6.5	12.7	2.32
ENE	332.4	0.4	20.9	1.81
WNW	201.2	4.8	11.8	1.80
NNW	246.0	10.3	12.0	1.08
SubH	334.0	87.0	10.4	1.61

Table A-7-10. P_{21} values from data and simulations for outcrop. In this case r_0 is held constant and k_r is varied to find the best match.

r_0 = 0.04m								
Set	**P_{21} ASM100235**	**k_r**						
		2.9	2.8	2.7	2.6	2.5	2.4	2.3
NNE	1.03	0.38	0.45	0.54	0.67	0.77	0.85	0.89
ENE	0.38	0.24	0.24	0.29	0.37	0.45	0.44	0.51
WNW	0.26	0.30	0.34	0.42	0.48	0.53	0.61	0.68
NNW	0.25	0.19	0.21	0.23	0.25	0.34	0.41	0.41
Sub-H	0.26	0.10	0.12	0.14	0.16	0.22	0.20	0.21
Total	**2.18**	**1.21**	**1.36**	**1.62**	**1.92**	**2.31**	**2.51**	**2.70**

Table A-7-11. P_{21} values from data and simulations for outcrop. In this case k_r is held constant and r_0 is varied to find the best match.

k_r=2.9							
Set	**P_{21} ASM100235**	**r_0 (m)**					
		0.04	0.06	0.08	0.10	0.15	0.2
NNE	1.03	0.38	0.56	0.75	0.91	1.26	1.62
ENE	0.38	0.24	0.33	0.42	0.52	0.72	0.91
WNW	0.26	0.3	0.43	0.58	0.67	0.97	1.25
NNW	0.25	0.19	0.27	0.34	0.41	0.58	0.76
Sub-H	0.26	0.10	0.15	0.18	0.22	0.34	0.46
Total	**2.18**	**1.21**	**1.74**	**2.27**	**2.73**	**3.87**	**5.00**

Simulation of fracture connectivity

The final step in the fracture geometrical analysis was to perform connectivity analyses and determine the fracture intensities for connected open fractures. The crucial assumption in this section of work is that the simulated intensity of connected open fractures, $P_{10,cof,corr}$, simulates the intensity of PFL-f features, $P_{10,PFL,corr}$. To illustrate the role of fracture size distribution in the P_{10} intensity of connected, open fractures four cases were tried initially, with the fracture size parameters described in Table A-7-8. The basic input data is listed in Table A-7-7.

In Figure A-7-11 the fracture intensities for simulated connected open fractures for the individual fracture sets and all sets combined for the above models are compared with the measured fracture intensities for PFL-f features around KLX11 for the initial fracture size cases. (It assumed that all simulated connected open fractures have transmissivities above PFL-f measurement limit). None of these initial models are a particularly good match.

The next cases considered were based on the two fracture size parameterisations which produced the best match to the measured ASM100235 outcrop data. The fracture size parameters were identical for each fracture set. The results of these simulations are shown in Figure A-7-12 (assuming all simulated connected open fractures have transmissivities above PFL-f measurement limit). The case with r_0=0.04m and k_r=2.5 represents a reasonable match, whereas the case with r_0=0.08m and k_r=2.9 under-represents all the fracture intensities by around a factor of ten.

In order to understand this difference one needs to consider the assumptions made in the modelling with respect to the fracture size distributions. The fracture size parameters for the outcrop calibration were conditioned based on simulating the P_{21} intensity for *all* fractures, whereas for the calibration of intensity of connected open fractures against PFL-f features only the open fractures were simulated. The outcrop simulations assumed that only fractures larger than 0.5m contribute to P_{21}, while the open fracture connectivity calculations allow fractures as small as 0.038m to contribute. Using these two different types of calibration target potentially allows the size distribution to be better constrained, although it has to be accepted that outcrop data informs the size distribution for *all* fractures, and PFL-f informs the size distribution of open fractures, and these are not necessarily the same. One would be large fractures to be more likely to containing openings, and consequently the slope, k_r, for open fractures to be shallower than that for all fractures.

Since the connectivity analysis suggests cases with high k_r do not yield sufficiently connected networks then the case with r_0=0.04m and k_r=2.5 was used as the basis for refining the calibration on fracture connectivity in more detail. The approach used was to hold r_0 constant at 0.038m and vary k_r from a base value of 2.5 and adjust the k_r until the simulated Terzaghi corrected intensity of connected open fractures matched that measured for PFL-f features. The resulting match is shown in Figure A-7-13 and the corresponding parameters used are described in Table A-7-12. The values for k_r were reduced for 3 sets (WNW, NNW and SubH), and increased for ENE relative to the outcrop calibration. This might be expected as the fracture size distribution for open fractures compared to all fractures is typically biased slightly towards larger fractures, implying a shallower slope, k_r.

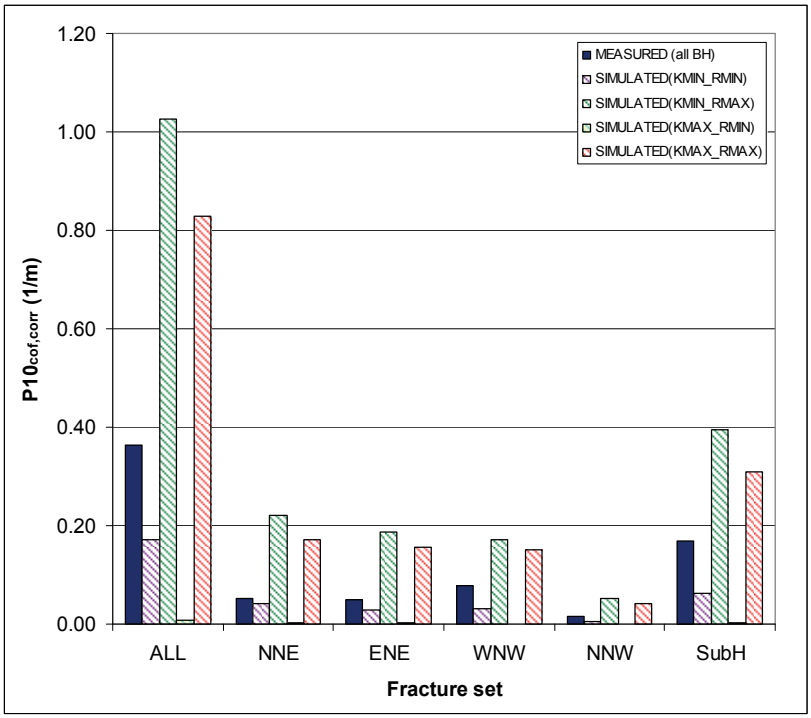

Figure A-7-11. *Comparison of the simulated Terzaghi corrected fracture intensities for connected open fractures for the 4 model cases described in Table A-7-8 against the measured fracture intensities for PFL-f features. The intensities are broken down by set as well as being given as a total.*

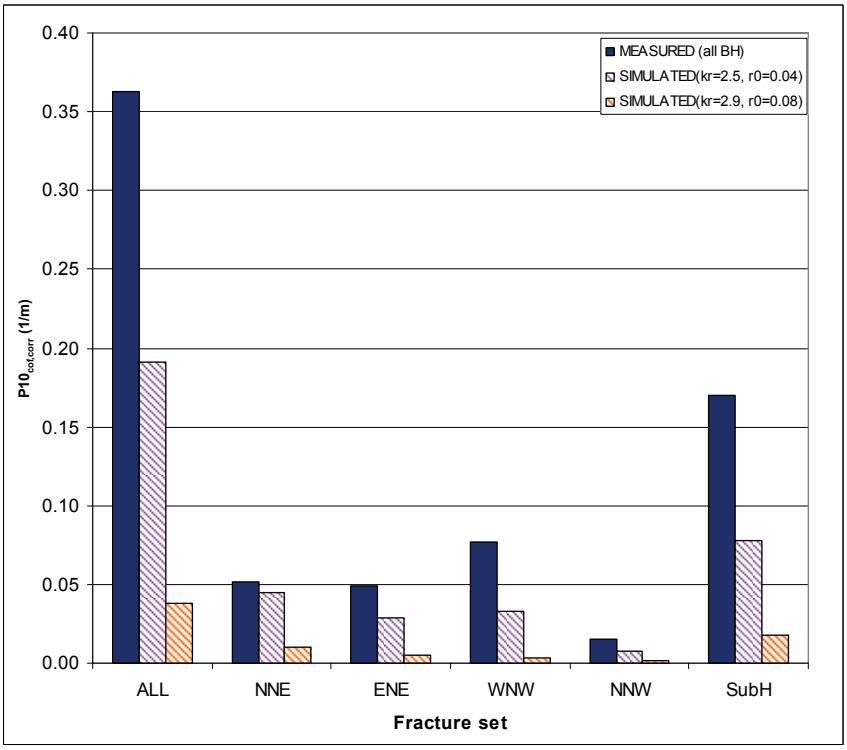

Figure A-7-12. *Comparison of the simulated Terzaghi corrected fracture intensities for connected open fractures for the 2 model cases identified in the outcrop calibration against the measured fracture intensities for PFL-f features. The intensities are broken down by set as well as being given as a total.*

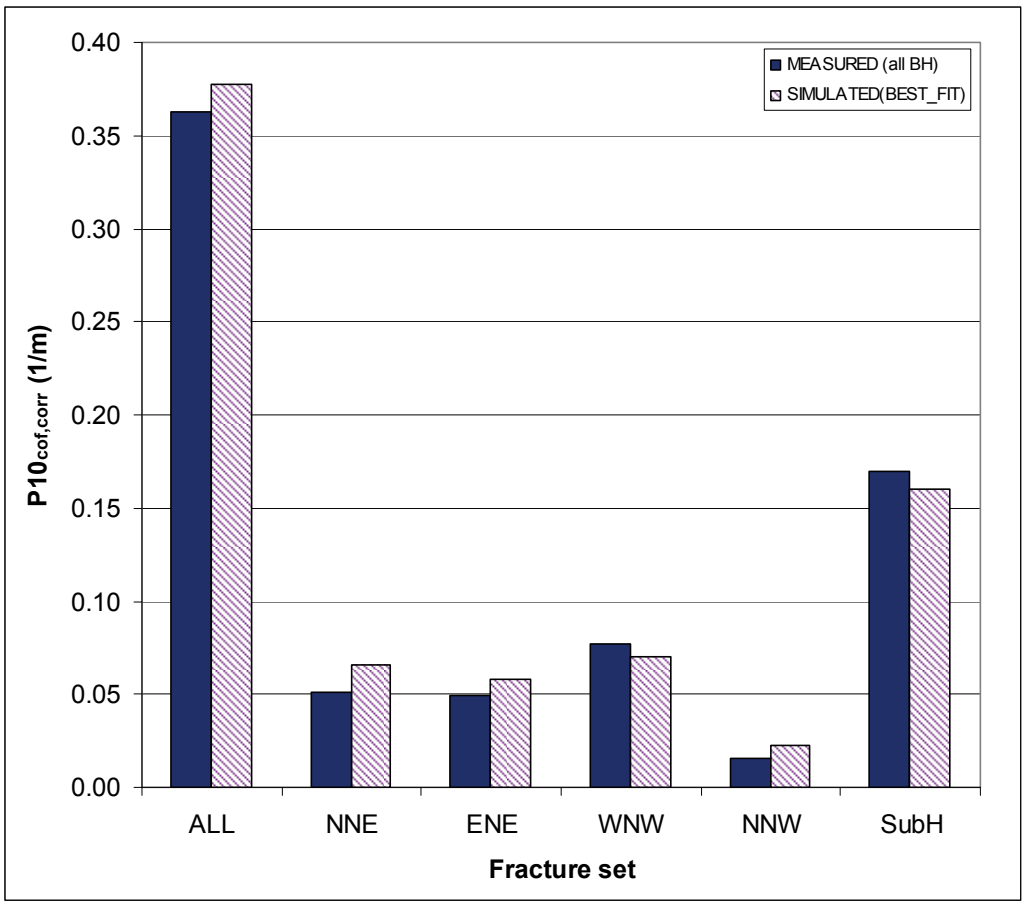

Figure A-7-13. *Comparison of the simulated Terzaghi corrected fracture intensities for connected open fractures for the parameters given in Table A-7-12 against the measured fracture intensities for PFL-f features. The intensities are broken down by set as well as being given as a total.*

Table A-7-12. Power-law size parameters for open fractures by fracture set for the best fit case to intensities of PFL-f features based on a geometrical connectivity analysis.

Case	Size parameters	NNE	ENE	WNW	NNW	Sub-H
BEST_FIT	r_0	0.04 m	0.04 m	0.04 m	0.04 m	0.04m
	k_r	2.50	2.60	2.40	2.40	2.35
	P_{32}	0.36	0.29	0.30	0.08	0.55

A.7.5 Simulations of the Posiva Flow Log tests

Simulations of single-hole tests

Five single-hole pump tests have been performed in the KLX11 boreholes /Sokolnicki and Kristiansson, 2007/. Each of the boreholes KLX11B-F was pumped, one at a time.

The holes were pumped between 2 and 8 days, but all reached a drawdown of about 10 m. A suitable recovery time was used after each borehole pumping test. The recovery time varied between 1 and 4 days. The undisturbed pressures and flow rates for into each borehole at each identified fracture were measured. The equivalent data was recorded during each of the pumping tests to give the differences. Hence, this data yields 5 single-hole standard PFL-f tests as well as a series of interference tests. However, only the interference tests for pumping at KLX11B, KLX11D and KLX11E gave a complete set of data useful for modelling.

A methodology for hydrogeological DFN modelling of PFL based interference tests was developed using data from the KLX09 array of boreholes /Hartley et al, 2007/. The approach is to first calibrate the hydraulic parameters, mainly transmissivity, on the single-hole tests, and test or adjust the models based on their ability to predict the drawdowns and intra-hole flows observed in the monitoring boreholes.

One issue of potential importance identified there was that the PFL tool might constrict intra-hole flows within the monitoring during measurements. The solution was to specify an effective hydraulic conductivity of 0.3 m/s to the full length of all boreholes and represent flow along a borehole by a 1D connection that provides a hydraulic connection between the fractures which it intersects. The flux along the borehole between any two adjacent fractures is then equal to the hydraulic conductivity multiplied by the cross-sectional area of the borehole times the head gradient between the fractures. A no-flow boundary condition was imposed on the top surface. In modelling both the single-hole and interference tests it was assumed that appropriate boundary conditions for steady-state flow calculations were a fixed head of zero on all vertical sides.

As a starting point for the calibration, the fracture size distribution parameters that gave the best overall match in the simulations of fracture connectivity (see Table A-7-7 and Table A-7-12) were used. The fracture size parameters were modified with the objective of obtaining the right number of fractures carrying flow above the detection limit in determined flow intervals. The measurement limit of Q/s was taken to be 4.0 10^{-10} m^2/s, based on the lowest flow rate recorded in the PFL-f data.

For the single-hole tests, 3 main calibration targets are used to quantify how well the model simulates the data (more calibration targets were introduced for the complete set of boreholes considered in Section 10.5):

1. A histogram of the distribution of flow-rates, *Q/s*, is compared with a bin size of half an order of magnitude;

2. The total flow to the borehole, sum of *Q/s* (calculated as arithmetic average over the realisations);

3. The numbers of PFL-f features associated with each fracture set and the distribution of *Q/s*, for each set. This distribution is quantified in terms of the mean, plus/minus 1 standard deviation, minimum and maximum of Log(*Q/s*).

As part of the calibration some minor adjustments were made to the fracture size parameters by keeping r_0 constant at 0.038m and altering k_r values as necessary, usually downwards to compensate for some small connected open fractures yielding flow-rates

below the PFL detection limit. Three different transmissivity models were tested; correlated, semi-correlated and uncorrelated in terms of fracture size. The matches for each of these 3 simulations cases compared to the PFL-f data are shown in Table A-7-13 and Figure A-7-14 through Figure A-7-19. The parameters corresponding to these results are summarised in Table A-7-14.

Table A-7-13. Total flow rates divided by drawdown (Q/s) to the borehole, from the PFL-f data and as predicted by the various models.

Data source	Total flow rate (Q/s) m^2/s
PFL_f data	$1.21\ 10^{-5}$
Semi-correlated model	$1.94\ 10^{-5}$
Correlated model	$1.11\ 10^{-5}$
Uncorrelated model	$1.45\ 10^{-5}$

Table A-7-14. Description of the hydrogeological DFN input parameters calibrated on the KLX11B-F single-hole test. The transmissivity parameters are given for each set and the semi-correlated (SC), correlated (C) and uncorrelated (UC) models.

Fracture set name	Orientation set pole: (trend, plunge), conc.	Fracture radius model power-law (r_0, k_r)	Intensity P_{32} (m^2/m^3)	Transmissivity model T (m^2/s)
NNE	(283, 6.5) 13	(0.038, 2.5)	0.23	SC: ($1.5\ 10^{-8}$, 0.7, 1.0) C: ($1.7\ 10^{-8}$, 0.9) UC: ($1.5\ 10^{-7}$, 1.1)
ENE	(332, 0.5) 21	(0.038, 2.45)	0.18	SC: ($3.0\ 10^{-9}$, 0.7, 1.0) C: ($7.5\ 10^{-9}$, 0.9) UC: ($3.0\ 10^{-8}$, 1.1)
WNW	(201, 5) 12	(0.038, 2.3)	0.19	SC: ($4.8\ 10^{-9}$, 0.7, 1.0) C: ($8.4\ 10^{-9}$, 0.9) UC: ($5.1\ 10^{-8}$, 1.1)
NNW	(246, 10) 12	(0.038, 2.3)	0.05	SC: ($2.3\ 10^{-8}$, 0.7, 1.0) C: ($6.7\ 10^{-9}$, 0.9) UC:(μ,σ) ($3.1\ 10^{-8}$, 1.1)
Sub-H	(334, 87) 10	(0.038, 2.2)	0.35	SC: ($2.0\ 10^{-8}$, 0.7, 1.0) C: ($7.0\ 10^{-9}$, 1.2) UC: ($2.2\ 10^{-7}$, 1.1)

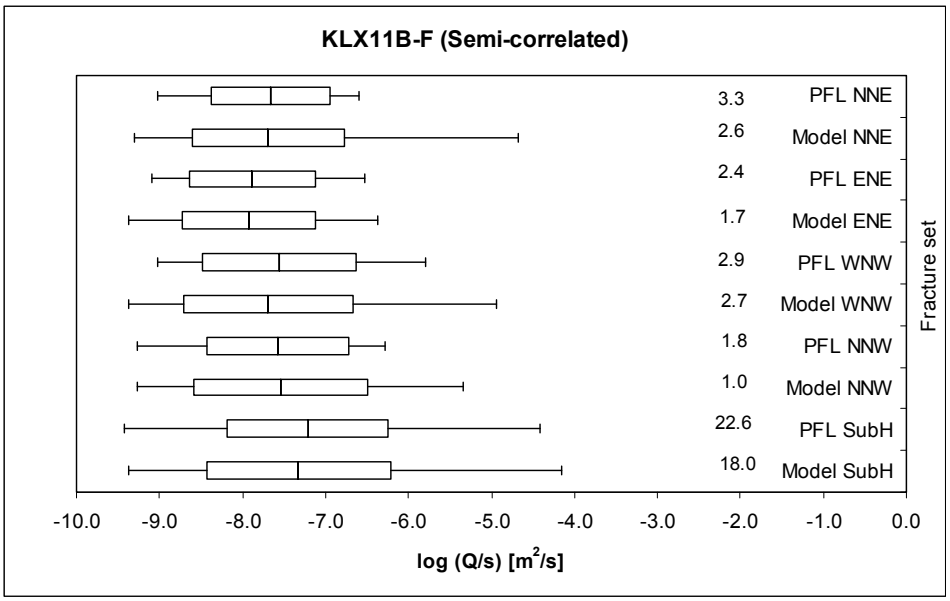

Figure A-7-14. *Bar and whisker plots comparing statistics taken over each fracture set for the individual inflows, Q/s, for the PFL-f measurements from KLX11B-F against the mean over 10 realisations of the model. The centre of the bar indicates the mean value, the ends of the bar indicate ±1 standard deviation, and the error bars indicate the minimum and maximum values. The total numbers of fractures with inflow above the detection limits within each set are also given normalised to a 100m borehole interval. For the PFL-f data, the statistics are taken over the identified PFL-f features within each set. For the model, statistics are taken over the fractures generated within each set and over 10 realisations. The semi-correlated transmissivity model is shown.*

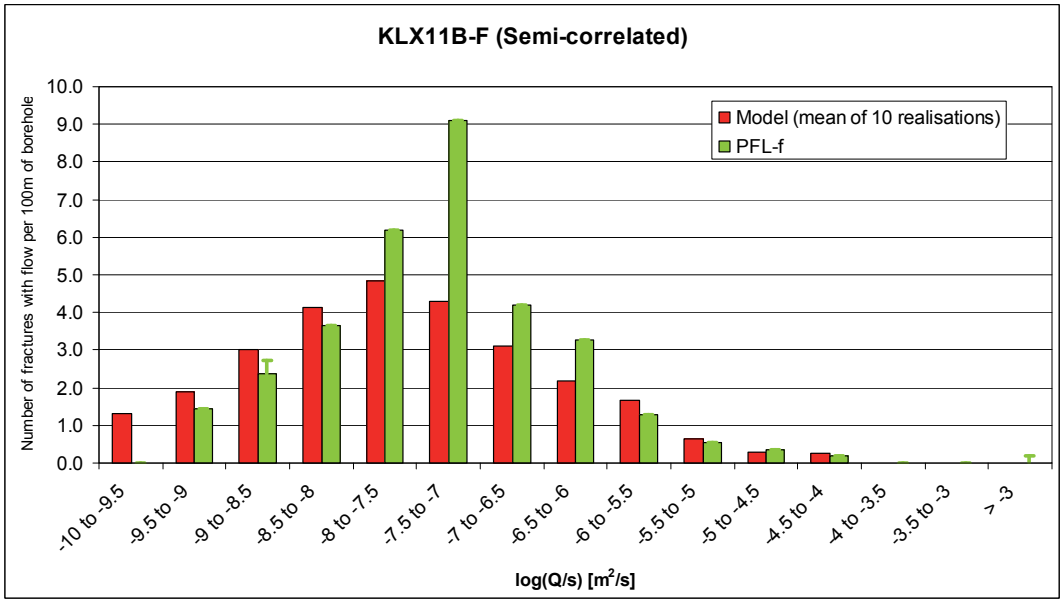

Figure A-7-15. *A comparison of the distributions of individual fracture inflows, Q/s, for the PFL-f measurements from KLX11B-F against the mean over 10 realisations of the model and a semi-correlated transmissivity to size. The numbers of intersections are normalised to a 100m length of borehole. For the PFL-f data, the error bars indicate values close to the detection limit which are estimated*

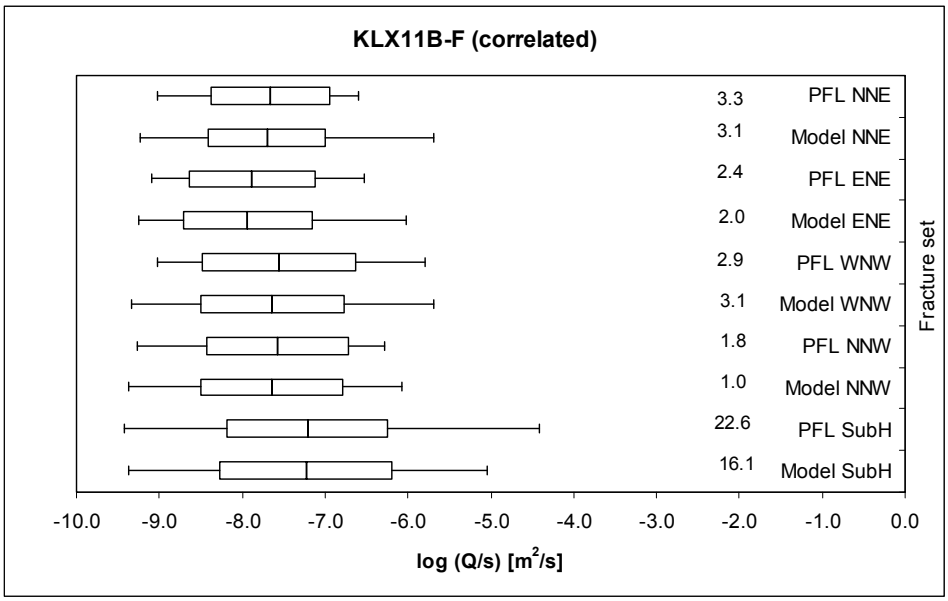

Figure A-7-16. *Bar and whisker plots comparing statistics taken over each fracture set for the individual inflows, Q/s, for the PFL-f measurements from KLX11B-F against the mean over 10 realisations of the model. The centre of the bar indicates the mean value, the ends of the bar indicate ±1 standard deviation, and the error bars indicate the minimum and maximum values. The total numbers of fractures with inflow above the detection limits within each set are also given normalised to a 100m borehole interval. For the PFL-f data, the statistics are taken over the identified PFL-f features within each set. For the model, statistics are taken over the fractures generated within each set and over 10 realisations. The semi-correlated transmissivity model is shown.*

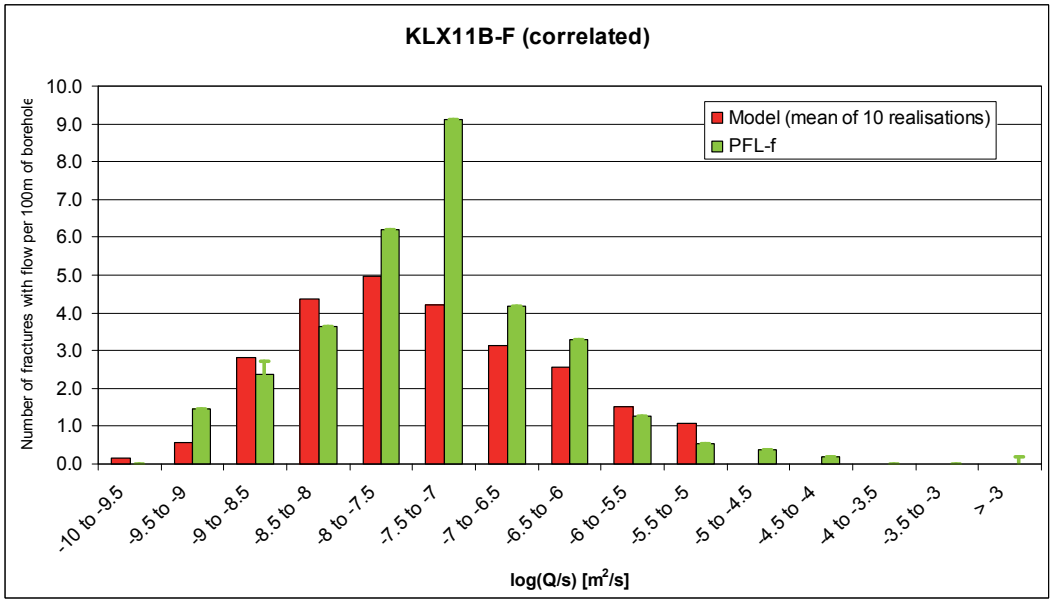

Figure A-7-17. *A comparison of the distributions of individual fracture inflows, Q/s, for the PFL-f measurements from KLX11B-F against the mean over 10 realisations of the model and a correlated transmissivity to size. The numbers of intersections are normalised to a 100m length of borehole. For the PFL-f data, the error bars indicate values close to the detection limit which are estimated.*

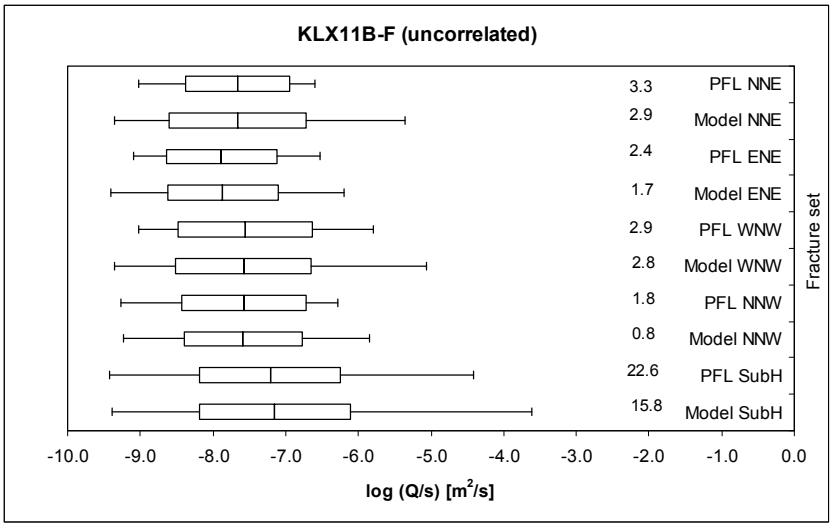

Figure A-7-18. *Bar and whisker plots comparing statistics taken over each fracture set for the individual inflows, Q/s, for the PFL-f measurements from KLX11B-F against the mean over 10 realisations of the model. The centre of the bar indicates the mean value, the ends of the bar indicate ±1 standard deviation, and the error bars indicate the minimum and maximum values. The total numbers of fractures with inflow above the detection limits within each set are also given normalised to a 100m borehole interval. For the PFL-f data, the statistics are taken over the identified PFL-f features within each set. For the model, statistics are taken over the fractures generated within each set and over 10 realisations. The semi-correlated transmissivity model is shown.*

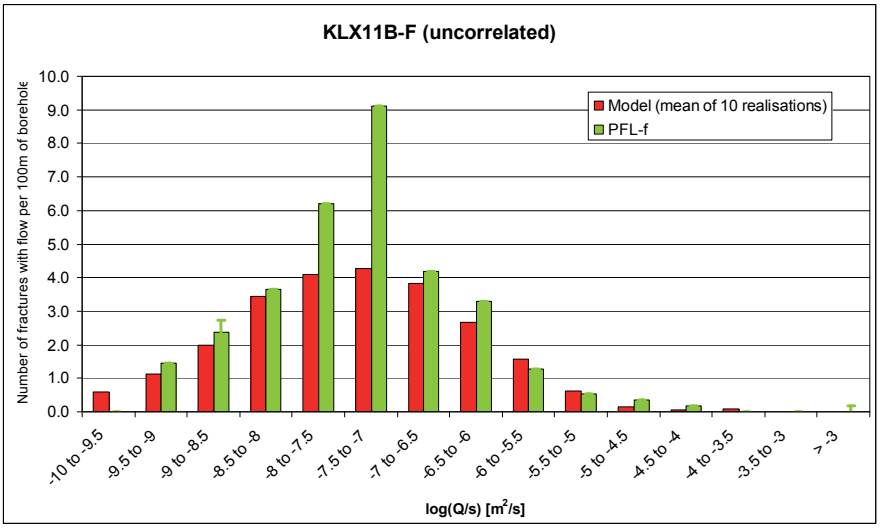

Figure A-7-19. *A comparison of the distributions of individual fracture inflows, Q/s, for the PFL-f measurements from KLX11B-F against the mean over 10 realisations of the model and an uncorrelated transmissivity to size. The numbers of intersections are normalised to a 100m length of borehole. For the PFL-f data, the error bars indicate values close to the detection limit which are estimated. For the model, the error bars indicate predicted flows below the measurement limit.*

Visualisation of interference test responses

Before trying to simulate the interference test it is instructive to visualise the main structures and flow connections that are responsible for the observed flow and head responses by identifying the PFL-f features corresponding to the highest measured inflows/outflows. They were visualised as square fractures assumed to have a length of 10 m, centred on the interpreted location of the PFL-f feature and oriented as interpreted from boremap data. The visualisation is shown in Figure A-7-20 with fractures coloured by the transmissivity inferred from the single-hole tests and selected PFL-f features are tabulated in Table A-7-15, which shows that all but one of the fractures intersecting the KLX11 boreholes with transmissivities above 10^{-6} m^2/s is in the sub-horizontal set. The only other fracture shown is assigned to the WNW set.

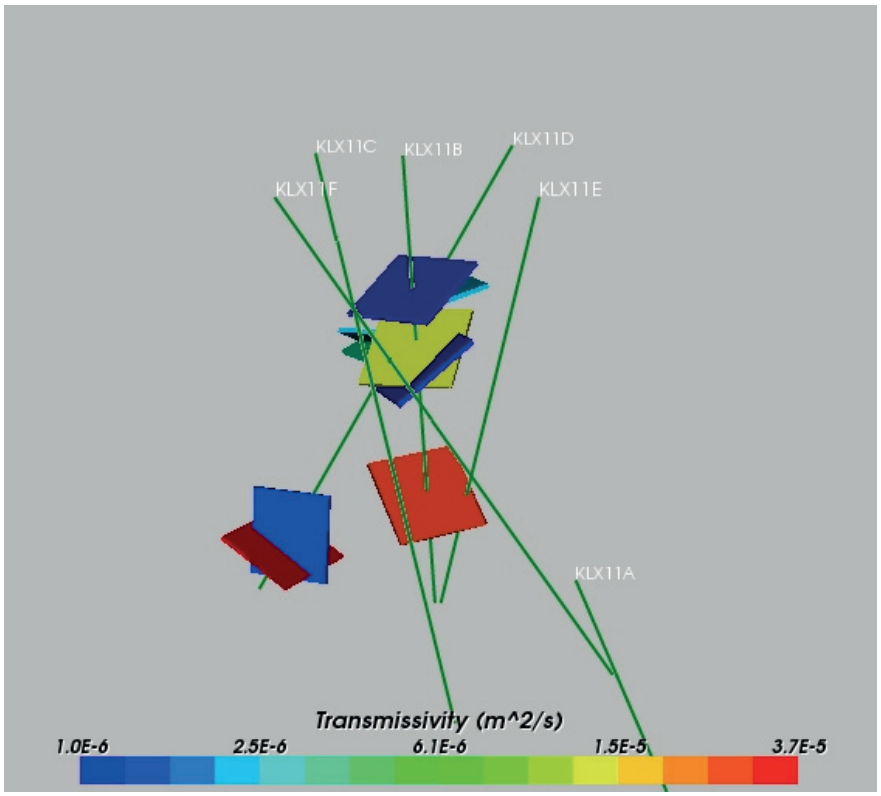

Figure A-7-20. *Speculative visualisation of most transmissive fractures contributing to intra-borehole flows during the interference tests. The fractures are drawn as square fractures of length 10 m centred on the borehole with orientations taken from integration of PFL-f and borehole image analysis. The fractures are coloured according to the transmissivity interpreted from the single-hole test interpretations. All but one of the fractures is assigned to the sub-horizontal fracture set.*

Table A-7-15. Properties of the fractures with highest interpreted transmissivities (above 10^{-6} m^2/s) in the KLX11 boreholes from the single-hole abstraction tests.

Borehole	Elevation (masl)	Strike (º)	Dip (º)	Interpreted transmissivity (m^2/s)
KLX11B	-3.78	310.3	25.0	1.21E-06
KLX11B	-16.03	294.2	36.3	1.36E-05
KLX11B	-19.18	342.0	32.0	1.08E-06
KLX11B	-48.08	248.1	42.9	2.98E-05
KLX11D	-9.06	341.9	11.1	2.15E-06
KLX11D	-18.86	330.8	17.4	3.53E-06
KLX11D	-19.63	120.2	27.0	2.41E-06
KLX11D	-62.66	301.8	75.7	1.56E-06
KLX11D	-65.7	219.8	26.1	3.74E-05

Simulation of interference tests

The aims of the interference modelling was to assess the validity of the fracture set parameters derived from the single-hole analysis above in explaining the observed behaviour of the flows and head drawdowns in the interference tests. The fracture parameters used for the interference test modelling are recorded in Table A-7-14.

The performance of the model in simulating the data considered the intensity and magnitude of the intra-hole flows measured in the monitoring borehole (here referred to as cross-hole flows), and the size of drawdowns observed in the monitoring holes. This was quantified by making the 3 following comparisons:

1. The distribution of fluxes within the monitoring boreholes. Here the measured fluxes into or out of the monitoring holes at each PFL-f feature location for all combinations of interference test (4 monitoring holes and 3 pumped boreholes) were collected together as an ensemble and the values divided into half order of magnitude bins to give a distribution. For the model, 10 model simulations were generated and flow calculations made for pumping in each of the 3 boreholes to give equivalent set of histograms for each of the 10 simulations. An average histogram for the model was calculated by averaging the numbers of flows in each bin over the 10 realisations and this average histogram was compared with the data. The data was normalized to give the values per 100m of borehole.

2. A second comparison was made using bar and whisker plots using statistics taken over each fracture set for the individual flows into and out of the monitoring boreholes divided by drawdown, Q/s, for the PFL-f measurements from KLX11B-F against the mean over 10 realisations generated by the model. The data was normalized to give the values per 100m of borehole.

3. A third comparison was made against the drawdowns in the monitored boreholes. Since for a particular pumped borehole the average drawdowns in all of the monitoring holes are quite similar, the average drawdown over all the monitored boreholes (ordinate) is shown for each pumped borehole

(abscissa). The first histogram bar represents the measured data for each of the 5 boreholes, followed by 10 data series for each of the model realisations. For the measured data the drawdown in the monitored holes has been normalised linearly to a 10 m drawdown at the pumped borehole to make it easier to compare across the boreholes.

The overall distribution of the magnitude of cross-hole flows, calibration target 1 above, was matched well for all 3 transmissivity models. Comparing the measured and modelled distributions of cross-hole flows by set (calibration target 2 above) suggested there was a tendency in the model to under-predict the mean transmissivity, but compensate with having more spread, especially for the correlated and semi-correlated transmissivity models. The distribution of drawdowns in heads was probably the most sensitive to the choice of transmissivity to size relationship, and hence these are the results we describe first. The measured drawdowns vary between about 0.7m and 3m for different monitoring boreholes, i.e. far more variable than what would be expected for a radial flow system were the effective hydraulic properties of the rock homogeneous and isotropic. Figure A-7-21 through Figure A-7-23 show comparisons of the measured average drawdowns and the results of 10 realisations for the 3 transmissivity models.

For a stochastic model it is unreasonable to expect the model to reproduce the spatial differences in the responses; instead the models were expected to mimic the variation between boreholes within and between realisations. One quick observation is that the correlated model predicts low variability in the predicted drawdown at the monitoring boreholes, about 0.8 to 1.6m. This is thought to be caused by the tendency of this model to consistently generate large fractures with a high transmissivity that dominate the responses and smooth out the drawdown distribution. The semi-correlated and uncorrelated models predict higher variability more consistent with data. The uncorrelated model shows more variability within a realisation, whereas the semi-correlated model shows mostly variability between realisations. This suggests spatial variability of transmissivity within a fracture on scales smaller than the spacing between the boreholes is an important control on the observed responses. The semi-correlated, and uncorrelated model in particular, tend to distribute high transmissivity on smaller scale fractures, and so they are just one way of reducing the length scale of hydraulic variability. Another would be to include spatial variability in transmissivity on fractures larger than a certain scale (a few tens of metres would seem appropriate based on these tests).

As an example the results for calibration targets 1 and 2 measuring cross-hole flows are shown for this model in Figure A-7-24 and Figure A-7-25 for the uncorrelated model, noting that the other 2 transmissivity models gave similar results for these two types pf comparison.

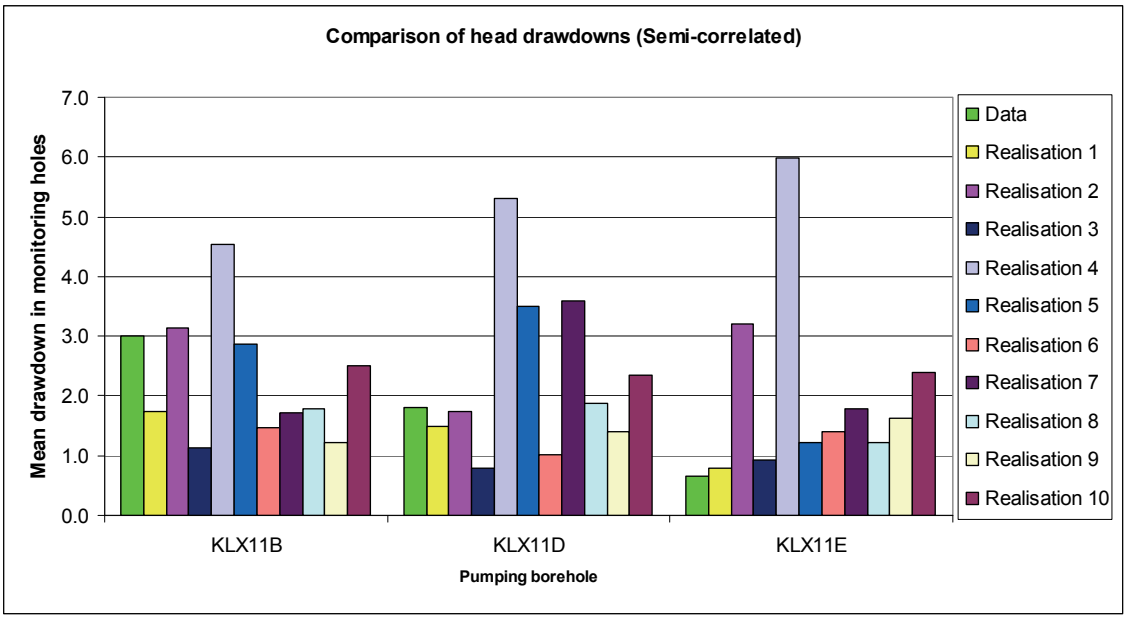

Figure A-7-21. *Comparison of the mean drawdown response measured in the monitoring holes for pumping in the 3 abstraction boreholes KLX11B, KLX11D and KLX11E against the mean simulated head drawdown for each of 10 realisations. The model has a semi-correlated transmissivity (see Table A-7-14 for parameter values).*

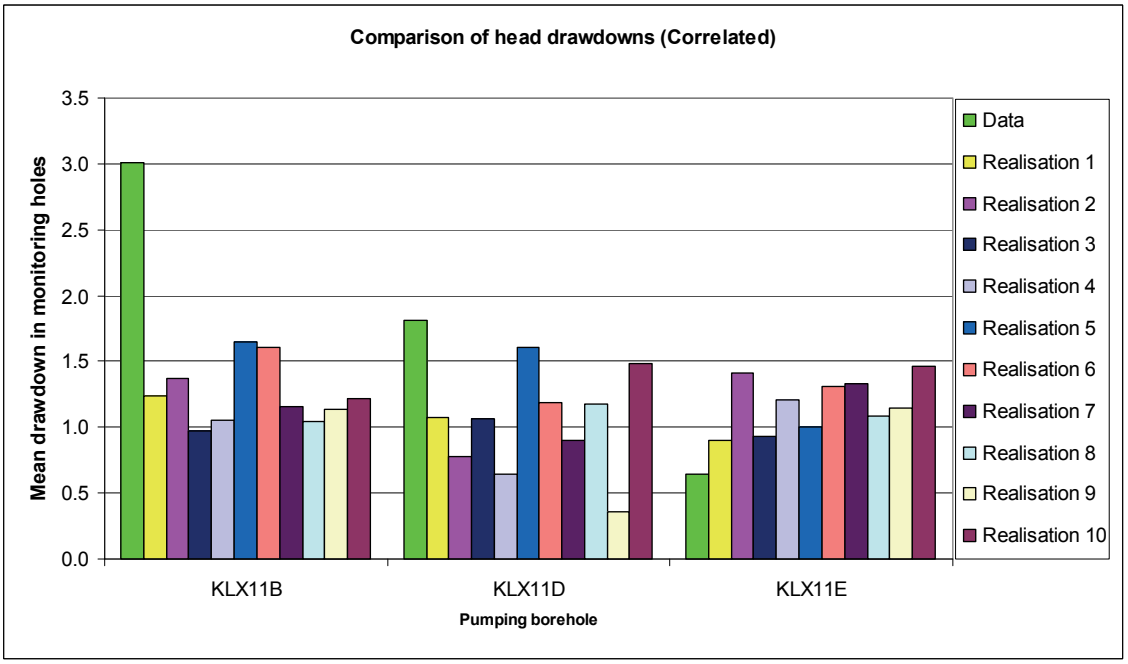

Figure A-7-22. *Comparison of the mean drawdown response measured in the monitoring holes for pumping in the 3 abstraction boreholes KLX11B, KLX11D and KLX11E against the mean simulated head drawdown for each of 10 realisations. The model has a correlated transmissivity (see Table A-7-14 for parameter values).*

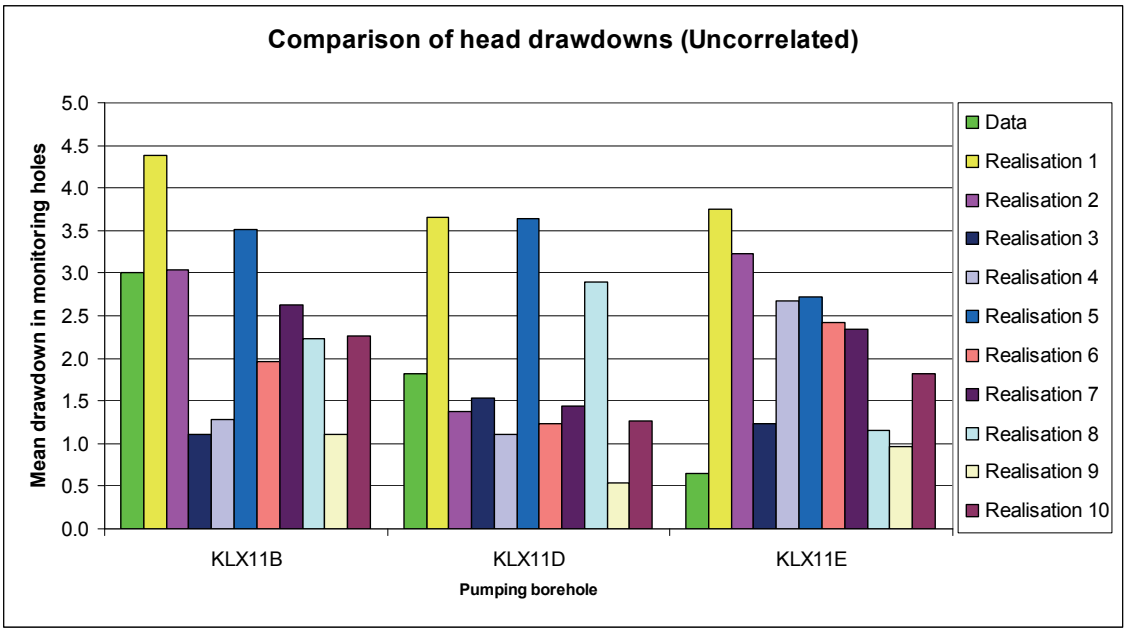

Figure A-7-23. *Comparison of the mean drawdown response measured in the monitoring holes for pumping in the 3 abstraction boreholes KLX11B, KLX11D and KLX11E against the mean simulated head drawdown for each of 10 realisations. The model has an uncorrelated transmissivity (see Table A-7-14 for parameter values).*

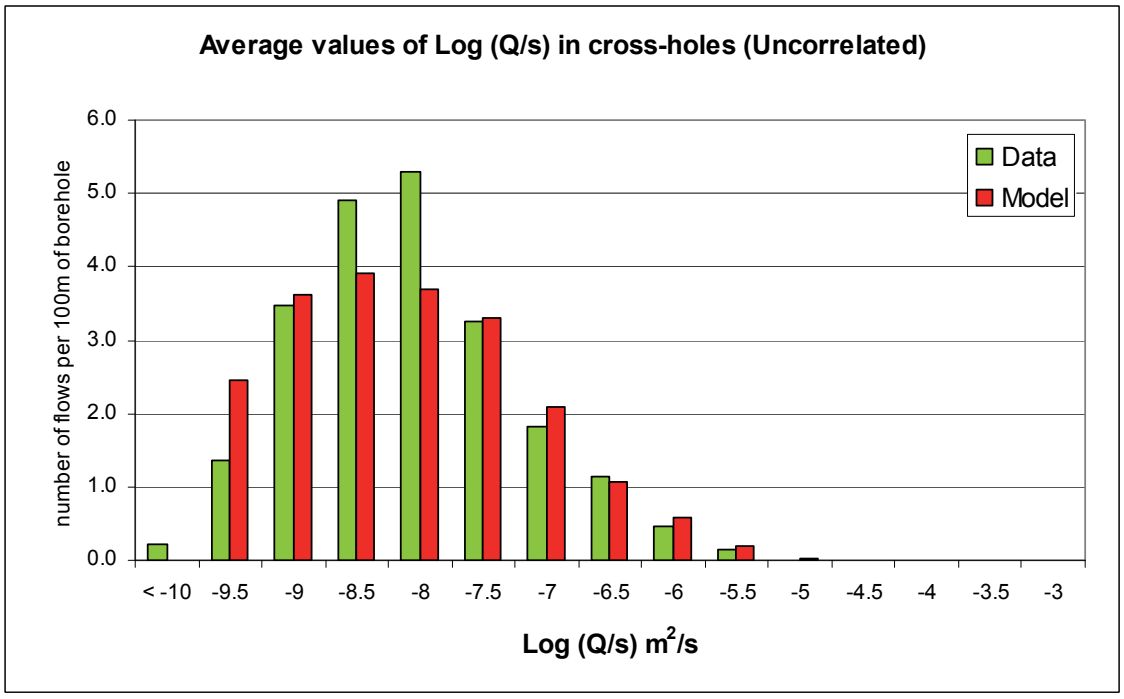

Figure A-7-24. *Histogram comparing the distribution of the magnitude of inflows/outflows divided by drawdown, Q/s, to the monitoring boreholes averaging over an ensemble of all possible combinations, i.e. three abstraction boreholes multiplied by 4 monitoring boreholes each. The PFL-f interference measurements in KLX11B-F (green) are plotted against the mean over 10 realisations of the model with an uncorrelated transmissivity.*

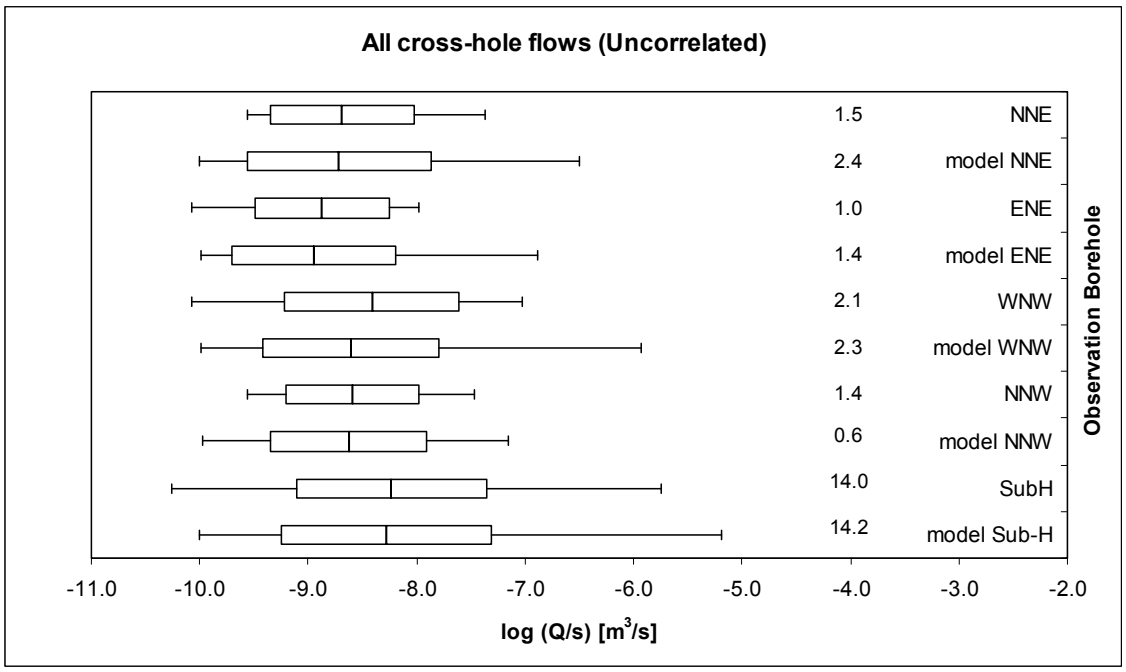

Figure A-7-25. *Bar and whisker plots comparing statistics taken over each fracture set for the individual inflows, Q/s, for the PFL-f measurements from KLX11B-F against the mean over 10 realisations of the uncorrelated transmissivity model. The centre of the bar indicates the mean value, the ends of the bar indicate ±1 standard deviation, and the error bars indicate the minimum and maximum values. The total numbers of fractures with inflow above the detection limits within each set per 100m of borehole are also given. For the PFL-f data, the statistics are taken over the identified PFL-f features within each set, and over the fractures generated within each set and over 10 model realisations.*

A.7.6 Summary and conclusions

This analysis developed a hydrogeological DFN model for the near surface Ävrö Granite based on one vertical and four inclined boreholes around the KLX11 drill site area and integrating core descriptions, borehole image and outcrop data together with hydraulic data from single-hole and multi-hole PFL-f tests.

Based on the power-law concept for fracture size, distribution parameters have been determined for DFN models consistent with the following data:

- Data from the ASM100235 outcrop, giving surface P_{21} fracture intensity values;
- The intensity of open fractures for boreholes KLX11A to KLX11F. This was equated with the intensity of connected fractures in simulations;
- Inflow rates, freshwater heads and transmissivity values from single-hole tests for boreholes KLX11B to KLX11F;
- Intra-hole flow rates and drawdowns in the monitoring boreholes when pumping boreholes KLX11B, KLX11D and KLX11E.

An analysis of the orientations of PFL-f features suggests the sub-horizontal fractures are responsible for the majority of higher flow-rates. The WNW set is the next most

important set. This is reasonable since the sub-horizontal set is the most abundant and the WNW set correlates with the direction of maximum horizontal in-situ (see Chapter 9).

The outcrop data could be modelled by power-law size parameters for *all* fractures of either (k_r, r_0) = (2.5, 0.04) or (k_r, r_0) = (2.9, 0.08). Considering the network connectivity of open fractures and assuming it is the main control on the intensity of PFL-f detected features suggested that the parameter pair (k_r, r_0) = (2.5, 0.04) could be suitable for describing both the hydraulic connectivity of open fractures and the intensity seen on the outcrop for trace lengths > 0.5m. This choice was therefore used as the basis for more detailed modelling of the single-hole and interference test modelling.

Hydro-DFN models of the open fractures were developed with correlated, uncorrelated and semi-correlated transmissivity relationships which each gave a reasonable match to the single-hole results. However, when these parameters where used to model the interference test results, the correlated model predicted drawdown responses in the monitoring boreholes uncharacteristic of the measurements (too homogeneous). The semi-correlated, and in particular the uncorrelated model, gave the predictions of drawdowns and cross-hole flows most consistent with data. This is considered to indicate that there must be significant heterogeneity of transmissivity within or between the on a length scale smaller than the borehole spacing, i.e. a few tens of metres.

A.8 Modelling Connected Open Fractures: Sensitivity to changes in methodology

A.8.1 Introduction

This appendix describes the results of a study to investigate sensitivities to the methodology used in the Hydro-DFN calibrations of fracture size distributions. The calibration process matches Terzaghi corrected intensities of connected open fractures to that of PFL-f features by varying the power-law fracture size distribution parameters. If there are uncertainties in the method used to calculate the Terzaghi corrected intensities of connected open fractures predicted by the model, then this will lead to uncertainties in the power-law fracture size distribution parameters. In particular, there are two aspects of the calibration process that are considered:

- Whether the borehole is added to the model before or after the connectivity calculation is made. If a borehole is added before the connectivity calculation, then it has the possibility to enhance fracture connectivity in its vicinity (see schematic examples in Figure 10-1).

- How sensitive the results are to the fracture size truncation limit used in the simulations. Two cases are considered r_{min} = 0.28m truncation and $r_{min} = r_0$ = 0.038m (i.e. no truncation).

Possibly the most realistic method would be to insert the borehole before the connectivity calculation and use r_{min} = 0.038m truncation. However, due to practical constraints in running many realisations in reasonable time, and due to limitations in the flexibility of the current version of ConnectFlow, the approach used for calculating the open fracture size distribution described in Section 10.4 uses the following:

- perform a connectivity analysis with r_{min} = 0.038m;
- and the borehole is added to the model after the connectivity calculation.

For the calibration of fracture transmissivity based on simulated flow-rates as described in Section 10.5 a different approach is used:

- apply a truncated fracture size distribution, r_{min} = 0.28m, to make flow calculations more tractable, assuming very small fractures do not contribute to flows above the PFL-f detection limit;
- and the borehole is added to the model before the connectivity calculation and subsequent flow simulations.

This section quantifies uncertainties with respect to the methodology used by considering the four different model configurations described in Table A-8-1. The two "AFTER" cases follow the procedure used in calibration of the open fracture size distribution based on a geometrical connectivity calculation, but different fracture size truncation are tested. Such calculations are computationally inexpensive and so 40 realisations were performed. The two "BEFORE" cases follow the procedure used in

the flow simulations, but consider a lower fracture size truncation. In this case 10 realisations were performed as the flow calculations take longer to run. The case which best reflect reality then is the BEFORE_04 case as it includes the effect of the borehole potentially enhancing local connectivity and has $r_{min}=r_0$. This approach was not used to determine the fracture size distribution because it is often computationally expensive.

Table A-8-1. Summary of the methods used in the sensitivity study.

Variant name	Borehole included in model before or after connectivity calculation	Fracture size truncation limit: r_{min}(m)
BEFORE_04	Before	0.038 (i.e. r_0)
BEFORE_28	Before	0.28
AFTER_04	After	0.038 (i.e. r_0)
AFTER_28	After	0.28

A.8.2 Example

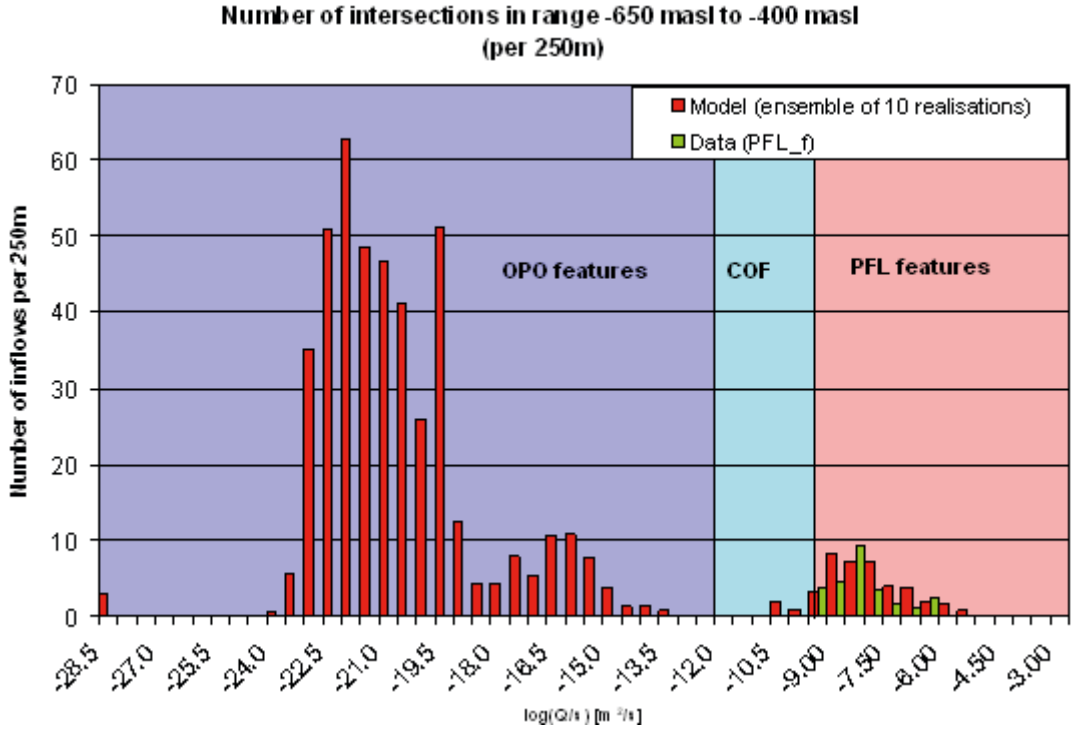

Figure A-8-1. *Illustration of how the open features intersecting the borehole can be classified according to their fracture inflow distribution: This histogram compares the modelled and measured distribution of the magnitude of inflows divided by drawdown, Q/s. The PFL-f measurements are treated as an ensemble over all boreholes sections within HRD_C. For the model, ensemble statistics over 10 realisations of the Hydro-DFN model (BEFORE04 case) are calculated. The numbers of intersections are normalized to the length of borehole indicated in the heading of the graph and have been Terzaghi corrected. Below about 10^{-13} m^2/s the calculated inflows are essentially numerical noise.*

This illustration is based on HRD_C, semi-correlated transmissivity model, and OPO features. Results are presented for depth zones -650 to -400 masl and -400 to -150 masl.

For all 4 cases described in Table A-8-1 a connectivity analysis is performed. For the BEFORE cases this is done prior to the flow calculations to avoid trying to calculate flows in unconnected fractures. When performing a connectivity analysis, ConnectFlow currently eliminates all isolated fractures or dead-end fractures apart from those intersecting a borehole. For transient flow, all fractures connected to the borehole, including unconnected ones, can provide storage. For steady-state calculations, only the fractures connected to the flowing network provide inflows, and this situation is the most appropriate to modelling the PFL-f tests. Hence, in all 4 cases both isolated and dead-end fractures are removed.

The 2 cases where the borehole is included in the model after the connectivity analysis, AFTER_04 and AFTER_28 in Table A-8-1, correspond to the approach described in Section 10.4, and consider 2 different fracture truncation limits. The borehole is inserted afterwards to avoid the borehole contributing to connectivity, and hence these 2 cases give results for the in-situ intensity of connected open fractures.

The 2 cases where the borehole is included in the model before the connectivity analysis, BEFORE_04 and BEFORE_28 in Table A-8-1, correspond to the approach described in Section 10.5, and consider 2 different fracture truncation limits. Adding the borehole before removing unconnected fractures could be significant since it includes the potentially enhanced connectivity near the borehole that may result from it connecting to otherwise isolated or dead-end parts of the fracture network. Since in these cases all open fractures connected to the borehole are retained there needs to be some way of discerning which ones are connected to the wider network and can therefore conduct flow. Hence, for the 2 "BEFORE" cases, steady-state flow calculations are performed to identify the connected network by analysing the distribution of inflow in the fractures connected to the borehole. Doing the simulations is a more realistic representation of how fractures are classified in the field. Based on inflows, fractures fall into 3 classes (see Figure A-8-1):

1. If a fracture or fracture cluster is isolated and is only connected to the borehole it will have a negligible flow-rate, $Q/s < \sim 10^{-13}$ m^2/s, and so can be identified and excluded. These represent unconnected OPO fractures in Figure A-8-1 that in the field would be recorded as open fractures, but would not be identified as PFL-f features irrespective of the detection limit. (The distribution of $Q/s < \sim 10^{-13}$ m^2/s is erratic and an artefact of the accuracy of the numerical scheme used to obtain the steady-state flow (i.e. a consequence of the convergence criterion set for the iterative solver used) and should be viewed as effectively zero.);

2. If a fracture has a flow rate (Q/s) above the PFL-f detection limit it is classified as a PFL feature and is included in the flow calibration;

3. If a fracture has an intermediate flow rate ($Q/s > 10^{-12}$ m^2/s and $Q/s <$ detection limit $\sim 10^{-9}$ m^2/s) it will contribute to the count for connected open features (COF), but will not contribute to the count of PFL-f features.

Considering Figure A-8-1, fractures in the part of the inflow range coloured pink correspond to simulated PFL-f features, those in the ranges coloured pink or blue correspond to connected open fractures, and the full range covers all OPO fractures.

Performing steady-state flow simulations consumes more computational time than connectivity analysis, and so this method of classifying fractures based on inflows was not performed in calibrating the fracture size distributions as described in Section 10.4. Therefore, the results of the 4 cases described in Table A-8-1 are used to here to quantify the sensitivities to choices made in the modelling approach.

A.8.3 Results and conclusions

First, we consider the sensitivity of predicting the Terzaghi corrected intensity of connected open fractures based on a connectivity analysis alone, i.e. only considering the geometry of network connectivity and not any consideration of inflow magnitude. This is equivalent to considering a hypothetical case where the PFL-f method was able to detect much lower magnitude flows. The values of the simulated connected open features using each of the 4 cases described in Table A-8-1 are displayed in Figure A-8-2 and Figure A-8-3 for the middle 2 depth zones. These cases also indicate the sensitivity to a truncation of r_{min}. The effect of the truncation limit of r_{min} = 0.28m on $P_{10,cof,corr}$ is more significant for the "BEFORE" variants than the "AFTER" variants. This suggests that small fractures are forming localised additional connected networks on the order of a few decimetres around the borehole. Since they are small and localised they are unlikely to enhance the magnitude of flow to the borehole, although the simulations suggest that they could potentially increase the number of inflows observed by up to 50% if the PFL method had a sufficiently low detection limit. Presumably these additional inflows occur as clusters of small fractures around the borehole intersect with a large connected fracture which carries the flow from distance. The important WNW set is least affected since these fractures are typically long, while the intensity of other sets is almost double for the r_{min}=0.038m case. However, when the fracture size distribution is truncated at r_{min} =0.28m then the simulated connected open intensities are close to the 2 "AFTER" cases.

Second, we consider if the simulated connected open fractures were filtered according to predicted inflows to eliminate ones below the PFL-f detection limit, then how sensitive are the results to the connectivity methodology and size truncation. Figure A-8-4 and Figure A-8-5 show the equivalent plots where the simulated fractures with inflows < 10^{-9} m^2/s eliminated for the 2 "BEFORE" cases. The results are for more self-consistent, which demonstrates that the extra connected open fractures resulting from the insertion of a borehole correspond to small fractures giving small inflows to the borehole, and the results are then much less sensitive to the fracture size truncation used.

The results quantify a number of sensitivities related to decisions made in the Hydro-DFN modelling procedure. Sensitivities are largest to the approach used to calculating connected open fractures seen in a borehole. Based on a purely geometrical analysis of the connected network surrounding a borehole, connected open intensity depends strongly on whether the borehole is assumed to alter local connectivity or not, and this sensitivity is a result of swarms of connected decimetre scale fractures surrounding the intersect between a larger fractures and the borehole. Since these fractures have very little effect on inflows above the PFL detection limit, then it is perhaps not appropriate to include these in the counts, and hence using the methodology described in

Section 10.4 that focuses on fractures connected in-situ, i.e. in the absence of the borehole, perhaps best reflects what the PFL method is measuring. Still, this study shows that these issues need to be considered carefully as the decisions made in the methodology could have a strong influence on the ultimate size distribution parameters that are interpreted.

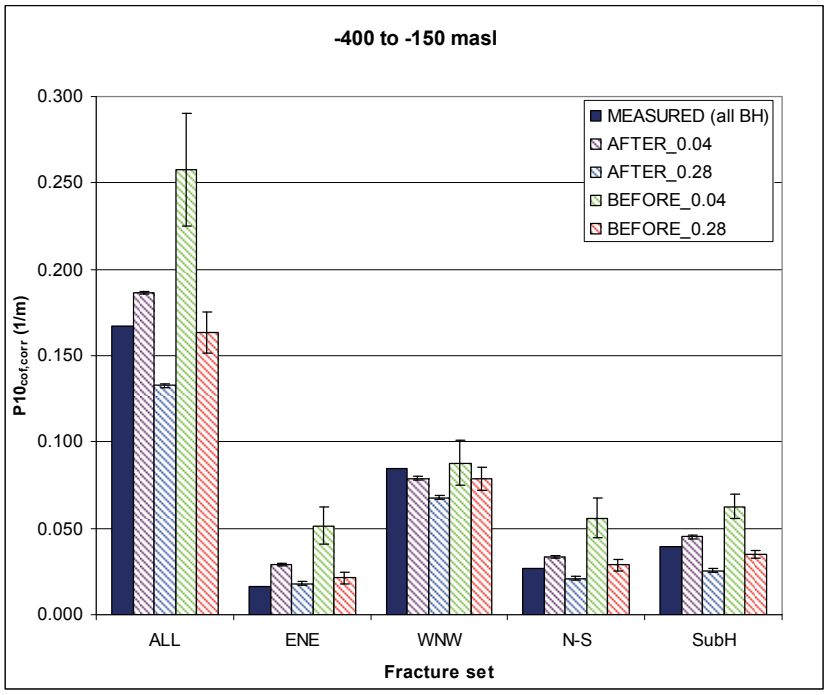

Figure A-8-2. *Comparison of the Terzaghi corrected fracture intensities of connected open, $P_{10,cof,corr}$ for the individual fracture sets with the measured fracture intensities for PFL-f features for depth zone -400 to -150 masl. For each model variant the error bars show the standard error in the mean.*

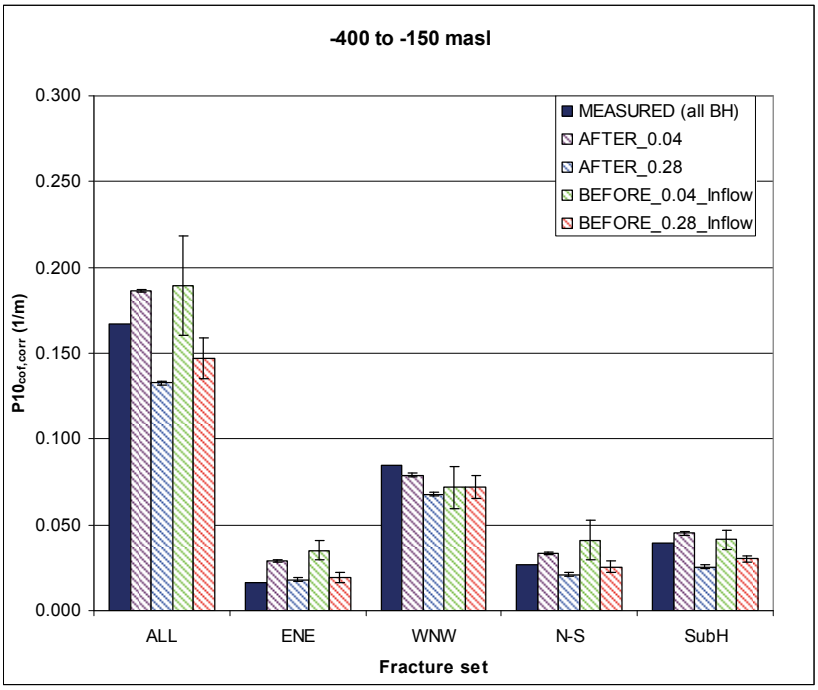

Figure A-8-3. *Comparison of the Terzaghi corrected fracture intensities of connected open, P_{10},cof,corr for the individual fracture sets with the measured fracture intensities for PFL-f features for depth zone -650 to -400 masl. For each model variant the error bars show the standard error in the mean.*

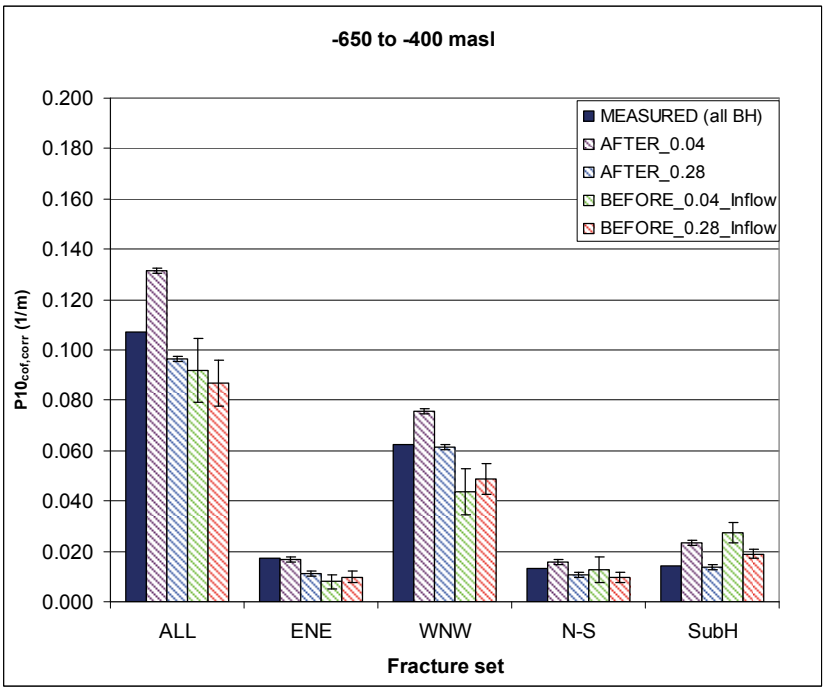

Figure A-8-4. *Comparison of the Terzaghi corrected fracture intensities of PFL-f features, $P_{10,PFL,corr}$ for the individual fracture sets with the measured fracture intensities for PFL-f features for depth zone -400 to -150 masl. For each model variant the error bars show the standard error in the mean. Simulated fractures with inflows < 10^{-9} m^2/s are eliminated.*

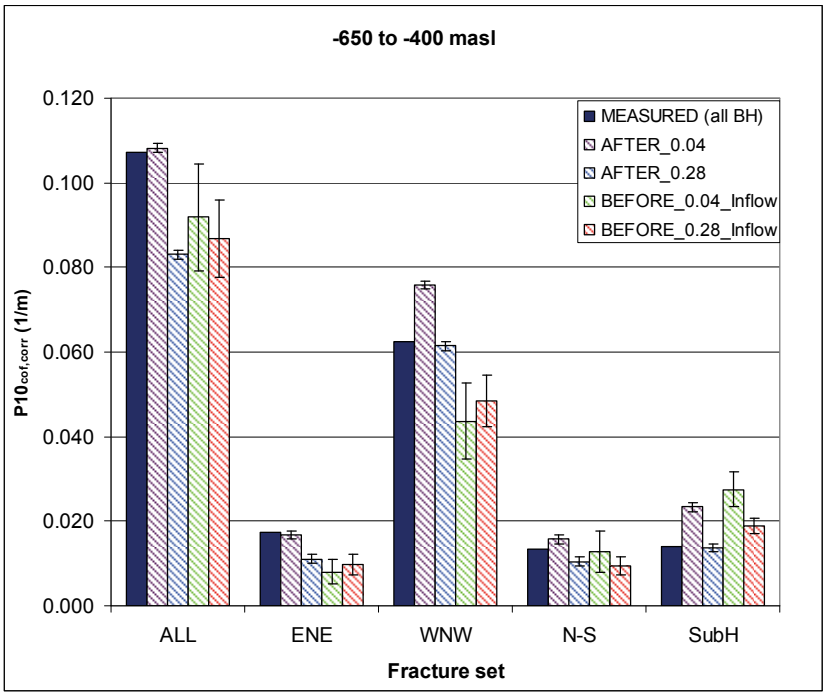

Figure A-8-5. *Comparison of the Terzaghi corrected fracture intensities of PFL-f features, $P_{10,PFL}$,corr for the individual fracture sets with the measured fracture intensities for PFL-f features for depth zone -650 to -400 masl. For each model variant the error bars show the standard error in the mean. Simulated fractures with inflows < 10^{-9} m^2/s are eliminated.*

A.9 Hydraulic conductivity estimated from injection tests

A.9.1 Hydraulic conductivity in test scales 100,20 and 5m

A large number of tests have been performed at test scale 100, 20 or 5m, using PSS, HTHB, or tests with similar methods employing older equipment in coreholes or percussion holes. These tests have been divided in three groups; "HCD": Test sections that includes one or several HCDs, "HRD": Test sections that includes HRD but no HCDs, "All": including all tests (both HRD and HCD). The data are based on the so called best Choice (BC) transmissivites, mainly based on transient evaluation. The methodologies for the tests providing the data were described in Chapter 4.

The elevation intervals used in the HydroDFN model, cf. Section 9.5, have been used for analysing possible depth dependence in the test data; >-150m, -150- to -400m, -400 to -650m, <-650m.

The estimation of distribution characteristics is based on the assumption of a lognormal distribution and censored data are taken into account to provide distributions that fits the values above the measurement limit in an appropriate way (see e.g. /Helsel, 2004/ and /Jensen et al., 2000/).

Statistics are provided based on regional data and some time on local data. The use of regional data yields a better statistical support as the sample becomes larger.

Results are presented in a number of tables and below it is explained the contents in the tables in this appendix.

- **Obj.:** Objects referrs to the sample analysed. All: All data analysed, HCD: only test sections covering HCD are analysed; HRD: only test sections between HCD are analysed.
- **Data type:** Describes in more detail what part part of "Object" that is analysed. (e.g. Reg.mod.: Reginal model area, Loc.mod.: Local modela area,
- **Sel.:** (in some tables) defines a selection of a subsample from Obj.+Data type.
- **Test type:** Type of hydraulic tests, cf. Ch 4.
- **Elevation interval:** Elevation interval for the data analysed.
- **Mean elev.:** Mean elevation (mid point of elevation interval).
- **Test scale:** Test section length used when performing hydraulic tests.
- **Sample size (Tot/left cens./ right cens.):** Total sample size analysed /No of data below lower measurement limit/ No. of data above upper measurement limit.

- **Mean Log10(K-xxx):** Evaluated mean of Log10(K-xxx) from the fitted distribution. xxx: Test type
- **STD Log10(K-xxx):** Evaluated standard deviation of Log10(K-xxx) from the fitted distribution. xxx: Test type.
- **95% Conf. Int. Log10(K-xxx) Low/High:** In tables the confidence interval of 95% is based on a two-tailed test; that corresponds to cumulative probabilities of 2.5% and 97.5%. xxx: Test type
- **Corr. Coef.:** Correlation coefficent for the fitted distribution.

Test scale 100m

In total 304 tests of test scale 100m are available and are discussed in Section 9.6.1. The trend models are shown in Section9.6.1 and are summarised in to Table A9-1 through Table A9-5.

The following basic trend models for hydraulic conductivity (K), with variable X as K, cf. Table A9-5:

- Power-law trend model (Power) : $X = a * (-Z)^B$,
- Linear trend model (Linear) : $X = a + B * (Z)$
- Exponential trend model (Exp) $X=(10^Y=)10^{(a+B*Z)}$

Z: Elevation in m (masl) (Z defined positive up). The coefficients in the Exponential trend model are based on a linear regression of $Log10(X_i)$ and Exponential trend model is generally just used for transmissivity and hydraulic conductivity.

Table A9-1. Table of results for all data samples made up of data on test scale 100m. Statistics for elevation intervals. Confidence interval for Mean Log_{10}(K-PSS). Obj.: HCD; Test sections including one or more Hydraulic Conduction Domains and surrounding rock, HRD; Test sections including only Hydraulic Rock Domains All; Covers all data (includes HRDs and HCDs). Test Type: "PSS" includes PSS, HTHB and similar older tests. (Data: regional model volume.)

Obj.	Data type	Test type	Elevation interval	Mean elev.	Test scale	Sample size (Tot/left cens./ right cens.)	Mean Log_{10}(K-PSS)	STD Log_{10}(K-PSS)	95% Conf. Int. Log_{10}(K-PSS) Low	95% Conf. Int. Log_{10}(K-PSS) High	Corr. Coef.
			(masl)	(masl)	(m)		(K: m/s)	(K: m/s)	(K: m/s)	(K: m/s)	
All	Reg.mod	PSS	> -150	-75	100	126/ 2/ 0	-6.95	1.11	-7.15	-6.76	0.97
All	Reg.mod	PSS	-150 to -400	-275	100	76/ 1/ 0	-7.47	1.56	-7.82	-7.11	0.98
All	Reg.mod	PSS	-400 to -650	-525	100	63/ 0/ 0	-8.57	1.71	-9.00	-8.14	0.98
All	Reg.mod	PSS	< -650	-825	100	39/ 0/ 0	-9.38	1.76	-9.95	-8.81	0.96
HCD	Reg.mod	PSS	> -150	-75	100	32/ 1/ 0	-6.95	1.35	-7.44	-6.47	0.93
HCD	Reg.mod	PSS	-150 to -400	-275	100	23/ 0/ 0	-6.78	1.29	-7.33	-6.22	0.92
HCD	Reg.mod	PSS	-400 to -650	-525	100	19/ 0/ 0	-7.59	1.20	-8.17	-7.01	0.97
HCD	Reg.mod	PSS	< -650	-825	100	12/ 0/ 0	-8.97	1.85	-10.15	-7.80	0.93
HRD	Reg.mod	PSS	> -150	-75	100	94/ 1/ 0	-6.96	1.04	-7.18	-6.75	0.98
HRD	Reg.mod	PSS	-150 to -400	-275	100	53/ 1/ 0	7.81	1.63	7.36	8.26	0.99
HRD	Reg.mod	PSS	-400 to -650	-525	100	44/ 0/ 0	-9.05	1.78	-9.59	-8.51	0.96
HRD	Reg.mod	PSS	< -650	-825	100	27/ 0/ 0	-9.66	1.70	-10.33	-8.99	0.94

Table A9-2. Table of results for all data samples made up of data on test scale 100m. Statistics for elevation intervals. Confidence interval for Mean Log_{10}(K-PSS). Object (Obj.): HCD: Test sections including one or more Hydraulic Conduction Domains and surrounding rock: HRD: Test sections including only Hydraulic Rock Domains All: Covers all data (includes HRDs and HCDs). Test Type: "PSS" includes PSS, HTHB and similar older tests. (Data: local model volume.)

Obj.	Data type	Test type	Elevation interval (masl)	Mean elev. (masl)	Test scale (m)	Sample size (Tot/left cens./ right cens.)	Mean Log_{10}(K-PSS) (K: m/s)	STD Log_{10}(K-PSS) (K: m/s)	95% Conf. Int. Log_{10}(K-PSS) Low (K: m/s)	95% Conf. Int. Log_{10}(K-PSS) High (K: m/s)	Corr. Coef.
All	Loc.mod	PSS	> -150	-75	100	67/ 2/ 0	-6.74	0.98	-6.98	-6.50	0.94
All	Loc.mod	PSS	-150 to -400	-275	100	49/ 1/ 0	-7.69	1.78	-8.20	-7.18	0.96
All	Loc.mod	PSS	-400 to -650	-525	100	47/ 0/ 0	-8.51	1.59	-8.98	-8.05	0.98
All	Loc.mod	PSS	< -650	-825	100	26/ 0/ 0	-9.59	1.66	-10.26	-8.92	0.98
HCD	Loc.mod	PSS	> -150	-75	100	20/ 1/ 0	-6.77	1.33	-7.39	-6.15	0.89
HCD	Loc.mod	PSS	-150 to -400	-275	100	17/ 0/ 0	-7.04	1.45	-7.79	-6.29	0.95
HCD	Loc.mod	PSS	-400 to -650	-525	100	15/ 0/ 0	-7.57	1.10	-8.18	-6.96	0.94
HCD	Loc.mod	PSS	< -650	-825	100	9/ 0/ 0	-8.94	1.26	-9.91	-7.96	0.91
HRD	Loc.mod	PSS	> -150	-75	100	47/ 1/ 0	-6.77	0.90	-7.03	-6.50	0.97
HRD	Loc.mod	PSS	-150 to -400	-275	100	32/ 1/ 0	-8.11	1.95	-8.81	-7.40	0.97
HRD	Loc.mod	PSS	-400 to -650	-525	100	32/ 0/ 0	-9.02	1.57	-9.58	-8.45	0.98
HRD	Loc.mod	PSS	< -650	-825	100	17/ 0/ 0	-10.05	1.76	-10.95	-9.14	0.99

Table A9-3. Table of results for all data samples made up of data on test scale 100m. Statistics for elevation intervals. Confidence interval for Mean Log_{10}(K-PSS). Object (Obj.): HCD: Test sections including one or more Hydraulic Conduction Domains and surrounding rock: HRD: Test sections including only Hydraulic Rock Domains All: Covers all data (includes HRDs and HCDs). Test Type: "PSS" includes PSS, HTHB and similar older tests. (Data: regional model volume.)

Obj.	Data type	Test type	Elevation interval (masl)	Mean elev. (masl)	Test scale (m)	Sample size (Tot/left cens./ right cens.)	Mean Log_{10}(K-PSS) (K: m/s)	STD Log_{10}(K-PSS) (K: m/s)	95% Conf. Int. Log_{10}(K-PSS) Low (K: m/s)	95% Conf. Int. Log_{10}(K-PSS) High (K: m/s)	Corr. Coef.
All	HRD_Wa	PSS	> -150	-75	100	18/ 0/ 0	-6.57	0.66	-6.89	-6.24	0.96
All	HRD_Wa	PSS	-150 to -400	-275	100	12/ 1/ 0	-8.56	0.65	-8.98	-8.15	0.86
All	HRD_Wa	PSS	-400 to -650	-525	100	10/ 0/ 0	-9.25	1.68	-10.45	-8.04	0.95
All	HRD_Wa	PSS	< -650	-825	100	3/ 0/ 0	-12.05	0.80	-14.05	-10.05	1.00
HRD	HRD_Wa	PSS	> -150	-75	100	14/ 0/ 0	-6.67	0.59	-7.01	-6.33	0.94
HRD	HRD_Wa	PSS	-150 to -400	-275	100	9/ 1/ 0	-9.05	3.00	-11.36	-6.75	0.90
HRD	HRD_Wa	PSS	-400 to -650	-525	100	8/ 0/ 0	-9.63	1.64	-11.00	-8.26	0.94
HRD	HRD_Wa	PSS	< -650	-825	100	3/ 0/ 0	-12.05	0.80	-14.05	-10.05	1.00
All	HRD_C	PSS	> -150	-75	100	12/ 1/ 0	-6.94	1.02	-7.59	-6.30	0.94
All	HRD_C	PSS	-150 to -400	-275	100	16/ 0/ 0	-8.80	1.26	-9.47	-8.13	0.99
All	HRD_C	PSS	-400 to -650	-525	100	19/ 0/ 0	-9.09	1.73	-9.92	-8.26	0.99
All	HRD_C	PSS	< -650	-825	100	18/ 0/ 0	-9.66	1.50	-10.40	-8.91	0.97
HRD	HRD_C	PSS	> -150	-75	100	12/ 1/ 0	-6.94	1.02	-7.59	-6.30	0.94
HRD	HRD_C	PSS	-150 to -400	-275	100	14/ 0/ 0	-8.92	1.18	-9.60	-8.23	0.98
HRD	HRD_C	PSS	-400 to -650	-525	100	12/ 0/ 0	-9.82	1.47	-10.76	-8.89	0.95
HRD	HRD_C	PSS	< -650	-825	100	9/ 0/ 0	-10.52	1.40	-11.60	-9.44	0.99

HRD_Wa: KLX13A not included

Table A9-4.Table of results for all data samples made up of data on test scale 100m. Statistics for elevation intervals. Confidence interval for Mean Log_{10}(K-PSS). Object (Obj.): HCD: Test sections including one or more Hydraulic Conduction Domains and surrounding rock: HRD: Test sections including only Hydraulic Rock Domains All: Covers all data (includes HRDs and HCDs). Test Type: "PSS" includes PSS, HTHB and similar older tests. (Data: regional model volume.)

Obj.	Data type	Test type	Elevation interval (masl)	Mean elev. (masl)	Test scale (m)	Sample size (Tot/left cens./ right cens.)	Mean Log_{10}(K-PSS) (K: m/s)	STD Log_{10}(K-PSS) (K: m/s)	95% Conf. Int. Log_{10}(K-PSS) Low (K: m/s)	95% Conf. Int. Log_{10}(K-PSS) High (K: m/s)	Corr. Coef.
All	HRD_N	PSS	> -150	-75	100	13/ 0/ 0	-6.35	0.74	-6.80	-5.90	0.91
All	HRD_N	PSS	-150 to -400	-275	100	7/ 0/ 0	-6.62	1.36	-7.88	-5.36	0.85
All	HRD_N	PSS	-400 to -650	-525	100	4/ 0/ 0	-7.83	1.04	-9.48	-6.18	0.91
All	HRD_N	PSS	< -650	-825	100	2/ 0/ 0	(-9.14)	-	-	-	-
HRD	HRD_N	PSS	> -150	-75	100	7/ 0/ 0	-6.41	0.39	-6.77	-6.05	0.89
HRD	HRD_N	PSS	-150 to -400	-275	100	3/ 0/ 0	-6.28	0.60	-7.76	-4.80	1.00
HRD	HRD_N	PSS	-400 to -650	-525	100	4/ 0/ 0	-7.83	1.04	-9.48	-6.18	0.91
HRD	HRD_N	PSS	< -650	-825	100	2/ 0/ 0	(-9.14)	-	-	-	-
All	HRD_EW007	PSS	> -150	-75	100	12/ 1/ 0	-6.71	1.15	-7.44	-5.98	0.93
All	HRD_EW007	PSS	-150 to -400	-275	100	12/ 0/ 0	-6.56	1.22	-7.34	-5.79	0.85
All	HRD_EW007	PSS	-400 to -650	-525	100	12/ 0/ 0	-8.01	1.22	-8.78	-7.24	0.93
All	HRD_EW007	PSS	< -650	-825	100	1/ 0/ 0	(-7.00)				
HRD	HRD_EW007	PSS	> -150	-75	100	6/ 0/ 0	-6.69	1.04	-7.78	-5.60	0.94
HRD	HRD_EW007	PSS	-150 to -400	-275	100	4/ 0/ 0	-6.45	1.15	-8.28	-4.62	0.99
HRD	HRD_EW007	PSS	-400 to -650	-525	100	8/ 0/ 0	-8.40	1.35	-9.52	-7.27	0.92
HRD	HRD_EW007	PSS	< -650	-825	100	1/ 0/ 0	(-7.00)				

(xxx): values within brackets show the mean value of the few observations, that is very uncertain.

Table A9-5. Table of results for all data samples in test scale 100m. Trend models for hydraulic conductivity (m/s) in rock mass. Object (Obj.): HCD: Test sections including one or more Hydraulic Conduction Domains and surrounding rock: HRD: Test sections including only Hydraulic Rock Domains All: Covers all data (includes HRDs and HCDs). (Data: Regional and local model volume.)

Model ID	Depth trend model	Obj.	Data type	Coeff. a	Coeff. B	Corr, coeff. r^2
All-100-R-K1	Exp	All	Hydraulic conductivity. X=K, Regression on means for interval (4 data points). Regional model data.	-6.6752	0.003252	0.98
All-100-R-K2	Power	All	Hydraulic conductivity. X=K, Regression on means for interval (4 data points). Regional model data.	0.002741	-2.2088	0.89
HCD-100-R-K3	Exp	HCD	Hydraulic conductivity. X=K, Regression on means for interval (4 data points). Regional model data.	-6.3614	0.002558	0.86
HCD-100-R-K4	Power	HCD	Hydraulic conductivity. X=K, Regression on means for interval (4 data points). Regional model data.	0.0001797	-1.4886	0.57
HRD-100-R-K5	Exp	HRD	Hydraulic conductivity. X=K, Regression on means for interval (4 data points). Regional model data.	-6.8070	0.003562	0.96
HRD-100-R-K6	Power	HRD	Hydraulic conductivity. X=K, Regression on individual points. Regional model data	0.009268	-2.52758	0.94
All-100-L-K1	Exp	All	Hydraulic conductivity. X=K, Regression on means for interval (4 data points). Local model data.	-6.55094	0.003596	0.99
All-100-L-K2	Power	All	Hydraulic conductivity. X=K, Regression on means for interval (4 data points). Local model data.	0.013377	-2.49447	0.93
HCD-100-L-K3	Exp	HCD	Hydraulic conductivity. X=K, Regression on means for interval (4 data points). Local model data.	-6.30310	0.002761	0.93
HCD-100-L-K4	Power	HCD	Hydraulic conductivity. X=K, Regression on means for interval (4 data points). Local model data.	0.0006071	-1.71229	0.70
HRD-100-L-K5	Exp	HRD	Hydraulic conductivity. X=K, Regression on means for interval (4 data points). Local model data.	-6.674365	0.004020	0.97
HRD-100-L-K6	Power	HRD	Hydraulic conductivity. X=K, Regression on individual points. Local model data.	0.063167	-2.88754	0.98

Test scale 20m

A total of 775 test results with test scale 20m are available and are commented in Section 9.6.2 The associated statistics are shown in Table A9-6 through Table A9-8.

Table A9-6. Table of results for all data samples made up of data on test scale 20m. Statistics for elevation intervals. Confidence interval for Mean Log_{10}(K-PSS). Object (Obj.): HCD: Test sections including one or more Hydraulic Conduction Domains and surrounding rock: HRD: Test sections including only Hydraulic Rock Domains All: Covers all data (includes HRDs and HCDs). Test Type: "PSS" includes PSS, HTHB and similar older tests. (Data: regional model volume.)

Obj.	Data type	Test type	Elevation interval (masl)	Mean elev. (masl)	Test scale (m)	Sample size (Tot/left cens./ right cens.)	Mean Log_{10}(K-PSS) (K: m/s)	STD Log_{10}(K-PSS) (K: m/s)	95% Conf. Int. Log_{10}(K-PSS) Low (K: m/s)	95% Conf. Int. Log_{10}(K-PSS) High (K: m/s)	Corr. Coef.
All	Reg.mod	PSS	> -150	-75	20	95/ 0/ 0	-7.39	1.75	-7.75	-7.03	0.98
All	Reg.mod	PSS	-150 to -400	-275	20	279/ 25/ 0	-8.58	2.09	-8.83	-8.33	0.98
All	Reg.mod	PSS	-400 to -650	-525	20	247/ 36/ 0	-9.46	1.97	-9.70	-9.21	0.98
All	Reg.mod	PSS	< -650	-825	20	154/ 41/ 0	-10.02	1.77	-10.30	-9.74	0.98
HCD	Reg.mod	PSS	> -150	-75	20	17/ 0/ 0	-6.96	2.04	-8.01	-5.91	0.95
HCD	Reg.mod	PSS	-150 to -400	-275	20	58/ 0/ 0	-7.46	1.85	-7.95	-6.97	0.96
HCD	Reg.mod	PSS	-400 to -650	-525	20	43/ 3/ 0	-8.00	1.57	-8.48	-7.51	0.94
HCD	Reg.mod	PSS	< -650	-825	20	30/ 1/ 0	-8.57	1.13	-8.99	-8.15	0.94
HRD	Reg.mod	PSS	> -150	-75	20	78/ 0/ 0	-7.51	1.70	-7.89	-7.13	0.98
HRD	Reg.mod	PSS	-150 to -400	-275	20	221/ 25/ 0	-8.90	2.08	-9.17	-8.62	0.99
HRD	Reg.mod	PSS	-400 to -650	-525	20	204/ 33/ 0	-9.78	1.92	-10.05	-9.52	0.99
HRD	Reg.mod	PSS	< -650	-825	20	124/ 40/ 0	-10.48	1.82	-10.81	-10.16	0.98

Table A9-7. Table of results for all data samples made up of data on test scale 20m. Statistics for elevation intervals. Confidence interval for Mean Log_{10}(K-PSS). Object (Obj.): HCD: Test sections including one or more Hydraulic Conduction Domains and surrounding rock: HRD: Test sections including only Hydraulic Rock Domains All: Covers all data (includes HRDs and HCDs). Test Type: "PSS" includes PSS, HTHB and similar older tests. (Data: local model volume.)

Obj.	Data type	Test type	Elevation interval (masl)	Mean elev. (masl)	Test scale (m)	Sample size (Tot/left cens./ right cens.)	Mean Log_{10}(K-PSS) (K: m/s)	STD Log_{10}(K-PSS) (K: m/s)	95% Conf. Int. Log_{10}(K-PSS) Low (K: m/s)	95% Conf. Int. Log_{10}(K-PSS) High (K: m/s)	Corr. Coef.
All	Loc.mod	PSS	> -150	-75	20	83/ 0/ 0	-7.29	1.79	-7.68	-6.89	0.98
All	Loc.mod	PSS	-150 to -400	-275	20	243/ 24/ 0	-8.55	2.18	-8.82	-8.27	0.98
All	Loc.mod	PSS	-400 to -650	-525	20	205/ 36/ 0	-9.61	2.12	-9.91	-9.32	0.98
All	Loc.mod	PSS	< -650	-825	20	108/ 41/ 0	-10.67	1.90	-11.03	-10.31	0.97
HCD	Loc.mod	PSS	> -150	-75	20	17/ 0/ 0	-6.96	2.04	-8.01	-5.91	0.95
HCD	Loc.mod	PSS	-150 to -400	-275	20	58/ 0/ 0	-7.46	1.85	-7.95	-6.97	0.96
HCD	Loc.mod	PSS	-400 to -650	-525	20	38/ 3/ 0	-7.96	1.64	-8.50	-7.42	0.93
HCD	Loc.mod	PSS	< -650	-825	20	25/ 1/ 0	-8.63	1.10	-9.08	-8.17	0.92
HRD	Loc.mod	PSS	> -150	-75	20	66/ 0/ 0	-7.40	1.75	-7.84	-6.97	0.98
HRD	Loc.mod	PSS	-150 to -400	-275	20	185/ 24/ 0	-8.92	2.22	-9.25	-8.60	0.98
HRD	Loc.mod	PSS	-400 to -650	-525	20	167/ 33/ 0	-10.01	2.05	-10.33	-9.70	0.99
HRD	Loc.mod	PSS	< -650	-825	20	83/ 40/ 0	-11.45	1.73	-11.83	-11.08	0.98

Table A9-8. Table of results for all data samples made up of data on test scale 20m. Statistics for elevation intervals. Confidence interval for Mean Log_{10}(K-PSS). Object (Obj.): HCD: Test sections including one or more Hydraulic Conduction Domains and surrounding rock: HRD: Test sections including only Hydraulic Rock Domains All: Covers all data (includes HRDs and HCDs). Test Type: "PSS" includes PSS, HTHB and similar older tests. (Data: regional model volume.)

Obj.	Data type	Test type	Elevation interval (masl)	Mean elev. (masl)	Test scale (m)	Sample size (Tot/left cens./ right cens.)	Mean Log_{10}(K-PSS) (K: m/s)	STD Log_{10}(K-PSS) (K: m/s)	95% Conf. Int. Log_{10}(K-PSS) Low (K: m/s)	95% Conf. Int. Log_{10}(K-PSS) High (K: m/s)	Corr. Coef.
All	HRD_Wa	PSS	> -150	-75	20	24/ 0/ 0	-8.23	1.90	-9.03	-7.43	0.96
All	HRD_Wa	PSS	-150 to -400	-275	20	46/ 10/ 0	-10.02	2.59	-10.78	-9.25	0.99
All	HRD_Wa	PSS	-400 to -650	-525	20	40/ 12/ 0	-10.76	2.64	-11.60	-9.91	0.97
All	HRD_Wa	PSS	< -650	-825	20	8/ 7/ 0	(c. <-10)	-	-	-	-
HRD	HRD_Wa	PSS	> -150	-75	20	13/ 0/ 0	-8.36	2.08	-9.62	-7.11	0.94
HRD	HRD_Wa	PSS	-150 to -400	-275	20	39/ 10/ 0	-10.41	2.65	-11.27	-9.55	0.99
HRD	HRD_Wa	PSS	-400 to -650	-525	20	34/ 11/ 0	-11.10	2.55	-11.99	-10.21	0.95
HRD	HRD_Wa	PSS	< -650	-825	20	8/ 7/ 0	(c. <-10)	-	-	-	-
All	HRD_C	PSS	> -150	-75	20	30/ 0/ 0	-7.31	1.34	-7.81	-6.81	0.99
All	HRD_C	PSS	-150 to -400	-275	20	86/ 13/ 0	-9.52	1.89	-9.93	-9.11	0.98
All	HRD_C	PSS	-400 to -650	-525	20	97/ 18/ 0	-10.22	2.01	-10.62	-9.81	0.99
All	HRD_C	PSS	< -650	-825	20	87/ 29/ 0	-10.48	1.89	-10.88	-10.08	0.97
HRD	HRD_C	PSS	> -150	-75	20	30/ 0/ 0	-7.31	1.34	-7.81	-6.81	0.99
HRD	HRD_C	PSS	-150 to -400	-275	20	75/ 13/ 0	-9.61	1.82	-10.03	-9.19	0.98
HRD	HRD_C	PSS	-400 to -650	-525	20	81/ 17/ 0	-10.57	1.75	-10.95	-10.18	0.99
HRD	HRD_C	PSS	< -650	-825	20	62/ 28/ 0	-11.40	1.67	-11.83	-10.98	0.98

HRD_Wa: KLX13A not included in HRD_W

(c. <xxx): Values within brackets and < sign shows that all or almost all measurement below measurement limit value estimated to xxx.

Test scale 5m

A total of 898 test results with test scale 5m are available and are commented in Section 9.6.3. The associated statistics are shown in Table A9-9 to Table A9-11. As almost all tests in 5m test scale have been performed between elevation -300m and -700m, the statistics based on the few samples above elevation -150m and below -650m are considered very uncertain.

Table A9-9. Table of results for all data samples made up of data on test scale 5m. Statistics for elevation intervals. Confidence interval for Mean Log_{10}(K-PSS). Object (Obj.): HCD: Test sections including one or more Hydraulic Conduction Domains and surrounding rock: HRD: Test sections including only Hydraulic Rock Domains All: Covers all data (includes HRDs and HCDs). Test Type: "PSS" includes PSS, HTHB and similar older tests. (Data: regional model volume.)

Obj.	Data type	Test type	Elevation interval (masl)	Mean elev. (masl)	Test scale (m)	Sample size (Tot/left cens./ right cens.)	Mean Log_{10}(K-PSS) (K: m/s)	STD Log_{10}(K-PSS) (K: m/s)	95% Conf. Int. Log_{10}(K-PSS) Low (K: m/s)	95% Conf. Int. Log_{10}(K-PSS) High (K: m/s)	Corr. Coef.
All	Reg.mod	PSS	> -150	-75	5	3/ 0/ 0	-5.76	2.07	-10.91	-0.61	-
All	Reg.mod	PSS	-150 to -400	-275	5	304/ 81/ 0	-9.75	2.19	-10.00	-9.51	0.98
All	Reg.mod	PSS	-400 to -650	-525	5	558/ 0/ 228	-10.45	2.25	-10.64	-10.26	0.98
All	Reg.mod	PSS	< -650	-825	5	33/ 0/ 15	-10.34	1.85	-11.00	-9.69	0.96
HCD	Reg.mod	PSS	> -150	-75	5	1/ 0/ 0	(-6.65)	-			-
HCD	Reg.mod	PSS	-150 to -400	-275	5	40/ 2/ 0	-7.79	1.40	-8.24	-7.35	0.92
HCD	Reg.mod	PSS	-400 to -650	-525	5	81/ 17/ 0	-8.78	1.97	-9.21	-8.34	0.97
HCD	Reg.mod	PSS	< -650	-825	5	5/ 1/ 0	-8.86	2.61	-12.10	-5.62	0.93
HRD	Reg.mod	PSS	> -150	-75	5	2/ 0/ 0	(-4.44)	-			-
HRD	Reg.mod	PSS	-150 to -400	-275	5	264/ 79/ 0	-10.15	2.27	-10.42	-9.87	0.99
HRD	Reg.mod	PSS	-400 to -650	-525	5	477/ 211/ 0	-10.76	2.18	-10.95	-10.56	0.99
HRD	Reg.mod	PSS	< -650	-825	5	28/ 14/ 0	-10.63	1.64	-11.26	-9.99	0.94

(xxx): values within brackets show the mean value of the few observations, that is very uncertain.

Table A9-10. Table of results for all data samples made up of data on test scale 5m. Statistics for elevation intervals. Confidence interval for Mean Log_{10}(K-PSS). Object (Obj.): HCD: Test sections including one or more Hydraulic Conduction Domains and surrounding rock: HRD: Test sections including only Hydraulic Rock Domains All: Covers all data (includes HRDs and HCDs). Test Type: "PSS" includes PSS, HTHB and similar older tests. (Data: local model volume.)

Obj.	Data type	Test type	Elevation interval	Mean elev.	Test scale	Sample size (Tot/left cens./ right cens.)	Mean Log_{10}(K-PSS)	STD Log_{10}(K-PSS)	95% Conf. Int. Log_{10}(K-PSS) Low	95% Conf. Int. Log_{10}(K-PSS) High	Corr. Coef.
			(masl)	(masl)	(m)		(K: m/s)	(K: m/s)	(K: m/s)	(K: m/s)	
All	Loc.mod	PSS	> -150	-75	5	3/ 0/ 0	-5.76	2.07	-10.91	-0.61	-
All	Loc.mod	PSS	-150 to -400	-275	5	260/ 80/ 0	-9.77	2.35	-10.06	-9.49	0.96
All	Loc.mod	PSS	-400 to -650	-525	5	456/ 196/ 0	-10.52	2.39	-10.74	-10.30	0.98
All	Loc.mod	PSS	< -650	-825	5	20/ 12/ 0	-11.60	2.71	-12.87	-10.34	0.96
HCD	Loc.mod	PSS	> -150	-75	5	1/ 0/ 0	(-6.65)	-			-
HCD	Loc.mod	PSS	-150 to -400	-275	5	40/ 2/ 0	-7.79	1.40	-8.24	-7.35	0.92
HCD	Loc.mod	PSS	-400 to -650	-525	5	63/ 14/ 0	-8.53	1.92	-9.01	-8.05	0.95
HCD	Loc.mod	PSS	< -650	-825	5	3/ 0/ 0	-7.41	0.20	-7.91	-6.92	-
HRD	Loc.mod	PSS	> -150	-75	5	2/ 0/ 0	(-4.44)	-			-
HRD	Loc.mod	PSS	-150 to -400	-275	5	220/ 78/ 0	-10.35	2.02	-10.61	-10.08	0.98
HRD	Loc.mod	PSS	-400 to -650	-525	5	393/ 182/ 0	-10.88	2.32	-11.11	-10.65	0.98
HRD	Loc.mod	PSS	< -650	-825	5	16/ 11/ 0	-11.55	1.22	-12.20	-10.90	0.88

(xxx): values within brackets show the mean value of the few observations, that is very uncertain.

Table A9-11. Table of results for all data samples made up of data on test scale 5m. Statistics for elevation intervals. Confidence interval for Mean Log_{10}(K-PSS). Object (Obj.): HCD: Test sections including one or more Hydraulic Conduction Domains and surrounding rock: HRD: Test sections including only Hydraulic Rock Domains All: Covers all data (includes HRDs and HCDs). Test Type: "PSS" includes PSS, HTHB and similar older tests. (Data: regional model volume.)

Obj.	Data type	Test type	Elevation interval (masl)	Mean elev. (masl)	Test scale (m)	Sample size (Tot/left cens./ right cens.)	Mean Log_{10}(K-PSS) (K: m/s)	STD Log_{10}(K-PSS) (K: m/s)	95% Conf. Int. Log_{10}(K-PSS) Low (K: m/s)	95% Conf. Int. Log_{10}(K-PSS) High (K: m/s)	Corr. Coef.
All	HRD_Wa	PSS	> -150	-75	5	2/ 0/ 0	(-4.44)	-	-	-	-
All	HRD_Wa	PSS	-150 to -400	-275	5	75/ 25/ 0	-10.56	2.93	-11.24	-9.89	0.97
All	HRD_Wa	PSS	-400 to -650	-525	5	145/ 67/ 0	-11.59	2.98	-12.08	-11.10	0.97
All	HRD_Wa	PSS	< -650	-825	5	0/ 0/ 0					
HRD	HRD_Wa	PSS	> -150	-75	5	2/ 0/ 0	(-4.44)	-	-	-	-
HRD	HRD_Wa	PSS	-150 to -400	-275	5	63/ 25/ 0	-11.58	3.20	-12.39	-10.78	0.98
HRD	HRD_Wa	PSS	-400 to -650	-525	5	126/ 61/ 0	-11.96	2.77	-12.45	-11.47	0.98
HRD	HRD_Wa	PSS	< -650	-825	5	0/ 0/ 0					
All	HRD_C	PSS	> -150	-75	5	0/ 0/ 0					
All	HRD_C	PSS	-150 to -400	-275	5	85/ 46/ 0	-10.93	2.34	-11.43	-10.42	0.97
All	HRD_C	PSS	-400 to -650	-525	5	226/ 118/ 0	-10.39	2.19	-10.68	-10.10	0.98
All	HRD_C	PSS	< -650	-825	5	17/ 11/ 0	-12.49	3.47	-14.28	-10.70	0.96
HRD	HRD_C	PSS	> -150	-75	5	0/ 0/ 0					
HRD	HRD_C	PSS	-150 to -400	-275	5	85/ 46/ 0	-10.93	2.34	-11.43	-10.42	0.97
HRD	HRD_C	PSS	-400 to -650	-525	5	182/ 110/ 0	-10.91	2.01	-11.20	-10.61	0.97
HRD	HRD_C	PSS	< -650	-825	5	14/ 11/ 0	-12.60	1.79	-13.64	-11.57	0.97

HRD_Wa: KLX13A not included in HRD_W

(xxx): values within brackets show the mean value of the few observations, that is very uncertain.

Hydraulic conductivity of rock types and sections with crush

The hydraulic conductivity of the rock mass (between the deterministically defined deformation zones) based on PFL-s (5m section) has been analysed with regards to rock type. The influence of smaller veins of fine-grained granite on the hydraulic conductivity is also studied in this section.

The mapping of the cores differentiates between"rock type" and "rock occurence". The rock type is mapped under "rock type" if the mapped length is >1m borehole length and under "rock occurrence" if the mapped length is <1m borehole length. The rock types, and related rock codes, for "rock types" and "rock occurrences" used in the geological mapping is shown in Table A9-12.

Table A9-12. Igneous rock types in the Laxemar-Simpevarp area and their relative age relationships. The rock codes for each rock type employed by SKB are shown within brackets. Reproduced from /Wahlgren et al. 2008/

Rock type	Relative age
Dolerite (501027)	Youngest
Götemar and Uthammar granites (521058)	
Fine-grained granite (511058) and pegmatite (501061)	
Fine-grained diorite-gabbro (505102)	
Granite, equigranular (501058)	
Ävrö granite (501044)/Ävrö quartz monzodiorite (501046)	
Quartz monzodiorite (501036)	
Diorite-gabbro (501033)	
Fine-grained dioritoid (501030)	Oldest

The statistics for different subsets of the entire data sets of PFL-s data are shown in figures in Section 9.7 and Table A9-13 through Table A9-19.

The entire sample of 5m PFL-s measurements comprises 4036 tests of which 3379 are associated with rock between deterministic deformation zones (corresponding to HCD). Table A9-13 shows the statistics for the entire sample of data between HCDs. In this table also a subset including all sections with fine-grained granite (511058) is shown.

Test sections intersected by a crushed zone are significantly more conductive than sections without a crushed zone, see Table A9-14 .

In Table A9-15 through Table A9-19 the statistics are shown for all rock types. Concerning Dolerite (501027) the only data available were from borehole sections intersected by deformation zones, but still used in the statistics here.

Table A9-13. Tabulation of results for all defined data samples (data sets) of test scale 5m (3m in KLX02). Statistics for elevation intervals. Statistical models for hydraulic conductivity (m/s) between deterministically interpreted deformation zones (DZ). Confidence interval for Mean Log_{10}(K-PFL-s). Obj.: HRD: Data from test sections includes only Hydraulic Rock Domains (No HCDs). Data type: All RT: All rock types, All RT R-occ:511058: All rock types and with test section with rock occurrence=511058, Selection (Sel.): D: Test section with rock type dominating. (Data: Regional model volume)

Obj.	Data type	Sel.	Test type	Elevation interval (masl)	Mean elev. (masl)	Test scale (m)	Sample size (Tot/left cens./ right cens.) (1)	Mean Log_{10}(K-PFL-s) (K: m/s)	STD Log_{10}(K-PFL-s) (K: m/s)	95% Conf. Int. Log_{10}(K-PFL-s) Low (K: m/s)	95% Conf. Int. Log_{10}(K-PFL-s) High (K: m/s)	Corr. Coef.
HRD	All RT	D	PFL	> -150	-75	5	703/ 228/ 11	-8.31	1.56	-8.43	-8.20	0.99
HRD	All RT	D	PFL	-150 to -400	-275	5	1087/ 702/ 3	-10.03	1.94	-10.15	-9.92	0.99
HRD	All RT	D	PFL	-400 to -650	-525	5	954/ 764/ 1	-10.89	1.91	-11.02	-10.77	0.97
HRD	All RT	D	PFL	< -650	-825	5	635/ 569/ 0	-11.60	2.02	-11.76	-11.44	0.94
HRD	All RT, R-occ: 511058	D	PFL	> -150	-75	5	334/ 111/ 5	-8.30	1.55	-8.46	-8.13	0.99
HRD	All RT, R-occ: 511058	D	PFL	-150 to -400	-275	5	436/ 304/ 0	-10.33	1.98	-10.52	-10.14	0.98
HRD	All RT, R-occ: 511058	D	PFL	-400 to -650	-525	5	326/ 258/ 0	-10.83	1.96	-11.04	-10.62	0.97
HRD	All RT, R-occ: 511058	D	PFL	< -650	-825	5	257/ 236/ 0	-11.97	2.06	-12.22	-11.71	0.93

(1): Lower measurement limit c. =$2 \cdot 10^{-10}$ m/s, Upper measurement limit ca=$2 \cdot 10^{-6}$ m/s assuming a drawdown of 10m. Left censored values are below lower measurement limit and right censored values are above upper measurement limit.

Table A9-14. Tabulation of results for all defined data samples (data sets) of test scale 5m (3m in KLX02). Statistics for elevation intervals. Statistical models for hydraulic conductivity (m/s) between deterministically interpreted deformation zones (DZ). Confidence interval for Mean Log_{10}(K-PFL-s). Object (Obj.): HRD: Data from test sections includes only Hydraulic Rock Domains (No HCDs). Data type: All RT, No crush: no crush in test section, All RT, crush: crush in test section: All RT, crush-MDZ: crush in test section witch is within a MDZ, Selection (Sel.): D: Test section with rock type dominating. (Data: Regional model volume)

Obj.	Data type	Sel.	Test type	Elevation interval (masl)	Mean elev. (masl)	Test scale (m)	Sample size (Tot/left cens./ right cens.) (1)	Mean Log_{10}(K-PFL-s) (K: m/s)	STD Log_{10}(K-PFL-s) (K: m/s)	95% Conf. Int. Log_{10}(K-PFL-s) Low (K: m/s)	95% Conf. Int. Log_{10}(K-PFL-s) High (K: m/s)	Corr. Coef.
HRD	All RT, No crush	D	PFL	> -150	-75	5	668/ 226/ 8	-8.40	1.54	-8.51	-8.28	0.99
HRD	All RT, No crush	D	PFL	-150 to -400	-275	5	1038/ 692/ 3	-10.11	1.83	-10.22	-10.00	0.99
HRD	All RT, No crush	D	PFL	-400 to -650	-525	5	894/ 742/ 0	-11.15	1.91	-11.28	-11.03	0.97
HRD	All RT, No crush	D	PFL	< -650	-825	5	582/ 541/ 0	-12.18	2.02	-12.34	-12.01	0.92
HRD	All RT, crush	D	PFL	> -150	-75	5	35/ 2/ 3	-6.78	1.25	-7.21	-6.36	0.97
HRD	All RT, crush	D	PFL	-150 to -400	-275	5	49/ 10/ 0	-7.65	1.49	-8.07	-7.22	0.95
HRD	All RT, crush	D	PFL	-400 to -650	-525	5	60/ 22/ 1	-8.60	1.42	-8.97	-8.23	0.98
HRD	All RT, crush	D	PFL	< -650	-825	5	53/ 28/ 0	-9.08	1.58	-9.52	-8.65	0.93
HRD	All RT, crush-MDZ	D	PFL	> -150	-75	5	21/ 0/ 3	-6.47	1.03	-6.94	-6.00	0-97
HRD	All RT, crush-MDZ	D	PFL	-150 to -400	-275	5	27/ 6/ 0	-7.51	1.66	-8.17	-6.86	0.92
HRD	All RT, crush-MDZ	D	PFL	-400 to -650	-525	5	25/ 6/ 1	-8.29	1.37	-8.86	-7.73	0.99
HRD	All RT, crush-MDZ	D	PFL	< -650	-825	5	6/ 3/ 0	-9.05	1.28	-10.40	-7.70	0.88

(1): Lower measurement limit ca=$2 \cdot 10^{-10}$ m/s, Upper measurement limit ca=$2 \cdot 10^{-6}$ m/s assuming a drawdown of 10m. Left censored values are below lower measurement limit and right censord values are above upper measurement limit.

Table A9-15. Tabulation of results for all defined data samples (data sets) of test scale 5m (3m in KLX02). Statistics for elevation intervals. Statistical models for hydraulic conductivity (m/s) between deterministically defined deformation zones (DZ). Confidence interval for Mean Log_{10}(K-PFL-s). Object (Obj.): HRD: Data from test sections includes only Hydraulic Rock Domains (No HCDs). Object (Obj.): HRD: A Test section includes only Hydraulic Rock Domains (No HCDs). Selection (Sel.): D: Test section with rock type dominating, 100: 100% of rock type (in Data type) in test section. (Data: Regional model volume)

Obj.	Data type	Sel.	Test type	Elevation interval	Mean elev.	Test scale	Sample size (Tot/left cens./ right cens.) (1)	Mean Log_{10}(K-PFL-s) (2)	STD Log_{10}(K-PFL-s)	95% Conf. Int. Log_{10}(K-PFL-s) Low	95% Conf. Int. Log_{10}(K-PFL-s) High	Corr. Coef.
				(masl)	(masl)	(m)		(K: m/s)	(K: m/s)	(K: m/s)	(K: m/s)	
HRD	501027	D	PFL	> -150	-75	5	10/ 10/ 0	< -9.7	-	-	-	
HRD	501027	D	PFL	-150 to -400	-275	5	2/ 2/ 0	< -9.3	-	-	-	
HRD	501027	D	PFL	-400 to -650	-525	5	10/ 10/ 0	< -9.3	-	-	-	
HRD	501027	D	PFL	< -650	-825	5	0/ 0/ 0	-	-	-	-	
HRD	501027	100	PFL	> -150	-75	5	7/ 7/ 0	< -9.7	-	-	-	
HRD	501027	100	PFL	-150 to -400	-275	5	2/ 2/ 0	< -9.3	-	-	-	
HRD	501027	100	PFL	-400 to -650	-525	5	7/ 7/ 0	< -9.3	-	-	-	
HRD	501027	100	PFL	< -650	-825	5	0/ 0/ 0	-	-	-	-	
HRD	501030	D	PFL	> -150	-75	5	20/ 10/ 0	-8.97	1.22	-9.54	-8.40	0.89
HRD	501030	D	PFL	-150 to -400	-275	5	92/ 63/ 0	-9.77	1.39	-10.06	-9.48	0.94
HRD	501030	D	PFL	-400 to -650	-525	5	88/ 73/ 1	-11.37	2.26	-11.85	-10.89	0.91
HRD	501030	D	PFL	< -650	-825	5	95/ 83/ 0	-11.56	2.16	-12.00	-11.12	0.85
HRD	501030	100	PFL	> -150	-75	5	18/ 9/ 0	-8.86	1.27	-9.49	-8.23	0.85
HRD	501030	100	PFL	-150 to -400	-275	5	72/ 51/ 0	-10.11	1.53	-10.47	-9.75	0.96
HRD	501030	100	PFL	-400 to -650	-525	5	61/ 53/ 0	-11.96	2.32	-12.55	-11.36	0.82
HRD	501030	100	PFL	< -650	-825	5	74/ 66/ 0	-11.97	2.30	-12.51	-11.44	0.77

(1): Lower measurement limit ca=$2 \cdot 10^{-10}$ m/s, Upper measurement limit ca=$2 \cdot 10^{-6}$ m/s assuming a drawdown of 10m. Left censored values are below lower measurement limit and right censord values are above upper measurement limit.

(2) Values within brackets; (-7.8) indicate that there are 1-2 measurement above measurement limit, Values indicated; < -9.7 shows that all measurement are blow a certain measurement limit, in this case -9.7.

Table A9-16. Tabulation of results for all defined data samples (data sets) of test scale 5m (3m in KLX02). Statistics for elevation intervals. Statistical models for hydraulic conductivity (m/s) between deterministically defined deformation zones (DZ). Confidence interval for Mean Log_{10}(K-PFL-s). Object (Obj.): HRD: Data from test sections includes only Hydraulic Rock Domains (No HCDs). Object (Obj.): HRD: A Test section includes only Hydraulic Rock Domains (No HCDs). Selection (Sel.): D: Test section with rock type dominating, 100: 100% of rock type (in Data type) in test section. (Data: Regional model volume)

Obj.	Data type	Sel.	Test type	Elevation interval	Mean elev.	Test scale	Sample size (Tot/left cens./ right cens.) (1)	Mean Log_{10}(K-PFL-s) (2)	STD Log_{10}(K-PFL-s)	95% Conf. Int. Log_{10}(K-PFL-s) Low	95% Conf. Int. Log_{10}(K-PFL-s) High	Corr. Coef.
				(masl)	(masl)	(m)		(K: m/s)	(K: m/s)	(K: m/s)	(K: m/s)	
HRD	501033	D	PFL	> -150	-75	5	11/ 9/ 0	-12.53	3.02	-14.56	-10.50	-
HRD	501033	D	PFL	-150 to -400	-275	5	30/ 23/ 0	-10.89	1.74	-11.54	-10.24	0.88
HRD	501033	D	PFL	-400 to -650	-525	5	39/ 32/ 0	-11.17	2.31	-11.92	-10.42	0.91
HRD	501033	D	PFL	< -650	-825	5	0/ 0/ 0	-	-	-	-	
HRD	501033	100	PFL	> -150	-75	5	0/ 0/ 0	-	-	-	-	
HRD	501033	100	PFL	-150 to -400	-275	5	17/ 13/ 0	-9.80	0.20	-9.90	-9.69	0.79
HRD	501033	100	PFL	-400 to -650	-525	5	26/ 24/ 0	-16.34	4.60	-18.20	-14.48	-
HRD	501033	100	PFL	< -650	-825	5	0/ 0/ 0	-	-	-	-	
HRD	501036	D	PFL	> -150	-75	5	303/ 94/ 5	-8.31	1.45	-8.48	-8.15	0.99
HRD	501036	D	PFL	-150 to -400	-275	5	284/ 237/ 0	-11.78	2.53	-12.08	-11.49	0.99
HRD	501036	D	PFL	-400 to -650	-525	5	273/ 235/ 0	-11.70	2.33	-11.98	-11.43	0.97
HRD	501036	D	PFL	< -650	-825	5	219/ 211/ 0	-13.71	2.23	-14.00	-13.41	0.98
HRD	501036	100	PFL	> -150	-75	5	286/ 88/ 5	-8.30	1.45	-8.47	-8.14	0.99
HRD	501036	100	PFL	-150 to -400	-275	5	266/ 225/ 0	-12.02	2.57	-12.33	-11.71	0.99
HRD	501036	100	PFL	-400 to -650	-525	5	237/ 208/ 0	-12.01	2.39	-12.32	-11.70	0.98
HRD	501036	100	PFL	< -650	-825	5	187/ 182/ 0	-12.93	1.66	-13.17	-12.69	0.90

(1): Lower measurement limit ca=$2 \cdot 10^{-10}$ m/s, Upper measurement limit ca=$2 \cdot 10^{-6}$ m/s assuming a drawdown of 10m. Left censored values are below lower measurement limit and right censord values are above upper measurement limit.

(2) Values within brackets; (-7.8) indicate that there are 1-2 measurement above measurement limit, Values indicated; < -9.7 shows that all measurement are blow a certain measurement limit, in this case -9.7.

Table A9-17. Tabulation of results for all defined data samples (data sets) of test scale 5m (3m in KLX02). Statistics for elevation intervals. Statistical models for hydraulic conductivity (m/s) between deterministically defined deformation zones (DZ). Confidence interval for Mean Log_{10}(K-PFL-s). Object (Obj.): HRD: Data from test sections includes only Hydraulic Rock Domains (No HCDs). Object (Obj.): HRD: A Test section includes only Hydraulic Rock Domains (No HCDs). Selection (Sel.): D: Test section with rock type dominating, 100: 100% of rock type (in Data type) in test section. (Data: Regional model volume)

Obj.	Data type	Sel.	Test type	Elevation interval	Mean elev.	Test scale	Sample size (Tot/left cens./ right cens.) (1)	Mean Log_{10}(K-PFL-s) (2)	STD Log_{10}(K-PFL-s)	95% Conf. Int. Log_{10}(K-PFL-s) Low	95% Conf. Int. Log_{10}(K-PFL-s) High	Corr. Coef.
				(masl)	(masl)	(m)		(K: m/s)	(K: m/s)	(K: m/s)	(K: m/s)	
HRD	501044	D	PFL	> -150	-75	5	326/ 99/ 5	-8.15	1.57	-8.32	-7.98	0.99
HRD	501044	D	PFL	-150 to -400	-275	5	623/ 345/ 3	-9.59	1.83	-9.74	-9.45	0.99
HRD	501044	D	PFL	-400 to -650	-525	5	482/ 377/ 0	-10.81	1.85	-10.97	-10.64	0.97
HRD	501044	D	PFL	< -650	-825	5	244/ 222/ 0	-11.33	1.83	-11.56	-11.10	0.85
HRD	501044	100	PFL	> -150	-75	5	280/ 79/ 5	-8.11	1.58	-8.29	-7.92	0.99
HRD	501044	100	PFL	-150 to -400	-275	5	549/ 294/ 3	-9.50	1.80	-9.65	-9.35	0.99
HRD	501044	100	PFL	-400 to -650	-525	5	407/ 321/ 0	-10.99	1.98	-11.18	-10.80	0.96
HRD	501044	100	PFL	< -650	-825	5	192/ 169/ 0	-11.24	1.85	-11.51	-10.98	0.84
HRD	501058	D	PFL	> -150	-75	5	2/ 2/ 0	(-7.8)	-	-	-	
HRD	501058	D	PFL	-150 to -400	-275	5	23/ 12/ 0	-9.64	1.77	-10.41	-8.88	0.96
HRD	501058	D	PFL	-400 to -650	-525	5	10/ 7/ 0	-10.93	2.52	-12.73	-9.13	0.97
HRD	501058	D	PFL	< -650	-825	5	14/ 13/ 0	(-9.2) , low	-	-	-	
HRD	501058	100	PFL	> -150	-75	5	0/ 0/ 0	-	-	-	-	
HRD	501058	100	PFL	-150 to -400	-275	5	10/ 7/ 0	-11.15	2.23	-12.74	-9.56	-
HRD	501058	100	PFL	-400 to -650	-525	5	4/ 3/ 0	(-5.9)	-	-	-	
HRD	501058	100	PFL	< -650	-825	5	6/ 5/ 0	(-9.2)	-	-	-	

(1): Lower measurement limit ca=$2 \cdot 10^{-10}$ m/s, Upper measurement limit ca=$2 \cdot 10^{-6}$ m/s assuming a drawdown of 10m. Left censored values are below lower measurement limit and right censord values are above upper measurement limit.

(2) Values within brackets; (-7.8) indicate that there are 1-2 measurement above measurement limit, Values indicated; < -9.7 shows that all measurement are blow a certain measurement limit, in this case -9.7.

Table A9-18. Tabulation of results for all defined data samples (data sets) of test scale 5m (3m in KLX02). Statistics for elevation intervals. Statistical models for hydraulic conductivity (m/s) between deterministically defined deformation zones (DZ). Confidence interval for Mean Log_{10}(K-PFL-s). Object (Obj.): HRD: Data from test sections includes only Hydraulic Rock Domains (No HCDs). Object (Obj.): HRD: A Test section includes only Hydraulic Rock Domains (No HCDs). Selection (Sel.): D: Test section with rock type dominating, 100: 100% of rock type (in Data type) in test section. (Data: Regional model volume)

Obj.	Data type	Sel.	Test type	Elevation interval (masl)	Mean elev. (masl)	Test scale (m)	Sample size (Tot/left cens./ right cens.) (1)	Mean Log_{10}(K-PFL-s) (2) (K: m/s)	STD Log_{10}(K-PFL-s) (K: m/s)	95% Conf. Int. Log_{10}(K-PFL-s) Low (K: m/s)	95% Conf. Int. Log_{10}(K-PFL-s) High (K: m/s)	Corr. Coef.
HRD	501061	D	PFL	> -150	-75	5	0/ 0/ 0	-	-	-	-	
HRD	501061	D	PFL	-150 to -400	-275	5	0/ 0/ 0	-	-	-	-	
HRD	501061	D	PFL	-400 to -650	-525	5	5/ 4/ 0	(-8.9)	-	-	-	
HRD	501061	D	PFL	< -650	-825	5	0/ 0/ 0	-	-	-	-	
HRD	501061	100	PFL	> -150	-75	5	0/ 0/ 0	-	-	-	-	
HRD	501061	100	PFL	-150 to -400	-275	5	0/ 0/ 0	-	-	-	-	
HRD	501061	100	PFL	-400 to -650	-525	5	1/ 1/ 0	(-9.7)	-	-	-	
HRD	501061	100	PFL	< -650	-825	5	0/ 0/ 0	-	-	-	-	
HRD	505102	D	PFL	> -150	-75	5	17/ 2/ 1	-8.08	1.34	-8.77	-7.39	0.99
HRD	505102	D	PFL	-150 to -400	-275	5	26/ 20/ 0	-12.18	3.61	-13.63	-10.72	0.97
HRD	505102	D	PFL	-400 to -650	-525	5	26/ 16/ 0	-9.78	0.99	-10.18	-9.38	0.97
HRD	505102	D	PFL	< -650	-825	5	13/ 12/ 0	(-7.8), low	-	-	-	
HRD	505102	100	PFL	> -150	-75	5	4/ 1/ 0	-9.03	0.92	-10.50	-7.56	0.99
HRD	505102	100	PFL	-150 to -400	-275	5	6/ 4/ 0	-9.94	0.56	-10.52	-9.35	-
HRD	505102	100	PFL	-400 to -650	-525	5	13/ 9/ 0	-10.20	1.26	-10.96	-9.44	0.96
HRD	505102	100	PFL	< -650	-825	5	2/ 1/ 0	(-7.8)	-	-	-	

(1): Lower measurement limit ca=$2 \cdot 10^{-10}$ m/s, Upper measurement limit ca=$2 \cdot 10^{-6}$ m/s assuming a drawdown of 10m. Left censored values are below lower measurement limit and right censord values are above upper measurement limit.

(2) Values within brackets; (-7.8) indicate that there are 1-2 measurement above measurement limit, Values indicated; < -9.7 shows that all measurement are blow a certain measurement limit, in this case -9.7.

Table A9-19. Tabulation of results for all defined data samples (data sets) of test scale 5m (3m in KLX02). Statistics for elevation intervals. Statistical models for hydraulic conductivity (m/s) between deterministically defined deformation zones (DZ). Confidence interval for Mean Log_{10}(K-PFL-s). Object (Obj.): HRD: Data from test sections includes only Hydraulic Rock Domains (No HCDs). Object (Obj.): HRD: A Test section includes only Hydraulic Rock Domains (No HCDs). Selection (Sel.): D: Test section with rock type dominating, 100: 100% of rock type (in Data type) in test section. (Data: Regional model volume)

Obj.	Data type	Sel.	Test type	Elevation interval	Mean elev.	Test scale	Sample size (Tot/left cens./ right cens.) (1)	Mean Log_{10}(K-PFL-s) (2)	STD Log_{10}(K-PFL-s)	95% Conf. Int. Log_{10}(K-PFL-s) Low	95% Conf. Int. Log_{10}(K-PFL-s) High	Corr. Coef.
				(masl)	(masl)	(m)		(K: m/s)	(K: m/s)	(K: m/s)	(K: m/s)	
HRD	511058	D	PFL	> -150	-75	5	13/ 1/ 0	-7.73	1.34	-8.54	-6.91	0.98
HRD	511058	D	PFL	-150 to -400	-275	5	9/ 2/ 0	-9.05	0.88	-9.73	-8.37	0.96
HRD	511058	D	PFL	-400 to -650	-525	5	31/ 20/ 0	-9.92	1.42	-10.44	-9.40	0.95
HRD	511058	D	PFL	< -650	-825	5	33/ 16/ 0	-9.14	1.58	-9.70	-8.58	0.96
HRD	511058	100	PFL	> -150	-75	5	1/ 0/ 0	(-7.1)	-	-	-	
HRD	511058	100	PFL	-150 to -400	-275	5	4/ 1/ 0	-8.84	1.51	-11.25	-6.43	0.00
HRD	511058	100	PFL	-400 to -650	-525	5	16/ 9/ 0	-9.81	1.30	-10.50	-9.11	0.95
HRD	511058	100	PFL	< -650	-825	5	23/ 11/ 0	-9.11	1.75	-9.86	-8.35	0.95

(1): Lower measurement limit ca=$2 \cdot 10^{-10}$ m/s, Upper measurement limit ca=$2 \cdot 10^{-6}$ m/s assuming a drawdown of 10m. Left censored values are below lower measurement limit and right censord values are above upper measurement limit.

(2) Values within brackets; (-7.8) indicate that there are 1-2 measurement above measurement limit, Values indicated; < -9.7 shows that all measurement are blow a certain measurement limit, in this case -9.7.

A.9.2 Comparison of PSS hydraulic conductivity data from surface boreholes at Äspö and Laxemar, test scales 3-5m and 30-20m

Background

PSS tests were performed in tests scales 3, 30 and 100m during the site investigation program for ÄspöHRL. During Site investigation for a deep repository the test scales have been 5, 20 and 100m. In this section tests located on Äspö from surface drilled core hole with test scales 3 and 30m are compared with tests on Laxemar in HRD_C, HRD_W and HRD_EW007, south of deformation zone ZSM_EW007, with test scales 5, 20m. Data plotted includes HRDs and HCDs.

Test sections and data used

The number of data available from the two sites and depth intervals is shown in Table A9-20 and the boreholes that are used for the comparison are shown in Table A9-21. 3m tests sections cover KAS02-08 boreholes but 30m test sections are only available in boreholes KAS02 and KAS03 on Äspö. 20 m tests are available in KLX02-05, KLX07A, KLX08, KLX10, KLX11A, KLX12A and KLX15A – KLX21B. 5m tests in the KLX boreholes are limited to KLX01, KLX04, KLX10-15A, KLX17A-KL19A and KLX21B. There are tests of 5 and 20m scale in KLX27A but they are not included as the data are not used in the SDM-Site Laxemar modelling.

Table A9-20. The number of data available from the two sites and depth intervals.

Elevation (m)	Number of Äspö data scale 3 m	Number of Laxemar data scale 5 m	Number of Äspö data scale 30 m	Number of Laxemar data scale 20 m
0 to -150	135	3	4	63
-150 to -400	646	243	18	198
-400 to -650	276	456	19	183
-650 and downwards	47	19	7	97
Total	1104	721	48	541

Table A9-21. Boreholes sections compared.

Borehole	Data used from section (3 or 5 m)	Data used from section (20 or 30 m)
KAS02	102 – 801	102 – 812
KAS03	103 – 550	103 – 733
KAS04	133 – 457	-
KAS05	157 – 541	-
KAS06	105 – 591	-
KAS07	106 – 592	-
KAS08	106 – 580	-
KLX02	300 – 545	204 – 1004
KLX03	-	106.31 – 992.41
KLX04	385.47 – 685.78	385.47 – 983.05
KLX05	-	111.30 – 947.34
KLX07A	-	186.88 – 827.56
KLX08	-	304 – 823
KLX10	120.20 – 716.50	105.20 – 992.50
KLX11A	303 – 683	103 – 883
KLX12A	304 – 567	104 – 584
KLX15A	380 – 880	80 – 975
KLX16A	-	12.50 – 426.00
KLX17A	339 – 694	69 – 689
KLX18A	299 – 599	104 – 604
KLX19A	104 – 781	111 – 791
KLX20A	-	102.20 – 307.50
KLX21B	323 – 743	103 – 843

CDF plots and quantile-quantile plots

Data is presented for the elevation intervals used in the HydroDFN modelling for Laxemar site. The points in the quantile-quantile plots represent percentiles 5, 10, 15……90, 95 and corresponding estimated K-values from the two distributions; Laxemar and Äspö.

Elevation down to -150m

There are very few Laxemar data above -150 so the comparison is not considered relevant. However, the CDF is shown for the data.

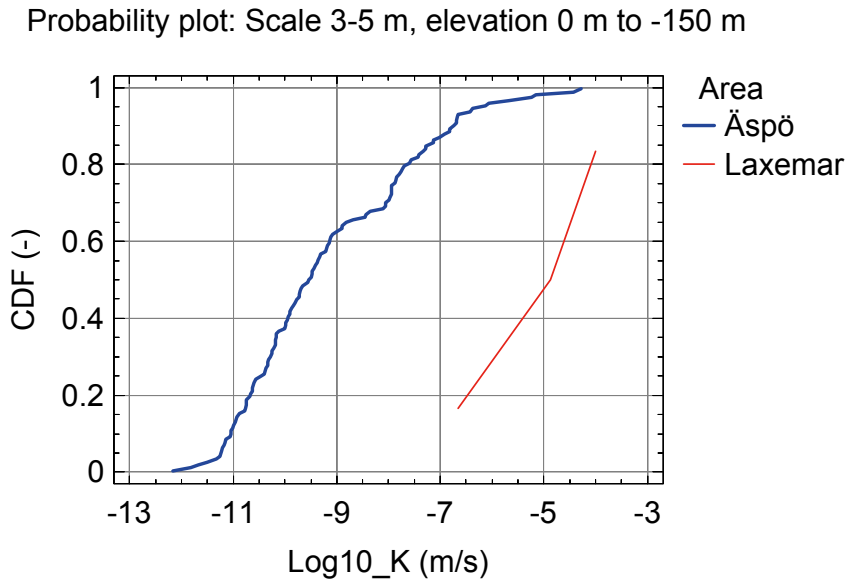

Figure A-9-1. *CDF plot (top), tests scale 3-5m, elevation 0 to -150m.*

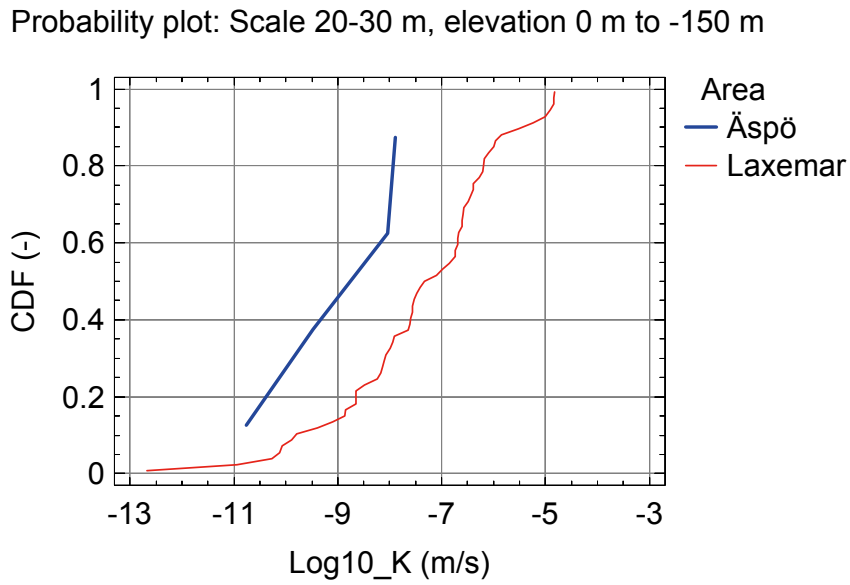

Figure A-9-2. *CDF plot (top), tests scale 30-20m, elevation 0 to -150m.*

Elevation -150 to -400m

Laxemar hydraulic conductivity distribution is slightly lower than Äspö data for both 3-5m data and 30-20m data. The number of 30m tests is limited and the comparison between 30 and 20m scales is considered uncertain.

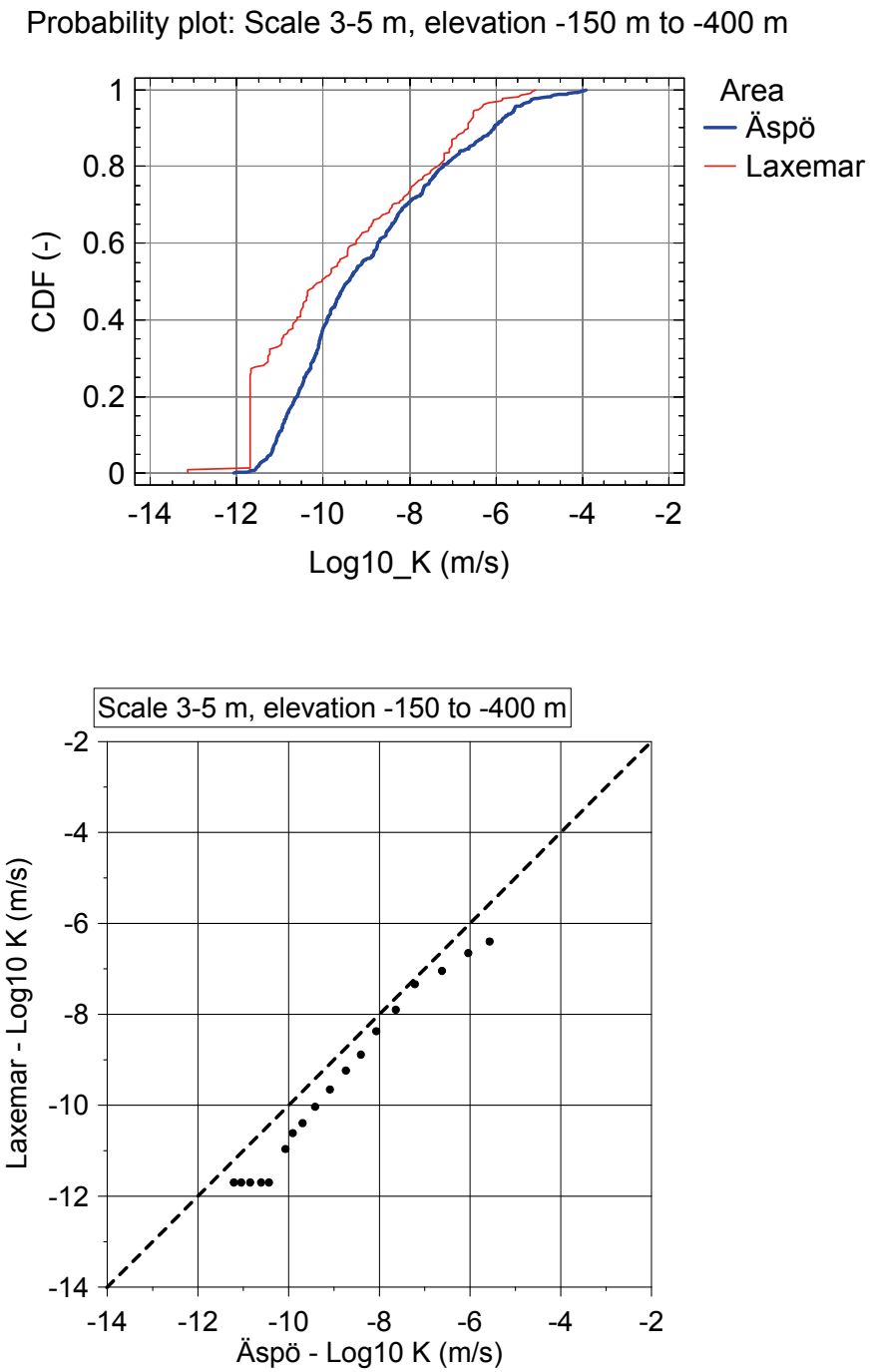

Figure A-9-3. *CDF plot (top) and Quantile-Quantile plot, tests scale 3-5m, elevation -150 to -400m.*

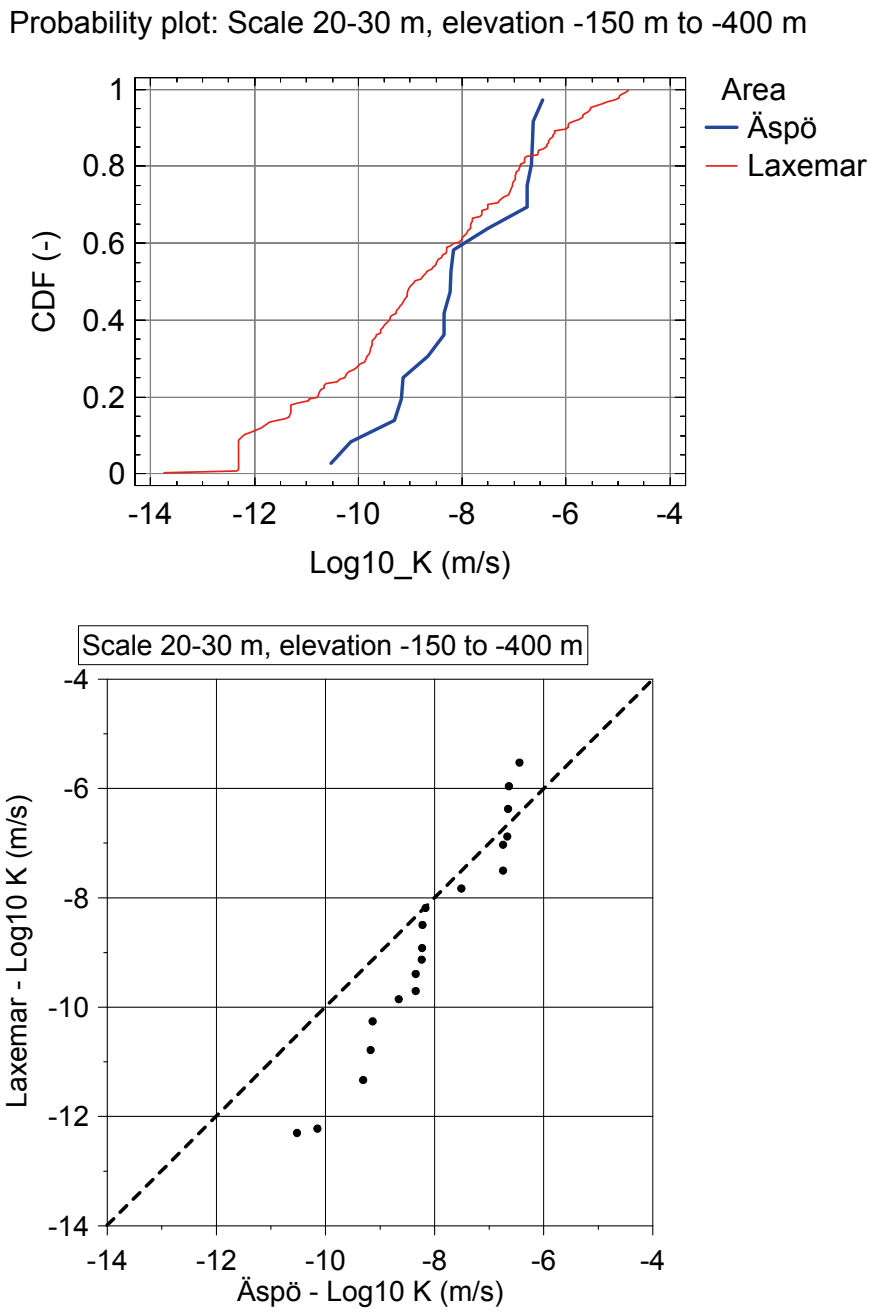

Figure A-9-4. *CDF plot (top) and Quantile-Quantile plot, tests scale 30-20m, elevation -150 to -400m.*

Elevation -400 to -650m

The Laxemar hydraulic conductivity distribution is lower than Äspö data for both 3-5m data and 30-20m data. The number of 30m tests is limited and hence the comparison between 30 and 20m scales is considered uncertain.

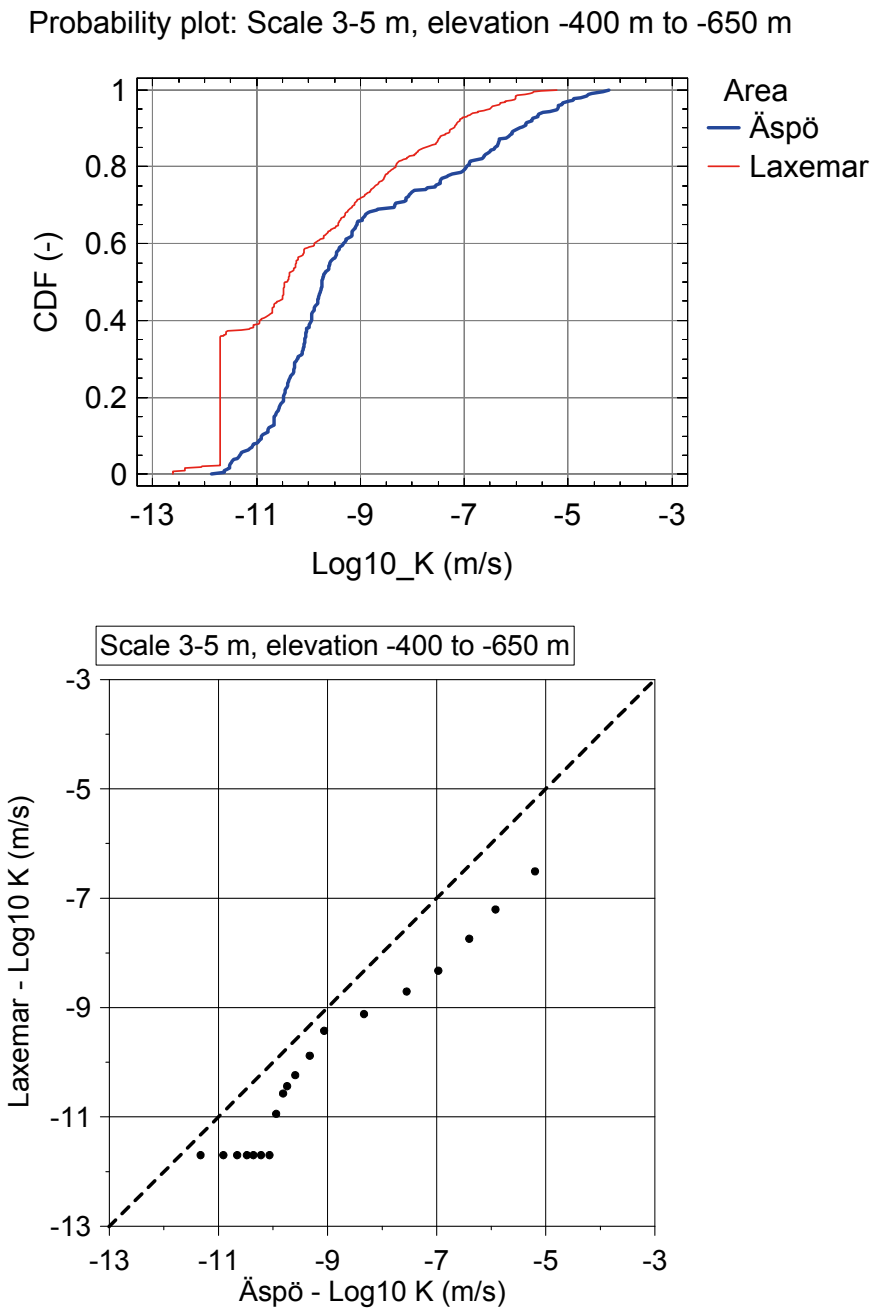

Figure A-9-5. *CDF plot (top) and Quantile-Quantile plot, tests scale 3-5m, elevation -400 to -650m.*

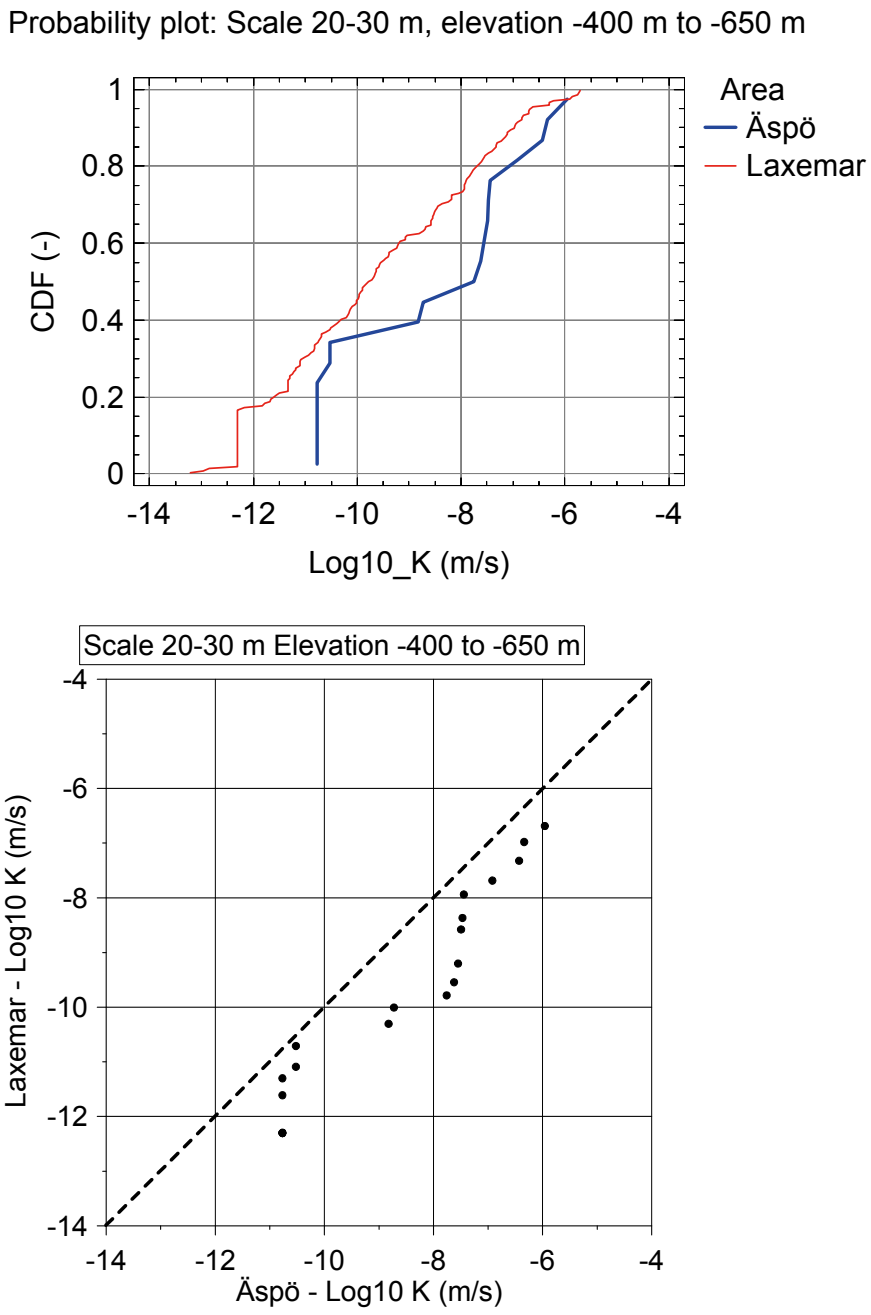

Figure A-9-6. *CDF plot (top) and Quantile-Quantile plot, tests scale 30-20m, elevation -400 to -650m.*

Below -650m

The Laxemar hydraulic conductivity distribution is lower than Äspö data for both 3-5m data and 30m/20m data for most sections but the frequency of high conductivity sections seem to be higher in Laxemar looking at 3m/5m data, but is not seen in the 30m/20m data. The reason is probably that there are rather few 5m data from Laxemar below -650m and the comparison is consequently considered uncertain. The number of 30m tests from the Äspö site is also limited.

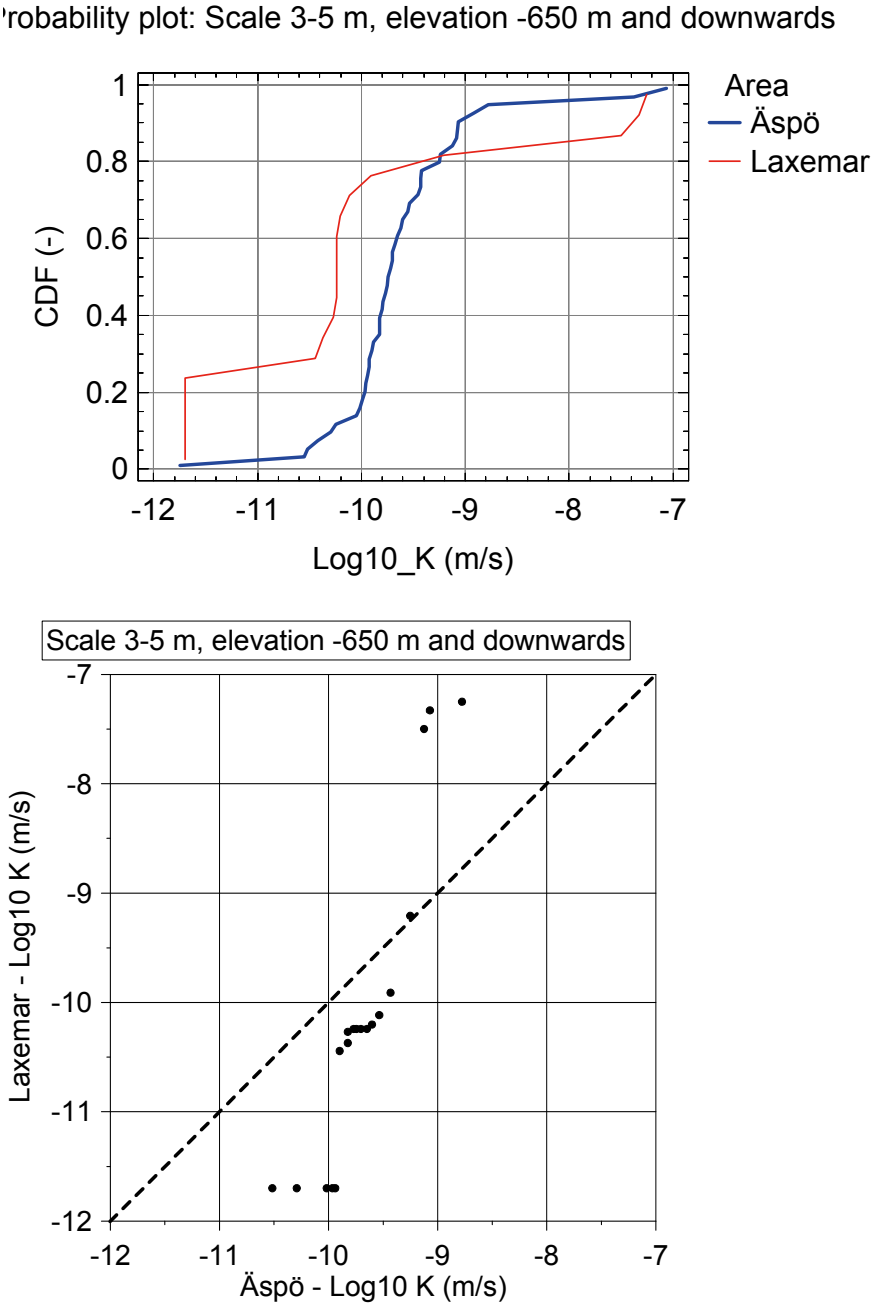

Figure A-9-7. *CDF plot (top) and Quantile-Quantile plot, tests scale 3-5m, elevation below -650m.*

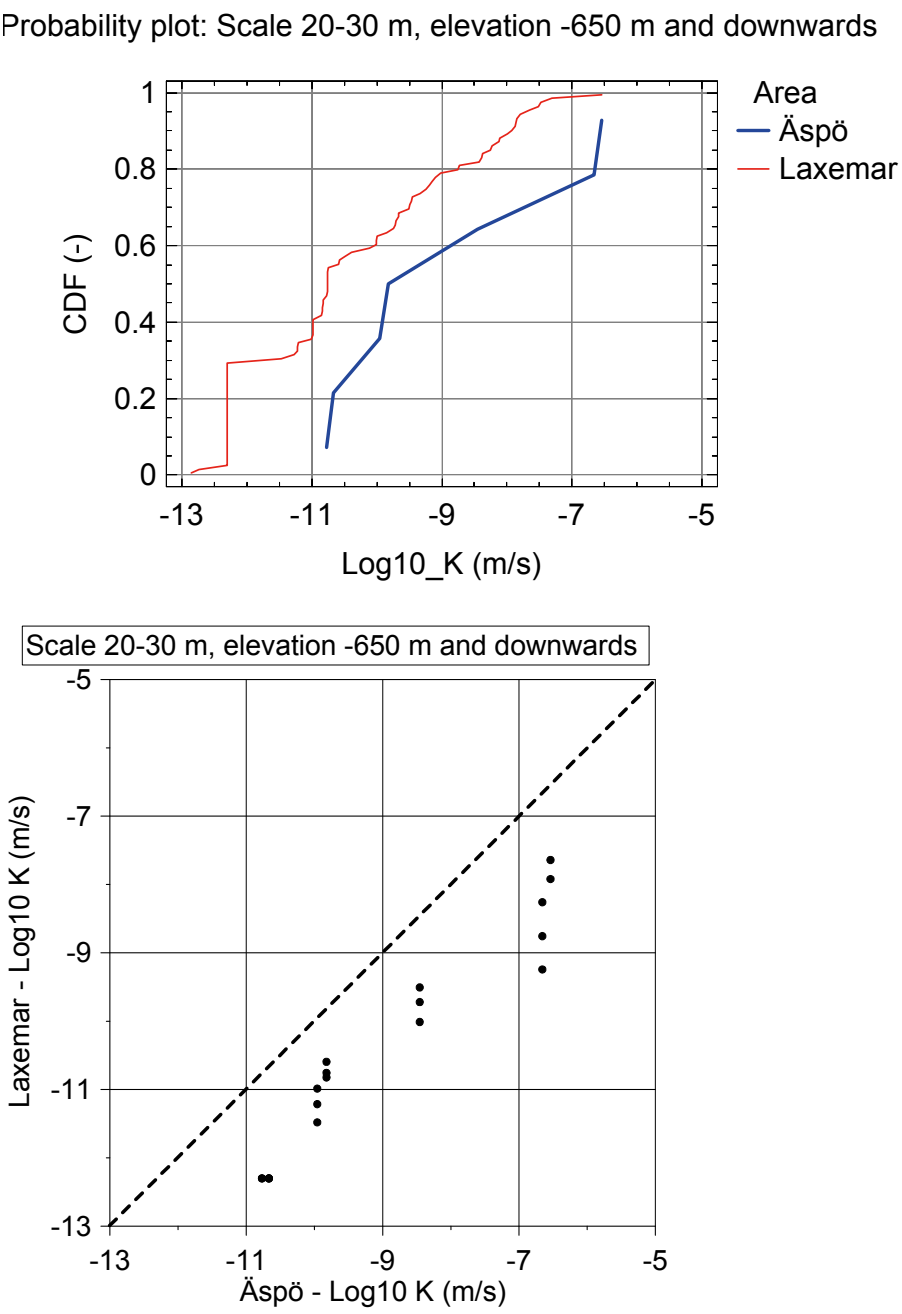

Figure A-9-8. *CDF plot (top) and Quantile-Quantile plot, tests scale 30-20m, elevation below -650m.*

Conclusions

The hydraulic conductivity within elevation interval -150 to -400m is slightly lower in Laxemar compared with Äspö and lower within elevation interval -400 to -650m in Laxemar compared with Äspö.

Below -650m the hydraulic conductivity in Laxemar is possibly lower than in Äspö, but the number data points are limited at both sites.

Above elevation -150m the data are too few to make any conclusion.

A.10 Using data from KLX27A to validate the hydrogeological DFN model

A.10.1 Introduction

KLX27A is a core-drilled borehole in the South-West corner of the Laxemar site. It is approximately 645m long and dips northwards, starting in HRD_C, crossing the ZSMNW042A deformation zone, and ending in HRD_W. About 408m of the borehole is in HRD_W (excluding major deformation zones); only this data is used in the validation study. Data from KLX27A was excluded from the data used to calibrate the hydrogeological DFN model, and therefore it may potentially be used to validate the model.

Before the comparison with the hydrogeological DFN model, we must first consider whether KLX27A is consistent with the hydro-geological properties assigned to HRD_W, i.e. check that KLX27A is appropriate to use for the validation exercise. Assuming this is the case the validation exercise is then to see if the current hydrogeological DFN model for HRD_W can be used to predict KLX27A. This is essentially an exercise in determining if the variation in hydrogeological properties produced by different realisation of the model can be used as an analogue for the spatial variations indicated by measurements made in different boreholes within HRD_W.

The comparisons are made in terms of Terzaghi corrected fracture intensities of all fractures, fractures classified as open or partly-open (OPO) and fractures identified as PFL fractures. A second type of comparison is made in terms of the flow-rates observed or predicted by the model. The hydrogeological DFN model used for the comparison has a semi-correlated transmissivity, and the input fracture intensity is based on OPO fractures.

A.10.2 Results of the comparison

Comparisons of fractures intensities are shown in Figure A10 - 1 and Figure A10 - 2. Figure A10 - 1 indicates that KLX27A has slightly atypical fracture intensities for ALL and OPO features for a borehole within HRD_W. The number of ALL fractures in depth -150 to -400 m is quite low and the number of OPO fractures in depth -400 to -650 m is unusually high. However, it is the PFL-f intensity that exhibits the most obvious difference between KLX27A and the ensemble mean intensity in HRD_W. This is shown most clearly in Figure A10 - 2. Figure A10 - 2 shows that the PFL-f intensity in KLX27A in depth interval -150 to -400 m is zero, but this can be accommodated by the spread of data within HRD_W. The model exhibits slightly less variation, and cannot accommodate this value, although here only 10 realisations were performed. The PFL-f intensity in KLX27A in depth interval -400 to -650 m is very high; which is neither consistent with the rest of the boreholes drilled within HRD_W nor the model.

The reason for the high PFL intensity in KLX27A in depth interval -400 to -650 m is a group of 13 WNW fractures at around -540 m (+/- 20 m). There are several MDZs

defined around this depth, but they only encompass two PFL fractures since they are typically c. 0.9-4.3m thick (borehole length). Hence, the anomalously high PFL-f feature intensity may simply be a result of the geological interpretation of MDZs not being wholly appropriate for identifying the hydraulic characteristics associated with minor deformation zones /cf. Hermanson et al., 2008, Section 10.9/. If PFL-f features within a distance (along the borehole) of less than 3m from a MDZ is assessed to belong to the MDZ, two more MDZ with flowing features will be defined for HRD_W. DZ8: 3 PFL-fs (PFL-f number 37-39) and DZ9 3 PFL-fs (PFL-f number 48-50) with transmissivities $4.6 \cdot 10^{-7}$ m^2/s and $3.6 \cdot 10^{-6}$ m^2/s respectively. This would reduce the difference in intensity between model and KLX27A seen in the plots.

Figure A10 - 3 shows the total inflows to the boreholes calculated from PFL-f statistics. Figure A10 - 4 shows the geometric mean inflows to 100m borehole sections based on PSS data. In both cases, KLX27A shows unusually low inflows in depth zone -150 to -400 m and unusually high inflows in depth zone -400 to -650 m. These results can be accommodated within the variation of the geometric mean inflow to 100m section data. However, such variation is not consistent with the hydrogeological DFN model when considering the total inflows. The inflows to borehole sections observed in KLX27A reflect the relative abundance of PFL anomalies within the two depth zones. These PFL intensities are shown to be atypical so the difficulty in matching the inflows is unsurprising.

A.10.3 Conclusions

The sections of KLX27A within HRD_W are atypical of borehole sections drilled within HRD_W in a number of respects. The intensity of all fractures is consistent with the other boreholes. The intensity of open fractures in the interval -400 to -650 m is abnormally high in KLX27A. The intensity of PFL-f features in the interval -150 to -400m is zero in KLX27A, which is also seen in other boreholes, while the hydrogeological DFN predicts there should be only c. 2% of 50m sections that are dry. Conversely, in the interval -400 to -650 m, the PFL intensity is about 5 times the mean value seen in the other boreholes and predicted by the hydrogeological DFN. This is outside the variability of both the other boreholes drilled through HRD_W and the hydrogeological DFN. This may be related to the difficulties in associating geologically interpreted MDZs, typically just a few decimetres to a few meters thick, with possibly associated swarms of PFL-f features that are typically a few metres wide. The overall conductivities of both depth intervals as measured by PSS in KLX27A are accommodated by the variability within both the other boreholes drilled through HRD_W and the hydrogeological DFN.

The comparison between the model and the borehole data in KLX27A, cf. premises in Section 10.5 and results in Appendix A.10, demonstrates that a number of the observed hydraulic characteristics fall within the predicted variability, but some properties such as the intensity of PFL-f features below –400m in KLX27A is exceptional. Considering the large spatial variability of PFL-f features (cf. Chapter 9, plots of intensities of PFL-f in FSMs) occurrence and the use of only one borehole for the comparison, the conditions for statistically significant comparison cannot be expected. It is therefore not possible to draw stronger conclusions from the comparison, other than that the outcome of KLX27A confirms that HRD_W is characterised by a strong element of heterogeneity and is also probably more difficult to predict than HRD_C.

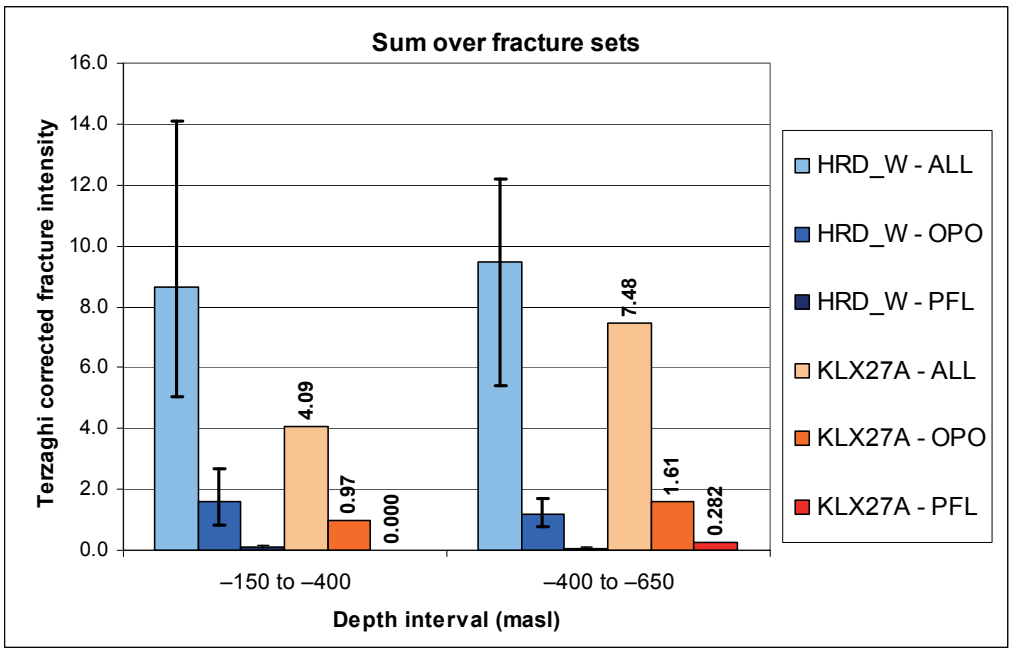

Figure A10 - 1: *A comparison of the total Terzaghi corrected fracture intensities for ALL, OPO and PFL fractures between KLX27A and the ensemble of boreholes within HRD_W. For HRD_W the error bars indicate the maximum and minimum values recorded for any borehole within HRD_W.*

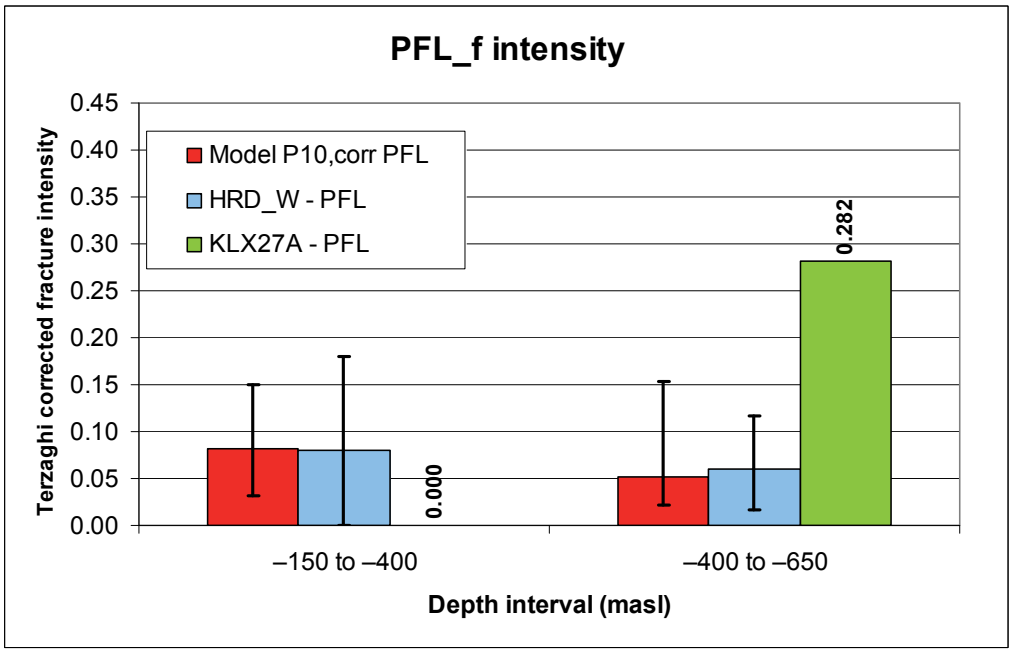

Figure A10 - 2: *A comparison of the total Terzaghi corrected fracture intensities for PFL fractures between the hydrogeological DFN model, KLX27A and the ensemble of boreholes within HRD_W. For HRD_W the error bars indicate the maximum and minimum values recorded for any borehole within HRD_W. For the model the error bars indicate the maximum and minimum values obtained over 10 realisations of the model.*

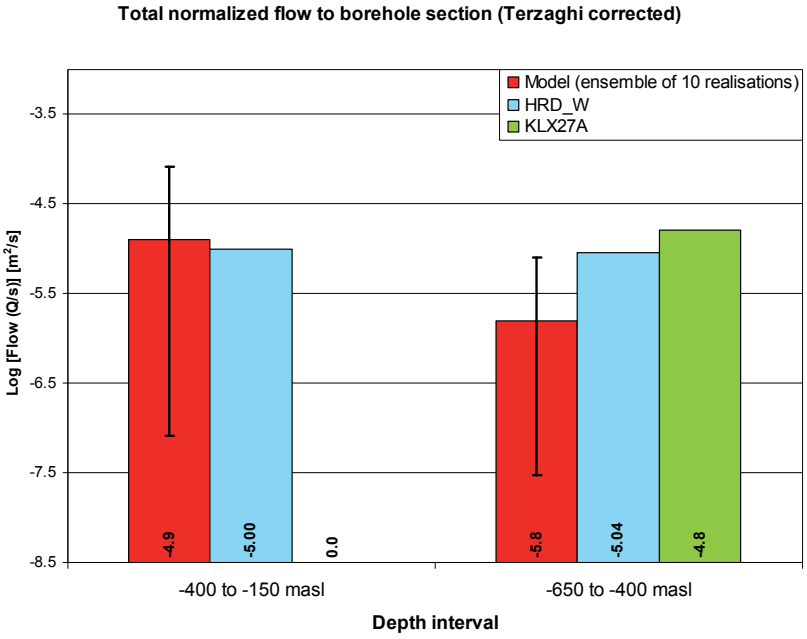

Figure A10 - 3: *Comparison of the sum of individual flows, Q/s, for the PFL-f data from borehole sections within HRD_W and for KLX27A against the hydrogeological DFN model. For the model, the arithmetic mean is taken over 10 realisations. The error bars indicate the maximum and minimum values over the 10 realisations. The flows are normalized to the borehole length indicated by the range on the horizontal axis and Terzaghi weighted.*

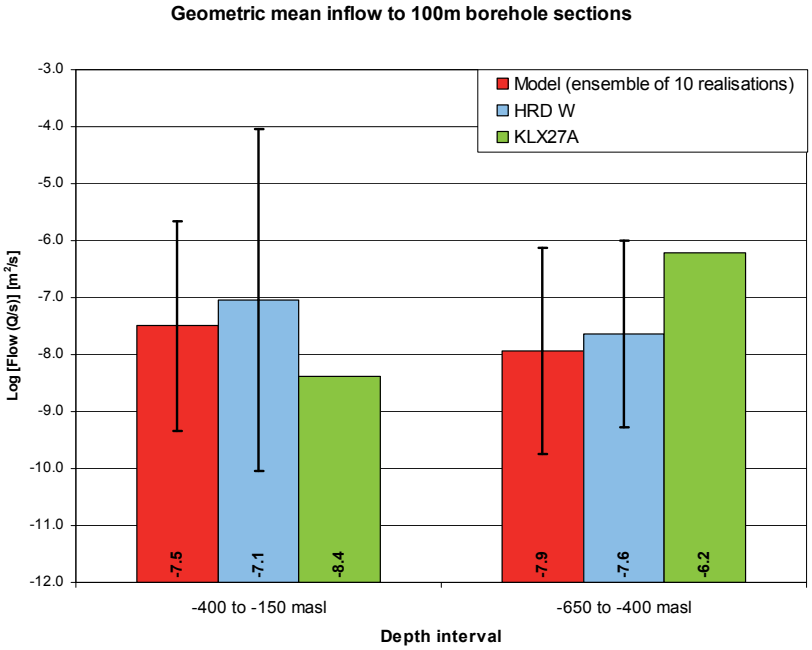

Figure A10 - 4: *Comparison of the geometric mean of total flows, Q/s, to 100m borehole intervals for the PSS data from borehole sections within HRD_W and for KLX27A against the hydrogeological DFN model. For HRD_W the error bars show 1 standard deviation. For the model the mean value of total flow is taken over 10 realisations and the error bars show 1 standard deviation.*